

A11100 984602

NAT'L INST OF STANDARDS & TECH R.I.C.



A11100984602

Space Simulation Con/Space simulation; p.
QC100 .U57 V336;1970 C.1 NBS-PUB-C 1970

A UNITED STATES
DEPARTMENT OF
COMMERCE
PUBLICATION



PUBLICATION

336

Space Simulation

U.S.
DEPARTMENT
OF
COMMERCE

National
Bureau
of
Standards

DATE DUE

JAN 24 2001

UNIVERSITY PRODUCTS, INC. #859-5503

UNITED STATES DEPARTMENT OF COMMERCE
Maurice H. Stans, *Secretary*
NATIONAL BUREAU OF STANDARDS • Lewis M. Branscomb, *Director*

Space Simulation

Proceedings of a Conference held at NBS
Gaithersburg, Maryland
September 14-16, 1970

J. C. Richmond, Editor
NBS, Institute for Basic Standards
National Bureau of Standards
Washington, D.C. 20234

Sponsored by
The American Society for Testing and Materials
Institute of Environmental Sciences
The American Institute of Aeronautics and Astronautics
and The National Bureau of Standards



U.S. / Nat. Bur. Stand. (U.S.), Spec. Publ. 336, 984 pages (October 1970)
CODEN: XNBSA

Issued October 1970

For sale by the Superintendent of Documents,
U.S. Government Printing Office, Washington, D.C. 20402
(Order by SD Catalog No. C13.10:336), Price \$5.25

FEB 12 1971

149903

62100

.057

No. 336

1970

Copy 3.

FOREWORD

The National Bureau of Standards served as a co-sponsor of the Fifth Space Simulation Symposium, made its facilities available for the meeting and, with this special volume, is making the conference proceedings available to participants and to the public.

Space exploration has posed the most challenging technical difficulties man has ever faced and successfully overcome. The National Bureau of Standards is proud to have played a significant role in meeting both scientific and technological needs of the space program, particularly in the field of accurate and meaningful physical measurements. The standards and new methods being developed to meet space requirements find their way into the national measurement system so that everyone ultimately benefits.

NBS is pleased to cooperate with the American Society for Testing and Materials, Institute of Environmental Sciences, and the American Institute of Aeronautics and Astronautics, in advancing the frontiers of knowledge in the important area of space simulation, and to make these proceedings available to other areas of science and technology.

Lewis M. Branscomb, Director
National Bureau of Standards

PREFACE

The series of Space Simulation Conferences of which this is the fifth, is sponsored jointly by the American Society for Testing and Materials, the Institute of Environmental Sciences, and the American Institute of Aeronautics and Astronautics. Each society in turn assumes the responsibility for organizing and conducting the conference and publishing the Proceedings. The reasons for this cooperative action are threefold: first to provide a forum for the presentation of papers before a large audience of listeners who are interested and knowledgeable in this important interdisciplinary area of technology; second to provide a mechanism by which a majority of the papers in this area can be published in a single volume annually, rather than being scattered in a multiplicity of technical and scientific journals; and finally to reduce the number of annual meetings, and hence the cost in both time and money to the sponsoring societies and participants. The Technical Committees of the Sponsoring Societies that participate in organizing and conducting the conferences include ASTM Committee E-21 on Space Simulation, the IES Committees on Solar Simulation and Vacuum, and the AIAA Technical Committee on Ground Testing and Simulation.

Three committees are involved in the organization and conduct of each conference, a Permanent Policy Committee, a General Committee, and a Program Committee. The committees for this conference are listed on the following pages.

The Permanent Policy Committee is made up of two representatives from each of the sponsoring societies. The chairman is elected by the members of the committee. Each sponsoring society designates its own members on the committee, who serve for an indefinite term. This committee formulates general policy for the organization of the conferences, and sees that they are conducted in conformity with the rules and regulations of the sponsoring societies, so far as that can be done in a jointly sponsored conference.

The General Committee is responsible for arranging for the physical facilities required for the meeting, for conducting the meeting and for publishing the Proceedings. The General Chairman and most of the members of this committee, as well as the Chairman of the Program Committee, are from the society that is responsible for organizing and conducting the meeting.

The Program Committee is responsible for arranging the program, and is made up of representatives of all three sponsoring societies.

The Fifth Space Simulation Conference was held at the National Bureau of Standards, Gaithersburg, Maryland, and was co-sponsored by the National Bureau of Standards in addition to the three societies. The American Society for Testing and Materials was responsible for organizing and conducting the Conference, with the assistance of the National Bureau of Standards. The Proceedings were published by the National Bureau of Standards.

Joseph C. Richmond
Editor

COMMITTEES FOR
FIFTH SPACE SIMULATION CONFERENCE

General Committee

General Chairman - Joseph C. Richmond
National Bureau of Standards

Co-Chairman - Rodney W. Johnson
NASA Headquarters

Program Chairman - Eugene N. Borson
The Aerospace Corporation

Arrangements Chairman - John Bidwell
ASTM Headquarters

Local Arrangements - Robert T. Cook
National Bureau of Standards

Program Committee

Frank J. Koubek U.S. Naval Ordnance Lab.	R. E. (Zeke) King McDonnell Douglas Astronautics
William F. Carroll Jet Propulsion Laboratory	Charles H. Duncan NASA Goddard Space Flight Ctr.
D. William Conner NASA Langley Research Ctr.	John H. Boeckel NASA Goddard Space Flight Ctr.

Robert S. Shane
National Materials Advisory Boards
National Research Council -
National Academy of Sciences

Joint Permanent Policy Committee

John C. Simons - ASTM	John D. Campbell - IES
Rodney W. Johnson - ASTM	Thomas Miller - IES
Aleck Bond - AIAA	
R. E. Covey - AIAA	

TABLE OF CONTENTS

Session I, Contamination

- Session Organizer - E. N. Borson
The Aerospace Corporation
- Session Chairman - J. Dozier
NASA Marshall Space Flight Center
- Session Co-Chairman - Kenneth Taylor
NASA Marshall Space Flight Center

Paper No.		Page
1	Introduction, Arthur Reetz, Jr., National Aero- nautics and Space Administration*	*
2	Molecular Contamination in Environmental Testing at Goddard Space Flight Center J. C. Goldsmith and E. R. Nelson, NASA Goddard Space Flight Ctr.	1
3	Contamination Measurement in Space Environment Simulation Chambers, C. M. Wolff and M. L. Ritter, Brown & Root-Northrop, Inc., SESL, P.O. Box 34416, Houston, Tx.	25
4	Contamination Studies in a Space Simulated Environ- ment, D. L. Enlow, General Electric Co.	51
5	External Spacecraft Contamination Modeling and Countermeasures, T. Baurer, M. H. Bortner and I. M. Pikus, General Electric Co. and A. M. Cooper, Grumman Aerospace Corporation	79
6	Particulate Contaminant Measurement by Quartz Crystal Microbalance, R. L. Chuan, Atlantic Research Corporation	105

*Not available for publication.

7	Space Measurements of the Contamination of Surfaces by OGO-6 Outgassing and their Cleaning by Sputtering and Desorption, D. McKeown and W. E. Corbin, Jr., Faraday Laboratories	113
---	---	-----

Session II, Instrumentation

- Session Organizer - J. C. Richmond
National Bureau of Standards
- Session Chairman - J. J. Triolo
NASA Goddard Space Flight Center
- Session Co-Chairman - D. F. Stevison
Air Force Materials Laboratory

Paper No.		Page
8	Simulation of Radiation from RTG Power Sources, P. A. Newman, Jr., NASA Goddard Space Flight Center	129
9	In Situ Vacuum Gage Calibration by the Reference Transfer Method, L. D. Blado and R. H. Lilienkamp, McDonnell Aircraft Company	141
10	Methods of Determining Residual Gas Composition from Residual Gas Analyzer Data, R. H. Lilienkamp, McDonnell Aircraft Company	151
11	Spectral Absolute Reflectance Measurements of CO ₂ Frosts in the 0.5 to 12.0 Micron Region, B. E. Wood, A. M. Smith, B. A. Seiber, ARO, Inc., J. A. Roux, University of Tennessee Space Institute	165
12	NBS Radiometry Standards - Present and Future, H. J. Kostkowski, National Bureau of Standards . .	185
13	Apparatus for Laboratory Simulation of Ionospheric Flow Over On-Board Instruments of an AES, E. N. Evlanov, V. B. Leonas and S. V. Umansky, USSR Space Sciences Laboratory USSR Academy of Sciences	189

14	Thermal Conductivity Measurements of a Candidate Viking Heat-Shield Material After Sterilization, and During Exposure to Vacuum, and to a Simulated Martian Atmosphere, L. R. Greenwood, NASA Langley Research Center, and Roy M. Fleming, N. C. State Univ.	197
----	---	-----

Session III, Special Topics

Session Organizer	- D. W. Conner NASA Langley Research Center
Session Chairman	- D. W. Conner
Session Co-Chairman	- Emile S. J. Wang McDonnell Douglas Corporation

Paper No.		Page
15	Method for Rock Property Determination in Ultrahigh Vacuum, E. R. Podnieks and Peter G. Chamberlain, Twin Cities Mining Research Center, U. S. Bureau of Mines	209
16	Friction Between Solids and Simulated Lunar Soils in Ultrahigh Vacuum and Its Significance for the Design of Lunar Roving Vehicles, Leslie L. Karafiath, Grumman Aerospace Corp. . . .	225
17	Real Time Simulation of Atmospheric Balloon Environment, A. Paillous and M. Roussel, ONERA - CERT - Department d'Etudes en Technologie Spatiale	245
18	Analysis of the Simulation of the Solar Wind, David Zuccaro, Hughes Research Laboratories	261
19	Solar Wind Simulator, H. J. King, Hughes Research Laboratories	279
20	Laboratory Experiment on Solar Wind Interaction with Geomagnetic Field, E. M. Dubinin, G. G. Managadze and I. M. Podgorny, Institute for Space Research, Academy of Sciences, USSR	297

Session IV, Degradation of Materials by Simulated
Space Environments

- Session Organizer - Charles H. Duncan
NASA Goddard Space Flight Center
- Session Chairman - Charles H. Duncan
- Session Co-Chairman - Malcolm A. Lillywhite
Martin Marietta Corp.
Denver, Colorado

Paper No.		Page
21	Effect of Photodegradation on Organic Coatings, P. J. Hearst, U.S. Naval Civil Engineering Lab . .	299
22	Relation Between Dose Rate Effects and Labora- tory Simulation of Space Radiation Damage, A. Roizès and R. Schuttler, ONERA - CERT - Dept. d'Etudes et Recherches en Technologie Spatiale	313
23	Some Problems Concerning the Simulation of Plastic Films Degradation by Ionizing Radiations, A. Paillous, ONERA - CERT - Dept. d'Etudes et Recherches en Technologie Spatiale, Ph. Fayet, Centre National d'Etudes Spaciales . . .	323
24	Ultraviolet and Charged Particle Degradation of Aluminum and Silver Coated FEP Teflon Second Surface Mirrors, F. G. Cunningham, NASA Goddard Space Flight Center, B. L. Bean and S. G. Park, Electromechanical Research, Inc.	345
25	The Interaction of Low Energy Electrons with Polymeric Perfluorinated Ethylene-Propylene (FEP), J. B. Schutt, NASA Goddard Space Flight Center	359
26	The Degradation of Alzak by Short Wavelength Ultraviolet Radiation, M. J. Donohoe, R. McIntosh, Jr., and J. H. Henninger, NASA Goddard Space Flight Center	383

27	The Photo-Response at an Alkaline Paint Interface with Aluminum, W. A. Wappaus, NASA Goddard Space Flight Center	393
----	--	-----

Session V, Predictive Testing I

Session Organizer - Robert S. Shane
National Materials Advisory Board -
National Academy of Sciences

Session Chairman - James D. McClelland
The Aerospace Corp.

Session Co-Chairman - Robert S. Shane

Paper No.		Page
28	Plans and Status of NMAB ad hoc Committee on Testing for Prediction of Material Performance in Structures and Components Robert S. Shane, National Materials Advisory Board - National Academy of Sciences	403
29	Monitoring Service Testing by Nondestructive Testing, Robert W. McClung, Oak Ridge National Laboratory	405
30	Signature Analysis - Non-Intrusive Techniques for Incipient Failure Identification Application to Bearings and Gears, B. Weichbrodt and K. A. Smith, Research & Development Center, General Electric Co.	407
31	Measurement Methods for Microcircuits, W. Murray Bullis, National Bureau of Standards . .	449
32	Life Testing Using Continuous Acceleration, Ernest Rabinowicz, Massachusetts Institute of Technology, and B. Shiralkar, General Electric Nuclear Energy Div., San Jose, California	457

Session VI, Predictive Testing II

Session Organizer - Robert S. Shane
National Materials Advisory Board -
National Academy of Sciences

Session Chairman - James D. McClelland
The Aerospace Corporation

Session Co-Chairman - Robert S. Shane

Paper No.		Page
33	Establishment of an Optimum Duration for Spacecraft Component Thermal Vacuum Tests, William L. Harvey, Martin Marietta Corp., Denver, Colorado	473
34	Equipment to Study High Velocity Dislocations in Materials, V. R. Parameswaran and J. Weertman, Northwestern University	487
35	Some Effects of Equalization on Acceleration Response and Fatigue Life Expectancy, Robert M. Mains, Washington University, St. Louis, Mo.	509
36	Charged Particle Track Implications for Accelerated Testing, Terence M. Flanagan and Victor A. J. van Lint, Gulf General Atomics, Inc. .	525
37	A Simulation to Validate Future Space Missions, T. P. Foley, A. W. Metz and A. W. Yonda, Sudbury Engineering Facility, Raytheon Co.	535
38	General Purpose Centralized Automatic Testing for Improvement of Shipboard System Performance Frank Zupan, U.S. Navy Electronics Lab. Center . .	549

Session VII, Simulation and Effects - Manned Environments

Session Organizer - R. E. King
McDonnell Douglas Astronautics Co.
McDonnell Douglas Corp.
Huntington Beach, Calif.

Session Chairman - R. E. King

Session Co-Chairman - A. H. Bay
McDonnell Aircraft Company
McDonnell Douglas Corp.
St. Louis, Missouri

Paper No.		Page
39	Explosive Oxidations Initiated by Simulated Meteoroid Penetration into Spacecraft Atmospheres, William H. Carden, ARO, Inc.	569
40	The Dynamic Environment Simulator, A Multi-environmental Man-Rated Centrifuge, D. B. Rogers and M. McCally, M.D., USAF Aerospace Medical Research Lab, and K. L. Cappel, Franklin Institute	587
41	Use of the Ben Franklin Submersible as a Space Station Simulator, M. J. Ferguson, Grumman Aerospace Corp., and C. B. May, Advanced Systems Office, NASA	599
42	Development of an Open Circuit Cryogenic Life Support System for Use in Neutral Buoyancy Space Simulation, Clifton M. McClure III, and Charles W. Williams, Hayes International Corp. . .	623
43	Advanced Diving Techniques Applicable to Extended Mission Neutral Buoyancy Space Simulation, J. B. MacInnis, M.D., Ocean Systems, Inc., and C. M. McClure III, Aquaspace	651

Session VIII, Facilities

Session Organizer - R. E. King
McDonnell Douglas Astronautics Co.
McDonnell Douglas Corp.
Huntington Beach, Calif.

Session Chairman - H. Allgauer
Hughes Aircraft Co.

Session Co-Chairman - J. Ratliff
Martin Marietta Corp.
Denver, Colorado

Paper No.		Page
44	A Method to Obtain an Ultraclean Environment, Maurice S. Cridlin and Joseph W. O'Connor, NASA Goddard Space Flight Center	661
45	A Programmable Dynamic Thermal Vacuum System For Solar Array Component Testing, John W. Fairbanks, NASA Goddard Space Flight Center, Marshall B. Eck, H. C. Slack & Associates	669
46	The Cryopumping System for the Space Simulation Chamber, Hiroshi Nakagawa and Ryuji Tsunoda, Japan Oxygen Co., Ltd., (Nippon Sanso K.K.)	683
47	Simulation of Surface - Atmosphere Interaction Processes for Mars, K. M. Foreman, Grumman Aerospace Corporation	699
48	Operation of a Large Thermal Vacuum Chamber at Martian Pressure Levels, T. Buna and J. R. Ratliff, Martin Marietta Corporation	725
49	A Cryopump for Steady-State Testing of Rocket Engines Under Altitude Conditions, M. J. Triplett and W. E. Riggs, ARO, Inc.	749

Session IX, Ablative Reentry Materials

Session Organizer - Frank J. Koubek
U.S. Naval Ordnance Laboratory
Silver Spring, Md.

Session Chairman - Frank J. Koubek

Session Co-Chairman - Robert L. Bierman
General Electric Co.

Paper No.		Page
50	Ablative Heat Shields for Planetary Entries - A Technology Review, G. D. Walberg and E. M. Sullivan, NASA Langley Research Center . . .	751
51	Ablation Phenomena in Supersonic Laminar and Turbulent Flows, E. M. Winkler, M. T. Madden, R. L. Humphrey and J. A. Koenig, U.S. Naval Ordnance Laboratory	813
52	Prediction of Mechanical Erosion of Charring Ablators, Lauri H. Hillberg, The Boeing Company . .	837
53	Heating in Cracks on Ablative Heat Shields, E. M. Winkler, R. L. Humphrey, M. T. Madden and J. A. Koenig, U.S. Naval Ordnance Laboratory .	853
54	Apparent Operating Limits of Arc Heaters with Respect to Total Enthalpy and Stagnation Pressure, R. Richter, Electro-Optical Systems	879
55	Operating Characteristics of the Air Force Flight Dynamics Laboratory Reentry Nose Tip (RENT) Facility, John C. Beachler, Air Force Flight Dynamics Laboratory	893

Session X, Testing in Simulated Space Environments

- Session Organizer - E. N. Borson
The Aerospace Corporation
- Session Chairman - E. N. Borson
- Session Co-Chairman - Fritz Benning
Spectrolab Div. of Textron Corp.
Sylmar, California

Paper No.		Page
56	Investigation of the Characteristics of Fluids Vented into a Vacuum, R. Steddum, Dupree Maples and F. M. Donovan, Louisiana State Univ. . . .	905
57	Micrometeroroid Impact Simulation System, R. A. Golub and J. R. Davidson, NASA Langley Research Center	915
58	A Space Radiation Environment Simulator for the Evaluation of Solar Cells, P. A. Newman, J. J. Hirschfield and H. E. Wannemacher, NASA Goddard Space Flight Center, and M. Eck, H. G. Slack & Associates	935
59	Properties of Optical Materials in Space, Fred W. Paul, NASA Goddard Space Flight Center . .	949

Workshop and Panel Discussion

- Moderator - Charles H. Duncan
NASA Goddard Space Flight Center

Author Index	961
------------------------	-----

SPACE SIMULATION

ABSTRACT: This volume contains all of the papers presented at the Fifth Space Simulation Conference held at the National Bureau of Standards September 14-16, 1970, that were available for publication. The general scope of the conference was the effect of the space environment on materials, components, structures and man. The range of topics is too wide to permit a simple classification, but contamination, ablation, degradation of materials by the space environment and predictive testing account for approximately half of the papers presented. Other topics range from purely laboratory problems such as radiometry standards, calibration of vacuum gages, cryopumping and operation of space simulation facilities to gravity simulation, with neutral buoyancy for zero gravity and a man-rated centrifuge for high gravity, use of a drifting submarine to study the psychological aspects of long-duration missions in a space station, and simulation of (1) atmospheric balloon environments, (2) radiation from nuclear power sources, (3) solar wind, (4) micro-meteoroid bombardment, (5) soil friction on the moon and (6) the Martian atmosphere.

KEY WORDS: ablation, particulate radiation, re-entry, space simulation, thermal radiation, vacuum, weightlessness

INTRODUCTION

The purpose of this conference, as stated in the Call for Papers, was to provide a forum for the presentation of new information on the technology of space simulation. This technology encompasses all aspects of simulating the environment of space and determining its effect on materials, components and spacecraft. Specific aspects of the space environment that are of interest include vacuum, solar and planetary radiation, particle radiation, meteoroids, weightlessness, magnetic fields, temperature extremes, planetary atmospheres, and re-entry. All of these topics are covered in the papers presented on the following pages. In addition, two other topics are included in this conference that have not been adequately covered in previous conferences; Contamination and Predictive Testing.

The 59 papers accepted for presentation were separated into 10 sessions and are grouped by sessions in these Proceedings. All papers were subjected to careful technical

review prior to final acceptance and comments of the reviewers were sent to the authors prior to preparation of the final draft in form suitable for photo-offset reproduction, but the final drafts have not been reviewed. For this reason each author must assume full responsibility for the content of his paper.

MOLECULAR CONTAMINATION IN ENVIRONMENTAL TESTING AT GODDARD SPACE FLIGHT CENTER

J. C. Goldsmith¹ and E. R. Nelson²

REFERENCE: Goldsmith, J. C. and Nelson, E. R., "Molecular Contamination in Environmental Testing at Goddard Space Flight Center," ASTM/IES/AIAA Space Simulation Conference, 14-16 September 1970.

ABSTRACT: A discussion of the various techniques used to detect and analyze materials outgassing from a spacecraft during the environmental test is presented. In addition, a number of compounds that have been detected and their parent outgassing sources are listed. The two major methods for reducing the threat of contamination (i.e., proper choice of spacecraft materials and proper operation of the test facility) are also discussed.

KEY WORDS: contamination, outgassing, polymeric materials, residual gas analysis, vacuum, test facility, chemical analysis, organic residues

This paper describes the techniques presently being used at Goddard Space Flight Center (GSFC) to detect and minimize molecular contamination of spacecraft or spacecraft subsystems and experiments during the environmental test.

The methods described are an outgrowth of work done to determine the test readiness of oil-diffusion-pumped test chambers for spacecraft having UV reflective optics.

¹ Senior Engineer—Sperry Rand Corp. Space Support Division, Goddard Space Flight Center, Greenbelt, Md.

² Polymer Chemist—National Aeronautics and Space Administration, Materials Research and Development Branch, Goddard Space Flight Center, Greenbelt, Md.

DEFINITION

Molecular contamination can be defined simply as a deposition of molecules upon a surface that would affect some physical property of that surface (i.e., reflectance, transmittance, absorptance, or surface resistivity). These contaminants are chiefly composed of water vapor and organic molecules of medium to high molecular weight (50 to 800 atomic mass units) and low vapor pressure. The low-molecular-weight organic compounds and residual gases are too volatile to adhere to any surface in a vacuum unless the surface temperature is in the order of -60°C or lower. Hence, these compounds do not ordinarily present a problem since spacecraft surface temperatures are generally above this level.

However, recently there have been some spacecraft experiments flown that utilize detectors that are cooled to 0°C or lower. In this temperature range, some gases, volatile, low-molecular-weight compounds, and water vapor will condense, thus obscuring the detector's view.

EFFECTS OF CONTAMINANTS

Molecular contamination can affect spacecraft performance in four major ways.

1. Loss of Optical Reflectance

A film of silicone oil approximately seven molecular layers ($0.4\text{ }\mu\text{g}/\text{cm}^2$) thick will cause a loss of approximately 8 percent in the reflectance measured at 1216\AA (1).³ Thus, the output of an optical experiment operating in the ultraviolet region in which the beam is reflected from several consecutive reflective surfaces can be seriously reduced.

2. Loss of Optical Transmittance

If the mass accretion upon an optically transmissive surface is sufficient, it can reduce optical and near infrared transmittance (0.4 to $18\text{ }\mu\text{m}$ region). This may result in the degradation of the output of solar-cell arrays, the loss of sensitivity of optical experiments or sensors, or the loss of vision, as in the case of the Gemini 11 where severe clouding of the spacecraft window occurred (2).

³The numbers in parentheses refer to the list of references appended to this paper.

3. Degradation of Thermal-Control Coatings

The molecular contaminants that condense on thermal-control surfaces can alter the solar absorptance-to-emittance ratio. At this time, however, the relationships between the type and amount of molecular contaminant and the extent of degradation for polymeric materials are not clearly understood.

4. Malfunction or Failure of Electronic Systems

Outgassed contaminants condensing on a circuit board assembly, on open contacts, or in waveguide subassemblies can alter effective circuit impedances to the point that malfunction or failure of an experiment or subsystem may result. In addition, molecules outgassing in a confined enclosure may maintain pressure in the corona region. Consequently, when sensitive experiments, transmitters, and high-voltage power supplies are commanded on, they can fail in orbit due to high-voltage corona breakdown if these circuits are turned on before the volatilized organics and residual gases have had a chance to diffuse into space.

SOURCES OF MOLECULAR CONTAMINATION

In any specific test there are two basic sources of contaminants: the test facility and the spacecraft.

1. Possible Test Facility Contamination Sources

- Compounds adsorbed on chamber wall from previous tests.
- Cracked oils from the diffusion or mechanical pumping system.
- Paint volatiles or cutting oils used in spacecraft mounting fixtures.
- Outgassed compounds from cabling, potting compounds, adhesives, flexible heaters, etc., used to support the test.
- Water or other compounds adsorbed from the ambient air environment.
- Cleaning solvents.

2. Possible Spacecraft Contamination Sources

- Outgassed compounds from cabling, potting compounds, sealants, circuit boards, adhesives, etc., in the electronic subsystems.

- Paint volatiles from improperly cured thermal coatings.
- Water or other compounds adsorbed from the ambient air environment.
- Cleaning solvents.

METHODS OF MEASUREMENT

The following complementary analytical techniques are available for the quantitative and qualitative analysis of contaminants outgassed during environmental test:

- Residual gas analysis (RGA).
- Infrared spectroscopy (IR).
- Gas chromatography (GC).
- Gas chromatography-mass spectrometry (GC-MS).
- Quartz-crystal microbalance gravimetry (QCMB).
- Ultraviolet reflectance.

The use of all of these techniques may be necessary for the environmental test of a large spacecraft.

1. Residual Gas Analysis

A residual gas analyzer (Fig. 1). is used to quantitatively and qualitatively identify the molecules present in the spacecraft test environment. This analyzer is a mass spectrometer of relatively low resolution and mass range that ionizes molecules present in the environment and separates them by atomic mass. The data presented by this instrument is in the form of a plot of the molecular weight of the molecules detected versus their relative abundance or partial pressure. A typical RGA spectrum is shown in Fig. 2.

A cursory inspection of the spectrum is all that is required to determine the presence and amounts of residual gases such as air, nitrogen, and water because of their relatively simple molecular formulas.

However, to determine the presence of the higher molecular weight contaminants, those molecules that originate from the spacecraft materials, one must have prior knowledge of the characteristic mass spectra or "fingerprint" spectra of all compounds likely to be found in the test environment. The problem is further complicated by the fact that the mass spectrum presentation represents a summation of the mass spectra of each individual compound in the test environment at that particular instant. The resolution of this mass spectrum

into its individual compounds requires a sophisticated computer program. Such a program has recently been developed for this purpose (3).

Fingerprint mass spectra of known compounds are fitted to the unknown mass spectrum. The computer then determines the combination of fingerprint spectra that gives the best fit to the unknown spectrum and prints out the results. The use of this program thus far has been limited only by the sensitivity of our analyzers and the limited amount of available fingerprint spectra of commercial compounds.

2. Infrared Spectroscopy

A cold plate (Fig. 3) located in the test volume is operated at 77 K for the duration of the test, during which it collects a fraction of all condensable contaminants in the test environment. At the conclusion of the test, the cold plate is washed with isopropanol solvent.

The mixture of solvent and contaminant is then transferred to the analytical chemical laboratory where the solvent is evaporated and the residue (i.e., contaminants) is analyzed, chiefly by infrared spectroscopy. In this technique of analysis, the infrared spectra of the contaminant is taken in the range from 2.5 to 25 μm . Figure 4 shows a typical infrared spectrum obtained from the OAO thermal-vacuum test. The absorption pattern in this band is representative of the chemical bonds between atoms of these molecules and is thus a fingerprint of the molecules.

However, as with RGA, the resulting infrared absorption spectrum represents a summation of all outgassed compounds that have condensed on the cold plate. Thus, the mixture spectrum is capable of giving general information on the functional groups present: aliphatic, aromatic, hydrocarbon, silicone, ester, amide, etc. For a more complete identification of the individual compounds in the mixture, the mixture must either be separated for individual identification or a computer solution, similar to the one used for mass spectral identifications, must be applied to the mixture spectrum.

3. Gas Chromatography

The gas chromatograph is an analytical instrument that separates a mixture of compounds into pure compounds. The sample obtained from the residue from the cold plate is vaporized and bled into a stream of helium that then passes through a column of absorbing material. The column packing absorbs the less volatile compounds more readily than it absorbs the more volatile compounds. Thus, the material will emerge from the column as a series of time-spaced peaks

in the helium stream with each peak representing a unique compound. These peaks are usually detected by either flame ionization or thermal conductivity detectors at the column exit or both.

The results are displayed as a series of roughly gaussian peaks plotted versus time on a strip-chart recorder. The data are taken as time of peak height (column traverse time) versus area under the curve, which is proportional to the amount of the compound. Though this technique does give a very good fingerprint, it, unfortunately, does not uniquely determine a given compound and may and usually does vary somewhat from run to run. Hence, the gas chromatograph cannot be used for identification without running reference compounds or trapping the eluted compound for subsequent infrared or mass spectrometric analysis.

4. Gas Chromatography-Mass Spectrometry

In addition to the infrared spectrometer and gas chromatograph, the analytical laboratory utilizes a combination gas chromatograph-mass spectrometer for analysis of the contaminant residue. This combination overcomes the difficulties of the use of the gas chromatograph alone. The combination enables one to separate the mixture into its pure molecular constituents and to obtain a mass spectrum for each constituent from 10 to 1000 atomic mass units.

As a consequence of this capability, thirty or more mass spectra may be generated from an average cold-plate sample containing a mixture of up to thirty compounds. For expediting the resolution of these spectra, automatic data reduction is a necessity. Figure 5 shows the gas chromatograph-mass spectrometer data acquisition unit in use at GSFC.

5. Quartz-Crystal Microbalance Gravimetry

The QCMB measures gravimetrically the mass accretion of contaminant over the surface of an oscillating crystal. The change in the frequency of oscillation of the crystal is directly related to the mass accreted upon it. With proper precalibration and temperature compensation, this instrument⁴ is capable of measuring as little as $01 \mu\text{g}/\text{cm}^2$.

⁴Hanyok, J., "Crystal Microbalance Vacuum Contamination Monitor," NASA X-Document X-324-69-404, National Aeronautics and Space Administration, Goddard Space Flight Center, Greenbelt, Md. Sept. 1969.

If the QCMB is placed at or near a critical surface, such as an optical or thermal-control surface, and the QCMB crystal is configured so as to have the same "view" relationship and temperature as the surface in question, then the mass accretion on the QCMB will approximate the mass accretion on that surface. Figure 6 shows the QCMB system.

6. Ultraviolet Reflectance

As mentioned previously, small amounts of condensed contaminants will cause a significant loss of reflectance in the ultraviolet region. Hence, with proper precalibration, a mirror sample (Fig. 7) can be used to measure directly contaminant levels on a critical surface. As in the case of the QCMB, the mirror must be configured so that it has the same "view" and temperature relationship of the surface in question. Pretest and post-test reflectivity measurements are made at 1216\AA with a vacuum monochromator. Most organic chemicals absorb ultraviolet radiation at this wavelength but in varying amounts, depending on their chemical structure. Consequently, some prior knowledge of the type of contaminant is required for accurate measurement.

A change of reflectivity at 1216\AA is indicative of contaminant. The exact level of contaminant deposited is, however, somewhat in doubt.

THE RELATIONSHIP BETWEEN CONTAMINANT MEASUREMENTS AND ACTUAL SPACECRAFT CONTAMINATION

Although each of the measurement methods previously described will give some quantitative picture of the contaminant levels within the test volume, the actual quantities of material outgassed or desorbed from the spacecraft can only be inferred. This is due to the fact that, in the average test, the majority of the outgassed compounds are pumped out and only a small percentage will return to the spacecraft and condense as a surface contaminant. (Figure 8 shows schematically the relationship among these measurement methods.)

As shown by R. Chaun,⁵ the fraction of outgassed material actually condensed on the spacecraft is a function of the chamber wall capture coefficient, the spacecraft surface capture coefficient, and the ratio of internal chamber area to total spacecraft surface area.

⁵Notes from "Vacuum Technology," a course at the University of California at Los Angeles (Extension), Feb. 14-18, 1966.

For a precise measurement of the amount of contaminant condensed on a spacecraft surface (aside from physically wiping the surface which has been done in a few cases, i.e., OAO 2), it would be necessary to precalibrate the particular spacecraft-chamber system. Modeling techniques can be used to determine the relationship of the material condensed on the spacecraft to the quantitative amounts measured by the techniques described previously.

In solar-vacuum testing, the chamber shrouds are at 77 K or lower; therefore, a molecule that desorbs from the outgassing source will be quickly cryopumped on the cold shroud. Consequently, the analysis of the cold finger sample may show only a small percentage of the outgassed compound, and the RGA or reflective mirror sample may indicate no trace of contaminant molecules, depending on their respective "views" and capture coefficients relative to the outgassing source. In fact it has been found at GSFC that the cold finger will often pick up traces of compounds not detected by the RGA. This is due, possibly, to the integrating effect of the cold plate as well as the limited mass range of the RGA.

In the thermal vacuum test, however, the outgassing molecule will collide several times with the warm wall or spacecraft before coming to rest, thus establishing a relatively uniform molecular flux throughout the test environment. Consequently, all contaminant sensors will "view" the outgassing compound(s). However these compound(s) may or may not condense, depending on their relative surface capture coefficients.

CLASSES OF COMPOUNDS OBSERVED

A qualitative identification of the major compounds observed in the test environment is shown in Table 2. These compounds, collected chiefly from the cold plate, are grouped into three classes according to their percentage of the total condensed sample.

In addition to the compounds listed in Table 2, traces of many more compounds associated with plastics have been observed. Compounds such as 2,6-di-*t*-butyl-*p*-cresol, biphenyl, and butyl ethyl ether of ethylene glycol, have been observed in quantity but infrequently, and so far, it has not been possible to determine their source.

Backstreaming silicones from the chamber pumping system are conspicuous by their absence. A positive gas chromatographic technique has been developed that is able to detect 1 μ g or less of tetramethyltetraphenyl-trisiloxane compound (DC 704). With this technique, backstreaming silicones have been observed in only six tests, with over six hundred samples thus far analyzed.

In general, outgassing levels of polymeric compounds, will be seriously affected by the following factors: their "cure" cycle (i.e., the correct time-temperature relationship following their preparation), the amounts of plasticizer and antioxidants added to the parent compound to modify its basic physical properties to fit the application, and the operating temperature of the compound.

METHODS OF REDUCING CONTAMINATION

1. Choice of Materials

The ideal method for reducing contaminant levels is to reduce the outgassing rate at the source. This can best be accomplished by the proper choice of materials in the design phase.

The criterion that is used at GSFC for nonmetallic spacecraft materials is based on the work of Muraca and Whittick (4) at the Stanford Research Institute for the Jet Propulsion Laboratory. These criteria limit the use of materials to those with less than 1-percent total weight loss (TWL) and 0.1-percent vacuum condensible material (VCM). The VCM value tends to be far more important than the TWL value because the difference between VCM and TWL is accounted for by the light gases and water. Normally, if a material has a high TWL and a low VCM, it still can be used on a spacecraft if the material is free to outgas into space.

At present, the Material R&D Branch at GSFC is continuing the certification of additional nonmetallic materials for inhouse application. This is being done with a highly automated material outgassing facility developed at GSFC and based on the original design of Muraca and Whittick.⁶

Where a specific requirement can only be met by a material with a high outgassing rate, it is recommended that the material or subassembly be preprocessed (i.e., exposed to a high-temperature and vacuum environment before integration into the spacecraft). Thus, the material whose initial gas load is composed largely of gases, water, and lower-molecular weight fractions is "cleaned out." At the present state of the art, it is not possible to prepare a spacecraft free of all sources of molecular contaminants, but the contaminant hazard can be significantly reduced by the use of the correct nonmetallic materials.

⁶Fisher, A. and Marmelstein, B., "Micro-Volatile Condensable Material System for Polymer Outgassing Studies," NASA X-Document X-735-69-47, National Aeronautics and Space Administration, Goddard Space Flight Center, Greenbelt, Md., Oct. 1969.

2. Operation of The Vacuum Chamber

Several practical steps may be taken to minimize the contamination threat to a spacecraft during environmental test:

- Pretest bake-out. This will remove contaminants condensed on the chamber wall from previous tests. This can best be accomplished by a high-temperature long-term bake-out (100 C for 48 h is a recommended minimum level).
- Maximum pump-speed to test-volume ratio. Cryopanel and high-capacity pumping system will maximize chamber capture coefficients, thus effecting the rapid removal of the contaminant from the test volume.
- Minimum spacecraft-chamber temperature differential. The temperature differential between the chamber wall and the spacecraft during cold-to-hot temperature transition should be held to a minimum, preferably 10 C or less. This will extend transition time; however, it will decrease chamber-to-spacecraft contamination.
- Backfill chamber. In order to hold contaminants that have been trapped on the cryopanel, it is desirable to backfill the test volume to approximately 0.1 torr with dry GN₂ when concluding a test in which large cryopanel are used. This will reduce the molecular mean free path in the test volume to less than 2.5 mm while still maintaining the environment below the region of convective heat transfer. Thus, the probability that a trapped contaminant released by the cryopanel during the warm-up phase will reach the spacecraft is considerably reduced.
- Protective cryopanel. A relatively small cryopanel interposed between a sensitive experiment and the chamber cryopanel will occlude the experiment's "view" of the larger chamber cryopanel, thus reducing the contaminant hazard due to outgassing from the chamber wall. In addition, larger cryopanel surfaces that are kept cold during chamber warmup will act as a molecular sink for molecules released from the chamber wall.
- Sweep purging. Backstreaming of a diffusion pumping system is at a maximum when the diffusion pump is operating in a transition mode (i.e., pumpdown or repressurization). A small leak or purge of nitrogen bled into the chamber during this transition period will stabilize molecular flow outward (i.e., from the test volume to the atmosphere) (5), thus minimizing the risk of backstreaming.

CASE HISTORY—AN EXPLORER SPACECRAFT

A contaminant case history is given in the succeeding paragraphs, for one of the Explorer series spacecraft.

1. Spacecraft Description

The spacecraft had a mass of approximately 140 kg and carried six experiments. The nonmetallic materials used in the fabrication of the spacecraft were

- Polyurethane foam potting compounds.
- Epoxy and silicone potting compounds.
- Silicone and ester lubricants.
- Silicone adhesives.
- Epoxy adhesives.

2. Test Procedure

The spacecraft was subjected to ten-day thermal-vacuum test followed by a six-day solar-vacuum test. A three-day thermal-vacuum retest was performed finally to assure that malfunctions that had occurred during the first test had been corrected.

3. Test Instrumentation

- Residual gas analyzers
Consolidated Electrodynamics Corp. 21-613
General Electric Monopole
- Cold plate sample analysis
Perkin Elmer 621 Spectrophotometer
Hewlett Packard 5750 Gas Chromatograph
Perkin Elmer 270 Gas Chromatograph - Mass Spectrometer

4. Analysis of Outgassed Compounds

A complex mixture of almost 2.5 g of outgassing products was found on the condenser plate following the first thermal-vacuum test. This sample was analyzed by infrared, gas chromatographic, and mass spectrometric techniques. Figure 9 shows an RGA spectrum taken during the second retest phase, Fig. 10 shows the IR spectrum of the cold plate sample mixture, and Fig. 11 shows the gas chromatogram of the cold plate sample mixture.

The mixture of at least fifty components, twenty of them major in quantity, was found to have the following composition: a complex mix-

ture of aliphatic or alicyclic hydrocarbons or both, 50 to 60 percent; a series of phenylmethyl siloxanes, 5 to 10 percent; six members of a homologous series of dimethyl silicones, 15 to 20 percent; and pure bis(2-ethyl hexyl) phthalate, 20 percent. The hydrocarbons could come from several sources such as lubricating oil (i.e., a petroleum-based lubricant) or perhaps from the outgassing of some O-rings, which quite often use plasticizer with white oils of this type. The dimethyl-silicones and phenylmethyl silicones are most likely due to outgassing of RTV and other silicone resins. The bis (2-ethyl hexyl) phthalate is one of the most common plasticizers used in the United States and thus could come from outgassing of various compounds. It should be noted that the use of such compounds is discouraged at GSFC.

This mixture did not contain any of the oil from either the chamber diffusion pumps (Dow Corning 704) or from the mechanical pumps (Sunvis 931). These results were obtained by running Dow Corning 704 and Sunvis 931 through a gas chromatograph under the same conditions as those of the outgassing mixture. The fingerprint obtained did not match any peaks in the outgassing mixture. During these thermal vacuum tests, a sun gun (quartz-iodine photoflood lamp) was used to excite the spacecraft solar-aspect sensor. This sun gun was suspected of being a source of the hydrocarbon contaminants seen in the analysis because of its high operating temperature. Consequently, a separate outgassing test was performed on the sun gun. Gas chromatographic and infrared spectra of the condensed cold plate residue failed to show any similarity with spectra from the thermal-vacuum test. Hence, the sun gun was ruled out as a possible contributor of hydrocarbons.

For the subsequent solar-vacuum test and thermal-vacuum re-test, the condensor plate samples taken after these tests showed almost the same infrared patterns and gas-chromatographic patterns as had been obtained from the thermal-vacuum test, only in much less quantity. Results of the RGA scans were inconclusive during both the initial thermal-vacuum and initial solar-vacuum tests because of a loss of resolution during the thermal-vacuum test and a loss of sensitivity in the solar-vacuum test. In the solar-vacuum test, no peak above atomic mass 57 could be detected.

SUMMARY AND CONCLUSIONS

With the measurement techniques described, it has been possible to partially identify and roughly approximate the contaminants outgassed in a specific test. However, a great deal more analytical and experimental work must be done before exact quantitative and qualita-

tive contaminant data can be determined. Two general observations may be made:

- (1) It has been found that, in most of the tests, the test item is the prime source of contaminants.
- (2) Contamination traceable to the chamber diffusion-pump system occurred in a very small percentage of the tests (0.1 percent).

Future spacecraft missions involving extended orbital life such as the Grand Tour deep-space probe and the next generation of communication satellites and orbiting observatories will require a functioning lifetime of three years and longer. This imposes a severe constraint on the spacecraft designer in his choice of materials.

Longer orbital lifetimes also will mean an extended environmental-testing program; consequently, it will be necessary that the environmental test engineer be assured that his test facility is clean and that his methods of operation minimize the contaminant hazard.

REFERENCES

1. Shapiro, H., "Monomolecular Contamination of Optical Surfaces," NASA Technical Note D-4612, National Aeronautics and Space Administration, Washington, D.C., June 1968.
2. Blome, J. C., and Upton, B. E., in "Effects of the Space Environment on Materials," Society of Aerospace Material and Process Engineers National Symposium and Exhibit, 11th Symposium, Science of Advanced Materials and Process Engineering Proceedings, Vol. 11, p. 217, 19YQAE.
3. Babst, R. W., "Computerized Analysis of RGA Scans," Final Report SP 923-0054, Sperry Rand Corporation, April 1970.
4. Muraca, R. F., and Whittick, J. S., "Polymers for Spacecraft Application Final Report," SRI Project ASD-5046, JPL Contract No. 950745, Menlo Park, California, Sept. 15, 1967.
5. "Technology and Space Simulation," NASA Publication SP-105, National Aeronautics and Space Administration, Washington, D.C., 1966.

Table 1—Comparison of measurement techniques.

Measurement	Technique				
	RGA	Cold Plate or Wipe Sample (Residue)			Mirror Reflectance
		IR	GC	GC-MS	
Minimum Detectable Quantity	Molecular Quantities	50 μg^a	1 μg	1 to 5 μg	0.01 $\mu\text{g}/\text{cm}^2$
Range of Measurement Sensitivity	Lower Organics Only	All Organics Which Will Volatize and Condense on Cold Plate ^b			All Organics Which Will Volatize and Condense ^b
How Measured	Instantaneous	Integrated Over Test			
Type of Measurement	In Test	Post-test		In test	Post-test
What Is Measured	Outgassing Compounds in Environment	Condensed Contaminants			

^aThis is an upper figure; analysis can be performed, if necessary, on as little as a 10 μg sample.

^bGenerally pure compounds with molecular weights over 1000 will not volatize in a vacuum environment and hence will not outgas.

Table 2—Major compounds observed in the test environment.

Class I (10 to 60%)			Class II (0-10%)		Class III (Trace)	
Compound	Source		Compound	Source	Compound	Source
Phthalate Esters	Common Plasticizer Used in Processing Polymers Used as a Test Aerosol in Clean Room Filters		Butyl, Decyl Esters of Adipates and Sebecates	Specific Purpose Plasticizers	Ketones	Solvents, Plasticizers in Vinyl Polymers
Dimethyl Siloxanes	Low-Molecular-Weight Species Desorbed From High-Molecular-Weight Silicones Silicone Fluids		Phenylmethyl Siloxanes	Low-Molecular-Weight Species Desorbed From High-Molecular-Weight Special Purpose Silicones	Chlorinated Biphenyl and Other Chlorinated Hydrocarbons	Solvents Used for Cleaning, Plasticizers
Saturated and Unsaturated Hydrocarbons	Paraffinic Lubricants and Residual Cutting Oils Solvents			Resistant to Radiation and Temperature Extremes (i.e., Adhesives, Diffusion Pump Oils, O-Ring Seals)	Glycidyl Ethers and Other Low-Molecular-Weight Epoxy Compounds	Epoxy Resins
			Halogenated Siloxanes	Special Silicones for Various Specific Uses	Amines and Amides	Curing Agents From Epoxies Nylons
					Polyesters	Polyurethanes (i.e., Potting Compounds)
					Fluorinated Hydrocarbons	Solvents Used for Cleaning

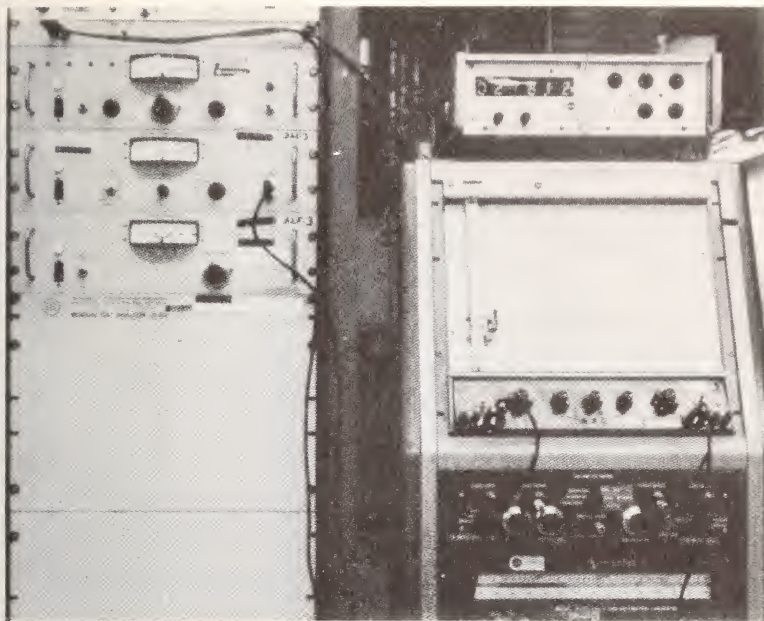


Fig. 1—Residual gas analyzer (RGA).

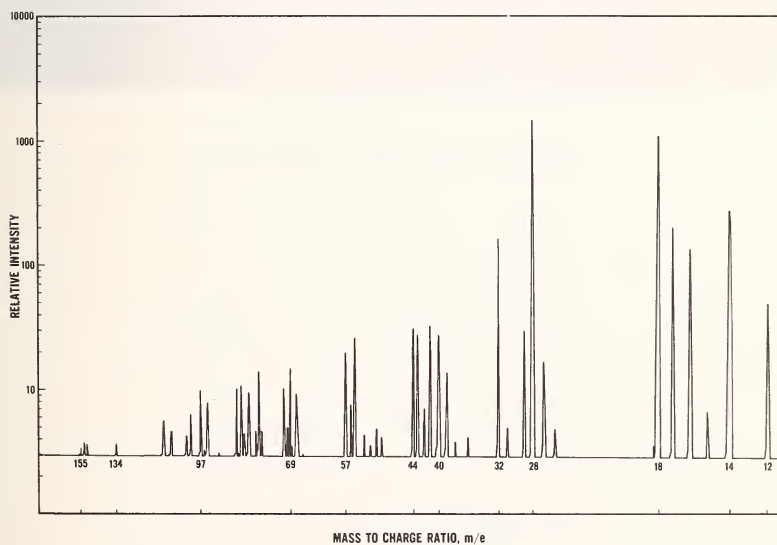


Fig. 2—RGA mass spectrum.



Fig. 3—Chamber cold plate.

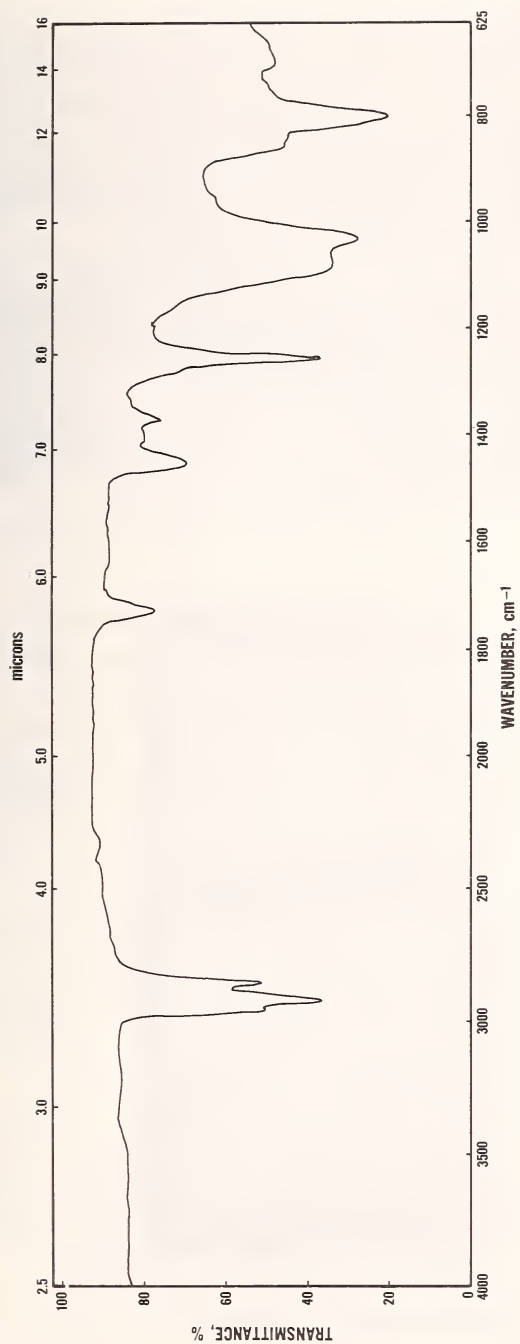


Fig. 4—Surface contamination from OAO 2, infrared spectrum.

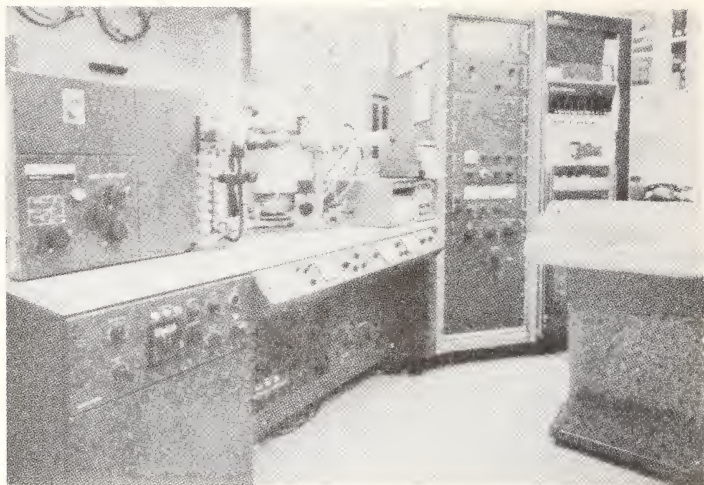


Fig. 5—Gas chromatograph-mass spectrometer (GC-MS) and data reduction system.

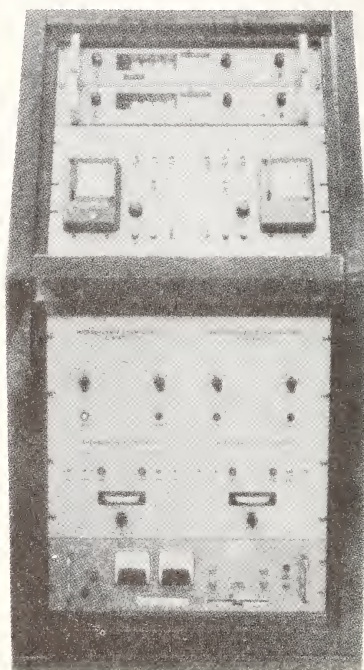


Fig. 6—Quartz crystal microbalance (QCM) system.

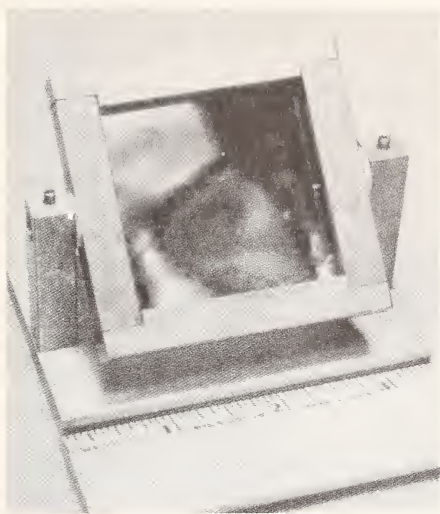


Fig. 7—Mirror sample.

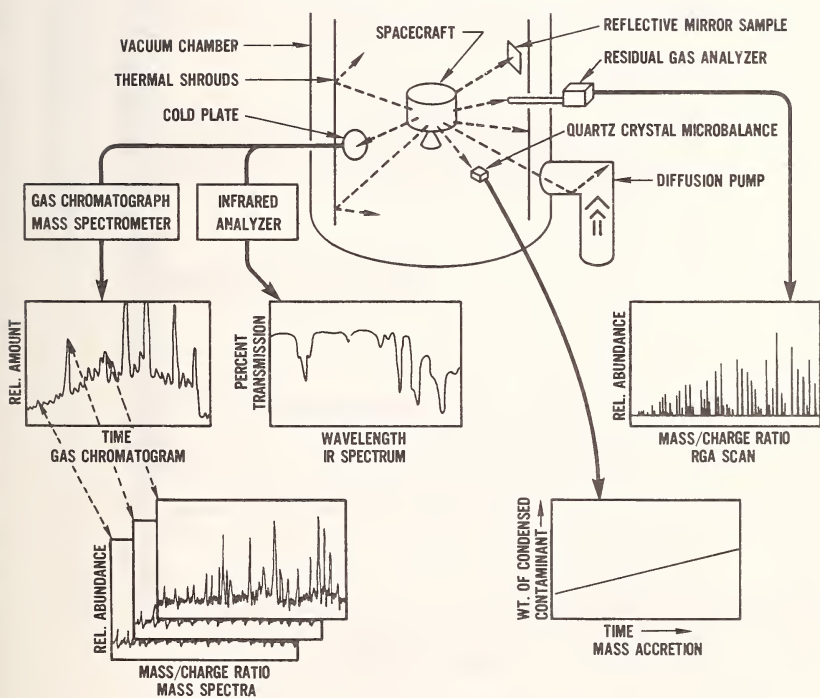


Fig. 8—Relationship of measurement methods.

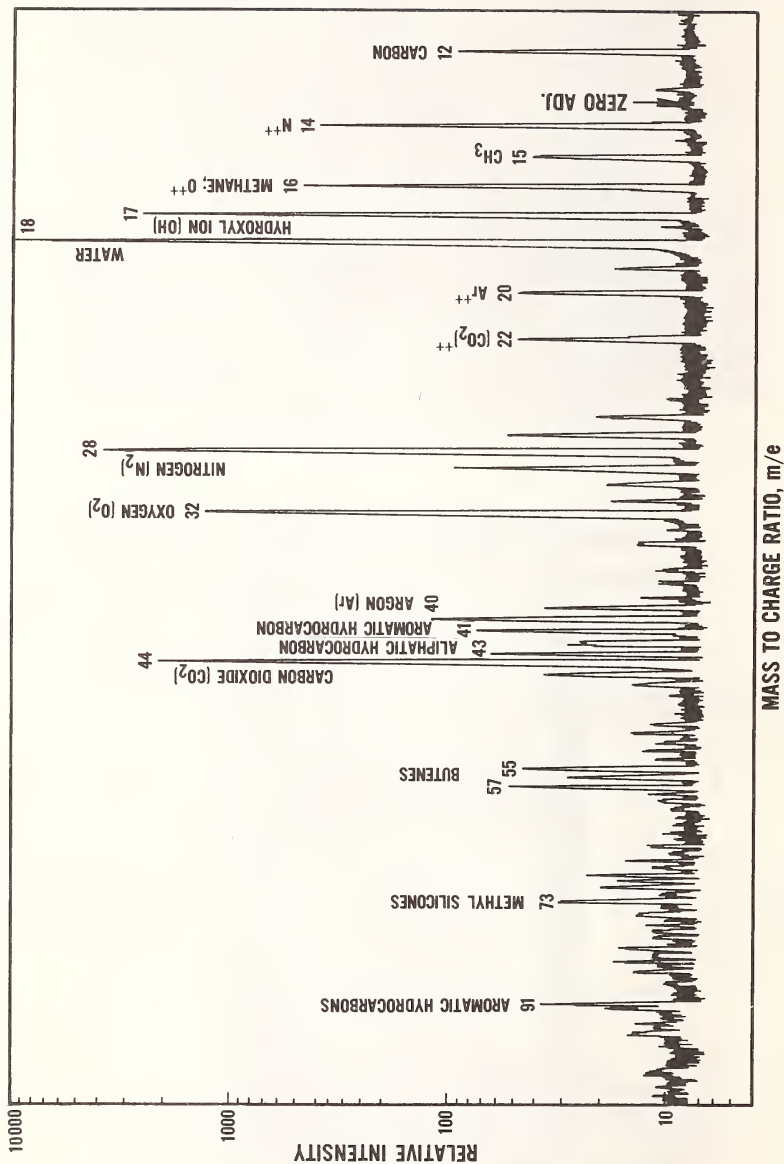


Fig. 9—RGA spectrum, Explorer spacecraft.

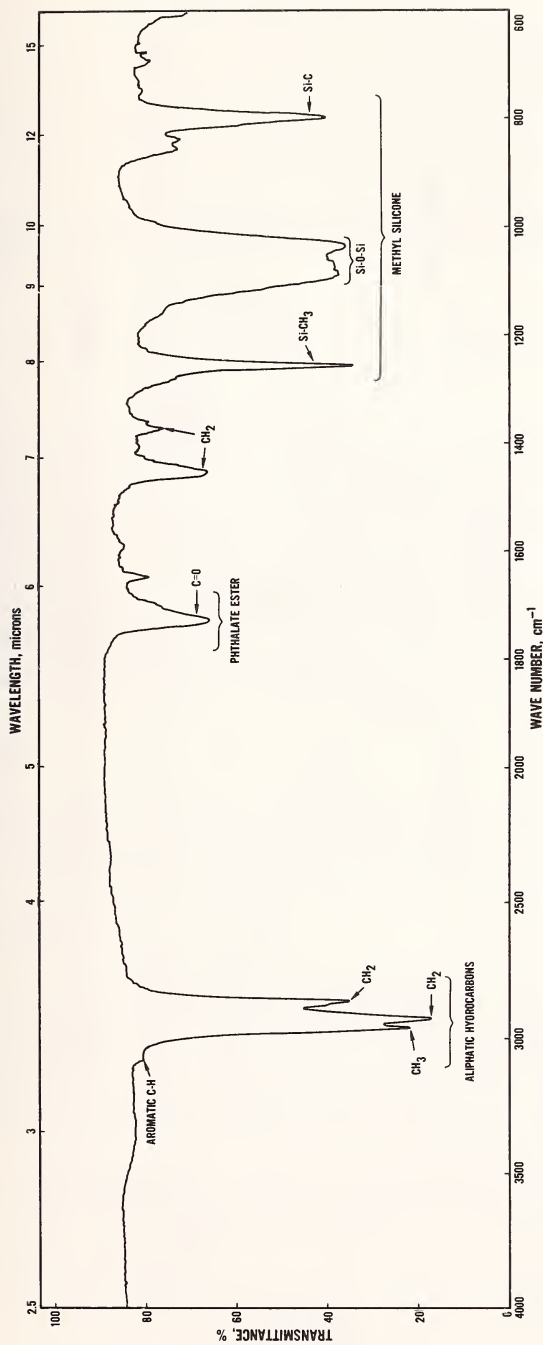


Fig. 10—Explorer cold plate sample, infrared spectrum.

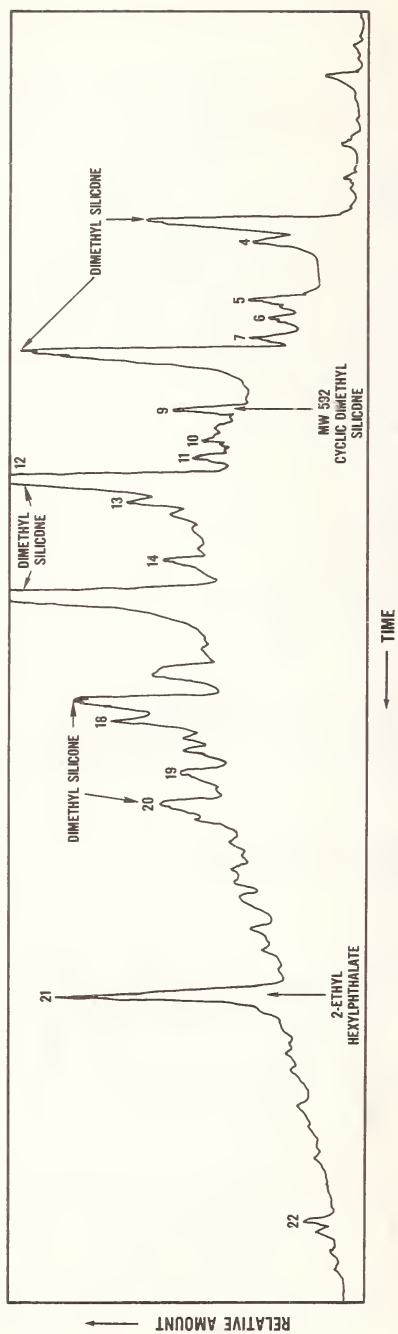


Fig. 11—Gas chromatogram of cold plate sample, Explorer spacecraft.

CONTAMINATION MEASUREMENT IN SPACE ENVIRONMENT SIMULATION CHAMBERS

Calvin M. Wolff and Melvin L. Ritter*

ABSTRACT

Contamination measurement is classified according to the requirements; i.e., the identity, sources, and effects of contamination by active and passive sampling. The chemical nature of the most common contaminants found in space environment simulation is discussed. Qualitative and quantitative techniques for contaminants analyses are described and evaluated. These techniques include mass spectrometry, quartz crystal oscillator mass monitors, infrared spectrometry, and gas-liquid chromatography. Also, the uses of optical surfaces and thermal control coatings as contaminants effects monitors are described.

KEY WORDS

Space environment simulation chambers, mass spectrometry, infrared spectrometry, gas-liquid chromatography, contamination collection units, quartz crystal oscillator mass monitors, reflectometry, radiometry, thermal control coatings.

INTRODUCTION

The increasing sophistication and flight duration of space vehicles and related hardware is imposing more stringent cleanliness requirements of space environment testing facilities. The need of controlling contamination and measuring its effects is thus becoming of great importance. Measurement of contamination may yield the following information:

1. The source and nature of contamination
2. The identity and quantity of contamination
3. The effects of contamination on test articles.

*Brown & Root-Northrop, Inc., SESL, P.O. Box 34416, Houston, Tx.

THE SOURCE AND NATURE OF CONTAMINATION

Contamination in space environment chambers may be considered as twofold: particulate and molecular. Particulate contamination, such as lint and dust, is, in most instances, of less concern than molecular contamination, because the particulates can be easily and completely removed. Particulate removal may be made by forced air or other gas, by bombardment with soft α -particles (anti-static technique), or by brushing or wiping if contact is permissible. Also, particulate contamination affects only extremely small fractions of test article surface area; however, particulate contamination may be dangerous when it is not found and removed, for it degrades delicate electronic contacts, miniature mechanical systems, and blocks slits of spectrometers. Particulate contamination in space environment testing can occur at all times when the test article is at ambient conditions, during the initial pumpdown phase, and during the final (high pressure) repressurization phase. Particulate contamination is very improbable under high vacuum conditions, being that there is no external source of particles and no matrix for the mobility of particles, save for the gravitational field. The effects of particulate contamination on thermal-vacuum test data are negligible because the fraction of affected area involved in heat transfer is minute. Likewise, the effects of particles on facility heat transfer surfaces, such as cryopanelling and solar simulator and radiometer optics, are negligible. Several references are available describing detection and removal of particulate contamination (references 1 thru 8).

Molecular contamination is a serious problem in thermal-vacuum testing. Molecular contamination may be defined as that which migrates and deposits in the test volume as individual molecules, rather than the relatively massive molecular conglomerates and polymers that we refer to as particulates. Molecular contamination may emanate by evaporation, sublimation, chemical decomposition, or desorption. These processes are described in references 9 thru 21.

Because molecules migrate individually and randomly, they also will deposit in a random manner, that is, tend to cover an exposed surface uniformly. Since molecular masses are so low, surfaces are quickly coated with monomolecular layers of contaminants, even though the partial pressures of contaminants may be quite small. For example, one milligram of molecular contaminant will deposit, roughly, one monolayer over a surface area of ten square feet. The time of a contaminant remaining on a sur-

face after it has deposited is governed by desorption rate parameters. The contamination level on a surface is dependent on the rate of deposition and desorption or evaporation. The contamination level will be high for any combination of a high and continuous deposition rate, a very high tenacity of the contaminants on the surface, and a very low surface temperature. The situation becomes worse when the ultraviolet radiation of solar simulation breaks intramolecular bonds of contaminants on test article surfaces and which in turn may bond chemically with the test article surface and each other. Since the chemical adsorption (chemisorption) energies are much higher than other types, the desorption rate of contaminants on the test article would be greatly reduced, causing essentially permanent contamination.

One important facet of desorption is that when a surface is exposed to a gas on the order of one atmosphere pressure, as in "ambient" conditions, desorbed molecules are reflected back onto the contaminated surface by the gas molecules to an extent that elevating the surface's temperature is not sufficient for decontamination; that is, elevated temperatures and vacuum are required. Further, the adsorption energies of many molecules on a foreign surface are generally much greater than the heat of vaporization or sublimation of that molecule, such that the final monolayer of contaminant is very difficult to remove. This monolayer must be removed either by vacuum "bake-out" or by chemical decomposition (such as oxidation) of the contaminant into gaseous and particulate material.

The "permanent" gases (oxygen, nitrogen, hydrogen, helium, methane, carbon monoxide, argon, and neon) will always be present in vacuum chambers; however, they are of little concern as contaminants because even if they should adsorb, their effects on thermal and optical properties of test surfaces are negligible and quantities greater than a monolayer will desorb above cryogenic temperatures. Carbon dioxide and moisture (water vapor) will always be present, since they will be adsorbed in large quantities on the chamber and test surfaces during ambient conditions and migrate extensively during pumpdown and repressurization phases. If sufficient time is allowed during pumpdown to degas and pump away most of the carbon dioxide and water, and if leakage is controlled, these contaminants should be of no consequence. However, if these gases are allowed to migrate from warm surfaces or enter the chamber when the test article is cold, then contamination may build up (sheets of ice and frozen CO_2) to a point as to seriously affect heat transfer at thermal control surfaces. These materials have no absorption in the near ultraviolet and visible regions of the spectrum, so that portion of solar absorptance would not be affected; however, they have con-

siderable infrared absorption and can affect the emittance of the coatings. These contaminants could be removed by solar simulation without permanently affecting thermal or optical properties. In fact, the saving grace of carbon dioxide and moisture contamination is that they are reversible; i.e., they are removed, except for a few monolayers, when the test article is returned to ambient temperatures.

The vapor pressures of ionic and of most metallic compounds (14) are sufficiently low as not to be of general concern as contaminants. There are exceptions, of course, such as mercury and cadmium, but these materials should be restricted from use in space environment facilities. The standard inorganic materials recommended for vacuum usage, such as stainless steel, copper, aluminum, gold, quartz, pyrex glass and porcelain, are so stable and of such low vapor pressure as not to be of concern as contaminants in space environment simulation testing.

Organic materials, however, are the most troublesome contaminants. Organic materials must often be used in space environment chambers where non-brittle adhesives and flexible electrical and thermal insulators are required, and are also used as vacuum sealants, lubricants, insulative structural materials, hydraulic oils, diffusion and mechanical pump oils, and thermal control coatings. To minimize contamination, polymer materials are preferred. Since polymer molecules (many relatively small molecules linked together) are very heavy (molecular weights in the range of several thousand or greater), their mobilities are very small, and the great number of chemical bonds present furnish many modes in which to dissipate and distribute thermal energy other than in evaporation. When non-polymers must be used, they are of high molecular weight (several hundred or more), to minimize evaporation. The contamination source of polymer and non-polymer organic compounds is not the very heavy molecules, but the lighter impurities initially present (16). Most organic materials used in vacuum work show continually decreasing vapor pressures as the time of vacuum exposure increases. The materials outgassed from polymers are usually the monomers, i.e., the "building block" molecules or link of the polymer chain and also catalyst compounds (19, 20, 21). In non-polymers, the outgassed materials are usually lower boiling fractions or impurities in the oil, which may be initially present, and may also be generated by very slow "cracking," or decomposition, of the larger molecules into smaller more volatile molecules. These materials will eventually outgas themselves to a state at which they are quite involatile, and the only outgassing would be from very slow decomposition. Common classes of organic materials are briefly discussed below.

Heavy Hydrocarbons, Oils, and Esters

Commercial heavy hydrocarbons in vacuum use are high boiling petroleum fractions. Their infrared (36) and mass spectra are essentially identical, as are their chemical behavior, including their effects as contaminants. A large number of hydraulic oils, mineral oil, motor oils, lubricating oils, and vacuum oils, greases, and waxes (Apiezon) are of this nature. Many natural organic oils are not hydrocarbons but are fatty acids or their ester derivatives. The fatty acids have a ten-to-thirty carbon atom chain which terminates in carboxyl ($O = \overset{|}{C}-OH$) group (22). The existence of the polar ($-C=O$) (carbonyl) group and of possible double bonds in the carbon chain cause the compound to remain in the liquid state despite the high molecular weight. Esters of these oils (hydrocarbon chain terminating in $-COO(CH_2)_n-CH_3$ group, $n = 0, 1, 2, 3$) have even lower melting points, that is, have more of a liquid nature. When the size of the carbon chain becomes large (ten or more), the chemical and physical nature of hydrocarbons, acids, and oils become similar. These types of compounds often fluoresce, making them detectable upon visual inspection with black (ultraviolet) light, and are easily soluble in organic solvents and detergents. They may form stubborn tars when exposed to solar simulation, however.

Halocarbons

Halocarbons are organic compounds containing carbon and at least one halogen atom. Halogens are fluorine (F), chlorine (Cl), bromine (Br), and iodine (I).

The most important halocarbon in vacuum use is Teflon, a perfluoroethylene polymer whose repeating monomer is $(-CF_2-CF_2)_n$; Teflon is the least troublesome of the organics, as the outgassings, nearly 100% monomer, C_2F_4 , are stable and are reluctant to adsorb even on very cold surfaces (23). Halocarbons containing fluorine and some other halogen atom, such as Kel-F and freons, are of more concern, because their outgassings are decomposed by ultraviolet radiation from solar simulation, the decomposition products being very reactive with and detrimental to first surface aluminum, SiO , and SiO_2 coated mirrors of solar simulators (24).

Silicones

Silicones are silicon containing organic compounds usually containing several continuous silicon-oxygen-silicon linkages (sil-

oxanes). The silicone oils, greases, and rubbers used in vacuum work are commonly polymers of dimethyl siloxane, $\{O-Si(CH_3)_2\}_n$. These compounds have common and very characteristic mass and infrared spectra (27,31). They are difficult to dissolve with any solvent and are very stubbornly adsorbed on foreign surfaces. They are known to "creep" over very large continuous surfaces, forming a very fast monomolecular layer of silicone in their wake. When light silicone polymers and monomers are outgassed and deposited on foreign material, they may easily repolymerize, especially with the aid of ultraviolet light from solar simulation.

The DC-700 series silicone oils are used frequently as diffusion pump oils. They are non-polymers, being phenylmethyl trisiloxanes, that is, $R_3Si-O-SiR_2-O-SiR_3$, where the R's are methyl or phenyl (benzene) groups in varying distributions about the molecule.

Epoxies

Epoxy polymers vary greatly in chemical structure, but they all were created from monomers containing the epoxide group, $-C-O-C-$, which decomposes and cross-links to form the polymer.

Many of the high emittance thermal control coatings used in space technology are epoxy paints, whose monomer is an ester containing the epoxy group. Heavy esters, alkyd resins, drying oils, and alcoholic ethers (cellosolves) are used as matrices for these paints and are the major outgassed materials (34). The esters and epoxy monomers are quite soluble in most organic solvents, but are also subject to tar formation and polymerization by ultraviolet light (35).

THE SAMPLING OF CONTAMINANTS

Contaminants may be analyzed according to their quantity, identity, directionality, and effects. They can be analyzed on an in situ, real time basis (active), or samples can be removed from the test site after testing and analyzed in the laboratory (passive). An important factor in either active or passive sampling is that the sampling surface be at or near the same temperature as the test article surface of concern. It has been found, for example, that some fairly heavy oils will not deposit on surfaces above 4° C. Also of importance is the condition that the sampling surface be of the same material as that of the test article. An outstanding example of this requirement is that many compounds will not adsorb on Teflon regardless of its temperature, and conversely, methane and carbon dioxide are re-

tained on highly activated charcoal, alumina, and silica at room temperatures. Another parameter that is of concern in sampling is that the sampling surface be as near as possible to the test article and have the same directionality and field of view as the test surface. The most desirable sampling conditions would be, then, to sample the test article surface itself on a real time basis for identity and quantity of contaminants and for the effects of the contaminants on the test surfaces. Unfortunately, this is not feasible, and the sampling conditions must be selected to satisfy the most important requirements of contaminant analysis. For example, it is often important to know the sources of contamination in a vacuum chamber, so that they may be found and eliminated. After they are eliminated, it is desirable to evacuate the chamber again and repeat the measurements to determine the effect of the cleaning. In this case, passive devices at cryogenic temperatures, and at locations all about the chamber, are sufficient. On the other hand, when it is important to know the effects of contamination during testing, as in long duration simulated flights, only active effects measuring devices with close matching of surfaces, temperatures, locations, and field of view will suffice. The various modes of sampling and analysis techniques available shall be described to assist in the satisfaction of contamination measurement requirements.

Mass Spectrometry

This active or passive sampling technique has the greatest analysis potential; however, a great amount of effort is required to make it usable, and caution is recommended in considering its application.

Mass spectrometers, with the exception of the leak detection type instrument which is "tuned" to one peak, were formerly used in a more passive contamination sampling role better suited to discrete samples and slower analysis scan times not related to real time test monitoring. With the recent advent of fast scanning and recording mass spectrometers, it is now advantageous to use the instrument on a real time basis.

Generally the mass spectrometer can be coupled either externally or internally to the test volume under consideration. For external use, the mass spectrometer has an ultra-high vacuum system which draws an in-chamber atmospheric sample through a heated sample line into a heated mass analyzer tube. The sampling line should extend into the chamber test volume in order to obtain the most significant sample and to avoid sample con-

densation on the coldwalls. Externally coupled instruments are generally useful only for pumpdown and repressurization test phases, when sample pressures are sufficient for migration through the line to the instrument. Each sample line will have its own time constant, i.e., the time necessary for the entrance of the sample into the line until its exit at the entrance to the ionization source region of the mass spectrometer. The time constant of the sample line will depend on line length, sample pressure, line diameter, sample line temperature, and material of tube wall.

At high sample pressures, the fastest response is obtained with a small diameter (3 to 7 mm.) line, which keeps the gas volumes low. At lower sample pressures, where an auxiliary pumping line which ordinarily helps reduce the gas flow into the analyzer would not be used, a large diameter (7 to 25 mm.) line would give the highest pumping speed and fastest time response. The sample line design must be optimized for best response with any given set of operation conditions, be it a single line with variable orifices or a series of sample lines valved in at differing pressure ranges.

An internal mass spectrometer is a type known as the Remote Residual Gas Analyzer (RRGA) which is essentially a mass analyzer mounted in the test volume and depends on the chamber itself for vacuum. Of necessity, this instrument can operate only when the chamber pressure falls below the 10^{-4} torr region and must be provided with automatic filament protection should there be a sudden pressure surge. Since the instrument control consoles are located external to the chamber, the necessary pre-amplifiers must also be located with the analyzer to enhance the signal-to-noise ratio. The RRGA mount may allow rotation through two mutually perpendicular axes to provide directional sampling capability. The usual magnetic sector instrument mounted in-chamber requires its own magnet, and its weight can present a mounting problem in directional sampling. A recent popular trend in test volume mass spectrometers has been the small, lightweight monopole and quadropole type instruments which lessen mounting constraint and provide good linear spectral display (magnetic type mass spectrometer mass scans are usually non-linear with respect to mass numbers).

For either internal or external instruments, once the sample is obtained in the ion-source region and ionization of the gas is effected, the types of analyzer methods used may be widely differing. Upon electron impact, the ions produced are electrically accelerated and filtered from the source region into the analyzer region, where the ion sorting may be accomplished by use of any combination of magnetic, electrostatic, or electrodynamic

fields. Various mass analyzer types are the magnetic (180° Dempster, 60° and 90° sectors), quadropole, and monopole types already mentioned, and also the cycloidol, omegatron, RF, and pulsed time-of-flight analyzers which are less commonly used. Each of the above types has its own advantages and disadvantages, and the choice among them for use in chamber sampling depends on the requirements of resolution, scan speed, mass range, sensitivity, clean-up time, and inlet system. A very good listing and specification comparison of commercially available mass spectrometers is contained in reference 32.

The mass spectrometer is an "absolute" analyzer which can be made both qualitative and quantitative. One recurring problem with the present rapid scan instruments is that there is too much useful data, and complex data reduction methods have to be employed. Analyses of mixtures of compounds, without appropriate working conditions and on a poor resolution instrument, can be futile. The problem is the indeterminability of percentage of contribution of each component for a selected mass value. Identification of possible chamber contaminants requires a very extensive program of library referencing or "fingerprinting" spectra of the suspected single components. If possible, these single components should be run as series of mixtures of various compositions under differing simulated chamber temperature and pressure environments to serve as a standard for the instrument sensitivity, resolution, and times of appearance. The end result of the previous work will be an in situ calibration, a formidable task, indeed, for multicomponent compounds such as oils, paint samples, or surface outgassings. Published fingerprint data are not very useful, as a mass spectrum of a compound is unique for any mass spectrometer and may vary for different sampling systems for the same instrument. However, general rules of fractionation of molecules in mass spectrometer ionizing chambers are applicable in determining the type of compound present. This is a very delicate exercise, however, since mass peaks from several different types of molecules tend to make each other's spectra ambiguous, i.e., there are often too many peaks. To begin, mass numbers of unknown peaks must be matched to, or interpolated between, mass peaks from a known mass marker. One then searches for the mass peak of the unfractionated molecular ion, if possible, and proceeds to smaller mass peaks, trying to recognize any patterns representative of certain functional groups. For example, m/e peaks of 29, 39, 42, 43, 55, and 57 are representative of hydrocarbons; m/e 31, 45, or 59 peaks of alcohols; m/e 45 and 60 of carboxylic acids; m/e at $30 + (14)_n$ of amines; m/e 30 and 46 of nitro compounds; and m/e 65, 77, 78, 79, $91 + (14)_n$ for aromatic hydrocarbons. The above functional group

patterns are only a very few of many. Several excellent texts are available for functional group identification and description of typical cracking modes in mass spectrometry (30, 31, 32, 33); however, considerable expertise must be developed in reading mass spectra before this technique can be useful.

Mass spectrometers are now being linked directly to gas chromatographs, so that individual components of a mixture may be analyzed, thus eliminating ambiguities caused by the presence of unknown mixtures. Gas chromatographic sampling of gases whose vapor pressures are less than 10^{-5} torr is not possible, however, so that this powerful separating technique cannot be used with mass spectrometers for real time contaminant analyses.

Again, one is cautioned in considering mass spectrometry as a contaminant analysis technique, because, though it is a very powerful method, it also requires very great effort and expertise to analyze the wealth of data from each mass scan.

Quartz Crystal Mass Monitors

These devices measure the mass of contaminants deposited and are capable of active or real time sampling with directionality, field of view, and temperature control. They consist of small, thin quartz crystal pieces cut at the AT plane. The crystals have aluminum or noble metal films deposited on each face which are electrodes. An electric field is applied across the faces of a crystal, which distorts piezo-electrically in a direction perpendicular to the field (parallel to the faces). The natural oscillating frequency is dependent upon the mass and temperature of the crystal, although it is quite temperature insensitive in the range 0° to 70° C. Thus with controlled temperature, the natural frequency of the crystal will decrease as the crystal becomes contaminated; i.e., its mass will increase, and the effect is analogous of adding mass to a vibrating spring. The crystal mass is on the order of 0.1 grams, and its natural oscillating frequency is in the range of 5×10^6 Hz. The frequency (f) of an oscillator, within limits, is inversely proportional to its mass (m), $f = c/m$, where c is a constant. In differential terms $df/f = dm/m$, (5) which can be approximated to $\Delta m = -m \Delta f/f$, (6); as long as $\Delta f/f$ is small, the approximation is quite accurate.

The valid range of Δf is about 10^5 Hz, and the typical stability and sampling area of the system are such that contaminants can be measured in the range of 10^{-4} to 10^{-1} g/m², or approximately 0.1 to 100 monolayers of a heavy organic material.

The frequency of the oscillator may be monitored directly with an electronic counter, but problems are generally encountered in transmitting the weak radio frequency signal through the chamber; a preferred method is to beat the sampling crystal's natural oscillating frequency against that of a reference crystal that is completely shielded from contamination and located only a few centimeters distance from the sample crystal. This results in an audio frequency signal which is easily transmitted and measured with an electronic counter. It is interesting to note that electronic counters, which are very stable, must use an oscillating quartz crystal as a clock, so that the beat method actually involves three crystals. Several sample crystals may be beat against a single reference crystal in a multidirectional apparatus. It is important when using the beat method that the sample and reference crystal temperatures be identical, at least to within 1°C . An interesting phenomenon in the use of quartz crystal mass monitors is that during the pumpdown phase, the frequency may often increase, due to desorption of CO_2 and H_2O from the crystal faces.

The above technique cannot discern the nature of the contaminants, and the sampling surfaces are limited to the type of electrode material (metallic) that can be employed. The crystals begin to lose their linear frequency-mass relationship when the contaminant becomes too heavy ($\Delta f > 10^5\text{ Hz}$), and this limit may be lower if the contaminant is in the liquid, rather than the solid, state. The crystals are apt to change oscillating planes, and thus the principal frequency, if mechanical stresses develop. The crystals may be cleaned with organic solvents and reused. To remove the final monolayer of contaminant, the crystal may be boiled in an aqueous solution of 3 percent hydrogen peroxide and 1 percent ammonia. This type of mass monitor is in common use as rate indicators in thin film vacuum deposition processes.

In Situ Reflectometers

This active sampling technique provides crude relative information on the quantity of contamination and is of most benefit in measuring the effect of contamination on specularly reflecting surfaces. The device is comprised simply of a light source, a mirror, and a detector, which are mounted as a unit in the space environment chamber and monitored throughout a test. A decrease in detector signal will result from contamination on a mirror. Whereas transmitting optics are quite insensitive to contamination, specular reflectance of mirrors is very much affected. The reflectometer system may be sophisticated and tailored to satisfy the requirements of the investigation. Sources, detectors, and optical filters may be selected to view only a given

band of the spectrum. For complete spectral analysis, a sophisticated scanning monochromator system might be employed; however, increasing the complexity of a system increases the number of susceptible optical surfaces, and also increases the probability of self-contamination. A sophistication of a non-scanning system is monitoring the intensity of the incident beam, so that the ratio of reflected to incident light, or specular reflectance, may be monitored directly. This avoids errors due to drifts in source intensity and detector sensitivity. An important factor in the design and employ of in situ reflectometers is to assure that the obstruction of the view of the mirrored surface by the instrument itself is minimized. Temperature control of the mirror is desirable. An additional detector may be included that receives light reflected from the mirror that is not specular (diffusely reflected light). This is a delicate system because the aperture of the detector must be low to avoid view obstruction of the (sampling) mirror; the scattered, or diffusely reflected, light from small amounts of contamination would be very weak. However, diffuse reflectance increases dramatically with contamination and is more sensitive to contamination than specularly reflected light. The only value of diffuse reflectance measurement, though, would be to monitor the relative extent of contamination.

A typical decrease of specular reflectance at 253.7 nm wavelength due to two or three monomolecular layers of heavy oil would be on the order of 1 percent. The increase of diffuse reflectance of a mirrored surface, which is initially very low, for the same contamination would be around 50 percent. The mirrors used in reflectance monitoring must be first surface coated.

Painted Radiometers

This is an active, effects measuring technique which also serves as a radiative heat transfer monitoring method. This approach involves placing a nude radiometer or calorimeter, whose coating is identical to that of the test surface of concern, on the test surface and in good thermal contact with it. The radiometer must be so constructed that the temperature differential between its back and sensing surface is less than 0.5°C . A thermocouple must be located on the radiometer body to monitor radiometer temperature, T_R . The output of the radiometer, V , is directly proportional to the radiative heat transfer at the test article surface by the equation (7):

$$V = \frac{\alpha_S E_S - \epsilon_H \sigma T_R^4}{S_R} = \frac{M_{\text{rad, net}}}{S_R} \quad (7)$$

where

α_S = solar absorptance (for solar simulation)

E_S = solar simulation irradiance

ϵ_H = total hemispherical emittance for radiometer temperature T_R

σ = Stefan-Boltzman constant, $5.67 \times 10^{-8} \text{ wm}^{-2} \text{ deg K}^{-4}$

S_R = sensitivity of radiometer based on absorbed flux

$M_{\text{rad, net}}$ = net radiative heat transfer at the surface.

If the radiometer is monitored when the solar simulation is off,

the emittance may be directly measured
$$\epsilon = \frac{E_S}{\sigma T_R^4} \quad (8)$$

This value may be substituted into equation (7) to determine α_S , the absorptivity of the surface for solar simulation. Of course, the value of solar simulator irradiance at the location of the painted radiometer must be known. The best data the painted radiometer technique will afford, however, are changes in net radiative heat transfer at the test surface. Provided radiometer temperature measurement is accurate, these data will indicate the effects of solar simulation spectrum and irradiance, and of contamination on the test surface; however, it cannot discern between the two effects unless solar is off, at which time the effects of contamination on emittance can be measured. Should the coating material itself photochemically degrade, however, emittance monitoring would not distinguish this degradation from that of contamination.

Contamination Collection Units (CCU's)

This is a passive sampling, quantitative and qualitative analysis method. It can provide bountiful information regarding identity, extent, and source of contamination. The sampling is very simple and inexpensive. This technique collects low levels of contamination over large surface area in order to obtain enough sample to analyze. For example, if one monomolecular layer of heavy oil is approximately 10^{-5} g/m^2 , then about 0.1 milligram will be collected from a sampling area of one square foot, or 929 cm^2 . Microgram quantities of organic materials can be analyzed with gas chromatographs (with hydrogen flame ionization detectors) and with mass spectrometers. Quantities as small as ten micro-

grams can be analyzed with infrared spectrophotometers using beam condensing attachments.

A contamination collection unit is simply a 300 x 300 mm glass or polished metal plate with 25 mm diameter quartz discs attached to each face. A thermocouple is attached to the plate to monitor its temperatures during a test in the space environment chamber. These units may be placed anywhere in the chamber, e.g., near pump ports, test articles, and solar simulators. These units may be sophisticated by placing them in thermally controlled mounts with covers that can be removed and replaced during various phases of a test in a space environment chamber; for example, one might be exposed only during the pumpdown phase, another only during the test conditions, and still another only during repressurization. After they are removed from the chamber, the quartz discs are detached from each face, and their transmittances are measured at 200 nm on an ultraviolet spectrophotometer. They are cleaned with ethyl alcohol or carbon tetrachloride, and their transmittances at 200 nm are measured. The log of the ratio of transmittance of the cleaned to that of the contaminated disc (absorbance) at 200 nm affords a quick indicator of the relative contamination on that disc. This may be very crudely converted to a quantitative value if a molar extinction coefficient of $10^3 \text{ m}^2/\text{mole}$ (typical of many organic compounds at 200 nm) is used in the relationship:

$$\frac{m}{A} = 300 \frac{\log_{10} T_0/T}{\epsilon}$$

where $\frac{m}{A}$ is the mass per unit area

T_0 and T are the transmittances at 200 nm of the cleaned and contaminated quartz disc, respectively

ϵ is the molar extinction coefficient

300 is the assumed molecular weight of a typical heavy organic contaminant.

The assumptions of extinction coefficient and molecular weight make the quantitative values obtained from the quartz discs very uncertain; however, a comparison of absorbances of the quartz discs provides a quick look evaluation of the relative severity of contamination about the chamber.

Each face of the CCU plate is rinsed down with 100 cm^3 of spectroquality carbon tetrachloride. The rinsing has been shown to

be better than 90 percent effective in removing contaminants in excess of one monolayer. One monolayer of some organic material will remain on the plate surface. This monolayer may be subject to competitive displacement by other more adsorptive materials. If the existing, pretest monolayer is of a sufficiently stubborn material, such as silicones, then at least 90 percent of all the contaminants accrued during testing will be collected by the rinsings. The rinsings of each face are concentrated to a volume of 3 cm³, and the absorbances (log of the inverse of the transmittance) of the contaminants in the solvent are measured in the region 2.5 to 10 micrometers on an infrared spectrophotometer. The optical path is from one to two millimeters. The quantitative estimate of contamination is determined from absorbance and extinction coefficients similarly to the method used for quartz discs. The calculation is from the formula

$$\frac{m}{A} = \frac{\epsilon_{\lambda}^{-1}}{\ell} \frac{\log_{10} T_{0\lambda} / T_{\lambda}}{A_{CCU}} V$$

where $T_{0\lambda}$ and T_{λ} are the transmittances of the solvent (CCl₄) and CCl₄ solution containing the contaminant, respectively, at wavelength λ .

ϵ_{λ}^{-1} is the extinction coefficient of the contaminant, on a mass rather than molar basis, at wavelength λ .

ℓ is the optical path of the infrared absorption cell (1 to 2 mm).

A_{CCU} is the area of one face of a CCU.

V is the total volume of solution (typically 3 cm³).

Some values of ϵ_{λ}^{-1} for various compounds, with λ selected at minima of bands characteristic of the compound, are:

COMPOUND	$\lambda_{1, \mu\text{m}}$	$\lambda_{2, \mu\text{m}}$	$\epsilon_{\lambda_1}^{-1} \text{ g/m}^2$	$\epsilon_{\lambda_2}^{-1} \text{ g/m}^2$
Nujol Mineral Oil	3.4	---	3.18	---
SunVis 706 Hydraulic Oil	3.4	---	2.79	---
DC-705 Silicone Oil	3.2	7.0	18.5	7.9
Houghtosafe 1055 Tricresyl Phosphate Oil	8.6	---	7.5	---
Polydimethyl Siloxane oil, grease, or rubber	8.6	12.0		

The sensitivity of this method is about 0.3 monomolecular layers of heavy oil on a 300 x 300 mm CCU surface. A different infrared solvent may be used, such as carbon disulfide, if contaminant absorbances in the region 7.5 to 15 μm are sought.

The solvent, CCl_4 , is very transparent in the region 2.5 to 6.0 μm where absorption of O-H, N-H, C-H, and C = O bonds occur. From these data, an estimate of the total hydrocarbons, alcohol and amines, and carbonyl (C = O) containing compounds can be made. The solution is then evaporated to dryness on a small (12 x 12 mm) piece of KRS-5 infrared transmitting material (non-hygroscopic) or in 25 milligrams of potassium bromide (KBr) pellet powder and pelletized in a microdie (1.5 millimeter diameter).

The sample - KBr powder mixture may be mechanically mixed, or the sample may be transferred to the KBr by the lyophilization (freeze drying) technique (28). Lyophilization is a time consuming and tedious process, but affords quantitative spectra because of resulting homogeneity of the sample in the pellet (29). The KRS-5 piece or the pellet is placed in a beam condensing attachment of an infrared spectrophotometer, and the spectrum can be measured from 2.5 to 40 micrometers without interference from the media. If the KRS-5 piece is used, the sensitivity of the technique is about 10 micrograms, corresponding to about 0.1 monolayer of a heavy oil on a 300 x 300 CCU. The spectra may be matched against "fingerprint" spectra of known materials used in and about the space environment facility. Figure 1 depicts infrared spectra of materials commonly used in vacuum chambers. In some cases the contaminants may be readily identified; i.e., their spectra are unique, as in epoxy paint outgassings (alkydresins) and DC-700 series oils (27, 34). In other in-

stances, where the contaminants are basically of the same compositions such as petroleum based fluids and polydimethyl siloxane compounds (silicone rubber and many silicone oils and greases), identifications would be restricted to the type of compound (petroleum based hydrocarbon, polydimethyl siloxane, etc.) (27, 36). One very misleading consequence in matching contaminant infrared spectra to fingerprints is that perhaps the volatile component of a contaminating compound may constitute only a very small fraction of the compound fingerprinted, in which case this compound would be erroneously exonerated by fingerprint matching as a contamination source. It is preferable, if possible, to collect only the outgasings of materials for fingerprinting, in order to avoid this pitfall. Identification of contaminants becomes difficult when small quantities of some contaminants are present with large quantities of the others. In this case, the infrared spectra of the lesser contaminants becomes obscured by those of the more dominant ones. It is preferable to fractionate, or separate, the contaminants, and this is facilitated in a very sensitive fashion by gas chromatography.

If the contaminants concentrated on the KRS-5 piece or in the KBr pellet are redissolved in an organic solvent, such as CCl_4 , they may be injected in a gas chromatograph. This instrument separates the contaminants according to chemical composition (fractionates) from a stream of inert carrier gas flowing through a long, narrow "column" (usually coiled tubing) packed with a solid material of uniform mesh size, each particle of which is coated with a low vapor pressure organic material known as the stationary phase. The effluent of the column passes through an electronic detector whose current is sensitive to impurities (fractions of contaminants) in the carrier gas. For most detectors, change in detector current is directly proportional to the amount of the sample's fractions in the effluent stream. The gas chromatograph is strictly a relative instrument, that is, the time between sample injection and occurrence of a fraction of the sample at the detector is a function of the individual column used, flow rate of carrier gas, and column temperature, which is often increased at reproducible rates after injection. Thus if materials are to be "finger-printed" for gas chromatography, the procedure must be performed for each type of column, preferably each individual column, used. A general purpose system consists of a dual column, dual hydrogen flame ionization detector chromatograph using 2 meter long columns of 2 to 4 millimeters internal diameter packed with 60 to 70 mesh solid coated with 5 percent (by weight) SE-30 silicone gum rubber and operated at 300, 310, 315° C for column, detector, and injector, respectively (37). This technique provides an accurate quantitative analysis of contaminants if the fractions can be reliably matched to fingerprints. The sensitivity of gas chromatography is now typically in the sub-microgram range, so that quantities of contaminants much less than

0.1 monolayer on a CCU face can be identified and their masses measured. It is also possible, but with great difficulty, to individually collect the effluent fractions of the CCU contaminants from a gas chromatograph. When this is done, their infrared spectra may be recorded (if the sample is heavy enough) and also their mass spectra may be measured. This is a very powerful technique, as it allows the infrared and mass spectra of individual compounds to be unambiguously measured, under which conditions the infrared and mass spectra are very capable of identifying the fractions, to the extent of determining most of the molecular structure, including molecular weight of the compounds. The linking of a gas chromatograph effluent stream to a mass spectrometer inlet system is now becoming a common practice, and this combination is highly recommended in CCU analysis. The combination GC-MS eliminates the one great disadvantage of mass spectrometry in identifying compounds from multi-component mixtures.

Optical Samples

Optical samples may be mirrored, transparent, or opaque and non-specular. The use of first surface mirrors permits the determination of the effects of contamination on similar mirrored surfaces. For this application, it is recommended that the coating, view factor, directionality, location, and temperature of the sample mirrors be as similar as possible to the same parameters of the test surfaces of concern. The specular reflectance and diffuse reflectance spectra of the sample mirrors and of one or more laboratory control mirrors are measured immediately before the environmental test begins and again immediately after the test is concluded. The control samples are maintained in a sealed container in the measurement laboratory and serve to indicate changes in the reflectometer and errors in handling technique that occur between pre- and post-exposure measurements. The wavelength range of specular reflectance measurement should be selected to match that range in which the test surfaces are intended for use (soft X-ray, vacuum ultraviolet, near-ultraviolet, invisible, near infrared, infrared, or far infrared). The diffuse reflectance spectrum is most conveniently and advantageously measured in the range 200 to 750 nm (near ultraviolet and invisible) and is a sensitive indicator of the extent of contamination. Integrating sphere attachments for spectrophotometers using magnesium oxide or barium sulfate coatings are commercially available. Likewise, specular reflectance attachments are available for vacuum ultraviolet, ultraviolet, visible, and infrared spectrophotometers. Absolute accuracy is not necessary in this type of measurement, the important information required is only the extent of change, or degradation, of the optical surfaces due to environmental testing. The same approach is applicable to transparent samples, wherein these samples are matched to

the pertinent test surfaces, and their transmittance spectra, and that of control samples, are measured before and after exposure to simulated space environment.

Samples coated with thermal control coatings identical to those of the test article may be also employed in the same manner. Integrating sphere attachments for spectrophotometers also lend themselves to absorptance measurements in the solar region, and precise emmisometers can be employed for the measurement of normal total emittances (in the infrared region) of such samples.

It may be commendable to control the exposure of optical samples to selected phases of the environmental test by remote, controlled shuttering. The shutters and actuating mechanisms should be very thoroughly cleaned, preferably including vacuum bakeout, in order to avoid their own contamination of the optical samples.

Optical samples will indiscernably indicate degradation by environmental conditions other than contamination, such as ultraviolet radiation and thermal shocking, and thus contamination may be erroneously blamed for such degradation when optical samples are employed.

Microscope Slides

This is a passive technique for the determination of particulate contamination. Microscope slides, preferably with calibrated grids imprinted on them, are cleaned and are photographed through a microscope at significant times before being placed in the environmental chamber. The slides are again microphotographed at significant times after removal from the chamber and the amounts of particles in successive size ranges are counted. Control slides are photographed and counted at the same time the sample slides are, except they are maintained in a particle-free environment while the slides are being exposed. The exposure of the samples may be controlled by remote shutterings. Cleanliness in this type of measurement is understandably critical (1, 7, 8).

REFERENCES

Particulate Contamination

1. Sivinski, H. D.; Whitfield, W. J.; Pauhamus, J.A.: Contamination Control Principles, NASA Special Publication SP-5045, National Aeronautics and Space Administration, Washington, D. C., 1967, pp. 41-46.
2. Method of Test for Continuous Counting and Sizing of Airborne Particles in Dust-Controlled Areas by the Light Scattering Principle (for Electronic and Similar Applications), ASTM F50, American Society of Testing Materials, 1916 Race St., Philadelphia, Pa.
3. Whitfield, W. J.: Monitoring a Class 100 Clean Room, SC-R-956, Sandia Corp., Oct. 1966.
4. Procedure for the Determination of Particulate Contamination of Air in Dust Controlled Spaces by the Particle Count Method, SAE-ARP-743A, Society of Automotive Engineers, Inc., New York.
5. Johnson, J. D.: Contamination Analysis and Monitoring, Proceedings of the National Conference on Spacecraft Sterilization Technology, NASA Special Publication SP108, National Aeronautics and Space Administration, Washington, D. C., 1967, pp. 293.
6. Dwyer, J. L.: Contamination Analysis and Control, Reinhold, New York, 1966.
7. Handbook for Contamination Control on the Apollo Program, NASA Handbook NHB 5300.3, National Aeronautics and Space Administration, Washington, D. C., Aug. 1966.
8. Sivinski, H. D.: Contamination Control Handbook, NASA Special Publication SP-5076, National Aeronautics and Space Administration, Washington, D. C., 1969, pp. 63-82.

Desorption, Sublimation and Evaporation

9. Moelwyn-Hughes, E. A.: Physical Chemistry, 2nd Ed., Pergamon Oxford, 1961, pp. 921-983, 1051-1113.
10. Santeler, D. J.; Holkeboer, D. H.; Jones, D. N.; Pagano, F.: Vacuum Technology and Space Simulation, NASA Special Publication SP-105, National Aeronautics and Space Administration, Washington, D. C., 1966, pp. 175-213.
11. Deboer, J. H.: Dynamical Character of Adsorption, Oxford, Toronto, 1953.
12. Dayton, B. B.: Outgassing Rate of Contaminated Metal Surfaces, Transactions of Eight National Vacuum Symposium and the Second International Congress on Vacuum Science and Technology, Vol. I, Pergamon, 1962, pp. 42-57.
13. Dushman, S.: Scientific Foundation of Vacuum Technique, Wiley, New York, 1962, pp. 491-587.
14. Gray, D. E. (Ed): American Institute of Physics Handbook, McGraw-Hill, New York, 1957, pp. 4-131 ff.
15. Ehrlich, G.: Molecular Processes in Adsorption on Metals, Transactions of the Eight National Vacuum Symposium and the Second International Congress on Vacuum Science and Technology, Vol. I, Pergamon, 1962, pp. 126-145.
16. Espe, W.: Materials of High Vacuum Technology, Vol. 3, Pergamon, Oxford, 1968, pp. 235 ff.
17. Fulk, M. M.; and Horr, K. S.: Sublimation of Some Polymeric Materials in Vacuum, Transactions of the Ninth National Vacuum Symposium, Macmillan, 1962, pp. 324-333.
18. Boebel, C. P.; Mackie, N. A.; and Quaintance, C.C.: Outgassing Studies of Space Materials, Transactions of the Ninth National Vacuum Symposium, MacMillan, 1962, pp. 307-310.

Decomposition and Chemistry

19. Brandrup, J.; and Immergut, E. H. (Ed): Polymer Handbook, Wiley, New York, 1966, pp. V-5 - V-12.
20. Lenz, R. D.: Organic Chemistry of Synthetic High Polymers, Interscience, New York, 1967, pp. 733-767.
21. Madorsky, S. L.: Thermal Degradation of Organic Polymers, Interscience, New York, 1964.
22. Fieser, L. F.; and Fieser, M.: Organic Chemistry, Heath, Boston, 1956, pp. 399-408, 412-416.
23. Madorsky, S. L., Ibid, p. 132.
24. The Boeing Co., Kent, Washington, June 30, 1966. Results of an Investigation on the Effects of Solar Simulator Ultraviolet Irradiated Freons on First Surface, SiO_x Over-coated Aluminized Solar Simulator Mirrors.

Infrared Spectroscopy

25. Silverstein, R. M.; and Bassler, E.C.: Spectrometric Identification of Organic Compounds, 2nd Ed., Wiley, New York, 1967, pp. 64-109.
26. Henniker, J. C.: Infrared Spectrometry of Industrial Polymers, Academic, New York, 1967.
27. Hummel, D. O.: Infrared Spectra of Polymers, Interscience, New York, 1966, pp. 152-153.
28. Instructions for KBr Microdie, Perkin-Elmer Corp., Norwalk, Conn., 1966.
29. White, R. G.: Handbook of Industrial Infrared Analysis, Plenum, New York, 1964, pp. 123.

30. Silverstein, R. M.; and Bassler, E.C.: Ibid, pp. 4-63.
31. Bieman, K.: Mass Spectrometry, Organic Chemical Applications, McGraw-Hill, New York, 1962, pp. 171-172.
32. Industrial Research, 1970 Instruments Specifier, Industrial Research, Inc., Beverly Shores, Ind., 1970, pp. 32, 39-41.
33. McLafferty, F. W. (Ed): Mass Spectrometry of Organic Ions, Academic, New York, 1963.
34. Hummel, D. O.: Ibid, pp. 112-113.
35. Lenz, R. W.: Ibid, pp. 307.
36. Hummel, D. O.: Ibid, pp. 179.
37. Langdon, W. M.; and Ivanuski, V.R.: Backstreaming from Oil Diffusion Pumps, Report No. IITRI-C6030-10, IIT Research Institute, Technology Center, Chicago, Ill., July 1966, pp. 17, 163-170.

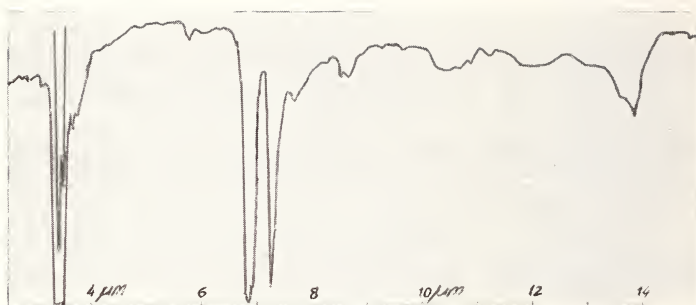


Figure 1A. Infrared Spectrum of Petroleum Based Oil or Grease (Hydrocarbon)

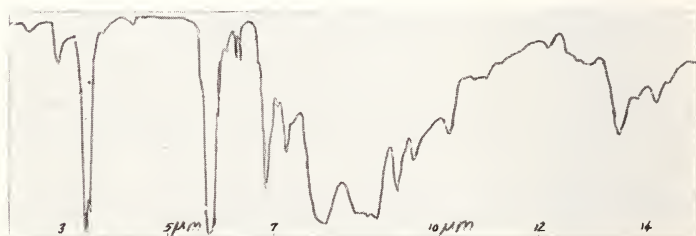


Figure 1B. Infrared Spectrum of Tall Oil Alkyd - Used in Paints - Outgassed From 3M Nextel® Paints

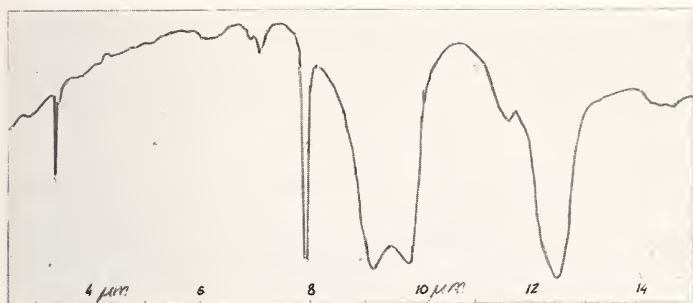
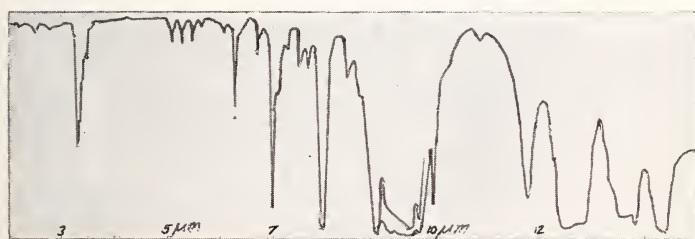


Figure 1C. Infrared Spectrum of Polydimethylsiloxane--
Common to Most Silicone Oils, Greases and Rubbers



Figutr 1D. Infrared Spectrum of DC-700[®] Series Oils
(Methyl-phenyltrisiloxanes)

CONTAMINATION STUDIES IN A SPACE SIMULATED ENVIRONMENT

David L. Enlow, Research Physicist, Environmental Sciences Laboratory, Re-entry and Environmental Systems Division, General Electric Co., Phila, Pa.

ABSTRACT: Biological and optical contamination problems can be best investigated experimentally. Studying the dynamics of microorganisms in a vacuum environment showed that shock forces in the order of a 1000 g's will liberate 20 percent of the previously bound particles and the effect of simulated attitude control gas jet firing will remove more than 50 percent of the bound particles.

A potential source for optical degradation to infrared systems is identified as the absorption phenomena of condensed volatile products from certain polymeric materials. The effects of this condensation were analyzed by a combination of surface photography and IR spectroscopy. These preliminary investigations point out the need for proper materials selection for far infrared space-borne optical systems.

KEY WORDS: planetary quarantine, shock force, fluid dynamic force, microorganisms, contamination control, testing, evaluation, space simulation, optical properties, condensation, volatile products, polymers, far infrared, absorption.

INTRODUCTION

Contamination problems in previous space system programs have to varying extents endangered full mission objective realization. In particular, the problems of biological and optical contamination have in the past and will be in the future, increasingly important. This is evidenced by the planetary constraints which are placed on the current Viking Mars Landing Program and the ever increasing level of sophistication and operational sensing requirements of space-borne optics. This paper will discuss analytical and experimental investigations for both of these areas of contamination.

1.0 BIOLOGICAL CONTAMINATION

Biological contamination is of prime consideration for the Viking Mars Landing program in which a sterile lander will investigate the existence of life on Mars. The overall Martian planetary biological integrity will be insured by the provision of an International Planetary Quarantine Agreement which specifies the overall probability contaminating Mars within the next twenty years shall be less than 1×10^{-3} . The constraints imposed by the Planetary Quarantine Requirements on the Viking Program will consist of designing, fabricating, and launching a sterile lander which will be protected during the trans-planetary cruise by a bioshield. To realize these requirements, extensive experimental evaluation (we will discuss sterile lander recontamination only) under space simulated, as well as space-mission mission event simulated environments, must be performed.

1.1 Analytical Studies

Recontamination refers to the phenomena of the sterile lander becoming contaminated via any source at any time after terminal lander sterilization. Detailed analytical studies on the recontamination phenomena for a Mars Lander Mission were performed. First, a definition of recontamination mechanisms was generated (see Fig. 1). The attitude control gas particle transport mechanism is one whereby particulates may be removed from non-sterile portions of the spacecraft and transported to sterile areas. The availability of micro-organisms is determined by the interactions of bound particles and micro-meteoroid impacts, shock and vibration events.

To determine the importance of each mechanism, they were singularly analyzed in terms of their controlling forces. The controlling forces were found to be orderable in three main areas: (1) Removal forces (input forces) - shock and vibration, fluid dynamic, surface sublimation, and impact; (2) Adhesive forces (force bounding particles to surface) - capillary and electrostatic; (3) Dynamic Forces (forces controlling unbound particles) - electrical gravitational, and fluid dynamic. Attempts to quantify these forces analytically turned out to be tractable in some cases but for the most part very difficult. In summarizing the analytical work [1], it should be pointed out that the key properties to understanding the recontamination phenomena were the adhesion and electrostatic characteristics of small particles and their interaction with surfaces; that

[1] The number in brackets refer to the list of references appended to this paper.

analytical analyses was not sufficient to define the controlling forces; and that experimental investigations must be performed under simulated space flight conditions.

1.2 Experimental Program

1.2.1 Introduction

An experimental test program was designed to investigate the adhesive and electrostatic surface interactions for microorganisms on surfaces [2]. The experimental approach (Fig. 2) consisted of developing a particulate deposition technique to enable uniform and repeatable depositions be performed on various types of surfaces. To determine the number of microorganisms removed or remaining on a test surface, bio-assay methods were selected and validated for high removal efficiency and repeatability. To investigate the adhesion phenomena of potential contaminating particles, force produce test assembly systems were designed and fabricated to simulate specific forces; i.e., centrifugal, shock impulse, and fluid dynamic flow. The necessity for space simulation in the investigations required that force producing systems be implemented under vacuum conditions, and therefore must be vacuum system compatible.

The aerosol deposition technique (Fig. 3) was finally selected after many variations, consisted of placing 100 mg. of microorganism B. subtilis var. niger in the spore form into the aerosol head behind a paper diaphragm. Pressure was applied to the head and the dispersed cloud was allowed to circulate in the chamber for a half an hour, the planchets (1 in. diameter test metal discs) were then exposed for several hours. This technique enabled a deposition uniformity of ± 15 percent to be attained. The microbe-deposited planchets were used as the test specimens. The ultrasonic rinse bioassay technique was selected because of its high removal efficiency (>97 percent repeatability).

The two major recontamination events to be simulated were the shock environment and the thruster (altitude control firing) flow. The techniques used to simulate these mission events in terms of evaluating their importance as a recontamination mechanisms were greatly controlled by the requirement for vacuum environment.

1.2.2 Vacuum Shock Experiment

To simulate the shock environment, that is, impart a maximum of 1000 g's (1 millisecond duration) to a test surface under vacuum

proved difficult. Since the problem of absorbing the shock recoil energy by any vacuum chamber, its connections, and seals, is a very serious threat to maintaining vacuum integrity, an approach was taken to connect a small highly durable test assembly to a vacuum chamber by a flexible connector, with the test assembly mounted rigidly to a shock test machine. Several designs were conceived; the final assembly (shown in Fig. 4a) was made of stainless steel 304, with removable top lid and vacuum gasket of Viton. It was connected to the vacuum system by a stainless steel flex hose which was found to be far superior to earlier used thick wall tygon (shown in Figure 4a, which was found to present a wall diffused gas load thus preventing a test low base pressure.) The sterilizable test chamber accommodated four planchets at one time. The supporting hardware (Fig. 4b) shows the flex hose mounted to the vacuum chamber via a pneumatic safety valve, connected to the test assembly which in turn is mounted to the shock test machine. The vacuum pressure was measured at the test assembly by a hot cathode ionization gauge which was connected to the test assembly via a valve so that the tube could be removed at the time of the shock pulse. The shock pulse was measured for permanent record by a microminiature accelerometer, charge amplifier, peak-hold meter, and oscilloscope/camera. The vacuum system used in those tests and in all the biological contamination experiments was a Kinney Vacuum System (Fig. 5). It consisted of a 6 in. diffusion pump (400 ℓ /s) backed by a 0.9 ℓ /s holding pump. The pump down from ambient was done by a (7.1 ℓ /s) Roughing pump. The diffusion pump had both water and LN_2 trapping, with the LN_2 level maintained by a controller. The pressure was measured at several pump locations by thermocouples and the vacuum chamber by an ionization tube, with an identical tube and gauge at the end of the test assembly. Since the testing required reasonably long term durations, a pneumatic safety valve was mounted between the vacuum chamber and test assembly. Since the testing required reasonably long term durations, a pneumatic safety valve was mounted between the vacuum chamber and test assembly to prevent excessive backstreaming in the event of a power failure. The pressure profiles were maintained on both the vacuum chamber and test chamber, a typical run is shown in Fig. 6. The pressure in the test assembly was in high 10^{-6} torr range, whereas the vacuum chamber pressure was at 5×10^{-8} torr. This large difference is due to the low conductance of the 1 in. diameter connection hose.

The procedure for the vacuum shock experiments was to place four planchets into the previous sterilized test assembly, mount it to the shock machine, connect the hose and vacuum pump to a pressure in the 10^{-6} torr range and allow the system to remain under vacuum for varying lengths of time; then close the valve to the test assembly

ionization tube, remove the tube, and shock the assembly. To remove the test assembly, a noninterfering bleed-up technique was required. The turbulent flow conditions can occur during equilibrium balancing of a test chamber [3]. The results of analysis and an attempt to analytically determine bleed-up effect on microbial removal showed that an experimental evaluation was required. To determine the appropriate bleed conditions, the shock test procedure was repeated without imparting a shock impulse and the microbes removed as function of time duration of bleed-up (which was controlled by a precision leak valve; sensitivity 10^{-13} cm³/s at standard atmosphere). It was found that if the time exceeded one-half hour there were virtually no microbes dislodged. Therefore, all shock tests were bleed up to ambient over an hour duration to insure isolation of the removal forces (Fig. 7).

The shock tests measured the percent removal of microorganisms as a function vacuum level duration, the pulse impulse was taken as worst case - 1000 g's (1 millisecond sine pulse). The summarized results of tens of tests are shown in Fig. 8. The removal was shown to be dependent on vacuum level duration and that the removals are not large; these two factors point up that the prediction that the strong capillary forces are in effect as the water at the particle surface is probably still present. It is well known that water vapor can remain in vacuum systems after long pumping [3]. For this reason, future experiments will have to either be longer term (> 200 hours) and/or include a moderate non-interfering thermal bake of the test surface (less than 100 C).

Conclusions from our limited investigations showed that shock impulse removal forces did not present a major removal force thus shock generating spacecraft sequencing events did not present a clear threat as a recontamination mechanism.

1.2.3 Fluid Flow Vacuum Tests

The next potential recontamination event to be simulated was the thruster (attitude control gas jet) firing and its effect on the removal of microorganisms. At various points in a trans-planetary cruise, the thrusters on a spacecraft will fire to modify the trajectory, lock on to earth signals, or stabilize. The analytical evaluation of the effect of a gas jet plume expanding into a vacuum, colliding with particles on a surface, was found to be very difficult without proper experimental data. An experimental program was planned, designed, and performed. A chamber was designed that would accommodate one planchet, be sterilizable, and vacuum compatible. The chamber (Fig. 9) was fabricated from a small stainless steel cylinder with

the central portion bored out. The platchet was placed looking downward and into the vacuum. The test chamber was connected to a filter assembly which trapped microbes moving during a molecular flow condition. The attitude control jet firing was simulated by a rapid pressure excursion controlled by a precision leak valve. To indicate why this analogy and simulation was selected, the topic of free expansion in a vacuum environment is discussed.

The expansion of a gas jet plume in space has been investigated by NASA-Langley [4] and others [5, 6] initially to increase understanding of the lunar landing problems. This work can be directly applied to the same phenomena in interplanetary space since the near surround density is very low relative to the jet plume.

The expansion of a gas jet into the vacuum environment is such that the majority of mass and momentum of the plume are in its center section in which the density decreases along and normal to the centerline axis. The mathematical investigations of this phenomena have led to the following expressions (4):

$$P_s = P_{r_e} \left(\frac{(k+2)}{2} \right) \left(\frac{h}{r_e} \right)^{-2} (\cos \theta)^{k+4} \quad \text{where}$$

$$P_{r_e} = P_o \left(1 + \gamma M_e^2 \right) \left(1 + \frac{\gamma-2}{2} M_e^2 \right)^{-\left(\frac{\gamma}{\gamma-1} \right)}$$

$$k = \frac{\gamma}{\gamma-1} M_e^2 = \frac{\text{exhaust gas kinetic energy}}{\text{exhaust gas internal energy}}$$

where $\gamma = C_1/C_v$ ratio of ideal gas specific heats, M_e = Mach number, h = distance along streamline from nozzle exit, r_e = radial coordinate normal to axis, r_e = nozzle exit radius, θ = streamline inclination angle relative to axis, P_s = static pressure on surface beneath nozzle, P_{r_e} = normal shock recovery pressure at nozzle exist, P_o = nozzle stagnation pressure, and θ_∞ = maximum angle of plume off centerline. See Fig. 10 for the Nozzle Geometry Configuration.

Using the NASA-AMES report on compressible flow, expressions for P_e (pressure at nozzle exit) in terms of P_c (pressure in the jet chamber) were generated [7]. Fig. 11 shows a listing of calculated exit pressures and surface pressures considering nozzle configurations for exit to throat ratios of 10, 100, and 1000 and a chamber pressure of 100 times ambient pressure ($\sim 10^5$ torr). Most attitude control gas jets have a nozzle ratio of 5 to 100; therefore, looking at Fig. 11, this corresponds to a surface pressure rise from interplanetary vacuum, 10^{-16} torr to 2×10^{-2} torr (for 30 degrees off the

centerline and 3.05m from the nozzle exit) for $A_e/a_t = 10$, for $A_e/A_t = 100$ the pressure at the plume impinged surface would rise to 1.7×10^{-4} torr. The analytical predictions of the equations for the flow field of an exhaust plume were shown to correspond very well with experimental studies [5] when the distance from nozzle exit (h) is greater than r_e (i.e., $h > 50 r_e$). It was shown, however, that the approximation does hold to a reasonable extent even for $h \geq 10 r_e$ [4]. Considering the validity of the analysis it can be stated that the experimental technique should follow a procedure whereby the pressure is allowed to rise to levels near 2×10^{-2} torr in varying time durations. One difference in the two events is that the time of the pressure excursion under a jet firing is probably very fast (< 1 s) whereas the laboratory experiment was found to be limited to a 5 second minimum.

The fluid flow experiments procedure was similar to that of the vacuum shock tests except no flex-hose was used with the test assembly being mounted directly to the pneumatic valve; and the force producing system was a precision leak valve with the entrance port parallel to the planchet test surface (see Fig. 9). The experiments were performed determining the percentage of particles removed as a function of vacuum level duration and time duration for the pressure excursion (typical 10^{-5} to 10^{-6} torr to 10^{-2} torr). A characteristic pump down pressure profile and bleed-up, with the pressure measured by an ionization tube or thermocouple, is given in Fig. 12 and 13 respectively. Fig. 14 and 15 show the results of these experiments. In the dependence of the percent microbes removed on the vacuum duration is shown. As expected, the longer the duration the larger the number removed. This is understandable since the adhesive forces are decreasing as the capillary force component is being diminished by desorbing vapors at the particle-surface interface. More positive discussion of this phenomena would be possible if heating of the test surface could be performed on a microbiological non-interference basis. Fig. 15 shows the dependence of the time excursion of the percent removed. The shorter the time the more removed. All runs were done under similar vacuum conditions to accurately isolate the variables. The shorter time duration for the pressure excursion corresponds to a comparatively larger mass rate flow, i.e., \dot{m}/dA where $\dot{m} = dm/dt$. This would imply a large dp/dt , where p is the composite momentum which is imparted to the surface or particles on the surface. This is assuming that for the time domain of interest no significant boundary layer is established at the surface of test planchets. The increasing dp/dt corresponds to an increasing imparted force. This analog is simplistic but of probable validity for free molecular flow regimes.

1.2.4 Conclusion: Biological Contamination Experiments

It can be observed that the particle removal by shock forces are not large as was predicted. This may be due to the still present bound surface water allowing the adhesive force to remain large. The potential recontamination threat presented by shock impulse producing events (bioshield separation, staging, positioning of panels) is not as significant as previously proposed. This is not to preclude the necessity for longer duration vacuum testing.

The effect of the fluid flow forces on microbial removal under a simulated space environment show the importance of attitude control gas jet firing as potential recontamination mechanism. There are critical events during a Mars Landing Mission when this phenomena may present its greatest threat (i.e., at the time of bioshield separation). In considering these results one must evaluate the simple direct approach of simulation and determine how well this approach meets the real case.

2.0 OPTICAL CONTAMINATION

Contamination effects on space-borne optical systems have presented problems that can degrade a mission performance. Optical contamination may be defined as any surface phenomena which causes the incident radiation's optical path to be deviated or intensity attenuated from the design specifications for the optical system. The effects of optical contamination have been observed on Gemini through Apollo, as well as some military programs. The cause stems from several sources: liquid dumps, plume interactions, cryogenic dumps and space thermal vacuum effects on polymeric materials. Most of the past contamination studies have considered optical systems which operate in the ultraviolet and visible sensing region of the spectrum. Discussed herein will be optical contamination for optical systems which will operate in the mid to far infrared. Especially those systems requiring thermal control at cryogenic temperatures. The rationale for such a study is that the previously known second order material effects due to the space thermal-vacuum environment may well become first order considerations. The program objective is, to analytically and experimentally investigate the physical phenomena of optical degradation for cooled space-borne optical sensing systems detecting in the mid to far infrared. Fig. 16 shows flow chart outlining the approach taken and will be discussed in the following sections.

2.1 Analytical Studies

To best evaluate and understand the occurrence and effect of contamination on optical systems (cooled, mid to far infrared) analytical studies were initiated. Considered are the contaminating events that can occur due to the sublimation and outgassing of bonding, sealing, and encapsulating polymeric materials that selectively condense on critical optical surfaces (for temperatures lower than the materials). To do this task, the past studies on space vacuum effects on materials were reviewed. One of the most comprehensive reports (8), investigated the outgassing behavior (i.e., total weight loss and volatile condensables) of some 350 polymeric materials. These experiments were performed under the thermal-vacuum conditions of 125 C and approximately 10^{-6} torr. The total weight loss for the materials tested (at a temperature of 125 C) ranged up to 30 percent for some sealents. The effect of curing conditions was found to be significant with the weight loss decreasing for increasing thermal (> 25 C) duration curing (see Fig. 16) [8,9]. This is due to the various chemical curing mechanisms that are occurring for each specific cure condition. Long term curing cycles or elevated temperatures will minimize the various effects. The sample size has been shown to be important, with thicker samples (greater than 1/2 in. cube) exhibiting long term outgassing [8,9]. In Reference 9, volatile condensable material (VCM) experiments were performed in which the percent of volatile condensable mass collected at 25 C to sample total mass was determined. For most sealents and adhesives the VCM was under two percent with the majority under one percent (see Fig. 17). Information of this type is most significant for optical contamination effects because it is the condensable materials that may cause degradation. To identify the constituents of the VCM and outgassed materials mass spectroscopy and qualitative infrared spectrophotometry were performed. The IR spectral analysis was found to be useful for determining optical effects of these potential contaminants and will be discussed later. Other studies have been performed that determine total weight loss and VCM for thermal vacuum conditions of $< 10^{-7}$ torr and < 200 C with the VCM collectors at 25 C [10].

Consider now the outgassing effects coupled with the phenomena of condensation, nucleation and growth. One of the most important factors in the investigation of optical contamination is the amount of condensable materials that is collected on cooled optical surfaces. This determination depends on differences in the rates of outgassing (evaporation) of materials.

For a pure compound the expression for loss of material by evaporation and/or sublimation is: $W \approx 6 \times 10^{-1} P (M/T)^{1/2}$ where W = rate of evaporation in $\text{kg/m}^{-2}\text{s}^{-1}$, M = molecular weight, T = absolute temperature, $P(T)$ = vapor pressure (in torr), and A , B = constants for each material.

Fig. 19 shows the vapor pressure of pure compounds is a function of its temperature and may be expressed by $\text{Log } P = A - B/T$ or $P = 10^{A-B/T}$. It also points out the obvious that as the temperature is increased, the vapor pressure increases, and similarly the evaporation rate increases. The evaporation rates for silicone polymers (shown in Fig. 20) shows the dependence on temperature as well as molecular weight (given by n - the number of dimethyl-siloxane groups in a molecule). Thus one can see that low molecular weight polymers have a much greater evaporation rate hence the expulsion of low n polymers are first to be observed under thermal vacuum conditions. This effect does not follow directly the above given expression for the rate of evaporation. For polymeric materials composed of various molecular weight molecules it is not simple to estimate the rate of evaporation because of the effects of diffusion of particular molecular species through the bulk material, distribution of stages of curing, and nonideal and non-equilibrium vapor pressures.

The absorption or condensation of the outgassed material onto a cooler surface is a commonly observed phenomena since the high vacuum pumping speeds at pressures $< 10^{-6}$ torr use cryosorption techniques as a standard practice. The build up of molecules on a surface may be expressed by: $N = nt$ (molecules/ m^2) [12] where N = molecules/unit area, n = number of molecules striking a unit surface/unit time, and t = average remaining time. The number of molecules striking a surface 1 m^2 per second is: $n = 3.52 \times 10^2 P (MT)^{-1/2}$ where M = molecular weight, T = absolute temperature (K), P = vapor pressure of material (torr). The average sitting time (t) of a molecule on a specific surface can be expressed by the Frenkel equation: $t = t_0 \exp (Q/RT)$ (12), where $t_0 \approx 10^{-12} - 10^{-14} \text{ s}$ and is related to the lattice vibrations of the solid surface. where: Q = heat of adsorption (J), R = gas constant ($8.314 \times 10^3 \text{ J/Kgmol.K}$ and T = absolute temperature of the surface (K). A listing of some characteristic values for this expression and the significance of cryogenic temperatures for molecular trapping are shown in Fig. 21.

Another approach to the condensation and adsorption phenomena is by surface energy considerations. When a molecule hits a surface three conditions are possible: (1) the molecule may return to the gas phase, (2) it may be trapped in the shallow potential well (minimum for physical adsorption), (3) it may be trapped in the deep potential well (minimum for chemisorption) [13]. The possibility that item (2) is the result of a collision is defined as the condensation coefficient c

and the possibility (3) is the result of a collision is defined as the sticking probability s . The effect of substrate temperature on a c and s is shown in Reference 13. For example, H_2 and Ne gas depositing on glass both show a 30 percent increase in c for a temperature decrease 100 C down to 0 C. Similar quantitative data is not known to exist or be available for polymeric condensable products. However, the overall trend of increasing c and s values for decreasing collector substrate temperatures ($T < 273$ K) are realistic for these materials. Similarly little information can be found describing the nucleation and growth of a polymeric film for temperatures less than 273 K. The experimental program to be discussed in the next section will hopefully help to increase the understanding of these phenomena at least, in particular, for the effect on optical components. However, Muraca [8] has shown that for some materials collected on a cold collector (298 K), they evaporate slowly, and that the weight of material on the cold collector is never stable. This does not apply in general to specific polymeric bonding materials that may have spacecraft application because of the fact that the volatile condensed material which is different from the initial bulk source may polymerize or chemisorb to varying extents.

2.2 Optical Effects

Mid to far infrared optical systems are of two basic types: (1) refractive-utilizing lenses, and (2) reflective-utilizing mirrors. Each approach has its own advantages and disadvantages for each specific sensing application. The performance of an IR system to accurately sense and detect radiation at required levels of sensitivities is a function of the individual system component performances which is shown simply in Fig. 22. Item number one (Fig. 22) lists the transmission of IR radiation through windows or lens of Irtran, Germanium, or other similar materials would be affected by a contaminant build up on the component's surface. Analytically, the transmission may be expressed by:

$$T = \frac{\hat{t}_1 \hat{t}_2 \exp(-i\sigma_1)}{1 + r_2 r_1 \exp(-2i\sigma_1)} \quad [14]$$

where T is the transmittance and $r_1, r_2, \hat{t}_1, \hat{t}_2$ are the Fresnel coefficients at the n_0/n_1 and n_1/n_2 interfaces, $\sigma_1 = [2\pi/\lambda] n_1 t \cos \theta$, is the phase thickness of the film, and λ is the radiation wavelength in vacuum (see Fig. 23) This expression assumes a parallel-sided, isotopic film. For the case of reflective optics, the reflectance is expressed by:

$$R = \frac{r_2 + r_1 \exp(-2i\sigma_1)}{1 + r_2 r_1 \exp(-2i\sigma_1)} \quad \text{For the real case of an}$$

absorbing medium n_1 must be expressed in complex form $n_1 - ik$ where k is the extinction coefficient. From these expressions one can see how the film absorbance characteristics, film thickness, and film morphology play a controlling role. It is difficult however, to analytically compute the specific T and R values for various contaminant films on surfaces because of the many unknown required input factors. Our solution to this problem is an experimental investigation. In addition to transmission and reflection property changes, the presence of a contaminant film, which is probably not planar, will scatter radiation. For a transmitting surface the effect of scattering sites (Fig. 24a) not only reduces further the amount of radiation emergent on opposite side of the lens but also disperses the directionality. For the reflective optics case the effect is enhanced, as shown in Fig. 24b. The reflected radiation will be scattered and absorbed going into the film as well as coming out of the film. This will cause a further reduction in signal intensity and directionality. These factors will present serious stray radiation problems (off-axis inputs, increased detector cross-talk) as well as reductions in resolution and contrast capability for an Infrared System.

To determine the effect of scattering one must know the film-surface characteristics, i.e., film morphology, thickness, and index of refraction. These explicit factors have been found unavailable for specific materials in question, and it appears that an experimental approach is best. The extent of this effect will be further evaluated in the near future.

2.3 Experimental Program

To evaluate optical contamination due to polymeric material thermal vacuum effects two basic experiments were planned. The first would involve photomicroscopic analysis of contaminant build-up. This would be done by first determining the size, thickness, and where possible, composition of the condensed volatile material. Then predict the corresponding optical degradation using analytical analysis developed as a function of optics temperature, bonding material, its temperature, and vacuum level duration. The materials selected for evaluation include single and double component methyl-siloxanes of both the condensation and addition type. These experiments would be done to evaluate the previously discussed transmission loss, scattering increases, and corresponding effect on resolution. It should be pointed out that a computer simulation capability already exists at GE-RESO to predict IR system performance as a function of operational conditions (i.e., selective adsorption, increased detector noise due to thermal loads, etc.).

Type two experiment will be in situ-infrared transmission property measurements. That is, the transmission properties of IR optical materials (Irtran 4, 6, Germanium, and Chalcogenide glass) subjected to a simulated contaminant environment. The transmission properties would be evaluated as a function of the following parameters: optics materials, bonding material, temperature of optics and bonding material, and vacuum level duration. The performance of these experiments would establish directly the effect of contaminant build-up on the transmission properties of IR collection optics, thereby, clarifying the significance of proper materials selection.

To determine the transmission properties of volatile condensable products a vacuum distillation system with a cold trap for collecting VCP was fabricated and utilized. A diagram of this simple system is shown in Fig. 25. Showing the glass assembly connected directly to the Kinney Vacuum System (Fig. 5). The flask connecting the polymeric material was placed in an oil bath to provide the 125 C temperature. The glass valving (Apiezan T lubricant was used) is such that the outgassed material must pass through the tubing connecting the tube in the LN_2 bath and the flask. The VCP would therefore collect in the base of the tube. The LN_2 level was monitored by a controller and the vacuum level by a gauge at the far end of the assembly. This assembly has been used for Methyl phenyl siloxane RTV bonding material and Platinum vinyl siloxane. The procedures used consisted of placing 30 g's of the material chopped in 2 cm pieces (approximately 0.8 cm thick) into a flask after various curing cycles. The first tests were performed with methyl siloxane RTV for both the accelerated cure of 8 hours at 65 C, and the seven day room temperature cure. Each batch of at least 100 g's was mixed the same: dip coat clean petri dishes in a primer and allow to dry, add a given weight of the bonding material along with 0.1 percent curing agent (dibutyl tin dilaurate) and mix thoroughly and separated for different curing. For the Platinum vinyl siloxane it was mixed according to manufacturers directions, separated for a four hour (65C) accelerated cure, and cured at room temperature for seven days.

The results of the initial tests (the program will consist of six to eight different polymeric materials) which remained under vacuum for 24 hours ($\sim 10^{-5}$ torr) showed a 0.5 percent mass loss for the methyl siloxane (accelerated cure). The collected condensable material when first taken out of the LN_2 bath was semi-solid, as it was allowed to warm up (isolated from rest of the system) two liquid phases were observed. Later IR analysis showed this to be water to a large extent which was attributed to the filler used in this RTV. For the vinyl siloxane (accelerated cure) and seven day room temperature, under similar test conditions, smaller amounts of condensable products were collected. There was not a two phase liquid visible. Each sample

was analyzed by Infrared Spectroscopy (Perkin Elmer) and the corresponding spectra are shown in Fig. 26 and 27. The spectra were obtained with the samples at a temperature of 25°C. Plans are being made to adapt the experiment to perform low-temperature IR spectral effect of contaminants absorbing radiation on cooled optical window. The spectra in Fig. 26 shows the large selective absorption for the 9 to 10 micron, 12 to 13, and 14 to 15 micron bands. The samples were run in the pure form with cell absorbance spectrally subtracted out of the results. Fig. 27 shows a similar spectrum in the original absorbance data form for the vinyl siloxane. However, the thickness of film are not the same with the latter being (one half the former) approximately 1 micron. Selective absorption of this type if realized on an operational spaceborne IR optical system would cause serious loss of sensing capability; for example, for Earth's limb measurements the resulting IR output spectra would show false absorptions in the peaks previously discussed.

To assess how significant this selective absorption might be, the size, thickness, and surface state of condensed off-gassed polymeric products must be determined. This would have to be performed in a space simulated ultra-clean vacuum facility. The requirements for such an experimental facility are the following: (1) multi-test capability; (2) thermal control and monitoring (77K to 673K); (3) elimination of synergistic vacuum system contamination; (4) high vacuum pumping to maintain simulation requirements during initial contaminant source outgassing; (5) bakeable for rapid clean-up; (6) ultra-high vacuum capability (cryopanneled); (7) provision for in-situ optical measurements. The design of a system to meet these requirements is shown in Fig. 28. It is a stainless steel chamber approximately 46cm x 46cm x 25.4cm. The rotatable optical specimen mount (which is thermally controlled by strip heater underneath the plate and cryogenics on top of the plate) accommodates four test optical materials. Each specimen can be rotated into the visible or IR optical train as the specific experiment requires. This platform is removable from the chamber and will fit through the entrance port. A detailed view of the optical specimen mount is shown in Fig. 29. Each of the four holders is cryogenically cooled by boring out the center of each holder's sides (as shown). The LN₂ is supplied by a flexible stainless steel hose that will rotate as the whole table is turned. The contaminant source configuration is also graphically shown. The materials will be easy to change as it is placed in a removable boat for each specific experiment.

The walls are cryopaneled (LN₂) with the fin-type panel which has been shown to have the best trapping efficiency. The outside walls have strip heaters attached to facilitate rapid bake-out up to

The thermal excursions that occur at the various locations in the assembly are monitored by Copper-Constantan thermocouples.

There are various support feedthroughs to provide LN_2 , voltage for heaters, and thermocouple connections. The major vacuum pumping will be done by an 30 l/s ion pump (after the base pressure has reached 10^{-5} torr via a diffusion pump). The mating of the test assembly to main vacuum system (see Fig. 30) is by a pneumatic safety valve. This is required between chambers as well as between the test chamber and ion pump to effectively isolate the components in the event of a power failure. The major vacuum systems consists of a 2000 l/s 11 in. diffusion pump, cryotrapped; cryopanelled (LN_2) chamber walls, circular heaters for the main chamber exterior, and a 19 l/s roughing pump. The pressure level is measured by the ion pump controller and by ionization gauges at various locations. The performance of this system with test chamber isolated and cryo-cooled walls after a moderate bake-out of 250 C for four hours is in the high 10^{-8} torr range. The ion pumped test assembly will achieve pressures in the low 10^{-8} torr range with moderate bake-out.

The in-situ optical measurements can be performed for either the visible or IR range of the electromagnetic spectrum. The visible optics investigations are possible through metal-gasketed viewports which are aligned across from each other, with the test specimen being positionable in the viewport field-of-view. The in-situ surface photography utilizes a stereo microscope which is focused outside the chamber on the optical component being tested. A camera is attached to the microscope for a permanent record. The visible light source will be a mercury arc lamp (500 watt) which provides sufficient illumination for low power magnifications. Difficulty has been experienced in gaining sufficient resolution for film thickness determination for the long working distances (~6 inches). This problem is currently being addressed to enable in-situ thickness determination as well as surface morphology definition. As an intermediate approach, microphotographs were taken under ambient conditions of condensed material from methyl siloxane based polymer using the set-up as shown in Fig. 25 by placing glass slide into the tube (discussed in Appendix A). The infrared observations will use specially designed IR viewports (Irtran 6). The radiation source for the infrared (yet to be acquired) will be a precision blackbody radiator, with the detector (also yet to be acquired) being a thermopile.

The vacuum test assembly (Fig. 31) in its present state of development is operational for the surface photography investigations. The infrared transmission experiments will be commenced shortly upon receipt of the IR source and detector.

2.4 Conclusions

An experimental program has been defined and developed to investigate the optical degradation effects due to the thermal vacuum performance of polymeric materials that are used on spacecraft programs. It has been shown analytically that the presence of cold (cryogenic) collection surfaces do enhance the contaminant build-up. In addition, a major degrading effect may be due to the far infrared absorption properties of condensed volatile out-gassed materials. The scattering effects are predicted to cause serious off-axis rejection problems as well as loss of detection sensitivity. From these preliminary investigations, it is apparent that care must be exercised in the selection of a far infrared space-borne optical subsystem bonding materials as the degradation of the resulting contaminating film may severely decrease the signal/noise ratio for an operational optical sensing subsystem and thereby minimize the overall system sensitivity.

ACKNOWLEDGEMENTS

The author wishes to acknowledge the assistance of Dr. A.E. Binks of the Environmental Sciences Laboratory in the area of polymer chemistry and Dr. E.L. G. Odell also of the Environmental Sciences Laboratory in the area of optical physics, Frank Pancoast, Vacuum Technologist in the area of vacuum system fabrication, performance and evaluation, and B. Schein for graphical displays.

APPENDIX A

A.1 Preliminary Photomicroscopic Investigation of Contaminate Build-up

In the contamination collection vacuum assembly, glass slides were placed in the bottom of the collection tube which was submerged in LN_2 . After 24 hours with the polymer material (methyl siloxane) at 125 C. at 10^{-5} torr pressure, the collection tube with the enclosed slide was isolated and removed from the LN_2 . The sample was allowed to warm up under reduced pressure to minimize the ambient vapor condensation effect when it was removed for microscopic investigations. The slide was then removed and analyzed under a reflected light (metallurgical) microscope. This microscope was operated in the 100X to 500X magnification range with the attached camera assembly (Bausch-Lomb L Camera and Polaroid Film Holder)

operating in the 50X to 200X range. The light source was a mercury arc lamp filtered to provide good color match for the film. Some of the first photos taken are shown in Fig. A-1. They show the variation in contaminate morphology. The size of the droplets was determined by a calibration with a precision stage micrometer and the corresponding linear distances are recorded on the figure. The thickness of the condensed material was determined by interference techniques. That is for an index of refraction for the film n_f such that $n_{air} < n_f < n_{glass}$, $2tn = (m + 1/2)\lambda$ for a minimum, $2tn = m\lambda$ for a maximum $m = 0, 1, 2, 3, \dots$. t = thickness. In Plate a) at least 8 fringes can be counted on the large droplet assuming $n_f = 1.4$; $n_{glass} = 1.5$ and $\lambda = 0.45$ microns we get $t = 1.3$ microns with its linear size being approximately 100 microns. Clearly this is a large formation and was not observed in general. The majority of the cases were as shown in c) an agglomerate of smaller particles. It was observed that as the substrate was allowed to remain at ambient, there was a tendency for the droplet to coalesce; however, a continuous film was not observed in the cases of this particular RTV.

REFERENCES

- [1] Enlow, D., "A Physical Study of Microbe Surface Interactions", Re-entry and Environmental Systems Division, General Electric Company, Technical Memorandum 8126-15, October 1967.
- [2] Enlow, D. and Cheater, D., "Experimental Investigations of Microbe Surface Interactions", Re-entry and Environmental Systems Division, General Electric Company, Technical Memorandum 9821-006, February 1970.
- [3] Vacuum Science and Engineering, C.M. Van Atta, McGraw Hill, New York, p. 328-334, 1965.
- [4] Roberts, L., and J.C. South, Jr., "Comments on Exhaust Flow Fluid and Surface Impingement", AIAA Journal, Volume 2, #5, p. 971-973, May 1964.
- [5] Eastman, D., and Radtke, L., "Flow Field of an Exhaust Plume Impinging on a Simulated Lunar Surface", AIAA Journal, Volume 1, #6, p. 1430-1431.
- [6] Sibulkin, M., and Gallaher, W.H., "Far-Field Approximation for a Nozzle Exhausting into a Vacuum", AIAA Journal, Volume 1, #6, p. 1452-1453.

- [7] Equations, Tables and Charts for Compressible Flow, NASA-AMES Report 1135, 1953.
- [8] Muraca, R.F., and Whittick, J.S., "Polymers for Spacecraft Hardware", Final Report, Stanford Research Institute, SRI Project #ASD 5046, September 1967.
- [9] Whipple, C.L., and Curtindale, E.G., "Performance of Silicone Materials in Thermal Vacuum Environments", Trans. 10th National Vacuum Symposium, 1963, p. 63-68, MacMillan Company, New York.
- [10] Poehlmann, H.C., "Vacuum Weight-Loss and Contamination Tests of Some Materials for Space Application", Proceedings of the Fourth International Vacuum Congress, 1968, p. 809-813.
- [11] Vacuum Science and Engineering, C.M. VanAtta, McGraw Hill Publ., 1965, p. 410.
- [12] "ATM Contamination Study Task IV", Final Report Ball Brothers Research Corporation, Report F67-06, March 1967.
- [13] The Physical Basis of Ultrahigh Vacuum, P.A. Redhead, J.P. Hobson, E.V. Kornelsen; Chapman and Hall Publ., London, 1968, p. 59-80.
- [14] Thin Film Phenomena, K.L. Chopra, McGraw Hill Publ., New York, 1969, p. 723-725.

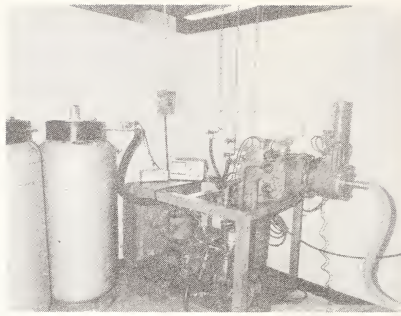


Fig. 5. Kinney Vacuum System

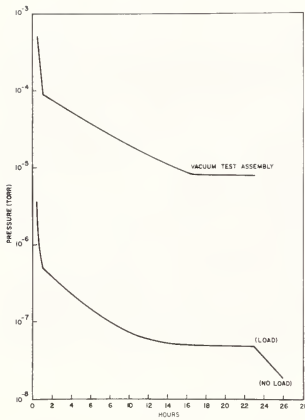


Fig. 6. Typical Pressure Profile

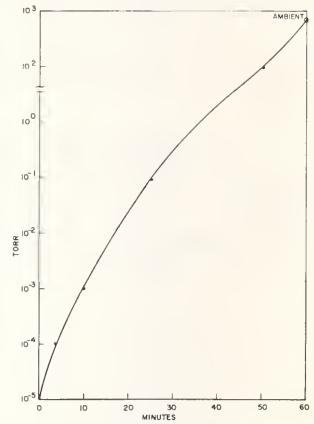


Fig. 7. Shock Test Bleed Rate

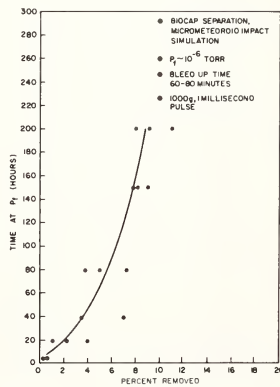


Fig. 8. Shock Test Results

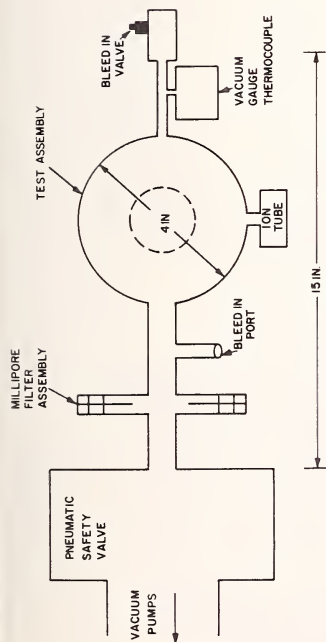


Fig. 9. Fluid Flow Test Chamber (Top View)

NOZZLE RATIO	MACH NUMBER	HEIGHT	ANGLE FROM CL	MAX ANGLE	EXIT PRESSURE	SURFACE PRESSURE
$\frac{A_2}{A_1}$	M_∞	h, ft	ϕ	ϕ_{max}	P_2 TORR	P_1 TORR
10	4	10	30	160	6×10^3	2×10^{-2}
	4	10	0	180	6×10^3	1.3×10^{-1}
100	7	10	30	75	2.5×10^1	1.7×10^{-4}
	7	10	0	75	2.5×10^1	1.2×10^{-2}
1000	18	10	30	45	0.38×10^{-1}	1.4×10^{-16}
	18	10	0	45	0.38×10^{-1}	1.3×10^{-4}

Fig. 11. Summary of Flow Field Calculations

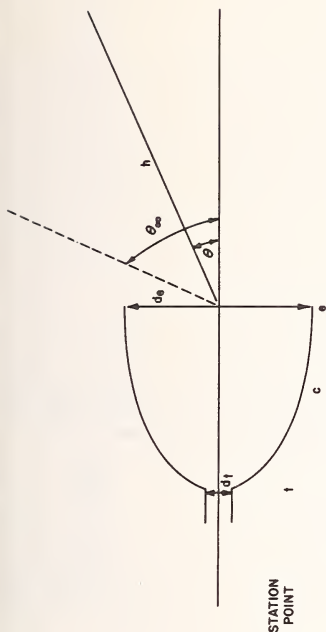


Fig. 10. Nozzle Geometry Configuration

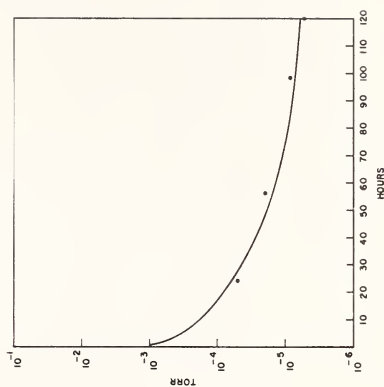


Fig. 12. Pressure Profile (Fluid Flow Tests)

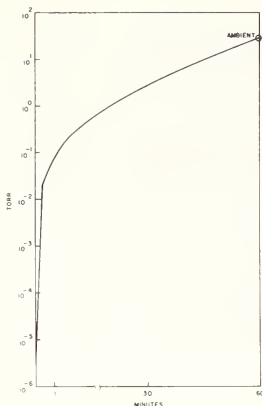


Fig. 13. Typical Bleed Rate

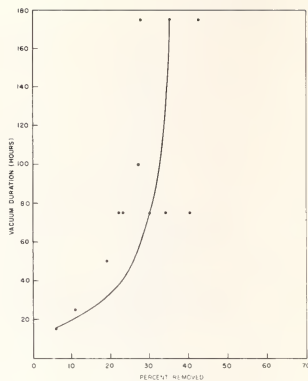


Fig. 14. Fluid Flow: Percent Removed as a Function of Vacuum Duration

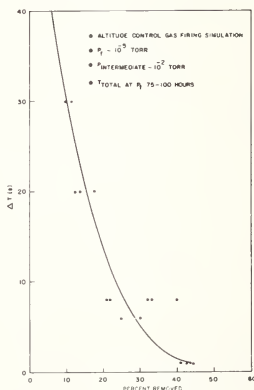


Fig. 15. Fluid Flow: Percent Removed as a Function of Duration of Pressure Excursion (Δt)

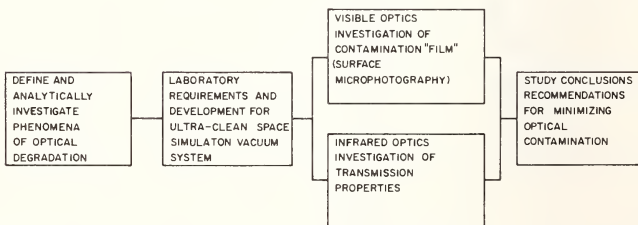


Fig. 16. Approach to Optical Contamination Investigation: Flow Diagram

Fig. 17. Effect of Cure on Vacuum Weight Loss of Sylgard 182 and RTV 501

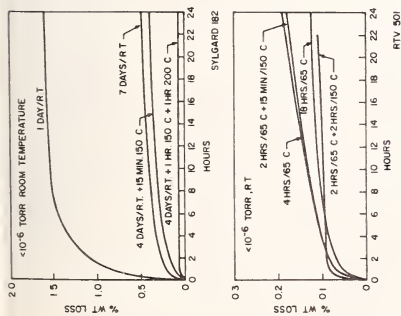


Fig. 18. VCM Data for Sealants

EROXY SCOTCHCAST 260	TREATMENT AS RECEIVED, 30 MIN /150 C	TOTAL MASS LOSS 0.32	VCM MASS % 0.03
SILICONE E691-22E (EXPERIMENTAL "CLEANED-UP SYLGARD IB4)	USED AS RECEIVED	0.19	0.04
RTV 60	MANUFACTURING SAMPLE, POSTCURED 24 h /150 C	0.69	0.54
RTV 102	AS RECEIVED, 24 h /25C	5.45	1.63
RTV 560	MANUFACTURING SAMPLE, POSTCURED 24h /150C	1.03	0.68
SYLGARD IB4/CAT	90 PARTS /IB4/10 PART CAT 4 h /65 C	1.77	0.89

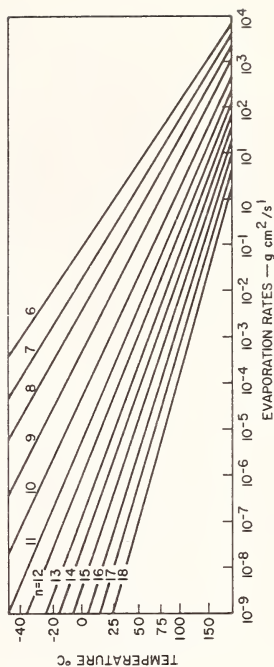


Fig. 20. Evaporation Rates of Silicone [8]

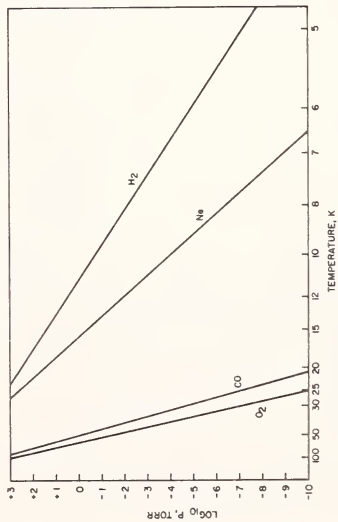


Fig. 19. Vapor Pressure Dependence on Temperature [11]

$t = 10^{-13} \text{ S exp}(Q/RT) \quad R = 8.314 \times 10^{-3} \text{ J/kg mol K}$					
HEAT OF ABSORPTION Q (J/KG MOL)	SITTING TIME (S) SURFACE TEMP 73 K	SITTING TIME (S) SURFACE TEMP 173 K	SITTING TIME (S) SURFACE TEMP 293 K	SITTING TIME (S) SURFACE TEMP 373 K	
4.184×10^5	1.9×10^{-13}	1.4×10^{-13}	1.2×10^{-13}	1.2×10^{-13}	
6.25×10^6	2.2×10^{-9}	1.5×10^{-11}	1.2×10^{-12}	1×10^{-12}	
1.47×10^6	1.2×10^{-7}	1.63×10^{-8}	4×10^{-11}	2.4×10^{-11}	
1.67×10^6	3.5×10^{-3}	1.0×10^{-7}	1×10^{-10}	5.5×10^{-11}	
4.184×10^7	7.3×10^{15}	27	3×10^{-6}	7.2×10^{-7}	
8.368×10^6	5.3×10^{44}	7.3×10^{15}	1×10^2	5	
1.26×10^7	*	*	4×10^9	4.3×10^7	
1.67×10^7	*	*	1×10^{17}	2.6×10^{14}	

NOTE: 1 YEAR = 3.1×10^7 S * MUCH GREATER THAN 1 YEAR

Fig. 21. Setting Time of Molecules on a Surface

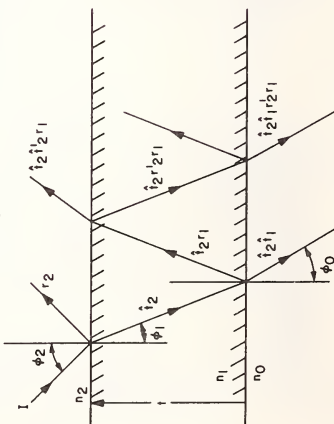


Fig. 23. Thin Film Optical Ray Diagram (INCIDENT LIGHT BEAM (ϕ_0), FILM OF THICKNESS t , r 'S AND t 'S ARE THE FRESNEL COEFFICIENTS)

FUNCTION	COMPONENT	PROPERTIES
(1) COLLECTION OPTICS	LENS, MIRRORS	TRANSMISSION REFLECTION SCATTERING THERMAL STABILITY
(2) RADIATION SELECTION	FILTERS	ABSORPTION THERMAL STABILITY
(3) SIGNAL ENHANCEMENT	AMPLIFIERS	NOISE MINIMIZATION
(4) SENSING	DETECTORS	THERMAL STABILITY
(5) OVERALL SYSTEM		RESOLUTION SENSITIVITY

Fig. 22. IR Optical Components

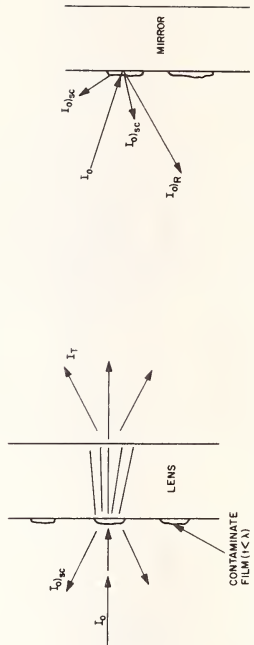


Fig. 24a. Thin Film Scattering for Transmission Optics

Fig. 24b. Thin Film Scattering for Reflective Optics

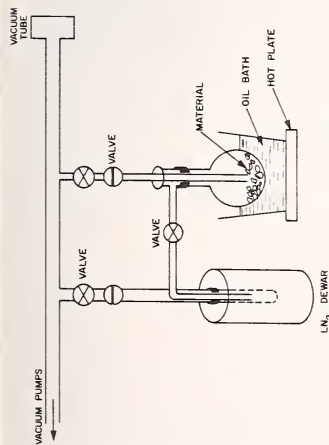


Fig. 25. Condensable Contaminates Collection Vacuum Assembly

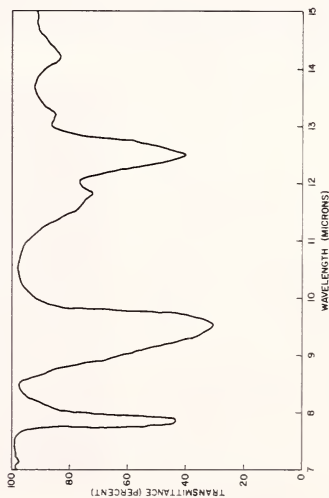


Fig. 27. Infrared Spectrum of Volatile Condensable Products from Platinum Vinyl Siloxane Material

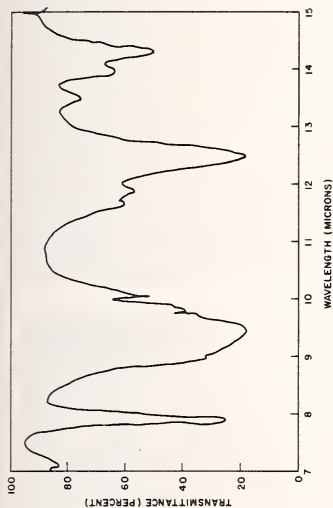


Fig. 26. Infrared Spectrum of Volatile Condensable Products from Methyl Siloxane Material

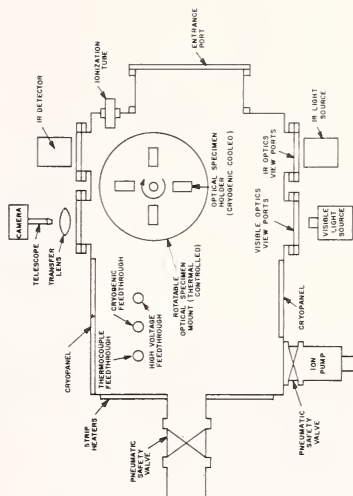


Fig. 28. Optical Contamination Test Assembly

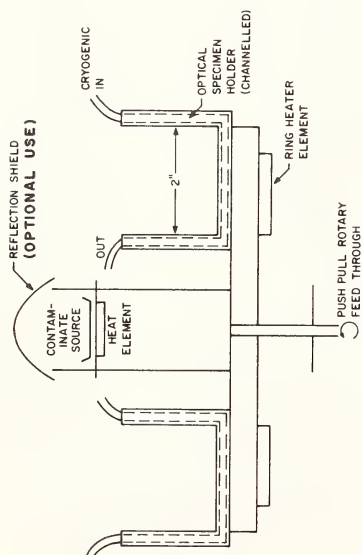


Fig. 29. Optical Specimen Mount

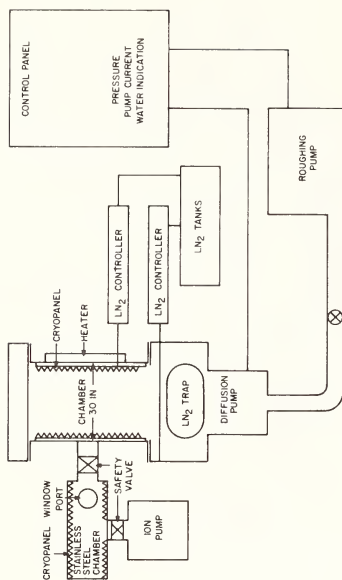


Fig. 30. Optical Degradation Ultra-Clean Vacuum System

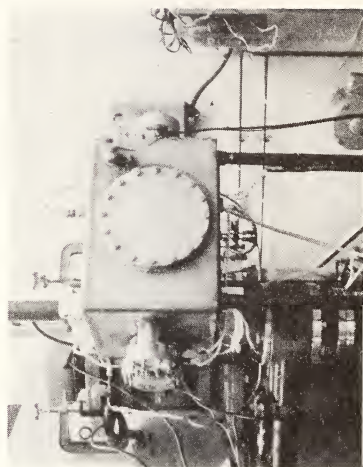
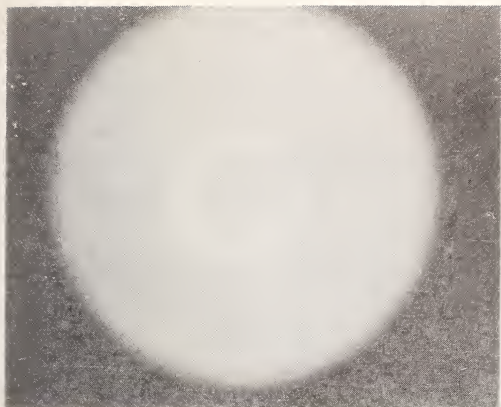
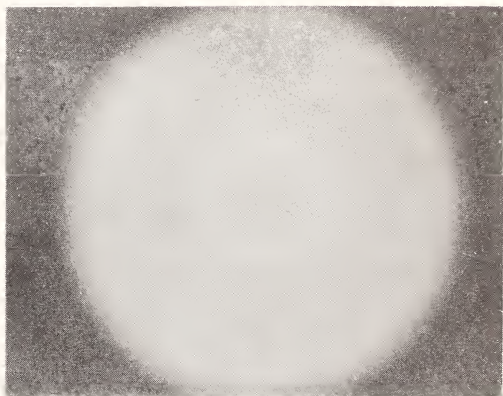


Fig. 31. Optical Test Assembly Photography



a. MAG 185 x
ICM = 55 μ



b. MAG 45 x
ICM = 220 μ



c. MAG 45 x

Fig. A-1. Contaminate Photomicrographs

EXTERNAL SPACECRAFT CONTAMINATION MODELING AND COUNTERMEASURES

Theodore Baurer¹, M. H. Bortner¹, Irwin M. Pikus¹, and
Arnold M. Cooper²

REFERENCE: Baurer, Theodore, Bortner, M. H., Pikus, Irwin M., and Cooper, Arnold M., "External Spacecraft Contamination Modeling and Countermeasures," ASTM/IES/AIAA Space Simulation Conference, 14-16 September 1970.

ABSTRACT: The problem of spacecraft external contamination is a function of both the spacecraft and the receptors, in relation to the natures and quantities of contaminants involved, i.e., the problem depends on both design and mission. The relevant phenomenology may be conceptualized in a model which assumes that a mass-transfer mechanism is operative, including sources, transport modes, and sinks. Typical sources include engine debris, jettisoned wastes, outgassing, and cabin leakage. Gaseous contaminant transport is based on the complex interaction of gas-surface interaction potentials and hydrodynamic, electrostatic, and magnetic fields. Condensed-phase materials are subject to hydrodynamic coupling, induced polarization, and electrostatic field effects. The sink or deposition mechanism assumes differential charge development on conducting (e.g. vehicle skin) and dielectric (e. g. windows, lenses) external surfaces, such as to cause preferential attraction to the latter. The net electrostatic potentials at the dielectric surfaces cause charge neutralization of impinging ions, followed by bonding, scattering, and desorption. Impacting particulates adhere or scatter at the dielectric surface depending on the relative magnitudes of local surface potential, strength of induced dipoles, and particle

¹Space Division, General Electric Company, Philadelphia, Pa.

²Research Dept., Grumman Aerospace Corp., Bethpage, N. Y.

velocity vectors normal to the surface. Flowing and adhering contaminants continually cover the surface, preserving its dielectric nature. This model suggests the applicability of at least three complementary approaches to the problem of counteracting contamination, viz., passive prevention of the appearance of contaminants, active removal measures during the transport of contaminants which do appear, and means of counteracting or discounting the effects of contaminants which complete their transit to sensitive surfaces.

KEY WORDS: contamination, spacecraft, mass transfer

1: INTRODUCTION

The external environmental contamination of manned spacecraft has been recognized as a problem since the actual sighting of contaminant particles was first reported by the early Mercury astronauts (Refs. 1, 2),³ and the origin of these particles as effluents from the vehicle was then shortly confirmed (Ref. 3). Subsequently, similar phenomena were observed photographically on unmanned rockets (Ref. 4) and satellites (Ref. 5). Gaseous environmental contamination was observed as well (Ref. 6).

The implications of a self-generated contaminated environment immediately adjacent to manned or unmanned spacecraft, in terms of its effects upon the ability of men or instruments to perform scientific missions in space, were explored analytically three years ago (Refs. 7-9). However, in the absence of definitive experimental verification, the results of these early analyses were inconclusive. Indeed, a specific item of experience brought into these considerations (Ref. 7), viz., the reported inability of the astronauts to see stars in the daytime, was attributed elsewhere (Ref. 10) to factors having more to do with human ocular adaptability to varying background luminance than with any effects of the spacecraft environment.

The whole problem came into fresh focus with the well-publicized window contamination observed on Gemini spacecraft (Ref. 11). Specific experiments (Ref. 12) carried out in conjunction with the later Gemini missions, and involving exposures to the space environments of test coupons, reaffirmed the gravity of the situation. Still more recent experience under the Apollo program (Ref. 13) has

³The numbers in parentheses refer to the list of references appended to this paper.

tended to reinforce the general concern over contamination.

It is now well recognized that, whereas certain manned and unmanned satellite-based experiments projected for this and later decades have as their primary objective the observation and measurement of radiation emanating from solar, stellar, and other non-terrestrial sources, unimpeded by atmospheric absorption, this aim now faces the possibility of severe compromise. Specific dangers arising from the presence of external contaminants include: (1) the development about the experimental vehicle of its own localized "atmosphere" comprising off-gas and cabin leakage products, human and fuel cell wastes, and engine effluent particles and gases; (2) the deposition and adhesion of both particulate matter and gaseous condensates from this "atmosphere" upon sensitive optical, thermal-control, solar cell, and other external surfaces; and (3) the interference, through light absorption and scattering, with signal reception aboard the spacecraft, owing to the passage of gaseous and particulate contaminants across optical paths. These effects, if permitted to proceed unchecked, would tend to destroy the very basis of the several experimental packages now projected, by virtue of both the presence of undetermined foreign matter in the respective optical fields, and the actual fouling of the receptor elements themselves.

The present concern is with the reduction of the external spacecraft contamination phenomenology to a model which assumes that the mechanism is essentially one of mass transfer, including sources, transport modes, and sinks. This model, which is based insofar as possible upon information available from the NASA manned space-flight program, serves in turn as the basis for the consideration of countercontamination concepts.

2: THE MODEL: DEVELOPMENT

As indicated above, the GE/SSL effort to model the external contamination phenomenology of spacecraft has been based on the simple concept that the entire process is an example of classical mass transfer, under highly specialized conditions. The practical approach to modeling, based on this concept, has comprised preliminary definition of the specific sources of contaminant materials insofar as they are known, followed by the attempted description of probable transport modes, and identification of the sink or deposition mechanisms, while relating the totality of these efforts to actual experience, as derived from chemical analyses of contaminant deposits returned from space.

2.1: CHEMICAL COMPOSITION AND SOURCES OF CONTAMINANTS

2.1.1: GEMINI

The results of semi-quantitative emission-spectrographic chemical analyses (Ref. 13) of window contaminant material from manned Gemini (GT4-7, 9-12) space capsules were examined (Ref. 14), and an estimate of the percent of each element was derived therefrom. These estimates are presented in Table 1. A number of possible sources of Gemini window contamination were examined critically (Ref. 14), and their probable importance was evaluated. This information is also contained in Table 1.

While several relatively unimportant constituents of the window deposits may not be fully accounted for, such elements contribute no more than 2.5% by mass to the overall contamination analyses, while the others are attributed in Table 1 to just five major sources, viz., the throat ablator, propellant impurities, waste dumps, window seals, and the sea. Needless to say, while the sea may be accountable as a partial source of the deposit material as analyzed, it certainly is not a source of anything in space.

2.1.2: APOLLO

The available analytical data relating to contaminant composition on the Apollo windows were compared (Ref. 14) with the corresponding information elucidated with respect to the Gemini missions. In this effort, analytical data were obtained for several unmanned flights (I-IV and VI), not all of which were orbital missions, and one manned flight (XI).

Table 2 presents a summary of the analytical data from the flights enumerated above, along with presumptive sources, as deduced by NASA/MSC personnel (Ref. 13), which apply only to the five unmanned flights. These sources are of interest, inasmuch as they coincide, to a degree, with the conclusions expressed above, with respect to Gemini. One additional major source is listed, viz., the launch escape system (LES), and the launch escape tower (LET) components, which had not been considered in evaluating the Gemini deposits.

The Apollo XI analyses in Table 2 roughly parallel those of Apollo II-IV, which were unmanned orbiting or high-heat reentry vehicles. Thus, the residual contaminants found on the windows of both manned and unmanned orbiting spacecraft may have come from the same sources. However, those contaminants which may have impacted the windows and bounced away, or which may have washed away on splashdown, could have had other sources, e.g. waste dumps, propellant impurities.

An important distinction which must be drawn in comparing Gemini and Apollo is to be found in the different number (two and five, respectively) and disposition of windows in the two vehicles. The Apollo window configuration comprises the hatch window situated in the middle, two flanking rendezvous windows, and two outlying side windows. Of these, the hatch and side windows are flush with the conical vehicle surface and are reputedly the most vulnerable to contamination in flight; the rendezvous windows are inset facing the apex of the cone, i.e., in a forward flight direction, and have remained relatively clean.

2.1.3: PASSIVE PREVENTIVE MEASURES AT THE SOURCE

The above discussion and those of Ref. 14 relate to a variety of conceivable contaminant sources, the importance of which is a function of both the operational characteristics of a spacecraft and its mission. For example, where deposition largely of a siliceous nature (Table 1) was markedly noted upon the Gemini windows (Ref. 11) and upon test coupons (Ref. 12), it appears that such gross sources as the phenolic-Refrasil ablatively-cooled attitude-control thrusters and silicone-based window sealants were among the probable primary sources of the visual interference noted by the astronauts. Those lesser sources such as surface outgassing and cabin leakage which may have produced as much as 2-3% of the contaminant mass were relatively less important within the context of these missions. On the other hand, the optical surfaces associated with projected flights of space experiments such as the Apollo Telescope Mount (ATM) cluster are likely to be much more sensitive than were the Gemini windows to minor forms of contamination. Therefore, every conceivable source of foreign matter must be regarded, a priori, as a potential threat to the latter type of mission.

It is tempting, having identified the principal contaminants, and their major and minor sources, to cast about in an effort to find means of suppressing the contaminants at the source by the application of control measures which are essentially passive in nature. Table 3 lists the passive measures which might be utilized in efforts to control contamination in space at the source. Some of the remedies suggested in Table 3 appear to be relatively easy to implement, e.g. cleaning up the engine fuels, modifying the waste handling procedures. Others would require major vehicle redesigns, e.g. substituting radiatively for ablatively cooled engines, retaining window and lens coverage until well after LET jettison. Still others require extensive materials searches, evaluations, and trade-off studies, e.g. for

new window sealants and for the several minor external surfaces listed.

In the case of the window sealants, a change in procedure, viz., the introduction of a pre-launch bakeout, and the substitution of a newer, less volatile silicone product, have been credited (Refs. 13, 16) with a partial improvement in the contaminant picture as regards silicon. However, still further improvement is possible, and it has been argued (Ref. 17) that the utilization of Viton, a synthetic fluorinated heat-molded elastomer, in place of the silicones, could be expected to eliminate or strongly reduce this aspect of the contamination problem. This is based on cumulative experience with Viton as a laboratory vacuum seal, and as a test substance in materials degradation experiments (Ref. 17).

As for the concept of passive controls generally, and notwithstanding the worth of some of the remedial approaches suggested in Table 3, or discussed above in relation to window sealants, it does seem evident that the number of conceivable sources, for unwanted matter capable of condensing on windows and optical surfaces, is so great, and their variety is so diverse, as virtually to preclude the successful application of passive control techniques at every single source. Accordingly, it is suggested that no reliance be placed at this time on passive control as an overall remedial measure or cure-all for the contamination problem. At best, this type of technique may be relied upon to reduce somewhat the level of contaminant emissions at the source, but not necessarily to the point of threshold tolerance by experimental instruments whose protection is of utmost importance to a given space mission.

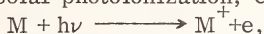
2.2: TRANSPORT OF CONTAMINANTS

The transport of gaseous contaminant matter is dependent upon the superposition of thermal and photoionization processes upon the ambient flowfields, followed by the complex interaction of gas-surface interaction potentials and hydrodynamic, electrostatic, and magnetic field effects. Particulate matter is dependent for transport on phase equilibration followed by hydrodynamic coupling, induced polarization, and electrostatic field effects. Thus, the number and variety of forces involved are such that the complete quantitative definition of these processes is very difficult. However, certain aspects of the transport mechanisms for gaseous and particulate contaminants have been examined individually (Ref. 14). They include the ionization and field interactions of gases, and the two-phase flow and interactions of solids, and will be summarized here.

2.2.1: IONIZATION OF GASEOUS METAL ATOMS

The transport of gaseous contaminants, e.g. metal vapors, is dependent upon their ionization prior to electrostatic field interaction with the charged surface of the vehicle. A variety of ionization mechanisms may be postulated with respect to the metallic constituents found in Gemini and Apollo window deposits. The most obvious of these mechanisms include:

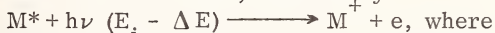
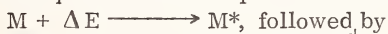
- a. Direct solar photoionization, e.g.



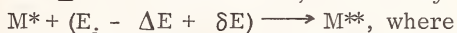
where M represents a metal atom and $h\nu$ a photon of appropriate energy.

- b. Thermal ionization, e.g. in the course of OAMS or other engine combustion processes.

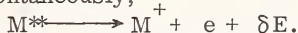
- c. Indirect solar photoionization, e.g. via metastable-state formation and subsequent solar-flux photoionization:



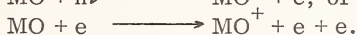
M^* is the metastable state into which quantities of M are first pumped, and having an energy ΔE above that of the ground-state M; or via metastable-state formation and subsequent autoionization:



δE is a small increment of energy representing the difference in ionization limits between two different state series available to M, and M^{**} is M in the limiting state for one (the higher) of the two series, then spontaneously,



- d. Metallic vaporization as the oxide, either in the original emission, via oxidation in the vehicle environment, or on the surface after deposition; followed by ionization of the gaseous oxide, e.g.



It was concluded (Ref. 14) that, pending further experimental investigation, none of these processes appear to be important, and that the metallic constituents reported in spacecraft window deposits probably arrived in condensed form, as solid particles or liquid droplets, and not in the gas phase.

2.2.2: FIELD INTERACTIONS RELEVANT TO THE TRANSPORT OF IONIZED GASEOUS CONTAMINANTS

Significant quantities of ionized gases are nevertheless present

in the vehicle flowfield, e.g. ambient ionic species such as O^+ . Aside from purely hydrodynamic considerations such as were treated in Ref. 8, other forces appear to play a possibly significant role in determining the transport modes of gaseous contaminant ions. These include the forces arising from ionic interactions with local electrostatic fields, and to a lesser extent with the earth's magnetic field.

The development of a surface electrostatic charge upon conducting surfaces of the vehicle (Refs. 18-27) may arise from:

a. The transfer of positive charge to the surface, e.g. through trapping of ions and by Auger emission of electrons;

b. Electron ejection through the absorption by a sunlit surface of sufficiently energetic photons; and

c. Subsidiary mechanisms, e.g. motion of the vehicle through the earth's magnetic field which gives rise to an effective electric field in the vehicle's coordinate system, and the operation of electrical equipment inside the vehicle which can produce a change of surface charge state if there is a conducting path to the surface.

The field produced about the vehicle by the charge upon its surface is weakened and distorted by the flowing plasma environment. The details of this problem have been considered for a number of years (Refs. 28, 29). Even assuming that the charge on the vehicle is uniform or that the vehicle is an equipotential surface, the field in the vicinity of the vehicle is not easily described. The principal features of these results which seem applicable to the problem are the following: The negative charge on the front of the vehicle is well shielded by the incoming positive ions. Toward the rear, however, the potential is much less effectively screened. Furthermore, there is significant distortion of the field caused by the effect of the earth's magnetic field on the surface charge distribution.

It was concluded (Ref. 14) that, with respect to the transport of contaminant gaseous ions through an electrostatic mechanism:

a. Significant charge differences can be established between dielectric and conducting surfaces.

b. Windows facing out of the flow, especially those facing rearward, probably achieve the most negative potentials on the spacecraft.

c. Thruster firing not only supplies new contaminant material but also changes the charge state of the vehicle at least during the firing period.

2.2.3: THE TRANSPORT OF CONDENSED-PHASE CONTAMINANTS

The forces under which solid and liquid contaminant material acts include:

a. Those due to the ambient conditions, e.g. aerodynamic drag, radiation pressure, solar wind, and interactions with the space magneto-plasma (Refs. 8, 30).

b. Those due to plume interactions, e.g. two-phase coupling (Ref. 31).

c. Those due to the presence of the vehicle, e.g. the electrostatic force arising from the existence of charge upon the vehicle surface, and charged contaminant material.

The ambient forces were found (Ref. 14) to be negligible in comparison with the other effects considered.

The problem of purely gaseous plume interactions is not understood sufficiently well for the purposes of impingement predictions. A purely continuum formulation of plume expansion would provide a solution which would obtain in the vicinity of the gas exit port. However, far from the exit any continuum formulation breaks down since the mean free path of the molecules in the plume increases downstream, while the length scale associated with the spatial gradients of the flowfield, as predicted by the continuum solution, is scaled by the exit diameter. That is to say, far from the source, situations exist for which the local mean free path is comparable in magnitude to the scale of the local flow gradients. Then the molecular distribution function can no longer be near equilibrium, and any continuum formulation breaks down, necessitating recourse to a kinetic formulation.

In recent years there has been substantial progress in understanding rarefaction effects in underexpanded free jets. However, this progress has been concentrated in the vicinity of the plume axis where the basic symmetry of the flow enables an accurate modeling of the plume by a supersonic spherical source expansion (Ref. 32). Utilizing the spherical source model, numerous theoretical studies (Refs. 33-35) have provided predictions of the nature and location of the rarefaction effects in the centerline region. These studies have been for pure monatomic and polyatomic gases and for binary gas mixtures.

The problem of predicting particle migration in the plume flowfield is more formidable in that the general case presents an extremely complicated coupled two-phase flow. The nature of the resultant flowfield is dependent upon a number of fundamental parameters, e.g. the size distribution of particles, the concentration field at the exit, and the average mass density ratio of particles to gas. This last parameter determines the nature and degree of coupling between gas and the particles in an overall sense. The details of particle size distribution are necessary to determine the distribution of this coupling over the particle size distribution.

There are basically two coupling situations which are important

in gas-particle plumes, viz., strong and weak coupling. Strong coupling occurs when the mass densities of the two phases are comparable and the resulting flow is such that the gas and particle characteristics are dependent upon each other. Weak coupling occurs when the particle loading is very low. In this case the gas-phase characteristics are independent of the particle phase, but the particle-phase characteristics are determined by interaction with the gas phase. The weakly coupled case is, of course, the more convenient for calculation since the gas flowfield can be determined independently and can then be utilized to produce the required particle field.

Finally, a preliminary examination of electrostatic effects between a vehicle and a charged droplet was undertaken (Ref. 14) because of the importance of droplets in window contamination on spacecraft. The mechanism proposed for the interaction involved summing the coulombic forces between charges on the vehicle and the droplet, and the forces between the vehicle and an induced dipole moment on the droplet. In order to compute these forces it is necessary to know the vehicle charge, and the charge and polarizability of the droplet. The latter problem is one of considerable difficulty since the chemical composition of the droplet is essentially unknown, the physical state is unknown, the equilibrium charge on a small droplet cannot be extrapolated from the calculation of vehicle charge because of the differences in composition and size, and the effective polarizabilities of mixed-phase (solid and liquid) droplets of various geometries and compositions are not available nor easily computed. Model calculations of the interaction can, however, be made by first assuming values of the necessary properties.

2.2.4: ACTIVE PREVENTIVE MEASURES IN TRANSPORT

It is implicit in the concept of ionized gases, polarized liquids, and charged solids traveling in predictable trajectories defined by known or readily estimated force fields, that the magnitudes and directions of artificially imposed counterforces which would comprise the basis of active countercontamination measures are at least calculable. Whether such measures are also realizable in terms of actual devices has yet to be determined. However, despite the lack of demonstrated feasibility of such devices at this time, it is nevertheless possible to indicate several general principles upon which they might be based, such as to implement the general idea of force-counterforce measures. These principles include: outright expulsion from the total spacecraft environment, deflection

to nonsensitive surfaces comprising integral parts of the vehicle structure, deflection to sacrificial surfaces deliberately added to the spacecraft, and trapping upon grids or other special filtering devices imposed across the contaminant paths. Each of these approaches offers the potential of providing a credible means of countercontaminant control; Their further analytical and experimental development is strongly recommended.

2.3: DEPOSITION OF CONTAMINANTS

The sink or deposition mechanism assumes differential charge development, with the resultant generation of surface currents, on different external surfaces of the vehicle, i.e., the conducting vehicle skin vs. the essentially dielectric functional areas, e.g. windows, lenses, thermal-control coatings. The resulting net electrostatic potentials at the dielectric surfaces may cause charge neutralization of impinging gaseous ions, followed alternatively by physical and chemical bonding, scattering, and desorption phenomena. Charged particles and polarized droplets impacting the vehicle adhere or scatter depending on the relative magnitudes of the local surface potential, the strength of induced dipoles, and the particle velocity vectors normal to the surface. Some of the factors affecting this phenomenology were examined (Ref. 14).

2.3.1: CONTAMINANT-SURFACE ENCOUNTERS

Contaminant material, in atomic or molecular form, originating at the spacecraft, may encounter the vehicle surface even in the absence of a long-range attractive force. Its speed at encounter depends upon its initial thermodynamic state and the degree to which it has thermalized in the ambient medium.

Gas-surface interactions have been investigated (Refs. 36-38) where the surface was metallic and the gas was a monatomic or diatomic species. A marked dependence of capture probability upon surface temperature has been found, in addition to the expected dependence on molecular velocity (Refs. 36, 38). Studies of the trapping of gas on an impure surface have indicated that the coupling between impurity and substrate is very important. For certain combinations of molecule and surface species the interaction potential at encounter is of dominant importance (Ref. 37). In such chemisorption interactions it frequently has been found that there exist a number of binding states between molecule and surface. Sometimes the adsorbed molecule has sufficient mobility to travel

along the surface until it meets a location even more favorable energetically. In certain cases it is expected that the trapped molecule will react at the surface, either dissociating or combining with other surface species, to form new structures.

The impingement of contaminant particles on spacecraft surfaces is predicted from considerations of contaminant transport, and the prediction is confirmed by observations. Particles generally are expected to impinge at relatively low speeds. Thus, the trapping of particles is highly probable. Solid particles, even at low speeds, can produce surface damage, i.e., defects in surface structure, before coming to rest. Liquid droplets may spread out over a considerable portion of the surface or may remain as globules. This is determined by the relative importance of surface tension of the droplet and forces of interaction with the surface. The tendency for small droplets to coalesce into larger ones, and the likely distribution of droplet sizes on the surface, are also determined by these factors.

Interaction modes between trapped particulates and the surface material include chemical bonding and surface alloying. However, even in the absence of these very strong interactions, other modes of interaction exist. In particular, Vander Waals forces, which are relatively long-range on an atomic scale, and electrostatic (or double-layer) forces are important (Ref. 39). These can give rise to trapping of the solid particles and to the viscous creeping of liquid droplets, leading to their gradual spread over the surface.

2.3.2: CONTAMINANT-SURFACE BONDING

It is necessary to take account here of the competing forces which may cause on the one hand, bonding or sticking, or alternatively, reflection or scattering, of positive ions approaching a negatively-charged dielectric surface. A rigorous solution of the problem is precluded at this time. Furthermore, virtually all the previous efforts in this area have been concerned with gas-surface bonding. Therefore the subject of bonding between condensed-phase contaminants and spacecraft surfaces has not been considered, beyond the few remarks on interaction modes which concluded the previous paragraph.

The interaction of fast gaseous species, both neutral and charged, impinging on solid surfaces, has been a matter of concern for some years (Refs. 38, 40-43). The experimental approach has been based largely on the results of molecular and atomic beam testing. A second area of phenomenology bearing on the gas-surface interaction problem is that arising from studies of sorption, both

physical and chemical (Refs. 38,44). However, much of the work in this area deals essentially with equilibrated systems, and hence is of limited applicability to the present problem. On the other hand, the results of these investigations do shed some light on the nature of bound states resulting from dynamic encounters.

A number of analytical approaches to the problem have been reported as well. For example, one model assumed simple, classical "hard-cube" scattering (Ref. 45), which in one version (Ref. 38, p. 392) was treated in conjunction with an increasingly detailed lattice model of the solid, such as to project possible generalizations to quantum interaction models. This model was succeeded by a more sophisticated concept based on exponential interaction between a gas atom and a single one-dimensional oscillator, at a flat surface assumed to consist of "soft-cube" atoms (Ref. 46).

Another classical approach was based on lattice dynamics. This treated a two-dimensional independent - oscillator lattice, with harmonic potentials connecting the lattice sites, and Morse-type potential functions operating between the incident gaseous atom and each lattice atom (Ref. 47). The model was subsequently expanded to a three-dimensional independent-oscillator lattice; nine movable lattice sites were each connected both to the incident gas atom by a Morse potential, and to fixed lattice points by harmonic springs (Ref. 48).

One further modeling concept (Ref. 37) considers, as a first approximation, a triangular interaction potential with impulsive energy transfer in a rigid-spheres high-speed head-on collision, after the attractive potential has acted. Here, the target atom is coupled to the solid through an effective spring constant, and the lattice model is assumed to be two-dimensional in depth, i. e., straight down into the solid, rather than in breadth, i. e., across the surface of the solid, as in other models (cf. Ref. 47). Three-dimensionalization was contemplated in a projected extension of this study (Ref. 37), which unfortunately was not completed. This was to have included considerations of off-center, as well as head-on, collisions.

With regard to all the lines of investigation reviewed above, they all are concerned with crystalline solid surfaces. Thus their applicability to interaction systems involving glassy surfaces is very much open to question. In the present area of concern, the stress is upon the latter type of surface, as exemplified primarily by the spacecraft windows. A second significant limitation of the current state of the art is the emphasis upon neutral gaseous atoms as the colliding species. The problem presently under consideration involves the impingement of gaseous ions. Thus most of the previous

experimental and analytical work in gas-solid interactions is only marginally applicable to the current area of interest.

2.3.3: REMEDIAL MEASURES AT THE POINT OF DEPOSITION

By contrast with the passive and active preventive measures suggested above for implementation, respectively, at the source and in transport, many of the countercontamination procedures which might be brought into operation at the point of deposition would more likely be compensatory or remedial in nature.

For example, a totally permissive approach to countercontamination would be one in which the amount of deposit accumulated upon a given window or lens was routinely monitored up to some limit of acceptable performance loss, after which remedial procedures would be undertaken. These might include cleaning of the affected surfaces, either by some mechanism controlled from within the spacecraft, e.g. using an external N_2 - methanol jet (Ref. 16), or during extra-vehicular activity (EVA) by an astronaut. Or contaminated optical components might be replaced by retracting the instrument within the vehicle for overhaul. By the same token, a temporary flux of contaminant gases passing through a given optical path might be deemed tolerable if the extent of light absorption and/or scattering caused thereby did not exceed some acceptable noise level. If such a limit were exceeded, observation via the affected light path would be shut down for the duration of the contamination episode.

On the other hand, a preventive-permissive approach would involve advance knowledge of major contaminating events, e.g. engine firings, waste dumps, plus advance calculation of the resulting contaminant trajectories. Then all sensitive surfaces likely to be affected could be shut down temporarily, i.e., protected by retractable covers, or drawn within protective housings or the spacecraft itself. This would last until normal operations could be resumed safely, according to the indications of strategically emplaced monitoring instruments. Minor (and unpredictable) contaminating events, e.g. the loss of surface material by outgassing or upon micrometeorite impact, would then be treated in a totally permissive manner.

The difficulty with adopting a strategy of tolerance and/or remedial treatment after the fact is that in a large and complex future spacecraft, many potentially contaminating events are likely to be occurring simultaneously. Hence the problem of predicting the total contaminant flux at any one point and at all times is likely to become rather involved. Furthermore, the time that a given sensitive element spends out of service may be excessive. Likewise, a commitment to the totally permissive approach may turn out to

require unacceptable levels of "down-time" for cleaning or replacement of contaminated sensitive surfaces, and corresponding onerous burdens on logistics systems responsible for supplying the necessary cleaning materials or replacement optics.

3: THE MODEL: SUMMARY AND CONCLUSION

A conceptual model has been tentatively developed to describe the phenomenology of spacecraft external contamination. This model is based on the processes classically involved in mass transfer, i.e., sources, transport modes, and sinks or deposition points.

3.1: SOURCE MECHANISMS

The primary contaminant sources arise from engine firings, waste dumps, and flowing or outgassing window sealants. Secondary sources include outgassing paints, solders, and other structural surface materials, and leakage from the spacecraft interior. These may be summarized as follows:

- a. Engine firings (e.g. OAMS, RCS, LES, SPS)
 - (1) Propellant impurities
 - (2) Ablation products
 - (3) Ablator impurities
 - (4) Combustion products and intermediates
 - (5) Nozzle and explosive-bolt materials
- b. Jettisoned wastes
 - (1) Human and animal excreta
 - (2) Fuel-cell effluents
- c. Window mounting materials
 - (1) Sealants
 - (2) Gaskets
 - (3) Insulation
 - (4) Grommets, brackets
- d. Outgassing of vehicle surfaces
 - (1) Structural components, e.g. LET, structural ablators
 - (2) Paints and lacquers
 - (3) Sealants and binders
 - (4) Flanges and gaskets, e.g. cork liners, docking flanges
 - (5) Wire, solders, weldments
- e. Cabin atmosphere leakage and venting
 - (1) "Normal" cabin atmosphere
 - (2) Cabin interior contaminants

3.2: TRANSPORT MECHANISMS

a. Regarding the transport of gaseous matter:

(1) Uncharged gaseous metal atoms emitted in the ground electronic state undergo neither thermal nor photoionization to any significant extent and are therefore unrelated to window contamination, but may be responsible for absorption and scattering of light in the optical paths of instruments in space.

(2) Uncharged gaseous metal atoms emitted in excited electronic states may be capable of photoionization or autoionization in the solar flux, especially if the states concerned are metastable; otherwise, they are more likely to return to the ground state, with the loss of a photon. Those ions which may be formed in this manner would be subject to the effects of electrostatic fields originating on the spacecraft surface itself.

(3) Gaseous metal oxides may be subject to photodissociation in the solar flux; in some instances, this may produce metastable-state metal atoms. In no case, however, are ionized gaseous metallic oxides important components of the contaminant flux.

(4) Significant charge differences can be established between dielectric and conducting surfaces on the spacecraft, which may affect the transport of ionized gases.

(5) Dielectric surfaces facing out of the flow, especially those facing rearward, probably achieve the most negative potentials, of the order of -10 to -15 volts, on the spacecraft.

(6) The firing of thrusters changes the charge state of the vehicle for at least the duration of the firing period.

(7) The net transport motion of gaseous ions with respect to the spacecraft is a highly complex aggregate function of hydrodynamic forces characterizing the vehicle flow field, a gas-surface interaction potential, the superimposed electrostatic field potential, and possibly forces arising from interaction with the earth's magnetic field.

b. Regarding the transport of particulate matter:

(1) The metallic constituents reported analytically among Gemini and Apollo window deposits probably were transported there by entrainment within, or as an integral part of, particulate contaminants.

(2) Liquid matter, e.g. as droplets, undergoes phase equilibration with respect to the corresponding solid and gaseous states of the substances concerned.

(3) Solid matter in two-phase flow is coupled hydrodynamically to the enveloping gas; this coupling may be strong or weak, depending on the relative mass densities of the two interacting phases.

(4) Therefore the net transport motion of particles with respect to the spacecraft is determined either by interactions between roughly equivalent mass densities of the two phases (strong coupling), or by significant dependence of the particle flow upon a dominant gaseous flowfield (weak coupling).

(5) Particles approaching the spacecraft may undergo an induced polarization effect, regardless of their net charge, by electrostatic interaction with the vehicle; if this happens, the resulting field effects are superimposed upon the purely hydrodynamic effects.

3.3: DEPOSITION MECHANISMS

a. To recapitulate pertinent aspects regarding electrostatic attraction:

(1) A net negative charge develops on the vehicle surfaces, both conducting and nonconducting; magnitudes of the potentials on nonconducting surfaces are dependent on their orientation with respect to the flow, but are greatest (of the order of -10 volts or more) on rearward-facing areas.

(2) The charge state of the vehicle is affected by thruster firing.

(3) Currents are generated through conducting surfaces by virtue of potential gradients.

(4) Gaseous ions are attracted electrostatically to the vehicle, and especially to sideward or rearward-facing dielectric surfaces.

(5) Particles carried toward the vehicle by flowfield coupling to the gaseous envelope may be subject to induced polarization, with subsequent attraction to the vehicle, and especially to the sideward or rearward-facing dielectric surfaces.

b. Regarding the impingement and adhesion of contaminants:

(1) Gaseous ions impacting the vehicle are neutralized; both physical and chemical bonding processes may be active but some of the impinging species may be lost by scattering or desorption.

(2) Particulate matter impacting the vehicle adheres or scatters depending on the relative magnitudes of the local vehicle potential, the strength of the induced dipole, and the velocity vector of each particle relative to the surface.

(3) Liquids spread or coalesce depending on their surface tension in comparison to their interaction forces relative to the surface.

(4) Flowing window sealants and/or adhering particulates cover the surface and seal previous layers of deposited materials in

place; the dielectric nature of the contaminated surface is preserved for repetitions of the mechanism.

4: COUNTERCONTAMINATION: SUMMARY AND CONCLUSIONS

The above contamination model suggests the applicability of certain corrective or countercontamination measures, for it is implicit in the notion of predictable mass transfer that the process may be interrupted at any stage, given a suitable procedure or device. Thus there appear to be at least three types of approach to the practical problem of counteracting contamination, viz., prevention of the appearance of potential contaminants by passive measures, active removal measures to prevent or inhibit mass transfer for contaminants which do appear, and compensatory means of counteracting or discounting the degrading effects of contaminants which complete their transit to sensitive surfaces.

4.1: PASSIVE PREVENTION

The number of conceivable contaminant sources is so great, and their variety so diverse, as practically to preclude successful passive prevention at each source. Passive prevention appears to be at best a means of reducing contaminant emissions, not necessarily to the point of threshold tolerance by sensitive optics, but at least to the level of subsequent manageability by other means of control, e.g., active prevention.

4.2: ACTIVE PREVENTION

The interception of contaminant materials in transit between the various sources and the sensitive optical and other instruments which are to be protected appears to be technically feasible. Furthermore, since the point of interception can be chosen anywhere in the contaminant flow-field, convenience of operation will dictate that this type of control be applied where it is most needed, in the immediate vicinity of the surface being protected. In this manner, the effects of active devices should be readily predictable in terms of actual effectiveness (as determined by suitable monitoring instruments) within the operational locus of the protected sensitive surfaces. It remains to translate the concept of active countercontamination into the construction and testing of hardware.

4.3: REMEDIATION

If all else fails, there is always the final resort of a remedial approach, i.e., either the tolerance of deposition (with subsequent cleanup), or the shutdown of functional surfaces during major contaminating events (and permissiveness toward minor ones). However, for complex spacecraft reliance on this strategy alone is expected to lead to excessive "down-time" of the instrumentation being protected.

4.4: A GENERAL STRATEGY OF COUNTERCONTAMINATION

It may be concluded from the foregoing discussions, that each of the three approaches to countercontamination has something to recommend it, and each has certain drawbacks. Furthermore, one may also conclude that the three in fact tend to complement one another, such that an effective countercontamination strategy ought to be based upon their integration into one system.

Thus, passive prevention would be applied, in the selection of components and materials during the design and construction of spacecraft, such as to minimize the efflux of contaminants in space. In order to compensate for those events which, despite all precautions, would still release unacceptable amounts of contaminants into the spacecraft environment, active controls accompanied by suitable local monitoring stations would be mounted in the vicinity of all functional instruments. Finally, remedial procedures would be devised and standardized for utilization either on the rare occasions when a particular contaminating event might be of such a magnitude as to overcome all preventive measures, or, equally rarely, at periodic intervals when the aggregate deposits of subthreshold amounts of contaminants slipping by the preventive controls have accumulated to an unacceptable degree and must be removed.

5: REFERENCES

1. Glenn, J. H. , Pilot's Flight Report in Results of the First United States Manned Orbital Space Flight, February 20, 1962; (National Aeronautics and Space Administration, Washington, 1962).
2. Carpenter, M. S. , Pilot's Flight Report in Results of the 2nd US Manned Orbital Space Flight, May 24, 1962 (National Aeronautics and Space Administration, Washington, 1962).
3. O'Keefe, J. A. , "Preliminary Report on the Results of the MA-6 Flight in the Field of Space Science", in Results of the First

United States Manned Orbital Space Flight, February 20, 1962; (National Aeronautics and Space Administration, Washington, 1962).

4. Tousey, R., Koomen, M. J., McCullough, R. E., and Seal, R. T., "Photographs of Particles from an Aerobee Rocket at 130- to 204- km Altitude", Meteor Orbits and Dust, ed. G. S. Hawkins, NASA SP-135, SCA Vol. II, 333-344 (1967).

5. Grenda, R., Neste, S., and Soberman, R. K., "Contaminant Particle Trajectories near a Spacecraft", Space Research, Vol. IX, eds. K. S. Champion, P. A. Smith, and R. L. Smith-Rose, North Holland Publishing Co., Amsterdam (1969).

6. Hinton, B. B., Leite, R. J., and Mason, C. J., "Neutral Particle and Positive Ion Data Obtained from OGO-C", Trans. AGU 48, 74 (1967).

7. Ney, E. P., and Huch, W. F., "Optical Environment in Gemini Space Flights", Science 153, 297 (1966).

8. Newkirk, G., Jr., "The Optical Environment of Manned Spacecraft", Planet. Space Sci. 15, 1267 (1967).

9. Osborne, F. J. F., and Kasha, M. A., "The VXB Interaction of a Satellite with its Environment", Can. J. Phys. 45, 263 (1967).

10. Schmidt, I., "Optical Environment in Gemini Space Flight," Science 155, 1136 (1967).

11. Tilly, M. J., "Foreign Deposits on Gemini XI Optical Windows," Final Report, McDonnell Aircraft Corp., NASA-MSC-G-R-66-8, Supplemental Report 7, August 1967.

12. Muscari, J. A., and Cunningham, A. C., "Gemini 12 Contamination Study," Martin Company, Report R-67-2, January 1967.

13. Leger, L. J., NASA Manned Spacecraft Center, private communication (1969).

14. Baurer, T., et al., "External Spacecraft Contamination Modeling and Countermeasures", GE TIS R 70 SD 260, June 1970.

15. Dushman, S., Scientific Foundations of Vacuum Technique, John Wiley and Sons, New York, 1949.

16. Gibson, W. C., and Modisette, J. L., "A System for Removing Contaminants from Spacecraft Optical Systems", J. Spacecraft Rockets 7, 353 (1970).

17. Goldstein, H. W., GE Space Sciences Laboratory, Private communication (1968).

18. Belton, M. J. S., "Dynamics of Interplanetary Dust", Science 151, 35 (1966).

19. Wyatt, S. P., "The Electrostatic Charge of Interplanetary Grains", Planet. Space Sci. 17, 155 (1969).

20. Brundin, C. L., "Effects of Charged Particles on the Motion of an Earth Satellite", AIAA J. 1, 2529 (1963).

21. Liu, V. C., "Ionospheric Gas Dynamics of Satellites and Diagnostic Probes", *Space Sci. Rev.* 9, 423 (1969).
22. Jen, N. C., "Satellite Potential in an Ionized Atmosphere", *AIAA J.* 3, 714 (1965).
23. Samir, U., and Wren, G. L., "The Dependence of Charge and Potential Distribution Around a Spacecraft on Ionic Composition", *Planet. Space Sci.* 17, 693 (1969).
24. Beard, D. B., and Johnson, F. S., "Ionospheric Limitations on Attainable Satellite Potential", *J. Geophys. Res.* 66, 4113 (1961).
25. Sehna, L., "The Motion of a Charged Satellite in the Earth's Magnetic Field", *Smithsonian Astrophysical Observatory Special Report 271*, April 1968.
26. Singer, S. F., ed. Interactions of Space Vehicles with an Ionized Atmosphere, Pergamon Press, New York (1965).
27. Al'pert, Ja. L., Gurevich, A. V., and Pitaevskii, L. P., Space Physics with Artificial Satellites, Consultants Bureau, New York (1965).
28. Shay, J. J., "Collisionless Plasma Flow Around a Conducting Sphere in a Magnetic Field," *Rarefied Gas Dynamics 5th Symposium*, Academic Press, New York (1967); P. 1671.
29. Maslennikov, M. V., and Sigov, Yu. S., "Discrete Model of the Medium in a Problem on Rarefied Plasma Stream Interaction with a Charged Body," *Rarefied Gas Dynamics 5th Symposium*, Academic Press, New York (1967); p. 1657.
30. Kovar, N. S., Kovar, R. P., and Bonner, G. P., "Light Scattering by Manned Spacecraft Atmospheres", *Planet. Space Sci.* 17, 143 (1969).
31. Carlson, D. J., Lewis, C. H., Jr., and Bartky, C. D., "Solid Propellant Rocket Exhaust Plume Study" (Unclassified), *J. Missile Defense Research*, Vol. IV, No. 1, Summer 1966.
32. Ashkenas, H., and Sherman, F. S., "The Structure and Utilization of Supersonic Free Jets in Low Density Wind Tunnels", Rarefied Gas Dynamics, ed. de Leeuw, Supplement 3, Vol. II, Academic Press, New York (1965).
33. Hamel, B. B., and Willis, D. R., "Kinetic Theory of Source Flow Expansion with Application to the Free Jet", *Phys. Fluids* 9, 829 (1966).
34. Willis, D. R., and Hamel, B. B., "Nonequilibrium Effects in Spherical Expansions of Polyatomic Gases and Gas Mixtures", Rarefied Gas Dynamics, Supplement 4, Vol. I, Academic Press, New York (1967).
35. Cooper, A. L., and Bienkowski, G. K., "Asymptotic Theory for Steady Source Expansion of a Binary Gas Mixture",

Rarefied Gas Dynamics, Supplement 4, Vol. I, Academic Press, New York (1967).

36. Ehrlich, G., "Atomic Processes at Solid Surfaces," GE TIS 66-C-023, February 1966; "Atomistics of Metal Surfaces", GE TIS 67-C-432, November 1967.

37. Pikus, I. M., "High Speed Gas-Surface Interactions, I. Preliminary Model," GE TIS R67SD16, April 1967.

38. Saltsburg, H., Smith, J. N., Jr., and Rogers, M., Fundamentals of Gas-Surface Interactions, Academic Press, New York (1967).

39. Krupp, H., "Particle Adhesion Theory and Experiment", *Advan. Colloid Interface Sci.* 1, 111 (1967).

40. Proceedings of the Atomic and Molecular Beams Conference, University of Denver, Denver, Colo., 20-22 June 1960.

41. Wise, H., "Energy Exchange between Gases and Solids", Project Squid, Technical Report SRI-15-P, Stanford Research Institute, February 1963.

42. Saltsburg, H., and Smith, J. N., Jr., "Molecular-Beam Scattering from the (111) Plane of Silver", *J. Chem. Phys.* 45, 2175 (1966).

43. Harris, R. E., "On the Determination of Thermal Accommodation Coefficients in the Temperature - Jump Region", *J. Chem. Phys.* 46, 3217 (1967).

44. "The Role of the Adsorbed State in Heterogeneous Catalysis", *Disc. Far. Soc.* No. 41 (1966); entire volume.

45. Logan, R. M., and Stickney, R. E., "Simple Classical Model for the Scattering of Gas Atoms from a Solid Surface", *J. Chem. Phys.* 44, 195 (1966).

46. Logan, R. M., and Keck, J. C., "Classical Theory for the Interaction of Gas Atoms with Solid Surfaces", *J. Chem. Phys.* 49, 860 (1968).

47. Raff, L. M., Lorenzen, J., and McCoy, B. C., "Theoretical Investigations of Gas-Solid Interaction Phenomena. I", *J. Chem. Phys.* 46, 4265 (1967).

48. Lorenzen, J., and Raff, L. M., "Theoretical Investigations of Gas-Solid Interaction Phenomena. II. Three-Dimensional Treatment", *J. Chem. Phys.* 49, 1165 (1968).

TABLE 1 -- Summary of contaminant sources: Gemini

Element	Probable Sources:		Urinary Waste	Window Seals	The Sea	Possible Sources:		Estimated Analysis (Mass %)
	Refrasil (as oxides)	Propellant Impurities				Paints	Solders	
Si	Major		Minor	Major				90-95
Na		Intermediate	Major		Major			1.5-2.5
B	Major							1.0-1.5
Mg	Major	Minor			Minor			.75-1.25
Ca	Major	Major	Major		Minor			.25-.75
Fe	Major	Intermediate						.2-.5
Sb						pigment	Minor	~.3
Ag						pigment	Minor	.2-.3
Pb		Major				base	Minor	.2-.3
Cr		Minor				pigment		.2-.3
Al	Major		Minor		Minor	pigment	Minor	.20-.25
Cu	Minor*	Minor				pigment	Minor	.1-.2
Sn		Minor				pigment	Minor	.1-.2
Co						pigment		~.1
Ni		Minor				pigment		~.1
Cd						pigment	Major***	~.1
Ti	Minor**					base		.07-.09
Mn						pigment	Minor	.07-.09
Sr				Minor		pigment		~.06
V						pigment		~.05
Mo		Minor				pigment		~.04
Zn		Intermediate				base	Major***	~.03

* Owing to low analysis in virgin Refrasil

** Owing to low vapor pressure of oxide at 1500 K.

*** Owing to appreciable vapor pressure at 500 K. (Ref. 15)

TABLE 2 -- Apollo window contaminant analyses and sources

Element	Unmanned Apollo Window-Deposit Compositions (Mass %)*					Presumed Apollo Sources*	Manned Flight* Apollo XI***
	Apollo I (S/C 002)	Apollo II (S/C 009)	Apollo III (S/C 011)	Apollo IV (S/C 017)	Apollo VI (S/C 020)		
Aluminum	0.1-0.5	5-10	0.5-1.0	5-10	0.1-0.5	LES rocket gases	1-5
Antimony	0	<0.01	0.01-0.1	0	0	Fire Retardant	0
Barium	0	<0.01	0	0	0	Tower (TJM)	0
Boron	0.1-0.5	0.1-0.5	0.5-1.0	0.1-0.5	0	LET igniter	0
Cadmium	0	0.01-0.1	0	0	0	LET bolts	0 - 0.1
Calcium	0.01-0.1	10-20	5-10	>20	0.1-0.5	Sea	1-5
Chromium	<0.01	0.5-1.0	0.1-0.5	>20	<0.01	Cork Liners-Binders	0 - 0.1
Copper	0.01-0.1	1-5	1-5	1-5	0.01-0.1	Wire	0.01-1
Iron	5-10	5-10	5-10	5-10	0.01-0.1	LET	1-10
Lead	>20	10-20	10-20	>20	0.5-1.0	LET Leadliner	0.01-1
Magnesium	0.01-0.1	10-20	10-20	10-20	0.01-0.1	LET, Sea	1-5
Manganese	<0.01	0.01-0.1	0.1-0.5	0.01-0.1	<0.01	LET, Sea	0
Molybdenum	0	<0.01	0	0	0	RCS Nozzle Lining	0
Nickel	<0.01	<0.01	0.01-0.1	<0.01	<0.01	Structure	0.01-1
Silicon**	1-5	>20	>20	5-10	0.5-1.0	RTV (Window Seals)	1-15
Silver	0	<0.01	0.01-0.1	0.01-0.1	0.01-0.1	Solder	0.01-1
Sodium	5-10	>20	>20	Not given	5-10	Sea-Binders	10-15
Tin	0.01-0.1	0.01-0.1	0.1-0.5	<0.01	<0.01	Solder	0.01-1
Titanium	0.5-1.0	0.5-1.0	0.01-0.1	0.01-0.1	0.01-0.1	Ablator (structural)	0.01-0.1
Vanadium	0	0.01-0.1	1-5	0.01-0.1	0.01-0.1	Steel structure	0.01-0.1
Zinc	10-20	0.5-1.0	>20	0	0	Ablator (structural)	0.01-0.5
Zirconium	0	<0.01	0	0	0	None Given	0

* From Ref. 13

** Reported as Silicones, in Apollo (Ref. 13)

*** Also Lithium 0.01-0.1%

TABLE 3 -- Available passive control measures

Contaminant Source	Passive Control
Engine Throat Ablators	Use Radiatively Cooled Engines
Engine Propellant Impurities	Clean up Propellants
Waste Dumping	Desiccate, Bag, and Save Wastes; Recycle Water; Modify Dumping Procedures
Window Seals	Change Sealants; Utilize Non- Flowing, Non-Volatile Materials
LES and LET Components	Keep Windows Covered and Delay Deployment of Optical Experiment until Complete Jettison of LET.
Paints, Solders, Wire, Liners, Binders, Structural Ablators, All Other External Surfaces	Undertake Careful Materials Selection; Find Trade-Offs be- tween Functional Performance and Contaminant Emission Behavior for Each External Area Considered.

PARTICULATE CONTAMINANT MEASUREMENT BY QUARTZ CRYSTAL MICROBALANCE

R. L. Chuan¹

REFERENCE: Chuan, R. L. "Particulate Contaminant Measurement by Quartz Crystal Microbalance," ASTM/IES/AIAA Space Simulation Conference, 14-16 September 1970.

ABSTRACT: A piezo-electric crystal executing vibrations in a shear mode can be used as a mass balance with very high sensitivity. Various methods have been used by investigators in diverse fields to bring the mass to be measured to such a balance. Some of these are: absorption of a gas into the surface of the crystal; condensation of a gas onto a cooled crystal; chemical reaction with material bonded to the crystal surface; and impaction of particulate matter onto the crystal surface. The present paper deals with this last mass-accretion mechanism as applied to the measurement of contamination in the form of particulate matter present in space environment (actual and simulated).

The QCM (quartz crystal microbalance) responds to a mass change on its surface typically in the following manner: $\Delta f = -Cf^2\Delta m$, where Δf is the change in the crystal resonant frequency due to the addition of mass Δm , and C is a constant whose magnitude is about 10^6 . For a nominal frequency of 10^7 Hz the sensitivity, $\Delta f/\Delta m$, is of the order of 10^8 Hz/gm, from which it is seen that the mass resolution of the QCM depends directly on frequency resolution. Frequency resolution, in any given oscillator, depends on the characteristic time within which measurements are taken - the resolution generally degrading as the time increases. Thus for small mass change occurring in a long time (by which we mean seconds or tens of seconds) the frequency resolution is commonly not better than about 0.1 to 1 Hz for a 10^7 Hz oscillator. However, if the characteristic measurement time is less than, say, 10^{-2} sec, the frequency resolution can be quite good - being of the order of 10^{-2} Hz or

1

Manager, Advanced Technology Group, Atlantic Research Corporation, Costa Mesa, California.

better. This consideration lends itself to the sensitive and accurate measurement of discrete particulate mass, because when such a mass is deposited on the crystal there is an almost instantaneous, though small, frequency shift. By utilizing this very high rate of frequency shift it is possible to measure particulate mass down to the order of 10^{-11} gm. This is equivalent to a single particulate of 2 micron diameter with mass density 2 gm cm^{-3} .

In addition to measuring the mass of particulate matter, the technique also provides information on whether the material is volatile. If subsequent to its impaction onto the crystal surface, with an accompanying frequency shift, the particulate material evaporates, there will not only be a loss of mass but, more importantly, there will be cooling of the crystal. The crystal can be chosen so as to exhibit a frequency change of a sign opposite to that caused by mass addition. Then the instantaneous frequency change caused by the impaction of particulate will be followed closely by an opposite frequency change due to evaporation.

Experimental data will be presented showing the response of the QCM to non-volatile and volatile particulate matters.

KEY WORDS: spacecraft contamination, particulate sampling, quartz crystal microbalance.

INTRODUCTION

The recognition in recent years that a spacecraft can contaminate itself both in actual space environment and in laboratory simulated space environment has led to a variety of devices with high sensitivity to detect the presence of contaminants. As more data becomes available, from both flight and laboratory experiments, it appears that a significant amount of the contaminants released by a spacecraft (particularly on manned spacecraft) is in the form of particulates rather than vapors. This paper describes an instrument system which measures the flux of vapor and particulate contaminants, and can distinguish between the two types as well as measure the mass of discrete particulates. In addition, it can distinguish between solid and volatile particulate matters.

What is required basically as a pertinent measure of spacecraft contamination is the determination - directly, in real time, if possible - of the mass flux per unit area per unit time incident on the surface in question. Depending on the criticality of the effects of contamination, the resolution in such a mass flux measurement may be between 10^{-10} kg/sm^2 and 10^{-6} kg/sm^2 (those corresponding roughly to monolayer

formation times of 3 hours to 1 second). If the contaminant is in particulate form, the resolution in discrete mass measurement need be of the order of 10^{-14} kg (corresponding to the mass of a 2 micron diameter particle of mass density 2×10^3 kg/m³).

The quartz crystal microbalance can be used quite adequately for such measurements. The QCM is a piezo-electric crystal vibrating in a shear mode such that the addition of mass on its surface results in a change in its resonant frequency. The device is compact and operates largely free from environmental influences such as pressure, temperature and gravity, and thus is well suited for use on a spacecraft as well as inside a laboratory chamber. Several configurations of the QCM are described in this paper, together with typical experimental results.

CHARACTERISTICS OF THE QCM

The basic sensor is a small disc of piezo-electric crystal (about 1 cm in diameter and 0.014 cm in thickness) which forms part of a resonant circuit whose frequency is controlled by the mechanical resonant frequency of the crystal. In our application the crystal, cut from quartz operates in a shear mode whereby the opposite faces execute parallel displacements. In this oscillation mode the frequency is affected by the mass on the crystal surface. For small amplitudes of oscillation and small variation in mass, the resonant frequency is inversely proportional to mass:

$$\Delta f = -Cf^2 \frac{\Delta m}{A}$$

where f is the change in frequency caused by a mass change Δm on an active area A of the crystal, and C is a constant which in our case has the nominal value of 2×10^{-5} , with f expressed in Hertz, and m in kg and A in square meters.

Figure 1 shows a pair of crystals with nominal frequency of 10^7 Hz. The sensitivity, by the above formula, is then

$$\Delta f = -2 \times 10^7 \frac{\Delta m}{A} \text{ Hz}$$

In practice this change in resonant frequency of the sensing crystal is detected by the change in the beat frequency created by mixing the frequency of the sensing crystal with that of a reference crystal with slightly higher frequency, as shown schematically in Figure 2. The beat frequency, being much lower than the sensing frequency, makes it much easier to measure a small frequency change. Instead of measuring a change, of, say, 10^{-2} Hz in 10^7 Hz, it is only necessary to measure 10^{-2} Hz out of 10^3 Hz or less. An increase in mass shows as an increase in the beat frequency. The type of quartz crystal used exhibits a slight sensitivity to temperature variation (about 5 Hz k⁻¹). By placing the reference crystal in

the same thermal environment as that of the sensing crystal (but without being exposed to the impaction air jet) temperature compensation is automatically achieved.

DISCRETE MASS SENSING

In order to ensure that particulates incident on the crystal surface will attach to the surface and not bounce off, a thin layer (about 1 micron thick) of adhesive substance, which is inert and has very low vapor pressure, is applied over the crystal. The arrival of a particulate mass on the crystal results in a step-wise rise in the beat frequency. If the beat frequency is converted to an analog voltage and then differentiated, the step-wise frequency rise becomes a pulse whose height is proportional to the mass of the particulate. The sensitivity attainable for such a means of measuring particulate mass is estimated in the following manner.

With conventional circuitry it is possible to resolve a frequency change, over a short time interval, of the order of 10^{-2} Hz. Referring to the crystal sensitivity formula given above, it is seen that a frequency shift of 10^{-2} Hz results from a mass change per unit sensing area of

$$\frac{\Delta m}{A} = 5 \times 10^{-10} \text{ kg/m}^2$$

The area typically employed is about 10^{-5} m^2 (10 nm^2), so that the attainable mass resolution is $5 \times 10^{-15} \text{ kg}$. Actual test results to date have reached a mass resolution of about $1 \times 10^{-14} \text{ kg}$. This is the mass of an equivalent sphere of diameter 2 microns with a mass density of $2 \times 10^3 \text{ kg/m}^3$.

Figure 3 shows an actual recording trace of a differentiated analog signal from the beat frequency change. The five readily discernible pulses represent discrete masses of from 5×10^{-14} to $6 \times 10^{-13} \text{ kg}$. These are produced by particulates of mass density $3 \times 10^3 \text{ kg/m}^3$; thus the largest pulse represents a single particulate of diameter 7.5 microns.

If the particulate matter incident on the crystal is of a volatile material, some of the mass initially captured may be lost due to evaporation, which is also accompanied by some cooling of the crystal surface. The resulting response in the differentiated analog signal is a pulse followed by a negative pulse - the former due to the arrival of the mass, and the latter due in part to mass loss and in part to cooling. An example of this is shown in Figure 4. The pulses here are produced by water droplets - the difference from the signals in Figure 3 are quite apparent. The largest pulse here represents a water droplet of diameter 13 microns.

EXAMPLES OF PARTICULATE SENSORS

Figure 5 shows a sensor used primarily for space chamber monitoring. The main feature of it is the crystal sandwich

in which the sensing and reference crystals are bonded together so as to achieve good thermal compensation, as well as to conserve space. The two oscillators and the mixer are built into a single board closely behind the crystal sandwich. The output beat frequency is brought out of the space chamber for further processing.

Another example of the particulate sensor is one designed for use on a spacecraft to protect sensitive optical surfaces. Figure 6 shows a unit built for the Apollo Telescope Mount. A thermister is attached to the crystal sandwich to monitor its temperature so that corrections can be made to compensate for slight shifts in frequency over a wide range of temperature variation (from about -10°C to $+100^{\circ}\text{C}$). There is a heater behind the crystal assembly which is used to clean off volatile materials if too much accumulates.

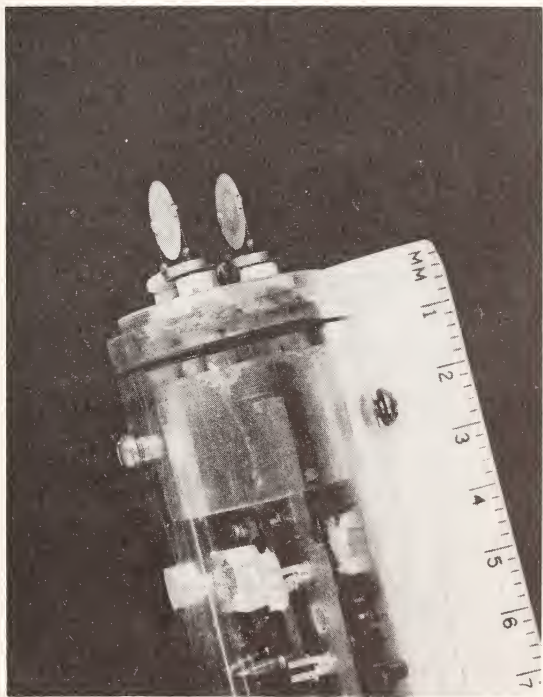


Figure 1. Quartz Crystals

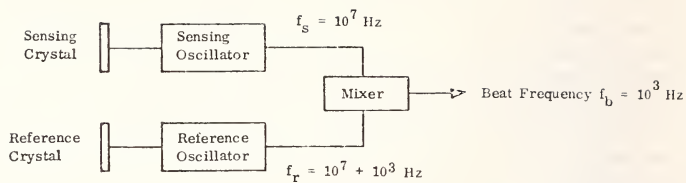


Figure 2. Schematic Diagram of Particulate Instrument

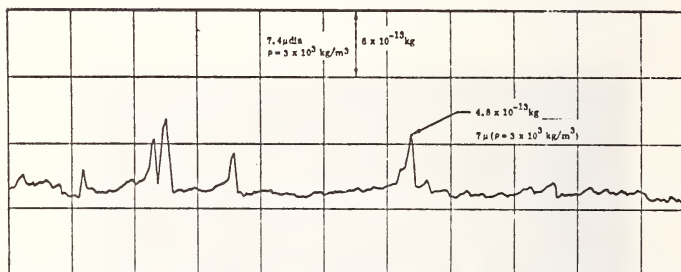


Figure 3. Solid Particulates

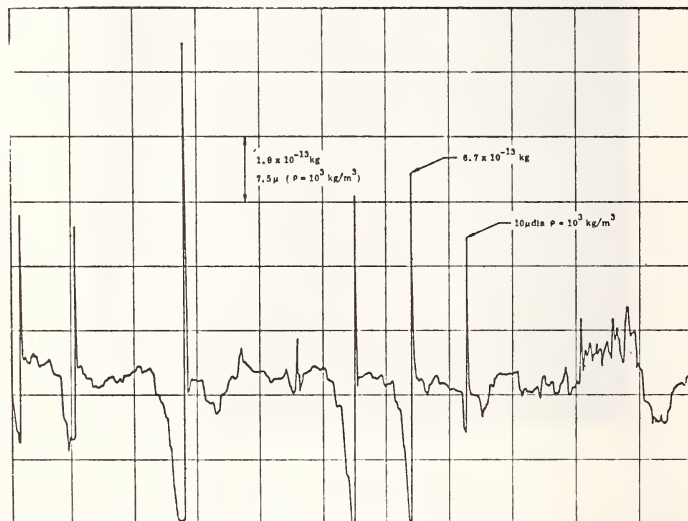


Figure 4. Liquid Particulates



Figure 5. Microbalance for Space Chamber Contamination Monitoring

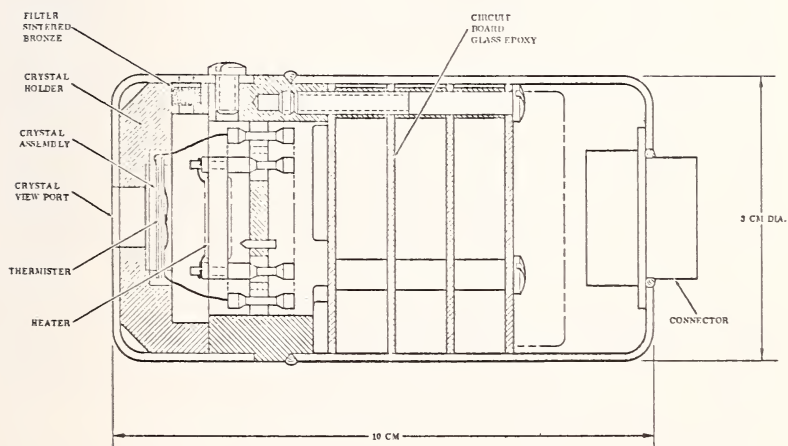


Figure 6. Microbalance for Spacecraft Contamination Monitoring

SPACE MEASUREMENTS OF THE CONTAMINATION OF SURFACES BY OGO-6 OUTGASSING AND THEIR CLEANING BY SPUTTERING AND DESORPTION²

D. McKeown and W. E. Corbin, Jr.¹

REFERENCE: McKeown, D. and Corbin, W.E. Jr., "Space Measurements of the Contamination of Surfaces by OGO-6 Outgassing and Their Cleaning by Sputtering and Desorption," ASTM/IES/AIAA Space Simulation Conference, 14-16 September 1970.

ABSTRACT: Results of the contamination of surfaces by outgassing of the OGO-6 satellite and the rates at which these surfaces are now being cleaned by sputtering and desorption after being in space for five months are given. The contamination measurements are being made with a quartz crystal microbalance to define the conditions of Al and Au surfaces used in an experiment to measure gas-surface energy transfer. It was found that the primary source of outgassing on the satellite was its two solar panels baking out in the sun. The time constant for the exponential decay of the outgassing is 1,000 hours. The maximum amount of contamination adsorbed by the surfaces exposed to the outgassing was reached after five months in orbit and is 96 mg/m² for the Al surface and 52 mg/m² for the Au surface. The contamination has a desorption activation energy of 26 kcal/g mol which falls into the energy range of materials, such as, epoxies and vacuum oils. The surfaces are now undergoing cleaning by desorption at 1.2×10^{-9} g/m²s and sputtering by upper atmospheric neutral impacts at 2.3×10^{-9} g/m²s. A method to greatly increase the cleaning rate by removal of the contamination by sputtering with upper atmospheric ions is discussed.

KEY WORDS: Surface contamination, space, outgassing, solar panels, sputtering, desorption, cleaning, ions, quartz crystal microbalance

¹ Staff Members, Faraday Laboratories, La Jolla, California

² This work was supported by NASA Goddard Space Flight Center under Contract NAS5-11163 and the Office of Naval Research under Contract N00014-68-C-0373.

INTRODUCTION: With the planned orbiting of large manned space laboratories in the 70's, the space environment has taken on a new dimension. Not only must problems be considered concerned with the effects of the environment on the laboratory but also the effects of the laboratory on the environment. One area of concern is the contamination of surfaces, such as, telescope mirrors and windows by the outgassing of materials used in the construction of the craft. The contamination problem is especially troublesome because of the free molecular flow conditions that exist in the hard vacuum of space. Molecules issuing from the contamination source flow freely in straight lines to exposed surfaces. If these contaminated surfaces also point towards the sun, solar UV will compound the problem by polymerizing the oil and grease contaminants and a hard carbon glaze will form resulting in significant changes in the optical properties of the surfaces and in the accommodation coefficients for gas-surface energy transfer.

At present we are conducting a space experiment to measure gas-surface energy transfer by upper atmospheric atomic and molecular impacts to determine how satellite drag is effected by various surface materials (1)¹. The experiment is being flown on OGO-6 launched on 5 June 1969 into a polar orbit with a perigee of 397 km and an apogee of 1098 km. The experiment uses four quartz crystal probes as dual microbalances and energy transfer probes. One important part of the experiment is to monitor the rate at which material is outgassing from the satellite, how much of this material is adsorbed by the experimental surfaces, and after the outgassing rate drops to low levels, at what rate do the surfaces clean by desorption and sputtering erosion? Because the rates at which surfaces are contaminated by satellite outgassing and cleaned by desorption and sputtering are of importance to the understanding of surface contamination on other spacecraft, we would like to present here the results of measurements on the effects of a space environment on surfaces obtained from OGO-6.

INSTRUMENTATION: The flight experimental instrumentation is shown in Fig. 1 and is 11.4 x 17.8 x 19.1 cm, weighs 2.2 kg, and operates at 28 Vdc on 3.5 W. The experiment has been described in early work (1,2) and only the general operation of the instrumentation will be given here. The surfaces used in the experiment are housed in the four gold plated probes located behind the shutter wheel. The experiment is pointed along the velocity vector of the satellite into the air stream. To

1 The numbers in parentheses refer to the list of references appended to this paper.

minimize weight in the OPEP appendage of OGO-6 which has attitude control for pointing into the upper atmospheric stream, the experiment was flown in two parts. The four probe sensor package is located in the OPEP and connected by a 3 m cable to the L-shaped electronics package located in the main body of the satellite.

Four different measurements are being made on two Al and two Au surfaces. The surfaces are plated by vacuum evaporation on 15 MHz, 1.27 cm diameter, optically polished Y-cut quartz crystal sensors shown in Fig. 2. The sensors are located in gold plated probes 3.3 cm in diameter and 9 cm long, and view space through a 1.8 cm diameter window. The field of view of the surface is 0.13 steradians and the probes effectively colimate the contaminate flux reaching the surfaces.

The probes are designated A through D. Probe A is instrumented with an Al plated sensor mounted normal to the probe axis. Probe B and C have Au plated sensors mounted normal to the probe axis. Probe D has an Al plated sensor mounted at 14 degrees to the probe axis. Probes A, C, and D are pointed into the molecular stream and both contamination and energy transfer measurements are made with these probes. Probe B is pointed away from the stream by 13 degrees and the molecular stream loses its energy by multiple impacts on the wall of the probe, and only contamination measurements are made with this probe.

An eight position shutter, shown in Fig. 1, is mounted in front of the probes. Two of the 1.8 cm diameter apertures in the shutter have a 0.5 mm thick BaF_2 blank mounted over it for chopping the beam. BaF_2 is used for the shutter because its wide IR band minimized temperature changes during shutter operation. The shutter can be periodically stepped open to permit the upper atmospheric molecular stream to simultaneously impact on the Al and Au surfaces to measure gas-surface energy transfer. The shutter is programmed to remain open a total of 67% of the time and closed for 33% of the time and 67% of the outgassing flux reaches the surfaces. On every apogee pass (100 min) the frequency outputs of the probes are read out to determine the mass loading caused by contamination. The contamination measurement is made at this point in the orbit because the upper atmospheric kinetic energy flux falls below 100 mW/ m^2 , the energy transfer threshold of the probe, and energy transfer does not interfere with contamination measurements.

The probe output frequency is the beat frequency between the sensor crystal and a matched reference crystal. The beat frequency is used because it effectively cancels out ambient temperature changes and any variation in the power supply voltage driving the probe. The reference crystal is mounted in a chamber just behind the sensor crystal. The chamber front wall is 0.05 mm thick gold plated stainless steel with a 1.27 cm hole cut in it and is attached to the circumference of the sensor crystal. This does not affect the crystal oscillation because an amplitude node exists at its edge. The chamber keeps

any contamination from reaching the back surface of the sensor crystal or either surface of the reference crystal which would effect the accuracy of the measurements. The Q or quality factor of the crystals is 200,000 which assures high frequency stability from aging and any changes in the transistors used to drive the crystal oscillators. The general equation for the frequency change, ΔF , of the sensor crystal caused by mass loading (3) is

$$\Delta F = (\Delta m F_S^2 / k \rho A) + F_S(T) - F_R(T) \quad (1)$$

where Δm is the contaminant loading in g, F_S , the fundamental frequency of the crystal in Hz, k , constant of quartz = 1.66×10^6 mm, A , the motional area of the crystal in cm^2 , and ρ , the density of quartz in g/cm^3 , and $F_S(T)$ the frequency dependence of the sensor and reference crystal to ambient temperature changes. $A = 0.1 \text{ cm}^2$ and letting $\Delta F_T = F_S(T) - F_R(T)$

$$\Delta m = (2.5 \times 10^{-9} \text{ g/cm}^2 \text{ Hz}) (\Delta F - \Delta F_T) \quad (2)$$

The ambient temperature of the probes is monitored to $\pm 1^\circ\text{C}$ and $\Delta F_T = 20 \text{ Hz}/^\circ\text{C}$ for Probes A, B, and C and these probes can measure contaminant mass loading to an accuracy of $\pm 5 \times 10^{-8} \text{ g/cm}^2$ ($\pm 0.5 \text{ mg/m}^2$). The sensor in Probe D is affected to a greater degree by temperature because it is mounted at a 14° angle to the axis of the probe. Its accuracy is $\pm 2 \times 10^{-7} \text{ g/cm}^2$ ($\pm 2 \text{ mg/m}^2$).

SURFACE CONTAMINATION MEASUREMENTS: The surfaces were prepared in the laboratory by vacuum evaporation and sputtered atomically clean before instrumentation in the experiment. From the laboratory until insertion into orbit the Al surface collected 32 mg/m^2 and the Au surface 14 mg/m^2 of mass from exposure to atmospheric contamination on the ground (Los Angeles smog).

Results of contamination of Al and Au surfaces on OGO-6 are shown in Fig. 3. Data given from launch until 31 July are production data from the continuous readout of the experiment. From 1 August on, the data is "quick look" received every few days for several minutes at a time which accounts for the gaps in the measurement points.

The Al surface placed normal to the direction of the contamination flux has adsorbed approximately four times as much contamination as an Al surface mounted 14° to the flux and shows that the outgassing is external to the experiment and not internally generated. The Al surfaces have adsorbed about twice as much mass as the gold surfaces. The Al is probably gaining more mass because the outgassing material has a larger sticking coefficient for Al than Au. The Au surface in the air stream has gained a little more mass than the Au surface

shielded from the stream. One explanation for this is that the contamination layer on the surface in the molecular stream is picking up a small amount of atomic oxygen by chemisorption while the control surface shielded from direct atmospheric impacts is not reacting with O.

The contamination flux reaches a maximum when the surfaces are pointed towards either one of the two solar panels on the satellite in June and drops to near zero in August when pointed into deep space because of rotation of satellite orbit plane to the earth-sun line, and shows that the panels are the primary source of contamination.

The satellite outgassing flux consists of two main components, volatile gases such as O_2 , N_2 , CO_2 , and H_2O and relatively low-volatile materials such as oil and paint that require a long period to outgas.

The volatile materials boil off the satellite and reach very low levels in the first few days after launch. The cloud that enveloped the satellite apparently shielded it from direct atmospheric impacts for many hours and incoming atmospheric molecules lost a significant portion of their kinetic energy by particle-particle interactions before impacting on surfaces. We were unable to detect any gas-surface energy transfer from the upper atmosphere until 72 hours after launch. Because these volatile gases are not adsorbed to any significant amount by the surfaces used in the experiment, no quantitative measurement on the flux of these particles was made.

The low volatile materials outgassing from the satellite stick to the experiment surfaces and an estimate of the flux of the low-volatile material was possible. Assuming a sticking coefficient of the flux on aluminum of 0.7 at the start of adsorption (4) and taking into account the time the shutter is closed and the view angle of the surface, the mass flow to the experiment at zero revolutions from Fig. 3 is

$$[dM/dt]_{t=0} = 9.2 \times 10^{-11} \text{ g/cm}^2 \text{ s} \quad (3)$$

In the International System units the flow is $9.2 \times 10^{-7} \text{ g/m}^2 \text{ s}$. Assuming the molecular weight averages 200 g, because low-volatile oils have large molecular weights, the outgassing flux in the vicinity of the experiment is

$$F = 2.7 \times 10^{11} \text{ part/cm}^2 \text{ s} \quad (4)$$

In SI units the flux is $2.7 \times 10^{15} \text{ part/m}^2 \text{ s}$. This flux rate decreases exponentially with time as the panels outgas. Fitting an exponential curve to the A1 curve for the first three days after launch gives a time constant of 1,000 hours for the exponential decay and

$$F = 2.7 \times 10^{11} e^{-t/10^3} \text{ part/cm}^2\text{s} \quad (5)$$

The decay in the outgassing flux is plotted in Fig. 4 from launch through January 1970.

The flux plotted in Fig. 4 is for the case of the experiment remaining fixed relative to the solar panel. Since the experiment is constantly turning to remain pointed into the air stream and the panels are turning to remain pointed at the sun, the flux reaching the face of the experiment is

$$F = [2.7 \times 10^{11} e^{-t/10^3}] [k + \cos(\theta - \pi/4)] \quad (6)$$

where F is in $\text{part/cm}^2\text{s}$, t in hours, k a constant < 0.1 to account for outgassing other than from the panels, and θ the angle between the experiment face and the solar panels. The rate of rotation of the orbit plane to the earth-sun line determines the angle, θ , between the experiment and the panels where $\theta = 4.5 \times 10^{-4} \pi t$ where t is in hours.

DESORPTION: The desorption or outgassing of materials from OGO-6, although easily measured by a quartz crystal microbalance, is very small and reflects the care with which materials were chosen in the construction of the satellite. The maximum amount of the outgassing material adsorbed by the aluminum surface was $9.6 \mu\text{g/cm}^2$ (96 mg/m^2) which represents less than 50 monolayers, assuming an average molecular weight of 200 g.

It has been pointed out that the solar panels are the primary outgassing source on OGO-6. The front surfaces are solar cells and the back surfaces of the panels are painted with ZrO_2 pigmented potassium silicate inorganic paint. Because this material has a low vapor pressure, epoxies used in assembling the panels and contamination absorbed in vacuum tests must be the contaminant sources.

This material is now deposited on the Al and Au test surfaces. The preliminary desorption rate of the material can be found when the experiment was pointed toward deep space in August. The amount of adsorbed gas, S_r , on the Au surface (4) at time t is

$$S_r = S_0 \exp(-t/\tau_r) \quad (7)$$

where S_0 is the amount on the surface at $t = 0$, and τ_r the average residence time of the gas.

$$\tau_r = \tau_0 \exp(\Delta E/RT) \quad (8)$$

where τ_0 is the vibrational period of the lattice, ΔE the desorption activation energy, R the gas constant, and T the abso-

lute temperature.

The desorption activation energy for the contamination is

$$\Delta E = -RT[\ln(2.8 \times 10^{-17}/t)(\ln S_0/S_r)] \quad (9)$$

The average temperature of the surface was 7°C and from Fig. 3 during August for Probe B: $S_0 = 4.5 \times 10^{-6} \text{g/cm}^2$, $S_r = 4.1 \times 10^{-6} \text{g/cm}^2$, $t = 750 \text{ h}$, and

$$\Delta E = 26 \text{ kcal/g mol} \quad (10)$$

Griffith (4) points out that diffusion pump oils and epoxies have desorption activation energies of about 25 to 30 kcal/g mol and begin to vaporize in significant amounts at temperatures above 45°C. In full sun light the OGO-5 solar panels operate above 45°C. The contamination outgassing from the panels is then most probably epoxy assembly materials and diffusion pump oil absorbed during pre-launch vacuum tests.

RADIANT ENERGY EXCHANGE: In designing the experiment, a thermal model was made of the instrumentation to minimize the energy radiated from the surfaces generated by gas-surface interactions to maximize the temperature increase of the sensor to attain large output signals.

Radiant energy exchange between elements of a system of nonblackbodies were computed by

$$q_{ij} = \sigma F_{ij} F_{eij} A_i (T_i^4 - T_j^4) \quad (11)$$

where σ , is the Stefan-Boltzman constant, F_{ij} , the ordinary view factor for blackbodies, A_i , the area of the i 'th element, T_i , the temperature of the i 'th element, T_j , the temperature of the j 'th element.

F_{eij} is a factor which accounts for the energy transferred between i and j where heat transfer is a function of multiple reflections between i and j themselves and other elements of the system. F_{eij} is a function of both the geometry of the system and the emittance of the various elements. The exchange of energy is directly related to the emissivity of the surfaces and would be reflected in the exchange rate measurements made during calibration.

The energy transfer sensors are calibrated periodically at the several power levels. Fig. 5 is an 878 μW calibration of the aluminum plated sensor made on 7 June 1969 soon after launch and Fig. 6 is the same level calibration made on 9 August 1969 after accumulation of 8 $\mu\text{g/cm}^2$ of contamination. A constant power was applied to the sensor for 110 sec. The probe frequency output was 1475 Hz in Fig. 5 and 1450 Hz in Fig. 6 and changed less than 2% which is the accuracy of reading out the

probe frequency. The near normal emittance of Al surface was measured in the laboratory and found to be 0.02 and has not changed significantly after being contaminated in space because the power calibration has not changed significantly.

Figs. 5 and 6 are typical of the output of the probes when energy transfer is taking place produced by molecular impacts. An exponential curve fit is made by computer of the frequency increase of the probe, $F(t)$, to find the beam energy transferred when the shutter opens.

$$F(t) = F_1(1 - e^{-t/\tau_1}) + F_0 \quad (12)$$

where τ_1 is a time constant and F_1 is the asymptotic frequency increase of the probe when the shutter opens. The constants are found by calibrating the probes in space (1).

SPUTTERING: Sputtering is the ejection of surface atoms by energetic impacts of neutral atoms or ions. For impact energies below 50 keV the interaction between the bombarding particle and target atom is treated as a hard sphere collision. For normal incidence the bombarding particle undergoes at least one collision to reverse its momentum vector before a second collision can produce sputtering. The bombarding ion strikes a target atom and rebounds in such a direction as to sputter another atom from the surface. The other possibility is that the bombarding particle displaces from its site the first atom it meets and is subsequently lost in the interstitial spaces of the lattice. Meanwhile, the displaced atom uses up its excess kinetic energy to collide with other atoms in the lattice. A certain percent of the time, this atom will strike an atom near the surface with enough energy to cause sputtering. At oblique incidence a single collision can lead directly to the ejection of a surface atom.

The sputtering yield is defined as the number of surface atoms ejected per impacting particle. The yield is dependent upon the angle of incidence, the energy, and the mass of the impacting particle and the mass of the target atom, the average binding energy of an atom in the lattice, the crystal structure of the solid, the heats of sublimation of the different crystal planes, the collision cross section of the target atoms, and the energy dissipated in the lattice as heat. Henschke (5) points out the dependence of the yield below impact energies of 100 eV on the collision radii. This dependence reveals a marked periodicity of this energy as a function of the atomic number of the target atom. More specifically, this behavior is seen to be related to the filling of the d subshells, (electronic orbital angular momentum $\ell = 2$) in the electronic structure of the elements. It is observed that for these atoms with nearly completely filled d shells, the collisions are more elastic and less energy is lost in the lattice. This results in higher

sputtering yields for these solids. Unfortunately no theoretical relationship exists to predict the sputtering yield for any arbitrary particle-surface combination and yields must be measured experimentally for particular combinations.

Rol et al (6) and Almen and Bruce (7) have proposed that the dependence of the yield on impact energy and mass is

$$\mu = \beta N \sigma(E) [4mME/(m + M)^2] \quad (13)$$

where μ is the yield in atoms/particle, β a proportionality constant to fit the experimental data, N the number density of surface atoms, $\sigma(E)$ the energy dependent scattering cross section, m the mass of the impacting particle, M the mass of the surface atom, and E the particle impact energy.

The impacting particle energy, E , is expressed in eV. From Eq. 13, the following observations can be made. The scattering cross section is known to increase with energy so yields will increase strongly with impacting energy. The yield will be maximized when the mass of the impact particle equals the mass of the surface atom ($m = M$).

Experimentally it has been found that for most particle-surface combination yields as a function of energy fall in the following ranges:

$$\begin{aligned} 0 < \mu < 0.5; 0 < E < 100 \text{ eV} \\ 0.5 < \mu < 15; 100 \text{ eV} < E < 10 \text{ keV} \\ 15 < \mu < 50; 10 \text{ keV} < E < 100 \text{ keV} \end{aligned}$$

Measurements for Au in noble gas ions in Fig. 7 illustrate the effect of impacting particles of different masses between 100 eV and 800 eV.

As the beam energies are reduced below 100 eV to 10 eV the sputtering yields fall exponentially to values of less than 10^{-3} atom/ion. It is not possible to conduct sputtering experiments at yields below 10^{-3} because laboratory beams are not intense enough to produce measureable mass losses in the few hours time required in the best vacuum systems before system impurities contaminate the surface. In the upper atmosphere, an orbiting satellite generates a molecular beam in the 10 eV range about 1,000 times more intense than is possible in the laboratory. Sputtering can then be measured on a satellite if the surface is placed in the molecular stream pointed towards space so that outgassing cannot contaminate it.

During August in Fig. 3, it was possible to determine the sputtering on OGO-6 when the surfaces were pointed into space. The desorbing mass loss rate of the Au surface shielded from impacts is 1.2×10^{-9} g/m²s. The mass loss rate for the other surface caused by sputtering and desorption at normal incidence is $M_{Al} = 3.5 \times 10^{-9}$ g/m²s, $M_{Au} = 3.5 \times 10^{-9}$ g/m²s, and M_{Al} at 14° incidence = 3.8×10^{-9} g/m²s. Subtracting the desorption mass loss rate of 1.2×10^{-9} g/m²s from the surfaces gives the

sputtering rates. The average particle flux over an orbit is 1.1×10^{17} molecules/m²s, and assuming the contamination has a molecular weight of 200 g, the sputtering yields are

$$\begin{aligned}\mu_{14^\circ} &= 3 \times 10^{-4} \text{ atom/molecule} \\ \mu_{90^\circ} &= 7 \times 10^{-5} \text{ atom/molecule}\end{aligned}$$

These yields are not for Al and Au but the contamination on the surfaces. The grazing angle of incidence produced higher yield because the impacting molecule can eject atoms without having to reverse its momentum direction.

The sputtering yields are in agreement with the Au yield, $\mu = 1 \times 10^{-6}$ atom/molecule, measured on Discoverers 26 and 32 (8) with a quartz crystal microbalance mounted on an appendage pointed continually into space. The lower yield for atomically clean Au is indicative of the higher heat of vaporization for Au than for the oil type contamination measured on OGO-6.

DISCUSSION: The measurements on OGO-6 show that outgassing of low-volatile materials which cause surface contamination is produced primarily by structures baking out in the sun such as solar panels. The contaminated surfaces can be cleaned by desorption and sputtering.

Desorption requires that the surfaces be heated to temperatures above 45°C to produce acceptable cleaning rates. The heating should be done electrically or indirectly by solar heating because if the surface is exposed to the sun, UV will polymerize the oil contamination leaving behind a permanent carbon glaze which in most cases could cause more problems for a surface than a coating of oil.

Sputtering is another cleaning method. It has a big advantage in that it can remove carbon contamination which desorption cannot. To sputter carbon, the impacting particles must transfer at least 5 eV, to the surface to break the carbon lattice bond. The neutral upper atmosphere impacts between 5 eV and 10 eV and will sputter carbon but is impractical because the yield is too low. A better source of sputtering particles is upper atmospheric O⁺ ions. Metallic surfaces would be biased to a potential of several hundred eV. A biased wire grid, 95% open, would be moved in front of a non-conductor, to accelerate the ions. Space charge would spread the ion beam and no grid shadow would form on the surface. The surface would be kept from charging up by impacting ions by directing about a 1 mA/m² flux of electrons at the surface.

During the day at altitudes below 1,000 km, the ion density is about 10^9 ions/m³ (9). An orbiting satellite sweeps out 8×10^{14} ions/m²s. At impact energies of 500 eV, the sputtering rate is about a million times greater than the rate measured at 10 eV on OGO-6. The ion sputtering cleaning rate would be about 1 mg/m²s, which would clean the 100 mg/m² of

contamination from the surfaces on OGO-6 in 100 seconds.

Above 1,000 km, ion densities will be too low for sputtering cleaning. At these altitudes an ion gun would be employed using an onboard gas supply to sputter the surfaces. The electronics already developed for use in ion engines would be a good starting point for the design of such a gun.

REFERENCES

- (1) McKeown, D. and Dummer, R.S., IEEE Geoscience Electronics, Vol. GE-7, No. 2, April 1969, p. 98.
- (2) McKeown, D., Rarefied Gas Dynamics, J.A. Laurmann, Ed., Academic Press, New York, 1963, p. 315.
- (3) McKeown, D., Review of Scientific Instruments, Vol. 32, No. 2, Feb. 1961, p. 133.
- (4) Griffith, J.S., Proceedings 4th Space Simulation Conference, AIAA/ASTM/IES, Los Angeles, Sept. 1969.
- (5) Henschke, E.B., Physical Review, Vol. 106, No. 5, March 1961, p. 1286.
- (6) Rol, P.K., Fruit, J.M., Vielbock, F.P., and de Jong, M., Ionization Phenomena in Gases, N.R. Nilsson, Ed., North-Holland Publication Co., Amsterdam, 1962, p. 257.
- (7) Almen, O. and Bruce, G., Nuclear Instruments and Methods, Vol. 11, 1961, p. 279.
- (8) McKeown, D., Fox, M.J., Schmidt, J.J., and Hopper, D., AIAA Journal, Vol. 2, No. 2, Feb. 1964, p. 400.
- (9) Hanson, W.B. and Sanatani, S., Proceedings AGU Annual Meeting, SPA59c, Washington, D.C., April 1970, p. 32.

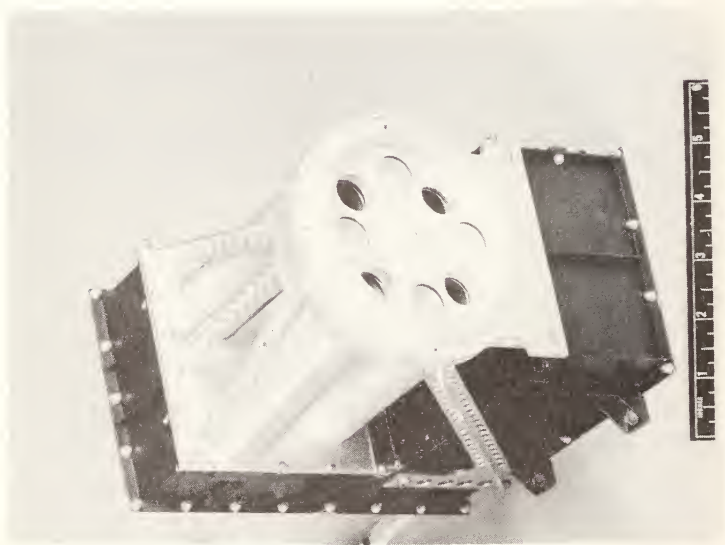


Fig. 1 : Flight instrumentation

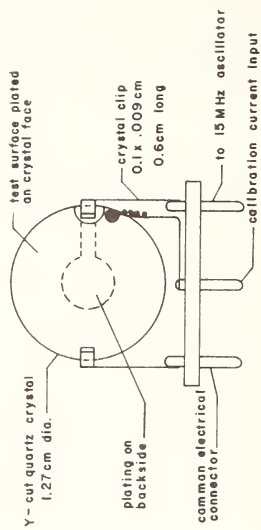


Fig. 2 : Quartz crystal sensor

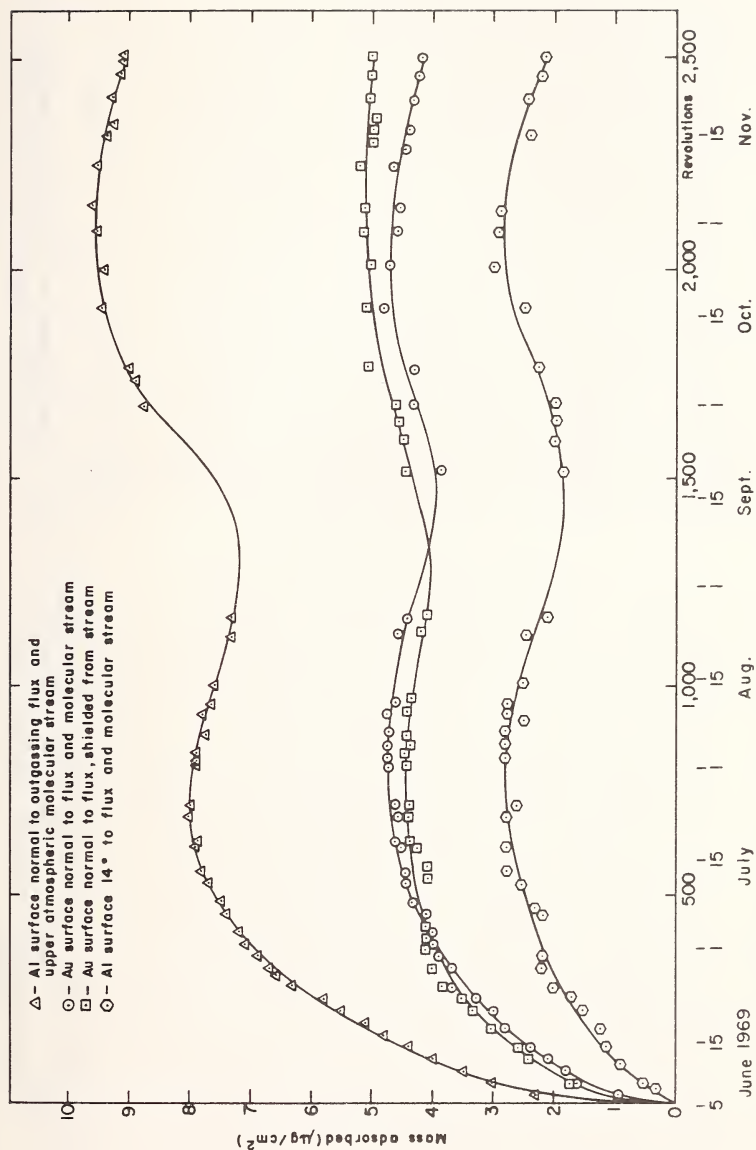


Fig. 3 Contamination loading of surfaces by outgassing of OGO-6 under various environmental conditions.

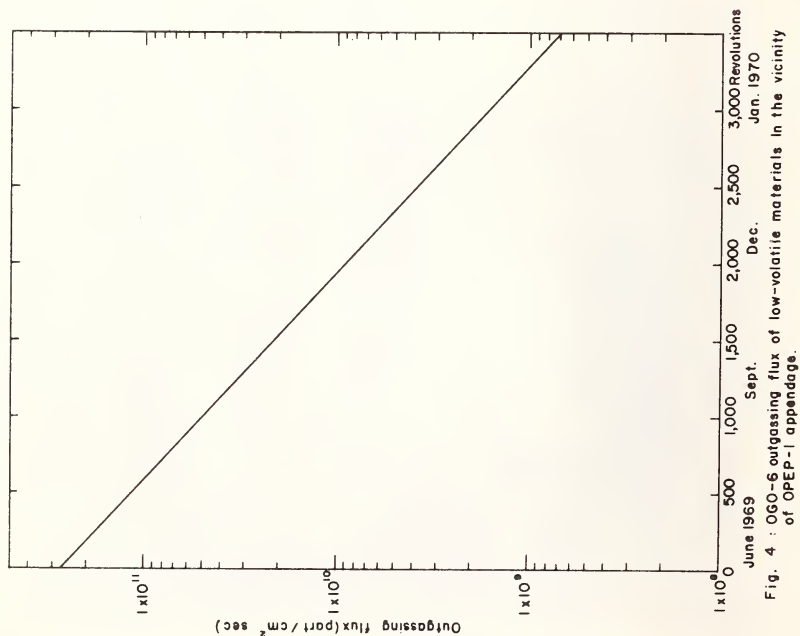


Fig. 4 : OGO-6 outgassing flux of low-volatile materials in the vicinity of OPEP-1 appendage.

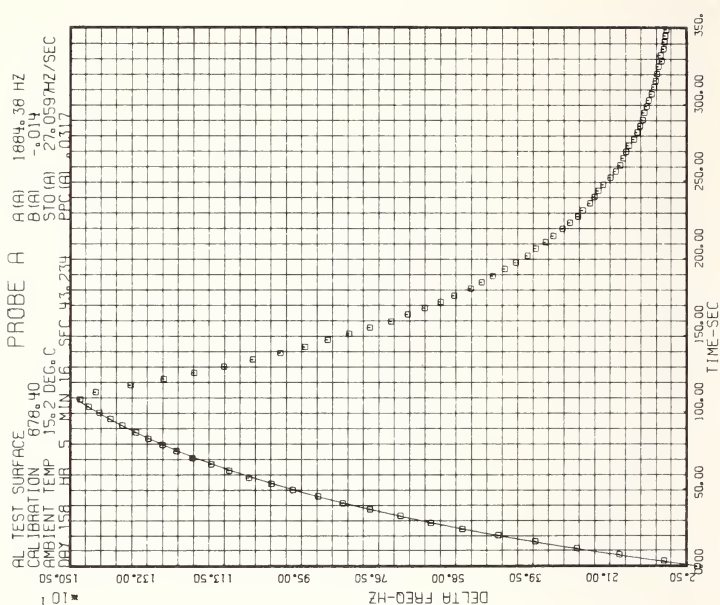


Fig. 5 : Probe A output for 878 μ W calibration with 1.8 μ g/cm² of surface contamination on 7 June 1969.

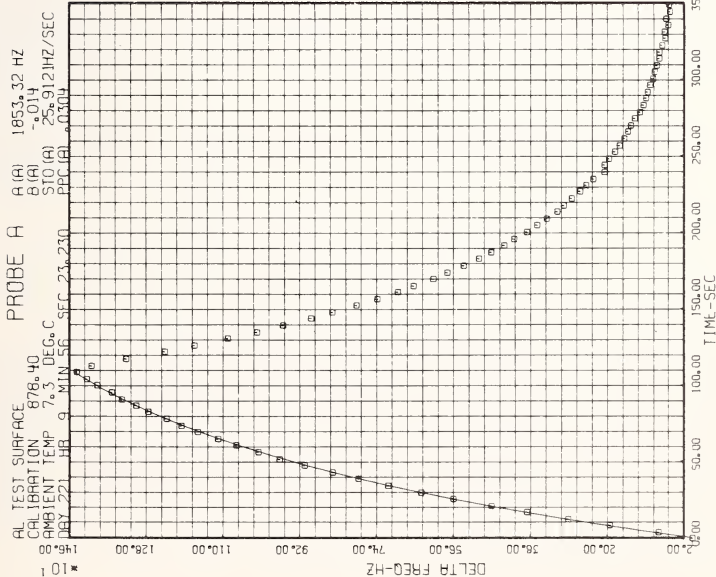


Fig. 6 : Probe A output for 878 μ W calibration with 7.7 μ g/cm² of surface contamination on 9 Aug. 1969.

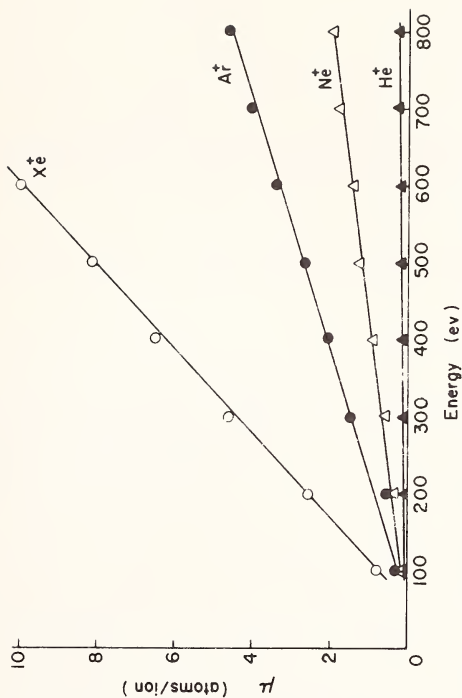


Fig. 7 : Sputtering yields of Au in noble gas ions of impact energies between 100 eV and 800 eV.

SIMULATION OF RADIATION FROM RTG POWER SOURCES

Phillip A. Newman, Jr., NASA, Goddard Space Flight Center, Greenbelt, Md.

ABSTRACT: The recent interest in Radioisotope Thermoelectric Generator (RTG) power systems for deep space missions and the ever increasing use of the radiation sensitive MOSFET in spacecraft electronics has made it essential that an assessment of the radiation effects for this combined application be determined. An RTG with its continuous flux of neutrons and gamma photons provides a long term hostile environment for electronic components. This paper deals with a radiation source (Pu^{239} -Be) selected to simulate, for the most part, the neutron effects of the RTG. Preliminary experiments with this source have indicated that for most electronic applications the neutron contributions of the RTG over a five year mission in present spacecraft configurations will not be a major problem. An analysis of the data from several experiments indicate that predictions of the radiation effects can be made for "hotter" configurations with a reasonable degree of confidence.

KEY WORDS: radiation simulation, neutrons, MOSFETS, RTG, test, evaluation, Pu^{239} -Be

INTRODUCTION

Until recently NASA has not been interested in the effects of neutrons on spacecraft electronics since neutrons do not exist to any substantial degree in the space environment. The proposed use of Radioisotope Thermoelectric Generator (RTG) power systems on deep space missions has made it essential that an assessment of the effects of the radiation on the more sensitive electronic components be determined.

RADIATION EFFECTS ON SPACECRAFT ELECTRONICS

Most of the advanced spacecraft electronic systems being designed today are making extensive use of MOSFETs (metal-oxide-semiconductor field effect transistor) both as discrete devices and as integrated circuits because of the substantial power and weight savings and the decrease in circuit complexity. Prior work⁽¹⁻³⁾ has shown that MOSFETs are the most sensitive of all commonly used electronic components to ionizing radiation. While some neutron work has been done on MOSFETs none has been done at the low levels expected from the RTG.^(4, 5)

It is well known that radiation can cause permanent damage to semiconductors in two basic ways, ionization damage and displacement damage. Ionization damage, when it occurs, takes place at a much lower dose level than does displacement damage. For the predicted levels here, ionization damage should be the dominant effect. In discrete MOSFET devices the most prominent ionization effect is the shift of the gate threshold voltage (and consequently the gate voltage-drain current characteristic) due to a charge build-up in the gate insulator. This shift is strongly dependent on the gate bias during irradiation.⁽⁶⁾ While this threshold shift certainly takes place in integrated circuits it is not always accessible for measurement. Since gamma radiation effects on MOSFETs have been studied in the past and have been done extensively in this laboratory this preliminary experiment was largely an effort to isolate the effects of the neutron.

SIMULATION REQUIREMENTS

Figure 1 shows a possible spacecraft configuration for a deep space mission using an RTG power system. The RTG fuel, a special form of PuO_2 (Pu^{238}), emits a flux of neutrons and gamma photons which are impractical to shield against in the spacecraft situation. The location of the RTG, about 2 m from the main part of the spacecraft, indicates that the spacecraft electronics package will be subject to a long term hostile environment.

An ideal source to simulate this radiation would be an RTG itself. Certain problems would exist in the handling and storage of such a source in the laboratory not to mention its cost. However an RTG was not available for this work so the problem did not arise. The basic

Numbers in parentheses refer to the list of references appended to this paper.

problem was to find a radiation source to do some preliminary work on the most sensitive electronic components to determine the extent of the problem.

Both reactor neutrons and neutrons produced indirectly by an accelerator were considered. However they were both rejected because of the difficulty in controlling the accompanying gamma flux. In addition reactor fluxes are somewhat high for this problem while accelerator produced neutron fluxes are so low that an inordinate amount of manpower would be required to reach the desired levels.

The proposed deep space application using the RTG power system will generate a total fluence on the order of 4×10^{10} neutrons/cm² at the electronics package during a 5 yr mission. The gamma fluence depends on a number of factors including the purity of the fuel element and the gamma build-up. It has been estimated to be 1×10^{12} photons/cm².

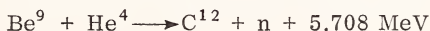
In view of the nature of the radiation damage and other practical considerations the source had to satisfy the following criteria:

1. The level be such that the fluence produced during a typical deep space mission could be achieved in a reasonable time.
2. A gamma level that was low enough so that over the period of irradiation its effects on the MOSFET would not be dominant over that of the neutron.
3. The neutron energy spectrum be similar to that of the RTG.
4. The activity of the source should be low enough so that handling problems are not excessive.

Criteria 1 and 4 are in some contradiction but can be resolved with safety in mind. This has the added benefit that although the irradiation will take longer it will be closer to real time and help to eliminate possible rate effects.

NEUTRON SOURCE

An available source that seemed to satisfy all of our criteria pretty well was a cylindrical 9 curie source of Pu²³⁹-Be (Fig. 2). The reaction that produces the neutron flux is an (α , n) reaction where the alpha particle emitted by the Pu²³⁹ reacts in the following way:⁽⁷⁾



The neutron spectrum that results⁽⁸⁾ is believed to be (Fig. 3) similar

Numbers in parentheses refer to the list of references appended to this paper.

enough to that of the RTG to permit an unambiguous assessment of the radiation effects of the neutron on the MOSFET. The gamma spectrum has been measured and found to have peaks at 40 KeV and 2.4 MeV.

The major problem in using a source of this size and geometry is in the dosimetry used to determine the neutron and gamma fluences at the point where the devices were irradiated.

EXPERIMENT

For the first experiment a total of eight devices, two each of four off-the-shelf commercial p-channel enhancement types from three manufacturers, were used. The devices were mounted on a circuit board so that the top of the device can was against the source cylinder (Fig. 4). In this way the maximum neutron flux was encountered. The devices were all irradiated with a bias of -10 V on the gate during irradiation. The gate threshold voltage for each device was measured periodically by an automatic data acquisition system. Four control samples, one of each type used in the irradiation, were biased and measured in the same way as the irradiated samples. This experiment was run for a total of 230 days. A second experiment was run for 30 days to give a better idea of the data spread among the device types.

A third experiment using a Co^{60} source for a pure gamma flux was used on the same device types to determine the portion of the damage that could be attributed to the neutrons in the original experiment.

FLUX DETERMINATION

Although many dosimetry techniques, including calorimetry, neutron long counter, thermoluminescent dosimeters, a nemo counter, ion chambers, activation analysis, R-chambers and film, were used for various parts of the experiment, in the final analysis, only two of the methods were relied upon. The neutron flux was computed⁽⁹⁾ from the total emissivity supplied by the manufacturer. The gamma flux was determined from film. Assuming that the calculated neutron flux is correct and that the neutron-gamma ratio remains constant away from the can, the gamma flux computed at the surface of the can from the ratio agrees fairly well with the measured value. The neutron flux

Numbers in parentheses refer to the list of references appended to this paper.

was taken to be 1.7×10^{10} n/cm²-day and the gamma flux at 5 rads/day.

RESULTS

The gate threshold shifts for a typical device type is shown in Figure 5. On the abscissa the calculated neutron fluence and the measured gamma fluence is plotted in addition to the exposure time on a logarithmic scale. Curves are shown for both the neutron experiment and the Co⁶⁰ experiment with the latter being plotted on the same scale as the measured gamma contribution of the neutron source. The curves for almost all of the neutron exposed devices fit an equation of the form

$$\Delta V_t = K (\Phi)^{.76}$$

where ΔV_t is the change in the gate threshold voltage and Φ is the fluence.

On the other hand all of the Co⁶⁰ data show that the change in gate threshold voltage is linear with respect to fluence.

DISCUSSION

The results of using this experimental neutron source show that while the total number of gamma photons emitted is somewhat less than the number of neutrons their relative effect is large but not large enough to mask the effect of the neutrons. From this data one can assess the radiation damage of the MOSFET due to neutrons and can determine with some degree of confidence the problems that will be encountered on a deepspace mission. It is clear that at the radiation levels anticipated for the configuration shown the neutron damage to the spacecraft package will not be significant, while the gamma level is at the threshold of damage. Another consideration that must be taken into account for determining the vulnerability of the electronics is the electronic application to which the MOSFET devices or integrated circuits will be put. For most digital applications a shift of one volt in the characteristic can be tolerated. For some types of linear applications lower thresholds must be used.

There is probably some small amount of displacement damage due to the neutrons in these devices. The fact that the neutrons showed a slightly non-linear relationship and that the damage could not be annealed at temperatures that will ordinarily anneal ionization damage in MOSFETs shows that another type of damage is present.

CONCLUSION

While the Pu^{239} -Be source served nicely for preliminary experiments the results show that for practical RTG configurations the gamma effects will dominate. From the nature of the curves it seems reasonable to expect to be able to predict the radiation effects of the RTG for other configurations once the expected neutron and gamma fluxes are determined.

A number of other radioisotope sources have been considered but they do not appear to be any better than the one used. Short half-life, excess gamma and poor neutron spectrum match seem to be the major problems.

ACKNOWLEDGEMENTS

The author would like to thank Mr. Kirk King for his extensive dosimetry efforts, Mr. William Larimer for handling many of the experimental details, especially toward the windup of the experiment, and Mr. Jule Hirschfield for many useful discussions concerning the simulation of the radiation environment.

REFERENCES

- (1) J. P. Mitchell, "Radiation-induced spacecharge buildup in MOS structures," IEEE Trans. Electron Devices, vol. ED-14, pp. 764-774, November 1967
- (2) E. H. Snow, et al., "Effect of ionizing radiation on oxidized silicon surfaces and planar devices," Proc. IEEE, vol. 55, pp. 1168-1185, July 1967
- (3) P. A. Newman and H. E. Wannemacher, "Radiation induced peaking effect in open geometry p-channel MOSFETS," IEEE Trans. Nuclear Science, vol. NS-14, pp. 299-302, December 1967
- (4) G. Messenger, et al., "Displacement damage in MOS transistors," IEEE Trans. Nuclear Science, vol. NS-12, pp. 78-82, October 1965
- (5) A. A. Witteles, "Neutron irradiation effects on MOSFETS," IEEE Trans. Nuclear Science, vol. NS-15, December 1968
- (6) A. G. Stanley, "A model for shifts in the gate turn-on voltage of insulated-gate field effect devices induced by ionizing radiation," IEEE Trans. Electron Devices, vol. ED-14, pp. 134-138, March 1967
- (7) J. B. Marion and J. L. Fowler, "Fast Neutron Physics," Interscience Publishers, Inc., New York, 1960, p. 6.
- (8) M. E. Anderson and W. H. Bond, Jr., "Neutron spectrum of a Plutonium-Beryllium source," AEC R&D Report, MLM-1131, UC-34 Physics, TID-4500 (18th Ed.), September 1964
- (9) T. Rockwell, "Reactor Shielding Design Manual," D. Van Nostrand Company, Inc., Princeton, N.J., 1956, p. 360.

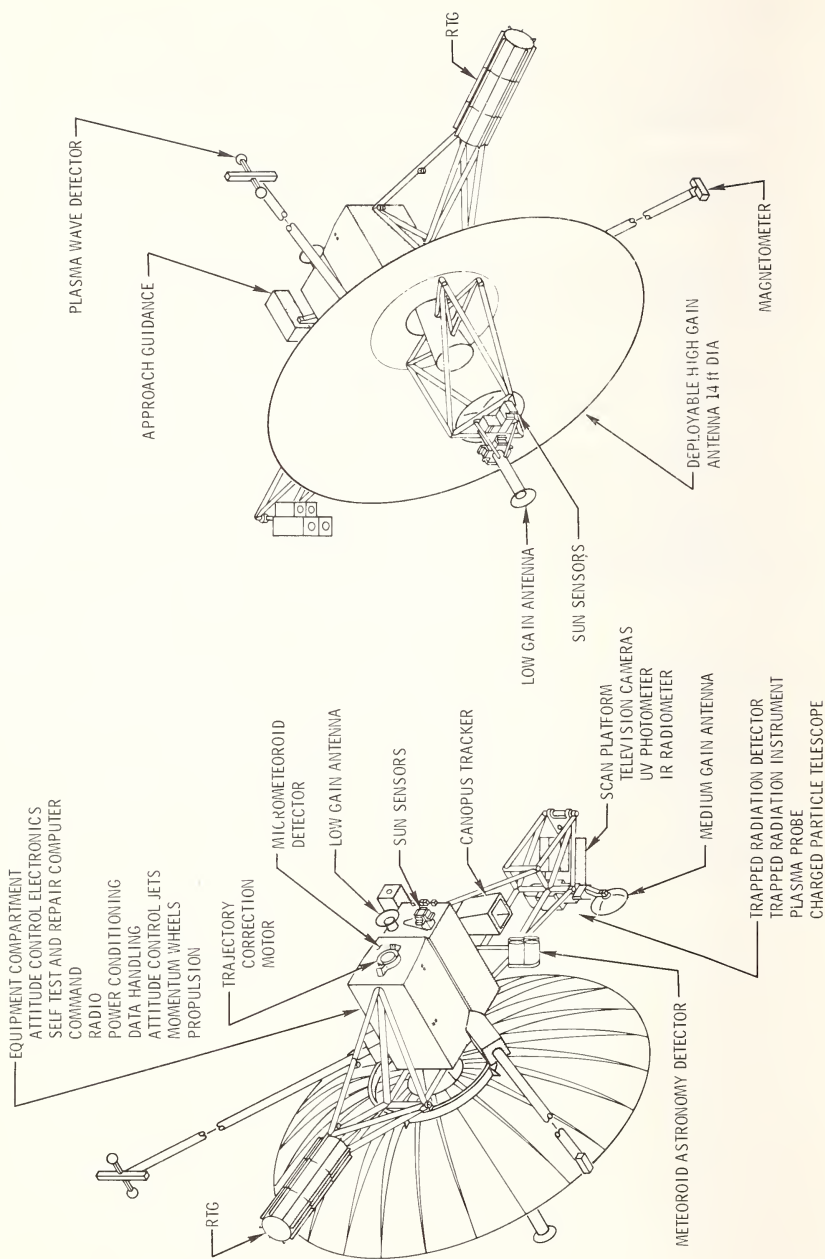


Fig. 1—Typical Spacecraft Using RTG Power

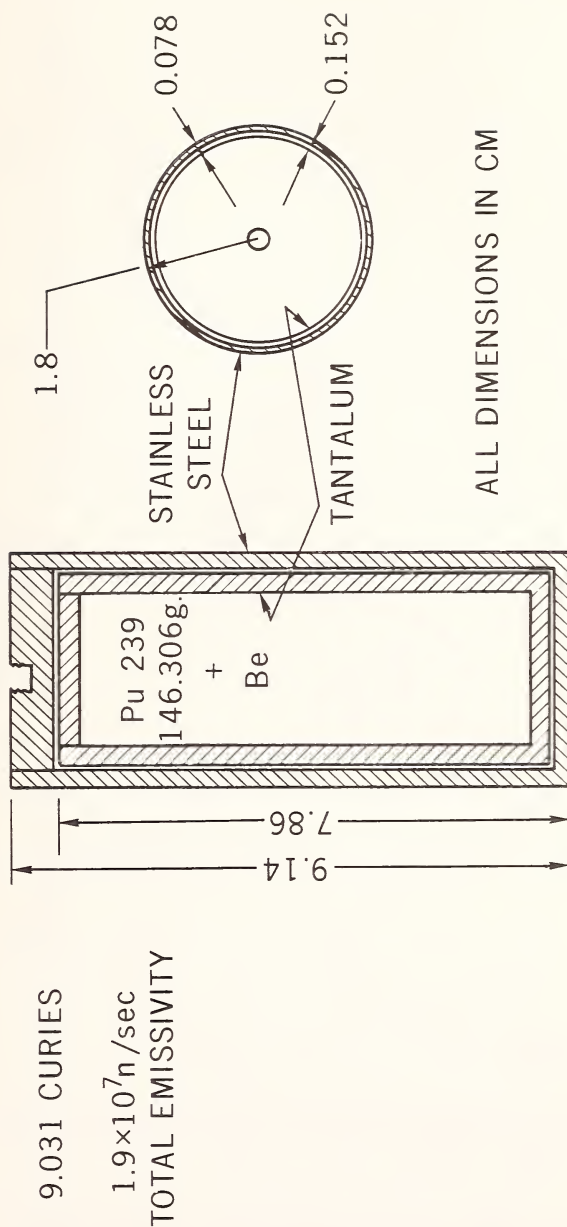
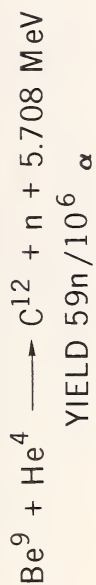


Fig. 2—Pu ²³⁹-Be Neutron Source

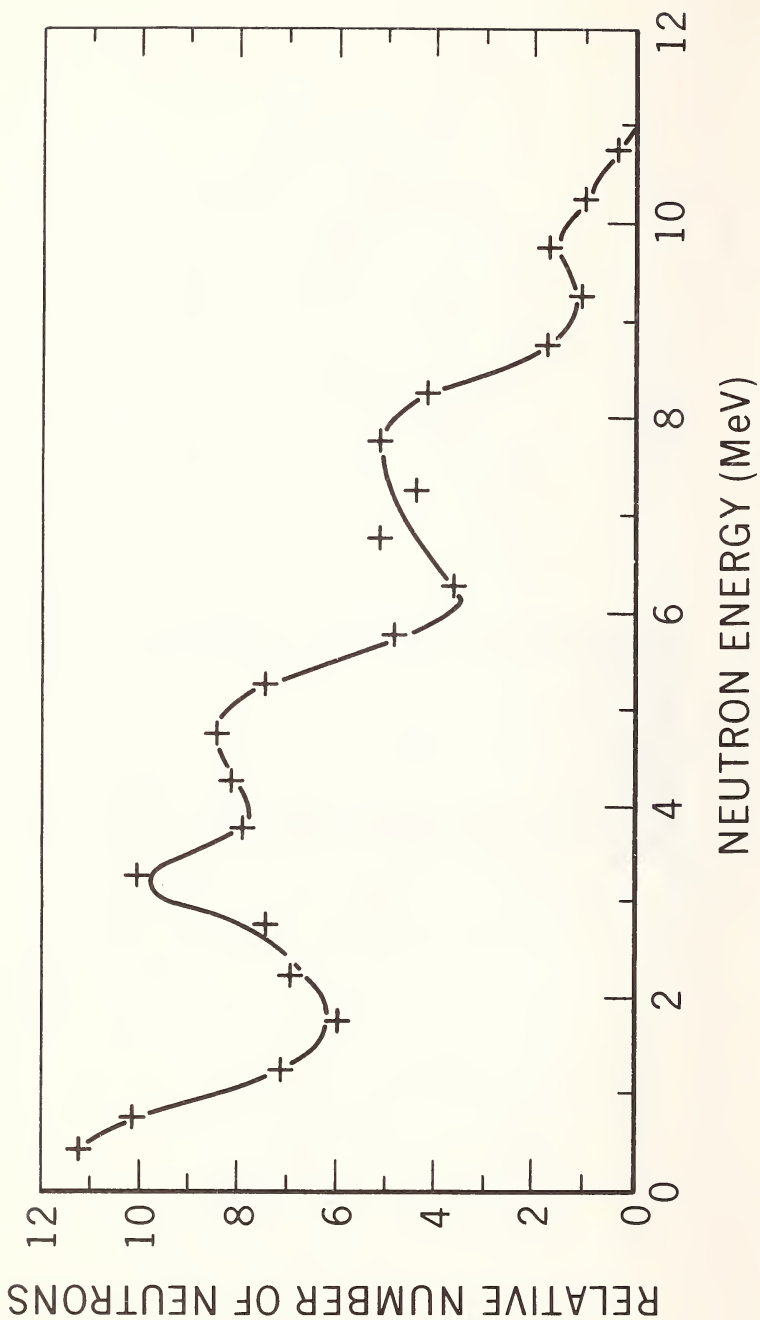


Fig. 3—Neutron Spectrum of Pu^{239} -Be Source

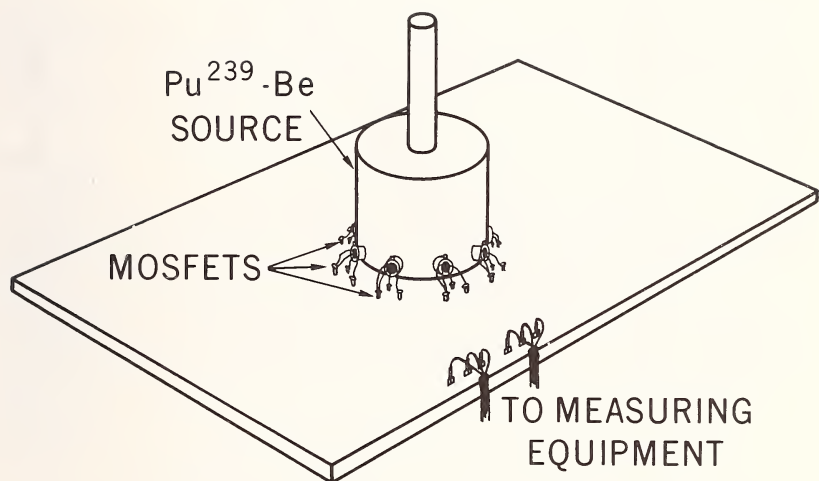
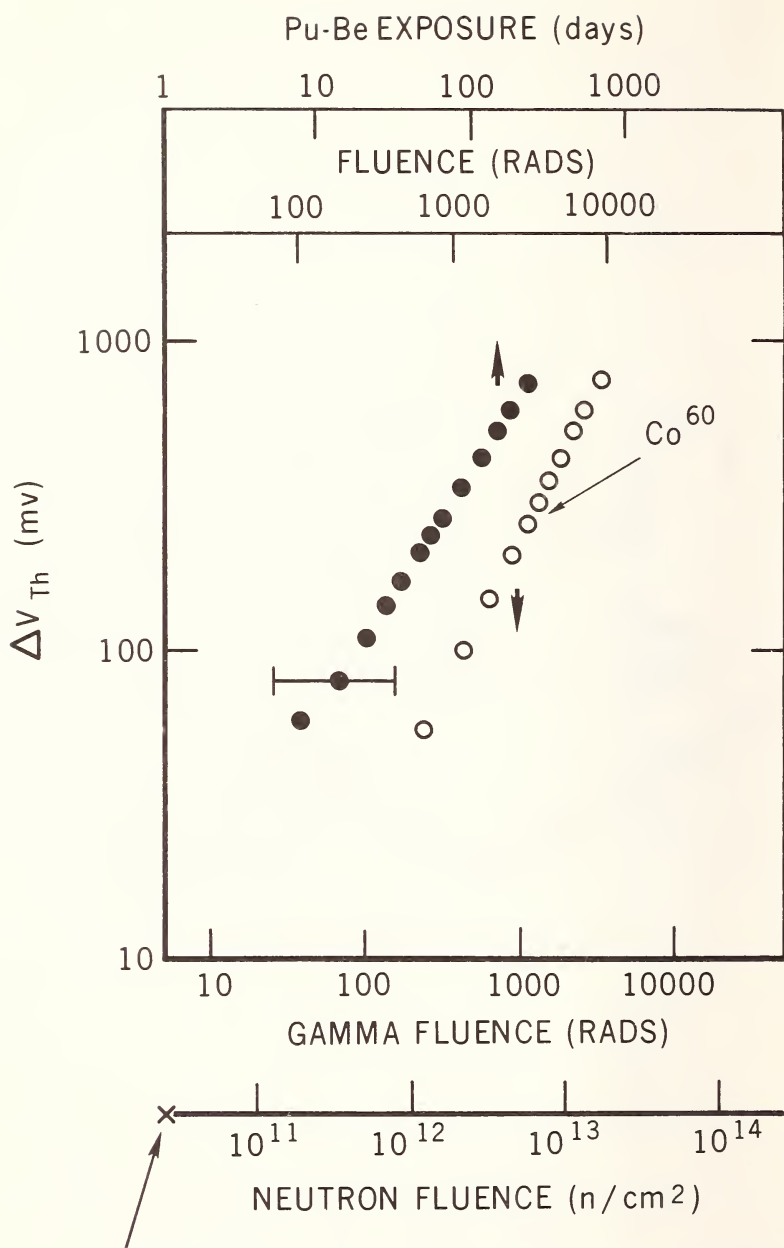


Fig. 4—Neutron-MOSFET Experiment



FLUENCE EXPECTED AFTER 5 YR RTG MISSION

Fig. 5—Typical Neutron-MOSFET Results

IN SITU VACUUM GAUGE CALIBRATION BY THE REFERENCE TRANSFER METHOD

L.D. Blado¹ and R.H. Lilienkamp²

REFERENCE:

Blado, L.D. and Lilienkamp, R.H., "In Situ Vacuum Gauge Calibration by the Reference Transfer Method," ASTM/IES/AIAA Space Simulation Conference, 14-16 September 1970.

ABSTRACT:

Application of the Reference Transfer Method to in situ calibration of ionization gauges was evaluated in order to ascertain the effectiveness of the method when applied in a manner determined both by the commercial availability of equipment and by the restraints of an operating space environment simulation facility. A prototype Reference Transfer Calibrator (RTC) was assembled from standard vacuum components. Transfer ratio determinations were made in the range 10^{-4} to 10^{-8} torr. These experimental measurements were then compared with theoretical calculations, thereby verifying the feasibility of the technique.

KEY WORDS: Vacuum Gauge Calibration, Reference Transfer Method

The problem of calibrating vacuum gauges for accurate measurement in pressure ranges below 10^{-4} torr has long been recognized. A technique for calibration in this range, proposed by Charles Morrison⁽¹⁾ in 1966, is the Reference Transfer Method. This method, by virtue of its simplicity and the fact that it relies upon a single pump, is ideally suited for in situ calibrations. The purpose of the work described here was to assemble a prototype Reference Transfer Calibrator (RTC) with commercially available hardware and to evaluate the efficacy of this technique for in situ operations.

¹Test Engineer, Engineering Laboratories, McDonnell Aircraft Company, St. Louis, Mo.

²Senior Group Engineer, Engineering Laboratories, McDonnell Aircraft Company, St. Louis, Mo.

Superscript numbers in parentheses refer to the list of references appended to this paper.

The lack of an acceptable pressure standard below 10^{-4} torr requires that a means be found to relate lower pressures in some known manner to pressures in a region where an acceptable standard does exist. Reference transfer, like other calibration techniques for this pressure range^(2,3,4,5) takes advantage of the well-known fact that a molecular flow of gas through an orifice will produce a pressure ratio across that orifice.

A hypothetical two-orifice system (Figure 1) can be used to determine the pressure ratio in the general case. The pressure ratio across the orifice O_{AB} can be obtained for equilibrium conditions with flow through the chamber. The flow into B is $(P_A - P_B) F_{AB}$, where P_A and P_B are the pressures, in torr, of Chambers A and B, respectively, and F_{AB} is the conductance (liters per second) of the orifice O_{AB} . The flow out of B is $(P_B - P_C) F_{BC}$, where P_C is the pressure of Chamber C and F_{BC} is the conductance of the orifice O_{BC} . Thus,

$$(P_A - P_B) F_{AB} = (P_B - P_C) F_{BC} \quad (1)$$

Rearranging Equation 1 gives

$$P_A/P_B = (F_{AB} + F_{BC})/F_{AB} - (P_C/P_B)(F_{BC}/F_{AB}) \quad (2)$$

From Equation 2, it follows that if P_C is small with respect to P_B , the second term is negligible, and

$$P_A/P_B = (F_{AB} + F_{BC})/F_{AB} = U \quad (3)$$

This ratio can now be used to generate a series of pressures having a known relationship. Since we know the interrelationship of all series members, the comparison of one element to a standard will yield a standard value for all the elements. If we let P_R be the standard and P_N be the N^{th} pressure in the series, we can write

$$P_N = P_R U^{N-R} \quad (4)$$

The foregoing development does not consider background gas loads which may be neglected in a well-baked calibration system but which could become significant in a typical space simulator. With a gas load Q_B in Chamber B, Equation 1 becomes

$$(P_A - P_B) F_{AB} + Q_B = (P_B - P_C) F_{BC} \quad (5)$$

Rearranging Equation 5 gives

$$P_A/P_B = (F_{AB} + F_{BC})/F_{AB} - Q_B/P_B F_{AB} - (P_C/P_B)(F_{BC}/F_{AB}) \quad (6)$$

Similarly, for Chamber C with gas load Q_C ,

$$(P_B - P_C) F_{BC} + Q_C = P_C S \quad (7)$$

where S is the pumping speed in liters per second.

Superscript numbers in parentheses refer to the list of references appended to this paper.

Rearranging Equation 7 gives

$$P_C/P_B = F_{BC}/(S + F_{BC}) + Q_C/P_B (S + F_{BC}) \quad (8)$$

Combining Equations 6 and 8 gives

$$P_A/P_B = K_1 - K_2/P_B \quad (9)$$

where

$$K_1 = (F_{AB} + F_{BC})/F_{AB} - F_{BC}^2/(S F_{AB} + F_{AB} F_{BC}) \quad (10)$$

and

$$K_2 = [Q_B (S + F_{BC}) + F_{BC} Q_C]/F_{AB}(S + F_{BC}) \quad (11)$$

The first term of Equation 10 corresponds to U and the second term is negligible when the pumping speed is large. (The pumps used in our experimental work had effective pumping ranging from 400 to 25,000 liters per second, giving errors due to this term of 0.5 to 0.03 percent)

The first term of Equation 11 corresponds to the ultimate pressure of Chamber B and the second term is approximately equal to F_{BC}/F_{AB} multiplied by the ultimate pressure of Chamber C.

Thus, if P_B remains large compared to K_2 , P_A/P_B remains constant, and if the pumping speed is large, P_A/P_B equals U . The relative error in the pressure ratio due to outgassing can now be expressed as

$$\frac{dU}{U} = \frac{K_2}{P_B K_1} \quad (12)$$

This relation is shown in generalized form in Figure 2.

The relative error in a final calibration can be determined from Equation 4. Letting P_N be the N^{th} pressure in the series, we had

$$P_N = P_R \quad U^{N-R}$$

Therefore,

$$\frac{dP_N}{P_N} = \frac{dP_R}{P_R} + (N-R) \frac{dU}{U} \quad (13)$$

The first term in Equation 13 gives the error contribution due to the standard chosen. Bromberg⁽⁶⁾ has shown that a capacitance manometer is accurate to within 0.5 percent in the 10^{-4} to 1 torr range.

From Figure 2 and Equation 13, it follows that the closer we get to the chamber's ultimate pressure and the more steps we need to get there, the larger the error in the calibration will be. In the process of an experimental

Superscript numbers in parentheses refer to the list of references appended to this paper.

determination of U , an approximation of the constant K_2 can be made by observing the pressure at which a drastic change in the pressure ratio occurs.

The prototype RTC shown in Figure 3 was assembled from standard 1.5-inch vacuum components, such as crosses, valves, and flexible couplings, employing sexless flanges with copper seals. The orifices O_{AB} and O_{BC} shown in Figure 4 are 0.32 and 0.95 cm in diameter, and have conductances of approximately 1 and 9 liters per second, respectively. The orifices were given a 100° chamfer to approximate a zero thickness condition. The transfer gauge is a Bayard Alpert type ionization gauge operated at an emission setting of 0.9 ma for a rated sensitivity of 10 amps per torr. Before each data gathering attempt, the entire system was baked at 400°F for a minimum of 24 hours.

Figure 5 shows a schematic of the RTC attached to a space simulation chamber designated as Chamber C. The two chambers (A and B) of the calibrator are connected through orifice O_{AB} and can both be valved independently into a transfer gauge G_t . Chamber B is connected to Chamber C through a second orifice O_{BC} . Chamber C can also be valved independently into the transfer gauge. The gas source was a regulated supply of room temperature dry nitrogen admitted into Chambers A and C through separate variable leak valves attached to each of those chambers. The Baratron capacitance manometer used as a pressure standard attaches to the remaining flange on the cross designated as Chamber A.

A typical calibration sequence proceeds in the following manner:

- (1) With Valves A, B, and C open and variable leak Valves L_A and L_C closed, evacuate the entire system until a stable equilibrium is reached.
- (2) Close Valves A and C. Open Valve L_A to admit gas to Chamber A. Monitor Chamber B pressure until it is at least 1 decade higher than its original value. Record the transfer gauge reading.
- (3) Close Valve B and open Valve C.
- (4) Using Valve L_C , admit gas to Chamber C until the pressure as seen by the transfer gauge is the same as that recorded in Step 2. Record the reading of Gauge G_C ; this is the first calibration pressure. Close Valves C and L_C .
- (5) Open Valve A and record the transfer gauge reading. Close Valve A.
- (6) Open Valve B. Increase the gas flow through L_A until the pressure in Chamber B is the same as the value recorded in Step 5. Record the transfer gauge reading.

Steps 3 through 6 in the above procedure are repeated until the pressure generated in Chamber A is high enough to be compared to the available standard. Once this comparison is made and an absolute value for this pressure is known, we can extrapolate to the other members of the series, and the calibration is complete.

Obtaining the desired pressures in Chamber B by the control of the gas flow through the leak valve L_A was very difficult. To obtain the fine control needed, the supply pressure to the leak valve was reduced to 1 torr.

The majority of our effort has been in the experimental determination of the pressure ratio U . For this work the transfer gauge is used to determine

the pressure in Chambers A and B and from these data the pressure ratio is calculated. The transfer gauge need not be calibrated for these measurements since the determination of U requires that the measured pressures be correct relative to each other. The symmetry of the valving system that connects the transfer gauge to the chambers, coupled with the well established linearity of the Bayard-Alpert type ionization gauge over the pressure range under consideration, ensures a high degree of confidence in the individual ratio determinations. The results of two determinations of the pressure ratio U , with the RTC mounted on two different space simulators, are given in Table 1. The first set of data was obtained on a system having a pumping speed of 25×10^3 liters per second during the space conditioning of spacecraft components. The second set of data was obtained on a system having a pumping speed of 400 liters per second with the chamber empty. From both sets of data we can see the change in the pressure ratio as the pressure in Chamber B approaches the ultimate pressure of Chamber C.

For these chambers the ultimate pressures were 1×10^{-7} and 1×10^{-8} torr. K_2 for these chambers was approximately 10^{-6} and 10^{-7} torr, respectively. Figure 6 presents the variation of the pressure ratio with Chamber B pressure. The data from Table 1 is also shown on this figure.

We have operated the reference transfer system somewhat differently than Morrison. He used a flow measurement to establish the reference pressure, but we are using the capacitance manometer for this purpose. We believe that this instrument is accurate enough for most work and is far simpler to operate than a flow measuring device or a McLeod gauge.

For our particular system a pressure ratio of 10 was selected. With this ratio the number of steps in each calibration sequence is kept reasonably small. The ease of obtaining the reference pressure allows rerunning the sequence several times to obtain intermediate points.

Because the experimental determination of the pressure ratio is limited by our ability to measure the ion current in the transfer gauge and our control of the operating voltages and currents supplied to the transfer gauge, it may become necessary to use the calculated values of the pressure ratio obtained from calculated values of conductance based on measurements of the orifices to obtain the accuracy expected.

The following main conclusions can be drawn from this work:

- 1) Reference transfer is well suited to an in situ calibration. Compactness and design simplicity coupled with the use of a single pumping system are a near-ideal set of characteristics for in situ calibration.
- 2) Relative calibrations in a facility with several vacuum chambers can be achieved quite easily. An RTC such as the one used in this work can be readily assembled from available hardware. Its operation does not require the high level of vacuum technique sophistication characteristic of even most relative calibrations. Our prototype RTC was mounted on two operating vacuum chambers without making any attempt to bring those chambers to their maximum operating efficiency. In one case, the RTC was mounted and the pressure ratio determined while the chamber was being used to degas several spacecraft components. The fact that calibrations can be performed to within 1 decade of the chamber ultimate with a reasonable degree of

accuracy, regardless of what that ultimate is, can prove to be a valuable capability. In addition, the compactness of the RTC makes transport relatively easy. Thus, it is feasible to calibrate all the vacuum systems of a company relative to each other, regardless of plant location, by shipping an RTC from one plant to another.

3) The absolute accuracy of a reference transfer calibration can be improved dramatically by careful operations, using accepted high vacuum techniques. Equations 13 and 14 show that minimizing the error in the transfer ratio by reducing the background gas load (i.e., lowering the system ultimate pressure) will permit the accurate calibration range to be extended into the ultra-high vacuum region. Morrison has estimated that the error in the transfer ratio can be kept below 1 percent in the 10^{-9} torr range, thus allowing the operator to fit the degree of effort involved in a calibration to the degree of accuracy he desires.

4) The flexibility of the Reference Transfer Method is a definite advantage. Any adequate standard that is valid in the 10^{-4} torr range may be used.

References

- 1 Morrison, Charles, F. "Reference Transfer Method of Vacuum Gauge Calibration," *Journal of Vacuum Science and Technology*, Volume 4, Number 5, September/October 1967.
- 2 Choumoff, P.S. et. al, "Absolute Calibration of Ion Gauges by Means of a Bakeable Adjustable Conductance," *Journal of Vacuum Science and Technology*, Volume 7, Number 1, January/February 1970.
- 3 Florescu, N.A., "Reproducible Low Pressures and Their Application to Gauge Calibration," *Transactions of the 8th Vacuum Symposium and 2nd International Conference*, Volume 1, pp. 504-510.
- 4 Roehrig, J.R. and Simons, J.C., "Accurate Calibration of Vacuum Gauges to 10^{-9} Torr," *Transactions of the 8th Vacuum Symposium and 2nd International Conference*, Volume 1, pp. 511-518.
- 5 Normand, C.E., "Use of a Standard Orifice in the Calibration of Vacuum Gauges," *Transactions of the 8th Vacuum Symposium and 2nd International Conference*, Volume 1, pp. 534-543.
- 6 Bromberg, J. Phillip, "Accurate Pressure Measurements in the Region 0.1 to 1000 millitorr; The Intercalibration of Two McLeod Gauges and A Capacitance Manometer," *Journal of Vacuum Science and Technology*, Volume 6, Number 5, September/October 1969.

Table 1 – Determination of Pressure Ratio

High Pump Speed; Chamber Ultimate 1×10^{-7} Torr		
Chamber A	Chamber B	Ratio
1.70×10^{-6}	3.45×10^{-7}	4.9
2.15×10^{-6}	4.15×10^{-7}	5.1
2.80×10^{-6}	5.15×10^{-7}	5.4
4.70×10^{-6}	6.95×10^{-7}	6.7
5.10×10^{-6}	7.20×10^{-7}	7.0
5.30×10^{-6}	7.40×10^{-7}	7.2
9.80×10^{-6}	1.15×10^{-6}	8.5
1.05×10^{-5}	1.20×10^{-6}	8.7
1.40×10^{-5}	1.50×10^{-6}	9.3
2.35×10^{-5}	2.45×10^{-6}	9.7
2.40×10^{-5}	2.40×10^{-6}	10.0
3.95×10^{-5}	4.00×10^{-6}	9.8
5.40×10^{-5}	5.40×10^{-6}	10.0
6.10×10^{-5}	6.05×10^{-6}	10.0
7.10×10^{-5}	6.80×10^{-6}	10.4
9.50×10^{-5}	9.10×10^{-6}	10.4
9.70×10^{-5}	9.40×10^{-6}	10.3
1.40×10^{-4}	1.40×10^{-5}	10.0
2.00×10^{-4}	2.00×10^{-5}	10.0
3.90×10^{-4}	3.60×10^{-5}	10.8
4.40×10^{-4}	4.30×10^{-5}	10.2
5.40×10^{-4}	4.95×10^{-5}	10.9
9.10×10^{-4}	9.00×10^{-5}	10.1
Low Pump Speed; Chamber Ultimate 1×10^{-8} Torr		
Chamber A	Chamber B	Ratio
4.60×10^{-8}	1.00×10^{-8}	4.6
1.70×10^{-7}	3.56×10^{-8}	4.7
3.10×10^{-7}	5.35×10^{-8}	5.7
5.00×10^{-7}	7.50×10^{-8}	6.6
6.60×10^{-7}	9.20×10^{-8}	7.1
1.50×10^{-6}	2.00×10^{-7}	7.5
4.80×10^{-6}	5.00×10^{-7}	9.6
7.50×10^{-6}	7.55×10^{-7}	9.9
3.00×10^{-5}	3.00×10^{-6}	10.0
6.60×10^{-5}	6.50×10^{-6}	10.0
9.40×10^{-5}	9.20×10^{-6}	10.2
4.00×10^{-4}	4.00×10^{-5}	10.0
8.25×10^{-4}	8.20×10^{-5}	10.0

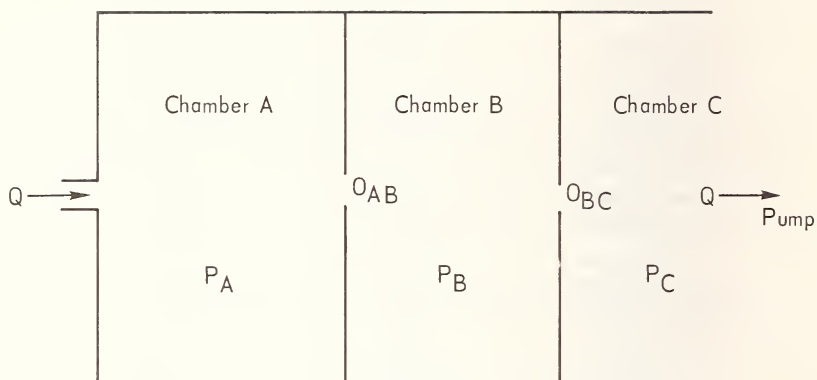


Figure 1 – Molecular Flow of Gas Through Fixed Orifices

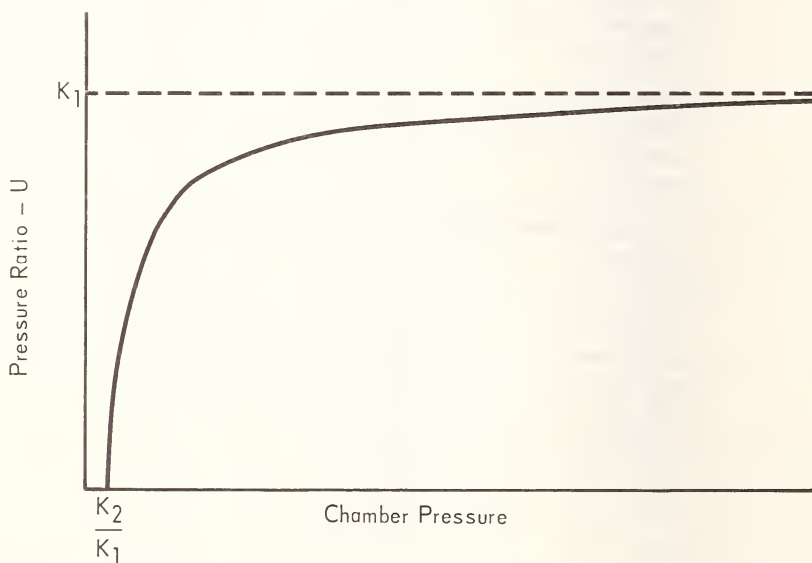


Figure 2 – Generalized Deviation in U Due to Background Gas Load

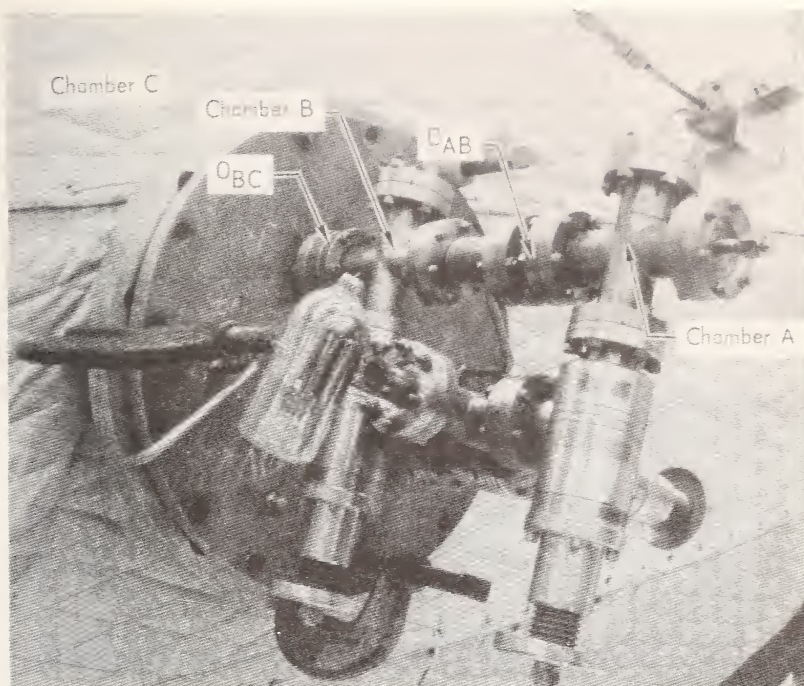


Figure 3 – Reference Transfer Calibrator

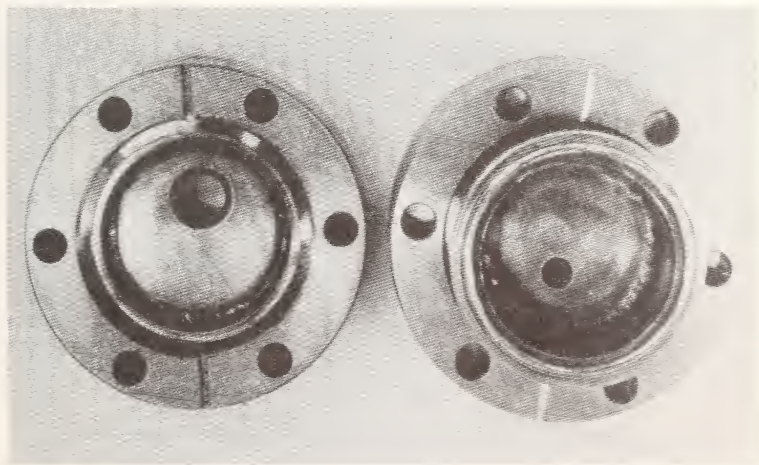


Figure 4 – RTC Orifice

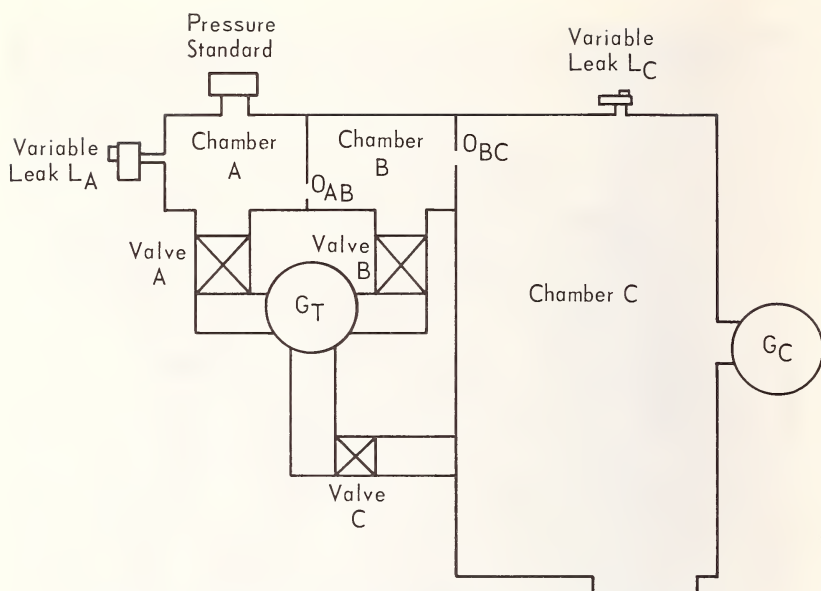


Figure 5 – Reference Transfer Comparison System Schematic

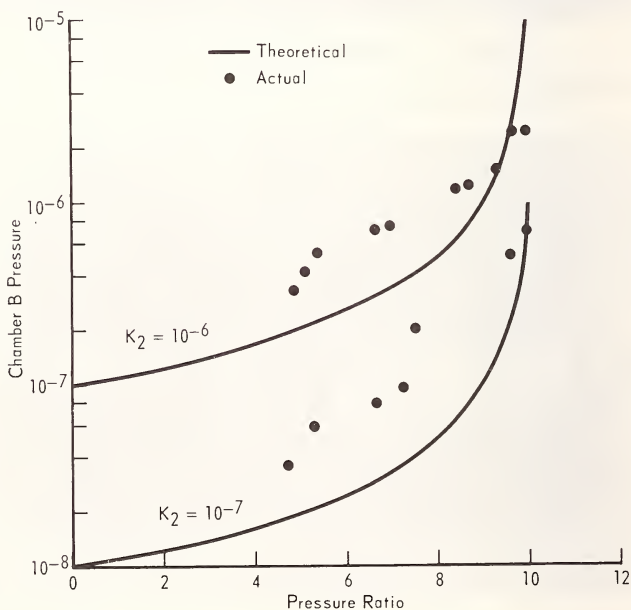


Figure 6 – Variation of Pressure Ratio – Chamber B Pressure

METHODS OF DETERMINING RESIDUAL GAS COMPOSITION FROM RESIDUAL GAS ANALYZER DATA

R.H. Lilienkamp¹

REFERENCE: Lilienkamp, R.H., "Methods of Determining Residual Gas Composition From Residual Gas Analyzer Data," ASTM/IES/AIAA Space Simulation Conference, 14-16 September 1970.

ABSTRACT: Three methods of determining residual gas composition from Residual Gas Analyzer (RGA) data are compared using a computer simulation of an RGA to generate the data for analysis. Typical vacuum system gas mixtures and errors from shot noise were simulated. Errors were also introduced into the calibration data used to interpret the RGA data. The first method is an iteration technique which proved to be inferior to the other methods. The second is a matrix inversion method which worked well for the gases used in this study but which must be evaluated for each gas mixture. The third method is a multiple regression analysis giving least squares fit to the data. This method uses all of the data from the RGA and is usable with any mixture of gases. The effect of the calculation of the residual gas composition is also shown.

KEY WORDS: Mass Spectrometry, Residual Gas Analysis Data Reduction, Residual Gas Analysis Computer Simulation, Space Vacuum System Gas Analysis

Introduction

The residual gas analyzer (RGA) is a very useful instrument for monitoring the performance of the vacuum system of a space simulator, and the reaction of the test specimen to the environment. In general, these instruments are used for qualitative analysis because of the complexity involved in analyzing the data to obtain quantitative results. A recent application of the residual gas analyzer required quantitative results, and a method of computerizing the system was

¹Senior Group Engineer, Engineering Laboratories, McDonnell Aircraft Company, St. Louis, Mo.

developed.⁽¹⁾ In this application only five gases were monitored and three of these had unique peaks which simplified the analysis.

For the more complex gas mixtures which can be expected in a space simulator, a more general method of data reduction would be required. The following methods of analyzing residual gas data have been investigated: iteration technique, matrix inversion method, and multiple regression analysis.

In the iteration technique⁽²⁾, an estimate of the partial pressure of each gas in the mixture is made. These estimates are used to calculate a mass spectrum which is then compared to the original data. From this comparison, corrections are made to the original estimates and the process is repeated until two successive estimates are sufficiently close.

In the matrix inversion method, a subset of N equations in N unknowns is selected and matrix algebra is used to solve these equations. A logical choice of equations to be used in this subset was made by basing the choice on the cracking patterns for each of the gases expected to be in the mixture.

Multiple regression analysis⁽³⁾ gives a least square fit to the data, using all the data from the RGA. With this technique it is possible to weight the data so that the data with larger errors is not as important as the data with smaller errors.

The RGA Model

To evaluate the methods of data reduction, a computer simulation of a mass spectrometer was used to generate mass spectra for analysis. This model assumes that there is linearity and no interaction between gas species. These are the same assumptions that are used in the data reduction techniques.

Gas mixtures typical of vacuum system operations⁽⁴⁾ were used to generate the mass spectra. Eight gases (hydrogen, methane, water vapor, carbon monoxide, nitrogen, oxygen, propane and carbon dioxide) were possible in these mixtures. The proportions of the mixtures, listed in Table 1, correspond to those present in an unbaked vacuum system, a vacuum system during bakeout, and a well-baked vacuum system.

Cracking patterns and sensitivities published for mass spectrometers⁽⁵⁾ were used in the model to calculate the peak heights (i.e., ion current) for these mixtures. The cracking patterns used are tabulated in Table 2.

Shot noise effects were simulated by adding errors, which were random both in magnitude and sign, to the spectra. The shot noise was proportional to the square root of the peak height. A proportionality constant was chosen to make the shot noise equal to 1 percent of the peak height for the major peak of a 100 percent concentration of a gas having a sensitivity of 100. Provisions were made to vary the constants to simulate varying amounts of shot noise.

Random errors were also introduced into the calibration data (i.e., sensitivity and cracking pattern) used to reduce the mass spectra data. These errors were directly proportional to the magnitude of the calibration data to which they were applied.

Superscript numbers in parentheses refer to the list of references appended to this paper.

The calibration errors and the magnitude of the shot noise were varied to evaluate their importance in obtaining a good gas analysis. For each combination of gas mixture, shot noise, and calibration errors, five different sets of noise data were generated. These noise data were both added to and subtracted from the basic mass spectra, thus producing 10 spectra to be analyzed. For each pair of spectra, a different set of calibration errors was used. Thus, a small statistical sample was obtained to compare the techniques.

The matrix equation for the simulated mass spectrometer is

$$(S \times [A] \times [P]) \pm [N] = [h] \quad (1)$$

where h , a column matrix of 22 rows, is the peak height. P , a column matrix of eight rows, is the composition of the gas. A , a rectangular matrix of 22 rows and eight columns, is the true calibration data for the spectrometer.

S is a constant used to convert relative sensitivities to absolute sensitivities; its value was selected so that the major peak of a 100 percent concentration of a gas having a sensitivity of 100 equals 10^{-4} .

The noise matrix N is a column matrix of 22 rows, and is added to or subtracted from the true peak heights. Each element of this matrix is related to the true peak height H by

$$N_{j,i} = (\text{Random Number}) k H_{j,i} \quad (2)$$

where the Random Number is random in sign and magnitude between 0 and 1, and k is the proportionality constant.

The matrix equation for calibration data with errors is

$$[A] = [C] + [E] \quad (3)$$

where A is the calibration data with the errors, C is the true calibration data, and E is the error. All three matrices are rectangular with 22 rows and eight columns.

Each element of the E matrix is related to the corresponding elements of the C matrix by

$$E_{j,i} = (\text{Random Number}) k_1 C_{j,i} \quad (4)$$

where the Random Number is random in sign and magnitude between 0 and 1, and k_1 is a proportionality constant.

Iteration Technique

The values of the partial pressure are estimated by calculating the value from each peak height and calibration factor in the spectrum for a given gas and using the lowest of these values as the partial pressure.

These partial pressures are used with the calibration factors to calculate a spectrum which is subtracted from the original spectrum to obtain an error spectrum. A correction to the partial pressures is obtained from the error

spectrum in a manner similar to that used to make the first estimate.

The second approximation is obtained by adding the correction to the original estimate.

Iterations are made by calculating a new spectrum which is used to calculate another new error spectrum from which new corrections are calculated and then added to the current estimate. The iterations are continued until the peaks in the error spectrum become small compared to the corresponding peaks in the original spectrum or until the error spectrum ceases to change with successive iterations.

In the initial evaluation of this technique the results from each iteration were printed, and based upon a comparison of these results with those of the previous iteration, a decision was made by the operator to continue or stop the iteration process. From these data it was concluded that it is unlikely that all the peaks in the error spectrum will become small compared to the corresponding peaks in the original spectrum even if "small" is defined as 1 percent.

The Matrix Inversion Technique

Matrix algebra is a conventional method for solving a set of N simultaneous linear equations in N unknowns. Starting with an equation set

$$[A_{j,i}] \times [P_i] = [h_j] \quad (5)$$

to solve for the P_i 's, the inverse of matrix A is used and

$$[A_{j,i}]^{-1} \times [h_j] = [P_i] \quad (6)$$

To have an inverse, the matrix A must be square and must not be singular. The original matrix A was not square; therefore, to use this technique, a subset of N equations must be chosen to produce a N x N matrix.

Out of the complete set of 22 equations, it is possible to choose 341,088 subsets of eight equations. This number can be reduced by following two simple rules:

(1) The matrix must not be singular. Thus, if any rows are either equal or proportional to each other, only one can be used in the matrix.

Examination of the matrix in Table 2 reveals that the 22 equations are reduced to 14 and the number of possible subsets is reduced to 3003.

(2) The matrix must include the major peak or at least one prominent peak in the spectrum of each gas. Using the major peaks gives seven equations corresponding to m/e 2 (hydrogen), 16 (methane), 18 (water vapor), 28 (carbon monoxide and nitrogen), 29 (propane), 32 (oxygen), and 44 (carbon dioxide).

The remaining equation must further define the carbon monoxide and nitrogen concentrations, and thus it is limited to m/e 12, 13, 14 and 30.

The m/e 12 and 13 peaks are formed by methane and carbon dioxide in addition to carbon monoxide. The m/e 14 peak is formed by both carbon monoxide and nitrogen as well as methane. The m/e 30 peak is formed by only carbon monoxide, but is quite small. The m/e 14 peak was chosen for this study.

A more mathematical approach is presented by Stanton⁽⁶⁾. The N rows of the matrix are vectors in N dimensional space. If the vector is perpendicular to all other vectors, it is ideally suited to be in the subset. If the angle between two vectors becomes small, then the two equations are ill-conditioned and only one can be used in the subset. The angle between the two vectors is given by

$$\cos^2 \theta_{j,k} = \frac{\left[\sum_{i=1}^N (a_{j,i} a_{k,i}) \right]^2}{\left[\sum_{i=1}^N a_{j,i}^2 \sum_{i=1}^N a_{k,i}^2 \right]} \quad (7)$$

where j and k are the two rows of the matrix being tested. For the 22 row matrix used in this study, there are 231 values of $\cos^2 \theta_{j,k}$.

Table 3 presents the values of the $\cos^2 \theta_{j,k}$ for the seven major peaks with respect to each other. From these data, the worst pair are m/e 28 and 29. The $\cos^2 \theta_{j,k}$ is 0.144152, which means $\theta_{j,k}$ is about 68 degrees.

Table 4 presents the values of $\cos^2 \theta_{j,k}$ for m/e 12,13,14 and 30 with respect to the seven major peaks. The largest $\cos^2 \theta_{j,k}$ occurs with m/e 13, the next largest with m/e 12, and the third largest with m/e 30. The m/e 14 peak, while having the smallest values of $\cos^2 \theta_{j,k}$, has two values larger than 0.3. To determine if it is better to have two pairs of equations with some ill-conditioning or one pair more ill-conditioned, the subset of equations used in the matrix inversion was modified by removing the data for the m/e 14 peak and adding the data for the m/e 30 peak.

Multiple Regression Analysis

Multiple regression is used to obtain the best fit of a set of observations of independent and dependent variables to an equation of the form

$$y = b_0 + b_1 X_1 + b_2 X_2 + \dots + b_M X_N \quad (8)$$

where y is the dependent variable and the X's are the independent variables. The b's are the constants to be determined for the set of observations. For residual gas analysis, the y's are the peak heights, the b's are the pressures, and the X's are the calibration constants. Thus, Equation 13 becomes

$$h_j = h_0 + P_1 A_{j,1} + P_2 A_{j,2} + \dots + P_N A_{j,N} \quad (9)$$

which, except for the h_0 term, is the same as Equation 5. The least squares fit determines the values of the P's in such a way that the error is minimized and results in N simultaneous linear equations in P. These N simultaneous linear equations can be solved by any appropriate method. The computer technique described by Efroymsen⁽⁷⁾ and used by Tunnicliff and Wadsworth⁽³⁾ solves these equations by the Gaussian elimination method. At each step in the elimi-

Superscript numbers in parentheses refer to the list of references appended to this paper.

nation, either a variable is removed or a new variable is added to the regression. The criteria used to select the variable to be added to or removed from the regression are as follows:

1. If the various contributions of a variable in the regression are insignificant, this variable is removed. If no variable is to be removed, then the following criterion is used.
2. The variable providing the greatest variance reduction is added to the regression if the variance reduction is significant. If the variance reduction is not significant, the regression is complete and the remaining variables are set equal to zero.

The application of these criteria to an actual problem is shown in Table 5, which presents the results for each step in the regression. The gas mixture used corresponds to that for a baked system, and a 0.1 percent calibration error and a 0.1 percent shot noise contribution to the maximum signal are assumed. In the first step the hydrogen partial pressure is the most significant. In the second step carbon monoxide partial pressure is added to the regression but with a value about twice that actually present. At Step 5, when nitrogen partial pressure is added to the regression, the value of the carbon monoxide partial pressure is reduced to a more reasonable value. The regression is completed in the seventh step, since adding the oxygen partial pressure will not produce a significant variance reduction. The oxygen partial pressure is then set equal to zero. In addition to the calculation of the partial pressures, the method also calculated the standard error for each of the partial pressures and for the peak height. The method also includes provisions for including weighting factors, which Tunnicliff and Wadsworth⁽³⁾ have done. They also have incorporated a method of rounding off the partial pressures based on standard errors. The majority of the work reported in this paper does not use weighting factors.

Results

A comparison of the gas composition calculated by analyzing the same data with the three techniques is presented in Table 6. A comparison of the errors in mass spectra computed from these results is presented in Table 7 along with the sum of the squares of these errors. The iteration method produced the most inaccurate data reduction of the three methods. The errors shown in Table 7 for the peak height calculation from the iteration method are zero for nine of the peaks (m/e 2, 12, 15, 18, 29, 30, 32, 34 and 38). The 32 and 34 peaks are redundant. Therefore, the method solved eight simultaneous equations in eight unknowns. Of the eight peaks, six (m/e 2, 15, 18, 30, 32 and 38) are unique to one of the gases in the mixture. The $\cos^2 \theta_{j,k}$ was calculated for these eight equations. For m/e 12 and 30, the value of $\cos^2 \theta$ was 0.312474, and for m/e 29 and 38, the value was 0.999741. All other values were very small or zero.

Following the procedure of Sherrell and Mathews⁽²⁾, the smaller peaks were deleted and the iteration was repeated. The results are presented in Table 8. The results were unchanged for four of the gases (hydrogen, methane, water

Superscript numbers in parentheses refer to the list of references appended to this paper.

vapor and oxygen). For nitrogen, propane and carbon dioxide, the results improved, but for carbon monoxide, the error increased. A comparison of the computed spectra from this composition with the original spectra reveals that the sum of the squares of the differences has increased from 1.61966×10^{-12} to 1.7599×10^{-12} . In this iteration only seven of the peaks, m/e 2, 15, 18, 29, 32, 34 and 39, produced zero error. Again, 32 and 34 were redundant, so that, effectively, only six peaks produced zero error. However, the m/e 14 and 44 peak errors were very small; these peaks had been controlling the iteration of nitrogen and carbon dioxide, respectively, until the m/e 29 error went to zero.

Again, the $\text{Cos}^2 \theta_{j,k}$ was calculated for these eight equations. The value of $\text{Cos}^2 \theta$ for m/e 14 and 15 was 0.402002, and for m/e 29 and 39 it was 0.999741, indicating that this choice of equations was worse than the first in this particular example.

Deleting the small peaks from the calculation removed the unique peak for carbon monoxide. This resulted in the number of iterations increasing from 2 to 28 in this example. In general, removing the small peaks resulted in an increase in the number of iterations. In some cases the iterations would not converge for all gases, but would oscillate between two values. In one of these examples the carbon monoxide varied between 6.5487 and 6.66516, and the nitrogen varied between 9.26273 and 7.42821. Their actual values were 7.6 and 7.5, respectively.

The choice of subsets of equations to be used in the matrix method was verified by comparing results from two different subsets. Both subsets included m/e 2, 16, 18, 28, 29, 32 and 44, which are the major peaks in the cracking patterns of the eight gases. One subset included m/e 14, while the other included m/e 30. The results for hydrogen, methane, water vapor and oxygen were not affected by this equation, but the results for carbon monoxide and nitrogen were the most affected. Results from one set of calculations are presented in Table 9. These results are typical and clearly favor the choice of the subset which includes the m/e 14 peak. These results illustrate the importance of the choice of the subset and the limitations of the matrix inversion technique.

For these mixtures of gases, the matrix technique using the m/e 14 peak and the multiple regression technique gave about equally valid results. Rounding off the results to a reasonable number of significant figures is required. The round-off technique of Tunnicliff and Wadsworth⁽³⁾ was tried on several calculations and appeared to work reasonably well. With this technique the last significant figure should have an accuracy of approximately one to five digits. Some adjustments are required to account for calibration errors.

Weighting of the data was investigated by using two weight factors, one proportional to the square root of the peak height and the other proportional to the reciprocal of the square root of the peak height, except for the very small peaks. The first weighting is based on the fact that the percent error increases as the peaks become smaller, and the second weighting is based on the

Superscript numbers in parentheses refer to the list of references appended to this paper.

fact that the absolute error decreases as the peaks become smaller. Neither of these weighting factors improves the results enough to warrant their use.

The effects of errors in the calibration factor and errors due to shot noise have been investigated by varying the magnitudes of these errors and observing the results. For this investigation the same set of random numbers was used, and only the order of magnitude of the errors was changed. The standard errors of the peak heights are presented in Table 10. The effect of increasing the noise is shown in the first row of data. A tenfold increase in noise produces a tenfold increase in the standard error. In this first column of data the effect of increasing the calibration error is shown, and again a tenfold increase in the calibration error produces a tenfold increase in the standard error. When both errors are present, these relationships begin to break down and now a tenfold increase in both errors is required to produce a tenfold increase in the standard error. This most likely is the result of some of the errors canceling the effects of other errors.

The errors in the calculation of the hydrogen concentrations are presented in Table 11. The same basic pattern seen in Table 10 is repeated in Table 11, with an interesting variation occurring when the noise error and calibration error are of the same order of magnitude. Under these conditions the errors become smaller than any other in that row or column, further suggesting the cancellation of errors. A similar effect is noted in the errors in the calculation of the methane concentrations presented in Table 12. In this case, the minimum errors are obtained when the calibration error is ten times that of noise error.

It would be expected that if both sources of error were eliminated, perfect solutions would be obtained. This is not necessarily the case, since the multiple regression analysis technique employed uses a significance test for the addition of a variable. By eliminating the calibration and shot noise errors, one of the minor gases in each of the mixtures was excluded from the regression. For the unbaked system the nitrogen (0.79 percent) was dropped, for the system during bakeout the oxygen (0.4 percent) was dropped, and for the well baked system the water vapor (0.2 percent) was dropped. By modifying the regression technique to include all variables, the concentrations of all gases were correctly obtained. With the inclusion of very small errors, these minor gases are no longer excluded from the regression and thus should not be of any concern in the analysis of data taken from a real RGA.

Conclusions

The iteration method gives the illusion that it is using all of the data in the mass spectra, but it is actually picking out a subset of equations which can be ill-conditioned and therefore produce quite erroneous results.

If a suitable subset of equations can be found, the matrix inversion technique is fast and produces results consistent with the accuracy of the data used. The technique is well-suited to on-line calculations for quick-look data.

The multiple regression analysis is the best of the techniques. This technique does use all of the data in the mass spectra. The large number of gases which can be included in the multiple regression analysis makes possible the detection of unexpected gases in the mixture. This method also provides standard errors for the results.

Both the matrix inversion and the multiple regression analysis techniques require reasonable accuracy in data and calibrations to obtain significant results. Experimental techniques to reduce the influence of noise on the data have been developed. Employment of these techniques should provide the quality of data necessary to achieve quantitative results with the residual gas analyzer.

References

1. R.J. Lilenkamp, H.F. McKinney, and D.I. Fiste,
 - a. "A Computerized Mass Spectrometer System", AIAA/ASTM/IES 4th Space Simulation Conference, Los Angeles, California, Sept. 8-10, 1969 (AIAA Paper No. 69-1016).
 - b. "A Computerized Mass Spectrometer System for Spacecraft Ground Test", Journal of Spacecraft and Rockets, Volume 7, 1970, pp.110-111.
2. F.G. Sherrell and A.J. Mathews, "Data Reduction Techniques for Vacuum Measurements by Mass Spectrometry", AIAA/ASTM/IES 1st Space Simulation Conference, Houston, Texas, Sept. 7-9, 1966, pp. 215-223.
3. D.D. Tunnicliff and P.A. Wadsworth, "A Stepwise Regression Program for Quantitative Interpretation of Mass Spectra", Analytical Chemistry, Volume 37, 1965, pp. 1082-1085.
4. Anonymous, "Test Your Knowledge", Varian Vacuum Views, March/April, 1969.
5. A. Cornu and R. Massot, "Compilation of Mass Spectral Data", Hayden and Son Limited, London, England, 1966.
6. R.G. Stanton, "Numerical Methods for Science and Engineering," Prentice-Hall, New Jersey, 1961.
7. M.A. Efroymson, "Multiple Regression Analysis in Mathematical Methods for Digital Computers", A. Ralston and H.S. Wilf, Eds., Wiley, New York. 1960.

Gas	Composition (%)		
	Unbaked	During Bakeout	Well-Baked
H ₂	0	21.9	75.7
CH ₄	0.8	2.63	6.67
H ₂ O	79.0	17.5	0.2
CO	16.0	21.9	7.6
N ₂	0.79	17.5	7.5
O ₂	3.1	0.4	0
C ₃ H ₈	0	17.15	2.2
CO ₂	0.3	0.87	0.2

Table 1– Typical Residual Gases in Vacuum Systems

Gas		H ₂	CH ₄	H ₂ O	CO	N ₂	O ₂	C ₃ H ₈	CO ₂
Column		1	2	3	4	5	6	7	8
M/e	Row								
1	1	1	0	0	0	0	0	0	0
2*	2	1000	0	0	0	0	0	0	
12	3	0	8	0	47	0	0	0	69
13	4	0	29	0	1	0	0	0	9
14*	5	0	75	0	8	52	0	0	0
15	6	0	754	0	0	0	0	0	
16*	7	0	1000	9	17	0	36	0	94
17	8	0	12	211	0	0	0	0	0
18*	9	0	0	1000	0	0	0	0	0
26	10	0	0	0	0	0	0	53	0
27	11	0	0	0	0	0	0	316	0
28*	12	0	0	0	1000	1000	4	615	82
29*	13	0	0	0	12	7	0	1000	1
30	14	0	0	0	2	0	0	0	0
32*	15	0	0	0	0	0	1000	0	0
34	16	0	0	0	0	0	1	0	0
38	17	0	0	0	0	0	0	43	0
39	18	0	0	0	0	0	0	165	0
41	19	0	0	0	0	0	0	149	0
42	20	0	0	0	0	0	0	61	0
43	21	0	0	0	0	0	0	336	0
44*	22	0	0	0	0	0	0	402	1000

* Peaks used in matrix inversion technique.

Table 2 – Cracking Patterns

m/e	16	18	28	29	32	44
2	0	0	0	0	0	0
16		1.41499×10^{-4}	1.36289×10^{-3}	5.59433×10^{-7}	2.5438×10^{-3}	3.58113×10^{-2}
18			0	0	0	0
28				0.144152	3.86872×10^{-6}	2.88122×10^{-2}
29					0	9.44378×10^{-2}
32						0

Table 3 – Values of $\text{Cos}^2 \theta_{j,k}$ for the Seven Major Peaks

Major Peak	Candidate Peaks			
M/e	12	13	14	30
2	0	0	0	0
16	5.22741×10^{-2}	0.852571	0.39062	1.19731×10^{-3}
18	0	0	0	0
28	0.202258	5.82893×10^{-3}	0.304761	0.51036
29	8.28862×10^{-5}	2.41448×10^{-6}	5.40778×10^{-5}	2.08387×10^{-4}
32	0	0	0	0
44	0.621188	0.280373	0	0

Table 4 – Values of $\text{Cos}^2 \theta_{j,k}$ to Select the Eighth Peak

Gas	Actual	Step 1	Step 2	Step 3	Step 4	Step 5	Step 6	Step 7
H ₂	75.5	71.5293	73.7899	74.5893	75.3757	75.3722	75.3888	75.4246
CH ₄	6.67			5.85851	6.52495	6.63657	6.61605	6.65286
H ₂ O	0.2							0.199035
CO	7.6		14.4206	14.6568	13.775	7.62461	7.51718	7.51973
N ₂	7.5					7.41275	7.56472	7.56177
O ₂	0							0
C ₃ H ₈	2.2				2.22568	2.24266	2.18402	2.20731
CO ₂	0.2						0.200304	0.204763

Baked System

Calibration Error 0.1 Percent

Shot Noise 0.1 Percent for Maximum Signal

Table 5 – Results of Each Step in the Regression

		Iteration Method		Matrix Method		Regression Method	
Gas	Actual	Calculated	Difference	Calculated	Difference	Calculated	Difference
H ₂	75.5	75.4954	4.64835×10^{-3}	75.4954	4.64835×10^{-3}	75.4906	9.4038×10^{-3}
CH ₄	6.67	6.70745	-3.74526×10^{-2}	6.70143	-3.14347×10^{-2}	6.70101	-3.10143×10^{-2}
H ₂ O	0.2	0.201330	-1.32975×10^{-3}	0.20133	-1.32975×10^{-3}	0.198251	1.74917×10^{-3}
CO	7.6	7.51186	8.81354×10^{-2}	7.76979	-0.169791	7.69521	-9.52123×10^{-2}
N ₂	7.5	9.59221	9.59221	7.30213	0.197865	7.38658	0.113419
O ₂	0	0	0	0	0	0	0
C ₃ H ₈	2.2	2.17572	2.42754×10^{-2}	2.18815	1.18469×10^{-2}	2.19320	6.80313×10^{-3}
CO ₂	0.2	0.289488	-8.94883×10^{-2}	0.198073	1.92661×10^{-3}	0.194518	5.48246×10^{-3}

Table 6 – Comparison of Composition Calculated by Three Techniques

m/e	Peak Height	Errors		
		Iteration	Matrix	Regression
1	4.18604×10^{-7}	6.68012×10^{-9}	6.68102×10^{-9}	6.70606×10^{-9}
2	1.96417×10^{-5}	0	3.38813×10^{-21}	1.23723×10^{-9}
12	3.07419×10^{-7}	0	-4.42107×10^{-9}	-1.52820×10^{-9}
13	7.74480×10^{-7}	-2.32419×10^{-9}	-1.79984×10^{-9}	-1.71235×10^{-9}
14	4.7688×10^{-7}	-7.47515×10^{-8}	-3.97047×10^{-23}	-2.33766×10^{-9}
15	1.87109×10^{-6}	0	1.67871×10^{-9}	1.79594×10^{-9}
16	2.59784×10^{-6}	5.73121×10^{-9}	6.35275×10^{-22}	1.41230×10^{-9}
17	5.11147×10^{-8}	9.64329×10^{-11}	1.23143×10^{-10}	4.49942×10^{-10}
18	1.00631×10^{-7}	0	2.64698×10^{-23}	1.53895×10^{-9}
26	7.62449×10^{-8}	2.40678×10^{-9}	1.98499×10^{-9}	1.81382×10^{-9}
27	4.51453×10^{-7}	1.12183×10^{-8}	8.70354×10^{-9}	7.68298×10^{-9}
28	1.15251×10^{-5}	-1.26839×10^{-6}	-4.23516×10^{-22}	1.57104×10^{-9}
29	1.50456×10^{-6}	0	6.35275×10^{-22}	-2.91341×10^{-9}
30	1.15625×10^{-8}	0	-3.97009×10^{-10}	-2.82215×10^{-10}
32	0	0	0	0
34	0	0	0	0
38	5.99302×10^{-8}	0	-3.42343×10^{-10}	-4.81274×10^{-10}
39	2.33961×10^{-7}	4.15767×10^{-7}	2.84495×10^{-9}	2.31222×10^{-9}
41	2.13783×10^{-7}	6.37356×10^{-9}	5.18877×10^{-9}	4.70795×10^{-9}
42	8.59945×10^{-8}	1.04179×10^{-9}	5.56515×10^{-10}	3.59576×10^{-10}
43	4.77394×10^{-7}	9.56445×10^{-9}	6.89204×10^{-9}	5.80751×10^{-9}
44	7.21304×10^{-7}	-6.99986×10^{-8}	-2.64698×10^{-23}	1.55005×10^{-9}
Sum of the squares of the error		1.61966×10^{-12}	2.33036×10^{-16}	2.02381×10^{-16}

Table 7 – Comparison of Errors in Mass Spectra Computed From Compositions of Table 6

Gas	Actual	Iteration (All Peaks)	Iteration (Small Peaks Deleted)	Difference from Actual
H ₂	75.5	75.4954	75.4954	4.64835×10^{-3}
CH ₄	6.67	6.70745	6.70745	-3.74526×10^{-2}
H ₂ O	0.2	0.201330	0.201330	-1.32975×10^{-3}
CO	7.6	7.51186	5.72381	1.87619
N ₂	7.5	9.59221	7.67615	-1.176153
O ₂	0	0	0	0
C ₃ H ₈	2.2	2.17572	2.21509	-1.50884×10^{-2}
CO ₂	0.2	0.289488	0.189422	1.05776×10^{-2}

Table 8 Effect of Deleting Small Peaks on Composition Calculations by the Iteration Method

	N ₂ Actual = 0.79 Matrix		CO Actual = 16 Matrix	
Case	m/e 14	m/e 30	m/e 14	m/e 30
1A	0.795487	-0.233733	15.9602	16.8174
1B	0.791744	1.76231	16.0119	15.2036
2A	0.732669	2.02149	16.0729	14.9983
2B	0.850865	-0.470798	15.9118	17.0137
3A	0.802927	1.15697	15.9586	15.6631
3B	0.775903	0.45944	16.0703	16.3344
4A	0.654809	2.02425	16.1389	14.9981
4B	0.925431	-0.475565	15.8665	17.0336
5A	0.738217	1.96145	16.0546	15.0344
5B	0.847726	-0.380303	15.9547	16.9789

Table 9 Effect of Choice of Subset in the Matrix Inversion Technique

Noise Error %	0	0.01	0.1	1.0
Calibration Error %				
0		3.38×10^{-10}	3.38×10^{-9}	3.383×10^{-8}
0.01	2.468×10^{-11}	3.40×10^{-10}	3.38×10^{-9}	3.383×10^{-8}
0.1	2.578×10^{-10}	4.345×10^{-10}	3.405×10^{-9}	3.385×10^{-8}
1.0	3.571×10^{-9}	2.608×10^{-9}	4.347×10^{-9}	3.413×10^{-8}
10.0	2.50×10^{-8}	2.50×10^{-8}	2.541×10^{-8}	4.366×10^{-8}

Table 10 Standard Errors of Peak Height

Noise Error %	0	0.01	0.1	1.0
Calibration Error %				
0		-4.019×10^{-3}	-4.019×10^{-2}	-0.4019
0.01	4.950×10^{-3}	9.411×10^{-4}	-3.523×10^{-2}	-0.396904
0.1	4.957×10^{-2}	4.555×10^{-2}	9.404×10^{-3}	-0.3521
1.0	0.4928	0.4888	0.4528	9.328×10^{-2}
10.0	4.655	4.651	4.617	4.276

Table 11 Actual Errors in H₂

Reading Error %	0	0.01	0.1	1.0
Calibration Error %				
0		-3.215×10^{-3}	-3.215×10^{-2}	-0.3215
0.01	1.137×10^{-4}	-3.102×10^{-3}	-3.204×10^{-2}	-0.3214
0.1	1.137×10^{-3}	-2.078×10^{-3}	-3.101×10^{-2}	-0.3204
1.0	1.37×10^{-2}	8.154×10^{-3}	-2.077×10^{-2}	-0.3100
10.0	0.1134	0.1102	8.144×10^{-2}	-0.2064

Table 12 Actual Errors in CH₄

SPECTRAL ABSOLUTE REFLECTANCE MEASUREMENTS OF CO₂ FROSTS IN THE
0.5 to 12.0 MICRON REGION*

B. E. Wood, A. M. Smith, and B. A. Seiber, Aerospace Division,
von Karman Gas Dynamics Facility, Arnold Engineering Develop-
ment Center, Arnold Air Force Station, Tennessee and J. A.
Roux, The University of Tennessee Space Institute, Tullahoma,
Tennessee.

ABSTRACT: In situ absolute reflectance measurements have been made for carbon dioxide frosts formed on liquid-nitrogen cooled substrates. Data were obtained spectrally in the wavelength range from 0.5 to 12.0 μ using an infrared integrating sphere. CO₂ frosts were found to exhibit an anomalous dispersion reflectance peak at 4.3 microns which was shown to be a very sensitive indication of the presence of solid CO₂. Also CO₂ frosts scatter short wavelength radiation ($\lambda < 1.0\mu$) significantly and is semi-transparent for much of the wavelength range between 2.0 and 12.0 . The application of these results to problems associated with cryogenically cooled surfaces is discussed.

KEY WORDS: carbon dioxide, reflectance, infrared, frost, cryo-deposit, simulation, spectral, cryogenics, Mars, integrating sphere, scattering, absorbing, anomalous dispersion

INTRODUCTION - The thermal radiative properties of cryogenic-ally cooled surfaces are being studied with increased interest as more and more applications of cryogenic coolants appear. Examples of situations where knowledge of these properties is important are: (1) simulation of cold outer space in ground test facilities by liquid nitrogen (LN₂) cooled black surroundings, (2) reflective and emissive properties of cooled optics (3) formation of frosts on cold surfaces to approximate the

*The research reported in this paper was sponsored by the Arnold Engineering Development Center, Air Force Systems Command, under Contract No. F40600-69-C-0001 with ARO, Inc.

formation of planetary frosts (i.e., polar caps on Mars), (4) variation in transmission of cryogenically cooled optical windows caused by thin film interference effects of thin deposited films, (5) problems associated with absolute calibration of low temperature black bodies as reference sources, and (6) reduction in visibility through spacecraft windows caused by condensation of water and other contaminants.

Many of the previous cryogenic reflective property measurements have suffered somewhat due to the deposits being formed and measured at atmospheric pressure or because the measurements were obtained by a calorimetric technique or within a narrow wavelength range. This study presents the reflective properties of LN_2 cooled surfaces in vacuum, with and without the presence of CO_2 cryodeposits. The reflectance measurements were made in situ and covered the wavelength range from 0.5 to 12.0μ .

Absolute reflectance measurements of scattering type (non-specular) surfaces are ordinarily made using an integrating sphere. Integrating spheres having MgO or BaSO_4 coatings are limited to wavelengths less than about 2.6 microns due to the low reflectance of the coating for longer wavelengths. However, it was established in Ref. 1 that the usable wavelength range can be extended if powdered sodium chloride (NaCl) is substituted as the sphere coating. By using the NaCl coating, and developing a new radiation source, the usable wavelength range was extended out to 12.0μ . Cryodeposit reflectance measurements were obtained as functions of wavelength, deposit thickness, τ , substrate material and deposition rate, $\dot{\tau}$.

APPARATUS - The infrared integrating sphere (Fig. 1) was composed of two stainless steel hemispheres 8 inches in diameter. The interior of the sphere was coated with powdered reagent grade NaCl which was applied by first coating the sphere interior with a thin layer of low vapor pressure vacuum grease (10^{-11} torr at 300°K). This served as a bonding agent and then the previously ground NaCl was pressed onto the sphere wall until a thickness of approximately 5 mm had been obtained. This technique of coating has the advantage of eliminating highly absorbing water which was present when the water slurry method described in Ref. 1 was used.

The cryosurface (Fig. 2) was a hollow, 1 by 1-1/2 by 1/2-in. rectangular, stainless steel block which was cooled by continuously flowing LN_2 through it. The test surface was one of the 1 by 1-1/2-in. faces and was either polished stainless steel or black epoxy paint. A copper-constantan thermocouple was silver soldered to the surface to allow monitoring of the test surface temperature. To restrict the cryopumping area to that of only the cryosurface, the LN_2 supply lines inside the chamber were vacuum jacketed. The pumping system consisted of an ion pump and an LN_2 -trapped 4-inch oil diffusion pump backed by a mechanical pump. This system allowed pressures in the 10^{-7} torr range to be routinely achieved.

One of the problems associated with using an infrared integrating sphere is that of obtaining an infrared source which emits enough energy at the longer wavelengths. In this study, a 1000 watt tungsten-halogen lamp was enclosed in a housing which was cooled at both ends (see Fig. 3). This allowed the middle of the housing to heat up to glowing red thereby providing an extra source of infrared energy. With this arrangement the source was usable over the wavelength range from 0.3 to at least 25μ . Radiation from the source was chopped at 13 Hz and focused onto the wall of the integrating sphere after passing through a sodium chloride window (Fig. 1). After striking the sphere wall behind the test surface face, the radiation was reflected diffusely throughout the sphere so that the portions of the sphere which were not illuminated directly were uniformly irradiated. Radiation reflected from either the test surface or a portion of the wall not directly irradiated was collected by an off axis paraboloidal mirror and focused on the entrance slit of the monochromator.

The monochromator was a prism type single pass system. For most of the measurements a NaCl prism was employed since it was usable over the entire wavelength range from 0.5 to 12.0μ . In one set of experiments a CaF_2 prism was used since it has a much higher dispersion than NaCl in the $1-6\mu$ range. The monochromator and paraboloidal mirror were mounted on a table which could be rotated about the vertical centerline of the viewport, thus allowing radiation from either the test surface or sphere wall to be collected. The detector was a Charles M. Reeder[®] thermocouple which had a sensitivity of $25 \mu\text{V}/\mu\text{W}$. From the detector the output was amplified, synchronously rectified, and displayed on a strip chart recorder.

Formation of the CO_2 cryodeposit was accomplished by flowing CO_2 gas into the chamber at a known flow rate and allowing the gas to be cryopumped by the LN_2 cooled cryosurface. The flow system consisted of two calibrated standard leaks with a forepressure of one atmosphere. The deposition rate, \dot{r} , of the gas depended on the standard leak used.

PROCEDURE - The hemispherical-angular technique was used for obtaining spectral absolute reflectance measurements. In this technique the spectral hemispherical-angular reflectance is determined from the relations (Refs. 1 and 2)

$$\rho_{\text{ha}}(\theta, \lambda) = \frac{I_r(\theta, \lambda)}{e_{i,h}(\lambda)/\pi} = \frac{I_r(\theta, \lambda)}{I_i(\lambda)} \quad (1)$$

where $I_r(\theta, \lambda)$ is the reflected intensity within the small collection solid angle $\Delta\omega_r$ (0.02 steradians) inclined at the angle θ and $e_{i,h}(\lambda)$ is the hemispherically incident energy with the associated diffusely incident intensity $I_i(\lambda)$. Since the same collection solid angle $\Delta\omega_r$ is used for both

quantities, the absolute reflectance can be obtained from Eq. 1. Even though the exact quantities $I_r(\theta, \lambda)$ and $I_i(\lambda)$ are not measured, the detector outputs are directly related to these quantities by multiplicative constants which depend on the transfer optics and detection system. The measurements were accomplished by first viewing the sample and obtaining a detector output for a given wavelength. This was followed by viewing a portion of the sphere wall (not directly irradiated) at the same wavelength and again recording the detector output. Since the sphere wall is uniformly irradiated by multiple reflections, the intensity of the radiation reflected from the sphere wall is equal to the intensity incident on the test surface. From these two detector outputs, the absolute reflectance can be determined from Eq. 1.

Prior to cryodeposit reflectance measurements, the integrating sphere system was evacuated to approximately 5×10^{-7} torr and then reflectance measurements were made on the bare test surface.

After obtaining the reflectance as a function of wavelength, LN_2 was used to cool the test surface to 94°K . Upon valving off the integrating sphere from the pumping system the CO_2 gas flow into the sphere was started. By allowing the gas to condense on only the test surface, a given flow time resulted in a certain thickness, τ , of the deposit. The average thickness over the entire surface could be calculated by knowing the mass flow rate, cryosurface pumping area, and density of deposit. The cryosurface pumping area was 40.2 cm^2 , and the mass flow rate either $2.25 \times 10^{-3} \text{ g/sec}$ or $2.39 \times 10^{-4} \text{ g/sec}$. The cryodeposit density was taken to be 1.67 (Ref. 3) since the deposits were formed at pressures approximately the same as those in Ref. 3. In-situ thickness measurements were made in order to verify the deposit thickness as calculated. This was done using thin film interference techniques discussed in Refs. 3 through 5. The thicknesses determined by the two methods were in good agreement.

The chamber pressure during deposition varied between 10^{-3} and 10^{-1} torr and depended on the flow rate and cryodeposit thickness. For the majority of the measurements the deposition pressure varied between 10^{-2} and 10^{-1} torr. After each thickness of deposit had been formed, reflectance measurements were made over the complete wavelength range from 0.5 to 12.0μ . This procedure was continued until the deposit had reached the desired thickness (usually 3-4 mm).

RESULTS - Black Epoxy Paint Substrate - The reflectances of CO_2 cryodeposits formed on an LN_2 -cooled black epoxy paint substrate are shown in Fig. 4 for wavelengths between 0.5 and 12.0μ . The view angle, θ , was 10 degrees for all thicknesses. These deposits were formed using a deposition rate of $0.335 \mu/\text{sec}$ which resulted in a deposition pressure of 1×10^{-2} to 5×10^{-2} torr, for deposits 0.44 mm thick or less. For the 3.38 mm

thick deposit the final pressure during deposition was 1.25×10^{-1} torr. The flow time required to form a deposit 3.4 mm thick was approximately 2-3/4 hours.

Figure 4a shows the reflectance of the bare substrate prior to deposition. The reflectance is essentially independent of wavelength with only a slight increase from 5 percent up to 8-9 percent in the vicinity of 9.1μ . Figures 4b to 4d show the reflectance of cryodeposits ranging from 0.13 mm up to 3.38 mm thick.¹ As can be seen by comparison of the data for different thicknesses, the reflectance begins to increase first at the short wavelengths ($\lambda < 1.5\mu$) and continues to increase for the long wavelengths as the deposit thickness is increased. The increased reflectance at the shorter wavelengths has been previously reported (Ref. 5). For wavelengths greater than about 2.0μ the reflectance is seen to be less than the bare substrate reflectance for the 0.13 and 0.23 mm thick deposits. This is also typical of the reflectance for shorter wavelengths ($\lambda < 2.0\mu$) but the effect shows up for deposits thinner than any shown in Fig. 4. As the thickness is increased further, the reflectance increases for all wavelengths, Figs. 4b and 4d. For the thickest deposit investigated, $\tau = 3.38$ mm, the reflectance has risen to about 77 percent for $\lambda = 0.5\mu$ but drops off rapidly with increasing wavelength.

In Figs. 4b and 4c the single most prominent spectral feature is the sharp rise in reflectance in the region of 4.3μ . As the thickness of the deposit increases this feature becomes less prominent due to the increase in bulk scattering of other wavelengths around the 4.3μ region. The reflectance peak is attributed to anomalous dispersion (Ref. 7) wherein a strong absorption band in a liquid or solid has associated with it a very high index of refraction so that both absorption and reflection coefficients are quite high. It is well known that in the gaseous phase, CO_2 exhibits its strongest absorption at 4.25μ . As can be seen in Figs. 4b through 4d the rapid increase in reflectance in this region results in a sensitive technique for identifying the presence of solid CO_2 . The peak at 4.3μ has been seen for deposits as thin as 1 micron.

For deposits less than 3.38 mm thick there is relatively little spectral structure seen in the reflectance spectra in Fig. 4 due to the transmission of the deposit and the highly absorbing black substrate. However, for the 3.38 mm thick deposit the scattering has increased significantly which enhances the absorption bands due to the increased reflectance for the nearby wavelengths. Absorption bands can now be seen to occur at 2.0μ , 2.85μ and what appear to be bands at 3.85

¹Additional experimental data are contained in Ref. 6.

and 4.55μ . However, the latter two are really part of the strong absorption band centered around 4.25μ with the reflectance peak occurring in the middle of the absorption band. Other spectral features to be seen in Fig. 4d are a broad reflectance increase extending from 7.9 to 10.5μ and a gradual rise in reflectance from 10.5μ to 12.0μ . For all of the CO_2 deposits formed on the black substrate, it can be seen that the reflectance will be less than 20 percent for wavelengths between 2.7 and 12.0μ . This could be a result of the deposits being highly absorbing or the deposits being somewhat transparent with most of the energy being absorbed by the black substrate. As will be shown later, the latter is the most significant factor.

The reflectance dependence on deposit thickness is presented in Fig. 5. The view angle is again 10° and the dependence on thickness is shown for the selected wavelengths of 0.5 , 1.0 , 2.0 , 4.0 , 8.0 , and 12.0μ . For 0.5μ radiation, the 3.38 mm thick deposit effectively behaves as one of infinite thickness since the reflectance has leveled off. However, for $\lambda = 1.0$ and 2.0μ , the reflectance is still increasing with thickness at 3.38 mm. The $\lambda = 2\mu$ curve is essentially linear with thickness above $\tau = 0.4$ mm. At the other 3 wavelengths, the deposit reflectance is still dependent on thickness at 3.38 mm but much less so than for the 2.0μ curve. The increase in reflectance for $\lambda = 8.0$ and 12.0μ is only slight due to the relatively small scattering coefficient at these wavelengths. For the $\lambda = 4.0\mu$ curve, very little thickness dependence is present, as expected, since the CO_2 deposit is highly absorbing at this wavelength.

To determine the reflective properties of thin CO_2 deposits on the black epoxy paint and to determine possible deposition rate effects, a series of measurements was made using a deposition rate, \dot{t} , of $0.0355\mu/\text{sec}$ which is about a factor of 10 less than the deposition rate used for the previously discussed measurements. For these investigations, the wavelength range covered was from 0.5 to 5.0μ since it had already been established that relatively little change was observed for the longer wavelength radiation for the thinner deposits. In Fig. 6, the reflectances of thin deposits formed at a deposition rate of $0.0355\mu/\text{sec}$ on the black substrate are shown for deposits 2 , 27 , 54 , 108 , and 215 microns thick. Notice that even for the thinnest deposit, 2 microns thick, that the 4.3μ anomalous dispersion band is already quite apparent. The only other significant change in reflectance for all thicknesses and wavelengths is the gradual increase in reflectance for wavelengths between 0.5 and 1.5μ due to internal scattering. In the thickness region of overlap between Figs. 4 and 6 it appears that the deposits formed at the lower deposition rate are less reflecting. For example, at 231 microns, for the larger deposition rate, the reflectance is about 32 percent at $\lambda = 0.5\mu$ whereas for 215 microns formed at the lower deposition rate, the reflectance is only 21

percent at the same wavelength. For the 2 micron thick deposit, the reflectance is lower than the bare substrate reflectance for wavelengths less than 1μ . This effect is usually present for all wavelengths although it is not so noticeable in Fig. 6. The deposition pressure for the lower deposition rate varied from 10^{-3} torr for the 2 micron thick deposit up to 2×10^{-2} torr for the 215 micron thick deposit and was a little lower than for the deposits formed at the higher deposition rate.

Stainless Steel Substrate - To understand more fully the radiative properties of CO_2 deposits, a polished LN_2 -cooled stainless steel substrate was employed. This was the same test surface used in the previous measurements but with the black paint removed and the surface repolished. In Fig. 7a the reflectance of the bare polished stainless steel surface is shown with an absorption band occurring around 3.0μ . This band could not be eliminated although various methods were attempted such as mild bakeout under vacuum, repolishing with various types of abrasives, and finally, cleaning with freon in an ultrasonic cleaner. Since the band shows up at 3.0μ and increased scatter in the reflectance data is seen in the 5 to 6μ region, it would appear that some form of water was permanently entrenched in the steel. As shown in Fig. 7b-d reflectances of CO_2 deposits of thicknesses, 0.13, 0.44, and 3.38 mm were formed on the stainless steel substrate. The pressure during deposition varied from 2 to 4×10^{-2} torr for the 0.13 to 0.44 mm thick deposits, and was 2×10^{-1} torr for the 3.38 mm thick deposit. Notice that for the 0.13 mm deposit the reflectance at the shorter wavelengths ($\lambda = 0.5\mu$) has decreased from the bare substrate reflectance of 58 percent to 40 percent. Further increase in deposit thickness, however, causes the reflectance to increase due to internal scattering until eventually it levels off. For longer wavelengths, $\lambda > 2.0\mu$, the reflectance is influenced by strong absorption bands in some regions, and a gradual decrease in the reflectance in other wavelength regions as the thickness is increased. It was expected in these non-highly absorbing regions that the reflectance would gradually decrease with thickness since only a slight increase in reflectance was seen for similar thicknesses of deposits formed on the black surface. In contrast to the reflectance curves for the black epoxy paint substrate, the absorption bands are quite pronounced even for the smaller deposit thicknesses. In the wavelength regions near these bands the deposits are somewhat transparent with the result that the stainless steel substrate reflectance continues to influence the amount of radiation reflected. The high reflectance at wavelengths near the absorption bands accentuates the absorption in these regions.

By comparing the reflectance data for deposits formed on the two substrates, it becomes apparent that the CO_2 deposits transmit appreciably in the wavelength region from 1 to 12μ .

If the deposits were not somewhat transparent, the reflectances observed for cryodeposits of equal thickness formed on the two different substrates would be more nearly the same. For instance, the reflectance at 5.5μ for a 3.38 mm thick deposit on stainless steel is 65 percent whereas for an equal thickness on the black substrate the reflectance is only 19 percent. This indicates that even at this relatively large thickness the substrate reflectance still influences the reflectance of the cryodeposit-substrate complex which can only be explained by the deposit being transparent for radiation at these wavelengths.

As mentioned previously, the absorption bands of CO_2 shows up more clearly in Fig. 7 than in Fig. 4. Absorption bands for the 3.38 mm thick deposit can be seen to be centered around 2.0, 2.85-3.0, 4.3, 6.1, 6.85, and 7.55μ . The location of the absorption band in the 2.85-3.0 μ region seemed to vary with deposits. For instance in Fig. 7b the band is centered at 2.85μ while thicker deposits exhibited the same absorption band centered at 3.0μ . This variation was also seen for other deposits (not shown). As shown in Fig. 7c and 7d, the reflectance peak at 4.3μ is again present but is not so noticeable as in Fig. 4. Notice, however, that the peak heights are about the same in each case (20-25 percent). For wavelengths between 10 and 12μ , there is a significant reduction in reflectance. For the 3.38 mm thick deposit the reflectance has dropped to 25 percent at 12.0μ .

The change in reflectance as the deposit thickness is formed on stainless steel is shown in Fig. 8 for a wavelength of 0.705μ . The reflectance was monitored continuously as the deposit was being formed. Figure 8 shows that the experimental reflectance curve has a sharp decrease initially, followed by a more gradual decrease until reaching a minimum, and then increasing until the reflectance levels off at a value much higher than the bare surface. The explanation of this behavior will be explained in detail in the next section where a theoretical study is made.

Analytical Results - Figure 8 shows that the reflectance initially undergoes a decrease, then descends to a minimum and finally increases with deposit thickness until reaching a plateau. Due to this interesting behavior an analytical investigation was conducted to obtain a fundamental understanding of cryodeposit reflectances and their variation with thickness, view angle, substrate, and refractive index. The theoretical study was conducted with the objective of formulating a mathematical model for the cryodeposit reflectance based on the results of the present experimental work.

In the search for a realistic reflectance model several combinations of boundary conditions were considered for the substrate and vacuum deposit interface. Based on the magnitude of the reflectances and the general trend of the data presented

in this report and in Ref. 1, it was decided that the best model would be to consider the substrate and vacuum deposit interfaces as Fresnel surfaces. The internal structure of the deposit was considered as an absorbing and isotropic scattering medium; that is, the probability of energy being scattered into every direction is equal.

This model for the cryodeposit reflectance required the solution of the radiative transport equation:

$$\frac{dI}{d\bar{\tau}} = \frac{-I}{u} + \frac{W}{2u} \int_{-1}^1 I(u) du \quad (2)$$

where

$$\bar{\tau} = \int_0^{\tau} (K + \sigma) d\tau \quad (3)$$

is the local monochromatic optical thickness at physical thickness τ . The transport equation is an integro-differential equation and was reduced to a system of ordinary linear differential equations by the method of discrete ordinates which employed the Gaussian quadrature:

$$\int_{-1}^1 f(x) dx = \sum_{j=1}^m f(x_j) a_j \quad (4)$$

where x_j is the quadrature point and a_j is the quadrature weight. Therefore,

$$\frac{dI(\bar{\tau}, u_i)}{d\bar{\tau}} = \frac{-I(\bar{\tau}, u_i)}{u_i} + \frac{W}{2u_i} \sum_{j=1}^m I(\bar{\tau}, u_j) a_j \quad (5)$$

$i = 1, 2, \dots, n$

The solution of the system of simultaneous differential equations together with the diffuse irradiance boundary conditions is extremely lengthy and complex and will be discussed in detail in Ref. 8. It should suffice to mention that the system of equations was solved numerically using the Milne predictor-corrector method.

The theoretical investigation was conducted with the point of view of matching the hemispherical-directional reflectance measured for cryodeposits. This led to a computer program that employs two experimental data points (the reflectance at two different thicknesses) to calculate a monochromatic absorption and scattering coefficient. Once the coefficients were calculated they were used to "predict" reflectance values at other thicknesses.

Figure 8 shows a comparison between the theoretical and experimental results for a CO_2 cryodeposit on a stainless steel substrate at $\lambda = 0.7\mu$. The arrows indicate the two data points used in the computer program to calculate the monochromatic absorption and scattering coefficients. All other points were predicted using these coefficients. The theoretical results are in very good agreement with the data which indicates that the analytical model proposed is realistic.

Since the cryodeposit reflectance model has proven to be a reasonable one, it can be used to explain the shape of the curve in Fig. 8. For small deposit thicknesses near zero, there is a sharp (almost discontinuous) drop in reflectance due to the relative refractive index change. This reflectance decrease is from 0.49 to 0.388 and is denoted as the first decrease. As the deposit thickness increases there is a second reflectance decrease from 0.388 to 0.325. In view of the theoretical model, this second decrease is a result of internal scattering occurring in the deposit. Some of the internally scattered intensity is incident internally on the vacuum-deposit interface at angles greater than the critical angle and undergoes total internal reflection. The reflectance decreases since the thickness increase causes a higher probability that more intensity will be scattered past the critical angle and eventually will be absorbed by the substrate before being rescattered. As the thickness increases further, the total internally reflected intensity has an even higher probability of being rescattered before reaching the substrate and being rescattered into directions less than the critical angle and hence partially escaping the cryodeposit. At larger thicknesses the internal scattering dominates causing more intensity to escape the deposit due to the rescattering effect and resulting in a reflectance that now monotonically increases with thickness. Now each ray is multiply scattered and is less likely to reach the absorbing substrate. For greater deposit thicknesses, the curve levels off at a reflectance plateau of about 0.71. The reflectance should stay at approximately this value as the thickness increases further since there is a small but finite amount of absorption.

DISCUSSION - The results presented in Figs. 4 through 8 show the reflectance of carbon dioxide cryodeposits formed on stainless steel and black epoxy paint substrates and ranging from 2 microns to 3.38 mm in thickness. These thicknesses cover the range of concern for most of the situations listed in the introduction. From the results discussed previously, it is apparent that several aspects should be considered in determining the reflectance of CO_2 frosts. These are: wavelength, deposit thickness, and substrate material.

Possible applications of the data to some of the problems mentioned earlier are apparent. The presence of thin CO_2 deposits ($\tau < 100$ microns) on black surfaces will have a

relatively small effect; the reflectance in the visible and near infrared wavelength range will show only a slight increase and for infrared radiation the reflectance will be reduced for these same thicknesses. For even thinner deposits, $\tau < 20$ microns, the reflectance in the visible and near IR can also be reduced. For most applications in space simulation chambers these changes will be negligible. The reflectance changes for the larger thicknesses ($\tau > 100$ microns), however, will not be negligible.

The thin deposits may also have a significant effect in the calibration of low temperature black body reference sources. The presence of thin deposits will, in general, increase the emittance, especially in the wavelength range from 3.0μ to 12.0μ . Although no data were taken for $\lambda > 12.0\mu$ it is believed that emittance values would also be increased for longer wavelengths. With the current interest in absolute calibration of low temperature black bodies, these thin film effects become increasingly important.

Cooled optics are often used in situations where the surrounding pressure is relatively high, e.g., in balloons or aircraft. Under such conditions it is impossible to keep cryogenically cooled surfaces free from contamination due to condensation of CO_2 and H_2O gases. For determination of effects of the CO_2 frosts on cooled optics (such as mirrors), Fig. 7 shows some of the changes one could expect. In addition to the reflectance considerations, the increase in emittance, and the reduction in image quality due to scattering by the cryodeposit may also have to be considered.

Finally, the recent findings of the Mariner 6 and 7 probes have increased the interest in the reflective properties of both carbon dioxide and water frosts. According to Herr and Pimentel (Ref. 9) the reflectance data obtained from Mariners 6 and 7 indicate that the Martian polar caps are carbon dioxide. They also reported that absorption bands at 3.34 and 3.04μ , which had earlier been designated as methane and ammonia bands, respectively, were also due to CO_2 . They verified this by obtaining the same absorption bands for CO_2 frosts formed under laboratory conditions. This was the first reported observation of these two bands for CO_2 . These two bands were not seen in the measurements presented in Figs. 4 and 7 and the data in Fig. 7 were, like the laboratory data for Herr and Pimentel, for CO_2 formed on stainless steel.

In order to obtain higher resolution data, the NaCl prism was replaced by a CaF_2 prism. Figure 9 shows the results of the reflectance of a CO_2 deposit 4 mm thick. The pressure during deposition was 1.80×10^{-1} torr or less and the view angle, θ , was 18 degrees. With the higher resolution an absorption band was seen at approximately 3.36μ which is probably the same band reported by Herr and Pimentel in Ref. 9. The other band reported by Herr and Pimentel at approximately 3.04μ was not seen. The anomalous dispersion reflectance

peak at 4.3μ was not observed in the reflectance data of the Martian polar cap shown by Herr and Pimentel in Ref. 9. This was probably due to the fact that the reflected radiation from the polar cap was in turn absorbed by the surrounding CO_2 gas. However, in a later article (Ref. 10) Herr and Pimentel report seeing the anomalous dispersion peak at 4.3μ but not while viewing the polar caps but when viewing the bright limb of the planet. This indicated to them that the solid CO_2 was somehow suspended above the planet in some type of particle cloud in a manner not completely understood. This observation establishes conclusively the presence of solid CO_2 either on the surface or in the atmosphere of Mars. Herr and Pimentel suggest that since the peak does show up, the CO_2 cloud must be suspended high enough up so that the atmosphere can be considered optically thin as far as gaseous absorption in the 4.3μ region is concerned.

Further comparison of the data of Herr and Pimentel of Ref. 9 with Fig. 9 indicates some significant differences. First, of all, Herr and Pimentel show a strong broad absorption band in the vicinity of 5.3 microns, which is even stronger than the 4.3μ CO_2 band. This was not observed in any of the measurements reported herein, nor was this band seen in Ref. 11 where CO_2 frosts formed at atmospheric pressure were studied. This might be due to the difference in the ordinate scale since this report and Ref. 11 measured the reflectance whereas Herr and Pimentel in Refs. 9 and 10 use intensity which probably corresponds to unnormalized detector output. The present study and Ref. 11 both observed narrow absorption bands near 5.0 and 5.24μ , whereas neither of these two bands were reported by Herr and Pimentel in Ref. 9 either in the Martian polar cap data or in their laboratory data. Bands located near these two were seen in the CO_2 gas in the Martian atmosphere and were found to be at 4.76 and 5.13μ .

As seen in Fig. 9 for the 4 mm thick CO_2 deposit, there is a broad absorption band centered around 3.0 microns which is probably due to a small trace of water which was present in the chamber from outgassing. The band centered around 6.2 microns also indicates the presence of water impurities even though the chamber was initially pumped down to approximately 5×10^{-7} torr. To determine the effect of water contamination in this wavelength range, a thin film of water frost ($\tau = 11$ microns) was formed on top of the 4 mm thick CO_2 deposit (see Fig. 9). Even for this small thickness, the reflectance was reduced for all wavelengths with the most noticeable reductions occurring in the 2.9 to 3.4μ region and the 5.0 to 6.4μ range. This means that the 3.04μ band seen in Ref. 9 would not have been seen due to the trace of water which obscured any recognizable band in this wavelength region. However, it is possible that the slight band at 3.04μ of Ref. 9 may also be attributable to water particles sparsely scattered throughout the polar cap.

SUMMARY - In situ reflectance measurements on LN₂-cooled surfaces within a vacuum were carried out in a powdered sodium chloride coated integrating sphere from 0.5 to 12.0 μ . Reflectance measurements of CO₂ cryodeposits formed on black epoxy paint coated and stainless steel surfaces were obtained for deposit thicknesses ranging from 2 microns to 4.0 mm. A reflectance peak at 4.3 μ was found to be due to anomalous dispersion. The presence of this peak in a reflection spectra was shown to be a very sensitive method of detecting solid CO₂ since a deposit only 2 microns thick on black epoxy paint shows the peak quite clearly.

CO₂ deposits were seen to absorb strongly at 2.0, 2.85, and in the vicinity of 4.3 μ . With a higher resolution instrument, weaker absorption bands were also seen at 3.36, 5.0 and 5.24 μ . Thick CO₂ deposits were highly reflecting at the shorter wavelengths ($\lambda < 2.0\mu$) and transmit appreciably at longer wavelengths (excluding absorption bands).

Finally, the applicability of the experimental results to several current problems was discussed. These included: determination of the composition of the Martian polar caps, thermal radiative properties of cooled optics, effects on space simulation chamber cold walls, and effects on emittance of low temperature black body reference sources.

REFERENCES

- (1) McCullough, B. A., Wood, B. E., Smith, A. M., and Birkebak, R. C., "A Vacuum Integrating Sphere for In Situ Reflectance Measurements at 77°K from 0.5 to 10.0 μ ," Progress in Astronautics and Aeronautics, Vol. 20, Academic Press, Inc., New York, 1967, p. 137.
- (2) Sparrow, E. M. and Cess, R. D. Radiation Heat Transfer, Brooks/Cole Publishing Company, Belmont, California, 1966, p. 57.
- (3) Müller, P. R., Frost, W. and Smith, A. M., "Measurements of Refractive Index, Density, and Reflected Light Distributions for Carbon Dioxide and Water Cryodeposits," AEDC-TR-69-179 (AD692714) September 1969.
- (4) Smith, A. M., Tempelmeyer, K. E., Müller, P. R., and Wood, B. E., "Angular Distribution of Visible and Near IR Radiation Reflected from CO₂ Cryodeposits," AIAA Journal, Vol. 7, No. 12, 1969, p. 2274.
- (5) Wood, B. E. and Smith, A. M., "Spectral Reflectance of Water and Carbon Dioxide Cryodeposits from 0.36 to 1.15 μ ," AIAA Journal, Vol. 6, No. 7, 1968, p. 1362.
- (6) Wood, B. E., Smith, A.M., Seiber, B.A., and Roux, J. A., "Infrared Reflectance of CO₂ Cryodeposits," AEDC-TR-70-103.

- (7) Jenkins, F. A. and White, H. E. Fundamentals of Optics, McGraw-Hill Book Co., Inc., 1957, p. 469.
- (8) Roux, J. A., PhD Thesis, (In Preparation), University of Tennessee Space Institute, Tullahoma, Tennessee.
- (9) Herr, K. C. and Pimentel, G. C., "Infrared Absorptions Near Three Microns Recorded Over the Polar Cap of Mars," Science, Vol. 166, No. 3904, 1969, p. 498.
- (10) Herr, K. C. and Pimentel, G. C., "Evidence for Solid Carbon Dioxide in the Upper Atmosphere of Mars," Science, Vol. 167, No. 3914, 1970, p. 47.
- (11) Keegan, H. J. and Weidner, V. R., "Infrared Spectral Reflectance of Frost," Journal of the Optical Society of America, Vol. 56, No. 4, 1966, p. 523.

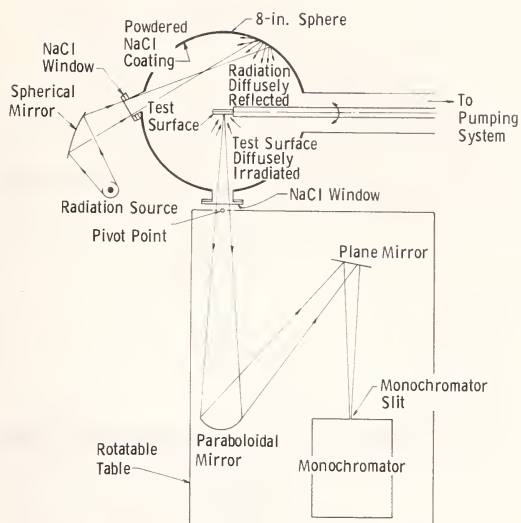


Fig. 1 Schematic of Infrared Integrating Sphere and Components

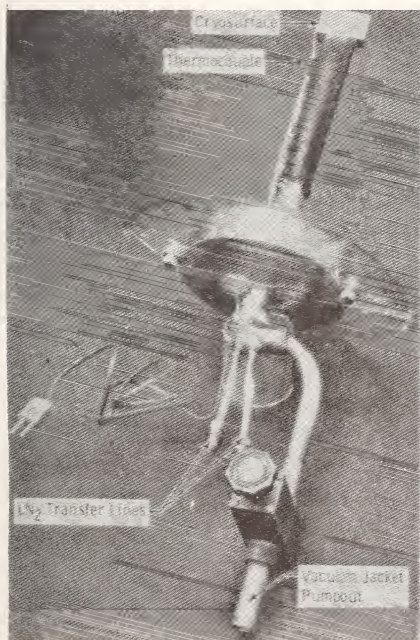


Fig. 2 Cryogenic Test Surface

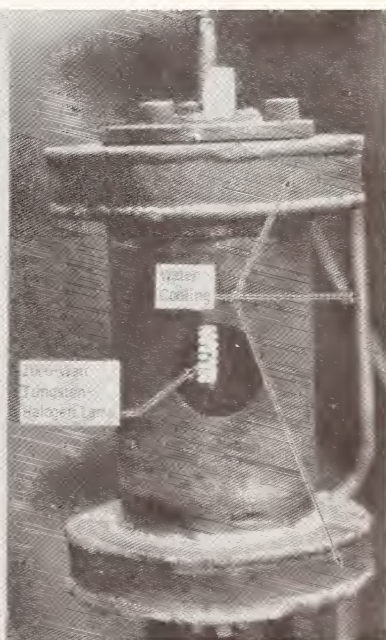


Fig. 3 Radiation Source

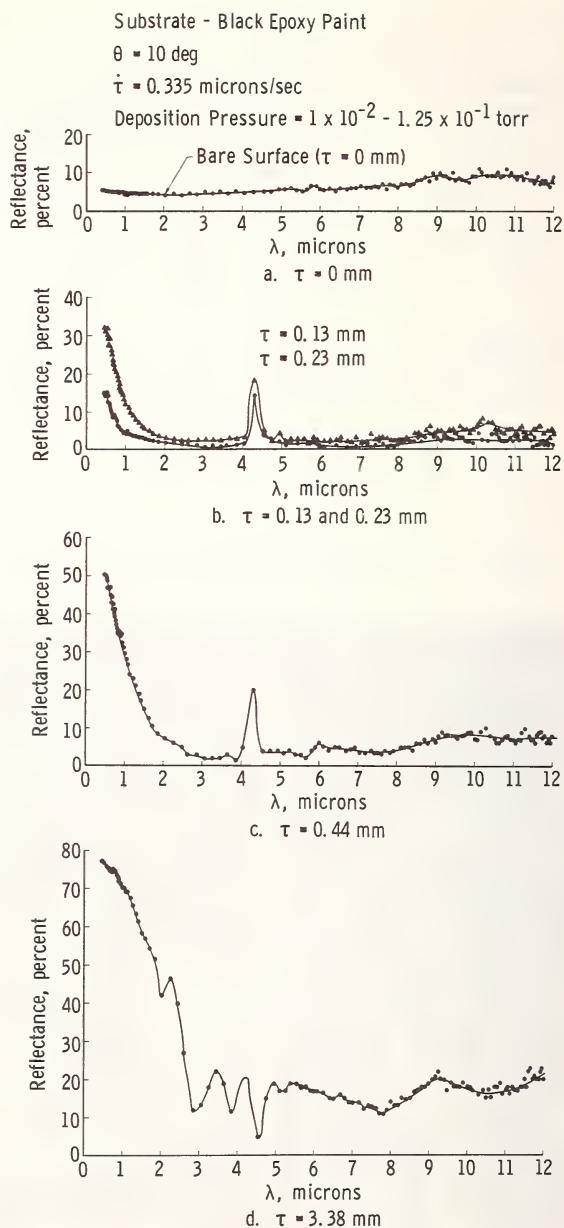


Fig. 4 Reflectance of CO_2 Cryodeposits Formed on a Black Epoxy Paint Substrate

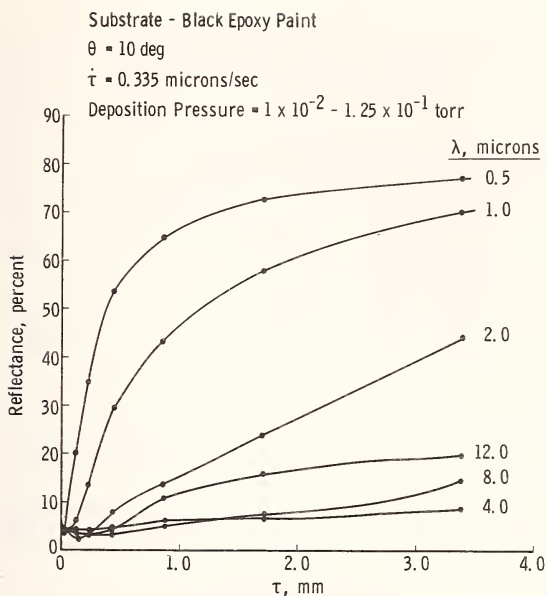


Fig. 5 Reflectance as a Function of Deposit Thickness-Black Paint Substrate

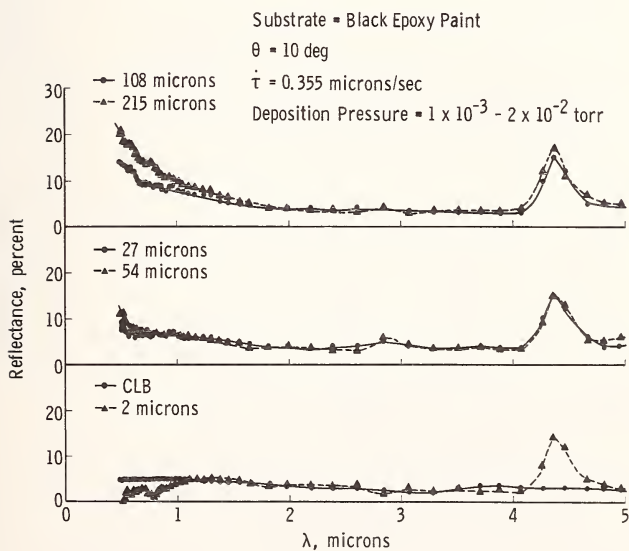
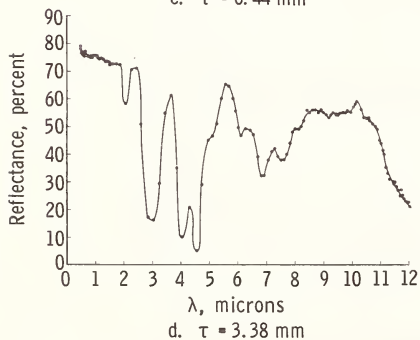
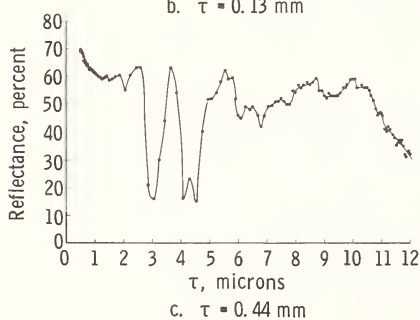
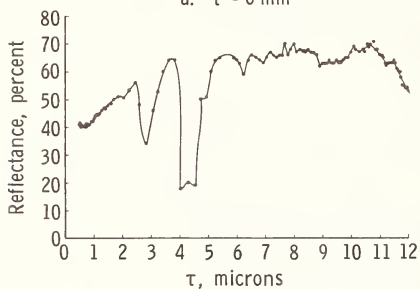
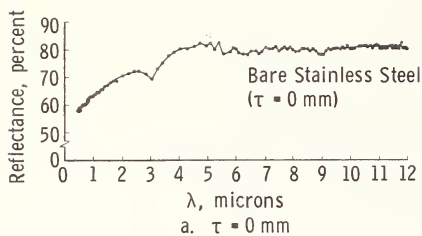


Fig. 6 Reflectance of CO_2 Deposits Formed on a Black Substrate for $\dot{r} = .0355 \mu/\text{sec}$.



Substrate - Stainless Steel

$\theta = 10$ deg

$\dot{\tau} = 0.335$ microns/sec

Deposition Pressure = $2 \times 10^{-2} - 2 \times 10^{-1}$ torr

Fig. 7 Reflectance of CO_2 Cryodeposits Formed on a Stainless Steel Substrate

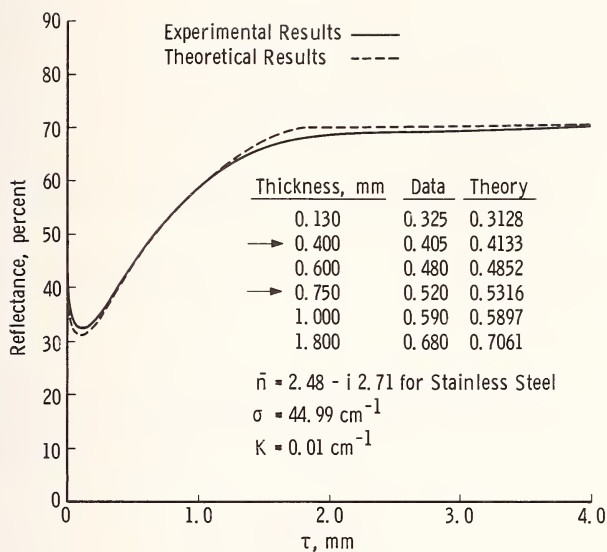


Fig. 8 Comparison of Experimental and Analytical Results for Deposits Formed on a Stainless Steel Substrate for $\lambda = 0.7\mu$

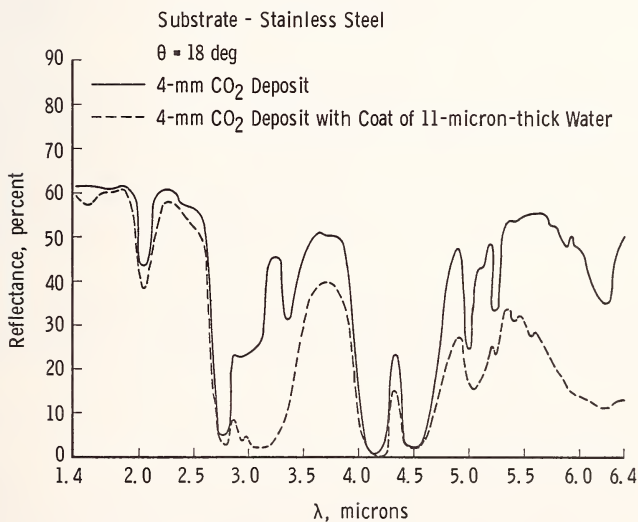


Fig. 9 Reflectance of a 4 mm Thick CO_2 Deposit and a 4 mm Thick CO_2 Deposit with a 11 micron Thick Layer of H_2O

NBS RADIOMETRIC STANDARDS -- PRESENT AND FUTURE²

Henry J. Kostkowski¹

REFERENCE: Henry J. Kostkowski, "NBS Radiometric Standards -- Present and Future", ASTM/IES/AIAA Space Simulation Conference, 14-16 September 1970.

ABSTRACT

One of the primary functions of the National Bureau of Standards is to realize, maintain and disseminate national standards of measurement. In radiometry, the currently available standards consist of various types of tungsten lamps or blackbodies that have been calibrated in terms of spectral radiance, spectral irradiance or total irradiance.

The standards of spectral radiance are either tungsten strip lamps or blackbodies, have temperatures from 500 K to 3000 K, and are calibrated, depending on the temperature and source, from 0.2 μm to 15 μm . Their uncertainty varies from about 0.1% to 5% depending on the temperature and wavelength (1,2)³. Two additional, useful standards that do not require calibration and are available commercially are the graphite arc (3) and the copper-point blackbody (4).

At present, there are two standards of spectral irradiance. The first is a 1000-watt coiled coil tungsten filament quartz-halogen lamp (5) and the second consists of this lamp mounted

¹Heat Division, National Bureau of Standards, Washington, D.C., 20234.

²This presentation concerns itself only with incoherent type radiometric standards.

³The numbers in parentheses refer to the list of references appended to this paper.

in a ceramic reflector (6). Their spectral irradiances at a wavelength of 0.9 μm and working distances of 50 and 40 cm are about 25 and 105 $\mu\text{w cm}^{-2} \text{ nm}^{-1}$ respectively, and they both vary with wavelength roughly as a 3200 K blackbody. These standards are uncertain by values ranging from 3% at 2.5 μm to 8% at 0.25 μm . However, a research effort is now under way which is expected to reduce these uncertainties within a year by a factor of about 3.

The standards of total irradiance consist of the same lamps used for spectral irradiance standards (6) and in addition 100, 500 and 1000 watt projection lamps (7). They have irradiances varying from about 0.5 to 135 mw cm^{-2} at working distances from 100 to 40 cm. The uncertainty of these sources has been estimated to be about 1%.

Radiometric detectors that can be calibrated electrically are becoming commercially available and appear useful in replacing irradiance source standards for some applications, particularly at the upper levels of approximately 100 mw cm^{-2} . Such absolute or calorimetric detectors, as they are sometimes referred to, are being developed and extensively evaluated at NBS. An uncertainty and reproducibility of a few tenths of a percent is anticipated for some models of these detectors.

A description of the standards, of how they are realized, of current attempts and limitations in extending their range or reducing their uncertainties, and the present NBS policy for their dissemination will be included in the verbal presentation.

KEY WORDS: radiometry, radiometric standards, spectral radiance, spectral irradiance, irradiance.

REFERENCES

1. Kostkowski, H.J., Erminy, D.E., and Hattenburg, A.T., "High-Accuracy Spectral Radiance Calibration of Tungsten-Strip Lamps", Advances in Geophysics 14, 111 (1970).
2. Yokley, C.R. and Kostkowski, H.J., "High-Accuracy Infrared Calibrations of Blackbodies", J. Opt. Soc. Am. 58, 1553A (1968).
3. Hattenburg, A.T., "Spectral Radiance of a Low Current Graphite Arc", Applied Optics 6, 95 (1967).
4. Lee, R.D., "Construction and Operation of a Simple High-Precision Copper-Point Blackbody and Furnace", Nat. Bur. Stand. (U.S.), Tech. Note 483, 15 pages (May 1969).
5. Stair, R., Schneider, W.E., and Jackson, J.K., "A New Standard of Spectral Irradiance", Applied Optics 2, 1151 (1963).

6. Schneider, W.E., "A One-Solar-Constant Irradiance Standard" Applied Optics 9, 1410 (1970).

7. Stair, R., Schneider, W.E., and Fussell, W.B., "The New Tungsten-Filament Lamp Standards of Total Irradiance", Applied Optics 6, 101 (1967).

APPARATUS FOR LABORATORY SIMULATION OF IONOSPHERIC FLOW OVER
ON-BOARD INSTRUMENTS OF AN AES.

E.N. Evlanov, V.B. Leonas, S.V. Umansky

Space Research Institute Academy of Sciences USSR, Moscow.

ABSTRACT: An apparatus for a simulation of ionospheric plasma flow over on-board instruments of an artificial earth satellite (AES) is described. The simulated fluxes of nitrogen, hydrogen and other ions have energies in the range of $5-10^2$ eV, current density of $1 \cdot 10^{-8}$ A/cm and provide good simulation of the natural working conditions of on-board instruments. A description of diagnostic means which are used for analysis of the flow parameters is given.

KEY WORDS: laboratory space simulation, apparatus, ion source, vacuum system, beam diagnostic, ion transportation.

1. **INTRODUCTION.** The advent of explorations with the help of AES leads to the necessity of creating installations for simulation of the space environment parameters and, in particular, for the construction of apparatus for laboratory simulation of ionospheric plasma.

In this report the apparatus designed for laboratory calibrations of on-board instruments for ionospheric studies is described. For the solution of such a problem the parameters of the laboratory plasma must be close to those which accrue in the ionosphere [1] so one needs to have a weakly divergent monoenergetic ($\Delta E = 1$ eV) ion flux with an energy of 5-100 eV of a certain mass composition and with a current density of $10^{-9}-10^{-1}$ A/cm². The ion beam diameter must be an order of magnitude larger than the entrance apertures of typical on-board instruments. ($D = 100$ mm). Neutralization (charge compensation) of the ion beam charge is desirable. The residual gas pressure in the apparatus must be sufficiently low ($10^{-7}-10^{-8}$ torr) and must correspond to the working conditions of on-board instruments in the upper atmosphere.

2. GENERAL DESCRIPTION [2] OF THE APPARATUS. Fig. 1 is a schematic diagram of the apparatus which provides ion flows with the noted parameters. Its appearance is shown in fig. 2. The apparatus may be schematically divided into three main parts: I. Ion source 1 (fig. 1), with a neutralizer, for production of the rarefied plasma. The ion source is mounted in a single tube 1 (fig. 2), which is attached by means of a flange to the main vacuum vessel. II. Vacuum system with manometric tools. The main vacuum vessel is connected to the preliminary pumping equipment; inside of it a solenoid coil is installed which is used for restricting divergence of the simulated flux. III. Test chamber III (fig. 1) with movable equipment holders and instruments for the control of simulating flux parameters. The test chamber 4 (fig. 2) is separated from the main vessel by a tube 3 (fig. 2) in which diagnostic instruments are installed. These instruments are removed during operation from the path of the simulating flux.

3. ION SOURCE. For production of wide ion beams with a weak divergence, sources with electron bombardment ionization were used. The use of electron bombardment is conditioned by the necessity to obtain ion fluxes of low energy (up to 5 eV) with sufficiently narrow energy spread (~ 1 eV).

Two modifications of the ion source were used. The first ion source (fig. 3) consists of an ionizer (Pears system) which forms the rectangular electron beam. The directly heated flat tantalum cathode (100 x 1.5 mm) is covered with yttrium oxide. This electron gun provides a current of 30 mA; the electron beam expansion along the ionization length (≈ 100 mm) due to a space charge is ~ 10 mm. A positive potential which determines the energy of ions in the beam is applied at grids 3, 4 (fig. 3) while the accelerating grid 6 is under ground potential. Ions leaving the ionization space with thermal velocities are accelerated and further move in the equipotential space of the main vessel.

The ion source provides an ion beam with energy of 5 eV with current density of $1 \cdot 10^{-8}$ A/cm² (Current was measured at 15 cm from the source). The source of the second type provides currents 1 or 2 orders of magnitude higher due to an increase of the ionizing electron current. The source consists (general view is shown in fig. 4) of two hollow cylinders; one of which is anode 1 and the other is an electron reflector 2 (fig. 4). There are four 8 slots (2 x 4 cm) in the anode screened by tungsten grids above which, at a distance of 2 mm, directly heated tantalum cathodes are installed. The total emission current is ~ 2 A with electron energy of 100 V. The inside surface of the anode has the shape of a truncated cone (grid-

covered bases are of 40 and 50 mm diameter respectively) which narrow in the ion extraction direction. Such a configuration is an inverse ionizer of the Weiss type [3] in which the ion expulsion from the ionization region is actualized by the ions space charge field (but not electrons as by Weiss). The source's functioning heavily depends on the pressure and optimal conditions are selected empirically. The ions coming out from the ionizer are first accelerated and then decelerated by an ion-optical system [4]. A system of this type effectively enables one to extract from the ion beam fast background electrons and to reduce substantially widening of the ion beam during deceleration.

4. VACUUM SYSTEM. A number of special requirements are imposed on the vacuum system of the apparatus.

Under working conditions the residual gas pressure must be sufficiently low in order that charge-exchange and scattering of the beam ions by the residual gas will be as small as possible. Keeping in mind the considerable gas load on the vacuum system during an intense ion beam extraction, one needs a powerful pumping system for maintenance of low pressure. The presence of vapours of organic matter (oil), which form films on the sensitive elements of the instruments, is highly undesirable; i.e. the vacuum system of the apparatus must be oilless.

Titanium sublimation pumping is best for fulfilling the above mentioned requirements [5] and this kind of pumping is used in the apparatus.

The main vacuum vessel of the apparatus II (fig. 1) has a near spherical shape ($D \sim 1m$). Inside of the vessel a near spherical liquid nitrogen cooled copper shield is installed. In the lower part of the vessel an electron-beam evaporator 10 (fig. 1) is installed ($0.1g/min$) which sputters out the titanium on to all the inside surface of the shield. The primary pumping of gas is done with a high-vacuum oil-diffusion pump. (pumping speed of 500 l/sec) provided with a reliable hydrogen trap. The shield walls on the diffusion pump side are solid and this sharply limits the oil vapour migration to the working volume. The measured values of pumping speed for the pressure of $1 \cdot 10^{-7}$ torr are $8 \cdot 10^5$ l/sec (H_2), $2 \cdot 10^5$ l/sec (N_2), $2 \cdot 10^5$ l/sec (O_2). The titanium sublimation pumping is not effective for noble gases and their pumping out was done by the diffusion pump.

Ultimate vacuum ($1 \cdot 10^{-9}$ torr) in the apparatus without gas supply is reached in several hours. In the working condition

under the total gas load the pressure is $1 \cdot 10^{-7}$ torr.

5. THE TEST CHAMBER AND DIAGNOSTIC TOOLS. The test chamber III (fig. 1) is separated from the main vacuum vessel by the tube 3 (fig. 2) with diagnostic equipment. The test chamber is equipped with a rotating device which provides alignment of the sensor position relative to the beam and facilitates studies of the effects of the direction of ion incidence on the sensors. The use of the separate chamber along with the practical convenience enables one to eliminate sensor contamination with titanium vapours.

Beam diagnostics is carried out by means of the following tools: Faraday cup 5 (fig. 1), Collimated channel multiplier 6 (fig. 1), and a sectional plate-condenser 7 (fig. 1). The Faraday cup was used for absolute ion current density measurements. It was mounted on boom 2 (fig. 5), which permits determination of beam profile.

An analysis of the ion beam divergence is performed by means of a well-collimated channel electron multiplier 3, which is mounted on the same boom (fig. 5). Multiplier amplification coefficient is 10^7 and the accuracy of divergency measurement is $\sim 1^\circ$.

For the ion beam energy and mass composition determination the time of flight method was used. For successful use of the method a high-speed shutter for the ion beam break and a quick sensor is needed. In the given case an open electron multiplier was used for ion registration. Ion beam pulsing was actuated by the sectional plate-condenser. It consists of parallel connected plate-condensers (the distance between the plates is 3 mm, width is 100 mm, number of plates is 30 for first type source) and is mounted directly on the source 5 (fig. 4). The composite design of the condenser with transparency of 90% permits its size to be decreased significantly and exclude the effect of a distorting field on ion motion that is important in diagnostics of low-energy and large diameter ion beams.

A typical TOF-oscillogram for a 20 eV ion beam is presented in fig. 6. As can be seen the ion beam consists of Ar^+ , N_2^+ and H_2^+ ions (the initial gas mixture). An energy spread for argon ion (Ar^+) is ~ 1.5 eV in the given case.

6. THE ION BEAM TRANSPORTATION. Due to the ion beam divergence for low (~ 5 eV) energies which is caused by the effect of the thermal velocity normal components, defocusing in the

accelerating grid cells and mainly by coulombic repulsion ion current density rapidly decreases with distance. This effect may be seen from the data presented in fig. 7, which shows beam current dependency on the accelerating voltage. Ion current density was measured both in the sources vicinity (15 cm) and at a distance of 150 cm. In the first case current saturation is already observed for the accelerating voltage at ~5V; i.e. the ion current is not limited by the space charge effect. At a distance of 150 cm the ion current continuously increases with an increase of accelerating voltage and only for 300V does it become comparable with that at a distance of 15 cm.

Ion beam divergence due to coulomb repulsion can be considerably decreased compensating the ion-beam space charge by electrons. To accomplish this a neutralizing filament assembly was mounted behind the source 6 (fig. 4) which injected slow electrons into the beam (electron energy ~10 eV). It is difficult to hold low energy electrons in the ion beam along its whole track (~2 m), hence, a solenoid is mounted inside the main vessel 4 (fig. 1) producing a constant magnetic field directed along the beam.

Fig. 8A shows the dependence of ion electron currents, which are measured by the collector, on the magnetic field in the solenoid. As can be seen, the beam transport optimum conditions are achieved with a field of 20 G. In this case the ion current increases by two orders of magnitude as compared to the case of a beam without neutralization (fig. 7B and fig. 8B). Such a magnetic field has a small effect on ion motion and the operation of the gauges studied.

7. CONCLUSIONS. An apparatus is described that provides simulation of the conditions of the ionospheric plasma flow about satellite on-board gauges.

REFERENCES

1. Y.L. Alpert, A.V. Gurevich and L.P. Pitaevsky.
"Artificial satellites in rerefied plasma".
"Nauka", 1966.
2. E.N. Evlanov, V.B. Leonas and S.V. Umansky.
"Interplanetary medium and physics of magnetosphere".
Chodarev Y.K. ed. "Nauka" in press.
3. R. Weiss. "Rev. Sci. Inst." 32. 397.1961.
4. Von Koch. H. Lindholm E. "Ark Fys." 19.123.1961.
5. V.A. Simonov, G.F. Klamenov and V.A. Kochnev.
"Nucl. Synthes." Part 1, 325, 1962.

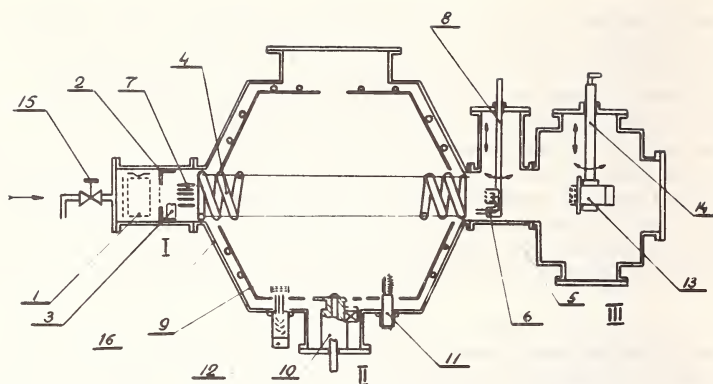


Fig. 1. Schematic of apparatus. I. Ion source chamber. II. Main vacuum vessel. III. Test chamber. 1. Ion source. 2. diaphragm. 3. neutralizing assembly. 4. solenoid. 5. Faraday cup. 6. channel multiplier. 8, 14. movable holder. 9. liquid nitrogen cooled shield. 10. titanium evaporator. 11. vacuum gauge. 12. residual gas analyser. 13. gauge studied. 15. gas input.

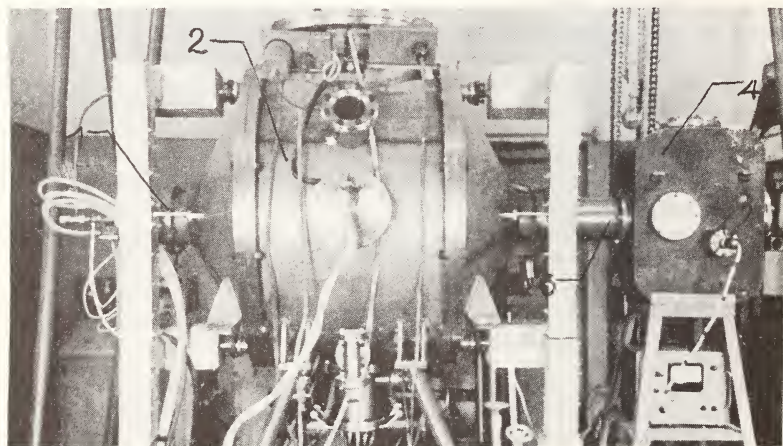


Fig. 2. General view of apparatus. 1. ion source chamber. 2. main vacuum vessel. 3. tube with diagnostic tools. 4. test chamber.

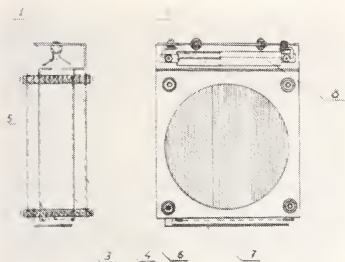


Fig. 3. Schematic of ion-source (first type). 1. electron gun. 2. cathode. 3, 4. ionization space. 5. repelling grid. 6. accelerating grid. 7. electron collector. 8. reflector.

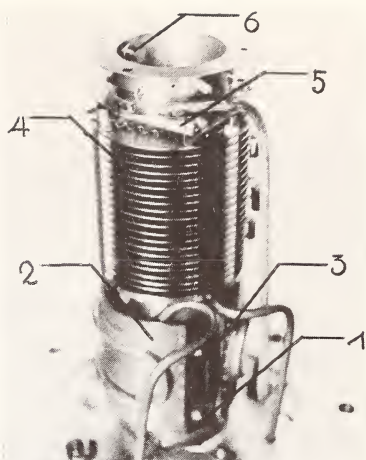


Fig. 4. General view of the sources of second type. 1. anode. 2. reflector. 3. cathode. 4. ion optical systems. 5. TOF-condenser. 6. neutralizer.

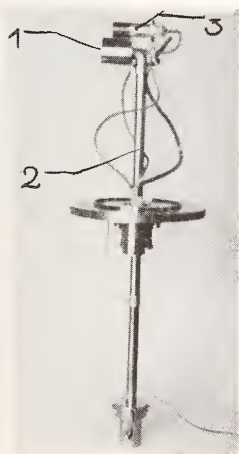


Fig. 5. Ion Beam diagnostic tools. 1. Faraday cup. 2. Moveable boom. 3. collimated channel multiplier.

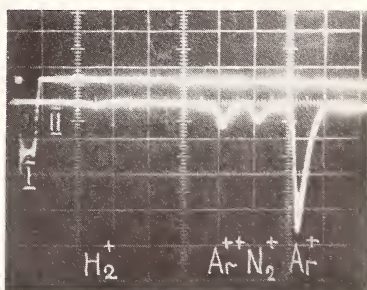


Fig. 6. TOF-oscillogram. 1. ion start pulse. 2. TOF-spectrum.

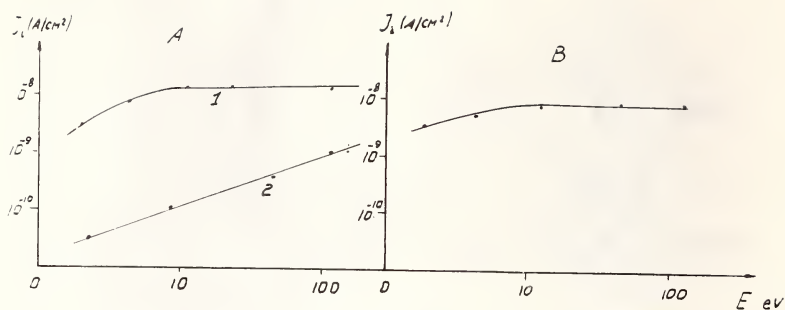


Fig. 7. Ion (N_2^+) current ver. ion energy for the source of first type. A. without beam space charge compensation. 1. Source-collector distance 15 cm. 2. source-collector distance 150 cm. B. With space charge compensation. Source-collector distance 150 cm.

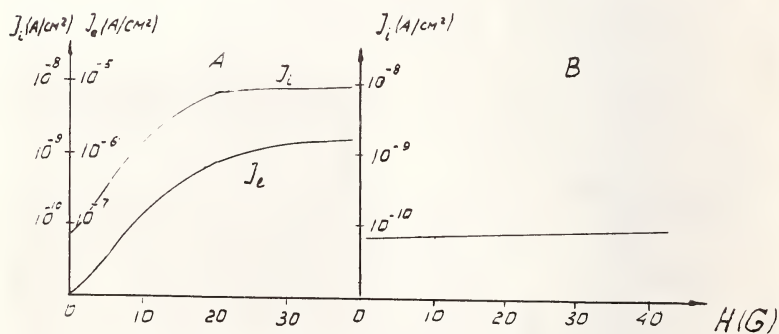


Fig. 8. The ion (N_2^+) current and electron current ver. magnetic field for the source of first type (energy ions 10 eV). A. I_i and I_e dependence on solenoid field. B. I_i dependence on solenoid field without beam space charge compensation.

THERMAL CONDUCTIVITY MEASUREMENTS OF A CANDIDATE VIKING HEAT-SHIELD MATERIAL AFTER STERILIZATION, AND DURING EXPOSURE TO VACUUM, AND TO A SIMULATED MARTIAN ATMOSPHERE

Lawrence R. Greenwood¹ and Roy M. Fleming²

REFERENCE: Greenwood, Lawrence R. and Fleming, Roy M., "Thermal Conductivity Measurements of a Candidate Viking Heat-Shield Material After Sterilization, and During Exposure to Vacuum, and to a Simulated Martian Atmosphere," ASTM/IES/AIAA Space Simulation Conference, September 14-16, 1970.

ABSTRACT: An experimental program has been conducted to measure the thermal conductivity of the proposed Viking heat-shield material, Martin SLA-561, after sterilization (60 hours at 276° F) and during exposure to vacuum and to a simulated Martian atmosphere (74.4 percent CO₂, 12.8 percent N₂, 12.8 percent Ar). In situ thermal conductivity measurements were made at 75° F using the line-source technique. The thermal conductivity of SLA-561 was measured to be 0.0298 Btu/ft-hr-°F at atmospheric pressure. In the first environmental sequence consisting of atmosphere, vacuum, and simulated Martian atmosphere exposure, a 60-percent reduction in thermal conductivity was measured in vacuum. After a 4-hour exposure to a 7-torr pressure in the simulated Martian atmosphere, the thermal conductivity increased 67 percent from the value measured in vacuum. The second environmental sequence consisted of measurements in the atmosphere, after sterilization and during exposure to vacuum and the simulated Martian atmosphere. The results of these measurements showed that sterilization had no effect on the thermal conductivity measured at atmospheric pressure nor on the changes measured in vacuum and in the simulated Martian atmosphere. Thermal conductivity was measured at varying pressures during both environmental sequences

¹Head, Space Vacuum Laboratory, Applied Materials and Physics Division, NASA Langley Research Center, Hampton, Virginia.

²Student, N.C. State University (Employed as a Co-operative Engineering Student at LRC)

and the results showed the thermal conductivity to be essentially independent of pressure below 10^{-4} torr with the transition from molecular to continuum flow occurring in the 10^{-2} to 10 torr pressure range.

KEY WORDS: thermal conductivity, vacuum effect, ablation material

Recent experimental results have shown that the thermal and mechanical properties of spacecraft materials can be altered by exposure to the space environment.^{1,2,3} In particular, results have shown that the thermal and mechanical properties of ablative heat-shield materials may change due to sterilization and exposure to vacuum. To determine the thermal conductivity of a candidate Viking heat-shield material during the mission environmental sequence, an experimental program has been conducted wherein in situ thermal conductivity measurements were made after sterilization and during exposure to vacuum and a simulated Martian atmosphere.

EXPERIMENTAL PROGRAM

Thermal Conductivity Measurements

The line-source technique was used for measuring thermal conductivity.¹ In this technique a heater wire and thermocouple wire are placed inside a sample as shown in Fig. 1. Heat is generated in the sample by passing a known heater current through the heater wire, and the variation of temperature with time is measured with the thermocouple located on the heater wire. The heater circuit consisted of a 6-volt battery, an ammeter, and a variable resistor for presetting the heater current prior to initiating sample heating. After initiating the heater current, the temperature-time history of the heater wire is recorded using the thermocouple located on the heater wire, a reference junction and a recorder. From the recorder output, a computer program is used to fit a least-squares straight line to the data and calculate the thermal conductivity from the slope of the line. The thermal conductivity was calculated from⁴

$$K = \frac{q}{4\pi(\Theta_2 - \Theta_1)} \ln \frac{t_2}{t_1}$$

where

K = thermal conductivity

q = heat input

Θ = temperature

t = time after initiation of heat generation

Fig. 2 is a photograph of the thermal conductivity instrumentation and Fig. 3 is a photograph showing details of the sample instrumentation. All measurements were made at 200 mA heater current with a heating period of 5 minutes. A second thermocouple was inserted 1/4 inch (see Fig. 3) below the sample surface and monitored during the tests to determine if the surface temperature was changing. Also, a plot of the logarithm time-temperature output was also examined to check the linearity. All measurements reported are the average of the thermal conductivity measured on three samples at a given time.

Environmental Chamber

The sterilization, and exposure to vacuum, and a simulated Martian atmosphere was done in the 20-cu-ft-ultrahigh vacuum chamber shown in Fig. 2. This is a stainless steel chamber capable of achieving pressures of 10^{-10} torr. A complete description of the chamber is given in Ref. 5.

Material

The candidate Viking heat-shield material studied was SLA-561, made by the Martin Marietta Corporation. The SLA-561 has a density of 0.201 g/cc and is composed of a silicone elastomer filled with silica spheres, phenolic microballoons, silica fibers, and cork. A complete description of the material, including its ablative properties, can be found in Ref. 6. Thermal conductivity samples were 4 by 4 by 6 inches, and typical samples are shown in Fig. 4. The 0.010-inch manganin heater wires and the 30-gage copper-constantan thermocouple wires were cast into the heat-shield samples during sample preparation. The material was preconditioned several weeks at 45 percent relative humidity in a class 100 clean room prior to testing.

Environmental Sequence

Thermal conductivity measurements were made during two environmental sequences: (1) atmosphere, vacuum, and simulated Martian atmosphere exposure, and (2) atmosphere, sterilization, vacuum, and simulated Martian atmosphere exposure.

The first sequence began by making several thermal conductivity measurements on the three samples in the vacuum chamber at atmospheric pressure (see Fig. 3). The chamber was then evacuated and thermal conductivity measurements were made as a function of time during the 128.5-hour vacuum exposure time. After 146.1 hours, the pressure was increased to 7.0 torr with a simulated Martian atmosphere consisting of 74.4 percent CO_2 , 12.8 percent N_2 , and 12.8 percent Ar. Thermal conductivity

measurements were made at 7.0 torr. The chamber pressure was then reduced to 1.0, 0.5, and 0.1 torr and thermal conductivity measurements were made at each of these pressures. The pressure time history for sequence 1 is shown in Fig. 5. All environmental exposures and thermal conductivity measurements were at 75° F.

At the start of the second sequence, three different thermal conductivity samples were sterilized in the chamber by heating the samples of 276° F for 60 hours at a pressure of 600 torr in a dry nitrogen atmosphere. After sterilization the thermal conductivity was measured at 75° F and the vacuum exposure begun. Thermal conductivity measurements were made as a function of vacuum exposure time for 95.0 hours and after 96.5 hours the pressure was raised to 7.0 torr with the simulated Martian atmosphere. The pressure time history for this sequence is also shown in Fig. 5.

EXPERIMENTAL RESULTS

Sequence 1 - Atmosphere, Vacuum, Simulated Martian Atmosphere

The thermal conductivity measured at atmospheric pressure was 0.0298 Btu/ft-hr-°F as shown on Fig. 6. After 1.8 hours in vacuum, the average thermal conductivity had been reduced 46 percent to 0.0161 Btu/ft-hr-°F. For the first 20 hours in vacuum the thermal conductivity continued to decrease, and after 31.5 hours the conductivity was 0.0120 Btu/ft-hr-°F and remained approximately constant for the remainder of the vacuum exposure period. After 146.1 hours the pressure in the chamber was raised to 7 torr with the simulated Martian atmosphere. Measurements were made immediately after reaching 7 torr and after 4, 8, and 12 hours. The thermal conductivity measured at these times was 0.0186, 0.0200, 0.0191, and 0.0193, respectively. The pressure was then reduced to 1.0 torr for 4 hours, after which time the thermal conductivity was 0.0145 Btu/ft-hr-°F. The pressure was then reduced to 0.5 torr for 4 hours after which time the thermal conductivity was 0.0140 Btu/ft-hr-°F. Finally, the pressure was reduced to 0.1 torr for 4 hours after which time the thermal conductivity was 0.0131 Btu/ft-hr-°F.

Sequence 2 - Sterilization, Vacuum, Simulated Martian Atmosphere

A second environmental sequence on three different SLA-561 samples was conducted wherein thermal sterilization was included. The thermal conductivity measured at 600 torr in a nitrogen atmosphere after sterilization was 0.0296 Btu/ft-hr-°F (see Fig. 7). Since the thermal conductivity for the unsterilized samples discussed in sequence 1 was 0.0298 at atmospheric pressure, there was essentially no effect of sterilization on the thermal conductivity. After sterilization the vacuum

exposure began, and the measured thermal conductivity values are shown in Fig. 7. The vacuum-induced changes for the sterilized samples (sequence 2) were similar to the vacuum-induced changes for the unsterilized samples (sequence 1). For instance, after 2 hours in vacuum, the thermal conductivity of the sterilized samples (sequence 2) was 0.0161, whereas the thermal conductivity of the unsterilized samples (sequence 1) was 0.0155 Btu/ft-hr-°F. After 95 hours in vacuum, the thermal conductivity of the sterilized samples (sequence 2) was 0.0140 Btu/ft-hr-°F compared with 0.0124 Btu/ft-hr-°F for the unsterilized samples (sequence 1).

After 96.5 hours the pressure was increased to 7.0 torr with a simulated Martian atmosphere. Three hours later the thermal conductivity for the sterilized samples (sequence 2) was 0.0212 Btu/ft-hr-°F. The thermal conductivity for the unsterilized samples (sequence 1) was 0.0200 Btu/ft-hr-°F after 4 hours in a 7-torr atmosphere of the simulated Martian environment. The sterilization had very little effect on the thermal conductivity of SLA-561 during vacuum exposure and exposure to the simulated Martian atmosphere at 7 torr.

Effects of Pressure

The effect of pressure for both the unsterilized (sequence 1) and sterilized (sequence 2) samples is shown in Fig. 8. First, it should be noted that there are no discernible differences in the thermal conductivity measured at the same pressure for either of the sequences studied. The measurements do indicate that at pressures below 10^{-4} torr the thermal conductivity may be independent of pressure. In the pressure region 10^{-2} to 10 torr, the characteristic knee in the thermal conductivity curve (due to transition from molecular to continuum flow) was observed. At about 10^{-1} torr, there appear to be differences in the thermal conductivity measured during the vacuum chamber pumpdown and those measured in the simulated Martian atmosphere. This is difficult to confirm because the vacuum pumpdown measurements were made while the pressure was changing as a function of time (see Fig. 5) and thus it cannot be assumed that the samples were allowed sufficient time to establish equilibrium with their environment.

CONCLUSIONS

The results of making in situ thermal conductivity measurements on SLA-561 during sequence 1 (atmosphere, vacuum, simulated Martian atmosphere) and sequence 2 (atmosphere, sterilization, vacuum, simulated Martian atmosphere) resulted in the following conclusions:

1. The thermal conductivity of the unsterilized samples (sequence 1) was reduced by 46 percent after 1.8 hours in vacuum and by 60 percent after 31.5 hours. The thermal

conductivity after 12 hours in a 7-torr pressure of a simulated Martian atmosphere was 0.0193 Btu/ft-hr-°F. The thermal conductivity did not appear to be a function of time in vacuum after 31.5 hours of exposure.

2. There was essentially no effect of sterilization on either the thermal conductivity measured at atmospheric pressure or on the vacuum-induced changes in thermal conductivity. Measurements at 7 torr for both sterilized and unsterilized samples were approximately the same.

3. The thermal conductivity measured for both environmental sequences was essentially independent of pressure below 10^{-4} torr. In the 10^{-2} to 10 pressure region the thermal conductivity was a function of pressure.

BIBLIOGRAPHY

1. Greenwood, Lawrence R.; and Comparin, Robert A.: Application of the Line-Source Technique for Vacuum Thermal Conductivity Measurements. Presented at the AIAA/ASTM/IES Fourth Space Simulation Conference, Los Angeles, California, September 8-10, 1969.
2. Pyron, C. M.; and Pears, C. D.: Effects of Sterilization and Vacuum Exposure on Potential Heat Shield Materials for Unmanned Mars Mission. NASA CR-66557, 1968.
3. McCrary, Leon; and McCormick, Carl: Effects of Sterilization and Vacuum Environment on Ablation Materials. Presented at the IES 14th Annual Technical Meeting, St. Louis, Missouri, April 29-May 1, 1968.
4. Carslaw, H. S.; and Jaeger, J. C.: Conduction of Heat in Solids. Oxford, Clarendon Press, 1947.
5. Bradford, James M.: Operating Parameters of the Omegatron Mass Spectrometer in Ultrahigh Vacuum. NASA TN D-3129.
6. Strauss, Eric L.: Superlight Ablative Systems for Mars Lander Thermal Protection. Journal of Spacecraft and Rockets, Vol. 4, No. 10, pp. 1304-1309.

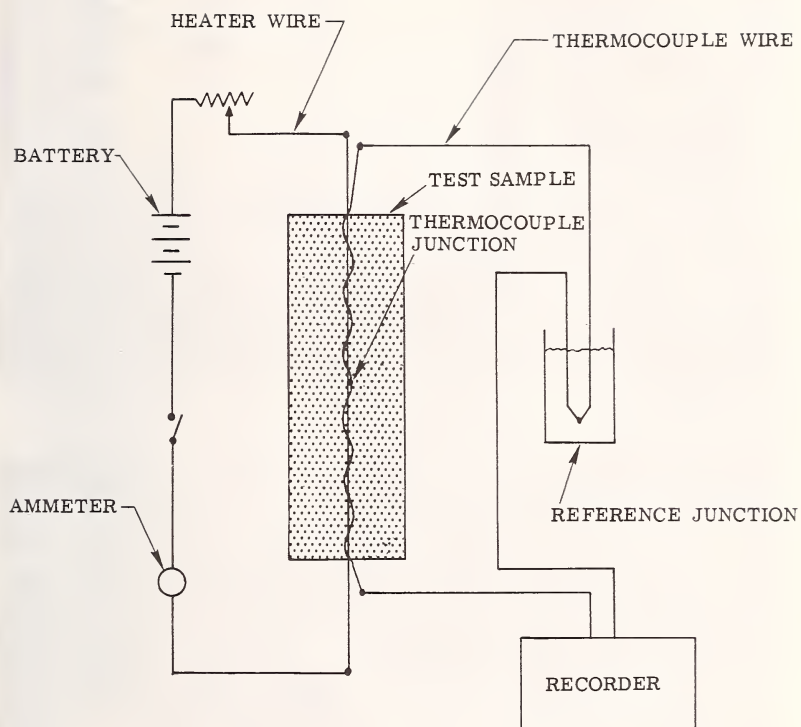


Figure 1.- Experimental technique used for measuring thermal conductivity.

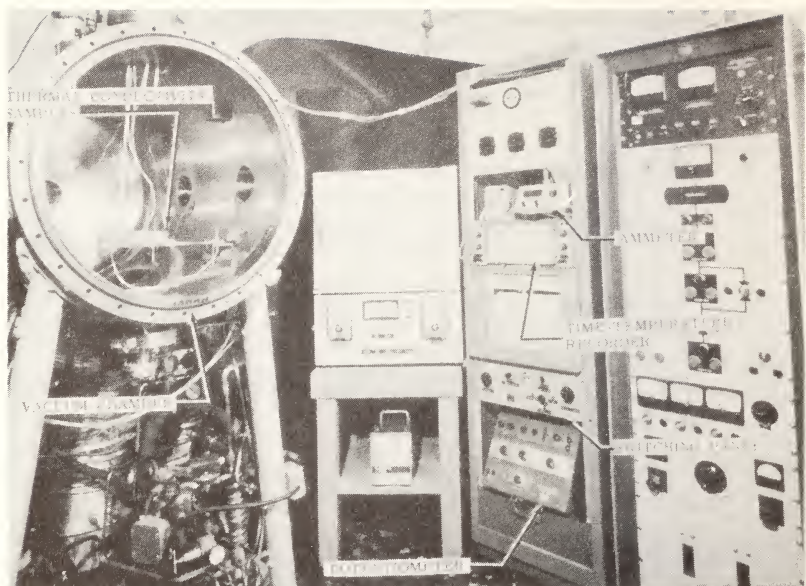


Figure 2.- Experimental apparatus used in making the thermal conductivity measurements.

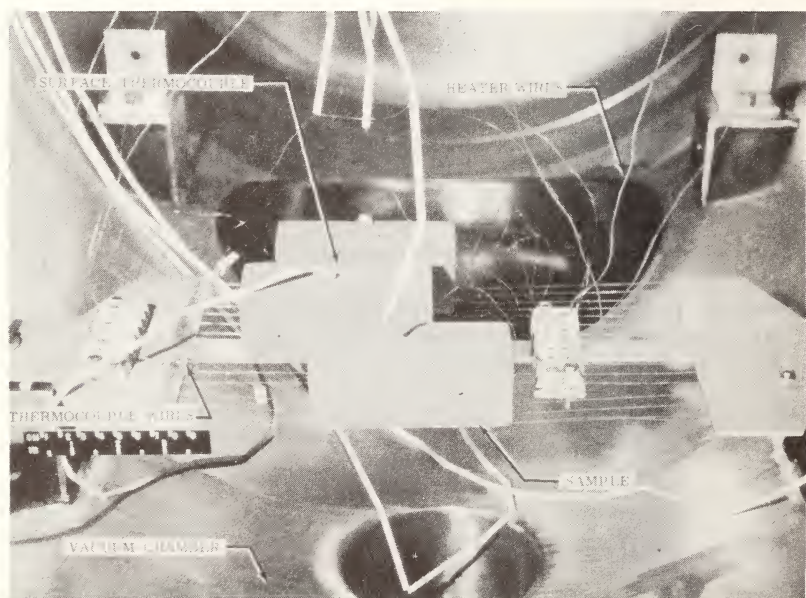


Figure 3.- Heat-shield samples located in the 20-cubic-foot ultrahigh vacuum chamber.



Figure 4.- Heat-shield samples used in the thermal conductivity study.

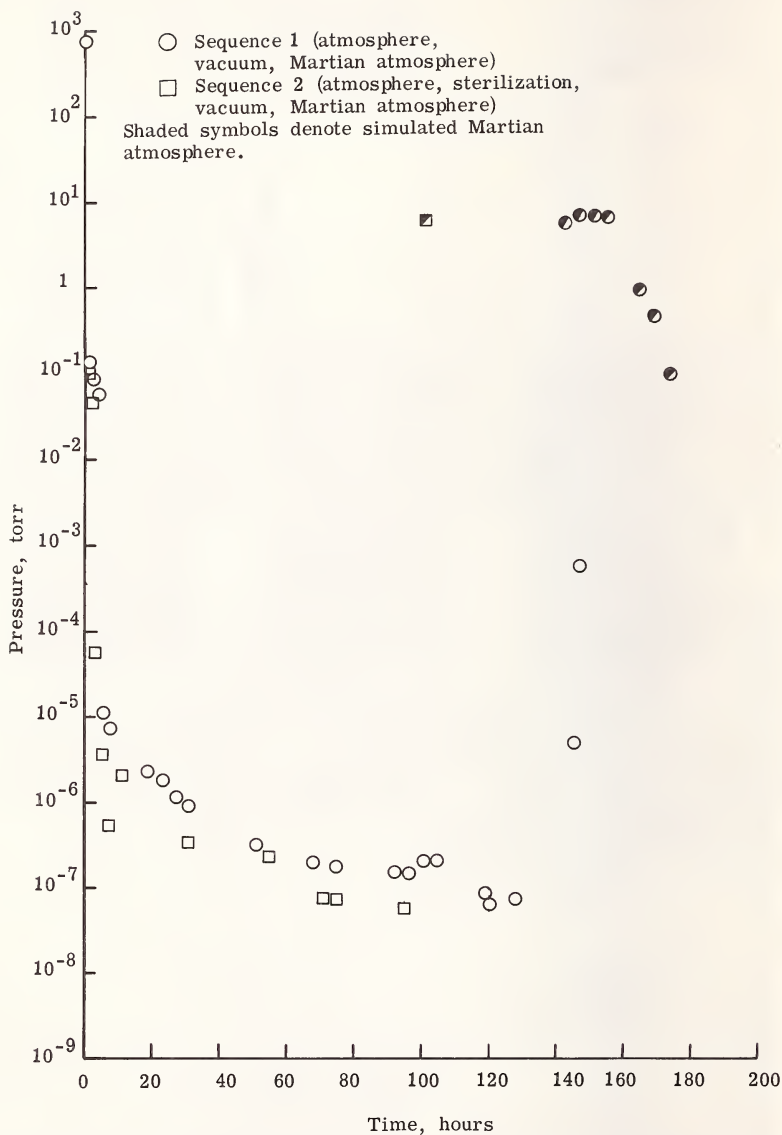


Figure 5.- Pressure time history during thermal conductivity study.

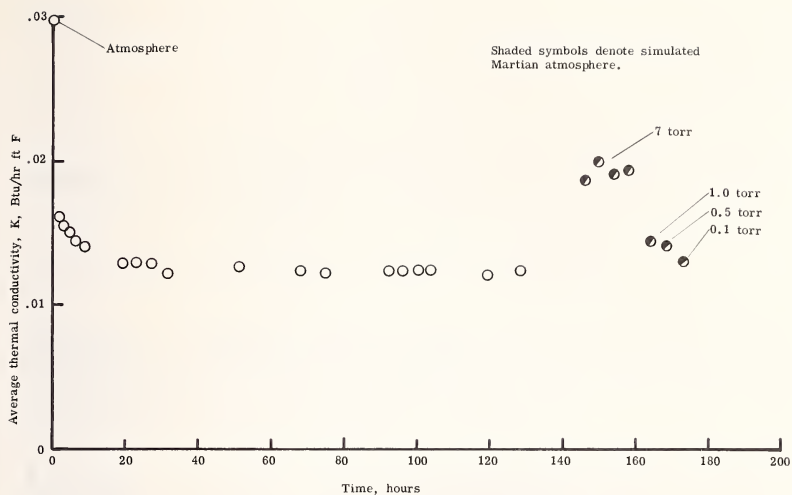


Figure 6.- Thermal conductivity of SLA-561 measured for sequence 1 (atmosphere, vacuum, Martian atmosphere).

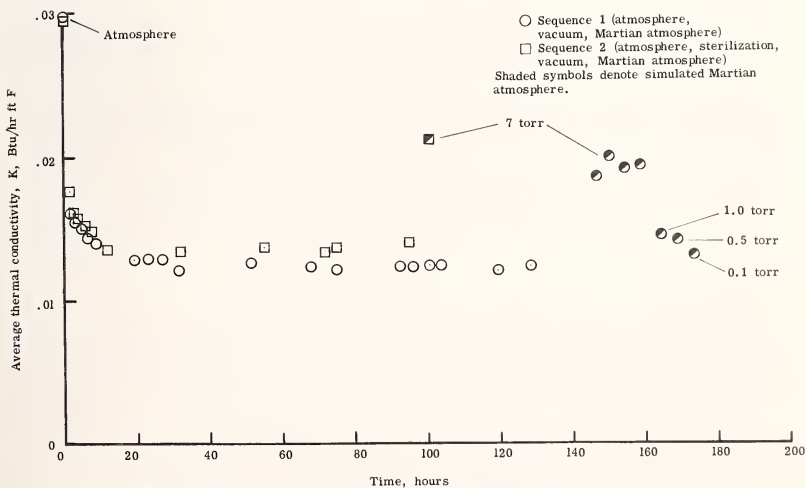


Figure 7.- Thermal conductivity of SLA-561 measured for sequence 1 and sequence 2.

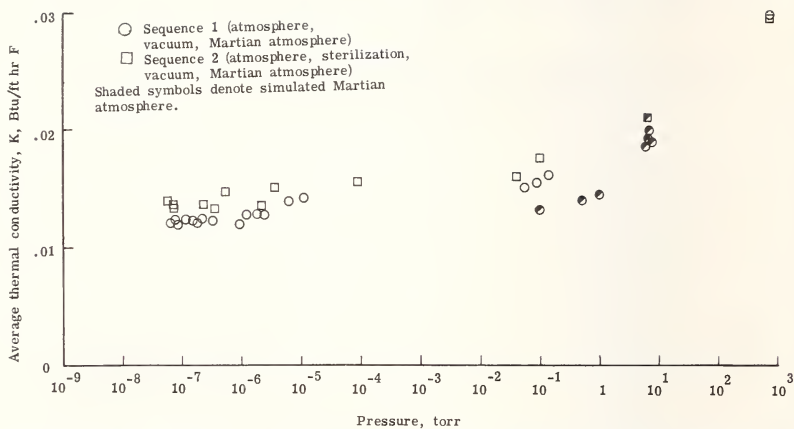


Figure 8.- Effect of pressure on the thermal conductivity of SLA-561.

METHOD FOR ROCK PROPERTY DETERMINATION IN ULTRAHIGH VACUUM

by Egons R. Podnieks¹ and Peter G. Chamberlain¹

REFERENCE: Podnieks, Egons R. and Chamberlain, Peter G., "Method for Rock Property Determination in Ultrahigh Vacuum", ASTM/IES/AIAA 5th Proceedings of Space Simulation Conference, Gaithersberg, Maryland, Sept. 14-16, 1970.

ABSTRACT: A special ultrahigh vacuum system was designed for determining deformational and strength properties of simulated lunar rocks. The system provides a vacuum of 10^{-9} to 10^{-10} torr (10^{-7} to 10^{-9} N/m²) depending on the specimen size and rock type. The vacuum was measured by various types of gages and also by ion pump current measurements. The partial pressure measurements of the various gas components were obtained by a quadrupole residual gas analyzer. The vacuum chamber has two stainless steel bellow-type feedthroughs for loading and a spring mechanism to compensate for the atmospheric pressure effect on the rock specimen. The uniaxial load was applied to the specimen by a servo-controlled hydraulic testing machine. Specimens of tholeiitic basalt, dacite, and semiwelded tuff were used. Special procedures in specimen preparation and preconditioning were developed. During the pumpdown period, prolonged roughing and an initial bakeout produced significantly low final pressures in the chamber. Test data presented include a typical load-deformation curve from rock specimen in ultrahigh vacuum, outgassing characteristics during loading in terms of pressure variation, and changes in the composition of gases being released by the specimen.

KEY WORDS: rock mechanics, space environment simulation, ultrahigh vacuum, pressure measurements, outgassing, mass spectroscopy, mechanical properties, anisotropy, compression tests.

¹Supervisory Mechanical Engineer and Geophysicist, respectively, Twin Cities Mining Research Center, Bureau of Mines, U. S. Department of the Interior, Minneapolis, Minn.

Since 1965 the Bureau of Mines has been engaged in NASA-sponsored multidisciplinary research leading to the use of extraterrestrial resources. As a part of this broad program, rock failure processes and the strength and elastic properties of rock in simulated lunar pressure environment have been investigated. To facilitate these studies a special ultrahigh vacuum system has been designed that can be readily moved in and out of a hydraulic testing machine, to permit axial loading of a rock specimen through a set of bellow feedthroughs. This vacuum system is equipped with a variety of pumps incorporating both momentum transfer and capture types. With this system an ultrahigh vacuum of 10^{-9} to 10^{-10} torr (10^{-7} to 10^{-8} N/m²) can be obtained in 2 days depending on the rock type and specimen size. During the axial loading of a specimen, the rock deformation behavior is determined and compared with simultaneously obtained outgassing data. Total pressure rise in the chamber and the partial pressure measurements of the outgassing components, made by a quadrupole residual gas analyzer, are correlated with the deformational and fracture characteristics of the test specimen.

EXPERIMENTAL EQUIPMENT

The vacuum chamber consists of a 14-in. (35.5 cm) stainless steel cylinder 26-in. (66 cm) long equipped with ports for attaching pumps, gages and other accessories (Fig. 1). The purpose of this chamber is to provide an ultrahigh vacuum environment for rock testing in simulated lunar pressure environment. Since the first phase of this research covers only the effect of vacuum on rock strength, a relatively compact test chamber is quite satisfactory.

The pumping system (Fig. 2) consists of a 400 l/sec ($0.4\text{m}^3/\text{sec}$) ion pump supplemented by titanium sublimation and cryopumping. The ion pump is directly attached to the chamber by a 6-in. (15.8 cm) port. The sublimator deposits titanium film directly on the wall of the test chamber and onto a chilled copper coil with the test specimen and the gaging protected by proper baffling. The cryopumping is accomplished by flowing liquid nitrogen (LN₂) through a coil of copper tubing lining the chamber near the test specimen. The initial pumpdown of the system is performed by three cryosorption pumps supplemented by a mechanical carbon vane pump.

The vacuum conditions in the chamber are first monitored by thermocouple and alphasatron gages mounted on the roughing manifold. After the roughing cycle the vacuum measurements are obtained directly from inside the chamber by a nude ionization gage and/or a cold cathode (Kreisman) gage and also by ion pump current measurements. A quadrupole residual gas

analyzer is used intermittently first for leak detection and second for giving partial pressure measurements of the various gas components originally present in the system or being released by the rock specimen during the test.

The vacuum chamber is specially adapted for compression testing of rock specimens in vacuum (Figs. 3 and 4). Both of the axial loading platens are connected with the chamber by stainless steel bellows to allow platen movement during the test and also to provide a positive bakeable vacuum seal. In addition the platens are spring mounted to compensate for the force applied to them by the pressure differential during the pumpdown of the system. The rock sample is surrounded by a metal screen to prevent rock particles that spall away during the compression test from damaging other components in the chamber. The load applied to the specimen is measured by a load cell located underneath the specimen and by a second load cell exterior to the vacuum chamber. The specimen deformation is measured by a strain gage - cantilever beam type extensometer which indicates the deflection between the platens.

The vacuum chamber assembly is mounted on wheels and is moved into position in the compression testing machine when a test is to be made (Fig. 5). A servo-controlled hydraulic testing machine is used to apply the axial load to the specimen at a controlled load or deformation rate (Fig. 6). During the compression tests an X-Y recorder handles load-deformation data, a strip chart recorder monitors pressure changes in the vacuum chamber, and an oscilloscope camera documents mass spectrometer traces at various stages of specimen deformation.

EXPERIMENTAL TECHNIQUES

Rock Selection

The rock materials chosen for this program were earth-formed rocks assumed to simulate lunar rocks. In establishing the rock standards for lunar research the following criteria were used for rock selection (1)²: 1) they should represent lunar rocks on the basis of lithology, texture, and composition, 2) they should meet specific requirements for the particular research likely to be performed on the rocks, 3) they should be uniform in composition and texture and 4) they should be convenient to collect in sufficient quantity.

Following these criteria the Bureau of Mines selected fourteen simulated lunar rocks covering a broad range of possible lunar rocks (2). From this suite of fourteen rocks three were first tested in this program: 1) a tholeiitic basalt (from N. E. of

²"The numbers in parentheses refer to the list of references appended to this paper."

Madras, Oregon) to simulate rock from large basaltic flows; 2) a dacite (from west of Bend, Oregon) to simulate an extrusive rock with a composition intermediate between rhyolite and basalt; and 3) a semiwelded tuff (from Bend, Oregon) to simulate possible ash flows on the Moon. These three rocks represent a wide range of properties: bulk density - 1.15 to 2.84 g/cc (1150 to 2840 kg/m³), Young's modulus - 0.3 to 10.3 x 10⁶ psi (2.1 to 71 GN/m²) and compressive strength - 850 to 53,000 psi (5.9 to 370 MN/m²).

Rock Specimen Preparation and Preconditioning

Preparing rock specimens for compression testing requires special attention because of the time consuming preparation and preconditioning processes involved. Since most rocks are anisotropic and nonhomogeneous, i.e., their properties vary with direction and location within a rock mass (3), their properties have to be measured and analyzed with respect to fixed reference directions. At the Twin Cities Mining Research Center a standard procedure has been developed for obtaining oriented rock specimens. If possible, rock blocks are oriented with respect to in situ principal geologic and geographic directions. From each block a 3- or 4-in. (7.6- or 10.1 cm) spherical specimen is prepared maintaining reference directions with respect to the source block throughout the process (4). Longitudinal pulse velocity measurements are performed on these spheres in many diametrical directions. These measurements are plotted on equal area nets and contoured, resulting in velocity symmetry patterns that provide information on the orientation of rock fabric features, e.g., elongated vesicles, which control other property anisotropy as well (3). From the velocity symmetry patterns meaningful directions in which to measure the compression properties are selected, and since the sphere orientation is carried throughout the process, it is possible to prepare oriented specimens from the source block. Cores were drilled from the source block in the selected directions with a diamond impregnated bit, and cut to size with a diamond-blade saw. For these tests cylindrical specimens were used with a length to diameter ratio of 2:1. The tholeiitic basalt and dacite specimens were 1-in. dia. (2.54 cm), whereas the semiwelded tuff specimens were 2-in. (5.08 cm) in diameter because of large inclusions in the rock. The dimensional tolerances being formalized into ASTM Standards were used in the preparation of rock specimens (5). The ends were cut and surface ground perpendicular to the axis of the specimen within 0.25°, the diametrical variations were held within 0.005 in. (.1270 mm), and the end roughness within 0.001 in. (.0254 mm). During the cutting, drilling and grinding operations the only coolant was water. Before being placed in the vacuum chamber, the rock specimens were dried in a vacuum oven for one week at 135°C and about 50 x 10⁻³ torr (6.66 N/m²).

pressure. After being cooled to room temperature, the specimens were backfilled with dry air so that they could be transferred to desiccator for storage under moderate vacuum.

Test Procedure

The preconditioned rock sample was placed in the vacuum chamber while the chamber was in the testing machine to assure proper alignment, preloading and checkout of interior instrumentation. While the chamber is open to the atmosphere, dry nitrogen gas was forced through it to minimize moisture contamination. After the specimen was properly mounted on the test platens, the system was closed and the rough pumpdown started by a carbon vane vacuum pump. At that time the pressure differential across the platens forced the bellows to extend until both platens contacted the specimen and created a preload on the specimen. This preload was held to the desired value by the compensating springs. With the specimen secured between the platens, the vacuum chamber was moved out of the testing machine for the pumpdown cycle.

The initial rough pumpdown of about 15 minutes by the carbon vane pump reduced the chamber pressure to approx. 25 torr (3340 N/m^2). Thermostatically controlled electrical band heaters encircling the exterior of the chamber were then turned on and final roughing by cryo-sorption pump was initiated and continued for 4-hr. During this pumpdown phase the chamber pressure was monitored with an alphanatron gage located in the manifold section of the vacuum system. After the 4-hr. roughing, when the pressure in the chamber is in the middle of 10^{-4} torr (high 10^{-2} N/m^2) region, the manifold was closed and the ion and the sublimation pumps were started. During the following pumpdown ion and cold cathode (Kreisman) gages were used to monitor the chamber pressure. A 24-hr. bakeout was initiated when the ion pump was turned on. This bakeout was thermostatically controlled at 135°C and was automatically interrupted if pressure in the chamber rose above the 10^{-5} torr level. During the bakeout the system was checked for leaks with a mass spectrometer using helium gas. After bakeout the system was cooled for 24-hr. period before the rock specimen was tested. Figure 7 shows typical pumpdown curves for the empty chamber and for chamber containing specimen of basalt, tuff and dacite.

After the desired vacuum has been reached, usually in the low 10^{-9} or 10^{-10} torr (low 10^{-7} or 10^{-8} N/m^2) range, the vacuum chamber was positioned in the testing machine and the pretesting alignments were made. Shortly before the start of the compression test, the cryoshroud was cooled off with LN_2 resulting in a 0.5 - 1.0 decade pressure drop within the test chamber. The rock specimen was compression-tested to complete failure at a constant deformation rate of $1 \times 10^{-5} \text{ cm/cm/sec}$.

During the tests the load applied to the specimen and the deformation of the specimen were recorded on an X-Y plotter (Fig. 8). The chamber pressure variation (Fig. 9) as well as partial pressure changes indicated by the mass spectrometer traces (Fig. 10) were recorded simultaneously with the load-deformation data.

RESULTS AND CONCLUSIONS

Applying vacuum technology to rocks requires a modification of the conventional methods of simulating a space environment. The problems of space technology usually deal with man-made materials that are specifically designed to meet the extraterrestrial environment requirements. In this program, however, natural rock material, being studied under simulated lunar vacuum conditions, cannot be chosen by its adaptability to vacuum technology. This factor requires special attention to establish valid preconditioning methods in order to approach conditions in the rock specimen (that have been selected because of the likelihood of their occurrence on the Moon) that are similar to those in actual lunar rocks.

Previous studies at the Twin Cities Mining Research Center of vacuum and moisture effects on rocks (5,6,7) have helped to establish specimen preconditioning requirements for various rocks and specimen sizes. These studies have shown that it is nearly impossible to obtain complete equilibrium between the vacuum environment surrounding the rock specimen and the entire volume of the specimen. Equally evident from the experiment is the effect of preconditioning treatment on the pumpdown and bakeout procedures. Since terrestrial rocks normally contain gases and moisture either in pores or interstitially, the preconditioning treatment and the initial rough pumping have to be prolonged enough to remove the most of the gas load before the chamber is sealed for high vacuum pumping with ion and sublimation pumps. Because of the rock structure, the bakeout process requires caution. To avoid causing irreversible structural changes in the rock, bakeout temperatures should be kept to the minimum required to discharge water vapor.

As the rock undergoes deformation during the compression test, cracks are formed and existing cracks either opened or closed. This formation of new surfaces and opening of interior cavities causes a very distinct increase in pressure (Fig. 9) which continues until the specimen fails (compressive strength). During the post-failure loading when mostly redistribution of broken rock particles takes place, few new fracture surfaces are formed and the pressure tends to drop because the outgassing rate falls below the pumping capacity

of the system. The outgassing during a compression test depends greatly on the rock type. Rocks with interconnected pores tend to release a smaller amount of gasses because of the ease with which they are removed during preconditioning and pumpdown. Whereas relatively dense rocks with interstitially held gas loads tend to release larger amounts during the deformation and failure process (5). Mass spectrometer analyses indicate that for the three rock types used the principal outgassing components were: water vapor, nitrogen, hydrogen, and carbon dioxide (Fig. 10). The principal increase in outgassing during the compressive loading cycles was contributed by water vapor and nitrogen.

The prime objective of this presentation is to describe the problems associated with research in rock properties in simulated space vacuum environment that were encountered in our study on the compression properties of simulated lunar rock in ultrahigh vacuum. The main emphasis is directed toward obtaining the deformation and strength properties of rock under carefully controlled conditions of vacuum. These studies also have shown that the analysis of outgassing characteristics of rock in vacuum gives highly significant data on the basic mechanism of rock deformation and failure.

ACKNOWLEDGEMENTS

The work presented in this paper was performed at the Twin Cities Mining Research Center under a NASA contract on Multidisciplinary Research Leading to Utilization of Extraterrestrial Resources.

The authors wish to express their appreciation for the valuable consultation provided by W. W. Roepke during establishment of pumpdown procedures and for the efforts of R. C. Rosenquist and K. G. Pung in standardizing and conducting the test program. They also wish to thank L. Sunda for his contributions towards the design of certain vacuum chamber modifications.

BIBLIOGRAPHY

1. Green, Jack. "Selection of Rock Standards for Lunar Research," Ann. N. Y. Acad. Sci., v. 123, Art. 2, July 15, 1965, pp. 1123-1147.
2. Fogelson, David E. "Simulated Lunar Rocks," Proceedings, Working Group on Extraterrestrial Resources, Brooks Air Force Base, Feb. 1968, NASA SP-177, pp. 75-95.
3. Thill, R. E., R. J. Willard, and T. R. Bur. "Correlation of Longitudinal Velocity Variation with Rock Fabric,"

Journal of Geophysical Research, v. 74, No. 20, Sept. 15, 1969.

4. Vickers, B. L., and R. E. Thill. "A New Technique for Preparing Rock Spheres," J. Sci. Instr. (J. of Physics E), 1969, Series 2, v. 2, pp. 901-902.
5. Podnieks, E. R., P. G. Chamberlain, and R. E. Thill. "Environmental Effects on Rock Properties," Proceedings, Tenth Symposium on Rock Mechanics, May 20-22, 1968.
6. Roepke, W. W., and C. W. Schultz. "Mass Spectrometer Studies of Outgassing From Simulated Lunar Materials in Ultrahigh Vacuum," Proceedings, 14th National Vacuum Symposium of the American Vacuum Society in Kansas City, Mo., October 4-27, 1967.
7. Roepke, W. W. "Friction Tests in Simulated Lunar Vacuum," presented at the Seventh Annual Meeting of the Working Group on Extraterrestrial Resources (WGER) in Denver, Colorado, June 17-20, 1969. To be published as a NASA - SP.

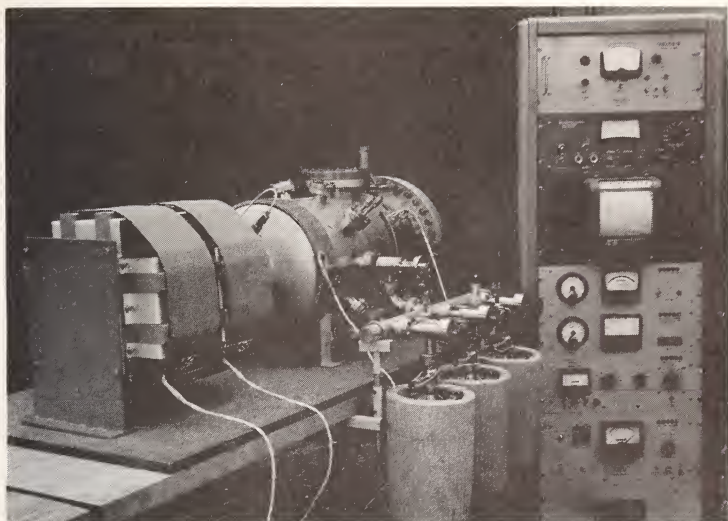


Fig. 1--Ultrahigh Vacuum System.

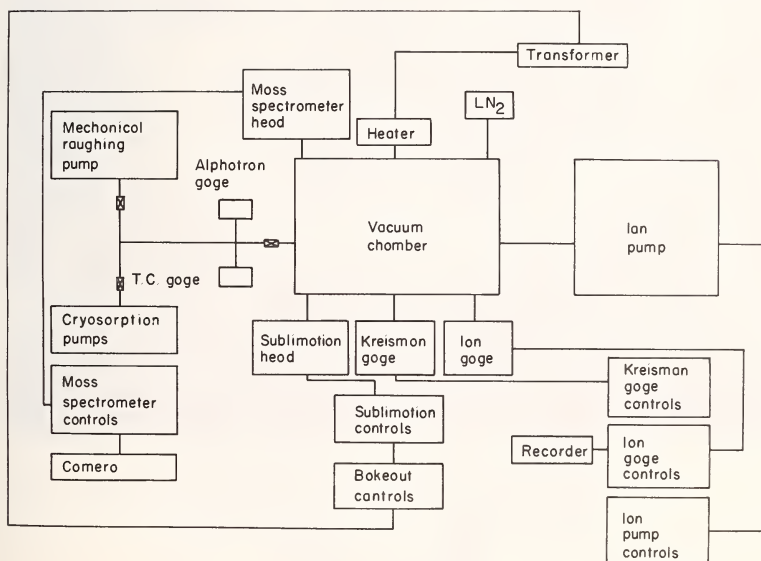


Fig. 2--Ultrahigh Vacuum System.

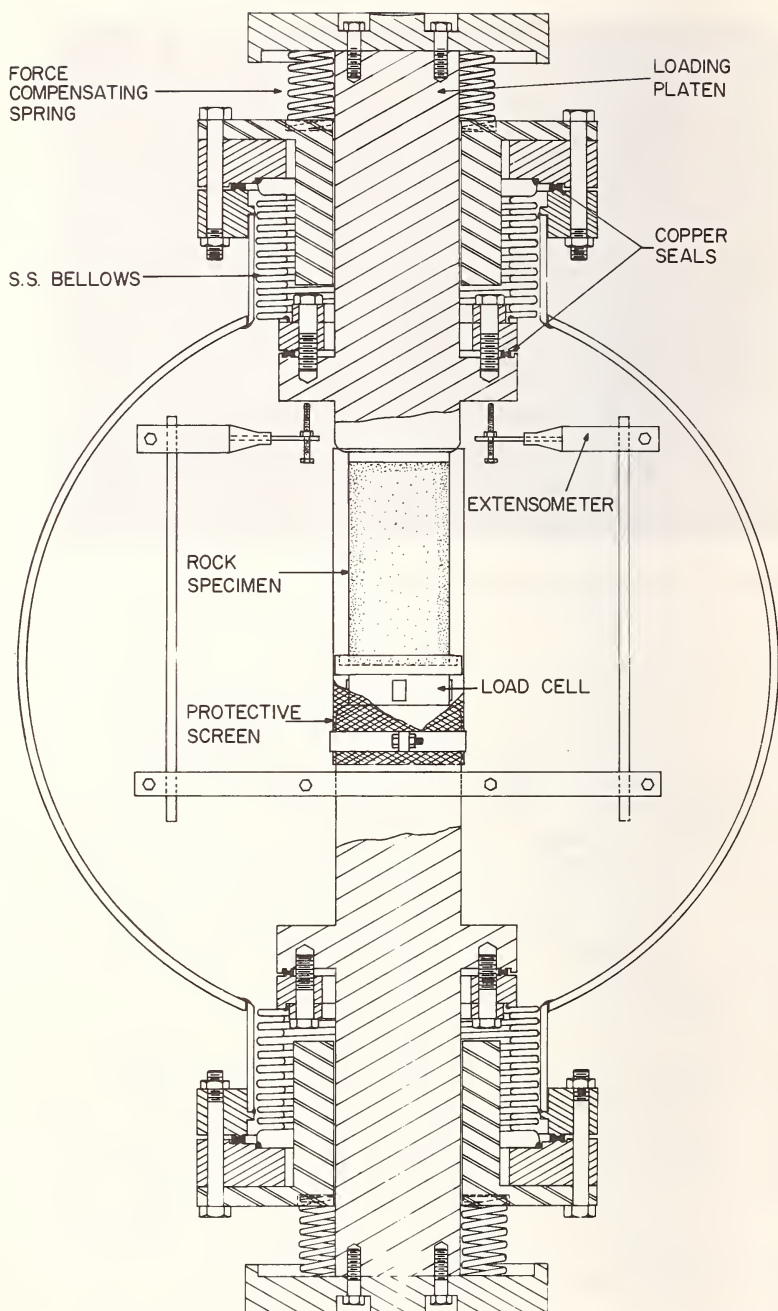


Fig. 3--Adaptation of Vacuum Chamber for Compression Tests.

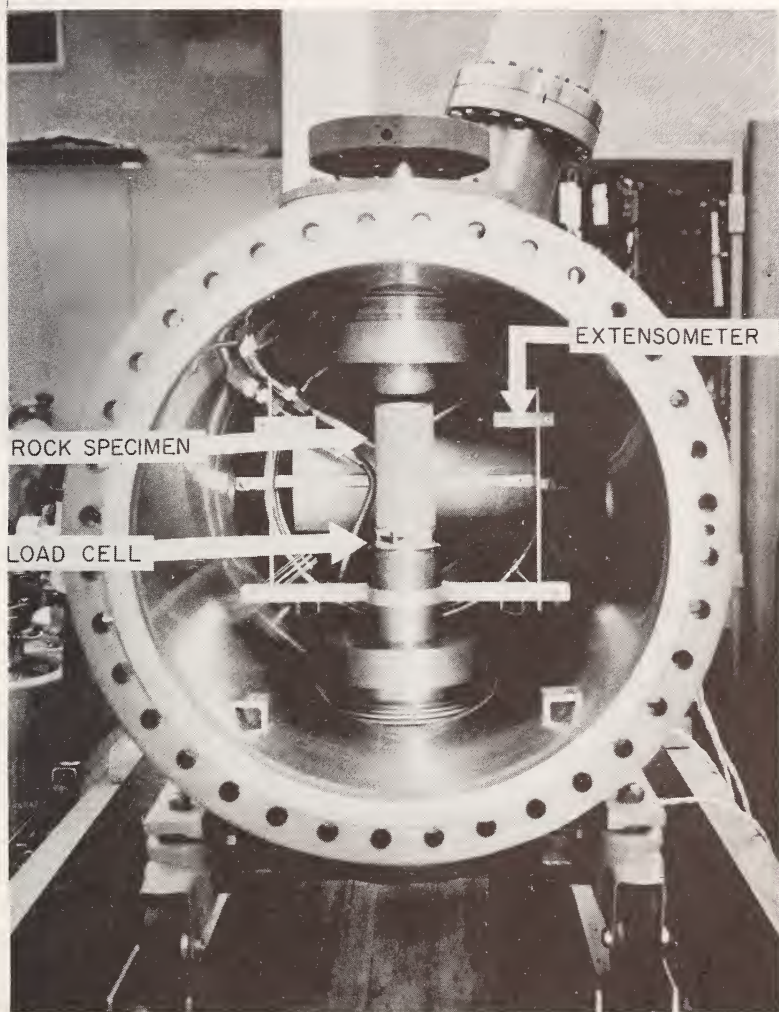


Fig. 4--Specimen in Position Within Vacuum Chamber.

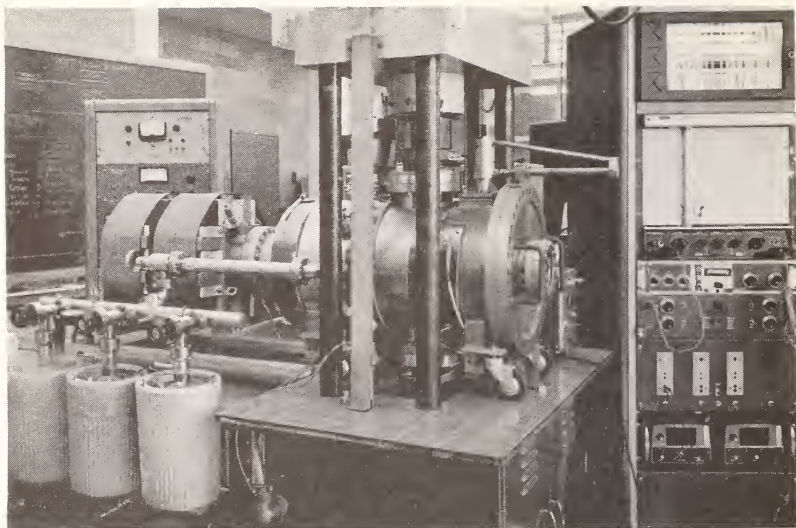


Fig. 5--Vacuum Chamber Positioned in Compression Testing Machine

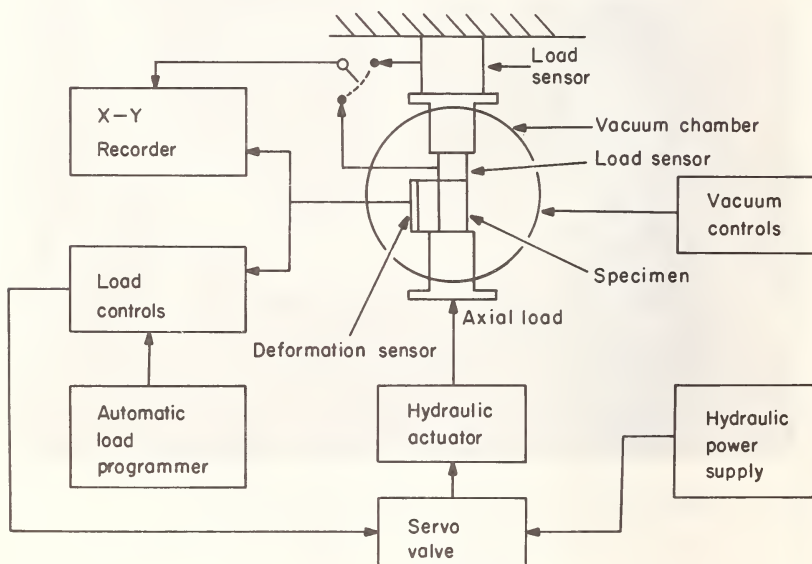


Fig. 6--Compression Testing System.

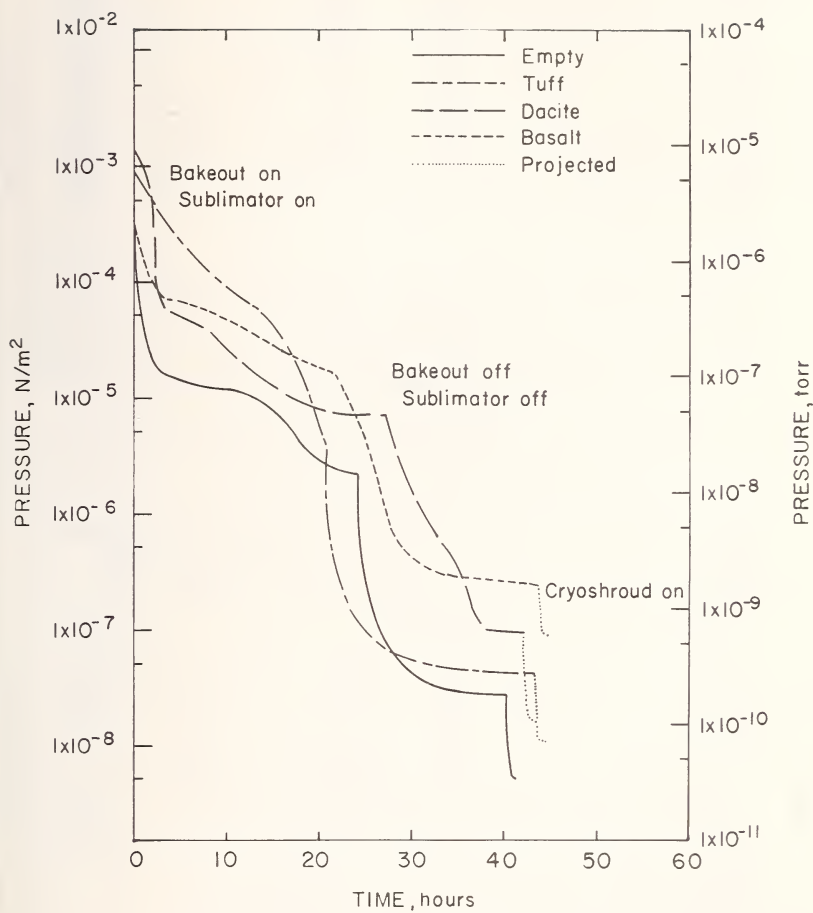


Fig. 7--Typical Pumpdown Curves.

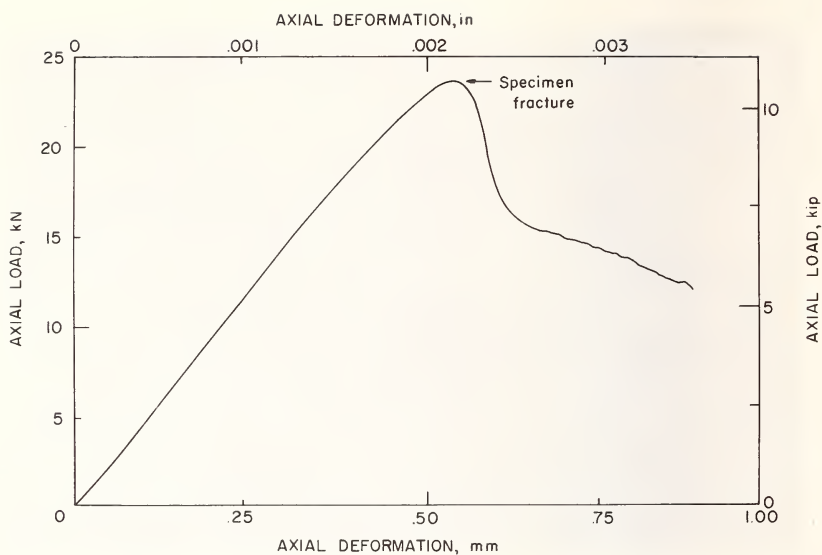


Fig. 8--Typical Load - Deformation Curve for Tuff.

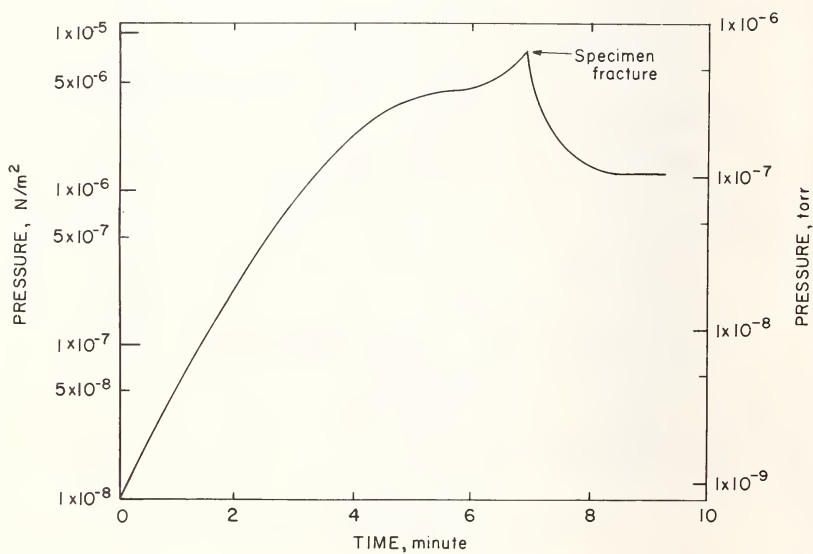
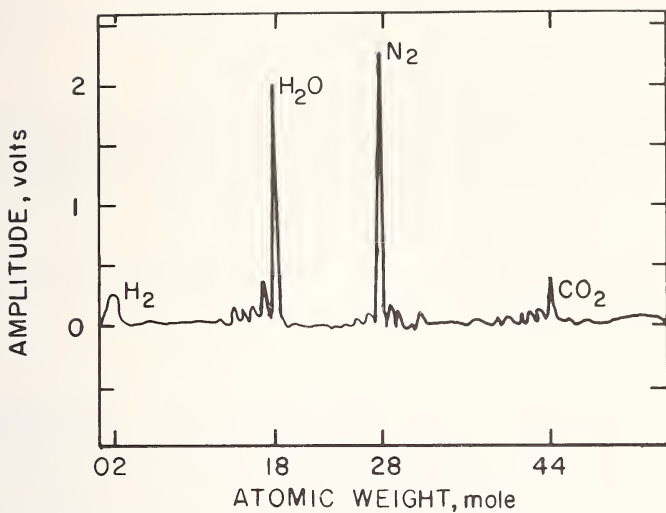
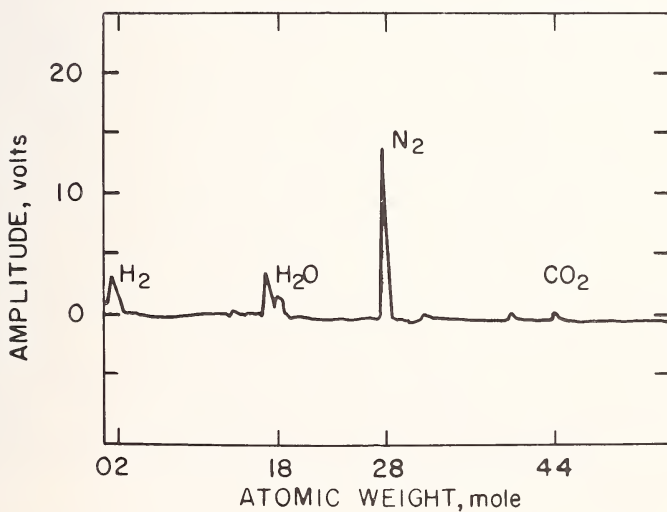


Fig. 9--Chamber Pressure During Compression Test on Tuff.



(a) - At Initiation of Compressive Loading.



(b) - At Specimen Fracture.

Fig. 10--Mass Spectrometer Traces for Tuff During Compression Test.

FRICITION BETWEEN SOLIDS AND SIMULATED LUNAR SOILS IN
ULTRAHIGH VACUUM AND ITS SIGNIFICANCE FOR THE DESIGN
OF LUNAR ROVING VEHICLES

Leslie L. Karafiath¹

REFERENCE: Karafiath, Leslie L., "Friction between Solids and Simulated Lunar Soils in Ultrahigh Vacuum and Its Significance for the Design of Lunar Roving Vehicles," ASTM/IES/AIAA Space Simulation Conference, 14-16 September 1970.

ABSTRACT: The initial and kinetic friction between various solids and ground basalt, simulating the lunar soil, was measured in ultrahigh vacuum with a rotating disk-type apparatus designed for this purpose. Pressures below $p = 10^{-9}$ torr have been routinely reached with the vacuum system consisting of a turbomolecular, a getter-ion and a liquid-N₂-cooled titanium sublimation pump. The testing program included tests with steel, titanium, and fiberglass disks and ground basalt in two particle size ranges, coarse (250-500 μ) and fine (38-62 μ). The experimental results show that both the initial and kinetic friction invariably increase in ultrahigh vacuum. For the range of normal stresses applied in the experiments, the total kinetic friction was highest for fiberglass followed by titanium and steel; the total initial friction was highest for fiberglass followed by steel and titanium.

¹Research Scientist, Grumman Aerospace Corporation, Bethpage, New York 11714

KEY WORDS: adhesion, friction, ultrahigh vacuum, basalt, fiberglass, steel, titanium

INTRODUCTION

On earth it is possible to perform full scale performance tests of off-the-road vehicles to determine traction, slip, and other wheel characteristics under various soil conditions. For the design of lunar roving vehicles these characteristics have to be estimated on the basis of wheel geometry, soil properties, and the friction that develops between the soil and the contacting solid surfaces of the wheel. On earth the layers adsorbed on both the surface of the soil particles and of the solid govern the mechanism of friction; in the ultrahigh vacuum environment of the Moon these layers are absent allowing direct contact between the solid and mineral constituents of the soil, and thus a change in the frictional properties of these materials. The purpose of the experimental investigations reported in the paper is to determine the friction between various solids and simulated lunar soils in ultrahigh vacuum environment.

METHOD OF FRICTION MEASUREMENT

The frictional resistance which develops between solids and granular materials upon mutual displacement has the following characteristic features. At the beginning of the relative displacement the frictional resistance rises sharply and reaches its peak value after a small displacement. Upon continuing displacement between the solid and the granular material the frictional resistance may stay at this peak level (curve a in Fig. 1), or, as is more frequently the case, drop somewhat and stabilize at a lower level (curve b in Fig. 1).

In this paper the term initial friction is used to designate the peak value of frictional resistance.

Sometimes this initial friction is considered as static friction, since very little mutual displacement is necessary for its mobilization. The frictional resistance which develops when continuous motion of the sliding solid is maintained is termed kinetic friction. If the frictional resistance shows a linear relationship with the normal load, and uniform distribution of stresses is assumed, then

$$\tau = a + \mu \sigma , \quad (1)$$

where τ is unit frictional resistance, a is adhesion, σ is normal stress, and μ is coefficient of friction (initial friction is indicated below by subscript i and kinetic friction by subscript c).

For the purpose of estimating shear stresses at the soil-wheel interface at various performance levels it is necessary to know the magnitude of both the initial and kinetic friction. The testing apparatus designed to determine both of these values under both atmospheric and ultrahigh vacuum conditions is shown in Fig. 2. It consists of two sections: a rotating section with an annular metal disk 4 cm in diameter and a surface area of 10 cm², and a strain gauge balance carrying a stainless steel cup 6 cm in diameter and 1.8 cm deep, containing the soil specimen. The rotating section is free to move up and down so that the test surfaces can be separated during baking of the vacuum system. Loads were varied by changing weights. For transmission of motion into the vacuum chamber, a flexible coupling connects the drive shaft of a variable speed motor to the input shaft of a NRC-rotary harmonic feedthrough.

A diaphragm section about the center of the strain gauge balance is instrumented to measure axial loads; a thin-walled cylindrical member is instrumented to measure torsional forces. The important feature of the testing apparatus shown in Fig. 2 is that the geometry of the contacting surfaces does not change upon mutual displacement allowing the determination of both the initial and kinetic

friction. The kinetic friction observed in the tests corresponds to the friction at 100 percent slip in locomotion theory.

Assuming uniform distribution of the stresses beneath the disk the following relations hold for the disks used in these experiments:

$$\tau(\text{g/cm}^2) = 0.066 T(\text{g cm})$$

$$\sigma(\text{g/cm}^2) = 0.103 N(\text{g}) ,$$

where T = torque and N = normal load. It is noted that any error arising from the nonuniform distribution of stresses is negligible as was shown for triangular distribution in (1).

The determination of the friction between solids and granular materials by the above method is valid as long as the shear failure induced by the rotation of the disk occurs at solid-granular material interface. If the frictional resistance at this interface and the normal load is relatively high, shear failure may occur laterally in the granular material before the frictional resistance reached its limit at the interface. Figure 3 shows the principal stress planes for these conditions. Lateral failure in the granular material is accompanied by excessive sinkage of the disk; in the experiments reported herein both the normal load and the frictional resistance was relatively low and no lateral failure occurred.

ULTRAHIGH VACUUM SYSTEM

The ultrahigh vacuum system includes a working chamber equipped with several different pressure gauges, including a residual gas analyzer, electrical and instrumentation feedthroughs, internal heaters, a gas handling system, and various pumps. For baking the whole system, a combination of ovens, heating strips and tapes, and baking mantles are available. Normally, a turbomolecular pump with a

nominal pumping speed of 260 liter/s is used for roughpumping and pumping during part of the baking cycle. With very fine soils, the start of the turbomolecular pump is preceded by the activation of two sorption pumps in order to avoid disturbing the specimen. Ultrahigh vacuums are obtained by the operation of a getter-ion pump with a nominal pumping speed of 270 liter/s and a liquid-N₂-cooled titanium sublimation pump with an estimated pumping speed of 700 liter/s. Pressures below 1×10^9 torr were routinely reached within 2 or 3 hours after baking.

TESTING PROCEDURES

a. Preparation and Properties of Soil Samples

Chunks of basalt from Somerset County, New Jersey were comminuted in air and sifted to obtain the desired grain sizes. The container was filled with 66 g of loose soil and carefully evened to the same level in each test with the help of an Airite vibrator. Table 1 shows data pertinent to the preparation of samples.

To compare the frictional resistance of solids on granular soil specimens with the internal friction of the soil, triaxial tests were performed on both coarse and fine basalt in air-dry condition. The shear strength envelope for both materials was found to be a curve which at pressures lower than 1 kg/cm^2 could be approximated by a straight line corresponding to a friction angle of 45 degrees.

Sieve analyses performed on specimens tested either for solid-on-soil or for internal friction did not show a discernible change in the grain size distribution, an indication that the stresses applied in the tests did not break down the individual grains significantly.

b. Preparation and Properties of Solid Disks

The annular metal disks were fabricated by machining, and were checked for concentricity before and after polishing. Only disks with a total runout of less than 0.01 mm were accepted; their degree of finish was measured with a profilometer. Most tested disks had finishes between 0.050 and 0.1 μ (rms).

The annular fiberglass disks were cut from $\frac{1}{8}$ -in. thick laminated fiberglass (cloth fibers) sheets and fastened by two screws to aluminum disks fabricated in a previous program. The sides of the fiberglass sheet differed slightly in texture; in the friction tests, the side with the coarser texture was used as the sliding surface.

The steel disks were manufactured of steel AISI 1020, the titanium disks of the titanium alloy Ti-6Al-4V. Properties of the latter are given in (2). The metal disks were submitted to a thorough cleaning procedure after manufacturing and prior to testing.

The fiberglass sheets were manufactured according to Grumman specifications (3). Outgassing experiments performed with fiberglass material showed that with the fiberglass inside the chamber the ultimate pressure reached with the vacuum system was about $1\frac{1}{2}$ decades higher than with empty chamber (4).

c. Pumpdown

To avoid lengthy pumpdowns, the granular basalts used in the vacuum tests were outgassed in a special desiccator prior to their transfer to the experimental chamber. Besides reducing pumpdown time considerably, the nearly constant gas loads produced by the processed specimens made the achievement of a certain uniformity of the vacuum history of each test easier.

Baking temperatures varied from section to section of the vacuum system; their limitations were set by high temperature sensitive components in the system; e.g., strain gauges and ion pump magnets. During the entire baking cycle, a temperature gradient ranging from 250° to 300°C at the TSP-cryopump combination to 200° to 220°C at the ion pump was maintained. The chamber itself was usually kept at 200° to 210°C. Total baking times ranged from 22 to 92 hours. When the system pressure showed a tendency to fall and reached the 10^{-7} torr level, the heat was shut off. From this point, it took approximately 3 to 6 hours to produce a reasonably stable pressure. Although the achieved ultimate pressure varied from test to test within a decade, they were without exception in the 10^{-10} torr range, or lower. Pressure readings were taken with a G.E. Model 22 GR214 trigger gauge.

The pressure was normally kept below 1×10^{-9} torr for an exposure time of about 20 hours. In two instances, however, scheduling necessitated performing a test exposure times between 3 and 4 hours; the effect, if any, of this shorter exposure time on friction was within the experimental error.

d. Performance of Tests

Once an acceptable pressure level was obtained, the loaded stationary disk was lowered to rest on the granular basalt for 5 minutes; then three clockwise revolutions were executed at 3 rpm. The torque required to rotate the disk and the normal load were recorded throughout the test on a Brush Mark 280 dual recorder.

Pressure evolution during the tests was recorded on a G-14 Varian recorder. At the start of disk rotation, pressure readings increased by a factor of 2 or 3; as soon as motion stopped, the pressure decreased rapidly until it reached the original pressure level.

RESULTS OF TESTS

a. Repeatability of Tests

The testing procedure as described in the preceding section consists of several operations each of which may be a source of error in the measured friction. To determine the accuracy of the whole system a series consisting of 10 tests in ultrahigh vacuum and 10 parallel tests in air was performed on coarse basalt with a normal load of 682 g. The average values of the measured torque as well as the standard deviation of the 10 observations are shown in Table 2, together with estimates of the percentage error intervals that occur with 95 percent probability when averages of observations are used to represent the theoretical mean.

Because of the time required for bakeout and pumpdown it was not possible to incorporate 10 repetitions for each measurement in the testing program. The error interval for a series of 5 tests is 1.7 times that shown in Table 2, and for 3 tests it is 3.5 times greater.

b. Testing Program

Table 3 shows the number of tests performed to date in ultrahigh vacuum with various solids and particle sizes of ground basalt. For each test in ultrahigh vacuum a parallel test was performed in air.

c. Presentation of Test Results

The results of tests performed on coarse basalt in both ultrahigh vacuum and air are represented in Figs. 4 through 7, which show the averages of the measured torque values for each normal load and their best fitting linear relationships, determined by the method of least squares.

The coefficient of friction, as defined by Eq. (1) is determined by the slope of the best fitting straight line and is shown in the figures. The adhesion can also be evaluated from Eq. (1). However, in many instances the adhesion determined by the best fitting straight line was found to be negative indicating that at low loads the relationship between normal load and frictional resistance is not linear. For this reason the best fitting straight lines are shown only in the range of normal loads where it represents the best approximation to the test results.

Figure 4 shows the effect of ultrahigh vacuum on the friction between steel and coarse basalt. The best fitting straight lines indicate that the coefficients of friction, as defined by Eq. (1), were not affected by the ultrahigh vacuum. The adhesion due to the ultrahigh vacuum was found to be $a_i = 18 \text{ g/cm}^2$ for the initial friction and $a_c = 9 \text{ g/cm}^2$ for the kinetic.

In the tests performed on fine basalt, the frictional resistance versus displacement curve was invariably found to be that of type "a" in Fig. 1. For these tests $\mu_i = \mu_c$. The results of these tests are shown in Fig. 5; the coefficient of friction is $\mu_i = 0.20$ for ultrahigh vacuum and $\mu_i = 0.18$ for air. The adhesion represented by the distance between the two straight lines varied from $a = 6 \text{ g/cm}^2$ to 9 g/cm^2 , within the range of normal loads.

The scatter of the measurements experienced with the fine basalt was greater than that for the coarse basalt. This is attributed to the difficulties of controlling the surface of the soil bed. Because of the lower gas permeability of the fine basalt, gas pressures may build up within the soil bed and loosen the surface during outgassing.

The results of two series of tests performed on coarse basalt with titanium disks in both ultrahigh vacuum and air are shown in Fig. 6. In these two

series of tests the difference between the initial and kinetic friction was in the range of the noise level of electronic recording and, therefore, was not evaluated quantitatively.

The results of two series of tests, one in ultrahigh vacuum, the other in air, on coarse basalt with fiberglass disks are shown in Fig. 7. In contrast to the tests with titanium disks, well pronounced initial friction was observed in all fiberglass disk tests. The coefficients of initial and kinetic friction are shown in the figure.

The results of the first two tests with fiberglass disks performed under the same test conditions were found to be almost identical within the accuracy of recording. Further tests at the two other normal loads showed the same degree of repeatability, therefore, it was deemed unnecessary to perform more than two tests at each normal load.

EVALUATION OF TEST RESULTS

The test results show that the frictional resistance between the various solids and soils tested invariably increases in ultrahigh vacuum but in a different way for the various combinations of materials. A valid comparison of the frictional properties of the various materials in ultrahigh vacuum can best be made by evaluating total frictional resistance within the range of normal stresses of interest. The normal stresses in experiments varied from 46 to 91 g/cm², approximately corresponding to the expected range of normal stresses under the wheels of a lunar roving vehicle. Thus comparison of the total frictional resistance within the range of normal stresses applied in the experiments is also meaningful for the applications.

Figure 8 plots average shear stresses representing the total frictional resistances developed by various materials sliding on coarse basalt in ultrahigh vacuum against the normal stresses. The upper graph shows the kinetic, the lower the initial

frictional resistances. As can be seen from Fig. 8, fiberglass develops more initial and kinetic friction than any of the metals tested. This may, however, be partly due to the texture of the fiberglass. Comparable results were obtained with the titanium and steel disks, both having the same surface finish. The titanium disk exhibited somewhat higher kinetic friction than the steel. The initial friction developed by the titanium disk, on the other hand, was so low that it could not be quantitatively evaluated; the dashed line in Fig. 8 represents a very rough guess offered for comparison only. The differences in friction exhibited by these two metals are probably due to their different hardnesses.

From the point of view of lunar locomotion it is significant that both the initial and kinetic friction increased in ultrahigh vacuum. Preliminary tests performed with titanium disks and ground basalt simulating the particle size distribution of the Apollo 11 samples showed friction values very close to that found with coarse basalt.

APPLICATION OF TEST RESULTS TO THE DETERMINATION OF TRACTION

In the application of experimentally obtained frictional relationships to the determination of traction that a driven wheel can exert, it is essential to pay attention to the following considerations.

Friction and Slip

The kinetic friction determined by the experiments corresponds to 100 percent slip of the wheel. There is no direct correlation between slip and the rotational displacements associated with the development of initial friction in the tests.

Lateral Failure

The results of friction experiments apply to wheel-soil friction as long as sliding occurs only at the wheel-soil interface. If the stresses transmitted to the soil by the wheel cause lateral failure in the soil mass before the full frictional resistance at the interface is mobilized, the traction exerted by the wheel can no longer be computed on the basis of the friction developed at the contact area. Failure in the soil mass would occur along an oblique plane causing lateral displacement of the soil; hence the term lateral failure.

An analysis of potential lateral failure beneath a wheel may be made by considerations similar to that applied to the friction experiments (Fig. 3). The principal stresses in the plane of the normal load and shear stress at the interface may be determined and the minor principal stress compared with that in the lateral direction.

Consideration of Tread or Lugs

Tread or lugs force the sheared surface to pass through the soil between the tread bars or lugs mobilizing thereby the internal frictional resistance of the soil which is generally higher than that between solids and soil. The total traction which a wheel with tread or lugs can exert is composed in such a case of two components, one due to the frictional resistance on the face of the tread bars or lugs and the other one due to the internal frictional resistance of soil between the tread bars or lugs (Fig. 9).

An estimate of the contribution of the two components to the total traction may be made by considering the distribution of normal stresses at the sheared surface. Normal stresses at the face of the lugs will be generally higher than between them because the soil immediately beneath the face of lugs is compressed more than between lugs. Experiments with treaded tires showed high stress concentrations

at the face of lugs. A crude approximation of the distribution of normal stresses may be made by assuming that a firm bottom exists at some depth beneath the wheel and the normal stresses are inversely proportional to the depth of the compressed layer (Fig. 9). The total traction can then be computed by applying the respective relationships between frictional resistance and normal stress to the areas in question.

CONCLUSIONS

An experimental apparatus suitable to determine in ultrahigh vacuum both initial and kinetic friction between solids and granular materials under various normal loads has been developed. The experimental results clearly show that with every material tested in UHV there is an increase in frictional resistance between the solid disk and the granular basalt simulating lunar soil. Since the magnitude of this increase in relation to the normal stress varies with each of the solid materials tested, no general conclusions as to effect of ultrahigh vacuum on the friction between solids and soils can be drawn.

The friction that develops between a wheel operating in ultrahigh vacuum and the soil significantly affects wheel performance. In the selection of materials for the wheels of lunar roving vehicles consideration should be given to the frictional properties that these materials exhibit in ultrahigh vacuum.

ACKNOWLEDGMENT

Acknowledgment is due to G. Mohr who designed the ultrahigh vacuum system and performed part of the experiments and to G. Homfeld who assisted in the operation of the ultrahigh vacuum system and in the performance of experiments.

REFERENCES

1. Karafiath, L. L., Some Aspects of the Determination of the Coefficient of Friction between Metals and Soils and Its Application to Lunar Locomotion Studies, Grumman Research Department Memorandum RM-379, October 1967.
2. Properties of Ti-6Al-4V Titanium Engineering Bulletin No. 1, Titanium Metals Corporation of America, New York.
3. Grumman Standard Specification No. 11100A, "Glass Fiber Base-Plastic Laminates for Structural Application," June 1968.
4. Karafiath, L. L. and Mohr, G., The Effect of Ultrahigh Vacuum on the Friction between Various Solids and Granular Soils, Grumman Research Department Report RE-376, March 1970.

Table 1

PROPERTIES OF SOIL SAMPLES

Material	Particle Size Range (microns)	Sample Weight g	Specific Gravity g/cm ³	Moisture Content % (in air)	Dry Density g/cm ³	Porosity %
Basalt	250-500	66	2.914	0.26	1.73	40.4
	38-62	66	2.990	0.7	1.72	42.5

Table 2

ACCURACY OF TESTS BASED ON A SERIES OF TEN TESTS

	Initial Friction			Kinetic Friction		
	Average Torque g-cm	Standard Deviation	Error Interval %	Average Torque g-cm	Standard Deviation	Error Interval %
Ultrahigh Vacuum < 10 ⁻⁹ torr	632	69	±8	346	22	±4
Air	251	38	±9	209	19	±7

Table 3

TESTING PROGRAM — NUMBER OF TESTS PERFORMED IN UHV

Coarse Basalt:

Disk	Normal Load (g)		
	455	682	910
Steel	5	10	6
Titanium	7	5	5
Fiberglass*	3	2	2

*Normal load 7gs higher than shown.

Fine Basalt:

Disk	Normal Load (g)		
	455	682	910
Steel	3	5	4

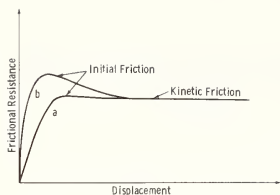


Fig. 1 Development of Frictional Resistance with Displacement

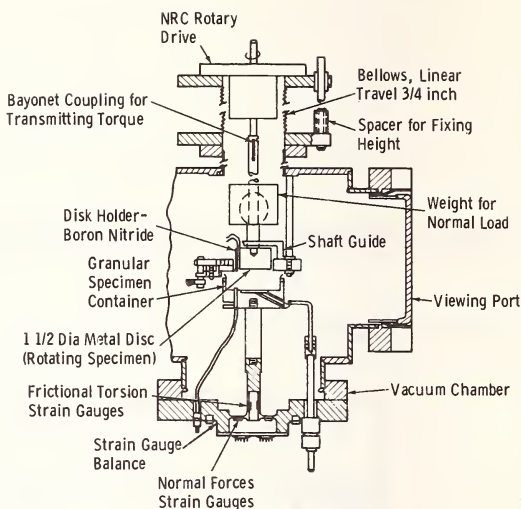
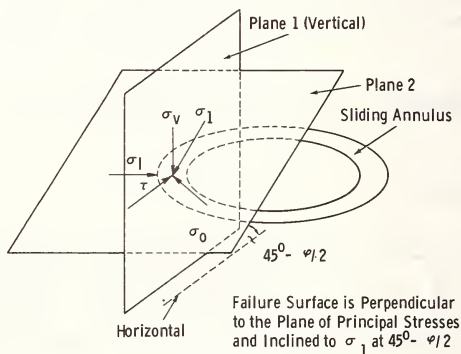


Fig. 2 Friction Measuring Apparatus



- σ_v = Vertical Normal Stress
- σ_l = Lateral Stress
- τ = Shear Stress
- σ_1, σ_3 = Principal Stresses
- $\sigma_v, \tau, \sigma_l, \sigma_0$ in Plane 1
- σ_l, σ_1 in Plane 2

Fig. 3 Planes of Principal Stresses:
 Plane 1 $\sigma_0 < \sigma_1$; $\sigma_0 = \sigma_3$
 Plane 2 $\sigma_l < \sigma_0$; $\sigma_3 = \sigma_1$

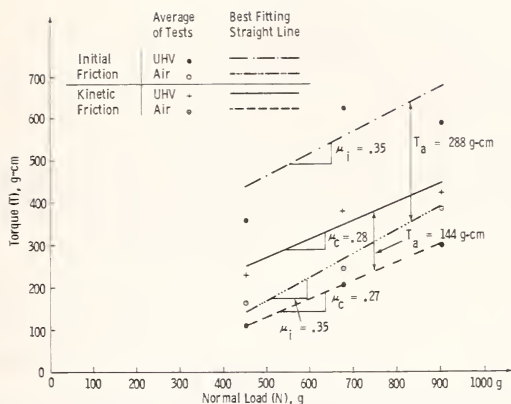


Fig. 4 Friction Between Steel and Coarse Basalt, Results of Test

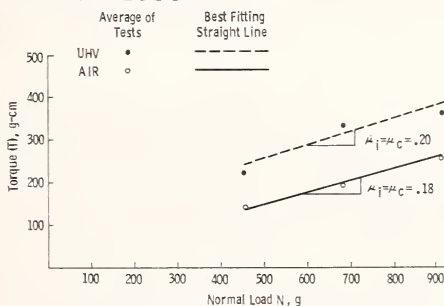


Fig. 5 Friction Between Steel and Fine Basalt, Results of Tests

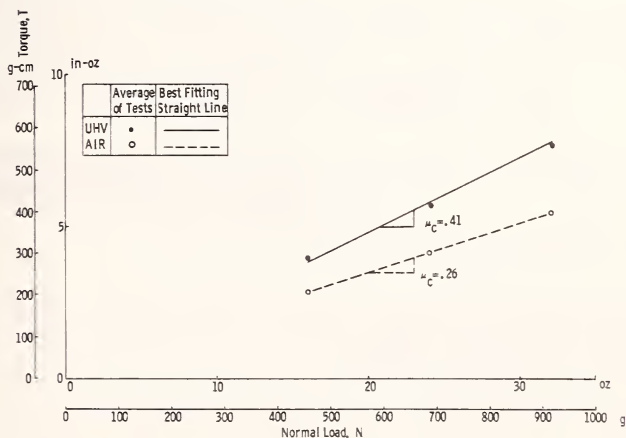


Fig. 6 Kinetic Friction Between Titanium and Compacted Coarse Basalt - Results of Tests

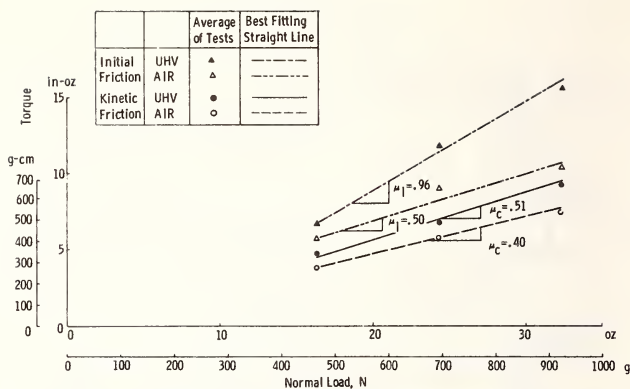


Fig. 7 Friction Between Fiberglass and Compacted Coarse Basalt - Results of Tests

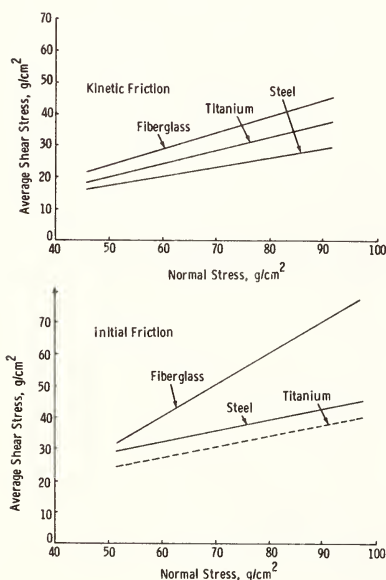


Fig. 8 Comparison of Friction Between Coarse Basalt and Various Materials in Ultrahigh Vacuum

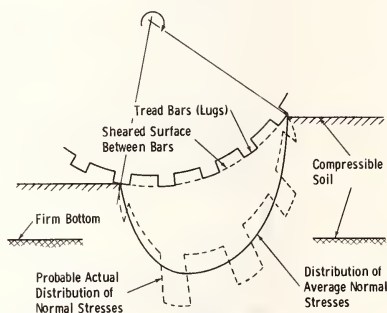


Fig. 9 Treaded Wheel - Distribution of Normal Stresses

REAL TIME SIMULATION OF ATMOSPHERIC BALLOON ENVIRONMENT²

A.J. Paillous¹ and M. Roussel¹

REFERENCE: Paillous, A.J. and Roussel, M., "Real time Simulation of Atmospheric Balloon Environment," ASTM/IES/AIAA : Space Simulation Conference, 14-16 September 1970

ABSTRACT: A simulation chamber was designed in order to study the behaviour of several balloon materials during long time flights. Solar ultraviolet radiation, pressure, temperature and atmospheric composition are the simulated constituents of the atmospheric balloon environment. Samples are irradiated without mechanical strain. A computer program, taking the values of different parameters (of the environment and of the material) against wavelength into account, gives the information for conducting the simulation. Experiments are performed in real-time. Exact ultraviolet energy doses, in each spectral wavelength interval, between 300 and 410 nm, are delivered every day to samples. A night-day cycle is simultaneously achieved with a thermal cycle.

KEY WORDS: Simulation, Balloon, Solar ultraviolet Radiation, Atmospheric environment, Ozone, Temperature, Plastic material, Computer.

¹ONERA/CERT - Département d'Etudes et de Recherches en Technologie Spatiale, 51, rue Caraman 31-TOULOUSE FRANCE.

²This work was supported by a CNES contract

1 - INTRODUCTION

The Eole Project (1)¹ includes the flight of several hundred superpressure balloons at a constant altitude (200 or 300 mbar) for some months (Superpressure balloons are non-extensible balloons which are sealed to prevent gas release. See reference(2)).

In order to test and select the balloon materials, a chamber allowing the simulation of a real long-lasting flight was realized. This chamber can reproduce, in the laboratory, all the parameters of the balloon environment at a chosen altitude [i.e. solar ultraviolet radiation, pressure, temperature and atmospheric composition (ozone concentration)]. All these components have a role in the degradation of the physical properties of plastic films used in the present state of superpressure balloon technology.

The selected exposition process enables one to carry out a real-time study. Exact ultraviolet energy doses, in each spectral wavelength interval between 300 and 410 nm, are delivered every day to samples. Samples are alternately illuminated and darkened ; a thermal cycle is simultaneously used.

2 - OVERALL SIMULATION EQUIPMENT

The simulation equipment is shown in Figure 1. It includes a stainless steel irradiation chamber, a light source, a cooling system and an ozone source.

2-1 Irradiation chamber : The stainless steel irradiation chamber is formed by two portions of a sphere separated by a cylindrical part (diameter 120 cm). All internal surfaces are black.

In the chamber, twelve sample-holders (12x21 cm) are regularly laid out around the light source (Figure 2). They can be adjusted at a variable distance from the source (32 - 41 cm). Taking the light

¹The numbers in parentheses refer to the list of references appended to this paper.

emission diagram of the source into account, the shape of the sample-holder was found to produce a high uniformity of light on the sample (4%). Each sample-holder is connected to the cooling system by a flexible pipe.

The irradiation chamber is also equipped with several pass-throughs for thermocouples, four pyrex windows for direct observation of the samples, a quartz window for the determination of the ultraviolet intensity and a vent valve. These elements are seen in Figure 1.

2-2 Ultraviolet source : A 2 500 watts Xenon short arc lamp (OSRAM, XBO 2 500 Watts) is used as the source of ultraviolet radiation. The lamp is centered in a quartz cylinder through which an air flow cools the lamp and carries along the ozone formed in its vicinity.

2-3 Sample positioning and temperature control : The film samples are fixed close to the sample-holders by clips and small U-Shaped springs (Figure 3). Thus, samples are irradiated without mechanical strain.

The sample-holders are cooled by a fluid circulation allowing the temperature control of samples. The heat exchanger used for this purpose has an output range of from -80°C to $+100^{\circ}\text{C}$. The irradiation temperature is greater than the night temperature. This thermal cycle is obtained by an automatic change of the working conditions of the cooler when irradiation stops. Two temperature control devices are employed. Thermocouple leads run from behind each sample to a temperature recorder ; these thermocouples, placed between two plastic films (Figure 3), give a fair estimation of the sample temperature. An other thermocouple is placed in the return pipe of the cooling fluid. It is connected to a safety device which stops irradiation when the temperature is higher than a fixed value (See Figure 2).

2-4 Atmospheric composition control : Total pressure and ozone partial pressure, in the chamber, are controlled every day during long periods of experimentation.

A mercury manometer measures pressure in the chamber which is evacuated by a mechanical pump.

The ozone concentration in the chamber is determined by a chemical method (3). A constant volume of the chamber atmosphere is drawn at a constant rate through a solution contained in three gas-traps (Figure 1). The absorption of the solution is then read at 412 nm in a spectrophotometer. The loss in extinction per cm after sampling gives the ozone concentration, which can be adjusted by the introduction of pure ozone, or pure air, and further pumping.

2-5 Measurement of ultraviolet light

intensity : The spectral energy distribution of our light source, in the irradiation device, at the sample location, has not been yet accurately measured, because we are lacking a convenient spectrometric device. As an approximation of the truth, we assumed that the Xenon short arc had an output similar to the one given in previously published works (4).

Before a long experiment is carried out, and while the irradiation chamber is open, a calibrated thermopile is used to measure the total light intensity given by the Xenon source (with the quartz cylinder and pyrex filters) on the sample-holders. If necessary, the positions of the sample-holders are adjusted in order to achieve the desired value.

During experimentation, solar cells, fixed on a sample-holder (see Figure 3), monitor the light intensity through the solar region. One of these solar cells is behind a wide band filter (300-400 nm) and gives an estimate of the intensity of ultraviolet radiation. Another device is used behind the quartz window to give the variations in ultraviolet intensity of the Xenon arc lamp. This device consists of a sensor cell attached to a compact metering unit and an ultraviolet filter. To measure the variation in ultraviolet intensity of the lamp, two readings are taken ; one reading with the sensor cell by itself, then a second reading while holding the ultraviolet filter between the source and the sensor cell. The difference between these two readings gives a proportional value of the ultraviolet intensity of the Xenon arc lamp.

3 - PRINCIPLE OF THE ULTRAVIOLET SOLAR SIMULATION

The solar spectral irradiance for a given wavelength interval, and the solar constant, are well known (5). Terrestrial albedo and light attenuation by the atmosphere are also tabulated for various altitudes (6).

The ultraviolet energy dose received by the balloon at a given altitude is a function of solar spectral irradiance, terrestrial albedo and light transmission through the atmosphere.

All these terms are used in a computer program which gives at any latitude, every day in the year, every hour in the day, at a fixed altitude, the ultraviolet flux density on a horizontal unit surface (top of the balloon).

The computer writes also the energies $I_{\Delta\lambda_i}$ received by this unit area ($I_{\Delta\lambda_i}$ are expressed in J/m^2) for different contiguous wavelength intervals $\Delta\lambda_i$, during one day; this calculation takes the solar radiation reflected by the earth through the balloon into account.

Then the program assumes that the Xenon arc source provides to the sample, in a given time T and in the wavelength interval 350 - 370 nm, exactly the same energy as provided by the sun to the balloon in 24 hours; it takes also the $I_{\Delta\lambda_i}$ values and the spectral irradiance¹ of the Xenon arc lamp into account. Then the computer writes for each $\Delta\lambda_i$, the duration $T_{\Delta\lambda_i}$ of the illumination required to deliver the $I_{\Delta\lambda_i}$ energy.

4 - VALIDITY OF THE SIMULATION

A first experiment was carried out in order to simulate equatorial conditions at 300 mbar. Materials were irradiated 12 hours out of 24, during 6 months.

¹The spectral irradiance of the Xenon arc lamp was computed from the ratio of lamp energy to Johnson's solar irradiance values (4), taking the new values of solar spectral irradiance into account (5).

4-1 Ultraviolet Solar Radiation Simulation

The data used by the computer program for this experiment and the results of the calculation are respectively given in Table 1 and Table 2. In these conditions, three filters are required for the ultraviolet light simulation.

Spectral transmission plots of these filters are shown in Figure 4. The pyrex filters fixed in the chamber (see Figure 2) cut off the wavelength shorter than 300 nm. The two other filters, fixed on a polygonal support (Figure 5) can be interposed between the lamp and the samples, to cut off respectively wavelengths shorter than 315 and 333 nm.

The Xenon short arc lamps do not possess a satisfactory solar spectral match in the visible and near infrared regions (800 to 1 100 nm region) (4). But it is quite unimportant for the sample degradation, which is due to ultraviolet radiation when samples are very well cooled. So, as a matter of fact our purpose was not the simulation of the whole spectrum at a given altitude, but the simulation of only the ultraviolet solar radiation at this altitude.

The total light intensity given by the experimental device (having only the pyrex filter) and measured by the thermopile, is adjusted in order to obtain on the samples, in the wavelength interval 350 - 370 nm the exact computed value. In the wavelength range 300 - 335 nm an exact agreement between the $I_{\Delta\lambda_i}$ values calculated and those given by the Xenon

source can be obtained by interposition of the mobile filter during a time in accordance with the computed $T_{\Delta\lambda_i}$. In the wavelength range 300 - 410 nm, for the

considered altitude (300 mbar), the agreement is theoretically better than 20%, provided that there is no spectral aging of the light source. In order to be sure that the facility achieves its intended purpose of adequately simulating the ultraviolet solar radiation, an accurate measurement of the spectral irradiance, at the sample location, ought to be used, at first at the beginning of irradiation, and then at even time intervals. We plan to use soon a convenient spectrometric device. Meanwhile a preventive replacement of the lamp must be done every 250 hours (20 startings).

4-2 Atmospheric environment simulation :

The other environmental parameters are ozone concentration and air temperature. The following values are given in the Handbook of Geophysics (6), at 300 mbar, at the Equator :

Ozone concentration : 0.2 to 0.4 ppm

Air temperature : -37°C (January) to -33°C (July)

Actual temperatures of the balloon materials in flight are a function of the thermo-optical properties of these materials.

The experimental device allowed to achieve the following conditions during the long lasting (6 months) experiment :

Pressure : 300 ± 10 mbar

Ozone concentration : 0.1 to 0.5 ppm

According to the facts that different materials are simultaneously tested in the chamber and that there is only one cooling circuit a same temperature was maintained for all the samples : for nights, the chosen temperature was approximately the average air temperature (-35°C) ; during the days, the sample temperature was allowed to be higher and higher as the samples were aging (the difference with the average air temperature was fixed at $+1^{\circ}\text{C}$ at the beginning of irradiation, and at $+10^{\circ}\text{C}$ three months later) ; this is in order to simulate the increase in solar absorptance with time.

5 - CONCLUDING REMARKS

The equipment, described above, allowed a convenient real-time simulation of a six-months flight at 300 mbar at the Equator. All the environmental parameters, which contributed to the balloon material degradation, were reproduced : ultraviolet energy dose, pressure, atmospheric composition, sample temperature.

This equipment can be adapted for the ultraviolet Solar Radiation Simulation on balloon, satellite or aircraft materials, in varying atmospheric conditions (pure air, ozone, or others gases) for different pressures from one atmosphere to vacuum (a high

vacuum system can be adapted), with a night and day cycle, and a thermal cycle (from -120°C to $+150^{\circ}\text{C}$).

ACKNOWLEDGEMENT

The authors wish to acknowledge the comments and suggestions offered by Mr. D.W. CONNER of NASA Langley Research Center.

REFERENCES

- (1) P. MOREL - "Preliminary flights of Eole Balloons" COSPAR Space Research, London 1967
- (2) VINCENT E. LALLY - "Superpressure Balloons for Horizontal Soundings of the atmosphere" NCAR - TN 28 - June 1967
- (3) T. NASH - "Colorometric determination of ozone by diacetyl-dihydrolutidine" Atmospheric Environment, 1, 679 (1967)
- (4) M. LILLYWHITE, R. Mc INTOSH, C. DUNCAN and J. COLONEY - The Journal of environmental Sciences p. 9, Avril 1968
- (5) "The solar constant and the solar spectrum measured from a research aircraft at 38 000 feet" GSFCX 322-68-304
- (6) "Handbook of geophysics and Space Environment" Scientific editor SHEA L. VALLEY - Air Force Cambridge Research Laboratories - Mc Graw Hill Book Company, Inc.

Wavelength interval (nm)	280-300	300-315	315-335	335-350	350-370	370-390	390-410	410-490
Solar irradiance (W/m ²)	8.75	9.62	19.60	15.92	21.91	22.50	28.50	153.10
Optical transmission of material	0	0.01	0.43	0.54	0.59	0.64	0.66	0.70
Terrestrial Albedo	0.010	0.180	0.106	0.200	0.200	0.200	0.200	0.200
Atmospheric optical thickness	7.5	1.15	0.34	0.210	0.162	0.129	0.099	0.065
Ratio of Xenon lamp energy to solar irradiance	0.92	0.92	0.77	0.92	0.90	0.93	0.93	0.66

TABLE 1 - Solar Ultraviolet radiation simulation
Data used by the computer program, for
the latitude $\phi = 0$, at pressure $P = 300$ mb

Date : 84th Day (equinox)
 Altitude : 300 mbar
 Latitude : 0.00 degree
 Daytime : 12.00 hours

Energies $I_{\Delta\lambda_i}$ received by a unit area of the balloon during 1 day :	$\Delta\lambda_i$ (nm)	$I_{\Delta\lambda_i}$ (J/m ²)
	280-300	0.51814315×10^2
	300-315	0.60157099×10^5
	315-335	0.34373990×10^6
	335-350	0.35551321×10^6
	350-370	0.52827901×10^6
	370-390	0.57579393×10^6
	390-410	0.76368446×10^6
	410-490	0.43386885×10^7

Irradiation time T = 12 00 Hours

Necessary light intensity for accurate simulation in the wavelength interval 350-370 nm = 0.1223×10^2 W/m²

$\Delta\lambda_i$ (nm)	Xenon Arc Irradiance (W/m ²)	$T_{\Delta\lambda_i}$ Simulation Time (Hours)
280-300	0.4575×10^1	0 00
300-315	0.5576×10^1	3 00
315-335	0.9257×10^1	10.31
335-350	0.8172×10^1	12 08
350-370	0.1223×10^2	12 00
370-390	0.1320×10^2	12.12
390-410	0.1490×10^2	14.23
410-490	0.6366×10^2	18 03

TABLE 2 - Calculated results given by the computer for one day (equinox)

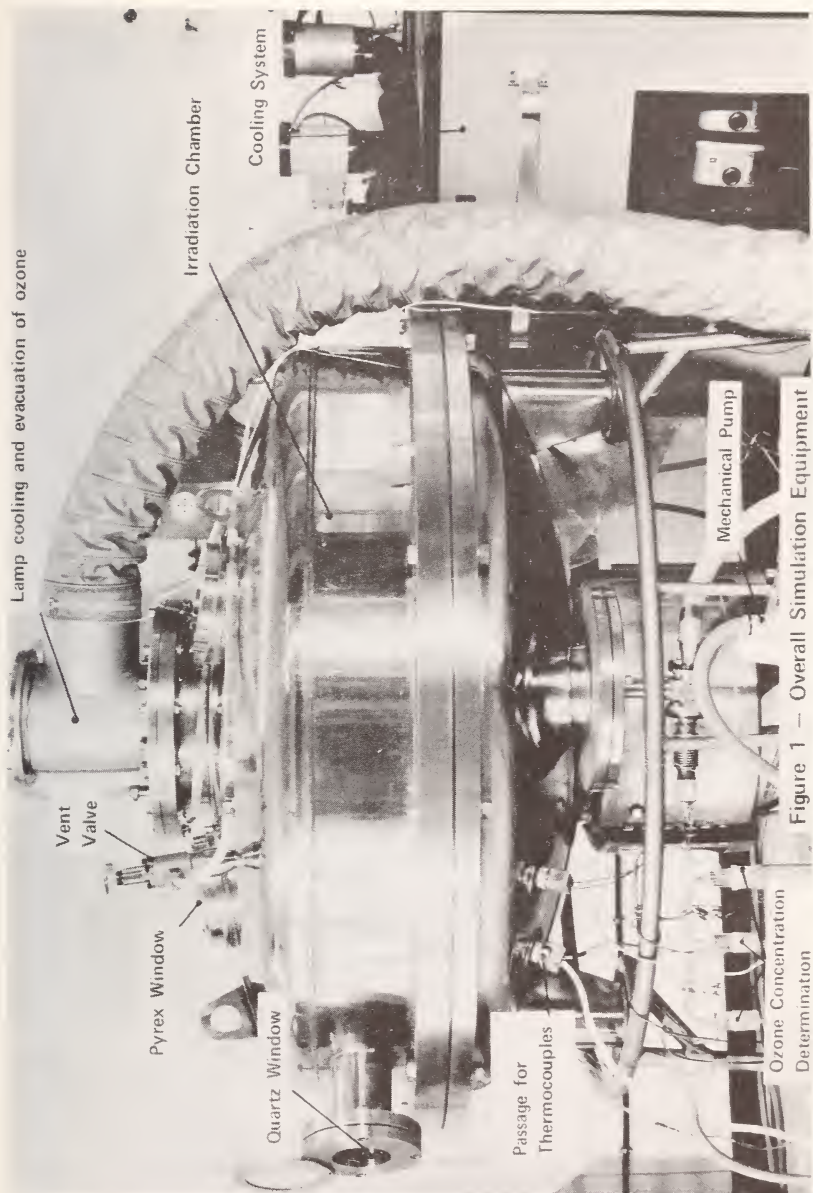


Figure 1 — Overall Simulation Equipment

Ozone Concentration
Determination

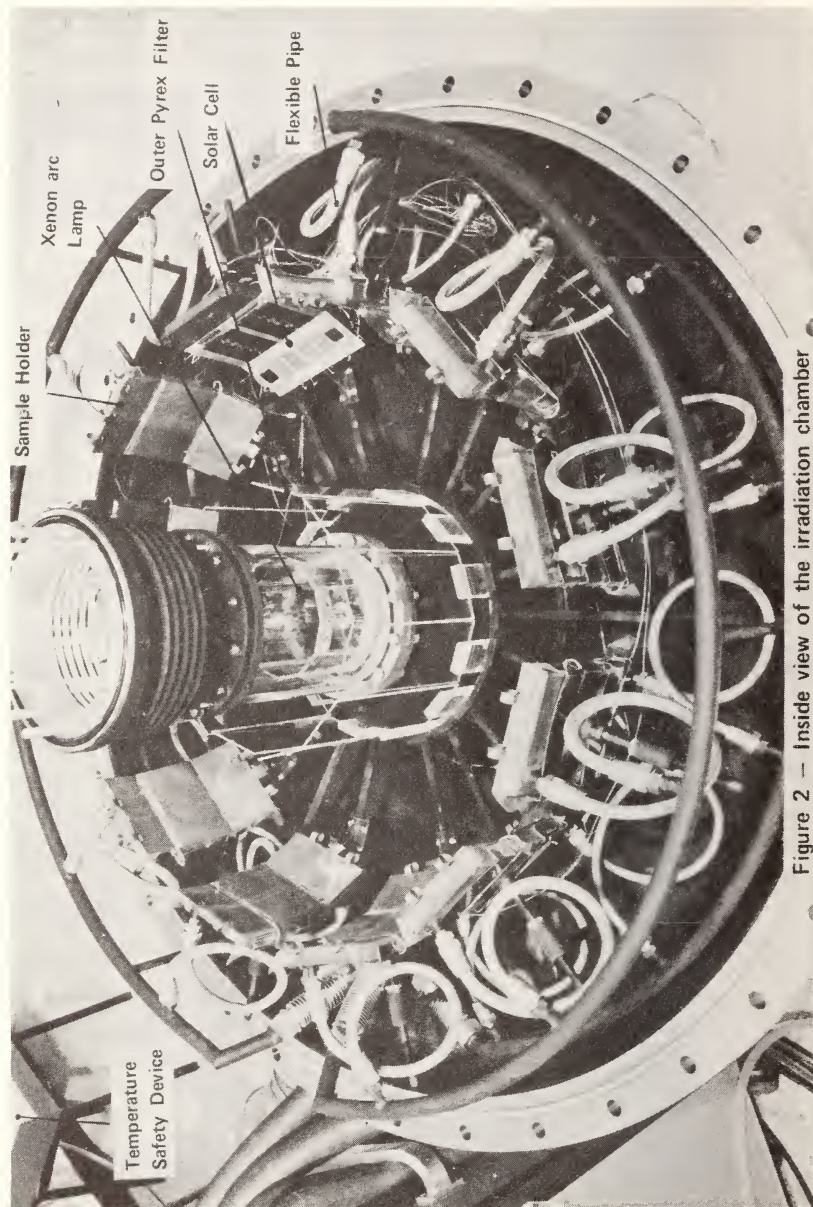


Figure 2 — Inside view of the irradiation chamber

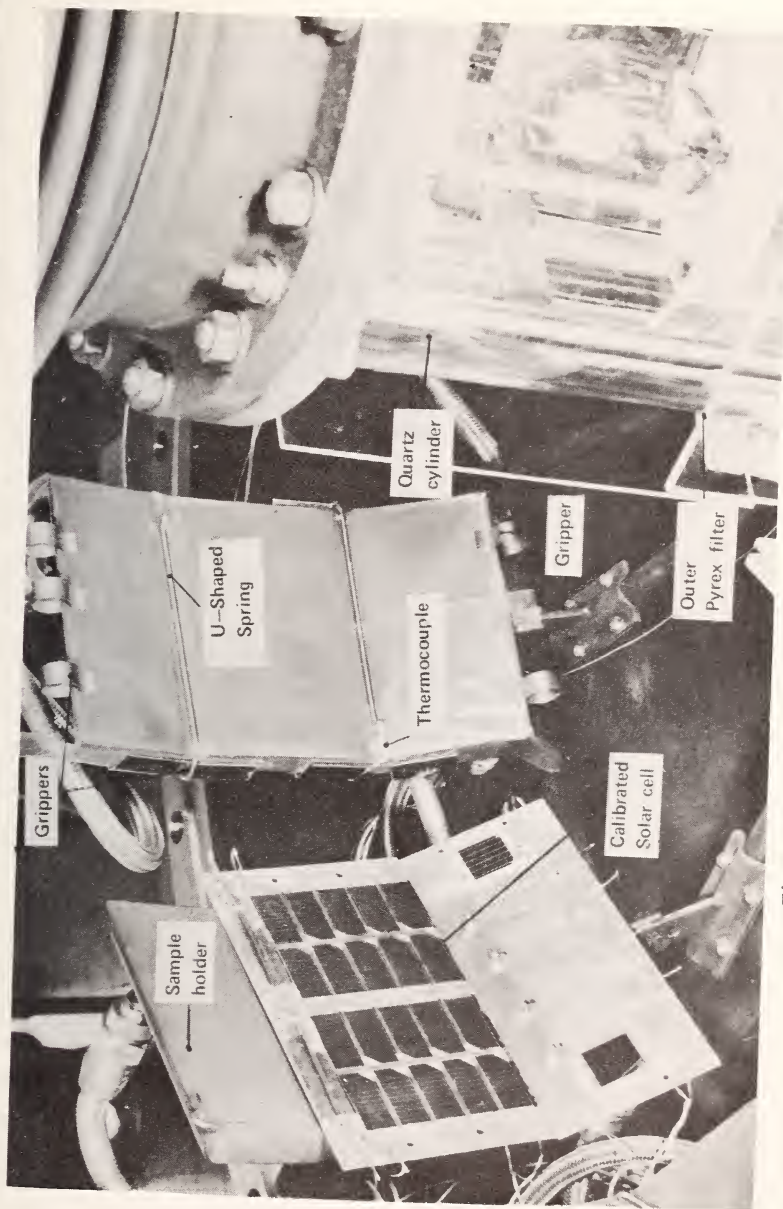


Figure 3 - Sample Positioning

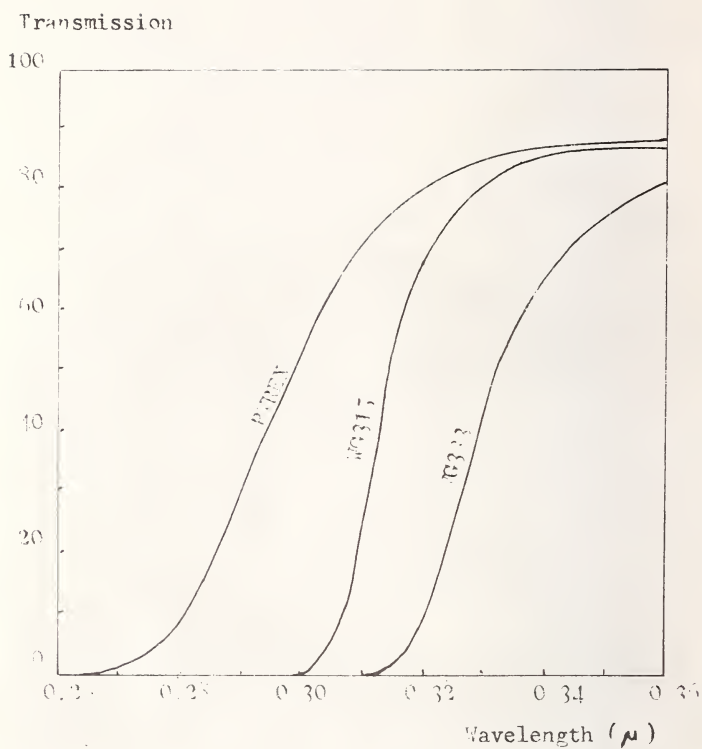


Figure 4 - Spectral transmission plots of sharp cut filters

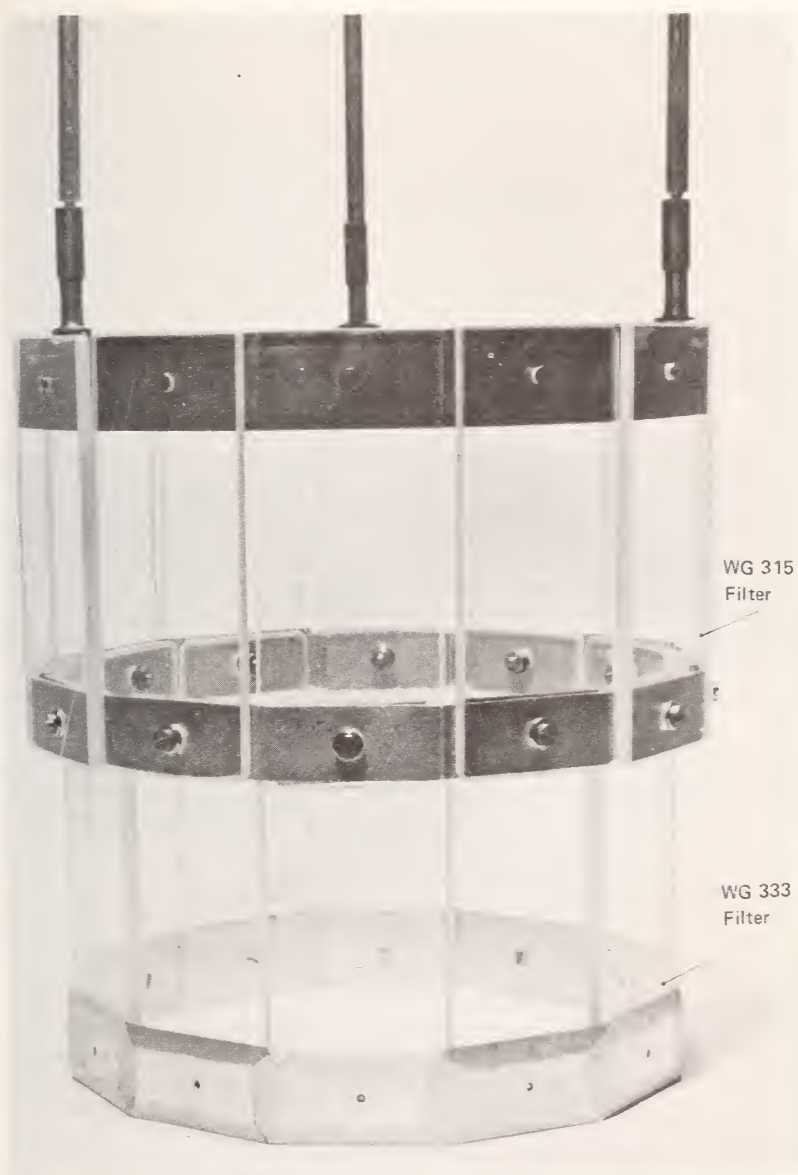


Figure 5 - Polygonal support of mobile filters

ANALYSIS OF THE SIMULATION OF THE SOLAR WIND²

D. E. Zuccaro¹

REFERENCE: Zuccaro, D. E., "Analysis of the Simulation of the Solar Wind," ASTM/IES/AIAA Space Simulation Conference, 14-16 September 1970.

ABSTRACT: This analysis surveys the properties of the solar wind, establishes a set of requirements for solar wind simulation, and develops a conceptual design of a simulator system. The significant features of the design are the following. The protons are formed in an r-f excited plasma discharge ion source. A 20° deflection magnetic mass separator is used to purify the proton beam of other ions, energetic charge exchange neutrals, and Lyman alpha photons. The use of a small diameter beam permits differential pumping of the ion source and the sample chamber. The proton beam either can be expanded to flood the sample, or it can be scanned over the sample.

KEY WORDS: solar wind, charge exchange, charge neutralization, sputtering, proton sources, mass separators, ion optics, ultra-high vacuum systems.

I. INTRODUCTION

The development of spacecraft thermal control coatings requires the laboratory evaluation of the coating's resistance to damage induced by solar photon and particulate radiation. As the characteristics of the solar wind (or solar particulate radiation) have been determined rather recently, various types of simulators, which had different operating and performance characteristics, were fabricated. The Hughes Research Labora-

¹Ion Device Physics Dept., Hughes Research Laboratories, Malibu, California.

²This work was performed under Contract NAS 2-5585.

tories has performed a study of the simulation of the solar wind for the Ames Research Center of the National Aeronautics and Space Administration. The goals of this program were to survey the properties of the solar wind, to establish the requirements for a solar wind simulator, to analyze the techniques and apparatus to be used in the system, and to establish an optimized system and its operating techniques.

This publication is one of a pair that report the results of this study. The companion paper by King⁽¹⁾ analyzes the ion sources, mass separators, and ion optics systems needed to form a proton beam that uniformly irradiates a 10 cm diameter sample. This paper will survey the solar wind properties, the simulator requirements and, using the results of King's analysis, establish a conceptual optimized simulation system.

II. SOLAR WIND COMPOSITION

The particle environments in space that are of principal interest to the designers of spacecraft are the solar wind and the radiation that exists at synchronous orbit. The latter has been summarized in an extensive survey by Stanley and Ryan.⁽²⁾ The properties of the solar wind, which have been measured by a number of satellite probes, will be summarized in this section of this paper.

The solar wind is the term applied to the streaming plasma that is evolved from the sun. Because the energy of the particles is much greater than that which can be associated with the corona temperatures, it is believed to result from a supersonic expansion of the corona's charged particles coupled to the sun's magnetic field. The plasma is neutral, having an equal number of positive charges and electrons per unit volume. The ions and electrons have much different velocities.

The most abundant type of ion is the hydrogen ion, H^+ (i.e., a proton). The second most abundant type is the doubly charged helium ion, He^{2+} (i.e., an alpha particle). The He^{2+} to H^+ ratio (η_α/η_p) has been measured by the Vela 3A and 3B satellites.⁽³⁾ During a two year period, the ratio varied over the range of 1 to 8%, with an average value of 3.7%. The variation is believed to reflect time changes in the plasma composition. During periods of solar activity, i.e., solar flares, the plasma contains a much greater He^{2+} content. In a recent class 3B flare, an η_α/η_p ratio of 0.22 was observed.⁽⁴⁾ Under this condition nearly half the charge of the solar wind is carried by the He^{2+} ions.

(1) The numbers in parentheses refer to the list of references appended to this paper.

Although there are spectroscopic data indicating the presence of many other elements in the sun, only multiply charged oxygen ions O^{5+} , O^{6+} , and O^{7+} have been identified⁽⁵⁾ at this time. The heavy ion component could be resolved only under quiet sun conditions. During this period it was about 0.5% (by number ratio) of the proton flux.⁽⁵⁾ Other ions are believed to be present,⁽⁶⁾ but their low relative abundance and the number of ionic states makes it very difficult to identify them by means of energy per charge detectors. The foil collector experiments made during the recent Apollo flights should provide more information about the heavy ion composition of the solar wind.

The solar wind proton energies were first accurately measured by the Mariner 2 satellite⁽⁷⁾ in the final third of 1962. The average of the daily average proton energies for the period was 1325 eV. The 3 hour averages ranged from a low energy of 540 eV (which is associated with quiet sun conditions) to a high energy of 3100 eV. The Vela 2A and 2B satellites made about 13,000 measurements⁽⁸⁾ during a period of minimum solar activity from July 1964 to July 1965. The mean value of the proton energy was 920 eV. The largest number of cases was for a 550 eV particle energy, which is associated with the quiet sun condition that was prevalent throughout most of the period. This distribution of proton energies is shown in Fig. 1.

The energy of the He^{2+} ions was 4 times that of the solar wind protons. The highly charged heavy ions (O^{7+} , O^{6+} , and O^{5+}), which could be resolved only during quiet sun periods,⁽⁵⁾ had energies of about 20 times that of the protons.

The solar wind ion flux is about $2 \times 10^8 \text{ cm}^{-2} \text{ sec}^{-1}$ during quiet sun conditions.⁽⁶⁾ This value is relatively constant, and its variation with solar activity generally less than a factor of 2.

The determination of the solar wind electron properties is difficult because the low energy of the electrons means the spacecraft potential can perturb the measurements and the solar induced photoelectrons can cause erroneous measurements. The most accurate measurements are the recent Vela 4B observations⁽⁹⁾ which showed that electron energy spectrum has a broad maximum in the energy range of 20 to 40 eV.

III. SOLAR WIND SIMULATOR REQUIREMENTS

The requirements for the laboratory simulation of the solar wind are established mainly by the solar wind properties that have been summarized in the previous section. Additional factors such as the duration of the tests, the cost and com-

plexity of the equipment, the need for accelerated testing, and the size and number of samples must be considered.

A. Particle Composition

The most important parameter to be specified is that of the ion composition. All efforts to date to simulate the solar wind have used either proton beams that were purified by mass separation, or mixed (unpurified) ion beams. The latter contain molecular hydrogen ions (H_2^+ and H_3^+) as well as other ions.

Although it is possible to rule out total simulation of the solar ion plasma (H^+ , He^{2+} , O^{7+} , O^{6+} , and O^{5+}) because of the prohibitively expensive and complex apparatus required to produce such a plasma, it is important to note some of the possible effects of these minor constituents. For example, the sputter yield of oxygen ions is 100 times that of protons.⁽¹⁰⁾ Thus, the oxygen ion component would have about the same sputtering effect as the proton component of the solar wind. The interaction of highly charged ions, such as O^{7+} , O^{6+} , and O^{5+} , with the surface results in the formation of x-ray photons or Auger electrons. Both of these can produce secondary ionization in the target. In this case, the effect of the heavy ions is much greater than that of the protons.

Based on the present limitations, simulation of the solar wind is limited to the use of pure proton beams. Nevertheless, one of the first tasks of this optimized simulator will be to determine if the simulation of the minor constituents of the solar plasma is necessary. This could be done with a less complex O^+ or O^{2+} source in combination with an x-ray source.

B. Particle Flux

The simulation of the solar wind requires a proton flux of $2 \times 10^5 \text{ cm}^{-2} \text{ sec}^{-1}$, which corresponds to a ion current density of $3 \times 10^{-11} \text{ A cm}^{-2}$. Because this value is based on satellite data that were obtained during a period of decreasing and minimum solar activity, it may be necessary to modify the value for the period of maximum solar activity. The change should be a small one. A much higher flux level may be required to accelerate the testing rate. This will be particularly true when radiation resistant coatings are developed. At present, accelerated testing of photon (light) induced damage is performed with 5 to 50 equivalent suns, where limitation is the output of the sources and the reciprocity failure of the samples. A proton beam of $2 \times 10^{11} \text{ cm}^{-2} \text{ sec}^{-1}$ (ion current density of $3 \times 10^{-8} \text{ A cm}^{-2}$), which corresponds to a level of 1000 times the normal solar plasma flux, is readily obtained. This is an acceptable design goal as far as the engineering aspects are con-

cerned. The operating limit may be less than 1000 times the normal plasma flux because of reciprocity failure of the sample.

C. Particle Energy

The simulator should be capable of producing a proton beam of uniform energy that can be varied over the range of 500 to 3000 eV, which corresponds to the range of solar proton energies. The mean energy of the solar protons is about 1000 eV.

The simulator also requires an electron emitter which is capable of providing sufficient electron current to the target to neutralize the proton beam charge at any proton beam operating level. Based on observations of the electrons in the solar plasma, these electrons should have energies of about 20 to 40 eV.

D. Beam Purity

A specification for the ion beam purity must take into account the nature of the impurity. For example, the molecular hydrogen ion (H_2^+), which is the major impurity, has chemical and physical effects that are quite similar to those produced by protons. Therefore, the effect of the molecular ions should scale approximately as does its concentration. A heavy ion, such as OH^+ , will have a sputter yield over 100 times that of a proton of the same energy. Thus, in this case, a 1% OH^+ concentration will have an effect equal to the 99% proton component.

Another aspect of beam purity that must be specified is the presence of energetic neutrals formed by charge exchange. As the fast neutrals will have the same mass effects on the surface as ions, and because they are not registered as a current and are therefore not included in the dose measurements, it is essential that the number of charge exchange neutrals not exceed 1% of the proton flux. This factor is an important element in the selection of the mass separator system.

The beam purity requirement should specify a limit for energetic photons (Lyman α radiation) that are produced in the ion source. These photons, which are due to the excitation of hydrogen by electron bombardment, have energies of 10 to 13 eV. They can cause a very marked effect on the degradation of thermal control coatings.(11) The production of photons is negligible in the low pressure electron bombardment ion sources and pronounced in the plasma type ion sources. This factor is considered in the selection of the mass separator.

E. System Requirements

The specification of the operating pressure of the system must be set in terms of the partial pressures of the residual gases that can be present in the system. This is important because gases containing oxygen are known to cause bleaching of some of the color centers formed in the degradation of the thermal control coatings. The tolerance limits for these gases must be set to ensure that they will not interfere with the experiments.

Duplication of the vacuum conditions that exist in the interplanetary space (i.e., a random gas with a pressure of the order of 10^{-13} Torr and a directed pressure of the order of 10^{-11} Torr due to streaming from the sun⁽¹²⁾) is unrealistically expensive. However, the results of solar wind simulation performed at 10^{-6} Torr are different from the effects of operating the same coatings in space. Experiments have been performed⁽¹³⁾ that show marked changes in the reflectivity of thermal control coatings that are exposed to 10^{-5} Torr partial pressure of oxygen (after irradiation). This can also be shown by comparing the arrival rate of oxygen at 1×10^{-7} Torr to that at 1×10^{-14} Torr. The former will accumulate on a surface to form a monolayer in about 10 sec, while the later condition will require 3 years to form a monolayer.

The significance of this estimate is that it will be necessary to perform experiments on the irradiation of identical samples under a range of vacuum conditions to determine if the experiments are sensitive to the presence of specific gases. This is a standard procedure when operating an experiment in the presence of additional factors that can influence the results.

Because of the uncertainties in the estimation of residual gas effects on the experiments, the a priori establishment of partial pressure limits is not possible. Instead, it is necessary to set up guidelines which will result in the design of a system that has the capability to operate at pressures below the 5×10^{-7} Torr level. This will permit the establishment of these basic partial pressure parameters. In view of the fact that hydrogen will be the major gas present (due to the operation of the proton source), it is possible to set the total operating pressure limit at 5×10^{-7} Torr and to set, as a design goal, the limit on the total of all other gases at about 1×10^{-8} Torr.

In addition to controlling the sample temperature it is necessary to duplicate the condition that exists in space where none of the radiation from the surface and none of the gas desorbed from the surface is returned to the surface. The 3°K

black body condition of space must be simulated by cryogenic shrouds treated to have a high absorptivity.

Another design requirement is that the simulator system have a continuous operating lifetime that is greater than the test period. This could be of the order of 1000 hours. The reason is that the pressurization of the system to repair a component would cause the loss of the samples due to the bleaching of the irradiation damage. An alternative is to design a system in which the beam-forming components can be isolated from the samples by means of a high vacuum valve. This permits the pressurization of either element while maintaining the rest of the system under vacuum.

The specification of a proton beam area of 10 cm diameter is based on two considerations. This represents about the smallest area which can contain about 6 to 8 samples 2.5 cm diameter, which is the size normally used. This size beam is an upper limit for an expanded single proton beam. Thus, this system makes possible a direct comparison of the continuous beam and the intermittent rastered beam. This is important because larger samples will require the use of a rastered beam to obtain uniform irradiation.

IV. DESIGN ANALYSIS OF A SOLAR WIND SIMULATOR SYSTEM

This solar wind simulator system is based on the preceding discussion of the solar wind characteristics, the solar wind simulator requirements and on King's⁽¹⁾ analysis of the techniques and apparatus for proton beam formation. An outline drawing of the proposed system is shown in Fig. 2. It consists of an r-f excited plasma ion source, the ion optics system (which includes the mass separator), and the sample chamber. The discussion of the components is organized about these three basic elements.

A. Ion Source

King's analysis of proton sources indicated that the r-f ion source and the electron bombardment ion sources are the types best suited for use in a simulator system. The r-f ion source was selected for this design because it is capable of operating at the maximum ion current (1000 times the solar wind ion density) without causing an excessive gas load in the system. The r-f source also has the advantages of a long operating life and a high proton production efficiency.

If the accelerated testing was limited to less than about 50 times the solar wind level, the electron bombardment ion source could be used in the simulator system. This source is

readily adjustable over a wide range of ion currents, and produces ions with a narrow energy spread.

B. Ion Optics System

The beam extraction system is designed so that only the source is at high voltage. The beam is kept small until it reaches the last lens, to reduce aberrations in the lenses and separator and to reduce the size of the components. This also permits the beam to be rastered. The small size of the beam also means that it is possible to separate the source chamber from the main chamber with a small orifice without affecting the beam. Thus, the two chambers may be pumped separately and the large gas load from the source removed without interacting with the target. This system is shown in Fig. 3.

The ion extraction system or ion accelerator focuses the ions from the source into a beam with a divergence angle compatible with the rest of the ion optical system. It is operated in the accel/decel mode to prevent electron backstreaming and to permit adjustment of the beam voltage and thus the proton energy without affecting the field gradient at the surface of the plasma in the source from which the ions are extracted. The single small aperture provides adequate current while still acting as an effective flow impedance to reduce neutral hydrogen efflux from the discharge chamber.

The first or focusing einzel lens focuses the ion beam through the mass separator onto the aperture $\frac{1}{4}$ cm from the exit plane of the magnetic sector. By adjusting the beam size at this aperture, the intensity of the beam which arrives at the target may be adjusted by a factor of 100.

The proton component is separated from the ion beam, which also contains molecular ions, by means of a 20° sector magnetic mass separator. King⁽¹⁾ has shown that this type of mass separator is superior to the $E \times B$, the Bennett r-f field, and the magnetic lens types. It fulfills the two basic requirements - separation of the proton beam from both the charged and uncharged (i.e., photons, charge exchange neutrals) contaminants from the source without seriously defocusing the beam. King has discussed the tradeoff, between adequate separation of charged species and beam defocusing due to energy dispersion, that must be made in choosing the separator angle. The 20° sector separates the protons from the H_2^+ beam by 0.6 cm at the aperture stop located $\frac{1}{4}$ cm downstream of the exit plane of the separator. The increase in diameter of the 1 mm diameter, 1000 V beam due to a 50 eV energy spread when passing through this 20° separator is less than 0.5 mm. Thus, a 2 mm aperture will pass all of the proton beam and block other charged species. This separator will nominally operate at a magnetic

field of 300 gauss and consume less than 200 W. It should not require water cooling. The final design of such a separator that is to be actually constructed should involve careful consideration of the shape of the magnet pole entrance and exit surfaces and of the magnetic gap itself, in order to minimize aberrations.

This 2 mm diameter aperture also serves to limit the flow of neutral gas molecules into the chamber. It is thus possible to differentially pump the gas that is released by the ion source and thus maintain the sample chamber at a better vacuum.

The second einzel lens controls the size of the beam at the target. It is capable of expanding the beam that passes through the aperture to 10 cm diameter at the target plane or maintaining the beam size at 0.1 cm so that it may be rastered.

As shown in the insert in Fig. 2, a set of deflection plates may be inserted between the second lens and the target to raster the beam.

The above four elements will provide a 10 cm diameter beam at the target in which no proton trajectory has an angle of more than 3° with respect to the normal from the target plane.

C. Sample Chamber

The proton beam then passes through an all-metal high vacuum valve that serves to isolate the proton beam forming part of the simulator system from the sample chamber. This serves two functions:

1. to permit the samples to remain under vacuum in the event it is necessary to pressurize the ion source section,
2. to permit the ion source region to remain under vacuum and thus protected from exposure to water vapor during the loading of samples.

The sample chamber shown in Fig. 4 contains the neutralizer; the cryogenic shroud; the sample transfer arms; and the sample mounting plate (which supports the samples); and the proton, electron, and photon detection and measurement apparatus. The neutralizer consists of an electron emitter operating in an accel-decel mode that produces up to 3×10^{-6} A of 30 eV electrons. The cryogenic shroud is liquid nitrogen-cooled and is treated so as to have an absorptivity of 0.95 or larger.

The sample mounting plate is a constant temperature plate to which the samples are mechanically attached. Fluid is cir-

culated from an external reservoir to maintain the plate temperature. The plate is moved in the x-y plane by means of bellows sealed rotary motion drives in order to make possible sample transfer and to scan the proton and photon beams.

The sample transfer operates in the following manner. The plate is positioned above the z-axis transfer arm (see Fig. 4). The arm is extended to engage the sample holder, and the rotary motion then is used to unlock the sample. The sample is carried upward by moving the z-axis transfer arm, and the sample is transferred to the y-axis sample transport arm. The y-axis transfer arm moves the sample into the integrating sphere.

D. Beam Measurement Apparatus

The sample mounting plate also supports the apparatus for determining the flux, energy, and profile of the proton and electron beams and the flux and profile of the photon beam. These detectors, as well as some pressure sensors, are part of the control loop that regulates the operation of the ion source and the neutralizer.

The determination of the flux, energy, and density profile of the proton beam is accomplished by use of a Faraday collector located below the sample mounting plate. The collector should have a length-to-diameter ratio of about $\frac{1}{4}$ to 1 to ensure that the potential within the collector is very small and thus prevents the loss of secondary electrons or ions. Shielding and operation of the collector at a small positive bias may be necessary to prevent errors due to photoelectron currents that can result from the solar photon radiation simulation.

The proton energy is determined by measuring the beam potential as a function of bias potential on the collector. The proton beam energy spread is determined by plotting the first derivative of the beam current as a function of proton beam energy. The proton beam density profile is determined by measuring the beam flux (at a fixed set of operating conditions) at a number of points by moving the mounting plate in the x-y plane. Simultaneous measurement of the proton and electron beams is needed to regulate the operation of both sources, to provide a measurement of the proton dose rate during the run, and to verify the degree of neutralization. This can be accomplished by passing the combined beam (protons and electrons) through an aligned electric and magnetic field. The electrons are swept out by fields to another collector, thus giving an electron and an ion current.

Some of the experimental problems that should be anticipated in the design of the measurement apparatus include both extremely low signal levels and the high noise levels that can

result from the r-f generator used in the ion source, the plasma in the ion source, stray electron currents in the chamber, and photoelectrons. While there is little that can be done about the low signal levels (e.g., signal of the order of 10^{-12} A), there are a number of remedies for the high noise level. The r-f and plasma noise can be reduced by the use of π or T section filters or by the use of ferrite beads. The design of the filters can be obtained from any standard text. Carefully designed shields are the most effective way of preventing the stray electron currents from measurement as part of the signal. Photoelectric currents can be suppressed by operating the collector at a slightly positive bias with respect to the surroundings.

The ion-electron converter^{(14),(15)} can be used for visual check of the beam shape and density variations. This consists of a fine metal mesh mounted near an electron excited phosphor on a plate. The ions strike the mesh, generating secondary electrons that are attracted to the phosphor, which is held at a high positive potential. Use of an electroformed nickel mesh of 400 wires cm^{-1} gives resolution on the order of 25 to 50 μm .

E. Vacuum Pumps

The vacuum pumps shown in Fig. 2 consist of two pairs of sputter ion and titanium sublimation pumps. The combination is necessary because the pumping mechanism for hydrogen in a sputter ion pump is limited to chemical reaction (gettering) with the cathode material.^{(16),(17)} The titanium sublimation pump is added to increase the pumping of the hydrogen (as well as any other chemically reactive gases). The sputter pump must handle the gases that are not gettered by the titanium.

The use of liquid helium cooled cryogenic pumps is not advisable for a system in which the predominant gas load is hydrogen. The reason is that the vapor pressure of hydrogen is of the order of 10^{-6} Torr at a cryopump temperature of the order of 4.5 to 4.2°K.⁽¹⁸⁾ This value is poorer than that which can be obtained from the TSP and ion pump.

V. SUMMARY

The design that has been produced satisfies the requirements for simulation of the solar wind. The most significant features are:

- a. the magnetic mass separator to purify the beam of other ions, energetic charge exchange neutrals, and Lyman alpha photons,
- b. the small ion beam that makes possible differential pumping of the system,
- c. the direct comparison of the expanded versus the scanned beam, and
- d. the isolation valve between the beam forming system and the sample chamber.

VI. REFERENCES

1. H. J. King, "Solar Wind Simulator, to be given at Space Simulation Conference, 14-15 September 1970, Gaithersburg, Maryland.
2. A. G. Stanley and J. L. Ryan, "Charged Particle Radiation Environment in Synchronous Orbit," Technical Report 443, Contract AF 19 (628)-5147, MIT Lincoln Laboratory, 15 May 1968.
3. D. E. Robbins, A. T. Hundhausen and S. J. Bame, J. Geophys. Res. 75 , 1178, (1970).
4. J. Hirshberg, A. Alksne, D. S. Colburn, S. J. Bame, and A. J. Hundhausen, J. Geophys. Res. 75 , 1 (1970).
5. S. J. Bame, A. J. Hundhausen, J. R. Asbridge, and I. B. Strong, Phys. Rev. Letters 20 , 393 (1968).
6. A. J. Hundhausen, Space Sci. Rev. 8 , 690 (1968).
7. M. Neugebauer and C. W. Snyder, J. Geophys. Res. 71 , 4469 (1966).
8. I. B. Strong, J. R. Asbridge, S. J. Bame, and A. J. Hundhausen, in "Zodiacal Light and Interplanetary Medium," J. Winberg, Ed., NASA SP-150, 1967.
9. M. D. Montgomery, A. J. Bame, and A. J. Hundhausen, J. Geophys. Res. 73 , 4999, (1968).
10. F. Grönlund and W. J. Moore, J. Chem. Phys. 31 , 1132 (1959).

11. D. D. Swofford, V. L. Mangold, and S. W. Johnson,
Thermal Design Principles of Spacecraft and Entry Bodies,
J. T. Bevans, Ed. (Academic Press, New York, 1968), p.667.
12. L. A. Nelson, Handbook of Solar Simulation for Thermal
Vacuum Testing, J. S. Griffith, Ed. (Institute for
Environmental Sciences, 1968). p.3-1.
13. J. E. Gilligan and G. A. Zerlant, AIAA Paper No. 69-1025,
AIAA/ASTM/IES 4th Space Simulation Conf., Los Angeles,
8-10, September 1969.
14. G. Kuskevics, J. Appl. Phys. 39, 4076 (1968).
15. D. M. Jamba and O. Husmann, J. Appl. Phys. 38, 2630
(1967).
16. S. L. Rutherford and R. L. Jepsen, Rev. Sci. Instr. 32,
1144 (1961).
17. S. L. Rutherford, S. L. Mercer, and R. L. Jepsen,
1960 Seventh National Symposium on Vacuum (Pergamon
Press, New York, 1961).
18. E. S. Borovik, S. F. Grishin, and Ya. Grishina, Soviet
Phys. Tech. Phys. 5, 505 (1960).

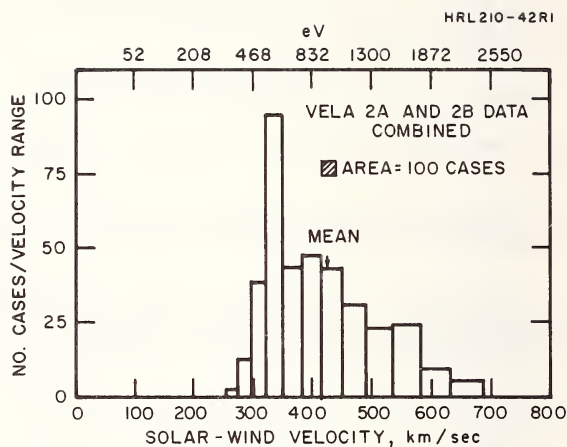


Fig. 1. Distribution of solar-wind ion energy and velocity from July 1964 to July 1965 (from ref. 8).

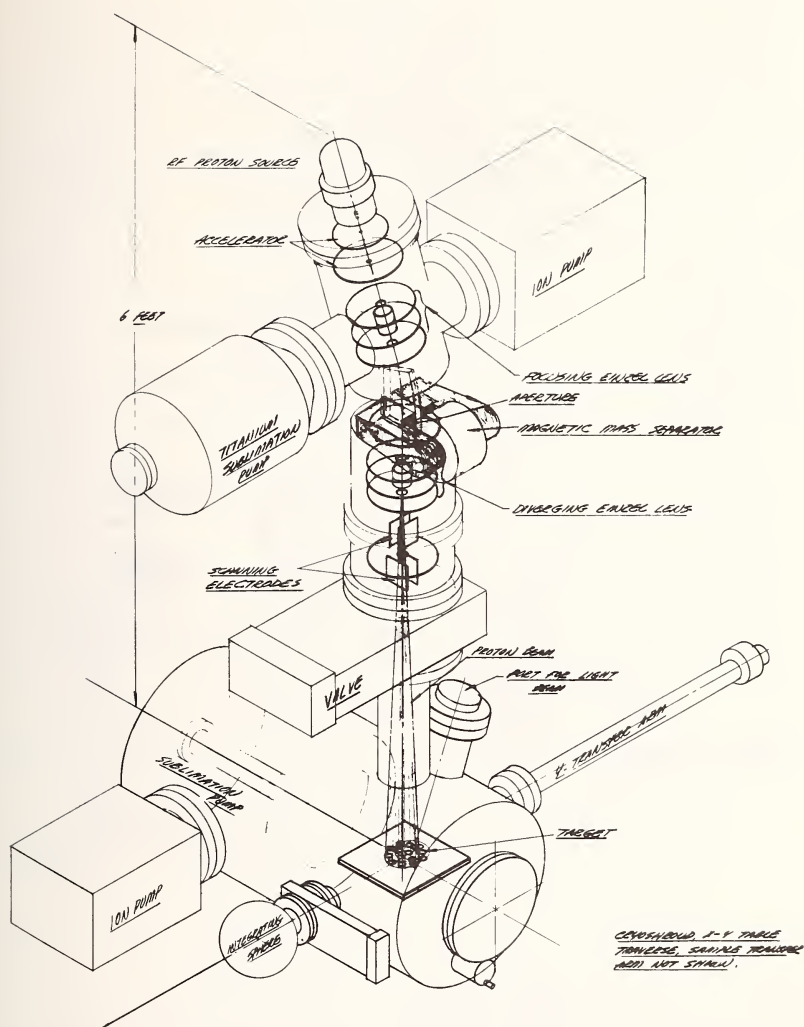


Fig. 2. Solar wind simulator system.

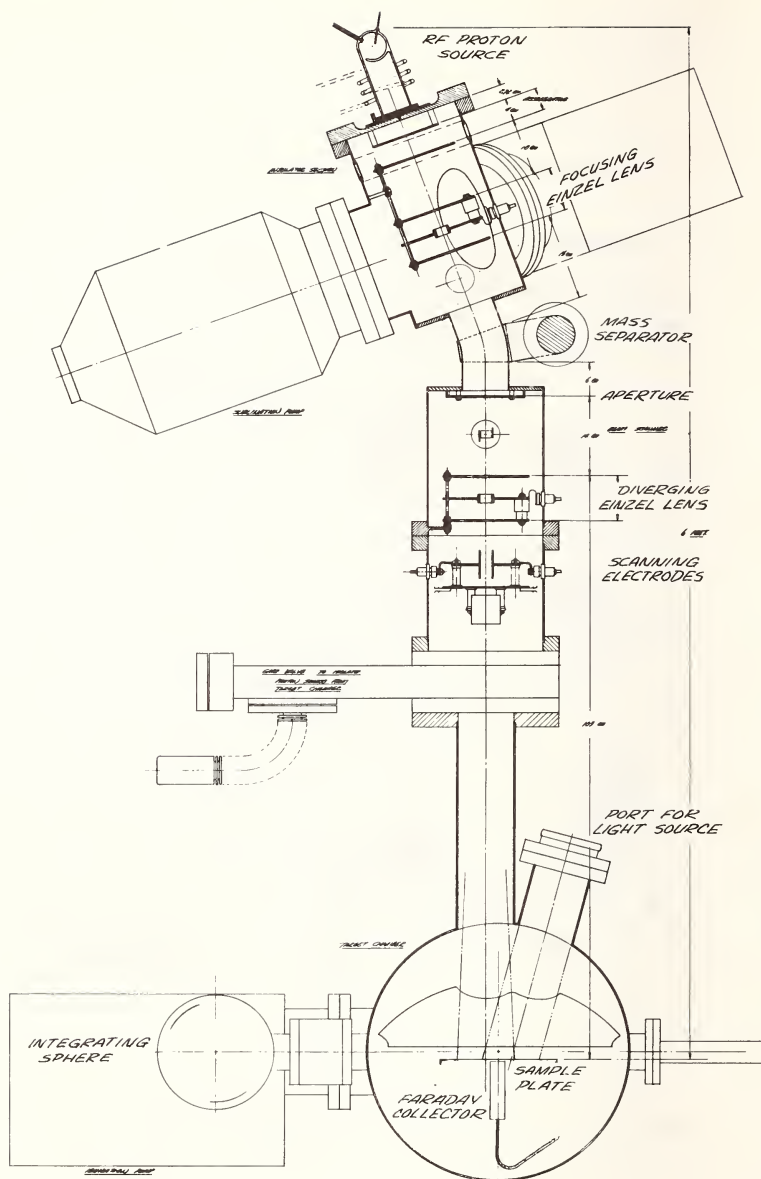


Fig. 3. Layout of solar wind simulator.

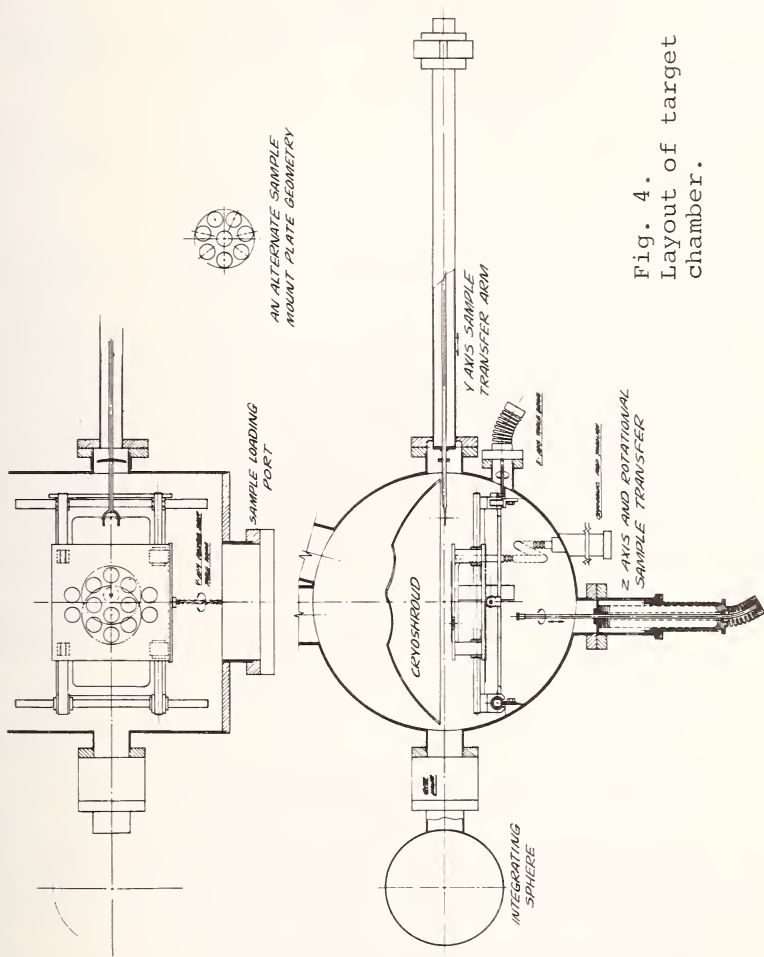


Fig. 4.
Layout of target chamber.

SOLAR WIND SIMULATOR²

H. J. King¹

REFERENCE: King, H. J., "Solar Wind Simulator," ASTM/IES/AIAA Space Simulation Conference, 14-16 September 1970.

ABSTRACT: It is necessary to expose samples of thermal control coating materials to a proton flux in the laboratory in order to estimate the stability of their reflective and absorptive properties when exposed to the solar wind. The choice of the ion source, mass separator, and beam transport system which make up an experimental apparatus to perform these tests is discussed. A final system design is presented which is capable of irradiating 10 standard samples 2 cm in diameter with a proton beam ranging in energy from 0.5 to 3.0 KeV and in intensity from 1 to 1000 times that of the nominal solar wind.

KEY WORDS: solar wind simulator, proton source, mass separator, ion optics, ion beam deflection

INTRODUCTION

Scientific probes traveling through space encounter several types of particle fluxes. A primary class are those emanating the sun—the so-called solar wind. A companion paper (1)³ describes these particles, their intensity and their relation to the activity cycle on the sun. This paper deals with the design of apparatus to simulate the solar wind in laboratory facilities.

¹Head, Propulsion Technology Section, Hughes Aircraft Research Laboratories, Malibu, California.

²This paper is based on NASA CR 73443 prepared for the Ames Research Center under contract NAS 2-5585. Please see the final report under this contract for a quantitative discussion of the material presented here.

³The numbers in parentheses refer to the list of references appended to this paper.

The solar wind simulator discussed herein is intended to be used for evaluating the synergistic effects of the combined particulate and photon radiation on thermal control coatings. Zuccaro (1) has discussed the basic requirements for apparatus to reliably evaluate these materials and the techniques to perform the experiments. This paper presents the design rationale behind the selection of the major components of the simulator.

SYSTEM DESIGN

The design of the apparatus such as shown in Fig. 1 requires the selection and design of the ion sources, the mass separator, and the beam transport system. The system must be capable of irradiating 10 standard samples 2 cm in diameter with a proton beam ranging in intensity from 1 to 10^3 times that of the nominal solar wind. The nominal solar wind is defined as a pure proton flux of 2×10^8 protons/cm²-sec (3.2×10^{-11} A/cm²) ranging in energy from 0.5 to 3.0 KeV with a nominal mean energy of 1.0 KeV.

A. ION SOURCES

1. Physical Characteristics

The characteristics of the ion source affect all the other major components of the system — the ion optics, the mass separator, and the vacuum station itself. Fortunately, for this study, proton sources have played an important role in nuclear physics for many years, so that a large body of information is available to define and compare the various possible source configurations. Before considering individual ion sources in detail, it is appropriate to interpret the previous section in terms of the conditions which it imposes on the ion source.

Considering the nominal intensity of the solar wind, the desire to accelerate the test time by a factor of 1000, the target size and attenuation in the apparatus, the ion source must generate a proton current of approximately 10^{-5} A. The bulk of the protons in the solar wind range in energy from 0.5 to 3.0 kV. In order to provide the necessary experimental flexibility, the apparatus must be designed so that the proton energy is variable, at least over this range. While it is well within the capability of the designer to make the instantaneous ion energy a variable, this should not be confused with the virtually impossible task of providing an ion beam which contains a controllable mixture of all ion energies at a given time. Fortunately, the latter is not required for an accurate simulation of solar wind.

A related characteristic is the energy spectrum of the ions inside the ion source. This energy spread appears as an uncertainty in the final proton energy at the target. While this may not be detrimental to the experiment itself, it does impose severe limitations on the design of the ion beam transport and separation systems. Therefore, an ion source with a small energy spread is desirable.

Mass efficiency n_m is used to define the percentage of hydrogen atoms that actually leave the source as protons. A high mass efficiency is desirable to reduce the neutral density in the region immediately downstream of the source. This reduces the creation of charge exchange ions which contaminate the beam. (See Ref. 1)

The useful lifetime of the source is important for an apparatus in which experimental simulation may be conducted in real time. The arbitrary, but realistic, lifetime goal set for this design was 1000 hours (~6 weeks).

The above characteristics provide a scale against which the various sources may be compared. Where possible this comparison is made quantitatively in Table 1.

2. Types of Proton Sources

There are a large number of generic types of ion sources, each with many individual designs, which will produce a proton beam. An excellent review of the basic types was presented by Hoyaux and Dujardin (2). All of these sources dissociate and ionize the hydrogen by electron bombardment. They differ radically in power requirements and general operating conditions. Of particular interest for this application are two requirements mentioned earlier; namely, a minimum kinetic ion energy spread in the source and the ability to vary the source output current intensity over a wide range to accommodate the required flux variations.

a. Radio Frequency Ion Sources (See Ref. 3)

The radio frequency ion source, sometimes called an electrodeless discharge source, has been a standard for many years in high voltage particle accelerators used for nuclear physics experiments. RF power is coupled into a quartz (or other insulating material) tube containing hydrogen gas at a pressure ranging from 10 to 100 μm of mercury. The mean free path of an electron in the source is on the order of 1 cm. Thus, electrons will be accelerated by the imposed electromagnetic field and will, under the proper conditions, generate a stable plasma from which an ion beam may be extracted.

The most common method of coupling rf power into the discharge is to place the discharge chamber inside a solenoid which is activated with rf power at approximately 10 MHz. The alternating magnetic field generated in the discharge chamber accelerates the electrons. Generally, the induced electric fields are relatively small here and the circulating currents rather large. Energy spreads ranging upward from 20 eV have typically been reported (4, 5) for this device. Quite frequently an axial magnetic field is used to increase the electron path length and to improve stability.

Beam currents up to 1 mA are typically reported for this type of source. Proton fractions up to 90% of the total ion current in the beam have been observed under optimum conditions; 50 to 70% is common for well designed sources. Hydrogen consumption varies according to source design but is typically of the order of $4 \text{ cm}^3/\text{hour}$ at STP for 1 mA of output beam. It may not be possible to scale down the gas flow directly with beam current. Operating frequency varies as well, ranging from 1 to 400 MHz; 10 MHz is common and rf power requirements are a few hundred watts. Source lifetimes of 1000 hours at the current levels required for this application are reported (6).

Of the various sources surveyed, the electromagnetic rf ion source most nearly meets all the requirements. It fully meets the beam requirements and is adequate in terms of mass efficiency and proton yield. If this type of source is to be designed or adapted to this application, care should be taken to assure stable operation over long periods by choosing high quality materials for its construction and designing both the power supplies and the hydrogen feed system with stability as a primary consideration.

b. Electron Bombardment Sources

As the name implies, electron bombardment sources ionize by direct impact of electrons on the hydrogen molecule or atom. The distinction here is that in contrast to other types of sources conditions are such that no plasma is created nor is any arc or discharge struck. While several designs are possible only the low voltage source is of interest here. Typical of the type most useful for the purpose at hand is that described by Redhead (7). Hydrogen gas is introduced into the ionization region where it is bombarded by electrons with the resulting production of protons. An axial magnetic field significantly increases the electron path length and hence the source efficiency. The electrons may be axially restrained by holding both ends of the discharge chamber at cathode potential, thus making it energetically impossible for electrons to reach them after any energy loss. Redhead has reported that this type of source is capable of trapping ions in the source for

periods as long as 1 sec. This is desirable in a proton source because when a proton collides with the metal wall of the source, it is re-emitted as part of a hydrogen molecule and must be both dissociated and ionized again to be useful.

This type of ion source has several advantages. Primary among these is that it fulfills the two desirable criteria mentioned earlier. It is adjustable in current over several orders of magnitude and produces ions with a relatively small energy spread, ranging down to less than 1 eV for specially designed sources⁽⁸⁾. The primary difficulty with this type of ion source is that the mass efficiency is of the order of 1% or less. Thus, it presents a large gas load to the system when operating at high output currents. A second, and less important, disadvantage is that the source requires a thermionic cathode, which is subject to contamination and has a finite lifetime.

A simple source of this type is in use at Hughes Aircraft Company⁽⁹⁾. It is capable of producing a proton current equivalent to 2000 times the nominal solar wind value over a 2.5 cm diameter circle. Input power is about 20 W. The entire vacuum station, including the source chamber and the integrating sphere, is pumped by a single 400 liter/sec ion pump. A single feedback loop that monitors the emitted ion beam current and adjusts the cathode emission to compensate for drift in line voltage or hydrogen flowrate serves to stabilize the beam for periods of several days.

c. Other Proton Sources

All other ion sources investigated were considered unsuitable for this application for a variety of reasons. These types included the high voltage and crossed field electron bombardment sources mentioned above, gas discharge sources such as the Penning or Finkelstein source, the duoplasmatron and the capillary arc. The reasons for this selection have been discussed in detail in the final report from which this paper was taken⁽¹⁰⁾ and are summarized in Table 1.

3. Ion Extraction Systems

The foregoing sections have discussed a number of proton sources. To be useful, these protons must be extracted from the source and focused into a beam. The ion extraction system which accomplishes this forms a critical interface between the source and the ion transport system which controls the beam shape en route to the target.

The theory of charged particle focusing has been investigated extensively in the development of electron guns used for many purposes. Because the focal properties of electrostatic

lenses are independent of particle mass, the theories derived for electrons are equally valid for protons. The principal difference is that the currents that may be carried with a given set of lenses and accelerating voltages are much less for protons than for electrons because the particle velocities for a given accelerating voltage vary inversely as the square root of the mass

The simple, but important, concept of operating the extraction system in an accel : decel mode is often overlooked by those designing ion transport systems. The ions are extracted with a total voltage greater than the desired beam voltage and then decelerated. This accomplishes two things. First, it prevents electrons from the beam or target from entering the source and damaging components or disturbing the control system which often operates on total emitted current. Second, it separates the extraction voltage from the beam voltage and permits a higher beam current to be extracted than would be possible at the beam voltage alone. It also permits adjustment of the beam voltage without disturbing the position of the plasma sheath because the total voltage may be held constant as the ion beam voltage is varied.

B. MASS SEPARATORS

All of the ion sources discussed above produce an ion beam output which is a mixture of protons, H_2^+ , H_3^+ , and many other ions. The sources may also produce a high flux of fast neutral particles by charge exchange and a number of ultraviolet photons which can degrade the test sample. The photons can create photo electrons if they are allowed to strike the target or the Faraday cup which monitors the beam. The mass separator, which is located between the proton source and the target, must purify the beam which passes through it so that only the protons will strike the target.

The physical separation of the protons from the rest of the beam can be accomplished in two basically different manners. An appreciation of the two concepts plays an important role in choosing the most desirable type of mass separator. All ion sources produce a mixture of protons, other positive ions, fast and slow neutral particles, photons from the discharge within the source and sputtered material from the ion extraction system or focusing lenses. The first method is to design a separator which selects only the protons from this beam. The trajectories of the protons are controlled so that they alone reach the target, which is shielded from the source so that none of the contaminants may reach it by line of sight. The magnetic sector magnet is an example of such a device. The second system concept is to provide a series of filters to prevent the unwanted particles from reaching the target while

permitting the desirable proton beam to pass. The difficulty here is first to identify all of the contaminants which may exist in the beam and then to devise filters which will selectively stop the contaminants but transmit the protons. This is particularly difficult in the case of photons and fast neutrals. The rf separator is an example of this type of system. As will be shown, a separator which deflects the proton beam is clearly superior for this application.

1. Physical Characteristics

The various separators were compared on the basis of their ability to produce a pure proton beam; transmit a large fraction of the incident photons; provide a continuous rather than pulsed beam; introduce minimum aberrations into the ion beam transport system; provide continuous, stable operation; accommodate a full range of ion velocities; and their ease of design and use.

2. Types of Mass Separators

Three general types of mass separators were considered:

- Radio Frequency - which utilizes resonance between particle inertia and an alternating electromagnetic field.
- Homogeneous Magnetic Field - in which the ions of different mass are spatially separated due to their different radius of curvature in a magnetic field.
- Crossed Field or $E \times B$ - where perpendicular static electric and magnetic fields cause different trajectories for different masses.

a. Radio Frequency

The basic concept of a linear rf mass spectrometer was first described by Bennett.⁽¹¹⁾ The operation had been analyzed by a number of authors, particularly Redhead and Crowell⁽¹⁷⁾, who list all the critical performance parameters for both sinusoidal and square wave operation.

The experimental performance for a system of this design has been reported recently (Ref. 13). This device has 13 grids, three rf stages, and two drift spaces. The complete system is 25 cm long and operates at 10 MHz. Assuming that each grid is 95% transparent but that the individual wires are randomly oriented with respect to those of the other grids, approximately 50% of the particles from the source will impinge on the grids. While the beam may be purified by this device to greater than

95% , it can be accomplished only at the expense of reducing the transmission to less than 10% . This in itself may be quite tolerable if a source with a sufficiently high output current is used. The difficulty arises because the photon output from the source and the beam of fast charge exchange neutrals created at the source aperture are not attenuated by the electric fields. Thus they are increased in relation to the proton beam by at least an order of magnitude using this type of separator. The effects of these contaminants may thus easily be greater than those of the proton beam for many operating conditions. A further complication is that the impurity beam may not be uniform over the target area and may be very difficult to measure accurately.

Therefore, even though this system has many advantages in terms of minimum energy dispersion, astigmatism, cost, and size, it is suggested that serious consideration be given to the problem of beam contamination before it can be used for any simulation.

b. Homogeneous Magnetic Field

This is a "conventional" type of mass separator which operates on the principle that the trajectory of a charged particle will be deflected by a magnetic field. A great deal of developmental work devoted to understanding and improving this type of mass spectrometer has been reviewed by Inghram and Hayden (14).

Of Primary importance to the overall system performance are two parameters of the separator design. The first is the angle through which the beam of interest (protons) is deflected. It is directly related to the strength of the magnetic field and the path length in the field. The second factor is the dispersion of the various masses at the target. In order to preserve the minimum beam size, the dispersion through the separator should be minimized. This may be done by establishing the minimum sector angle for the separator which will spatially separate the proton beam from the H_2^+ beam.

The magnetic sector mass separator is well suited for this task, provided that the beam is kept small in diameter until after separation and then expanded to cover the target area. The power requirements increase rapidly as the beam size increases, because of the resultant increase in magnetic gap. The magnetic fringing fields also become very difficult to adjust at large gap spacings, thus introducing unwanted aberrations in the final beam. This type of separator accomplishes the two necessary functions of bending the proton beam to physically remove it from the efflux of photons and neutrals from the ion source (which travel line of sight), and of dispersing the charge particles of various masses so that a pure

proton beam results. Care must be taken in the design to reduce the ion optical aberrations and to minimize the dispersion due to the energy distribution in the ion source.

c. Crossed Field or ExB

In a crossed field separator, the magnetic field B , the electric field E , and the velocity of a charged particle are all mutually perpendicular. If the signs are properly chosen, it is clear that by adjusting the magnitudes of the electric and magnetic field strengths the electric and magnetic forces on the particle may be made equal and opposite and the particle trajectory will be unchanged. Particles with the same kinetic energies but a different mass will follow a curved trajectory. The properties of this type of separator have been discussed by Bleakney and Hipple (15). The simplified analysis of Wahlin (16) is recommended as clearly illustrating the important processes. This type of separator will serve equally as well as the simple magnetic sector in many cases. The extra variable of the electric field strength provides the opportunity to design the system to achieve first order focusing.

3. Selection of the Mass Separator

The properties of the three types of mass separators discussed above are summarized in Table 2. Of the three, only the rf separator is clearly rejected because it does not prevent uncharged particles and photons from striking the target. The remaining two—the sector and crossed field separators—are similar in many respects. The crossed field separator contains aberrations from nonuniformities in both the electric and magnetic fields, while only a magnetic field is present in the sector. In particular, it is difficult to generate a uniform electric field when the magnetic and electric pole pieces of the crossed field separator must of necessity be in close proximity. This problem has recently been solved analytically and appears manageable for low energy applications such as that required for the present program.

The sector magnet was chosen over the crossed field device for the system design here, principally because it requires one less power supply and is a well understood, proven device. Techniques have been derived to produce very sophisticated instruments of this type, if they are required. Special attention should be devoted to the defocusing of the beam due to energy dispersion in the source. Careful design of both source and separator can keep this well within tolerable limits.

C. BEAM TRANSPORT SYSTEM

1. Introduction

The beam transport system must accept the ion beam from the source, focus it through the mass separator, and expand it to 10 cm diameter at the target plane. It must also be capable of providing adjustment of beam intensity by a factor of 1000. Finally, it must perform satisfactorily over the full range of proton energies from 0.5 to 3.0 kV. Two general concepts are possible. The first is to extract from the source a small, relatively high current density beam which is expanded in size only after it has passed through the mass separator. This considerably simplifies the design of the einzel lens, because all the beam ions pass through the lens near the axis where aberrations are small and the paraxial ray equation is valid. The mass separator is simplified as well because the magnet gap widths can be minimized. The single small aperture in the source serves to minimize the effluent hydrogen gas and the pumping speed necessary to maintain satisfactory chamber pressure. Finally, the small beam permits a series of apertures to be installed between the source and the main vacuum chamber, to reduce the diffusion of hydrogen from the source into the chamber. A separate pump is provided near the source.

The second approach is to extract a large beam from the source and transport this broad beam through the mass separator to the target. This virtually eliminates the need for an ion optical system, but entails a number of other difficulties which are obvious from the preceding paragraph. The only mass separator which readily accommodates a broad beam is the rf separator, although large aperture crossed field and even magnetic sector separators are possible at the low beam energies used here. Only the first type of system (i. e., small beam) will be treated here.

2. Computer Simulation of Ion Trajectories

As the name implies, each element in the ion optical system may be treated mathematically by techniques used in conventional geometrical optics. For instance, the einzel lenses have an equivalent thick lens analogy, and a sector magnet is equivalent to a cylindrical lens bounded on the entrance and exit sides by thin lenses. The focal properties of the lenses are a complicated function of the geometry, beam voltage, and lens voltage for each.

It has been shown (17) that where the paraxial ray equation is applicable, this problem may be readily treated by a matrix technique which is easily adaptable to computer calculation. Assuming circular symmetry, the trajectory of a particle may

be defined at any time by its radial distance and radial momentum and represented by a column vector. The effect of each ion optical element on the trajectory is represented by a two-by-two matrix so that the total transfer matrix for the entire system is thus a product of n matrices, where n is the number of ion optical elements in the system. It is clear that this formulation is suitable for computer calculation.

Only electrostatic lenses are considered here because they consume no power and are independent of the mass of the particle being focused. The most versatile type is the einzel lens which is composed of three apertures, or cylinders. The two end elements are connected together electrically so that the beam leaves the lens with the same kinetic energy with which it entered. The central element is biased to retard the beam (i.e., biased positively for positive ions). The focal length of the lens is a direct function of the ratio of the voltage on this central element to the beam voltage. While such lenses are simple in concept, they introduce sizable aberrations if the beam is not kept small relative to the lens aperture.

Three einzel lenses are used in the beam transport system for focusing purposes. The first, in conjunction with the weak focusing properties of the mass separator, focuses the beam through the aperture following the mass separator. This aperture also provides the pressure differential needed between the target and source chambers. The second lens produces a magnified image of the aperture, resulting in a 10 cm diameter image at the target. The third lens (optional) provides the slight collimation needed to produce an exactly parallel beam at the target. Without this last einzel lens the long "throw" of the second einzel produces a landing angle of $\tan^{-1} (5/100) \approx 2.7$ deg.

Because of the large number of elements in the system, the operation of the beam transport system is too complex to describe quantitatively here. Interested readers are referred to the final report on NASA Contract NAS 2-5585 (10) for a detailed description.

The total system must be able to change the target current by three orders of magnitude. Because it is not possible to operate the rf source over such a wide dynamic range, it is necessary that the beam transport system provide approximately a factor of 100 intensity variation, which together with a variation of source current by a factor of 10 provides the total dynamic range required. The source current will be varied by changing the neutral H_2 flow and/or the rf excitation power. The variation provided by the beam transport system is accomplished by flooding an aperture and allowing only a small fraction of the current to pass through the aperture by changing the

first einzel focusing voltage. This means the beam size at the aperture may be varied from a radius of less than 0.1 cm to greater than 1.1 cm by the first einzel. This is about the maximum intensity ratio possible with this method because the image size at the target is limited by the maximum magnification (minimum focal length) of the lens.

3. Beam Rastering System

The system illustrated in Fig. 2 is based on the requirement that the simulation requires a large dc proton beam which covers all of the target area uniformly. It has been estimated (10) that the simulation would not be impaired if the protons arrived at the target as a series of discrete pulses at rf frequencies. If it can be demonstrated experimentally that this is indeed true, a system employing a small diameter proton beam which is swept over the target surface is a pattern similar to the electron beam in a TV raster has many advantages. The system shown in Fig. 2 is easily converted to this design by changing the operating voltage of diverging einzel lens No. 2 to focus the beam to a spot on the target and introducing two pairs of orthogonal electrostatic deflecting plates in place of optional collimating einzel lens No. 3.

The advantages of a rastered system are

1. By sweeping a small beam over the large target area, the beam nonuniformities are smeared out and the coverage may be made as uniform as desired, even if some lens aberrations exist.
2. By programming the rate at which the beam is swept, the dose rate to each individual sample may be controlled (as a function of exposure time if desired).
3. The dose rate may be attenuated over several orders of magnitude while the source operates at the single fixed point where it performs best. This is achieved by deflecting the small beam off the target area entirely for some fraction of each raster period. This not only extends the operating range of the system, but simplifies the design of the ion source and its control system.
4. The accuracy of the dose measurement is improved by this technique because the total proton beam (which may be measured accurately) is projected onto each area of the target for a time, which also can be measured accurately. The result is a far more accurate measure of dose than sampling a small fraction of the beam and relying on a prior measurement of beam homogeneity.

It is also much easier to design a dynamic control system for this system than for one that samples a fraction ($\sim 1\%$) of the beam current (i.e., $\sim 10^{-11}$ A).

D. CONCLUSIONS

The discussion in the preceding section illustrates that a system of the general design shown in Fig. 1 can indeed be designed and that the requirements on each of the various components required is within the current state of the art. The most critical area requiring experimental verification and possibly further development is the design of the ion extraction system which draws protons from the source and focuses them into a parallel, laminar flow beam. This interface between proton source and the rest of the system is the key to successfully producing a beam of uniform current density at the target.

Two important design principles were formulated as a result of this study. The first is that the proton beam should be bent during its traversal of the system so that it is possible to completely shield the target from photons, fast neutrals and possibly sputtered material that are inadvertently produced by the source. The second design philosophy is that if it does not reduce the experimental accuracy it is more desirable from a system designer's viewpoint to irradiate the target with a small beam which is rastered over the surface than with a broad, uniform dilute beam.

References

1. Zuccaro, D. E., companion paper this conference.
2. Hoyaux, M. and Dujardin, L, *Nucleonics*, 4, 7; 4, 12; 5, 67 (1949).
3. Blanc, D. and Deghilh, A., *J. Phys. Radium* 22, 230 (1961).
4. Hall, R. N., *Rev. Sci. Instr.* 19, 905 (1948).
5. Thoneman, P. C., Moffatt, J., Roaf, D., and Sanders, J. H., *Proc. Roy. Soc.* 61, 483 (1948).
6. ORTEC Model 320 RF Ion Source Data Sheet.
7. Redhead, P. A., *Can. J. Phys.* 45, 1790 (1967).
8. Dworetzky, S. Novick, R. Smith, W. W. and Tolk, N., *Rev. Sci. Instr.* 39, 1721 (1968).
9. Constructed by H. J. King and D. E. Schnelker; unpublished.
10. Solar Wind Simulation Techniques Final Report Contract NAS 2-5585 HRL Staff (1970).

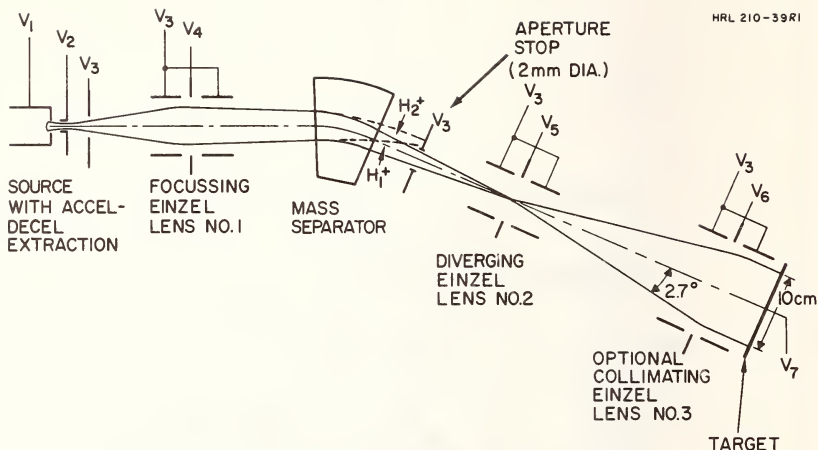
11. Bennett, W. H., J. Appl. Phys. 21, 143 (1950).
12. Redhead, P. A. and Crowell, C. R., J. Appl. Phys. 24, 331 (1953).
13. Lebduska, R. and Meckel, B., "Solar Wind Simulator and Advanced Design with Extended Operational Capabilities," AIAA Paper No. 70-31, January 1970.
14. Inghram, M. G. and Hayden, R. D., Handbook on Mass Spectroscopy (Nuclear Science Series, National Academy of Science, Washington, D.C., 1954), No. 14.
15. Bleakney, W. and Hipple, J., Phys. Rev. 53, 521 (1938).
16. Wahlin, L., Nucl. Instr. Methods 27, 55 (1967).
17. Cotte, M., Ann. Phys. (Paris) 10, 333 (1938).

Table 1--Ion Sources

Type of Source		Advantages	Disadvantages
Radio Frequency	Electromagnetic	Long life and high percent of protons	Narrow beam current range
	Electrostatic	Low operating pressure and beam current	Wide energy spread
Electron Bombardment	Low Voltage	Wide range of beam current	Low mass utilization
	High Voltage (Canal Ray)		High power and large energy spread
	Crossed Beam	Low energy spread and wide range of beam current	Low beam current
Gas Discharge	Capillary Arc	Monoenergetic	Short life, complicated electronics, hard to stabilize
	C crossed Field (H x B)	High Density	Current too high
		Low Density	Trade m_{mass} for proton yeild, cathode life, or energy spread

Table 2---Mass Separators

Type	Advantages	Disadvantages
Radio Frequency	<ul style="list-style-type: none"> • Handles large beam • Small size • Low total power • Easy intensity adjustment 	<ul style="list-style-type: none"> • $< 100\%$ purity • Low transmission of protons • Transmits fast charge exchange neutrals • Must trade beam purity for transmission • Photons from source strike target
Homogeneous Magnetic Field	<ul style="list-style-type: none"> • Pure beam • High transmission • Compatible with scanned beam 	<ul style="list-style-type: none"> • High power for large beam • Energy dispersion
Crossed Field or ExB	<ul style="list-style-type: none"> • Pure beam • Will take large beam 	<ul style="list-style-type: none"> • Two-power supplies • Electric and magnetic aberrations



Proton Energy	V ₁	V ₂	V ₃	V ₄	V ₅	V ₆	V ₇
One Equivalent Sun							
500 V	500	-1250	0	400	465	375	0
1000 V	1000	- 750	0	800	930	750	0
3000 V	3000	- 500	0	2400	2825	2250	0
100 Equivalent Suns ^b							
500 V	500	-1250	0	310	460	375	0
1000 V	1000	- 750	0	605	920	750	0
3000 V	3000	- 500	0	1855	2800	2250	0
^a All voltages measured with respect to ground (target at ground). ^b Source provides additional factor of 10 intensity variation.							

Figure 2--System Schematic

LABORATORY EXPERIMENT ON SOLAR WIND INTERACTION WITH
GEOMAGNETIC FIELD

E.M. Dubinin,¹ G.G. Managadze,¹ I.M. Podgorny¹

It is impossible to reproduce in a laboratory all phenomena which exist at the interaction of the solar wind and the Earth magnetic field. In previous works it was shown that choice of experimental conditions permits one to simulate some of the most interesting effects, for example, the collisionless shock near the Earth magnetosphere. According to the principle of limited simulation, to reproduce the magnetosphere and the collisionless shock the parameters of the artificial solar wind should be:

plasma density - $n = 10^{13} \text{ cm}^{-3}$, electron temperature - $T_e = 15 - 20 \text{ ev}$, embedded magnetic field - $B \sim 40 \text{ Oe}$, ion temperature - $T_i \sim 5 \text{ ev}$, stream velocity - $V = 3 \cdot 10^7 \text{ cm/sec}$.

At these conditions the plasma flux compressed the dipole magnetic field on the day side and formed a configuration of the magnetic field similar to the magnetic field of the Earth tail. Between the artificial magnetosphere and the plasma flow the collisionless shock is displayed. The thickness of the shock is in agreement with plasma theory and has the same order of magnitude in dimensionless expression as in space measurements. In the shock high level magnetic field microfluctuation was discovered. The dimension of the fluctuations is about that of the Larmor radius of ions. The microfluctuations were predicted in plasma theory as a result of Alfvén and magnetosound instability.

In addition to the shock investigations, measurements of the plasma density, velocity and magnetic field strength were carried out before and behind the shock.

KEY WORDS: earth magnetic field, earth tail, magnetosphere, plasma theory, shock wave, solar wind

(Paper not available for publication)

¹Institute for Space Research AN USSR, Moscow, Russia

EFFECT OF PHOTODEGRADATION ON ORGANIC COATINGS

Peter J. Hearst
Naval Civil Engineering Laboratory
Port Hueneme, California 93041

ABSTRACT: Clear and pigmented coating films were irradiated with a mercury arc, a xenon arc, and sunlight. Strips of the free films, consisting chiefly of alkyd, vinyl, and epoxy coatings, were exposed in a quartz chamber. The major volatile product, as determined by infrared spectroscopy, was carbon dioxide, but the products varied depending on the irradiation, the pigmentation, and the type of coating. Internal reflection spectra indicated primarily the formation of carbonyl groups, and the greatest changes were obtained for coatings that did not have high initial carbonyl absorption.

KEY WORDS: Photodegradation, organic coatings, infrared analysis, volatile degradation products, internal reflection spectroscopy, ATR spectroscopy, surface degradation, clear and pigmented films, mercury-arc irradiation, xenon-arc irradiation, atmospheric exposure.

As coatings become more durable, there is an increasing need for better methods of predicting their performance. Much of the deterioration of coatings exposed in the atmosphere is due to the effect of sunlight. Photodegradation of coatings produces volatile products and the formation of these products should be related to coating performance. Because the deterioration - and especially the photodegradation - of coatings occurs primarily at the surface, it should also be possible to relate changes at the surface to coating performance. Internal reflection spectra give infrared absorption data for thin surface layers and should therefore be valuable in following chemical changes at coating surfaces.

Many studies have been made of the volatile decomposition products of polymers, especially under ultraviolet irradiation and at very low pressures. However, comparatively little

attention has been given to the photodegradation of organic coatings in a natural atmospheric environment. The volatile degradation products of linseed oil films exposed to sunlight in an atmosphere of oxygen was studied in 1927, [1]¹ and more recently other studies of the decomposition of oil and alkyd films have been reported. [2,3,4] We have investigated the volatile products from the irradiation of various clear and pigmented organic coating films, [5] and the results are summarized below.

Internal reflection spectroscopy is being used widely to study coatings and polymers, but chiefly to determine the gross composition. Gedemer [6] was the first to use internal reflection spectroscopy to investigate surface changes caused by photodegradation. He studied polycarbonates and found that, except for the formation of one new peak, the chief changes in the spectra were a general weakening of the absorption peaks. In the study of the photodegradation of organic coatings we have found evidence for carbonyl formation and again a general weakening of other absorption peaks.[7] More recently Chan and Hawkins in a study of polyethylene and other plastics have related carbonyl formation, as determined by internal reflection spectra, to the brittleness temperature of irradiated samples.[8]

Experimental Procedure

The coating films consisted primarily of alkyd, vinyl, and epoxy films. Both clear films and films pigmented with titanium dioxide were employed, and the thicknesses of these free films were approximately 40 micrometers.

The films were irradiated with a mercury arc, with a xenon arc, or with natural sunlight. The approximate spectral distribution of these light sources is shown in Figure 1. The relative intensities for each light source are shown but no direct comparison between sources are available.

For the mercury-arc irradiations and most of the xenon-arc irradiations, the coating films were placed in an exposure chamber whose sides were made of quartz to allow the transmission of the irradiating ultraviolet and visible light, and whose ends were made of Irtran windows so that the chamber could be used as a cell in a infrared spectrophotometer for the identification of the volatile products. The cell was filled with air at 50 percent relative humidity at 25°C, and the films were exposed to 6 hours of mercury-arc irradiation or 54 hours of xenon-arc irradiation. In other experiments, without the exposure

¹The numbers in brackets refer to the list of references appended to this paper.

chambers, the films were exposed for 500 hours to the xenon arc or for 5 months to atmospheric sunlight.

The significant infrared absorption peaks of the volatile degradation products from some of the irradiated films are presented graphically in Figures 2 to 4. The absorption peaks of the vapors obtained from the clear vehicle films are indicated by vertical bars. The heights of the corresponding absorption peaks from similar irradiations of the pigmented films are shown by short horizontal bars which generally bisect the vertical bars. The wavenumbers of the significant peaks and their assignments are given. The yield of any individual product was proportional to the percent absorption, except for the yield of carbon dioxide. (The absorption peak of the latter was of such magnitude that the percent absorption was no longer proportional to the absorbance.) Water was also produced, but no quantitative measurements could be made. Some of the minor products also have been omitted from the figures.

The effects of mercury-arc irradiation on the internal reflection spectra of clear alkyd, vinyl, and epoxy films are shown in Figures 5 to 7. Other experimental results are summarized in Table I.

Volatile Products from Clear Films

In the photodegradation studies of various clear vehicle films, ten different products had been identified and five functional groups characteristic of these products, or of additional products, were also identified. The products identified included carbon dioxide, carbon monoxide, methane, acetone, formic acid, methanol, ethylene, acetylene, hydrogen chloride, and water; the functional groups included carbon-hydrogen linkages, carbonyl groups, acetyl groups, vinyl groups, and vinyl ester groups. The major product was carbon dioxide.

Both the rate of production of volatile products, and the relative yields of products from the same film, were dependent on the type of irradiation. Thus, 6 hours of irradiation with the mercury arc and 54 hours of irradiation with a xenon arc produced approximately equivalent decomposition of the clear alkyd film, as judged by the yields of carbon dioxide, carbon monoxide, and compounds with carbon-hydrogen and carbonyl groups, and as shown in Figure 2. The same 6-hour and 54-hour exposure periods were used in the study of other vehicle films even though the relative yields were somewhat different for different types of vehicles.

The oxidatively drying vehicles gave greater yields of carbon dioxide than did the vehicles that dried by solvent

evaporation or by polymerization and this difference was accentuated in the xenon-arc irradiations. The oxidatively drying vehicles also gave greater yields of ethylene and of formic acid. The vinyl and epoxy films, on the other hand, gave greater yields of acetone and compounds with vinyl groups. Methane and acetylene were obtained from the mercury-arc irradiations of all the clear vehicle films, and this might have been caused by the shorter wavelength, and higher energy, light of the mercury arc.

Volatile Products from Pigmented Films

The yields of volatile products from the pigmented films were generally much lower than the yields from the clear films, as might be expected, but the addition of pigment had no uniform quantitative effects on the yields of individual volatile products. The differences in these yields is shown for alkyd films in Figure 2, for vinyl films in Figure 3, and for epoxy films in Figure 4.

The predominant product from the irradiation of both the clear and pigmented films was carbon dioxide. The possibility was thus raised that the carbon dioxide production might in itself be used as an indication of the degree of photodegradation. In the xenon-arc irradiation of several air-drying films, the reductions in the carbon dioxide yields from the pigmented films as compared to the clear films paralleled similar reductions in yields of other volatile products. In similar irradiations of vinyl films the yields of other volatile products were reduced much more by pigmentation than the yields of carbon dioxide, and the yields of vinyl groups and acetone were essentially eliminated by pigmentation. Further work is thus needed to determine whether the carbon dioxide production can in itself be used as an indication of film deterioration.

Light of sufficiently short wavelength to be strongly absorbed will penetrate a clear coating film less than light of longer wavelengths. In a pigmented film in which the pigment is covered by a thin layer of clear vehicle, the pigment therefore would be expected to have comparatively little effect on the photodegradation produced by light of very short wavelength. This was borne out in the experiments. Acetylene and methane were produced by the shorter wavelength light from the mercury-arc irradiations, and the yields were only slightly affected by pigmentation. Acetone and vinyl groups apparently were produced by light of longer wavelength, and the yields were greatly affected by pigmentation. Generally, pigmentation reduced the yields of volatile products from the mercury-arc irradiation less than it reduced the products from the xenon-arc irradiation.

Surface Changes Detected by Internal Reflection Spectroscopy

In internal reflection spectroscopy, or attenuated total reflectance (ATR) spectroscopy, the light beam is reflected at the prism-sample interface in such a way that the beam travels essentially within the prism except for a slight penetration into the sample. This penetration is dependent on the relative indices of refraction of the prism and the sample, and on the angle of incidence of the light; and it is directly proportional to the wavelength of the light.[9] For ordinary infrared internal reflection spectroscopy the penetrations may be in the neighborhood of 2 to 10 micrometers. The spectra obtained are similar to the transmission spectra which would be characteristic of this upper layer.

The chief changes in the spectra, which resulted from the irradiation of the coatings, were increases in absorbance in the region of $1600\text{--}1800\text{ cm}^{-1}$ ($5.6\text{--}6.2\text{ }\mu\text{m}$) and decreases in the peak heights in other regions. The increases in absorbance presumably were due to the formation of various types of carbonyl groups in ketones, esters, or organic acids that were produced in the photodegradation processes. No specific reaction products could be identified, probably because of the large variety of products that are formed and because of their relatively low concentration as compared to the unreacted film constituents. The decreases in peak heights that are observed in other regions of the spectra are often due to a broadening of the peaks and lowering of the baseline. These changes can be caused by the disappearance of specific functional groups, by a proliferation of the types of chemical linkages, or by poorer contact because of surface roughness.

There is no one specific change common to all the internal reflection spectra that would be a good indicator of the degree of photodegradation. Different changes were observed in the spectra of the various generic types of coatings or of the different polymers. The type of irradiation greatly affected the relative effects on the spectra, and the presence of pigment had varying effects.

The mercury-arc irradiations produced large changes on the surfaces of clear vehicle films, whereas the xenon-arc irradiations produced comparatively small surface changes, as indicated by the spectra. This difference in effect of these sources of radiation is again due to the difference in penetration of the irradiating light. The clear films are comparatively transparent to most of the light from the xenon arc. On the other hand the same films have a high absorbance for much of the shorter-wavelength light from the mercury arc. The mercury arc thus causes much greater surface degradation of the clear film, even though the same total amounts of volatile products may be formed in the xenon-arc irradiation.

The presence of pigment in the coating films greatly reduced the changes in the internal reflection spectra that were produced during the same periods of mercury-arc irradiation. On the other hand, the pigmented films exposed to the xenon-arc irradiation showed slightly greater changes in the spectra than those produced for the clear films, in spite of the fact that the yield of volatile products was reduced. It is possible that this greater change at the surface was due to reflection of the light within the film.

The results of five-month atmospheric exposure were much more similar to those of xenon-arc irradiation than to those of mercury-arc irradiation. General reductions in peak heights were obtained in the spectra of alkyd, vinyl, and epoxy films, and there was an increase in the carbonyl peaks of the epoxy films. The 500-hour xenon-arc irradiations had lesser effects on the alkyd film, approximately the same effects on the vinyl film, and greater effects on the epoxy film, as compared to the five-month atmospheric exposures.

The results described above, as well as those of other investigators, show that the chief effect of photodegradation on the internal reflection spectra is an increase in carbonyl absorption. It thus appears likely that such spectra will be most useful in studying the degradation of those coatings and plastics which do not have high initial carbonyl absorption.

Changes in Spectra of Various Polymers

The changes in internal reflection spectra that were obtained for coatings of different generic types, under various sources of irradiation, and for clear and pigmented films are discussed below. Also listed are the major changes noted by other authors in the spectra of other polymeric materials.

Alkyd Films. Mercury-arc irradiation of clear alkyd films produced increased carbonyl absorbance in the 1600 to 1800 cm^{-1} (5.6 - $6.2\text{ }\mu\text{m}$) region which resulted in a widening of the base of a large absorption peak at 1720 cm^{-1} ($5.8\text{ }\mu\text{m}$), as shown in Figure 5. This part of the new carbonyl formation was masked by the carbonyl peak originally present. A new peak, or intensified peak was obtained at 1165 cm^{-1} ($8.6\text{ }\mu\text{m}$), but there was a marked decrease in other individual peak intensities at frequencies below 1600 cm^{-1} (above $5.6\text{ }\mu\text{m}$).

Mercury-arc irradiation had a much reduced effect on the spectra of pigmented alkyd films, as noted in Table I. Xenon-arc irradiation had only a slight effect for either clear or pigmented films. Exposure of clear or pigmented films to the atmosphere produced small reductions in peak heights.

Vinyl Films. Mercury-arc irradiation of clear vinyl films produced considerably increased carbonyl absorbance in the 1600-1800 cm^{-1} (5.6-6.2 μm) region, which was less strongly masked by the original carbonyl peak than was the case for the alkyd film. The other peaks were again greatly decreased, as shown in Figure 6.

Mercury-arc irradiation of pigmented vinyl films gave a small increase in the carbonyl peak and considerable decreases in other peaks, as noted in Table I. Xenon-arc irradiation produced only slight effects on clear or pigmented films. Atmospheric exposure also produced only slight effects. Slight effects after weathering for eighteen months also were reported for the internal reflection spectra of several PVC formulations by Chan and Hawkins.[8]

Epoxy Films. Mercury-arc irradiation of clear epoxy films produced strong carbonyl peaks at 1720 and 1655 cm^{-1} (5.8 and 6.0 μm). Other peaks were decreased, as shown in Figure 7.

Mercury-arc irradiation of pigmented epoxy films produced somewhat weaker peaks at 1720 and 1655 cm^{-1} as shown in Table I, but had relatively little effect in decreasing other peaks. Xenon-arc irradiation (54 hr) of the clear film had slight effects but xenon-arc irradiation of pigmented films produced somewhat greater increases at 1720 and 1655 cm^{-1} without affecting other peaks. Atmospheric exposure (5 mo) of both clear and pigmented films gave greater increase in the two carbonyl peaks and did decrease the heights of other peaks; however the effects were not as great as in the mercury-arc irradiation (6 hr) of the pigmented film. Longer xenon-arc irradiation (500 hr) of the pigmented film, produced greater effects than the atmospheric exposure, even though this irradiation had comparatively little effect on the alkyd and vinyl films.

Polycarbonates. Mercury-arc irradiation of the polycarbonate samples was studied by Gedemer.[6] He found an increase in a peak at 1600 cm^{-1} (5.6 μm), a general decrease in other peaks, and changes in the relative intensities of some of the peaks.

Polyethylenes. Exposure in a weathering machine, which produced higher relative amounts of ultraviolet light than the xenon-arc, and also outdoor exposure, produced a strong carbonyl peak at 1710 cm^{-1} (5.9 μm) in the internal reflection spectra of polyethylene samples, according to the studies of Chan and Hawkins. [8] There was also increased absorbance in a broad area centered near 1050 cm^{-1} (9.5 μm).

ABS Resins. Outdoor exposure of acrylonitrile-butadiene-styrene resins, produced hydroxyl peaks near 3300 cm^{-1} (3.0 μm)

and carbonyl peaks near 1710 cm^{-1} ($5.9\text{ }\mu\text{m}$), according to Chan and Hawkins. [8]

References

1. J. D'Ans and S. Merzbacher, Chem. Umschau Fette, Oele, Wachse, Harze, CUGFA, Vol. 34, 1927, pp. 283-291, 295-296 [Chem. Abst., CHABA, Vol. 22, 1928, p. 1860].
2. E. B. Fitzgerald, Ind. Eng. Chem., IECHA, Vol. 45, 1953, pp. 2545-2548.
3. E. B. Fitzgerald, ASTM Bull., ASTBA, No. 207, 1959, pp. 65-77.
4. R. S. Yamasaki, Journal of Paint Technology, JPTYA, Vol. 39, No. 506, 1967, pp. 134-143.
5. P. J. Hearst, ACS, Division of Organic Coatings and Plastics Chemistry, Papers Presented, ACOCA, Vol. 26, No. 1, March 1966, pp. 205-215; Vol. 27, No. 1, April 1967, pp. 197-206.
6. T. J. Gedemer, Applied Spectroscopy, APSPA, Vol. 19, No. 5, September 1965, pp. 141-146.
7. P. J. Hearst, ACS, Division of Organic Coatings and Plastics Chemistry, Papers Presented, ACOCA, Vol. 28, No. 1, April 1968, pp. 672-681.
8. M. G. Chan and W. L. Hawkins, ACS Polymer Preprints, ACPPA, Vol. 9, No. 2, September 1968, pp. 1638-1643.
9. N. J. Harrick, Internal Reflection Spectroscopy, Interscience Publishers, New York, 1967, p. 30.

Table 1. Effect of irradiation on internal reflection spectra of coating films.

Pigmentation	6-hr Mercury Arc	54-hr Xenon Arc	5-mo Atmospheric
Alkyd Films			
Clear film	Wider at 1600-1800 ^d Peak at 1165 Decreased Peaks	No significant change	Slightly decreased peaks
Pigmented film	Slightly decreased peaks	No significant change	Slightly decreased peaks
Vinyl Films			
Clear film	Strong increase 1600-1800 Shoulder at 1625 Decreased peaks	Slight increase 1740 Slightly decreased peaks	
Pigmented film	Increase 1740 & 1700 Decreased peaks	Slightly decreased peaks	Slight increase 1740 Slightly decreased peaks
Epoxy Films			
Clear film	Strong increase 1720 & 1655 ($\Delta A \sim 0.15$ & ~ 0.11) Decreased peaks	Slight increase 1655 ($\Delta A \sim 0.03$) No other effect	Increase 1720 & 1655 ($\Delta A \sim 0.04$ & ~ 0.04) Strongly decreased peaks
Pigmented film	Strong increase 1720 & 1655 ($\Delta A \sim 0.11$ & ~ 0.07) Slightly decreased peaks	Increase 1720 & 1655 ($\Delta A \sim 0.04$ & ~ 0.02) No other effect	Increase 1720 & 1655 ($\Delta A \sim 0.04$ & ~ 0.03) Decreased peaks

^d The four-digit numbers are the frequencies (in cm^{-1}) in the spectra.

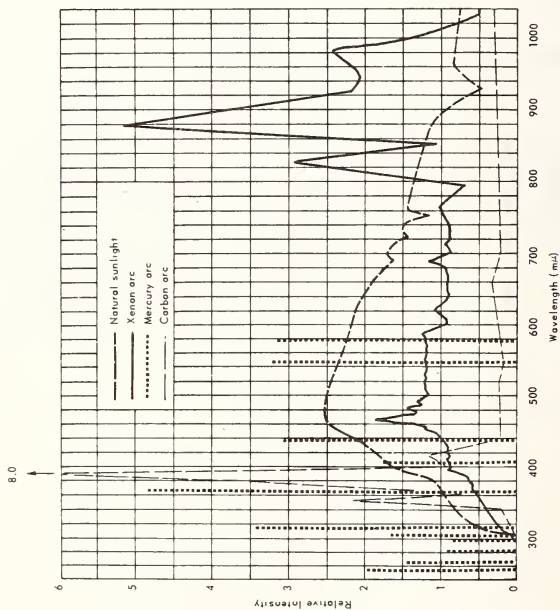


Figure 1. Spectral distribution of light sources.

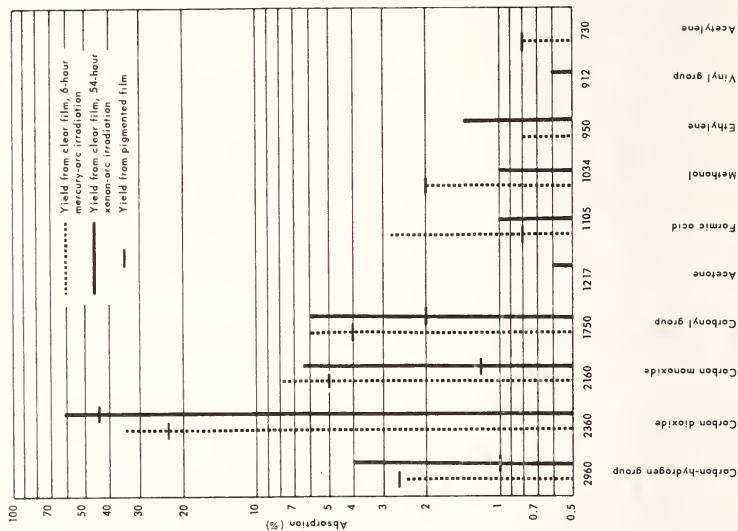


Figure 2. Relative yields of volatile products from alkyl films.

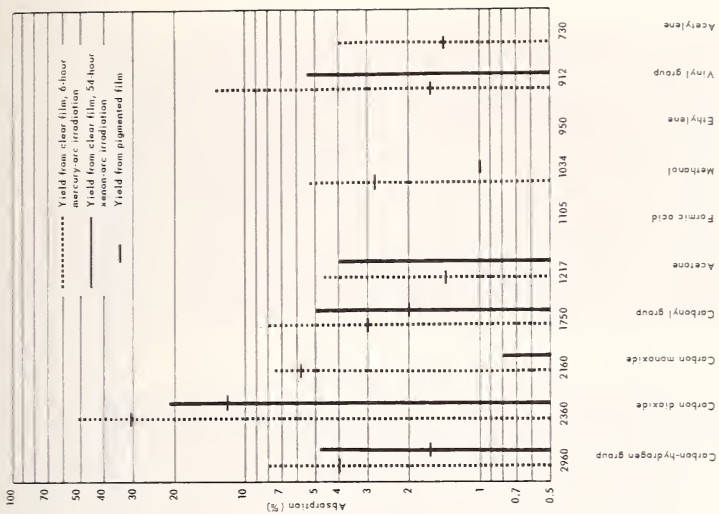


Figure 3. Relative yields of volatile products from vinyl films.

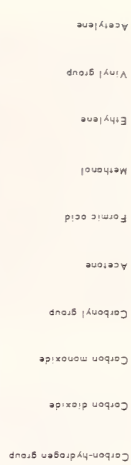


Figure 4. Relative yields of volatile products from epoxy films.

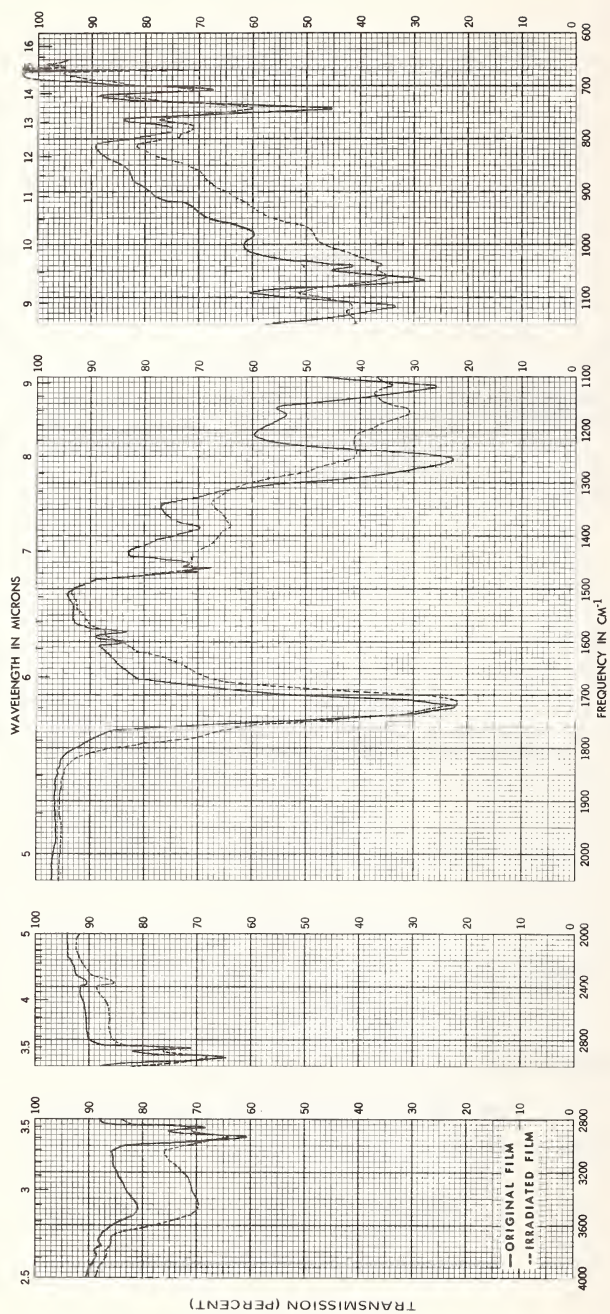


Figure 5. Internal reflection spectra of a clear alkyl film irradiated with a mercury arc.

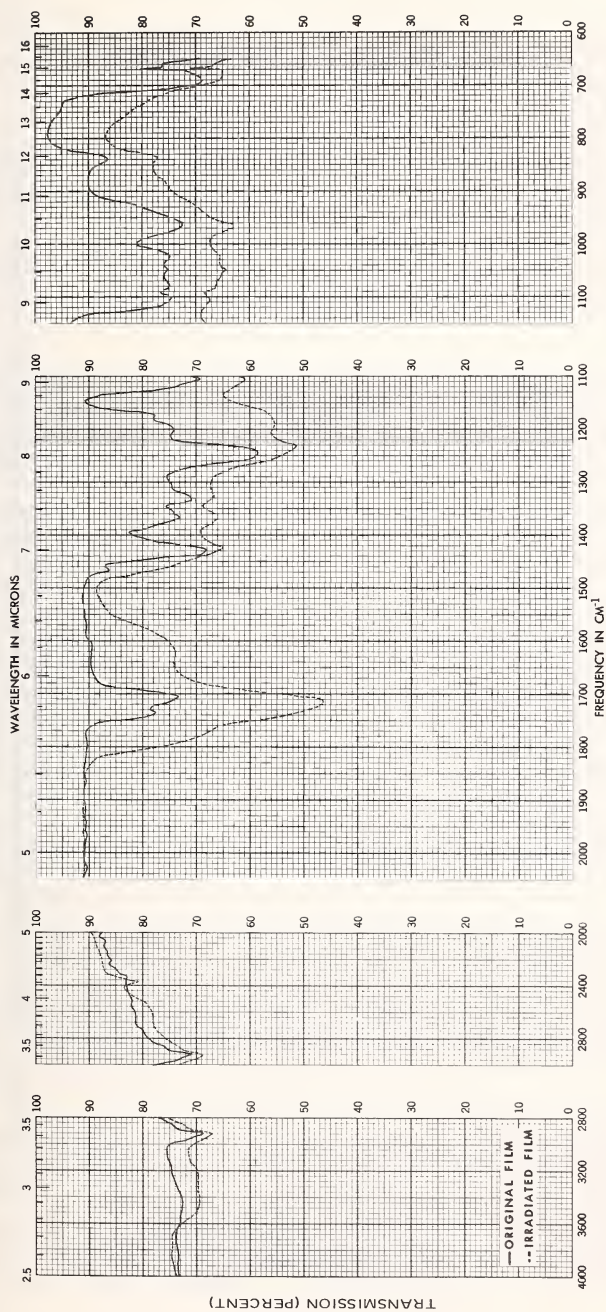


Figure 6. Internal reflection spectra of a clear vinyl film irradiated with a mercury arc.

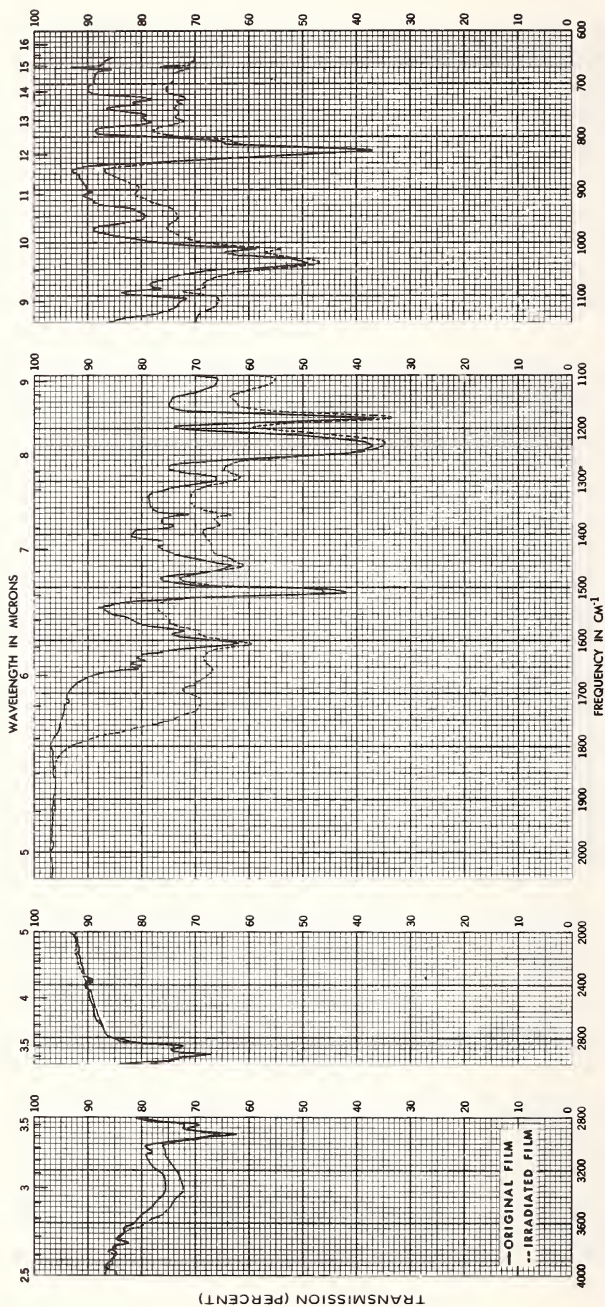


Figure 7. Internal reflection spectra of a clear epoxy film irradiated with a mercury arc.

RELATION BETWEEN DOSE RATE EFFECTS AND LABORATORY
SIMULATION OF SPACE RADIATION DAMAGE

A. Roizès¹ and R. Schuttler²

REFERENCE: Roizès, A. and Schuttler R., "Relation Between Dose Rate Effects and Laboratory Simulation of Space Radiation Damage," ASTM/IES/AIAA, Space Simulation Conference, 14-16 Septembre 1970.

ABSTRACT: The experimental simulation of space radiation damage is usually done on a much shorter time scale than the satellite lifetime. The defect annealing in the semiconductor may lead to an overestimation of the real space degradation ; indeed the irradiation time may be of the same magnitude order than the annealing time constant. Cleland's experiments (1) on germanium show that for a sufficient dose the defect number electron induced may be half as much in the long irradiation case than in the shorter one.

The higher density of ponctual defects introduced by a greater flux rate enhances the production of multiple defects as reducing the production of vacancy-impurity complexes.

Different factors that can influence the defect center distribution are analysed in the range -100°C to + 100°C.

It is shown that to improve the device hardness against radiation, we must study the production rate of defects in the bulk material coming from different growing methods and makers, as we know that the damage depends on impurity constant.

¹ONERA/CERT - Département d'Etudes et Recherches en Technologie Spatiale 51,rue Caraman 31-TOULOUSE FRANCE.

²Institut National des Sciences Appliquées et Département d'Etudes et Recherches en Technologie Spatiale 31-TOULOUSE - FRANCE.

Moreover a second improvement can be reached by annealing enhancement. Thus we must choose a material whose defect annealing temperature is as near as possible than the device temperature operation. A combination of these two requirements can help to select an optimal crystal for devices in space environment.

It is shown that with a better knowledge of the recovery process it will be possible to simulate long irradiation time with reasonable operation time of a particle accelerator by irradiating devices at a controlled temperature higher than the usual temperature operation.

For example, calculations made on the E center defect (vacancy - phosphorous association) show that one year irradiation at 300°K can be simulated with the same dose, in one hour irradiation at 400°K.

We deduced than in a room temperature simulation the number of defects, in this case, is overestimated by about 50% approximately.

KEY WORDS: Silicon, defect annealing, Space simulation, impurities.

1 - INTRODUCTION

Ground simulation of a semiconductor where radiation produces degradation in a much shorter interval of time than under real conditions.

In such a way we neglect all defect annealing, and thus we overestimate the degradation effect of energetic particles.

The higher density of punctual defects introduced by a greater flux rate enhances the productions of multiple defects as reducing the production of vacancy-impurity complexes.

As different defects have different influences on measured physical properties, the degradation coefficient becomes to be dependent upon the flux rate.

The improvement of device properties against space radiations can be obtained through a careful study of the material electrical properties. Indeed,

the device characteristics before irradiation depend much less upon the impurities nature than the bulk properties after irradiation.

Previous studies by Stein et Gereth (2), have shown that one could select a material whose annealing temperature was near the working temperature of devices, thus lowering the sensibility to a slow irradiation.

We show that it is possible to take into account the annealing phenomena during an irradiation by high flux rates if one maintains the devices at a higher temperature than the device working temperature.

The study of the major defect annealing enables us to show that a simple relationship exists between irradiation duration and irradiation temperature.

Calculations concerning the E center (vacancy-phosphorous association) show, for example, that space irradiation at 300°K can be simulated by a one hour ground simulation at 400°K.

In classical simulations one overestimates the defect number by about 50%.

2 - INFLUENCE OF IRRADIATION CONDITIONS ON THE PRODUCTION RATE

2-1 Temperature : The creation defect production rate varies with temperature in the low temperature ranges (3), (4), where a correlation exists between the vacancy and the interstitial of the primary defect. This effect vanishes above 200°K in Silicon.

2-2 Flux rates : The experiment performed shows that the defect production rates does not depend on flux rates up to a limit of 10^{14} el/cm²s for Silicon (5).

3 - DEFECT ANNEALING

3-1 Simple defect : For studying the defect annealing at room temperature one must define exactly the material characteristics.

The following equation gives the variation of the number N of defects with temperature T and time t:

$$\frac{dN}{dt} = K_0 \exp \left(- \frac{E_a}{kT} \right) \cdot N^\gamma$$

E_a is the activation energy

K_0 is the jump frequency

very often $1 < \gamma < 2$

Well known defects are of type E center i.e vacancy-impurity associations.

HIRATA et Al.(6) have shown that annealing depended on the kind of impurity : we choose the vacancy-phosphorous defect to show the importance of defect annealing. It is characterised by an activation energy $E_a = 0.94$ eV and a jump frequency $K_0 = 6 \cdot 10^8 \text{ s}^{-1}$.

Keeping the crystal at ordinary temperature, only 35% of created defects remain one year after the irradiation.

If we work using the real space conditions of temperature, we have approximated the temperature cycles of the solar pannels, as following. In shadow, the temperature is constant and equal to -20°C and in sunlight the temperature is 27°C . The corresponding intervals of time for these temperatures are respectively 30 and 90 mn in one cycle. We assume there is a sharp temperature transition between these states.

We have calculated the ratio $\frac{N}{N_0}$, between the number of defects N effectively remaining after one year of irradiation and the number N_0 , obtained by irradiation at 300°K , by delivering the same total dose over a short period prior to the diffusion times of the defects.

We have found $\frac{N}{N_0} = 0.7$, for a 3 years irradiation

$\frac{N}{N_0} = 0.47$, for 4 year irradiation $\frac{N}{N_0} = 0.18$, the

effect increases with temperature and the irradiation time, for a given integrated dose.

The same calculus for a maximum temperature of 60°C and a one year irradiation time gives $\frac{N}{N_0} = 0.01$.

The E center will disappear for another center of greater stability, the A center for example. In this condition the physical meaning of a spatial irradiation is not the same as a classical irradiation on the ground.

3-2 Complexe defect : Above a threshold dose, the defect density can be so high that interaction among defects takes place and there is a new defect non existant in a real irradiation. This result was obtained by FANG (7) who compared solar cell degradations after successive cycles of irradiation followed by a recovery.

For the other defects, the effect will be more important if the annealing temperature is nearer the device temperature operation : for example this is the case of doped lithium solar cells.

4 - SPACE IRRADIATION SIMULATION

The semiconductor devices degradation simulation is not possible during their space exposure periods.

We propose to accelerate the diffusion phenomena by irradiating the samples, with accelerators dose rate i.e. about 10^{11} el/cm²s at a temperature rather higher than the real temperature of irradiation, for a reasonable period.

We consider a first order kinetics annealing, the result obtained can be generalized for any kinetic order.

The recovery is governed by a differential equation of the form :

$$\frac{dN}{dt} = - N(t) K_0 \exp - \frac{E_a}{kT}$$

$$\text{i.e. } \text{Log } \frac{N(t)}{N(0)} = - K_0 t \exp - \frac{E_a}{kT}$$

N(t) is the number of defects remaining at the time t after irradiation

N(0) is the number of defects introduced just after irradiation

If we perform irradiation with the same dose on two identical samples kept at different temperatures T_1 and T_2 , the number of defects present in the samples will be identical at the end of the respective time t_1 and t_2 such that :

$$K_0 t_1 \exp - \frac{E_a}{kT_1} = K_0 t_2 \exp - \frac{E_a}{kT_2}$$

that is the ratio of the observation times in the two experiments will be

$$\frac{t_2}{t_1} = \exp - \frac{E_a}{kT} \left(\frac{1}{T_1} - \frac{1}{T_2} \right)$$

Example - In the case of the vacancy-phosphorous defect $E_a = 0.94$ ev,

the ratio of the irradiation times for $T_1 = 300^\circ\text{K}$ and $T_2 = 400^\circ\text{K}$, will be :

$$\frac{t_1}{t_2} = 1.2 \cdot 10^4$$

It is evident than a continuous irradiation of one year at 300°K could be simulated by an irradiation of one hour at 400°K with the same dose.

5 - CALCULATION OF DOSES OF PARTICLES RECEIVED : EFFECT OF RECOVERIES

If we used as dose accumulator a device sensitive to minority carrier lifetime , the annealing effect will induce an error that we evaluate here.

The measured dose ϕ' is lesser than the real dose see figure 1 .

The quantity $\frac{1}{\tau} - \frac{1}{\tau_0}$ is proportional to the number of defects N.

τ is the minority carrier lifetime after irradiation
 τ_0 is the minority carrier lifetime before irradiation

$$\frac{1}{\tau} - \frac{1}{\tau_0} = K \phi = K' \phi' \quad \text{thus} \quad \frac{\phi}{\phi'} = \frac{K}{K'}$$

In one case after a one year's irradiation $\frac{K}{K'} = 1.43$
 a four years irradiation $\frac{K}{K'} = 5.5$

The annealing defect become appreciable during a lesser irradiation time.

6 - PREDICTION OF A SEMICONDUCTOR DEVICE DEGRADATION

We consider a device sensible to the minority carrier diffusion length,

$$\frac{1}{L^2} - \frac{1}{L_0^2} = K \phi$$

A 20% degradation prediction after one year's irradiation will be 17%.

A 20% degradation after four years will be 5%.

7 - CONCLUSION

The degradation prediction of semiconductor device working in a space radiation environment requires the degradation study of the bulk material. It is better to select a low annealing temperature material, nearest to the working temperature : for example the lithium doped Silicon is an extreme case.

Many years of irradiation can be better simulated by accelerating the annealing phenomena : we have defined a new irradiation procedure which gives a better prediction of a semiconductor device degradation. We have shown that there is a simple relation between time and temperature irradiation. In a particular case, a one year room temperature degradation can be simulated by a one hour irradiation of a sample maintained at 400°K with the same dose.

This problem will be important for long duration satellites, this is the case with technological application satellites.

$$\frac{1}{\tau} - \frac{1}{\tau_0} \propto N$$

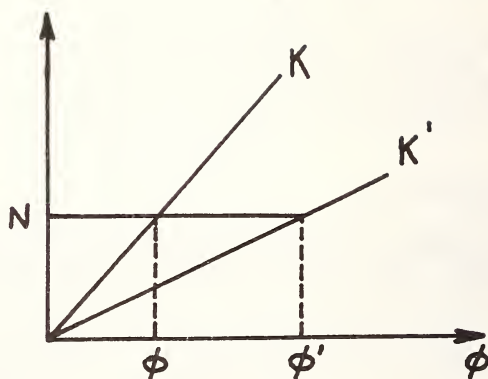


Figure 1 - Number of defects as a function of irradiation integrated flux

BIBLIOGRAPHY

- (1) A. HIRAKI, J.W. CLELAND, J.H. CRAWFORD -
Radiation effects in Semiconductors
Proc. of the Santa Fe Conference (1967)
- (2) H.J. STEIN and R. GERETH -
J.A.P. 39, 2890, (1968)
- (3) R.E. WHAN and F.L. VOOK -
Phys. Rev. 153, 814, (1967)
- (4) H.J. STEIN - Bull. Am. Phys. Soc. 11, 194 (1966)
- (5) D.E. HILL - Phys. Rev. 114, 1414, (1959)
- (6) M. HIRATA et al. - J.A.P. 38, 2433, (1967)
- (7) P. FANG - Phys. Rev. Letters, 20, (1966)

SOME PROBLEMS CONCERNING THE SIMULATION OF PLASTIC FILMS DEGRADATIONS BY IONIZING RADIATIONS

A.J. Paillous^{1,2} and Ph. Fayet³

REFERENCE: Paillous, A.J. and Fayet, Ph., "Some Problems Concerning the Simulation of Plastic Films Degradations by Ionizing Radiations," ASTM/IES/AIAA Space Simulation Conference, 14-16 Septembre 1970.

ABSTRACT: Simulation in the laboratory, of the action of polyenergetic proton-and electron-fluxes encountered in Space is necessary for a convenient estimate of polymeric film materials. In order to select the best simulation conditions, the following points were experimentally investigated on Poly (ethylene terephthalate) films, irradiated in vacuum by 1.5 MeV-protons and by 0.35-, 0.6-, 2.0 MeV-electrons : a) dose rate effects b) effects of interruptions during irradiation (samples being kept in vacuum) c) recovery during post-irradiation exposures to air or to vacuum d) effect of the sample temperature during irradiation e) effect of particles' energy f) effect of the particles' nature.

It appears that accelerated tests in a vacuum can be used to predict the damage created during missions in Space which are of a longer duration than

¹To whom correspondance must be adressed.

²ONERA/CERT - Département d'Etudes et Recherches en Technologie Spatiale 51, rue Caraman 31-Toulouse FRANCE.

³Centre National d'Etudes Spatiales - Direction des Programmes et du Plan B.P. n° 4
91 - Brétigny-sur-Orge - FRANCE.

that of the tests themselves. Electron damage in Space can be simulated by a monoenergetic electron irradiation which introduces into the sample the same absorbed energy dose than the computed dose which would be absorbed in Space. For plastic films there is no practical equivalence in the effects of proton- and electron-irradiation, except for the optical transmission properties. The need for an in-situ testing of mechanical and optical properties is outlined.

KEY WORDS: tests, evaluation, plastic films, Poly (ethylene terephthalate), radiation effect, space simulation, proton damage, electron damage, radiation intensity, recovery, temperature effect, electron energy, proton energy, optical properties, mechanical properties, viscosity, solubility, gel, electron spin resonance.

I - INTRODUCTION

Simulation in the laboratory, of the action of ionizing polyenergetic isotropic radiations encountered in Space (i.e. chiefly protons and electrons) is necessary for a convenient estimate of materials to be used for a particular mission.

Such a simulation depends on existent irradiation apparatuses (particle accelerators providing a monoenergetic non-isotropic irradiation with a limited range of energies) ; moreover it must be short-lasting and easy to bring into use (simultaneous irradiations by electrons, protons and ultraviolet radiations, must be done separately in the laboratory).

In order to select the best simulation conditions (which must be compatible with our own existing apparatuses) for testing polymeric films, the following problems were studied:

- a) recovery of defects during an exposure to the air, following irradiation
- b) dose rate effects, for same absorbed dose deposited in a sample maintained in vacuum (particles being the same)
- c) effect of interruptions during irradiations

(samples being kept in a vacuum during breaks)

d) effect of the sample temperature during irradiation

e) equivalence of effects for particles of same nature but having different energies

f) equivalence of effects for same absorbed dose delivered by radiations distinct in their nature (electrons, protons)

II - EXPERIMENTAL PART

Material used in this study

The plastic material used in this study was Poly(ethylene terephthalate) (P.E.T.). The sample of P.E.T. was Terphane¹ film of thickness 0.0050 cm.

Electron exposure apparatuses

Two 600-KeV electrostatic SAMES accelerators and a 2 MeV Van de Graaff electron accelerator were used.

A same exposure device was used for these accelerators :

The electron beam was diffused by a thin Aluminum foil (25 or 30 μm thick). The diameter of the irradiated surface was 150 mm. Flux homogeneity was better than 10% (measured by five small cups) ; multi-diffused electrons were eliminated by use of a collimating system.

Samples were irradiated in a vacuum better than 10^{-5} Torr.

Film specimen were generally fixed on a frame at 4 cm from the irradiation chamber back-part, and were not externally cooled.

In the experiments reported in Tables 1 and 2, and in figures 1 and 3, small film specimens were laid on an Aluminum sample-holder ; the sample-holder temperature was adjusted by the use of a circulating fluid.

In all experiments, the maximum sample-temperature was estimated by the use of temperature-indicating thin plates (Temp-Plates², Mylar support).

¹Société La Cellophane, 110 boulevard Haussmann, Paris 8e - FRANCE

²Williams Wahl Co. Santa Monica - California

Proton exposure apparatus

A 2 MeV Van de Graaff proton accelerator was used. A mechanical scanning system allows an homogeneous irradiation of specimens which are fixed on a rotating drum ; the diameter of the proton beam is 20 mm². The specimens are irradiated in a vacuum better than 10⁻⁴ Torr. The maximum temperature of samples was estimated by the use of temperature indicating thin-plates.

Optical measurements

Optical transmission measurements, in the 200-2700 nm wavelength interval, were performed in air with a Beckman DK2A Spectrophotometer. Except for the measurements given in Tables 1 and 2, and in Figures 1 and 3, spectra were recorded with an integrating sphere attachment. The reproducibility at any wavelength was within + 1 per cent. Measurements given in Tables 4, 5 and Figures 3 and 4 are obtained after only a post-irradiation exposure to air at the end of irradiations (samples being kept at room temperature). For recovery experiments (Tables 1,2 ; Figure 1), procedure is given in the text.

Mechanical measurements

Tensile stress-strain curves were recorded on a Lhomargy testing machine. The speed of testing was 30 mm/mn. At the end of irradiation, samples were exposed to air for less than 5 minutes ; then they were kept in a 10⁻² Torr vacuum for one hour ; they were subsequently kept in air (20°C ± 1°C, 65% ± 2% relative humidity) for 23 hours ; measurements were performed in air at 20°C. For each irradiation, 6 rectangular specimens (105 x 80 mm ; 5 cm between grips) were tested : the average measurement is given in the text). For recovery experiments, samples were exposed for less than 5 minutes to air ; they were subsequently kept in a container in a 10⁻² Torr vacuum, at ambient temperature for 20 minutes during their transport ; then access of air to these samples was allowed, and curves were recorded at intervals.

Viscosity measurements

Viscosity measurements were carried out at

40°C + 0,02°C in an Ubbelohde viscometer. Specimens were dissolved at 60°C, for 15 mn, in a phenol-tetrachlorethane (1 : 1 vol.) mixture.

Solubility analysis and equilibrium swelling values

We used the experimental methods described by MARCOTTE and Al. (10) for the measurements of the insoluble fraction and of the equilibrium swelling value.

Electron spin resonance

Irradiated films were examined in a Thomson-Houston THN 252 Spectrometer (X band) at room temperature.

Spectra were either recorded in air (the irradiated plane film, 5 x 0.6 cm, was contained in an open Suprasil tube) or recorded in vacuo (the irradiated plane film, 5 x 0.6 cm, was sealed in a Suprasil tube in a 10^{-6} Torr vacuum). Film was examined with different orientations in the magnetic field ; measurements reported below were performed with the irradiated film perpendicular to the magnetic field.

III - RESULTS

Post-irradiation recovery

. Variations of optical properties

A yellowish-brown coloration is produced by gamma irradiation (1)¹ or electron-irradiation (2) of Poly (ethylene terephthalate) in a vacuum. This coloration is less intense in samples irradiated in air. A rapid post-irradiation decrease (3) in optical density of P.E.T. in air, was explained (1) by the reaction between the trapped radicals and the oxygen which diffused into the polymeric film. The recovery is limited : a rapid fading of the ultraviolet absorption occurs until a stable level is reached after a about 12 hours ; this stable value may be attributed to the formation of cross-links between phenylrings.

In order to evaluate the extent of recovery, the following experiments were carried out. Three samples, A,B and C, were irradiated by 600 KeV electrons in a vacuum at 15-20°C ; after this period of

¹The numbers in parentheses refer to the list of references appended to this paper.

irradiation, the samples were in contact with air for 5 minutes ; then they were kept at 77°K under vacuum (10^{-2} Torr) for 10 minutes ; they were subsequently warmed for 5 minutes up to 20°C ; then access of air to the samples was allowed. Optical transmission of sample A was recorded at intervals. Sample B was kept in a vacuum (10^{-2} Torr) in darkness at 20°C for 75 hours ; its spectrum was then recorded in air.

Table 1 gives optical transmission variations during the exposure of A to air. Table 2 gives measurements for the sample B.

It can be seen that the recovery extent at room temperature after 75 hours under a 10^{-2} Torr vacuum is comparable with the recovery extent after 3.5 hours in air.

Therefore it can be inferred that the optical recovery for sample A in a vacuum is quite weak during the earliest minutes. On account of this observation, it is therefore possible to overvalue and undervalue the transmission which would be presumably recorded in-situ on sample A at the end of irradiation without any contact with air. The upper value is given by extrapolation to zero-time of the transmission variations ; the lower value is given by the first measurement in the air ; values deduced from Table 1 by this method, are shown in Table 3.

Such a method must be used when in-situ recording of spectra is not possible.

It is worthy of note that the recovery we observed for sample B during a 75 hours-exposure in a 10^{-2} Torr vacuum, at the end of a short exposure to air (5 minutes), may be greater than the recovery which would be actually observed in-situ after 75 hours without any contact with air.

Similar optical changes are recorded during exposures to air following in vacuum irradiations (by 1.5 MeV protons, or by 600 KeV electrons) of all the plastic films we tested (Polyimides, Pyrroles, Polychlorotrifluoroethylene, polyvinyl fluorides...). The extent of changes and their algebrical sign (degradation or improvement in optical transmission) depends on the nature of the plastic, and, in some cases, of wavelength interval.

. Radical Decay

Biaxially oriented films of Poly(ethylene

terephthalate) are reported to give E.S.R. spectra after exposure to high energy radiations in vacuum (4). The spectrum comprises either 6 or 8 lines according to the orientation of film in the magnetic field. During a post-irradiation exposure to air, a decay of radicals is observed, owing mainly to a destruction of radicals by oxygen (leading to formation of carboxyl groups) and also to a recombination.

In order to compare the evolution of ultraviolet transmission with ESR signal decay, by exposure to air, the sample C, which was treated in the same way as sample B (see the paragraph above), was examined by ESR at 20°C. The decay of radicals was studied by following the decrease in height of the central peaks of the first derivative ESR spectrum, with time. In air, radical decay is directly related (see Figure 1) to transmission variations, specially at 495 nm where there is no permanent optical damage (cf. Table 4), and where recently irradiated films present a weak absorption band (cf. Figure 4).

No signal decay is noted after 20 days for a film which was irradiated in vacuum at 20°C, then allowed to be in contact with air for 5 minutes, then sealed in a good vacuum (10^{-6} Torr) in a Suprasil tube and kept in darkness. This observation leads us to think that no correlative transmission variation of irradiated films would have been recorded in-situ for such a long time.

. Variations of mechanical properties

A very fast variation of mechanical properties was observed during the very earliest minutes following the beginning of exposure to air of an in vacuo-irradiated sample. Samples which are, at the end of irradiation, qualitatively very brittle and difficult to handle, become flexible again within a few minutes. Tensile stress-strain curves of Terphane films irradiated by electrons (600 KeV ; flux : $4.3 \cdot 10^{16}$ e.cm⁻²) were recorded after different times of post-irradiation exposure to air. The curves in Figure 2 show that an important change is produced quite rapidly : experimental conditions are described above (see Experimental Part).

We must thus conclude that there is an imperious need for an in-situ mechanical testing device for plastic films.

Dose rate effect

Table 4 contains optical, mechanical and viscosimmetrical measurements of Terphane films irradiated in vacuum up to $2.16 \cdot 10^{16}$ electrons. cm^{-2} , with flux densities ranging from $2.5 \cdot 10^{11}$ e. $\text{cm}^{-2} \cdot \text{s}^{-1}$ to $2.0 \cdot 10^{12}$ e. $\text{cm}^{-2} \cdot \text{s}^{-1}$. Nearly all of the measurements are the same which show that there is no dose rate effect. However slightly more damage can be observed for the film irradiated with the highest intensity ; in this particular case, we noted an important increase in sample temperature during the irradiation : 80 or 90°C, which corresponded to a temperature much higher than the glassy transition of P.E.T. (70-80°C). It is significant to note that a conservation of a non-irradiated Terphane film in vacuum at 90°C for 3 hours does not change its optical transmission.

All of the electron-irradiated samples quoted in Table 4 were easily solubilized in a phenol-tetrachlorethane (1 : 1 vol.) mixture at 60°C. Only slight variations in limiting viscosity number $\{\eta\}$ (except for the highest dose rate) were measured in the dose-rate interval investigated (0.46 - 3.73 Mrad. mn^{-1}). These results are different from those of TURNER, PEZDIRTS and SANDS (5) who found a dose-rate effect on electron - and gamma-induced viscosity changes in Mylar, for dose rates ranging from 0.17 Mrad. mn^{-1} to 1.4 Mrad. mn^{-1} . This discrepancy may be due to the different origins of the materials. In any case, if $\{\eta\}$ is considered as a direct evaluation of the ratio of crosslinks N_c to fractures N_f , it appears that a simultaneous increase of N_c and N_f will not affect $\{\eta\}$; no quantitative measurement of carboxylic groups was performed on our samples ; however an important increase observed in the infrared absorption band at $3\,000\text{ cm}^{-1}$, leads us to believe that there is simultaneously cross-linking and degradation during electron-irradiations.

Intermittent irradiations

When exposure is segmented by interruptions in irradiation (these interruptions are necessary, for the longest exposures, during the nights for example) results are the same as those noted after unsegmented exposures, provided that the samples are kept in vacuum, in the irradiation chamber, during breaks.

In Table 4, irradiations n°5 and n° 6 refer to such unsegmented and segmented irradiations at the same flux density (10^{12} e.cm⁻² .s⁻¹ during exposure) ; in the latter experiment the total duration of the interruptions is equal to eight times the true irradiation time.

Temperature effect

In order to confirm temperature effects, during an electron exposure, two irradiations were performed above and below the glassy transition of Poly (ethylene terephthalate). The first experiment was carried out with a sample holder cooled at 15°C by a cooling fluid ; the second was carried out at 92°C, other conditions being the same (flux density : $1.5 \cdot 10^{12}$ e.cm⁻².s⁻¹; 1.5 MeV ; 1.5 hour). Transmission spectra were recorded in air 30 minutes after the end of irradiation. Shape differences between curves are observed (Figure 3 (a)) : the absorption band at 495 nm is more intense in the cold-irradiated sample. Moreover spectra recorded 24 hours after the end of irradiation show (Figure 3 (b)) a less intense absorption, in the whole wavelength interval 350 - 700 nm, for the cold-irradiated sample. It can be inferred that both transient and permanent effects of irradiations, are different for irradiations performed above and below the glassy transition of P.E.T. Similar difference may be expected for the mechanical properties of cold- and hot- irradiated samples. We believe that synergistic effect of temperature and irradiation (see the paragraph above) would be further investigated by E.P.R. measurements. We intend very soon to develop these studies at various temperatures and also to investigate the effect of sample temperature during a post-irradiation storage.

Energy dependence experiments

These experiments were performed only with electrons at 350 and 600 KeV. Computed values of stopping power in P.E.T. at these energies are respectively 3.02 and 2.67 MeV.cm⁻¹ ; corresponding ranges are 0.78 mm and 1.67 mm (to compare with film thickness 50 μ m). Two samples were irradiated to the same absorbed dose : 670 Mrad. Sample 3 was irradiated by 600 KeV electrons with a flux density equal to $2.5 \cdot 10^{11}$ e. cm⁻² .s⁻¹ for 24 h 00 ; sample 7 was

irradiated by 350 KeV electrons with the same flux density for 21 h 15 mn. Slightly higher optical and mechanical degradations are observed in the case of the low-energy irradiation : see Table 5. Both samples are easily soluble in trifluoroacetic acid ; however in a phenol-tetrachlorethane (1 : 1 vol.) mixture, microgels are formed when attempt is made to dissolve the low-energy irradiated sample 7 : these microgels prevent viscosimetric measurements. A greater number of cross-links is suggested by the ultraviolet absorption spectrum and by the microgel formation in the case of the low-energy irradiated sample. The weak differences in stopping powers cannot satisfactorily explain the greater extent of damages recorded at the lower energy. It is worthy of note that degradation differences between electron-irradiated samples at 350 KeV and 600 KeV are slight in comparison with the differences between irradiated and non-irradiated samples.

No attempt was made to perform such experiments with protons : observation would be further complicated by differences in range of protons (for energies lower than 2.0 MeV, these ranges are less than the film thickness ; see below).

Effect of particle nature

Computed range and stopping power for 1.5 MeV protons in P.E.T. are (8) respectively $4.94 \cdot 10^{-3} \text{ g.cm}^{-2}$ and $1.89 \cdot 10^2 \text{ MeV.cm}^2.\text{g}^{-1}$. Thus exposure to 1.5 MeV protons irradiates only 35 μm , to compare with the film thickness 50 μm . The absorbed energy dose is not homogeneously distributed in these 35 μm : a greater dose is expected at the end of the proton penetration. In Table 6 are given the average absorbed-energy dose D (expressed in Mrad), and the energy W absorbed by square centimetre, for three 1.5 MeV-proton irradiation and one 600 KeV-electron irradiation.

Figure 4 shows the transmission spectra of Terphane films irradiated, in vacuum, under comparable conditions, by 1.5 MeV protons and 600 KeV electrons. It appears that, when comparing proton- and electron-irradiation, the optical degradation can better be correlated with the energy W absorbed by unit area, than with the absorbed - energy dose D. In Polymers, defects created by electrons and protons

are qualitatively the same : ionized and excited species, and radicals ; but optical transmission properties are more directly related to the total number of created defects than to their spatial distribution within the solid (The case of optical reflective properties may be quite different).

Mechanical properties depends on the penetration depth of the particle and cannot be directly connected with energy doses. From only the mechanical measurements reported in Table 6, it is impossible to conclude that a non-equivalence of effects of different particles, in the same absorbed-energy scale, exists (owing to the limited penetration of 1.5 MeV protons in P.E.T.).

Network formations during proton -and electron -irradiations can be easily compared. Samples irradiated by electrons at 350 KeV and at 600 KeV, up to 670 Mrad are easily soluble in trifluoroacetic acid ; all samples irradiated by protons have a limited solubility in trifluoroacetic acid, even at the lowest dose. Measured values of insoluble fractions and swelling of gels are given in Table 6. These observations lead us to think that molecular weight evolutions are different, for same absorbed energy doses, in the case of protons and in the case of electrons, owing to the spatial distribution of the created defects.

Generally speaking, it must be outlined that, at low doses (for instance lower than 100 Mrad), the great density of ionized and excited species and radicals along the 1.5 MeV protons track, does not ensure a "homogeneous" irradiation in bulk, contrary to irradiation ensured by 600 KeV electrons at the same dose. A "homogeneous" irradiation by protons, with a random distribution of intermediate species created in different tracks, will be only ensured for doses higher than a D_1 value ; for these high doses, and for penetration depths much greater than the film thickness, there will be actually equivalence of effects after electron-and proton-irradiations. Taking an approximative mean distance (10 \AA) between ions or excited species created in a 1.5 MeV-proton track into account, a D_1 value equal to a few hundred Mrad is plausible for temperatures lower than the glassy transition T_g (7) (9) ; a lower value of D_1 is expected for $T > T_g$ owing to a limited diffusion of created defects in the polymer. According to our solubility measurements, D_1 appears to be higher than 670 Mrad for 1.5 MeV protons at $T < T_g$.

IV - CONCLUSIONS

a) From the great extent of the recoveries observed during a post-irradiation exposure to air of in-vacuo irradiated polymeric films, we must conclude that all samples should be measured without any contact with air.

For a convenient estimate of in vacuo-irradiated samples, an in-situ mechanical and optical testing device is absolutely necessary.

b) When in-situ measurements of optical transmission are not possible, an extrapolation method can be used.

c) In-vacuo recovery is very weak according to optical and E.S.R. measurements.

d) No dose-rate effect was observed during exposures with flux densities ranging from $2.5 \cdot 10^{11} \text{ e.cm}^{-2} \cdot \text{s}^{-1}$ to $2.0 \cdot 10^{12} \text{ e.cm}^{-2} \cdot \text{s}^{-1}$.

e) Intermittent irradiations and unsegmented exposures lead to the same sample degradations (even for breaks so long as eight times the true irradiation time).

f) From the three latter statements, it can be inferred that long-lasting irradiations in Space can be validly simulated by much shorter experiments (some dozen hours or so).

g) Optical properties show a clear temperature effect, near the glassy transition point. A correlative effect is expected for mechanical properties of the irradiated sample. Thus a strict control of the sample temperature is necessary during irradiations.

h) Energy dependence experiments show a slightly greater extent of degradations during a 350 KeV-electron irradiation than during a 600 KeV-electron irradiation for the same absorbed energy dose. Such an effect should be confirmed at low energy (150 - 300 KeV).

This effect being apparently slight, it seems possible to simulate the polyenergetic electron irradiation which takes place in Space, by a monoenergetic electron irradiation delivering approximately the same energy dose (Mrad) into the material. However, according to the above observation, it seems more advisable to simulate the degradation of plastic films by electrons in low orbite (for which 80 or 90 % of the observed energy dose is due to electrons with energies lower than 250 KeV), by a low-energy electron irradiation (200 KeV for instance); care must be

taken than the range corresponding to the selected energy will ensure irradiation of the whole film thickness.

i) For the highest absorbed doses ($D > D_1$), provided that the range of the used protons is much greater than the film thickness, proton- and electron-induced degradations are expected to be equivalent.

However, the range of the majority of protons encountered in Space being short with regard to the film thickness, it is not practically possible to use this equivalence in order to simulate a proton-irradiation by an electron-irradiation, or reciprocally.

ACKNOWLEDGMENTS

The authors wish to express their gratitude to Messrs. LEVI, TALAGRAND, AUROUX, AMBROSI and MAROT of Laboratoire Central de l'Armement (ARCUEIL - FRANCE) for their assistance in irradiating the samples. They also wish to acknowledge the very valuable assistance of Mrs. HENOUX of L.C.A. (ARCUEIL, FRANCE) in performing most of the optical tests, and of Mr. BELLOC of Laboratoire Central des Industries Electriques (FONTENAY-AUX-ROSES, FRANCE) in performing mechanical tests on samples.

REFERENCES

- (1) D. CAMPBELL, D.T. TURNER - "Influence of dose-rate on Radiation induced network formation in Poly (ethylene terephthalate)" Polym. Letters 5, 471-475, (1967)
- (2) N.A. SLOVOKHOTOVA, G.K. SADOVSKAYA, V.A. KARGIN "Effects of high speed electrons on the structure of P.E.T." J. Polym. Sc. 58, 1293-1299, (1962)
- (3) J.W. BOAG, G.W. DOLPHIN, J. ROTBLAT - "Radiation dosimetry by transparent plastics" Radiat. Res. 9, 589-610, (1958)

- (4) D. CAMPBELL, K.ARAKI, D.T. TURNER - "ESR Study of free radicals formed by γ -Irradiation of Poly(ethylene terephthalate)" J. Polym. Sc. 4, 2597-2606, (1966)
- (5) D.T. TURNER, G.F. PEZDIRTZ, G.D. SANDS - "Influence of dose rate on radiation induced network formation in Poly(ethylene terephthalate)" J.Polym. Sc. 4, 252-254, (1966)
- (6) A. PAILLOUS - "Action of ionizing radiation on Poly(ethylene terephthalate)" A bibliography. 21 ref. ONERA/CERT/DERTS NP-O3-1-68, Oct. 1968.
- (7) A. PAILLOUS - "Simulation of ionizing radiation acting in Space - The case of structural polymeric materials" ONERA/CERT/DERTS NT-O3-3-69, July 1969.
- (8) R.P. HENKE, E.V. BENTON - "Charged particle tracks in polymers : n° 3 - Range and energy loss tables" USNRDL TR-1102 (1966)
- (9) A. CHARLESBY - "Atomic radiation and Polymers"- Pergamon Press Oxford - London - New York (1960)
- (10) F.B. MARCOTTE, D. CAMPBELL, J.A. CLEAVELAND, D.T. TURNER - "Photolysis of Poly(ethylene terephthalate)" J. Polym. Sc. A1, 5, 481-501, (1967).

Time after the end of irradiation (mn)	Optical Transmission (%)									
	350 nm	375 nm	400 nm	450 nm	490 nm	550 nm	600 nm	700 nm		
20	9.8	26	43	61.5	65.9	72.4	75	79.5		
35	10.2	27.5	44.5	62.8	66.9	73.1	75.2	79.7		
65	11.7	30	47	64	68.1	73.8	76	79.9		
110	12.8	32	48.5	65.1	69.1	74.2	76.5	80.2		
155	14.0	34	50	66.3	70.1	75	77.1	80.3		
220	15.2	36.2	52.5	67.7	71.3	75.3	77.5	80.3		
305	17	39	54.8	69	72.5	76	78	80.5		
435	19	42.5	58	71	74.1	76.7	78.1	80.5		
485	20	43.5	59	71.6	74.5	78	78.5	80.5		
4000	22	47	62	73	75	78.6	78.6	80.5		
—	—	—	—	—	—	—	—	—		
Before irradiation	65	70	72	74.7	75	78	78.2	80.5		

TABLE 1 - Optical recovery during a post-irradiation exposure to air of sample A

	Optical Transmission (%) at							
	350 nm	375 nm	400 nm	450 nm	490 nm	550 nm	600 nm	700 nm
Before irradiation	66.8	71.2	73.5	76.5	77.5	79	79.8	81.2
75 hours in-vacuum after the end of irradiation	16	36.5	52	67	70.5	75	77	80

TABLE 2 - Sample B - Optical transmission after a post-irradiation storage in-vacuum (10^{-2} Torr)

Wavelength (nm)	Initial Transmission (%)
350	7.8 - 9.8
375	22.4 - 26.
400	40.3 - 43.
450	59.5 - 61.5
490	63.9 - 65.9

TABLE 3 - Presumed transmission in-vacuum at the end of irradiation

№	Fluence (e.cm ⁻²)	Flux density (e.cm ⁻² .s ⁻¹)	Duration(hours)		Maximum Sample temperature (°C)	Breaking strength (daN/mm ²)	Elongation (%)	Optical transmission (%)				[η] (dl/g)
			exposure	inter- ruption				325 nm	350 nm	400 nm	500 nm	
	0	-	-	-	-	17.0±1.0	120±20	70	79	84	85	0.60±0.02
1	2.16 10 ¹⁶	2.10 ¹²	3	0	83<t<93 locally 120°(?)	8.7±0.7	3.0±1.0	{ ⁰ 2	{ ¹ 7	{ ³¹ 55	{ ⁷⁰ 84	0.42±0.02
2	" "	5 10 ¹¹	11+1 = 12	14	43<t<48	9.9±0.3	23±18	{ ¹ 2	{ ² 10	{ ³³ 60	{ ⁷⁶ 84	0.62±0.01
3	" "	2.5 10 ¹¹	11+11+2 = 24	13+15	t<43	9.7±0.3	7.2±4	{ ⁰ 1	{ ¹ 9	{ ³⁴ 59	{ ⁷⁰ 84	0.62±0.01
4	" "	10 ¹²	2+2+2 = 6	5+15+24	60<t<82	9.6±0.6	7.6±1	{ ⁰ 1	{ ¹ 9	{ ³² 61	{ ⁷⁰ 84	0.59±0.01
5	" "	"	6	0	71<t<76	10±0.2	17.3±7	{ ⁰ 0	{ ^{3.5} 11	{ ³² 59	{ ⁶³ 83	0.57±0.01
6	" "	"	2+2+2 = 6	24+24	60<t<65	10±1.2	16.5±12	{ ⁰ 1	{ ³ 12	{ ³¹ 62	{ ⁶⁷ 83	0.55±0.01

TABLE 4 - Optical, mechanical and viscosimetric measurements after 600-keV-electron irradiations in-vacuum

N.B. - The first value given for optical transmission corresponds to a 15 minutes post-irradiation exposure to air at room temperature.
The second value corresponds to a 15 days exposure to air.

№	Fluence (e.cm ⁻²)	Flux- density (e.cm ⁻² .s ⁻¹)	Ener- gy (keV)	Duration(hours)		Maximum sample temperature (°C)	Breaking strength (daN/mm ²)	Elongation (%)	Optical transmission (%)				η_p (dl/E)
				exposure	inter- rup- tion				325 nm	350 nm	400 nm	500 nm	
	0	-	-	-	-	-	17.0±1.0	120±20	70	79	84	85	0.60±0.01
3	2.16 10 ¹⁶	2.5 10 ¹¹	600	11+11+2 = 24	13+15	t<43	9.7±0.3	7.2±4	{ 0 1	{ 1 9	{ 34 59	{ 70 84	0.62±0.02
7	1.93 10 ¹⁶	2.5 10 ¹¹	350	4h40+2h20 +9h15+5h = 24	24+16 +15	48<t<54	7.1±1.8	2.7±2.1	{ 0 0.5	{ 1.5 6	{ 23 53	{ 68 83	g±l

TABLE 5 - Optical, mechanical and viscosimetric measurements after 350 keV- and 600 keV-electron irradiation of terphane films in vacuum.

N.B.-The first value for optical transmission corresponds to a 15 minutes post-irradiation exposure to air at room temperature. The second value corresponds to a 15 days exposure to air.

Non irradiated	1.5 MeV-Proton flux				600 keV-electron flux
	7.07 10^{13} p/cm ²	1.54 10^{14} p/cm ²	3.07 10^{14} p/cm ²	2.16 10^{16} e/cm ²	
Absorbed dose (Mrad)	0	377 Mrad (35 μ m)	754 Mrad (35 μ m)	1503 Mrad (35 μ m)	670 Mrad (50 μ m)
Absorbed dose by 1 cm ² (erg.cm ⁻²)	0	1.70 10^8	3.39 10^8	6.79 10^8	4.59 10^8
Duratica (hours)	-	3	6	12	6
Breaking strength (daN/mm ²)	17.4 ± 0.7	a) 14.9 b) 13.3	a) 13.6 b) 12.9	a) 9.1 b) 10.1	10 ± 0.2
Ultimate elongation(%)	121 ± 16	a) 50.5 b) 97.5	a) 74 b) 62	a) 14.5 b) 14.5	17.3 ± 7
Insoluble fraction (%)	0	2 ± 0.2	43 ± 0.2	61.5 ± 1.2	0
Swelling value (%)	-	$\approx 10^4$	6 $\pm 2.3 \cdot 10^3$	2 $\pm 0.6 \cdot 10^3$	-

TABLE 6 - Comparison of 1.5 MeV-proton irradiations and 600 keV-electron irradiation

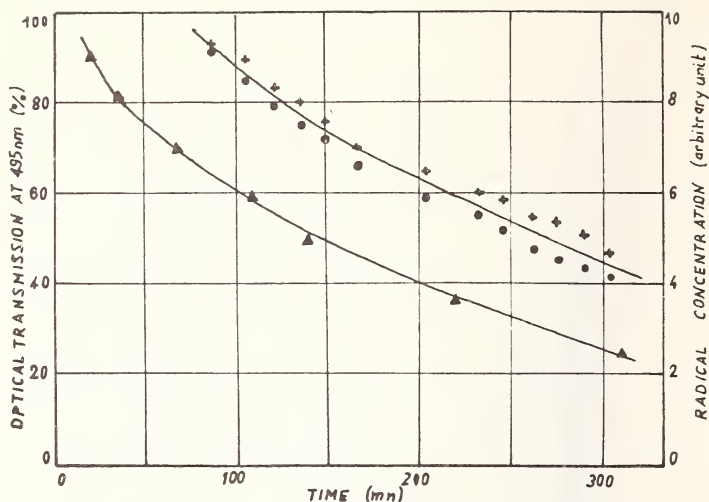


Fig. 1 - ESR Signal decay and transmission variations during a post-irradiation exposure to air at room temperature

- ▲ Optical transmission
- + Central Peak, left part of the ESR Spectrum
- Central Peak, right part of the ESR Spectrum

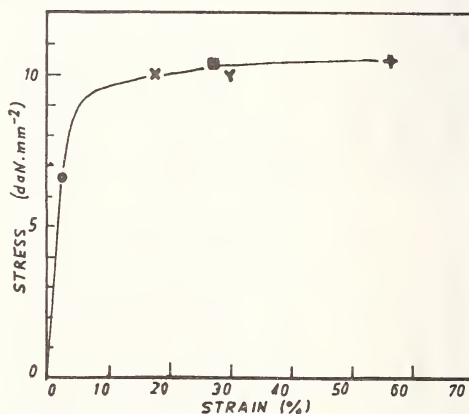
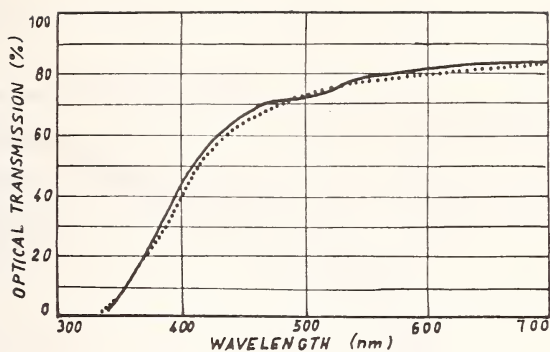
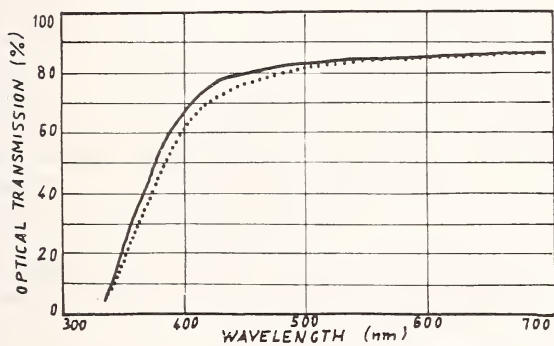


Fig. 2 - Tensile Stress-Strain curves of Terphane films irradiated by electrons (dose $4.3 \cdot 10^{16} \text{ e.cm}^{-2}$) The curves are drawn as a result of the following times of post-irradiation exposure to air

- 1 mn 20 s
 - + 10 mn 30 s
 - x 3 mn 50 s
 - 6 mn 30 s
 - Y 15 mn 20 s
- Time origin corresponds with opening of the container



(a)



(b)

Fig. 3 - Temperature effect during irradiation
Spectra recorded after a 30 mn (a), 24 hours (b).
post-irradiation exposure to air at room
temperature

... Irradiation at 92°C
— Irradiation at 15°C

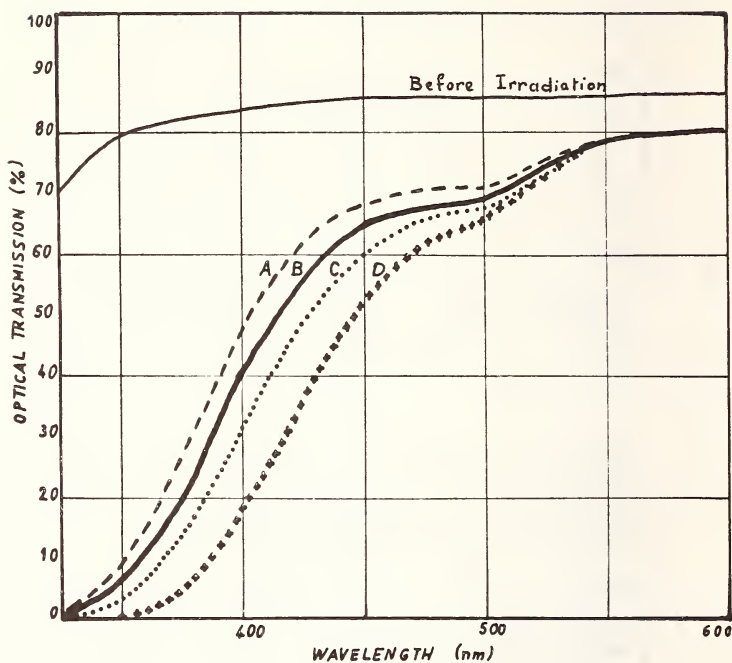


Fig. 4 - Transmission Spectra of Terphane Films irradiated by protons or electrons (after a 15 mn exposure to air)

A	1.5 MeV-protons	$\Phi = 0.77 \cdot 10^{14} \text{ p.cm}^{-2}$
B	1.5 MeV-protons	$\Phi = 1.54 \cdot 10^{14} \text{ p.cm}^{-2}$
D	1.5 MeV-protons	$\Phi = 3.08 \cdot 10^{14} \text{ p.cm}^{-2}$
C	600 keV-electrons	$\Phi = 2.16 \cdot 10^{16} \text{ e.cm}^{-2}$

ULTRAVIOLET AND CHARGED PARTICLE DEGRADATION OF ALUMINUM AND SILVER COATED FEP TEFLON SECOND SURFACE MIRRORS

F. G. Cunningham¹, B. L. Bean and S. G. Park²

ABSTRACT: An experimental program has been undertaken in which bare FEP Teflon films were subjected to ultraviolet irradiation and charged particle bombardment, and in which five mil aluminum and silver coated FEP Teflon films were: i) ultraviolet irradiation in vacuum and oxygen; ii) irradiated with 5, 10 and 25 or 30 KeV electrons and protons; and iii) exposed to simultaneous ultraviolet-proton and ultraviolet-electron bombardment.

The charged particle irradiations indicate that a measurable change occurs in the spectral reflectance of both silver and aluminum backed material at a dose of about 1×10^{15} particles/cm², and that this degradation increases as the total dose is increased. This spectral reflectance change appears first and is the most pronounced in the ultraviolet for a given total dose. At a total dose of 1×10^{16} particles/cm² the surfaces generally look cloudy and oftentimes mottled. Upon closer examination this mottling is found to be due to the presence of Lichtenberg figures within the teflon—especially in the case of electron irradiation—which are caused by charge storage and subsequent electric discharge. The calculated changes in integrated solar absorptance generally agree with those reported by other observers. The ultraviolet results confirm that silver coated teflon is stable when irradiated in vacuum and indicate that aluminum coated material undergoes a small decrease in integrated solar absorptance (i.e., an improvement) when so irradiated.

KEY WORDS: aluminum coated teflon, electron degradation, proton degradation, silver coated teflon, teflon film, ultraviolet degradation.

¹NASA/Goddard Space Flight Center, Greenbelt, Maryland

²Electromechanical Research, Inc., College Park, Maryland

INTRODUCTION

Metalized type A FEP¹ Teflon² films, used as second surface mirrors, have shown much promise as suitable thermal control coatings for spacecraft. In particular five mil silver backed FEP film has been chosen, pending the outcome of the experiments now in progress, to be a part of the thermal control coating on the following spacecraft: IMP I, scheduled for launch in October 1970; OAO-B, scheduled for launch in late 1970, S³, scheduled for launch 1 May 1971 and OAO-C. This tentative certification for flight use is based upon findings to date which indicate that teflon second surface mirrors exhibit exceptional ultra-violet stability, and have shown no change in integrated solar absorptance for low energy electron and proton bombardment at total fluxes less than 1×10^{15} particles/cm².

These data are the results of thermal data interpretation obtained from limited flight testing as well as from several series of laboratory studies. Five mil aluminum coated FEP Teflon was flown as the outer layer of the lower thermal shield (sunlit) on Mariner II (Venus), while 1 mil aluminum coated FEP film was used in the same capacity on Mariner V (also Venus). Results from measurements made on this surface from Mariner V indicate an apparent Δa of about 0.043 after 5000 equivalent sun hours.³

On OGO-6, launched in June 1969, two mil silver coated FEP has been used in conjunction with black paint (75% FEP and 25% black paint) as the control surface of the solar facing side of one of the experimental packages. To date (May 1970) this package has performed satisfactorily, and no gross change in the solar absorptance of the teflon has been noted. OGO-6 also has a coatings experiment, one sample of which is five mil silver coated teflon. After 5000 sun hours, performance was still quite satisfactory.⁴ Laboratory investigations with which we are aware have been carried out by: i) The Boeing Co.⁵,

¹FEP is the acronym for the copolymer fluorinated polyethylenepropylene.

²Teflon is a registered trademark of E. I. du Pont de Nemours company.

³W. F. Carrol; "Mariner V Temperature Control Reference Design, Test and Performance," AIAA paper 68-791 presented at AIAA 3rd Thermophysics Conference, Los Angeles, June 1968.

⁴Archie Fitzkee; Private Communication.

⁵L. B. Fogdall and S. S. Cannaday; "Dependence of Thermal Control Coating Degradation Upon Electron Energy." Final report to NASA/GSFC for contract NAS5-11164, May 1969. (Also AIAA paper 69-643); and L. B. Fogdall and R. R. Brown; "Degradation Tests on Thermal Control Materials," Contract NAS5-11219, Final report to NASA/GSFC, May 1970.

ii) The General Electric Co.¹ and iii) Electro-Mechanical Research, Inc.² It is with this latter work that this paper is concerned.

APPARATUS DESCRIPTION AND EXPERIMENTAL PROCEDURE

A. Irradiation System

A diagram of the irradiation system is given in Figure 1. The system can be used for three kinds of irradiation: solar simulation, proton or electron beam, and solar simulation plus proton or electron beam.

The solar simulator consists of an ultraviolet source lamp, focusing optics, and two separate vacuum chambers. The source, a 1000 watt Xenon gas filled arc lamp,³ is focused and collimated by two quartz lenses and transmitted through a quartz window onto a sample holder in the vacuum chamber. The level of radiation at the sample surface is adjustable from zero to five solar constants (one solar constant = 1350 watts/m²) and monitored with a solar cell detector. For solar simulation work alone, the gate valve to the accelerator is closed.

The proton and electron beam source is an RF ion source,⁴ electrostatic collimating lens, and magnetic analyzer. Hydrogen gas is admitted into the source through a palladium leak and ionized by an RF field. Depending upon the applied potential, protons or electrons are drawn from the discharge and formed into a uniform beam. The magnetic analyzer is used to remove neutral atoms from the beam as well as ions of other than the desired charge-to-mass ratio. The uniform beam then passes through a four foot long drift tube and is scanned with a Beam Scanner.⁵ The beam scanner is mounted in a tee as shown in Figure 2, and it can scan either the vertical or horizontal dimension of the beam. The beam finally falls on the sample holder, where flux ranges are available from 1×10^{10} particles/cm²-sec to 1×10^{13} particles/cm²-sec.

¹B. Linder and R. N. Griffin; "Development of Series Emittance Thermal Control Coatings," NASA CR-66820; Final report to NASA/LRC for Contract NAS1-8603, September 1969.

²M. J. Brown and S. G. Park; NASA/GSFC Contract NAS5-9469, completed August 1969; and R. Thompson, B. L. Bean and S. G. Park, NASA/GSFC Contract NAS5-9469, completed May 1970.

³Hanovia model

⁴Ortec, model C-SO-173K

⁵Physicon, Model 512

B. In Situ Measurement System

The In Situ Measurement System consists of the sample holder inside a quartz finger, a double beam recording spectrophotometer,¹ and an absolute integrating sphere.² The sample holder is adjustable so that the sample can be removed from the sphere for a 100% reflectance measurement. For this portion of the measurement, both a reference beam and a sample beam are alternately incident on the barium sulfate coated sphere wall, the sample beam traversing the quartz finger while the reference is positioned so as to miss it entirely. The two beams are diffusely reflected and detected with either a lead sulfide cell or a photomultiplier tube. The spectrophotometer then automatically ratios the two beam energies and plots the result as a function of wavelength. The sample is then lowered into the quartz finger, and the sample beam is now reflected from the sample surface before it hits the sphere wall. The reference beam is still in the same position, and the spectrophotometer again ratios the energies of these two beams.

The vacuum is maintained by a 25 L/S ion pump at the sample end and a 4-inch diffusion pump at the accelerator end. Rough pumping is accomplished with several sorption pumps. Pressures in the 10^{-7} torr range are maintained at all times.

C. Experimental Procedure

The ultraviolet in situ experiments were conducted first. Three initial and three final reflectance measurements were made on each sample: in air, in air in the quartz finger, and in the proper environment. The two environments investigated were vacuum and oxygen. The oxygen was allowed to leak slowly through the system so that a positive pressure of oxygen was always maintained. The samples were five mil teflon coated with aluminum or silver, and they were clamped directly to the water-cooled sample holder. The reflectance measurements were made with the wavelength and detector ranges shown in Table 1; and this table was used for all other reflectance measurements as well. The irradiation rate was at five solar constants, and each sample was irradiated for 120 hours.

The electron beam in situ experiments were conducted using a different accelerator port. The samples used were five mil teflon coated with silver; and these samples were generally clamped directly to a sample holder. Further discussion of the various experiments will follow later in the paper.

¹Beckman Instruments, Inc., Model DK-2A

²Gier Dunkle, Inst.

The proton beam and proton beam plus ultraviolet experiments were done in the same chamber as the earlier ultraviolet experiments. The samples used were five mil teflon coated with silver; and they were glued to 3/4-inch squares of 0.060-inch aluminum with an aluminum filled epoxy putty. These samples were clamped to the sample holder, with several small squares of aluminum foil placed between the 60 mil aluminum mount and the sample holder, as in Figure 3. This method was used to obtain better sample cooling. The ultraviolet irradiation was at a five solar constant rate; and the proton flux was 1×10^{11} p/cm² - sec to 10^{15} p/cm² and then 10^{12} p/cm² - sec to 10^{16} p/cm², with measurements made at 1×10^{15} p/cm², 5×10^{15} p/cm², and 1×10^{16} p/cm².

EXPERIMENTAL OBJECTIVES AND DIFFICULTIES

The proximity of EMR to GSFC has made it possible for close collaboration throughout the entire period of this work. Our original objective was to conduct a systematic investigation of bare, aluminum and silver backed 2, 5 and 10 mil (later changed to 7.5 mil) Type A FEP Teflon film. The initial investigations were simply screening tests, involving short term ultraviolet (240-280 ESH) studies and low energy electron and proton bombardment of the various thicknesses of bare material and of five mil silverized and aluminized teflon, undertaken for orientational purposes and possible indication of the correct approach for a more through investigation.

These screening tests showed that bare and metalized Teflon were stable to short term ultraviolet irradiation, even though a mercury lamp was used instead of the Xenon lamp incorporated with the in situ facility previously described. The preliminary charged particle irradiations indicated quite clearly that teflon when so irradiated tends to turn brown. Measurements showed a general decrease in transmission with the greatest decrease occurring in the ultraviolet region. As the results were similar for the various film thicknesses employed and since five mil film seems to be most desirable from a thermal control viewpoint, the systematic investigation of charged particle effects was limited to a study of five mil silver and aluminum coated material. No quantitative transmission data from these early irradiations is presented here, however, since certain nonuniform patterns were present on these samples, particularly on those irradiated with electrons. This manifested itself, in some cases, by a change in the degree of brownness at various parts of the sample, and in other cases as a browning of only a portion of the sample. This nonuniform pattern was not a regular geometrical figure but looked rather like a shadow graph of a moving starfish.

A subsequent and systematic series of electron and proton irradiations was begun. Alignment of the beam was made and monitored by visual means using a phosphor and the irradiations were made as carefully as possible. No beam nonuniformities were apparent and the current as measured by a Faraday cup, about the same size as the sample and placed adjacent to it, remained steady. Measurements made by moving the Faraday cup with the sample absent showed no beam irregularities. However, the irradiated samples continued to show nonuniform irradiation patterns, albeit to a lesser extent than previously, and the electron irradiated samples were still the worse as viewed by eye. The damage as shown by the spectral reflectance curves was quite extensive at a total dose of 1×10^{16} particles/cm² and the damage as measured by the increase in integrated solar absorptance was greater (sometimes excessively) than that reported by other investigators.

This latter fact, in itself, is no particular reason to suspect the data. But, before this series of irradiations was completed and before we were able to devise a better method for monitoring the beam an electrical storm connected power failure coupled with the failure of a "fail safe" device on the accelerator allowed a backflow of diffusion pump oil into the system. After the subsequent cleaning, a preoperational check showed that a beam misalignment located at the exit of the ion source did, in fact, exist. Because of this, it is our belief that the nonuniformities were due to extraneous particles hitting the sample at angles different from the primary beam. This secondary beam could be reflecting or scattering from a wall of the beam tube and would not necessarily be picked up by the Faraday cup. It is probable that it was picked up but that the resolving power of the cup was too low to show it. For subsequent measurement of charged particle fluxes the idea of a separate Faraday cup was abandoned and the sample holder itself, electrically isolated from the sample chamber, was so used. In any case, we believe that the severe damage observed during this series of measurements was excessive and was due to a radiation dose larger than was intended and what we believed it to be. For this reason the quantitative data obtained during this period will not be reported here.

After accelerator repair further irradiations were held in abeyance until a beam scanner consisting of a vibrating tungsten wire could be installed in the beam tube. With this device it was possible to continuously monitor the beam during irradiation and in this way we were assured that the beam was properly aligned and that it remained reasonably uniform.

Since the problem of beam nonuniformity was most apparent with electrons an anticipated complete rerun of the electron irradiation program was begun, using a flux rate of 3×10^{11} e/cm² - sec. This program was again suspended after two samples had been irradiated with electrons; the first at 10 KeV to a total dose of 1×10^{16} e/cm² and the

second at 25 KeV to a total dose of 2×10^{16} e/cm². When the first sample was removed from the in situ chamber, after completion of the in situ measurement and during the preparation for the air measurement, a small circular brown spot 2-3 mm in diameter was discovered, located at the very center of the circular sample. The in situ measurement included this brown spot, while the air measurements were made both on and off spot. The second sample developed a similarly located small brown spot. Because of this the regular irradiation procedure was suspended until a series of studies pertaining to this brown spot formation could be conducted. These experimental results will be discussed elsewhere.

The browning phenomenon did not occur for proton irradiation but time and financial limitations, created by the unexpected brown spot studies, made it necessary to reduce the planned scope of the proton irradiation studies. We were, therefore, unable to repeat all of those irradiations made prior to the discovery of the misalignment of the beam at its source. Studies were limited to five mil teflon and the irradiation limited to two beam energies, 5 KeV and 25 KeV.

In toto, with the properly aligned and continuously monitored beam, four samples were irradiated with 25 KeV protons and two with 5 KeV protons. Each group of samples was divided in half; one half was irradiated with protons only and the other half was irradiated with simultaneous ultraviolet light and protons. In all cases the proton irradiations were the same for each pair. All samples were proton irradiated at a dose rate of 1×10^{11} p/cm² -sec. to a total dose of 1×10^{15} p/cm²; then one pair of the 25 KeV irradiated samples and the pair of 5 KeV irradiated samples was further irradiated at a rate of 1×10^{12} /cm² -sec. to a total dose of 1×10^{16} p/cm². The simultaneous ultraviolet irradiation was done with an Xenon lamp at an intensity of five suns.

Internal bureaucratic delay in the negotiation of a new contract to continue and finish the experimental effort has precluded the acquisition of any additional data. We can only hope that the experimental program will have been completed in time for the results to be given when this paper is read in September.

Concurrent with the charged particle studies, eight samples (four each of aluminum backed and silver backed) of five mil FEP were irradiated in the in situ chamber at a rate of 5 ultraviolet suns with an Xenon lamp, to a total dose of 600 ESH. Four samples were irradiated in vacuum and four in an oxygen atmosphere. We believe a total ultraviolet dose of 600 ESH is sufficient to confirm the previous work which has indicated that FEP films are very resistant to damage or changes brought about by ultraviolet irradiation. The irradiation in an oxygen environment was undertaken to determine whether or not irradiation in the presence of an active gas would introduce any differences.

EXPERIMENTAL RESULTS

Even though the beam was nonuniform and total dose uncertain, the preliminary charged particle irradiations on bare FEP Teflon films indicated quite clearly that the samples have a tendency to turn brown. The intended flux rate was 3×10^{11} particles/cm² -sec. and total intended dose 1×10^{16} particles/cm²; the actual dose appears to be greater than this figure, but its true value is unknown.¹ This browning was distributed over the irradiated portion of the samples, total dose differences being indicated by a varying degree of brownness. This browning is generally more apparent on the bare samples than on those with metal backing. The widespread browning, when it occurs, appears to be distributed through the material and the material remains clear. Often, however, the surface of charged particle irradiated teflon becomes cloudy or milky in appearance; i.e., a fine white powder appears on the surface which can be wiped off. Its presence often helps obscure the browning. This powder may be depolymerized teflon or a chemical reaction product of the monomer or, even, some residual catalyst. The transmission of the browned teflon decreases slightly in the visible and near infrared, and (as would be expected) much more strongly in the ultraviolet. The ultraviolet cutoff moves noticeably to longer wavelengths.

The results of the ultraviolet (Xenon lamp, 600 ESH exposures) irradiations are: i) five mil silver backed teflon ultraviolet irradiated in vacuum and left in vacuum is essentially stable, showing improvement after re-exposure to a normal laboratory atmosphere; i.e., its reflectance increases. The integrated solar absorptance decreased on the order of 7.5 percent.; ii) five mil aluminum backed teflon ultraviolet irradiated in vacuum and left in vacuum tends to improve slightly; i.e., the reflectance increases overall. The reflectance actually decreases in the ultraviolet but increases in the visible and near infrared. The integrated solar absorptance decreases on the order of six percent. However, when these samples were reintroduced to a normal laboratory atmosphere the reflectance changed, having decreased from its initial value in the ultraviolet and visible regions while remaining essentially the same in the near infrared. The net effect was a degradation. The integrated solar absorptance increased on the order of 5.8 percent; iii) five mil aluminum backed teflon ultraviolet irradiated in oxygen tends to improve; i.e., the reflectance increases. The decrease in integrated solar absorptance was on the order of 8.5 percent; and iv) five mil silver backed teflon ultraviolet irradiated in oxygen

¹For clarification see preceding section.

undergoes a large degradation; i.e., the reflectance decreases. The increase in integrated solar absorptance was on the order of 76 percent.

The spectral reflectance of the two electron irradiated samples, on which the localized central brown spots first appeared, was measured from 0.25 to 2.4 microns. The initial value of the integrated solar absorptance of the 10 KeV irradiated sample, measured in vacuum, was 0.071. After an exposure of 1×10^{15} e/cm² the integrated solar absorptance had become 0.076; and finally, after a total dose of 1×10^{16} e/cm² the integrated solar absorptance had increased to 0.108—an increase of 52 percent. However, this in situ measurement was made prior to the discovery of the central brown spot and, therefore, included it. The samples were remeasured in air (as is customary) off center; i.e., the beam did not strike the central brown spot. The initial and final values of the integrated solar absorptance were 0.070 and 0.089 respectively; representing an increase of 27 percent. The general appearance of the sample off the spot was typical for charged particle irradiated samples and, hence, the latter measurement is probably reasonable. The initial and final values of the integrated solar absorptance for the 25 KeV irradiated sample, measured in air and off spot, were 0.071 and 0.104 respectively; representing an increase of 46 percent. However, this sample received approximately twice the dose of the 10 KeV irradiated sample or about 2×10^{16} e/cm². The electron irradiation studies are not yet complete, but our experiments have indicated that avoidance of the brown spot formation is probably not possible. We shall simply make all measurements off spot and note them as such.

Microscopic examination of the first sample which developed the browning of the central spot showed it to be clear and uniformly brown while the overall surface of the sample was somewhat cloudy. Several additional samples were electron irradiated at varying dose rates in an attempt to determine the nature of this browning and what might be done to prevent it. All of these samples were five mil silver coated teflon.

Sample number one (1) was irradiated with 30 KeV electrons at a rate of 1×10^{12} e/cm² -sec. to a total dose of 1×10^{16} e/cm². A central spot appeared but it was not brown. The entire surface of the sample, except for the central spot, did appear cloudy; i.e., covered with a thin layer of fine white powder. The central spot itself looked, upon microscopic examination, as if the electron beam had not struck it at all.

Sample number two (2) was irradiated with 30 KeV electrons at a rate of 1×10^{13} e/cm² -sec. to a total dose of 1×10^{16} e/cm². A centrally located, extremely bright, white opaque spot was formed. It had no visible structure. No attempt was made to determine its thickness or if it were composed of a white powder which could be wiped off.

Sample number three (3) was covered with a coarse mesh screen which was grounded. This screen was in contact with the metal retaining ring clamping the sample, and thereby, to the sample holder itself. This sample was irradiated with 30 KeV electrons at a dose rate of $1 \times 10^{13} \text{ e/cm}^2 \text{ -sec.}$ to a total dose of $1 \times 10^{16} \text{ e/cm}^2$. The grid pattern of the screen was quite visible on the sample surface. In the center of a majority of the grid squares a brown spot had been formed. Under microscopic examination the central brown spots do not appear clear and dendritic patterns are quite visible around each of these spots. These dendritic patterns are similar to the well known Lichtenberg figures created by electrical discharge in insulators. In fact, this is precisely what they are. Bridges or conducting paths exist across the gaps left by the grid lines. It is indisputable that these paths have been created by electrical discharge.

Sample number four (4) was covered with a coarse mesh screen and it and the sample holder were biased at +300 volts during the irradiation. The sample was irradiated with 30 KeV electrons at a rate of $1 \times 10^{13} \text{ e/cm}^2 \text{ -sec.}$ to a total dose of $1 \times 10^{16} \text{ e/cm}^2$. No centrally located brown spots were formed this time within each grid pattern; in fact, it appeared that little or no damage exists near the center of each grid pattern. Damage does appear to be most severe near the grid lines themselves. Dendritic pattern or electrical discharge paths exist around most grid markings: These are very large in some cases and bridges exist across the grid lines.

Sample number five (5) was irradiated with 25 KeV electrons at a rate of $1 \times 10^{12} \text{ e/cm}^2 \text{ -sec.}$ to a total dose of $1 \times 10^{16} \text{ e/cm}^2$. A small barely visible brown spot exists in the center of the sample and the sample appears cloudy overall, but clear.

Sample number six (6) was covered by a coarse mesh screen placed 2-3 mm in front of but not touching it. The sample holder and the screen were grounded. The sample was irradiated with 25 KeV electrons at a rate of $3 \times 10^{11} \text{ e/cm}^2 \text{ -sec.}$ to a total dose of $1 \times 10^{16} \text{ e/cm}^2$. The entire sample now showed an overall browning. The grid outlines of the screen were visible but were a darker shade of brown than were the central portions of each grid square. Surface scratch marks developed dendritic growth patterns extending outward and normal to the scratch marks; these dendritic patterns were not present on the same scratch marks wherever they extended into a portion of the sample which was not irradiated. The structure stopped abruptly at the boundary between irradiated and unirradiated parts of the sample. This structure looks as if electrical discharge occurred from the teflon itself to the surface scratches which acted as a conducting path to ground. We know that there is visible arcking of the sample during irradiation because a view port was installed during a portion of these side experiments so that the samples could be observed during irradiation. This arcking coincided

with a jump in the instantaneous current being collected by the Faraday cup and measured. At intervals of from five to thirty seconds (depending upon the irradiation rate) the current measuring indicator would jump suddenly to a higher value, perhaps fluctuate a bit for a second or two and then settle down to its steady state value. We have no alternative but to conclude that electrons are being stored in the teflon. Some continually leak off, to be sure, to be captured by the Faraday cup, and much of this is probably via surface conduction. However, enough charge is apparently stored to create local electric fields of enormous values; values so large that discharge is inevitable. Sufficient repetition of this gives rise to the dendritic patterns or Lichtenberg figures in the teflon, and may be causing the browning of the sample center. Presumably, at low enough flux rates, the leak current would be sufficiently high to prevent significant charge accumulation. Visual observation of a decreased amount of arcking at lower flux rates confirms this. If, however, this leak current is predominately due to surface conduction caused by vacuum system contaminates it may not occur in space unless the contaminates found there due to the outgasing products of the spacecraft itself are sufficient. On the other hand, space bombardment is predominately neutral beam outside the Van Allen belts and no localized fields may ever materialize.

The results of the proton and simultaneous proton-ultraviolet irradiations are presented in Table 2.

These results tend to confirm the presumption that damage is energy dependent, certainly for low proton energies. The 25 KeV data seem to indicate an anti-synergistic effect; i. e., that simultaneous ultraviolet and protons tends to retard the damage that occurs with protons alone. Certainly, no positive synergistic effect is evident. However, the 5 KeV data do not support such a conclusion. With the limited statistical sample herein represented it is impossible to say. We hope to have more to say upon completion of the work.

TABLE 1

WAVELENGTH RANGE (nm)	DETECTOR	LAMP
250 - 360	Lead Sulfide	Xenon
350 - 750	Photomultiplier	Tungsten
750 - 2500	Photomultiplier	Tungsten

TABLE 2

	Integrated Solar Absorption		Measured in Vacuum	
	Sample #24 25 KeV protons	Sample #25 25 KeV protons	Sample #26 5 KeV protons	Sample #27 5 KeV protons
Type	5 mil Silver	5 mil Silver	5 mil Silver	5 mil Silver
Initial	0.074	0.079	0.071	0.072
1×10^{15} p/cm ²	0.079	x	0.072	x
1×10^{15} p/cm ² plus uv (13.9ESH)	x	0.079	x	0.071
5×10^{15} p/cm ²	0.083	x	0.075	x
5×10^{15} p/cm ² plus uv (19.4ESH)	x	0.081	x	0.075
1×10^{16} p/cm ²	0.092	x	0.079	x
1×10^{16} p/cm ² plus uv (26.4ESH)	x	0.095	x	0.082

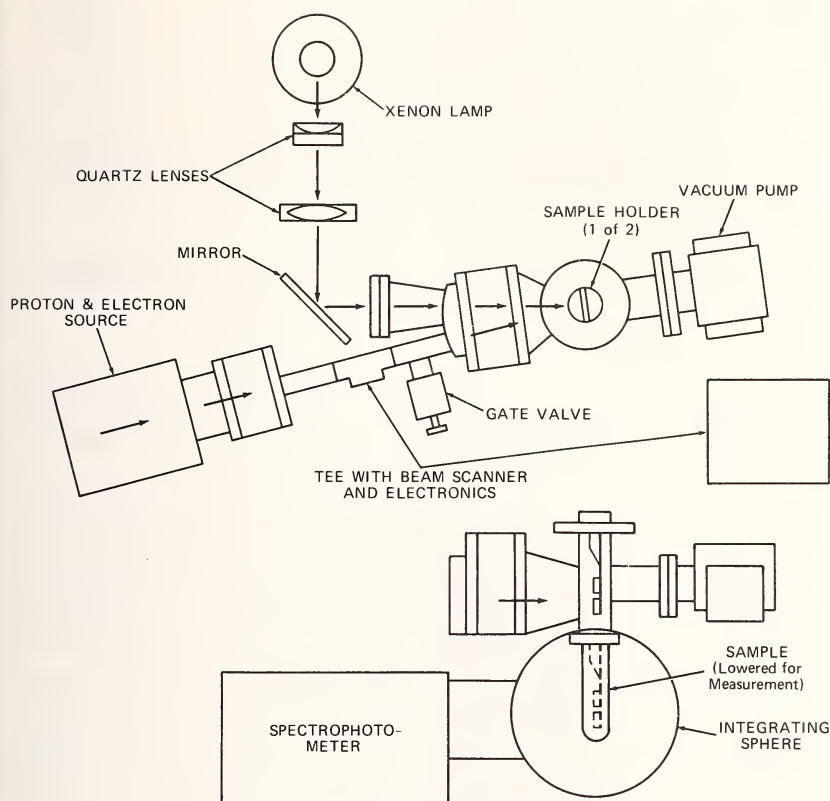


Fig. 1—Test facility for in situ measurement

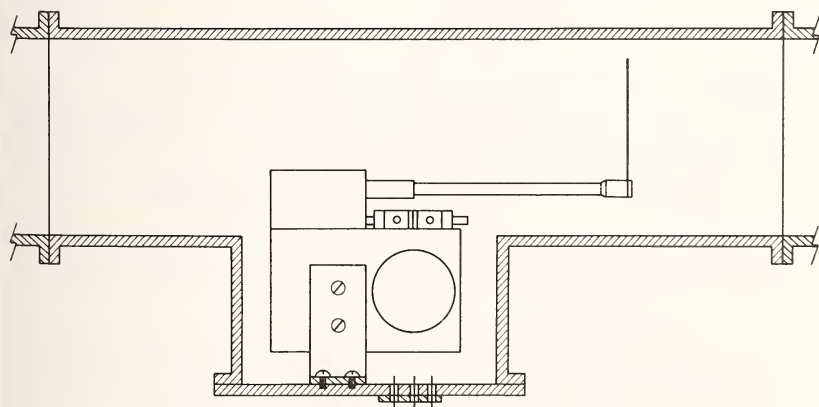


Fig. 2—Beam scanner installed in facility

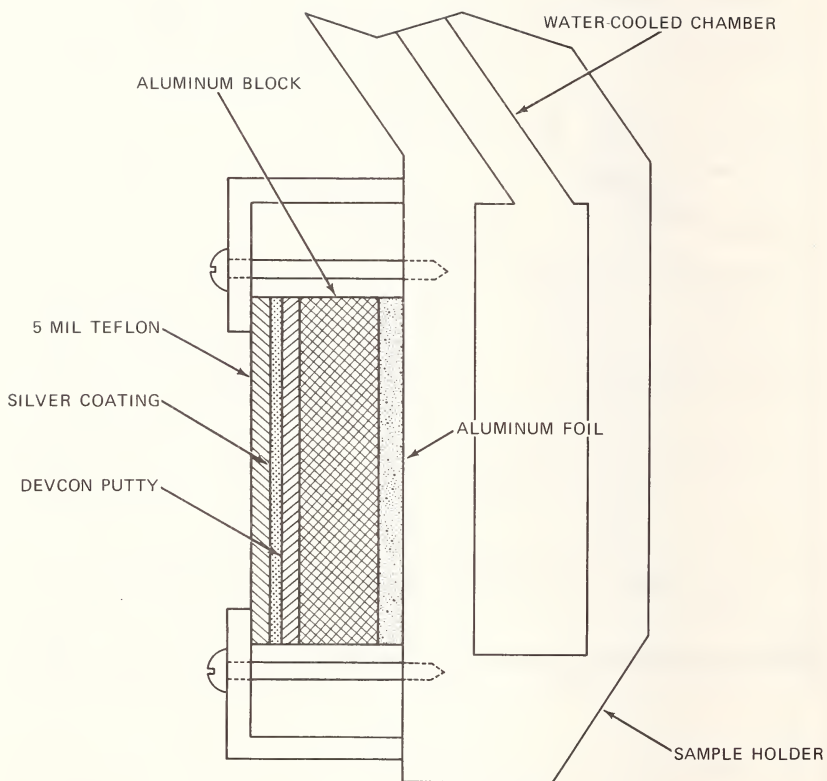


Fig. 3—Cross section of sample and sample holder

THE INTERACTION OF LOW ENERGY ELECTRONS WITH
POLYMERIC PERFLUORINATED ETHYLENEPROPYLENE (FEP)⁽¹⁾

John B. Schutt¹

REFERENCE: Schutt, John B., "The Interaction of Low Energy Electrons With Polymeric Perfluorinated Ethylenepropylene (FEP)," ASTM/IES/AIAA Space Simulation Conference, 14-16 September 1970.

ABSTRACT: Photomicrographs are presented showing the effects of 30 Kev electrons on FEP. Depicted are Lichtenberg patterns, bubbles and a buckling effect. The attempt to explain these observations is derived from a theoretical analysis based on a diffusion mechanism for charge flow using beam current as a source term. The solution is used to demonstrate that charge is stored centrosymmetrically with respect to ground. These effects are discussed in terms of an "electrolysis" mechanism resulting from charge storage and beam energy thermalization. Explicit expressions are given for surface charge storage and voltage across the sample resulting from such charge accumulation. Buckling is treated from a thermodynamic basis using the Helmholtz free energy and assuming the distortion develops isothermally. "Electrolysis" is postulated via a mechanism selecting the tertiary carbon as the active site for mobile moiety generation.

The usefulness of optical data for purposes of thermal design taken from samples irradiated with low energy electrons in the laboratory is questioned. Because FEP is an electrical insulator, these experiments must, therefore, be carried out in a neutral laboratory environment, or be characterized in the space environment from carefully designed electrical experiments.

KEY WORDS: degradation mechanising, electron bombardment, electron degradation, polymeric perfluorinated ethylenepropylene. proton bombardment, thermal control coatings

¹Goddard Space Flight Center, Greenbelt, Maryland 20771

(¹) The numbers in parentheses refer to the list of references appended to this paper.

Introduction

Few spacecraft thermal control materials have received as much undocumented attention as perfluorinated polyethylenepropylene (FEP). This unusual ascendancy of FEP into prominence occurred because encouraging thermal information obtained from flight data^(2,3) were available prior to laboratory tests qualified from optical measurements.

That the performance of metallized FEP as a second surface mirror appreciably surpasses white paints cannot be doubted;⁽⁴⁾ yet, its qualification in the laboratory cannot be judged as altogether routine. For example, irradiating with ultraviolet photons or 2 - 30 Kev protons gives reproducible data under carefully controlled conditions, whereas irradiations carried out with electrons characterized similarly to their proton counterpart will not give a degradation sufficiently uniform for optical measurement. This treatment provides an elucidation of this "unconventional" behavior of FEP toward electrons.

In the following section, experimental observations of electron irradiated FEP are presented and discussed with the detailed objective of providing a basis for a theoretical development of the charge storage function $c(r, z, t)$. Subsequently, the stability problem is discussed in a heuristic manner using some notions of control theory and simple electric circuits. A brief thermodynamic description is presented and a solution to the complete problem is outlined accounting for chemical reactions or "electrolysis" of the film. Finally, recommendations are put forth regarding electron stability testing of electric insulators.

Experimental Observations

Perfluorinated polyethylene copolymer units comprise the FEP⁽⁵⁾ network in a manner yielding a material susceptible to sublimation. That FEP is indeed subject to vaporization, resulting from thermalization of a 30 Kev proton beam, is shown in Figure 1. The area surrounding the puncture contains proton beam generated charge rearrangements detectable by optical means as additional ultraviolet absorption sites having the usual long wavelength cutoff extending deep enough into the visible portion of the spectrum to create a brown color. The puncture occurred near the center of unmetallized material or at the point furthest from ground. The experiment was

(2,3,4,5) The numbers in parentheses refer to the list of references appended to this paper.

repeated using a grid placed about 30 mils above silver coated 5 mil FEP. Experiments were performed with both grid and sample holder at ground potential and with the grid at +300 volts above ground. Results were similar and reproducible for both cases. Figure 2 shows the configuration. Figure 3 is a photograph of the area comprising one section of the grid.

Although not clearly shown in Figure 3, the mesh centered portions of the FEP generate ultraviolet centered optical changes possessing absorption tails extending far enough into the visible portion of the spectrum to show the familiar brown color. Again, heating appeared to take place in portions furthest below ground electrically. Clearly visible are dendrite-like Lichtenberg patterns⁽⁶⁾ emanating from the center of the sample and extending toward portions shadowed from the electron beam by the grid. Figure 4 reveals the existence of these dendritic patterns amid clusters of bubbles. It appears likely therefore that charge is stored at least in the neighborhood of the surface of the material, preferably at its geometric center relative to the mesh. Referring again to Figure 3, it is apparent that the surface of the sample is not in relative focus owing to the buckled central region where charge storage and thermalization occur. Figure 5 shows this effect schematically. Notice that the metallic film maintained its adhesion to the FEP.

In summary then, it appears reasonable to assume that 5 mil FEP whether metallized or not can at least store charge in the neighborhood of its surface and in a region furthest from ground. The conversion of beam kinetic energy into thermal energy in the presence of stored charge gives rise to an "electrolysis" or bubbling of the material and, therefore, the formation of dendrites capable of carrying charge to ground; ground itself being made more accessible via the grid by means of a buckling mechanism. Figure 6 depicts the veined network common to virtually all beam shadowed areas where charge also arcs to ground. It is the charge storage problem and its relationship to the grounding of the sample that forms the basis for the following section.

The Charge Storage Problem

The phenomenology of electron storage in electrical insulators and dielectrics can be treated in a manner formally identical to a

⁽⁶⁾ The numbers in parentheses refer to the list of references appended to this paper.

corresponding thermal problem. Our starting point is, therefore, the diffusion equation:

$$\frac{\partial c(r, z, t)}{\partial t} = D \nabla^2 c(r, z, t) + \nabla F(z) \quad (1)$$

where:

$c(r, z, t)$ = number of charges at the point (r, z, t) ,

t = time,

D = a diffusion constant and,

(r, z) = an arbitrary point in cylindrical space.

Because we take for simplicity that charge is incident normal to the surface at $z = 0$, the angular dependency is automatically eliminated from the equation. The function $F(z)$ or source term is the solution of

$$-\frac{dF(z)}{dz} = kN_0 F(z), \quad (2)$$

the usual penetration equation governing spatial dependencies normal to the incident particles. The parameter k represents a number characterizing the capture cross-section of the storage site, while N_0 is the site density. Solving (2) and substituting into (1) gives

$$\frac{\partial c}{\partial t} = D \nabla^2 c - N_0 k F_0 e^{-kN_0 z} = D \nabla^2 c - f(z) \quad (3)$$

where F_0 is proportional incident particle momentum. We obtain the solution of (3) as the sum of two functions,⁽⁷⁾

$$c(r, z, t) = u(r, z) + w(r, z, t), \quad (4)$$

with $w = 0$ when $z = 0$. It follows that

$$\frac{\partial^2 u}{\partial r^2} + \frac{1}{r} \frac{\partial u}{\partial r} + \frac{\partial^2 u}{\partial z^2} - \frac{f(z)}{D} = 0 \quad (5)$$

⁽⁷⁾The numbers in parentheses refer to the list of references appended to this paper.

and

$$\frac{1}{D} \frac{\partial w}{\partial t} = \frac{\partial^2 w}{\partial r^2} + \frac{1}{r} \frac{\partial w}{\partial r} + \frac{\partial^2 w}{\partial z^2} \quad (6)$$

A solution to (5) is sought in the form

$$u = \sum_i \phi_i(r) \psi_i(z) \quad (7)$$

with $\phi_i(r)$ forming an orthonormal set. Substitution of (7) into (5) shows that the ϕ_i 's are Bessel functions of zero order with ψ_i being a solution of

$$\frac{\partial^2 \psi_i}{\partial z^2} - \left(\frac{\alpha_i}{R} \right)^2 \psi_i = \frac{1}{\alpha_i} \frac{J_1(\alpha_i)}{D} \frac{2 f(z)}{J_0^2(\alpha_i) + J_1^2(\alpha_i)} = g(z) \quad (8)$$

where α_i is a zero of $J_0(\mu R)$, since the sample is assumed at ground potential for $r = R$. The parameter μ is a separation constant. $Y_0(\mu r)$ was eliminated as a solution, since $c(0, z, t)$ must be finite. The Greens function solution of (8) was obtained using the usual symmetric boundary conditions,

$$G_{<}(0) = 0 \text{ and } G_{>}(d) = 0, \quad (9)$$

where d is the thickness of the sample. The result is

$$G = \theta(\xi - z) \frac{\sin h \mu (d - \xi)}{\mu \sin h \mu d} \sin h \mu z + \theta(z - \xi) \frac{\sin h \mu \xi}{\mu \sin h \mu d} \sin h \mu (d - z) \quad (10)$$

$$= G_{<}(\xi, z) + G_{>}(z, \xi),$$

with θ representing the Heaviside step function. The particular solution to (8) is then given by

$$\psi_P(z) = \int_0^z G_{<}(\xi, z) g(\xi) d\xi + \int_z^d G_{>}(z, \xi) g(\xi) d\xi$$

$$\begin{aligned}
&= \frac{M \sinh \mu z}{2\mu \sinh \mu d} \left[\frac{e^{\mu d}}{(\mu + kN_0)} (1 - e^{-(\mu + kN_0)z}) + \frac{e^{\mu d}}{(kN_0 - \mu)} \right. \\
&\quad \left. (1 - e^{-(kN_0 - \mu)z}) \right] + \frac{M \sinh \mu(d-z)}{2\mu \sinh \mu d} \left[\frac{1}{(kN_0 - \mu)} \right] e^{-(kN_0 - \mu)z} - e^{-(kN_0 - \mu)d} \\
&\quad + \frac{1}{(\mu + kN_0)} (e^{-(\mu + kN_0)z} - e^{-(\mu + kN_0)d}) \quad (11)
\end{aligned}$$

where

$$M = \frac{1}{\alpha_i} \frac{J_1(\alpha_i)}{D} \frac{2F_0 N_0 k}{J_0^2(\alpha_i) + J_1^2(\alpha_i)}$$

The homogeneous solution is of the form

$$\psi_H = \bar{A} e^{\mu z} + \bar{B} e^{-\mu z}$$

with the total solution written as

$$\psi_T = \psi_H + \psi_P \quad (12)$$

or

$$\psi_T = \sum_i \frac{2}{\alpha_i} \frac{J_1(\alpha_i)}{J_0^2(\alpha_i) + J_1^2(\alpha_i)} \frac{F_0}{DkN_0} \left[1 + \frac{e^{-\mu d}}{\sinh \mu d} \sinh \mu z \right] + \psi_P \quad (13)$$

where ψ_P is given by equation (11). The complete solution is now reduced to the form

$$c(r, z, t) = \sum_i \left(\psi_{H_i} + \psi_{P_i} \right) \phi_i + w, \quad (14)$$

where the solution for w remains to be determined.

If we choose

$$w(r, z, t) = w_1(r) w_2(z) w_3(t) \quad (15)$$

then

$$w_1 = A_1 J_0(\mu r) + B_1 Y_0(\mu r)$$

and $B_1 = 0$ since w_1 must be finite for $r = 0$, and as before $J_0(\mu R) = 0$ to satisfy our grounding condition. Therefore,

$$w_1 = A_1 J_0(\alpha_i x)$$

with $0 < x < 1$ in place of $0 < r < R$. Continuing the partitioning to obtain equations for w_2 and w_3 , we obtain

$$\frac{\partial^2 w_2}{\partial z^2} + \lambda^2 w_2 = 0 \quad (16)$$

and

$$\frac{1}{w_3 D} \frac{\partial w_3}{\partial t} = -\lambda^2 - \mu^2 \quad (17)$$

If we write

$$w_2 = A_2 \sin \lambda z + B_2 \cos \lambda z$$

and

$$w_3 = A_3 e^{-(\lambda^2 + \mu^2) D t}$$

equation (15) becomes

$$w = \sum_i e^{-(\lambda^2 + \mu^2)Dt} J_0(\alpha_i r) \left[A_2' \sin \lambda z + B_2' \cos \lambda z \right] \quad (18)$$

The constant B_2' is determined from the grounding requirement that $w = 0$ when $z = d$ for $0 < x < 1$ ($0 < r < R$) giving $B_2' = 0$. The parameter λ is determined from the zeros of $\sin \lambda d$ or

$$\lambda = 2n\pi/d$$

and

$$w(r, z, t) = \sum_i \sum_n A_2 e^{-\left\{ \left(\frac{2n\pi}{d} \right)^2 + \left(\frac{\alpha_i}{R} \right)^2 \right\} Dt} J_0(\alpha_i k) \sin \left(2n\pi \frac{z}{d} \right) \quad (19)$$

Thus far we have demonstrated that our charge storage solution can be put into the form

$$\begin{aligned} c(r, z, t) = & \sum_i \left\{ \left(\bar{A}_i e^{\mu z} + \bar{B}_i e^{-\mu z} \right) + \psi_P J_0(\alpha_i k) \right\} \\ & + \sum_i \sum_n A_{ni} e^{-\left\{ \left(\frac{2n\pi}{d} \right)^2 + \left(\frac{\alpha_i}{R} \right)^2 \right\} Dt} J_0(\alpha_i \psi) \sin \left(\frac{2n\pi z}{d} \right) \end{aligned} \quad (20)$$

To determine \bar{A}_i , \bar{B}_i , and A_2 we apply our grounding condition

$$c(r, d, t) = 0, \quad 0 < r < R, \quad 0 < t < \infty \quad (21)$$

followed by the surface requirement

$$c(r, 0, t) = F_0/kN_0 D, \quad 0 < r < R, \quad 0 < t < \infty \quad (22)$$

and finally the initial condition that the sample carries no initial charge, or

$$c(r, z, 0) = 0. \quad 0 < r < R, \quad 0 < z < d \quad (23)$$

Applying the boundary conditions (21), (22), and (23) in the order listed gives

$$\bar{A}_i = \frac{J_1(\alpha_i)}{\alpha_i} \frac{F_0 e^{-\mu d}}{k N_0 D \sinh \mu d} \frac{1}{\{J_0^2(\alpha_i) + J_1^2(\alpha_i)\}}$$

$$B_i = -A_i e^{2\mu d}$$

and

$$A_{ni} = \frac{2F_0 J_1(\alpha_i)}{k N_0 D \alpha_i \{J_0^2(\alpha_i) + J_1^2(\alpha_i)\}} \frac{1}{(2\pi n) \left\{ \frac{(\alpha_i)^2}{R} + \left(\frac{2\pi n}{d} \right)^2 \right\}} \quad (24)$$

with A_i being determined from a Fourier-Bessel's expansion and A_{ni} from both Fourier and Fourier-Bessel's expansions.

Discussion of the Relationship Between Charge Storage and Stability

There exist two conduction paths for the escape of absorbed charge to ground: along the surface and through the bulk. Brief consideration determines that these routes can be represented most simply as two resistances connected in parallel. Let us write expressions for local resistances in the form

$$R_{\text{bulk}} = R_z = \frac{\rho(d-z)}{\pi r^2} \quad \text{and} \quad R_{\text{surface}} = R_r = \frac{\rho(R-r)}{2\pi r z}$$

where the locality is given by (r, z) for a sample of size (R, d) and ρ is the resistivity. Combining these expressions in parallel, the local equivalent resistance, $R(r, z)$ becomes

$$R(r, z) = \frac{\rho}{\pi r} \frac{(d-z)(R-r)}{2z(d-z) + r(R-r)} \quad (25)$$

Taking the limit for $z \rightarrow 0$ we obtain

$$R(r, 0) = R \lim_{z \rightarrow 0} = \frac{\rho d}{\pi r^2},$$

while if in addition the limit for r approaching zero is taken,

$$R(0, 0) = R(r, 0) = \infty, \lim_{r \rightarrow 0}$$

a divergent expression results.⁽⁸⁾ In both cases the local resistance about the origin gives a divergent result, suggesting that the closer an electron is to the origin the more difficult its migration to ground becomes. Hence the conjecture that charge is stored in the center of the sample or farthest from ground appears to be a reasonable one. Using this approach, however, the divergence of $R(0, 0)$ cannot be removed; but, having anticipated this result the diffusion equation was solved in the previous section to remove this divergence. From equations (14) and (15), the storage function is most compactly written in the form

$$c(r, z, t) = \sum_i \phi(\alpha_i x) \{ \psi_H(z) + \psi_P(z) \} + \sum_i \sum_n \phi(\alpha_i x) w_2(z) w_3(t), \quad (26)$$

where use has been made of the identity $\phi(\alpha_i x) = w_1(\alpha_i x)$. Our boundary condition on the radial solution to equation (15), demanding the convergence of $c(r, z, t)$ at $c(r, 0, t)$ and $c(0, 0, t)$, eliminated the divergent Neumann function. Inspection of equation (11) for ψ_P , equation (13) for ψ_H , and the result $J_0(0) = 1$, gives an expression for the number of charges stored in the neighborhood of the origin:

$$c(0, 0, t) = \sum_i \psi_H(\alpha_i) + \psi_P$$

⁽⁸⁾The numbers in parentheses refer to the list of references appended to this paper.

$$= \sum_i \frac{2}{\alpha_i} \frac{J_1(\alpha_i)}{\{J_0^2(\alpha_i) + J_1^2(\alpha_i)\}} \frac{F_0}{DkN_0} \quad (27)$$

$$+ \frac{M}{2\mu} \left[\frac{1}{(kN_0 - \mu)} (1 - e^{-(kN_0 - \mu)d}) + \frac{1}{(kN_0 + \mu)} (1 - e^{-(kN_0 + \mu)d}) \right]$$

with M being given in equation (11).

By inspecting the above result the generalized surface charge storage expression is obtained:

$$c(r, 0, t) = \sum_i c(0, 0, t) J_0(\alpha_i x). \quad (28)$$

Equation (26) shows that the charge stored at (0,0) is indeed finite and that

$$\bar{F} R(r, 0) = e c(r, 0) C \quad (29)$$

where

e = electronic charge,

C = surface capacitance at $(r, 0)$, and

\bar{F} = electron current.

Equations (27) and (28) show that $\bar{F} R(0, 0) = V(0, 0)$ is finite.

However, $R \sim \rho = 1/\sigma$

where σ is the conductivity. Writing

$$\sigma = c(0, 0, t) e \mu_e$$

where e and μ_e represent electronic charge and mobility, respectively, we can conclude that $R(0, 0)$ is finite. Next we wish to calculate the number charges stored on the surface of the sample. The result is obtained by integrating $c(r, 0, t)$ over the surface of the sample:

$$\begin{aligned}
c_s &= \sum_i \int c(0,0,t) J_0(\alpha_i x) r dr d\theta \\
&= 2\pi R^2 c(0,0,t) \sum_i \frac{J_1(\alpha_i)}{\alpha_i}
\end{aligned} \tag{30}$$

The number of charges per unit area is then given by

$$\bar{c}_s = \frac{c_s}{\pi R^2} = 2 c(0,0,t) \sum_i \frac{J_1(\alpha_i)}{\alpha_i} \tag{31}$$

Since the voltage supported by a capacitor is given by definition as

$$V = qC, \tag{32}$$

where q and C are charge and capacitance, respectively, we automatically have an expression for the voltage across any undamaged sample,

$$V = e c_s C, \tag{33}$$

a quantity subject to calculation and measurement.

At the on set of this section, we discussed the conduction paths as a parallel arrangement of resistances, purposefully neglecting their respective path capacitances. It is clear from the photographs discussed in the first section, that material instabilities can be generated under quite moderate irradiation conditions. Further, it has been suggested that thermalization and charge storage cooperatively induce material changes. In a heuristic manner, then, we suggest that the initial charge storage sites become inductively altered once saturation has been reached, and propose a black box scheme to model the course of events. Shown in Figure 7 is a simple feedback loop represented by the transfer function $Y_2(p)$ or a time delayed degradation mechanism serving to modify the voltage generated across the circuit with transfer function $Y_1(p)$, the initial charge storage mechanism. The circuit transfer function $Y_0(p)$ is given by

$$Y_0(p) = \frac{V_0}{V_s} = \frac{Y_1(p)}{1 - Y_1(p) Y_2(p)}, \quad (34)$$

where the stability conditions are related to the voltage discharge frequency (p) to ground via the grid. It follows that stability will be determined by the zeros and poles of the function

$$Y_1(p) Y_2(p) - 1 = 0$$

The transfer functions are accordingly generated from the circuit analogy selected to represent the physical situation. This aspect of the problem will not be carried further here, but rather reserved for a future publication.

Before concluding this section, by reviewing the problem from a mechanisms point of view, the buckling phenomenon will be briefly discussed using a thermodynamic approach. As a starting point we assume that the occurrence of buckling could take place isothermally, that is,

$$\left(\frac{\partial F}{\partial \nu} \right)_T = -p_v + \mu \left. \frac{\partial c(r, z, \infty)}{\partial \nu} \right|_T + \frac{1}{2} \epsilon \left(\frac{V}{d} \right)^2 \quad (35)$$

where

F = Helmholtz free energy,

p_v = vapor pressure of the FEP,

μ = chemical potential,

$c(r, z, \infty)$ = terminal number of stored charges ($t = \infty$),

ν = volume, and

ϵ = dielectric constant.

Next we make the substitution for the dielectric constant

$$\epsilon = 1 + 4\pi P \frac{d}{V} \quad (36)$$

and take

$$\left(\frac{\partial F}{\partial \nu}\right)_T = 0$$

to obtain

$$p_v = \mu \frac{\partial c(r, z, \infty)}{\partial \nu} \Big|_T + \frac{1}{2} \left(\left(\frac{V}{d} \right)^2 + 4\pi P \frac{V}{d} \right), \quad (37)$$

where P is the polarization. Equation (37) expresses the charge buckling effect in terms of the vapor pressure p_v , of the expanded surface. To rewrite the equation in terms of the vapor pressure p_∞ of the undeformed material and the surface energy, use is made of the relationship between surface pressure and curvature:

$$p_v = p_\infty - \frac{\gamma}{R_1} - \frac{\gamma}{R_2} \quad (38)$$

where γ is the surface energy and R_1 and R_2 the principal radii of curvature. Our final result is

$$\mu \frac{\partial c(r, z, \infty)}{\partial \nu} \Big|_T = p_\infty - \gamma \left\{ \frac{1}{R_1} + \frac{1}{R_2} \right\} + \left(\frac{V}{d} \right)^2 + 2\pi P \frac{V}{d} \quad (39)$$

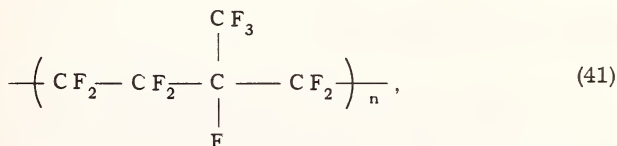
If FEP is "electrolyzed" under the influence of an electron beam and an expansion or buckling results, the surface curvature effect enters in a way such that the vapor pressure of the material will tend to be maintained at its original level. To simplify the argument we take $p_\infty = 0$ and $R_1 = R_2$ or

$$\mu \frac{\partial c}{\partial \nu} \Big|_T = -\frac{2\gamma}{R_1} + \left(\frac{V}{d} \right)^2 + 2\pi P \frac{V}{d} \quad (40)$$

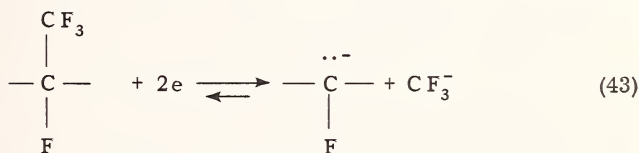
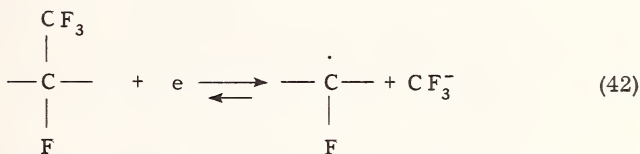
when

$$\frac{2\gamma}{R_1} > 2\pi \frac{PV}{d} + \left(\frac{V}{d} \right)^2$$

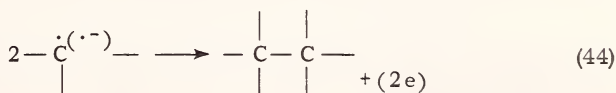
Then $\mu \frac{\partial c}{\partial \nu} \Big|_T < 0$, and the tendency toward volume charge storage is diminished and γ becomes a factor in the behavior. On expansion d will increase allowing for some increase in P and V if field strength is maintained. The relationship of the surface effect to bulk storage suggests buckling and charge escape to the grid is manifested by an "electrolysis" effect. We are now prepared to relate the stability problem to the chemical nature of FEP. Quite generally we can write the copolymer in the form



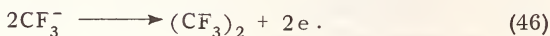
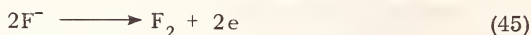
assuming the ethylene and propylene units are combined in equimolar amounts. If FEP stores appreciable charge prior to damage, then a small degree of unsaturation may be present. Next the tertiary carbon becomes suspect as a source of charge imbalance by virtue of the known stability of the carbanion. We are led to assume



and similarly for extraction of the fluoride moiety. A "crystallization" or cross linking reaction can be written for tertiary radicals,



with the products $\text{CF}_3^{(-)}$ and $\text{F}^{(-)}$ becoming suitable candidates for transporting charge to the grid⁽⁹⁾, where discharge or the "electrolysis" effect is formally completed:



Summary and Conclusions

Throughout this paper the assumption of beam uniformity and stability was maintained. That electron beam stability can be a problem is well known by experimenters in this field. However, it is felt that the paths to ground are the most critical aspect in the work, otherwise the observation of buckling might not have been made. Clearly, the grounding paths and physical effects in the material are in turn related to the charge storage and beam energy thermalization effects. Vaporization is probably related to the proclivity of hydrogen deficient organic materials containing side groups with small steric factors toward sublimation, (this behavior is related to the well known flammability problem). FEP is a highly charge compensated material by virtue of the orientation of its bond dipoles. That these orientations are easily disturbed is evidenced by the well known T^{-1} dependency.⁽¹⁰⁾ Combined with the charge storage property a temperature effect becomes reasonable.

Examining the buckling effect once more, the dominance of surface storage over bulk storage is suggested, since this distortion moved the surface of the sample closer to the grid or suspended ground as opposed to the bulk ground through the silver to the substrate. Heating combined with charge repulsion can then be used to justify the expansion. Once distorted, charged particle diffusion channels may be formed and the "electrolysis" effect may proceed. The observed browning effect follows as the result of FEP moiety reorientation and "electrolysis".

The electron irradiation of electrical insulators cannot be treated from an experimental approach in a routine manner. A spacecraft passes through space carrying a neutral charge cloud defined with respect to some finite volume, and departure from electrical neutrality

^(9,10) The numbers in parentheses refer to the list of references appended to this paper.

over the surface of this cloud likely exists only as minor electrical fluctuations. Consequently, it appears reasonable to conjecture that for laboratory test data on electron irradiation to be meaningful, data should most probably be obtained using a neutral beam environment. If laboratory simulation of low energy electron and neutral charge distribution fluctuation effects develop into a formidable task, then data from carefully designed spacecraft experiments provide an attractive alternative for two reasons: first, meaningful thermal design data are obtained and second, realistic inputs are obtained for materials development.

Acknowledgment

The author wishes to express his appreciation to Messers. Rebne Thompson, Segun Park and Bruce Bean of Electro-Mechanical Research Incorporated of College Park, Maryland, for helpful discussions. Their elaboration of experimental observations not readily recorded photographically were instrumental in establishing the scope of this paper.

References

1. The experimental portion of this work was supported by funds supplied by the OAO Project Office, Goddard Space Flight Center, Greenbelt, Maryland. Data were obtained under Contract No. NAS 5-9469 with the Electro-Mechanical Research Corporation, College Park, Maryland.
2. Carrol, W. F., "Mariner V Temperature Control Reference Design, Test and Performance", AIAA paper 68-791 presented AIAA 3rd Thermophysics Conference, Los Angeles, June 1968.
3. Private communication from Miss Archie Fitzkee, Thermal Control Section, Thermophysics Branch, of OGO-6 Flight Data on Silvered 5-MIL FEP.
4. Private communication from Miss Archie Fitzkee, Thermal Control Section, Thermophysics Branch, of OGO-6 Flight Data on Silicated Treated Zinc Oxide in Methyl Silicone.
5. Usually referred to as FEP Teflon Type A, Teflon is a Registered trademark of E. I. duPont de Nemours Company.
6. Gross, B. and Murphy, P. V., "Electrical Radiation Effects in Solid Dielectrics," "Nukleonik", 2. Band 7. Heft, 1961, S. 279-285.

7. Carslaw, H. S. and Jaeger, J. C., "Conduction of Heat in Solids", Second Edition, Clarendon Press (Oxford), London, 1959, pp. 29-30.
8. This difficulty may be overcome if $\frac{1}{r} \frac{\partial}{\partial r} \left(r \frac{\partial \rho}{\partial r} \right)$ exists, a result suggesting solution via a diffusion mechanism.
9. Lilly, A. C. and McDowell, J. R., "High-Field Conduction in Films of Mylar and Teflon", Journal of Applied Physics, Vol. 39, 1968, pp. 141-147.
10. Debye, P. D., "Polar Molecules", Rheinhold Press, New York, 1929, pp. 27-30.



Figure 1. Photomicrograph of FEP Film After Puncture Has Occurred Using 25 Kev Protons at 10^{12} p/cm.² -sec. to 10^{16} p/cm.² (Magnified 100×)

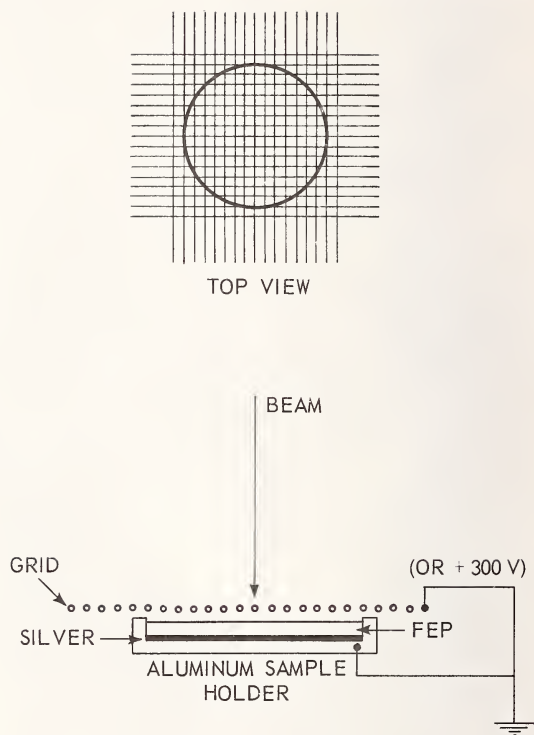


Figure 2. Pictorial Representation Showing Grid Placement Relative to Metalized Sample

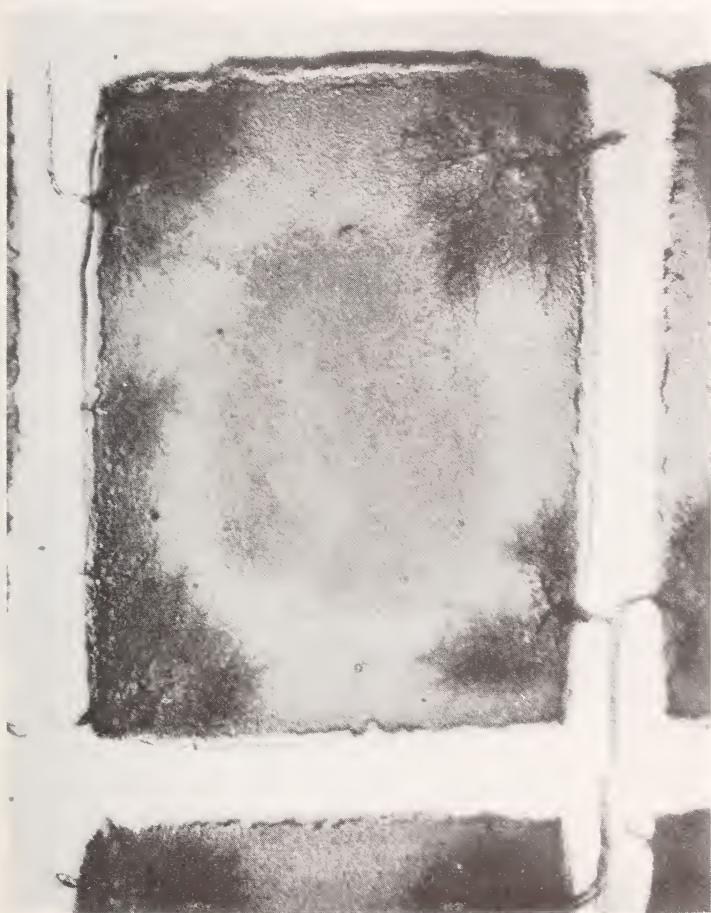


Figure 3. Photomicrograph of Silver Coated FEP Film After Irradiation With 30 Kev Electrons at 10^{12} p/cm.²-sec. to 10^{15} p/cm.² Showing Dendrites (Magnified 50x)

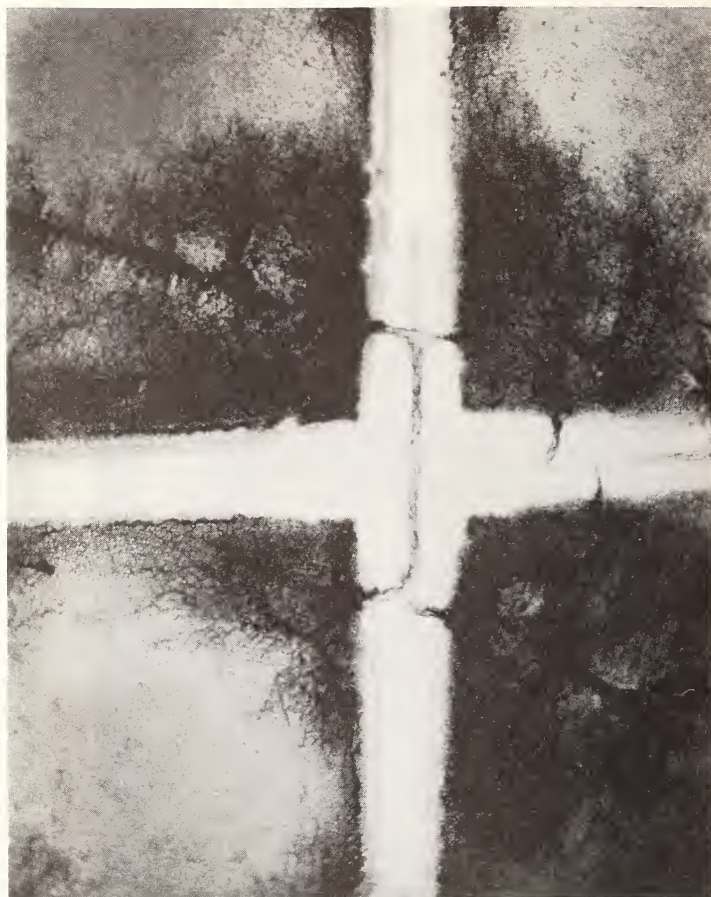


Figure 4. Photomicrograph of Silver Coated FEP After Irradiation
 With 30 Kev Electrons at 10^{12} p/cm.² - sec. to 10^{15} p/cm.²
 Showing the Bubbling Effect (Magnified 50X)

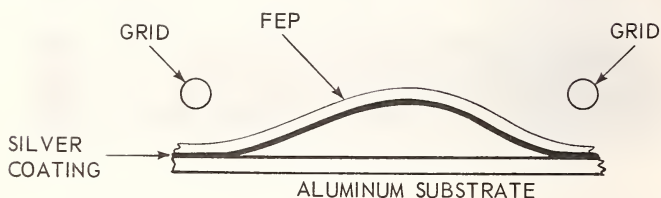


Figure 5. Sectional Representation of Metalized Sample Showing
 Buckling Position Relative to Two Grid Leads



Figure 6. Photomicrograph of Silver Coated FEP After Irradiation With 30 Kev Electrons at 10^{12} p/cm.² -sec. to 10^{15} p/cm.² Showing Extensive Veining Beneath Charge Shadowed Regions

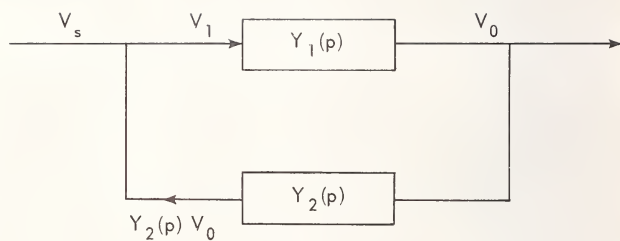


Figure 7. Simple Feed Back Loop Representing Effect of Material Changes on Intrinsic Charge Storage Capability

THE DEGRADATION OF ALZAK BY SHORT WAVELENGTH ULTRAVIOLET RADIATION

M. J. Donohoe, Roy McIntosh, Jr. and John H. Henniger, Thermo-physics Branch, NASA Goddard Space Flight Center, Greenbelt, Maryland.

REFERENCE: Donohoe, M. J., McIntosh, Roy and Henniger, John H., "The Degradation of Alzak by Short Wavelength Ultraviolet Radiation", ASTM/IES/AIAA Space Simulation Conference, 14-16 September 1970

ABSTRACT: Experimental evidence is presented to further support earlier findings on the UV induced degradation of Alzak, which was found to be inversely proportional to wavelength between 220nm and 300nm.⁽¹⁾ UV and vacuum UV exposures at selected wavelengths between 123.6nm and 300nm indicate degradation to be inversely proportional to wavelength down to 185nm. Equivalent exposure to 123.6nm radiation however, produced less degradation indicating a change in the damage dependency below 185nm. Degradation of up to 12% change in reflectance at 295nm is reported for Alzak exposed to less than 50 equivalent sun hours of vacuum UV radiation.

KEY WORDS: ultraviolet degradation, vacuum UV, thermal control coatings, Alzak.

There has recently been increasing interest in the damage of thermal control coatings produced by short wavelength ultraviolet radiation. This has occurred, in part, as a result of an apparent discrepancy in data returned from a coatings experiment aboard ATS-I.⁽²⁾ In addition, certain other findings indicate that, at least for some

Numbers in parentheses refer to the list of references appended to this paper.

coatings, degradation appears to be inversely proportional to the wavelength or irradiance.⁽¹⁾ Since the solar spectrum is rich in the vacuum and extreme ultraviolet regions, some experimenters have postulated that this could be a matter of great importance.⁽³⁾ If such a hypothesis could be demonstrated, it would mean that one more factor should be added to the growing list of requirements for synergistic ground based testing of spacecraft coatings.

At the Goddard Space Flight Center work has been underway for some time in an attempt to fully characterize the ultraviolet degradation of one of the important thermal coatings, namely, Alzak. Alzak is the designation given to a particular type of anodized and chemically polished aluminum sheet which is manufactured by the Aluminum Company of America. This material was chosen for the outer skin of the OAO spacecraft because it can be easily worked by ordinary sheet metal techniques and because it has an attractively low solar absorptance (α_s)/hemispherical emittance (ϵ_H) ratio of approximately 0.22. Work has been previously reported which showed that the degradation of alzak was strongly dependent upon the wavelength or irradiance at least down to $\approx 220\text{nm}$.⁽²⁾ The experiments which are described here were designed to provide data down to the solar Lyman α region (121.6nm).

EXPERIMENTAL

The experimental apparatus used in this study is shown in Figure 1. It consists of an irradiation cell and three UV sources with wavelengths at 123.6nm, 185nm, 206.2nm and 240nm. Not shown is a DK-2 Spectroreflectometer with an Edwards type integrating sphere used for in-air reflectance measurements on the samples. A 1-1/2 liter stainless steel vacuum chamber with a side port forms the irradiation cell. The cell is ion pumped with a trapped mechanical roughing pump. All vacuum seals are the copper gasket type and the valves have viton elastomer seats. Irradiations take place in the 10^{-7} torr region as measured by an ionization gauge. The irradiation port is a 2" diameter sapphire window or a 1" diameter lithium fluoride window, depending upon the wavelength or irradiation.

The sample was screw mounted on a temperature controlled¹ copper substrate opposite the irradiation port. Sample reflectance measurements were made before, during and after the irradiations by

¹Thermoelectric module — Cambion Corp., Cambridge, Mass.

Numbers in parentheses refer to the list of references appended to this paper.

removing the sample from the chamber. The sample could be removed, replaced and pumped down within 30 minutes. No detectable recovery in alzak took place during this time interval. During the earlier studies, in-situ reflectance measurements of Alzak damaged by irradiations from a 123.6nm source and a xenon arc indicated that recovery of damage was negligible when measurements were made within 8 hours after exposure to air. Reflectance measurements were made with an estimated error of $\pm 1/2\%$ due to variations across the sample face.

The UV irradiation sources were two low pressure microwave discharge lamps (krypton, iodine) and a high pressure xenon arc lamp² with a band pass filter³ centered at 240nm. The relative spectral output of the three sources is shown in Figure 2, together with a solar UV irradiance curve for reference.

The krypton lamp emits three lines, 117nm, 123.6nm, and 247nm. The 117nm line is weak, being approximately 10% of the 123.6nm line intensity. The 123.6nm line is the primary irradiating wavelength and is used to simulate the solar Lyman α line at 121.6nm. The 2nm difference between the two lines is assumed to have negligible effect on the results. The 247nm line contribution to sample degradation is evaluated by masking half the sample with a sapphire filter to eliminate the 123.6nm line, but pass the 247nm line. A reflectance measurement on both sample halves then isolates the 247nm line contribution. The krypton lamp output spectrum is blank from 247nm to approximately 330nm. The lamp is normally run gettered with a cold finger immersed in liquid nitrogen to eliminate contaminant lines. Krypton lamp intensities could be varied by the microwave generator from a fraction of an equivalent Lyman α sun (i.e., one equivalent Lyman α sun 5×10^{-7} watts/cm²) to approximately 20 equivalent Lyman α suns. The LiF window life was greatly reduced at the higher intensities due to the window sealing technique used.

The iodine lamp has a sapphire window and emits a group of lines centered at 185nm and a strong line at 206.2nm. The lamp is normally run with a cold finger immersed in water ice to maintain the proper pressure in the iodine reservoir shown in Figure 1. The lamp spectrum above 206.2nm is blank up to 400nm. Differentiation between the degrading contribution of the 185nm lines and the 206.2nm line is achieved using a gas filter of butene-1.⁽⁴⁾ The butene-1 cell absorbs the 185nm lines while reducing the 206.2nm line intensity by only 10%.

²Model XR-150, Eimac Corp., Palo Alto, California

³Optics Technology, Palo Alto, California

Numbers in parentheses refer to the list of references appended to this paper.

The iodine lamp output was variable up to 1/2 an equivalent sun at 185nm and 206.2nm (i.e., 40 Lyman α suns). The 185nm lines contributed approximately one half of the total, the balance was the 206.2nm line intensity.

The xenon arc lamp used, had a continuum at 240nm and the filter centered at 240nm had a band pass of 30nm. Maximum output was approximately equal to 1/2 an equivalent sun at 240nm (i.e., 75 Lyman α suns).

The intensity monitor for all the lamps was a sodium salicylate coated photomultiplier (1P28) referenced against a calibrated nitric oxide ionization chamber using the 123.6nm krypton line. The photomultiplier could be rotated to a position between the sample and the irradiating source. The calibration measurements were performed with the ionization chamber in the sample position as shown in Figure 1. The sodium salicylate quantum efficiency was assumed constant over the wavelength region of interest. This assumption is supported by the literature.⁽⁵⁾ The photomultiplier calibration was checked periodically during the experiments and found to remain within 5% of the original calibration.

Calculation of the equivalent sun irradiance for each source was based on Johnson's data using a 10nm band width of each line. The 185nm lines were treated as one line between 180nm and 190nm. Actually the band width of each line was known from the vacuum monochrometer measurements. Use of the actual band width, i.e., 2.5nm just increases the equivalent sun hour exposures. Since line sources were used to simulate the sun's continuum spectrum at select wavelengths, the 10nm interval was used. Another convenient way of looking at the data would be in terms of Lyman α suns since part of the experiment is aimed at studying the effect of Lyman α .

RESULTS

Plotted in Figure 3 are the changes in reflectance at 295nm of Alzak samples exposed to different irradiating wavelengths. Exposure to 123.6nm light used to simulate solar Lyman α produces the slowly developing damage shown in the lowest curve. Exposure to combined 185nm - 246.2nm light produces the steep curve at the left. This curve was constructed from 3 samples as indicated by the legend.

Shown in Figure 4 is a plot of % ΔR at 295nm versus wavelength for constant incident energy.

Numbers in parentheses refer to the list of references appended to this paper.

Before discussing the data in Figure 3 and Figure 4, two additional experiments should be mentioned. The first is a single Alzak exposure to 123.6nm irradiation at an intensity equivalent to the 185nm - 206.2nm irradiations shown in Figure 3. For a 36-1/2 exposure at 1.4×10^{-5} watts/cm² (i.e., ≈ 30 times Lyman- α), Alzak showed a 4% ΔR at 295nm compared to the 11% shown in Figure 3. The second result is a UV screening test on Alzak using a filtered 2.5kw xenon arc lamp (Spectrolab Solar Simulator model X-25). The UV irradiation tests performed through quartz vacuum chamber ports produced a 12% ΔR in Alzak after 57 equivalent sunhours at a one sun rate. Therefore, this sample saw the complete solar spectrum starting at the quartz cut off of the simulator and vacuum system optics. The UV content (i.e., below 220nm) for this test was not known, but the point is presented to emphasize the damaging effects of short wavelength UV. The energy output ratio in watts/cm² of the simulator versus the microwave discharge lamp is approximately 10,000 to 1.

DISCUSSION

The conclusions which can be drawn from the data presented are two: first, on a solar irradiance basis Alzak is damaged faster and further by wavelengths in the 180 - 210nm region than by Lyman- α (see Figure 3), and second, on an equivalent incident energy basis, Lyman does less damage than the 180 - 210nm wavelengths (see Figure 4). These two points, coupled with the previous studies on Alzak above 220nm, provide a general behavior picture for Alzak degradation; i.e., above approximately 300nm no degradation is observed for long exposures (100 hours), and below 300nm increasing degradation with decreasing wavelength is observed which peaks somewhere between 150-210nm (on a solar irradiance basis) and reaches a lower value at Lyman- α wavelengths. In addition, most of the damage caused by the 180-210nm wavelengths occurs within the first 50 hours of exposure and may approximate the damage observed under standard solar irradiation tests.

From the standpoint of solar environmental testing of Alzak, it is evident that Lyman- α wavelengths need not be included in laboratory testing. Every effort should be made, however, to include the wavelengths between 150 and 200nm. Other materials may behave differently and should at least be checked for their behavior under Lyman- α wavelengths.

At this point in the studies it is only of academic interest to determine the precise shape of the Alzak damage curve because of the large reflectance changes observed using the iodine lamp. However, efforts are being made to develop a bromine resonance lamp to provide a line source at 163nm which will bridge the wavelength interval between the iodine and krypton irradiation sources.

REFERENCES

- (1) McIntosh, R., "The Degradation of Alzak as a Function of the Wavelength of Irradiance," Symposium on Coatings in Space, December 1969, Cincinnati.
- (2) Reichard, P. J., Triolo, J., Progress in Astronautics and Aeronautics, Vol. 20, Academic Press, New York, 1967, 491.
- (3) Swofford, D. C., Johnson, S. W., Mangold, V. L., "The Effects of Extreme Ultraviolet on the Optical Properties of Thermal Control Coatings", AIAA Thermophysics Conference, June 1968, Los Angeles, Paper No. 68-783.
- (4) Liuti, G. and Mentall, J. E., "Monochromatic Iodine Lamp", Rev. Sci. Instr., 39, #11, 1767, Nov. 1968.
- (5) Samson, J. A. R., Techniques of Vacuum Ultraviolet Spectroscopy, John Wiley and Sons, New York, 1967, p. 212.

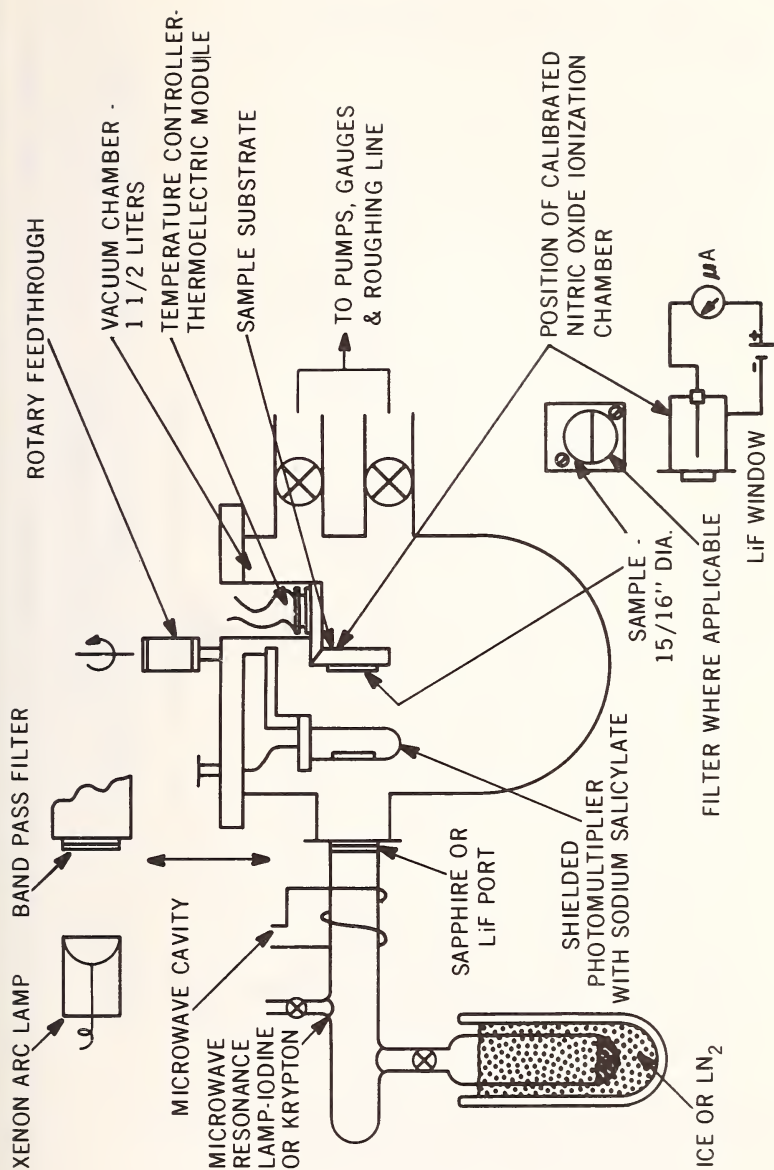


Fig. 1—Experimental apparatus.

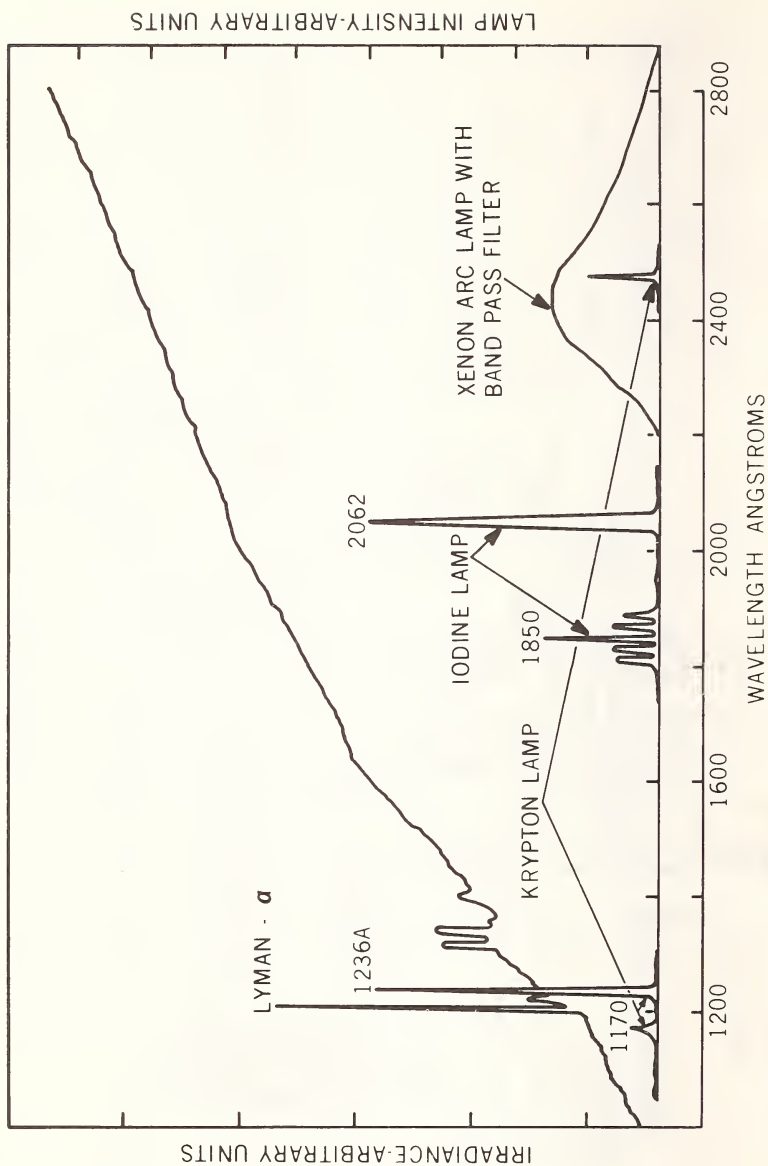


Fig. 2—Solar UV spectral irradiance — [Detwiler-1961] and UV irradiation source spectra.



Fig. 3—Comparison of Alzak degradation produced by 123.6nm, 185-206.2nm irradiation.

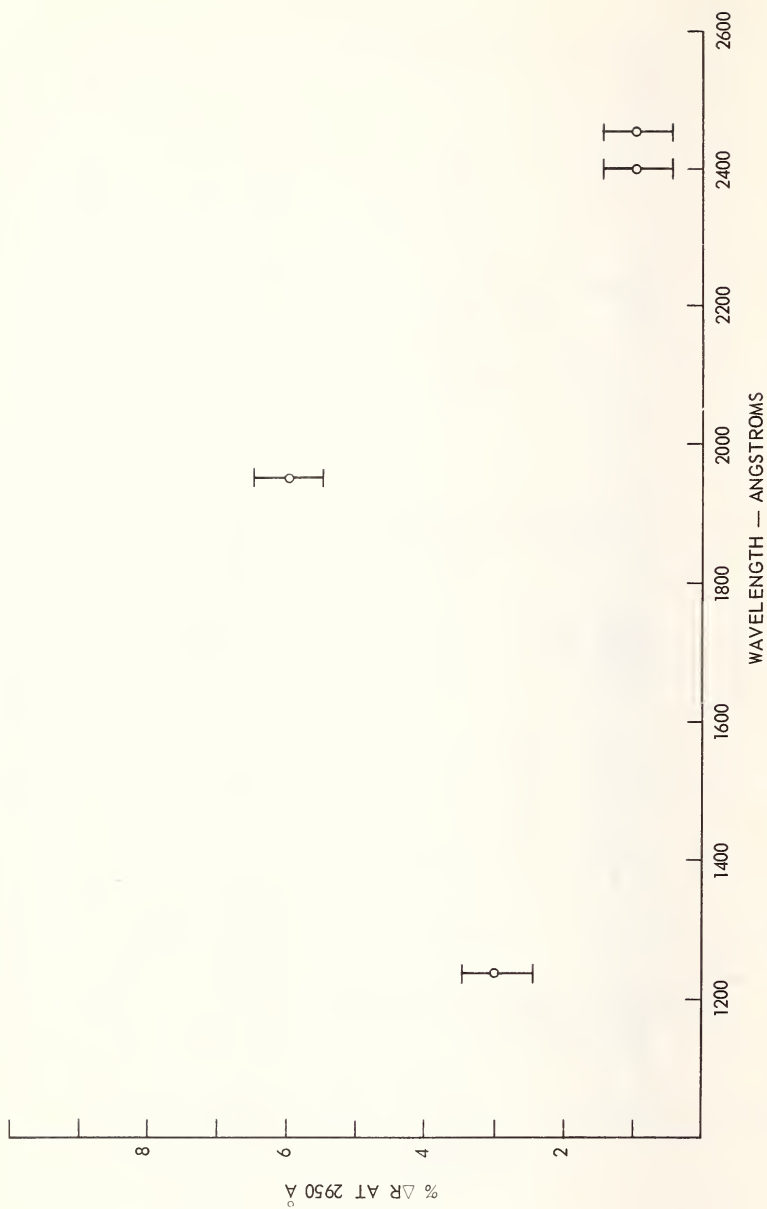


Fig. 4—Irradiation damage as a function of wavelength for constant incident energy (1×10^{-4} w/cm²).

THE PHOTO-RESPONSE AT AN ALKALINE PAINT INTERFACE WITH ALUMINUM

Walter A. Wappaus¹

REFERENCE: Wappaus, Walter A., "The Photo-Response at an Alkaline Paint Interface with Aluminum," ASTM/IES/AIAA Space Simulation Conference, 14-16 September 1970.

ABSTRACT: When a spacecraft coating comprised of aluminum oxide and potassium silicate is applied to an aluminum alloy (6061) substrate and subsequently partially coated with evaporated gold electrodes, a measurable potential is developed between the substrate and the gold electrodes. This effect is observed when the coating is in darkness and in vacuum. A dark current is also observed. Prior to observation, the specimen is heated in vacuum to 150°C for 24 hours.

When the coating is irradiated in situ with UV shorter in wavelength than 3600 Angstroms, the current and voltage is found to increase. Upon exposure to prolonged irradiation this current level decays exponentially with time. The voltage similarly decays with time in an exponential manner indicating that photo-degradation of the electronic transport properties is occurring.

The transport mechanism proposed to account for this behavior is a migration of protons toward the aluminum substrate and negative hydroxyl ions toward the gold electrodes resulting in the electrolysis of water in the coating. In the presence of UV this process is accelerated resulting in an increased current flow of three orders of magnitude. Since the current flow during UV radiation decays exponentially, this suggests a diffusion limited process.

KEY WORDS: alkaline paint, conduction of paints during ultraviolet exposure, electrode potential of paints, photo degradation, thermal control coatings, ultraviolet degradation

¹Goddard Space Flight Center, Greenbelt, Maryland 20771

INTRODUCTION

The stability of spacecraft coatings has been the object of much investigation. For successful satellite application a coating must exhibit stable properties for long periods of time when subjected to a space environment. One parameter, important to thermal control of a satellite is the absorptivity, or α , of the spacecraft coating. α is an optical property and usually changes when the coating is subjected to a space radiation environment. The object in coating formulation is to prepare a compound such that its time rate of change of α is very small when subjected to space radiation. The coating studied in this investigation, a mixture of aluminum oxide and potassium silicate, is stable with respect to α in a proton and electron radiation environment. However, it is unstable when subjected to ultraviolet irradiation. An attempt is made here to study the conduction characteristics of this coating by monitoring some electrical parameters of this coating while being subjected to ultraviolet radiation. This paper discusses an in-situ method for recording the behavior of a voltage across and a current through the thickness of a spacecraft coating applied to an aluminum alloy (6061) substrate. This coating when sprayed on an aluminum alloy substrate is representative of a typical spacecraft skin whose surface is painted for thermal control purposes.

In this paper conduction schemes are suggested and a model for ultraviolet degradation is proposed. As far as is known this particular approach in studying the in-situ degradation of spacecraft coatings has not been previously employed.

EXPERIMENTAL PROCEDURE

The coating which is discussed here is formulated from 1.0 micron alpha phase aluminum oxide² and potassium silicate³ mixed in a four to one solid ratio; that is,

$$\frac{\text{Weight Al}_2\text{O}_3}{\text{Weight K}_2\text{O} + \text{Weight SiO}_2} = 4$$

The mole ratio of SiO₂ to K₂O is 3.3; i.e.,

$$\left(\frac{\text{SiO}_2}{\text{K}_2\text{O}} \right)_{\text{mole}} = 3.3$$

²Manufactured by the Linde Division, Union Carbide Corp.

³Sylvania Corporation's electronic grade PS-7.

The pH at this ratio is 12.8 using water as the solvent. The preparation is sprayed on an aluminum alloy disc to a layer thickness of about 0.1mm. When air dried this coating has good hiding properties as well as low absorptivity values.

A set of gold electrodes is evaporated on the surface of a coated disc. The electrode configuration is shown in Figure 1. The disc is then mounted in a specimen holder which is designed to position a heater in contact with the uncoated side of the specimen. The heater is electrically insulated from the aluminum disc. The specimen holder firmly positions electrodes contacting the evaporated gold on the coated surface. A small amount of silver paste serves to insure electrical continuity between these contacts. The holder is mounted in a vacuum chamber such that it is electrically insulated from the chamber. An ultraviolet transmitting quartz port is provided through which radiation from a 500 watt medium pressure mercury lamp⁴ is directed normally onto the coated surface.

The two independent gold surface electrodes are electrically joined and connections are led outside the vacuum chamber via an electrical feed through. Another lead is attached to the aluminum substrate disc of the coated specimen and led externally in a similar manner. These two leads permit electrical measurements to be made across the coating layer.

The vacuum is ion pumped and capable of reaching the 10^{-9} torr region when empty. A sorption pump is used for roughing. All metal components are stainless steel. A light proof enclosure fitted with a shutter is placed over the quartz port and optically aligned with the ultraviolet beam. The specimen is in total darkness when not being irradiated with ultraviolet light. The pumping system and the light source are shown in Figure 2.

The radiation tests are designed to show the change of electrical parameters of the coating specimen as a function of total irradiation exposure time. At the start of the experiment the chamber containing the specimen appropriately mounted in the holder is roughed out and subsequently pumped down to the 10^{-6} torr region. The specimen is then heated to 150°C for a 24 hour interval and then allowed to cool. The pressure usually lowers to 10^{-7} torr after this procedure. The mercury ultraviolet source is positioned so that the specimen receives a one sun irradiance. The shutter is opened for a given time interval. The current and voltage are measured prior to and at the very beginning of the radiation time interval. Both light and dark current and voltage measurements are recorded with an electrometer.⁵

⁴Hanovia model 6730A10

⁵Keithley Instruments, Inc., Model 610B

At the conclusion of the irradiation time interval the shutter is then closed and a period of time is allowed to elapse before the next radiation interval in order to allow the specimen to return to initial temperature conditions. This cooling interval varies according to the length of time of radiation exposure, as the radiation interval is increased the cooling interval is also increased.

RESULTS

It is observed that, with the coating in darkness, a current flows through the paint compound. The sense of this dark current in the external measuring circuit is from the aluminum substrate electrode to the evaporated gold electrode. The dark current, when measured just prior to each radiation interval, was in the 10^{-12} ampere region for the duration of the experiment. A dark voltage is also observed and is developed across the two different electrodes. The gold evaporated electrode is of positive polarity. The dark voltage when measured just prior to the start of the experiment was found to be 0.35 volts. This dark voltage decreased linearly with time to a final value of 0.15 volts at the conclusion of the testing.

The results of the photo-response are presented in graphic form in Figures 3 and 4. Figure 3 shows the relationship between the current flowing through the coating, while being irradiated with ultraviolet light, versus the total accumulated time of this radiation. The time as plotted is the cumulative sum of the radiation intervals. Similarly, Figure 4 shows the relationship between the voltage developed across the coating electrodes, while being irradiated with ultraviolet light, versus the total accumulated time of radiation.

When a blocking filter was put into the light path, filtering out radiation of wavelength less than 3600 Å, no photo-response was detected. The original color of the coating was a chalk white, but at the conclusion of the irradiation the color had changed to a light brown. Upon re-exposure to light and a normal laboratory atmosphere for several months, the color of the coating did not bleach but remained brown.

DISCUSSION

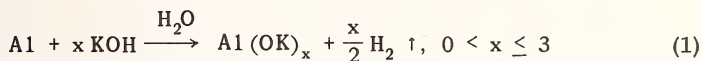
The coating material in contact with the aluminum substrate exhibits properties similar to a dry cell battery with a power output less than 10^{-12} watts. The voltage which is built up and maintained across the electrodes seems to occur spontaneously without the need for the application of an external voltage to initially polarize the system.

Contact potentials are certainly contributing to the voltage build up but their contributions are small compared to the total voltage in the dark condition.

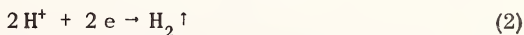
The mechanism for current production in the coating is different during the dark and illuminated conditions. In order to discuss these conduction schemes it is necessary to describe the various anodic and cathodic reactions occurring under these different conditions. The following reactions are suggested to account for the conduction mechanism.

Dark Conduction

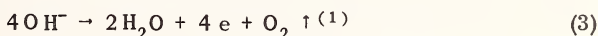
In considering a reaction at the cathode, one that is immediately suggested is,



due to the fact that the coating is strongly alkaline. Guided by (1), with the release of hydrogen at the cathode, the following competing cathodic reaction is also suggested,



The protons, which are furnished by dissociated H_2O , migrate toward the aluminum. At the gold anode the following reaction is suggested:



complementing (2). Here the hydroxyl ions migrate toward the gold electrodes releasing electrons for current flow in the external measuring circuit, accompanied by the release of oxygen as a gas. The hydroxyl ions are supplied by dissociated KOH or H_2O . In consideration of the K^+ ion and its migration to the cathode an equation similar to (2) may be written, resulting in a greater capacity for hydrogen formation. Reaction (1) is diminished as the water content of the coating is depleted. The conduction is ionic, resulting in the increased ionization of water at the cathode. The rate of these reactions determines

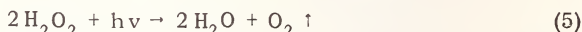
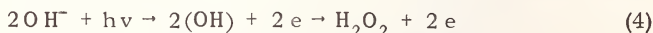
⁽¹⁾The numbers in parenthesis refer to the list of references appended to this paper.

how many electrons are furnished for current flow in the external measuring circuit but the mobility of the ions in the coating limits the conduction process.

Light Conduction

The above processes in the coating occur also during the illuminated condition but these are dominated by an additional reaction which supplies a much greater source of current.

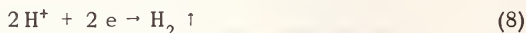
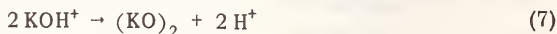
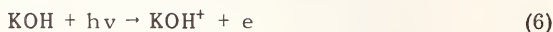
Since the photoresponse was detected at wavelengths less than 3600 Å an energy threshold greater than 3.4ev is required for photo-conduction. A suggested reaction for this photo-conduction at the anodic surface is



Here additional electrons are provided for external conduction and additional gas is evolved. The cathodic reaction is the same as in (1) and (2).

A contributing mechanism suggested for increased conduction in this condition is that the OH forms an amorphous-like valence band permitting hole conduction.⁽²⁾

It is further suggested that reactions may still occur to provide conduction even if all the water is depleted by electrolysis. The following reactions are speculated:



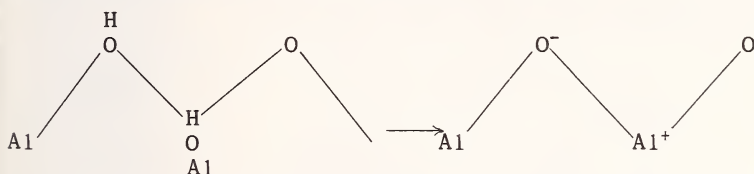
During the photo-response the data suggests that the resistivity decreases since an increase in voltage accompanies the increased output of current.

⁽²⁾The numbers in parenthesis refer to the list of references appended to this paper.

The curve in Figure 4 shows that there are two distinct rates of voltage decay indicating that the ability of the ions to polarize in the coating is changed after a certain length of radiation exposure time.

The curve in Figure 3 deviates initially from the exponential slope. This suggests that the ions are not initially diffusion limited and that surface conduction might take place due to contamination on the surface of the coating. The surface of aluminum oxide is strongly hydroxylized which might contribute to this effect.⁽³⁾ The dark current reactions seem unaffected, however, after a similar radiation exposure.

Water is present in the highly absorbent coating even after prolonged bakeout. As the photo-response progresses the coating dehydrates and this seems to be the dominating factor in attenuating the current and voltage output. This is supported by the fact that, at the conclusion of testing, the vacuum pump was shut off and the pressure in the chamber was allowed to rise slowly due to small leaks in the system. At 10^{-3} torr the voltage and current values were higher than the final values observed during the testing schedule performed at 10^{-7} torr. At the cathode, equation (1) suggests that along with the creation of aluminum ions, impurities in the aluminum alloy electrode would be mobilized via a related mechanism, and made available to influence optical properties. Proceeding toward the anode, dehydroxylation of the aluminum oxide according to the scheme



presents sites for charge transfer absorption. The doubtful oxidation states of the impurities are conducive to color center formation. The manner in which the impurities function is important.

GENERAL CONCLUSIONS

The decay of the conductivity processes of this aluminum oxide-potassium silicate coating is related to the dehydration of water from this coating. The conduction of the coating is normally ionic but when the coating is stimulated by UV, hole conduction is the predominant contributing factor to the conduction process. The coating is self

⁽³⁾The numbers in parenthesis refer to the list of references appended to this paper.

polarizing and is enhanced due to UV radiation. Under UV exposure, dehydroxylation of the surface of the coating coupled with the release of impurities at the cathode and their subsequent diffusion may combine these effects to form color centers in the coating, with a net resultant increase in absorptivity.

ACKNOWLEDGEMENTS

The author is indebted to Dr. John B. Schutt for his illuminating discussions and helpful suggestions. The author is also grateful to Charles M. Shai for preparing and applying the coating and to Robert N. Sheehy and his group for applying the gold electrodes to the coating.

REFERENCES

1. Latimer, W. M., "Oxidation Potentials", Prentice-Hall, New York 1952, p. 348
2. Ruff, I., J. Phys. Chem. 69, 3183 (1965)
3. Carter, J. L., Lucchesi, P. J., Corneil, P., Yates, D. J. C., and Sinfelt, J. H., J. Phys. Chem. 69, 3070 (1965)



Fig. 1—Configuration of vapor deposited gold electrode.

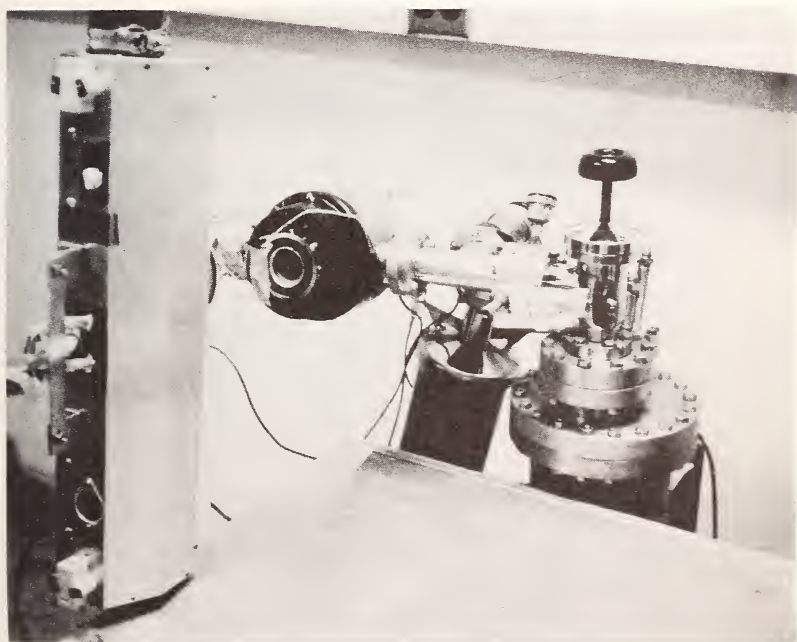


Fig. 2—Photograph of experimental apparatus; sample chamber and light source.

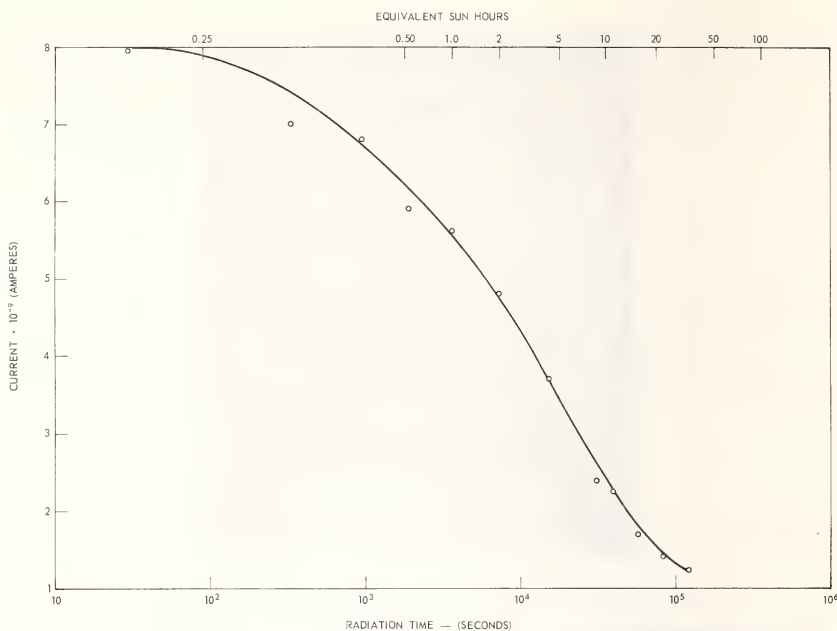


Fig. 3—Relationship between UV photo-response of current vs. radiation time.

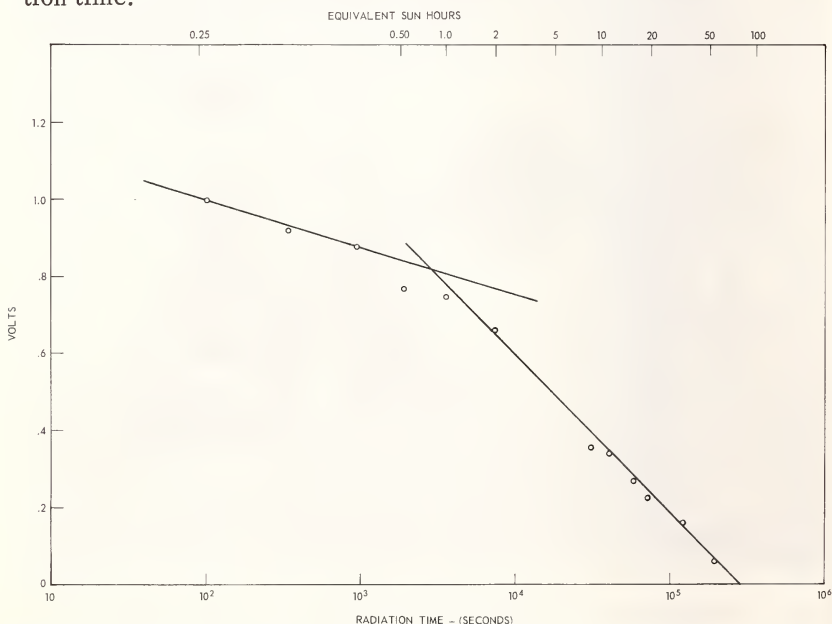


Fig. 4—Relationship between UV photo-response of voltage vs. radiation time.

PLANS AND STATUS OF NMAB ad hoc COMMITTEE ON TESTING FOR
PREDICTION OF MATERIAL PERFORMANCE IN STRUCTURES AND
COMPONENTS

Robert S. Shane

National Materials Advisory Board, National Research Council -
National Academy of Sciences, Washington, D. C.

ABSTRACT: National Materials Advisory Board - National
Research Council - National Academy of Sciences - ad hoc
Committee on "Testing for Prediction of Material Performance
in Structures and Components" - Interim Report

At the request of the Office of the Director of Defense
Research and Engineering, the National Materials Advisory
Board of the National Academy of Sciences has undertaken to
review "Testing for Prediction of Material Performance in
Structures and Components".

The basic purposes of the study have been identified as:
(a) make a selective survey of the needs for new and/or
improved predictive (including accelerated) testing techniques;
(b) consider predictive methods for forecasting the performance
of materials in structures and components under combined
stresses in service; (c) identify the factors of predictive
testing and explore approaches for development of methods and
techniques of predictive testing; (d) appraise the benefits of
predictive testing as well as the risks of predictive testing;
(e) provide guidance in establishing a policy for Government
and/or Industry interaction; (f) recommend mechanisms for
implementing this policy.

An ad hoc Committee has been appointed and convened. The
principal problem areas appear to be (a) interaction phenomena,
(b) design of multi-factor tests which forecast definitively
the behavior of structures and components in the presence of
known or foreseeable failure modes, involving materials
(c) lack of systematic accumulation of existing information so
that gaps in needed knowledge become apparent and remedial
action can be taken before design choices are irrevocably made,

(d) peripheral failure modes are frequently overlooked.

NMAB plans to co-sponsor the ASTM National Symposium on Predictive Testing, Anaheim, California, April 21-23, 1971.

KEY WORDS: combined environments, components, material performance, predictive testing, structures

(Complete paper not available)

MONITORING SERVICE TESTING BY NONDESTRUCTIVE TESTING

Robert W. McClung

Oak Ridge National Laboratory, Oak Ridge, Tennessee

ABSTRACT: Applications of nondestructive testing techniques to monitor tests include the use of x-rays with both film and television detection to monitor thermal cycling of fuel rods, neutron radiography on irradiation experiments, eddy-current measurement of space interval between components, and interim monitoring by ultrasonics of the wall thickness of a vessel in a reactor experiment. Studies during fabrication development include multiple interim measurements of compaction density of fuel rods and impregnation density of graphite using quantitative gamma and x-ray attenuation as well as use of eddy-currents to monitor changes in quality of sodium bonding in a fuel rod. Recommended approaches include the use of eddy-current methods to monitor changes in electrical properties, dimensions or flaw character, ultrasonics to measure changes in elastic properties, dimensions or flaw character, penetrating radiation to observe or measure changes in density, or dimensions and other forms of energy for similar applications.

KEY WORDS: compaction density, eddy current measurements, fuel rods, impregnation density, monitor tests, neutron radiography, ultrasonics, x-rays

(Complete paper not available)

SIGNATURE ANALYSIS - NON-INTRUSIVE TECHNIQUES FOR INCIPIENT
FAILURE IDENTIFICATION APPLICATION TO BEARINGS AND GEARS

B. Weichbrodt¹ and Kempton A. Smith²

REFERENCE: Weichbrodt, B. and Smith, Kempton A., "Signature Analysis - Non-Intrusive Techniques For Incipient Failure Identification Application to Bearings and Gears", ASTM/IES/AIAA Space Simulation Conference, 14-16 September 1970.

ABSTRACT: This paper describes how acoustic and vibration signals generated by operating machinery can be used to diagnose its internal condition without using internal sensors which might perturb the system of interest.

It is shown how characteristic "signatures" can be electronically extracted from the overall noise and vibration signals. By interpreting these signatures in the light of engineering knowledge of the machinery under study, it is often possible to identify incipient failure modes long before final failure. This technology opens up many new possibilities to avoid unscheduled maintenance, improve product quality and reduce testing time.

The paper discusses in detail specific applications to bearing and gear diagnostics and shows how the diagnostic process can be electronically implemented and automated. Several other application area are briefly discussed.

A major part of the work which is reported in this paper was sponsored by the Condition Monitoring Engineering Operation of General Electric's Aircraft Engine Group, for development of jet engine diagnostic systems.

¹Manager, Signature Analysis Unit, General Electric Research and Development Center, Schenectady, New York.

²Signature Analysis Unit, General Electric Research and Development Center, Schenectady, New York.

KEY WORDS: diagnostics, reliability, signature analysis, vibration, bearings, gears.

INTRODUCTION

Both mechanical and electrical systems generate secondary effects during their operation. These secondary effects, in contrast to primary effects, such as pressure and flow in a pump, are not directly utilized in the operation of the system. Examples of typical secondary effects are vibration, acoustic noise, heat generation, electrical and magnetic radiation. (Obviously, in some cases these are also primary effects.)

In fact, not only are the secondary effects not used, but in many cases these effects also represent major problems, and one would rather see that a system could be operated without them.

However, luckily there is also a positive side to these secondary effects, as this paper will attempt to illustrate. Generated inside a machine they are usually transmitted to the outside, carrying with them information about the internal action. Provided that the external observer can properly measure and interpret these effects, he has a new tool to gain an insight into the internal condition without actually having internal sensors.

During the last several years much work has been directed towards the development of machinery diagnostic techniques, using these secondary effects. This has generated both successes and frustrations. In the successful cases, it has been possible to establish effective communications with the internal action in a machine. This has led to several results. One has been the capability to predict failure of machinery much earlier than was previously possible by monitoring only the direct operating parameters. A second result has been the capability to predict life performance by testing only on the new product, i.e., better Quality Control and checkout techniques. This is of particular importance for space systems. A third result, and maybe the most important, has been the capability to actually identify specific failure modes without disassembly, by only studying the external secondary effects.

This paper will attempt to illustrate some of the more important results which have come out of machinery diagnostics work done at the Research and Development Center of the General Electric in Schenectady, New York. The diagnostics program, which initially was concentrated entirely to acoustic and

vibration techniques, "Mechanical Signature Analysis", now is broadened into mechanical, thermal, electrical and magnetic effects used for diagnostic purposes. It has been possible to develop technology and hardware, some of which is already being used in aerospace and industrial applications.

However, in this paper we will concentrate on mechanical effects, and how they can be used to diagnose machinery and structures. Since this is the area where work was first started, it has currently generated the largest number of successful applications. Subsequent papers will discuss non-acoustic diagnostic techniques as they are developed.

After a brief discussion of signature extraction techniques, we will discuss in detail the application to rolling element bearings and gears and in particular illustrate this discussion with results that have been obtained in diagnosing long life spacecraft gyros. After these detailed discussions we will briefly show how the diagnostic technology, developed at the General Electric Research and Development Center can also be applied to a much wider variety of systems, including nuclear reactors and artificial hearts.

SOUND AND VIBRATION AS DIAGNOSTIC TOOLS

As most readers will easily recall, sound and vibration have been used for diagnostic purposes for a long time. A classical example is the skilled automobile mechanic who with the help of a screwdriver and his "naked ear" can listen to an automobile engine and detect valve leaks and other defects long before they show up as performance changes.

Without elaborating on this example, it illustrates the proven fact that in order to successfully diagnose machinery by sound and vibration, it is necessary to recognize quite subtle differences between its normal and abnormal "signature". The automobile mechanic does not listen to the engine's overall loudness, but rather to the individual impacts from valves hitting valve seats and other similar effects. The same is true for most machinery diagnostics applications.

Thus, one of the primary requisites for successful diagnostics is to know what subtle sound differences to listen for. This, in fact, is the most important requisite of all, without which very few results have been obtained. It is necessary to understand the kinematics and kinetics of the mechanical system under study, and also to know something about the signal transmission through the machinery structure. In many cases it has been necessary to actually derive a dynamic mathematical model

of the system, and to mathematically calculate the differences caused by certain malfunctions.

Once the sound generating mechanisms and expected signatures are known, the next step is to devise means for extracting and analyzing these signatures from a complex total noise signal. This sometimes requires very special techniques, as will become evident later in this paper.

Finally, the techniques which have been developed must be electronically implemented and in many cases automated.

When applied with ingenuity and understanding of machinery dynamics, diagnostic techniques based on sound and vibration can detect machinery failure in its very early stages. At that time there is usually still time to take preventive action to avoid catastrophic failure or unscheduled maintenance. These non-intrusive techniques also have demonstrated their capability to actually identify specific failure modes, which is of prime importance since it strongly influences the preventive action to be taken.

SIGNATURE EXTRACTION VS SIGNATURE ANALYSIS

The task of analyzing subtle sound or vibration patterns in complex noise signals really consists of two problems. The first problem is to separate from the remaining noise the specific components in the signal, the "signature", which is generated by the part under study (i.e., one gear in a complex transmission). This is the signature extraction task.

The second problem is to analyze the features of the signature, once it has been separated.

The second problem is obviously closely related to the specific system under study, and the solutions tend to vary from one case to another. However, the first problem, that of signature extraction, is more general, and some specific extraction techniques have been developed which are used in most applications. In order to clarify the following discussions, a brief description will first be given of the most frequently used signature extraction techniques.

SIGNAL PROCESSING FOR SIGNATURE EXTRACTION

Because signature analysis as a practical tool utilizes secondary effects as a means of communicating with an operating component, it is frequently necessary to detect and extract very low level signals from high noise level backgrounds. As a result of this need, several specialized techniques of signal

processing have been developed which allow particular features of a signal to be enhanced.

Differing applications may of course call for different processing techniques, but the majority of these techniques fall into two categories; waveform analysis and spectral analysis. It is important to understand these techniques so that an appreciation can be gained for the wide variety of possible applications, previously not feasible without these techniques.

One of the most powerful tools available for extracting a periodic component waveform from a complex signal is the technique of signal averaging or summation analysis. A signal with known periodicity T is buried deep in noise. To extract that signal by averaging, the total signal plus noise is divided into n epochs of duration T . Each epoch is sampled at 1000 points between times $(n-1)T$ and nT . The samples are stored in a digital memory of 1000 words which algebraically adds together all n samples.

An event which always occurs with a period T will always be added in the same sample location; i.e., the resulting sum will be n times the average amplitude of that event. Events which do not repeat with a period T will result in a sum proportional to \sqrt{n} . Thus the desired signal has been enhanced over the noise by a factor of \sqrt{n} . This process is illustrated in Figure 1.

In practice it may be desirable to incorporate a weighting factor of one type or another or to select the period T as a multiple of a repetition period. A typical weighted average de-emphasizes old samples with respect to the samples just entered, allowing the operator to observe changing waveforms in real time.

In many cases waveform analysis is able to provide only a part of the total characterization of a signature. Much additional information may be obtained by real time spectral analysis. Frequency filtering provides optimum signal-to-noise relations and permits strong and weak components of different frequencies to be detected simultaneously. The Research and Development Center has developed a unique facility for the thorough exploration of signal characteristics by the use of frequency pattern analysis. The analyzer itself combines high quality crystal filtering with a high scanning rate to preserve both transient and steady state features. The analysis parameters are extremely versatile. Signal frequencies from 1/2 to 125,000 hertz have been analyzed with effective filter bandwidths ranging from 1/4 to 3,600 hertz. Many display formats are available, including cross section plots of amplitude

versus frequency, several forms presenting amplitude by intensity modulation, amplitude level and contour plots spectrum peak displays, and other combinations. In addition, computer processing of the analyzer output is available for the automatic extraction of information in signal spectra. An example of this type of analysis is included in the discussion of bearings below.

DIAGNOSTICS OF ROLLING ELEMENT BEARINGS

Ball and Roller bearings usually follow a characteristic wear/failure pattern. Since the sliding between metal surfaces is minimized, the wear rate is usually very low. But the rolling contact load between balls/rollers and the race is instead very high, and leads to sub-surface fatigue. Therefore, rolling element bearings have a tendency to fail by fatigue rather than wear-out.

Obviously, the statements above are very general, and can be challenged in special cases. But they describe the typical situation for bearings which are properly designed and maintained. All bearings can fail through many other mechanisms if they are not properly used, for example through corrosion or lack of lubrication.

Figure 2 shows a simplified but typical wear rate curve for a rolling element bearing.

Early in life the wear rate is often at a maximum. This is the running-in period. The maximum may be absent for very high precision bearings. After this initial period comes a long period with very low wear rate. This represents the major portion of the bearing life. During this period the wear rate is low, but both races and balls accumulate fatigue cycles.

The end of the low-wear period is marked by the appearance of some surface defects, usually on one of the races. This may be fatigue spalling but also corrosion spots or other effects. The surface defects are small at the beginning, but disturb the smooth rolling process, increase the friction, and therefore grow and increase the wear rate. When a sufficient amount of surface defects have accumulated, the bearing fails to perform its function. It may jam or fail to hold the position of the shaft, so that secondary damage occurs. It may overheat and burn the lubricant. This is the end of the bearing life.

As discussed above, the bearing goes through a number of stages on its way to final failure. Obviously, it is desirable to detect the problem some time before the final failure occurs.

But when? The timing is critical, because too late may be catastrophic but too early causes premature removal and is therefore uneconomical.

It can easily be shown that there is more than one answer to this question. In fact, different applications may result in completely different detection philosophy and completely different detection techniques.

Consider the situation where a radar antenna rotates resting on one roller bearing. Or a jet engine in an aircraft, where the main rotor is axially held by only one ball bearing. In both these cases final failure of the bearing would cause complete performance failure and heavy secondary damage. It is desirable in this case to detect the appearance of the first fatigue spalls, which would correspond to point A on the wear-rate curve. At that point most of the bearing life is expended, and the risk for rapid failure high. This is the time for requesting a replacement bearing for the antenna, or to schedule maintenance of the jet engine.

Consider now another situation - a spacecraft gyro undergoing final checkout before acceptance for a mission that requires long life. The components which usually fail first are the rotor bearings. In this case there is obviously no reason to look for fatigue spalls in the bearings, which are new. Instead one will want to look for the existence of initial imperfections such as misalignment, lack of roundness of bearing surfaces, etc., which may increase the load at some locations on bearing races and thereby cause early failure.

These are two entirely different definitions of a bearing malfunction, suited for different applications. Others may fit better in other cases. For the purpose of categorizing detection methods it has been found practical to distinguish between local defects (spalls, corroded spots, Brinelling) and distributed defects (misalignment, lack of roundness, unequal ball diameters) as Figure 3 illustrates.

Many different techniques are used to detect bearing malfunctions in operating machinery:

Oil contamination: Spalling of bearing surfaces generates metal chips which follow the lubrication oil and can be collected in filters or with magnetic plugs. Smaller wear particles may be detected with spectroscopic or radiographic oil analysis methods.

Temperature: The increased friction which precedes bearing failure generates heat that increases the temperature

of bearing and lubricant. Oil temperature is often measured.

Overall Noise Level: When the spalling has proceeded sufficiently the bearing gets noisy. The problem is that bearings are usually buried deep down in machinery, and there may be many other noise sources.

All these techniques and others, have been tried with varying degree of success in many cases. The problem is generally that the malfunction indication comes too late, so that there is no time to take preventive action before total failure has occurred. Another major problem is that these techniques do not identify the failure mode. This is unsatisfactory since failure mode identification is often necessary to decide what corrective action should be taken.

With this background, the work at the Research and Development Center has been directed toward developing methods for earlier detection of bearing malfunctions than what has previously been possible. This has involved diagnostic techniques based on vibration, or structure-borne sound, generated by the bearing and picked up with an external sensor. Analytical predictions have been made of specific vibration patterns generated by good bearings under various load conditions, and bearings with defects as discussed above. A number of projects, carried out at the R&D Center with the cooperation of several product departments, have given opportunities to compare analytical predictions with actual test results. It has been generally found that it is possible to make analytical predictions of vibration patterns from bearings with a number of defects. By employing selective data reduction techniques to extract the calculated patterns from the overall vibration signal, it has been possible to detect defects earlier than with other known methods.

In the following a few examples will be given to demonstrate how bearing malfunction signatures can be predicted and extracted from complex vibration signals. The examples will cover both local defects, very briefly since these have been discussed in earlier papers, (Reference 1) and distributed defects where the work has been done more recently.

DETECTION OF FATIGUE SPALLS AND OTHER LOCAL DEFECTS

A local defect in the inner or outer race of a bearing generates an impact every time a ball (or roller) rolls over it.

Likewise, if the defect is in a ball surface, an impact is generated every time it hits the inner or outer races. If the bearing rotates with constant speed each defect generates a regular set of impacts with an impact repetition rate that

depends upon bearing speed and location of the defect. Assuming that no sliding occurs in the bearing, those fundamental repetition rates can be calculated. The result is:

$$\begin{array}{ll} \text{Outer race} & f_e = \frac{n}{2} f_r \left(1 - \frac{BD}{PD} \cos \beta\right) \quad (\text{cps}) \\ \text{malfunction} & \end{array}$$

$$\begin{array}{ll} \text{Inner race} & f_i = \frac{n}{2} f_r \left(1 + \frac{BD}{PD} \cos \beta\right) \quad (\text{cps}) \\ \text{malfunction} & \end{array}$$

$$\begin{array}{ll} \text{Ball} & f_b = \frac{PD}{BD} f_r \left(1 - \left(\frac{BD}{PD}\right)^2 \cos^2 \beta\right) \quad (\text{cps}) \\ \text{malfunction} & \end{array}$$

where f_r is the relative speed between inner and outer race (revolutions per second), and BD , PD , β , and n as defined in Figure 4.

The vibration pattern, or signature, which can be expected from a single local defect in a bearing then consists of a series of transients with a repetition rate as calculated above. Figure 5 shows such an ideal pattern.

The problems in practical cases are that the signature from the bearing defect is often hidden behind background noise, and also that the repetition rate can only be calculated approximately. It has been discussed in an earlier paper (Reference 1) how a diagnostic system may be designed to extract this signature from a local defect, and thereby make the diagnostic system more selective. In addition to the mere transient repetition rate, there are many characteristic features associated with each individual transient. These details of the transient waveform depend on the load pattern for the bearings, and on the structural response to the impacts between rolling element and defect.

As an example, consider the effect of an unbalanced rotor, supported by the bearing under study. In addition to the gravity load, which always points in one direction, there will now be a rotating unbalance load acting on the bearing. This combination of loads will cause a modulation of the ball-race contact forces. A local defect on the outer race, for example, will see a 1/rev. modulation of the loads on the balls rolling over the defect. This effect will cause a modulation of the amplitudes of the impact transients. The calculated signature will look as shown in Figure 6a.

The modulation of the envelope is confirmed by Figure 6b which shows an analysis of vibration data measured on a jet engine with a large spall in one of the main ball bearings. The signal was analyzed through signal averaging as described previously in this paper, in this case programmed to enhance

events repeating with the envelope repetition rate rather than the individual transients.

The previous discussion has involved prediction of repetition rates and transient amplitudes, but not any details of the individual transient waveform. If the mechanical structure supporting the bearing is known, it may be possible to calculate its response to an impact at the bearing race. This is going to result in a number of "ringing frequencies" with which the structure will ring after the impact. It has been found in one case, for example, that the structural response to the impact from a local defect in a jet engine bearing can be described with a very low number of ringing frequencies. Figure 7 illustrates this case with analysis of a vibration signal measured inside a jet engine under idle conditions. The engine had a spall in one main bearing.

The signature shown in Figure 7 was extracted from the same raw vibration data as shown previously in Figure 6 through signal averaging as described in Reference 1, but without rectification before the summation. The analysis was here programmed to display the individual impact transients.

These are only a few examples, serving to illustrate the point that vibration signatures can be analytically predicted, and extracted from vibration data measured on machinery with local bearing defects. By knowing as many characteristics as possible in the predicted signature, the sensitivity of the diagnostic system can be maximized, and its false alarm rate minimized.

The success in detecting and identifying localized bearing defects has led to the development of an electronic system, which automatically performs the signature extraction and interpretation. This was developed in a joint program between General Electric's Research and Development Center and Aircraft Engine Group, Condition Monitoring Engineering. A laboratory model of this bearing condition monitor is shown in Figure 8. Miniaturized and further automated systems are currently being developed by the General Electric Company both for aircraft and industrial uses.

DETECTION OF DISTRIBUTED BEARING DEFECTS

In certain cases it is not sufficient to detect the first local surface defects in bearings. This was discussed above in connection with final checkout of gyros. The requirement is instead to detect such initial conditions which might cause high local forces in a bearing and therefore early failure. These are conditions such as misalignment, lack of roundness of

bearing races, unequal ball/roller diameters, etc., which are always built into the rotor system to some degree during assembly.

The capability which has been developed to detect such internal conditions through external measurements will be discussed in connection with a specific example.

The study was made to determine the feasibility of using vibration signals to predict the life of spacecraft components. As a first suitable test vehicle one type of rate gyro was selected. Eight similar gyros of this type were available for the study.

Rate gyros are critical components in spacecraft navigation systems. Therefore, much work has been devoted to generating rate gyros with long life expectancy. This work has resulted in gyros with long average life. However, the increase in average life of gyros achieved through higher quality and precision is not matched by a similar increase in the uniformity of individual gyro lives. In other words, even if average life of a certain type of gyro is long, there is still considerable variation around this average for an individual gyro. This large variation becomes of critical importance when the need for extremely high reliability arises.

In this situation, a screening tool with the capability to select the most long lived individuals within a group of gyros would offer one solution. However, a manufacturer of high quality gyros has already before delivery employed a number of sophisticated techniques to assure uniform performance. A useful screening tool must therefore be more sensitive than conventional checkout procedures.

The primary purpose of this study was to determine whether mechanical signature analysis might provide such a sensitive tool for gyro checkout.

The major failure reason in rate gyros is failure of the ball bearings which support the rotor. The work was therefore concentrated to such ball bearing defects which might be present in a new gyro motor and later cause early failure.

Initial vibration analyses of eight rate gyros, all performing within specifications, showed large variations between different gyros. This was interpreted as evidence that vibration analyses provided an extremely sensitive tool.

The initial test also showed that gyros generate a very

complex vibration spectrum, containing many hundred tones distributed over a very wide frequency band. Most of the effort in this study was therefore directed towards the interpretation of the complex gyro signature in terms of such parameters which might influence gyro life. This work included both mathematical modelling of the generation of bearing vibration signatures, and testing of gyros with inserted malfunctions. The analytical work was necessary in order to establish acceptable confidence in the results, since the eight gyros which were available did not by any means provide a statistically satisfactory sample.

MATHEMATICAL MODELLING - DISTRIBUTED DEFECTS

In order to predict the vibration signature from a bearing, it is necessary to first consider the source system, i.e., the bearing and its immediate support structure. This is where the signature is generated. In many cases it is not possible to locate the vibration sensor close to the bearing, and in such cases the transmission of the vibrations from bearing to sensor must also be considered.

Consider the source system in Figure 9. This is a ball bearing with six balls. The primary forces, which are the source of all vibration, are the six contact forces between balls and races.

In the figure it is assumed that the inner race is stationary and connected to the gyro frame. If instead the outer race is stationary, like in most electrical motors, the forces between balls and the outer race are considered.

The ideal situation, with no defects present in the bearing, is that all ball-race forces are equal and constant. (Gravity forces are negligible compared to pre-load forces in the gyro). The primary vibration source is then the six constant ball forces, rotating with the same constant speed as the ball cage, and acting on the stationary bearing ring.

When defects are present, the normal ball-race force pattern will be disturbed. Figure 10 shows the type of pattern which would be expected for a misaligned and an elliptic bearing race.

These disturbances of the normal force pattern are entirely different from the impacts generated in a bearing with spalls or other local defects. Therefore another approach to the analytical modelling must also be taken.

Without going into great detail here, it can be shown that most of the "initial" bearing defects can be represented by

disturbances of the force pattern similar to the examples shown in Figure 10. In a general approach to the problem, it is assumed that the ball-race force pattern follows a sinusoidal profile as shown in Figure 11. More complex solutions can then be constructed through Fourier analysis. The sinusoidal pattern may have an arbitrary angular velocity in order to simulate defects located on inner race, outer race, or balls/rollers.

The magnitude of each ball-race contact force is the following function of ϕ :

$$P = P_o \left\{ 1 + \epsilon \cos m (\phi - \beta t) \right\}$$

β = Force pattern angular velocity (rad/sec)

ϕ = Angular coordinate (radians)

m = Number of nodes of force pattern around race circumference

ϵ = Degree of force modulation

The dynamic radial deflection δ of the stationary bearing ring may be calculated by repeated solving of Lagrange's equations for the system.

$$\begin{cases} q_{n,\sin} + \omega_n^2 q_{n,\sin} = \frac{P_o}{M_n} \sin n\omega(t-\frac{\theta}{\omega}) \left\{ 1 + \epsilon \cos m (\omega t - \theta - \beta t) \right\} \\ q_{n,\cos} + \omega_n^2 q_{n,\cos} = \frac{P_o}{M_n} \cos n\omega(t-\frac{\theta}{\omega}) \left\{ 1 + \epsilon \cos m (\omega t - \theta - \beta t) \right\} \end{cases}$$

where $q_{n,\sin}$ and $q_{n,\cos}$ are generalized coordinates, and M_n are effective mode-masses. After a number of manipulations an expression for the dynamic deflection δ caused by all the ball forces is constructed:

$$\begin{aligned} \delta = \sum_{\theta} \sum_{n=1}^{\infty} \frac{P_o}{M_n} & \left\{ \frac{\cos n(\omega t - \theta - \phi)}{\omega_n^2 - \omega^2} \right\} + \\ & + \epsilon \frac{A \cos m \langle (\omega - \beta)t - \theta \rangle \cos n(\omega t - \theta - \phi)}{A^2 - B^2} - \end{aligned}$$

$$- \epsilon \frac{B \sin m (\omega - \beta)t - \theta \sin n (\omega t - \theta - \phi)}{A^2 - B^2} \quad \left. \vphantom{\frac{B \sin m (\omega - \beta)t - \theta \sin n (\omega t - \theta - \phi)}{A^2 - B^2}} \right\}$$

where

$$A = \omega_n^2 - \omega_n^2 - (\omega - \beta)^2 m^2$$

$$B = 2mn_\omega (\omega - \beta)$$

It can directly be seen that the solution for δ consists of several series of modulated tones, with frequencies and modulation patterns depending on the type of defect. By setting $\epsilon = 0$, the solution for a "perfect" bearing is obtained.

Further study of the effects of signal transmission from the bearing to the outside of the gyro shows that certain tone patterns propagate easily whereas other patterns are heavily attenuated through force cancellation.

The conclusions of these calculations is that characteristic vibration signatures, in the form of tone patterns, can be analytically predicted for most of the defects under study. This provides a tool with which the very complex vibration patterns generated by the gyros can be understood.

As an example of the highly complex tone pattern generated by the two rotor ball bearings in a gyro, Figure 12 shows a high speed spectral analysis of the vibrations measured on the outside of a gyro. Horizontal scale is time, vertical scale is frequency. Dark lines indicate tones in the signal. The gyro was first run at constant speed for twenty seconds, and then coasted down to zero speed.

In order to practically test the calculated bearing malfunction signatures, the eight rate gyros under study were sent back to the manufacturer for insertion of minor defects in six of the eight gyros. Three types of defects were selected as important for gyro life. They were:

- o Rotor Bearing Misalignment
- o Incorrect Pre-Load of Rotor Bearings
- o Rotor Unbalance

This selection was made in agreement with the gyro manufacturer. The three defects were inserted in two gyros each, thus making six defective gyros. The two remaining gyros out of the total group of eight were assembled without malfunctions.

The severity of the defects was generally such that all gyros were within or almost within performance specifications.

The eight gyros were run at the Research and Development Center, vibration signals were recorded and analyzed. The analysis results were compared to previously generated analytical models of predicted signatures for the inserted types of malfunctions. At the time when this was done it was known which malfunction types and how many of each were inserted in the gyros, but not which malfunction was inserted in each particular gyro. The result of this independent signature analysis is summarized in Table 1.

Thus of the eight inserted malfunctions seven were detected and identified correctly! As far as the gyro No. 6 with 3 pounds preload instead of 2 pounds, it is conceivable that the preload actually was lower than 3 pounds. It is generally very difficult to control bearing preload during gyro assembly, this is one of the major reasons why this type of defect was selected for the study.

The seven correctly detected defects were detected by ranking after study of spectral analysis plots and interpretation of the data based on previous mathematical modelling. It was at that time not attempted to assign numerical values to the defects.

As shown in Table 1, the evaluation resulted in prediction of several more bearing defects than those which were intentionally inserted. At the time when these predictions were made it was not possible to get them verified since all gyros had normal performance. However, all eight gyros were subjected to a life test and then torn down and inspected. The life test duration was approximately six months, during which none of the gyros failed to run. Shortly before the end of the life test, gyro No. 1 was shut down because of markedly increased overall noise level.

The inspection of the gyro bearings after teardown was done in considerable detail. As far as the two types of additional defects predicted by MSA before the life test, the result was:

Lack of roundness, outer bearing race, predicted for gyros No. 5 and 6. Completely confirmed by measurements! The two tested gyros have bearing housings with 150-200 micro-inches lack of roundness compared to normally 20-50 micro-inches for the other gyros.

Unequal ball forces, predicted for gyros No. 1, 2, and 8. Some indication also for gyro No. 7. The most likely

reasons for unequal ball forces would be unequal ball diameters within one bearing. The balls from gyros No. 2, 7, and 8 were measured and found to be well within specifications! The other gyros were not measured. This may initially look like a negative conclusion. However, one observation of great interest can be made. Of the eight tested gyros, only three showed heavy bearing wear after teardown. The rest were sometimes pitted and brinelled but did not show significant wear. The three gyros with worn bearings are the same three which showed the characteristic "unequal ball force" pattern when new. Thus even if the reason for the pattern is not unequal ball diameters, it may still be significant. If it can be further confirmed that this frequency pattern is reliably associated with early wear, it might well be the most important result of the study!

The techniques for bearing condition monitoring which were described above have later been further developed and refined, among other things to include the effects of multiple defects occurring simultaneously. These diagnostic techniques are currently being used in a program with NASA to evaluate gyros for the Apollo project (Reference 2).

APPLICATION TO GEAR DIAGNOSTICS

A pair of properly operating gears, running at constant speed and load can be expected to generate a signal which is periodic with the meshing frequency. The signal can be sound, vibration, stress, strain or something else, and all of the meshing events are similar when there are not mechanical imperfections in the gears. A typical waveform generated by a gear with ten teeth would look like the example of Figure 13.

Given the gear geometry and speeds, the repetition rate $1/T$ is very simple to calculate. The characteristic waveform $F(T)$ depends on gear profile, load, speed, coupling between gears and sensor and many other parameters, and is very difficult to calculate. Some predictions can be made, however, about the perturbations resulting from certain defects.

Generally gear defects can be separated into two categories:

1. Local Defects. These are defects which appear on one or more teeth but are not uniformly distributed around all teeth. Gears with these defects, cracked or deformed teeth, or scoring for example, will show the effects of those defects only when the defective tooth is in mesh. This makes interpretation a rela-

tively simple matter; when the waveform for one revolution of the gear is extracted, each tooth mesh can be compared with the others. If the waveforms are not all the same, within some limit, a defect is present.

2. Distributed Defects. These are defects which are distributed all around the gear and thus the effects will be seen everywhere on $F(T)$. A typical example is a gear which has a non-uniform load distribution on its teeth as a result of eccentricity of its shaft. Because of the changing load during each gear revolution the amplitude of the mesh waveforms is altered in a fashion proportional to the load. The resulting waveform appears as a carrier frequency at the mesh rate with amplitude modulation at the rotational frequency. Distributed defects may be either symmetrical or non-symmetrical. In the latter case, interpretation is facilitated by comparing individual teeth. In the former case, interpretation of the signature may be much more difficult.

A Gear Condition Monitor, shown in Figure 14 as part of a Jet Engine Diagnostic System, has been built at the Research and Development Center in a joint program with the Condition Monitoring Engineering Operation of the Company's Aircraft Engine Group to extract and automatically analyze the signatures of individual gears in a jet engine gearbox. The monitor pre-processes the signal by bandpass filtering and waveform averaging to isolate one gear signature from the total signal sensed externally on the gearbox housing. The extracted waveform is then analyzed automatically for the two defect categories mentioned above.

One part of the automatic analyzer, which identifies defects in the first category above, performs a crest factor analysis. A normal gear tone, with all tooth meshes equal in shape and amplitude will have a certain ratio of peak to root mean square amplitude. If the shape of a tooth mesh changes, (e.g., one tooth mesh signal is greater than the next) this change will be reflected in a different (in general increased) peak to RMS ratio. This ratio is displayed by the analyzer for every data analysis performed.

The second portion of the automatic analysis system is designed to detect and display the percent modulation of a gear tone, as an indication of the presence of distributed defects of the non-symmetrical type. The meter on the front panel is calibrated to read directly the percent modulation of the averaged signal stored in the memory of the digital averager. Permanent records of the waveform may be made.

Illustrations below are an example of how the signatures of these defects can be extracted and displayed. The data was collected from a large transmission operated on a test stand. The housing of the transmission was instrumented with accelerometers sensing the structure-borne sound generated internally by the many operating components.

The first figure is the averaged waveform of the planetary gear train, composed of a 76-tooth sun gear 15.2 inches in diameter, ten planets 5.4 inches in diameter with 27 teeth and a 26-inch diameter 134-ring gear fastened to the housing. The meshing frequency, at normal operating speed is 550 Hz. To extract this waveform, the sensor mounted over the ring gear support on the housing was interrogated. The signal was filtered and averaged in the waveform analyzer with the basic period T selected at one revolution of the carrier.

There are two basic features to the resulting averaged waveform. First, the higher frequency signal is the sound generated by the tooth meshing, in this case 550 hertz. Modulating this meshing frequency is a lower frequency, occurring at ten times per carrier revolution. Each modulation cycle is generated by one planet in mesh with the ring gear passing by the accelerometer. Since the acceleration measured at a point on the ring gear is dependent on the forces between the meshing teeth, the extracted signal indicates relative load sharing between the planets. In this case, one planet is obviously carrying less load than the rest. (This display shows parts of nine out of the ten planets).

The parameters of analysis for this gear were chosen to display the relative signals generated by each planet; hence, the selection of T at the carrier pass period. Other parameters are possible, for example, if T were selected at the tooth mesh period times the total number of teeth on the outer ring gear, the average waveform would be the average signal from each tooth. Thus, this technique permits isolation of defects that could not otherwise be studied.

Figures 16 and 17 are signatures of a bevel pinion gear. This 23-tooth gear is rotating at 13,800 RPM and is in mesh with a 92-tooth bevel gear. In Figure 16 a repeating pattern is visible every revolution of the pinion gear. The most obvious part of this repeating pattern are the three spikes across about one millisecond of the signal. When the transmission was inspected after several hours of running, the gear in question was found to have hard wear patterns on five teeth. The gear was replaced and the signature in Figure 17 resulted; some modulations present but generally a much more normal signature.

In this example, the driving gear and the driven gear have an integral ratio of teeth, making it possible to display the effects associated with both gears simultaneously. The more common occurrence is that the ratio of teeth is non-integral, requiring that the summation process be performed twice, with the period T selected for each gear.

Further discussion of gear diagnostics can be found in a previously published paper (Reference 3).

OTHER APPLICATIONS OF SIGNATURE ANALYSIS TO MACHINERY DIAGNOSTICS

Similar techniques and logic as described above for gears and bearings can also be applied to many other machinery systems. The following paragraphs will give a brief summary of some of these applications with reference to other papers where more detailed discussions can be found.

DIAGNOSIS OF PUMP SYSTEMS

Both reciprocating and rotating pumps generate repetitive signatures which can be extracted from background noise with signal averaging, performed so that speed variations are tracked by the processing system. This has been successfully done for both piston and vane pumps and has led to the development of an automated diagnostic system for hydraulic drives of satellite tracking antennas. (References 4 and 5) An example of signatures from a vane pump in normal and defective condition is shown in Figures 18 and 19.

DIAGNOSIS OF MACHINING PROCESSES

The metal cutting action during machining generated characteristic mechanical signatures which can be used to automatically detect low level tool chatter or cutting edge wear without stopping the machine for visual inspection. This capability is of great importance in developing adaptive machine tool controls (References 6, 7, and 8).

ANALYSIS OF HEART SOUNDS

Significant gains have been made in the field of Phonocardiology by the Research and Development Center by applying the techniques of Signature Analysis to the sounds of normal and abnormal hearts. It is now possible to specify characteristic waveforms associated with certain types of heart ailments

and to provide the medical profession with an advanced tool to aid them in diagnosis.

An outgrowth of the Phonocardiology Program has been the analysis of the sounds generated by a cardiac assist device. This program is providing the design engineers with information regarding the performance of the pumps - speeding the day when assist devices will be available for implantation.

Then these techniques will be used to monitor the condition of a patient with an assist device and keep the physician informed of its operation. Figure 20 is a typical example of the vibration signature of a left ventricular assist device. Points 1 and 3 are disc valve closures. At point 2 a valve is bouncing against the support structure. At point 4 the pumping bag fills and uncollapses. Deviation from this normal signature would indicate such defects as occluded valve seats or ruptured bags.

APPLICATION OF SIGNATURE ANALYSIS TO NON-REPETITIVE PHENOMENA

Although the applications of signature analysis discussed above have focused on repetitive signals, there are many times when a much simpler type of analysis may be possible. In particular, if the signal to noise ratio is high, no specialized extraction technique may be necessary and the characteristic signature of a non-repetitive event may be recognized. Two examples of this may be taken from work performed to develop diagnostic techniques for nuclear reactors.

Hydraulically operated control rod drives contain several mechanical systems which are critical to operation of the reactor, notably the latching mechanism for retaining the rods and the hydraulic control valves. Figure 21 illustrates the events which can be seen in the direct signal obtained from accelerometers mounted on the drive housing and the accumulator. At 1 the drive valves are opened, generating an impact transient followed by a high level of hydraulic noise. At 2 the retaining fingers latch. At 3 the drive valve closes, again creating an impact transient following by a high level of hydraulic noise. At 4 the settling valve closes and the cycle is complete. Here is a case where the relevant acoustic signature can be directly observed with little or no processing.

Often the only necessary processing may be wide band filtering. Another application to diagnosing nuclear reactors is in the location of steam leaks in heat exchangers. Several sensors around the exterior of the exchanger are tuned to "listen" for noise in a particular frequency band which is generated by the leak. Correlation and triangulation between

sensors then locates the source of the leak within the heat exchanger.

A similar approach has found application in studies investigating cavitation phenomena. A cavitating fluid transmits transient bursts of energy to the structure of the container. A sensor on the container walls is sensitive to these transients and evaluates them by the crest factor analysis technique already discussed.

CONCLUSIONS

The work which has been discussed in this and previously published papers has proven that Mechanical Signature Analysis techniques can successfully be applied to almost any type of machinery. Particularly when machines generate repetitive signatures, advanced signal processing techniques are available to extract signatures from background noise, and provide automated diagnostics. Of particular value is the fact that specific incipient failure modes can be identified, usually long before changes in operating parameters show up.

Today's diagnostic technology can often directly be applied to many types of bearings, pumps, gears, and reciprocating mechanical systems. In some cases, such as for bearings and gears, diagnostic hardware has already been developed and is presently in use for aerospace and industrial applications. In other cases, research and development efforts are currently underway.

With diagnostic systems, such as discussed here, considerable savings can be made in terms of reduced unscheduled maintenance, improved product quality, and reduced testing time.

Table 1

Results From Mechanical Signature Analysis
Of Eight Rate Gyros

<u>Gyro Number</u>	<u>Inserted Malfunction</u>	<u>MSA Independent Results</u>	
		<u>Prediction of Inserted Mal- function Types</u>	<u>Additional Conditions Predicted</u>
1	Rotor dynamic unbalance	Rotor unbalance Second highest in the group. CORRECT !	Unequal ball forces
2	High bearing preload (4 lb. instead of 2 lb.)	Preload highest in the group - significantly separated from all other tested gyros. CORRECT !	Unequal ball forces
3	Misalignment of outer bear- race	Outer bearing race misaligned. CORRECT !	Bearing preload almost totally absent
4	Misalignment of outer bearing race	Outer bearing race misaligned CORRECT !	None
5	None-gyro normal	Gyro normal as far as inserted malfunction types are concerned. CORRECT !	Lack of roundness outer bearing race.
6	High bearing preload(3 lb. instead of 2 lb.)	Gyro normal! INCORRECT!	Lack of round- ness, outer bearing race
7	Rotor dynamic unbalance	Rotor unbalance highest in group. CORRECT !	None
8	Normal	Gyro normal CORRECT !	Unequal ball forces

REFERENCES

1. Weichbrodt, B., "Mechanical Signature Analysis, a New Tool For Product Assurance and Early Fault Detection", presented at the Fifth Reliability and Maintainability Conference, New York, New York, July 18-20, 1966, sponsored by AIAA, SAE, and ASME. It was published in the "Annals of Reliability and Maintainability", vol 5, "Achieving System Effectiveness", American Insititute of Aeronautics and Astronautics, 1966.
2. Sturgeon, Lloyd, "Final Report on an Acoustic Signature Analysis of 32 Gyro Wheel Assemblies", prepared for the Massachusetts Institute of Technology Ref. P. O. No. IL-B-(M)-300207, Document No. 70SD4230, April 16, 1970.
3. Thompson, R. A., and Weichbrodt, B., "Gear Diagnostics and Wear Detection", published by the American Society of Mechanical Engineers, 69-VIBR-10, March 30-April 2, 1969.
4. Tatge, R. B., "Acoustic Techniques For Machinery Diagnostics", presented at the Seventy-fifth Meeting of the Acoustical Society of America, May 21-24, 1968, Ottawa, Ontario, Canada.
5. Tatge, R. B., "Final Report Study for Maintenance of Hydraulic Motors", prepared for National Aeronautics and Space Administration, Goddard Space Flight Center, under contract No. NAS5-10559, October 1968.
6. Thompson, R. A., "The Modulation of Chatter Vibrations", published in the Journal of Engineering for Industry, Paper No. 68-WA/Prod-21, also presented at the Winter Annual Meeting of the ASME, December 1-5, 1968.
7. Weichbrodt, B., and Weller, E. J., "New Development in Cutting Tools: 'Listen to Your Tools - They're Talking to You'", ASTME Paper No. MR67-144. Paper was also presented to the ASTME 1967 Engineering Conference and Tool Exposition, Chicago, Illinois, April 24-28, 1967. Paper was published in "The Tool and Manufacturing Engineer", July 1967.
8. Weichbrodt, B., Weller, E. J., and Schrier, H. M., "What Sound Can Be Expected From a Worn Tool?", ASME Paper No. 68-WA/Prod-4, presented at the Winter Annual Meeting, December 1-5, 1968, New York, New York of the American Scoeity of Mechanical Engineers.

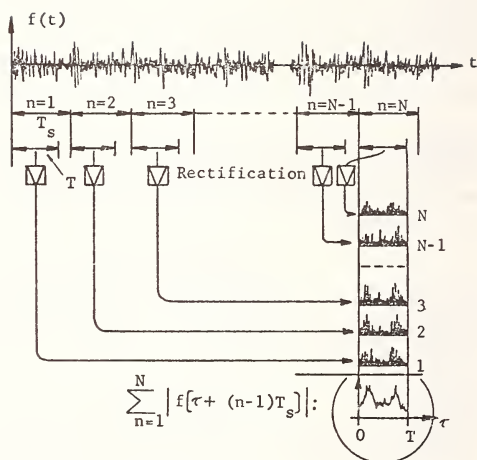


Figure 1
Signal Summation Analysis

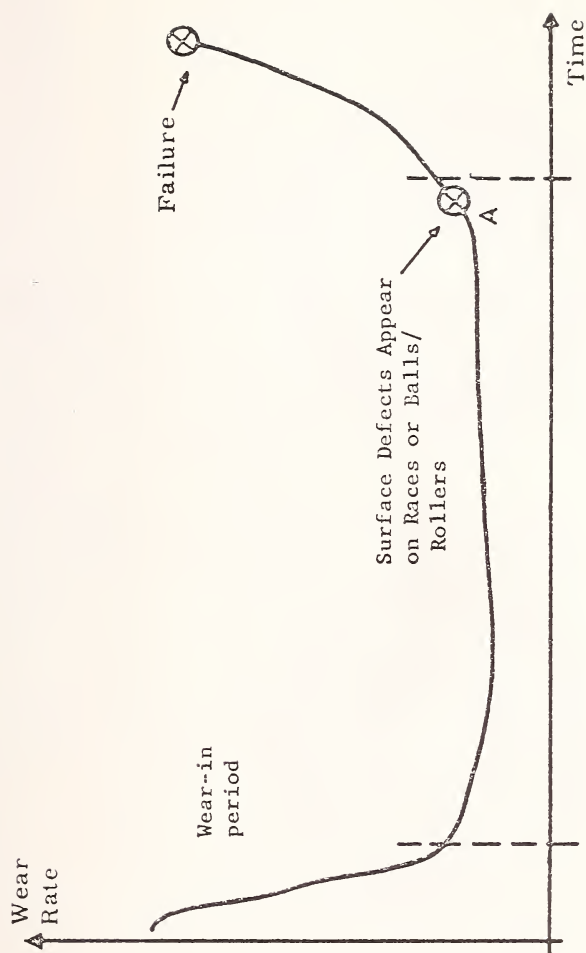


Figure 2 Typical Wear Rate Function For Rolling Element Bearings

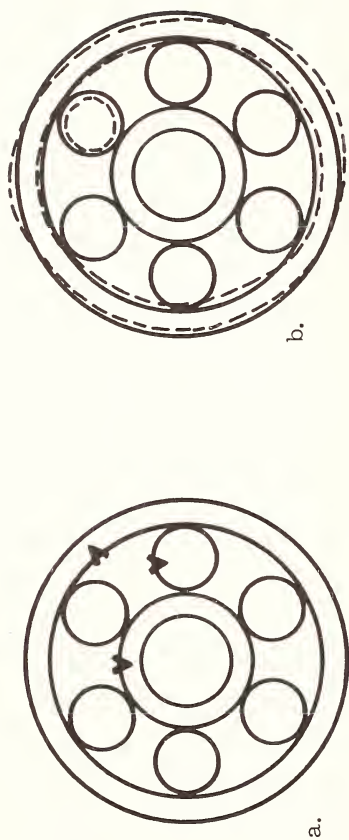
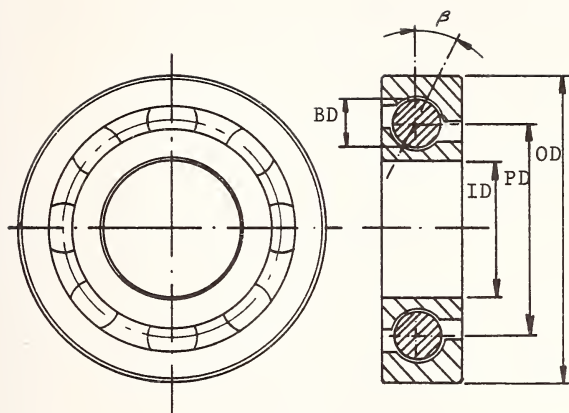


Figure 3 Illustration of Local (a) vs. Distributed (b) Bearing Defects



OD = Outer Diameter BD = Ball Diameter
 ID = Inner Diameter β = Contact Angle
 PD = Pitch Diameter n = Number of Balls

Figure 4 Basic Dimensions of Rolling Element Bearing

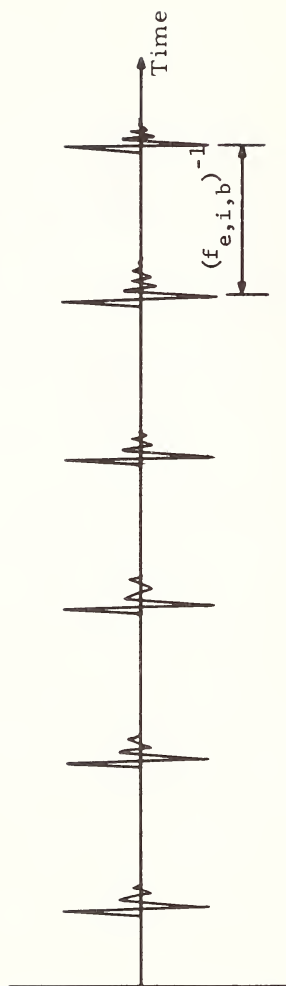


Figure 5 Ideal Vibration Signature From Local Bearing Defect

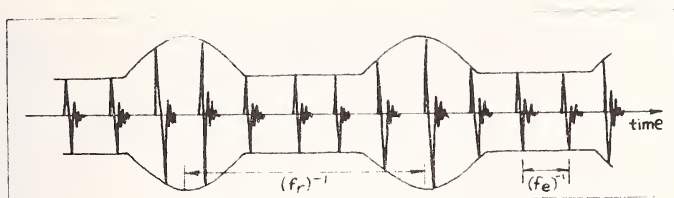


Figure 6a
Predicted Signal

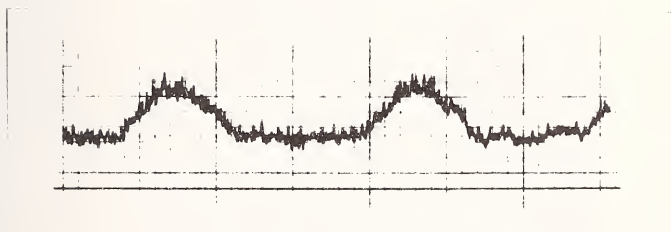


Figure 6b
Measured Envelope

Predicted and Measured Modulation of Impact Sequence From
Local Defect

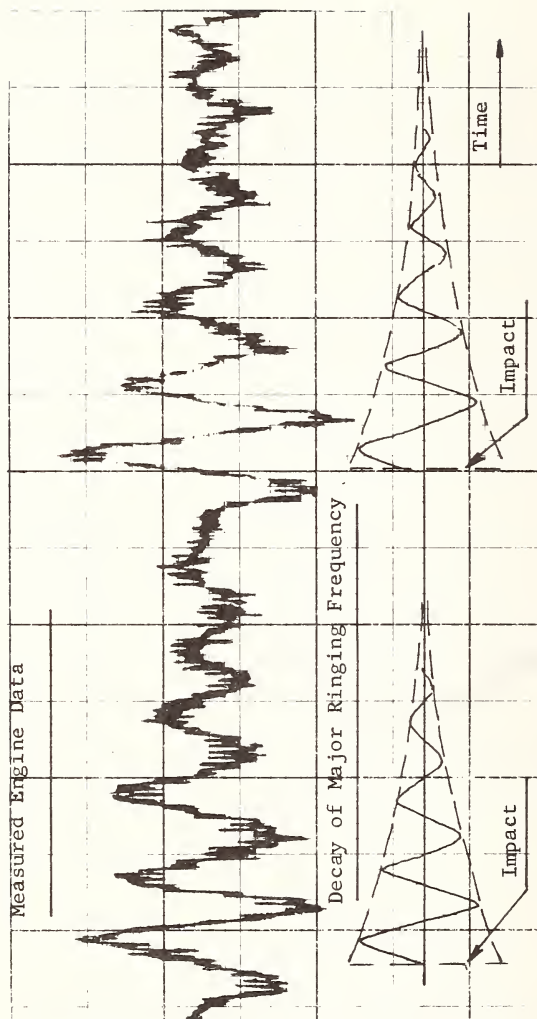


Figure 7 Details of Impact Sequence from Local Defect in Jet Engine Main Bearing. Signature Generated through Signal Summation.



Figure 8 Bearing Condition Monitor

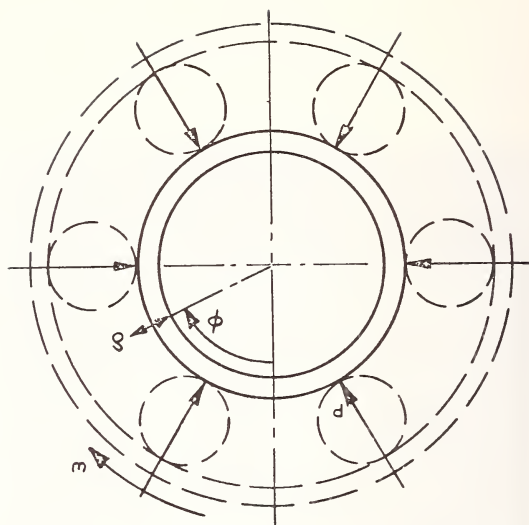


Figure 9 Ball Bearing with Primary Excitation Forces

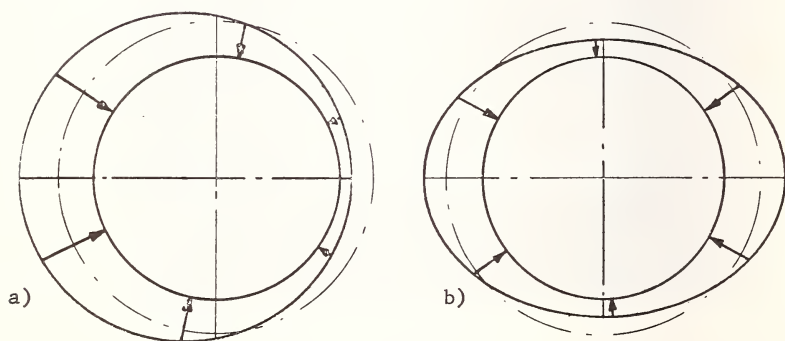


Figure 10 Ball-Race Force Pattern for Misaligned (a) and Elliptic (b) Bearing

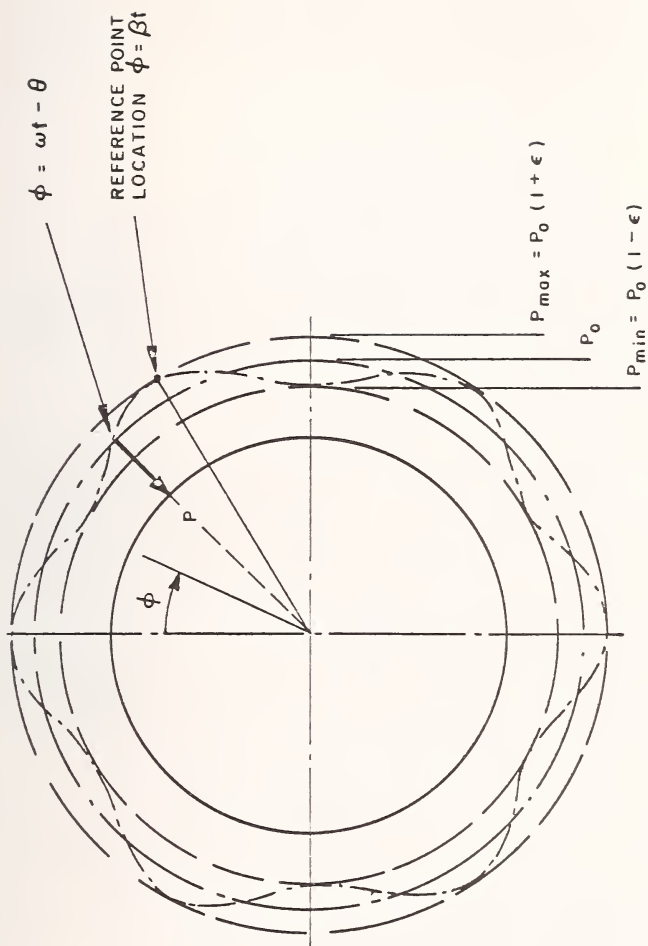


Figure 11 Model of Ball-Race Force Pattern in Bearing with Arbitrary Distributed Defect

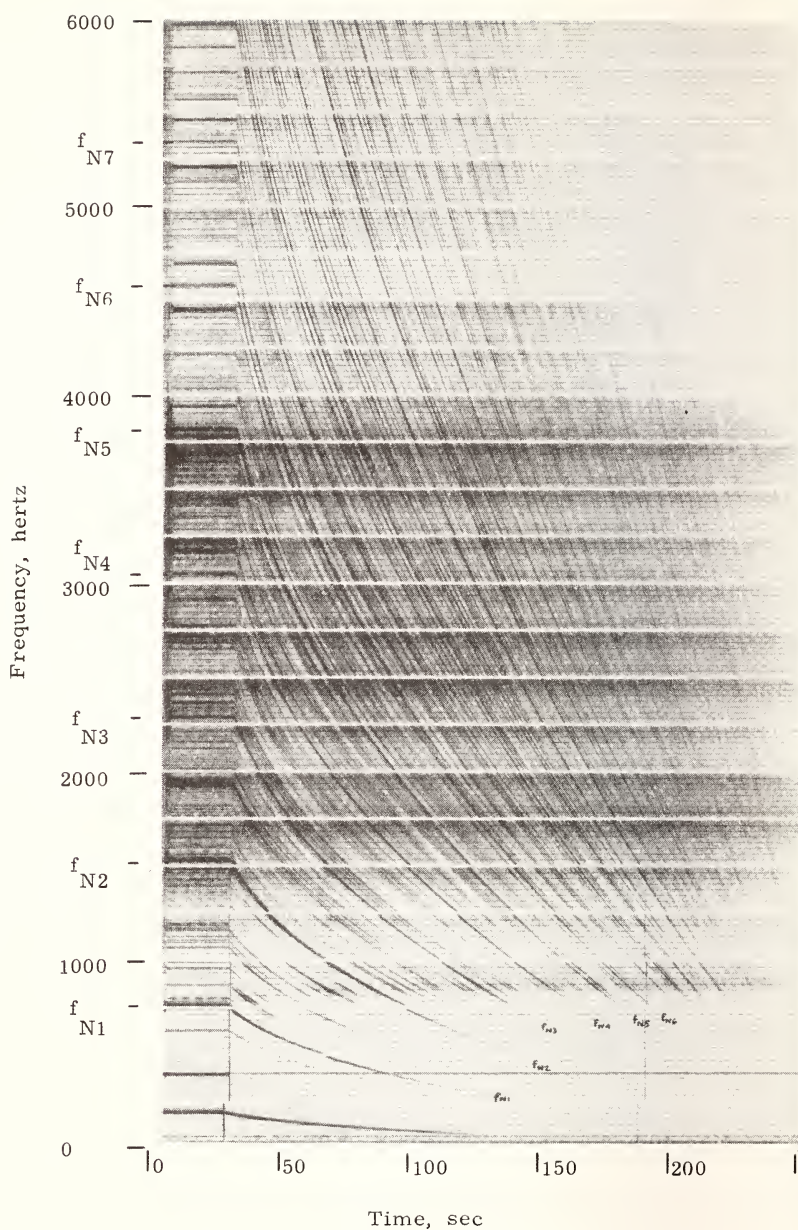


Figure 12 Intensity Modulated Spectrogram of Vibration Signal Steady State and Coast Down of Gyro.

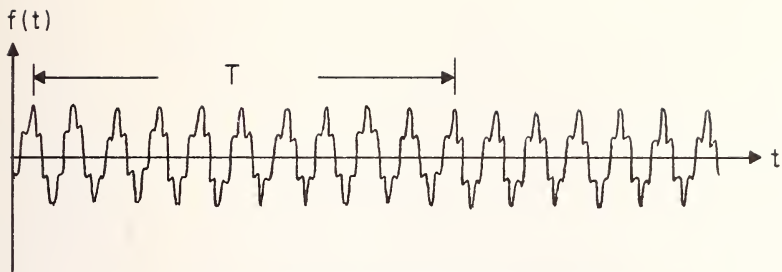


Figure 13 Gear Mesh Waveform

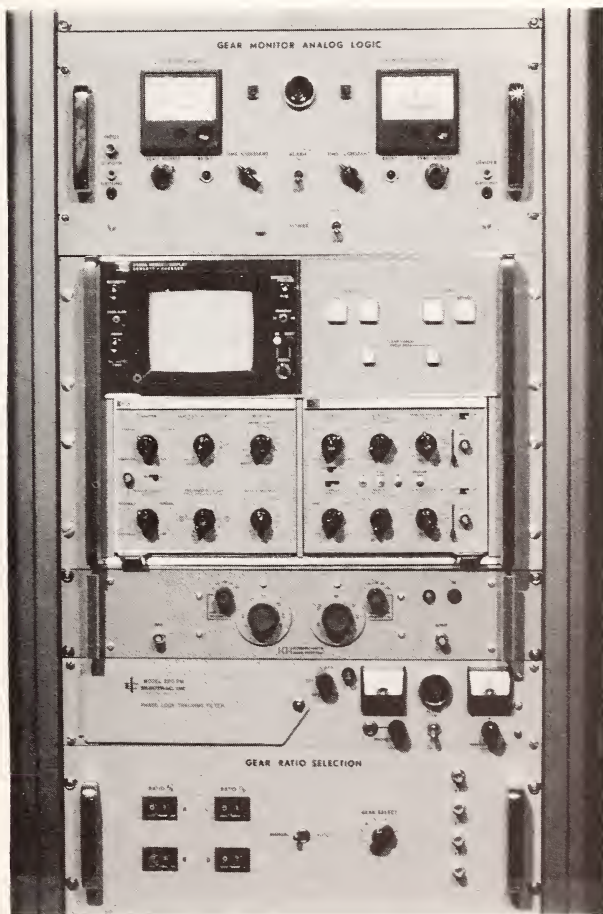
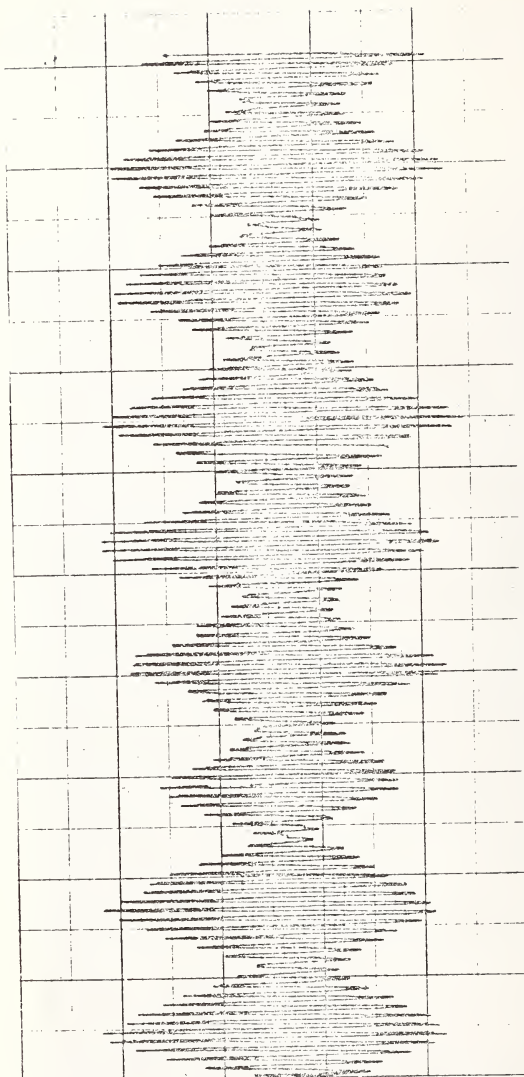


Figure 14 Jet Engine Diagnostic System



Time ↑

Figure 15 Signature of Planetary Gear

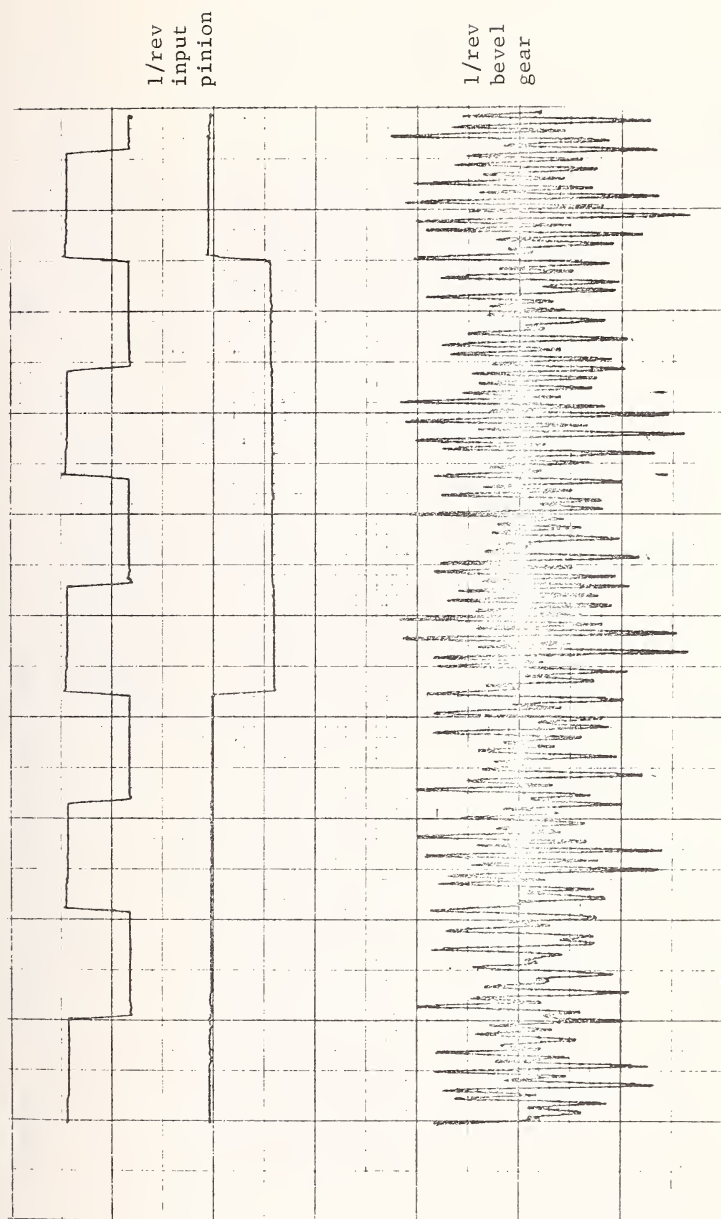


Figure 16 Signature of Bevel Gear With Abnormal Wear Pattern

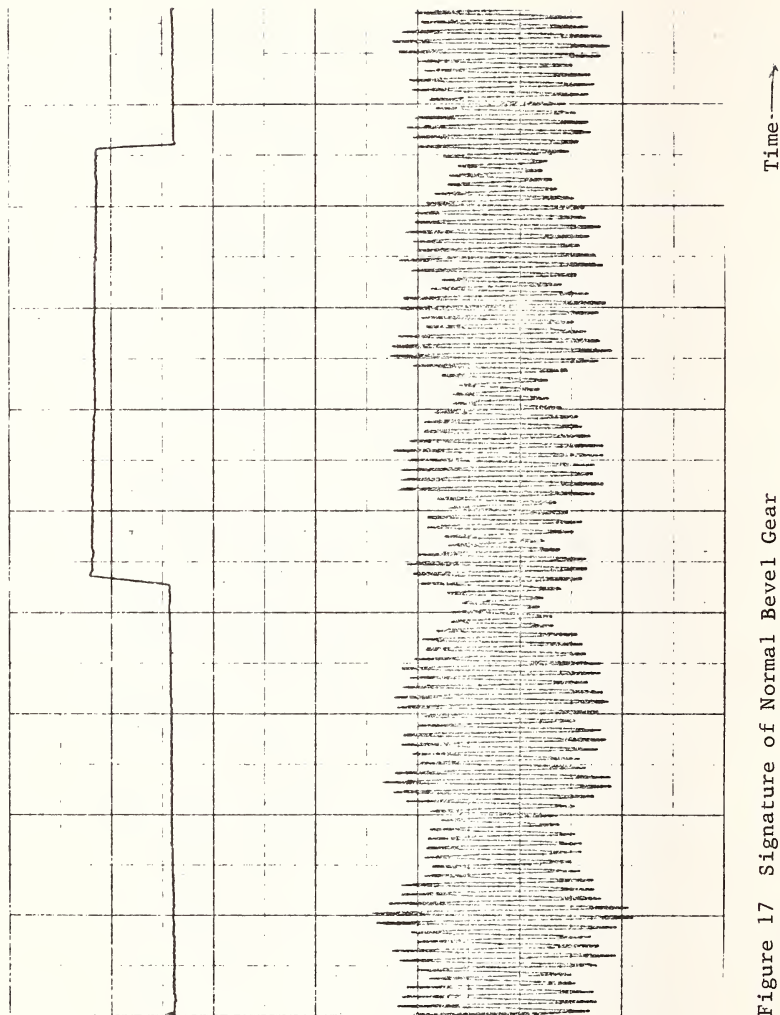


Figure 17 Signature of Normal Bevel Gear



Figure 18 Part of Vane Pump With Surface Defects

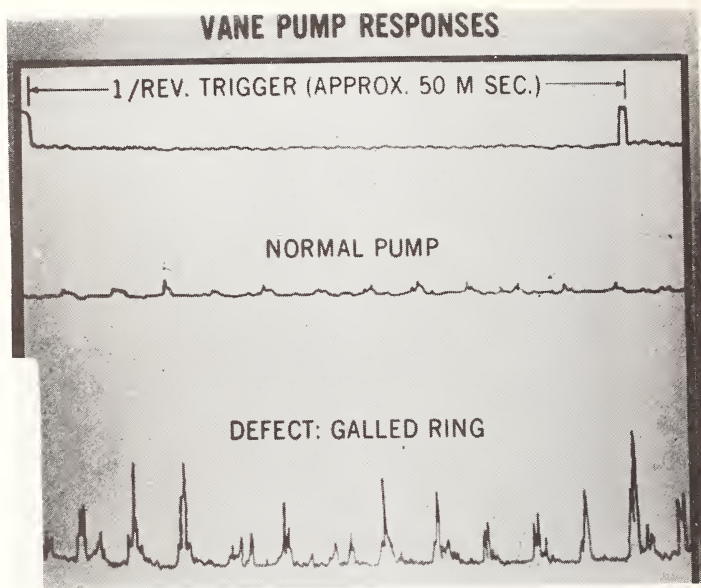


Figure 19 Mechanical Signatures From Normal
And Defective Vane Pump

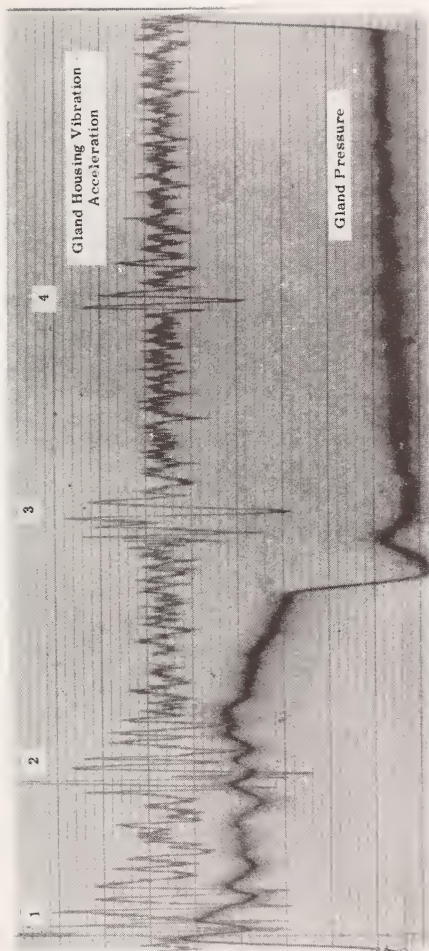


Figure 20 Pressure and Acceleration Display

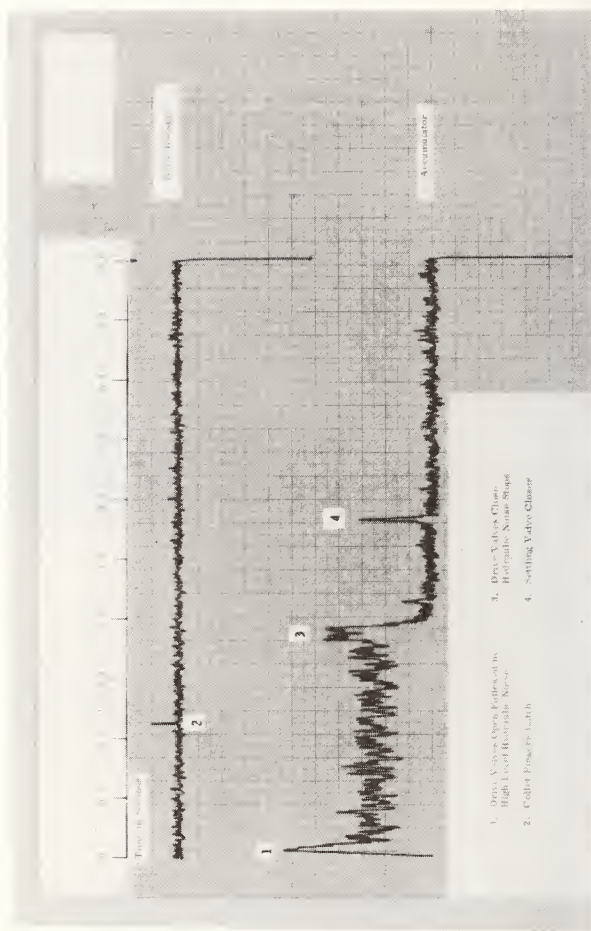


Figure 21 Test 15--Digital Envelope Display, Shim-up

MEASUREMENT METHODS FOR MICROCIRCUITS

W. Murray Bullis¹

REFERENCE: Bullis, W. Murray, "Measurement Methods for Micro-circuits," ASTM/IES/AIAA Space Simulation Conference, 14-16 September 1970.

ABSTRACT: One of the problems encountered with testing in either simulated or real environments is associated with the necessity of demonstrating that the failures observed are, in fact, due to the environment rather than random effects which would occur even in the absence of the environmental stimulus. This problem is particularly acute in the case of high-reliability electronic components such as silicon monolithic integrated circuits. For these parts, desired levels of reliability can be achieved only if all process steps in their manufacture can be carried out in a controlled and reproducible fashion. This paper surveys the status and availability of standard test methods suitable for making the measurements which are necessary to achieve such control. Consideration is given to standard measurement methods appropriate for thin film integrated circuits and hybrid microcircuits as well as those for silicon monolithic integrated circuits fabricated by the epitaxial, planar process.

KEY WORDS: device fabrication, environmental testing, integrated circuits, measurement methods, microcircuits, silicon

Testing in a simulated environment is usually undertaken in order to determine the effect of an environmental stimulus on the characteristics of the object being tested. Even if the simulation is assumed to be accurate, to obtain a valid test one

¹ National Bureau of Standards, Washington, D.C. 20234

must be able to demonstrate that the changes in characteristics are, in fact, due to the environment rather than to random effects which occur even in the absence of the environmental stimulus. In particular, it is frequently desired to establish whether the values of a certain set of parameters change to such an extent that the object will no longer perform its desired function. Objects in which one or more of the characteristics change to this degree are classed as failures. In addition an object may fail catastrophically, as by cracking or burnout, and thus may no longer be able to perform its function.

High-reliability electronic components such as silicon monolithic integrated circuits are designed to have extremely low failure rates even under the influence of various adverse environments. To show that the failure rate induced by environmental stress significantly exceeds the random failure rate requires large samples and carefully controlled experiments particularly when the two failure rates do not differ by very much.

As a result, tests to establish performance characteristics or failure rates under adverse environmental conditions are often unsuccessful. This is a particularly serious problem in connection with tests in nuclear radiation environments. When inconclusive results are obtained in underground tests with nuclear explosives the direct cost in dollars and resources which is wasted is self evident. Not so obvious is the costly but fruitless effort expended in design and analysis of the experiment. If the experiment should lead to incorrect conclusions the cost is even higher. These last costs are also encountered in tests conducted in simulated environments. Even though the environment can be carefully controlled in this case, experiments may fail because of parameter spread in the devices being tested.

There are two approaches to reducing the variability of devices and failures due to random causes. The traditional way is through the application of a variety of test procedures to completed devices in order to screen out defective units. Although this procedure has worked quite well for relatively simple devices, it becomes less and less effective as the complexity of the device and the variety of operating conditions to which it may be exposed increase. As a result, this "testing-in" of reliability is gradually being augmented or replaced by procedures which permit reliability to be built into the device. To do this requires that all process steps in the fabrication of the device be carried out in a controlled and reproducible fashion. Such control depends on the ability to determine and measure a large number of characteristics at the various process steps.

This involves a large number of tests on a variety of materials and structures. All the incoming materials including the substrate wafer, process chemicals, and miscellaneous parts must be inspected and accepted. Fabrication steps, such as epitaxial deposition, photomasking, diffusion, oxidation, and metallization, and assembly and packaging operations, such as

wire bonding, die bonding, and sealing, must be controlled. Finally the finished circuits must be tested.

Development of adequate measurement methods suitable for determining the necessary parameters during processing has also a secondary advantage; with the use of such measurements, increased understanding of the device operation can be achieved and improved values of various parameters can be obtained for use with models intended to enable device response to be predicted. This is particularly important in relating the results obtained in simulated environments to performance in actual environments. In addition, as such models become more refined, more efficient screening tests can be devised.

Much testing is presently carried out at the various producer-consumer interfaces and during the processing of semiconductor devices. Nevertheless, in a keynote speech at the Electrochemical Society's Symposium on Silicon last year, Willis Adcock of Texas Instruments emphasized that device production is "limited by broader than desired device parameter distributions due to the variability of the process-caused changes in material and device characteristics." (1)² In addition he noted that the area of silicon materials science which is concerned with the answer to the question "'What effect do the silicon processing operations...have on device performance?'" is in an early stage from the manufacturing viewpoint." As a solution he suggests that "quantitative correlations between the properties of the prepared slice and the subsequent device characteristics obtained through diffusion, interconnection, and packaging processes must be found and exploited." He also forecasts that "the greatest impact will likely come in improvement of the device property distribution through more effective material processing rather than in the form of the device structure." This effectively closes the circle because it is just this narrowing of parameter distributions which is essential in conducting effective tests in real or simulated environments.

The need, then, for adequate measurement methods is apparent. Where do we stand? What are we doing to improve the situation?

First, where do we stand? Many test methods are in daily use and a large fraction of these are written down on paper, either as in-house procedures, as military standards, or as standards issued by organizations such as ASTM, EIA, IEEE, and so forth. Unfortunately, users of these methods are all too often unaware of the limitations of the procedures they are using. Unless standard forms of the test method have been developed and unless the validity of the procedure has been demonstrated by a successful round robin experiment, these limitations are seldom documented. It is therefore of interest to

2

The numbers in parentheses refer to the list of references appended to this paper.

examine the kinds of methods which are available for use in various processing steps and the extent to which standards for them have been developed.

The prospect of increased standardization of measurement procedures for high-reliability of devices has improved over the past few years because of the almost universal use of silicon as the basic material for such devices and the wide adoption of the epitaxial, planar process for fabrication. The standard methods which are available have been developed principally because of their need in exchanges of materials or devices across a producer-consumer interface. As a result they cover the various requirements of microcircuit fabrication only incompletely.

The situation is best in regard to measurement methods for characterizing the silicon substrate wafer which is the basic starting material for monolithic circuits. Standard ASTM procedures (2) are available for most measurements, such as resistivity, conductivity type, orientation, and crystal perfection of the wafer. With suitable care and calibration, reliable results can be obtained in most cases. Nevertheless problems do exist in this area. In his review paper which opened a session on electrical characterization of silicon at last year's Symposium on Silicon, Paul Schumann of IBM Components Division observed that "the purchase of semiconductor materials is hampered by improperly specified and inadequately measured parameters, costing both vendor and customer time and money." (3) For other important characteristics such as gross geometry, flatness, and surface condition of the wafer, no standard procedures that have been validated by round-robin experiments exist. Some other parameters, such as oxygen content and carrier lifetime, are sometimes specified. The standard procedures for both these parameters are now undergoing investigation to determine if significant improvements in precision or sensitivity can be made.

Other materials such as water, acids and solvents, carrier and doping gases, silane or silicon halides, and photoresists are also necessary in the processing of semiconductor wafers. The methods for determining the properties of these materials are in various stages of development. Establishment of suitable standard procedures is hampered because of the difficulty of detecting and identifying the very small concentrations of impurities which are significant. Of these materials, water has been most intensively investigated. Although many of the standard methods for characterizing water were developed for a less pure water than is used in the electronics industry, tests appropriate to high-purity water have been developed in a few cases. In addition, standard methods are available for determining the resistivity of electronic-grade solvents, the concentration of certain impurities in hydrogen peroxide, and selected properties of photoresists. These represent only a very small beginning of an extremely large task.

Once the materials for processing are selected it is necessary to test each step of the process to verify that it is

being carried out reproducibly. This involves the determination of the characteristics of epitaxial, oxide, diffused, and metallic layers of various sizes and shapes. Because details of the procedures employed in fabrication are frequently highly proprietary, very little standardization has occurred in the measurement of these properties. Nevertheless measurement techniques with adequate and well-defined precision are essential whether to permit control and improvement in the processing for proprietary reasons or to permit the manufacturer to demonstrate that a process had been carried out reproducibly without revealing any of its proprietary details. This is particularly important in monolithic microcircuits because spurious interactions between circuit elements can be affected by the details of the fabrication process. Thus even devices which have the same electrical characteristics when measured under a given set of test conditions might perform differently in circuits where the conditions differ from test conditions.

Because minute particles can cause flaws (such as pinholes in thin films of oxides and metals) in the finished circuit, control of cleanness and particulate contamination during wafer processing is particularly important. Standard methods and specifications for clean room areas are available and are widely used and accepted. It is frequently necessary to control such other environmental factors as ambient temperature and moisture content at a specific temperature. No standard test methods appropriate to the control of these factors in microelectronics processing are now available.

The principal causes of failures which occur in high-reliability devices are related to problems encountered during assembly and packaging. As with fabrication, properties of incoming parts and materials must be determined, particulate contamination must be avoided, and the processes themselves must be controlled. Standard procedures for testing incoming parts are virtually nonexistent. Extension of general testing procedures is made difficult because of the small size and cleanness required of the parts. Particulate contamination can be monitored by the tests mentioned above. Control of assembly and packaging procedures is accomplished principally through visual inspections and environmental, mechanical, and electrical tests such as those found in MIL-STD-750 for discrete devices and MIL-STD-883 for microelectronics. Though these and similar tests are widely used, the procedures in most cases are quite general and considerable variations in test conditions can be expected to occur as a result of uncontrolled factors. Many of the electrical tests in these documents are applicable to testing of finished devices. Other standard methods for these electrical tests have been prepared by IEEE and EIA Committees.

One can conclude that although many standard test methods are available, much work remains to be done in nearly every area of semiconductor device processing. Now let us return to the question what is being done to attack this problem.

The ASTM is probably the leader in the development of standard testing methods which have been validated by round-robin experiment. The primary responsibility for developing ASTM standards in the semiconductor device field rests with Committee F-1 on Materials for Electron Devices and Microelectronics. Most of the ASTM documents mentioned previously originated with this committee. At the present time Committee F-1 has more than 70 additional documents in various stages of development as standards. These include methods for determining the characteristics of substrate wafers, the purity of various processing materials, the characteristics of photoresists and photomasks, and the electrical and crystalline properties of epitaxial layers. In addition test methods for evaluating both thin metallic films and the thick films used in hybrid microcircuits are under development. As with most other ASTM standards, the test methods developed by this Committee benefit from both user and producer participation and thorough evaluation before adoption.

The IEEE has recently reactivated its Electron Devices Standards Committee and is in the process of establishing task groups to work in a large number of areas of semiconductor device characterization. The Society of Automotive Engineers has a group which is working on specifications for certain electronic materials and processes. The International Society for Hybrid Microelectronics is also concerned with standardization activities but is relying on ASTM Committee F-1 for most test method development appropriate to this area.

The Electronic Industries Association is extremely active in the standardization of test methods for semiconductor devices. The various committees of this organization work closely with the military in the development and review of test methods to be incorporated in military standards. Unlike the committees concerned with discrete devices which are restricted to producer members, the committees concerned with microelectronics now have both user and producer representation. A number of these committees have undertaken round-robin testing of methods under development.

The Electronic Technology Division of the National Bureau of Standards is also assisting many of these standardizing committees as well as other government agencies in the development of the technology necessary for the establishment of new or improved standard measurement methods. This work is being carried out under the joint sponsorship of the National Bureau of Standards and several other government agencies (4).

From these various activities can be expected to come a set of measurement methods which will assist in the production of better characterized semiconductor devices with narrower parameter spread. The availability of such devices will assist in relieving one of the problems associated with testing high-reliability electronic components in real or simulated environments.

- (1) Adcock, W. A. in *Semiconductor Silicon*, R. R. Haberecht and E. L. Kern, Eds., The Electrochemical Society, New York, 1969, pp. 36-54.
- (2) A listing of ASTM standards pertinent to silicon and silicon processing is given in Bullis, W. M., and Scace, R. I., *Proc. IEEE*, Vol. 57, No. 9, September 1969, pp. 1639-1646. Most of these standards are published in Part 8 of the *Book of ASTM Standards* which appears annually in November.
- (3) Schumann, P. A., in *Semiconductor Silicon*, R. R. Haberecht and E. L. Kern, Eds., The Electrochemical Society, New York, 1969, pp. 662-692.
- (4) Joint Program on Methods of Measurement for Semiconductor Materials, Process Control, and Devices, supported by the National Bureau of Standards, the Defense Atomic Support Agency, the U. S. Navy Strategic Systems Project Office, the U. S. Navy Electronic Systems Command, and the National Aeronautics and Space Administration. For the most recent report on this work see Nat. Bur. Stand. (U.S.), Tech. Note 527, Issued May 1970.

LIFE TESTING USING CONTINUOUS ACCELERATION

E. Rabinowicz¹ and B. Shiralkar²

REFERENCE: Rabinowicz, E. and Shiralkar, B. "Life Testing Using Continuous Acceleration" ASTM/IES/AIAA, Space Simulation Conference, 14-16 September, 1970.

ABSTRACT: One method of carrying out accelerated tests consists of increasing the stress at a uniform rate with time until failure. It is shown that from such tests the life under normal stress conditions can be predicted by plotting the results on a stress-time curve on which the stress axis has been modified so that area represents amount of damage. Tests with electric light bulbs, whose failure obeys a cumulative damage criterion, give good agreement between predicted and measured life. The danger of the continuous acceleration procedure is that the stress may become so high that new failure modes are introduced.

KEY WORDS: life testing, accelerated testing, mechanical reliability, cumulative damage, failure.

¹ Department of Mechanical Engineering, Massachusetts Institute of Technology, Cambridge, Mass.

² Nuclear Energy Division, General Electric Co., San Jose, California

Introduction

The concept of continuous acceleration was introduced into life testing by Prot (1) in 1948, who determined the fatigue limit of mechanical specimens, not in the classic manner by running tests at constant stress levels, but rather by a procedure which involved starting at a low stress level and then increasing the stress continuously with time, until failure occurred. Tests at a number of different acceleration rates were carried out (Fig. 1), and then a mathematical procedure made it possible to deduce the fatigue limit from the measured failure points. The Prot procedure has been tested many times (2) - (8), and its theory has also been frequently evaluated (9) - (14).

Since that time two additional methods of running continuous accelerated tests have been developed. Fig. 2 shows a situation in which a specimen is first tested under a normal stress for a certain length of time which corresponds to its required life. After that time, the stress is accelerated at various rates until failure occurs, and from the location of the failure points the total life under normal stress conditions is estimated. This method is frequently used in situations in which government or other specifications require that a mechanism must run for a certain length of time on a test stand under constant operating conditions (the operational rectangle). Once the specimen has met the test, merely keeping the specimen running at normal stress is wasteful of valuable test facilities, while merely removing it from the test stand gives no information about how close to failure the specimen was at the end of the operational rectangle. Clearly, a change in operation characteristics to a high stress level is indicated, and a simple procedure for doing this is to raise the stress on the mechanism continuously until failure is experienced.

An alternative procedure uses specimens which are operated for part of the operational rectangle under normal stress conditions and then acceleration is applied at a constant rate until failure occurs (Fig. 3). This method is especially useful when a device is operated under field conditions for a certain length of time and is then brought back to the laboratory for testing to failure. To save time on the test stand, it is helpful to apply acceleration

The numbers in parentheses refer to the list of references appended to this paper.

procedures right from the start.

There is some discussion in the literature on whether acceleration must be carried out in a continuous fashion or whether it may be brought about by small but finite steps. However, no difference between these two procedures seems ever to have been demonstrated.

In the testing carried out in our program, the third type of continuous acceleration, that based on Fig. 3, was used, but in fact a limited amount of experimentation was carried out using the acceleration method of Fig. 2, and it seems that our procedures and modes of analysis are equally applicable to these methods of acceleration. Our study was part of a larger effort, part of which has been published (15), in which various methods of carrying out accelerated life tests were investigated, all the methods being based on the assumption that failure occurs as a result of cumulative damage (16). The cumulative damage criterion assumes that if a specimen is tested for a time t_1 under a stress at which its life would have been L_1 , and then for a time t_2 under a stress at which its life would have been L_2 , and so on, then if failure occurs at the n^{th} stress, we have

$$\frac{t_1}{L_1} + \frac{t_2}{L_2} + \dots + \frac{t_n}{L_n} = 1 \quad (1)$$

Theoretical Analysis

Accelerated testing procedures described in the literature generally start with the assumption that the effect on life of increasing the stress is known, i.e., it is assumed that the acceleration function is known. However, it was the aim of our study to develop accelerated test procedures which did not involve such assumption but rather, to develop empirical information on the influence of acceleration on life, and then to apply this information in as restricted way as possible to the analysis of the continuous acceleration procedure.

An important aid in comprehending accelerated life tests is the constant damage diagram. This is a diagram, rather analogous to the pressure-velocity plot used in thermodynamics, in which area under the curve represents the amount of damage. The ordinate of such a plot is a suitable function of the stress, while the abscissa is the time of operation of the mechanism.

The procedure for obtaining such a diagram is shown in Figs. 4 and 5. In Fig. 4 are shown the results of running life tests at various constant stress levels σ_0 to σ_3 . The times to failure are L_0 to L_3 . To lay out a vertical scale which obeys the constant damage relationship, any hyperbola

obeying the relationship

$$xy = \text{constant}$$

is drawn, as in Fig. 5, and then points are found on the vertical axis of Fig. 5 so that the horizontal distance from the axis to the hyperbola matches the parameters L_0 to L_3 , and these points correspond to the transformed values of σ_0 to σ_3 . Once the positions for the stresses σ_0 , etc. are found, other values can be inserted by interpolation. It remains to show that the diagram we have obtained is a constant damage diagram.

It is clear from Fig. 5, that the operational rectangles for specimens tested at constant stress σ_0 and σ_3 are equal in area, since this is a property of the hyperbola, and thus, if constant stress testing is undertaken, equal amount of damage yields equal area on the diagram. Now assume that testing is carried out under a more complex relationship until failure occurs (Fig. 6). The continuous curve can be approximated by a discontinuous series of steps, of length t_0 to t_3 . The total area A_t under the curve is then given by

$$A_t = \sum t_i f(\sigma) \quad (2)$$

But it is known from the construction of the constant damage diagram that

$$f(\sigma) = \frac{\text{constant}}{L} \quad (3)$$

Hence, equation 2 becomes merely

$$A_t = \text{constant} \sum \frac{t_i}{L} \quad (4)$$

and since the summed term is constant according to equation 1, so is A_t .

The main advantage of constructing a constant damage diagram rather than performing an equivalent mathematical manipulation for computing the amount of damage are twofold. First, a graphical visualization of damage is obtained and in some circumstances this can be very helpful. Second, it becomes possible to estimate the amount of damage when the theoretical function of damage against time is not known or is too complex, but failure times for various stress levels are known.

Experimental Program

The experimental testing was carried out with light bulbs. These were chosen from among several devices that were initially evaluated because of the following properties.

- A. It is easy to accelerate the damage rate in a continuous fashion merely by increasing the voltage.
- B. As will be seen below, it is found that the damage mechanism remains the same over a wide range of

voltages.

C. The life of commercial light bulbs is largely uniform with the standard deviation of life values less than one half of the mean life value.

D. The test specimens are very cheap and detection of the failure point is an extremely simple matter.

The eventual method arrived at for testing the light bulbs consisted of connecting them in parallel to the output of a Variac voltage transformer. The total current passing through all the bulbs was recorded continuously as a function of time, and the reduction in current which occurred when any bulb failed was directly detected.

Results

The first property studied was the statistical distribution of failure times for the light bulbs. The mean life of bulbs tested at a voltage of 110 volts was found to be 1190 hours, and the various lives were distributed about the mean in a normal distribution with a standard deviation of about 500 hours. These parameters agree well with published data (17). A second batch of rather different bulbs gave a mean life of 2050 hours. These mean lives were too long for our program and hence it was decided to operate at a standard voltage of 130 volts, i.e., it was hypothesized that these bulbs had been manufactured for use at 130 volts. The mean life under these conditions was 245 hours (Fig. 7).

Life tests on samples of 20 bulbs were then carried out at voltages of 145, 165, 190, 210, and 290 volts. At the higher voltages the life is drastically shortened and also the distribution of lives changes towards a bimodal shape suggesting that two different failure modes are operative (Fig. 8). These two failure mechanisms may be thinning and breaking of the tungsten wire (as at lower voltages) and detachment of the wire from its binding post (a new mechanism of failure).

The life results at various elevated voltages were used to lay off the vertical axis of the constant damage diagram shown in Fig. 9, and this diagram was used to plot the subsequent experimental data.

To carry out the accelerated tests, the procedure shown in Fig. 10 was employed. It was assumed that the operational rectangle consisted of service at 130 volts for 120 hours, and the acceleration procedures consisted of increasing the voltage at a rate of 4.3 volts per 4 hours. In fact, two different acceleration procedures were employed; in one case the voltage was increased every 4 hours while in the other case the voltage was increased three times as much every 12 hours. However, these produced no noticeable differences and the results have been combined. The failure points obtained are indicated in Fig. 10 and the voltage-time

curves are replotted on the constant damage diagram of Fig.9.

It is now required to estimate the life of the bulbs under nonaccelerated conditions, or more specifically, to see if a method can be found for estimating the true life under nonaccelerated conditions. The procedure is a relatively simple one, and it involves the use of at least two accelerated testing modes (say B and C). It is assumed that the position of the curves at high voltages is well established, but that the low voltage values are quite uncertain, since life tests at voltage of 130 volts have not been carried out. This state of affairs is represented on Fig. 11.

On comparing curves B and C on Fig. 11, it will be seen that they are identical in area, except that one has a region P and the other a region Q. If these areas are equated, then an estimate of the true position of the 130 volt line becomes available. Now compare curves C and D. These are identical except that one has region R and the other has region S. On equating the areas of these curves, an estimate of the position of point D becomes available. This procedure may be repeated by comparing the other pairs of curves, namely, A and B and then A and C.

Table 1 lists the value of the estimated life at a constant voltage of 130 volts obtained by comparing the curves A to C, also the directly measured life at 130 volts (curve D). It will be seen that the various estimates agree well.

It is of interest to note that before the use of the constant damage diagram was developed an attempt was made to use the results shown in Fig. 10 to deduce the life at the normal stress of 130 volts by various extrapolation procedures. For instance, Fig. 12 shows a plot of the log of the maximum voltage reached as a function of the log of the time of failure. It was hoped that a plot such as this might yield a straight line relationship thus allowing empirical extrapolation procedures to be used, but in fact no linear relationship was obtained. Many other plotting procedures were similarly unsuccessful.

Discussion

It has been the aim of this paper to show that a useful analysis of continuous accelerated life tests can be produced by first establishing a constant damage diagram and then analyzing accelerated life tests by means of such a diagram. It is not necessary that the acceleration function be known because during the initial stages of the testing program, a few points of the acceleration diagram can be experimentally determined, and can then be used.

As a matter of interest, we have found that the failure of light bulbs occurs by a process which follows the Arrhenius equation

$$\text{rate} = Ae^{-Q/RT} \quad (5)$$

where Q is the activation energy of the process

R is the gas constant

T is the absolute temperature

A is a constant

This equation must be modified to allow for the fact that for a wire heated electrically and cooled by radiation

$$\text{Heat in} \propto V^2$$

$$\text{Heat out} \propto T^4$$

and substituting this into Arrhenius equation gives

$$\text{rate} = Ae^{-Q/R \sqrt{V}}$$

$$\text{life} = Be^{Q/R \sqrt{V}} \quad (6)$$

Thus, the ordinate in Fig. 9 is in fact proportional to $e^{300/\sqrt{V}}$ and from the constant of 300, we may deduce an energy of activation of 120 kcal/mole. This figure is not out of line with activation energies for creep or evaporation of a strong metal like tungsten.

It may be of interest to compare the results of this investigation with earlier work. Prot assumed that a plot of alternating stress against testing time would be a hyperbola. He then established that such a diagram has constant damage characteristics and used this fact to devise his plotting procedure. However, since the fatigue life of materials at stress levels between the yield strength and the fatigue limit follows a relationship of the type:

$$\text{life} \propto \sigma^{-8} \quad (7)$$

rather than the hyperbolic relationship

$$\text{life} \propto \sigma^{-1} \quad (8)$$

It is clear that Prot's assumption is not a satisfactory one.

One of the advantages of the constant damage diagram is that it gives a realistic appreciation of how drastically accelerated testing raises the level of damage above the normal one. Anyone seeing the high spikes of Fig. 9 must wonder whether continuous acceleration has not taken the process into a region in which different failure laws apply.

One of the interesting findings of our study is that during accelerating testing, the distribution of failure times is not normal (Fig. 13a) but rather the long life part of the histogram is abruptly truncated. The data of Fig. 13 may be replotted in terms of the area under the constant damage curve rather than the time to failure, and the resultant relationship is much closer to being a normal one (Fig. 13b). This is perhaps an additional benefit of working with the constant damage diagram.

It should perhaps be pointed out that in all our tests, the average time to failure, which is the quantities used in plotting figures (9)-(12) is the mean value where the distribution is highly skewed.

The constant damage diagram of Fig. 9 as well as the simple stress-time plot of Fig. 10 from which it was derived, differ from some of the plots used in thermodynamics in that the position of a failure point depends on the path by which that point was reached. To illustrate this point, we show in Fig. 14 the results of tests on small electric motors, which were operated either unloaded or under an applied torque. Twelve motors or more were run at each loading condition. Two curves are shown, the higher one indicating the stalling load for units operated in the unloaded condition until the time indicated, the lower curve indicating the failure curve for units operated continuously under a uniform torque. In diagonal testing, as shown, the failure locus falls between the two previous curves, as might have been expected. A number of previous authors had not emphasized this influence of the mode of testing on the location of the failure point (6), (7), (11).

Perhaps an evaluation of the whole procedure of continuous acceleration is in order. The concept by which we keep raising the stress to 'punish' a specimen which has been a long time on the test stand, is psychologically a very attractive procedure, and perhaps the wide attention which Prot's procedure has received is partly attributable to this factor. However, there is a certain inefficiency in having a modest initial accelerated stress, and then compensating for this by having a very high final stress level. The alternative, two-step approach (15), is less likely to get the test into a realm where different modes of failure are brought into play, as a comparison of the two modes of testing shows (Fig. 15).

Acknowledgements

The authors wish to thank the Pratt and Whitney Division of the United Aircraft Company for sponsorship of this work, and R. Shevchenko, N. Gordon, P.F. Brown, K.A. Domeisen, and E.P. Saling, Jr., of that company for their advice and interest. Drs. P. Could and G.S. Reichenbach have made many helpful suggestions.

References

1. E.M. Prot, Fatigue Testing Under Progressive Loading, A New Technique for Testing Materials, *Revue de Metallurgie*, 45, 481-489, 1948. (Translated by E.J. Ward, WADC-TR-52-148, AD-2176, 1952).
2. F.H. Vitovec and G.J. Lazar, Strength, Damping and Elasticity of Materials under Increasing Reversed Stress with Reference to Accelerated Fatigue Testing, *Proc. ASTM*, 55, 844-865, 1955.
3. N. Enomoto, On Fatigue Tests Under Progressive Stress, *Proc. ASTM*, 55, 903-917, 1955.
4. L.S. Lazar, Accelerated Fatigue of Plastics, *ASTM Bulletin* 220, 67-72, 1957.
5. N. Enomoto, A Method for Determining the Fatigue Limit of Metals by Means of Sepwise Load Increase Test, *Proc. ASMM*, 59, 1959.
6. J.J. Bussolini and M.J. Ciarlariello, "Step Stress Testing to Failure for Reliability Analysis of Electronic Equipment," pp. 432-441, Aerospace Reliability and Maintainability Conference, SAE, New York, 1964.
7. G.E. Best, G.R. Bretts, H.T. McLean and M.M. Lampert, Determination and Application of Aging Mechanisms Data in Accelerated Testing of Selected Semiconductors, Capacitors, and Resistors, pp. 293-302, *Proc. Eleventh Symp. Reliability and Quality Control*, 1965.
8. M.N. Stepnov and Y.A. Shukhmin, Use of the Prot Method in the Fatigue Testing of Light Alloys, *Industrial Laboratory*, 33, 1018-1020, 1967.
9. W.A. Hijab, A Statistical Appraisal of the Prot Method for Determination of Fatigue Endurance Limit, *J. Applied Mechanics*, 24, 214-218, 1957.
10. H.S. Endicott and J.A. Zoellner, A Preliminary Investigation of the Steady and Progressive Stress Testing of Mica Capacitors, pp. 229-240, *Proc. Seventh Symp. Reliability and Quality Control*, 1961.
11. G.A. Dodson and B.T. Howard, High Stress Aging to Failure of Semiconductor Devices, pp. 262-272 of *Proc. Seventh Symp. Reliability and Quality Control*, 1961.
12. R.R. Gatts, Cumulative Fatigue Damage with Progressive Loading ASME Paper 62-WA-292, 1962.
13. G.E. Best, G.R. Bretts and H.M. Lampert, Physics of Failure and Accelerated Testing, *Electro-Technology*, 81-92, Oct. 1965.

14. G.A. Deryagin, U.K. Shtovba, E.I. Shneerova, Use of Rapid Methods in Determining the Fatigue Strength of D 16 T Aluminum Alloy, Industrial Laboratory, 33, 1021-1024, 1967.
15. E. Rabinowicz, R.H. McEntire and B. Shiralkar, A Technique for Accelerated Life Testing, ASME Paper 70-Prod-10, 1970.
16. M.A. Miner, Cumulative Damage in Fatigue, J. Applied Mechanics 12, A159-A164, 1945.

TABLE 1. Predicted Life of Bulbs at 130 Volts

<u>Source of estimate</u>	<u>Life</u>
Figure 9, Curves B and C	210 hours
Figure 9, Curves A and C	220
Figure 9, Curves A and B	310
Figure 7, Direct measurement	245

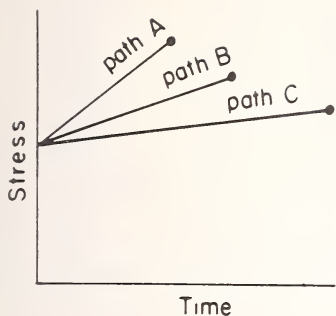


Fig. 1--Schematic illustration of the Prot method of accelerated testing.

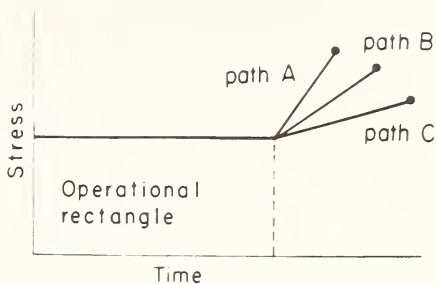


Fig. 2--An acceleration method especially applicable to devices which must first meet a specified duty cycle.

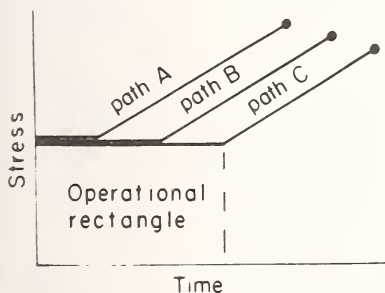


Fig. 3--An acceleration method to be used on devices which have used up part of their lives in field tests.

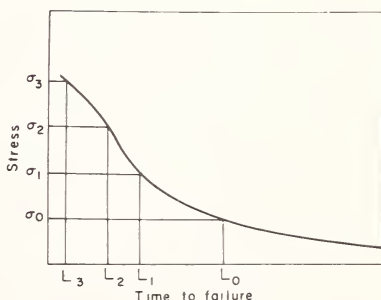


Fig. 4--Typical plot of time to failure as a function of constant test stress.

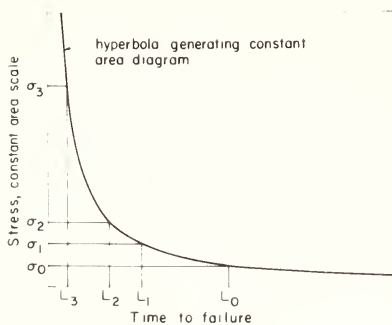


Fig. 5--Method of obtaining a constant damage stress scale from the data of fig. 4.

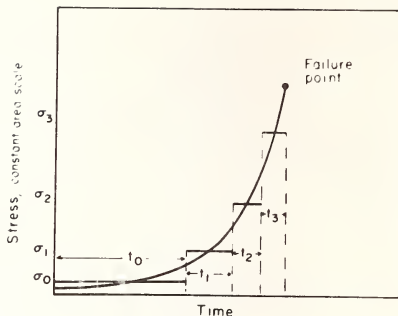


Fig. 6--A complex curve on a constant damage diagram may be approximated by a number of rectangular steps.

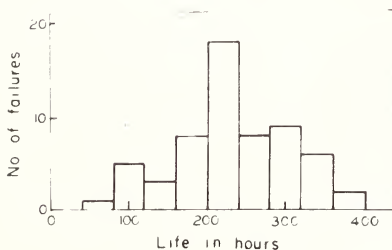


Fig. 7--Histogram for 60 light bulbs tested to failure at 130 volts. The distribution is nearly normal.

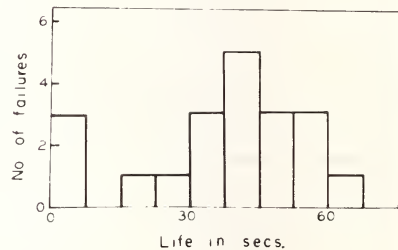


Fig. 8--Histogram for 20 light bulbs tested to failure at 290 volts. The shape of the diagram resembles that of fig. 7, but there are some very early failures.

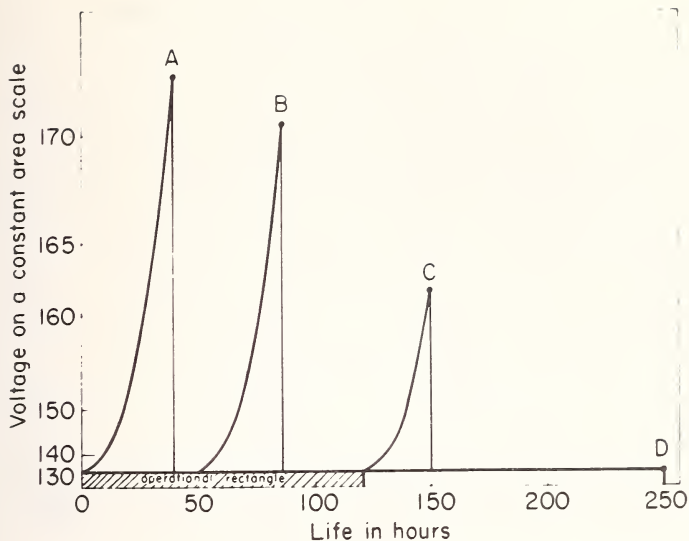


Fig. 9--Plot of the stress-time functions of fig. 10, but transformed to a constant area scale

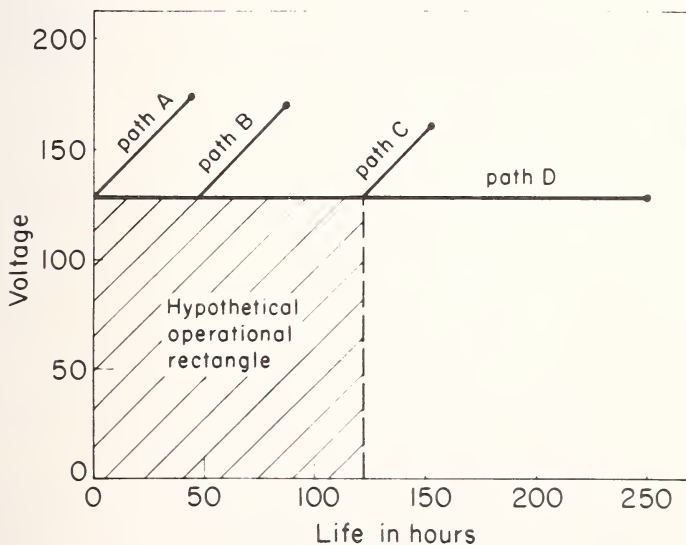


Fig. 10--Plot of the stress-time functions of light bulbs tested under continuous acceleration. Thirty specimens were failed along each path, and each median failure point is shown.

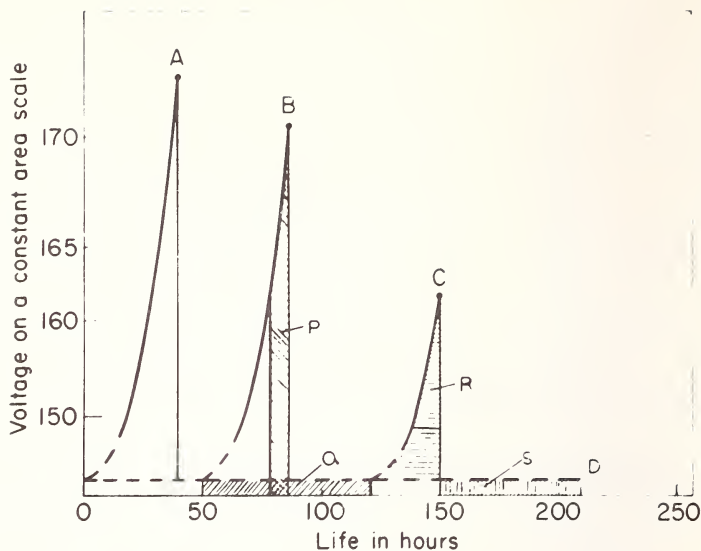


Fig. 11--Method of computing the life at 130 volts. Areas P and Q, and then areas R and S, are equated.

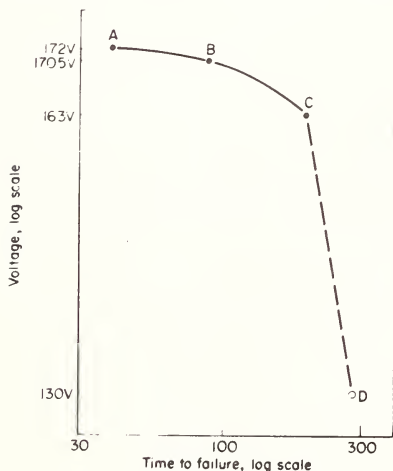


Fig. 12--Failure points from fig. 10 replotted on a log-log scale. Points A, B, and C do not readily extrapolate to D.

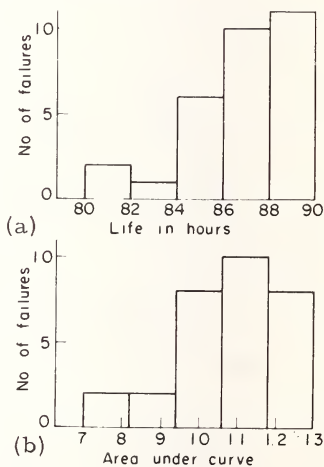


Fig. 13--Histogram of lives of 30 bulbs tested along path B of fig. 10 a) Life given in hours b) Life given as area under curve B of fig. 9.

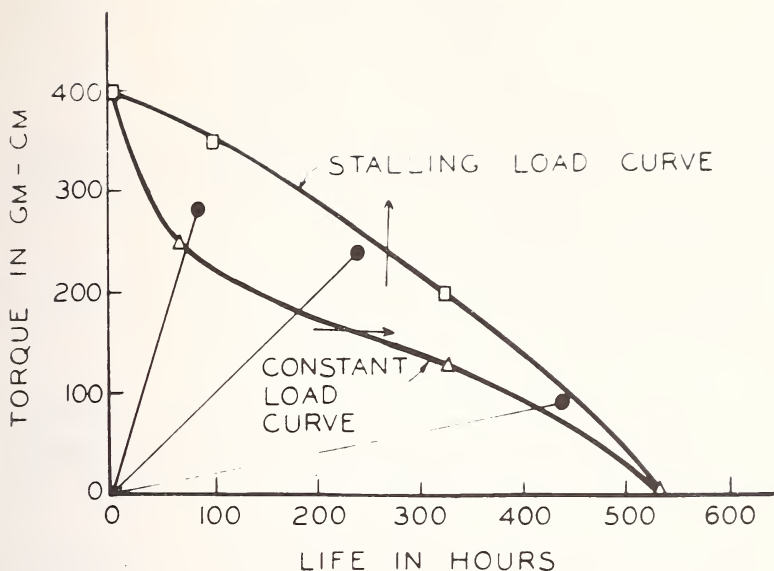


Fig. 14--Stalling curve, life curve at constant torque, and life data under continuous acceleration for electric motors. The stress-life function depends on the testing history.

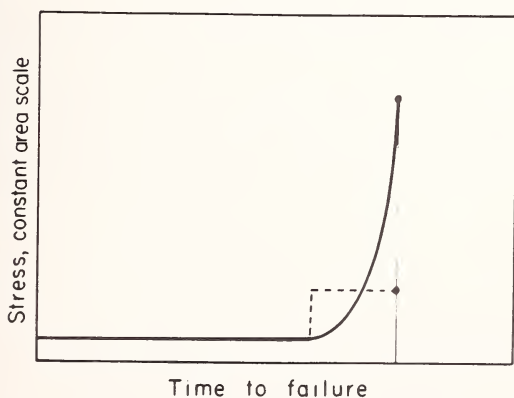


Fig. 15--Comparison of two-step and continuous acceleration testing. The full curve and the broken curve have the same area, but the broken curve (two-step testing) does not reach as high stress values.

ESTABLISHMENT OF AN OPTIMUM DURATION FOR SPACECRAFT COMPONENT
THERMAL VACUUM TESTS

W. L. Harvey¹

REFERENCE: Harvey, W. L., "Establishment of an Optimum Duration for Spacecraft Component Thermal Vacuum Tests," ASTM/IES/AIAA Space Simulation Conference, 14-16 September 1970.

ABSTRACT: The duration of planetary space missions precludes performing component thermal vacuum tests which simulate the mission time period. Many arbitrary approaches have been taken to establish adequate durations for these tests. This paper outlines an approach which considers the probable effects of the thermal vacuum environment on the components and their constituent materials. In general these effects are found to be related to outgassing rate which is time and temperature dependent. A test cycle is proposed which considers this situation and utilizes any prior "bake out" heat exposure to reduce the test duration to a reasonable period.

KEY WORDS: Thermal vacuum tests, components, simulation, environment, volatile constituents, outgassing, degassing, "bake out", thermal conduction, evaporation, sublimation, volatilization, decomposition, absorption, adsorption.

INTRODUCTION

Long duration space missions propose a unique problem to the engineer charged with establishing an appropriate test program to qualify and flight accept the spacecraft components. Since it is obviously not feasible to extend thermal vacuum test durations to coincide with a multi-month

¹ Staff Engineer, Martin Marietta Corporation, Denver, Colorado.

interplanetary cruise or orbital period, some compromise must be achieved.

A review of government and industry efforts at achieving this (as reflected in OGO, Mariner, Apollo, and other spacecraft test requirements) has indicated the absence of any consistent rationale in this area. Therefore, the purpose of this paper is to propose an approach to resolving this potentially costly and time consuming problem. Basically, the problem can be approached from two directions.

The first (and perhaps most reassuring) would be to correlate failure rates with time in the thermal vacuum environment from extensive ground tests. Unfortunately, this data is not readily available and, where available, is not in such a form that positive conclusions can be drawn from it. Such factors as component functional state, prior test history, and thermal cycling conditions have been observed to have a very pertinent effect on the occurrence of component failures under thermal vacuum conditions. For example, a component may be exposed to several days thermal vacuum conditioning while completely non-operative. It is then turned on and fails shortly thereafter. Was its failure a function of time in the chamber or initial operation under the thermal vacuum conditions? Similarly, a component may progress through a series of environments, including launch vibration, which simulates the spacecraft mission. It fails during simulated cruise thermal vacuum conditions. Should its failure be attributed to stresses induced by the thermal vacuum environment or to residual stress from the prior vibration testing?

The second approach involves restating the problem: "Establish a test (duration) which simulates the effects of the mission thermal vacuum environment rather than the precise environment itself." A step has already been taken in this direction with the realization that the hard vacuum of space (10^{-14} torr or less) cannot be readily simulated for normal component testing. Rather 10^{-5} to 10^{-6} torr² is generally

²Several rationales exist for supporting this compromise rather than the fact that it is exceedingly difficult if not impossible to provide a system for testing relatively dirty components at pressures much less than this. For example, at 10^{-5} torr the mean free path of gas molecules becomes several meters. Thus, gas molecules will be returned to the test surface only by condensing on the chamber walls and then re-subliming. This also means that the thermal conduction of the gas is quite small relative to radiant heat transfer. At 10^{-6} torr the dielectric strength of the chamber atmosphere has increased to the point where operating voltages in the kilovolt range may be applied without danger of arc or glow discharge.⁽¹⁾ Even at 10^{-6} torr, however, a monomolecular adsorbed gas layer may be built up on an initially clean surface in 2 seconds.⁽²⁾

considered adequate to simulate the effects and is nominally required for this type of testing.

In order to establish a test which adequately simulates the effects of the environment, it is necessary to determine what these are. Not surprisingly, these effects are directly related to the two prime characteristics of the space environment, i.e., temperature extremes and the absence of an atmosphere. The synergetic effect (absence of a convective atmosphere) appears to be minimal and definitely biased towards altering the effects of the thermal extremes. Consequently, it would appear that the primary effects of the space environment may be categorized as either thermal or vacuum related.

THERMAL EFFECTS

The thermal effects are essentially the same as those produced by any temperature condition. High temperature effects result in alteration of materials characteristics and include softening which may be either reversible or irreversible, loss of tensile strength or evaporation of volatile constituents as well as differential displacement which may create a physical stress. Low temperatures cause loss of resiliency or ductility and increased brittleness in addition to developing physical stress. While each of these effects is significant, two factors should be considered. First, each effect, with the exception of differential displacement, can be studied and evaluated at the materials level. The effects of differential displacement, however, can only be evaluated effectively at the component assembly level. Second, loss of resilience including dissolution of plasticizers can be produced under ambient pressure conditions as well as under vacuum.(3)³

VACUUM RELATED EFFECTS

The remaining thermal effect, evaporation of volatiles, leads directly to consideration of the vacuum related effects of the space environment. A review of references on materials for space usage indicates that exposure to space vacuum may produce essentially two categories of effects. First, and most prevalent, is weight loss through evaporation, sublimation, or volatilization of the material or its molecular fractions following decomposition or dissociation. The second effect, which is less common and certainly less understood, is

³The numbers in parenthesis refer to the list of references appended to this paper.

a direct change in mechanical properties without significant weight loss.⁽³⁾

The evaporation process is generally associated with the boiloff of entrapped water vapor or other residual fluids. Sublimation may occur where low molecular weight fractions exist in the polymer. Volatilization occurs where volatile constituents have much higher vapor pressures than the cured polymer. These volatile constituents may include:⁽⁴⁾

- Condensed reaction products from the curing process
- Processing additives
- Stabilizers
- Residual solvents
- Thermal or radiation induced decomposition or polymerization products
- Unreacted curing agents
- Impurities

In all of the situations the resultant rate of weight loss through outgassing is directly proportional to the vapor pressure of the outgassing materials as indicated by the Knudsen-Langmuir equation.

The total effect of weight loss on the engineering properties of the material presents another area of inconclusiveness. It is generally agreed that weight losses of 1 to 2 percent do not produce property changes of engineering importance unless large volumes of the material are present.^(2,4) In the latter case, the condensable volatiles produced by even a small weight loss of the bulk material might affect the performance of some other element of the system.⁽⁴⁾

Inorganic materials at nominal temperatures generally appear not to be adversely affected by vacuum conditions. In fact, electrical properties of inorganic dielectric materials may be enhanced through the boiloff of water.⁽²⁾

Changes in mechanical properties of polymers not accompanied by a weight loss include variations in elongation characteristics, tensile strength, hardness and elasticity. These poorly understood effects are generally believed to be a function of the relative rates of molecular cross linking and cleavage. Most sources, however, seem to feel that some weight loss must occur before vacuum conditions will have a significant detrimental effect on mechanical or electrical properties.⁽²⁾ Consequently, most materials studies have involved themselves with measuring weight loss or cataloging volatile condensable materials.⁽⁴⁾ For the purposes of analyzing and solving the problem of optimum component thermal vacuum test durations, weight loss and resultant degradation of engineering properties appear to be the prime parameters of concern.

THERMAL VACUUM EFFECTS ON COMPONENTS

Having considered the potential effects of the thermal vacuum environment on constituent materials it becomes necessary to determine the probable way in which these effects could manifest themselves at the component level. These include the following:

- 1) Physical failure as the result of mechanical degradation through outgassing and/or the introduction of stress from differential thermal displacement.^(5,6)
- 2) Degradation of lubricating properties (destruction of absorbed or chemisorbed oxide films with no healing possible) leading to cold welding, galling or seizure of bearing surfaces.⁽³⁾
- 3) Corona and arcing resulting from the loss of dielectric strength of an insulating material or through the development of a conductive atmosphere immediately adjacent to an outgassing source.^(3,6)
- 4) Contamination of critical surfaces through deposition of outgassed products.^(3,7)

At this point, the problem of establishing an optimum thermal vacuum test becomes one of establishing a test which adequately evaluates both the thermal and outgassing characteristics of components within a reasonable period. Temperature cycling, with the component operated while stabilized at each extreme and monitored during the transition time, appears to provide an excellent means of producing any potential problems related to thermal stress effects.

Outgassing, however, is time dependent. Therefore, it would appear that the test duration should be based on the time necessary to initiate, develop and essentially complete outgassing. The outgassing situation at the component level becomes a great deal more complex than it was at the materials level. Component geometry may provide for repeated condensation and resublimation of outgassed molecules in even a well vented "black box". Operating characteristics of the component may cause various parts within the component to operate at different temperatures during various phases of the functional profile. This could result in outgassing, condensation, resublimation, etc., occurring in a never ending cycle. While this is an extreme example it does point up the problem of basing a test duration on the time required to complete outgassing. In this case, the component might never complete outgassing.⁽⁵⁾ Worst case effects, however, could be evaluated at several points during the component operating cycle. Such a test might indeed be more severe than one wherein total

outgassing had been accomplished, including complete resublimation of miscellaneous outgassed products from critical internal surfaces. Certainly if arcing and corona discharge are potential problems, it would be better to conduct a test which evaluates the effect of outgassing while conductive gas molecules are still in the vicinity of high electrical potential sources.

OUTGASSING CHARACTERISTICS

From the foregoing it would appear that the development of outgassing is one of the prime if not the most important objective of the vacuum portion of a thermal vacuum test. As has been indicated previously the actual mechanics of outgassing vary from metals to non-metals and from non-metallic material to another. Outgassing in metals is related to the diffusion coefficient and true surface of the metal.⁽⁸⁾ The diffusion coefficient in turn is a function of temperature and, in some cases, concentration of gas within the solid.⁽⁹⁾ In addition to the same factors, outgassing of non-metals may be related to thermal degradation or molecular decomposition.⁽¹⁰⁾ The complexity of the situation is such that extensive materials thermal vacuum testing has been accomplished and will continue to be accomplished in order to select the most stable (and low outgassing) materials for space usage.

Numerous references reflect the weight loss (outgassing) characteristics of commonly used spacecraft materials. Metals, wherein outgassing is primarily a function of absorbed gasses, outgas at a log linear rate. Dayton⁽⁸⁾ has indicated that outgassing of clean metals is complete after 15 to 25 hours. Polymers, elastomers, etc., wherein outgassing may be related to chemical decomposition at higher temperatures also outgas at a log linear rate but at a higher initial level. Testing of these materials, which has been accomplished over the last 10 to 12 years, has established an extensive catalog of space qualified materials. As indicated in the references, outgassing of the low weight loss materials generally reaches equilibrium in as little as 25 to 50 hours depending on the temperature at which the evaluation is performed.^(11,12)

Without exception, outgassing may be initially accelerated and subsequently reduced or eliminated through the application of heat.^(5,11,13) This "bake-out" either at ambient pressure or under vacuum conditions, is a commonly accepted method of degassing materials.

The benefits of any such degassing process with polymers are further enhanced in that the subsequent reductions in outgassing appear to be permanent. Readsorption and reabsorption of ambient atmospheric constituents is generally less than one half that originally adsorbed.^(1,11,14) The weight gained by re-exposure to the atmosphere after degassing is quickly lost

when the material is again subjected to vacuum or elevated temperatures. Figure 1 shows this phenomena for a silicone base polymer.⁽¹¹⁾ This may be considered typical of most organic polymers.

One means of accomplishing this beneficial preliminary degassing occurs naturally where terminal sterilization is required for planetary probes. Current planetary quarantine constraints require exposures of up to 60 hours at 135°C. Such exposures may increase by an order of magnitude or more the initial outgassing rate and resultant weight loss of common aerospace polymers.⁽⁵⁾ Thus, where preliminary heat compatibility tests are required, a major portion of the probable outgassing would be accomplished even before thermal vacuum testing is initiated. This factor would permit an extensive reduction in the thermal vacuum test duration.

TYPICAL THERMAL VACUUM TEST PROGRAMS

Before proceeding to establish an optimum thermal vacuum test program a review of several major spacecraft programs appears to be in order.

The following reflects the test durations employed during some of these programs.

<u>Program</u>	<u>Component T/V</u>		<u>System T/V</u>	
	<u>FAT⁴</u>	<u>Qualification</u>	<u>FAT⁴</u>	<u>Qualification</u>
OGO	24 hrs	24 hrs	7 days	12 \pm days
Pioneer	24 hrs	24 hrs	14 \pm days	17 \pm days
Mariner Series	2-3 days	13 days	13 days	13 days
Surveyor	8 hrs	3 days	4 days	4 days
Nimbus, IMP, Etc.	2 days	2 days	13 days	13 days
Apollo (LM)	8 hrs	24 hrs	---	---
Lunar Orbiter	16 hrs	18 days	58.5 hrs	5 days

Discussions with the contractors involved with these programs indicated that even though they might run component qualification and system FAT or qualification for more than two days, the majority, if not all, of the failures encountered during the latter portions of the test could be related to one or more of the following circumstances.

- 1) Initial operation of the component during the test (even though it had been exposed to thermal vacuum for several days).

⁴FAT indicates flight acceptance environment tests applied to all flight components prior to installation in the flight spacecraft.

- 2) Operation during or immediately following a temperature cycle.
- 3) Accumulated deposition of outgassed materials from some bulk source (not related to a specific component).

In general, most contractors contacted indicated that the majority of the problems encountered during thermal vacuum testing were temperature related with only a small portion attributable to the vacuum environment. As an example, one contractor analyzed 134 FAT discrepancies occurring on 108 components with the following results.⁽¹⁵⁾

46.3%	- Thermal problems (drift, open circuits, etc.)
5.2%	- Vacuum (primarily arcing and corona on RF equipment)
31.3%	- Test error (procedure, test equipment, etc.)
17.2%	- Not thermal vacuum related - primarily residual from prior vibration test
<u>100.0%</u>	

It may be noted that all of the unmanned spacecraft programs required system thermal vacuum tests to both qualify and flight accept the spacecraft. Initially it was hoped that some guidance could be obtained from these system test durations in establishing component test durations.⁽¹⁶⁾ Unfortunately, a system cannot be treated as just a "big component" in this environment. Test durations at the system level must be of sufficient duration to permit thermal stabilization (if appropriate) in various operating modes. The effects of outgassing and deposition of bulk sources must be considered. Time must be allowed for degradation of thermal control surfaces. All of these factors make a system thermal vacuum simulation vastly different from that required for a component.

Component thermal stabilization may be accomplished in hours instead of days. The effects of self generated heat become apparent in minutes instead of hours. Bulk source outgassing either is not a factor as the bulk source is not present or manifests itself only in relation to its parent component.

System thermal vacuum testing does provide an indirect benefit to the engineer planning a component thermal vacuum test. The system test establishes an additional period of vacuum exposure outgassing, and resultant materials degradation if this is indeed a potential problem. Obviously, a system test may be a late point in the program at which to find a component design or materials application problem. However, it may also provide the "frosting on the cake" for those concerned with the risk of running an optimized component thermal vacuum test.

SUPPORTIVE MATERIALS TESTING

Throughout this entire analysis much reliance has been placed on materials test data. It should go without saying that similar reliance must be placed on actual materials testing in planning a valid component thermal vacuum test. Just as the system test is a late point in time to find a component design problem, so is a component test the wrong place to uncover a materials misapplication. Ideally all materials going into a spacecraft component will have been prequalified individually to the mission environments. This qualification can involve actual long duration thermal vacuum tests (coupled with ultraviolet radiation if appropriate) or cataloging of previously qualified materials. The component test may then be properly concerned with evaluating the interaction of the materials within the specific design.

This is not to say that all materials must have a low weight loss, non-thermal decomposition pedigree. This would be an ideal goal. Rather it should imply that all materials going into a specific component be identified. The presence of any unknown or suspicious materials or unusual application should then require consideration of additional testing.

THE OPTIMUM TEST

Certain positive conclusions can be drawn from the preceding discussion which should be considered in establishing the optimum test duration for spacecraft components. These include the following:

- 1) Adequate data concerning constituent materials should be available so that some prediction of their probable outgassing rates and time to equilibrium can be made.
- 2) Any prior thermal exposure should be considered for its preliminary degassing effects. [Even under ambient atmospheric conditions planetary quarantine sterilization temperatures (125 to 135°) should have the effect of degassing 50 to 90% of the adsorbed or absorbed gases]
- 3) The component should be operated and monitored during the pump down period as a means of detecting any potential conditions of arcing or corona. (This is a more effective evaluation than depending on component outgassing to establish potential conditions for this phenomena.)
- 4) Chamber pressure should be reduced to 10^{-5} torr or less to assure that all heat transfer occurs through

radiation and none through convection.

- 5) If no specific temperature cycle is required to simulate mission conditions the component should be exposed to the maximum test temperature initially for as long a period as reasonably possible. (A period of 12 to 24 hours would further promote outgassing and if accomplished following a prior high heat test should result in the earlier establishment of an equilibrium outgassing rate.)
- 6) The component should be operated near the conclusion of the high temperature exposure and its operation continued during reduction to the minimum test temperature. This will permit determination of any discontinuities over the total temperature range.
- 7) The transfer from high to low temperature should be accomplished at as high a rate as possible consistent with mission parameters. This action will promote any stresses developed through differential thermal displacement.
- 8) Time at the low temperature should be minimized to that required to stabilize the component. (Outgassing or other degradation is retarded at low temperatures in contrast with the action at higher temperatures.)
- 9) Transfer from low to high temperature should also be accomplished as rapidly as possible. (This action will promote any non-linear stresses not developed during the high to low temperature transfer.)
- 10) The foregoing temperature cycle should be repeated until the accrued time under high temperature conditions is sufficient to assure that the rate of outgassing for all constituent materials has reached equilibrium.
- 11) Or, if this is not predictable, the test should be extended to a minimum of 72 to 144 hours (four to eight cycles with nominal stabilization times). During this period most common materials will have achieved equilibrium outgassing 40 to 80 hours earlier. As a result the test duration will provide a margin over uncertainty of two or three times.
- 12) Operation during or following chamber repressurization need not be required unless this is necessary to simulate the mission. (Some solid state devices have

been known to develop an unexplained failure mode under these conditions.)

The test described here would provide adequate evaluation of component characteristics during the design development phase or could be used to demonstrate design maturity during qualification. Based on the data derived during these test programs the same or a shorter test could be used for flight acceptance. If no anomalous conditions attributable to vacuum produced effects are detected during either of these tests, consideration could be given to either a shorter test (24 to 72 hours - two to four cycles) or to a temperature cycling test under ambient atmospheric pressure conditions.

CONCLUSIONS

Based on this study, it now appears that the factors to be considered in establishing an optimum duration for component thermal vacuum testing should not be based totally on the actual mission environment itself. Rather, the factors of component design, materials used, prior environmental conditioning, and potential failure modes all should be considered. The test should be biased toward as complete evaluation of component characteristics early in the test profile as possible under the mission constraints. If it is desirable to establish a broad test to envelop a complete spacecraft family of components, it would appear that this could be based on consideration of the criteria used to select constituent parts and materials plus any prior thermal conditioning encountered as the result of planetary quarantine constraints.

APPENDIX

Definitions

Component	An assemblage of parts and materials which perform a specific function within a spacecraft system, i.e., a "black box."
System	A complete spacecraft element capable of accomplishing a major phase of the mission either separately or in conjunction with other systems.
Outgassing	Spontaneous evolution of gas from a material in a vacuum.
Degassing	Deliberate removal of gas from a material, usually by heat under vacuum.
Adsorption	Condensation of gas on the surface of a solid.
Absorption	Binding of a gas in the interior of a solid.

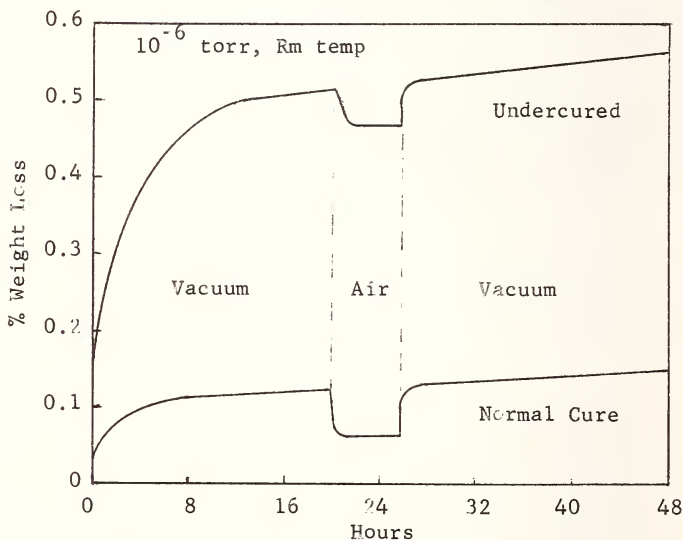


Fig. 1. Readsorption study of Sylgard 182.

REFERENCES

- (1) Santeler, D. J. et al, Vacuum Technology and Space Simulation, NASA SP-105, 1966, pg. 13, Chapter 9, pp. 223-229.
- (2) Jaffe, L. D. and Rittenhouse, J. B. in Materials for Missiles and Spacecraft, E. R. Parker, Ed., McGraw-Hill, 1963, Chapter 9.
- (3) Rittenhouse, J. B. and Singletary, J. B., Eds., Space Materials Handbook, Wright-Patterson Air Force Base, 1968.
- (4) Boundy, R. A., The Effects of the Space Environment on Materials, SAMPE, Volume 11, April 1967, pg. 194.
- (5) Lee, S. and Fewell, R., The Effects of the Space Environment on Materials, SAMPE, Volume 11, April 1967, pp. 151-156.
- (6) Dodge, H. S., Annals of the Assurance Science, Eighth Reliability and Maintainability Conference, AIAA, SAE, ASME, July 1969, pp. 101-104.
- (7) Duraetz, R. A. and Tuckerman, A. J., The Effects of the Space Environment on Materials, SAMPE, Volume 11, April 1967, pp. 228.
- (8) Dayton, B. B., Transactions of the Eighth National Vacuum Symposium of the American Vacuum Society, 1961, pg. 42.
- (9) Dayton, B. B., Transactions of the Ninth National Vacuum Symposium of the American Vacuum Society, 1962, pg. 293.
- (10) Fulk, M. M. and Horr, K. S., Transaction of the Ninth National Vacuum Symposium of the American Vacuum Society, 1962, pp. 324-338.
- (11) Shipple, C. L. and Curtindale, E. G., Transactions of the Tenth National Vacuum Symposium of the American Vacuum Society, 1963, pp. 63-68.
- (12) Boebel, C., Mackie, N. and Quaintance, C., Transactions of the Tenth National Vacuum Symposium of the American Vacuum Society, 1963, pg. 62.
- (13) Griffith, J. S., "Some Tests for Increase in Friction of Mechanisms of the Mariner Mars 1969 Spacecraft in the JPL Molsink Space Simulation Chamber," Technical Report 32-1446, JPL, Pasadena, California, September 1969.
- (14) Thorne, J. A. and Whipple, C. L., The Effects of the Space Environment on Materials, SAMPE, Volume 11, April 1967, pp. 244-247.
- (15) Vanderhorck, M., Private Discussion, TRW, January 20, 1970.
- (16) Timmims, A. R., "Time Required for an Adequate Thermal Test of Flight Spacecraft," NASA Report TN D-4908, National Aeronautics and Space Administration.

EQUIPMENT TO STUDY HIGH VELOCITY DISLOCATIONS IN MATERIALS

V. R. Parameswaran¹ and J. Weertman²

REFERENCE: Parameswaran, V. R. and Weertman, J.:
"Equipment to Study High Velocity Dislocations in Materials",
ASTM/IES/AIAA Space Simulation Conference, 14-16 September 1970.

ABSTRACT: The microstructural and physical properties of a material deformed under high strain rates are quite different from those of the slowly deformed material. This is attributed to the motion of a shock front consisting of an array of high speed dislocations through the shock loaded material. An equipment was constructed to shock load single crystals of metals by shooting small steel pellets using a gas gun. The slip bands generated on the surface of the crystals by the stress pulses give a measure of the dislocation mobility in the material. In this paper the equipment used to produce the stress pulses and that used to measure and record the stress pulses are described.

KEY WORDS: High speed dislocations, Impact stress pulse, Piezoelectric stress gauge, Quartz, Slip bands, Dislocation velocity.

¹Research Associate, Department of Materials Science,
Northwestern University, Evanston, Illinois 60201.

²Walter P. Murphy Professor of Materials Science, and
Professor in Geology department, Northwestern University,
Evanston, Illinois 60201.

INTRODUCTION

Many high-energy-rate deformation techniques are being used in aero-space industry to deform hard and refractory materials such as tungsten, niobium, titanium and their alloys, nickel and cobalt base alloys and high strength steels. When a material is deformed under high strain rates by one of the high velocity forming techniques such as explosive forming, electro-hydraulic forming, electromagnetic forming or pneumatic-mechanical forming, the plastic deformation of the material is rendered much easier than when deformed by conventional low-strain-rate techniques. This is due to the fact that under high strain rates, the dislocations in the material move with very high velocities close to their limiting velocities in the material. The limiting velocity V , of an ordinary dislocation pushed by a fixed applied stress lies in general in the transonic velocity range ($c \leq V \leq c_L$, where c is the shear sound wave velocity and c_L is the longitudinal sound wave velocity in the material). For a screw dislocation, the limiting velocity is equal to $V = c$. If the applied stress is made large enough, the limiting velocity of a gliding edge dislocation approaches $V = c_L$. The stress field of a moving screw dislocation shrinks in the direction of motion. Because of this shrinkage, the force parallel to the slip plane between fast moving screw dislocations in the same slip system goes to zero. The plastic flow of material is rendered easier under high strain rates due to this behaviour of high speed dislocations.

High speed dislocations are also thought to be the agents that bring about diffusionless transformations such as martensitic and bainitic transformations and twin transformations. Such transformations are brought about by the motion of an array of partial dislocations moving with sonic or supersonic velocities on an interface which can give up energy. Eshelby (1) has given the structure of such supersonic dislocations. Smith(2) has given the structure of the dislocation interface between the shocked and unshocked regions in very high pressure shock wave phenomena. The dislocations in Smith's interface travel at supersonic speeds with respect to both the shocked and unshocked regions in order to stay in the interface. For a review of the properties and behaviour of high speed dislocations, see Ref. (3-5).

The numbers in parenthesis refer to the list of references appended to this paper.

In order to study the mobility of high speed dislocations in single crystals of metals, an equipment was built to subject these crystals to impact stress pulses of short duration of a few microseconds. The length of the resulting slip bands on the surface of the crystals give a measure of the dislocation mobility. The results of the velocity measurements at different temperatures in lead and lead-indium alloys in both the normal and the superconducting states are described elsewhere (6,7). In this paper, the details of the equipment used are given.

A. THE GAS GUN:

A schematic diagram of the equipment is shown in Fig. 1. A stress pulse is applied by shooting a round nosed steel pellet A of diameter 3.2 mm onto an assembly consisting of a piezoelectric stress gauge B, the single crystal C under study, and a lead attenuator bar of length 12 cm. The assembly is kept in position by a perforated steel disc E of thickness 3 mm and 4 phosphorbronze springs F. Fig. 2 shows a photograph of the assembly. The pellets are shot out by means of a gas gun consisting of a vertical barrel G, a pressure chamber H, a solenoid valve I, and an electromagnet J. Pressure in the chamber is indicated by the gauge K. A pellet is held by the electromagnet over the barrel and the chamber is pressurized to the desired value by nitrogen gas. (Helium gas was used in tests at very low temperatures). Then, simultaneously, the current to the electromagnet is cut off and the solenoid valve is momentarily opened. Fig. 3 shows the electrical circuit to operate the solenoid valve and the electromagnet. The pellet, shot out through the barrel by the gas pressure in the chamber, strikes the top of the piezoelectric stress gauge. The piezo-voltage developed is fed to a dual beam oscilloscope which has been kept ready to be triggered by the pulse. X-cut quartz was used as the piezoelectric transducer. Details of the piezoelectric gauge are given in section B. Figures 4 & 5 show the photographs of the equipment.

The stress pulse in the form of a piezo-voltage vs time spike was photographed by a polaroid camera attached to the oscilloscope. The piezo-voltage is directly proportional to the applied stress. The dual beam scope used was Tektronix 555 with vertical plug-in units of the type L and 1A2 respectively, for the upper and the lower beams. The beams were triggered using the external triggering source position, since in the internal triggering source position, the beams were found to be triggered by any external transients in the vicinity of the system such as that caused by the switching of the electromagnet. A triggering circuit

was used to feed the piezo-voltage to the external source positions and the vertical amplifiers of the scope. Fig. 6 shows the triggering circuit used. The two beams were traced at different speeds to study the main pulse and the overall nature of the pulse after a longer duration.

The value of the applied shear stress was changed by altering the propellant pressure in the chamber. The length of the steel pellets was changed to vary the duration of contact of the steel pellet with the piezo-assembly, and hence the duration of the stress pulse. The stress pulses applied to the crystals were essentially single pulses, as can be seen from Figs. 7 & 8.

The stress pulse can be considered as a half sine wave, the stress increasing sinusoidally with time, reaching a maximum or peak value and then decreasing to zero. A mean stress $\bar{\tau}$ was calculated by dividing the area under the curve by the total time t of the pulse.

$$\bar{\tau} = (1/t) \int_0^t \tau(t') dt' \quad (1)$$

The magnitude of the stress applied by this equipment is of the order of a few kg/mm^2 and the duration is of a few microseconds.

B. THE PIEZOELECTRIC STRESS GAUGE

Many investigators (8-14) have used X-cut quartz discs as stress measuring gauges. Most of these investigations were carried out to study the voltage and current output obtained from quartz crystals by application of large stresses of the order of a few kilobars. Quartz has been extensively studied and it has been found that the piezoelectric strain coefficient d_{11} remains nearly constant from 4.2°K upto 473°K (15,16). Also, d_{11} is practically independent of stress. The dielectric constant of quartz is large enough so that edge corrections do not have to be made for bars or plates that are reasonably thin in the field direction. The crushing strength of quartz is about $300 - 400 \text{ kg/mm}^2$ and so quartz can withstand high stresses in compression. Due to these advantages of quartz, we decided to use X-cut quartz crystals received from M/S Hunt Corporation, Carlisle, Pennsylvania.

The quartz discs received were of diameter 1.25 cm and thickness 3.2 mm, with the two opposite faces lapped and polished to be parallel to each other, within 0.0001 cm. These faces were plated with a vapour deposited layer of silver of thickness of about 0.0075 cm. Fig. 9 shows the details of the piezoelectric stress gauge. The electrodes

attached to the quartz crystal are made of pure copper. On top of the upper electrode is a lead nose piece of diameter 1.25 cm and length 3.75 cm. On top of this is a hardened tool steel disc of diameter 1.25 cm and thickness 3.2 mm. These nose pieces make the wave front of the stress pulse reaching the quartz crystal essentially plane. The lead nose piece also cuts down the secondary pulses due to waves reflected from the sides. Since the double transit time in the bar supporting the piezoelectric stress gauge is much longer than the duration of contact of the steel pellet with the assembly, the difficulties due to wave reflections at the impact point are eliminated. Further, since the impacting pellet and the impacted surface were made from hardened tool steel drill blanks, there was hardly any indentation produced due to impact, showing the absence of plastic flow of material.

For bonding the quartz crystal to the top and bottom electrodes, either a thin layer of Duco cement mixed with silver paint and thinned down with a solvent, or Emerson and Cummings Eccobond solder 56 C mixed with catalyst 9 was used. The other joints were made with thin layers of Duco cement. After mounting the assembly into the outer copper tube, a suitable epoxy potting compound such as Eccobond 45 mixed with catalyst 15 was poured around the assembly inside the copper tube. The assembly was then allowed to cure overnight.

The stress gauge was calibrated against a dynamic stress of known value. This was accomplished with the help of a dynamic fatigue testing machine, where the assembly was subjected to a known alternating compressive stress. Fig. 10 shows the voltage-time curves for the calibration load cell of the fatigue machine (upper trace) and that of the piezoelectric stress gauge (lower trace) photographed simultaneously during stressing, using a dual beam scope. The calibration was done both at room temperature and at 77° with the assembly immersed in liquid nitrogen. Fig. 11 shows the stress calculated from the calibration curve for the load cell plotted against the peak voltage from the piezoelectric stress gauge. The piezo-voltage varies linearly with the applied stress and the slope of the straight line gives the stress required to produce an output of one volt from the piezoelectric stress gauge.

C. EQUIPMENT FOR TESTS AT LOW TEMPERATURES

For the tests at 77°K the assembly A to F fixed by rigid rods to the top plate L in Fig. 1 was lowered into an open dewar containing liquid nitrogen. The top part of the

piezoelectric stress gauge was above the liquid level. For the tests at 4.2°K the assembly was immersed into a liquid helium dewar placed inside an outer liquid nitrogen dewar. Fig. 5 shows the photograph of the assembly with the dewars in position. For the tests conducted above 4.2°K a heater was made by winding 100 cm length of fine manganin resistance wire on a grooved copper tube of length 1.9 cm and diameter 2.2 cm. This heater element was connected to an external variable D.C. power supply capable of supplying 0 - 25 volts at 0 - 800 milliamps. This heater was placed around the sample. A thermocouple with one element copper and the other element gold with 2 at.% cobalt was used to measure the temperature of the sample while heating. The thermocouple voltage was measured using a Leeds and Northrup K-3 Universal potentiometer and a Leeds and Northrup D C null detector. Ice with water was used as the reference junction and the standard calibration chart prepared by Richard Byrnes of M/S Andonian Associates was used after suitable zero point correction, to read the temperature from the millivoltage measured by the potentiometer. Since the temperature fluctuated, the measured and the actual temperatures could differ by as much as 1° .

CONCLUSIONS

Impact stress pulses of the order of a few kg/mm^2 and duration of a few microseconds could be applied to single crystals of metals by means of a simple equipment built in the laboratory to study dislocation mobility in metals. The stresses were measured by using a piezoelectric stress gauge using X-cut quartz as the transducer. The gauges were calibrated against a known alternating stress. Absolute values of the stress measured by the gauges are conservatively estimated to be within $\pm 10\%$. It is noteworthy here that recently, Brunton and Wilson (17) have used X-cut quartz to measure stresses in their study of the kinetics of twinning in zinc and tin crystals. They calibrated their quartz crystals against known impulsive loads produced by dropping hard steel balls. They quote a value of 328 N/V to produce one volt in the oscilloscope. This corresponds to about 0.27 kg/mm^2 for a quartz crystal of diameter 1.25 cm, as against our value of 1.96 kg/mm^2 (from the slope of the straight line in Fig. 11) to produce one volt in the oscilloscope. The difference could be due to the facts that (1)- we enclosed the quartz crystal with an epoxy potting compound within an assembly, and (2)- we used a lead nose piece over the quartz crystal. However, since the assembly was calibrated against a known stress, this difference does not affect our main conclusions of the dislocation mobility measurements (ref. 6,7).

ACKNOWLEDGEMENT

The authors would like to express their sincere thanks to M/S Hunt Corporation, Carlisle, Pennsylvania, for providing the quartz crystals used in the piezoelectric stress gauges.

This research was supported by the Advanced Research Projects Agency of the Department of Defense through the Northwestern Materials Research Center.

REFERENCES

1. J. D. Eshelby : Proc. Roy. Soc. (London), B 69, 1013 (1956)
2. C. S. Smith : Trans. Met. Soc. AIME, 214, 574 (1958)
3. J. Weertman : RESPONSE OF METALS TO HIGH VELOCITY DEFORMATION, Edited by Shewmon and Zackay, Interscience, (1961)
4. J. Weertman : J. Appl. Phys., 37, 4925 (1966)
5. J. Weertman : J. Appl. Phys., 38, 5293 (1967)
6. V. R. Parameswaran and J. Weertman : Scripta Met., 3, 477 (1969)
7. V. R. Parameswaran and J. Weertman : (to be published)
8. R. A. Graham : J. Appl. Phys., 32, 555 (1961)
9. R. A. Graham : Rev. Sci. Instr., 32, 1308 (1961)
10. R. A. Graham : J. Appl. Phys., 33, 1755 (1962)
11. O. E. Jones, F. W. Neilson and W. B. Benedick : J. Appl. Phys., 33, 3224 (1962)
12. O. E. Jones : Rev. Sci. Instr., 38, 253 (1967)
13. R. A. Graham, F. W. Neilson and W. B. Benedick : J. Appl. Phys., 36, 1775 (1965)
14. J. F. O'Brien and R. J. Wasley : Rev. Sci. Instr., 37, 531 (1966)
15. W. G. Cady : PIEZOELECTRICITY, McGraw-Hill, New York, London, (1946)
16. W. P. Mason : PIEZOELECTRIC CRYSTALS AND THEIR APPLICATIONS TO ULTRASONICS, D. Van Nostrand, New York, 1950
17. J. H. Brunton and M. P. W. Wilson : Proc. Roy. Soc. (London), A 309, 345 (1969)

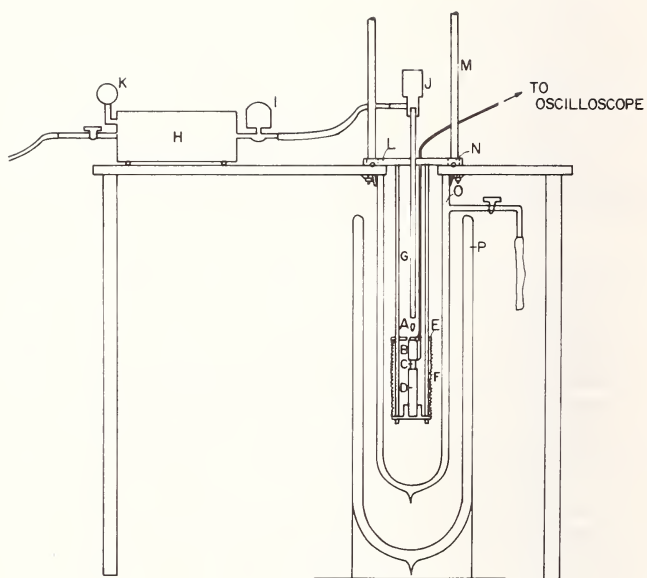


FIG. 1-- Schematic diagram of the experimental set up for the application of the stress pulse.

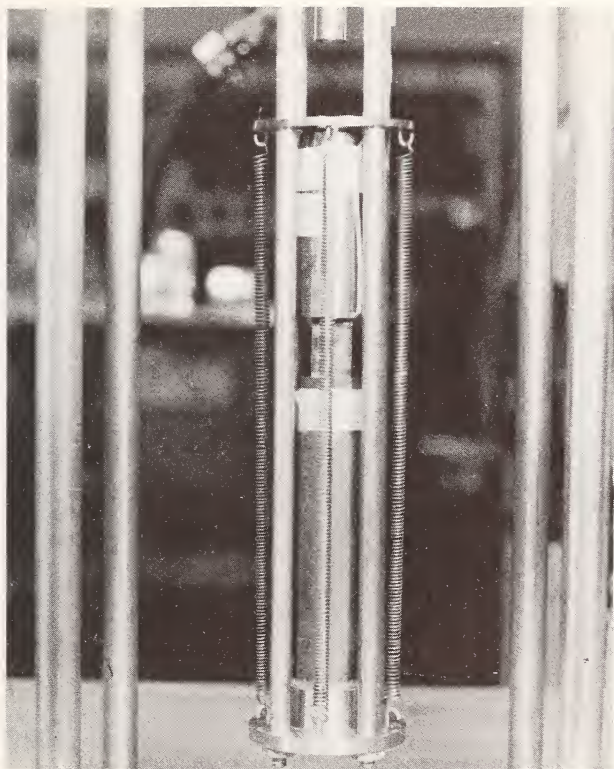


FIG. 2-- Photograph showing the piezoelectric stress gauge B, the single crystal C and the lead damper bar D.

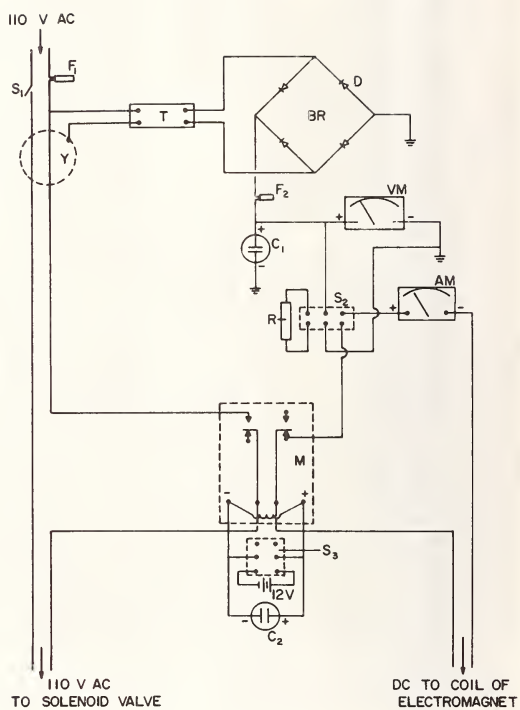


FIG. 3-- Electrical circuit used to operate the electromagnet and the solenoid valve.

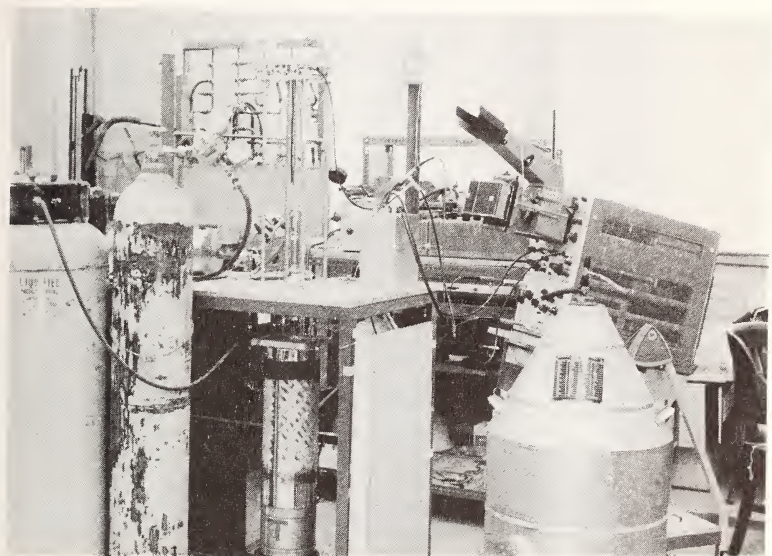


FIG. 4-- General view of the equipment.

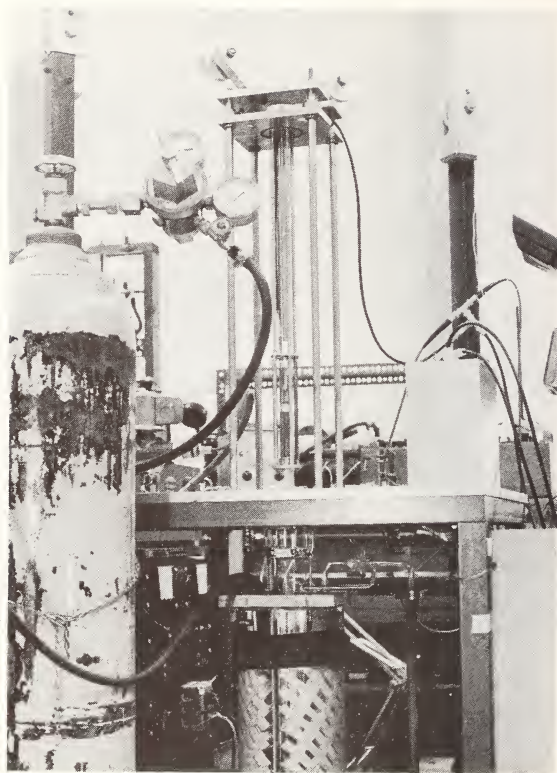


FIG. 5-- Photograph of the assembly with the dewars in position at the bottom.

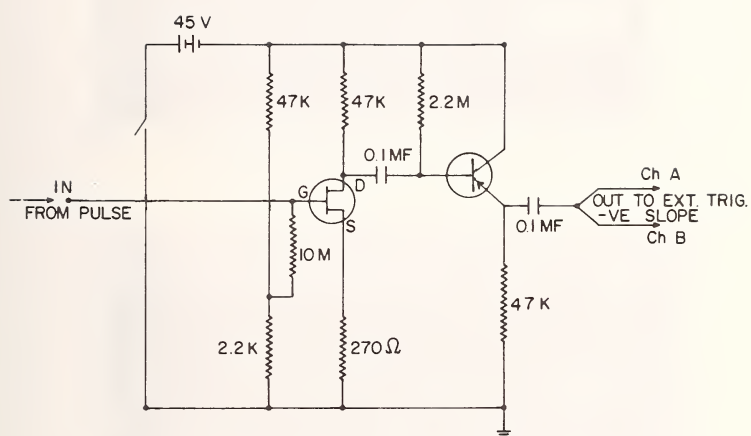


FIG. 6-- Triggering circuit.

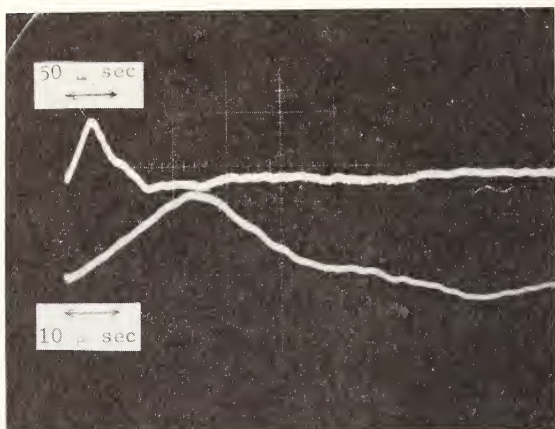


FIG. 7

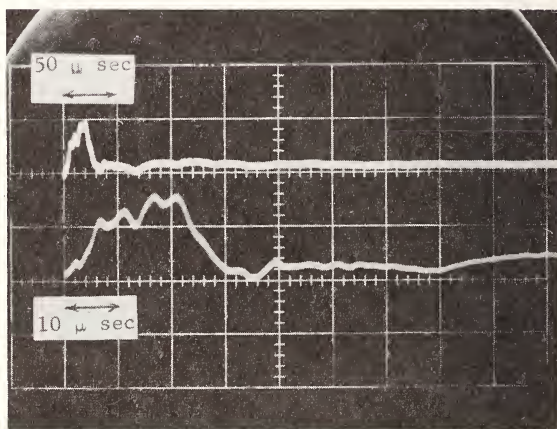
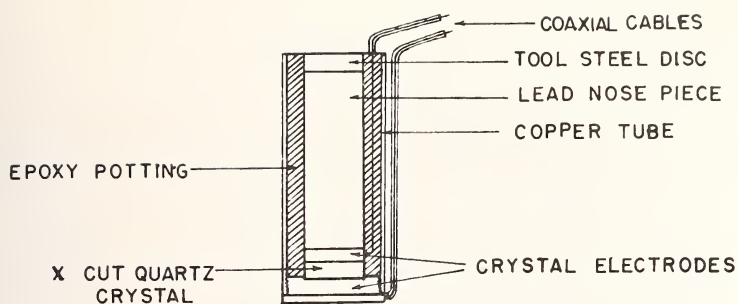


FIG. 8

Typical stress pulses obtained from the piezo-assembly.



PIEZOELECTRIC STRESS GAUGE

FIG. 9-- Schematic diagram of the piezoelectric stress gauge.

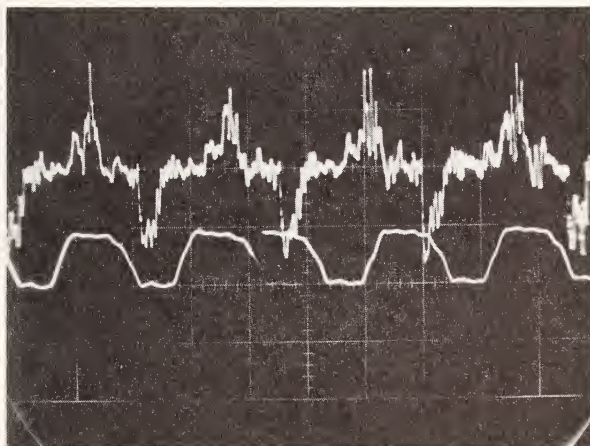


FIG. 10-- Voltage-Time pulses from the calibrated load cell (upper trace) and the piezoelectric stress gauge (lower trace).

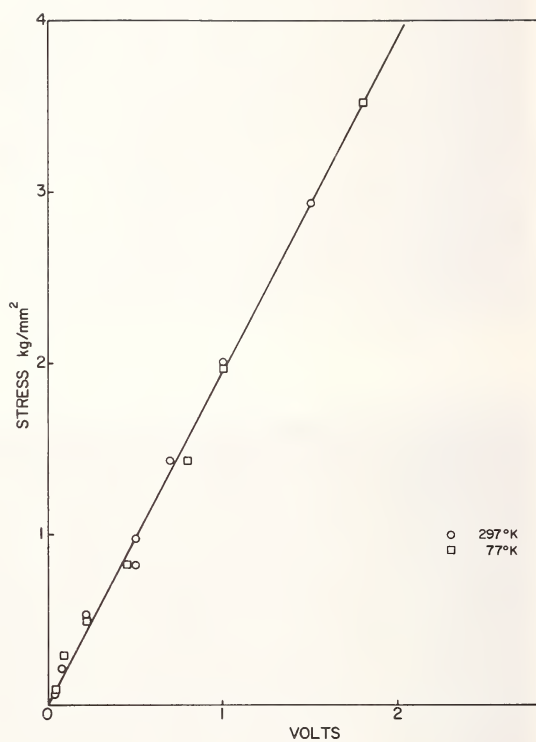


FIG. 11-- Calibration curve for the piezoelectric stress gauge.

APPENDIX

The equipment described in the text was used in the study of the mobility of high speed dislocations in metal single crystals. The method was to apply impact stress pulses of a few microseconds duration to the single crystal and to measure the lengths of the slip bands produced on the surface. A slip band is produced by the expansion of dislocation loops on a slip plane. The length measured on a surface gives the distance through which the screw components of these loops threading the surface have travelled along that slip plane for the duration of the stress pulse. This length divided by the total duration of the stress pulse gives the average velocity of the leading dislocation in that band. Fig. A-1 shows typical slip bands produced on the surface of a lead single crystal by the impact stress pulse.

Dislocation velocities were measured in high purity lead and lead-indium alloy single crystals at temperatures varying between 4.2°K and 298°K . Experiments were done in both the normal and the superconducting states of the metals. The velocities measured were in the range: $10^3 - 10^5$ cm/sec.

RESULTS

Fig. A-2 shows the dislocation velocity v plotted against the mean stress $\bar{\tau}$ (defined by equation (1) in the text), for pure lead at 298° , 77° and 4.2°K . The velocity varies linearly with stress in the lower regions of stress. At higher stresses, the variation is less than linear and the dislocation velocity approaches a limiting velocity equal to the shear sound velocity in lead at each temperature. In the linear region of the velocity-stress curve, the resistance to dislocation motion is proportional to the velocity itself and the slope of this linear region gives a drag coefficient or damping constant B defined as:

$$B = \bar{\tau}b/v \quad (2)$$

where $\bar{\tau}$ is the shear stress applied to maintain the velocity v . Fig. A-3 shows the damping constant B plotted for different temperatures for pure lead. The circles indicate the values of B calculated from velocity measurements at temperatures above 7.2°K in the normal lead. The value of B at 4.2°K is that of the superconducting lead.

In the case of the lead-indium alloys (lead with 0.1, 1, and 10 at% indium), the dislocation velocity was found to vary linearly with stress. The damping constants

calculated are given in Table I. The value of B increases with increasing alloy content. For a particular stress, the dislocation velocity in the alloys was always smaller than the corresponding value in pure lead. (The complete details of the results are given in a forthcoming paper to be published soon).

DISCUSSION

In the region where the dislocation velocity varies linearly with stress, at temperatures above about 60°K, most of the drag acting on the moving dislocations is caused by the effects of phonon viscosity and phonon scattering (Nabarro(1), Mason and Rosenberg(2), Leibfried(3)). These drag forces increase linearly with increasing temperature. At liquid helium temperatures, the phonon drag reduces to zero. But there is a drag due to conduction electrons which increases with decreasing temperature below about 60°K in a normal metal (Mason(4)). In a superconductor, the conduction electrons are paired into loosely coupled "Cooper pairs" and the electron drag is considerably reduced. Our experimental results are consistent with these theories of damping of dislocation motion by phonons and electrons.

REFERENCE

1. F. R. N. Nabarro : THEORY OF CRYSTAL DISLOCATIONS, Clarendon Press, Oxford, 1968.
2. W. P. Mason and A. Rosenberg : J. Appl. Phys., 38, 1929 (1967)
3. G. Leibfried : Z. Physik, 127, 344 (1950)
4. W. P. Mason : Phys. Rev., 143, 229 (1966)

TABLE I-- Values of damping constants in
lead and lead-indium alloys.

	Damping constant B (10^{-4} dyne sec/cm ²)	
	298°K	4.2°K
Pure lead	3.43	1.52
Pb - 0.1 at.% In	3.85	-
Pb - 1 at.% In	4.375	-
Pb - 10 at.% In	5.43	37.6



FIG. A-1-- Typical slip bands observed on the surface of the crystals after impact.

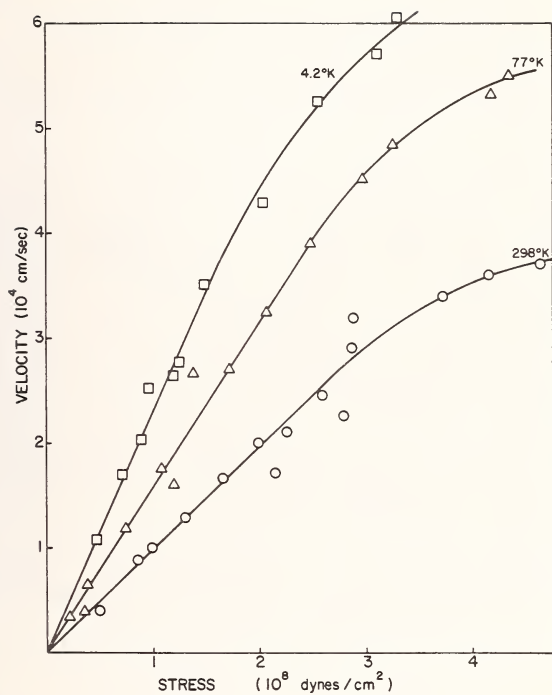


FIG. A-2-- Dislocation velocity vs stress for pure lead.

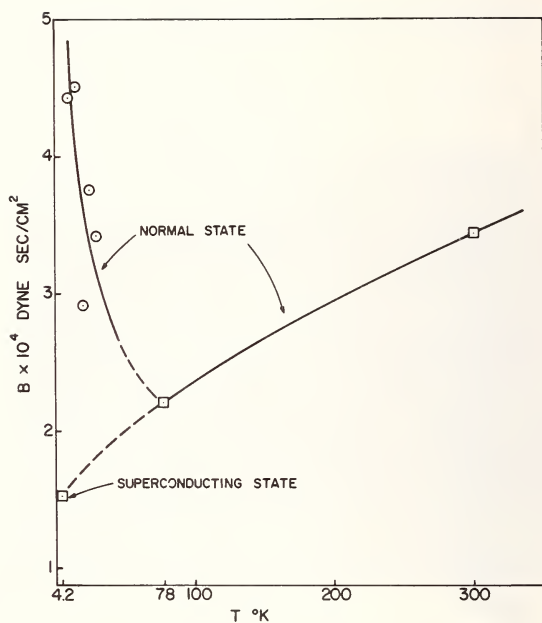


FIG. A-3-- Damping constant B vs temperature for pure lead.

SOME EFFECTS OF EQUALIZATION ON ACCELERATION RESPONSE AND
FATIGUE LIFE EXPECTANCY

R. M. MAINS¹

REFERENCE: Mains, R. M., "Some Effects of Equalization on Acceleration Response and Fatigue Life Expectancy," ASTM/IEC/AIAA Space Simulation Conference, 14-16 September, 1970.

ABSTRACT: A set of calculations is reported for various transmissibilities of a 10-mass system, intended to be representative of an exciter, fixture, test article arrangement. The difficulties of achieving equalization at some coordinate when it has a transmissibility range of 10^6 or more are noted. By comparison of r.m.s. responses to a level power spectral density input, it is shown that factors of 5 to 10 or more difference in acceleration response result from equalization at different coordinate locations. These differences in r.m.s. response would produce corresponding differences in predicted real-time behavior. The differences in r.m.s. spring stress responses were smaller for various equalization locations, but still large enough that predictions of fatigue life expectancy (for the system used) would be much affected by the choice of equalization location.

KEY WORDS: Vibration, test, evaluation, fatigue life, acceleration response, random vibration, transmissivity equalization, mechanical impedance, transfer impedance, lumped parameter system.

Introduction

At a symposium on reliability at Corona, California in 1954 (1)*, three papers were presented which discussed random vibration. Two of them (D.M. Ellett and R.M. Mains) showed the results of flight measurements and demonstrated the random nature of the vibration. The third paper (C.T. Morrow) showed

¹Professor of Civil Engineering, Washington University, St. Louis, Missouri 63130

*Numbers refer to the list of references at the end of the paper.

how the treatment of random noise in communications problems could be adapted for random vibration in mechanical systems. Since then, testing and measuring random vibration have become commonplace, and off-the-shelf equipment is available. Papers theorizing about random vibration abound in the literature, and there are several schemes for assessing damage under random vibration (2,3,4,5). As long as the vibration excitation spectrum is broad-banded and reasonably level, the responses of an elastic system to that excitation are best measured by the area under the curve of the square of the transmissibility vs. frequency (6). The smaller the area under that curve, the lesser the r.m.s. response of the phenomenon represented by the curve will be.

For some time, the author has been concerned over various practices in vibration testing, and in particular over the questions of whether, where, and how to "equalize" in a random vibration test. A study of the transmissibility curves for a system, and in particular the areas under the squared curves, could be expected to shed some light on the equalization problem. Differences in transmissibilities and in area under squared curves for various equalization locations would mean differences in real-time performance and life.

The System and its Analysis

A set of systems was devised, as shown in Figure 1, consisting of ten masses and springs in series, and constrained to move in one direction only. It was intended that these masses and springs would represent an exciter, fixture, test article combination, so nine different combinations of masses were tried with a given set of springs to see what the frequency patterns would be. Table 1 shows the various mass combinations and the natural frequencies for each. It is of interest to note how little change in the set of frequencies accompanys a considerable change in the arrangement of masses. There were no outstanding reasons for selecting any one of these systems over the others, so the author chose the first set.

In a system such as this, there are two phenomena of interest: the motions of the masses, usually in terms of acceleration; and the stresses or forces in the springs. The motions are associated with malfunction problems, short circuiting, gyro precession, relay chatter, and the like. The stresses are associated with fatigue damage accumulation and life prediction, as mentioned above.

In the random vibration test system, equalizing means the adjustment of the amplifier gain so that a level spectrum of input produces a level spectrum of response at the equalization

point. In the calculations, mass 1 was taken as the driving point (exciter armature), and masses 5 and 6 were taken in turn as the equalization points.

The general scheme of the analysis was to generate the complex impedance, invert this to complex mobility, and work with the mobility to get accelerations and stresses. First the natural frequencies of Table 2 were reduced to get a non-singular impedance matrix:

$$\omega_r^2 = \omega_o^2 * (1 - \zeta^2) \quad (1)$$

in which ω_o^2 = eigenvalue from undamped system

ζ = damping coefficient, taken as 0.03

ω_r^2 = reduced frequency, squared

Calculations with only these frequencies would not show enough shape to the curves, so three more ω^2 were calculated to divide the intervals between each ω_r^2 uniformly. The frequencies used are listed in Table 2.

The stiffness, K, and mass, M, matrices were constructed in the usual way, and the damping matrix, C, was calculated as:

$$C = 2\zeta [M^{\frac{1}{2}} K M^{\frac{1}{2}}] \quad (2)$$

where the square roots are term-by-term. Next the complex impedance, $Z(i\omega)$, was defined as:

$$Z(i\omega) = Z_{RE} + iZ_{IM} \quad (3)$$

$$Z_{RE} = K - \omega^2 M \quad (4)$$

$$Z_{IM} = \omega C \quad (5)$$

$$\text{Now } Z(i\omega) * X(i\omega) = f(i\omega) \quad (6)$$

$$\text{in which } X(i\omega) = X_{RE} + iX_{IM}, \text{ complex response} \quad (7)$$

$$f(i\omega) = f_{RE} + if_{IM}, \text{ complex excitation} \quad (8)$$

$$\text{From eq. (6)} \quad X(i\omega) = Z^{-1}(i\omega) * f(i\omega) \quad (9)$$

If $f(i\omega)$ is taken as real only, then

$$X_{RE} = Z_{RE}^{-1} * f_{RE} \quad (10)$$

$$X_{IM} = Z_{IM}^{-1} * f_{RE} \quad (11)$$

in which

$$Z_{RE}^{-1} = [(K - \omega^2 M) + \omega C(K - \omega^2 M)^{-1} C \omega]^{-1} \quad (12)$$

$$Z_{IM}^{-1} = Z_{RE}^{-1} * \omega C(K - \omega^2 M)^{-1} \quad (13)$$

Equations (10) and (11) are the responses in inches to one-pound driving forces, and from them the quantities of interest are calculated.

Results of the Calculations

To examine the feasibility of equalization, Table 3 shows the driving force on mass 1 required to produce 1 g at each mass and each frequency. For any given limit of exciter force, a row of the matrix shows whether the motion could be equalized within that force limit or not. Mass 5 is the best one for equalization over the full range of frequencies, while mass 6 would have attenuation above frequency 32. Masses past 6 would have more attenuation in the higher frequencies if equalization were attempted with them.

To show the range of driving forces involved, Figure 2 is a semi-log plot of the driving force at mass 1 for 1 g at mass 9. The range from 2.7 lbs at frequency 10, to 656,000 lbs at frequency 40 is of particular interest. Figure 3 is a semi-log plot of the driving force at mass 1 to produce 1 lb of force in spring 8-9. The range from 0.53 lbs at frequency 10, to 307,000 lbs at frequency 40 is of interest again.

Figure 4 is a semi-log plot of the acceleration of mass 9 for 1 g at masses 1, 5, 6. The differences between these curves are in the magnitude of the peaks in the lower frequency range. For 1 g at mass 1, mass 9 moved 6.5 at frequency 3 and 6.8 at frequency 10. For 1 g at mass 5, mass 9 moved 86.0 g at frequency 6 and 5.4 g at frequency 10. For 1 g at mass 6, mass 9 moved 15 g at frequency 9 and 12 g at frequency 17. These are significant differences, in that the prediction of real-time behavior or life from test data could differ by a factor of 5 or more depending upon which equalization point is used.

Figure 5 is a semi-log plot of the force in spring 8-9 for 1 g at masses 1, 5, 6. These curves show little difference in general level and are similar in many details. The resonance peaks in the low frequency range shift location with the change in equalization point.

The driving point impedance, pounds of force at mass 1 to produce 1 g at mass 1, is plotted in Figure 6. This is shown primarily for the shape and character of the curve.

Table 4 lists the r.m.s. pounds at mass 1 for a level power

spectral density of $1 \text{ g}^2/\text{cps}$ at the various masses. These values are prohibitively large, so that a p.s.d. level of $1 \text{ g}^2/\text{cps}$ could not be physically achieved with this system. This is because the system between mass 1 and mass 5 acts as a vibration absorber in the frequency range above number 20 or 25, and it is physically unreasonable to try to force a level spectral density of response. If a level response could be forced in the test, the results would be grossly misleading for conversion to real time.

Table 5 shows the r.m.s. pounds in the springs for a level power spectral density of $1 \text{ g}^2/\text{cps}$ at masses 1, 5 and 6. These values correlate with the similarity of the curves in Figure 5, in that the peak at frequency 6 for mass 5 produces a larger r.m.s. response by a factor of 4 or more. Predictions of real-time behavior or life of the springs would be significantly different according to which equalization point were used.

Table 6 shows the r.m.s. g's at the various masses for a level power spectral density of $1 \text{ g}^2/\text{cps}$ at masses 1, 5 and 6. Here is where the differences in equalization points show clearly. Equalization at mass 5 is about 6 times as severe as equalization at mass 1, while equalization at mass 6 is about $1\frac{1}{2}$ times as severe as at mass 1 and only $1/4$ as severe as at mass 5.

Conclusions

If data from a random vibration test are to be used to predict real-time behavior or life of an equipment, then care must be taken that the test fixture and the equalization process used do not lead to erroneous predictions. For the system used in this study, equalizing for a level response on any other mass than no. 5 could not be done. Equalizing at masses past 5 would require that attenuation in the higher frequencies be accepted. One alternative would be a redesign of the fixture for better transmissibility in the upper frequency range. Another alternative would be to reconsider the desirability of trying to use equalization at some point as a device for insuring correlation between test time and real time.

For the system calculated, factors of 5 to 10 or more difference in r.m.s. acceleration responses to a level power spectral density input, were noted for equalization at different locations. These differences in response would produce corresponding differences in prediction of real-time behavior. The r.m.s. spring stress responses showed factors up to 4 or 5 difference for the various equalization locations. These differences would produce appreciable differences in fatigue life estimates.

List of References

1. "Proceedings of the Symposium on Guided Missile Reliability," U. S. Naval Ordnance Laboratory, Corona, Calif., October 1954.
2. Clevenson, Sherman A. and Steiner, Roy, "Fatigue Life Under Various Random Loading Spectra," *Shock and Vibration Bulletin No. 35, II*, January 1966.
3. Root, L. W., "Random-Sine Fatigue Data Correlation," *Shock and Vibration Bulletin No. 33, II*, February 1964.
4. Bieber, R. E. and Fairman, J. H., "Random Fatigue Data," *Shock and Vibration Bulletin No. 31, III*, April 1963.
5. Fuller, J. R., "Cumulative Fatigue Damage Due to Variable-Cycle Loading," *Shock and Vibration Bulletin No. 29, IV*, June 1961.
6. Mains, R. M., Chapter 12 in *Random Vibration*, edited by S. H. Crandall, John Wiley and Sons, 1958, p. 12-32.

TABLE 1
VARIOUS MASS SEQUENCES AND FREQUENCIES

SEQUENCE OF MASSES - WTS. IN LBS.										MASS NO.
51	51	51	51	51	51	21	21	21	21	1
36	36	41	41	41	41	31	31	31	31	2
21	21	36	36	36	36	36	36	36	36	3
31	31	31	31	31	31	41	41	41	41	4
41	41	21	21	21	21	51	51	51	51	5
200	90	200	90	20	20	200	90	90	20	6
50	70	50	70	40	40	50	70	70	40	7
15	50	15	50	50	50	15	50	50	50	8
4	40	4	40	70	70	4	40	40	70	9
1	20	1	20	90	90	1	20	20	90	10

FREQUENCIES - CPS										FREQ. NO.
0.4660	0.4660	0.4660	0.4660	0.4660	0.4659	0.4660	0.4660	0.4660	0.4659	1
45.91	32.67	22.39	44.34	32.20	22.22	50.91	33.39	33.39	22.61	2
78.50	52.42	43.71	79.20	51.86	43.23	79.49	55.67	55.67	44.90	3
122.56	72.69	67.11	124.82	73.53	68.06	120.55	74.59	74.59	70.43	4
137.00	93.26	93.04	136.72	94.75	98.00	136.83	93.89	93.89	94.82	5
198.25	117.67	132.64	195.10	118.84	131.89	187.24	117.28	117.28	131.79	6
206.57	139.85	184.41	206.57	136.26	177.12	206.57	137.74	137.74	175.85	7
247.53	200.46	232.38	251.51	197.45	228.52	234.91	189.89	189.89	225.67	8
301.58	248.37	272.98	304.54	251.85	256.91	305.05	235.57	235.57	265.33	9
317.95	301.62	302.64	317.94	306.32	326.63	317.95	305.06	305.06	305.06	10

TABLE 2. FREQUENCIES
USED FOR COMPUTATION

FREQ. NO.	CPS	FREQ. NO.	CPS
1	0.4035	21	184.81
2	0.4659	22	198.21
3	22.955	23	200.32
4	32.459	24	202.41
5	39.753	25	204.48
6	45.902	26	206.53
7	55.860	27	217.49
8	64.293	28	227.92
9	71.742	29	237.90
10	78.488	30	247.47
11	91.508	31	262.03
12	102.89	32	275.81
13	113.14	33	288.95
14	122.53	34	301.51
15	126.30	35	305.68
16	129.95	36	309.80
17	133.51	37	313.86
18	136.97	38	317.88
19	154.57	39	321.84
20	170.36	40	325.76

TABLE 3. POUNDS AT MASS 1 FOR 1G AT MASS N

	1	2	3	4	5
1	0.270000 04	0.233480 04	0.182250 04	0.176040 03	0.484950 02
2	0.269980 04	0.233460 04	0.456620 04	0.232900 03	0.577560 02
3	0.269960 04	0.233440 04	0.116230 04	0.481300 03	0.396720 02
4	0.269930 04	0.233410 04	0.572090 03	0.160570 04	0.299650 03
5	0.269910 04	0.233390 04	0.419540 03	0.387970 03	0.362780 03
6	0.269900 04	0.233370 04	0.328380 03	0.212680 03	0.105020 03
7	0.269890 04	0.233360 04	0.296930 03	0.171530 03	0.739390 02
8	0.269880 04	0.233350 04	0.284900 03	0.157560 03	0.648650 02
9	0.269880 04	0.233350 04	0.279930 03	0.152060 03	0.514590 02
10	0.269880 04	0.233350 04	0.277830 03	0.149780 03	0.500780 02
	11	12	13	14	15
1	0.102580 03	0.223830 03	0.161690 03	0.104530 02	0.204860 02
2	0.711760 02	0.780480 02	0.904640 02	0.420330 02	0.426030 02
3	0.714180 02	0.567960 02	0.358520 02	0.961940 01	0.293810 02
4	0.102490 03	0.604930 02	0.286940 02	0.521150 01	0.124950 02
5	0.293730 03	0.113470 03	0.445570 02	0.693320 01	0.155430 02
6	0.170480 03	0.170470 03	0.105780 03	0.234120 02	0.614720 02
7	0.289420 03	0.168080 04	0.377320 03	0.265560 02	0.437710 02
8	0.841600 02	0.110310 03	0.715590 02	0.130550 02	0.280240 02
9	0.602390 02	0.703550 02	0.399570 02	0.623130 01	0.124010 02
10	0.530670 02	0.597670 02	0.326880 02	0.490200 01	0.959070 01
	21	22	23	24	25
1	0.701620 02	0.138260 02	0.137160 02	0.148910 02	0.167090 02
2	0.232540 02	0.128500 02	0.146440 02	0.182440 02	0.235040 02
3	0.218120 02	0.777920 01	0.812910 01	0.922710 01	0.107540 02
4	0.122960 03	0.588180 02	0.525270 02	0.510650 02	0.514540 02
5	0.272480 02	0.107150 02	0.112530 02	0.128000 02	0.149080 02
6	0.226440 03	0.105810 03	0.114020 03	0.132940 03	0.158500 03
7	0.711510 03	0.494860 03	0.549680 03	0.618860 03	0.661380 03
8	0.977580 03	0.202280 03	0.187700 03	0.190760 03	0.206020 03
9	0.332330 03	0.125790 03	0.126290 03	0.138380 03	0.160640 03
10	0.171400 03	0.557830 02	0.545110 02	0.580910 02	0.655360 02
	31	32	33	34	35
1	0.293320 02	0.346230 02	0.385850 02	0.372760 02	0.361940 02
2	0.385900 02	0.733290 02	0.736500 02	0.450230 02	0.435290 02
3	0.470860 02	0.405270 02	0.312810 02	0.278190 02	0.306090 02
4	0.320060 02	0.457970 02	0.497250 02	0.566510 02	0.669180 02
5	0.541150 02	0.952460 02	0.122710 03	0.161720 03	0.199870 03
6	0.995340 03	0.195540 04	0.278010 04	0.400670 04	0.509610 04
7	0.661390 03	0.148400 05	0.236760 05	0.377910 05	0.496500 05
8	0.152680 05	0.423410 05	0.814730 05	0.154550 06	0.212580 06
9	0.114530 06	0.182480 06	0.149670 06	0.138390 06	0.152610 06
10	0.733830 04	0.184870 05	0.293340 05	0.411710 05	0.507600 05

TABLE 3. CONTINUED

	6	7	8	9	10
1	0.340190 01	0.434200 02	0.707530 02	0.113080 03	0.182630 02
2	0.382250 01	0.445040 02	0.653090 02	0.852730 02	0.268080 02
3	0.536470 01	0.556170 02	0.731610 02	0.788260 02	0.817580 02
4	0.118200 02	0.931770 02	0.102780 03	0.871640 02	0.209380 02
5	0.421010 03	0.251890 03	0.193000 03	0.121610 03	0.145560 02
6	0.104500 02	0.216170 03	0.713410 03	0.530170 03	0.147000 02
7	0.625560 01	0.826840 02	0.101950 03	0.714530 02	0.587450 01
8	0.522670 01	0.623290 02	0.683200 02	0.417370 02	0.340640 01
9	0.486030 01	0.558370 02	0.588660 02	0.345230 02	0.269940 01
10	0.471460 01	0.533590 02	0.554050 02	0.319960 02	0.246290 01
	16	17	18	19	20
1	0.329670 02	0.438690 02	0.490420 02	0.861110 02	0.224100 03
2	0.486890 02	0.511010 02	0.517840 02	0.465880 02	0.363740 02
3	0.777850 02	0.166070 03	0.148660 03	0.111460 03	0.502730 02
4	0.234560 02	0.351350 02	0.395910 02	0.730450 02	0.100340 03
5	0.270900 02	0.374890 02	0.424860 02	0.574030 02	0.485670 02
6	0.129950 03	0.206630 03	0.155740 03	0.290260 03	0.326850 03
7	0.527910 02	0.465950 02	0.428130 02	0.356830 03	0.696430 03
8	0.425680 02	0.463720 02	0.520010 02	0.148110 04	0.414310 04
9	0.173400 02	0.172430 02	0.174710 02	0.196370 03	0.399510 03
10	0.131800 02	0.128770 02	0.128150 02	0.129770 03	0.235000 03
	26	27	28	29	30
1	0.187780 02	0.301660 02	0.412180 02	0.472930 02	0.304110 02
2	0.303830 02	0.920560 02	0.601330 02	0.310660 02	0.213490 02
3	0.124790 02	0.219080 02	0.288370 02	0.329860 02	0.391020 02
4	0.521800 02	0.498090 02	0.389700 02	0.261390 02	0.195040 02
5	0.172400 02	0.282490 02	0.316010 02	0.275970 02	0.253680 02
6	0.187330 03	0.343870 03	0.427730 03	0.411020 03	0.412120 03
7	0.687210 03	0.123890 04	0.185920 04	0.206710 04	0.233650 04
8	0.236830 03	0.868700 03	0.200250 04	0.296080 04	0.414460 04
9	0.197980 03	0.103330 04	0.331090 04	0.688460 04	0.142910 05
10	0.784320 02	0.342170 03	0.882650 03	0.139720 04	0.202030 04
	36	37	38	39	40
1	0.357570 02	0.358570 02	0.362420 02	0.367410 02	0.372690 02
2	0.451770 02	0.486820 02	0.531690 02	0.581460 02	0.633550 02
3	0.357200 02	0.427860 02	0.514180 02	0.613410 02	0.723750 02
4	0.833960 02	0.106190 03	0.135130 03	0.170130 03	0.211200 03
5	0.260090 03	0.345190 03	0.457080 03	0.597890 03	0.770080 03
6	0.681910 04	0.929900 04	0.126420 05	0.169660 05	0.224070 05
7	0.685380 05	0.962810 05	0.134640 06	0.185680 06	0.251810 06
8	0.300350 06	0.417320 06	0.563490 06	0.755710 06	0.102190 07
9	0.180090 06	0.225730 06	0.302880 06	0.435620 06	0.655930 06
10	0.662510 05	0.910180 05	0.132850 06	0.206530 06	0.334300 06

TABLE 4. RMS POUNDS
AT MASS 1 for $1g^2/cps$
SPECTRAL DENSITY

AT MASS	RMS LBS.
1	.10842+5
5	.87397+4
6	.67102+5
7	.71624+6
8	.29377+7
9	.20229+7
10	.84270+6

TABLE 5. RMS SPRING FORCES

SPRING NO.	RMS LBS. IN SPRING N FOR			RATIOS	
	$1g^2/cps@1$	$1g^2/cps@5$	$1g^2/cps@6$	$\frac{1g^2/cps@5}{@ 1}$	$\frac{1g^2/cps@6}{@ 1}$
5-6	6753	37300	7869	5.525	1.165
6-7	3012	14541	3440	4.825	1.442
7-8	1102	4820	1416	4.375	1.285
8-9	347	1297	469	3.785	1.352
9-10	67	264	99	3.957	1.492

TABLE 6. RMS G's AT MASSES

MASS	RMS G's AT MASS N FOR			RMS G's / .18077+2		
	$1g^2/cps@1$	$1g^2/cps@5$	$1g^2/cps@6$	$1g^2/cps@1$	$1g^2/cps@5$	$1g^2/cps@6$
1	.18077+2	.11440+3	.45804+2	1.000	6.330	2.533
5	.33482+2	.18077+2	.39869+2	1.853	1.000	2.205
6	.24246+2	.11527+3	.18077+2	1.342	6.380	1.000
7	.27356+2	.19218+3	.35147+2	1.513	10.63	1.945
8	.34157+2	.23064+3	.52449+2	1.890	12.77	2.903
9	.41427+2	.24870+3	.73529+2	2.293	13.75	4.070
10	.45800+2	.25680+3	.86931+2	2.534	14.20	4.810

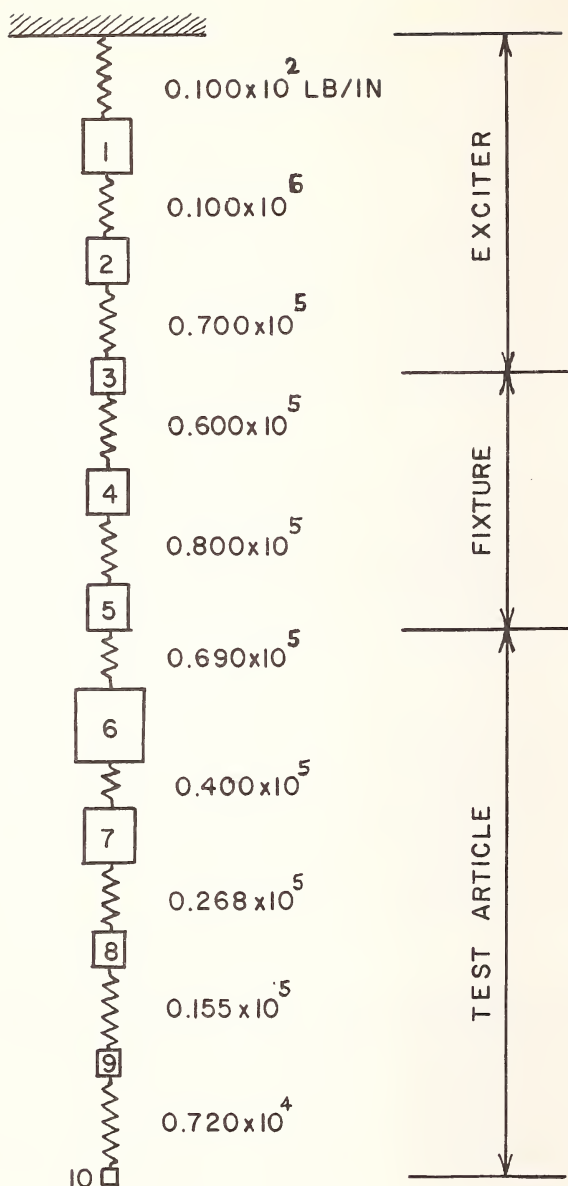
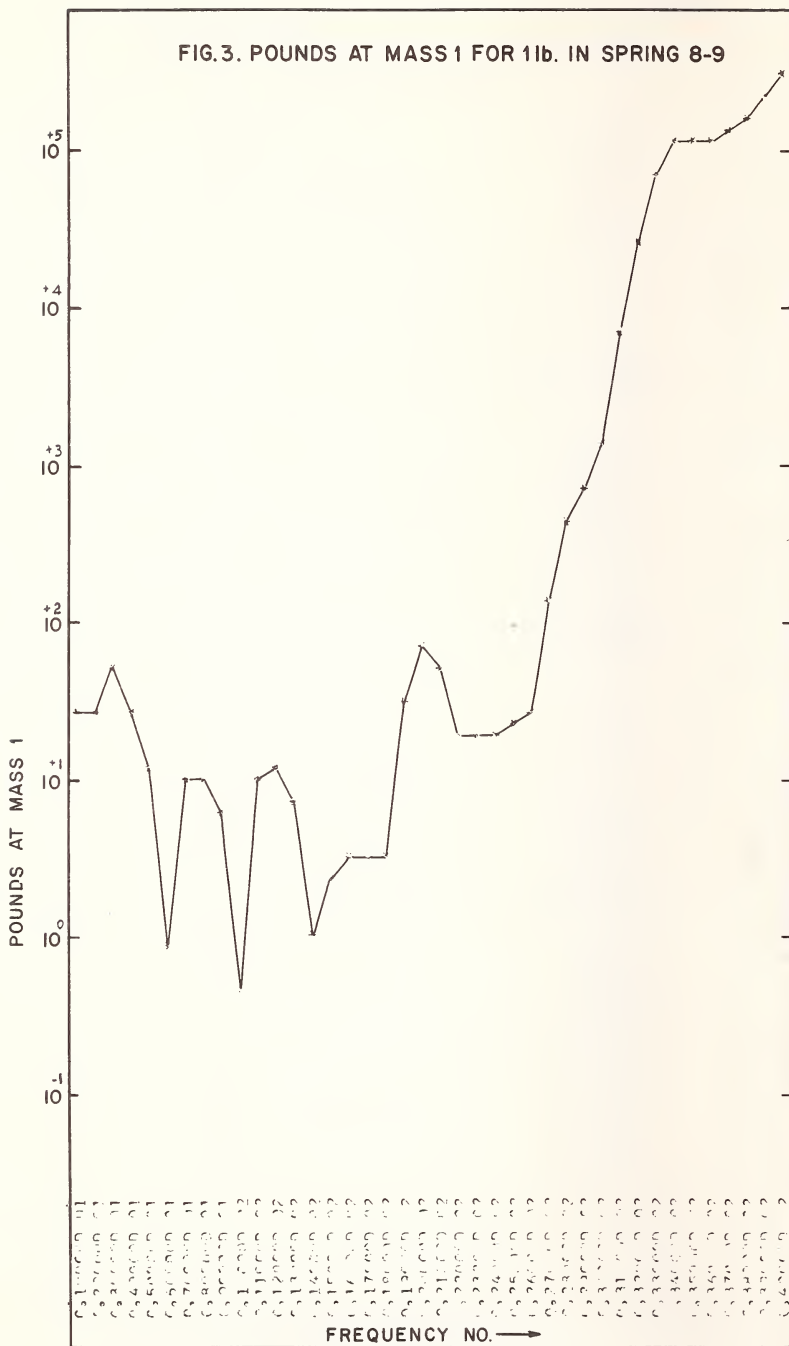
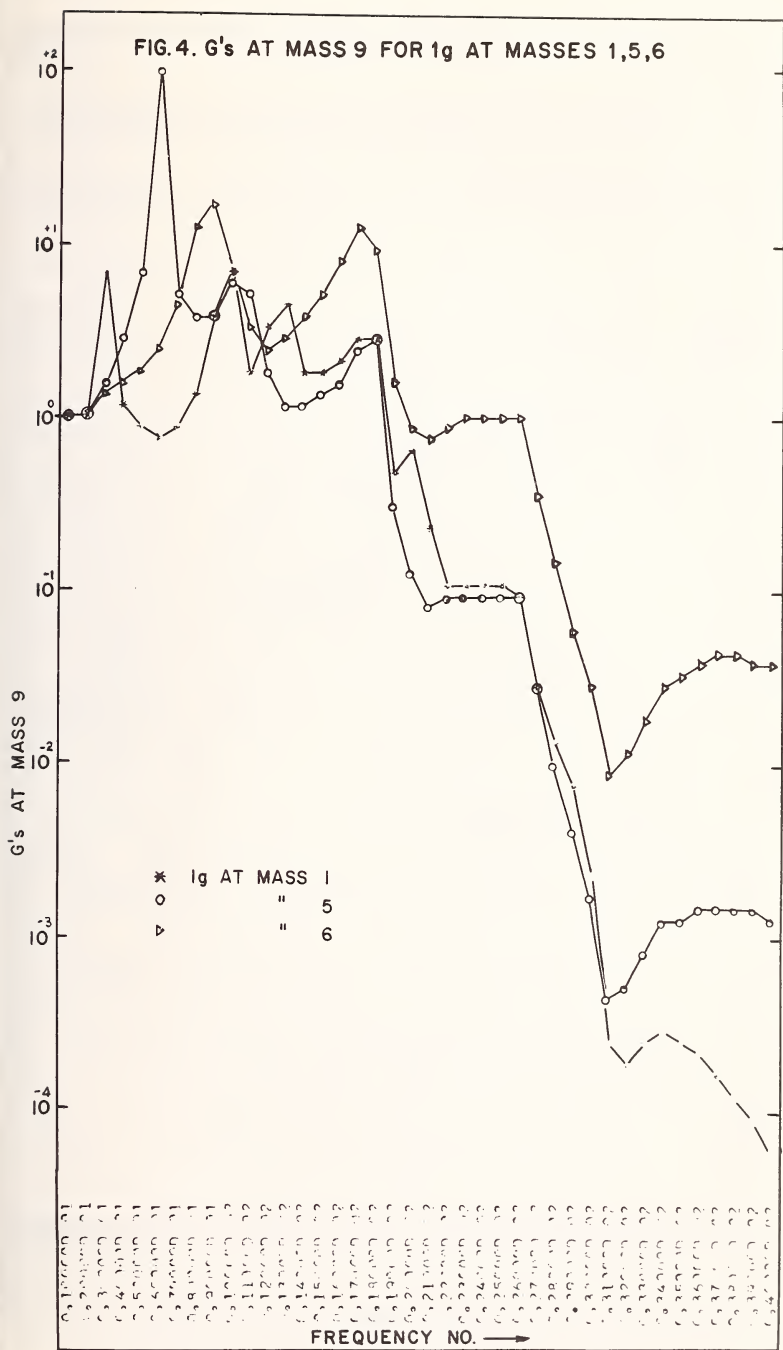


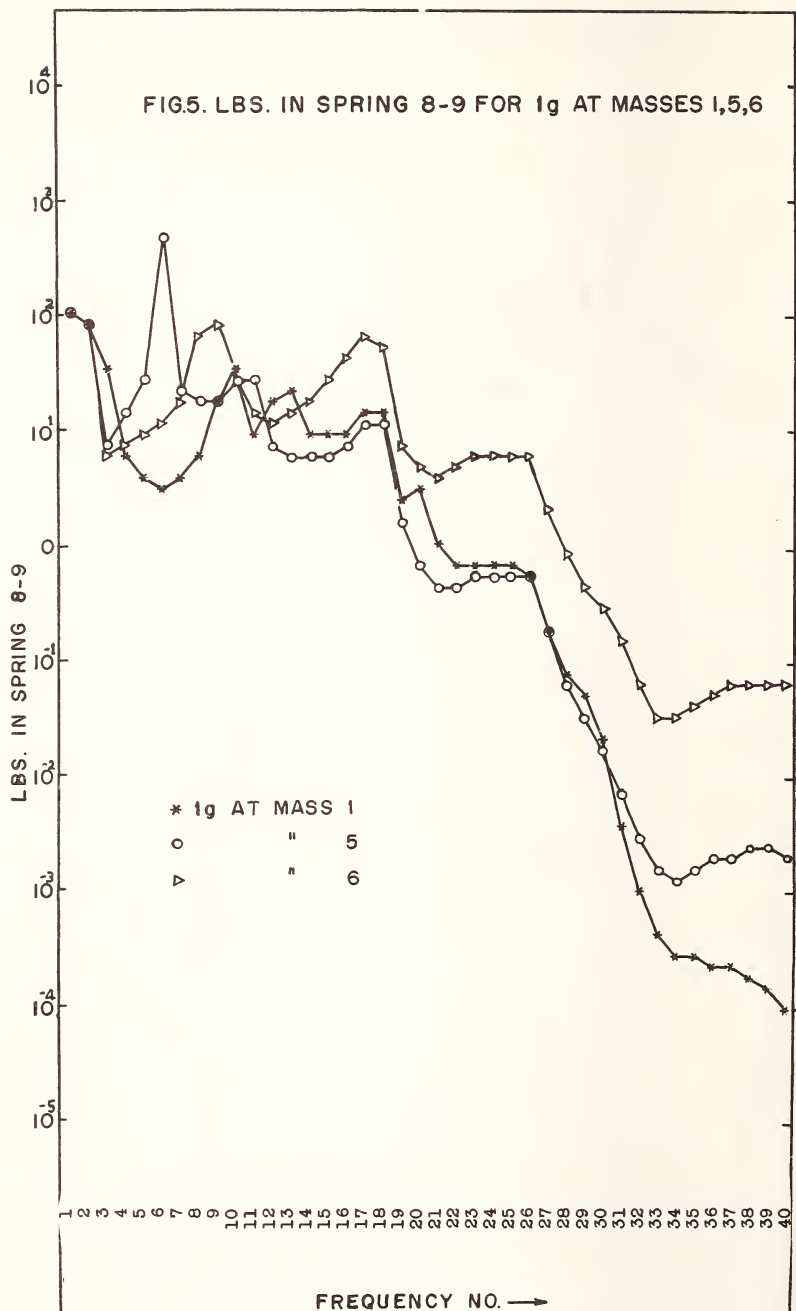
FIG.1. SCHEMATIC DIAGRAM OF SYSTEM



FIG.3. POUNDS AT MASS 1 FOR 11b. IN SPRING 8-9







CHARGED PARTICLE TRACK IMPLICATIONS FOR ACCELERATED TESTING

T. M. Flanagan¹ and V. A. J. van Lint²

REFERENCE: Flanagan, T. M., and van Lint, V. A. J., "Charged Particle Track Implications for Accelerated Testing," ASTM/IES/AIAA Space Simulation Conference, 14-16 September 1970.

ABSTRACT: This work considers the ionization effects produced by the passage of energetic particles through material, emphasizing the fact that the ionization is formed along particle tracks rather than being uniformly distributed throughout the material. Thus, the particle track through a material can be visualized as a cylinder centered on the particle path disturbed by ionization and carrier trapping. The dimension of the disturbed region is related to the range of the electron ejected by the ionization event, while the density of carriers within the disturbance depends on the ejected electron range and on the ionization efficiency of the energetic particle. The disturbed regions then relax with characteristic times ranging from the very short to the very long. The dose-rate dependence arises from the relationship of the characteristic relaxation times and the average time for two particles to disturb the same volume. At low doses, each particle track traverses primarily unirradiated material, and the effects are additive. At higher doses, nonlinearities are expected, since particles penetrating a previously disturbed region may find the carrier traps in a different charge state than in virgin material. Another source of nonlinearities is the density of ionization which will vary with particle type and energy. The size of the disturbance around a track varies from 100 to about 2000 Å, depending on the material. This quantity can be used to calculate the average overlap time for a given dose rate. The dose which must accumulate before nonlinearities are apparent can be estimated from the trap density of the material. Each of these factors must be taken into account when planning on assessing simulation of radiation effects.

KEY WORDS: radiation testing, radiation damage

¹Ionization Effects Group Leader, Defense Sciences Division, Gulf Energy and Environmental Systems, Inc., San Diego, Calif.

²Vice President, Gulf Energy and Environmental Systems, Inc., San Diego, Calif.

In radiation effects testing, it is usually impossible and often not even desirable to reproduce exactly the environment to which a component or system will be subjected. Especially for space applications, where real dose rates are very low and exposures to the space environment are long, some form of accelerated testing for radiation effects is dictated by economic necessity. The problem of assessing and perhaps designing a simulator for testing the system or component must then be faced. This paper develops some simulation requirements by considering the interaction of energetic radiation with materials from a microscopic point of view.

We consider the effects resulting from a single event—the passage of a single charged particle through a material.⁽¹⁾ The primary event produces a disturbance (primarily electron-hole pair production) at particular sites in the material; a line connecting these sites is the particle track. The density of disturbances along a track depends on the particle type and its energy; generally, increasing density results as the energy is decreased or the particles become more massive. A transport of the disturbance outward from the center of the track follows the passage of the particle and leaves behind the effect of the disturbance, i.e., trapped charge, along the track. Thus, at some time after the passage of the particle, a radius of disturbance is established around the track. Some relaxation processes associated with charge trapping, untrapping, diffusion, and recombination then take place as the disturbed region tends toward a new equilibrium.

DOSE-RATE DEPENDENCE

The origin of the dose-rate dependence can be understood by considering the relationship between the characteristic relaxation times of the disturbance and the average time for particles to disturb the same volume of the material (called the track overlap time). In general, the disturbance caused by the passage of a charged particle decays with a variety of relaxation times, ranging from the very short to the very long. If the track overlap time in the real environment is comparable to a relaxation time in the material, particles will be traversing material which is still disturbed by a previous particle passage, and the disturbance created will be modified by the existence of the previous track. Thus, lacking any knowledge of the physical processes occurring in the material, the track overlap time of the real environment must be reproduced by the simulator. This requirement can be relaxed somewhat if the relaxation times in the material are known. Then if the track overlap time for the real environment should fall between two relaxation times in the material, the track overlap time of the

Numbers in parentheses refer to the list of references appended to this paper.

simulated environment can fall anywhere in the time window bounded by these two relaxation times.

If enough is known about the relationship of the disturbance to the relevant effect, then some relaxation processes may not be important and the size of the time window for track overlap can be enlarged. For example, if transient optical absorption measurements following pulsed irradiation of a spacecraft thermal control material should reveal that the color centers are formed in a few microseconds, any longer-term relaxation processes could be neglected.

The relaxation processes often take the form of "annealing" or "self healing," which simply means that the radiation effect tends to disappear with time. The rate at which annealing takes place often depends on the average level of ionization in the material and, thus, on the dose rate. The effects of the total environment—i.e., particle irradiation, photon irradiation, temperature, and ambient gas—must be considered in evaluating the effect of annealing, since these are all important to annealing rates in various systems. This implies that it is just as important to study the annealing rates as it is to study the damage rates in any simulation test.

DOSE DEPENDENCE

Regardless of dose rate, for low doses a negligible fraction of the tracks overlap. In this case, the fundamental physical effects must be linear in dose—i.e., superposition must hold. This follows from the fact that, if the tracks do not overlap, they are independent of one another. For conductivity, the fundamental physical effect is the generation of free carriers, and the effects of carriers contributed by each track are additive if the tracks do not influence each other. This does not mean that all physical quantities which can be used to represent the effect are linear—e.g., resistivity is not—but only that the physical effect is linear in dose. As the dose accumulates in the material, a larger fraction of the volume has been previously disturbed by particle tracks, and no general statement can be made about the dose dependence. The relevant quantity at higher doses is the dose delivered in a time comparable to the relevant relaxation time; this dose is coupled to the dose-rate dependence.

SPECIFIC IONIZATION DEPENDENCE

The specific ionization of an irradiating particle is related to the density of ionization events along a track. Usually, it is defined as a dimensionless number (S) numerically equal to 1 for a minimum ionizing particle—e.g., a relativistic electron. Thus,

$S \equiv$ number of ionization events per cm of path for particle \div number of ionization events per cm of path for relativistic electron.

We can make no a priori assertions about the linearity of an effect as the value of S varies, since this quantity determines the distribution of charge within the disturbed volume. We can make a few general assertions:

1. The overlap dose must increase at least linearly with increase in the specific ionization, since the radius of the disturbance does not increase but the density of tracks is inversely proportional to specific ionization at a given dose.
2. The effect of an external electric field applied at an angle to the track will decrease with increased S due to the increased screening within the track.⁽¹⁾

SIZE OF THE TRACK

The radius of the disturbance around a particle track is generally in the range 100 to 2000 Å, depending on the material and the particle type. For a few special cases, such as very pure crystalline anthracene, the disturbance may be of larger dimension, but these special cases arise because of the migration of a long-lived exciton state (electron and hole move together).⁽²⁾ In most materials, the outward propagation of the disturbance is due to the secondary electrons ejected by the primary event. Then the size of the track can be deduced from the range-energy relation for very low-energy electrons.⁽¹⁾ Unfortunately, the exact range-energy relation for these very low-energy electrons in solids is unknown, and we must rely on experimental inference to deduce the size of the track.

For the aromatic hydrocarbons, the radius of the track is estimated to lie between 100 and 300 Å.^(3,4) In water,⁽⁵⁾ the ejected electron travels about 100 Å before being captured by a hydrogen ion or a water molecule, while in liquid hydrocarbons, the range is nearer 300 Å.⁽⁶⁾ For insulating solids which have some ionic bonding character, the range is longer (near 1000 Å in good single crystals),⁽⁷⁾ while in semiconductors a range of 2000 Å seems reasonable.⁽²⁾ Thus, once the class of material is known, range can be estimated.

NUMERICAL EXAMPLES

Scanning Simulators: Applying these concepts to a real simulation problem, let us discuss the simulation of proton (solar wind) damage to optical and thermal control materials. From the discussion, it can be asserted that the electrons ejected from a particular proton track will not influence more than a cylinder of radius of $\sim 10^3$ Å.

It is well known that the carrier trapping process (color center formation) can be a strong function of the carrier generation rate. The underlying cause of this dependence is that the simultaneous presence of a higher concentration of free carriers (electrons, holes) influences the dynamics of trapping and recombination by changing the average charge states of impurity centers that act as traps and recombination sites. The importance of this potential nonlinearity is that it depends on the microscopic carrier density, not on the spatially averaged value if the two are different. If one simultaneously exposes a sample to N proton tracks that do not interact (average spacing greater than 2000 \AA), the processes occurring within each track are unaware of, and unaffected by, the presence of the other tracks. They are strongly influenced by the ionization density within the track, but this is a property determined by the proton's energy, not by how many tracks there are.

There are important nonlinearities once the tracks overlap. A proton penetrating a previously ionized region may find the longer-lived traps in a different charge state than in virgin material. Furthermore, the charge state depends on a comparison of average time between overlaps and the trap relaxation time. In very impure or heavily displaced materials, there is almost a continuous spectrum of trap relaxation times; hence, there are likely to be some trap relaxation times in any range of interest.

This discussion suggests that important simulation requirements are to reproduce the proton specific ionization (same proton energy) and the average time between production of overlapping tracks. This latter requirement is particularly relevant to the evaluation of non-CW simulators (including RF mass separators or beam-scanning techniques). At the maximum expected solar flux ($\phi = 2 \times 10^{11} \text{ protons/cm}^2\text{-s}$), the mean overlap time, t_0 , for a track of $R_0 = 1000 \text{ \AA}$ radius is

$$t_0 = \frac{1}{\pi R_0^2 \phi} = \sim 0.02 \text{ s} \quad (1)$$

It is important to reproduce this overlap time, or any longer overlap time, at lower fluxes or electron ranges. This implies that for a scanning system the peak flux must not create overlap during a single pass, and that the pass repetition rate must be fast enough to create overlap between passes within 0.02 s . Both these criteria are met if the pass repetition rate is faster than 100 Hz . They are obviously met for an RF mass filter that operates in the 10^6-Hz regime.

Critical Dose: The dose at which significant track overlap occurs is called the critical dose. The exact choice of the critical dose is somewhat arbitrary, since tracks are produced randomly throughout the material. Harrity(7) has discussed this problem, and we will follow his analysis.

The rate at which the volume that has been irradiated at least once increases with fluence as

$$\frac{dV_I}{V_S \frac{d}{d}\Phi} = \frac{V_S - V_I}{V_S} \nu, \quad (2)$$

$$\int_0^{V_I} \frac{dV'_I}{V_S - V'_I} = \frac{\nu}{d} \int_0^{\Phi} d\Phi, \quad (3)$$

or

$$V_I = V_S (1 - e^{-\nu\Phi/d}), \quad (4)$$

where ν = volume ionized by a single incident particle,
 V_I = total irradiated volume,
 V_S = total sample volume,
 Φ = irradiating electron fluence,
 d = sample thickness.

If we consider ν as a cylinder with length d and radius R and realize that both V_I and V_S can be written as d times the equivalent areas, Eq. 4 may be rewritten as

$$A_I = A_S (1 - e^{-\pi R^2 \Phi}), \quad (5)$$

where A_I is the irradiated area of the total sample area A_S .

In recent work at this laboratory, Harrity(7) found that in Cz-grown single-crystal sapphire, the conductivity is linear in the dose for doses below 10 rads and above 500 rads. Between these doses is a nonlinear transition region which is interpreted as the result of particles traversing regions which have been previously irradiated. He uses this data to derive a value for R_0 of 1040 \AA .

We may use this data to find the value of A_I/A_0 for which significant overlap occurs. Deviations from linear behavior were observed at 10 rads (4×10^8 , 30 MeV e/cm²), and the value of A_I/A_0 for this point is 0.126 from Eq. 5. Thus, significant overlap occurs when about 1/8 of the total area has been influenced by a radiation track.

From a practical viewpoint, the track overlap is sufficient to produce nonlinearities only if enough carriers are generated within the track to fill a significant fraction of the traps.

A minimum condition for a significant perturbation of a track would be that enough carriers have been generated in the vicinity of the track to fill 50 percent of the traps, assuming all the carriers to be captured. That this is a reasonable criterion can be seen by applying it to Harrity's data. Harrity(7) estimates the trap density in his Cz-grown, single-crystal sapphire to be $6 \times 10^{14} \text{ cm}^{-3}$. At a generation rate of $3 \times 10^{13} \text{ carriers/cm}^3\text{-s}$, (8) 10 rads are required to fulfill

this condition, and Harrity's data show deviations from linearity just above 10 rads. For most insulators in technological use, a more reasonable trap density is of the order of 10^{13} to $10^{19}/\text{cm}^3$, and a dose greater than 10^5 rads is required to achieve critical dose.

Vacancy Motion in Silicon: So far we have considered only effects which are the results of ionization. However, accelerated production of displacement events can also be evaluated. Consider the displacement of atoms in silicon. At recoil energy transfers just greater than the threshold for displacement, it is likely that the displaced atom is still within the strain field of the vacancy, and it is most probable that it will return to its lattice position. A very small fraction of these displaced atoms may be favorably directed away from the track and escape as interstitials moving through the lattice. The vacancy moves also, and each will continue to move until it undergoes some type of immobilizing reaction at another defect. Since there is very little information on the interstitial, the remainder of this discussion will concentrate on the vacancy.

The questions are, what are the mechanisms by which the final defects are formed from diffusion of vacancies from the defect track, and how large can we allow the vacancy concentration to become—i.e., how much can we accelerate the test without perturbing the results?

As a vacancy diffuses away from its formation site, it has a choice of combining with various kinds of defects to form a stable complex. In a typical quartz crucible (QC) grown silicon crystal, these include:

1. Mobile radiation-produced interstitial atoms and vacancies (density 10^{12} to 10^{16} cm^{-3}),
2. Interstitial oxygen atoms (density 10^{17} to 10^{18} cm^{-3}),
3. Impurities such as donor or acceptors (density 10^{14} to 10^{18} cm^{-3}),
4. Dislocations (density 10^4 cm^{-2}); if we assume a strain field affecting a cross section of five atoms, the dislocations yield an effective density of approximately 10^{12} cm^{-3} ,
5. Surfaces.

It is clear from the foregoing that dislocations can normally be neglected. For equal capture cross sections, the interstitial oxygen atoms will dominate vacancy capture to form A-centers. Since the interstitial oxygen atoms are neutral in both n- and p-type silicon and the vacancy can be charged, it is possible that a charged impurity atom may compete with the oxygen atoms for the vacancies in heavily doped material, or in float-zone (FZ) material in which the oxygen concentration is much less. The effect of the surface can only be estimated by evaluating the mean free path for capture of a vacancy within the bulk of the crystal. It can be assumed that a neutral

capture cross section is 10^{-16} cm² and an attractive charged cross section is 10^{-14} cm². The average net distance, d , traveled by a vacancy prior to its being captured by a defect can be estimated from the mean free path for capture, λ_c , and the mean free path for scattering, λ_s . Let us assume that the mean free path for scattering, λ_s , is 5×10^{-8} cm or approximately equal to the interatomic spacing. Considering the random-walk nature of the process, and assuming the scattering to be random and isotropic at each site,

$$d = \sqrt{\lambda_c \lambda_s}.$$

Now

$$\lambda_c = \frac{1}{N\sigma},$$

where N is the density of capture centers and σ is the capture cross section. For A-center formation in QC silicon, let us take an oxygen atom density of 3×10^{17} cm⁻³. Then $\lambda_c \approx 3 \times 10^{-2}$ cm and $d \approx 4 \times 10^{-5}$ cm. For formation of E-centers (vacancy-phosphorus complexes) in n-type FZ silicon with an ionized donor concentration of 10^{15} cm⁻³, $\lambda_c \approx 10^{-1}$ and $d \approx 7 \times 10^{-5}$ cm. In either case, d is small compared to the size of typical samples, and surfaces are not likely to be sinks for mobile defects.

Addressing the second question above, the length of time elapsing before the stable defect is formed is

$$t = \frac{1}{v} \frac{\lambda_c}{\lambda_s},$$

where v is the jump frequency. For a defect which is not found at each lattice site, v is approximately equal to the lattice frequency and $t \approx 10^{-6}$ s.

In the actual case, the vacancy mobility is dependent on the charge state of the vacancy, and is an activated motion describable by a relation of the type

$$v = v_0 e^{-E/kT},$$

where v_0 and E are functions of the charge in the vacancy.(9) Assuming first-order formation kinetics, for which there is some evidence,(10) the equilibrium vacancy concentration is

$$[V] \approx [\dot{V}] t,$$

where $[\dot{V}]$ is the production rate for free vacancies and t is the time before capture.

Now, let us apply these calculations to a 1-MeV electron irradiation, and compute the equilibrium vacancy concentration in a steady 10-mA irradiation of a 1-cm² solar cell. This current is equivalent to 6×10^{16} e/cm² s which, at an introduction rate of 0.2 cm⁻¹ of free vacancies, yields $[\dot{V}] \approx 1.2 \times 10^{16}$ (cm³ s)⁻¹. The longest-lived vacancy occurs in p-type

silicon; therefore, this will be considered as a worst case. The time before capture for a vacancy in p-type silicon at 300 K is approximately 2×10^{-3} s.(9) This implies an equilibrium vacancy density of approximately $2.4 \times 10^{13} \text{ cm}^{-3}$, which is much smaller than either the oxygen concentration in QC material or most impurity concentrations of interest in FZ material. Thus, the irradiation rate used does not create enough vacancies to perturb the impurity vacancy interactions. The effect of the increased ionization caused by the increased dose rate in the test compared to the actual environment may change the charge state of the vacancy. However, this shortens the time during which the vacancy is free by increasing its mobility. Therefore, the enhanced dose rate tends to lower the steady-state vacancy concentration, which decreases further any perturbation of the vacancy-impurity interaction. Thus, the accelerated dose rate used in this example can be used to simulate displacement damage in silicon produced by all lower dose rates.

CONCLUSIONS

In assessing a radiation effects simulation experiment, some knowledge of the mechanisms of the relevant effects is necessary. The more that is known about the mechanism of the effects, the more confidence there is in the results. For that important class of radiation effects which depend on the disturbance created by the transport and trapping of charge around a particle track (ionization),

1. The average track overlap time in the simulated environment must appropriately represent that in the real environment;
2. Extrapolation to higher dose levels must take into account the potential nonlinearities which can occur when the critical dose is exceeded;
3. The influence of "self healing" or annealing must be taken into account.

In addition, consideration of the mechanisms of displacement defect formation, coupled with the ionization track model, can be used to evaluate the effects of accelerated testing on the damage formed.

REFERENCES

1. Kallman, H., "Mechanisms of Energy Transfer in Dielectrics," Technical Report ECOM-00129-F, January 1967.
2. Nichols, D. K., and V. A. J. van Lint, IEEE Trans on Nucl. Sci. NS-13, p. 119, December 1966.
3. Watanabe, Y., N. Saito, and Y. Inuishi, "Carrier Production and Transport in Anthracene," Osaka University Technology Reports, Vol. 18, Nos. 801-822, p. 143, March 1968.
4. Kepler, R. G., and F. N. Coppage, Phys. Rev. 151, 610 (1966).
5. Kupperman, A., in The Chemical and Biological Action of Radiation, Vol. V, M. Hassinsky (Ed.), p. 93, Academic Press, 1961.
6. Hummel, A., and A. O. Allen in Radiation Chemistry, Dobo and Hedvig (Eds.), p. 295, Akademiai Kiado, Budapest, 1967.
7. Harrity, J. W. (to be published in IEEE Trans. on Nucl. Sci., December 1970).
8. TREE Handbook, DASA 1420, September 1969.
9. Cesena, R., T. M. Flanagan, R. E. Leadon, C. E. Mallon, J. A. Naber and E. Wenaas, "Transient Radiation Effects," Summary Report on contract DAAG39-68-C-0060, Gulf General Atomic document GA-10098, p. 35, April 1970.
10. Harrity, J. W., and C. E. Mallon (to be published in IEEE Trans. on Nucl. Sci., December 1970).

A SIMULATION TO VALIDATE FUTURE SPACE MISSIONS

T. P. Foley¹, A. W. Metz¹ and A. W. Yonda¹

ABSTRACT: A simulation tailored to be responsive to the needs of aerospace systems analysts has been developed. The simulation is written in FORTRAN so that it can easily be transferred between different computers. The simulation is modularly structured so that new functions can be simulated and easily added. The level of detail of the simulation of model elements can vary widely. When macroscopic system aspects have been studied and optimal configurations established, then sub-systems of interest can be modeled in greater detail and embedded in the macroscopic simulation for more detailed study. Thus, design engineers can study the performance of their design in a total system environment before hardware is fabricated.

The parameters of the simulation permit the configuration of models rapidly. These can be run against a scenario of input parameters which when varied provide information on system performance. Thus, many different projected system configurations can be quickly exercised and discarded until only a few feasible system configurations remain. These then can be exercised with model elements being more detailed enabling a more comprehensive analysis. Provision is made for entry of errors into the system so that performance characteristics of the system in a degraded state can be studied. The exercising of Executive Program strategies is provided for. Thus, a tool which is oriented toward supporting the systems analysis requirements for studying dynamic system performance has been developed.

¹ Aerospace Systems, Equipment Division,
Raytheon Company, Sudbury, Mass.

KEY WORDS: Simulation, space systems, system test bed

1. INTRODUCTION

The reasons for developing this simulation are: To provide a design tool for design engineers and to provide a means to support systems analysts in the analysis of the operation of complex space systems. Due to limited resources and the need to quickly furnish support to engineers designing a data bus, it was decided to provide a data bus simulation which was general enough so that it could easily be expanded to simulate more comprehensive space systems.

The goals of the simulation are to provide design engineers and systems analysts with a tool which is easy to use and can quickly provide performance measures of the operation of asynchronously functioning interrelated elements of the systems being studied.

To attain the goal of ease-of-use, a user oriented language for describing the input parameters for simulation scenarios is provided. This input language minimizes the users scenario definition effort by providing stylized English statements for exercising control over the simulation process, and symbolic type inputs to specify the system parameters.

The goal of quickly providing relevant data in a timely manner is attained by designing the simulation so that it accepts more than one level of detail. That is, a sub-system designer can embed a detailed scenario of his sub-system in a macroscopically defined scenario of the entire system. Thus he will be able to run detailed experiments for his sub-system in a total system environment with considerably less delay than if he had to specify the total systems in fine detail. An additional advantage accrues from savings effected because of shorter computer runs.

The simulation is providing a viable test bed which economically exercises experiments in a controlled environment. Thus the systems analyst and design engineer are able to test out and validate concepts before building hardware.

2. METHODOLOGY OF THE SIMULATION

The simulation is modularly structured and table driven so that additional program modules are easy to add. That is, the professional programmers who wrote the simulation can quickly add new program modules to respond to new requirements. In addition to this type of modular construction, the simulation provides

for the user to write FORTRAN programs which implement the interpretation of any event the user wishes to specify for his simulation runs. Thus the simulation is flexibly structured so as to permit response to a wide variety of requirements. The primary advantage in this type of organization lies in the inherent capability to respond to new rules unthought of during the initial simulation design.

The simulation is written in FORTRAN in order to provide a tool which is easily transferred from one make or model computer to another.

A major requirement is to provide the systems analysts with the means to easily vary simulation parameters and thus be able to quickly reconfigure systems which are under consideration. Hence, by providing an easily varied system test bed at minimal cost, the systems analysts will be encouraged to try bolder and more innovative system configurations. How successful we will be in this endeavor has yet to be determined.

3. SIMULATION STRUCTURE

The purpose of this section is to describe the structure of the simulation program. Figure 1 is a block diagram of the simulation structure.

The simulation is divided into four parts. These are:

- . File Generation Processor
- . Preprocessor
- . Run Processor
- . Post-Processor

Their relationships are shown in Figure 1. The simulation starts with the hardware configuration, the software configuration, and the scenario in the form of punched card inputs. In addition, if the user wishes to define an entirely new type of element to augment the simulation, there may be a definition of that new element in punched card form.

The file generation program takes the punched card data and creates three magnetic tape files. These are:

- . Model Configuration File
- . Simulation System File
- . Scenario File

The model configuration file contains data on the particular hardware and software configuration for this run. The simulation system file contains the definitions of the various units (e.g., processors, memories, buses, and so forth) which are the building blocks of the simulation. The scenario file contains the definition of the scenario developed from the input cards.

The preprocessor, using the data on the three files listed above, creates tables in the memory describing the configuration and the elements (e.g., processors, memories, buses, and so forth) for the simulation run. It also creates an input event file, which is a listing of the events based on data coming from the scenario file. The scenario data can be the statistics of these events, an actual listing of desired events, or a mix of the two. There is no particular limitation on the allowable granularity of event times on the input file, and, in fact, the way that the run processor operates, additional granularity does not result in an increase in running time.

It should be noted that the input events remain on the input event file; therefore, if the analyst wishes, he can run the same input event file while making changes in the hardware configuration and software configuration. This means that if the performance of a configuration is sensitive to the exact sequence of input events, rather than simply to their statistical distribution, the analyst can repeat the identical sequence of input events, rather than a different sequence of input events having the same statistical properties.

The run processor executes the actual simulation. Our approach to the run processor is to make it "event driven", a technique which permits us to handle the simulation run in a fashion which is independent of real time. This technique is similar to that used in languages like GPSS and SIMSCRIPT. It does so by using an event table in which are stored a list of all events scheduled to occur in the future, in order of their time of occurrence. Some of these events in the event table come directly from the input event file. These include such things as incoming messages, requests for service, and external interrupts. Other events in the event table are a result of system action taken due to input events. For example, if a particular interrupt causes an application program to be started, the run processor will compute the time in the future at which that application program will terminate and will insert that time of termination into the event list. Each time the run processor "processes" an event, it determines some number (possibly zero) of future events, with their times, and puts these events into the event table. Each time the run processor goes to the next event in the event table, the "real time" becomes the time of that next event. The actual running time of the simulation is determined by the number of events which must be processed, rather than by

the granularity of the measurement of time.

The run processor creates an output event file, which is a record of every event that has occurred during the simulation. The post-processor extracts from that file the events and statistics which have been requested by the user. The reason for creating a separate output file, rather than creating the output data in the run processor, is that the simulation run will be the most time-consuming part of the simulation and, hence, the most expensive in elapsed computer time. After the completion of a run, the analyst may wish to examine the output data and then request other data for the same run. Rather than execute the run processor again, the user can simply change the input cards to the post-processor, which will then extract the new output data from the output events file.

Running time is, of course, heavily dependent on the particular scenario and on the size and complexity of the system configuration being simulated.

4. SIMULATION OUTPUTS

The reason for performing the simulation is to track the operation of the simulated system under the postulated scenario. The results of the run processor are much too detailed to be easily digested by the analyst; hence, a post-processor is required which can accumulate and reduce the data to a form that is more useful.

As described above, the post-processor operates somewhat as a report program generator, permitting the extraction of any data at all which is on the output file and the formatting of that data in the form desirable by the analyst.

There are essentially four kinds of reports which can be extracted by the post-processor. These are:

- . Event Reports
- . Time Line Reports
- . Snapshot Report
- . Summary Data Reports

Event reports are simply listings of specified events. Examples include listing of all interrupts from a particular external sub-system, listing of all executions of a particular application program, and so forth. The analyst can get a listing for the whole run, or he can have a listing of specified events from time T1 to time T2.

Time line data is a report of a continuous variable. For example, the percent loading of one of the CPU's as a function of time or the loading status of a specified bus or data channel would be a time line report. Of particular interest may be the time line

of certain operational programs with an identification of the processor used, or a time line for a specified device.

The snapshot is a third type of output report. The snapshot will consist of a complete report of the status of some area of interest -- for example, a complete map of a computer memory or a complete listing of the operational programs running in each of the processors. A snapshot may be taken at any point during the run, including the end. Memory map and processor task snapshots are particularly effective in comparison of Executive Program strategies.

The fourth type of output data is summary data, which requires that some processing or filtering of the event record be performed. Examples of this type of data are a record of percent device loading during a specified period of the simulation, the executive program overhead add factor, frequency of use of specified programs, or frequency of use of specified devices.

The four types of output data listed above provide the analyst with a complete and flexible tool for determining the performance of the simulated system.

5. SYSTEM ELEMENTS

The elements of a simulated system can range from individual logic elements such as flip flops to whole computers depending on the level of detail used and the needs of the user. With event driven simulators, it is a simple matter to combine many different levels of detail into a single system model.

In our initial application, a relatively simple data communication system was implemented. This system is modelled at the level of the major functions required to move messages from a central computer to remote device controllers by means of a data bus. The basic functional elements represented in the data bus communication system are described in the following sections.

5.1 COMPUTER

The computer exercises overall control over the entire system. It determines the order and frequency of the transfer of data to and from all remote devices. As the data transfer requirements build up the computer maintains the queues of data messages awaiting transmission and applies various scheduling algorithms to select the next message to be transmitted.

For multiple computer access to the data bus, a master computer, in addition to its normal message

processing also controls the data bus access of the remaining computers in the system.

5.2 MASTER DATA TRANSMISSION UNIT

The Master Data Transmission Unit (MDTU) provides the interface between a computer and the data bus. It controls the movement of individual messages via the bus to or from the remote controllers. The MDTU initiates synchronization, performs parallel to serial and serial to parallel data conversion, and performs a clock time-out as a check against lost messages.

5.3 REMOTE DATA TRANSMISSION UNIT

The Remote Data Transmission Unit (RDTU) controls up to thirty-two devices which can range from sensors to other computers. Each RDTU can be addressed separately and devices at an RDTU can be addressed separately or in groups. The functions performed by the RDTU include, address and message type decoding, serial to parallel and parallel to serial data conversion, device addressing and the control of all data transfers between itself and its devices.

6. SAMPLE MODELS

A candidate system model can be designed and studied at various detail levels.

For example, consider the model shown in Figure 2. This model, when exercised for a range of traffic loads provides data on:

- . the load on the bus
- . message delays
- . traffic scheduling effects

Next, the model is amplified so as to include more detail to the extent of introducing errors into the messages. For this configuration the model is as shown in Figure 3. Now, the simulation provides data on:

- . the effects of errors on bus
- . the effect on the load on the BUS because of repeat messages
- . the effect on system performance because messages are received by the wrong addressee.

For this same configuration, the same model can be further amplified so that the model as shown in Figure 4 now includes stored programs and executive programs. Here the simulation provides data on:

- . the CPU performance for a variety of Executive program strategies
- . the effect on system performance when erroneous messages are received by the CPU's
- . the effect on system performance when the compute power of any CPU is varied.

The detail level of each model can be further

amplified by putting more details in the program functions. In this manner, systems can be studied at various detail levels and when one model has areas that require greater depth of analysis, then the model detail level can be expanded.

7. SIMULATION PARAMETERS

The list of system variables which are parametric to the simulation and can be easily varied by the systems analyst follows:

- . CONNECTIVITY
 - Processors
 - Memories
 - Data Busses
 - Sensors
 - Controllers
- . PROCESSOR CYCLE SPEEDS
- . COMPUTER ASSIGNMENT OF MISSION PROGRAMS
- . DATA BUS
 - Bandwidth
 - Word Size
 - Block Size
 - Error Detection/Correction Techniques
 - Acknowledgement Techniques
- . NOISE ENVIRONMENT
- . MASS MEMORY SPEED
- . EXECUTIVE CONTROL FUNCTIONS
 - Data Bus Control Strategy
 - Priority Handling Techniques
 - Data Management Techniques
 - Checkout Techniques
 - Corrective Procedures in Event of Failure

Additionally, the following types of failures can be simulated during a simulation run:

- . SIMULATED FAILURE OCCURRENCES
 - Processor Failure
 - Memory Failure
 - Data Bus Failure
 - Out of Limit Sensor Reading

8. SIMULATION RESULTS

Results from a simulation run provide the following information:

- . PEAK AND AVERAGE BUFFER QUEUES
- . PEAK AND AVERAGE DATA BUS TRAFFIC
- . FLAGGING OF POSSIBLE SYSTEM FAILURES
- . DETAILED AND GROSS TRACES OF SYSTEM INTER-ACTIONS (ON REQUEST)
- . PEAK AND AVERAGE CENTRAL PROCESSOR LOADINGS AS A FUNCTION OF TIME
- . PERCENTAGE OF DATA BUS AND COMPUTATIONAL BANDWIDTHS REQUIRED FOR OVERHEAD (EXECUTIVE) FUNCTIONS

9. CONCLUSION

The simulation provides a viable tool to the systems analyst which by virtue of being problem oriented is highly responsive to his needs. The building block structure of the simulation makes it easy to expand the details of functions being simulated as well as to add new simulated functions unthought of in the initial design.

By judiciously varying the simulation parameters, it is possible for the systems analyst to derive enough information so as to be able to do the following:

- . Evaluate the performance of the specified system configuration
- . Optimize system control procedures
- . Minimize redundant elements in the system
- . Establish limits of system performance
- . Validate data bus scheduling strategies
- . Evaluate many projected system configurations

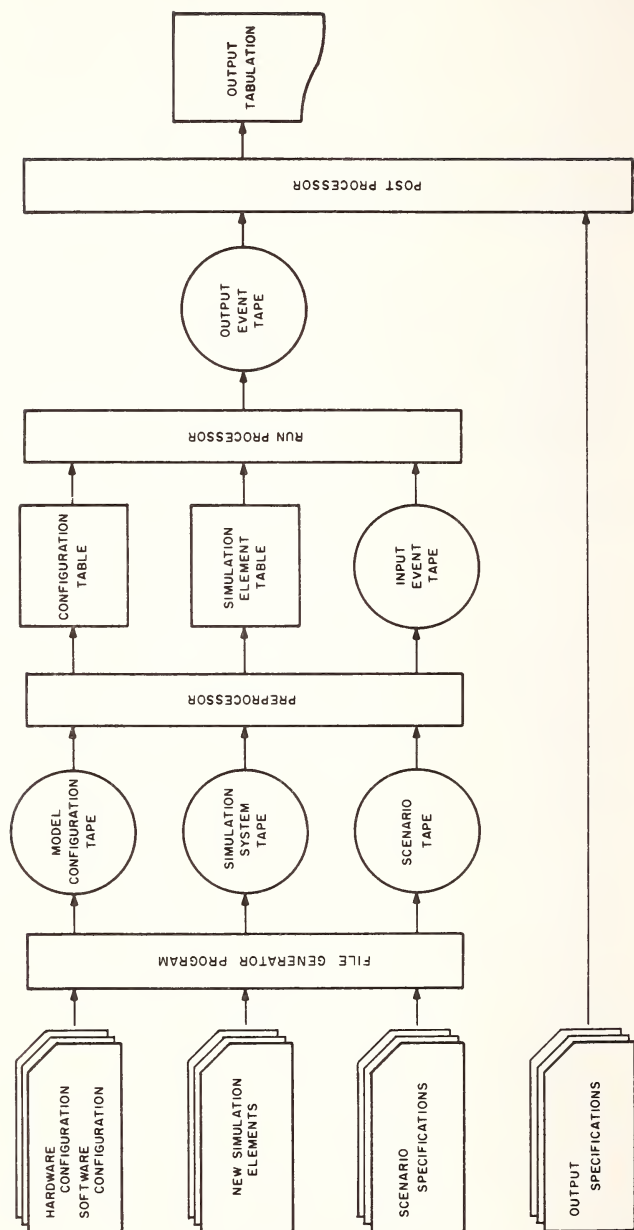


FIGURE 1 SIMULATION BLOCK DIAGRAM

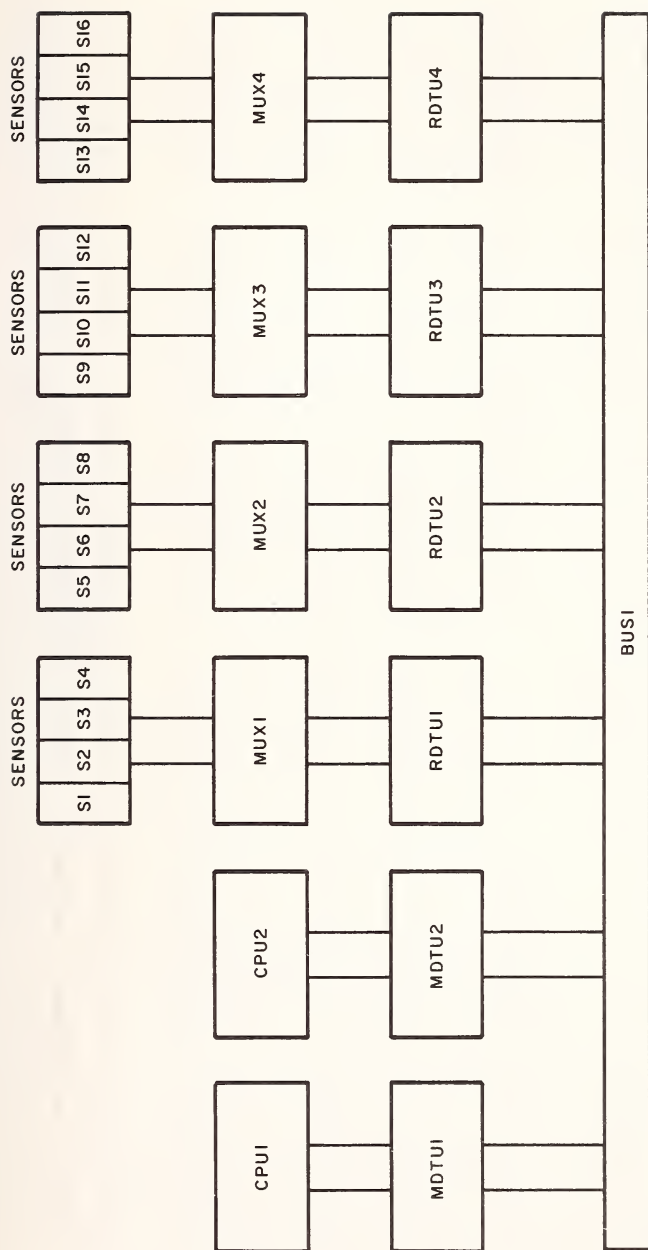


FIGURE 2

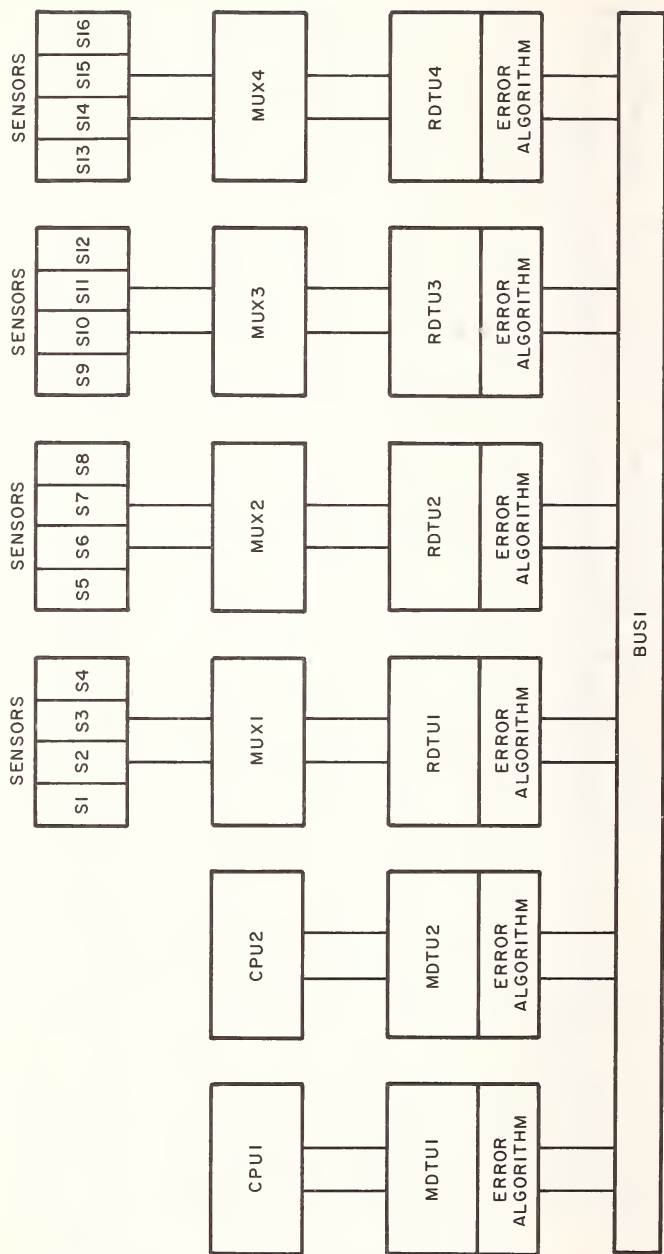


FIGURE 3

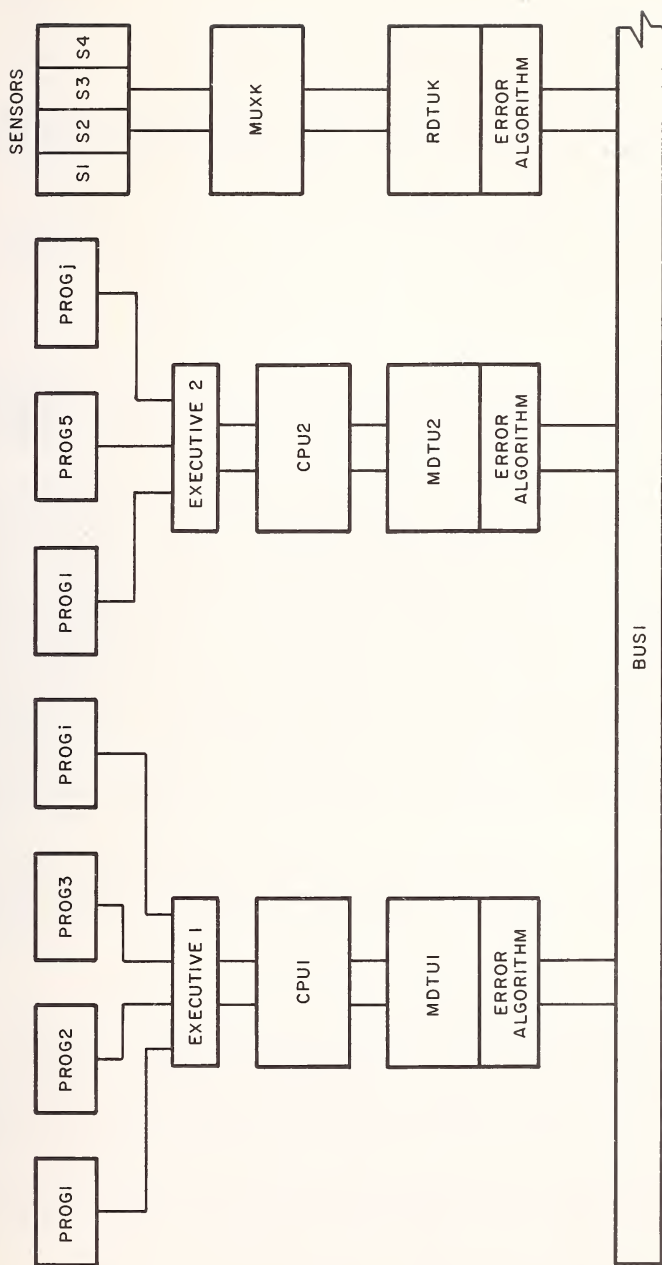


FIGURE 4

GENERAL PURPOSE CENTRALIZED AUTOMATIC TESTING FOR IMPROVEMENT
OF SHIPBOARD SYSTEM PERFORMANCE

F. J. Zupan¹

REFERENCE: Zupan, F. J. "General Purpose Centralized Automatic Testing for Improvement of Shipboard System Performance," ASTM/IES/AIAA Space Simulation Conference, 14-16 September 1970.

ABSTRACT: Increased operational effectiveness of Navy shipboard systems is the primary goal of the Navy automatic testing program. This paper discusses the rationale and techniques utilized in developing an experimental model which will help update and modernize traditional methods and approaches to systems monitoring and maintenance. Developments in acquisition, processing and dissemination of information as related to a centralized on-line performance monitoring system are covered. Both laboratory and shipboard functional tests were performed, with a laboratory model system monitoring typical Navy electronic and non-electronic systems. Test results, a discussion of problem areas, and a prediction of the impact of centralized testing on the shipboard maintenance and operating organization are included.

KEY WORDS: operational readiness, performance monitoring, testing, data acquisition, data processing, data dissemination, maintenance

The Navy Electronics Laboratory Center in San Diego has been engaged in exploratory development aimed at improvement of ship systems operational readiness. Efforts of a technical group which I represent are in response to a specific operational requirement which directs development of a Centralized

¹Performance Monitoring Systems Division, Naval Electronics Laboratory Center, San Diego, California

Automatic Test System (CATS). This system is intended to monitor the performance of complex and militarily essential shipboard systems and the environmental conditions under which these systems and personnel operate. A further requirement for CATS is that it shall have the capability to predict and locate failures in these shipboard systems.

A typical Navy Shipboard installation is comprised of many complex systems; all of these are necessary and essential to perform critical functions. The proposed monitoring system must somehow be able to converse with these ships' systems while they are operating, without adversely affecting this operation. A cursory consideration of these requirements might lead one to conclude that the magnitude of the task in terms of management problems, hardware complexity and the necessity for software would make this a difficult endeavor. Why then does the Navy elect to establish such a series of requirements?

One reason is that in terms of potential long term payoff, automation is a most promising approach to the Navy's need to improve or replace its outdated methods for performing shipboard maintenance. In the modern Navy, reaction time to detect and evaluate threats in combat ship operation has decreased, requiring more complex systems, increased automation and continuous optimum performance. Ship's command requires timely information regarding status and level of performance of systems in order to select from possible options such as alternate modes of operation or use of alternate systems to assure mission effectiveness. Extensive studies have shown that traditional manual methods of performance monitoring and fault detection are too cumbersome and time consuming. New techniques and methods must be adopted or developed to meet the requirement for quick reaction.

APPROACH:

Efforts at the Naval Electronics Laboratory Center with which we have been associated have been directed toward improving the monitoring and fault location tools and methods of the Navy technician, who is assigned responsibility for improving the performance of shipboard systems. His present aids which include manual portable test equipment, instruction manuals, built-in indicators, and localized testers, are insufficient in themselves to meet contemporary and advanced requirements for up to the minute system performance monitoring information. Since the technician is the ultimate source for systems status information which is eventually the basis for tactical and strategic decisions of command, improvements in his tools and methods will result in better status reporting and improved command decision and action.

In order to determine the effectiveness of Centralized Automatic Test Equipment with respect to General Purpose Manual,

Built-in, and Localized Automatic Test Equipment, the Naval Ship Systems Command directed that a special study be performed. The Naval Applied Science Laboratory conducted the study(1) which involved consideration of mixes of these support equipments. Mission simulation and mathematical analysis techniques were utilized. It was concluded that in the setting of typical situations studied, support mixes utilizing up to 80% centralized automatic test equipment were the most effective in terms of monitored systems availability and overall cost effectiveness. This study and other supporting evidence document the feasibility and effectiveness of centralized automatic testing aboard ship.

DESIGN PHILOSOPHY:

One of the most publicized criticisms of automatic testing systems developed in the past has been the enormous complexity and cost of software associated with these systems. In organizing and planning an automatic testing approach, means have been sought to make efficient use of automation. Since the earlier period, favorable advances in programming techniques as well as in hardware state of the art, have been helpful in achieving this goal. A substantial reduction in software requirements for our system has been achieved by application of the fundamental principle of retention of the man in the testing loop. Beginning with the conceptual model and continuing through the development period of a laboratory model system, the design philosophy has emphasized the man and his capability to exercise technical judgment based on a combination of the information presentation, his technical training, and his technical experience.

CATS is a computer-centered system which utilizes adaptive man-machine interfacing as an effective approach to the Navy's need to update ship's systems operational readiness. Displays, controls, and readouts are being planned and specified to exercise the man's capabilities and to eliminate or reduce routine, time-consuming tasks which increase maintenance and reporting times. System philosophy is such that a wide range of operator or machine control is possible, depending on the monitoring problem and/or the capability of the man.

Tracing performance data in monitored systems from the source to the ultimate shipboard user, capabilities may be grouped under the following broad categories: Information processing, presentation, recording, and system control and operation. These capabilities have been incorporated into a system that is designed to perform services for the ship's system operators, the ship's maintenance people and the ship's

The number in parenthesis refers to the list of references appended to this paper.

captain. In order to be effective the test and monitoring facility must supply this information when it is needed and in a form that is understandable to each of the various users.

DESCRIPTION OF SYSTEM STRUCTURE AND OPERATION:

The laboratory model of a centralized automatic test system has been tested under laboratory conditions while interfaced with several typical Navy equipments. Additional similar tests were also conducted aboard the USS NORTON SOUND. Figure 1 is a simplified functional block diagram of the model which was developed at the Naval Electronics Laboratory Center. Data utilized in the system is acquired from sensors (1) installed within the monitored prime equipment. These sensors (actually a part of the prime equipment) convert the parameters of interest into proportional d.c. voltages. These d.c. voltages are multiplexed in the Data Acquisition Unit (2) under control of the Central Processor (8) and are converted into a pulse duration. The pulse thus developed is transmitted to the Distribution and Data Conversion Unit (5). Conversion to digital form is accomplished in that unit to facilitate inputting to the Central Processor. The Central Processor formats, treats and compares this raw data, referring to the Mass Memory (7) for stored data pertaining to tests. Processed data is sent to the Operator Control Console (9) for display in a continuously updated manner and/or to the teletypewriter (4) for print out, and periodically is sent to the Status Panel (6) for use of controllers. The operator at the Control Console can initiate new data acquisition sequences, directing the Central Processor to address data to the various Data Acquisition Units via the Distribution and Data Conversion Unit. In the event of casualty to the Central portion of CATS, the Auxiliary Test Unit (3) can be used to access test parameters from sensors and to convert them to numbers which can be compared to pre-printed limits. This brief description is merely intended to convey the fundamentals of operation. The test system is capable of handling a wide variety of input parameters under actual operating conditions. Figures 2-4 show various equipments which comprise the CATS hardware.

INFORMATION GATHERING:

With this description as background let us examine the functional capabilities listed earlier, in terms of hardware and software development effort, conducted at the Naval Electronics Laboratory Center.

Some of the most challenging work performed during the entire program was the development of the data acquisition system. Work in this area spanned problems in both the systems monitored and in the CATS data gathering and monitoring facility.

Because of the critical nature of this effort, various data acquisition techniques were considered. Criteria used to gauge the effectiveness and suitability of various elements of the data acquisition system include the following: Cost, reliability, simplicity, speed, size, maintainability and repeatability. To emphasize the effectiveness of automatic data acquisition it might be instructive to compare the process with the manual method. In the latter case when equipment fails a technician commences a prescribed or improvised trouble-shooting routine fitted to his capabilities and those of the available manual test equipment (multimeters, oscilloscopes, signal generators, etc.). As he begins to probe for the defective area in a bewildering array of tightly packed circuitry he faces the frequent possibility of inadvertently shorting critical circuit terminals. His ability to acquire and evaluate data is such that several minutes per measurement are required. Automatic data acquisition circuitry developed for CATS supersedes these manual techniques with a substantial increase in data rate, and no damage from manual probing. Testing is accomplished at rates of 200 to 400 per second. Acquisition in the laboratory model is tailored to the unique requirements of automatic performance monitoring, comparing favorably with other candidate schemes which were evaluated against design criteria listed earlier. However, flexibility of CATS is such that advantages of state of the art developments in data acquisition can readily be incorporated. For example, if tradeoff studies indicate accuracy is more important than cost for a particular application, a potential candidate scheme might be a highly accurate analog to digital conversion facility located close to the monitored equipment. Specific details concerning data acquisition developments at the Naval Electronics Laboratory Center are available.(2)

Successful monitoring of shipboard systems is a function of both the test system and of the test logic design and sensor implementation in the tested system. Recognizing the need for some elements of standardization in test logic design and sensor implementation for shipboard systems, the Naval Ship Systems Command directed preparation and issue of Military Standard 1326 (Navy).(3) This document is intended to provide manufacturers of automatic test systems and shipboard operating systems with a standard guide to insure effective and compatible interfacing.

INFORMATION PROCESSING:

In CATS, raw data acquired from monitored systems is processed against stored data pertaining to the various tests being

The numbers in parenthesis refer to the list of references appended to this paper.

performed. Routine processing functions are performed automatically. In keeping with the overall system philosophy which attempts to make optimum use of the man, selection of displays on the central display device, and selection of other peripherals, as well as interpretation and analysis of the information presented, are manual functions.

INFORMATION PRESENTATION:

Information is disseminated to various users in a variety of display formats. Operational users are concerned with overall availability and performance of systems; therefore, readouts, status indicators and status type displays are the chief means of information presentation. Users directly concerned with maintenance are provided with several levels of information detail on the cathode ray tube display. Four general formats are presently available in the system (refer to Fig. 5-8). These illustrations were developed by photographing the CATS Central Display Device under operating conditions. Typical shipboard radar, communication and mechanical type systems were monitored. Identification of equipment as noted is readily understood by Navy operating and technical personnel. For example, AN/WRT-2 is the nomenclature for a generally used communication transmitter.

Informational: This type is static and is primarily used to convey static data of any type to the operator, Lists, tables and indices are examples of this type of display.

Bar Chart: This type combines static information, such as shown on the informational type display, with dynamic information resulting from performing tests on equipment being monitored. Test results are shown in the form of horizontal vectors, the length of the vector being proportional to the percentage that the measurement departs from the normal toward either the upper or lower limit for the test. The program can branch on the result of any test so that if a test is within tolerance one sequence of tests will be conducted, while if that test is out of tolerance, a different series of tests will be conducted. As vectors in the bar chart reach the length that represent 100% deviation from the norm, the vectors begin to flash. The 100% permissible deviation point is shown by the vertical cursor line.

Block Diagram: This type is similar to the bar chart except that in place of a list of tests a block diagram of the equipment or portion thereof is shown. Vectors are used as in the bar chart in order to show result of tests. Both the block diagram and the bar chart may have light pen targets for calling up other displays or tests and may have other displays referenced by number, indicating to the operator which displays to call up for continuation of signals or for more detailed information on areas of possible interest.

Diagnostic Display: This type is valuable for isolating faults when it can be predetermined that a series of out of tolerance tests infallibly indicates a particular fault. The diagnostic display shows a number of test numbers with dashed lines connecting them vertically and horizontally. As a test is performed, its vector is updated and if the test is in tolerance a solid line appears connecting the test number to the next test number to the right. As the next test is performed its vector is updated and a solid line is drawn to the next test to be performed. If a test is out of tolerance a solid line will appear connecting the test number to the number vertically below it. In this way tests are performed and the path through the diagnostic "tree" is indicated to the operator. Following the last test the solid line will extend to a block indicating the probable cause of failure or the fact that the equipment is in a stand-by, off, or no-fault condition. The operator has the option of calling for a rapid fault diagnosis sequence or one that progresses one step at a time with the capability of overriding the program's decision. Display formats described in this paper are typical; however, system flexibility permits a variety of others, - for example, logic diagrams.

INFORMATION RECORDING:

During the normal operation of CATS a large amount of data is gathered from various monitored systems. Properly used, the time history recording of this data is valuable in supplementing the human capabilities. In designing the system, attention has been given to implementation of this function. Comparison of current readings with past readings taken at various time increments is made possible by incorporation of the capability to retain desired sensed data in the memory store. How this data is used will be covered in detail under the discussion on Trend Analysis.

CONTROL OPERATION:

Functional controls in CATS are designed to complement machine functions and operator needs. The system can operate in both the unattended mode and the attended mode. In the unattended mode only discrete information such as "good", "bad" "marginal", or "indeterminate" is available. Alarms, both visual and aural are activated on the basis of this discrete machine assessment. In the attended mode more detail is available, including level of performance information for each test, combination of tests, and system tests which the operator interprets and analyzes. For example, a typical bar chart shows the immediate general status of the system it represents by a pictorial representation of the system in terms of dynamic

vectors showing test results with respect to nominal values, high limit values, low limit values and allowable deviation from nominal. Controls in the form of function buttons, keyset, typewriter keyboard and light pen provide a versatile array of access means to the computer program. Thus the operator is integrated with the machine in a manner which places emphasis on his ability to think and to exercise technical judgment.

TREND ANALYSIS:

Prediction of system behavior is a complex and many faceted subject. What has been accomplished as a result of technical efforts in our automatic testing program is merely an initial approach to a very broad problem. However, contrasted to present methods, it appears that several techniques not yet fully developed and implemented, have attractive features with the potential for practical application and long term benefits. Past methods are based on failure mechanisms and physics of failure studies which are costly and time consuming to implement and perhaps are not completely related to the particular system installation and its actual operational environment.

The prediction process is based on the capability to automatically and rapidly acquire, process and disseminate parametric data concerning the monitored system. Systems behavior is enhanced by the fact that on line monitoring may detect equipment and systems degradation before incipient failures become serious or catastrophic. This feature permits maintenance personnel to plan ahead. Repair or adjustment can be accomplished during scheduled preventive maintenance periods and therefore major casualties can be avoided, or at least reduced. In a broad sense, command and maintenance supervisory personnel are provided a gross behavior prediction capability by observation and study of the up to the minute display formats available on the cathode ray tube.

Several operator-oriented trend-analysis display formats are used in CATS. The operational program provides this capability by the technique of mark, store and recall of dynamic displays, including bar charts and block diagrams. By noting the overall change in the display or specific portions of the display on the basis of time, an estimate of probable equipment behavior can be projected. Figure 9 exemplifies this feature. A second method of trend analysis depends upon the use of the historical recording subroutine. Presently the program is written so that each hour and for the ensuing 15 hours all test measurements are stored in memory. This historical data can be recalled in various display formats and analyzed by the operator as an aid to trend prediction. Figure 10 is an example of this type display.

Actual experience in regard to systems behavior prediction was relatively limited during development assist tests with CATS aboard ship. However, sufficient data was acquired to conclude that further expansion of present techniques is warranted. Principal recommendations which resulted from this study are as follows:

(1) Increase the flexibility in rate and/or amount of data recording. For example, program modification to increase the sampling rate from a given point following detection of an intermittent fault should provide better information to judge the nature of the cause and prediction of possible complete failure.

(2) Optimize selection of data which is most useful in correlation and analysis. For example, in the automatic mode a program routine to collect and show the correlation of inter-related test point information would be helpful, once a most probable fault has been indicated. Putting it differently, a refinement of the program would permit concentrating both data and assessment automatically in the test point areas related to the difficulty, to provide a better basis for predicting the probable behavior trend.

(3) Increase use of the computer in automation of the analysis process. This of course involves a comprehensive analysis of failure modes and the earliest available indications of them, subject to automatic treatment.

This is a potentially fertile field. So far we have shied away from complete automatic analysis, as we mentioned previously, because of the size of this job of determining failures and most probable causes in an all encompassing manner. If the job of predicting faults and their causes in advance of experience were a straight forward process, we would agree that we should correct the deficiencies in advance rather than test for them. Some techniques related to computer aided design are undoubtedly relevant to computer aided fault analysis and we would like to explore this area more extensively in the future.

In considering the potential of system behavior prediction the value of information assessed from analysis of a number of systems would result in increased assurance that a particular trend is typical of a family rather than an isolated case. Recorded information could be analyzed to determine the patterns or trends. With appropriate statistical treatment, specific mathematical functions could be derived. When programmed into CATS automatic recognition of behavior patterns and trends would be achievable.

PRESENT STATUS AND FUTURE TRENDS:

Introduction of on-line automatic testing into the shipboard environment must be considered in terms of two general time frames. The present is called the retrofit time frame, one in which existing systems are not necessarily fully amenable to interfacing with an automatic test system. The CATS laboratory model has been interfaced with typical shipboard equipments in this time frame requiring an appendage-type data acquisition scheme. Tests indicate results are favorable despite the relatively unfavorable retrofit conditions.

Full exploitation of automation can be achieved during the new equipment time frame because automatic testing and new equipment interfacing problems can be effectively solved as a part of the design life cycle, rather than as a retrofit. At that point in time an optimized interface between tested and testing systems can be expected. System planning for automatic testing will be more integrated and correlated by the application of design principles discussed in this paper. One cannot minimize the technical problems which impact on effective implementation of centralized automatic monitoring. Questions like the following need to be studied in greater detail:

- (1) What is the optimum configuration of monitoring and testing hardware for various types ships?
- (2) Who needs displays and what type?
- (3) Should the system use dedicated processing or is shared processing more desirable?

Requirements of various shipboard maintenance departments and other user organizations need to be examined in terms of overlap and redundancy.

SUMMARY AND CONCLUSION:

This paper outlines the requirement for shipboard automatic testing; describes the development effort and philosophy of design for a centralized automatic test system; and points out salient features of CATS. Predicted long term worth of centralized automatic testing indicates that it will reduce down time for monitored systems; speed up the maintenance process; provide an increased system mean time before failure; reduce proliferation of test and monitoring facilities aboard ship; and generally increase the overall readiness of the ship.

Because of the revolutionary change to traditional approaches and methods, both technical and management problems must be solved. The laboratory model has demonstrated effectiveness during the difficult retrofit time frame. Application during the new equipment time frame will exploit the full capability and effectiveness of this concept.

REFERENCES:

- (1) System Formulation for a Centralized Automatic Test System (CATS) Vol. 1 (S46-23) July 1, 1968.
- (2) Development of Centralized Automatic Test Systems at NELC, Vol. 3, Data Acquisition, 3 Feb. 1969.
- (3) Military Standard 1326 Navy Test Points, Test Point Selection and Interface Requirements for Equipments Monitored by Shipboard On-Line Automatic Test Equipment.

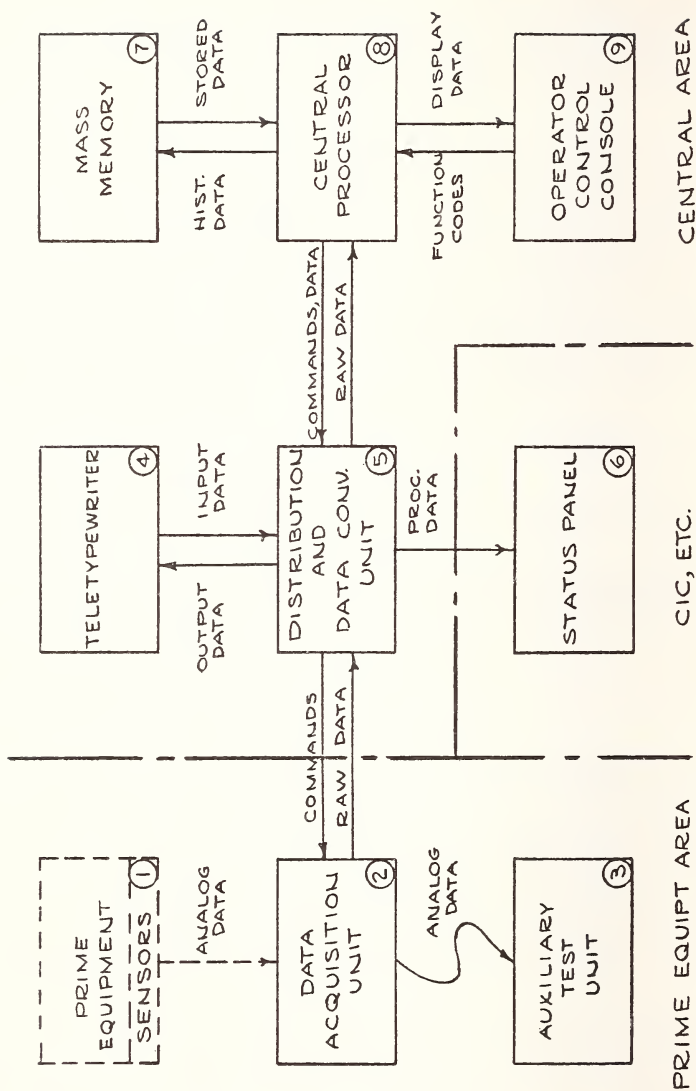


FIGURE 1 CATS MOD 0 SYSTEM BLOCK DIAGRAM.

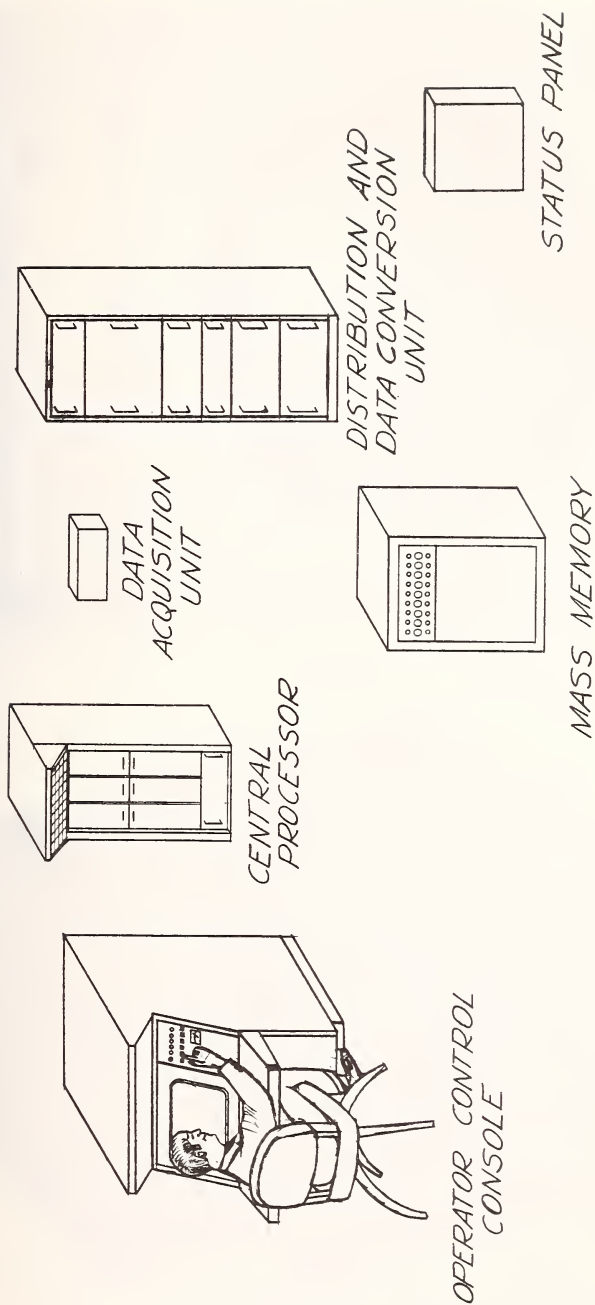


FIGURE 2

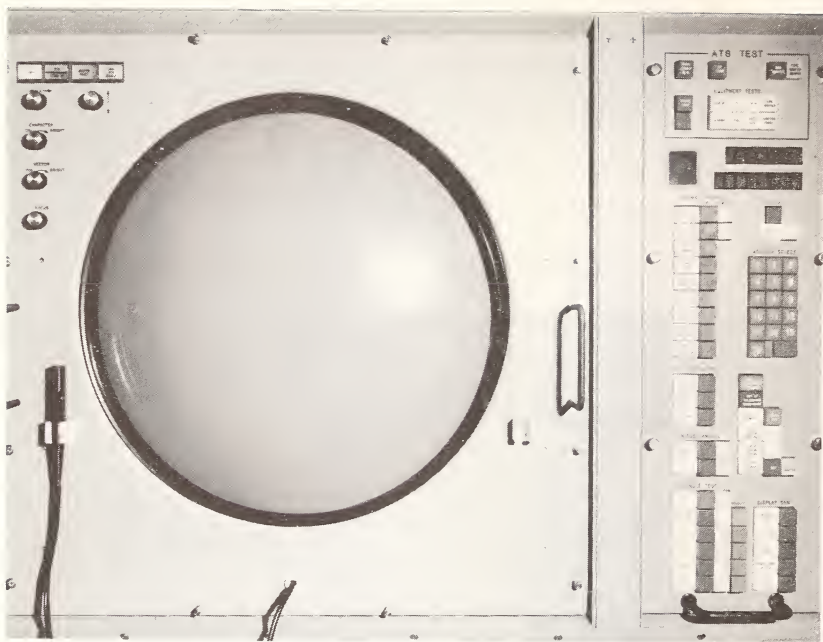


FIGURE 3

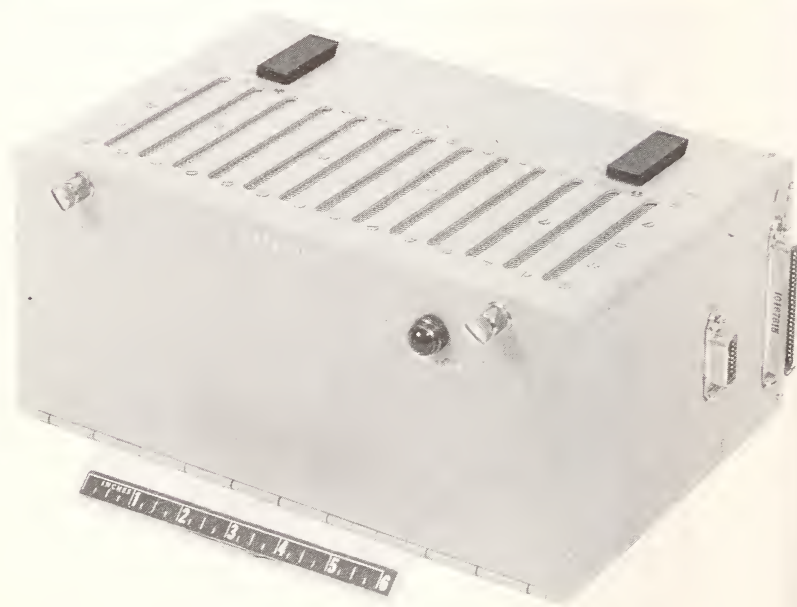


FIGURE 4

001 DISPLAY--EQUIPMENT INDEX

BAR CHART	BLOCK DIAGRAM	DIAGNOSTIC
R-1051	0051...ALL	0050...PWR / CONT 0055...SIG. PATH 0056...FREQ. GEN.
SPS-10	0004...ALL	0040...ALL
SRC-20	0053...ALL	0054...RX 0102...TX
URC-32	0072...ALL	0103...ALL
WRT-2	0060...ALL	0057...PWR. AMP. 0061...ALL 0062...MOD. 0063...R.F. GEN. 0005...POWER SUPPLIES
EVAP		0073...R.F. GEN. 0064...PWR. SUP. 0074...PWR. AMP. 0075...MODULATOR
SELF TEST	0015...CENTRAL AREA 0016...CALIB. CHAN.	0104...ALL

FIGURE 5

0051 DISPLAY
R-1051
ALL SENSORS
(PRIME EQUIPMENT NUMBER 002)
MODE.....AM, FSK

			100%
	POWER SUPPLY		
A2A8	+110 VDC	7121-	
	+28 VDC	7136—	
	-30 VDC	7135-	
	RF AMPS		
A2A4	V1 BIAS	7114—	
	V2 BIAS	7112—	
	TRANSLATOR		
	Q2 BIAS	7104—	
	Q3 BIAS	7123—	
A2A6A6	Q6 BIAS	7122-	
	Q7 BIAS	7126-	
	Q8 BIAS	7130—	
	Q9 BIAS	7125—	
	MC SYNTH		
A2A6A1	AFC VDC	7120—	
	MODE GATE		
A2A1	BIAS	7101—	
	500 CPS SYNTH		
A2A6A4	5KC SPECTRUM	7110—	
	7.1 MC AMP	7116-	
	100 KC SYNTH		
A2A6A2	AGC VDC	7106—	
	USB IF/AUDIO		
A2A2	IF OUTPUT	7132—	
	AUDIO OUTPUT	7102—	
	AUDIO GAIN	7111—	
	LSB IF/AUDIO		
A2A3	IF OUTPUT	7103	
	AUDIO OUTPUT	7133	
	AUDIO GAIN	7117	

SEE BLOCK DIAGRAM
0052^D

FIGURE 6

0052 DISPLAY/1
R-1051
TOTAL BLOCK DIAGRAM
(SEE EQUIPMENT NUMBER 002)
MODE..... AM, FSK

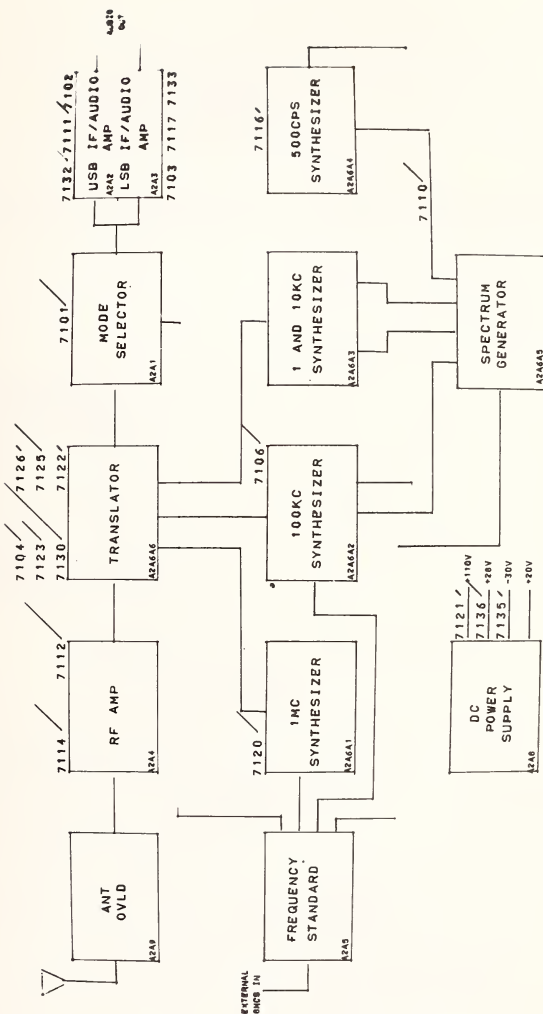


FIGURE 7

0050 DISPLAY
R-1051 DIAGNOSTIC
POWER, CONTROL SECTION
(PRIME EQUIP. NUMBER 000)

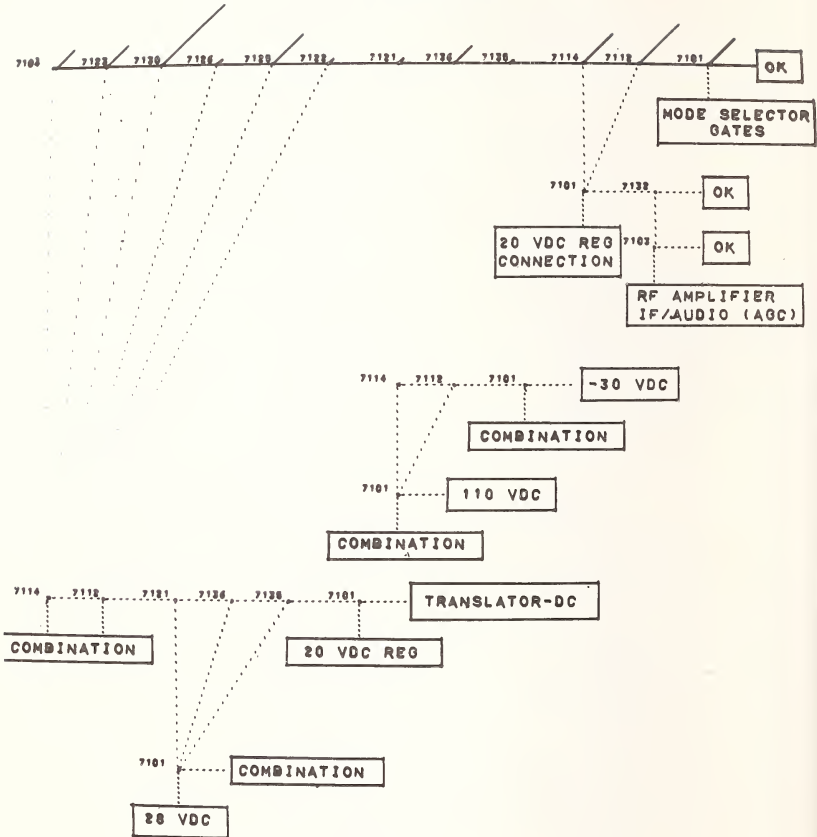


FIGURE 8

0051 DISPLAY¹
R-1051
ALL SENSORS

MODE..... AM,FSK

POWER SUPPLY	
A2A8	+110 VDC 7121 —•
	+28 VDC 7136 —•
	-30 VDC 7135 —•
RF AMPS	
A2A4	V1 BIAS 7114 —•
	V2 BIAS 7112 —•
TRANSLATOR	
A2A6A6	Q2 BIAS 7104 —•
	Q3 BIAS 7123 —•
	Q6 BIAS 7122 —•
	Q7 BIAS 7126 —•
	Q8 BIAS 7130 —•
	Q9 BIAS 7125 —•
MC SYNTH	
A2A6A1	AFC VDC 7120 —•
MODE GATE	
A2A1	BIAS 7101 —•
500 CPS SYNTH	
A2A6A4	5KC SPECTRUM 7110 —•
	7.1 MC AMP 7116 —•
100 KC SYNTH	
A2A6A2	AGC VDC 7106 —•
USB IF/AUDIO	
A2A2	IF OUTPUT 7132 —•
	AUDIO OUTPUT 7102 —•
	AUDIO GAIN 7111 —•
LSB IF/AUDIO	
A2A3	IF OUTPUT 7103 —•
	AUDIO OUTPUT 7133 —•
	AUDIO GAIN 7117 —•

SEE BLOCK DIAGRAM
0052^D

FIGURE 9

HOURS SINCE MEASUREMENT	PERCENT OF ALLOWABLE DEVIATION		
	0	100%	200%

CURRENT

1 HR.

2

3

4

5

6

7

8

9

10

11

12

13

14

15

16

TEST NO. 003-6114

PREVIOUS DISPLAY

P/P VAC
 U +1.000
 N +.9000
 M +.6401
 L +.7900
 H +.6420

FIGURE 10

EXPLOSIVE OXIDATIONS INITIATED BY SIMULATED
METEOROID PENETRATION INTO SPACECRAFT ATMOSPHERES

William H. Carden
Assistant Manager, Aeroballistics Branch, VKF
ARO, Inc., Arnold AF Station, Tenn.

ABSTRACT: Hypervelocity impact tests were conducted in an evacuated range on target samples which simulated a NASA S-IVB wall configuration since this stage is planned as the primary structure in the NASA Orbiting Workshop program. The samples formed part of the wall of a large tank which contained an oxygen-rich atmosphere. The explosive oxidations which occurred inside the tank as a result of perforation were observed and the results were analyzed. The bare thermal insulation on the inside of the wall further enhanced the otherwise severe reaction which occurs with a metallic wall in the presence of enriched oxygen.

KEY WORDS: hypervelocity impact, meteoroid penetration, spacecraft, combustion front, oxygen atmosphere, oxidative detonation, oxidative flash, blast over-pressure

INTRODUCTION

The perforation of the wall of a vessel by a hypervelocity projectile will produce an explosive-like reaction inside the tank if the tank contains an oxygen-rich atmosphere. Studies (1-10)¹ have shown that the extremely hot fragments of projectile and wall materials rapidly undergo a chemical reaction with the oxygen in the immediate vicinity of the perforation, producing a combustion front which penetrates into the tank. This violent reaction is accompanied by a brilliant flash of light.

The process just described is similar to the situation which could exist if the wall of a manned space vehicle were to be perforated by a meteoroid. There is ample reason for concern regarding the effect of such an encounter on the human occupants of

¹The numbers in parentheses refer to the list of references appended to this paper.

the space vehicle. Among the phenomena which could present a serious pathological hazard to human occupants are the blast overpressure, the intense light flash, and the high temperatures associated with the combustion front. The possibility that a spacecraft fire would be initiated by the combustion front and accompanying hot particles is a secondary, but perhaps equally serious, potential hazard. Ways to alleviate these problems are discussed in Refs. 9 and 11.

Roth (8) has presented a literature review and survey of this flash oxidation hazard from the biomedical point of view. Much of his discussion is focused on the work of Gell and his colleagues at Ling-Temco-Vought (1-3). These workers exposed white rats to this oxidative detonation inside a vessel which was perforated by a high-velocity projectile. These animals suffered various degrees of injury and incapacitation, and under some test conditions mortality occurred. It was impossible to determine whether death occurred primarily as a result of the blast effects or as a result of burns received by the animal.

Several recent studies (4-7) have produced additional information regarding the mechanism of this oxidative reaction and its potential hazards to spacecraft structures, systems, and personnel. However, all questions have not been answered, and any additional experimental information which becomes available should be welcomed by those concerned with spacecraft design.

In a recent test program (9) at AEDC, hypervelocity impact tests were conducted on target samples which simulated a wall configuration of the Saturn S-IVB stage. The S-IVB stage is planned as the primary structure in the NASA Orbiting Workshop program. On many of these tests, the target sample was attached to a large tank which permitted the rear of the wall sample to be exposed to an oxygen-rich atmosphere during perforation. The main purpose of these tests was to evaluate methods of preventing or minimizing combustion of the polyurethane foam which covered the inside of the wall sample. As a result of these tests, the decision was made to install a 3-mil aluminum foil fire-retardant liner to cover the insulation and to install a micrometeoroid bumper on the vehicle (11). At the same time, however, these tests provided an opportunity to observe the blast effects inside the test tank at the time of perforation. The combustion front was recorded photographi-

cally on a large number of these tests. In addition, on a limited number of these tests, transducers were placed inside the test tank to allow further observation of the phenomena associated with the combustion front. The purpose of this paper is to describe these observations and to relate them to previously available information on the subject. The present results, although limited in extent, provide information which applies specifically to an uncovered polyurethane insulation and unbumpered wall configuration.

TEST CONFIGURATION

LAUNCHER AND RANGE

These tests were conducted in the Hypervelocity Impact Range S-2 at AEDC. The range includes: (1) a two-stage launcher; (2) a blast tank into which muzzle gases expand and in which the projectile (1/8 in. diam., type 2017 aluminum spheres in these tests) is separated from the sabot; (3) a connecting tube along which velocity measuring shadowgraphs are located; and (4) a target tank where the test specimen is impacted by the projectile. The large size (6 ft. diam. by 21 ft. long) of this target tank permits the impact testing of unusually large configurations in a vacuum environment. In the present test, it permitted the use of a relatively large (3 ft. diam. by 5 ft long) test tank whose volume was greater than that of any vessel used in previous explosive oxidation impact studies (1-7).

TARGET CONFIGURATION

The wall specimen used on this test was designed to simulate the Saturn S-IVB basic wall structure. It consisted of a 0.125 in. thick, type 2014-T6 aluminum sheet to which a 1 in. thick layer of closed-cell polyurethane foam was bonded. The foam was sealed with a layer of glass fabric and a coat of polyurethane resin. A photograph of the rear of a wall specimen is shown in Fig. 1. This polyurethane insulation provides thermal insulation on the inside of the tank to prevent liquid hydrogen boil-off for the propulsive stage.

The target specimen was attached to the upstream end of the test tank, with the foam insulation on the

inside. The test tank was mounted inside the range target tank with its axis on the range centerline. Provisions were made for evacuating the test tank prior to charging it with the desired gas mixture.

INSTRUMENTATION

The combustion front inside the test tank was recorded photographically on a large number of those tests reported in Ref. 9. The tank was equipped with a side port (approximately 10 in. diam.) immediately behind the upstream tank flange, providing a view normal to the tank centerline. The uprange edge of this field of view was about 4 in. behind the rear of the wall specimen. In addition, another port was located in the rear end of the test tank, providing an unobstructed centerline view of the rear of the wall specimen. The side port was used most often for this high-speed camera coverage, because the rear port was usually occupied by other instrumentation systems. A 16-mm camera was used, and the framing rate during the event was usually about 3200 frames/sec.

For the shots which are of particular interest in this report, additional instrumentation devices were placed inside the test tank to record the passage of the combustion front. This additional instrumentation consisted of four quartz pressure transducers and four lead-zirconate piezoelectric "time-of-arrival" gages. These devices were mounted in four pairs at 12 in. intervals longitudinally in the tank. Each pair consisted of one of each type of gage. The devices were attached to a bracket which was cantilevered from the rear end of the test tank. The bracket was shock-mounted at its point of attachment to the tank. A sketch of this arrangement is presented in Fig. 2. The outputs of these devices were amplified and recorded on magnetic tape.

Three tests were also conducted with iron-constantan thermocouples located inside the test tank. The thermocouple junctions were resistance welded using 0.002 in. wires. These thermocouples were fabricated using a standard thermocouple connector and ceramic insulator as shown in Fig. 3, and the devices were mounted on the bracket inside the test tank with the exposed junction facing forward. The thermocouples were located at 8 in. intervals as shown in Fig. 2. The reference junctions were immersed in ice baths, and the thermocouple outputs were displayed and recorded on oscilloscopes.

The instant of projectile impact on the wall specimen was monitored by means of a radiometer which observed the initial impact flash. The radiometer output was recorded on the magnetic tape to provide a time reference for the pressure gages and time-of-arrival gages inside the test tank. The radiometer output was also used to trigger the oscilloscopes which were used to display the thermocouple outputs.

TEST RESULTS

TEST CONDITIONS

For the tests of interest in the present report, the test tank was charged with the desired gas mixture to a pressure of 5 psia. The test gases were nitrogen and oxygen, and individual tests were conducted with specific volumetric mixtures of 21 percent oxygen (air), 45 percent oxygen, 59 percent oxygen, 70 percent oxygen, as well as 100 percent oxygen or nitrogen. All tests of interest were conducted using 1/8 in. diam. aluminum spherical projectiles at velocities in the 20,000-26,000 ft/sec regime.

The target configuration previously discussed was used on all tests of interest in this report. Impact usually occurred within the target area covered on the rear by the polyurethane foam. However, on a few shots, including two of the shots made with the additional instrumentation devices inside the tank, target perforation occurred outside of the area covered by the foam. These shots provided a fortunate opportunity for comparing the test results for an insulated wall with the corresponding behavior for a simple aluminum wall.

PHOTOGRAPHIC OBSERVATIONS OF OXIDATIVE FLASH

Typical film sequences of the oxidative flash occurring inside the test tank at impact are presented in Figure 4. Film exposure resulted from luminosity inside the tank produced by the rapid oxidation of projectile and wall materials. The film clip at the left depicts perforation of the 1/8 in. thick aluminum wall without foam insulation. The duration of the event recorded on the film is about 6 msec. The second, third, and fourth film clips depict perforation of a typical wall specimen for the case of

45, 70, and 100 percent oxygen mixtures, respectively. The complete duration of the events on these tests, of which only the initial portions are shown in the figure, were 34, 44, and 53 msec for the 45, 70, and 100 percent oxygen mixtures, respectively. The exposure of the pictures indicates qualitatively that the intensity of the combustion front increases with increasing oxygen concentration. On other tests with 5 psia of air in the test tank, film exposure was too weak for printing. On tests using 100 percent nitrogen, no film exposure occurred.

The fifth film clip in Fig. 4 was obtained through the rear port of the test tank instead of the side port. The camera was focused on the rear of the test specimen, the outline of which is visible in the first frame. The sharpness of focus is reduced as the flame front propagates into the tank. Duration of the recorded event was about the same as for the adjacent film clip (100 percent oxygen). This view, unrestricted by port size, indicates that the flame front penetrates throughout the test tank.

These film clips demonstrate clearly the effect of the polyurethane foam on the oxidative flash. In the absence of the foam, the metallic wall and projectile provided the only particles available for oxidation. Furthermore, production of these particles is complete within a relatively short time interval after impact. However, with the addition of polyurethane foam to the wall, a large volume of low-density, highly combustible material is ejected into the oxidizing atmosphere inside the tank at impact. Also, the foam continues to be ejected for a long period of time compared with the single metallic wall condition. The overall effect of the presence of the foam is to significantly increase (by an order of magnitude) the duration of the oxidative flash inside the tank.

VELOCITY OF COMBUSTION FRONT

The "time-of-arrival" gages inside the test tank responded to the phenomena inside the tank. Typical oscillograph playback traces of the recorded data are presented in Fig. 5. The results shown in Fig. 5a are typical for those tests for which impact occurred within the area covered by the foam. The results for one of the two shots which missed the foam are shown in Fig. 5b. In the latter case, the type of response

obtained from these gages indicates that the leading edge of the disturbance is well defined as it passes through the tank. In the case of impact within the foam-covered area, however, the leading edge is somewhat "smeared out" by the interaction between the foam and the high-speed metallic particles.

The time interval from projectile impact to arrival of the disturbance at each gage location inside the tank was read from the oscillograph traces as indicated in Fig. 5. In the case of impacts through the foam, an attempt was made to define the instant of arrival of the strong part of the front instead of its weak leading edge. A degree of judgement was required in the definition of this "instant" because of the smearing of the front. These results are presented in Fig. 6. Although there is some scatter in these results, the data clearly indicate slopes on the distance-time plots corresponding to a propagation velocity of about 8000 ft/sec for impacts which perforated the foam and about 22,000 ft/sec for impacts which missed the foam. These results appear to be independent of the oxygen concentration in the test tank.

It is evident that the experimental distance-time measurements shown in Fig. 6 do not extrapolate back to the origin of the plot. This is largely because the bracket which held the instrumentation devices was mounted approximately 8 in. below the tank centerline. Since the disturbance front which propagated through the tank was non-planar and was, to a first approximation, hemispherical in shape, its arrival at a gage position could occur significantly later than its arrival at the corresponding centerline position. The general shifting in time of the results from shot to shot probably resulted from the random dispersion of the projectile impact location with respect to the tank centerline. It is believed that the large upward shift in the results for shot 300 (Fig. 6e) was the result of a premature impact flash signal from a small particle preceeding the projectile rather than the effect of a change in gas composition.

The velocity of the disturbance which produced the time-of-arrival gage response does not correspond with the velocity of cloud motions as observed on the 16-mm film (Fig. 4). In the later case, for impacts which perforated the bare foam, the leading edge of the luminous cloud which initially passes across the

camera field of view has a velocity of about 800 ft/sec, a full order of magnitude less than that indicated by the gage response. Therefore, there is reason to conclude that the billowing luminous clouds which are visible in the 16-mm camera pictures represent a stage of the impact process which is fundamentally different from the initial disturbance stage. These differences are worthy of further study.

PRESSURE MEASUREMENTS

When a thin wall is perforated by a hypervelocity projectile, the expanding debris cloud immediately behind the point of impact will contain fragmented, melted, and vaporized materials. It is convenient to visualize that a "pressure" exists within this expanding cloud. More precisely, the cloud contains momentum which produces an impulse acting on any surface the cloud strikes. If the cloud is completely vaporized, thereby consisting of a very large number of very small particles, the usual concept of pressure may be valid for time scales and space scales of interest. However, appreciable vaporization cannot be produced in most materials, including those of the present test, at velocities attainable with light-gas guns. Therefore, the debris cloud in these tests consisted of discrete solid and molten fragments instead of a "continuous" expanding vapor. Nonetheless, a piezoelectric pressure transducer located within a few projectile diameters of the impact location in the present tests would likely observe an apparent stagnation pressure on the order of a few kilobars (12,13).

The stagnation pressure in the debris cloud decreases as the cloud expands away from the target sheet. Furthermore, the radial pressure profile in the cloud falls off very rapidly with increasing distance from the axial centerline. The instrumentation bracket inside the tank (Fig. 2) on the present test was located below the tank centerline not only to prevent transducer damage from fragments within the debris cloud but also to minimize any contribution to the measured pressure which could result from the debris cloud rather than from the combustion front. It was hoped that any pressure observed by the transducers would result entirely from the explosive oxidation of the wall and projectile materials, the effects of which were expected to propagate throughout the tank.

None of the pressure transducers inside the tank on these tests recorded an overpressure exceeding the noise level generated by mechanical shock at impact. This mechanical noise level never exceeded the equivalent of 5 psi and was less than 3 psi for most tests. Therefore, these results imply that any overpressure which may have existed at the transducer locations never exceeded 5 psi.

This result is somewhat surprising in view of reported maximum overpressures of 38 psi (3), 100 psi (4), 75 psi (5), and 150 psi (6) obtained in previous investigations. It should be noted, however, that all of the investigations of this type have involved widely differing test configurations (projectile, target, tank volume, transducer location, etc.). Furthermore, the use of a piezoelectric transducer in a mechanical shock environment is no easy task since the crystal responds to acceleration as well as pressure. Finally, it is possible that some investigations may have indicated abnormally high overpressures because of the interaction of the expanding debris cloud with the blast overpressure. Nonetheless, it is not possible to explain with certainty the large difference in blast overpressure between the present measurements and those of other investigators. Nor is it possible to identify which particular sets of measurements, if any, are in error. The large differences between observations illustrate the need for additional testing to resolve the present uncertainty.

TEMPERATURE MEASUREMENTS

Temperature measurements were obtained on two tests using a 70 percent oxygen atmosphere and one test using air. An oscilloscope trace of the output of one thermocouple on a test with 70 percent oxygen is shown in Fig. 7. A rapid temperature increase is observed to begin about 5 msec after projectile impact. The signal then reaches a plateau corresponding to about 1600 F within 15 msec. The indicated temperature remains near this level for about 35 msec and then decreases steadily toward ambient conditions. This type of response was typical for all thermocouples used on these tests.

The maximum indicated temperatures recorded on these three tests are summarized in Table 1. The second thermocouple consistently recorded the higher temperature, indicating a spatial variation in maximum

temperature inside the tank. It is impossible to determine whether the impact velocity difference or the spatial variation in temperature was primarily responsible for the lower maximum temperature which occurred on the second test with 70% oxygen. It is clear that the indicated temperature is strongly dependent upon the oxygen concentration inside the test tank. The implication is that most (if not all) of the heating which occurs after impact is a direct result of the rapid combustion of impact debris. The contribution of the individual components (insulation and aluminum plate) to the heating effect was not determined.

DISCUSSION

The phenomena which occurred when the test specimen was perforated on these tests can be separated into two categories. The first category includes those phenomena which are associated with the impact and perforation events only, i.e., those which would occur even in the absence of an oxidizing atmosphere. The second category includes the additional phenomena which occur because of the presence of oxygen inside the test tank.

The first category includes the formation of the debris cloud of fragmented, melted, and vaporized projectile and wall materials which expand into the test vessel. The leading edge of this debris cloud is thought to have produced the initial response of the time-of-arrival gages on these tests. The presence of oxygen in the test tank apparently had little effect on the initial character of the debris cloud since the propagation velocity of the disturbance was the same with or without oxygen. On the other hand, the character of the debris cloud was obviously influenced by the presence of the polyurethane foam insulation which was bonded to the inside of the aluminum wall.

Although the oxygen concentration did not affect the initial character of the debris cloud, the quantity and state of the materials contained within the debris cloud strongly influenced the duration and severity of the oxidation process. In particular, the large quantity of finely divided, low-density, combustible material ejected from the insulated wall resulted in an order of magnitude increase in the

duration of the oxidative flash compared with the single metallic wall condition. The billowing luminous clouds visible in the 16-mm film records are probably the gaseous products of combustion of the foam with oxygen. The effects of these burning products on other spacecraft materials is not included in this paper. A limited study of secondary combustion is reported in Ref. 9.

The results presented herein have demonstrated the possibility that an exposed and unprotected internal thermal insulation could aggravate the reaction which would occur upon meteoroid perforation of an unbumpered spacecraft hull without a fire retardant liner. The phenomena treated in the present paper would occur only in the event of meteoroid perforation of the basic workshop wall. No attempt has been made in this investigation to assess the probability of such an occurrence or to evaluate methods of reducing this probability. The probability of this event can clearly be eliminated for all practical purposes by the use of meteoroid shielding techniques. As a result of tests reported (9), NASA elected to install an external micrometeoroid bumper and an internal fire retardant liner on the Saturn Workshop to alleviate these problems (11).

REFERENCES

1. Thompson, A. B. and Gell, C. F. "Meteoroids as a Hazard in Space Flight - A Survey of Present Information." American Rocket Society Space Flight Report to the Nation, October 9-15, 1961.
2. Gell, C. F., Thompson, A. B. and Stembridge, V. "Biological Effects of Simulated Micrometeoroid Penetration of a Sealed Chamber Containing Animal Specimens." Aerospace Medicine, Vol. 33, February 1962, pp. 156-161.
3. McKinney, R. and Stembridge, V. A. "Study of Optimum Environmental Protection against Meteoroid Penetration." NASA CR-50899, February 1963.
4. Caron, A. P. "Oxidative Detonations Initiated by High Velocity Impacts." AFFDL-TR-65-41, May 1965.

5. Gehring, J. W., Lathrop, B. L., Long, L. L., and Hammitt, R. L. "Meteoroid Hazards as Related to Internal Cabin Effects." Seventh Annual Symposium on Space Environmental Simulation, Seattle, May 23-24, 1966. Also, Long, L. L. and Hammitt, R. L. "Meteoroid Perforation Effects on Space Cabin Design." AIAA Paper No. 69-365, AIAA Hypervelocity Impact Conference, Cincinnati, Ohio, April 30-May 2, 1969.
6. Burch, G. T. "Hypervelocity Particle Penetration into Manned Spacecraft Atmospheres." Boeing Document D2-24149-1, May 1966.
7. Friend, W. H., Caron, A. P., et al. "An Investigation of Explosive Oxidations Initiated by Hypervelocity Impacts." AFFDL-TR-67-92, August 1967.
8. Roth, E. M. "Space-Cabin Atmospheres, Part II - Fire and Blast Hazards." NASA SP-48, 1964.
9. Carden, William H. and Payne, J. J. "Simulated Meteoroid Impact Testing on Wall Configurations for the NASA S-IVB Orbital Workshop." AEDC-TR-68-246 (AD845231), December 1968.
10. Carden, William H. "Simulated Meteoroid Impact Testing on a Composite Expandable Structure for Spacecraft Airlock Application." AEDC-TR-69-14 (AD850512), April 1969.
11. "Developments Leading to Material Modifications in the Saturn I Workshop Crewbay." NASA TM X-53732, April 1968.
12. Friend, W. H., Murphy, C. L., and Shanfield, I. "Review of Meteoroid-Bumper Interaction Studies at McGill University." NASA-CR-54857, August 1966.
13. Tillotson, J. H. "A Theoretical and Experimental Correlation of Hypervelocity Impact on Layered Targets." Edgerton, Germeshausen, and Grier, Inc. Technical Report S-425-R, May 1968.

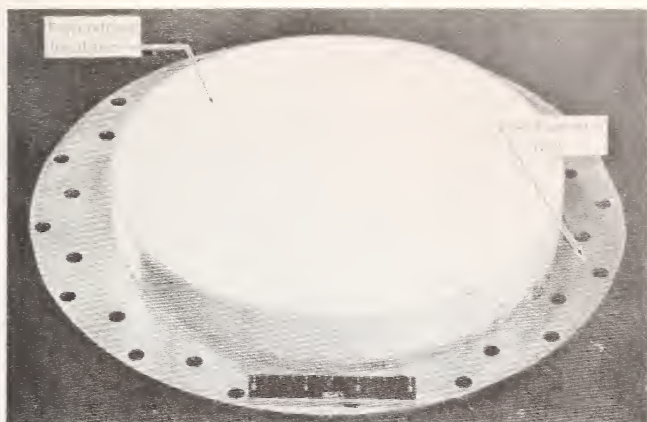


Fig. 1--Wall Specimen (Inside View)

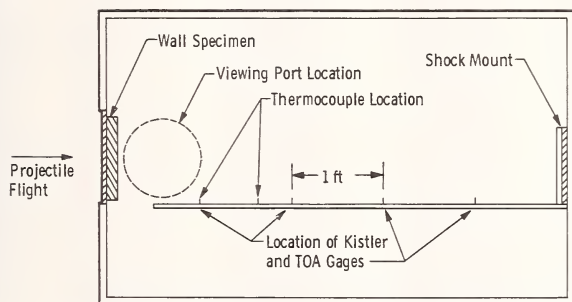


Fig. 2--Schematic of Test Tank

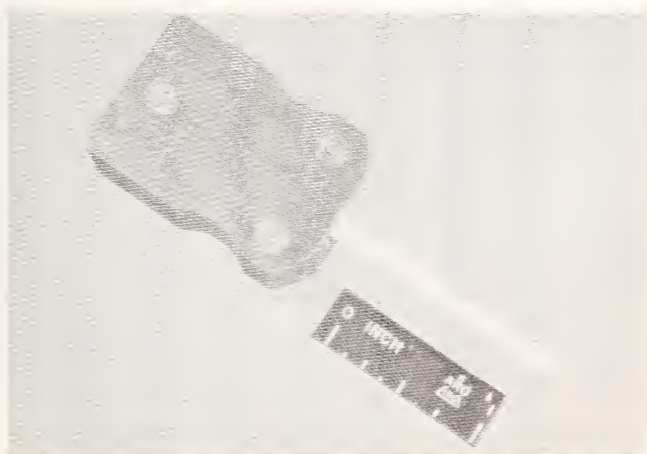


Fig. 3--Thermocouple

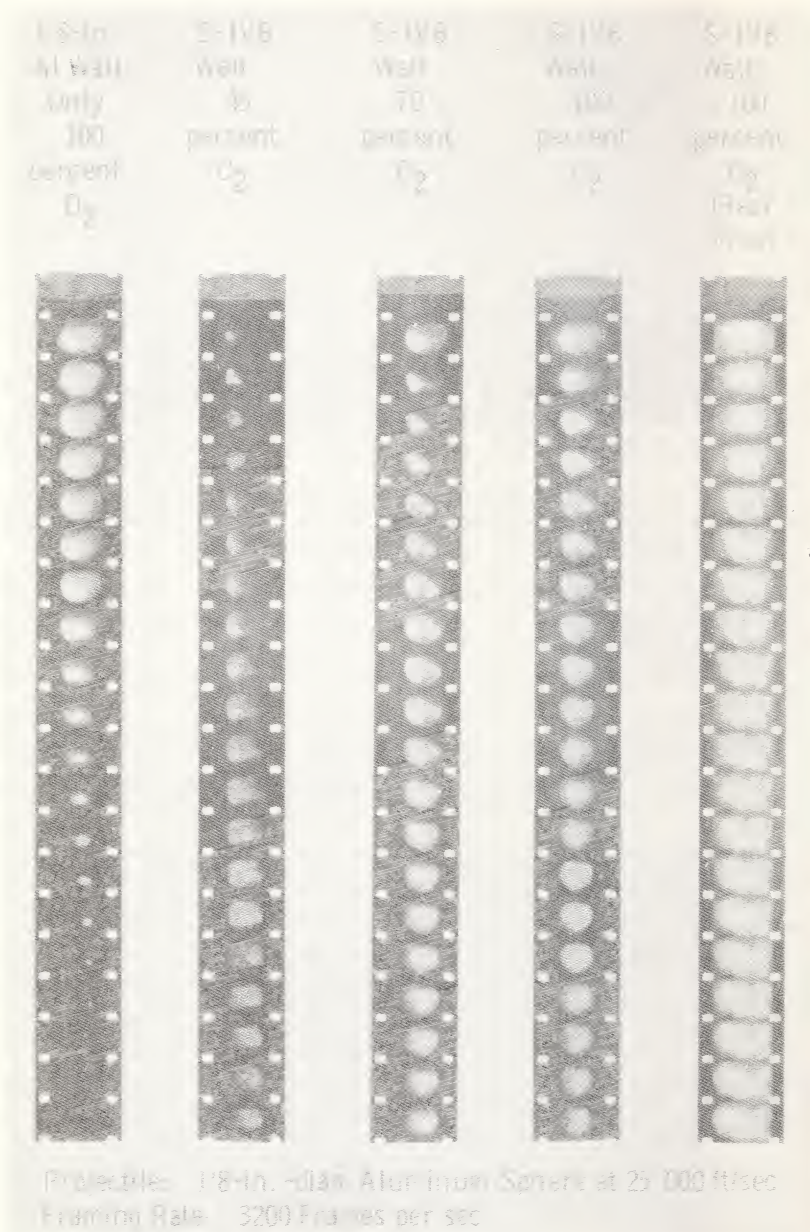
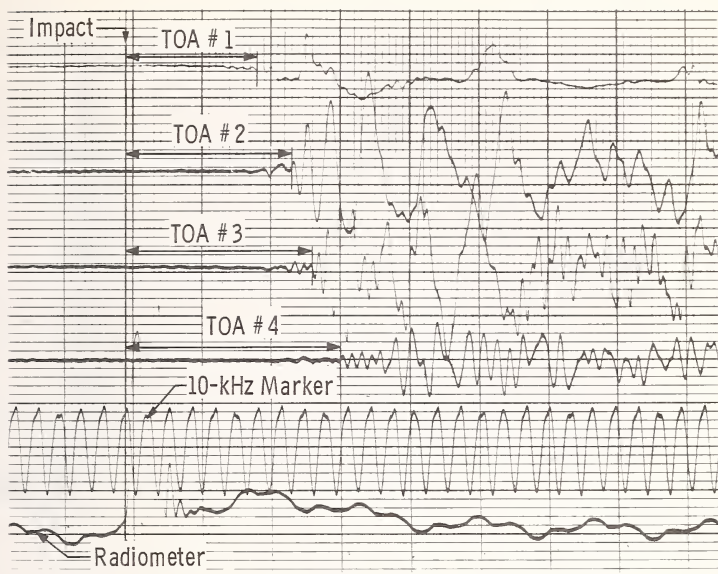
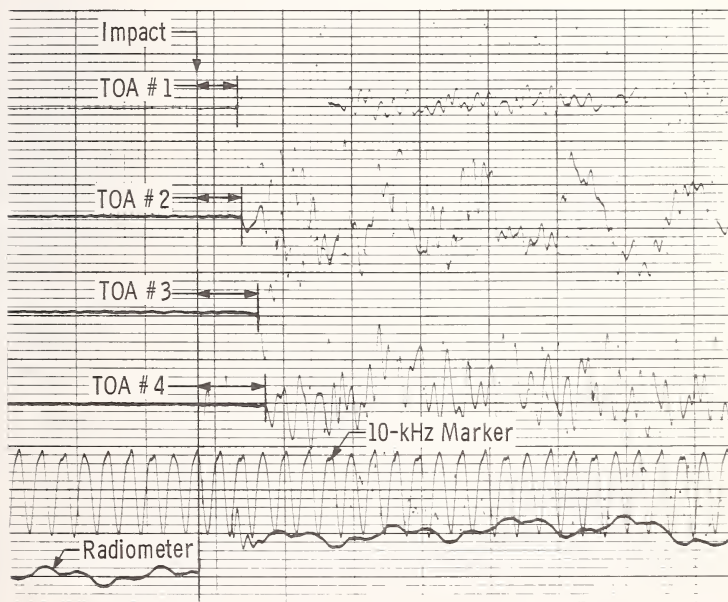


Fig. 4--Impact-Initiated Combustion Front



a. Impact through Foam



b. Impact through Aluminum Wall Only

Fig. 5--Oscillograph Traces

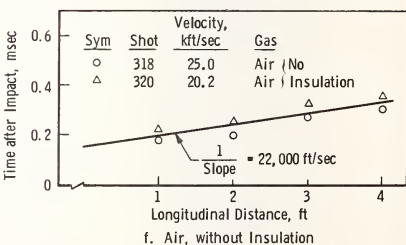
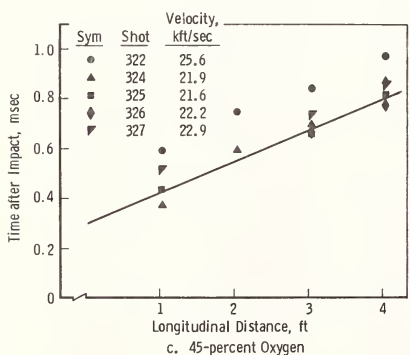
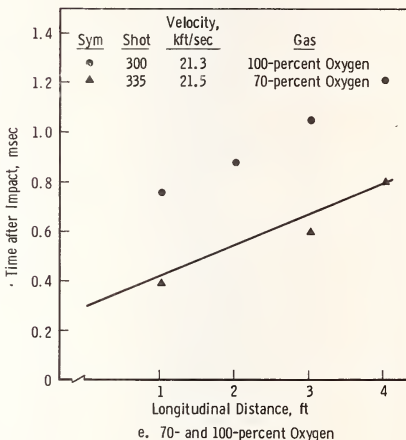
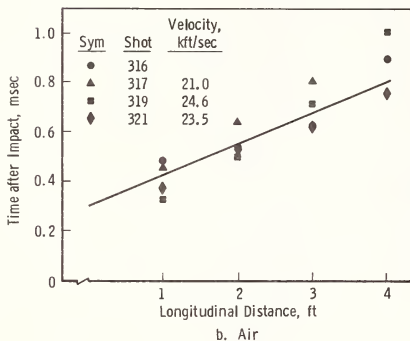
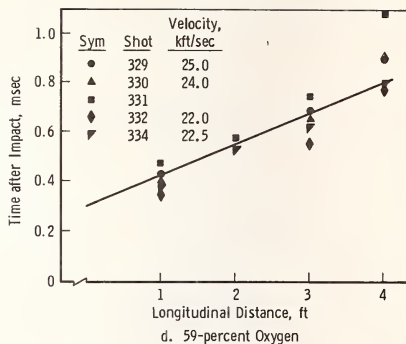
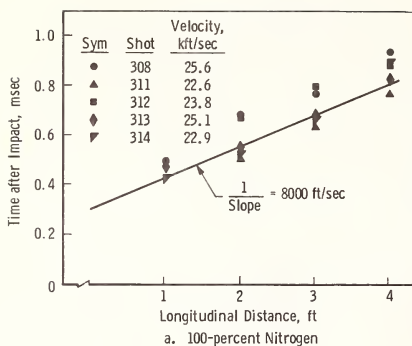


Fig. 6--Time-of-Arrival Results

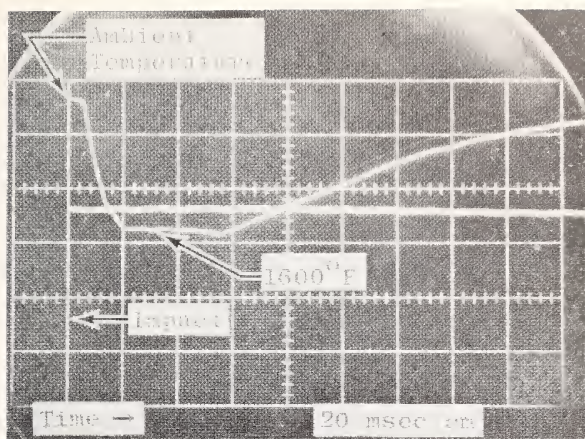


Fig. 7--Thermocouple Output

TABLE 1--Temperature Measurements

Shot	Velocity (ft/sec)	Gas Composition	Thermocouple No. 1 (F)	Thermocouple No. 2 (F)
1	26,300	70% O ₂ , 30% N ₂	1075	1600
2	24,300	70% O ₂ , 30% N ₂	825	1325
3	25,500	Air	200	300

The work reported in this paper was performed for the George C. Marshall Space Flight Center and sponsored by the Arnold Engineering Development Center (AEDC), Air Force Systems Command (AFSC), under Contract F40600-70-C-0002 with ARO, Inc. Further reproduction is authorized to satisfy the needs of the U. S. Government.

THE DYNAMIC ENVIRONMENT SIMULATOR - A MULTIENVIRONMENTAL MAN-RATED CENTRIFUGE

Dana B. Rogers, Captain, USAF¹, Michael McCally, M.D.¹ and Klaus L. Cappel, B.S.²

REFERENCE: Rogers, D. B., M. McCally and K. L. Cappel, "The Dynamic Environment Simulator - A Multienvironmental Man-Rated Centrifuge", ASTM/IES/AIAA Space Simulation Conference, 14-16 September 1970.

ABSTRACT: The U.S. Air Force Dynamic Environment Simulator is a man-rated centrifuge with multiple environment simulation capabilities. This facility can generate combinations, either simultaneous or sequential, of acceleration, vibration, temperature, barometric pressure, gas composition, noise and related environmental stresses. Simulation of a broad variety of aerospace flight mission environments is now possible using this facility. The man rating of this facility was carried out in the last six months of 1969 and resulted in the first manned run in December of that year. Although presently programmed to meet Air Force data requirements for the design of planned and proposed aircraft systems, the Dynamic Environment Simulator represents a national research capability capable of supporting the requirements of many R&D programs including manned space flight, high speed surface transportation and other systems or functions where man is exposed to physical environmental stresses in combination.

KEY WORDS: Dynamic Environment Simulator, man-rated centrifuge, combined environmental stress, man-machine system, simulation research

¹Aerospace Medical Research Laboratory, Wright-Patterson Air Force Base, Ohio.

²Franklin Institute Research Laboratories, Philadelphia, Pennsylvania.

The ultimate effectiveness of aerospace systems can be measured only by criteria or parameters taken from the total man-machine system. With the increasing complexity of present and future aerospace systems, the need is manifest for ground simulation of environments. The interactions of multiple concurrent sequential stresses is yet undefined; and the requirement for repeated exposure to mission environments demands that a centrifuge designed for simulation research should be capable of producing vibration, gas composition, pressure, acoustic, thermal and acceleration variables which may occur in aerospace vehicles during normal flight and emergency periods. The necessity to man rate aerospace simulation facilities cannot be avoided even though incorporation of man rating procedures adds significantly to the cost and complexity of the facility. Safety, of course, is the paramount consideration, and the well established medical ethics of experimentation with normal human volunteers demands complete fail-safe capabilities. In addition, the design requirements for a safe man rated device include consideration of mechanical, life support, control, communications, structures, emergency systems and associated medical facilities.

In 1960, after 18 years of continuous operation, the United States Air Force human centrifuge facility at the Aerospace Medical Research Laboratory, Wright-Patterson Air Force Base, developed excessive vibration and deflections. A study of alternative courses of action was conducted and three options became evident: (1) structural reinforcement of the existing quasi-operational device, (2) replacement of the current machine with an "off-the-shelf" centrifuge, or (3) design and installation of a specific motion simulator clearly based upon Air Force requirements evolving from aerospace operational needs foreseeable over the next two decades. Comparison of estimated costs, time, and, above all, the ability to solve Air Force scientific requirements directed the selection of the third alternative course of action. To meet this need, a complex multimode human centrifuge has been constructed at the Aerospace Medical Research Laboratory, Wright-Patterson Air Force Base, to replace a single mode simple centrifuge. The new facility called the Dynamic Environment Simulator (DES) is capable of providing acceleration, vibration, gas composition, pressure, acoustic and thermal environments as they may actually occur in an aerospace vehicle during normal flight or during emergency and escape conditions.

Simulation of a broad variety of aerospace flight mission environments is now possible using this facility. The man rating of this facility was carried out in the last six months of 1969 and resulted in the first manned run in December of that year.

PRIMARY SUBSYSTEMS

The Dynamic Environment Simulator has been called many

things. A schematic diagram of the major hardware assembly is seen in Figure 1. It is essentially a stiff arm human centrifuge and complex motion device with a multiple environment capability. The system includes the following major components or functions: (1) rotation capabilities, main arm, fork and cab axes; (2) vibration table; (3) power train; (4) hydraulics and bearing systems; (5) environmental control; (6) command and controls; (7) standard operating procedures and operator positions including the medical monitor's room, machine operating room and pit and (8) data acquisition systems. The subject is positioned in a 10 foot spherical chamber or cab located at the end of the main arm. The cab is hydraulic powered and can rotate at 150 rpm. The outer gimbal or fork which moves in a horizontal plane is used primarily for vector alignment, however, it is capable of reaching 30 rpm. The main arm length is 19-1/2 feet from the center of rotation to the center of the cab axis. The major structure can reach 56 revolutions per minute or 20G units at the cab. The main arm of the centrifuge with its two gimbals weighs about 170 tons. The structure is supported by externally pressurized "hydrostatic" bearings and rides on an oil film 0.005 of an inch thick on the thrust bearings. Similar radial bearings support the main shaft from all sides. This type of bearing was chosen because of its smooth operating characteristics and minimum friction. A solution of water and propylene glycol which is not only nonflammable but harmless to personnel coming into contact with it was chosen for the hydraulic fluid. The glycol fluid required special deaerators because of its capacity for retaining air bubbles.

The arm is driven by three electric motors acting through a common gear system. Together they deliver 330 horsepower. The main drive system is augmented by six flywheels deriving their power from small hydraulic motors. Energy is built up gradually in the flywheels over a period of 15 minutes or more and then transferred to the centrifuge by a set of aircraft disc brakes used as clutch. The flywheel drive adds about 15,000 horsepower for quick thrust during the brief period that it is in action. Although this capability is in place, it is not in use. The design calculations predict onset rates of 10G per second for the main arm using this "hi-drive system". The electric motors maintain the high velocity obtained by the rapid onset of acceleration from the flywheels.

In order to prevent large bearing forces due to unbalanced weight distribution, good main arm balance is essential. Conventional methods used for balancing centrifuges could not be used since they depend on measuring minute changes in length of the centrifuge arm under centrifugal force. The main arm of the Dynamic Environment Simulator is so stiff that its elongation under load cannot be measured. It

was, therefore, necessary to develop a special method of balancing that makes use of small changes in the hydrostatic bearing pressures as the arm is rotated at low speeds. In spite of the large weight of the arm (over 300,000 lb), the balancing method, which utilizes a digital computer, is able to detect an imbalance of less than 100 lb in the capsule.

When immediate medical attention is necessary, the machine must be brought to a stop in minimum time. Even unforeseen events, such as power failures, must not interfere with emergency procedures. The centrifuge can be brought to a stop from rotations at its maximum speed of 56 rpm, corresponding to 20G, in 35 seconds, or at the rate of about 1-1/2 rpm per second, even if electrical power used for dynamic braking is not available. This is achieved by three emergency brakes that are engaged automatically upon loss of power, or manually by the operator of the machine. At the same time, the bearings can remain pressurized by means of fluid stored in accumulators which maintain the oil film between the bearings and the journal of the main arm so that rotation could be continued for as long as 70 seconds, or twice the shutdown time, without damage to the machine.

In combination with the motion of the arm, the two outer gimbals make possible complex rotary movements about the three axes of pitch, roll and yaw. The maximum acceleration force at some portions of the gondola when all three systems are operated at top speed is 85G. Forces due to gyroscopic precession would probably limit such three mode rotations but the limitations of the machine have neither been calculated nor demonstrated in these modes.

One of the most important features of the new centrifuge is the cab mounted shake table capable of vibrations in all six degrees of freedom. It has a maximum vertical translation of 12 inches and rotations of $\pm 30^\circ$ and $\pm 19^\circ$ in pitch and yaw respectively. Smaller displacements are obtained in yaw and the other two lateral translations. Peak shake table accelerations will be 15G with a combined payload and shake table weight of 1500 pounds.

To simulate the internal environment of aerospace systems, the capsule can be evacuated to an absolute pressure of about 3 pounds per square inch or approximately 45,000 feet. Over pressure of approximately 1 atmosphere is also possible. In addition, the equipment is in place to vary the temperature within the cab between 40 and 120°F and relative humidity from 10 to 95%. In practice, however, it is likely that thermal stress will be applied to the subject with the use of a small cab-type enclosure or thermally controlled clothing. For efficiency in programming experiments, interchangeable gondola or cab capsules or shells are provided, thus one experiment may be set up in advance while another is in progress on the DES. A separate signal patchbox is available so that the entire experiment instrumentation can

be set up in the off line gondola and complete test checkout and nondynamic experimentation performed.

All motions of the Dynamic Environment Simulator are controlled by a digital computer which also monitors the status of the main subsystems and automatically initiates shutdown in case of malfunction or emergency. Emergency stops can be called for either by the medical monitor or the machine operator or the subject inside the capsule. The medical monitor is able to watch the subject by means of two closed circuit TV cameras and can also gauge the magnitude and direction of the G forces applied to the subject by means of a special display.

The standard operating procedures for the function of this device are built around three major operating areas. The operating areas are further composed of integrated teams. For example, in the medical monitor's room area, there are four stations: (1) test director, (2) medical monitor, (3) instrumentation, and (4) experimenter. Other areas are the machine operator's room and the pit.

The data acquisition and processing system provides for the collection, processing and display of experimental data. Approximately four hundred signal channels are available for either physiological signals, performance measures or power transmission. A hybrid data processing system composed primarily of an Adage Ambilog 200 system serves two functions: (1) The on line new real time processing of biomedical signals to be displayed to the medical monitor for medical monitoring of safety purposes. For example, EKG and respiration signals can be transformed into appropriate rates, heart and respiratory rates or rate of change of rate and displayed on a sequential time based display in front of the medical monitor. (2) The preprocessing of experimental data with the preparation of digital tape output of experimental data. At this point, it is readily seen that the system is designed with the concept of man rating safety and ease of function. It is necessary to formalize the safety concept and to provide a succinctly reviewable package describing the system and insuring that there are no omissions of safety requirements. This led to development of the man rating approach adopted for the DES.

MAN RATING THE SYSTEM

To satisfactorily resolve any unforeseen problems and meet the requirements for man rating a simulations facility, such as is described in the first part of this report, a man-machine team system philosophy was developed and utilized. A document which includes all subsets of the system was written and provides the backbone of the safety analysis. The document is intended to collect, analyze and collate all that material pertinent to man rating the DES. Safety considerations as applied to the DES operation are broken into three related considerations: subject safety, operator

safety including all industrial/occupational safety and environmental health considerations and facility safety.

The man rating procedure includes: (1) a detailed review of the safety considerations designed into all subsystems by reviewing as-built drawings of the major subsystems; (2) a detailed safety analysis conducted using the "worst possible case" or "failure mode" method. The pertinent components of each subsystem are identified as potential failure sources. The nature of the failure of a system or component is specified and its consequences established. The policies, methods and procedures to prevent such failure are listed. Systems studied include: structures, power/electrical, hydraulics/bearings, electronics, communications/control, data handling and air conditioning. Selected structural, electrical, control and operational failure modes are listed. Safety considerations are also implicit in operating procedures as well as the physical facility. Typical medical emergencies are manually inserted to develop reaction capabilities of the operating team. An ideal communication system for this facility was developed and implemented. The emergency system includes two types of planned shutdown, emergency air, power and fire protection systems. The man rating study provides logical organization and continuing analysis to achieve absolute or fail-safe safety standards for the operation of a manned environment simulator. The organization of the collected analyses provides a compendium of system information in the form of drawing files, specific safety analysis, industrial safety surveys, operating and administrative procedures.

The operation of this facility requires a well integrated team of approximately 12 people. Specific functions include test director, machine operator, pit operator, floor monitor, computer operator, medical instrumentation, investigator and medical monitor. The machine analysis currently reviewed is limited to the following configuration of the DES: main arm - rotation up to 35 rpm (approximately 8G) at 0.5-1G per second onset rate; fork - position holding capability for simple centrifuge runs with simple rotation up to 30 rpm with arm and cab locked; cab - position holding capability for simple centrifuge runs simple rotation up to 90 rpm as a short radius centrifuge; shells - perform as wind shield only; and restraint - seat design rated to 12G and direction perpendicular to platform with 500 lb subject payload. Subject restraint is designed to function in motion at G levels described above.

The heart of the analysis is developed in a tabular format listing Structures and Functions. The format forces a recognition of a potential system fault and a documentation of preventive measures. Table 1 shows selected portions of the analysis.

DES RESEARCH PROGRAM

The DES is presently programmed to support Air Force research efforts in two technical areas: biodynamics and combined environmental stress. A summary of the work units that the DES is to support in the next five years has been prepared. Specific support will be given to the development of the B-1 and F-15 systems in particular.

Although programmed to meet Air Force data requirements for the design of planned and proposed aircraft systems, the Dynamic Environment Simulator represents a national research capability capable of supporting the requirements of many R&D programs including manned space flight, high speed surface transportation and other systems or functions where man is exposed to physical environmental stresses in combination.

EPILOGUE AND ACKNOWLEDGEMENTS

The development of a complex state-of-the-art facility such as the DES includes personnel as well as technical considerations. The DES cost 6.5 million dollars and six years to build. That it exists is tribute to the foresight and dedication of a large group of scientists and managers. All of the problems of advanced systems development: technical administration and fiscal were present, and ultimately resolved. The list of credits is long. Well over 200 people devoted significant amounts of personal effort and energy over prolonged periods. Of the authors, Mr. Cappel of the Franklin Institute Research Laboratories was the principle investigator and design engineer, M. McCally, M.D., Chief of the Environmental Medicine Division of the Aerospace Medical Research Laboratory was the Air Force project engineer and monitor and Captain Rogers, Chief of the Dynamic Simulations Branch, accepted the system from the contractor and set up the systems operation program including final system testing, man rating and operation. Alvin S. Hyde, M.D., Ph.D., 11457 Washington Plaza West, Reston, Virginia, wrote the initial specifications and began the program, with Colonel A. S. Swan. Laboratory Commanders, Colonels A. Karstens, J. Quashnock, R. Yerg and C. Kratochvil provided the vital administrative support. The Raytheon Corporation designed the controls and the major subsystems and now support the maintenance and operations activities. Subcontractors selected for the construction of major components and subsystems deserve the highest credit for the excellence of their workmanship, and include: B. G. Danis Company, Dayton, Ohio; Digital Equipment Corporation, Dayton, Ohio; Foremans, Dayton, Ohio; General Electric Company, Cincinnati, Ohio; Goodrich Company, Troy, Ohio; Helldoerfer-Castellini Incorporated, Dayton, Ohio; Honeywell, Dayton, Ohio; Hughes Bechtol Incorporated, Dayton, Ohio; Walter M. Litsey Incorporated, Dayton, Ohio; Muth Brothers, Dayton, Ohio; Mutual Electric Company, Dayton, Ohio; Ohio Valley Painting

Company, Dayton, Ohio; Raytheon Company, Wayland, Massachusetts; Stevens Company, Fairborn, Ohio; Tibbetts Plumbing and Heating Company, Dayton, Ohio; Timons, Butt and Head Incorporated, Dayton, Ohio; Wiley Company, Huntsville, Alabama and finally, Mrs. Carole Smith who prepared this report and many others during development of the DES.

Figure 1. Dynamic Environment Simulator (Elevation)

1. Main Trunnion
2. Rotating Housing
3. Fork Shaft and Fork
4. Gondola
5. Flywheel
6. Sustaining Drive Motor
7. Fork Drive Motor
8. Gondola Drives
9. Acceleration Drive Pinion
10. Sustaining Drive Pinion
11. Thrust and Radial Hydrostatic Bearings
12. Slip Ring Tower
13. Motor Driven Counterweights
14. Multiple Disc Clutches

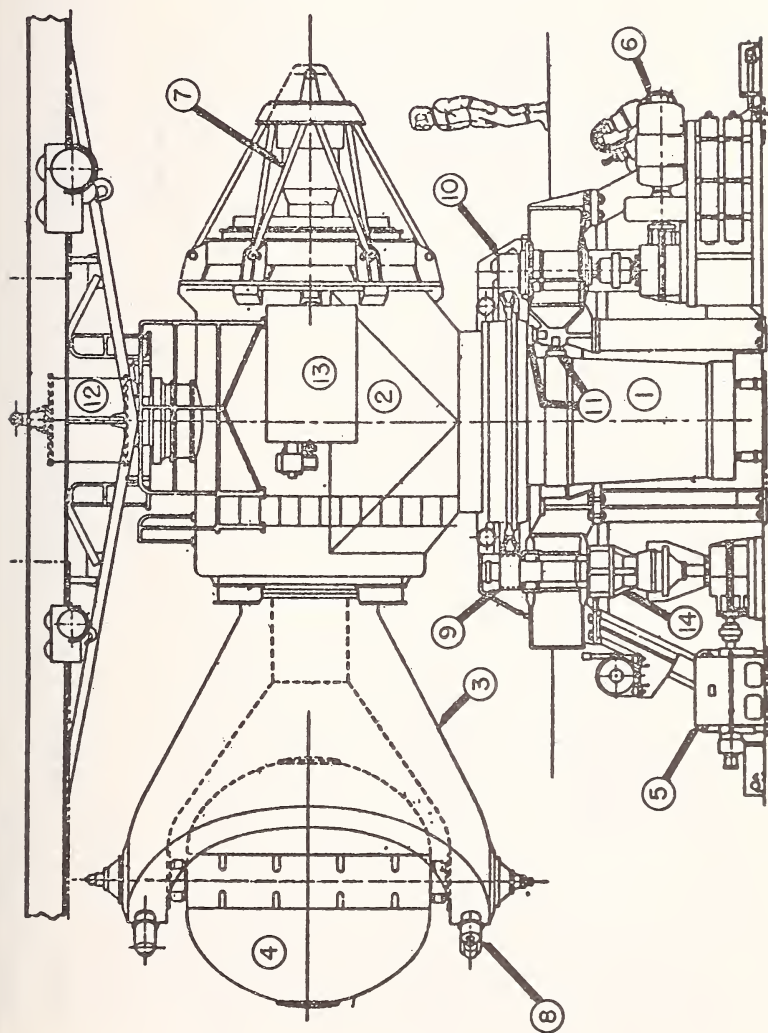


TABLE 1.

FAILURE MODE ANALYSIS

STRUCTURES

<u>SOURCE</u>	<u>FAILURE</u>	<u>CONSEQUENCES</u>	<u>PREVENTION</u>	<u>REFERENCES</u>
building	inadvertent door opening during operation	damage to the machine or injury to the involved personnel	a. control of all doors is achieved with interlock system b. positive control of all areas during operation is achieved by strictly enforced standard operating procedure c. warning lights system d. warning buzzer system	a. see standard operating procedures b. see standard machine operation procedures
power distribution	exposed electrical lines or terminals	electrical shock	a. routine maintenance, a. see surveys b. ground safety review	a. see maintenance procedures b. see consultation

TABLE 1 CONTINUED

<u>SOURCE</u>	<u>FAILURE</u>	<u>CONSEQUENCES</u>	<u>PREVENTION</u>	<u>REFERENCES</u>
hydraulic/fittings fracture anywhere in hydraulic supply to bearings - upstream of accumulators		loss of bearing	appropriate positioning of hydraulic accumulators assures hydraulic fluid source for duration sufficient to safely stop the machine	see test data and failure analysis
access to subject	access time greater than 1 minute	delay in medical diagnosis/treatment	a. standard operating procedures b. training c. emergency reaction plan	
	variables include: final cab position, magnitude and main arm velocity			

TABLE 1 CONTINUED

<u>SOURCE</u>	<u>FAILURE</u>	<u>CONSEQUENCES</u>	<u>PREVENTION</u>	<u>REFERENCES</u>
operations network	loss	test director goes to backup visual communication with machine operators/monitor with card system		

USE OF THE BEN FRANKLIN SUBMERSIBLE AS A SPACE STATION SIMULATOR

Matthew J. Ferguson¹

Chester B. May²

REFERENCE: Ferguson, Matthew J. "Use of the Ben Franklin Submersible as a Space Station Simulator," ASTM/IES/AIAA Space Simulation Conference, 14-16 September 1970.

ABSTRACT: This paper presents the NASA-sponsored effort using the Ben Franklin submersible as a space station analog during the 30-day drift mission in the Gulf Stream, starting 14 July and ending 14 August 1969. The areas of investigation include: (1) Psychological and physiological measurements during the pre-mission, mission, and post-mission phases were related to observed crew behavior. The results reveal that detailed consideration must be given early in the design to those aspects which could cause crew annoyance and frustration, and which could be further aggravated by long confinement. Selection of crew pairs for compatibility of personality will help reduce stress in small closed systems. (2) Habitability in a closed ecosystem was investigated. The objective was to determine the suitability of BEN FRANKLIN submersible habitability data for providing guidelines for future spacecraft design. These include provision for privacy, control of temperature and humidity, and adequate facilities for personal hygiene. (3) Microbiological investigation as a study of the effect of total biological isolation upon the flora of the crew, environmental and life support subsystems. The continuing shift and simplification of microbial flora on the 30-day mission indicates a need for investigation of the problem in association with longer space missions. (4) The maintainability experiment objective was to obtain detailed information on the frequency, duration, type, and complications of onboard maintenance during the mission.

¹Ocean Systems Dept., Grumman Aerospace Corp., Bethpage, N.Y.
²Advanced Systems Office, NASA, Huntsville, Ala.

KEY WORDS: space station simulator, submersible, closed ecological system, psychology, physiology, habitability, microbiology, microflora shift, maintainability prediction.

INTRODUCTION

Background. The 30-day Gulf Stream Drift Mission (GSDM) was conceived by Dr. Jacques Piccard in 1965 to explore the Gulf Stream from Florida to Nova Scotia using visual observations, bottom photography, biological surveys, and acoustical surveys. Early in 1967 the Grumman Corporation agreed to undertake the mission and established a program for the design, development, and construction of the BEN FRANKLIN (Figure 1).

During the design and development phase, the similarities between the GSDM and space missions became apparent. At the same time the NASA Office of Manned Space Flight awarded Contract NASW-1965 to Grumman to study the feasibility of using undersea facilities as space mission analogs. Final Report OSR-68-6, 11 March 1968, "Feasibility Study - Use of Submersibles as Space Mission Analogs," presents the results of the contractual effort. It was concluded that submersible missions would be reasonable analogs of space missions. Both types of missions would be manned by scientific and engineering crews motivated by a scientific purpose to work under operational hazards. Therefore the submersible could provide space programs with data on crew reactions, the man-machine interface, habitability, and the effects of complete biological isolation during a long mission. In support of these conclusions, NASA awarded Grumman a contract to study these factors during the GSDM.

The Naval Oceanographic Office (NAVOCEANO) agreed to support the ocean mission by providing a surface vessel and two BEN FRANKLIN crew members to perform ocean experiments. The remainder of the crew of six consisted of two pilots (including Dr. Piccard), a relief pilot and oceanographer, and a NASA crew member responsible for the NASA effort.

The GSDM began on 15 July 1969 when the BEN FRANKLIN submerged into the Gulf Stream off West Palm Beach, Florida. It terminated 30 days, 11 hours later when the BEN FRANKLIN surfaced 360 miles south of Nova Scotia. The drift covered 1444 n mi at an average depth of 650 ft. Ten excursions were made to depths between 1200 and 1800 ft. The mission was supported by two oceanographic ships, two land bases, and a mobile support van.

Submersible Advantages. The Gulf Stream Drift Mission (GSDM) generated data and information applicable to space missions which could not be acquired through other forms of ground-based simulators. The mission tasks, the diversified crew, the sealed environment, and complete physical separation from the outside world, produced unique problems. For example:

- The diversified crew and their interaction with the support team indicated potential command (organizational) problems.
- Microflora of the crew and within the vehicle tended to simplify and to move toward a microbial imbalance which might prove harmful over extended periods of time in isolation.
- Limitations of communications caused the crew to feel cut off from the world. In addition, a lack of private communications with the surface prevented personal discussions with families and physicians.
- Complete isolation and separation forced the initial provisioning of all food. Foods were pre-mission tested and accepted, but under mission conditions were found to be unsatisfactory.

The submersible provides a means for evaluating the operational effectiveness of crew habitability factors (food, clothing, accommodations), crew skill mix, command structure, and selected spacecraft subsystems checkout and maintenance during a real ocean mission.

To date, manned space operations, habitability provisions, and life support hardware have been tested in ground-based static simulators or chambers. However, as test durations have increased in manned testing, motivational problems have resulted due to a lack of meaningful work activities. The GSDM showed that the submersible overcomes this problem since a variety of meaningful scientific tasks are performed by the crew in support of the mission. At the same time, the effectiveness of candidate long-duration spacecraft hardware, operational procedures, and crew interactions can be evaluated in a closed, stressful environment.

Submersibles and ground-based chambers are complementary. Chambers are required for thermal, vibration, radiation, and life tests under simulated environmental conditions. The submersible offers a means for expanding on such tests by providing men and equipment an analogous mission environment. Figure 2 lists the many similarities between spacecraft and submersibles and compares them with chamber studies to date.

GSDM Inputs to Manned Spacecraft Systems Design. The objective of the NASA contract was to explore the areas of psychology and

physiology, habitability, microbiology, and maintainability to obtain spacecraft design criteria. The GSDM schedule precluded the acquisition and installation of space subsystems. BEN FRANKLIN subsystems and operations were, therefore, the basis for the space-related studies, and only incidental space equipment was provided. The following are a few examples of the types of spacecraft design guidelines supported by the data from the NASA contract:

Crew Accommodations

- Design and locate bunks for conversion to private lounges for relaxation, reading, and writing.
- Soundproof the crew quarters and locate them as far as possible from operating equipment and work areas.
- Separate work and living/recreation areas. Where limited volume prevents this, activities must be scheduled to avoid overlap and interference.
- Provide for private communications with family and friends.
- Provide privacy, recreation, and storage for personal belongings.

Food

- Provide home-type food and preparation facilities.
- The crew should not be forced to accept a monotonous diet and disagreeable foods.
- Variety and individual preference should be considered.

Clothing

- Daily underwear change is essential for comfort
- Provide for internal environment off-design temperature conditions.
- Provide two-piece garments rather than jumpsuits for ease of personal hygiene functions.

Biotechnology

- Develop automated on-line contamination monitoring and provide simple means for decontaminating the vehicle surfaces, internal atmosphere and water management subsystem.
- Compartmentize the spacecraft to reduce spread of contamination.
- Provide negative pressure in hygiene areas to prevent issue of contaminants into living areas.
- Choose materials and designs to minimize microbial nutrients and breeding grounds.
- Provide microbiological screening of crew to eliminate pathogen carriers.

- Monitor individual crew microbial makeup to detect potential spread of infection.
- Provide for microbe incineration, in addition to filters, to assist in atmosphere decontamination.
- Provide safe means for final disposal of microbially contaminated items.
- Provide an on-board microbiological laboratory to facilitate prompt analysis.

Maintainability

- Develop specific maintenance skill levels, experience and training requirements for crew members on long duration space missions.
- Develop the facilities required for on-board off-line repair of space equipment.

A study of the command structure during the GSDM was not part of the NASA contract, but it is evident that such a study would have provided valuable data for space missions. The BEN FRANKLIN crew comprised a "mini" crew of scientists and operational personnel similar in composition to spacecraft crew mixes. During the GSDM, operations problems arose related to command structure, scientific/operations personnel skill mix, and the mission control team decisions made on the support ship, PRIVATEER. These problems are analogous to those anticipated in space station operations. An investigation into the causes and resolution of such problems in submersible missions could help provide insight into the handling and prevention of similar situations on future space missions.

Recommendations - During BEN FRANKLIN ocean missions in the future, the space investigations of the GSDM should be expanded to further develop general space technology and to support the skylab, the space station, and the space base programs.

Psychology and Physiology

- Crew performance evaluation
- Biomedical instrumentation
- Crew selection test verification
- Work task unit

Habitability

- Personal hygiene provisions
- Food management
- Clothing

- Recreation provisions
- Noise control
- Personal accommodations

Biotechnology

- 60/90 day mission with crew rotation
- H₂O and atmosphere contaminant measurement and control
- Spacecraft and subsystems decontamination

Subsystems Operation

- Water management
- Waste management
- Atmosphere storage/supply

Maintainability (of space equipment)

- Failure prediction techniques
- Scheduled and unscheduled task analysis
- Spares and tools requirements
- Repair techniques/operations

Mission Operations

- Command Structure evaluation

PSYCHOLOGY AND PHYSIOLOGY

Objectives. The objectives of this portion of the study were:

- To relate observed crew behavior to variables (engineering design, choice and training of crew) which designers and mission planners can use to influence space systems performance.
- To investigate the physiological aspects of the 30-day confinement.

Approach. Pre-mission data were obtained to establish a personality profile of the crewmen, to establish a physical fitness index, and to develop a baseline on a motor skills test.

Data were obtained during the mission by means of a daily questionnaire or log that included, in addition to items related to the operation, the mission and the environment, the Cornell Medical Index, a Mood Scale Check List, a Subjective Stress Scale, a Sleep Recall Questionnaire, a number of tests to evaluate fitness, and daily tests of proficiency on the Langley Research Center Complex Coordinator.

Time-lapse photographs were obtained of most of the vehicle with 3 cameras, and approximately 1 hour of conversation each day, was recorded on tape.

Upon their return to Bethpage, N. Y., the crewmembers were given the following to complete for the debriefing with the psychologists:

- The Group Confinement Inventory (Retrospective)
- The Isolation Symptomatology Questionnaire (Retrospective)
- The Hostility Symptomatology (Retrospective)
- The Primary Affect Scale

Five of the men returned them immediately, and the sixth about a month later.

Results. Although selected only for special skills and desire to participate, the crewmen assigned to work together were reasonably compatible. Predictions of crew behavior based on pre-mission psychological tests, clinical interpretation and observation of the crew were proven reasonably accurate in the mission. However, the number of personality tests might be considerably reduced and still provide the same degree of insight.

Predicted annoyance and psychological stress were produced by the austere BEN FRANKLIN characteristics. These included the bunks, their location, food, the small galley, people noise, odors, lack of privacy, clothing, inaccessibility of equipment, limited personal hygiene facilities, and environmental control.

As time increased, the men showed a general trend toward withdrawal and an increased need for privacy. This was evidenced in part by the crewmen's tendency to eat more and more meals alone as the mission progressed. None of the crewmen reported psychosomatic or hypochondrical symptomatology. Depression was greatest and the sense of personal well-being lowest at the mid-point of the mission (scores for these factors were extracted by Naval Medical Research Institute's factor analysis computer program).

None of the crew suffered serious deterioration in proficiency. However, as judged from measurement of complex coordination, changes in proficiency in one instance could be related to a mood of depression. Potentially serious problems resulted from failures and misunderstandings in communications with the surface crew. This was especially true when expected personal news was inexplicably lacking.

Events in the GSDM indicate that expected communication of personal news at regular intervals probably is unwise because, if communications are delayed or interrupted, crewmen tend to feel anguish and concern. On the other hand, a lack of private communications to the surface was a source of annoyance during the mission.

Food provided a topic of conversation and possibly allowed for at least limited sublimation of psychological stress. Other topics such as daily questionnaires and the interactions with support personnel, accomplished the same result. These are not, however, appropriate avenues for the release of tension. Investigation is recommended to develop more acceptable techniques to relieve psychosocial tension.

The physiological investigation included analyzing data obtained prior to, during, and after the mission. These covered a physical fitness index, wrist and forearm strength, recovery pulse, blood pressure, oxygen utilization, and weight. None of the crewmen showed signs of physical deconditioning, although some had a weight loss. All were declared by the Grumman physicians to be medically fit subsequent to completion of the drift mission.

Inputs to Space. Detailed consideration must be given early in a design to those aspects which could cause crew annoyance and frustration, and which could be further aggravated by the long duration confinement. Particularly important are:

- Environmental control/life support system
- Privacy areas
- Illumination
- Noise
- Food/preparation/clean-up facilities
- Recreation
- Work areas
- Multiple use of spaces
- Personal hygiene

Selection of crew pairs for compatibility of personality characteristics will help reduce psychological stress in small closed systems. In addition, the mixed crews of future space missions should have a voice in the selection of teammates. A better understanding of the importance of this input is required and further investigations are recommended.

Performance rating both psychological (clinical) and operational can be obtained by self-reporting of the crew if they believe that the information they provide will be held in confidence. The development of improved techniques is recommended for obtaining self-evaluations by the crew with the intent of reducing the number of questions, eliciting observations not specifically called for, solicitations of reports about others and for reporting during a mission. An objective measure of skill by a device like the Langley Research Coordinator appears to be predictive and was accepted by the crew. Further investigation to develop its utility is recommended.

HABITABILITY

Objective. The objective was to determine the suitability of BEN FRANKLIN habitability data for providing guidelines for future spacecraft design. Factors considered in the study were food, clothing, control of environmental conditions, hygiene provision, crew equipment items, and crew reactions to these provisions.

Approach. The procedures and records used in the study included:

- Time-lapse cameras located at three places, set to function every two minutes.
- Environmental measurements (light, noise, temperature, etc.).
- Counters to measure use of toilet facilities, etc.
- Ship's log.
- Crewmen's personal logs and questionnaires.
- Debriefing
- Comparison of actual activities with planned activities in the Mission Plan.

Results. Analysis of the camera photos coupled with a study of the logs established a record of each man's location and activity throughout the mission. From these studies of area utilization and deviations from planned activities, it was determined that generally, half of the crew followed their plan and half did not. Figure 3 illustrates this type of analysis on day 1 of the mission, crewman #1 deviating from the plan and #6 following the plan. Also shown are the planned and actual hours spent at each location. These deviations are due in part to lack of pre-mission training establishing each man's role and to changes in work/rest cycles. The significant factor from this habitability standpoint is the overlap of work and recreation activities in a given area.

The ten top complaints on questionnaires and volunteered complaints are shown in Figure 4. These indicate items which demand man/machine consideration both in submersible and spacecraft design.

Food complaints stemmed principally from the difficulties in preparation. Cooking was ruled out since it would contaminate the atmosphere. Canned and freeze dried food was provided and was satisfactory from a nutritional and storage viewpoint. However, complaints about food increased with time.

The crew complaints on privacy and free space are presented in Figure 5. A maximum of four complaints were made on Day 15. The complaints decreased to one on Day 22 and started to increase to Day 29. It is interesting to note that no complaints were volunteered throughout the mission. The principal complaint was that each crew member needed a place other than his bunk.

Although the bunks were oversized, the crew complained that it was not possible to sit up or bend knees without hitting the pressure hull.

Atmospheric conditions were monitored and recorded throughout the mission. Variations were readily maintained within allowable physiological limits. Atmospheric constituents and trace contaminants were monitored with Drager Tubes and a gas chromatograph. The Drager tubes identified a continuing rise in CO throughout the mission to a maximum of 40 PPM, identifying the need for greater capacity in the CO removal apparatus.

On the basis of the habitability study during the drift mission the following guidelines are recommended for future spacecraft design:

- A separate area with soundproofing, adequate lighting and comfortable chairs, is needed for reading and writing.
- Sleeping quarters should be isolated from the noise of the work area.
- Food preparation devices and techniques should be simple.
- Environmental monitoring should be automatic to free the crew for more useful activity.
- Clothing and bedding for space stations should be evaluated at off-design conditions, to determine their adequacy.
- Illumination levels should be adequate for the task to be performed.

- The crew's use of the vehicle, crew activity, crew time lines, crew living and working areas require detailed consideration and integration.

MICROBIOLOGY

Objective. The 30-day submergence during the GSDM produced a unique internal environment which, with regard to biological isolation, closely resembles that of future spacecraft. The objective of the microbiological investigation was to study the effects of total biological isolation upon the flora of the crew, environment and life support subsystems.

Approach. For comparison purposes, pre-mission, mission, and post-mission sampling were scheduled. To make the bacterial counts, a variety of sampling media and devices were taken aboard including:

- Andersen samplers, (atmosphere)
- Swabs and agar plates (human and surface environmental sampling)
- Field-type water monitoring unit (field monitor kit).

Food was tested for bacterial count pre- and post-mission. Waste, garments and linen were stored on board until the completion of the mission and were then returned to the biotechnology lab for bacterial counts and identification of the types of bacteria present. Approximately 15,000 separate culturing steps were required to identify to Genus the 2230 isolates obtained.

Results. There appears to have been a general simplification and shift towards gram-negative organisms, (Figures 6 and 7), particularly *Pseudomonas* and *Aerobacter*. This has been postulated as an effect of long term isolation, but could have been biased by on-board sample incubation at low temperature, followed by long-term storage, or by the use of antimicrobial soap.

With the exception of one crew member (who had a history of Staph infections), there were only transitory occurrences of Staph Aureus in the crew and the environment (Figure 8.) Beta Hemolytic Streptococci were isolated from 5 of the 6 crew members (Figure 9). These 5 also developed upper respiratory infections during the early mission phase.

Contamination levels of the foods were well within acceptable limits both pre and post mission.

Garments and linen had generally low levels of contamination when cultured after use and onboard storage. It would appear that antimicrobial treatment of garments and linen were effective in suppressing bacterial proliferation and odor.

Iodine treatment was planned for control of the cold water system microbial contamination. However, the crew objected to the iodine taste in the water and the reconstituted food. In addition, the iodine treatment was difficult to perform and was not implemented. This contributed to cold water contamination.

Pseudomonas, which had been a problem during much of the pre-mission attempts at cleaning the system reappeared as a consistent contaminant. Later in the mission a variety of human associated organisms were recovered, including the fecal *E coli*. Several filters (head, galley, shower-sink) were found to be contaminated with *Pseudomonas* when cultured post-mission. Serious discrepancies existed between the on-board readings and base laboratory analysis of the same sets of samples. (Many samples read as "sterile" on-board were discovered by base lab analysis to be contaminated.) This was attributed to the limited facilities on board the BEN FRANKLIN:

- Low-temperature incubation
- Poor lighting
- Lack of experience

Provisions were made for dispensing germicides, replacing odor control canisters, and adding antimicrobial agents to the waste storage tanks. During the mission, macerator electrical problems prevented proper mixing of germicide with waste. This resulted in noticeable odor levels.

The effectiveness of odor control in the waste management contamination control system was not evaluated during the mission. At post-mission sampling, all waste tanks were found to be contaminated with between 10^6 to 10^7 micro organisms/ml, most of which were of intestinal origin.

As the mission progressed, the environmental flora reflected more and more of those organisms found on the men. The pattern of a shift towards gram negative organisms with respect to number of genera isolated was also similar to that of the human flora. Cleaning appeared generally effective in attaining a transitory reduction of total microbial level, although a general rise in contamination persisted as the mission progressed. The initial clean-up appeared to

lower the microbial load considerably, because on Day 2, all counts were low. The dips in contamination levels can be related to cleaning procedures with transient drops in microbial counts on the walls and floors noted at the general cleanups. However, after cleaning, there was a rapid rise of the contamination level on the floors and walls. The contamination of the table tops increased with time at a slower rate because of the daily washings.

Even with the limitations imposed by schedules and funding, the microbiology study produced guidelines for spacecraft design. Many unknowns exist in the area of space microbial technology, and this test should be considered only as a basis for much additional work, i. e. :

- The continuing shift and simplification of microbial flora on the 30-day mission indicates a need for investigation of the problem association with longer space missions.
- The personal hygiene areas, and humid areas in general, are fertile microbe breeding grounds and require microbial control.
- The water and waste management systems are particularly fertile areas and require suitable contamination monitoring and simple decontamination provisions.
- The use of anti-microbials offers temporary advantages but the overall effect may be to create an undesirable microbial imbalance. Additional work is required in this area.
- The stored hot water system was effective in controlling contamination and should be a candidate for spacecraft. It could eliminate the need for biocides such as iodine or chlorine which are disagreeable in food and drink.
- Further testing is required on the effects of crew rotation, i. e., putting a new crew member into an altered environment.

MAINTAINABILITY

Objective. The objective of the maintainability experiment was to obtain detailed information on the frequency, duration, type and complications of the onboard maintenance performed during the Gulf Stream Drift Mission. This would permit evaluation of existing maintainability techniques for application to space vehicle missions.

Approach. The maintainability study covered:

- Analysis of the systems and equipment in the BEN FRANKLIN to establish spares, tools, test equipment, and estimated work loads.

- Preparation of maintenance procedure and data sheets, crew training, and dock side maintenance time trials, etc.
- Maintenance recording during the mission
- Reducing and evaluating data

This maintainability experiment did not encompass all of the equipment aboard the vessel. Systems and equipment were selected on the basis of criticality and available information on which analysis could be performed. This became the "controlled" portion of the study. Actual mission data was collected for all maintenance performed.

Logistics preparation consisted of crew training and of maintenance procedures, troubleshooting information, checklists, computation charts, spares, tools, and test equipment for the equipment in the controlled maintenance portion of the experiment. This was successful in satisfying the maintainability objectives. Crew comments indicated that this preparation was precisely what they needed for approaching the mission with confidence.

Results. The crew performed 1354 individual maintenance tasks, an average of 45 per day. Figure 10 shows the percent of total available manpower expended on maintenance during the mission. The maintenance workload actually required from 12 to 31% of the crew's total available duty time each day. On the average maintenance occupied the equivalent of one man full time throughout the mission.

Scheduled maintenance accounted for 1312 of the 1354 maintenance tasks (Figure 11). Successful completion of the remaining 42 unscheduled repair actions, however, assured mission success.

Two crew members performed 58% of all the maintenance work, but more significantly they accomplished 96% of the unscheduled repair actions primarily because of their highly skilled and maintenance-oriented background. Figure 12 illustrates the maintenance workload assumed by the one crew member who was the prime mover in all of the unscheduled repairs. His skill contributed to the mission's success and attest to the need for this type of crew member on all such missions.

The statistical analysis of mission data indicated that maintenance tasks time predictions by Method II of MIL Handbook 472 were reasonably effective in determining task times. Figure 13 shows a comparison of the results when regression analysis was applied to these predictions in mission action dock-side time trials, and an aircraft program as a control case. In view of the results, we concluded that

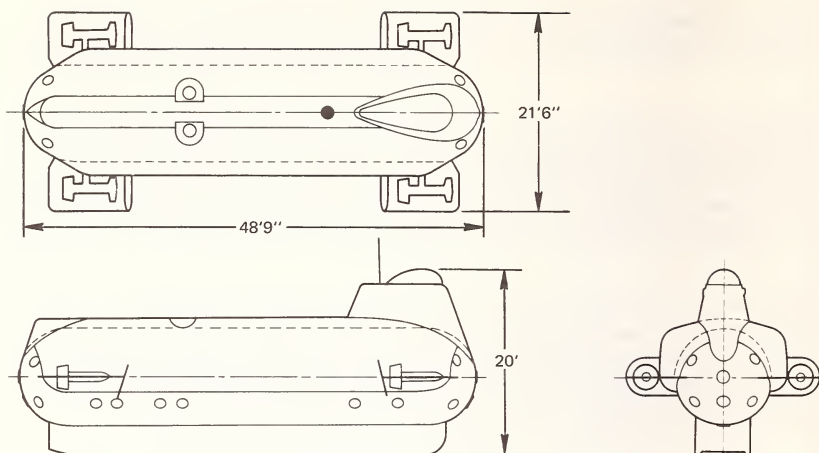
Method II was considerably better than Method III since it is more closely associated with actual hardware configuration and limitations.

Mission data analysis indicated that there was no discernible time differential for the performance of maintenance in the stress of this mission environment versus the relatively unstressed environment of the dock-side time trials. All crew members however, did admit to feeling the effects of stress at various points during the mission.

Since the GSDM maintainability studies were performed on submersible systems, no recommendations can be made concerning specific space systems. However, the study showed that the submersible could be used productively for testing maintainability techniques on space hardware under analogous mission conditions.

It was revealing to find that the equivalent of one man out of the six was required to perform maintenance tasks. Space stations will require many more highly complex subsystems, and mission duration will be measured in months and years rather than days. Hence, it appears that sophisticated analysis, training, and automatic failure detection methods will be required.

Since sophisticated training of many crewmen is expensive, it is apparent that means must be developed to reduce future space crew training. The submersible offers a facility to develop and evaluate alternative crew training procedures, with the aim of reducing crew training requirements and associated special skill needs.



GENERAL SPECIFICATION

DISPLACEMENT	130 TONS
LENGTH	48 FEET, 9 INCHES
BEAM (OVER MOTOR GUARDS)	21 FEET, 6 INCHES
HEIGHT	20 FEET
OPERATIONAL DEPTH	2000 FEET
COLLAPSE DEPTH	4000 FEET
SUBMERGED SPEED (MAXIMUM)	4 KNOTS
LIFE SUPPORT	6 MEN FOR 6 WEEKS
PAYLOAD	5 TONS
TOTAL POWER	756 KWH
VIEWPORTS	29

FIGURE 1 BEN FRANKLIN CHARACTERISTICS

	SPACECRAFT	SUBMERSIBLE	CHAMBER
CONFINEMENT	X	X	X
SOCIAL ISOLATION	X	X	X
DEPRIVATION	X	X	X
CLOSE QUARTERS	X	X	X
MEANINGFUL MISSION	X	X	
SUSTAINED MOTIVATION	X	X	
HOSTILE ENVIRONMENT	X	X	
OPERATIONAL STRESS	X	X	
REMOTE OPERATIONS	X	X	
ABORT DIFFICULTY	X	X	
REQUIRE REAL NAVIGATION	X	X	
SCIENTIFIC CREW	X	X	
DATA TRANSMISSION DIFFICULTIES	X	X	
ON-BOARD MAINTENANCE PROVISIONS	X	X	
COMPLETE BIOLOGICAL ISOLATION	X	X	
COMMAND STRUCTURE	X	X	

FIGURE 2 SIMILARITIES -SPACECRAFT/SUBMERSIBLE/CHAMBER

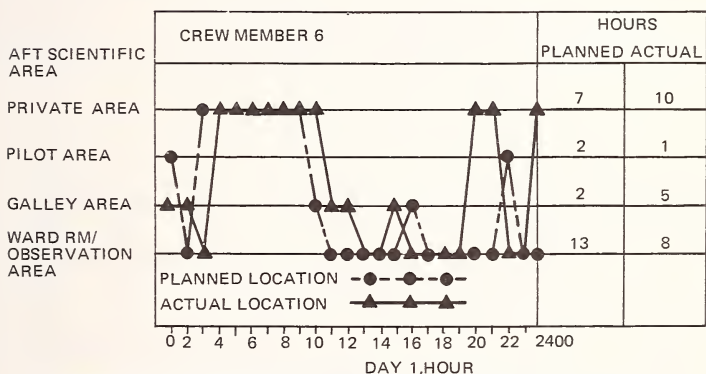
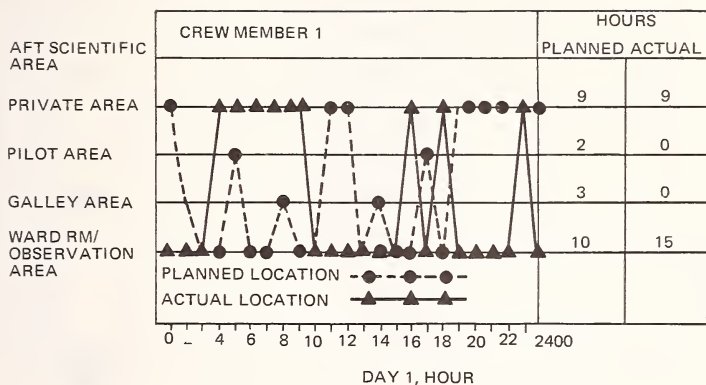


FIGURE 3 ACTUAL VERSUS PLANNED CREW MEMBER TIME LINES, DAY 1

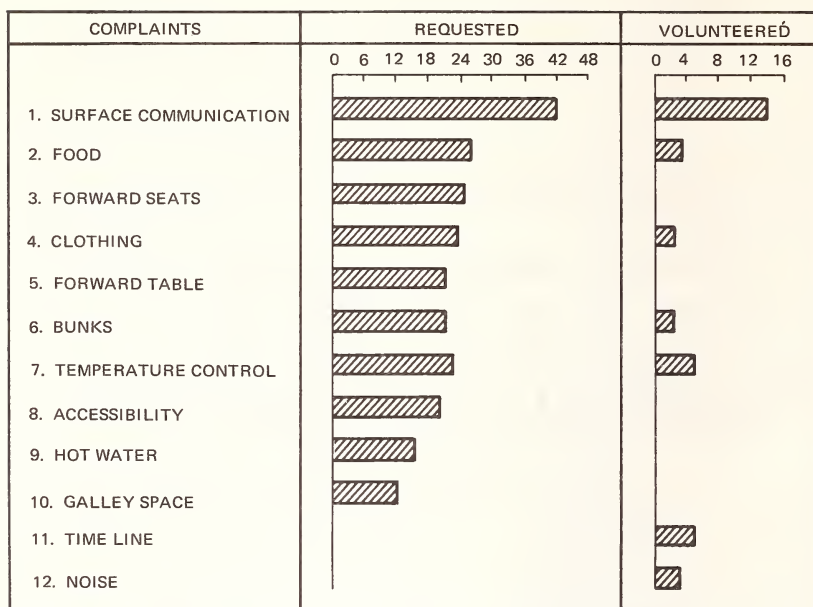


FIGURE 4 MAJOR HABITABILITY COMPLAINTS

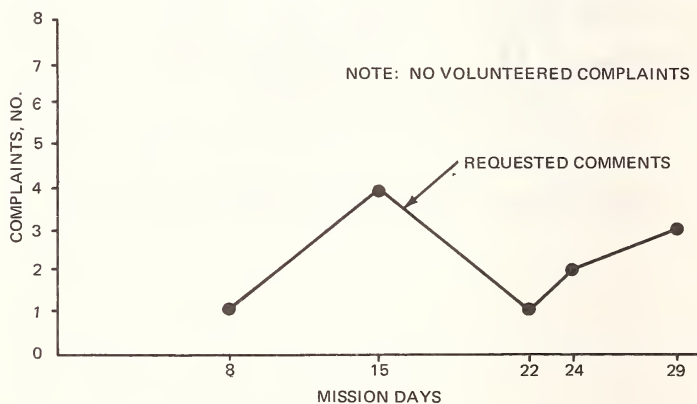


FIGURE 5 PRIVACY AND FREE SPACE COMPLAINTS

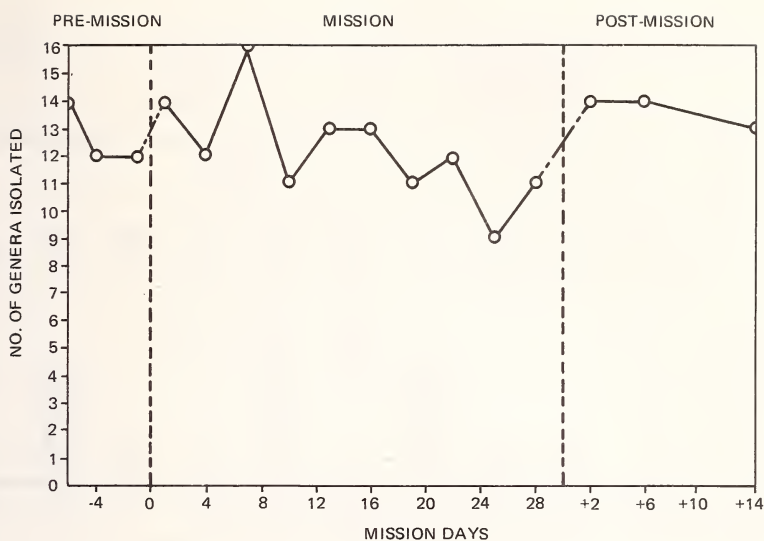
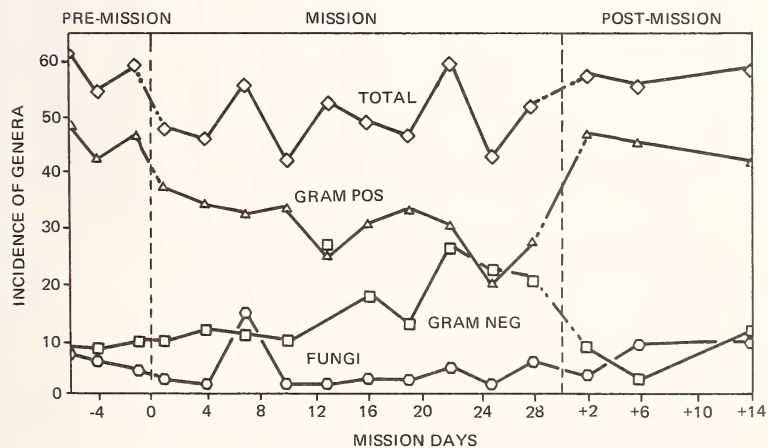


FIGURE 6 TREND OF TOTAL BODY SIMPLIFICATION



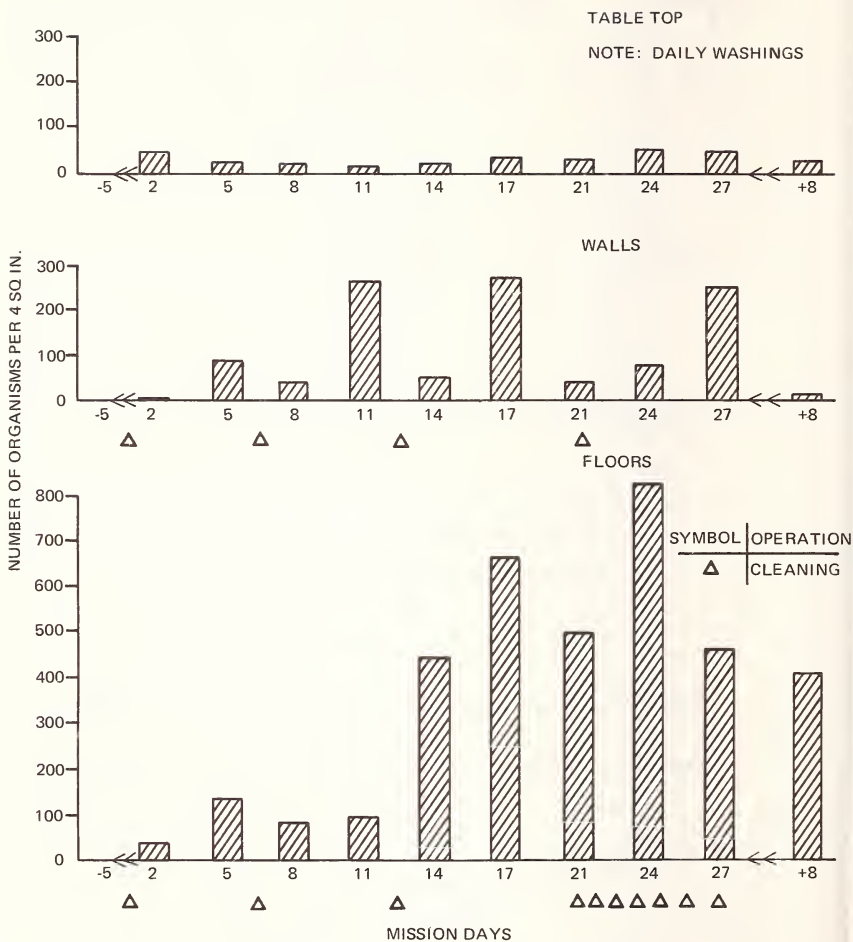


FIGURE 8 ENVIRONMENTAL CONTAMINATION

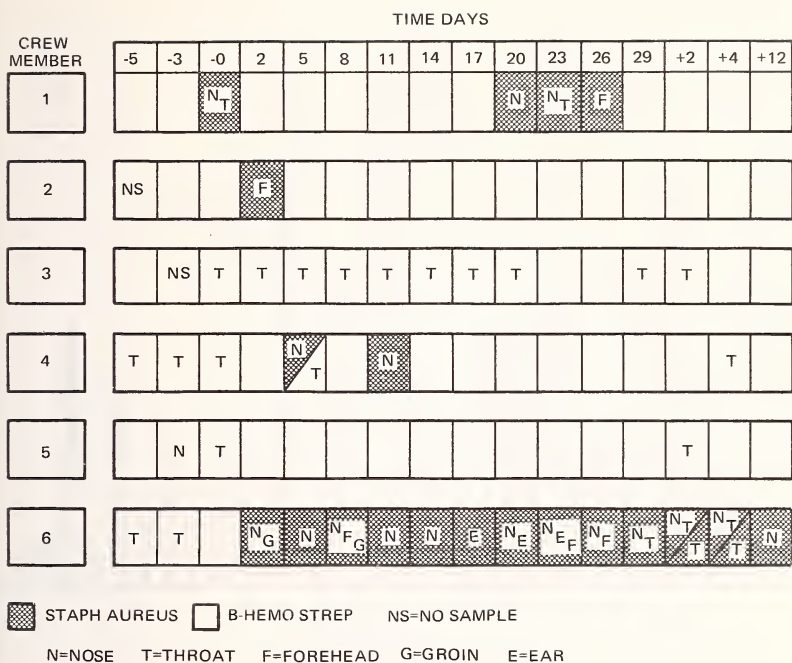


FIGURE 9 POTENTIAL PATHOGEN INCIDENCE

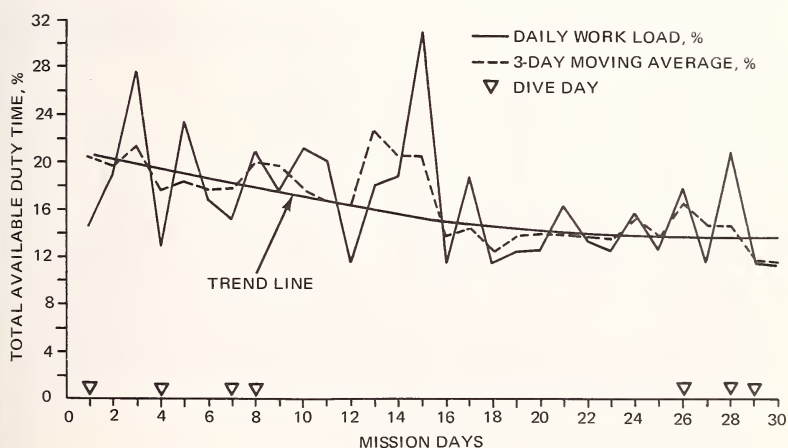


FIGURE 10 PERCENT MAINTENANCE MAN-HOURS OF TOTAL WORKING HOURS PER DAY

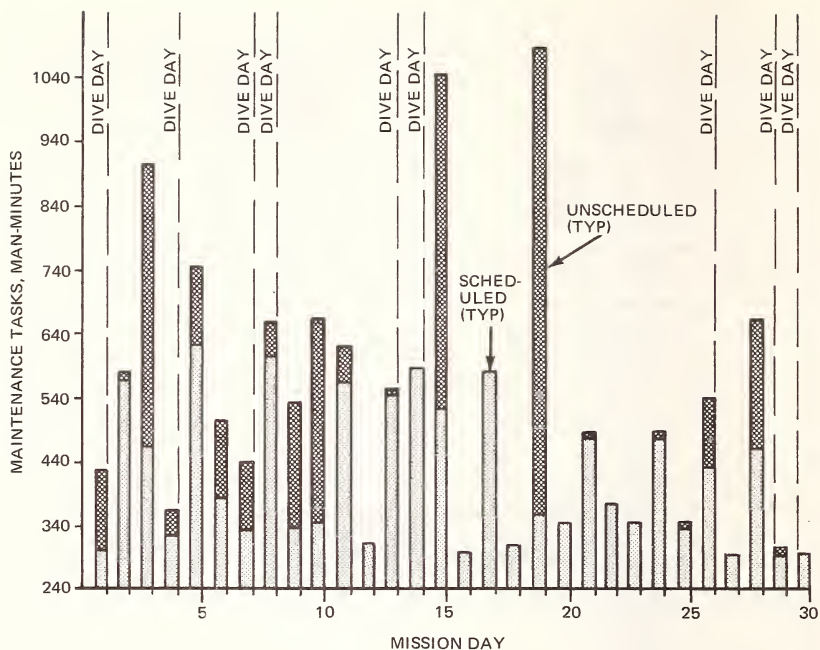


FIGURE 11 MAINTENANCE ACTION SUMMARY

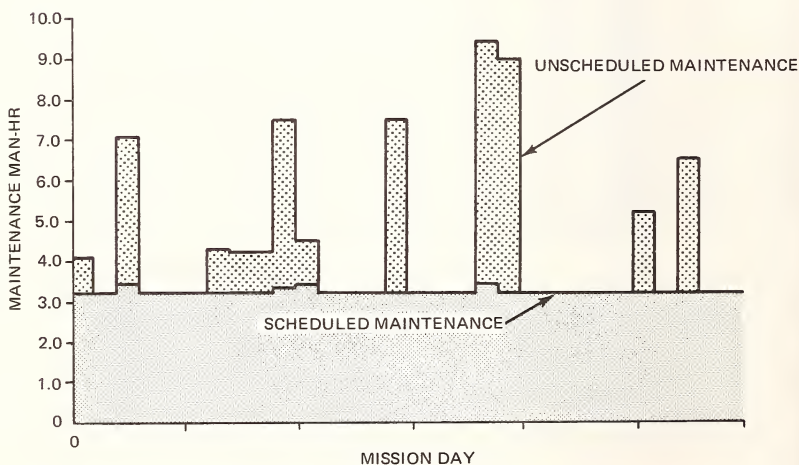


FIGURE 12 CREWMEMBER NO. 4 MAINTENANCE WORKLOAD BY DAY

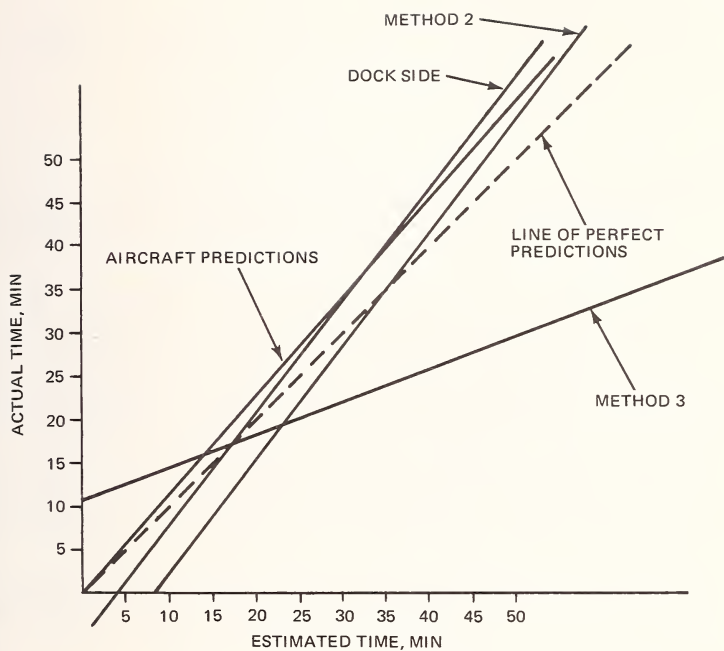


FIGURE 13 COMPARISON OF PREDICTION CHARACTERISTICS

DEVELOPMENT OF AN OPEN CIRCUIT CRYOGENIC LIFE SUPPORT SYSTEM
FOR USE IN NEUTRAL BUOYANCY SPACE SIMULATION.

1 2
C. M. McClure and C. W. Williams

REFERENCE: McClure, C. M. and Williams, C. W., "Development of an Open Circuit Cryogenic Life Support System for use in Neutral Buoyancy Space Simulation," ASTM/IES/AIAA SPACE SIMULATION CONFERENCE, 14-16 September 1970.

ABSTRACT: Marshall Space Flight Center has a need for a self contained underwater life support system which can supply a breathing mixture to the neutral buoyancy test subject, without the need for a surface tethered supply line. A prototype system has been developed which utilizes a mixture of liquid oxygen and liquid nitrogen contained in a single supply tank. Development and testing has shown that this system will supply the quantity and quality of gas required under completely controlled and predictable conditions to depths of at least 60 feet.

KEY WORDS: Neutral buoyancy, space simulation, cryogenics, liquid oxygen, liquid nitrogen, liquid air.

¹Senior Engineering Specialist, Hayes International Corporation, Missile and Space Support Division, Huntsville Alabama

²Scientist, Hayes International Corporation Missile and Space Support Division, Huntsville, Alabama

INTRODUCTION

Present neutral buoyancy space simulation techniques still model the tethered astronaut type of mission. Recent lunar surface operations and many future space missions under zero and sub-gravity conditions show the necessity for space simulation techniques which can model, with high fidelity, the umbilical-free astronaut missions. The present umbilical is used as the suit gas supply line. Therefore, a major type of equipment which is required to meet umbilical-free operations is a self-contained underwater breathing unit (SCUBA).

The Manufacturing Engineering Laboratory of the Marshall Space Flight Center has just completed the development of such a prototype system.

In order to develop the simplest system possible, it was decided to develop this backpack to be compatible with present suit systems in use in neutral buoyancy testing. This requirement results in retaining both the open circuit suit gas system and present suit through-flow gas rates. This combination could not be met without excessive weight and volume in a backpack using high pressure gas storage. Cryogenic liquid gas storage at subcritical pressure and high compressive potentials offered high storage efficiency without excessive weight or volume penalties. Further operational simplification was obtained by dictating that the diluent gas constituent be contained within a single liquid cryogen mixture. Neutral buoyancy depths easily allow choice of nitrogen as the diluent gas. Therefore the original design objective was for a single liquid mixture of liquid oxygen (LOX) and liquid nitrogen (LN₂) to be stored in a cryogenic system to feed the open circuit neutral buoyancy suit.

DESIGN REQUIREMENTS

Several design boundary conditions were established prior to starting this project; for principal importance were: (1) safety of operation, and (2) simplicity. Since the proposed apparatus must eventually be man-rated, the first condition follows as a natural consequence. The second requirement is merely a logical step towards achieving an operational state as soon as possible.

From these two basic conditions were developed certain specific design requirements:

1. The prototype was to be a breathing system of the "open circuit" type. "Open circuit" refers to the fact that the supply gas is dumped overboard after only one pass through the pressure suit. This system is currently used in Marshall Space Flight Center (MSFC) neutral buoyancy operations with an umbilical connection supplying a continuous flow of air through the pressure suit. Physiologically, this is the safest and simplest system; however, in addition to compromising simulation fidelity it is highly wasteful of the gases being supplied.
2. One hour duration was established as a target operational time for a single charging of the cryogenic tank.
3. Present suit through-flow rates of 5.0 ACFM (actual cubic feet per minute) were to be maintained at all depths. This means that as depth is increased, flow rate must also be increased to maintain 5.0 ACFM through the suit. If 45 ft. is established as the maximum operational depth, then the maximum standard cubic feet per minute (SCFM) rate on the bottom will be 2.36 times the surface rate, or 11.8 SCFM. In addition, it was felt that flow rates should be adjustable by the diver. From these considerations, a maximum flow capability of 16 to 18 SCFM was finally selected.
4. A cryogenic storage system was to be employed using a mixture of liquid oxygen (LOX) and liquid nitrogen (LN₂) in a single dewar. Cryogenic storage is necessary in order to supply the relatively large quantity of gas required.
5. Human safety and comfort parameters (breathing gas temperature, oxygen partial pressure, suit cooling, etc.) were to be maintained within the following limits:
 - (a) Air temperature should be maintained at a comfortable level between 68°F and 80°F.
 - (b) Oxygen partial pressure (PO₂) should be held within acceptable physiological limits. The minimum PO₂ of 0.20 atmosphere (152 mm Hg) is

the lowest allowable. The maximum PO_2 is less clearly defined; however, the Marine Technology Society has set a PO_2 of 1.33 atmospheres (1010.8 mm Hg) as the upper limit for continuous exposure. Other equally well qualified sources have set this figure at 1.25 atmospheres (950 mm Hg). In general, the spaceflight environmental control system (ECS) limits for maximum PO_2 have been set lower than either of these figures. The problem of maximum PO_2 is simpler in cabins sealed for spaceflight. These cabins have a total pressure which is 1.0 atmosphere or less. The hyperbaric PO_2 problem found in submerged operations is more difficult than for space cabins. With preset gas ratios, such as with air or any single liquid cryogen, the minimum (hypoxic) surface limit selected also presents the depth PO_2 curve. Therefore, under conditions of submergence with constant ratio gas mixtures a realistic maximum may well be those chosen by the quoted diving oriented-sources.

As a design goal, the PO_2 range from 0.20 atmosphere to 1.0 atmosphere was selected for this work.

THEORETICAL CONSIDERATIONS

Initial studies showed a major problem to be the positive control and delivery of safe oxygen partial pressures. Several important theoretical aspects relating to the overall problem are outlined in the following sections.

A. Oxygen Partial Pressure (PO_2) Control

In a vessel containing a cryogenic mixture of liquid oxygen and liquid nitrogen, the partial pressures of the individual gasses over the liquid components have been shown to obey Raoult's Law. This law, which applied for all possible concentrations, states that at any given constant temperature the partial pressures of the components of a mixture are equal to the mole fraction of the component multiplied by its vapor pressure in the pure state at the temperature of the liquid.

The liquid boiling and vapor condensing curve for oxygen and nitrogen mixtures is shown in Figure 1 and indicates that at 1 atmosphere pure nitrogen is saturated at about -320°F (-195°C) and pure oxygen is saturated at -298°F (-183°C). In

a binary mixture the simple terms "equilibrium or saturation temperature" do not exactly apply. In such a mixture, addition of heat and resulting liquid vaporization will shift both the mixture temperature and the gas and liquid phase composition. However, standard engineering terms are used throughout this section in reference to binary mixtures.

As an example consider a binary liquid mixture of 22% oxygen and 78% nitrogen contained as shown in Figure 1. The saturation temperature is about -317°F (-194°C). Under these conditions, this specific binary liquid mixture has in equilibrium with it a gas phase which contains only 8% oxygen which is well into the dangerous anoxic level. As this binary mixture continues to absorb heat, its sensible heat gain and subsequent temperature rise cause a disproportionate change in nitrogen and oxygen compositions. More of the liquid nitrogen boils off, resulting in a constant oxygen enrichment of the liquid phase, until the liquid is finally 100% oxygen.

As can be seen from the example above, any attempt to breathe the gas phase over the liquid mixture would be dangerous. From the analysis, it would seem possible to produce a gas phase containing 22% oxygen by starting out with a 50-50 liquid mixture. However, as useage continued, the partial pressure of oxygen would soon increase to a dangerous level especially in diving conditions. Thus, the situation in which a breathing gas phase is derived from a "pool" of a binary cryogen liquid mixture is undesirable. Such a situation will be inherently unstable and unpredictable with respect to the partial pressures of the gases being delivered. Because the oxygen partial pressure is life critical in this development, the instability which derives from "pool boiling" must be completely avoided.

If a system is considered whereby a volume of liquid is removed unchanged from one container and then totally vaporized and mixed in a separate container, the percentages of individual gaseous components will of course be identical to the percentages of individual components in the liquid. Continuous total vaporization and mixing of liquid unchanged from the tank composition can be accomplished by withdrawing liquid through an orifice small enough so that a constant flow of liquid in one direction is obtained followed by total vaporization and turbulent mixing in a sufficiently long, small diameter, heat exchanger.

B. FLOW CONTROL

Since pressurization and venting of present day spacesuits require a flow rate of approximately 5.0 ACFM, a flow control mechanism is needed to regulate flow according to changes in diving depth. To maintain 5.0 ACFM through the suit will require a gaseous flow rate which can be increased as depth increases. At a water depth of 40 feet (MSFC Neutral Buoyancy Tank depth), a flow rate of 10.9 SCFM is needed to yield a 5.0 ACFM flow rate through the suit.

Regulating the amount of liquid cryogen which can enter the heat exchanger can be used to regulate the output gas rate. The heat exchanger is allowed to operate at low pressure and only the amount of liquid required to give a selected flow rate enters the heat exchanger. The rate this liquid enters can be controlled by controlling the orifice and dewar pressure. Since a small volume of liquid will yield a large volume of gas, optimum flow control and PO₂ control can be obtained by using a small orifice, variable flow, control valve which meters liquid only. Therefore, the flow control valve can satisfy the flow control requirement discussed above and also the oxygen control requirement discussed in Section A.

C. TEMPERATURE CONTROL

The established comfort level for neutral buoyancy pressure suited subjects has been found to vary between 68°F and 80°F. The heat exchanger on Prototype II is overdesigned with respect to its heat exchange capacity so that extremely large flow rates can be accommodated without any appreciable drop in output temperature below ambient water temperature. Since the Prototype II unit was designed for underwater purposes, a heat exchanger suitable for an air environment was not considered.

D. STORAGE CONTAINER

The best available insulation would be a vacuum walled container possibly including multilayered "superinsulation". This type insulation would restrict heat loss to an insignificant value during the required one hour run time. The only significant operational contribution of vacuum insulation would be its extended "holding time" (16 to 20 hours might be expected). However, vacuum based insulation techniques have three distinct disadvantages: (1) cost, (2) fragility, and (3) heavy walls required as over pressure (depth) increases.

Preliminary calculations on other methods of insulation indicated that polyurethane foamed-in-place insulation would be inexpensive, lighter in weight, and more rugged than vacuum insulation. The only disadvantage of foamed polyurethane appeared to be a reduction of the dewar holding time to about three to five hours; this was considered adequate. Further, since neutral buoyancy simulation is a centralized operation, the combination of a standard high vacuum ambient pressure storage dewar plus the foam insulated diving dewar would allow a cryogen holding time of several days plus sufficient insulation for mission performance.

FINAL PROTOTYPE DESIGN

The final prototype design, known as Prototype IIA, is shown in Figure 2 and Figure 3. The unit can be loaded in a few minutes using a premix of the desired ratio of liquid oxygen and liquid nitrogen. For operation the vent valve is closed and the buildup valve is opened. Cryogenic tank pressure is built up and controlled by the build up circuit. The diver simply sets the flow control valve and plugs in to the outlet to obtain controlled delivery.

EXPERIMENTAL EVALUATION

A. TEST EQUIPMENT

In order to measure pertinent characteristics of the gas being discharged from the life support system an instrumented "analysis bar" (see Figure 4) was used in place of the pressure suited test subject. This analysis bar contained sensors for measuring the following parameters: (1) oxygen partial pressure, (2) system absolute pressure (3) actual flow rate output, and (4) output gas temperature.

Analog signals representative of these parameters were fed into a recorder so that all values could be recorded simultaneously on chart paper for future reference.

B. TEST TECHNIQUES

Preliminary testing of the unit was accomplished under standard atmospheric (ambient) conditions substituting liquid nitrogen for LOX/LN₂ (LON) mixtures. This phase of testing not only afforded the opportunity for gaining operational familiarity, but also permitted reliability testing of key components, valves and heat exchanger. Changes in the location of these components and changes in their operating conditions were made as dictated by the test results.

After establishing the operating reliability of the unit, tests were conducted using mixtures of LOX and LN₂ as the filling liquid. These tests, consuming over 2000 lbs. of cryogen, were conducted to establish PO₂ control and to determine any changes in PO₂ which may occur during filling. A performance chart for a typical run using LON is shown in Figure 5. Strip chart data for another run are given in the Appendix.

In addition to the standard 1-atmosphere tests, testing was also conducted at simulated diving depths up to 100 feet in the single chamber recompression facility located at MSFC. These tests were conducted to establish the effects of increased ambient pressure on PO₂, flow rates, output temperature, and the structural integrity of the unit. A performance chart for a typical simulated dive to 80 feet is shown in Figure 6. Strip chart data recordings for a dive to 50 ft. are given in the Appendix.

C. TEST RESULTS

Actual testing of the Prototype unit yielded the following results:

1. The basic cryogenic-gas cycle used by the Prototype II Unit provides reliable control of all parameters.
2. The special valve components of this cycle (pressure closing valve, relief valve and micrometer flow control valve) perform adequately and reliably under normal and special conditions including being submerged to a depth of 100 ft.

The build up valve provides for complete internal system pressurization within 6 minutes as shown by Figure 7. The build up circuit will hold the desired dewar pressure within 2% under normal flow conditions and within 10% of preset pressure under continuous maximum flow conditions. The pressure closing valve operates automatically to compensate for depth overpressure and will maintain pre-set dewar pressures over ambient pressure at depths up to 100 feet.

Figure 8 shows the performance of the micrometer flow control valve. This valve is linear and smooth under all conditions of cryogen flow required and can provide the flow control and orifice necessary for PO_2 control. Flow rates from 1 through 18.5 SCFM are possible at 80 or 125 psi dewar pressure.

Flow in SCFM from the Prototype II unit is dependent only on dewar ambient pressure and flow control valve setting. Testing showed that the pressure closing valve accurately maintained the preset differential pressure above ambient pressure. Consequently, flowrates (in SCFM) were found to be maintained at constant values dependent only on the flow control valve setting. Figure 9 shows for the Prototype II unit the relation between flowrates (in ACFM) and water depth for a given setting of the flow control valve. However, constancy of flow rate in SCFM is in basic contradiction to the requirements of a pressure-suited neutral buoyancy test subject; his situation demands that flowrate through the suit in ACFM be constant and that SCFM be adjusted with respect to depth to accommodate this requirement. Thus an important design feature of the Prototype II unit is a dive adjustable flowrate control which provides more than adequate gaseous flow levels under all neutral buoyancy depth-demand conditions.

3. The Prototype II unit will convert and deliver the oxygen content with high precision control as observed during

all LON testing (which included more than 2000 pounds of various LON mixtures).

Total PO_2 control includes accuracy of LON mixing, changes of LON ratio during storage, changes of LON ratio during dewar transfers (loading), and any change which might occur during operation. It is interesting to note that during the entire test program these cumulative factors never caused a PO_2 variation in excess of + 5%. If one considers a given run cycle only, eliminating the inaccuracies of mixing, storage and loading, PO_2 variation is reduced to less than $\pm 1/2\%$ (which approaches the accuracy limit of the PO_2 sensor).

Figure 10 represents total PO_2 variation for typical $LO_{20}N_{80}$ and $LO_{30}N_{70}$ mixtures for surface conditions.

The PO_2 depth control was also in excellent agreement with theoretical and precomputed values. In a constant ratio mixture such as gaseous air or liquid air ($LO_{20}N_{80}$) or any other specific liquid oxygen/nitrogen (LON) ratio mixture, hyperbaric operation will of course show PO_2 changes. The oxygen constituent must always contribute its relative fraction of the total hyperbaric pressure. Therefore as the ambient pressure is elevated on a constant ratio mixture the oxygen partial pressure must also be proportionately elevated.

Figure 11 shows a typical depth vs PO_2 performance curve for the Prototype II Unit. Two typical LON ratios are shown. The actual PO_2 depth curves are as linear and flat as the PO_2 curves obtained from an air dive (deviations are less than 0.1%). The PO_2 agreement with respect to precomputed values is also very good. The actual PO_2 curve in Figure 11 in all cases showed a slightly lower slope than the precomputed values. This type deviation is typical of all air dives and is felt to be due to a slight lag in the electrochemical PO_2 sensor from which all the PO_2 values were obtained.

Although PO_2 will vary with depth, this variance is in accordance with Dalton's Law and is exactly the same as for an air dive. The maximum PO_2 from any LON mixture used at any depth can be predicted and the Prototype II will deliver that value. For instance, in a $LO_{33}N_{67}$ mix, an oxygen partial pressure of 0.33 atmosphere (4.85 psia or 251 mm Hg) will be found at the surface, whereas this same mixture will show a PO_2 of 0.65 atmosphere at a depth of 40 feet.

4. Testing has shown that the Prototype II Unit will deliver positive, safe output gas temperatures under all submerged conditions down to depths of at least 60 feet. The

principle of an oversized heat exchanger effectively locks the output gas temperature so that it is always within 5°F of the water temperature in which the unit is immersed. Figures 5 and 6 show the output gas temperature and the water temperature vs. time and depth respectively. These curves show a slight decline in both the output gas temperature and water bath temperature. This is due only to the limited volume of water surrounding the unit and would not occur if the unit were operated in a large volume of water such as the neutral buoyancy tank.

The unit can be operated at 5.0 SCFM at surface ambient conditions (heat exchanger in air) only 5 minutes before the output gas temperature begins to drop. No attempt was made to size the heat exchanger or to provide auxiliary heat control for such ambient air operations.

The heat exchanger operated as expected under all conditions down to depths of 60 ft. and showed sensible cooling in the first few feet of exchanger length. This cooling did not produce ice at depths less than 60 feet. Ice was produced on the first few coils only when maximum flow rates were demanded at depths below 60 feet. This ice formation is due to the increased dwell time of the gas inside the heat exchanger as gas density is increased. Ice formation was never found to include a supercooled surface. Bare skin contact with an immersed and icing heat exchanger showed no tendency for skin adherence.

Thus, in actual testing, the heat exchanger design described here proved to be completely free of potential physiological hazards associated with low temperatures, cold gas or supercooled surfaces, at least for the pressures and flow rates of interest.

CONCLUSIONS

The MSFC Prototype II Cryogenic Life Support System will provide adequate gas for present neutral buoyancy operations. Flow is diver adjustable for comfort. Positive oxygen partial pressure control is inherent within the design and the performance of the unit with respect to oxygen partial pressures is exactly analogous to an air dive. The unit will deliver exactly that ratio of gas contained in the liquid phase in the tank. Selection of oxygen/nitrogen ratios other than air may be desirable and are easily possible with this system. Positive output gas temperature control is also inherent within the Prototype II design. During submerged operation, the output gas temperature is fixed directly by the

water temperature. Even under the highest flow conditions the gas temperature will not be more than a few degrees below water temperature.

This unit is being refined to include more efficient layout and packaging and to include the all-attitude dewar solution. It will then be put through man rating qualification tests for use within the MSFC neutral buoyancy facility.

Credits

The authors wish to thank Mr. W. D. Hand of the Hayes International Corporation and Mr. J D Bennight of Marshall Space Flight Center for their continued support and aid in accomplishing this project.

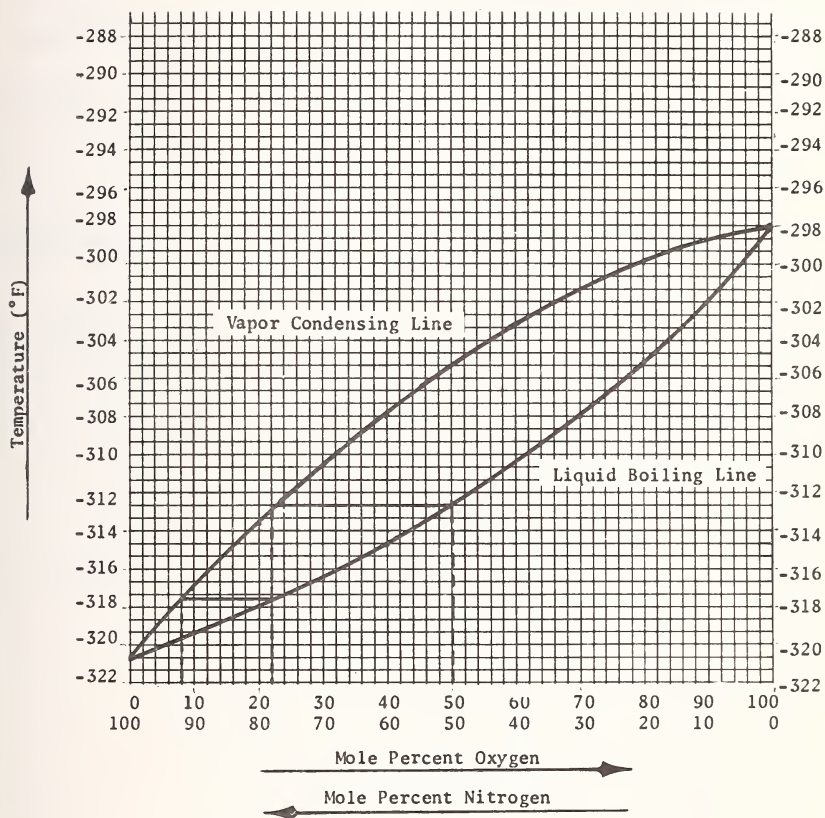


Figure 1. EQUILIBRIUM DIAGRAM FOR LIQUID OXYGEN-LIQUID NITROGEN MIXTURES

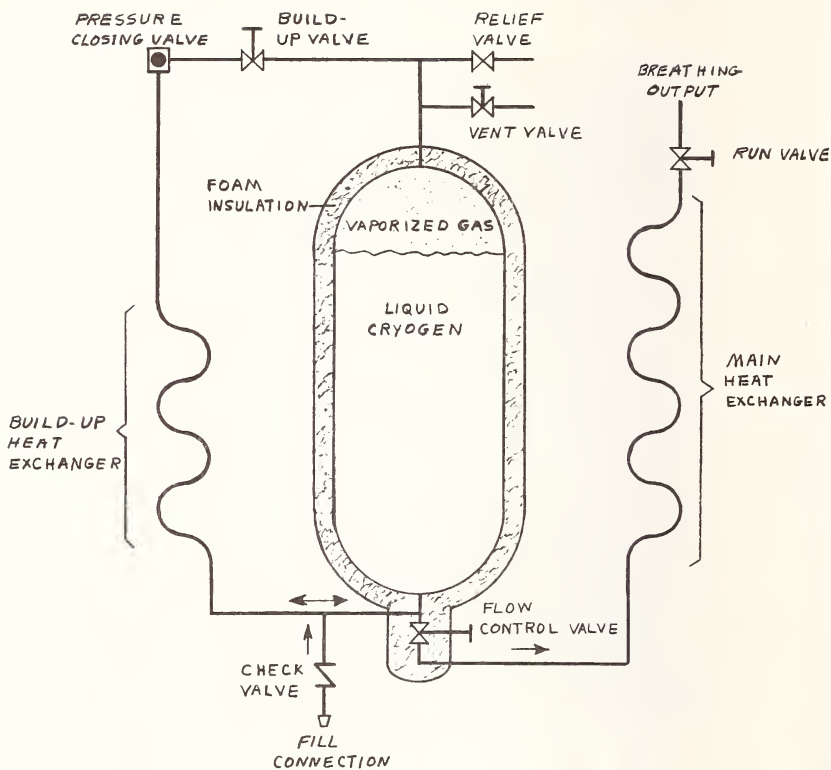


Figure 2. SCHEMATIC OF NSFC PROTOTYPE II UNDERWATER LIFE SUPPORT UNIT.

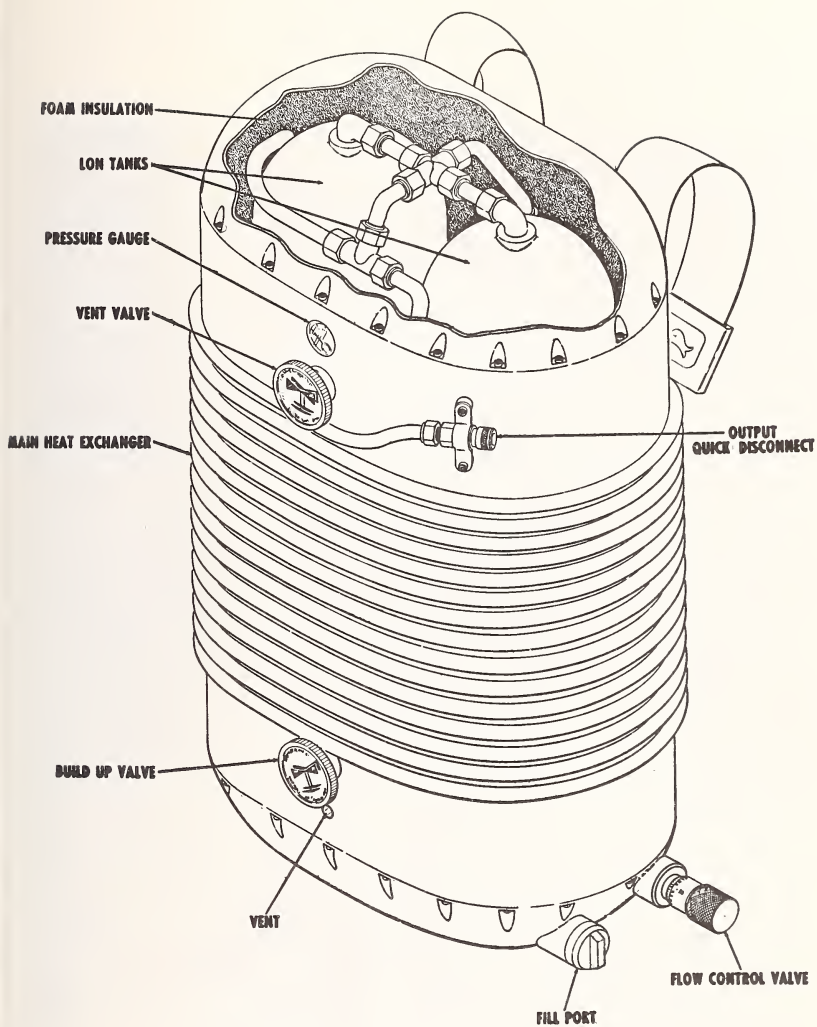


Figure 3. Prototype IIA Cryogenic Underwater Life Support System

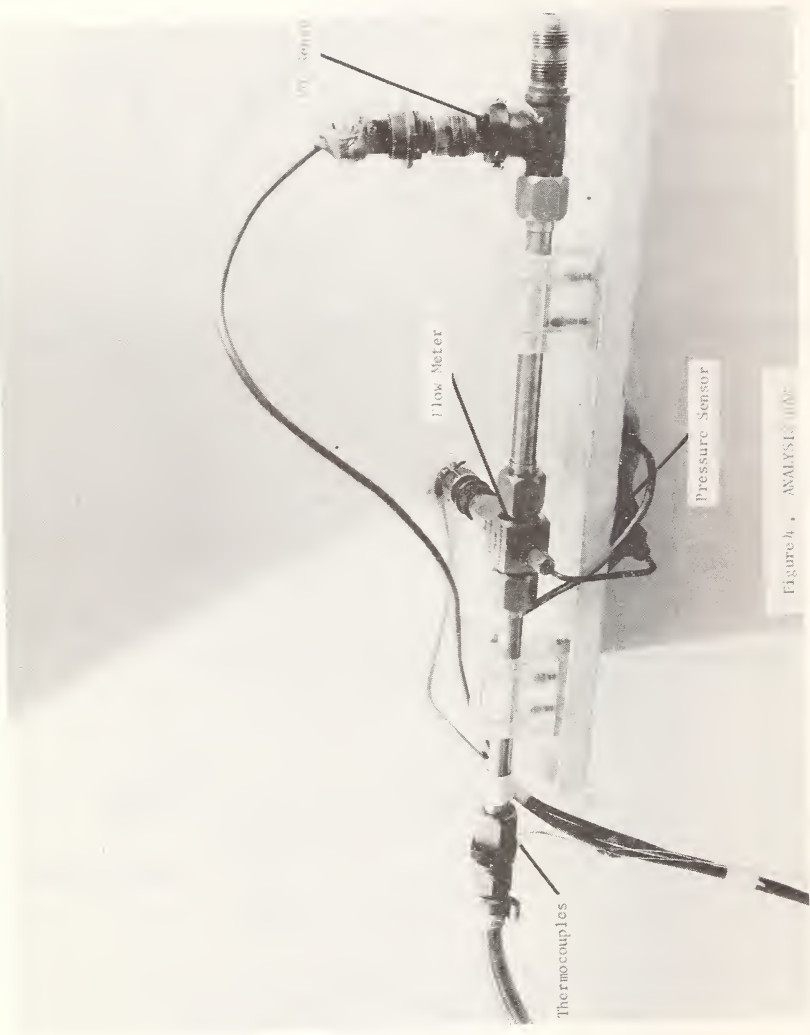


Figure 4. ANALYSIS 1102

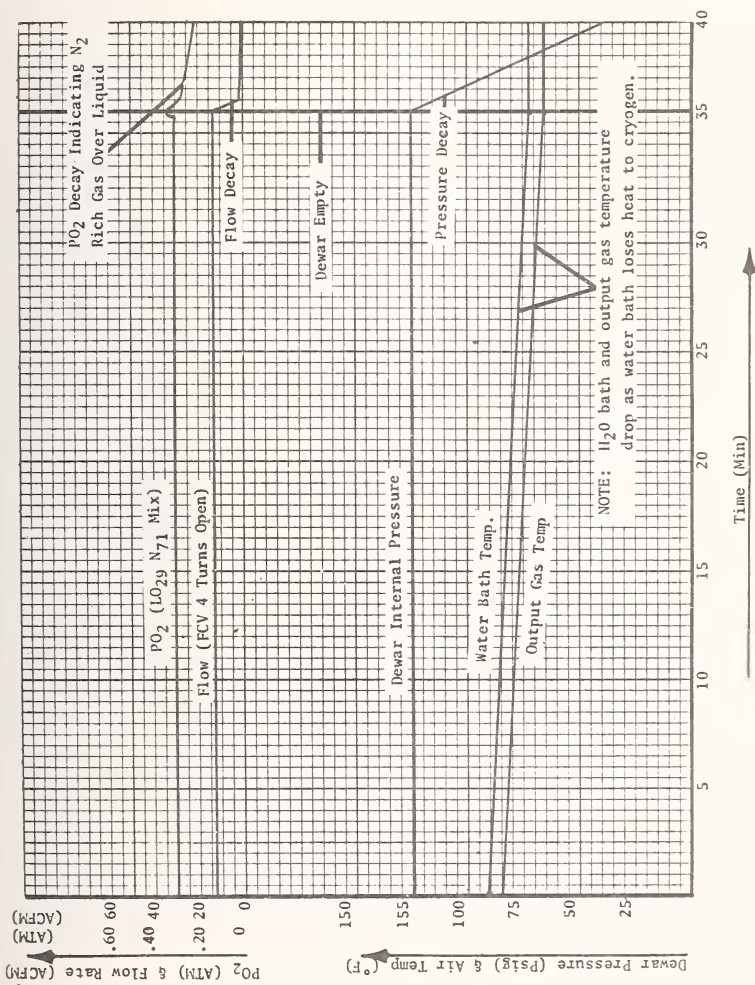


Figure 5. NSFC PROTOTYPE II PERFORMANCE CHART (SURFACE CONDITIONS)

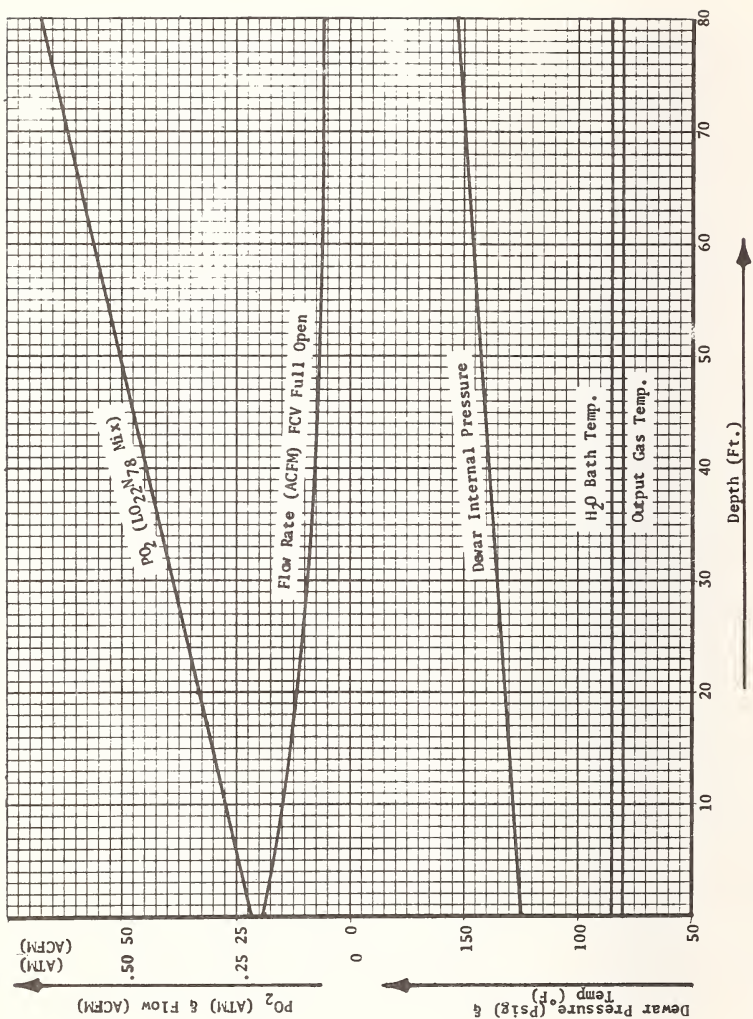


Figure 6. NSFC PROTOTYPE II PERFORMANCE CHART (DIVE CONDITIONS)

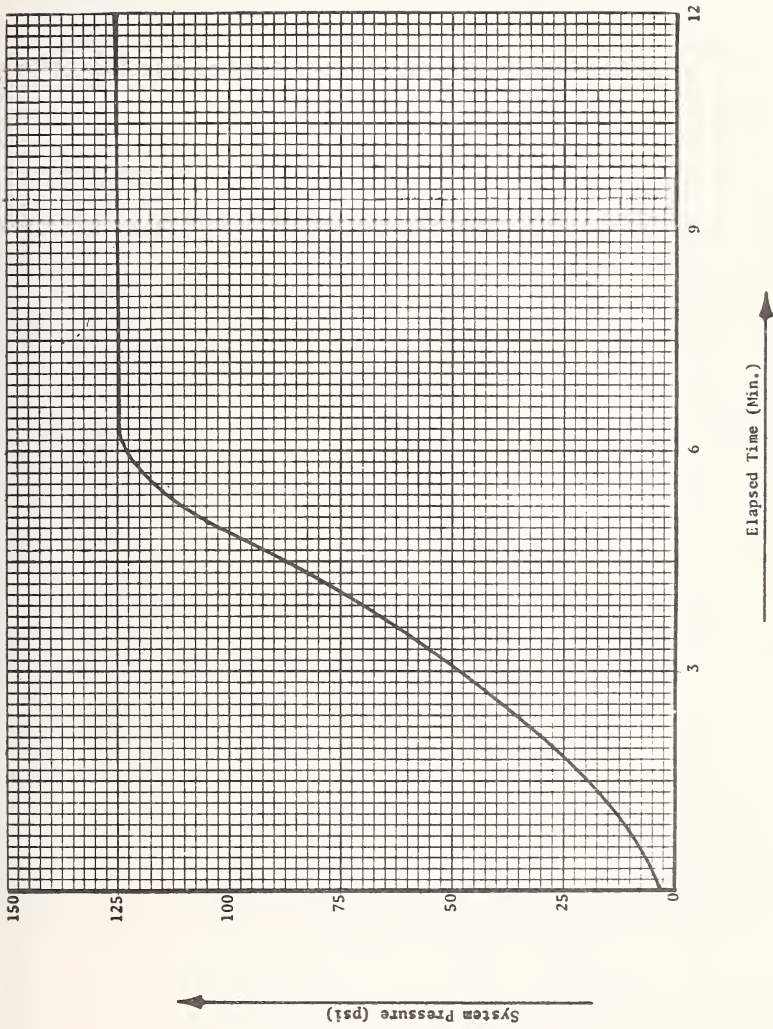


Figure 7. PRESSURE BUILD UP CURVE FOR PROTOTYPE II UNIT

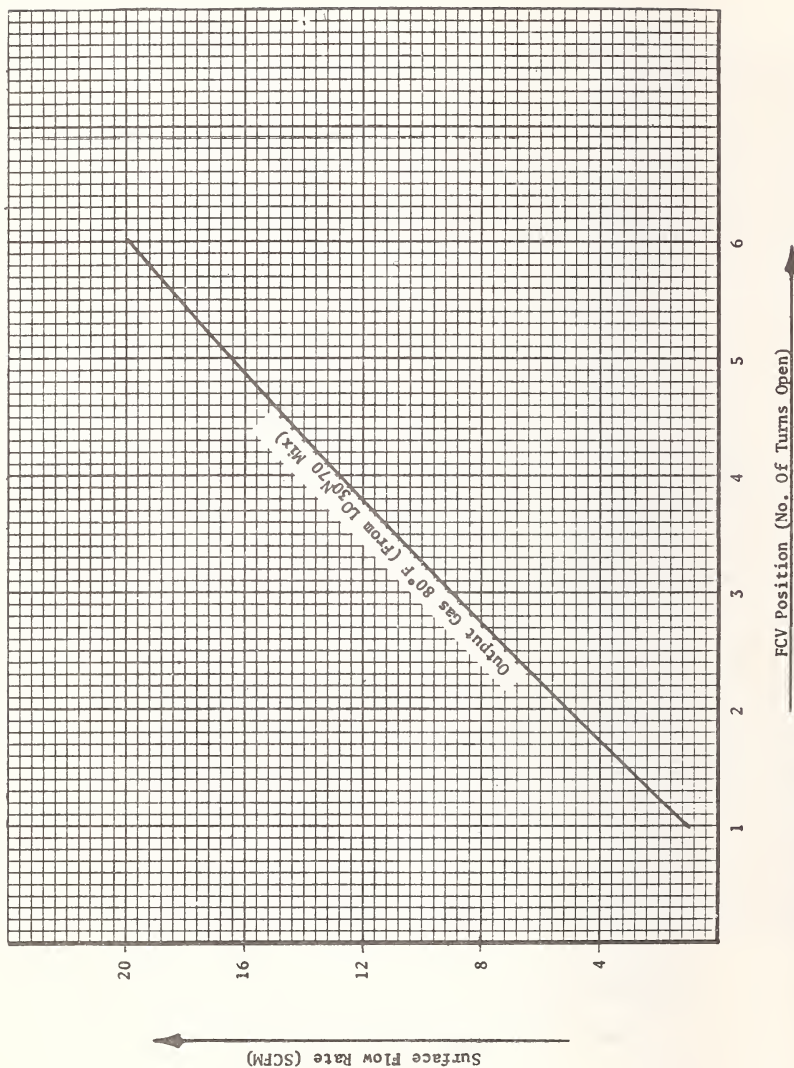


Figure 8. FLOW RATE VS. FLOW CONTROL VALVE POSITION (NSFC PROTOTYPE II UNIT)

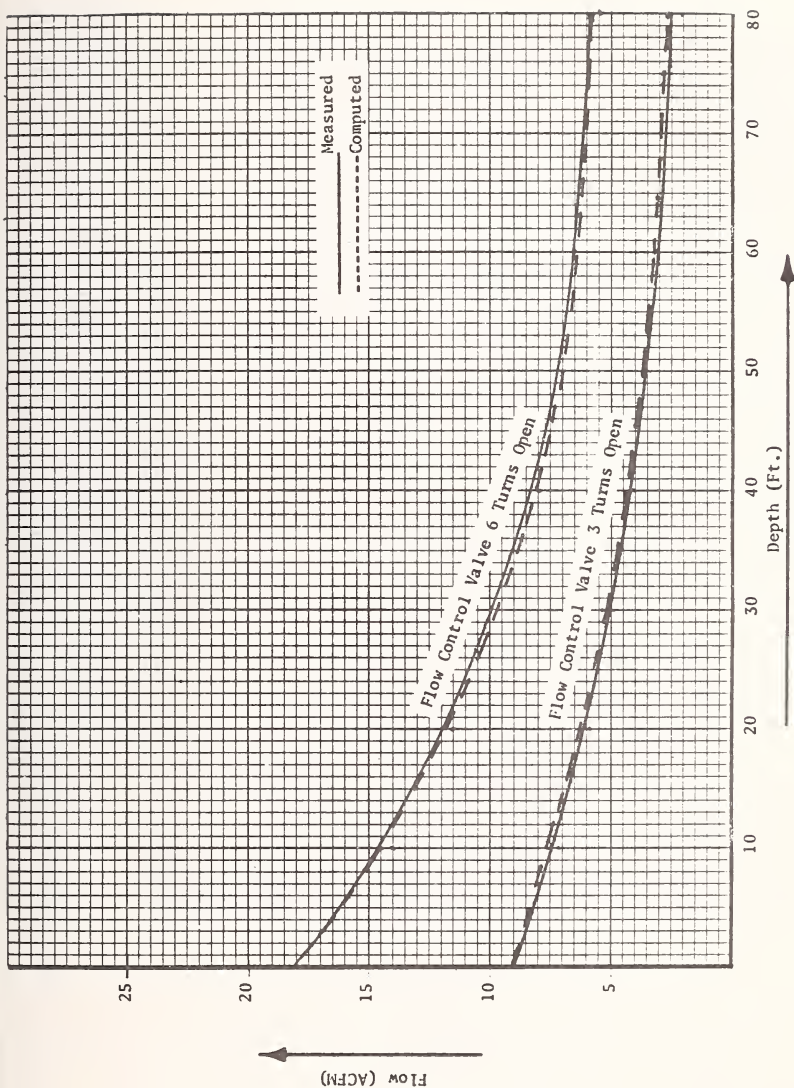


Figure 9 . FLOW RATE VS. DEPTH

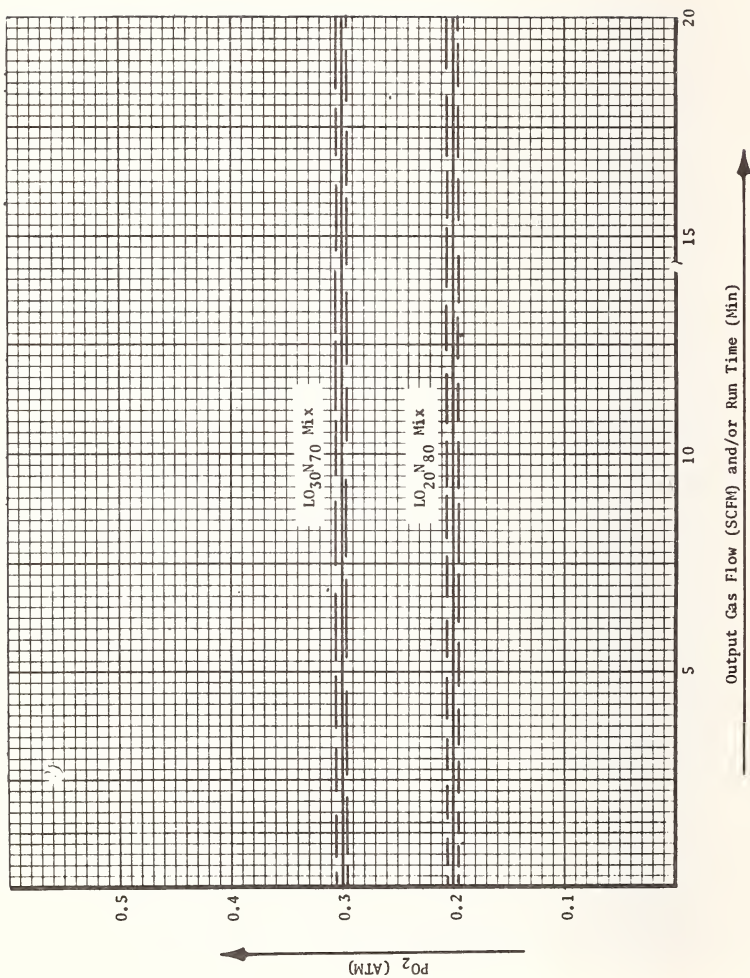


Figure 10. OUTPUT GAS ANALYSIS VS. FLOW RATE AND RUN TIME

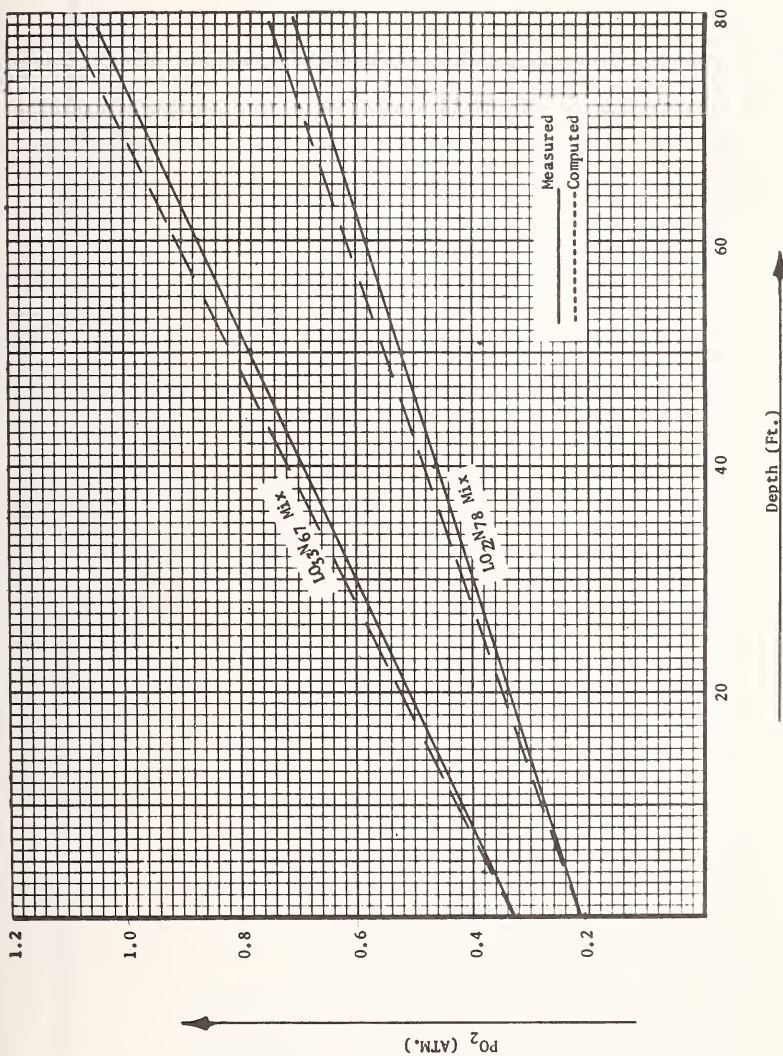
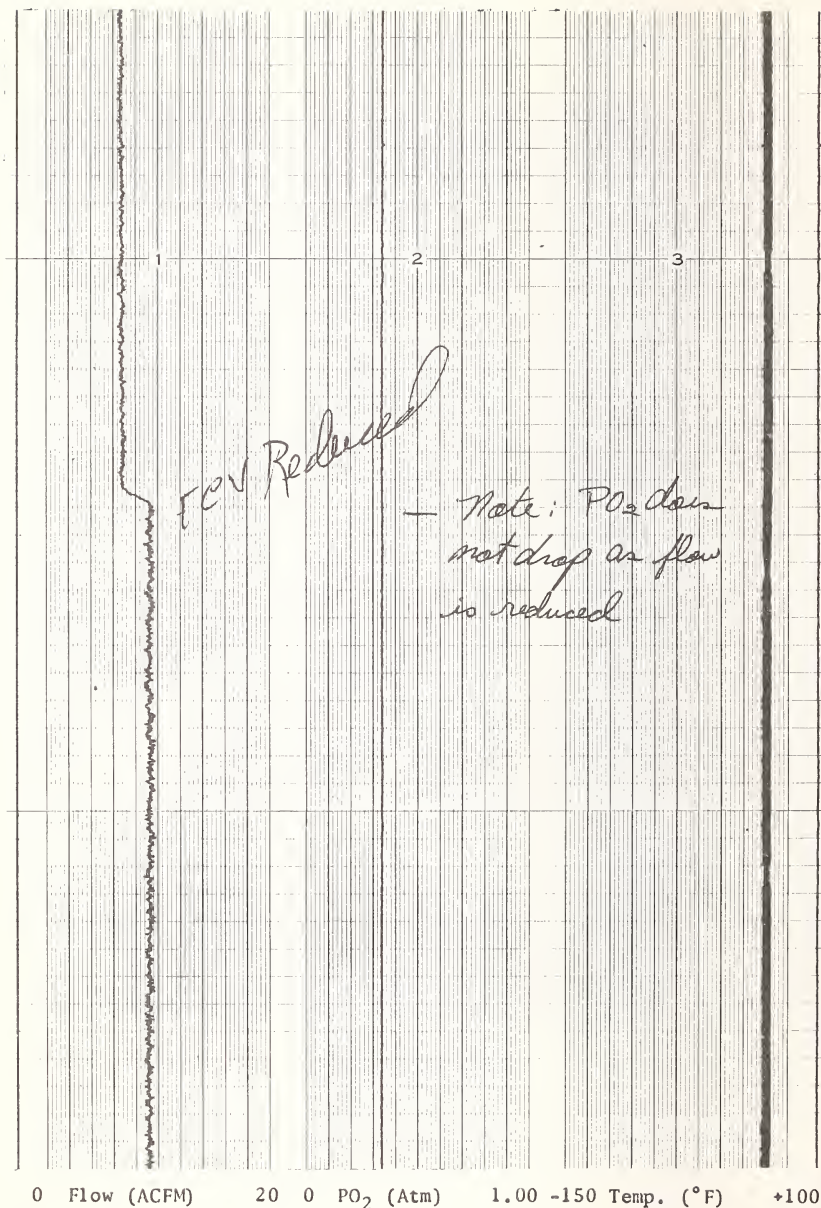
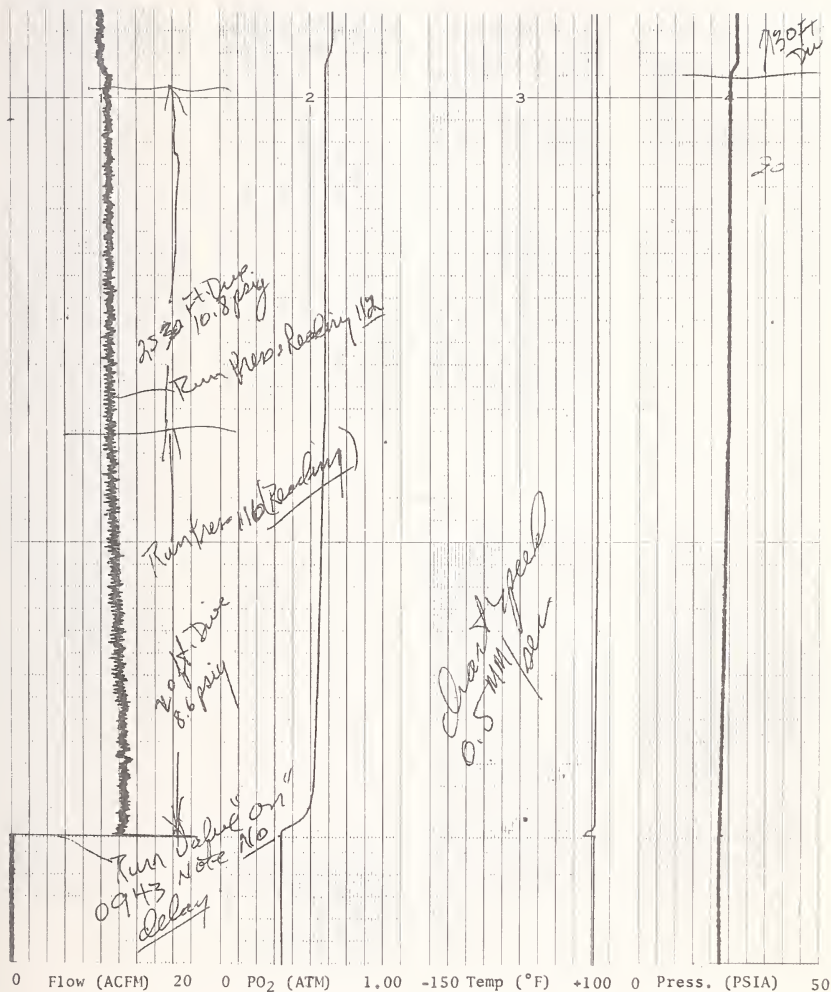


Figure 11. PO_2 VS. DEPTH (MSFC PROTOTYPE II UNIT)

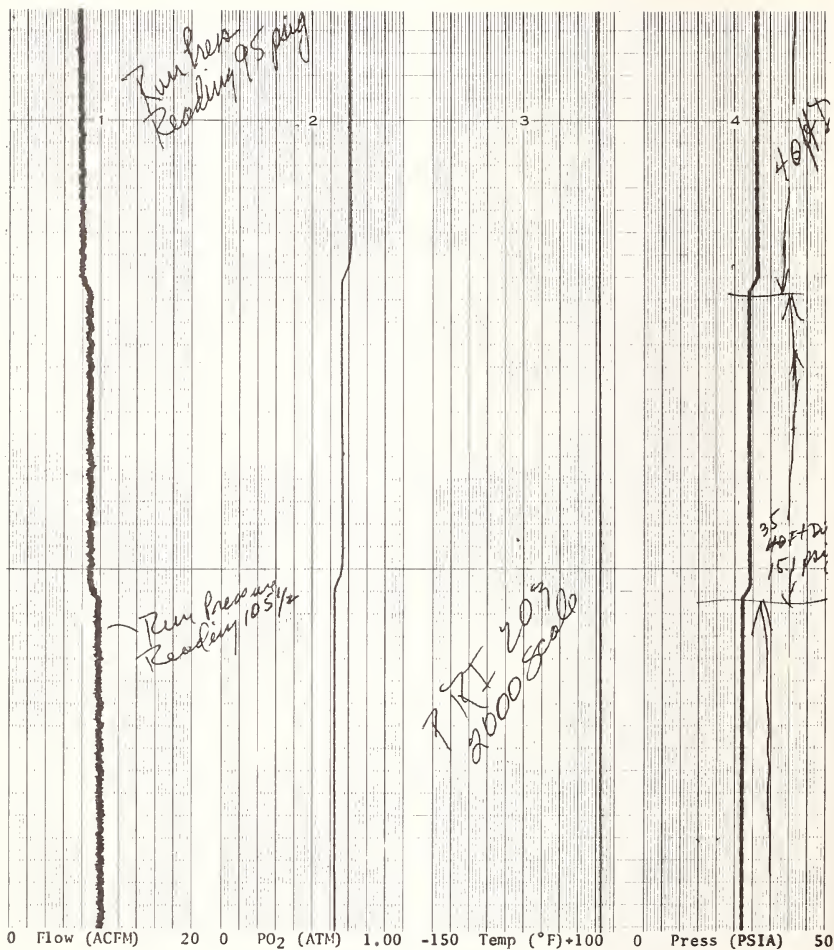
APPENDIX



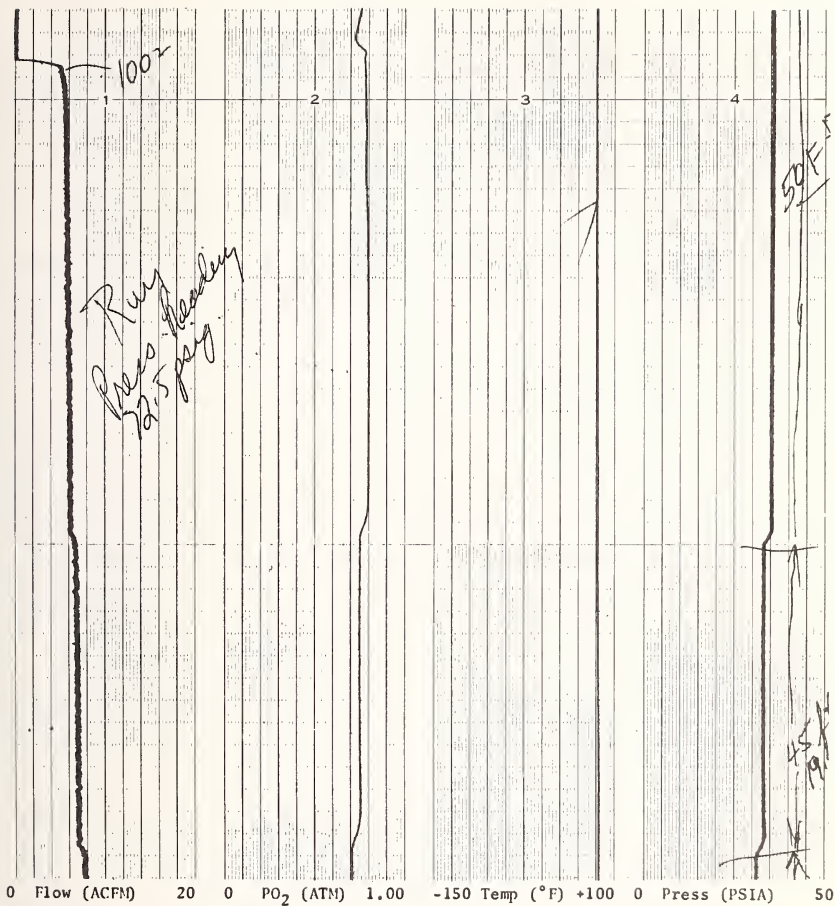
Strip Chart Data For MSFC Prototype
II Life Support Unit. (Surface Conditions)



Strip Chart Data For MSFC Prototype
Underwater Life Support Unit
(Dive Conditions, 25 Sept. 1969, Run #1, 24 Sept.
LON Mix, Initial Water Temp 87°F)



Run #1 24 Sept. 1969 Continued



Run #1, 24 Sept. 1969 (Continued from previous page).

MSFC-RSA, A16

ADVANCED DIVING TECHNIQUES APPLICABLE TO EXTENDED MISSION NEUTRAL BUOYANCY SPACE SIMULATION

Dr. Joseph B. MacInnis¹ and C.M. McClure²

REFERENCE: MacInnis, J.B., and McClure, C.M., "Advanced Diving Techniques Applicable to Extended Mission Neutral Buoyancy Space Simulation," ASTM/IES/AIAA SPACE SIMULATION CONFERENCE, 14-16 September 1970

ABSTRACT: Diving methodology is reviewed. Nonsaturated diving is recognized as the basis for almost all neutral buoyancy testing to date. Saturated diving methodology is reviewed and its possible special adaptation for extended duration mission neutral buoyancy simulation is proposed. The advantages of using the new closed circuit rebreather SCUBA gear is also reviewed and proposed as an aid to extended mission simulation.

KEY WORDS: Neutral buoyancy, space, simulation, hyperbaric, diving

INTRODUCTION

A requirement exists for high quality simulation of Space Flight. Simulation methods used to date have included gravity balance by underwater immersion, or "neutral buoyancy" methods.

¹Medical Director, Ocean Systems, Inc., Washington, D.C.

²Director, Aquaspace (Undersea Equipment and Technology), Huntsville, Alabama

Neutral buoyancy simulation to date has been basically a specialized industrial/scientific diving operation. It has been dependent upon and based on well-known and time-tested diving methodology. The depth to date has been relatively shallow, from 15 to 50 feet. The immersion times involved have also been relatively short and are usually less than from two to four hours. Future tests may dictate an increase in simulation depths, although depth per se is not a simulation requirement. It is foreseeable that the testing times may increase to equal the single-crew mission times for the extended duration space flights now planned. These times can be expected to be on the order of weeks and months, based only on the presently planned missions.

Immersion times of this duration will establish a simulation diving mode of operations very different from that mode upon which the past simulation diving procedures have been based.

It is the objective of this paper to review certain advanced diving techniques which may be of use when adapted to the special conditions of extended mission neutral buoyancy space simulation.

CURRENT DIVING TECHNIQUES

The present techniques on which neutral buoyancy simulation is based are those developed for and in use by military and commercial divers for many years. The equipment is primarily self-contained open-circuit, or surface air supplied open circuit types. The only significant difference between the standard commercial diving equipment and that used in neutral buoyancy simulation is the substitution of the pressure suit for the hard hat diver's dress. Also, the pressure suited test subject is purposely adjusted to be neutrally buoyant in simulation of zero gravity, whereas the hard hat diver is heavily weighted with lead shoes. There is little significant difference between the operation and physical performance of the pressure suit and ordinary commercial hard hat diving dress when both are air supplied at depths to 50 feet.

The methodology of present neutral buoyancy operations and ordinary commercial diving at similar depths is also similar. Of primary concern in this methodology is to accomplish the return to the surface without causing the diver clinical problems associated with decompression sickness. Briefly, these problems are usually attributed to the formation of tissue nitrogen gas bubbles during ascent back to the surface. To allow these bubbles to come out "silently", or without clinical problems developing, the diver must follow a decompression schedule during his ascent to the surface. Such a schedule may require the diver to stop

and wait a specified time at specified depths before surfacing. It is normal to find commercial divers being required to accomplish such a decompression schedule. In present neutral buoyancy operations, ascent schedules requiring decompression stops are not normally needed. This is only an apparent freedom from decompression procedures which is due to the particular combinations of depth and time being used in neutral buoyancy operations. The combination of depth and time are the critical parameters determining a possible decompression requirement.

The almost complete freedom from the necessity to follow decompression limited ascent schedules, a characteristic of neutral buoyancy operations to date, is due only to the particular combinations of shallow depths and short times used. Table I is an extraction of the U.S. Navy Standard Air Decompression Table and Standard Air Decompression Table for Exceptional Exposures. It shows that for durations less than 200 minutes at the forty foot level, no decompression stops are required. The only decompression procedure is a direct ascent to the surface at 60 feet per minute. This time of 200 minutes is known as the maximum no-decompression time for 40 foot depths. Beyond times of 200 minutes (3.3 hours) a decompression stop is required at the 10 foot depth. Excessive times (more than 1 hour decompression stop) at this stop level are not encountered up to immersion times as long as 6 hours.

At lesser depths the no-decompression time is increased and, according to these same tables, the no-decompression time is infinite at any depth less than 33 feet. This is shown by Curve 1, Table III.

The sharp departure from decompression procedures at immersion depths less than 33 feet is due to the fact that the human body can accommodate surfacing with a certain degree of tissue supersaturation without developing problems with decompression. The 33 foot depth limit, the critical supersaturation limit for direct surfacing without decompression stops, has been accepted for many years as the maximum depth for infinite time no-decompression exposures.

ADVANCED DIVING TECHNIQUES

During the last few years new diving techniques and equipment have been developed which are radical departures from the diving techniques on which almost all neutral buoyancy simulation has been based to date. The main new diving methodology is known as "saturation diving". Saturation diving is based on a single key idea, that the body tissues will absorb gases when subjected to new higher gas pressures (depths) only until the tissues are in equilibrium with the gases at the new

higher pressure. This absorption process to tissue "saturation" can be considered to be complete within 24 hours of continuous exposure at the new higher pressure.

Decompression procedures from saturation dives are different. Continuous pressure ascents are used, at the rate of 15 minutes per foot of depth, or four feet of ascent (sea water equivalent pressure) per hour. The ascent (decompression) time is the same for a depth stay of one day or any number of additional days at any given depth.

Depth stays of these extended durations are of course practical only with the use of a habitat or submerged station. The environmental pressure of the habitat is kept at the saturation depth pressure level. With no differential pressures, such habitats are of relatively lightweight structure and direct access from them to the water is easily accomplished.

The idea of being able to surface with a critical degree of supersaturation is still retained when saturation diving methodology is employed. However, recent experience has indicated that for saturation exposures, the critical maximum depth when breathing air is less than the 33 foot (sea water pressure equivalent) limit previously accepted. These experiences suggest that saturation dives to a maximum depth of 25 feet can be followed safely by direct ascent to the surface.

Additional diving advantages may be gained by using the technique of "excursion diving" from the submerged habitat level. Excursion diving can be described as dives from a submerged station to greater depths with subsequent return to the submerged station. Table III, taken from a paper given by Larsen and Mazzone in a symposium on Potential Advances in Deep Diving, shows these advantages. In this table the saturated divers are projected as operating from a station located at the 35 foot depth level. The no-decompression limits for direct ascent back to the station level are shown in curve 2. Considerably greater no decompression times are available at any depth when the divers are operating as saturated divers returning to the habitat level, than when operating as non-saturated divers returning to sea level surface pressure.

Curve 2 appears to be asymptotic to the 100 foot depth level. This implies that the maximum depth infinite time no-decompression limit is 100 feet for saturated divers operating out of a 35-foot depth level habitat. It is obvious that divers operating from such a submerged saturation station, even if the station is located at relatively shallow depths, will have a significant increase in the infinite time no-decompression maximum depth. More recent publications by Schreiner and

Kelley give methods for computation of decompression schedules for repetitive saturation-excursion dives. These schedules also show time advantages when compared to equal depth-time repetitive dives conducted from a surface base.

Advanced diving equipment may also have some bearing on long duration shallow water immersions. Habitat environmental control systems and closed circuit rebreathers (closed circuit SCUBA gear) have been in use recently. These systems can be set to supply the diver with oxygen/nitrogen ratios different from that found in air diving. If the oxygen partial pressure can be elevated, say from 0.2 atmospheres to a typical value of 0.4 atmospheres, then for any given depth the nitrogen partial pressure (pN_2) will be correspondingly lower than when using air at that depth.

With the adjustment stated, the maximum safe depth limit for no decompression of 25 feet would be increased to about 44 feet. Stated in another manner, the nitrogen partial pressure at 44 feet (gauge) depth breathing a 0.4/0.6 pO_2/pN_2 ratio gas would have an equal nitrogen partial pressure normally encountered with air breathing at immersion depths of only 25 feet.

NEUTRAL BUOYANCY APPLICATIONS OF ADVANCED DIVING TECHNIQUES

One of the simplest applications of advanced diving equipment and techniques to extended duration neutral buoyancy testing would be to utilize the new closed circuit rebreather SCUBA systems. Using these systems with a pO_2 elevated above the 0.2 atmosphere value available with air would increase the diving depths and times available with no-decompression dives. Using this method, the crew station (simulated) could be located at surface pressure and infinite time no-decompression dives to 40 or 50 feet would be possible, even with only moderate pO_2 elevation.

Should simulation needs develop for depths and times greater than would be feasible by the simple adjustment of the diver's pO_2/pN_2 breathing gas ratios, then selected application of saturation diving methodology could relieve the simulation series from involvement with limiting ascent schedules. For instance, if high fidelity simulation were required which involved space structures of sufficient size so that depths to 100 feet were necessary for complete mockup immersion, and if simultaneous with this depth requirement, continuous work/sleep schedules of several days were required to follow accurately the crew flight

program, then obviously new techniques would be required. Under simulation requirements just described, application of saturation diving techniques might yield the following typical solution:

The crew quarters could be located at a saturation depth equal to or less than the infinite time no-decompression maximum depth. With air ($pO_2/pN_2 = 0.2/0.8$ atm), this depth could be 25 feet. With pO_2/pN_2 ratio = $0.4/0.6$, the infinite time no-decompression depth would be in excess of 40 feet.

From this simulated space station base depth, the saturated simulated space crew could use excursion diving techniques to perform their work cycles under null gravity conditions at maximum mockup depths without decompression limited ascent back to the base station. Using such procedures, the simulation would not have space flight-irrelevant involvement with decompression procedures.

The situation would have three distinct categories of divers:

1. The non-saturated diver. These divers would be involved as safety and support divers, test engineers and directors, whose functions are in support of the simulation study. They would dive from the surface and return using standard decompression ascent procedures.

2. The habitat-saturated diver. These divers would be saturated at the habitat pressure level and would therefore have direct ascent to the surface without decompression involvement. This category would include simulated space crew members not required to perform work cycles exposing them to greater (excursion) depths. It would include those persons involved with conducting, supporting, and/or studying the simulation, whose needs included intimate stays aboard the station for long periods, but whose needs did not expose them to greater (excursion) depths.

3. The saturated-excursion diver. These divers would include those simulation crew members and other personnel whose duties required exposure to excursion depths. This category of diver would have some requirement for decompression before return to surface pressure. Assuming that a habitable saturation station is already available at shallow "no decompression" depths, in order that a multi-day simulation be made possible, then this shallow station could be used with pO_2 adjustments to reduce the category 3 diver to a category 2 diver. Such decompression might be possible without transfer to special decompression chambers other than the already available shallow saturation station. Such decom-

pression might be accomplished throughout the last rest and/or sleep period before returning the simulated space crewmember to the surface.

CONCLUSION

Advanced diving techniques and equipment are available which can facilitate simulation fidelity for extended duration simulation missions. These techniques primarily will involve special adjustments of saturation diving techniques and equipment, special use of advanced closed circuit SCUBA gear, and special pO_2 adjusted decompression methods. These advanced techniques will be especially useful where structure size dictates greater depths than are currently being used.

The adoption of such saturation methods will require extensive computations for the special case chosen. Also a thorough chamber testing program would be necessary to validate the computations, as is done for proposed new schedules.

TABLE I

Depth (Ft.)	Bottom Time		Time at 10 Ft. Decompression Stop (Min.)
	(Min.)	(Hr.)	
40	200	3.3	0
	210	3.5	2
	250	4.1	11
	300	5.0	19
	360	6.0	23
	720	12.0	69

TABLE II

Depth (Ft.)	Bottom Time	Decompression
40	Saturation Exposure (24 hours or more)	10 hours continuous ascent decompression

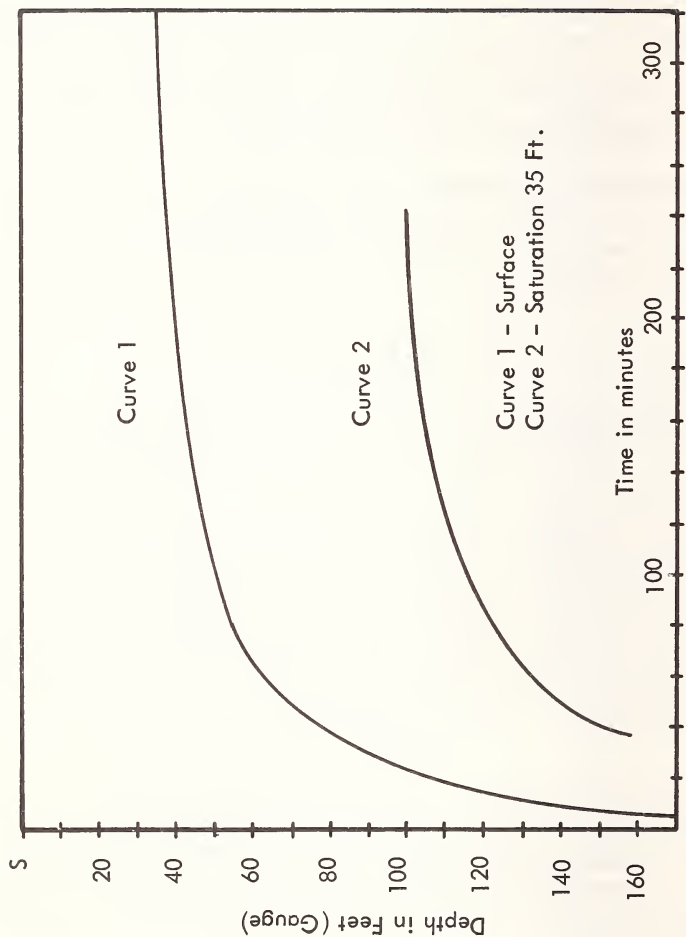


TABLE III. COMPARISON OF ALLOWABLE BOTTOM TIMES FOR TOTAL DEPTHS REACHED IN DIVES FROM THE SURFACE AND DIVES FROM A SATURATED 35-FOOT STATION ON COMPRESSED AIR

REFERENCES

1. Bornmann, Robert C. Decompression after Saturation Diving. Proc. Third Symposium on Underwater Physiology, Lambertsen, C.J., Ed., The Williams and Wilkens Co., 1967.
2. Hamilton, R.W. Jr., P. Fructus and X.R. Fructus: Physiological Surveillance and Performance Tests During A Seven-Day Exposure to 9.5 Atmospheres He-O₂ with Exercise Excursions at 13 Atmospheres. In Proc. International Congress Physiol. Sciences, Washington, D.C., 1968.
3. Hartman, H. and H.D. Fust: Pressure Chamber Experiments of Long Duration at Pressures Between 4 and 23 Atm., In Drager-Heft 265, Lubeck: Drager-Werke 1966.
4. Larsen, Reynold T. and W.F. Mazzone: Excursion Diving from Saturation Exposures at Depth. Proc. Third Symposium Underwater Physiology, Lambertsen, C.J. ed. The Williams & Wilkens Company, 1967.
5. Schreiner, H.R. Mathematical Approaches to Decompression. Int. J. Biometeor 11:301-310, 1967.
6. Schreiner, H.R. and P.L. Kelley. Computation Methods for Decompression from Deep Dives. In Proc. Third Symposium Underwater Physiology, C.J. Lambertsen, ed. Baltimore: Williams and Wilkins, 1967.
7. Schreiner, H.R. and P.L. Kelley. A Pragmatic View of Decompression. In: Proceedings Fourth Symposium Underwater Physiology, C.J. Lambertsen, ed., New York: Academic Press, 1970.
8. Schreiner, H.R. The Design of Decompression Schedules, A Symposium Man's Progress Into the Sea, Marine Technology Society, Washington, D.C. 1969.
9. Schreiner, H.R. and P.L. Kelley. Computation of Decompression Schedules for Repetitive Saturation-Excursion Dives. Aerospace Medicine 41(5), 491-494, 1970
10. Workman, R.D.: Calculation of Decompression Schedules for Nitrogen-Oxygen and Helium-Oxygen Dives. Research Report 6-65, Washington. U.S. Navy Experimental Diving Unit, 1965.

A METHOD TO OBTAIN AN ULTRACLEAN ENVIRONMENT

Maurice S. Cridlin, Vacuum Technologist, and Joseph W. O'Connor, Aerospace Technologist, NASA Goddard Space Flight Center, Greenbelt, Maryland.

ABSTRACT: The Goddard Space Flight Center has designed and fabricated a system which offers an effective approach toward solving the problems usually encountered in creating an ultra high vacuum. The vacuum techniques described find application in an Auger Spectrometry System.

This ionization pumped system is unconventional in that; (1) Interior chamber cryogenic shrouding is eliminated. In lieu of the internal shrouds the method is to submerge the entire chamber exterior in a dewar of liquid nitrogen. Eliminating the shrouds within the chamber eliminates sources of contamination and the exposing of the wall exterior to the cryogenics eliminates the typical ambient temperatures that chamber walls normally experience, (2) The ionization pump is located within the ultrahigh vacuum chamber, rather than outside. This eliminates the gate valve typically associated with an externally mounted pump and permits greatly increased realization of the conductance pump capacity. The pump is protected by use of gas purging when pressures are increased to atmospheric.

The method of precleaning, prior to bakeout, involving high temperature gas purging is described as well as the entire systems operation. Pressures in the order of 7×10^{-13} torr have been observed.

KEY WORDS: vacuum, pumping, ultraclean, cold shrouding, environment, contamination, low temperature, low pressure, ion pumping, anti-migration traps.

A METHOD TO OBTAIN AN ULTRACLEAN ENVIRONMENT

An ultraclean environment is often mandatory in space oriented research, particularly when experimental materials must be free of

surface contamination. The Goddard Space Flight Center has designed two ultra high vacuum systems using an effective approach to solve some of the problems usually encountered while attempting to create an oil-free environment. One of these systems is used to develop ultra high vacuum components and techniques. The other system is used for Auger Spectrometry research. The spectrometer can detect partial monolayers of materials and identify these materials. This unique system is one example clearly demonstrating the need for a noncontaminating experimental environment. Since an oil free environment for this Auger Spectrometer was mandatory, an ionization pumped system⁽¹⁾ was developed, which will be described here.

Conventionally, ion pumped ultrahigh vacuum systems employ an internal optically dense liquid nitrogen shroud⁽²⁾ in conjunction with a titanium pump, Figure 1(A). The ionization pump is mounted external to the chamber and isolated by a gate valve. Typically, the gate valve utilizes an elastomer⁽³⁾ O-ring. While this geometry and selection of components finds wide acceptability, improvement can be realized by locating the ionization pump inside the chamber, Figure 1(B); by eliminating the gate valve and the cyro shrouds and by slightly changing the typical pump down technique.

ULTRAHIGH VACUUM CHAMBER

The entire vacuum system, Figure 2, is constructed from metal and all seals are metallic. Ceramic to metal feedthroughs are used. Within the cylindrical chamber (20-inch diameter by 36-inch high) are the ionization pump, titanium sublimation pump, an electron trap and shelves for mounting experiments. Thermocouples monitor the chambers' wall at four separate elevations. The work area of the chamber is top loaded through a choice of metal sealed orifices up to 18 inches in diameter. The dome includes an observation port and a high intensity light port.

Surrounding the vacuum chamber on the sides and bottom is a metal thermos bottle. The annulus between the chamber and the thermos houses heater elements and when the heaters are activated, this area becomes an oven for bakeout. The area is also capable of being filled with liquid nitrogen, thus insuring the walls of the chamber being uniformly cooled to LN₂ temperature. Cryogenics are not allowed to contact feedthroughs directly, they are cooled through conduction. LN₂ can be gravity drained through a valve in the bottom of the thermos.

(1, 2, 3)Numbers in parentheses refer to the list of references appended to this paper.

Optically baffled titanium pump filaments are mounted through the center bottom of the chamber. When used, titanium is vaporized onto the LN_2 cooled walls of the chamber providing an intrinsic pumping speed in the order of 60,000 l/sec (approximately 60 l/in²/sec).

A 250 l/sec ionization pump is located above the titanium pump well, a position near the center of the chamber vertically. Conductance for the ion pump far exceeds its capacity and the solid angle of view it possesses is much improved over external mounting techniques.

An oven hood covers the top of the chamber and all feedthroughs during bakeout cycles. It is planned to seal this hood to the system at a later date so the oven/liquid nitrogen area can be used for a third beneficial function, a differently pumped area completely surrounding the vacuum chamber and feedthroughs. Currently, this feature does not exist.

GAGES

Three separate gages were used to evaluate the chambers' performance during the equipment checkout phase and installation. The location of two of these is shown in Figure 3. These included the ionization pump gage which reads pressures to 1×10^{-10} torr, a cold cathode-type gage and a hot cathode gage which cathode gage which read to 1×10^{-13} torr. The hot and cold cathode gages are mounted at the top of the chamber. As one might expect, variations in pressure readings were observed, however these were well within an acceptable range. Pressures presented in this report are from the hot cathode gage.

PUMPS

Five different types of pumping mechanisms are used in this system: a mechanical pump, a sorption pump, an ionization pump, a titanium pump and liquid nitrogen cooled surfaces which pump considerable gases and vapors.

The mechanical pump and the sorption pump are used for roughing the chamber. The mechanical pump also evacuates the double walled thermos bottle. Dry nitrogen is admitted into the chamber to maintain a pressure of 200 microns while roughing with the 15 cfm mechanical pump. This assures only viscous flow during the first stages of roughing. Roughing is completed by valving out the mechanical pump and the nitrogen gas supply and then activating the sorption pump.

The ionization pump, titanium pump and liquid nitrogen cooled walls are used to evacuate the vacuum chamber to lower pressures.

By location the ionization pump inside the vacuum chamber, the typical gate valve can be eliminated.

When rapid re-cycling of the chamber from atmosphere to ultra high vacuum is required, a feature not normally expected of an ultra-high vacuum system, elimination of the gate valve can offer some advantages. All gate valves decrease the conductance and reduce the throughput of a dynamic system. They also present additional surfaces to be cleaned and where elastomer O-rings are used, bakeout temperatures are often restrictive. Protection of the ion pump from contamination is accomplished by special operating procedures which are strictly adhered to. Venting the system to dry nitrogen while the system temperature is in the order of 125°C is necessary. The system is never allowed to see atmospheric pressure for over 15 minutes. Shorter exposures are more the rule.

BAKEOUT

All surfaces exposed to the ultra high vacuum are baked with good uniformity to 450°C. When it is desired to obtain a very low pressure (less than 1×10^{-13} torr), the chamber is cooled over a period of around eight hours so that all surfaces are cooled at nearly the same rate. Heat is added in ever decreasing increments during the cool down cycle to achieve this goal. When the chamber temperature approaches 50°C, liquid nitrogen is introduced until the entire chamber is submerged. By reducing the wall temperature the vapor pressure of all materials located thereon is reduced, consequently, even those gases exhibiting virtually no partial pressures on a mass spectrometer are affected. The mild bakeout, 450°C is very effective when the chamber is cooled to LN₂ temperature.

Since typical cryogenic shrouds are eliminated, their problems go with them. They are difficult, if not impossible, to bake out or cool uniformly. Reduction of surfaces exposed to the ultrahigh vacuum is of prime importance, to eliminate sources of contamination.

FORELINE TRAPS

Two traps are used in the foreline. A bakeable activated absorbent trap is located next to the mechanical pump. This trap eliminates much of the oil backstreaming from the mechanical pump. It eliminates some of the oil migration. To completely trap oil from the mechanical pump, the second trap employs a removable and throw-away section, Figure 4, so that oil cannot migrate through it when it is at ambient temperature. The second trap is activated with liquid

nitrogen such that oil cannot migrate through it when it is charged. In all cases, this trap is exposed to viscous flow in the direction of the mechanical pump, a feature which inhibits oil backstreaming.

Mechanical pump preliminary evacuation to 200 microns is an important feature of the operating procedure. Mechanical pumps evacuate all gases and are not selective as are sorption pumps.

OPERATIONAL SEQUENCE

Initial roughing of the chamber is accomplished with the double trapped mechanical pump to a controlled pressure of around 200 microns. Dry nitrogen is metered into the chamber to prevent the mechanical pump from evacuating the chamber to a lower pressure. Additional evacuation is completed with the sorption pump while the mechanical pump and gas bleed are valved out of the system. The entire evacuation procedure and sequence is performed after the chamber has been brought to at least 150°C. Roughing with the mechanical pump should continue for at least ten minutes. When the chamber pressure is below 10 microns, the sorption pump is valved out and the ionization pump is started. (The pressure can be reduced to around 1×10^{-4} torr with liquid nitrogen prior to starting the ionization pump if the pump seems hard to start.)

Within a few minutes, the ionization pump will have pumped the chamber to a pressure of 5×10^{-7} torr or lower. To achieve lower pressures, a bake cycle is initiated. Figure 5 illustrates a pump down cycle achieved with the Auger Spectrometry system. The newer system currently being evaluated is expected to better the pump down cycle exhibited by the first system.

ENVIRONMENT ACHIEVED

The initial cleaning of the system involved a long time (72 hours) bakeout. Normally a four hour bakeout will be sufficient to enable the chamber to achieve a vacuum in the 10^{-11} torr range or lower. The predominating gas species at 10^{-11} torr are H_2 , CO and He. In the 10^{-13} torr range H_2 and He were the dominant constituents.

REFERENCES

- (1) S. Dushman, J. M. Lafferty, Scientific Foundations of Vacuum Technique, John Wiley & Sons, Inc., 1962
- (2) C. M. VanAtta, Vacuum Science and Engineering, McGraw-Hill Co., 1965
- (3) H. A. Steinherz, Handbook of High Vacuum Engineering, Reinhold Pub. Corp., 1963
- (4) D. J. Santler, H. D. Holkerboer, D. W. Jones, F. Pagano, Vacuum Technology and Space Simulation, NASA SP-105, 1966

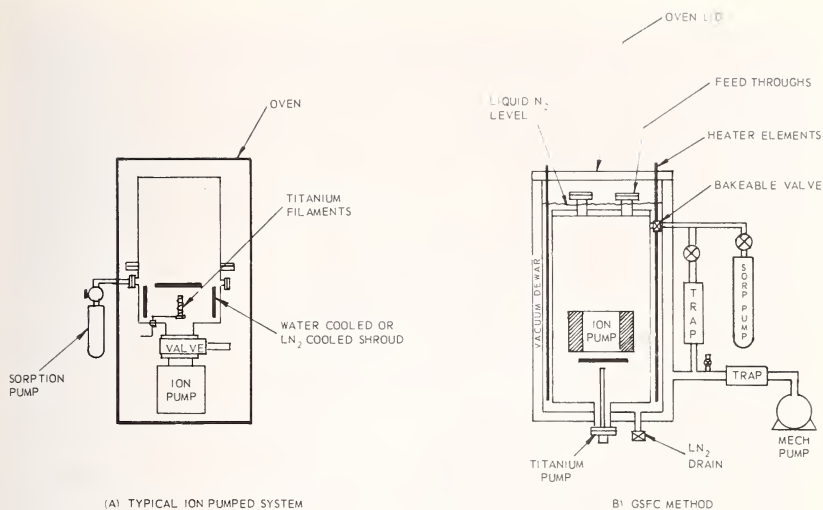


Fig. 1—Typical and GSFC ion pumping techniques.



Fig. 2—GSFC experimental ultra high vacuum system.

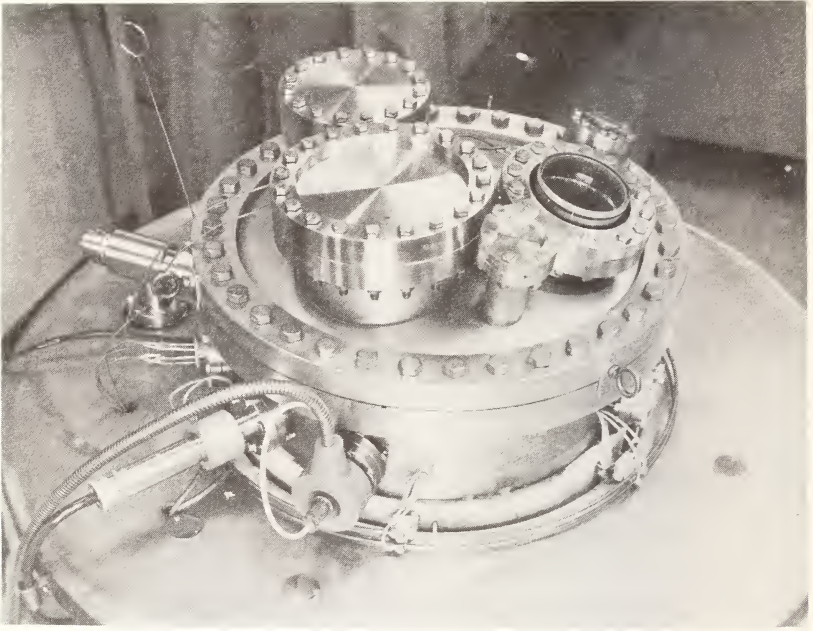


Fig. 3—Gage locations GSFC ultra high vacuum system.

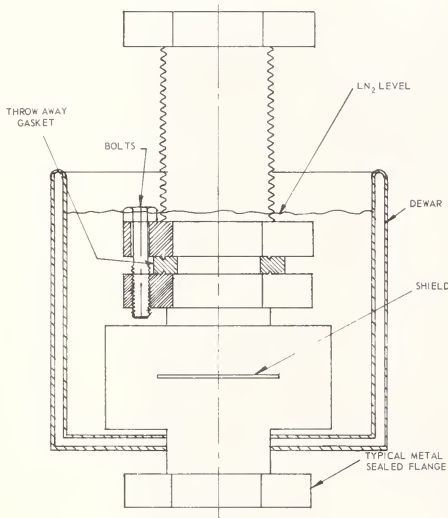


Fig. 4—Anti-migration trap.

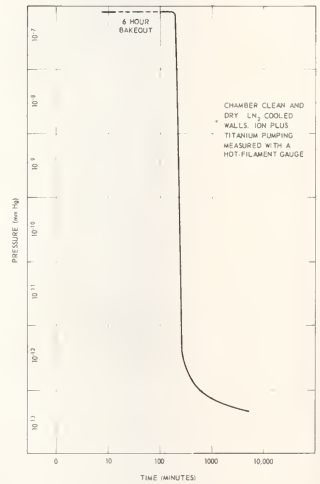


Fig. 5—Auger-spectrometer pump down cycle.

A PROGRAMMABLE DYNAMIC THERMAL VACUUM SYSTEM FOR SOLAR ARRAY COMPONENT TESTING

John W. Fairbanks¹ and Marshall B. Eck²

REFERENCE: Fairbanks, J. W. and Eck, M. E., "A Programmable Dynamic Thermal Vacuum System For Solar Array Component Testing," Fifth Space Simulation Conference, Gaithersburg, Maryland, September, 1970.

ABSTRACT: The Programmable Dynamic Thermal Vacuum System (PDTVS) was designed to provide long-term laboratory evaluation of solar array components undergoing thermal cyclic effects anticipated for specific missions. This system is capable of duplicating the temperature excursions, including rate-of-change of temperature, for practically all missions currently under consideration at NASA. The equipment can obtain test specimen temperatures between +150°C to -120°C with a rate-of-change of at least 6°C/min. The PDTVS can accommodate thirty-six 6"x6" test specimen holders and position each one in front of a illumination port for periodic in-situ electrical measurements with a solar simulator.

Basically, the facility consists of an ion-pump vacuum system with 2 bell jars, thermal conditioning equipment, a 3 stage blower, a programmable control unit and an LN₂ storage tank. The novel developments in this system include a high-energy low-mass heater which employs radiative-convective coupling of a gas stream to an IR source. The test carrousel shaft is used for specimen positioning and as an instrumentation penetration. Initial difficulties required modification of the blower bearings, shaft and housing to accommodate the wide range of gas stream temperatures without affecting performance.

KEY WORDS: Solar cell, solar array, thermal cycle vacuum testing, gaseous nitrogen heater, gas stream blower, thermal shroud, GN temperature conditioning.

¹AST Electrical Propulsion and Power Systems, NASA-Goddard Space Flight Center, Greenbelt, Maryland

²Chief Engineer, H. C. Slack & Associates, Baltimore, Maryland

INTRODUCTION

The ability of solar arrays to provide the power requirements for missions now in the conceptual and preliminary design stages at NASA require thermal cycling data which is not now available. Problems have been encountered on previous projects with the solar cell-interconnector solder joint and/or the solar cell contact integrity that have been solved primarily by "cut and try" techniques. Part of the problem stems from the broad range of thermal conductivities of the conductive and non-conductive components which comprise the solar array. The array assembly with this inherent thermal mismatch must undergo repeated thermal excursions typically with a ΔT as high as 230°C . Current design thermal flight qualification procedure generally consists of subjecting the prototype solar panel or paddle to a few thermal vacuum cycles to extremes about 10% beyond maximum and minimum flight predicted temperatures. Usually there are no more than rudimentary steps taken to ensure that the rate-of-change of temperature during shadow encounter and emergence is reproduced.

Consideration of some of the specific missions being planned, should assist in defining the test equipment requirements. The Orbiting Astronomical Observatory (OAO) program is seriously considering a ten-year life requirement for the solar array, which means approximately 50,000 thermal cycles (Ref. 1). Data on conventional solder connected cells indicates problems can be anticipated after 3,000 cycles (Ref. 2). The Astronomy Explorer (AE) C&D will encounter significant aerodynamic heating during a series of low perigee passes (Ref. 3). Considerable interest is also expressed in solar array capabilities on close-approach solar missions as well as the capability to operate in the vicinity of Jupiter. Perhaps of equal importance is the need to obtain comparative long-term thermal vacuum test data on solar array components or composites generated in Research and Development (R&D) programs which have the potential of cost saving, improved performance, weight reduction and/or increased reliability. The current conservative philosophy of flying with proven components has generated a significant time lag between R&D and flight utilization despite potential technical and/or economic advantages.

The Programmable Dynamic Thermal Vacuum System (PDTVS) was designed to support flight projects in the preliminary solar array design stage and as problems are encountered during flight qualification. In addition, the PDTVS provides meaningful long-term thermal cyclic effects data on R&D program developments which enhances their implementation in flight programs. In order to achieve these design objectives, the following system requirements were developed.

DESIGN REQUIREMENTS

The requirements generated for the PDTVS were as follows:

1. The system must be able to reproduce thermal conditions anticipated for essentially all NASA missions under consideration for the 70's which would employ solar arrays.
 - a. Specifically operate between $+150^{\circ}\text{C}$ to -170°C and produce a rate-of-change of at least $6^{\circ}\text{C}/\text{min.}$ between $+150^{\circ}\text{C}$ and -120°C .
2. Provision must be incorporated to accommodate in-situ periodic electrical measurements of test specimens through an illumination port.
 - a. Each of thirty six 6"x6" test specimens must be mounted so that it can be accurately positioned in front of the illumination port.
 - b. Also must be capable of accommodating an IMP-I solar panel.
3. Each test specimen must have a 99% view factor to thermally controlled surfaces.
4. Test instrumentation wiring shall produce minimum interference to the thermal view factor.
5. System must be capable of programmable thermal cycling performance.
6. System must operate automatically over long periods (on the order of 3 to 9 months).
 - a. Fail-safe features must be included.
 - b. Permit ready accessibility for operational and maintenance functions.
7. Must incorporate features that provide economical operation, including low-level maintenance requirements.
8. A second chamber shall be incorporated such that it could be thermally slaved to the programmed thermal cycle. This chamber would accommodate small numbers of samples which could be removed without affecting the long-term testing on the larger unit.
9. A common roughing system shall service both chambers with capability for a third chamber.

The above requirements have been incorporated in the PDTVS, which was built on-contract for the Goddard Space Flight Center.

OVERALL FACILITY

The PDTVS facility is shown in Figure 1.

The major components which comprise the PDTVS facility are a getter-ion pump vacuum system with two bell jars, a solar simulator, a test carrousel with automatic indexing, thermal conditioning system, programmable controls, liquid nitrogen storage tank and associated piping. Several innovative features were incorporated in the thermal conditioning equipment and in the test carrousel positioning scheme.

VACUUM SYSTEM

Roughing for both bell jars is achieved through physical adsorption of gas molecules by LN₂ cooled high-capacity molecular sieves. Pumping into the high vacuum region is accomplished by sputter-ion pump combined with titanium sublimation pumping. The sputter-ion pump operation involves trapping gas molecules and atoms through the interaction of gas ionization, titanium sputtering, chemical combination and ion burial. The titanium sublimation pump sublimates titanium from heated filaments which is deposited on a "line-of-sight" transmission to shielded non-working area. Pumping is affected as the active gases combine chemically with this deposited titanium film to form stable compounds. This system provides pressures of 10^{-6} torr and below under typical test conditions.

The getter-ion pumping system was chosen rather than systems that involve introduction of long-chain hydro-carbons. The combination sublimation and sputtering-ion pump system was considered developed sufficiently to meet the long-term automated operational requirements. This system is essentially immune from failures in power, water or air-service.

The 24" diameter bell jar was chosen as it could accommodate an Interplanetary Monitoring Platform (IMP)-I solar array panel within the thermal shroud. The IMP-I panel will probably be the standard design for the next series of in-house spacecraft at the Goddard Space Flight Center. This particular size bell jar was available as a standard size in the industry. The 12" bell jar was designed to accommodate a smaller number of test specimens. This feature would permit periodic removal of specimens for optical inspection and testing without interrupting the long-term thermal cycling test. Both bell jars are fitted with an illumination port of UV-grade fused quartz to permit in-situ solar

illumination measurements. Calibrated standard cells and disc radiometers are mounted to insure the desired solar illumination intensity level. The spectral distribution of the simulator can be checked with a spectrophotometer in the same lab.

THERMAL CONDITIONING SYSTEM

The Thermal Conditioning System (TCS) was designed to provide temperature stabilized GN or LN₂ to the cryoshroud of either of the two or both of the bell jars. The TCS supplies gaseous nitrogen to the selected bell jar shroud at any temperature between -170°C and +150°C with a maximum shroud temperature difference of $\pm 4^\circ\text{C}$ while the shroud is under a distributed thermal load of 140 watts. High flow rates of thermally conditioned gaseous nitrogen transform the shroud into the necessary radiation heat source and/or heat sink to obtain the desired test specimen temperature.

Test specimen heating and cooling is effected by radiation coupling between the shroud and the sample. The thermal shroud system includes a movable shutter in the illumination port and an optically dense baffle which shields the vacuum system internals. The only constraint preventing a 100% view or thermal shape factor from any point on a test panel to a controlled thermal surface is the carrousel shaft.

The shroud wall rate of temperature change is sufficiently rapid to produce a $6^\circ\text{C}/\text{min.}$ change in specimen temperature at any level between +150°C and -120°C. The specimen specific weight and surface emissivity have a large effect on the attainable rate-of-change of temperature. The value of $6^\circ\text{C}/\text{min.}$ is obtainable with silicon solar cells having fused silica coverslides attached such that the composite has a specific weight of 0.83 lbs/ft² or less.

Modulating butterfly valves proportion the gas flow through the GN to LN₂ heat exchanger. This flow variation combined with a controlled power input to the heaters produces a very precise means of affecting temperature control. There is also a large potential heat source or heat sink reserve. The response time and temperature overshoot of the system are minimized by biasing the system source and sink against each other.

The basic components in the TCS are (1) a high-energy density low-mass heater; (2) a three-stage centrifugal blower, and; (3) a liquid nitrogen boiler. These components, their inter-connecting piping and associated controls (LN₂ level, blower power, high and low temperature interlocks, etc.) are mounted in a caster mounted 2.5' x 4.5' x 6'

equipment cabinet. A block diagram of the system is shown in Figure 2. The TCS components are briefly described as follows:

- a. Blower: A three-stage centrifugal blower is used to circulate approximately 220 CFM of nitrogen gas through the system. This blower required considerable modification of a commercially available unit in order to operate with the range of gas temperatures involved. These modifications entailed the installation of super precision bearings, a polished stainless-steel shaft fitted with a specially designed fan and casing redesign to improve the heat dissipation. These modifications limited the bearing temperature excursions to a fraction of the GN temperature range.
- b. Heaters: Rapid transients require that system mass be minimized. This is particularly critical in the heater design as this element runs at the highest temperature of any system component. The system heater shells are fabricated from 3 inch diameter thin-wall stainless-steel tubing. Each heater module contains a 1.6 KW quartz IR lamp and a set of thin anodized aluminum fins. The fins are radiatively heated by the IR lamp and are convectively cooled by the GN stream. The weight of the heater extended surface is approximately one (1) lb.
- c. Boiler: The system heat sink is a LN_2 boiler. Gaseous nitrogen is pumped through the tube side of a shell and the tube heat exchanger. The shell side of this unit is flooded with LN_2 . The liquid level is maintained with a temperature probe, controller, and solenoid valve. Boil-off LN_2 is mixed with the exit gas flow stream to aid in lowering the circulating gas stream temperature. A pressure relief valve is located in the main gas stream to prevent excessive pressure buildup either from the introduction of boil-off gas or from gas expansion during increasing temperature transients in the loop. The relief valve maintains the GN loop pressure at 3 psig.
- d. Control: Operational control is provided by a solid controller having proportional band, rate and reset functions and a dynamic setpoint programmer. The controller has a set point accuracy of $\pm 2^\circ\text{C}$.

Control is obtained by sensing the shroud wall temperature and comparing the measured value to either a fixed or dynamically programmed set point. The resulting error signal is amplified and transformed into a control voltage. This voltage is used to control the output

of a silicon control rectifier (SCR) and a pneumatic valve positioner. The valve positioner operates two butterfly valves which are 90° out of phase. The amount of cooling provided is determined by the ratio of the flow through the boiler to the flow through the boiler by-pass. The amount of heating provided is a function of the magnitude of the error signal and the output of the SCR. There is sufficient overlap between the heating and cooling functions such that transitional operation is essentially continuous. This variation in flow combined with a variation in power input to the heaters produces a precise means of effecting temperature control. There is also a large potential heat source or heat sink reserve. The response time and temperature overshoot of the system can be minimized by biasing the system source and sink against each other. An over-temperature safety interlock using a pyrometer and relay automatically cuts out the heater voltage when the temperature hits a 150°C upper limit and automatically cuts the heater back in at 145°C if required by the programmed input. A schematic of the system control logic is presented in Figure 3.

TEST CARROUSEL

A carousel, or test specimen holder, was designed to accommodate the maximum number of test specimens such that each specimen can be accurately positioned at the illumination port. The system thermal performance objectives required the carousel to be extremely lightweight with minimal thermal mass. The carousel design that emerged was duo-decagon frame that could accommodate thirty six 6"x6" test specimens. The specimens are mounted along the periphery of the carousel in three adjacent rings. Thus, as the carousel is rotated and/or translated, each of the test specimen holders is positioned in front of the illumination port. Solar simulation is provided by a filtered 2500 watt Xenon arc lamp simulator which closely approximates the solar spectrum in space. This capability permits in-situ solar cell electrical characteristic measurements periodically during the test. A test section is included on the carousel to calibrate the solar simulator illumination at the test plane. The solar simulator can be rotated such that its beam is directed at a spectrophotometer to periodically analyze the simulator's spectral distribution.

CARROUSEL POSITIONING

The initial design efforts to provide positioning of the carousel at the illumination port involved various mechanical linkages with rotary and translatory motion feed throughs. These systems could be characterized as being complex, involving considerable thermal mass, imposing internal volumetric constraints, introducing conductive thermal paths and requiring more than one shroud penetration. A novel

approach to the positioning problem was suggested by Maurice Cridlin of the Goddard Space Flight Center. He had devised a sample positioning scheme for a facility that required in-situ measurements of particle radiation effects on the solar absorptance of materials (Ref. 4). This scheme involved attaching the carrousel to a hollow vertical shaft on the center-line. On the PDTVS the shaft penetrates the thermal shroud and bell jar and provides a means of indexing the carrousel through physical movement of the shaft. Additionally, the hollow shaft provides an instrumentation penetration.

The vacuum seal around this shaft is maintained by use of an ante-chamber with two viton "O" rings adjacent to the bell jar. This method requires a roughing pump to separately maintain approximately 10^{-3} torr vacuum in the ante-chamber.

Test specimen positioning accuracy was increased and test time was reduced by the addition of two remote controlled motors. One motor provides the desired vertical movement to align any one of the three rings of specimen holders at the plane of the illumination port by moving the shaft and the rotational indexing platform. The second motor, which is mounted on the rotary indexing platform, indexes each of the twelve specimen holders comprising the ring. This rotary motion is restricted by stops to $\pm 180^\circ$ in order to minimize instrumentation lead movement. The alternate approach of using instrumentation slip rings was considered to introduce unwarranted problems.

Instrumentation capability is increased by the use of a stepping switch installed in the carrousel. This switch connects the instrumentation leads to each of the three rings on command. Thus, only forty leads are fed through the shaft. The leads are potted in the shaft to sustain vacuum.

PERFORMANCE TESTING

The TCS was performance tested and found to meet the program design goals. The actual transient performance of the system is shown in Figures 4 and 5.

The initial cooldown rate from a steady state temperature of 20°C was 14°C per min. for the shroud wall and 6°C per min. for the test specimen.

The initial cooldown rate from a steady state temperature of 150°C was $25^\circ\text{C}/\text{min.}$ for the shroud wall and 11°C per min. for the test specimen.

The initial heat up rate from -140°C was reduced somewhat by the fact that the shroud wall and test specimen were not in thermal equilibrium at the time the test was initiated. The initial heat up rates from -140°C were approximately $10^{\circ}\text{C}/\text{min.}$ for the shroud wall and $7^{\circ}\text{C}/\text{min.}$ for the test specimen.

The initial heat up rate from a steady state temperature of 20°C was $4.1^{\circ}\text{C}/\text{min.}$ for the shroud wall and $3.4^{\circ}\text{C}/\text{min.}$ for the test specimen.

The rapid temperature change of the shroud wall and the close coupling between the wall and the specimen are particularly relevant.

Operation in the flooded LN_2 mode was conducted during Acceptance Testing. The results of the flooded LN_2 mode test are shown in Figure 6.

CONCLUSIONS

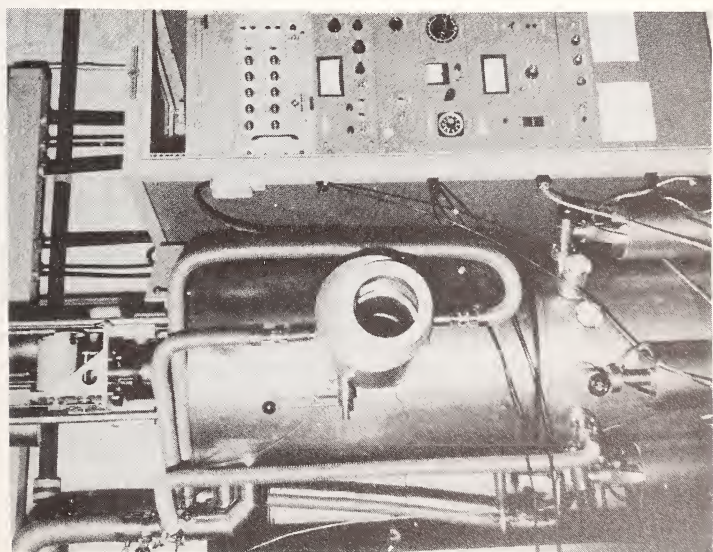
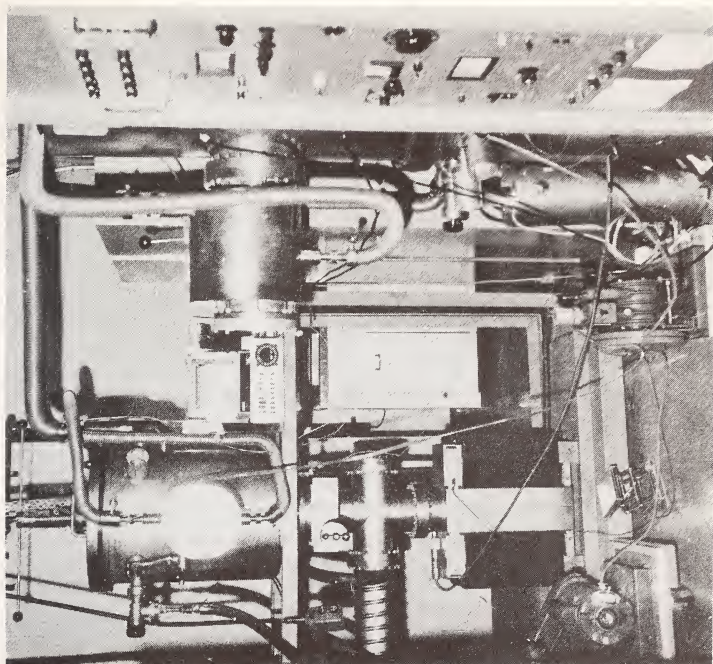
The PDTVS provides a test capability previously unavailable for solar array components. This capability is necessary to evaluate candidate components for the more exacting requirements of currently contemplated space missions. Specifically, it provides the following capabilities for solar array component testing:

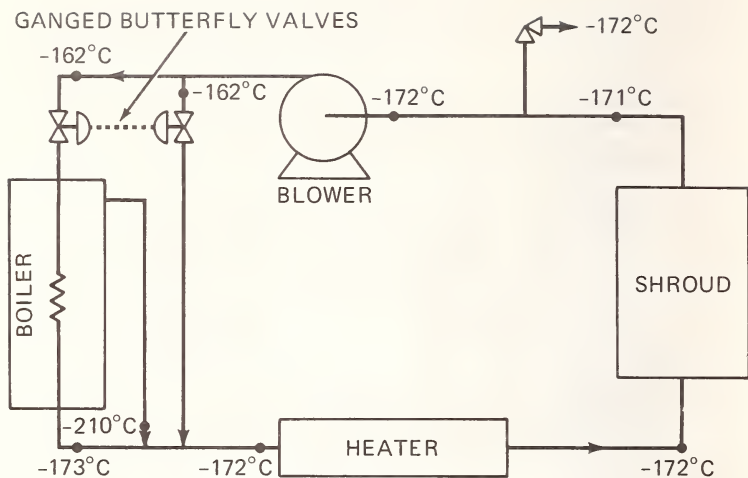
1. PDTVS can accurately reproduce the rate-of-change of temperatures experienced by solar arrays in typical orbits and in a wide range of probe missions.
2. It is programmable to reproduce desired thermal orbital conditions on a long-term basis and with a statistically significant number of solar array components.
3. It enables in-situ solar cell measurements to be taken periodically during long-term thermal vacuum testing.
4. PDTVS is automated for unattended operation. Safety devices will shut down equipment in the event of malfunction.

The PDTVS incorporates several novel design innovations. The high energy density-low mass heater developed for this system was a novel application of radiative-convective coupling of a gas stream to an IR source. The carousel shaft use for positioning and as an instrumentation penetration was an adaption of a recent GSFC development. Modification of the blower to allow operation over the potentially troublesome range of GN temperatures presented a formidable design challenge.

REFERENCES

1. Purcell, J. , "Space Astronomy Present Reality and Future Prospects," Proceedings of the IEEE International Geoscience and Electronics Symposium, Washington, D.C. , April 1970.
2. Ralph, E. , Roger, J. , "Silicon Solar Cell Interconnectors For Low Temperature Applications," Proceedings of the International Colloquium On Solar Cells, Toulouse, France, July 1970.
3. Grimes, D. W. , Spencer, N. W. , "GSFC Specification For Atmosphere Explorers AE-C and -D," S-620-P-1, Greenbelt, Maryland, April 1969.
4. Cridlin, M. S. , et al. "An In-Situ Facility For the Determination of the Effects of A Space Environment On The Solar Absorptance of Materials," X-713-69-257, Goddard Space Flight Center, Greenbelt, Maryland, June 1969.





NOTE:

GN temperature shown for steady state operation at -170°C .

Fig. 2—System block diagram

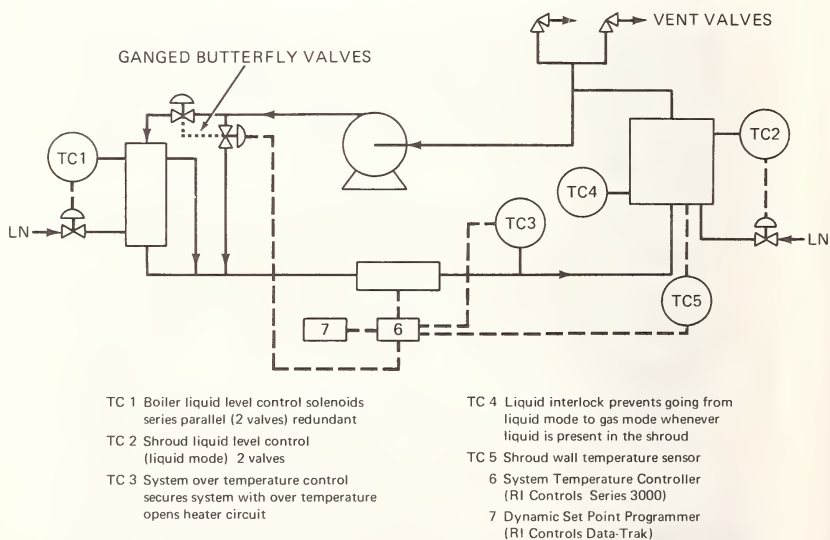


Fig. 3—Control schematic

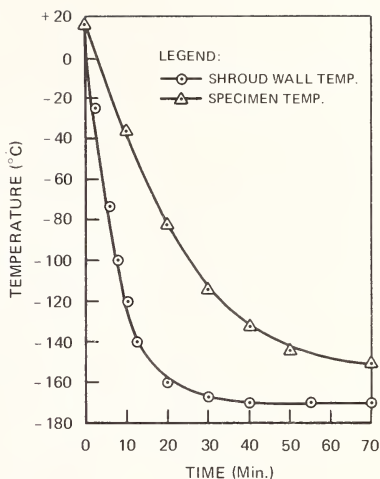
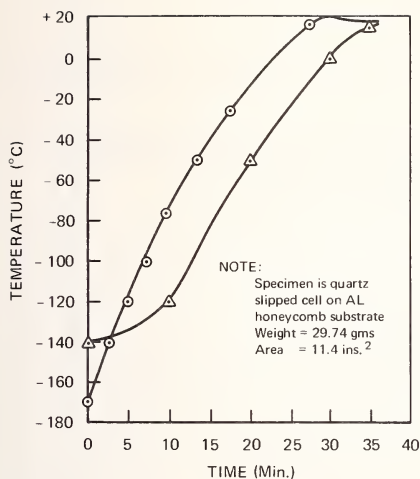


Fig. 4—System transient performance

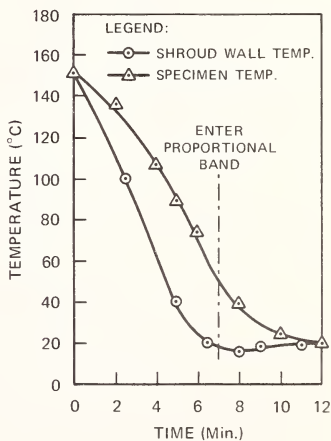
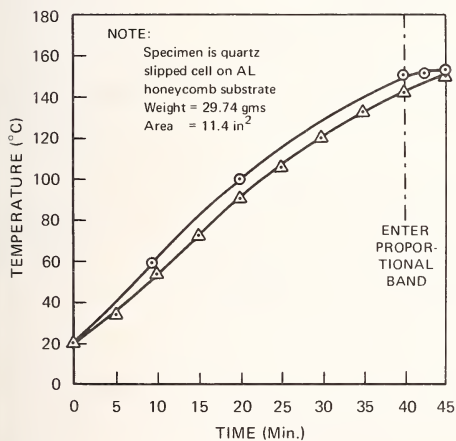


Fig. 5—System transient response

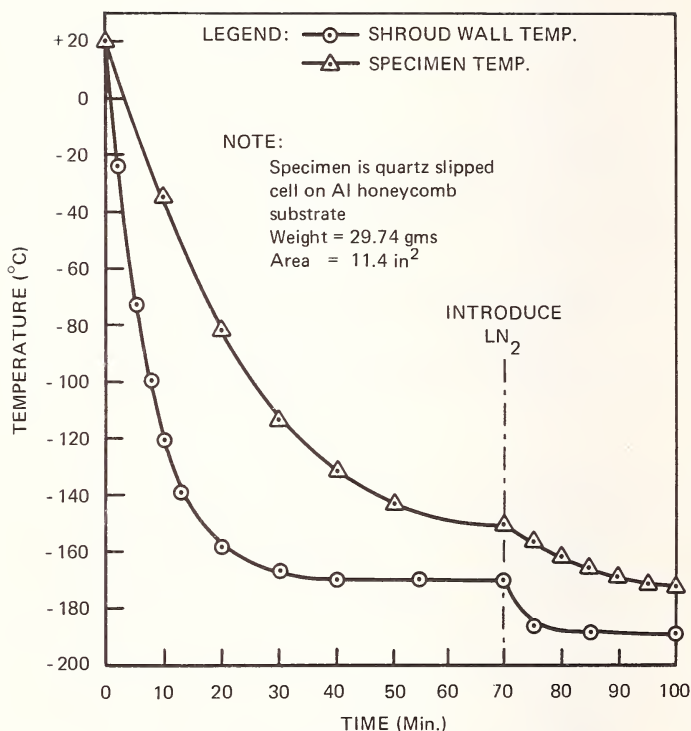


Fig. 6—Liquid nitrogen mode operation

THE CRYOPUMPING SYSTEM FOR THE SPACE SIMULATION CHAMBER

Hiroshi Nakagawa¹ and Ryuji Tsunoda²

ABSTRACT: Recently, the space simulation facility which has distinctive feature was completed in Japan. This facility consists of main- and sub-chamber and other necessary equipment. The main-chamber, having 1.8 m dia. and 6 m length, is accompanied by the pumping system of very high pumping speed. The pumping system consists of cryopump, diffusion pump, mechanical Roots booster pump and rotary vacuum pumps. The ultimate pressure of the order of 10^{-9} Torr was achieved by this system. The sub-chamber, having 60 cm dia. and 120 cm length, is accompanied by the pumping system which is completely oil free. The pumping system consists of cryopump, sputter-ion pump and cryosorption pumps. The ultimate pressure of the order of 10^{-10} Torr was achieved by this system. Determination of the pumping speed of the cryopump is a very complicated procedure and in this study we propose the new factor: "Arrival Probability" which is computed by Monte Carlo method. The dynamic performance of oil free pumping system, especially the using order of cryosorption pump was investigated, and the residual gases were analyzed by mass-filter. The concept of "Self-contamination Factor" proposed by Dr. R. Chuan is adopted to this study to determine the performance of this system, and the factors of 0.006 and 0.0012 were obtained under the actual operating condition.

KEY WORDS: cryopumping, ion pump, space simulation chamber, pumping speed, vacuum.

1. INTRODUCTION

As the Japanese space development project is rapidly progressing, the demand for the space environment chambers is also escalated. Some

^{1,2}Nippon Sanso K.K. (Japan Oxygen Co., Ltd.) Tokyo, Japan.

space chambers have been constructed and in operation in Japan for the purpose of testing satellite assembly, researching the adaptability of components and studying of fundamental properties of materials. But almost all of these chambers are rather small and simple, and are designed only to display the high vacuum condition, not considering carefully the true meaning of the simulation engineering for the space environments, especially from the viewpoints of "cleanness" and "contamination".

Recently, a complete simulation facility which has a distinctive feature of the reproduction of space environment and rationalized simulation system was constructed and delivered to the NASDA (National Space Development Agency of the Japanese Government) to satisfy the above mentioned requirements.

This facility consists of two chambers, main- and sub-chamber, high pumping speed and completely oil free evacuation system for the main-chamber and sub-chamber respectively, solar radiation sources and other necessary apparatus.

The main-chamber was designed for the thermal-vacuum testing of the Japanese artificial satellite under environment of high vacuum, solar radiation and heat sink, and the sub-chamber for research on the properties and effects of the components and materials to be used in the space under environment of oil-free ultra-high vacuum and solar radiation.

The vacuum pumping system for the main-chamber consists of a series of cryo(condensation)pump, diffusion pump, mechanical booster pump (Roots type blower), and rotary pumps, while the pumping system for the sub-chamber is completely oil free and consists of a cryo(condensation) pump, sputter-ion pump and cryosorption pumps.

Solar simulator for the main-chamber is a reflector type with a parabola mirror, using three of 6.5 KW xenon lamp and has an intensity of 1.5 KW/m^2 . Solar radiator for the sub-chamber is a direct projection type with a 2 KW xenon lamp and has an intensity of 1.8 KW/m^2 .

2. DESIGN OF FACILITY

a. Chambers

The main-chamber and sub-chamber are horizontal cylinders made of 18-8 stainless steel and general dimensions of these chambers are tabulated in Table 1.

Interior surface of both chambers is sand-blasted and polished to diminish the outgassing from the stains or rough spots on the surface.

The main-chamber can be baked up to 150°C for degassing purpose by circulating hot triethylene-glycol as a heat-transfer medium through pipes attached to the outer surface of the chamber, and it can also be quickly cooled down to the room temperature by circulating the cooled heat-transfer medium through the same pipes.

The sub-chamber can be baked up to 250°C by electric heater jacket. Warming and cooling of the chamber can be done by automatic programming.

The structures of chambers are illustrated in Fig. 1. The doors of both ends of the main-chamber can be moved by means of electric carts. The gaskets are made of Viton-A, which may release large quantity of

gas and vapor, but the total rate could be neglected because of the surface area of gaskets is very small comparing to that of chamber surface.

Satellite can be hung from the lod attached to the top of the chamber and rotated.

b. Shroud

The inside of both chambers are completely covered with double layers of aluminum shrouds and their configuration with cryopanel is illustrated schematically in Fig.2. The dimensions of shrouds are listed in Table 1. The shroud is designed to be cooled by liquid nitrogen so as to be a heat sink of radiation from the satellite and other test specimens and simultaneously to be a cryopump for vapors and gases which can be condensed at this temperature, and also as a heat shade of the cryopanel. Cryopanel is cooled by 10-15°K gaseous helium and this acts as a cryopump for the other gases.

The shrouds and the cryopanel are assembled from extruded aluminum pipes with fixed fins as the detailed structure as shown in Fig.3. Interior surface of the shrouds is coated by black epoxy paint, which has the emmisivity of more than 95% even in the infra-red range.

Welding of aluminum to stainless steel is usually very difficult and causes many of leak troubles, but in this study we used friction-welded joint which showed the reliable performance.

The configuration of shroud and cryopanel affects very seriously the pumping speed of cryopump, and this will be discussed in detail in section 3C.

c. Cryogenic System

Liquid nitrogen is supplied into the shrouds, to the helium refrigerator and to the cold baffles of pumping system from the pressurized 6,000 liter liquid nitrogen tank. A part of evaporated nitrogen can be recovered by the nitrogen liquefier.

Helium refrigerator is a closed cycle, liquid nitrogen pre-cooled type with a reciprocating expansion engine as shown in Fig. 4, the compressor is a completely leak free type with built-in motor. Leakage of the helium from the whole cryogenic system is guaranteed for less than 6 m³/year, therefore there is no need to supply helium for a long time.

As to ensure the utmost efficiency, the whole cryogenic system including gas helium pipe lines to the cryopanel in the chambers is completely super-insulated. The refrigerating capacity of the system was designed as much as 100 W at 15°K, and it was proved that more than 150 W of cold energy at 15°K could be available, and the ultimate temperature of refrigerator itself was measured as below than 10°K.

The heat loss at these pipes of gaseous helium was measured as the order of 0.025 W/m. The operating performance of helium refrigerator is shown in Table 2, wherein three cases using main-chamber, sub-chamber and only the refrigerator are shown respectively. In the latter case, the cold output was measured by means of a small heater as a dummy which was attached to the outlet part of the expansion engine.

d. Pumping System for the Main-chamber

The pumping system for the main-chamber consists of above mentioned 6 m^2 cryopump, a 36-inch diffusion pump, a Roots type mechanical booster vacuum pump and two rotary vacuum pumps. The capacities and specifications of these pumps are tabulated in Table 3, and the whole system is shown in Fig. 5.

The estimated outgassing rate from the wall and other parts in the chamber is listed in Table 4, and the total outgassing rate was believed as in the range of 1.5×10^{-2} Torr.L/sec., but this rate was mostly depending on the outgassing from the shroud. When the shroud is cooled down by liquid nitrogen, the rate should be decreased to be neglectable, and the total rate would be estimated at the order of 1×10^{-3} Torr.L/sec.

The surface area of cryopanel is 6 m^2 and conductance of opening area of cryopanel is about 6×10^5 L/sec., then the expected pumping speed of the cryopump could be presumed as 1.7×10^5 L/sec. at least. Therefore, the ultimate pressure could be expected as:
 $(1 \times 10^{-3}) / (1.7 \times 10^5) = 7 \times 10^{-9}$ Torr, when the shroud is cooled down and cryopump is operated

The outgassing rate from the actual satellite usually shows various values, but if the surface area of components of the satellite is supposed as 10 m^2 , and outgassing rate is estimated as 2×10^{-7} Torr.L/sec. cm^2 , then the total outgassing from satellite would be 2×10^{-2} Torr.L/sec.

Therefore the operating pressure of $(2 \times 10^{-2}) / (1.7 \times 10^5) = 1.2 \times 10^{-7}$ Torr could be achieved in actual simulation test.

e. Pumping System for the Sub-chamber

The system is designed to diminish the self-contamination of the sample and also to assure of completely oil free "clean" environment. The pumping system consists of the above mentioned 0.6 m^2 cryopump which has pumping speed of 20,000 L/sec, a sputter-ion pump of 400 L/sec and four of the liquid nitrogen-cooled cryosorption pump, each containing 1 Kg of Molecular Sieves 5A. The adsorptive capacity of the above four sorption pumps can be estimated as to evacuate the 300 L chamber to the pressure of 10^{-3} Torr from the atmospheric pressure.

After the cryosorption pumps are saturated, the sputter-ion pump and cryopump will be started to operate.

The outgassing rate from the inside of the sub-chamber is listed in Table 4, and the total rate would be the order of 1.1×10^{-5} Torr.L/sec when the shroud is cooled and the cryopump is operated. The surface area of cryopanel is 0.6 m^2 , and the conductance of opening area of shroud is 5.9×10^4 L/sec, then the pumping speed of cryopump is expected at the order of 2×10^4 L/sec. Therefore the ultimate pressure of:
 $(1.1 \times 10^{-5}) / (2 \times 10^4) = 6 \times 10^{-10}$ Torr could be expected when the shroud is cooled down and the cryopump is operated.

3. PUMPING-DOWN CHARACTERISTICS

a. Main-chamber

Fig. 6 shows some typical performance curves of pressure down of the main-chamber. Curve A denotes the case of the following procedure:

(1) the chamber is baked out and evacuated for a long period, (2) dry nitrogen gas is introduced into the chamber, (3) the chamber door is kept open for 30 min to be exposed to the atmosphere, then, (4) start to pump down. The ultimate pressure of 2×10^{-9} Torr was observed within 4 hours.

Curve B in Fig. 6 shows the following case, i.e. (1) and (2) are same as above, (3) is kept for 2 hours, closing the door, then, (4) start to pump down.

There is little difference between curve A and B at the final period of pumping down, when the cryopump is operated, there is a remarkable difference when the chamber is evacuated by diffusion pump only, and this seems attributable to the atmospheric moisture. By this figure it is confirmed that the evacuation system using cryopump can endure the high gas load, and especially it shows a good performance even when the large quantity of water vapor and other condensable vapors outgassed from sample.

b. Sub-chamber

Fig. 7 shows the pumping characteristics of the sub-chamber. Curve A is in the similar case to that of curve B in Fig. 6, while curve B is in the case where it is evacuated by cryopump after 24 hours of evacuation and degassing by sputter-ion pump.

In each case, the four cryosorption pumps are operated successively one after another, and this method shows better performance than the method of using these four pumps simultaneously, and these characteristics are proved by theoretical analysis. The sputter-ion pump should be used when the shroud is cooled by liquid nitrogen to diminish the quantity of outgassing from the shrouds and sputter-ion pump itself.

The ultimate pressures are 2×10^{-9} and 2.7×10^{-10} Torr in the cases of A and B respectively. These pressures are measured by nitrogen-calibrated nude B-A gauge.

c. Pumping Speed of Cryopump

The method of evaluating or estimating the pumping speed of cryopump has been investigated and discussed by many researchers (1), but they are devoted to deal with the phenomena concerning the sticking probability or condensation factor.

In such case where the cryopanel is surrounded by shrouds, we would like to emphasize as the most important factor which expresses the performance of cryopump: "Arrival Probability" (Pa). This is the ratio of the total number of molecules arriving to the cryopanel after several collisions with the shroud, which is the heat shade of cryopanel in this case, to the number of molecules which enter through the opening of the shroud. Considering this probability, the pumping speed of such cryopump is expressed as:

$$S = M.F.A.Pa.Km = C.Pa.Km \quad (1)$$

where F and A are open area ratio and overall area of shroud respectively, (F.A is area of opening of shroud), M is number of molecules entering through open area of shroud in the molecular flow condition expressed in L/sec per unit area. Km is sticking probability of molecules

reaching onto the cryopanel. Then, $M.F.A. = C$ is conductance of shroud in L/sec.

Of course, it is very difficult to analyze and define this probability theoretically, therefore it was computed by Monte Carlo method (2), as illustrated in Fig. 8. Briefly, the molecules entering through the opening area of shroud collide with the interior surface of shroud and reflected. Some of them escape out through the opening, some of them collide again with another spot of the surface, while the others arrive to the cryopanel. 3,000 molecules entering through opening of the shroud from various directions are counted, and numbers of arriving molecules to the cryopanel are summed up to the 20th collision with the shroud surface.

The result shows that this probability is strongly influenced by the slight difference of shape and dimension of shroud, as shown in Fig. 9. In the main-chamber, there are three parts of shroud of $L=300$ mm, 600 mm and 1,200 mm. The total of pumping speed of this cryopump shaded by shroud is shown in Table 5, using this "Arrival Probability" and equation (1).

4. PUMPING SPEED MEASUREMENT

The pumping speed of the cryopump of main-chamber is measured over the pressure range of 7×10^{-8} - 1×10^{-5} Torr by the method shown in Fig. 10. Dry nitrogen gas is introduced through a leak valve for the direction of sticking to the shroud of the door. The pressure is measured by two gauges: nude type B-A gauge which is hung at the center of the chamber and ordinary type B-A gauge attached to the wall of the chamber.

The pumping speed observed is shown in Fig. 11, in which line A denotes the value of 200,000 L/sec measured by the wall B-A gauge, while line B denotes the value of 150,000 L/sec measured by the nude B-A gauge.

There are many problems which require careful attention on the method of pressure measurement in the space which is surrounded by cold wall, but in this study only the temperature dependence of the reading of vacuum gauge is corrected.

5. ANALYSIS OF RESIDUAL GAS

The example of composition of residual gases in the sub-chamber when evacuated by the oil free pumping system is shown in Fig. 12, which is analyzed by the Varian-MAT Type AMP-3 Mass-filter at the pressure of 3×10^{-10} Torr. The pattern shows that the principal residual gases are H_2O , N_2 , Cl_2 and CO_2 . Chlorine seems to have come from the solvent which was used for cleaning the analyzer. Gases having mass-number of over 50 are very seldom, and this is the evidence of the merit of adopting the completely oil free pumping system. Also the pattern shows that there is no noticeable leak from the chamber and inside structures.

Fig. 13 shows the mass pattern of residual gases when the cryopump is being operated, while Fig. 14 shows the pattern of 10 minutes after the cryopump is stopped and the temperature of the cryopanel is raised up to $50^\circ K$. These two patterns were obtained in the same experiment, and these

denote that the quantities of H_2 , He, $Ne^{20,22}$, N_2 , and O_2 increase after cryopump was stopped. This confirms that some inert gases are co-condensed together with condensing gases such as O_2 and N_2 , and are released when the temperature of cryopanel is warmed up.

The composition of residual gases of chamber which is quickly evacuated after exposure to the atmosphere as in this study is quite different from that of the ordinary ultra-high vacuum system which is evacuated with a long period of baking up.

6. SELF-CONTAMINATION

Self-contamination factor which is proposed by Dr. R. Chuan (3) is expressed as:

$$Cs = 1 / (1 + \frac{\gamma_c}{1 - \gamma_c} \frac{1}{\gamma_m} \frac{Ac}{Am}) \quad (2)$$

In this study it can be presumed that $\gamma_c = 0.8$, $\gamma_m = 0.5$, and $Ac/Am = 20$ for main-chamber enclosing artificial satellite, then $Cs = 0.006$ is obtained. For the sub-chamber, $\gamma_c = 0.8$, $\gamma_m = 0.5$, and $Ac/Am = 100$ for small testing sample, then $Cs = 0.0012$ is obtained.

The self-contamination factor should be kept in a very low value to realize the true similar environment of space, and this is sufficiently achieved in this study by using large area of cryopump.

7. CONCLUSION

The newest Japanese space simulation facility is described. The pumping systems for main- and sub-chamber showed the distinctive features of very large pumping speed and oil free "clean" system respectively. These are certified by the residual gas analysis and by the concept of "self-contamination".

The new concept "Arrival Probability" to clarify the mechanism of cryopump is introduced, and the procedures of designing cryopump are described using this probability.

8. ACKNOWLEDGEMENTS

The authors wish to acknowledge the suggestions and helps to this study by Prof. Dr. K. Ohshima, Dr. K. Nakayama, and Dr. J. Asai.

REFERENCES

- (1). J.P. Dawson, A.W. Peck, 1962 Trans. 9th Natl. Vac. Symp. Am. Vac. Soc., 57 (1962)
- (2). Y. Akiyama, K. Nakayama, N. Saito, J. Vac. Soc. Japan. 14 (1969) 135.
- (3). R.L. Chuan, The Fluid Dynamics Aspects of Space Flight. 2, (1964) 41.

Table 1. Dimensions of Chambers and Shrouds

<u>Chamber</u>	<u>Main-chamber</u>	<u>Sub-chamber</u>
Type	Horizontal Cylinder	"
Inside Diameter	1.8 m	60 cm
Length	4.9 m	96 cm
Material	18-8 Stainless Steel	"
Surface Area	30 m ²	4 m ²
Capacity	12,600 liter	300 liter
<u>Shroud</u> (Cylindrical)		
Type, Material	Assembled from Extruded Al Pipe with Fins, Epoxy	"
Outside Diameter	1.64 m	50 cm
Inside Diameter	1.44 m	40 cm
Length	3.9 m	70 cm
Surface Area	89 m ²	6.3 m ²
<u>Shroud</u> (Door Part)		
Type, Material	Disk Assembled from the Same Al Pipe	"
Diameter	1.75 m	50 cm
Surface Area	4.5 m ²	0.33 m ²
<u>Cryopanel</u>		
Type, Material	2 Lines of Al Pipe	"
Surface Area	6 m ²	0.6 m ²

Table 2. Performance of Refrigerator

	<u>Main-chamber</u>	<u>Sub-chamber</u>	<u>Dummy</u>
<u>Expansion Engine</u>			
Inlet Pressure (ata)	27	31	28
" Temp. (°K)	20	24	21
" Enthalpy (Kcal/Kg)	26.8	31.5	27.7
Outlet Pressure (ata)	1.25	1.74	1.58
" Temp (°K)	8.5	11.0	10.5
" Enthalpy (Kcal/Kg)	13.4	16.7	15.5
Returning Pressure (ata)	1.25	1.74	1.58
" Temp. (°K)	13.2	13.9	15.2
" Enthalpy (Kcal/Kg)	19.4	20.4	21.9
<u>Capacity</u>			
Cold Out-put (Kcal/hr)	272	291	293
Efficiency of E.E. (%)	78	79	76
Heat Load (Kcal/hr)	94.0	94.5	129.1

Table 3. Pumping System

<u>For the Main-chamber</u>	<u>Specification</u>	<u>Pumping Speed</u>
15°K He Cryopump	Area 6 m ²	170,000 L/sec
Oil Diffusion Pump	36", Heater 30 KW	37,000 L/sec
Roots Blower	Motor 7.5 KW	34,000 L/min
Rotary Pump	Motor 11 KW	6,000 L/min
<u>For the Sub-chamber</u>		
15°K He Cryopump	Area 0.4 m ²	10,000 L/sec
Sputter-ion Pump	-	400 L/sec
Cryosorption Pump	4xl Kg. M-S 5A	-

Table 4. Outgassing Rate from Components

<u>Main-chamber</u>	<u>Area</u> (cm ²)	<u>Material</u>	<u>Outgassing Rate</u> (TorrL/sec.cm ²)	<u>Total</u> (TorrL/sec)
Interior Wall, Chamber	3.0x10 ⁵	18-8 S.S.	2x10 ⁻¹⁰	6.0x10 ⁻⁵
Exterior, Shroud	2.9x10 ⁵	Al	1x10 ⁻⁹	2.9x10 ⁻⁴
Interior, "	5.8x10 ⁵	Al, Epoxy	2x10 ⁻⁸	1.2x10 ⁻²
Cryopanel	6.1x10 ⁴	Al	1x10 ⁻⁹	6.1x10 ⁻⁵
Mirror	5.1x10 ³	Glass, Al	2x10 ⁻⁸	1.0x10 ⁻⁴
Gasket	1.0x10 ³	Viton-A	1x10 ⁻⁷	1.0x10 ⁻⁴
<u>Sub-chamber</u>				
Interior Wall, Chamber	3.9x10 ⁴	18-8 S.S.	2x10 ⁻¹⁰	7.8x10 ⁻⁶
Exterior, Shroud	2.3x10 ⁴	Al	1x10 ⁻⁹	2.3x10 ⁻⁵
Interior, "	3.8x10 ⁴	Al, Epoxy	2x10 ⁻⁸	7.6x10 ⁻⁴
Cryopanel	6.3x10 ³	Al	1x10 ⁻⁹	6.3x10 ⁻⁶
Gasket	3.0x10	Viton-A	1x10 ⁻⁷	3.0x10 ⁻⁶

Table 5. Pumping Speed of Cryopump

<u>Main-chamber</u>				
<u>Dimension</u>	<u>Pa</u>	<u>F.A (cm²)</u>	<u>C (L/sec)</u>	<u>Pumping S. (L/sec)</u>
L = 300	0.622	48,600	574,200	356,000
L = 600	0.306	16,200	191,000	58,500
L = 1,200	0.139	37,800	328,000	<u>62,000</u>
Total				477,000
<u>Sub-chamber</u>				
<u>Dimension</u>	<u>Pa</u>	<u>F.A (cm²)</u>	<u>C (L/sec)</u>	<u>Pumping S. (L/sec)</u>
c.f. Fig 9.	0.661	4,158	49,060	32,500

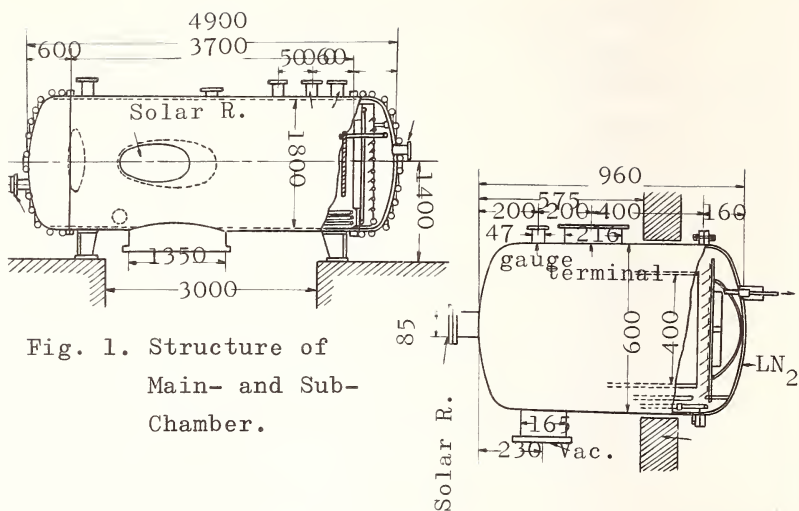


Fig. 1. Structure of Main- and Sub-Chamber.

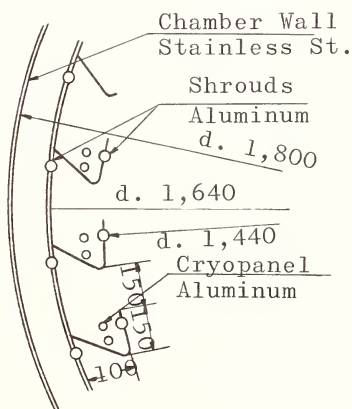


Fig. 2 Shroud and Cryopanel

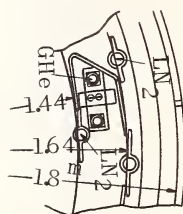


Fig. 3 Configuration of Shroud and Cryopanel

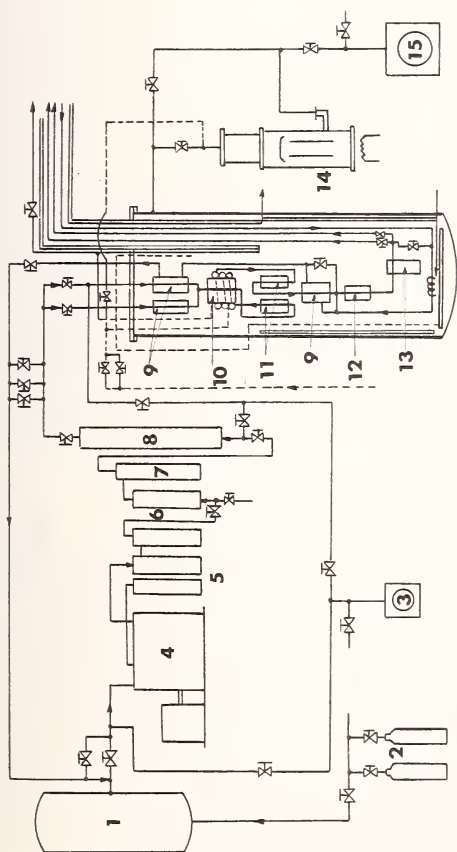


Fig.4 Flow Diagram of He-Refrigerator

- | | |
|------------------|------------------------|
| 1: He Holder | 9: Heat Exchangers |
| 2: He Cylinders | 10: LN_2 Bath |
| 3: Vac. Pump | 11: Absorbers |
| 4: He Compressor | 12: Absorber |
| 5: Separators | 13: Expansion E. |
| 6: Filters | 14: Diffusion P. |
| 7: Absorber | 15: Vacuum P. |
| 8: MS-Absorber | |

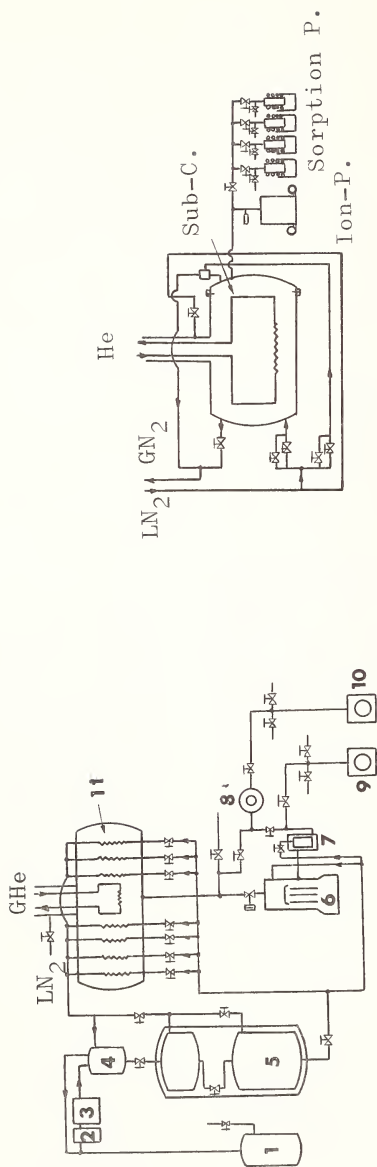


Fig.5 Pumping Systems for Main- and Sub-chamber

- | | |
|---------------------------------|-------------------------|
| 1: N ₂ Gas Holder | 7: LN ₂ Trap |
| 2: Absorber | 8: Roots Type Vac. P. |
| 3: N ₂ Gas Liquefier | 9: Rotary Pump |
| 4: Separator | 10: Rotary Pump |
| 5: LN ₂ Tank | 11: Main-chamber |
| 6: Diffusion Pump | |

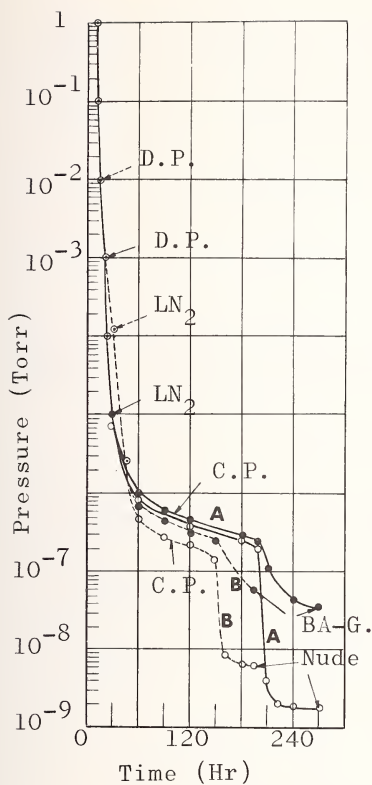


Fig. 6 Pump-down Curve
Main-chamber

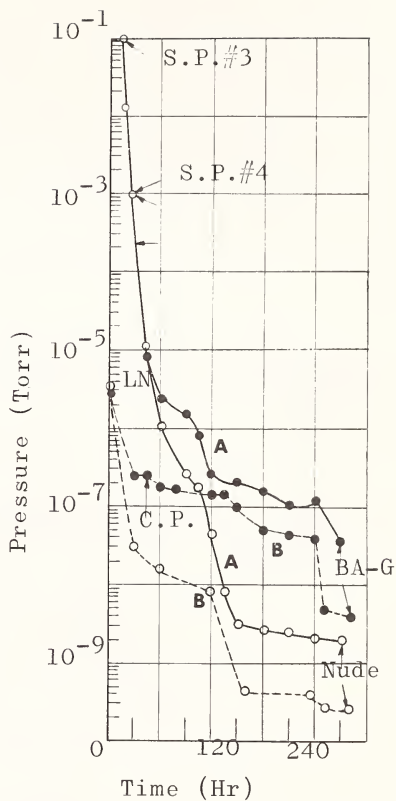


Fig. 7 Pump-down Curve
Sub-chamber

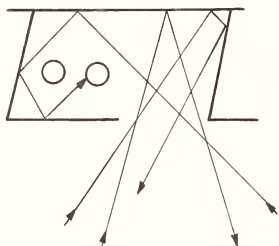
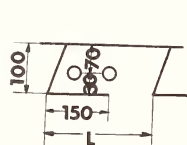
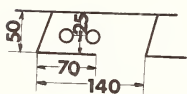


Fig.8 Monte Carlo Method



$L = 300, 600, 1,200$
 $P_a = 0.622, 0.306, 0.139$



$P_a = 0.661$

Fig.9 Arrival Probability P_a

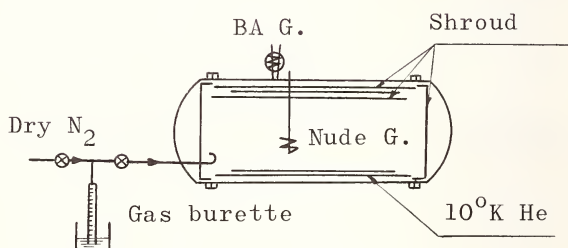


Fig.10 Pumping Speed Measurement

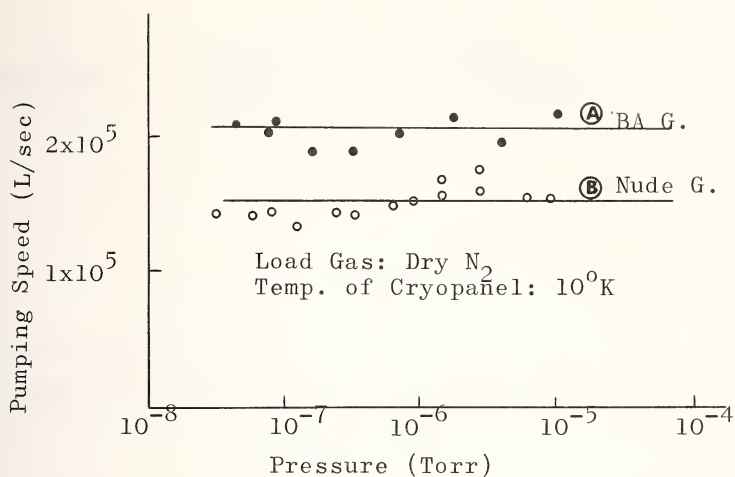


Fig.11 Pumping Speed of Cryopump for Main-chamber

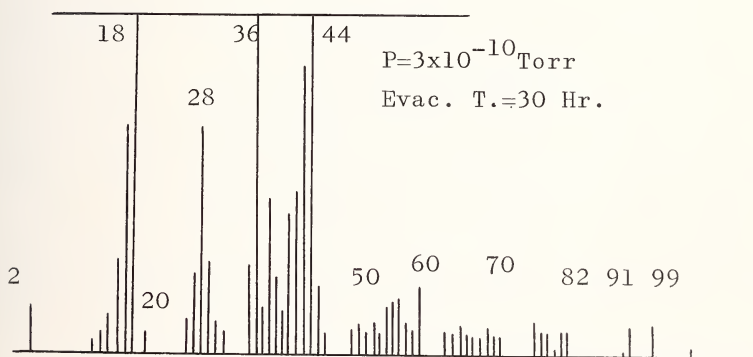


Fig.12 Gas Analysis of Residual Gases in Sub-chamber

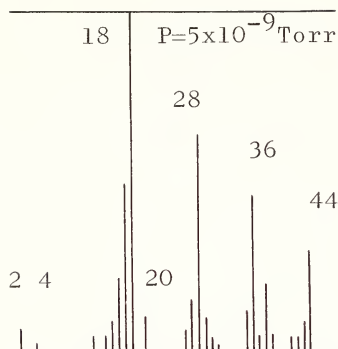


Fig.13 Residual Gas of Sub-chamber, Cryo-pump is operated

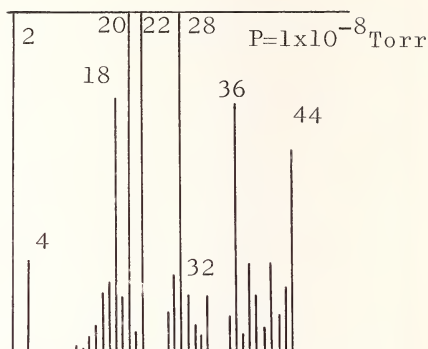


Fig.14 Residual Gas of Sub-chamber, Cryo-pump is stoped

SIMULATION OF SURFACE-ATMOSPHERE INTERACTION PROCESSES FOR MARS

K. M. Foreman¹

REFERENCE: Foreman, K. M., "Simulation of Surface-Atmosphere Interaction Processes for Mars," ASTM/IES/AIAA Space Simulation Conference, 14-16 September 1970.

ABSTRACT: Landings of unmanned spacecraft on Mars can be affected by the dynamics of the lower planetary atmosphere. In an effort to understand the convective motion and effect of surface topography and soil on local atmospheric motion, a laboratory-scale simulator has been designed and built to examine parameters of significance systematically. Scaling law relationships were used in sizing the facility and appropriate test conditions within the terrestrial gravitational environment. This facility is a 4-foot diameter by 8 foot high stainless steel chamber capable of maintaining test conditions to about 10 microns absolute pressure and gas temperatures between -85°C^b and $+65^{\circ}\text{C}^b$. The planetary surface is simulated by an electrically heated aluminum surface controlled to within $\sim \pm 0.7^{\circ}\text{C}^b$ of the initial set conditions.

Measurements of test gas temperature above the simulated planetary surface are made with a specially designed traversing mechanism carrying thin

¹Research Engineer, Grumman Aerospace Corporation
Bethpage, New York 11714

film and thermistor sensors. Temperature profiles above the surface are similar to theoretical calculations for equatorial Mars regions at midmorning, if the lower Martian atmosphere is assumed to have an eddy viscosity of about $5 \times 10^5 \text{ cm}^2/\text{s}$. Additional data show that temperature gradients increase near the surface as the gas pressure is decreased below atmospheric level, and that the degree of turbulence (as evidenced by temperature fluctuations) appears to diminish with lower pressure.

Exploratory tests of thin film sensors as wind speed indicators at simulated Mars surface pressure of 5mb show possible difficulty in differentiating velocity from temperature at wind speeds less than several m/s magnitude. However, thin films appear quite responsive as temperature sensors to pressures on the order of less than 1 mm Hg A.

KEY WORDS: Mars atmosphere exploration, simulation techniques, research facility, convective processes, space research, planetary atmosphere-surface interaction, planetary meteorology

INTRODUCTION

Man has already planted his automated laboratories, and his person, on an extraterrestrial body: the moon. And within the decade, the Martian surface will certainly be investigated by automated spacecraft. This involves a descent through the Martian atmosphere, and during the final, crucial moments just before touchdown the spacecraft will be subject to the dynamic processes of the Martian boundary layer.

Martian planetary meteorology has been the subject of many theoretical studies the past few years. Among the notable contributions are the numerical experiments of Leovy and Mintz¹ and the analyses and

computations of Gierasch and Goody,² Ohring and Mariano,³ and Neubauer.⁴

In all these attempts to explain the relatively few astronomical observations of Mars and predict operational environments with reliability sufficient for the spacecraft builders, there has been a free projection of our Earth experience onto what passes as meteorological data meaningful for Mars.

What is the nature of this information? We are fairly sure that Mars has a very high CO₂-content atmosphere (perhaps ~ 100 percent), with a surface pressure somewhere between 3 and 12 mb. Its gravity is about 1/3 the Earth's and it has characteristic light and dark regions, some of the latter looking like oases within the light regions. The surface temperature varies latitudinally, diurnally, and seasonally between 140°K^b and about 300°K^b.² From a flyby spacecraft, several thousand km from the planet, the surface appears extraordinarily cratered and rough, on a scale greater than what we know exists on the moon.

Mars exhibits dynamic meteorology if only by evidence of visible cloud formations and motions. Some clouds are white, others blue, still others yellow. With almost negligible moisture, the Martian atmosphere's dynamics are most probably unlike the Earth's and may be considered to be closely linked to surface heating and radiative transfer to CO₂ molecules.

Neubauer⁴ and Gierasch and Goody⁵ have noted the potentially strong radiative coupling that can exist because of the 15 micron absorption band of CO₂ and the corresponding IR wavelength emission of a 250°K^b soil, acting as a blackbody.

Clearly, the meteorological theories are approximate, and short of in situ data to be obtained (at this writing) in 1976, they remain somewhat conflicting and indecisive. We need some perspective to decide which theories and assumptions should be accepted, modified, or discarded.

Simulation of planetary processes in a laboratory is a convenient way to examine the various hypotheses, although there are inherent limitations to scaled physical experiments, such as physical size of instrumentation and its effect on the process being simulated. With this in mind, we set out to examine a few concepts of the Mars surface-atmosphere interaction problem. To bring the facility to manageable and economic dimensions, we limited our inquiry to the planetary boundary layer where geostrophic effects could reasonably be ignored. However, to create a quasi-Martian boundary layer environment we needed an enclosure that could maintain an approximately 5 mb CO₂ atmosphere.

The solution was an atmospheric boundary layer simulator. Previous efforts^{6,7} have been directed primarily toward simulating Mars dynamic pressure and properties of developed dust and sand storms relative to their effects on spacecraft materials. However, while composition, pressure, velocity, and temperature of the Martian atmosphere were duplicated to the extent believed to be represented by Mariner flyby data and Earth observations, there is no evidence that the previous experimenters were concerned with complete dynamic simulation of the atmosphere (including scale and gravitational effects) nor with the best estimates of the nature of the Martian surface (soil and topography).

Initially we are concerned with convective processes in a still-wind field. This involves the convection initiation mechanism where radiative transfer may not be negligible and the participation of particulate soil in the vertical transport of free convection or dust-devil type formations; the latter is believed to be the source of extensive yellow cloud formations that, according to the past 90 years of detailed observations, have an occurrence frequency comparable to hurricanes.

This paper will cover the design of the test facility, the operating procedure used to conduct tests, and some preliminary results of still-air convective simulation.

Equipment Design

Scaling laws make possible the dimensioning of the simulator; we considered the nondimensional Grashof and Rayleigh numbers for free convection. Incidentally, since two-phase flow (i.e., solids and gas) may be involved in the dust-devil formation, we can also use the Grashof number in the form where the buoyancy is produced by local density relative to the average density of the surroundings, $\Delta\rho/\rho$, instead of $\Delta T/T$, which relates the relative temperature difference.

Applying the Grashof number to likely conditions on Mars and appropriate test conditions in an Earth-bound simulator (ES) we have the relative dimensions given by

$$\frac{L_{ES}}{L_{Mars}} = \left[\left(\frac{g_M}{g_{ES}} \right) \left(\frac{\nu_{ES}}{\nu_M} \right)^2 \frac{(\Delta T/T)_M}{(\Delta T/T)_{ES}} \right]^{\frac{1}{3}}$$

where L is characteristic length; g , gravitational constant; ν , kinematic viscosity; and T , the temperature; from this we can size our facility.

For simulating a nominal 5 mb, 200°K^b, 100 percent CO₂ atmosphere on Mars, we find we could use a 1000 mb CO₂ test gas at room temperature in a 1 percent scale simulator, based on purely molecular thermal properties of the planetary and simulator gas. (More will be said on this point later in the paper.) However, for other relevant investigations, such as the thermal conductivity of particulate soils at low atmospheric pressure (~ 5 mb), there is also need for a vacuum capability to duplicate appropriate Martian surface conditions.

Among the interesting Martian phenomena are the yellow cloud formations. Initiation of these clouds may be a surface-atmosphere process involving advection and lifting to altitude — by saltation pickup

or turbulence — of top soil material into convective columns similar to dust devils. Ives's⁸ study of terrestrial dust devils indicates that a likely minimum $\Delta T/T$ of about 0.12 is needed to create dust devils with characteristic diameters on the order of 20 meters. In a 1 percent scale simulator, a ΔT in excess of about 40°C^b should be appropriate if unstable stratification can be created. Using Rayleigh number criteria for one fixed and one free surface (the planetary atmosphere case), centimeter-sized layer depths should yield convective flow for ΔT of 5°C^b or more.

On the strength of these studies and considerations, we designed and fabricated a 4 ft diameter by 8 ft high cylinder capable of maintaining test conditions of $10\mu\text{m}$ absolute pressure as well as 2 atm positive pressure over an operating temperature range from -85°C^b to $+65^{\circ}\text{C}^b$. The tank (see Fig. 1) consists of three interchangeable spool sections, each 2 ft high, and two dished end sections, all bolted together at matching flanges. To eliminate chemical corrosion problems, all major structural elements were made from type 304-SA 240 stainless steel. The spool sections were rolled and welded from 3/16 in. thick material and the end sections were made from standard 48-in. diameter dished heads of 1/4 in. thickness. The sectional approach was taken to provide maximum flexibility in setting up tests as well as to permit future extensions to greater heights, if desired. In each of the section flanges "O" ring installations prevent leakage even at micrometer-range vacuum despite the interchangeability feature. Two sections have 18 in. manholes that allow access to the interior for setting up test apparatus and instrumentation. These sections also have 4-in. diameter viewing ports with quartz windows for optical studies. These can be interchanged with solid flanges to carry special instrumentation or actuators. The center section has three 3-in. diameter ports to accommodate probe traversing apparatus and provide a connection to the pumping and gas feed system. An auxiliary valve also is located in this section to bleed off excess pressure rapidly or to permit

various gases, such as CO₂, neon, or custom mixtures of possible atmospheric gases to be introduced. At each of the end sections is an 8-in. diameter flanged port hole. These permit electrical vacuum feed-through connectors to be installed for supplying power to interior equipment or carrying instrumentation signals from sensors to exterior signal conditioning and recording equipment. An automatic pressure relief valve is installed at the top head to prevent excessive overpressures from being inadvertently introduced.

As currently used, the tank is supported upright by 4 legs welded to the bottom dish, and bolted to the concrete floor of the laboratory; there is six in. clearance between the bottom 8 in. flange and the floor. Another possible orientation for the tank is horizontal, as the test section for a closed-loop 8-in. diameter duct that is connected to the flanges at each end of the chamber. This configuration could be used to simulate cross-wind profiles arising from long fetches.

The chamber is connected by a stainless steel manifold to a Hyvac 45 vacuum pump. Various valves and bourdon type pressure gauges permit control of the pressure to particular set values in the 0.1 mm Hg Absolute to 1 atm pressure range; a McLeod gauge measures pressures between 10 micrometers and 5 mm Hg Absolute. One bourdon pressure gauge can be used either for vacuum to 10 mm Hg Absolute or positive pressures up to 2 atm; another gauge overlaps the vacuum pressure range of 0.1 to 20 mm Hg Absolute.

Experiment Procedure

The Martian surface is simulated by a 3-in. diameter area of an electrically heated hot plate mounted centrally within and at the bottom of the atmosphere simulator (see Fig. 2). By means of an externally located temperature controller connected to a temperature sensor attached to the plate, the test surface temperature is controlled to within

0.4°C^b of the desired average value. A 1/2 in. thick aluminum plate was intended to average out local hot spots caused by proximity of the underlying heating element. The degree of success in achieving surface temperature uniformity is evident from the sample distribution of average temperature shown by Fig. 3. The major profiles of air temperature above the heated surface were taken at 90 degrees (i.e., left of center) and 270 degrees (i.e., right of center) orientation angles. The mean positional variation from set temperature across this diameter is 0.7°C^b. This hot plate performance is considered satisfactory for experiments of qualitative objectives. For higher precision data, some modifications are planned to create more uniform surface temperature profiles. It may be of interest to note that the temperature profile of the initial surface simulator configuration exhibits similarity to a planetary surface heated by insolation, at about midmorning, with the "sun" rising at an orientation angle of about 180 degrees in the experiment's set of coordinates.

The hot plate surface outside of the central 3-in. diameter test area is insulated from the test gas by a double layer of asbestos sheet, separated by a 3/8 in. air gap. To prevent edge leakage of heat, a vertical metal radiation shield surrounds the hot plate at the outer edge of the asbestos insulation (not shown in Fig. 2).

Experimental Work

Measurement of gas temperature and velocity profiles above the heated surface is achieved with miniature quartz-coated thin film sensors (see Fig. 4). In addition, a less time-responsive thermistor temperature probe is mounted 7/16 in. to the right of the hot film sensor, which are attached to a traversing mechanism that allows very fine vertical positioning (viz., within 1/200 in.) and horizontal positioning to within 1/16 in. The vertical travel of the instrument carriage is controlled by a constant speed (Motomatic Model E-500 MG) motor

(speed regulation better than 2 percent) with continuous control variability possible up to about 2.5 cm/s linear motion. The motor is geared to a rotating drive tube (see Fig. 5) that runs into the chamber through an "O" ring seal. A miter gear at the end of this shaft engages a matching gear on a vertical threaded rod inside the chamber and causes the instrument carriage to move up or down, depending on the motion mode activated at the controller. Limit switches prevent the carriage from moving beyond desired travel limits. Dynamic braking by the drive motor stops motion within 1/400 in.

The thin film sensors are cylindrical, with an effective length of 0.080 in. and a diameter of 0.006 in. As employed in our tests, these sensors can be used either to indicate local gas temperature or velocity fluctuations caused by the convective motion above the hot plate. As a temperature sensor, the thin film acts as a very fast response linearly varying resistance thermometer. Connected to a resistance bridge and output amplifier, the analog signal output gives virtually instantaneous temperature values. Velocity at the same location is indicated by switching the sensor's signal processing electronics to a velocity mode. Here, the film is maintained at a constant temperature above the local gas (approximately 195°C^b greater) by a bridge servo loop that responds to the increased heat transfer from the film caused by gas motion. The output signal is proportional approximately to the 1/2 power of velocity, i.e., King's law

$$E^2 = [A + B(\rho V)^{\frac{1}{2}}](T_S - T_e)$$

where: E is output voltage; A and B are empirical constants; ρ is gas density; and V is gas velocity. However, there is a need for corrections at low gas velocities (i.e., below approximately 20 cm/s), see Ref. 9.

In the case where the temperature and velocity fluctuations occur simultaneously, the temperature effect can be isolated from the velocity effect by

running two such nearby hot films at somewhat different overheat temperatures, T_{S_1} and T_{S_2} , greater than the average gas mass. Then, the difference in the two sensor voltage outputs can be related to the velocity term in the expression

$$E_1^2 - E_2^2 = [A + B(\rho V)^{\frac{1}{2}}](T_{S_1} - T_{S_2})$$

if the gas density is considered essentially constant over the relatively small differences in operating temperatures and their fluctuations.

Discussion

Some interesting results of preliminary temperature surveys across and above the simulated heated surface are presented in the following discussion. A more detailed and complete analysis is planned for a future paper. Figure 6 shows vertical profiles of temperature above a 120°C^b heated surface for two pressures of air and two temperature instrumentation techniques. The profile at one atmosphere pressure gives evidence of greater convective turbulence than at 15 mm Hg Absolute. The greater heat energy transfer by convection at the higher pressure results in somewhat lower average temperature in the gas above the surface. This is further supported by Fig. 7 which shows the relative variation of temperature with decreased pressure at 0.125 in. above the center of the circular heat source. It is also interesting to compare in Fig. 6 the miniature fast-response thin film sensors to the larger slower responding thermistor probes. It should be noted that the thermistor is about 7/16 in. to the right of the hot film; the surface directly below it is at a negligibly ($\sim 0.25^\circ\text{C}^b$) higher surface temperature than at the center. However, there is evidence with both sensors of the highly variable temperature field within the first two inches above the heat source, and the large temperature gradient within the first 1/8 to 1/4 in. above the bare plate.

When CO_2 is used as the test gas instead of air, it would be expected that similar results would be obtained, except that the profile surveys should indicate slightly lower temperatures in CO_2 because its thermal conductivity is somewhat less than for air. This, in fact, is observed from the test data which shows CO_2 temperatures to be 2 to 3°C^b lower than for air at comparable positions above the heated surface. Thus, qualitatively, the air data presented here is representative for full Martian simulation.

The significance of these results to the planetary problem can be estimated by inspection of Fig. 8. There is a strong similarity between the average temperature profile, measured at 1 atm pressure, in the simulator with the detailed calculations made by Gierasch and Goody² for the equatorial regions of Mars at 10 A.M. Also shown for comparison are late afternoon (4 P.M.) calculations for Mars and the lab measurements at 15 mm Hg Absolute pressure.

The characteristic length for the similar profiles in the laboratory and for Mars calculations are in the ratio of about 10^{-5} . On the basis of the similarity criteria mentioned above in which only molecular gas properties were used, the Grashof number in the laboratory would be also about the same order of magnitude smaller than the planetary condition. However, Gierasch and Goody² used an eddy viscosity value on the order of $10^8 \text{ cm}^2/\text{s}$ (compared to the molecular viscosity value of the order $10^{-1} \text{ cm}^2/\text{s}$) to compute the case for equatorial Mars at 10 A.M. An eddy viscosity of $10^8 \text{ cm}^2/\text{s}$ is, perhaps, appropriate for an assumption of very strong turbulence. However, if a more representative terrestrial value for eddy viscosity on the order of $5 \times 10^5 \text{ cm}^2/\text{s}^{4,10}$ is introduced for the viscosity term in the Grashof number, we achieve practically exact thermodynamic similarity, in the laboratory, with the Mars conditions. Thus, Mars may not exhibit as strong a turbulent atmosphere as has been assumed. These qualitatively similar re-

sults, of course, need further physical simulation such as: CO₂ atmosphere, particulate surface covering (possibly granular limonite) and more uniformly distributed heat source. Nevertheless, the initial results give some perspective on the possible lower atmospheric motions, especially turbulence, that can be caused by convection. Comparison of the reproductions of two strip chart readouts of the hot film resistance thermometer, one at 1 atmosphere air pressure (Fig. 9) and the other at 5 mm Hg Absolute (Fig. 10), further emphasizes the strong temperature fluctuations near the heat source when close similarity (i.e., at one atmosphere pressure) to the planet is set up, as opposed to near-constant temperature at low pressure.

Velocity data is not presented here because the available in situ linear calibration speed range is too low with the existing constant speed motor drive. To remedy this restriction on test speeds, and extend the range to more significant speeds (i.e., at least an order of magnitude greater), we intend to install a linear motor on the traversing carriage to move the attached probes at shorter strokes but faster speeds.

Mars Lander Instrumentation

The hot film instrumentation used in our simulator is of the type that has been considered for wind measurements on Mars landers. Aside from the question of operational survivability in the total mission environment of a Viking-type lander, there has been some question about the suitability of this technique at Mars surface pressure.

To explore this area, we conducted a test at 5 mb pressure in the simulator. Two hot film sensors were mounted above a slowly increasing temperature heat source; one operated as a temperature sensor and the other as a velocity sensor at 1.5 overheat ratio. We found the temperature application to be highly responsive to temperature changes and we believe it could be successfully employed in

Martian pressures as low as 1 mb as a thermometer. However, we have had difficulty in discerning low speed velocity from temperature changes and circuit noise. So, unless improvements in signal processing equipment are introduced, wind speed resolution below several m/s appears questionable.

Future Tests

In addition to the bare-surface temperature surveys, we plan to conduct similar tests with the simulated planetary surface covered with particulate limonite to simulate the Martian soil. This hydrated iron oxide mineral has been found to exhibit thermal and optical properties that best match Martian observations.¹¹ There is a need for updated thermal transfer data on particulates under subatmospheric gas pressure conditions.

Another future test of Martian relevance involves cooling the test gas with liquid nitrogen shrouds to induce formation of solid CO₂ aerosols above the test area. It is believed that these sub-micrometer-sized aerosols can best explain data from experiments on-board Mariners 6 and 7¹² and have also been indicated by interpretation of Mie scattering calculations to explain Mars polarimetric observations.¹³

Conclusions

In anticipation of future spacecraft landings on Mars, a new facility has been designed and constructed to give thermodynamic simulation of atmospheric processes in the planetary boundary layer. Initial qualitative tests of free convection temperature profiles in a still wind field show distinct similarity to detailed theoretical calculations for equatorial Mars regions at midmorning if an eddy viscosity on the order of $5 \times 10^5 \text{ cm}^2/\text{s}$ is assumed for the planet. From these results it appears that the lower two km of the Martian atmosphere could prove quite turbulent under the condi-

tions described. Hot film sensors appear sufficiently responsive to indicate rapid temperature fluctuations in a turbulence field at Mars surface pressure conditions. However, unless extreme care is taken in signal conditioning and processing, one may anticipate difficulty in using hot film anemometry for wind speeds below tens of m/s.

The author thanks Mr. Frank Neumann for his patient assistance in conducting the tests and instituting equipment modifications where necessary. The design and checkout of the simulator were made possible by the energy of Messrs. Suey Jue, H. Rodenburg, V. Taibbi, and J. Wagner. Finally, we acknowledge the interest and support of Dr. N. Milford and the sponsorship of the Grumman Aerospace Corporation as part of its IR & D Program.

References

- [1] Leovy, C. B. and Mintz, Y., "A Numerical General Circulation Experiment for the Atmosphere of Mars," Rand Corporation Memorandum RM-5110-NASA, December 1966.
- [2] Gierasch P. and Goody, R., "A Study of the Thermal and Dynamical Structure of the Martian Lower Atmosphere," Planetary Space Science, Vol. 16, 1968, pp. 615-646.
- [3] Ohring, G. and Mariano, J., "Seasonal and Latitudinal Variations of the Average Surface Temperature and Vertical Temperature Profile on Mars," J. Atmospheric Sciences, Vol. 25, No. 5, September 1968, pp. 673-681.
- [4] Neubauer, F. M., "Thermal Convection in the Martian Atmosphere," J. Geophysical Research, Vol. 71, No. 10, May 15, 1966, pp. 2419-2426.
- [5] Gierasch, P. and Goody, R., "An Approximate Calculation of Radiative Heating and Radiative Equilibrium in the Martian Atmosphere," Planetary Space Science, Vol. 15, 1967, pp. 1465-1477.

- [6] Hertzler, R. G., Wang, E. S. J., and Wilbers, O. J., "Development of a Martian Environmental Simulation Facility," Proceedings of the AIAA/IES/ASTM Space Simulation Conference, Houston, Texas, September 7-9, 1966, pp. 172-178.
- [7] Dyhouse, G. R., "Simulated Martian Sand and Dust Storms and Effects on Spacecraft Coatings," Proceedings of the ASTM/IES/AIAA Space Simulation Conference, Philadelphia, Pa., September 11-13, 1967, pp. 97-103.
- [8] Ives, R. L., "Behavior of Dust Devils," Bulletin American Meteorological Society, Vol. 28, 1947, pp. 168-174.
- [9] Almquist, P. and Legnth, E., "The Hot Wire Anemometer at Low Air Velocities," DISA Information, No. 2, July 1965, p. 3.
- [10] Hanna, S. R., "A Method of Estimating Vertical Eddy Transport in the Planetary Boundary Layer Using Characteristics of the Vertical Velocity Spectrum," J. Atmospheric Sciences, Vol. 25, No. 6, November 1968 pp. 1026-1033.
- [11] Egan, W., "Polarimetric and Photometric Simulation of the Martian Surface," Icarus, Vol. 10, 1969, p. 223.
- [12] Herr, K. C. and Pimentel, G. C., "Evidence for Solid Carbon Dioxide in the Upper Atmosphere of Mars," Science, Vol. 167, No. 3914, January 2, 1970, pp. 47-49.
- [13] Egan, W. G. and Foreman, K. M., "Mie Scattering and the Martian Atmosphere," to be published in Proceedings of the IAU Symposium 40, Marfa, Texas, October 27-31, 1969, (also Grumman Research Department Report RM-461J, November 1969).

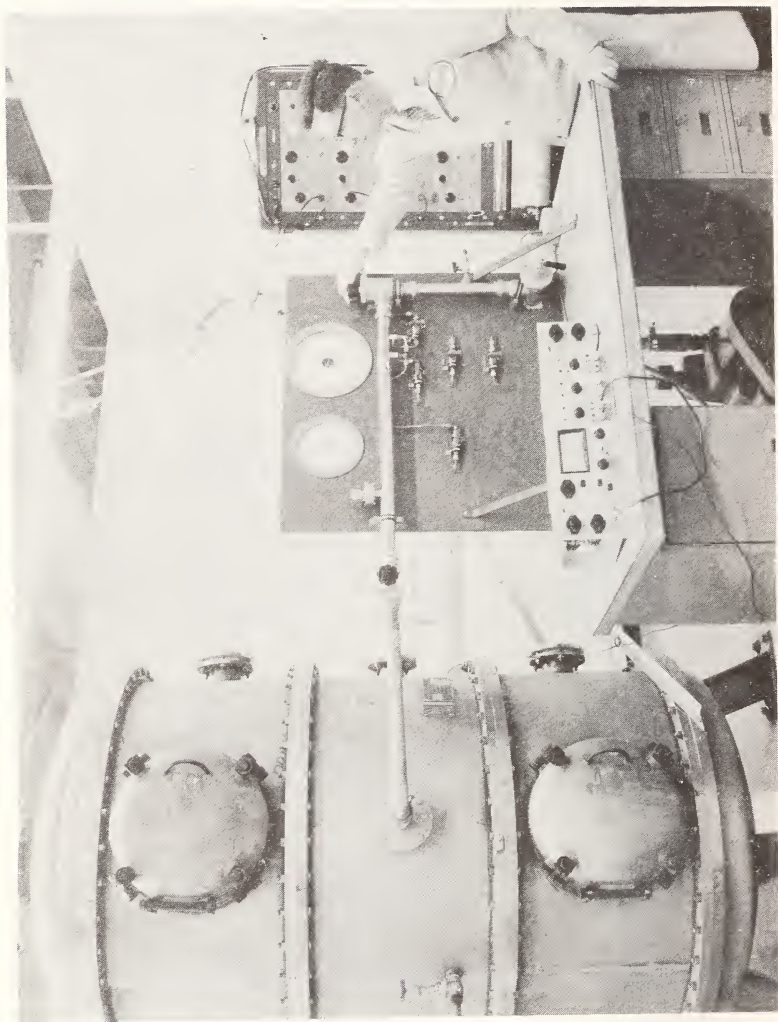


Figure 1. Over-all view of Mars Atmospheric Boundary Layer Simulator

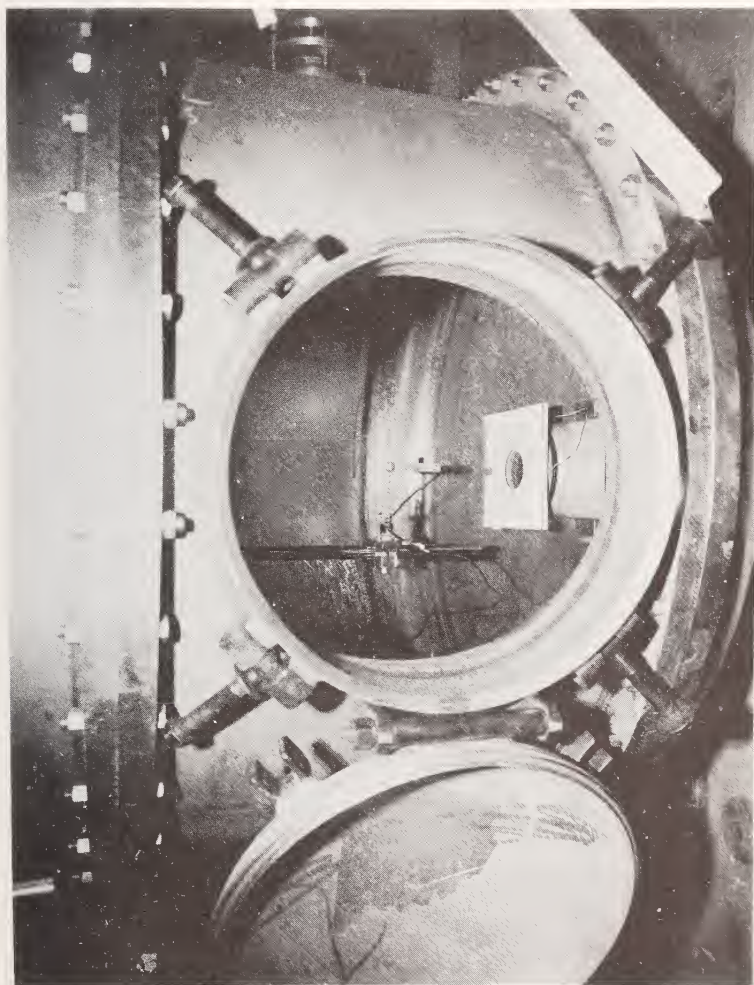


Figure 2. Interior of Mars Simulator Showing Heat Source, to Simulate Planetary Surface, and Instrumentation Carriage.

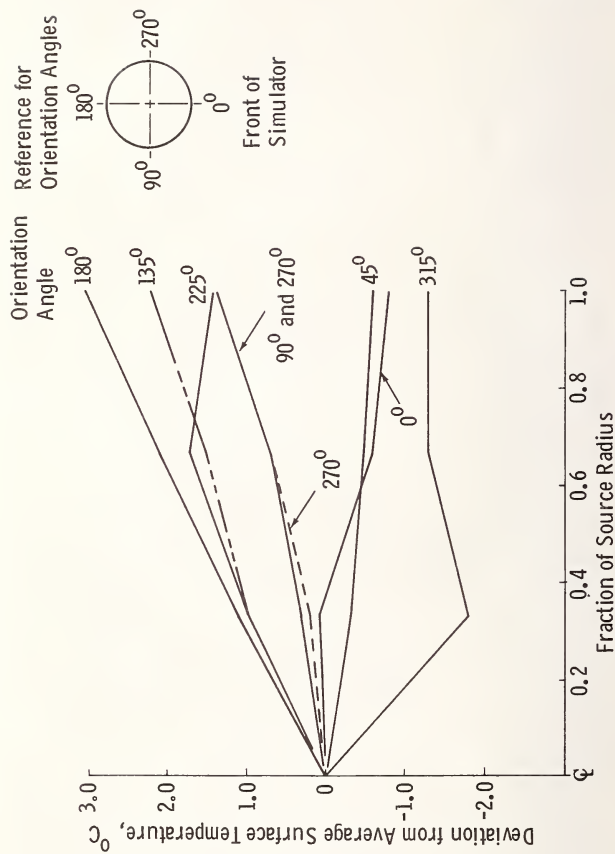


Fig. 3 Test Data of Surface Temperature Variation for a Bare Metallic Heat Source, -Average Temperature at Center = 120°C

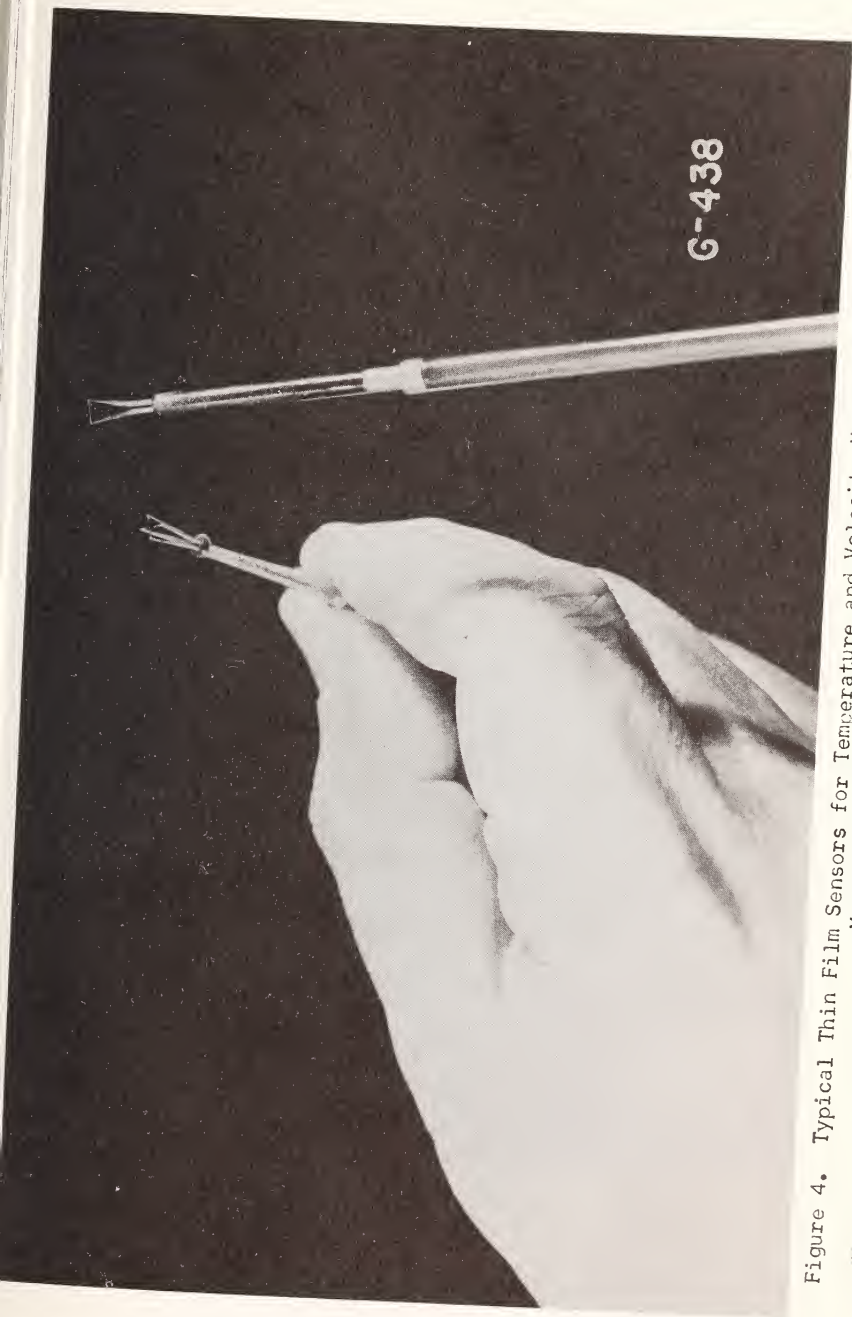


Figure 4. Typical Thin Film Sensors for Temperature and Velocity Measurements in the Mars Simulator.



Figure 5. Constant Speed Motomatic Drive for In-Situ Calibration of Hot Film Velocity Sensors, and Vertical Positioning of the Instrumentation Carriage.

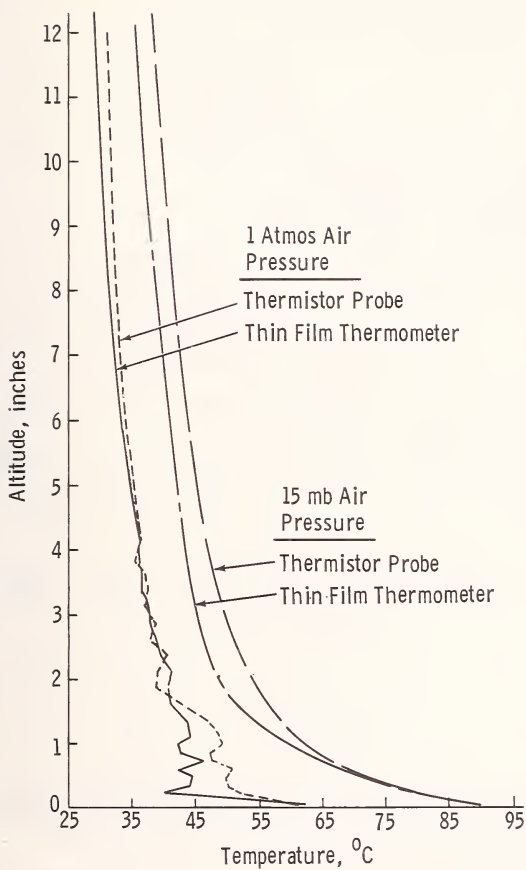


Fig. 6 Temperature Profile Above a 120°C Surface -
Comparison with Gas Pressure and Sensor Technique

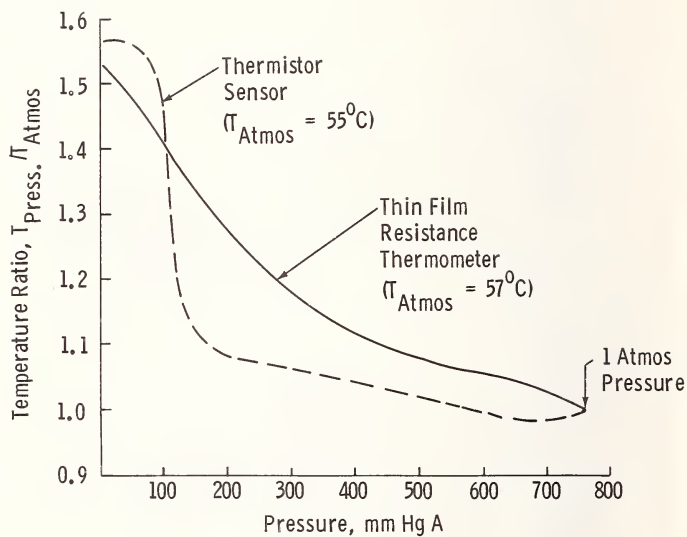


Fig. 7 Variation of Air Temperature with Pressure at 0.125 in. Above a 120°C Bare Surface - Comparison of Two Measurement Techniques

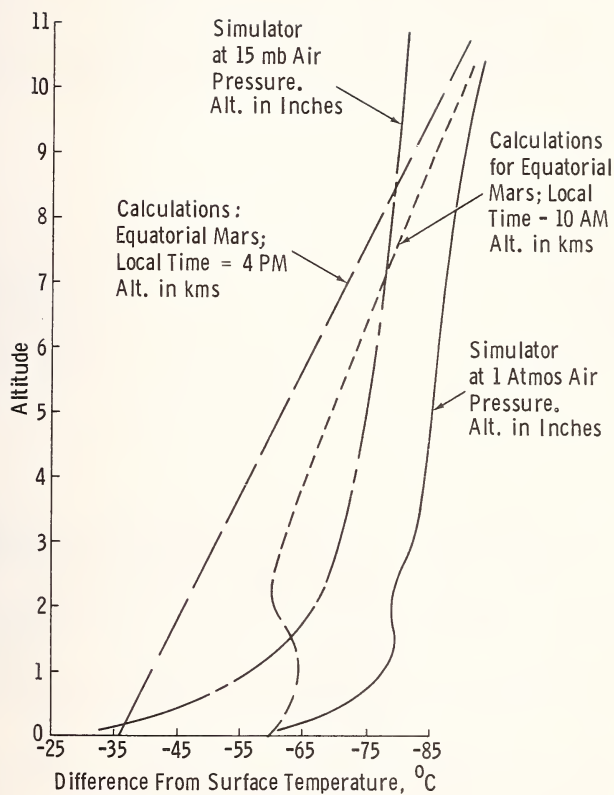


Fig. 8 Comparison of Temperature Profiles in Atmosphere Simulator with Mars Calculations (Ref 2)

THERMISTOR
TEMPERATURE
PROBE OUTPUT

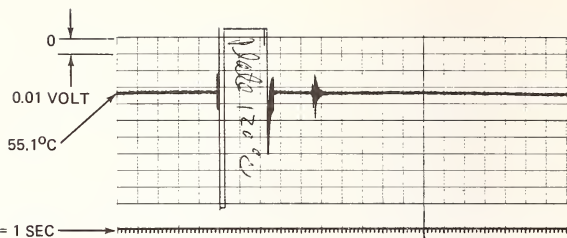
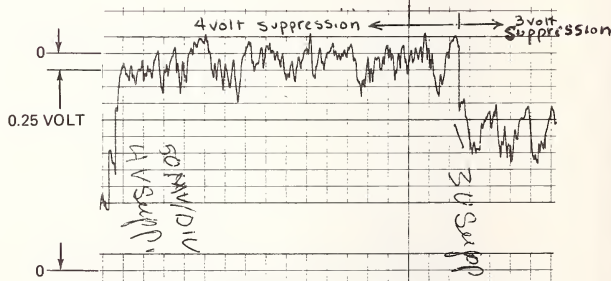
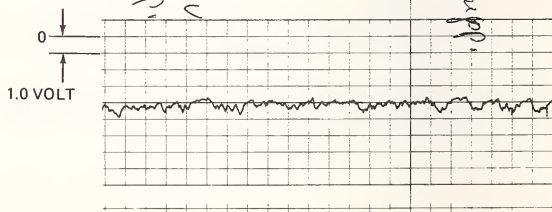


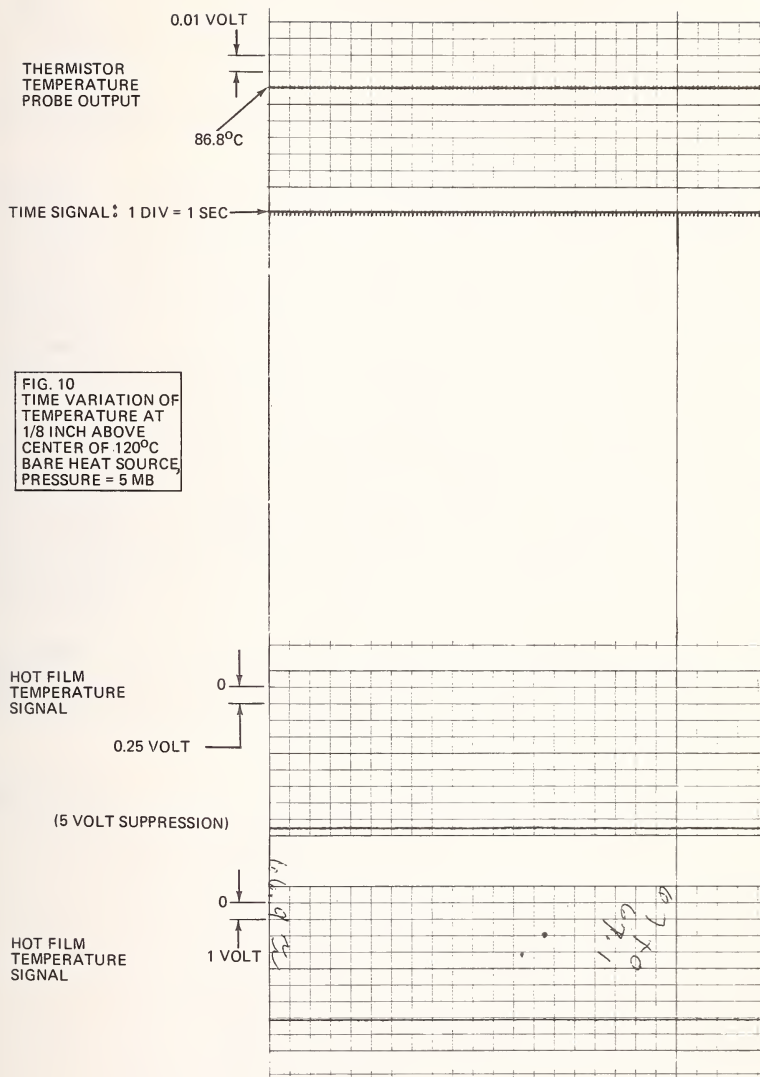
FIG. 9
TIME VARIATION OF
TEMPERATURE AT
1/8 INCH ABOVE CENTER
OF 120°C BARE
HEAT SURFACE,
PRESSURE = 1 ATMOSPHERE

HOT FILM
TEMPERATURE
SIGNAL



HOT FILM
TEMPERATURE
SIGNAL





OPERATION OF A LARGE THERMAL VACUUM CHAMBER
AT MARTIAN PRESSURE LEVELS

T. Buna

Staff Engineer, Thermal Technology Section

J. R. Ratliff

Senior Engineer, Thermal Technology Section

Martin Marietta Corporation, Denver, Colorado

ABSTRACT: A test program was conducted to evaluate techniques of insulating the cold shroud of a large thermal-vacuum chamber from its outer shell, in order to prevent excessive cooling of the latter during Mars environmental simulation tests. A fluidized insulation concept using polystyrene flakes in the shroud/shell interspaces was found to best meet both thermal and operational requirements. With 140 R (77.8 K) shroud, convective transport through the insulation was negligible up to 20 mm Hg chamber pressure, and did not exceed permissible levels up to 50 mm Hg. At the higher pressure levels local heat transfer through the insulation was found to be of a cyclic nature. Thermal data are presented in the form of Nusselt-Rayleigh type correlations. Unique techniques devised for rapid installation and removal of the insulation are described; chamber shell temperature monitoring techniques (including infrared scanning) are evaluated; and the pumpdown characteristics of the insulated chamber are established.

KEY WORDS: Mars environmental simulation, thermal-vacuum chambers, heat transmission, thermal insulation, infrared scanning, evacuating, outgassing.

NOMENCLATURE:

- C = constant in heat transfer correlations
- D = chamber diameter
- E = radiation interchange factor
- f = function symbol
- g = acceleration due to gravity
- h = convective heat transfer coefficient
- k = thermal conductivity
- Nu = Nusselt Number
- q = heat transfer rate per unit area
- Ra = Rayleigh Number
- T = temperature, deg abs
- α = thermal diffusivity
- ν = kinematic viscosity

ρ = density
 σ = Stefan-Boltzman constant

Subscripts:

av = average, pertaining to a convective zone
L = local
C = convection
g = gas
m = mean value
O = shroud
R = radiation
S = shell
 ∞ = ambient atmosphere

I. INTRODUCTION

It has been shown (1,2)¹ that the thermal extremes associated with windless conditions on the surface of Mars can be simulated in conventional thermal-vacuum chambers. The method requires that the chamber be operated at Martian pressure levels (2 to 20 mm Hg) with cold-shroud temperatures simulating the radiation heat sink of the Martian sky (3). With proper test margins the latter may vary between 140 R (77.8 K) and 400 R (222 K) depending on the environmental conditions simulated. There is one predominant problem associated with maintaining these conditions in a thermal-vacuum chamber originally designed for space environmental simulation: convective heat transfer between the outer shell of the chamber and the nitrogen-cooled shroud may cause the shell to cool below permissible levels, with potential catastrophic failure of the chamber's structural members. In addition, the increased (as compared to high-vacuum operation) external heat loads may overload the temperature control system of the shroud.

Outside of complete redesign and extensive modifications of the chamber, there are two possible approaches to minimizing the shell-cooling problem: external heating, and internal insulation. The subject of the present paper is the latter approach as applied to a large (29 ft diameter by 45 ft high) thermal-vacuum chamber intended for use in support of the early Mars programs. In order to preserve the high-vacuum capability of the chamber, it was required that the insulation be removable and its outgassing characteristics be compatible with chamber cleanliness requirements and available pumping capabilities. The temporary character of the insulation system introduced operational problems competing in significance with the thermal requirements: rapid installation and removal techniques had to be devised that were compatible with typical planetary program schedules; and means

¹The numbers in parentheses refer to the list of references appended to this paper.

had to be found to continuously monitor the thermal performance of the insulation once installed and in operation. Thus, the operational and thermal aspects played equal roles in the selection and evaluation of candidate insulation concepts.

Section II of the paper outlines the thermal analysis of the chamber shell/shroud system used for the purpose of providing a framework for planning and interpreting the test program. Section III discusses the test program entailing three phases: A) Full-scale problem evaluation; B) Reduced-scale development; and C) Full-scale performance verification. It is the results of the Series C tests upon which the case for the fluidized insulation concept rests. Section IV is an attempt at generalization of the results in the form of Nusselt-Rayleigh type correlations. Due to the limited nature of the supporting data, caution should be exercised when applying these correlations to conditions other than those of this program.

II. THERMAL CHARACTERISTICS OF THE SHELL/SHROUD SYSTEM

A thermal-vacuum chamber, when operated with a cold shroud in the presence of an internal atmosphere, represents a thermal system too complex to be amenable to purely analytical treatment, hence an empirical approach was considered mandatory in the present investigation. As an aid to planning and interpreting of the experimental program, it was found instructive to formulate some preconceived ideas about the convective processes in the chamber, and to examine them in the light of similarity theory. Such an analysis is presented in this subsection.

The Uninsulated Chamber

A plausible model of internal and external convective patterns is depicted on Figure 1. The convective flow field between the shroud and the outer shell is subdivided into three zones, corresponding to the interspaces of the bottom dome, cylindrical section, and upper dome, respectively. A fourth zone is shown to represent external (ambient) convection, interfacing with all three of the internal zones. The model further assumes that the effect of coupling between adjacent internal zones is negligible except in the vicinity of the zonal interfaces, and that local perturbations due to internal and external structures, penetrations, and liquid nitrogen lines, have a negligible effect on the overall convective patterns, although they may drastically influence local temperatures. These assumptions can be tested by experiment, as it will become apparent subsequently.

Of the three internal zones, the bottom dome interspace has the conditions most favorable for convective motion to develop: unlike Zone III, the Zone I-temperature gradients are unstable

(cold shroud on top, warm shell on bottom), their vertical components being considerably larger than in Zone II. Furthermore, Zone I has a more favorable geometry (shorter flow path lengths) than has Zone II.

Following Batchelor (4), the convective motion in Zone II is expected to be of the boundary layer type, with upward flow adjacent to the shell, and downward flow near the shroud. In the laminar range, the two boundary layers are contiguous, and horizontal convective motion can only develop near the two ends, i.e., at points C and E on Figure 1, whereas heat transfer within the central portion of the zone (Point D) is by conduction. At higher Rayleigh numbers, the two boundary layers become separated by a turbulent core, and convection is similar to that obtained with single vertical surfaces.

The upper dome interspace has the conditions least favorable for convection because of its stable overall temperature gradients (warm dome on top, cold shroud on bottom). Convective motion can, nevertheless, develop near the periphery of the dome (point F on Figure 1) where the dome intersects the shroud at an angle.

The above considerations indicate that, at moderate chamber pressures, the most likely areas affected by convective cooling are: the bottom dome (in its entirety), the upper and lower ends of the cylindrical portion of the shell, the periphery of the upper dome, and potential cold spots due to structural penetrations or nitrogen lines. It is further apparent, that with the possible exception of highly localized spots, the coldest temperatures will occur within Zone I of the chamber, to which our attention will be focused in the remainder of this subsection.

Dimensional analysis indicates that the heat transfer coefficient depends on the Rayleigh number, the Prandtl number, appropriate length ratios, and temperature ratios. Due to the restricted nature of the present investigation, the last three of these may be dropped from further consideration: the Prandtl number, because of restriction to gaseous media; the length ratios, because of limitation of the analysis to geometrically similar domes; and the temperature ratios, in view of the fact that both the shroud and shell temperatures were allowed to vary but slightly during this program. Thus, we may expect correlations of the form:

$$Nu_{av} = C_{av} f(Ra) \quad (1)$$

$$Nu_L = C_L f(Ra) \quad (2)$$

where, by definition

$$Nu_{av} = h_{av} D/k_g \quad (3)$$

$$Nu_L = h_L D/k_g \quad (4)$$

$$Ra = g(T_{av} - T_o) D^3 / \kappa \nu T_m \quad (5)$$

Note that the Rayleigh number is a characteristic parameter of the flow field as a whole within a zone, whereas the Nusselt number may be used to represent either average or local conditions within a zone. Equations (1) and (2) imply that: 1) for all thermally similar bottom dome interspaces the function f and the constant C_{av} are the same; and 2) within a single dome, the ratio C_L/C_{av} is a function of location only, independent of Ra . When comparing data from two different chambers, these statements may be expected to apply approximately at those locations on the shell sufficiently removed from anomalies due to penetrations or lines, and for geometrically similar shells that are sufficiently thin so that one-dimensional conduction may be assumed. This proved to be the case in the present investigation, as it will be discussed in Section IV.

The Heat Balance Equation

The determination of the Nusselt numbers from the test data requires that the heat balance equation of the shell be solved for the heat transfer coefficient. The procedure used in this program is outlined below.

Referring to Figure 1, and assuming one-dimensional steady state heat transfer, the heat balance of an elemental area dA of the shell may be written as

$$q_{R,\infty} + q_{C,\infty} = q_{R,o} + q_{C,o} = q_{net} \quad (6)$$

where the last term on the right hand side represents the net heat load to the shroud. Furthermore,

$$q_{R,\infty} = \sigma E_{\infty} (T_{\infty}^4 - T_s^4) \quad (7)$$

$$q_{R,o} = \sigma E_o (T_s^4 - T_o^4) \quad (8)$$

$$q_{C,\infty} = h_{\infty} (T_{\infty} - T_s) \quad (9)$$

$$q_{C,o} = h_o (T_s - T_o) \quad (10)$$

In equations (7-10), the temperatures are supplied by the test data; E_{∞} and E_o can be calculated from the surface optical

properties and radiation geometries of the chamber; h_o is the dependent variable, whereas h_{oo} can be estimated by the following procedure. Following McAdams (5), the average heat transfer coefficient in air at ordinary temperatures and atmospheric pressure, and for the turbulent regime, may be expressed in the form

$$h_{oo,av} = C_{oo,av} (T_{oo} - T_s)^{1/3} \quad (11)$$

Consequently, using a rationale similar to that in conjunction with Equations (1) and (2), we may assume, that:

$$h_{oo,L} = C_{oo,L} (T_{oo} - T_s)^{1/3} \quad (12)$$

where $C_{oo,L}$ is a function of location only. $C_{oo,L}$ may be determined experimentally for each location of interest from data obtained with the chamber pumped down to high vacuum. In this case, $q_{C,o} = 0$, and, by substituting Equations (7,8,9 and 12) into (6), the heat balance equation may be solved for $C_{oo,L}$.

The Insulated Chamber

The application of similarity relations to the insulated chamber would be of limited practical use, since thermal scaling of insulations is notoriously difficult, and, if successful, would probably result in a loss of identity of the insulation scheme from an operational standpoint. Since the principal aim in insulating the chamber is to suppress convection within the shroud/shell interspaces, the relative insensitivity of the shell temperatures to increasing chamber pressures may be taken as the principal measure of performance for any given insulation concept.

To permit direct comparison with the uninsulated chamber, this performance criterion can be expressed in the form of a Nusselt-Rayleigh correlation. Thus, complete suppression of convection means that the apparent Nusselt number as calculated from Equation (3) or (4) shows no dependence on the apparent Rayleigh number as determined from Equation (5) -the calculation being carried out by ignoring the presence of the insulation in the "convective" zone. Thus, with convection suppressed, we expect

$$Nu_L = \text{constant} \quad (13)$$

$$Nu_{av} = \text{constant} \quad (14)$$

where the constants are generally different at different locations and in different chambers, when using the same insulation scheme.

III. TEST PROGRAM

The test program consisted of three phases, hereafter

referred to as Series A, B and C tests, respectively, as described in detail below.

Series A Tests: Full-Scale Problem Evaluation

The purpose of these tests was to determine whether a potential problem existed, and to obtain preliminary data pertaining to the pressurized (i.e., other than high-vacuum) operation of the 29 ft chamber. The chamber consists of a 304 stainless steel outer shell, 0.625 in thick, externally reinforced with carbon steel stiffeners (see Figure 2). Because of the carbon steel structure, the recommended (by the manufacturer) lower temperature limit of the outer shell is 30 deg F. The chamber is equipped with liquid nitrogen cooled shrouds, normally operating at -320 deg F. There were no provisions for shroud temperature control at the time of this program.

The outer shell was equipped with eleven thermocouples, and data were recorded at 15-min intervals. Pressurization was accomplished by inbleeding gaseous nitrogen. Quasi-stabilized data were recorded at 120 and 500 microns, and 1, 2, and 4 mm Hg internal pressures. Since the lowest temperatures recorded were approaching the 30 F limit at 4 mm Hg, the test was terminated at that pressure.

The temperature data are summarized on Table 1. As anticipated (see (Section II)) the lowest temperatures recorded were on the bottom dome, with only a slight temperature drop experienced by Zone II, and, for all practical purposes, none by Zone III. The conclusion drawn from the data was that the 29-ft chamber could not be operated in its normal configuration at the pressure levels and shroud temperatures required for Mars environmental simulation.

Series B Tests: Reduced-Scale Development

These tests were conducted in a 4-ft diameter by 8-ft high chamber (see Figure 3), and had two main objectives: 1) to confirm and extend the uninsulated-chamber data obtained during the Series A tests; and 2) To evaluate potential schemes of minimizing the shell cooling problem. Initially, consideration was given to the use of external heaters as the sole means of preventing subcooling of the outer shell; the idea was abandoned, however, in favor of insulation, due to constraints imposed by available electrical power supply, the possible thermal overload of the shroud, and complexity of the full-scale installation.

In designing the tests, the guidelines of Section II were followed. The 4-ft chamber is made of stainless steel without carbon steel stiffeners and has no lower temperature limit as far as the present investigation was concerned. However, it was

found impractical to subcool its outer surfaces much below -90 F because of excessive frost buildup. Consequently, the range of Rayleigh numbers in the Series A and B tests were approximately equal. All Series B tests were run with liquid nitrogen cooled shrouds. The uninsulated tests were run at pressures ranging from high vacuum to 50 mm Hg, whereas all insulated tests were run at 50 mm Hg chamber pressure.

Candidate insulation materials were evaluated on the basis of ease of installation and removal, thermal performance, pump-down characteristics, mechanical integrity, outgassing properties, and cost. Following bell-jar screening tests on a number of candidate materials, three were selected for further investigation: polyurethane foam, crinkled aluminized Mylar sheets, and polystyrene flakes. It was found that there was no essential difference in their respective thermal performance when properly installed; however, the installation of the urethane foam and Mylar was extremely difficult and time consuming as compared to polystyrene flakes. Improper installation did result in convective voids and development of cold spots on the chamber shell.

The temperature data are summarized on Table 2. The uninsulated data again indicate that cooling occurs predominantly in Zone I, although some cold spots also developed in Zone II at higher pressures, near the Zone I/Zone II interface. The apparent inconsistencies in the Zone II minimum temperatures of Runs 5 through 8 are attributed to differences in the respective extensions of the bottom dome insulation into Zone II. The apparent increase in temperatures from Run 4 to 5 was due to a rearrangement of thermocouple locations.

The superiority of the polystyrene flake insulation concept was evidenced by two factors: the overall increase in Zone II temperatures during Run 10 as compared to Run 9; and by the lack of development of local frost deposits anywhere on the chamber's outer shell during Run 10. Because of its excellent thermal performance, fluidity (permitting rapid installation and removal by the use of mechanical or pneumatic conveyors), reasonable cost, and immediate availability, the polystyrene concept was selected for insulating the 29-ft chamber.

Series C Tests: Full-Scale Insulation Performance Verification

Objectives- The purpose of these tests was full-scale evaluation of thermal performance and operational characteristics of the fluidized polystyrene insulation concept. Detailed objectives included: 1) Evaluation of insulation and spot-heater effectiveness in maintaining the outer shell temperatures above the 30 F limit, with liquid nitrogen-cooled shrouds, and chamber pressures up to 50 mm Hg; 2) Establishing methods and procedures for rapid installation and removal of the insulation, consistent with typical program schedule requirements; 3) Evaluation of the pumpdown

characteristics of the insulated chamber; 4) Generation of heat transfer data for predicting shell-to-shroud heat loads; and 5) Evaluation of potential shell temperature monitoring techniques.

Setting the upper limit of chamber pressure at 50 mm Hg for the tests was somewhat arbitrary; it exceeded the maximum pressure levels anticipated during Mars simulation tests by a factor of 2.5. The inclusion of spot heaters as a supplemental means of protecting the shell from subcooling was a precautionary measure. Thirty 250-watt industrial heat lamps were made available for the purpose.

Temperature Instrumentation - Fifty thermocouples were used in addition to the permanent shroud-temperature instrumentation of the facility. Five of these were used to measure ambient temperatures at various elevations, twenty-four thermocouples monitored potential cold spots on the shell, whereas twenty-one were used to gather engineering data for heat transfer calculations. The potential cold spots were determined by inspection of the interspaces between the shroud and the shell, and thermocouples were attached in the vicinity of liquid nitrogen lines, and near potential conduction paths between nitrogen-cooled hardware and the outer surface of the chamber. Typical interspace areas are depicted by Figures 4 and 5. Local cooling was also expected near the periphery of the uninsulated upper dome. The engineering thermocouples were placed on predominantly smooth shell surfaces, through which most of the external heat load is transferred into the chamber.

Shell Temperature Monitoring - In addition to thermocouple instrumentation, two other techniques were evaluated: visual inspection, and infrared scanning. Data obtained during the Series B tests have indicated that incipient frost formation on a surface is a definite indication that its temperature is approaching 30 F. Periodic inspection of the outer surfaces of the chamber for the purpose of finding atmospheric moisture condensation or frost spots has proved to be a very effective monitoring technique during these tests.

The second technique employed an infrared television camera which converts the thermal image into a visual picture displayed on a picture tube. Permanent records of the infrared pictures could be obtained by a Polaroid camera attached to the display unit. Typical pictures are shown on Figure 6, with the white areas representing low temperatures. Infrared scanning of the lower dome (Figures 6a and 6b) has confirmed the anticipated locations of potential cold spots, although these areas remained above 30 F throughout the duration of the tests. Excessive cooling of the upper portion of the cylindrical shell due to insulation shrinkage (to be discussed subsequently) was also detected by the infrared camera, as shown by the bright white area on the upper portion of Figure 6c.

Insulation Installation and Removal - Before installation of the insulation could be started, it was necessary to seal all of the diffusion pump inlets, roughing ports, and internal repressurization lines. The sealing was accomplished with various combinations of galvanized wire screens, polyethylene sheeting, and polyurethane foam strips. Special handling fixtures were designed and fabricated for installation and removal of the insulation. Loading was accomplished with the help of the "elephant trunk nozzle" depicted on Figures 7 and 8. Figure 9 illustrates the unloading procedure by the use of a grain auger. The insulated volume consisted of Zones I and II of the shroud/shell interspace, comprising approximately 4300 ft³.

Pumpdown and Settling - After loading of the insulation was completed, a pre-test evacuation was made to determine the effect of vacuum on the mechanical integrity of the insulation. Some settling of the insulation was observed: approximately 50 ft³ additional insulation was required to return the level back to its initial height. The blankoff pressure of the roughing system was 2 mm Hg during this initial evacuation. Considerable contamination of the lubrication fluid of the mechanical pumps was experienced, however, no remedial action was required, since this fluid could be returned to its original condition after the required operating pressure was obtained. The final vacuum level at the start of the test was 0.02 mm Hg, with the liquid nitrogen shroud flooded. After temperature stabilization, the chamber was pressurized with gaseous nitrogen, and stabilized data obtained at 2, 4, 10, 20, 30, 40, and 50 mm Hg. Approximately two hours after the chamber pressure was increased to 4 mm Hg, frost spots were observed to develop at the periphery of the upper dome and the cylindrical area extending 2 to 3 ft just below the upper flange of the chamber. Subcooling in these areas was also indicated by infrared scanning. It was found after completion of the tests that the insulation had settled down to several feet from the upper flange of the chamber, as depicted on Figure 10. This settling is believed to be caused by vibrations of the shroud during cool-down with liquid nitrogen. Consequently, in the future, pre-test pumpdowns will be conducted with the cold shroud operating. The final pumpdown curve of the insulated chamber is shown on Figure 12.

Use of Spot Heaters - Excessive frost accumulation due to insulation settling was prevented by the use of the heat lamps discussed above. Due to the limited number of lamps available, it was necessary to periodically move the lamps to prevent excessive frost build-up in certain areas. The heat lamp arrangement is depicted on Figure 11. The lamps proved to be adequate to maintain the shell temperatures in the indicated areas above the 30 F limit.

Thermal Performance - The temperature data are summarized on Table 3. The performance of the insulation is shown to be pressure-dependent above 20 mm Hg, although it provides adequate protection to the shell up to 50 mm Hg. Typical temperature traces are depicted on Figures 13 and 14. Perhaps the most striking feature of the thermal data is the presence of temperature fluctuations at three distinct frequency levels: 1) The diurnal temperature cycle, with a period of 24 h and amplitude in the order of 5 deg F; 2) A thermal "noise" with amplitudes of a few tenths of a degree, and periods in the order of 1/2 h (temperature recording was at 15-min intervals); and 3) A random low-frequency oscillation at 50 mm Hg pressure displayed by the curve labeled "bottom dome engineering data" on Figure 14, with amplitudes in the order of 3 to 4 F and periods in the order of 2 to 4 h. Similar oscillations are indicated by a number of bottom dome thermocouples, as shown on Figure 15.

A possible explanation of the low-frequency random oscillations is that, at the 50 mm Hg level, a columnar-type convective flow develops through the insulation, with alternate upward flows originating from local hot spots, and downward flows towards the colder regions of the bottom dome. Due to convective heat transfer, the hot spots gradually cool down and lose their "activity", while other spots on the dome take over. During their periods of inactivity, the former hot spots become warm again, and the cycle is repeated.

IV. DATA CORRELATION

Nusselt-Rayleigh type correlations of the bottom dome data obtained from all three series of tests are shown on Figure 16. The curves were determined according to the procedure outlined in Section II. The curve on the left hand side applies to the uninsulated dome, and it may be used to predict internal heat transfer coefficients for conditions other than those of the present test program. Such predictions can be used to determine whether or not a significant shell-cooling problem exists when using a relatively warm shroud (300 to 400 deg R), and to establish heat load curves for the temperature control system of the shroud. Although there is considerable scatter in the data, the correlation is considered excellent in view of the complex geometries involved, the dissimilarities in the two chambers, and the numerous assumptions used in establishing the calculation procedure (see Section II). A log-log plot of local Nusselt numbers vs. Raleigh numbers for both chambers yielded approximately parallel lines (with a scatter similar to that on Figure 16). Hence, it is concluded that Equations (1) and (2) are basically correct.

The curve on the right hand side of Figure 16 pertains to the insulated 29-ft diameter dome. The Nusselt and Rayleigh numbers represent "apparent" values in this case, as discussed in

Section II. The most striking feature of this curve is the apparent sharp transition at $Ra = 10^{11}$ (20 mm Hg), indicating the onset of convective flow. Whether or not the low-frequency oscillations depicted on Figure 15 are associated with a second transition at a higher Rayleigh number is impossible to tell from the limited data available.

V. CONCLUSIONS

- 1) The polystyrene flake insulation concept provides adequate protection for the outer shell of the chamber to perform Mars environmental tests. It is reasonably priced, readily available, and easy to handle.
- 2) The use of spot heaters is an effective means of correcting eventual cold spots due to local voids in the insulation or insulation shrinkage.
- 3) Installation and removal of the insulation is consistent with typical program schedule requirements.
- 4) Chamber pumpdown with the insulation installed presents no problem. No harmful outgassing effects from the insulation have been detected to date.
- 5) Shell temperature monitoring can best be accomplished by a combination of thermocouple instrumentation, visual inspection, and infrared scanning.
- 6) The results of this test program can be extrapolated to other operating conditions by the use of Nusselt-Rayleigh type correlations.

VI. REFERENCES

- (1) Buna, T., "Thermal Testing Under Simulated Martian Environment", Progress in Astronautics and Aeronautics, Vol.21, pp 391-417, Academic Press, 1969
- (2) Buna, T., "Simulation of Planetary Environments", paper presented at the AIAA Test Effectiveness in the 70's Conference, Palo Alto, Calif., April 1-3, 1970
- (3) Wachter, J. P., Journal of Spacecraft and Rockets, Vol 7, No.3, pp 350-352, 1970
- (4) Batchelor, G. K., Quarterly of Applied Mathematics, Vol. XII, No. 3, pp 209-233, 1954
- (5) McAdams, W.H., Heat Transmission, 3rd ed, McGraw-Hill, 1954, pp 173-177

TABLE 1 - Series A test results, 29-ft diameter chamber

Run No.	Pressure, mm Hg	Zone I - Bottom Dome				Zone II - Side				Zone III - Top Dome				Zone IV	
		Temperature, deg F			No. ^a TCS	Temperature, deg F			No. TCS	Temperature, deg F			Temperature, deg F	Ambient	
		Avg	Max	Min		Avg	Max	Min		Avg	Max	Min			
1	0.12	52.7	54.2	50.3	4	63.8	67.7	57.7	2	66.4	66.6	66.2		---	
2	1	49.4	50.9	47.4	5	62.5	67.8	57.0	2	66.5	67.0	66.0		---	
3	2	45.9	48.5	43.2	5	60.5	66.8	54.6	2	66.2	67.6	64.9		---	
4	4	39.7	44.7	34.3	5	57.0	65.6	48.6	2	66.1	67.2	65.0		---	

^aNumber of Thermocouple Readings Reported

TABLE 2 - Series B test results, 4-ft diameter chamber

Run No.	Pressure, mm Hg	Zone I - Bottom Dome					Zone II - Side					Zone III - Top Dome					Zone IV	
		Insulation		No. ^a TCs	Temperature, deg F			Insulation		No. TCs	Temperature, deg F			No. TCs	Temperature, deg F		Ambient	
					Avg	Max	Min				Avg	Max	Min		Avg	Max		Min
1	0.013	None	4	49.8	50.7	49.3	None	8	54.2	59.9	48.4	None	2	64.1	65.7	62.6	77.0	
2	4	None	4	42.7	46.8	36.9	None	8	56.1	60.3	51.6	None	2	70.4	70.6	70.3	77.7	
3	25	None	4	2.0	24.2	-38.2	None	8	44.2	55.6	30.8	None	2	70.9	71.0	70.7	76.1	
4	37.5	None	4	-27.2	8.9	-75.2	None	8	36.6	52.5	-1.1	None	2	68.1	68.4	67.7	73.3	
5	50	None	4	-40.5	7.0	-90.6	None	8	38.1	52.3	13.0	None	2	70.6	70.8	70.5	75.0	
6	50	Mylar	4	57.4	58.9	54.7	None	8	27.6	46.5	-17.3	None	2	70.0	70.0	69.9	73.9	
7	50	Mylar	4	56.5	58.4	54.5	None	8	32.3	52.2	-18.2	None	2	68.3	68.5	68.2	72.8	
8	50	Polyu ^b	4	53.6	55.7	52.2	None	7	42.6	55.4	30.6	None	2	70.8	70.8	70.8	74.6	
9	50	Mylar	4	56.9	59.1	54.5	Mylar	7	43.0	52.9	38.5	None	2	70.1	70.1	70.1	74.9	
10	50	Polyu	4	56.5	58.4	54.4	Styro ^c	7	54.5	68.8	45.5	None	2	68.9	68.9	68.9	75.7	

^aNumber of Thermocouple Readings Reported

^bPolyurethane Foam

^cPolystyrene Flakes

TABLE 3 - Series C test results, 29-ft diameter chamber

Run No.	Pressure, mm Hg	Zone I - Bottom Dome						Zone II - Side						Zone III - Top Dome						Zone IV	
		Insulation	No. ^a TCs	Temperature, deg F			Insulation	No. TCs	Temperature, deg F			Insulation	No. TCs	Temperature, deg F			Ambient	Temperature, deg F			
				Avg	Max	Min			Avg	Max	Min			Avg	Max	Min					
1	0.020	Styro ^b	16	66.4	70.9	62.6	Styro	11	69.1	70.9	66.9	None	9	62.0	66.8	56.2				71.5	
2	2	Styro	16	63.6	69.7	58.2	Styro	11	68.1	70.0	63.4	None	9	60.6	64.1	52.4				73.1	
3	4	Styro	16	63.8	70.1	58.3	Styro	11	68.9	71.6	63.0	None	9	60.5	65.7	50.4				75.0	
4	10	Styro	16	62.7	69.2	57.1	Styro	11	68.2	70.7	62.3	None	9	57.5	65.6	45.0				73.0	
5	20	Styro	16	57.8	66.1	51.3	Styro	11	63.7	66.8	57.8	None	9	50.8	62.3	37.6				69.4	
6	30	Styro	16	54.9	63.7	49.6	Styro	11	62.1	67.1	53.8	None	9	49.6	62.0	31.2				70.0	
7	40	Styro	16	54.3	63.6	49.8	Styro	11	63.8	70.7	51.7	None	9	54.0	65.4	34.3				73.2	
8	50	Styro	26	47.3	58.1	41.7	Styro	11	58.4	66.3	44.3	None	9	51.7	60.5	31.9				69.0	

^aNumber of Thermocouple Readings Reported^bPolystyrene Flakes

LEGEND:

→ Heat Fluxes

- - - - - Convective Flow Patterns

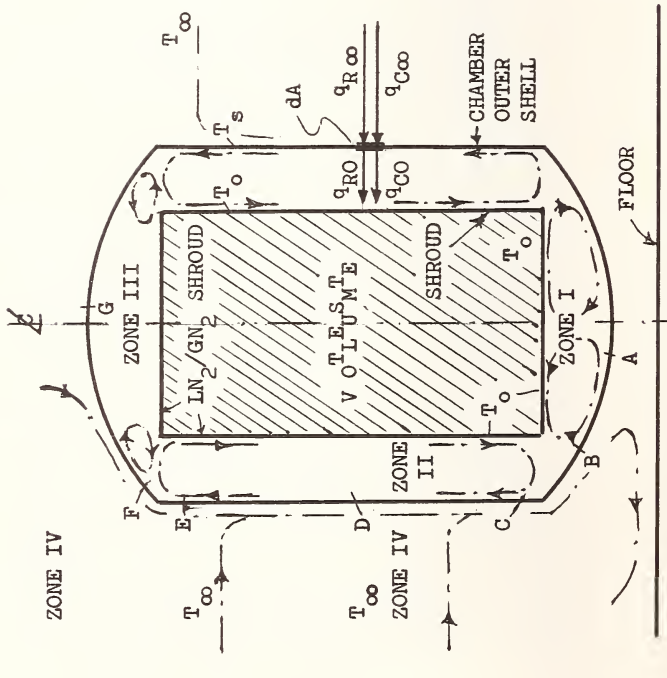


Fig. 1--Chamber Thermal Schematic

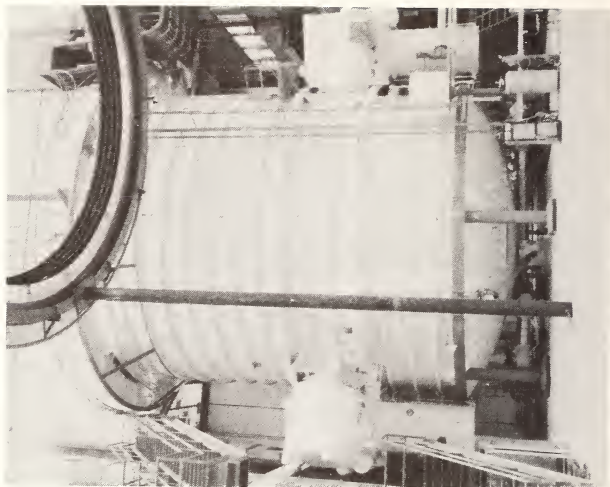


Fig. 2--29x45-ft Thermal Vacuum Chamber

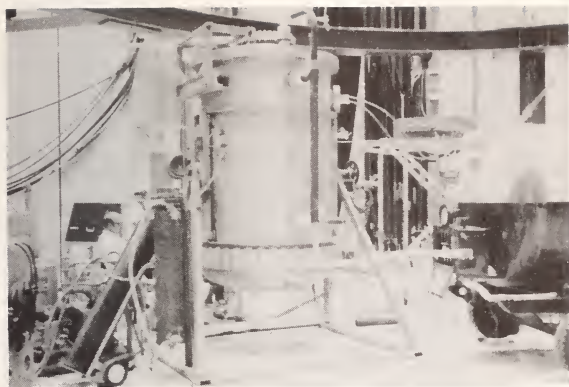


Fig. 3--4x8-ft Thermal Vacuum Chamber

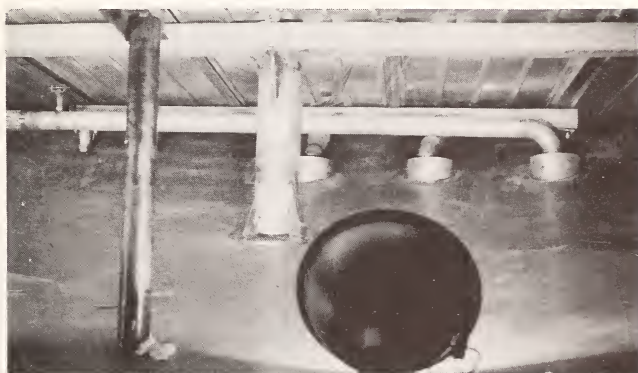


Fig. 4--29-ft Chamber Bottom Interspace



Fig. 5--29-ft Chamber Zone II Interspace



(a) Bottom Dome, Left (b) Bottom Dome, Center (c) Side, Upper Left
 Fig. 6--Infrared Monitoring of 29-ft Chamber Shell Temperatures

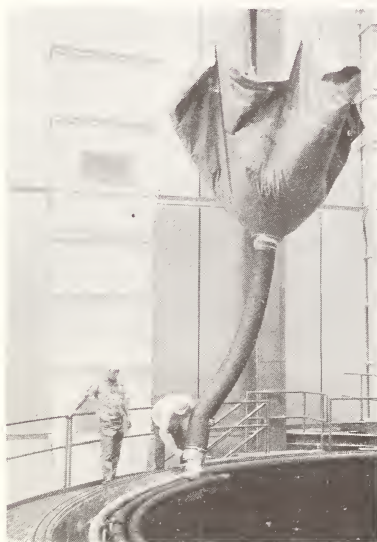


Fig. 7--"Elephant Trunk"
 Nozzle



Fig. 8--Loading the Nozzle



Fig. 9--Insulation Removal



Fig. 10--Insulation Settling



Fig. 11--Heat Lamp Application

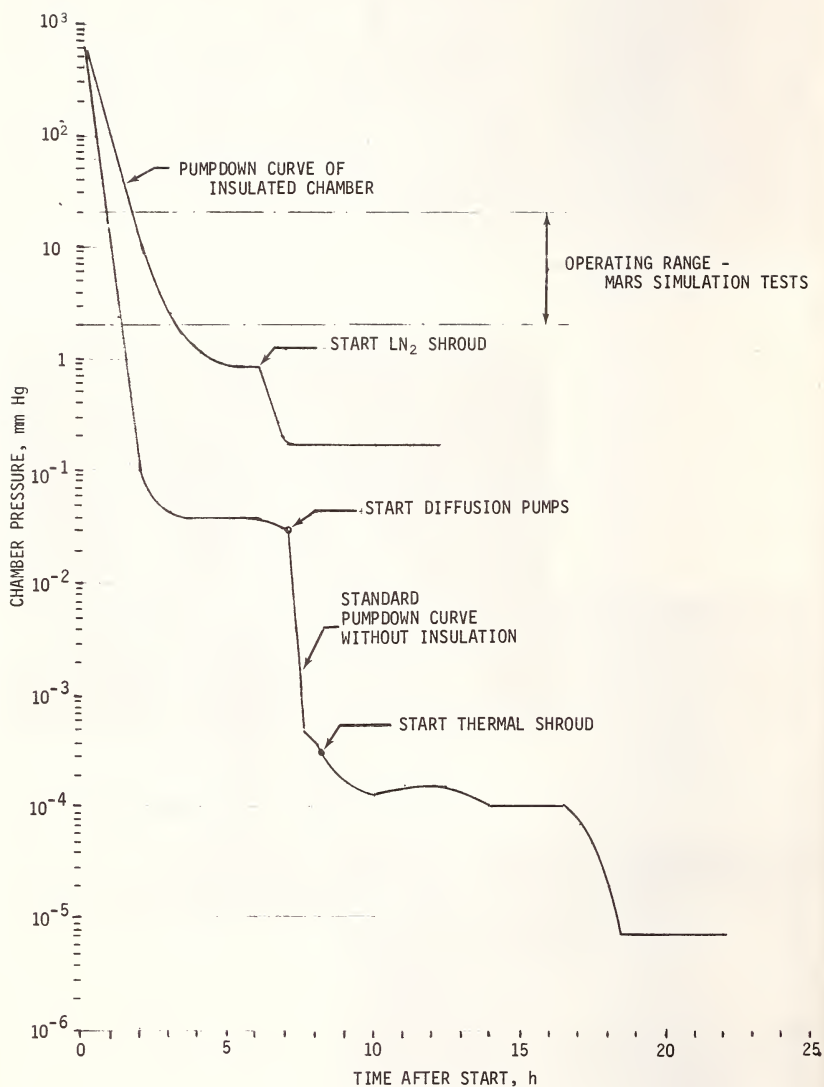


Fig. 12--Pumpdown Curves, 29x45-ft Chamber

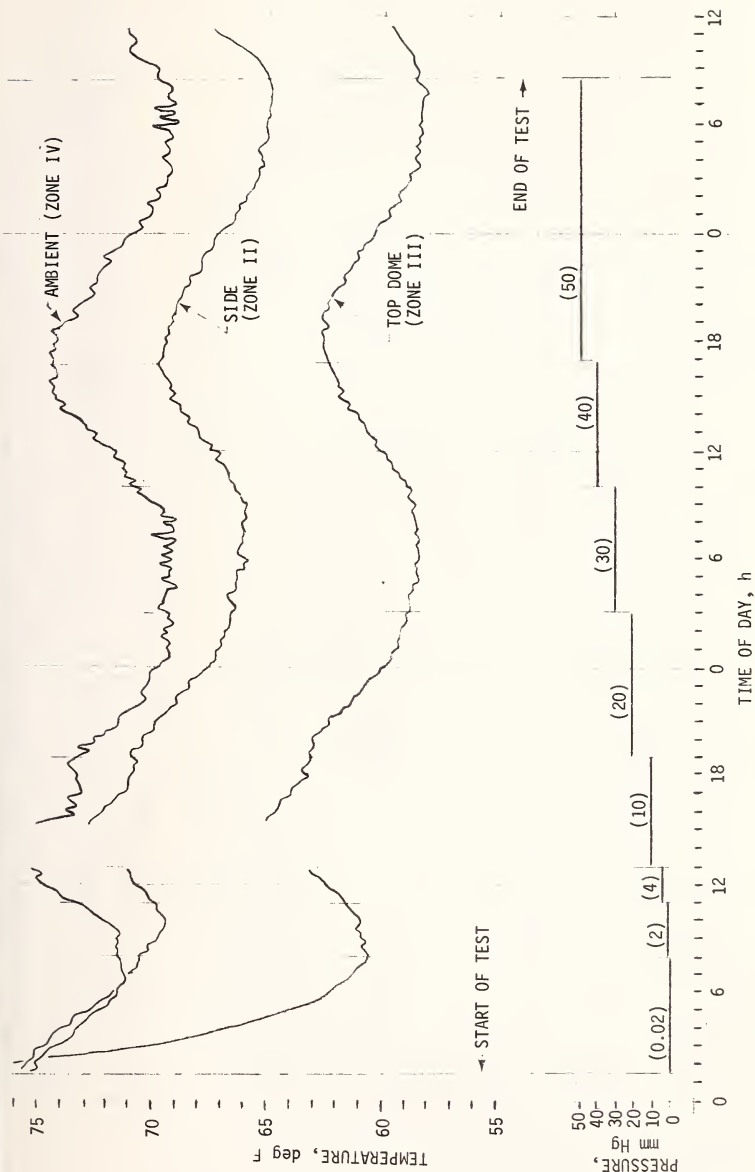


Fig. 13--Typical Outer Shell Temperature Profiles, Zones II and III, Series C Tests

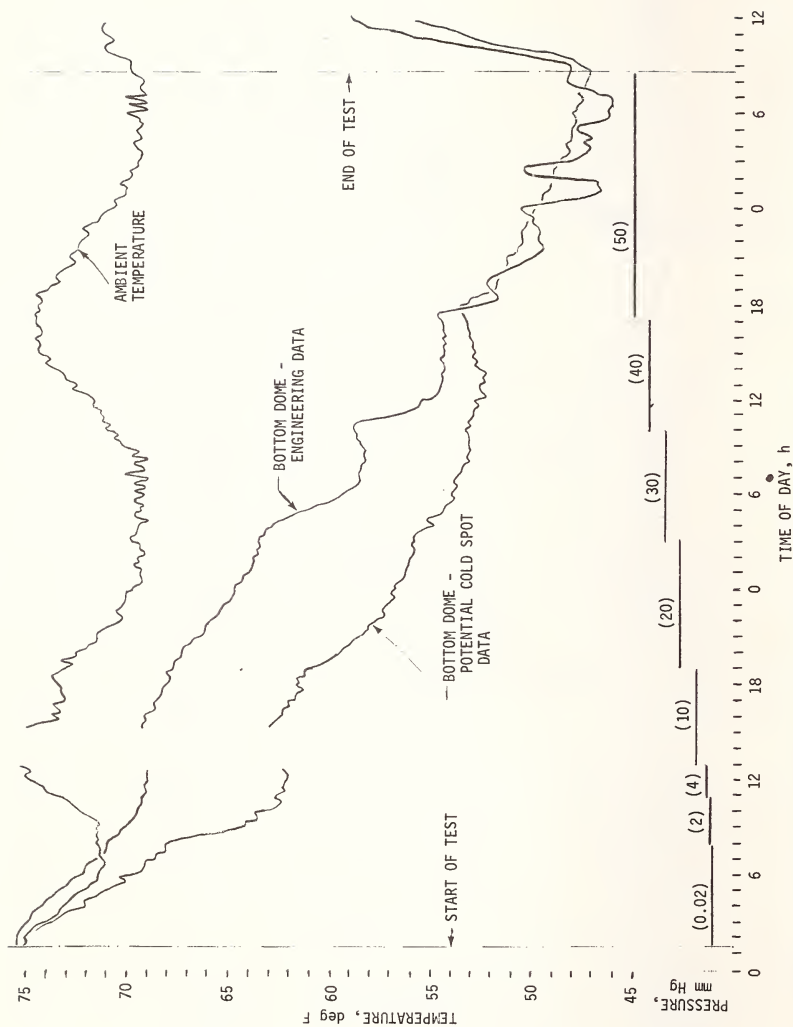


Fig. 14--Typical Outer Shell Temperature Profiles, Zone I, Series C Tests

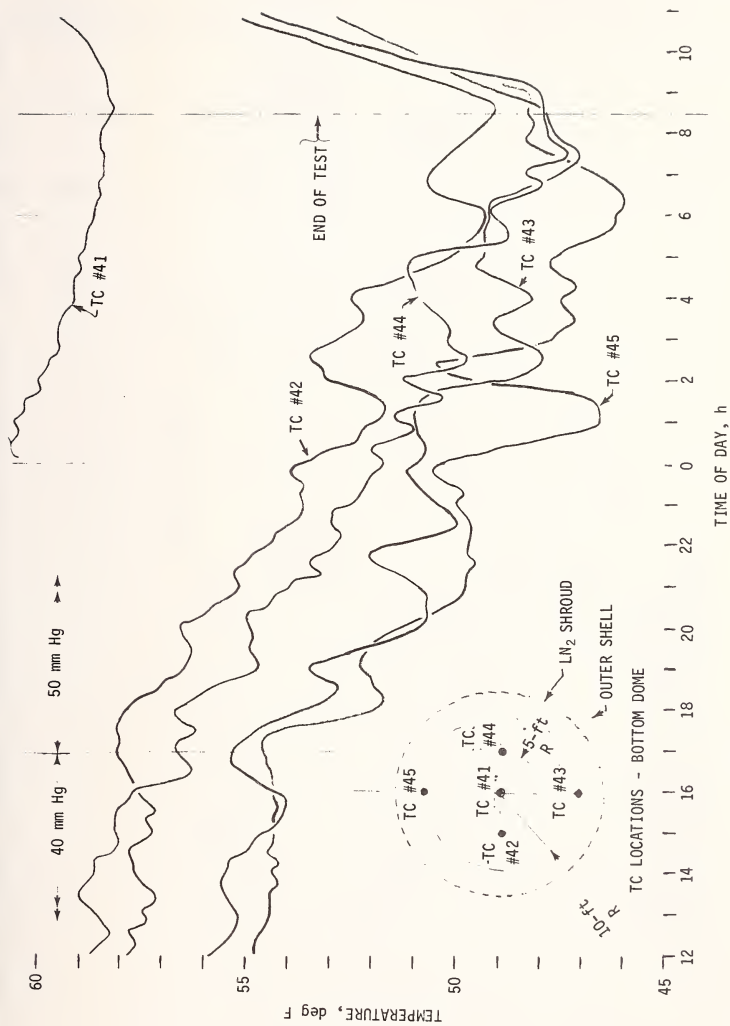


Fig. 15--Low Frequency Temperature Oscillations, Zone I, Series C Tests

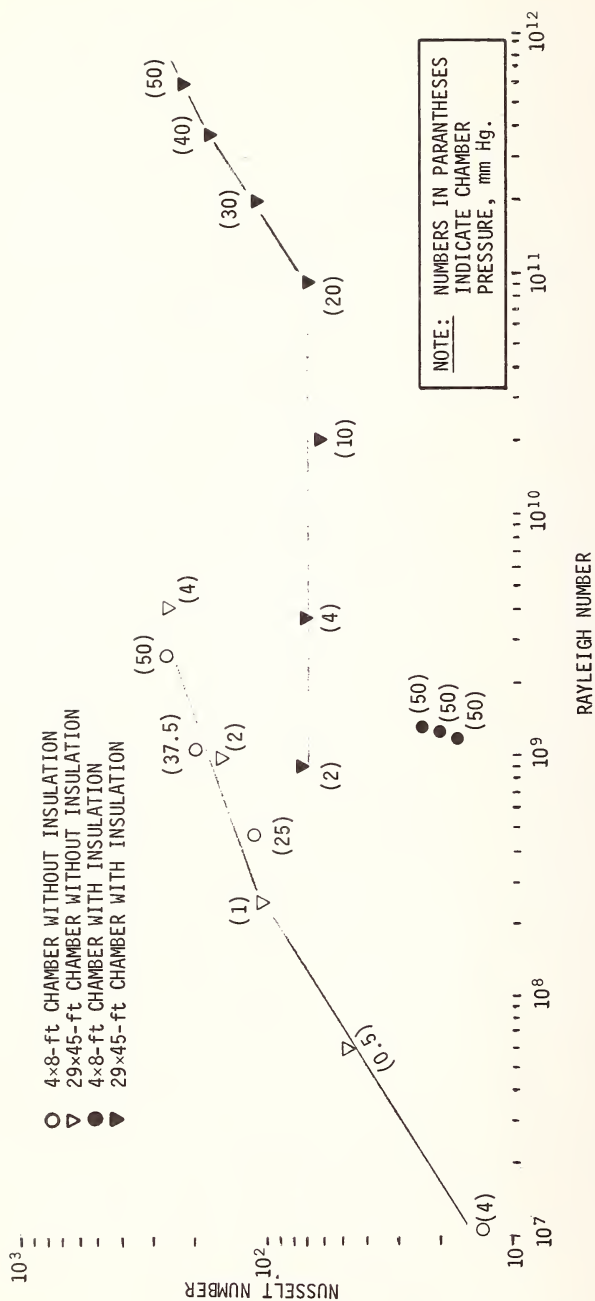


Fig. 16--Heat Transfer Correlation, Bottom Dome Shell, Series A,B and C Tests

Paper No. 49

A CRYOPUMP FOR STEADY-STATE TESTING OF ROCKET ENGINES UNDER
ALTITUDE CONDITIONS

M. J. Triplett and W. E. Riggs

AEF, ARO, Inc., Arnold Air Force Station, Tennessee 37389

PAPER AND ABSTRACT NOT RELEASED FOR
PUBLICATION

ABLATIVE HEAT SHIELDS FOR PLANETARY ENTRIES - A TECHNOLOGY REVIEW

G. D. Walberg¹ and E. M. Sullivan²

REFERENCE: Walberg, G. D. and Sullivan, E. M., "Ablative Heat Shields for Planetary Entries - A Technology Review," ASTM/IES/AIAA Space Simulation Conference, September 14-16, 1970.

ABSTRACT: A review of ablation technology is carried out to assess the present state of the art and point out areas in which further research is required for planetary entry heat shields. Analyses and test techniques which have been developed to treat heat shields for Earth entry with combined radiative and convective heating are reviewed. With the lessons learned from Earth-entry research in mind, the work carried out to date for entry into various planetary atmospheres is reviewed and technological problem areas are discussed. In defining significant phenomena, various mechanisms and processes are discussed and their relative importance is illustrated by describing the analysis of a manned planetary-return Earth entry. In discussing the work to date on planetary entry, two broad categories of research are considered: (1) entry into tenuous atmospheres and (2) entry into the dense atmospheres of Venus and the giant planets. In each of these categories, atmospheric characteristics, entry velocities and modes, vehicle geometries, heating levels and candidate ablation materials are discussed. Present ground and flight-test capabilities are summarized and compared with planetary entry conditions. Particular attention is paid to coupled ablative-radiative phenomena which require the radiation spectrum of the facility to essentially duplicate that of the planetary atmosphere under study.

¹Head, Thermodynamics and Combustion Section, Applied Materials and Physics Division, NASA Langley Research Center, Hampton, Va.

²Assistant Head, Fluid Mechanics Section, Applied Materials and Physics Division, NASA Langley Research Center, Hampton, Va.

KEY WORDS: ablation, heat shields, heat transfer, planetary entry, radiation, evaluation.

In August of 1957, the Army Ballistic Missile Agency successfully reentered and recovered an ablating nose cone for a 1500-mile range IRBM, (1)* and the practicality of the ablative heat shield was demonstrated. In the succeeding 13 years, the ablative heat shield has evolved from a dramatically new concept to a proven, reliable and reasonably light-weight means of protecting entry vehicles from aerodynamic heating. During this time, ablation analyses have developed from simple steady-state solutions which consisted basically of transpiration-cooling theory with additional heat-absorption terms, to complex computer codes which describe the transient, coupled, in-depth response of a char-forming plastic to the heating from radiating, chemically reacting shock layers and boundary layers. This is not to say that all the significant problems in ablation analyses have been solved. We shall see that there are areas in which large uncertainties still exist and in which much work remains to be done. None the less, the past decade has produced great advances in ablation technology.

In the late 1950's, much research was carried out on subliming and glassy ablators. Most analyses were steady-state solutions since the bulk of the research was concerned with the ballistic entry of vehicles having fairly high ballistic coefficients (M/C_{DA}) and entry heat pulses characterized by high heating rates and short duration.

In the early 1960's the emphasis swung toward charring ablators, and lower density materials began to be developed for lower M/C_{DA} manned entry vehicles. Much work was done on transient, in-depth ablation analyses. Military vehicles were developed with higher and higher M/C_{DA} 's. They penetrated deeply into the atmosphere before decelerating and hence their entries were characterized by extremely high stagnation-point heating, high pressures, transition to turbulent boundary layers, and high aerodynamic shears. Manned vehicles, on the other hand, tended to low M/C_{DA} 's and lifting entries to keep deceleration loads within human tolerance levels. These vehicles decelerated high in the atmosphere and their entries were characterized by low pressures, low shears, laminar flow, modest heating rates, and long duration.

* The numbers in parentheses refer to the list of references appended to this paper.

Since the entry environments of these two classes of vehicles are so different, two separate and quite different areas of heat-shield technology have developed. In the case of high $M/C_D A$ vehicles, high-density materials (such as high density nylon-phenolic, graphite-phenolic, carbon-carbon composites, and molded graphites) have been employed to resist mechanical erosion of the ablator surface, and to keep geometry change within reasonable bounds. In the case of manned vehicles, the trend has been to lower density materials since these materials provide superior insulating efficiency to protect against the long heat-soak characteristic of lifting, low $M/C_D A$ entries. Because of the low shears and pressures associated with manned entries, it has been possible to develop ablators having low densities but which produce char layers with sufficient strength to resist mechanical failure within the flight envelope of the vehicle.

Because of its higher entry velocity, the Apollo vehicle encountered radiative as well as convective heating. In a sense, the Apollo project ushered in the era of radiative heating. Of course, research on shock-layer radiation preceded the actual Apollo entries by many years (work was actively under way in the late 1950's) but the Apollo project served as a focal point for much of the radiative heating research.

In the late 1950's, many types of facilities were used to test ablation materials. Oxyacetylene torches, combustion heated wind tunnels, pebble bed tunnels, rocket exhausts, plasma torches, and arc-heated wind tunnels were used with varying degrees of success. By 1962, the arc-heated wind tunnel had established itself as the most versatile and capable of the ablation test facilities.

Intensive research was carried out to produce improved arc heaters, capable of operating over wider ranges of pressure and enthalpy; and radiation sources were added to allow tests with combined convective and radiative heating. Today's ablation test facilities have reached a high level of refinement and have played an invaluable role in the development of ablation technology. In spite of their refinement, however, these facilities provide only a partial simulation of reentry flight conditions. Because of this, the proper interpretation of ground-test results in terms of in-flight ablative behavior remains one of the most important areas of ablation research.

Throughout the past 12 years, much research in polymer chemistry has been carried out in an effort to produce improved ablators. This work has enhanced our understanding of the pyrolysis process and char formation mechanisms, but no "super" materials have been produced. In general, advances in heat-shield performance have come more through understanding the

significant phenomena of ablation than through development of greatly improved materials. When the effects of differing atmospheric compositions are accounted for, the phenomena involved in planetary entries and earth entries are the same. Hence, the technology developed for Earth entry heat shields can be used to, as a starting point, analyze the type of heat shields required for planetary entry vehicles.

In the present paper, the analyses and test techniques which have been developed to treat heat shields for Earth entry with combined radiative and convective heating are reviewed, and the significant phenomena are defined. The development of convective and radiative heat-transfer analyses, ablation layer analyses, and coupled heat transfer and ablation calculations are reviewed and, as an example of the current state of the art, a calculation technique developed for treating heat shields exposed to combined convective and radiative heating is described. With the lessons learned from Earth entry research in mind, the work carried out to date for entry into various planetary atmospheres is reviewed and technological problem areas are identified and discussed.

Symbols

A	projected cross-sectional area of entry vehicle
\tilde{C}_A	elemental mass fraction of ablation products
C_D	drag coefficient of entry vehicle
E_s	$\frac{1}{4} \kappa_p \sigma T_s^4$
f	dimensionless stream function
g	acceleration due to gravity
H	density scale height
h	enthalpy
h_s	stagnation enthalpy
K_O	oxygen mass fraction
M	mass of entry vehicle
\bar{M}	molecular weight
\dot{m}_g	gas injection rate

P	pressure
P_{t_2}	stagnation pressure
Q_c	convective heat load
Q_R	radiative heat load
\dot{q}_{BLK}	reduction in heat flux due to convective blockage
\dot{q}_c	convective heating rate
\dot{q}_{CHEM}	heat flux due to boundary-layer chemical reactions
\dot{q}_R	radiative heating rate
R_{eff}	equivalent nose radius for convective heating
$R_{e,l}$	Reynolds number based on wetted length
r_b	cone base radius
r_N	nose radius
T	temperature
T_s	post shock temperature
V	velocity
z	altitude
Γ	radiation loss parameter = $E_s \delta / \frac{1}{2} \rho_\infty V_\infty^3$
γ_e	entry angle
Δh	enthalpy potential
δ	gas cap thickness
θ_c	cone half angle
κ_p	Planck mean absorption coefficient
ρ	density
σ	Stefan-Boltzmann constant
τ	aerodynamic shear

Subscripts:

e entry condition
w evaluated at the surface
 ∞ free stream

Convective and Radiative Heating for Earth Entry

Convective Heating

Convective heating has been a source of serious concern ever since the early days of supersonic flight. (Remember the press having a field day talking about aircraft crossing the sonic barrier and landing in the thermal thicket?) We will briefly review the development of nonablating heating calculations. The coupling of heating and ablation analyses will be discussed later.

Several specific areas can be pointed out in the literature on convective heating. In particular, the problems of stagnation-point heating, laminar heating, and turbulent heating calculations for very high-speed entry were put on a firm footing by the work of Fay and Riddell(2), Cohen(3), and Hoshizaki(4). More recently the work of De Rienzo and Pallone(5) permits extension of stagnation-point convective heating up to entry speeds of 21.33 km/sec. This last paper also gives an excellent summary of convective heat-transfer studies including the shock-tube experiments which formed the basis for much of the theoretical work. The work of Boison and Curtiss(6) and Zoby and Sullivan(7) explored the influence of body geometry on stagnation-point heating.

Laminar heat transfer on flat plates, sharp cones, and off the stagnation point on blunt bodies has been well established by the work of Cohen(3) and Lees(8). The results of Cohen have been correlated by Zoby(9) to put them in a more usable form.

Turbulent heating is still a subject for extensive research. The Reentry F spacecraft has provided an extensive amount of turbulent heating data which are still being compared with existing correlation equations. The earlier work of Zoby and Sullivan(10) showed that turbulent heating for a large number of flight vehicles, blunt and sharp, could be predicted with fair accuracy using reference enthalpy methods.

No discussion of turbulent heating is complete without a discussion of the problem of boundary-layer transition. Transition is known or believed to be influenced by Mach number,

Reynolds number, leading-edge bluntness, surface roughness, and a host of other parameters including the ablation rate for an ablating surface. To date, no good correlation of boundary-layer transition is available. Any of the currently accepted correlations show a spread of the type shown in Figure 1 which is taken from Reference (11). Note that there is as much as an order of magnitude difference between the lowest and highest Reynolds numbers at which transition occurs. In addition, the influence of non-air gas mixtures on boundary-layer transition is not well known. However, barring major chemical effects which can significantly influence temperature and enthalpy profiles, there is no reason to believe that a transition correlation for air will not apply in non-air gas mixtures.

Radiative Heating

Radiative heating becomes an important design consideration when the gas-cap temperature exceeds approximately $10\,000^{\circ}\text{K}$. A history of radiative heating calculations is given by Anderson(12) who points out that calculations using an optically thin or a gray gas model seriously overpredict the radiative flux to the wall. Figure 2, which is copied from Anderson's paper, shows how the state of the art for radiation calculations has changed in the past decade. Calculation procedures have progressed from the transparent, continuum only, uncoupled calculations used by many early investigators through the nongray, coupled but continuum only calculations of Hoshizaki and Wilson(13) to the coupled with continuum and lines calculations which are current today. In Figure 2, the last category is demonstrated by results from Page et al.(14) but could be equally well demonstrated with results from Wilson(15), Olstad(16), Chin(17), or Rigdon(18). The radiation model used in the calculation procedure described below is that of Wilson(19) which includes continuum and atomic lines. Anderson further points out that due to uncertainties in gas absorption coefficients, the radiative flux "can probably be determined within 50 percent" and if the uncertainty in the absorption characteristics of ablation products is also taken into account the radiative flux "is known within a factor of two." It is obvious that if the entry environment is dominated by radiative heat transfer the heat-shield weight requirement can be a serious uncertainty.

Most of the radiative heating calculations made to date and referenced above apply to the stagnation region. It was recognized prior to 1962 that radiative heating to conical bodies was negligible because of the cooling of the gas as it moved out of the stagnation region and onto the conical afterbody. However, bodies with larger cone angles have become interesting (e.g., Viking) and attention has again turned toward this problem. A very recent paper by Callis(20) shows results

for sphere-cones with cone angles of 30° , 45° , and 60° . As anticipated, for the conditions investigated, the 30° and 45° cone heating rates fall to very small fractions of the stagnation-point values. The 60° cone, however, can experience radiative rates which may actually be higher than the stagnation-point values. Such results can have serious implications on both the heat-shield design and the aerodynamic characteristics of the entry vehicle. These results point out that radiative heating is a major unknown for the design of a vehicle flying in air. For vehicles flying in non-air gas mixtures, the uncertainty must be larger and requires further consideration.

Ablator Response

Ablation Analyses

During entry, an ablator responds to heat transfer and chemical attack from the adjoining shock layer. The ablator responds by receding, altering its internal temperature distribution, or both. The principal mechanisms of ablative response, as illustrated in Figure 3, are:

1. Sensible heat increase in the virgin plastic and char
2. Pyrolysis of the virgin plastic to form char and pyrolysis gases
3. Enthalpy increase in the pyrolysis gases as they flow through the char
4. Removal of the char surface by chemical attack and sublimation
5. Mechanical removal of the char
6. Reradiation of energy from the char surface

Most present-day ablation analyses assume one-dimensional flow of heat and mass normal to the local char surface. Such an assumption is valid for cases where the curvature of the heat shield is large compared to characteristic dimensions within the ablator (large nose radii), but for small ground-test models and for flight vehicles with small nose radii multidimensional solutions may be required. This is true in treating both temperature distributions and the internal flow of pyrolysis gases. At the present, complete multidimensional analyses have not reached a stage where they are suitable for routine use. Solutions have, however, been obtained for the important limiting cases of two-dimensional heat transfer with

one-dimensional mass transfer (subliming ablators and graphite - no char layer)(21,22), and two-dimensional pyrolysis gas flow with one-dimensional heat transfer (models with rapidly varying external pressure distributions)(23). In the present paper, for the purpose of illustrating basic phenomena, we shall, for the most part, restrict our attention to the one-dimensional case.

A typical one-dimensional ablation analysis is composed of a finite-difference solution of the transient heat conduction equation throughout the char, pyrolysis zone, and virgin plastic; a set of empirical kinetic equations that describe the pyrolysis process; a chemistry routine to determine the state of the pyrolysis gases; a set of equations which describe char removal by chemical and mechanical means; and a char surface energy balance(24,25,26,27,28).

In the early days of ablation analysis, it was often necessary to sacrifice some rigor in the solution of the heat-conduction equation in order to keep computing times reasonably short. This problem has now been overcome by improved programming techniques and increases in computer speed so that today's finite difference solutions are essentially exact and require reasonably short machine times. At the present time, the accuracy of predicted internal temperature distributions is limited mainly by the material properties required as input data (i.e., specific heats, thermal conductivities, etc.). Virgin plastic properties can be measured with reasonable accuracy at temperatures where pyrolysis of the material does not occur. Since the techniques used to measure specific heats and thermal conductivities are steady-state procedures, measurement made on a material which is pyrolyzing must contain some uncertainties(29). Hence, material properties in the pyrolysis zone are difficult to obtain. The largest difficulties with input properties are associated with the char layer. Most ablation analyses use a char thermal conductivity which is a lumped parameter and represents the net conductivity of the char and the pyrolysis gases flowing through it. This lumped conductivity cannot actually be measured and is often inferred from arc tunnel tests of ablation models. That is, the char conductivity is adjusted until the predicted temperature distributions agree with those measured in the tunnel tests(30,31). In spite of the foregoing difficulties, present-day ablation analyses usually predict reasonably accurate internal temperature distributions. In reference 30 for instance, after adjustment of the char thermal conductivity, internal temperatures were predicted to within 30 percent of the measured values.

Pyrolysis Kinetics and Pyrolysis Gas Chemical State

The pyrolysis kinetics, as obtained from DTA (differential thermal analysis) and TGA (thermo-gravimetric analysis) data, generally predict pyrolysis rates and energy absorption with reasonable accuracy(32).

The state of the pyrolysis gases remains one of the major unsettled questions in ablation analysis. Its significance is illustrated in Figure 4. Early ablation analyses usually treated the pyrolysis gases as frozen at the composition at which they left the pyrolysis zone. If this assumption is made, then the pyrolysis gases will absorb only a small amount of energy in being heated from the pyrolysis temperature to the char surface temperature. Later, gas phase equilibrium computer codes were employed to treat the gases as being in complete chemical equilibrium (including the deposition of carbon in the hotter regions of the char). This equilibrium assumption results in the prediction of large heat absorption by the pyrolysis gases. Experimental data have been obtained which support both the equilibrium and frozen assumptions. Data obtained by Lundel(33) which agree with the frozen assumption are presented in Figure 4. A more accurate approach would be to carry out a kinetic analysis which employed measured rate constants for the important reactions. Such an analysis was reported in Reference (34) and indicated that the equilibrium assumption would significantly overpredict the heat absorption by the pyrolysis gases. The available rate data are, however, limited to relatively low temperatures and, in many cases, are available only for overall reactions rather than the individual kinetic steps involved in the pyrolysis gas reactions. Hence, a true kinetic model for the pyrolysis gas reaction has not been established and, lacking such a model, analyses based on low temperature data cannot be extrapolated to the high char temperatures associated with lunar return, planetary return, and planetary entry missions.

Char Surface Recession

Another important area of ablation analysis that is still largely unresolved is the prediction of char surface recession. Most analyses for manned vehicles employ the assumption that char recession is due entirely to chemical reactions and sublimation. This is usually justifiable within the flight envelope and makes the problem more tractable than if mechanical char removal had to be accounted for; but the question of char surface kinetics still presents formidable problems. Most analyses treat chemical char removal as being jointly rate and diffusion controlled. At low temperatures, where oxygen can diffuse to the char surface faster than it reacts, the recession rate is governed by the kinetics of the solid-gas reaction. At high temperatures, the rate of char recession is governed by the rate at which oxygen (and other reactive boundary-layer gases) diffuses to the char surface. Between these two regimes, there exists a transition region of joint rate and diffusion control. At yet higher temperatures, sublimation causes additional char recession. Most investigators have assumed that the rate controlled regime could be described by a single

Arrhenius equation with a constant activation energy. This surface recession model has received such wide acceptance that its validity is seldom questioned. However, data recently obtained for various graphites strongly suggest that the activation energy is, in fact, a decreasing function of temperature and that char surface removal may be chemically controlled to temperatures much higher than previously thought possible(35,36). Sublimation is another area of considerable uncertainty. Several investigators have shown that accurate solutions require the inclusion of high molecular-weight gas phase carbon species (C_1 through C_{10} usually). The thermodynamic properties of these large carbon species are not well established. Depending on their treatment of these species, various investigators have predicted significantly different sublimation rates at high temperatures and pressures(37,38). When, as in the case of high $M/C_D A$ ballistic vehicles, mechanical char removal must be accounted for in addition to chemical removal, the prediction of char recession rates becomes uncertain indeed. Several theoretical treatments of char failure have appeared in the literature(39,40). Most of these analyses describe char removal as a cyclic process wherein the char builds up to a critical thickness and then is removed by a combination of thermal and internal pressure stresses. While this type of char failure has been reported for some materials, it is not encountered very often. The type of char failure that is most often seen in ablation tests involves the removal of relatively small fragments from the char surface. Figure 5 presents a typical set of test data for a carbon-phenolic ablation material. This type of char failure only occurs when the test stream contains oxygen. It is apparently a coupled chemical-mechanical process in which the char surface is weakened by oxidation and subsequently removed by aerodynamic shear. The phenomenon is particularly apparent under high-pressure test conditions and has been observed for graphites(41) as well as charring ablators(42). At the present time, this type of char removal must be described by empirical relations derived from ground tests.

Reradiation of Energy From Char Surface

The superiority of the charring ablator (over subliming and melting ablators) is largely due to its ability to reradiate large quantities of energy from a high-emissivity, high-temperature char surface. As will be shown in a subsequent section of this paper, this reradiation is one of the most important energy accommodation mechanisms for charring ablators. In most ablation analyses, the char surface is assumed to be a gray body and to have a constant emissivity. For most carbonaceous materials, this seems to be a reasonable assumption. However, materials which contain large amounts of silica often produce chars for which the gray-body assumption is significantly

in error(43). The counterpart to emissivity is char surface absorptivity, which becomes important when the ablator is subjected to radiative heating. As with emissivity, the absorptivity is usually assumed constant, though its value is usually assumed to be different from that of the emissivity to account for the fact that the shock-layer radiation and the char surface reradiation involve different wavelength ranges. Actually, little is known about char absorptivity for short wavelength, high-energy (ultraviolet) radiation.

Since, reradiation from the char surface varies as the fourth power of surface temperature, it becomes more important as heating rates (and hence surface temperatures) increase. At a temperature of approximately 4000° K (for pressures of the order of 10 atmospheres), however, carbonaceous materials sublime. Hence, an upper limit on the amount of energy that can be reradiated exists (around 1200 W/cm^2). For entries which involve heating rates of a few thousand W/cm^2 (manned planetary return earth entry, for instance), char surface reradiation will usually be the most important energy accommodation mechanism. For entries that involve tens of thousands of W/cm^2 (which, as we shall see, may be the case for Jupiter entry), reradiation may be small compared to other ablative mechanisms.

Categories of Ablators

A great many different materials and formulations have been investigated for use as ablative heat shields. It might be expected that each of these materials would have its own special characteristics and would require a separate research program to determine its ablative behavior. To an extent, this is true, particularly with regard to thermophysical and thermochemical properties. In a broad sense, however, ablators may be meaningfully categorized according to their elemental chemical composition (i.e., the number of atoms of carbon, hydrogen, etc.). The basis of such a categorization is the concept of complete (gas-phase and gas-solid) equilibrium at the char surface. If such equilibrium is obtained, then, in a diffusion limited situation, the char recession rate (which is one of the major determinants of ablator performance) is completely determined by the vehicle geometry, the flight conditions, and the elemental composition of the virgin plastic. The assumption of complete char-surface equilibrium has been studied, both analytically and experimentally by many investigators(26,44,45,46). In many cases, it has been shown to provide an accurate prediction of ablator behavior. As mentioned previously, there are data available which suggest significant pyrolysis-gas nonequilibrium, and in such cases, the concept would not hold. As a guide to the overall categorization of ablators, however, the equilibrium concept is quite useful. When considered in this way, most ablators can

be grouped into two classes: those which contain the elements carbon, hydrogen, nitrogen, and oxygen, and those which contain these four elements plus silicon. These two groups differ most significantly with respect to char chemistry. Materials which contain C, H, N, and O produce chars which are nearly 100 percent carbonaceous and whose chemical composition is virtually independent of test condition. Materials which contain Si, on the other hand, produce chars with surfaces composed primarily of solid SiO_2 , liquid SiO_2 , solid SiC , or solid C depending on the test condition. This behavior is particularly characteristic of elastomeric ablators and is illustrated by the results presented in Figure 6. Note that as the heating rate is increased, changes occur in both appearance and chemical composition of the char layers. Over this same range of test conditions, an ablator containing only C, H, N, and O would everywhere produce carbonaceous char. Silicon-dominated ablators (materials which behave as shown in Fig. 6) are best suited for use at low heating rates (low surface temperatures) where the char is primarily solid SiO_2 and, since it is an oxide, is virtually inert with respect to oxygen and hence is nonreceding. Carbon dominated ablators, on the other hand, are preferable at high heating rates since their carbonaceous chars do not suffer from the liquid layers and C/Si reactions characteristic of siliceous materials.

Coupling Between Heating and Ablator Response

One of the outstanding characteristics of an ablative heat shield is that it not only absorbs heat but, through the injection of gaseous ablation products, it also modifies the adjacent boundary layer and greatly reduces the level of aerodynamic heating. When the ablation products enter the boundary layer they are heated up, react with themselves, and (usually exothermically) with the boundary-layer and shock-layer gases; they thicken the boundary layer and alter its profiles of temperature, velocity, and species concentration, and they absorb radiation from the shock layer.

The exothermic reaction of the pyrolysis gases is both detrimental and beneficial. Because of its exothermic nature, it actually increases the heat flux to the ablator. However, these reactions also deplete the reactable oxygen in the boundary layer, reduce the oxygen flux to the char surface, and hence, in a diffusion limited situation, reduce the rate of char removal by chemical reaction. This combustive heating can be expressed as an effective increase in stagnation enthalpy. Hence, it is quite important at low flight speeds (low enthalpies) but becomes of lesser importance at high speeds. The oxygen depletion effect is important at both high and low speeds so long as chemical char removal is significant compared to removal by sublimation and mechanical processes. In treating

the ablation product boundary-layer reactions there is, once again, the question of reaction rates. The limiting cases of equilibrium and frozen chemistry are, of course, available. At higher boundary-layer and shock-layer temperatures (say above 2000° K), equilibrium is usually assumed since reaction rates are expected to be fast. A considerable amount of data supporting this assumption has been published, but in many cases the frozen assumption seems to give better results. The analysis that was most successful in predicting the performance of the Apollo heat shield treated the ablation products in the boundary layer as being frozen.

The thickening of the boundary layer and the alteration of its profiles constitutes the well-known "transpiration cooling effect." This is an important ablation mechanism under virtually all flight conditions, and becomes particularly important under conditions producing high radiative heating rates. Under these conditions, the resulting high mass injection rates "blow the boundary layer off" the char surface and reduce the convective heating to zero. This phenomenon is usually illustrated by a plot of the ratio of convective heat flux (or Stanton numbers) with and without blowing versus a nondimensional mass injection rate. From such a plot, presented in Figure 7, it is seen that the convective heat flux tends to zero with increasing blowing rate as shown by the solid curve. Experimental ablation data have been presented, however, indicating that, with increasing blowing rate, the convective heating approaches a finite asymptote (0.2 to 0.3 of the no-blowing value) rather than zero(47). This type of behavior should be expected when the blowing is produced by an ablator responding to purely convective heating. If the heating were actually reduced to zero, the ablator would stop ablating, the blowing rate would go to zero, and, with no mass injection, the heating rate would increase to its no-blowing value. Hence, some nonzero asymptote must be approached in convective heating situations. This type of behavior will not occur, however, in the presence of large radiative heating rates. In this case, the high mass injection rates (ablation rates) resulting from the radiative heating can, indeed, drive the convective heating rates to extremely low values.

Until a few years ago it was generally assumed that the gaseous ablation products would not absorb a significant part of the radiation from the hot shock layer. Then, a number of investigators carried out analyses in which the absorption by the ablation products could be accounted for(48,49). They found that the ablation products could actually be rather efficient absorbers (especially at ultraviolet wavelengths) and predictions of up to 50 percent reduction in radiative heat flux were published. Recently analyses of this type have been further refined and now reductions of around 25 percent are being predicted for typical planetary return

Earth entries(50). Analyses of this type are discussed in the following section of this paper.

State-of-the-Art Analysis for Planetary Return Earth Entry

In order to identify those ablative mechanisms which are most important during a high-speed entry, a typical up-to-date analysis is described and typical results for planetary return Earth entry are reviewed.

A state-of-the-art analysis which is being used to study some of the problems associated with Earth entry of a blunt body at planetary return speeds is given by Smith et al. in Reference (50). Figure 8 is taken from that reference to show the logic involved in developing such an analysis.

The analysis must begin with a trajectory if a transient ablation solution is required. If only simple, point calculations are required then velocity and altitude or velocity and density are all that are necessary to initiate the analysis.

The inviscid radiating solution is used to calculate all the flow parameters in the subsonic portion of the flow field behind the bow shock. In the analysis shown in Figure 8, the method used is that of Suttles(51) who combined the one strip integral method(52) with the radiation model of Wilson(19). The output from the inviscid flow-field program is used to provide local values of pressure, temperature, density, and velocity. This information can be used as local edge conditions with a conventional boundary-layer solution to provide initial estimates of the convective heating. In the analysis of Reference (50), these convective heating calculations were made using the correlation equations of Zoby(9) for equilibrium air.

The radiative flux calculated by the inviscid flow-field program and the convective heating rate calculated by the boundary-layer program are used as inputs to the ablation program (developed by Kendall, Rindal, and Bartlett(26)) which computes the transient, one-dimensional response of a charring material with heat conduction and in-depth pyrolysis governed by Arrhenius type rate equations. The pyrolysis gases are assumed to be in chemical equilibrium throughout the char, and two-phase chemical equilibrium is assumed at the char surface. All char recession is assumed to be caused by rate and diffusion-limited chemical reaction and sublimation.

When the ablation rates have been calculated, it is possible to compute the velocity profiles in the boundary layers using the technique described in Reference (50). By testing

the resulting stream function against a limiting value, the analysis decides whether or not the ablation rate is large enough to move the air-ablation products boundary layer away from the wall and replace it with an ablation products layer with an almost constant, low-value shear at the wall. If the ablation rate is sufficiently large the strong injection solution is used. This solution, described in detail in Reference (50), assumes that the boundary layer consists of a layer of ablation products next to the wall and a layer within which the viscous effects adjust the flow variables from the inner layer values to the inviscid outer layer values. In the layer next to the body, constant shear and negligible conduction are assumed. In the viscous layer, the elemental composition is computed by assuming a cubic variation from the ablation products composition in the inner layer to the air composition at the edge of the inviscid outer layer. If the ablation rate is moderate, a conventional boundary-layer solution is used in which the stream function at the wall is defined by the ablation rate.

The inviscid outer layer and the boundary layer for either strong or moderate injection are coupled to provide continuous enthalpy profiles across the shock layer. First, the inviscid layer is displaced from the wall by a distance equal to the displacement thickness of a boundary layer with mass addition. The boundary-layer edge enthalpy value is matched to a value in the inviscid layer near the edge of the boundary layer. This information provides a smooth enthalpy profile which is used by the radiation model to recompute the radiative flux. This flux is used as input for the next iteration on the mass loss rate calculations. The solution continues until a consistent set of flux and mass loss rate values is obtained.

There are several radiation models which might be used for calculation of radiative transfer through the ablation products layer. As previously noted, the radiation model used in Reference (50) was that of Reference (19). This model contains the major features for air radiation as well as the prominent features from a large number of the chemical compounds resulting from an equilibrium analysis of the ablation products from common ablators such as phenolic nylon and phenolic carbon. Thus, when this code is coupled with the boundary-layer solutions described above, the major influence of the ablation products on the radiative heating has probably been accounted for. The answers should certainly be within the factor of 2 mentioned by Anderson. Typical results from analyses of this type are presented in Figures 9 and 10. Figure 9 shows the extent of the ablation products layer and the temperature distribution through the shock layer, and presents the calculated shock stand-off distance, heating rates, and the char-surface temperature for conditions typical

of peak heating during a manned planetary return Earth entry. Blockage by ablation products reduces the inviscid heating by about 22 percent. It is of interest to see in which spectral regions the absorption is taking place. This is shown by the difference between the dashed and solid lines in Figure 10. Note that the absorption is almost entirely in the ultraviolet region.

Only by carrying out a coupled analysis such as that just described is it possible to accurately assess the heat-shielding requirements for severe radiation-dominated entries. Coleman, et al., carried out a thorough study of heat-shielding requirements for blunt and conical manned planetary return entry vehicles. Their analysis included all the important mechanisms mentioned previously. For a baseline theoretical model (which assumed a phenolic-nylon ablator, no mechanical char failure, equilibrium pyrolysis gases, laminar flow, equilibrium shock-layer chemistry, and no blockage of radiation by ablation products), they showed the magnitudes of the various heat absorption and blockage mechanisms as a function of time during entry. These data are reproduced (with some modification) in Figure 11. In constructing Figure 11, the data of Coleman et al. (49) were modified to reflect a 25-percent radiation blockage due to ablation products since, in light of recent developments, this is believed to be realistic. Results are presented for the center line of an Apollo-like vehicle. For the blunt Apollo-like vehicle, radiation is the dominant heating mechanism, and the significant energy accommodation mechanisms are radiation blockage by ablation products, transpiration cooling, surface reradiation, and the enthalpy increase in the pyrolysis gases. For conical vehicles, the dominant heating was found to be convective, and the significant energy accommodation mechanisms were transpiration cooling, reradiation, and pyrolysis enthalpy increase.

Ablative Response in Turbulent Flow

All the results presented thus far are rigorously applicable only to laminar flows. Actually, little is known about the response of ablators subjected to turbulent flows. Since arc tunnels are generally low-density facilities and can accommodate only small models, ordinary ablation tests never produce Reynolds numbers high enough to produce turbulent flow. Some ablation tests have also been carried out in turbulent pipe-flow and channel-flow facilities and have produced valuable data, but because of radiation exchange with facility walls and difficulties in precisely defining the flow, the application of these results to flight conditions is not straightforward. Some turbulent ablation data have also been obtained from flight tests. Data for several materials having densities from about 0.3 to 1 gm/cm³ were obtained from the NASA Pacemaker series of small flight

vehicles and data for a variety of high-density materials have been obtained from flights of military vehicles. Unfortunately, Mach numbers and enthalpies over which these data were obtained are considerably lower than those for severe planetary entries.

The analysis of the response of an ablator to turbulent flow is usually done by calculating the convective heating rates by available turbulent boundary-layer techniques and reducing the convective blocking effectiveness of the ablation products to $1/3$ or $1/4$ of their laminar values. Very little in the way of coupled radiative-convective analyses with turbulent flow has been attempted thus far since it has generally been assumed that radiative heating will be insignificant in the afterbody regions where the flow could be turbulent. In general, the approach used with nonmilitary vehicles has been to choose vehicle geometries and entry trajectories so as to avoid turbulent heating. This same approach will probably be used with planetary entry vehicles.

Planetary Entries

Ablation research for Earth entry has been reviewed. Now we shall use this background and consider the problems associated with planetary entries. From our review of Earth entry research, we have seen that ablative heat shields provide reliable, reasonably lightweight thermal protection systems, but because of uncertainties in several key technology areas (boundary-layer transition, chemical state of pyrolysis gases, char-surface recession mechanisms) a conservative design approach must be used. At the present time, these same uncertainties will require conservative designs for planetary vehicles. For severe Earth entries, the most significant ablative energy accommodation mechanisms were seen to be blockage of convective and radiative heat flux by ablation products, char surface reradiation, and pyrolysis enthalpy increase. Various planetary entries will now be considered and the most significant ablation mechanisms identified in each case.

At this point it should be pointed out that prelaunch and transit environments such as sterilization, vacuum exposure, and cold soak can significantly influence the choice of an ablation material for a particular mission. The study of these effects constitutes a broad technology area in itself and is outside the scope of the present paper. It must be remembered, however, that the material properties used in the analyses described herein must be those that the ablator possesses after its interplanetary trip, just prior to atmospheric entry.

In Table 1, properties of various planetary atmospheres(53,54,55,56,57) and unpublished Project Viking atmospheric

models are presented*. The near planets may be grouped into two categories, those with atmospheres considerably less dense than the Earth's and atmospheres more dense than that of Earth. In the low-density group, the planets of most current interest are Mars and Mercury. In the high density group, they are Venus and Jupiter.

In the present paper, we shall consider Mars as being representative of the planets with tenuous atmospheres. Pritchard(58) has considered the possibility of using a vehicle originally designed for Martian entry to explore Mercury, Titan (a moon of Saturn), and other planets with thin atmospheres. He concluded that, for surface pressures as low as 1 mb, an entry vehicle designed for Mars could be used for Mercury and Titan missions with appropriate changes in the terminal descent system and, perhaps, in the guidance system. Hence, Mars is a good focal point for low-density-atmosphere entries.

In the case of entry into dense atmospheres we shall consider two planets, Venus and Jupiter. Venus is selected for consideration since it is unique in posing entry problems somewhat comparable to those of Earth entry. Jupiter is chosen as being characteristic of the giant planets (Jupiter, Saturn, Uranus, Neptune). This is done for two reasons. First of all, interest in Jovian entry is currently high and, as a result, much more information is available for Jupiter than for the other giant planets. Second, Jupiter is thought to possess many of the atmospheric characteristics that would be encountered during Saturn, Uranus, and Neptune entries.

Entry Into Tenuous Atmospheres - Mars

The essential problem associated with entries into tenuous atmospheres is that of decelerating to conditions at which parachutes or other high drag devices can be deployed. This must be accomplished at altitudes which are high enough to allow atmospheric sampling in most planetary exploration missions. In order to achieve this high-altitude deceleration, low values of the vehicle ballistic coefficient, $M/C_D A$, are required. As pointed out by Roberts(59), deceleration within a given atmosphere requires that the atmospheric drag parameter,

$$P/(Mg/C_D A)$$

*

The values presented in Table 1 are intended only to roughly categorize the various atmospheres. It is recognized that many of these values are uncertain and debatable.

be less than approximately 10. Hence, a vehicle with an M/C_{DA} of 3.14 g/cm^2 will be decelerated by the Earth's atmosphere whereas, deceleration in the Martian atmosphere will require M/C_{DA} 's on the order of 3.14 g/cm^2 .

Atmospheric Characteristics

Our concept of the Martian atmosphere has changed drastically in the past few years. When Martian entry vehicles began to be seriously studied in 1961-62, it was recognized that much uncertainty existed regarding the pressure and composition of the Mars atmosphere. Early estimates of surface pressure ranged from 10 to 30 mb (0.01 to 0.03 atm), and compositions from 80 percent nitrogen, 20 percent CO_2 to 100 percent CO_2 were considered possible. In that time period most studies assumed significant amounts of both N_2 and CO_2 . Recent spectroscopic data and measurements of the occultation of radio-frequency transmission from the Mariner flyby spacecraft have, however, considerably improved our knowledge of the Martian atmosphere. The Project Viking Mars Engineering Model Working Group has reviewed these data and proposed a set of model atmospheres with surface pressures ranging from 4 to 10 mb (0.004 to 0.01 atm), compositions from 100 percent CO_2 to 71 percent CO_2 , 29 percent Ar, and density scale heights (in the stratosphere) from 4.5 to 12 km. These various atmospheres correspond to maximum and minimum surface densities and a mean model. Density and temperature profiles for these model atmospheres are presented in Figures 12 and 13.

Entry Vehicle Geometries, Entry Modes, and Velocities

By far the most often used geometry for Martian entry vehicles is the spherically blunted cone. This configuration has the advantages of low ballistic coefficient, good payload packaging characteristics, and good aerodynamic stability. The Project Viking entry capsule is shown in Figure 14 as an example of this type of configuration.

Nearly all the studies carried out to date have considered ballistic entries. While many early investigations featured vertical or near-vertical entries, the trend in recent years has been toward entry angles of -20° or less. For low ballistic-coefficient vehicles ($M/C_{DA} = 3 \rightarrow 5 \text{ gm/cm}^2$) entering at shallow angles, heating rates tend to be very low. The maximum heating rates on such vehicles as calculated in References (60), (61), (62), and (63) are summarized in Table 2. From this table it is seen that maximum heating rates range from 100 to 200 W/cm^2 for direct entry and are on the order of 20 W/cm^2 for entry from orbit. Furthermore, radiative heating is inconsequential for entries less than about 7 km/sec . Hence, for the Martian entries of greatest

current interest (e.g., orbital entries such as Project Viking), the heat-shielding problem is not severe. Only in the case of very high-speed advanced missions (such as the 11.5 km/sec Mars Surface Sample Return mission mentioned in Reference (62)) do the heating rates become high enough to really exercise present-day ablators. Since high-speed entries of this type have much in common with Venusian entries, they will not be discussed in this section.

Since the heating rates are so low, the selection of an ablative material for a Martian entry vehicle is influenced more by its ability to withstand such environments as prelaunch sterilization, in-transit cold soak, solar radiation, micro-meteorite bombardment, and vacuum exposure(63,64) than by its high ablative efficiency. From an ablative performance standpoint, the outstanding requirement is that the material be of low density and possess good insulating capability. Filled elastomeric materials seem to be well suited to these requirements. A typical material might be composed of silicone resin, silica microspheres, phenolic microballoons, and carbon and silica fibers. This type of material has been studied and tested extensively(46,65,66,67) and, for low heating-rate applications, is well proven.

The heat shield remains an important part of the overall vehicle design for a Martian entry vehicle. Most design studies(67,68) indicate that the heat shield will comprise 10 to 20 percent of the entry vehicle gross weight. The materials are developed and available, however, and the overall problem seems well within the present state of the art.

Entry Into Dense Atmospheres

As shown in Table 1, the near planets may be grouped according to atmospheric density. The planets of immediate interest which have atmospheres as dense or more dense than that of Earth are Venus and the giant planets, Jupiter, Saturn, Uranus, and Neptune. In most prior research, Venus and Mars have been considered together because of their similar atmospheric composition. If comparable entry velocities are considered for the two planets, this would be a logical grouping. In most cases, however (because of the difference in mass of the two planets), Venusian entry velocities are much higher than those for Mars. As a result, Venusian entries usually entail severe radiative and convective heating and pose a significant challenge to present-day ablative heat shields. As discussed in the preceding section, this is usually not the case for Mars. Except for the fact that they both pose appreciable heat-shielding problems, however, Venus entries and entries into the atmospheres of the giant planets have little in common. Hence, they will be discussed as separate categories.

Venus

Atmospheric Characteristics

Data obtained from the flights of Mariner V and the Russian Venera 4 vehicles have greatly reduced the uncertainties associated with the density, temperatures, and composition of the Venusian atmosphere. From analyses of these data(55), it appears that the altitude from which Venera 4 sent its last radio transmission is in doubt. Originally it was reported that Venera 4 had measured pressures of from 16.4 to 20.3 atmospheres at the Venusian surface. However, if it is assumed that the last Venera 4 transmission came from an altitude of approximately 30 km, then the Venera 4 data fit nicely with the Mariner V data, define the temperature and pressure profiles in the Venus atmosphere quite well, and surface pressures of 167 atmospheres are indicated. This interpretation of the data is appealing but there are still arguments pro and con. As a result, model atmospheres have been developed corresponding to surface pressures of 16.4 and 167 atmospheres and various degrees of solar activity. Density and temperature profiles for these atmospheres are presented in Figures 15 and 16. The composition of the Venusian atmosphere is now believed to be between 90 percent CO₂, 10 percent N₂, and 100 percent CO₂. From an entry heating standpoint, the atmosphere is reasonably well known since the important parameters are composition and scale height, and the scale heights in the sensible (from a heating standpoint) atmosphere are nearly the same for the various models shown in Figure 15.

Entry Velocities, Modes, and Vehicle Geometries

The entry velocities encountered for various missions range from 11 to 15 km/sec. The lowest velocities correspond to entry from orbit, and the highest velocities are those for a Mercury swing-by mission. For direct entries, as shown by Norman and Hart(69), the velocities can range from 11.6 to 13 km/sec depending on the year of the mission. Some early studies considered vertical entries but most recent investigations have studied entry angles from -30° to -50°. The Venus missions studied so far have utilized ballistic entries since it appears that heating rates can be kept within a manageable range without the use of lift and there is no problem in decelerating to subsonic speeds at sufficiently high altitudes for atmospheric studies.

The geometries considered by almost all investigators are, as was the case for Martian entry, spherically blunted cones. In general, nose radii and cone angles for Venusian vehicles are smaller than those used for Mars entry. This trend toward sharper, more highly sweptback vehicles reflects attempts at

minimizing the total heat load by reducing radiative heating. As shown by Norman and Hart(69), however, not all the effects of reducing nose radii are favorable. If transition to turbulent flow occurs (in Ref. (69), the assumption of a momentum thickness transition Reynolds number of 250 results in turbulent flow at the cone edge just prior to peak heating), then the thick entropy layer caused by a large nose radius can significantly reduce the levels of turbulent heating and shear. Most studies have indicated nose radii on the order of 1 foot and cone angles from 50 to 60° (Fig. 14).

Heating Levels

Studies of stagnation point and laminar convective heating in various atmospheres(70,71,72,73,74) have shown that CO₂ and CO₂/N₂ mixtures will produce nearly the same (actually about 10 percent higher) heat fluxes as air for comparable vehicles and flight conditions. It is to be expected that turbulent heating levels will be comparable for these gas mixtures.

On the other hand, radiative heating from air and from CO₂/N₂ mixtures differs considerably(75,76,77,78). One reason for this is that the temperatures at which these gas mixtures begin to radiate strongly are quite different. For example, at temperatures of approximately 8000° K, where air radiates weakly, CO₂ radiates strongly. Another reason is that because of the different radiating species involved the spectral distributions of radiation from these gases are quite dissimilar. This is shown in Figure 17 which was prepared using the radiation model of Nicolet(79). The reference conditions for this figure were selected from Reference (80) with a V-3 atmosphere(55) and the calculations were carried out for an isothermal slab. Three gas mixtures are shown: air, 90 percent CO₂ with 10 percent N₂, and 100 percent CO₂. The calculated equilibrium post-shock temperature varies between 9090° K for air and 9540° K for 100 percent CO₂. Note that there is almost no difference between the CO₂ and CO₂/N₂ spectral distributions except in the region from 3.0 to 4.5 eV. Nitrogen and cyanogen bands dominate in this region so this difference represents the effect to be expected by the presence of nitrogen in the atmosphere. This difference, while not negligible, will not make or break a design and, conversely, designs which allow for a reasonable nitrogen content will not be unduly penalized. It is evident that CN, while an important radiator, is not the dominant radiator which it was originally believed to be(75,81) for earlier Venus atmospheres which contained as much as 60 percent N₂.

A comparison of both of these atmospheres with the air results on Figure 17 shows significant differences. First of

all, it is noted that the air temperature is significantly lower than either of the others so that the radiation is expected to be lower. However, the difference shown indicates the importance of $\text{CO}(4+)$ which dominates the spectral region from approximately 5 to 11 eV. In air there are no comparable radiators in this region and, hence, the spectral distribution and radiative flux encountered during a comparable Earth entry will be significantly different from any Venusian entry.

Figure 17 suggests the importance of using an ablator which will absorb the $\text{CO}(4+)$ radiation. As shown in Figure 10 for air, the absorption by CO in ablation products is very noticeable in the spectral region from 5 to 11 eV. However, for air there are no prominent radiation sources in this frequency band and the effectiveness of the ablation products is minimized. These results suggest, however, that any ablator chosen for a Venus entry should be tailored to provide large quantities of CO in the ablation products so as to minimize the radiative heat load.

In Table 3, heating rates calculated by various investigators(60,69,75,80) for various Venus missions are presented. From this table, it can be seen that the maximum heating rates for out-of-orbit and direct entries are in the same range as those for high velocity Earth entry missions. For the out-of-orbit and direct entries, it is also seen that the pressures and aerodynamic shears are higher than those characteristic of manned entries but much less than those typical of high M/C_{DA} ballistic Earth entry vehicles. The duration of heating for these Venus entries is relatively short (on the order of 30 sec).

Candidate Materials

The levels of heating rate, pressure, and shear presented in Table 3 can be used to select a class of ablators for Venus entry missions. First of all, the high heating rates shown in Table 3 prohibit the use of silica-dominated materials such as those used for Martian entry vehicles. At high surface temperatures, chars which contain large amounts of SiO_2 will recede rapidly due to SiO_2 melting, Si/C reactions, or both. At these temperatures, char surface reradiation will be a primary energy accommodation mechanism and so a high emissivity, stable carbonaceous char layer is required. All of this dictates the use of a carbon-dominated material. As mentioned previously, the pressures and shears associated with Venusian entry are somewhat higher than those typical of manned entries. Because of this, mechanical char failure may become a significant consideration, at least for selected regions of the entry vehicle. In Earth entry research the usual approach has been to increase ablator density in an attempt to obtain increased char strength. To a degree this

has been successful, but large increases in ablator density have been found to result in only small changes in the test conditions required to produce mechanical char removal. As mentioned previously, the most commonly encountered type of mechanical char failure involves a weakening of the char skeleton by chemical reaction followed by removal of discrete char fragments by aerodynamic forces. This is not completely understood and is not analytically describable at the present time. It is probable that an ablator of somewhat higher density than those used on manned vehicles should be used on a Venusian entry vehicle. A density of about 0.7 gm/cm^3 seems a reasonable choice. The use of high-density materials is not desirable since their resistance to mechanical char failure is only slightly greater than that of the lower density materials, and their inferior insulating efficiency (resulting from their high density) would require large increases in heat-shield weight.

Hence, a carbon-dominated material of medium density is indicated. Some of the best-known materials of this type may, however, be unsuitable for planetary missions. Most phenolic-based and many epoxy-based materials have been found to be incapable of withstanding the prelaunch and transit environments of sterilization, vacuum, and cold-soak which were so influential in the choice of an elastomeric material for Martian entries. A possible approach may be to use a material composed of an elastomeric resin, carbon microspheres, and carbon fibers in an effort to utilize the good low-temperature properties of the resin; and with the high carbon-filler content, produce a stable high-temperature char. It would be interesting to know what type of ablator the Russians used on Venera 4.

Present State of the Technology

Since the levels of heating, pressure, and shear during Venusian entry are significantly higher than those for Martian entry, the heat-shield analysis and design is a more critical part of the overall vehicle design. Except for the most severe entries (Mercury swing-by), however, the entry conditions are close enough to those of high-speed Earth entries that the technology already developed for Earth entry is largely applicable. The situation then is that while there are significant uncertainties in both heating and ablation analyses, it appears that, through conservative design, workable heat shields can be produced within the present state of the art. Present indications are that for out-of-orbit and direct entries the thermal protection system will constitute from 10 to 25 percent of the entry vehicle weight. (A recent study by Jaworski and Nagler(82) indicates that, for the less severe Venusian entries, the weight of the actual ablation material may be less than 5 percent of the total vehicle weight. These numbers seem small and bear further study.)

In the analyses of aerodynamic heating, there are significant uncertainties associated with the prediction of boundary-layer transition, turbulent heating, and radiative heating levels. In predicting ablator response, the major uncertainties appear to be related to the kinetics of the pyrolysis gas reactions, ablator response to turbulent flows, the prediction of char recession rates, particularly recession due to mechanical char removal.

The prediction of boundary-layer transition has, for many years, been recognized as one of the most important problems in aerospace research. It is also one of the most difficult. In view of the great amount of research already devoted to the problem, it seems unrealistic to expect any breakthroughs in this area. Research should, of course, be continued, but in designing near-future planetary entry vehicles, we may have to accept transition Reynolds numbers with order-of-magnitude accuracies. On the other hand, it appears that the present uncertainties in radiative heating levels could be reduced by carrying out completely coupled analyses, such as those described earlier for high-speed Earth entry, in which all the significant phenomena such as self-absorption, radiation cooling, realistic (lines, band systems, and continuum) radiation models, and radiation blockage by pyrolysis gases are accounted for. In practically every study carried out so far for Venusian entry, one or more of these phenomena have been neglected. With regard to the uncertainties in ablator response, the greatest need is for more and better experimental data to better define the important mechanisms and to lead to more physically realistic analyses.

Jupiter

Atmospheric Characteristics

Our knowledge of the atmosphere of Jupiter is much less complete than for Mars or Venus. Because of the Jovian cloud layers, the planet's surface (if one exists in the usual sense) cannot be observed. The available data concern the atmosphere above the cloud layer. The makeup of the Jovian lower atmosphere is largely a matter of speculation. In 1967, Michaux, et al. (57), reviewed the status of our knowledge of Jupiter. They presented a possible makeup for the lower atmosphere and Jovian interior (based on models by Gallet and Peebles) which is presented in Figure 18 of the present paper. From this figure it is seen that the atmosphere is pictured as becoming denser and denser until a surface which may be liquid or solid is reached. From the standpoint of reentry vehicles, however, it is the atmosphere above the clouds that is of most interest since vehicles with moderate $M/C_D A$'s will decelerate to terminal conditions before reaching the clouds.

Table 4 presents a sampling of proposed Jovian model atmospheres(56,83). As shown in Table 4, there is general agreement that the main atmospheric constituents (above the cloud layers) are H_2 and He, but the proposed compositions range from predominantly H_2 to predominantly He. Proposed cloud-top pressures and temperatures range from 2 to 24 atmospheres and 150 to 168° K; the atmospheric scale heights range from 12 to 21 km.

Entry Velocities, Modes, and Vehicle Geometries

For Jupiter, escape velocity is approximately 60 km/sec and surface satellite speed is approximately 40 km/sec. Accordingly, most studies of Jovian entry have considered this range of entry velocities. The equatorial velocity of the planet is, however, about 13 km/sec and, hence, entry in the direction of planetary rotation and in the vicinity of the equatorial plane could reduce the relative direct-entry velocities to about 50 km/sec.

Most studies to date have considered ballistic entries and, again, the most widely considered configuration is the sphere cone. Because of the very high speeds and heating rates involved in Jupiter entry, there are some indications that guided (lifting) entries may be required to keep the heating within manageable limits(83). Tauber(83) has studied the relative merits of blunt and conical vehicles for Jovian entry. His conclusion is that the conical vehicles have a clear advantage with regard to required heat-shield weights. In fact, he suggests that if the atmosphere were primarily H_2 , a blunt (Apollo-like) vehicle might have to be composed almost entirely of heat shield. Present indications are that the cone angles for Jovian vehicles will be smaller than those for Martian and Venusian vehicles (Fig. 14). The most advantageous cone angle and, for that matter, the overall character of the entry heating appear to depend strongly on the atmospheric composition. This dependence will be discussed subsequently.

Heating Levels

Heating rates, for most Jovian entries, are predicted to be extremely high by Earth-entry standards. Tauber(83) studied the effects of vehicle geometry and atmospheric composition on radiative and convective heating rates for a spherically tipped, conical vehicle. Some of his results are presented in Figure 19. The results presented in Figure 19 were computed for a vehicle having a 30° cone half-angle, a base radius of 1 m, and a nose radius of 1 cm entering on a shallow ballistic trajectory at 50 km/sec. During entry, boundary-layer Reynolds numbers were limited to 5×10^6 in order to insure laminar flow. Both radiative and convective heating rates are presented for the stagnation point and the conical afterbody, as a function of

atmospheric H_2 content. As shown by Figure 19, a 100-percent H_2 atmosphere would produce heating rates that are sizable but comparable to those experienced during severe Earth entries. A He atmosphere, on the other hand, would produce radiative and convective heating rates far beyond those with which we have had experience. At the present time, it is difficult to pick a "most likely" Jovian atmosphere. The most recent papers on the subject do, however, seem to be indicating higher and higher H_2 contents. In 1963, Spinrad and Trafton(84) proposed a 60-percent H_2 atmosphere and, in 1967, Beckman(85) proposed an 82-percent H_2 atmosphere. If these high H_2 contents prove to be correct, the Jovian entry heating problem will be large but not unmanageable.

The theory of laminar convective heat transfer for H_2/He mixtures appears to be on fairly firm ground. Stagnation-point heating in H_2 has been treated by Scala(86) and Marvin and Deiwert(71), and correlated by Zoby(70). Stagnation-point heating in He was measured and correlated by Pope(87). Zoby(70) has proposed an approximate method (involving summation of terms weighted according to the mass fractions of the individual gases) for calculating stagnation-point heating in gas mixtures, and recent unpublished work by Sutton and Graves at the Langley Research Center has shown that the summation approximation gives accurate estimates of heating for Jovian atmospheres. With regard to laminar heating away from the stagnation point, Marvin and Deiwert(71) found that heating-rate distributions were only affected to a minor degree by gas composition. The prediction of transition and turbulent heating in H_2/He mixtures involves large uncertainties, just as it does in the case of air.

The radiation from H_2/He shock layers is significantly different from that produced by air. This is illustrated by Figure 20. In Figure 20, spectral flux is presented as a function of photon energy for a 61-percent H_2 , 36-percent He shock layer, and for an air shock layer. The results shown for the Jovian atmosphere were taken from the work of Stickford and Menard(88). They were obtained by carrying out an adiabatic calculation, which included self-absorption, for a 12 000° K, 1-cm-thick layer. The results shown for air are those previously presented in Figure 10(a) and include self-absorption, radiation loss, and, as indicated by the short dashed curves, absorption by ablation products. The H_2/He results include Lyman and Balmer line radiation while the air results are for continuum only. However, as Figure 10(b) indicates, the line radiation from the air will not change the comparison shown in Figure 20. The temperature of the air shock layer (12 900° K) is comparable to that of the H_2/He layer, but the air layer is nearly an order of magnitude thicker. From these curves it is seen that, for comparable shock-layer temperatures, the intensity

of radiation will be much greater for the H_2/He mixture than for air. Also, it can be seen that the relative amount of radiation in spectral regions not subject to absorption by ablation products is greater for H_2/He than for air. This suggests that absorption by ablation products may not be as important for Jovian entry as it is for Earth or Venus entry. Wilson(15) showed only about a 10-percent reduction in radiative heating due to ablation products.*

Candidate Materials

The extremely high heating rates and relatively high pressures that are predicted for Jovian entry (see Fig. 19) immediately suggest the use of high-density, carbonaceous materials. Graphites, carbon-carbon composites, and high-density graphite fiber reinforced plastics have all been suggested for use on Jovian entry vehicles. In the nose regions of the vehicle, such materials will probably be used. The requirement of reasonably small shape change, alone, may dictate high-density materials in this region. On the vehicle afterbody, moderate density ablators appear feasible. Materials similar to those discussed for Venusian entry may work well for these applications.

Actually, there are several basic phenomena which must be investigated before any reasonable choice of materials can be made. The first of these concerns the response of materials to very high radiative heating rates. At present, no realistic tests have been carried out at heating rates over a few kW/cm^2 . It has been suggested that materials may be torn apart by the high thermal stresses and internal gas pressures that heating rates on the order of tens of thousands of W/cm^2 will produce. Such a possibility cannot be discounted. What is needed is test data at these conditions. Second, there are questions concerning the absorptivity of ablative char layers in the different spectral ranges. Wilson and Spitzer(43) measured the absorptance of several chars and graphites at temperatures up to $3400^\circ K$ and over the visible and near-infrared wavelength ranges. They found that, for some chars, the assumption of gray-body behavior was invalid. In spite of such findings, most ablation analyses utilize constant values for char surface emissivity and absorptivity. For Jovian entry, large amounts of ultraviolet radiation from the shock layer are predicted (see Fig. 20). In the case of air shock layers, much of the ultraviolet radiation is absorbed by ablation products. It now appears that such will not be the case for Jovian entry. It has been suggested that the

*Recent calculations by the same author, using new absorption coefficient data for the polyatomic carbon species have indicated reductions in radiative heating of up to 80 percent. More work in this area is needed.

high energy, short wavelength ultraviolet radiation might penetrate deeply into the ablator rather than being absorbed at the surface as most ablation analyses currently assume. Wilson and Spitzer's data show increasing absorptance as ultraviolet wavelengths are approached and seem to suggest high ultraviolet absorptance values but absorptance measurements in the ultraviolet are not presently available. If the radiation should penetrate into the char, present analyses could give grossly incorrect predictions of ablator response during Jovian entry. Finally, there is the question of mechanical char failure in H_2/He atmospheres. As mentioned previously, the most commonly observed type of char failure is intimately associated with oxidation reactions at the char surface. When tested in inert streams, even low-density chars resist mechanical failure up to high levels of pressure and shear. If the Jovian atmosphere is essentially 100 percent He, mechanical char failure may not be a big problem even at relatively high pressures and shears. If large amounts of H_2 are present, however, it is possible that H/C reactions at the char surface could cause a type of char failure similar to that caused by O/C reactions in air.

Finally, the extremely high heating rates associated with He atmospheres may force us to reorient our thinking about the relative importance of the various ablative energy accommodation mechanisms. For severe Earth entries and for Venusian entries, we found that char surface reradiation is likely to be the most important single mechanism. As pointed out previously, however, the amount of energy that can be reradiated is limited (by the sublimation of carbonaceous materials) to around 1200 W/cm^2 . Hence, if the radiative heating rates reach levels of $12\,000 \text{ W/cm}^2$, char surface reradiation will be relatively unimportant while sublimation will become relatively more important. It has been suggested that, for such extreme conditions, materials with high surface reflectivity (to reflect the incident radiation) rather than high emissivity might be desirable, if such materials can be found.

State of Technology

Present indications are that the percentage of vehicle gross weight required for the heat shield will be significantly greater for Jovian entry than for Earth, Venus, or Mars entries. Jovian heat-shield technology is in an early stage of development and many fundamental phenomena require study before the Jovian entry problem can be accurately assessed.

Simulation Ground and Flight Testing

Ground Testing

While many types of ground test facilities were used in the early days of ablation research, the great majority of

present-day ablation tests are carried out in arc-heated wind tunnels. A typical arc tunnel, equipped to provide combined convective and radiative heating, is shown schematically in Figure 21. The test gas is passed through an electric arc where it is heated to high temperatures. It subsequently expands through a convergent-divergent nozzle and exits as a supersonic test stream in a free jet test section. The model to be tested is mounted on a swing arm which allows it to be inserted in the test stream after stable arc-jet operating conditions have been achieved and to be retracted from the stream after the desired test time has elapsed. The flow leaves the test section through a diffuser and flows through a heat exchanger to either a vacuum sphere or a steam ejector which provides the pressure ratio required to fill the supersonic nozzle. Arc heaters have been developed which operate well at high arc chamber temperatures (enthalpies) and low arc chamber pressures. Other heaters have been developed which operate at high chamber pressure but at modest temperatures. It has not been possible, however, to develop heaters which operate at both high temperatures and pressures, nor has it been possible to build a single heater that operates well over the entire range of possible conditions. Hence, most test complexes have several arc heaters, with each heater equipped with several nozzles of varying expansion ratio to provide a reasonably wide range of test conditions.

As shown in Figure 21, some test facilities are equipped with radiation sources (usually high-pressure arc lamps or lasers) so that the test models can be exposed to combined convective and radiative heating. The range of test conditions currently available is shown in Figure 22(89,90). This range of test conditions was determined for tests conducted in air and there is some question as to whether this extensive range of test conditions is available in gases such as CO_2 , H_2 , and He. For many years there were persistent reports of electrode failures resulting from CO_2 operation, but most facilities now seem to be capable of routine operation on CO_2 and the test conditions obtained are generally comparable to those obtained with air. All arc tunnels seem to run very well on He but, because of the safety problems involved, few tests have been run to date in H_2 or H_2/He mixtures. Some selected values of available radiative flux capabilities are also shown on Figure 22 to give an indication of the combined heating capabilities now available. Also presented on Figure 22 are representative Mars, Venus, and Jupiter entry conditions(89). As can be seen from Figure 22, our present ground-test facilities can produce conditions typical of Martian entry but not those typical of Venusian entry. Needless to say, Jovian entry conditions are considerably beyond our present test capabilities.

Even within the range of available test conditions, however, ground facilities do not actually simulate reentry flight conditions. This lack of simulation can be illustrated by considering the stagnation-point heating relation

$$\dot{q}_c \propto \left(h_s \frac{P_{t2}}{\sqrt{R_{eff}}} \right) \propto \left(v_\infty^2 \frac{P_{t2}}{\sqrt{R_{eff}}} \right)$$

Ground-test models are usually much smaller than the flight vehicles they represent. Hence, if the heating rate is the same for both, then either the pressure or the velocity must differ. This illustrates one of the basic difficulties of ground ablation testing. One or two aspects of a given flight condition can be duplicated, but when they are, other aspects, often important ones, must be in error. Because of this lack of complete simulation, ground-test results cannot be used directly to predict in-flight ablative behavior. Instead, the ground tests are used to define basic ablation mechanisms and to verify a theoretical ablation model (usually a digital computer code). The theoretical ablation model is then used to predict in-flight behavior.

Another problem associated with the small size of ablation test models is that multidimensional ablation effects can become important in ground tests even though they are negligible for the flight conditions that the ground tests are supposed to represent. One example of such an effect is the reduction in transpiration cooling effect caused by the pyrolysis gases flowing laterally through the char to the low pressure regions around the shoulders of the model rather than flowing perpendicular to the char surface as is assumed in one-dimensional ablation analyses. This effect, which can result in increased ablation rates, is described in Reference (23). Another effect of this type arises when lateral temperature gradients (due to small model size) become large enough so that significant amounts of heat are conducted laterally away from a given point on the char surface rather than perpendicularly to the char surface into the decomposing ablator below.

In Figure 22 it was seen that present radiative heating facilities cannot produce fluxes as high as those expected during advanced (especially, Jovian) planetary entries. These facilities also have another shortcoming which is possibly more important than the insufficient flux levels. That is, the spectral distribution of radiation from the lamps or lasers differs greatly from that of the gases in a radiating shock layer. This is illustrated in Figure 23. From this figure it is seen that the facilities are particularly deficient in the short wavelength ultraviolet region which constitutes a

significant part of the shock-layer radiation. As mentioned before, it has been often suggested that ablation materials may respond differently to ultraviolet radiation than to visible or infrared radiation. It is possible that the ultraviolet may penetrate deep into the ablator rather than being absorbed near the char surface (as is assumed in practically all existing ablation computer programs). Tests of models under ultraviolet radiation are needed to resolve this question. Another important phenomenon that cannot presently be studied in ground tests is the absorption of shock-layer radiation by ablation products. As was shown earlier, this energy absorption mechanism is quite significant for Earth entry and may be significant for many planetary entries (especially entries into predominantly CO₂ atmospheres). Since the incoming radiation is absorbed preferentially rather than uniformly across the spectrum (actually most of this absorption is in the ultraviolet), this phenomenon cannot be studied unless ground facilities with spectral distributions similar to those of an actual shock layer can be developed.

Flight Testing

Flight tests have played an invaluable role in the development of Earth-entry ablation technology. Flight tests are expensive and require large project teams and long lead times but, because of the previously mentioned difficulties in scaling ground-test ablation data to flight conditions, they are mandatory for cases (such as manned entry) where the ablator response must be known with great accuracy.

The great advantage of flight testing is the ability to expose the heat shield simultaneously to the correct levels of all the important entry parameters (i.e., heating rate, pressure, enthalpy, shear, etc.).

Since this situation cannot be achieved in ground testing, it usually happens that a given set of ground-test data can be satisfactorily explained by several theoretical ablation models, each of which predicts differing in-flight behavior for the ablator. One of the most significant contributions of a flight test is that it shows which (if any) of the proposed theoretical models is capable of predicting both ground and flight results.

The preceding comments apply when the flight test is carried out in the atmosphere of the planet for which the entry vehicle is designed. Suppose we are dealing with a vehicle designed for a Mars or Venus entry. Can meaningful flight tests of this vehicle be carried out in the Earth's atmosphere? This problem has been studied by several investigators(80,91,92). As far as phenomena which are largely

independent of atmospheric composition (i.e., decelerations, aerodynamic loads, etc.), the answer is yes. If one assumes a straight line ballistic trajectory(95) and an exponential atmosphere, it can be shown that, for the case where the entry velocities and ballistic coefficients are the same, we can select a path through the Earth's atmosphere along which the vehicle will encounter a density history equal to that which it would encounter along a different path in a different atmosphere. Beginning with this argument, Kennet(92) goes on to show that, along this equivalent trajectory, any quantity of the form

$$\rho_{\infty}^m V_{\infty}^n$$

can be duplicated so long as m and n do not depend on the atmospheric composition.

Laminar convective heating can be adequately correlated in terms of $\rho_{\infty}^m V_{\infty}^n$, but, of course, m and n will, in general, depend on the atmospheric composition. For air and CO_2 , N_2 mixtures, however, the correlations are nearly identical (≈ 10 percent difference) and, hence, it appears that for Martian and Venusian entries, the laminar convective heating could be adequately simulated. There also appears to be a possibility of simulating transition and turbulent heating in CO_2 - N_2 atmospheres, but this question has not been completely resolved at present.

Radiative heating, on the other hand, does not lend itself to simulation by these techniques. Since many of the most significant radiative heating phenomena (self-absorption, absorption by pyrolysis gases, possibly ablator response) are strongly dependent on the spectral distribution of the radiative flux, which is, in turn, strongly dependent on the chemical composition of the shock layer, this is to be expected. In Reference (80), Spiegel, Wolf, and Zeh carried out a detailed study of the degree to which the ablative response of a Venus-entry-vehicle heat shield could be studied and simulated in an Earth entry flight test. They found that convective heating could be simulated quite well, but that the radiative heating differed significantly, both with regard to flux level and spectral distribution, from that calculated for an actual Venus entry. Spiegel, Wolf, and Zeh went on to compute the in-depth response of a high-density phenolic-nylon heat shield for the Venusian and equivalent Earth entries and found that the ablator response was quite similar in spite of the differences in radiative heating. This would seem to imply that such an Earth entry might provide a proof test for a Venusian-entry heat shield. Such a conclusion, however, is predicated on the assumption that the Venusian-entry (and Earth-entry) radiative heating and the response of the ablator to it

has been accurately described by the theoretical models used in the analysis. This is precisely the assumption that we wanted to check with a flight test in the first place.

Hence, it appears that the simulation of planetary-entry heat-shield response by an Earth-entry flight test is only feasible for missions involving only convective heating. An out-of-orbit Martian entry is an excellent example of such a mission. Because of the low heating rates involved and the fact that the most likely candidate materials (filled elastomers) are not greatly sensitive to shock layer composition at the resulting low surface temperatures, it appears that nearly complete simulation could be achieved. For higher velocity Mars-entry missions and for missions to Venus and the giant planets, however, Earth entry flight tests do not appear capable of simulating the significant radiative phenomena.

Concluding Summation

A review of ablative heat-shield technology for planetary entries has been carried out to assess the present state of the art and to identify areas in which further research is needed.

To identify important phenomena and to provide a basis for comparison, research on Earth-entry heat shields was summarized as a first step in the review. Emphasis was placed on entries characterized by large radiative and convective heating rates, since less severe entries can be considered as limiting cases (the case of negligible radiative heating, for instance) of this more complex problem.

It was shown that realistic assessments of heating and ablator response for this type of entry required a coupled analysis in which convective and radiative processes in the shock layer influence one another, and both the radiative and convective heating are significantly modified by the introduction of gaseous ablation products into the flow field. From such analyses it was shown that, for moderate-density charring ablators, the significant energy accommodation mechanisms are: pyrolysis gas enthalpy increase, char surface reradiation, and the reduction of convective and radiative heat flux by the injection of ablation products into the flow field. Significant uncertainties were shown to still exist with respect to the chemical state of the pyrolysis gases (which determines their enthalpy content) and the calculation of radiative heating rates with absorption by ablation products. It was pointed out that most present-day ablation analyses assume that radiation of all wavelengths is absorbed at the char surface, even though little is actually known about the

absorptance of ablative chars at other than visible wavelengths. Shock-layer spectra were presented that showed large amounts of radiant energy at vacuum ultraviolet wavelengths. It was suggested that radiation at these wavelengths might penetrate deeply into the char and cause ablative behavior to be significantly different from that presently being predicted.

The rate at which the ablator is consumed in accommodating the incident heating is largely determined by the char recession rate which results from chemical reaction with boundary-layer gases, sublimation, and mechanical char failure. Significant uncertainties were shown to exist in the prediction of all three of these phenomena.

The prediction of convective heating rates was found to be on fairly firm ground so long as the flow remains laminar. The prediction of boundary-layer transition and turbulent heating rates still involve significant uncertainties, however, with transition Reynolds numbers being known only to within an order of magnitude. It was also pointed out that, because of experimental difficulties, the response of ablators to turbulent flow is a relatively unexplored area of research.

For entries into tenuous atmospheres such as those of Mars and Mercury, it was found that heat-shield design was well within the present state of the art. Because of the low entry velocities typical of out-of-orbit entries, radiative heating was found to be insignificant and convective heating rates were found to be low. It was pointed out that, for these entries, the most important ablation-material characteristics were low density (for high insulating efficiency) and the ability to survive prelaunch and transit environments such as sterilization, cold soak, and space vacuum.

In considering entries into the atmosphere of Venus, it was found that, because of the comparable entry velocities, the significant phenomena were essentially the same as those for planetary return Earth entry. Hence, most of the uncertainties discussed for severe Earth entry with combined radiative and convective heating apply as well to Venusian entries.

Since the Venusian atmosphere is primarily CO_2 (rather than air), the spectral distribution of shock-layer radiation is quite different from that for air and it was pointed out that most of the radiation from a Venusian shock layer was in a spectral range where it could be strongly absorbed by ablation products. Since very few coupled analyses (including absorption by ablation products) have been carried out for Venusian entries, it was suggested that this might be a fruitful field of research.

It was pointed out that the relatively high char surface pressures and aerodynamic shears which result from ballistic Venusian entries suggest significant rates of mechanical char failure. Considerable work is required in the area of char surface chemical reactions in CO_2 test streams, with particular emphasis on char failure by coupled chemical-aerodynamic mechanisms. Reference to Earth entry research showed that the mechanical char failure problem cannot be overcome by simply increasing the density of the ablator.

Because of the high Venusian-entry heating rates, elastomeric materials such as those proposed for Mars entries were considered unsuitable for Venusian entries. Because of their inability to withstand inter-planetary transit environments, many of the materials most often considered for severe Earth entries may also be unsuitable for Venus missions. Hence, it was suggested that a new class of materials that could withstand both the transit environments and the severe entries might have to be developed.

Jovian entry was considered as being typical of entries into the atmospheres of the giant planets (Jupiter, Saturn, Uranus, etc.). Because of the large mass of the planet (hence, high escape velocities), Jovian entry speeds and the resulting heating rates (especially radiative heating rates) were found to be potentially many times higher than those for Earth entry. The extent of the increase can not be evaluated because of uncertainties in the ablation products and their absorption coefficients, but it is almost certain that the radiative heating rates will be very large. It was pointed out that the behavior of materials under such high heating rates may be quite different than at lower heating rates. The possibility of catastrophic failure cannot be discounted. It was shown that, because the amount of energy reradiated from the char surface is limited by material sublimation temperatures, char surface reradiation could be a less important energy accommodation mechanism for Jovian entries than it is for Earth or Venusian entries. The possible significance of mechanical char failure was shown to depend to a significant extent on whether the Jovian atmosphere is mostly H_2 (which will react with carbonaceous materials) or He (which is inert). The state of the art for Jovian entry heat shields was found to be in an early stage of development.

The test capabilities of present-day ground-based facilities were reviewed and their inability to completely simulate entry conditions was pointed out. It was pointed out, however, that valuable partial simulation is available and, in particular, small test models can be subjected to convective heating rates up to the levels experienced in typical Venusian entries. It was also shown that radiative heating rates comparable to those of Venusian entry should be available soon. It was pointed out,

however, that one important aspect of the radiative heating, the spectral distribution, is not reproduced in any of the present radiative facilities. Because of this, it is not presently possible to validate existing theories of radiative heating with absorption by ablation products. It was shown that Jovian entry conditions are beyond the capabilities of present ground facilities.

The ability of Earth-entry flight tests to simulate entries into other atmospheres was reviewed. It was found that those phenomena, which are independent of atmospheric chemical composition, could be adequately simulated but that phenomena which depend strongly on shock-layer composition (such as radiative heating and char surface phenomena) could not be simulated. Hence it appeared that nearly complete simulation of an out-of-orbit Mars entry was possible (since char surface reactions are not too important at the low temperatures involved), but that the value of Earth entry tests in studying Venusian and Jovian entry phenomena is limited.

References

- (1) Adams, Mac C.: Recent Advances in Ablation, ARS Journal, Vol. 29, No. 9, p. 625, September 1959.
- (2) Fay, J. A.; and Riddell, F. R.: Theory of Stagnation Point Heat Transfer in Dissociated Air, Journal of the Aeronautical Sciences, Vol. 25, No. 2, February 1958.
- (3) Cohen, N. B.: Boundary-Layer Similar Solutions and Correlation Equations for Laminar Heat-Transfer Distribution in Equilibrium Air at Velocities up to 41 100 Feet Per Second, NASA TR R-118, 1961.
- (4) Hoshizaki, H.: Heat Transfer in Planetary Atmospheres at Super-Satellite Speeds, ARS Journal, Vol. 32, No. 10, p. 1544, October 1962.
- (5) DeRienzo, P.; and Pallone, A. J.: Convective Stagnation-Point Heating for Reentry Speeds up to 70 000 fps Including Effects of Large Blowing Rates, AIAA Journal, Vol. 5, No. 2, February 1967.
- (6) Boison, J. C.; and Curtiss, H. A.: Preliminary Results of Spherical-Segment Blunt Body Pressure Surveys in the 20-Inch Supersonic Wind Tunnel at JPL, RAD Tech. Memo 2-TM-57-77 (Aerod. Sec. Memo No. 152), AVCO Res. and Advanced Dev. Div., October 9, 1957.

- (7) Zoby, E. V.; and Sullivan, E. M.: Effects of Corner Radius on Stagnation-Point Velocity Gradients on Blunt Axisymmetric Bodies, NASA TM X-1067, (U), March 1965.
- (8) Lees, Lester: Laminar Heat Transfer Over Blunt Nosed Bodies at Hypersonic Flight Speeds, Jet Propulsion, pp. 259, April 1956.
- (9) Zoby, Ernest V.: Approximate Relations for Laminar Heat-Transfer and Shear-Stress Functions in Equilibrium Dissociated Air, NASA TN D-4484, April 1968.
- (10) Zoby, Ernest V.; and Sullivan, Edward M.: Correlation of Free-Flight Turbulent Heat-Transfer Data From Axisymmetric Bodies With Compressible Flat-Plate Relationships, NASA TN D-3802, January 1967.
- (11) Sullivan, E. M.; Erickson, W. D.; Smith, G. L.; and Suttles, J. T.: Some Aspects of Interplanetary Earth-Entry Simulation, Presented at the 15th Annual Meeting of the Institute of Environmental Sciences, Anaheim, California, April 21-24, 1969.
- (12) Anderson, John D., Jr.: An Engineering Survey of Radiating Shock Layers, AIAA Journal, Vol. 7, No. 9, pp. 1665-1675 September 1969.
- (13) Hoshizaki, H.; and Wilson, K. H.: Convective and Radiative Heat Transfer During Superorbital Entry," AIAA Journal, Vol. 5, No. 1, pp. 25-35, January 1967.
- (14) Page, W. A.; Compton, D. L.; Borucki, W. J.; Ciffone, D. L.; and Cooper, D. M.: Radiative Transport in Inviscid Nonadiabatic Stagnation-Region Shock Layers, AIAA Paper 68-784, AIAA Third Thermophysics Conference, Los Angeles, California, 1968.
- (15) Wilson, K. H.: Massive Blowing Effects on Viscous, Radiating, Stagnation-Point Flow, AIAA Paper 70-203, AIAA Eighth Aerospace Sciences Meeting, New York, N.Y., January 1970.
- (16) Olstad, W. B.: Blunt-Body Stagnation Flow With Nongray Radiation Heat Transfer - A Singular Perturbation Solution, NASA TR R-295, 1968.
- (17) Chin, J. H.: Radiation Transport for Stagnation Flows Including the Effects of Lines and Ablation Layer, AIAA Paper 68-664, AIAA Fluid and Plasmadynamics Meeting, Los Angeles, California, June 1968.

- (18) Rigdon, W. S.; Dirling, R. B., Jr.; and Thomas, M.: Stagnation Point Heat Transfer During Hypervelocity Atmospheric Entry, NASA CR-1462, February 1970.
- (19) Wilson, K. H.: RATRAP - A Radiation Transport Code, IMSC 6-77-67-12, Lockheed Missiles and Space Company, Palo Alto, California, March 14, 1967.
- (20) Callis, Linwood B.: Time-Asymptotic Solutions of Flow-fields With Coupled Nongray Radiation About Long Blunt Bodies, AIAA Paper 70-865, AIAA Fifth Thermophysics Conference, Los Angeles, California, June 1970.
- (21) Hurwicz, Henryk: Aerothermochemistry Studies in Ablation. Presented at Fifth AGARD Colloquium, on High Temperature Phenomena, Braunschweig, Germany, April 9-13, 1962.
- (22) Moyer, C. B.; Anderson, L. W.; and Dahm, T. J.: A Coupled Computer Code for the Transient Thermal Response and Ablation of Noncharring Heat Shields and Nose Tips, NASA CR-1630, 1970.
- (23) Bush, H. G.; and Dow, M. B.: Multidimensional Gas Flow Through Permeable Char Layers and Its Effects on Ablation, NASA TR R-296, January 1969.
- (24) Swann, Robert T.; Pittman, Claud M.; and Smith, James C.: One-Dimensional Numerical Analysis of the Transient Response of Thermal Protection Systems. NASA TN D-2976, September 1965.
- (25) Swann, Robert T.: Approximate Analysis of the Performance of Char-Forming Ablators. NASA TR R-195, June 1964.
- (26) Kendall, R. M.; Rindal, R. A.; and Bartlett, E. P.: Thermochemical Ablation. AIAA Paper No. 65-642. AIAA Thermophysics Specialist Conference, Monterey, Calif., September 13-15, 1965.
- (27) Hillberg, Lauri H.: The Convective Heating and Ablation Program (CHAP). The Boeing Co., Seattle, Washington. Code Ident. No. 81205, No. D2-36402-1, April 1966.
- (28) Kratsch, K. M.; Hearne, L. F.; and McChesney, H. R.: Theory for the Thermophysical Performance of Charring Organic Heat Shield Composites. Report No. 803099, Lockheed Missiles and Space Co., October 18, 1963.
- (29) Wilson, R. G.: Thermophysical Properties of Six Charring Ablators From 140° K to 700° K and Two Chars From 800 to 3000° K. NASA TN D-2991, October 1965.

- (30) Brazel, J. P.; Tanzilli, R. A.; and Begany, A. R.: Determination of the Thermal Performance of Char Under Heating Conditions Simulating Atmospheric Entry. AIAA Paper No. 65-640. AIAA Thermophysics Specialist Conference, Monterey, California, September 13-15, 1965.
- (31) McLain, Allen G.; Sutton, Kenneth; and Walberg, Gerald D.: Experimental and Theoretical Investigation of the Ablative Performance of Five Phenolic-Nylon-Based Materials. NASA TN D-4374, 1968.
- (32) Sykes, George F.; and Nelson, James B.: Thermoanalysis of Ablation Materials. Presented at the Am. Institute of Chemical Engineers Meeting, Houston, Texas, February 19-23, 1967.
- (33) Lundell, J. H.; Wakefield, R. M.; and Jones, W. J.: Hypervelocity Heat Protection. AIAA Journal, Vol. 3, pp. 2087-2096, 1965.
- (34) Pike, R. W.; April, G. C.; and Del Valle, E. G.: Nonequilibrium Flow and the Kinetics of Chemical Reactions in the Char Zone, Reacting Fluids Laboratory, Louisiana State University, NASA CR-66455, July 15, 1967.
- (35) Lewis, J. C.; Floyd, I. J.; and Cowland, F. C.: A Comparative Study of the Gaseous Oxidation of Vitreous Carbon and Various Graphites at 1500-3000° F. Paper presented at the Eighth Biennial Conference on Carbon, Buffalo, N.Y., June 1967.
- (36) Strickland-Constable, R. F.: Theory of the Reaction of Graphite With Oxygen in the Temperature Range 1000-2400° C. Paper presented at the Second Conference on Industrial Carbon and Graphite, London, April 1965.
- (37) Dolton, T. A.; Maurer, R. E.; and Goldstein, H. E.: Thermodynamic Performance of Carbon in Hyperthermal Environments. AIAA Paper No. 68-754, Presented at AIAA Third Thermophysics Conference, Los Angeles, California, June 24-26, 1968.
- (38) Kratsch, K. M.; Martinez, M. R.; Clayton, F. I.; Greene, R. B.; and Wuerer, J. E.: Graphite Ablation in High-Pressure Environments. AIAA Paper No. 68-1153, Presented at the AIAA Entry Vehicle Systems and Technology Meeting, Williamsburg, Va., December 3-5, 1968.
- (39) Scala, S. M.; and Gilbert, L. M.: Thermal Degradation of a Char-Forming Plastic During Hypersonic Flight. ARS Journal 32, Vol. 32, pp. 917-924, 1962.

- (40) Mathieu, R. D.: Mechanical Spallation of Charring Ablators in Hyperthermal Environments. AIAA Journal, Vol. 2, No. 9, September 1964.
- (41) Maahs, H. G.; and Schryer, D. R.: Particle Removal in the Ablation of Artificial Graphite. AIAA Journal, Vol. 7, No. 11, November 1969, pp. 2178-2179.
- (42) Sutton, Kenneth: Results of an Experimental Ablative Study of a Carbon-Phenolic Material. Proposed NASA TN (L-6455).
- (43) Wilson, R. G.; and Spitzer, C. R.: Visible and Near-Infrared Emittance of Ablation Chars and Carbon. AIAA Journal, Vol. 6, No. 4, April 1968.
- (44) Walberg, Gerald D.: An Analytical Study of Diffusion Controlled Char Oxidation and its Effect on the Steady State Ablation of Hydrocarbon Plastics. NASA TR R-242, 1966.
- (45) Wakefield, R. M.; Lundell, J. H.; and Dickey, R. R.: Effects of Pyrolysis-Gas Chemical Reactions on Surface Recession of Charring Ablators, AIAA Paper 68-302, Ninth AIAA/ASME Structures and Materials Conference, Palm Springs, California, April 1, 1968. Also J. Spacecraft, Vol. 6, February 1969, pp. 122-128.
- (46) McLain, Allen G.: Investigation of the Char Formation and Surface Recession Characteristics of a Silicone Resin-Based Composite Ablation Material. Proposed NASA TN (L-6359).
- (47) Vojvodich, Nick S.: Hypervelocity Heat Protection - A Review of Laboratory Experiments. J. Macromol. SCI. CHEM., A3(3), pp. 367-394, May 1969.
- (48) Hoshizaki, H.; and Lasher, L. E.: Convective and Radiative Heat Transfer to an Ablating Body. AIAA Paper No. 67-327, Presented at the AIAA Thermophysics Specialist Conference, New Orleans, Louisiana, April 17-20, 1967.
- (49) Coleman, W. D.; Hearne, L. F.; Lefferdo, J. M.; and Vojvodich, N. S.: A Study of the Effects of Environmental and Ablator Performance Uncertainties on Heat Shielding Requirements for Blunt and Slender Hyperbolic-Entry Vehicles. AIAA Paper No. 68-154. AIAA Sixth Aerospace Sciences Meeting, New York, N.Y., January 22-24, 1968.

- (50) Smith, G. L.; Suttles, J. T.; Sullivan, E. M.; and Graves, R. A., Jr.: Viscous Radiating Flow Field on an Ablating Blunt Body. AIAA Paper No. 70-218, AIAA Eighth Aerospace Sciences Meeting, New York, N.Y., January 19-21, 1970.
- (51) Suttles, John T.: A Method of Integral Relations Solution for Radiating Nonadiabatic Inviscid Flow Over a Blunt Body. NASA TN D-5480. Also, M.S. Thesis, Aerospace Engineering, Virginia Polytechnic Institute, Blacksburg, Virginia, March 1968.
- (52) Garrett, L. B.; Suttles, J. T.; and Perkins, J. N.: A Modified Method of Integral Relations Approach to the Blunt-Body Equilibrium Air Flow Field, Including Comparisons With Inverse Solutions, NASA TN D-5434, September 1969.
- (53) Vaughan, Otha H., Jr.: Model Atmospheres of Mercury, J. Spacecraft, Vol. 6, No. 10, pp. 1171-1175, October 1969.
- (54) Michaux, C. M.: Handbook of the Physical Properties of the Planet Mars. NASA SP-3030, 1967.
- (55) NASA Space Vehicle Design Criteria (Environment): Models of Venus Atmosphere (1968), NASA SP-8011, December 1968.
- (56) Sodek, Bernard A., Jr.: Jovian Occultation Experiment. J. Spacecraft, Vol. 5, No. 4, pp. 461-463, April 1968.
- (57) Michaux, C. M.: Handbook of the Physical Properties of the Planet Jupiter. NASA SP-3031, 1967.
- (58) Pritchard, E. B.; and Harrison, E. F.: Multipurpose Entry Vehicle Requirements for Unmanned Landings on Bodies Having Tenuous Atmospheres. J. Spacecraft, Vol. 5, No. 4, April 1968.
- (59) Roberts, Leonard: Entry into Planetary Atmospheres. Astronautics and Aeronautics, October 1964.
- (60) Strauss, Eric L.; and Sparhawk, H. E.: Ablative Heat Shields for Planetary Entry Vehicles, AAS Paper 68-8-5, Space Projections From the Rocky Mountain Region, Brown Palace Hotel, Denver, Colorado, July 15-16, 1968.
- (61) Hiltz, A. A.; Florence, D. E.; and Lowe, D. L.: Selection, Development, and Characterization of a Thermal Protection System for a Mars Entry Vehicle. AIAA Paper No. 68-304. AIAA/ASME Ninth Structures, Structural Dynamics and Materials Conference, Palm Springs, Calif., April 1-3, 1968.

- (62) Fixler, S. Z.; and Layton, D. M.: Thermostructural and Material Considerations for Mars Lander Heat Shields. In: Aviation and Space: Progress and Prospects; Proceedings of the ASME Annual Aviation and Space Conference, Beverly Hills, California, June 16-19, 1968.
- (63) Nagler, Robert G.: The Mars Transit and Entry Environment: A New Problem for Heat Shields. JPL TR 32-1145. Reprinted from Proceedings of Institute of Environmental Sciences, 13th Annual Technical Meeting, Washington D.C., April 10-12, 1967, Vol. 2, pp. 443-455.
- (64) Nagler, Robert G.: Ground Simulation of a Mars-Entry-Capsule Aeroshell Environmental History. JPL Tech. Report 32-1466, February 15, 1970.
- (65) Meltzer, J.; Rossoff, J.; and Slaughter, J. I.: Structure and Materials Aspects of the Prime Flight Test Vehicle. AIAA/ASME Seventh Structures and Materials Conference, April 18-20, 1966.
- (66) Strauss, Eric L.: Response of Superlight Ablators to Various Heat Pulses. AIAA Paper No. 68-301, AIAA/ASME Ninth Structures, Structural Dynamics and Materials Conference, Palm Springs, California, April 1-3, 1968.
- (67) AVCO Corp. Report: Comparative Studies of Conceptual Design and Qualification Procedures for a Mars Probe/Lander. Final Report, Vol. V. Subsystem and Technical Analyses, May 11, 1966.
- (68) Katz, G. D.; and McMullen, J. C.: Entry Vehicles for Unmanned Planetary Exploration. AIAA Entry Technology Conference, Williamsburg and Hampton, Virginia, October 12-14, 1964.
- (69) Norman, Herbert G.; and Hart, Paul M.: Mission Influence on the Aerothermodynamic Environment for a Venus Entry Vehicle, AAS Paper 68-4-6, Space Projections from the Rocky Mountain Region, Brown Palace Hotel, Denver, Colorado, July 15-16, 1968.
- (70) Zoby, Ernest V.: Empirical Stagnation-Point Heat-Transfer Relation in Several Gas Mixtures at High Enthalpy Levels. NASA TN D-4799, October 1968.
- (71) Marvin, Joseph G.; and Deiwert, George S.: Convective Heat Transfer in Planetary Gases. NASA TR R-224, July 1965.

- (72) Nerem, Robert M.; Morgan, C. Joe; and Graber, Bruce C.: Hypervelocity Stagnation Point Heat Transfer in a Carbon Dioxide Atmosphere. AIAA Journal, Vol. 1, No. 9, pp. 2173-2175, September 1963.
- (73) Collins, D. J.; and Horton, T. E.: Experimental Convective Heat-Transfer Measurements. AIAA Journal, Vol. 2, No. 11, pp. 2046-2047, July 1964.
- (74) Gruszczynski, J. S.; Warren, W. R., Jr.; and Diaconis, N. S.: Laboratory Simulation of Hypervelocity Heat Transfer Problem During Planetary Entry. Space Sciences Laboratory, General Electric Co. Report R64SD73. Paper presented at the 15th International Astronautical Congress, September 7-12, 1964, Warsaw, Poland.
- (75) James, Carlton S.: Experimental Study of Radiative Transport From Hot Gases Simulating in Composition the Atmospheres of Mars and Venus. AIAA Journal, Vol. 2, No. 3, March 1964.
- (76) Menard, Wesley A.; and Thomas, George M.: Experimental and Theoretical Study of Molecular, Continuum, and Line Radiation From Planetary Atmospheres. AIAA Journal, Vol. 6, No. 4, April 1968.
- (77) Gruszczynski, J. S.; and Thomas, K. M.: Equilibrium and Nonequilibrium Radiation in Simulated Planetary Atmospheres. AIAA Paper No. 66-183, AIAA Plasmadynamics Conference, Monterey, California, March 2-4, 1966.
- (78) Deacon, Howard Jr.; and Rumpel, William: Radiation Heating Characteristics of Venus Entry. AAS Paper 68-8-6, Space Projections From the Rocky Mountain Region, Brown Palace Hotel, Denver, Colorado, July 15-16, 1968.
- (79) Nicolet, William E.: Advanced Methods for Calculating Radiation Transport in Ablation-Product Contaminated Boundary Layers. Aerotherm Corp. Final Report No. 69-61, December 27, 1969.
- (80) Spiegel, Joseph M.; Wolf, Fred; and Zeh, Dale W.: Simulation of Venus Atmospheric Entry by Earth Reentry. AIAA Paper No. 68-1148, AIAA Entry Vehicle Systems and Technology Meeting, Williamsburg, Virginia, December 3-5, 1968.
- (81) McKenzie, Robert L.; and Arnold, James O.: Experimental and Theoretical Investigations of the Chemical Kinetics and Nonequilibrium CN Radiation Behind Shock Waves in CO₂-N₂ Mixtures. AIAA Paper No. 67-322, AIAA Thermophysics Specialist Conference, New Orleans, Louisiana, April 17-20, 1967.

- (82) Jaworski, W.; and Nagler, R. G.: A Parametric Analysis of Venus Entry Heat-Shield Requirements, JPL Technical Report 32-1468, April 15, 1970.
- (83) Tauber, Michael E.: Atmospheric Entry into Jupiter. J. Spacecraft, Vol. 6, No. 10, October 1969.
- (84) Spinrad, H.; and Trafton, L. M.: High Dispersion Spectra of the Outer Planets. I. Jupiter in the Visual and Red. Icarus, Vol. 2, pp. 19-28, 1963.
- (85) Beckman, J. E.: The Pressure at the Cloud Top and the Abundance of Hydrogen in the Atmosphere of Jupiter. Astrophysical Journal, Vol. 149, No. 2, 1967.
- (86) Scala, S. M.; and Gilbert, L. M.: Theory of Hypersonic Laminar Stagnation Region Heat Transfer in Dissociating Gases. R63SD40, Gen. Elec. Space Sci. Lab., April 1963.
- (87) Pope, Ronald B.: Stagnation-Point Heat Transfer in Arc-Heated Helium and Argon. AIAA Journal, Vol. 7, No. 6, pp. 1159-1161, June 1969.
- (88) Stickford, G. H., Jr.; and Menard, W. A.: Bow Shock Composition and Radiation Intensity Calculations for a Ballistic Entry Into the Jovian Atmosphere. AIAA Paper No. 68-787, AIAA Third Thermophysics Conference, Los Angeles, California, June 24-26, 1968.
- (89) Nagler, Robert G.: A Systematic Review of Heat-Shield Technology for Extraterrestrial Atmospheric Entry. JPL Tech. Report 32-1436, March 15, 1970.
- (90) Heister, N. K.; and Clark, C. F.: Feasibility of Standard Evaluation Procedures for Ablating Materials, NASA CR-379, 1966.
- (91) Beuf, F. G.; Katz, G. D.; and Kern, R. J.: Earth Flight Test of Mars Entry Vehicles. J. Spacecraft, Vol. 3, No. 4, April 1966.
- (92) Kennet, Haim; and Taylor, Roy A.: Earth Reentry Simulation of Planetary Entry Environment. J. Spacecraft, Vol. 3, No. 4, April 1966.
- (93) Allen, H. Julian; and Eggers, A. J., Jr.: A Study of the Motion and Aerodynamic Heating of Missiles Entering the Earth's Atmosphere at High Supersonic Speeds, NACA TN 4047, 1957.

TABLE 1-Planetary atmospheres

	Mercury	Mars	Earth	Venus	Jupiter
Surface Pressure, atm	1×10^{-3}	5×10^{-3}	1	167	1×10^5
Surface Temperature, °K	200	130	288	770	2000
Tropopause Altitude, km	11	19	11	55	20 (above cloud top)
Stratosphere Temperature, °K	122	100	217	220	86
Density Scale Height, km ^(a)	6	5	7.73	6	18
Molecular Weight	40	44	29	42-44	3.4
Composition	Ar, CO ₂	CO ₂	O ₂ , N ₂	CO ₂ , N ₂	He, H ₂
Entry Velocities, km/sec	3-4 ^(b)	4-8 ^(b)	8-20 ^(c)	7-15 ^(b)	40-60 ^(b)

(a) Stratosphere

(b) Orbital to escape

(c) Orbital to planetary return

TABLE 2-Maximum heating rates, integrated heat loads, pressures, and shears for sphere-cone vehicles entering the Martian atmosphere

Trajectory			Stagnation Point					Cone Edge				Ref.			
Entry Mode	$\frac{M}{C_D A}$	$-\gamma_e$	V_e	\dot{q}_c	\dot{q}_R	Q_c	Q_R	P	\dot{q}_c	\dot{q}_R	τ	P			
	$\frac{g}{cm^2}$	deg	$\frac{km}{sec}$	$\frac{W}{cm^2}$	$\frac{W}{cm^2}$	$\frac{J}{cm^2}$	$\frac{J}{cm^2}$	Atm	$\frac{W}{cm^2}$	$\frac{W}{cm^2}$	$\frac{N}{2} \times 10^{-2}$	Atm			
D	5.5	21	5.8	68	5.5	3270	329	0.16	31	2.1	1480	132	< 0.5	60	
D	5.5	21	5.8	125	6.0	2560	176	.41	57	2.5	1160	70	< .5	60	
O	4.7	15.7	4.6	26	N	2350	N	.05	12	N	1060	N	< .5	60	
O	-	10.9	4.0	7.2	N	-	N	.03	2.5	N	-	N	-	0.02	61
O	-	14.1	4.6	13	N	-	N	.04	4.1	N	-	N	-	.03	61
O	-	20	4.6	27	N	-	N	.22	9.1	N	-	N	-	.17	61
O	-	14.1	4.6	17	N	-	N	.07	5.7	-	-	-	-	.05	61
O	3.1	15	4.6	18	N	-	N	.01	-	-	-	-	-	-	62
O	3.1	15	4.6	34	N	-	N	.03	-	-	-	-	-	-	62
MSSR	31.0	21	10.7	785	510	-	-	.32	-	-	-	-	-	-	62
D	3.1	90	7.0	176	18	1790	77	.39	-	-	-	-	-	-	63
D	3.1	38	7.0	136	9.1	2380	63	.22	34	43	-	-	-	-	63
D	3.1	20	7.0	91	2.3	3820	47	.10	23	43	-	-	-	-	63

D Direct entry
O Out of orbit entry
MSSR Mars surface sample return mission
N Negligible
- Data not available

Table 3 -Maximum heating rates, integrated heat loads, pressures, and shears for sphere-cone vehicles entering the atmosphere of Venus

Trajectory			Stagnation Point					Cone Edge					Ref.	
Entry Mode	$\frac{M}{C_D A}$	$-\gamma_e$	V_e	\dot{q}_c	\dot{q}_R	Q_c	Q_R	P	\dot{q}_c	\dot{q}_R	Q_c	Q_R	τ	Ref.
	$\frac{g}{cm^2}$	deg	$\frac{km}{sec}$	$\frac{W}{cm^2}$	$\frac{W}{cm^2}$	$\frac{J}{cm^2}$	$\frac{J}{cm^2}$	Atm	$\frac{W}{cm^2}$	$\frac{W}{cm^2}$	$\frac{J}{cm^2}$	$\frac{J}{cm^2}$	$\frac{N}{m^2} \times 10^{-2}$	
VMF	9.4	45	13.4	4500	15450	-	-	7	-	-	-	-	-	89
D	9.4	45	12.2	2800	4550	-	-	6	-	-	-	-	-	89
O	4.7	45	11.0	1480	398	-	-	3	-	-	-	-	-	89
O	9.4	45	11.1	2600	590	8180	1135	-	1820	1080	4100	2260	-	80
VMF	4.7	40	13.4	2700	4200	7500	6600	1.8	-	-	-	-	33.0	69
D	4.7	40	11.6	1650	740	5400	1700	1.3	1870	738	3980	1250	24.0	69
O	4.7	40	9.8	910	284	3520	910	1	-	-	-	-	19.1	69
D	5.4	35	11.6	1640	727	-	-	3	1820	660	-	-	24.0	60
O	5.4	30	9.8	885	258	-	-	1	955	193	-	-	16.3	60

Table 4 —Model atmospheres of Jupiter
(compositions are in weight percent)

Parameter	Kuiper Model (A)	Kuiper Model (B)	Opik Model (O)	Spinrad and Trafton Model (K)	Sample Model (S)
H ₂ %	78.25	38.78	2.3	60	44.83
He %	21.65	60.94	97.2	36	53.95
Ne %	0.07	—	0.39	3	0.22
CH ₄ %	0.02	0.28	0.06	0.67	0.26
NH ₃ %	—	—	—	0.33	0.08
Ar %	0.01	—	0.04	—	0.01
T* °K	165	168	156	150	160
P* atm	24	2	11	2.8	5.5
H* km	21.45	16.41	12.27	14.05	16.12

*At top of cloud layer (from ref. 56)

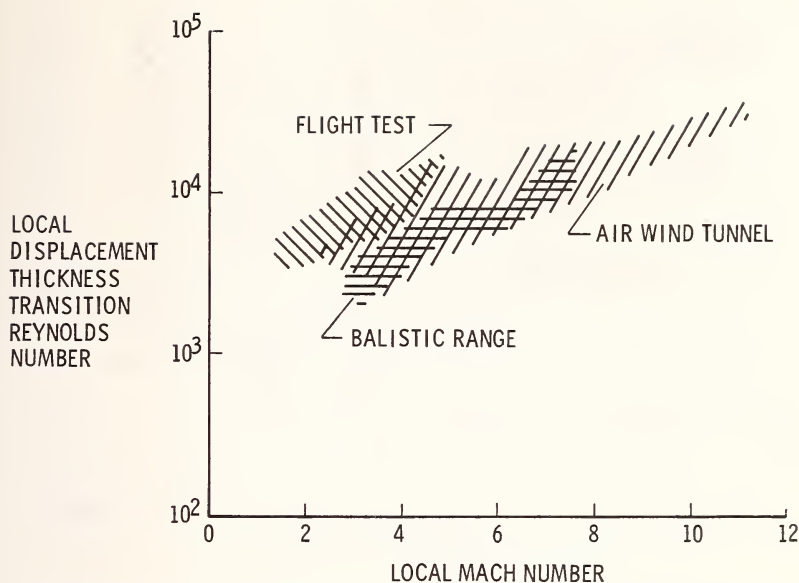


Figure 1.- Survey of transition data for nonablating sharp cones (from Ref. 11).

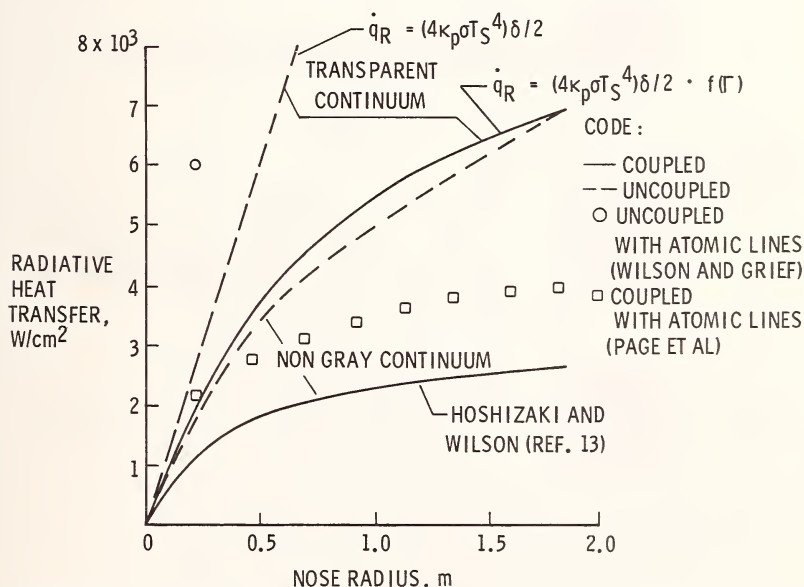


Figure 2.- Results for stagnation-point radiative heat transfer reflecting various stages of the state-of-the-art; $V_\infty = 15.24$ km/sec altitude = 61 km (from Ref. 12).

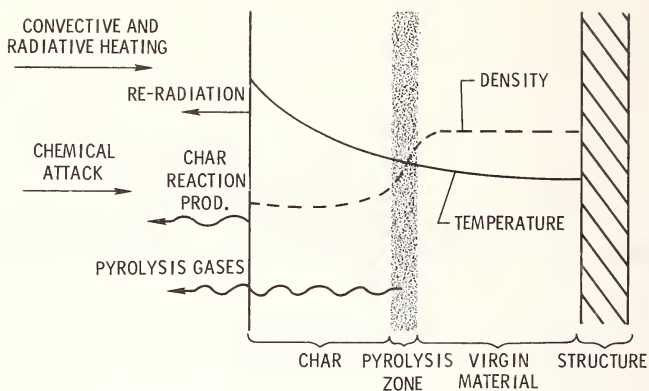


Figure 3.- Ablative mechanisms.

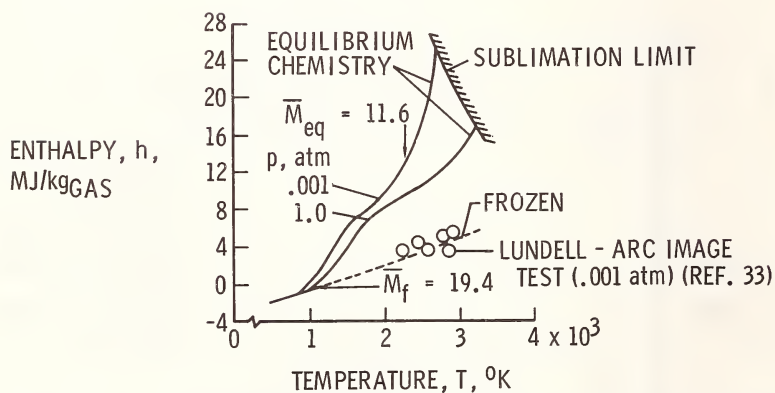


Figure 4.- Pyrolysis gas enthalpy as a function of chemical state (from Ref. 47).

CARBON-PHENOLIC

$$1.14 < \dot{q}_c < 13.6 \text{ MW/m}^2$$

$$1.86 < h_s < 23.2 \text{ MJ/kg}$$

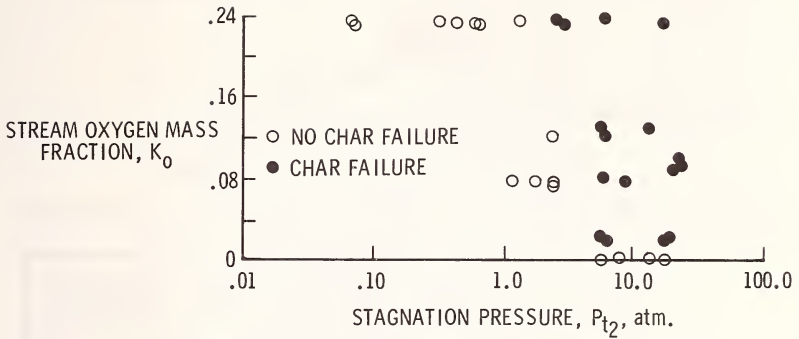


Figure 5.- Mechanical char failure for a carbon phenolic ablator (from Ref. 42).

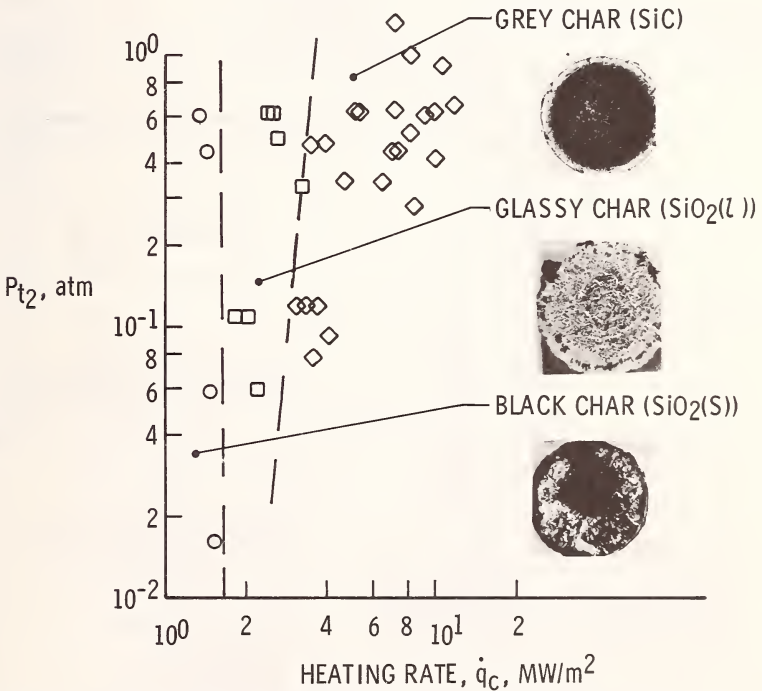


Figure 6.- Char surfaces produced by silicon dominated ablator (from Ref. 46).

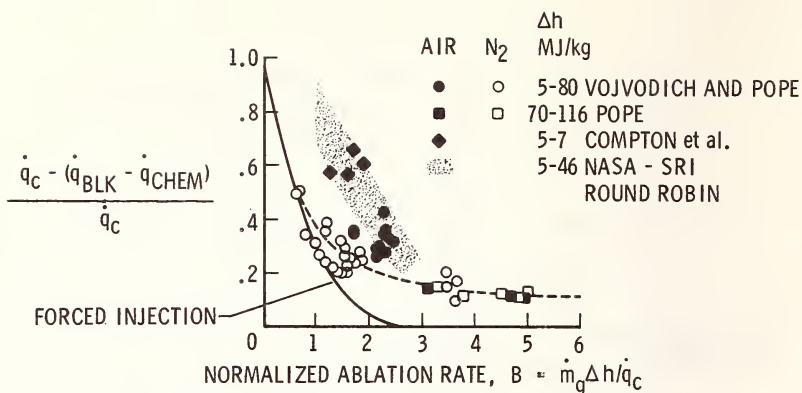


Figure 7.- Reduction of convective heating by pyrolysis gas injection (from Ref. 47).

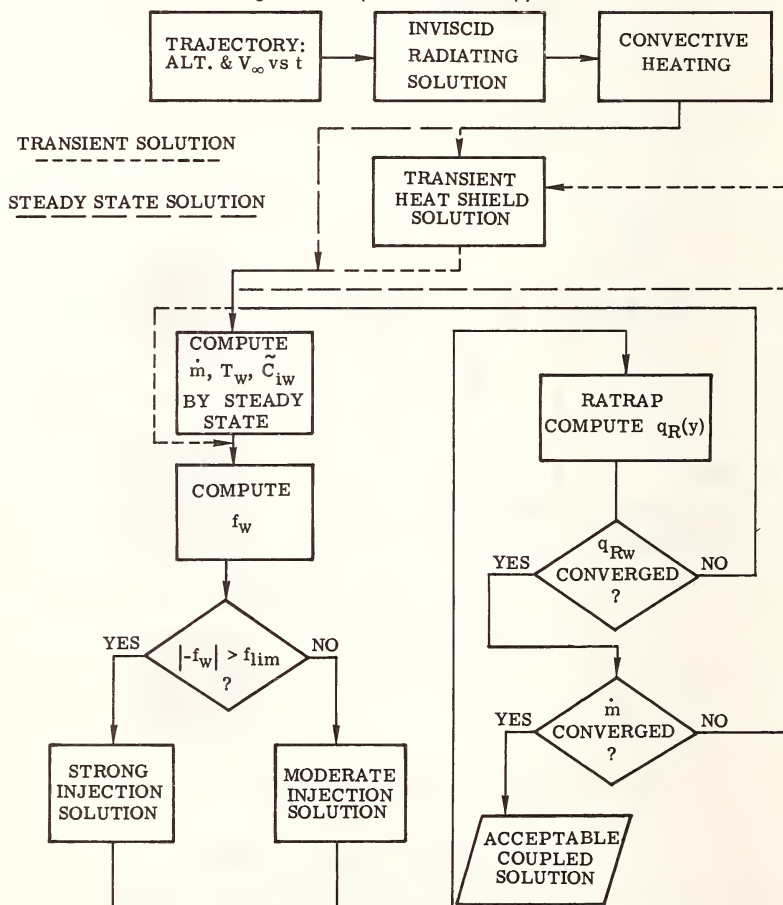


Figure 8.- Logic for coupled analysis (from Ref. 50).

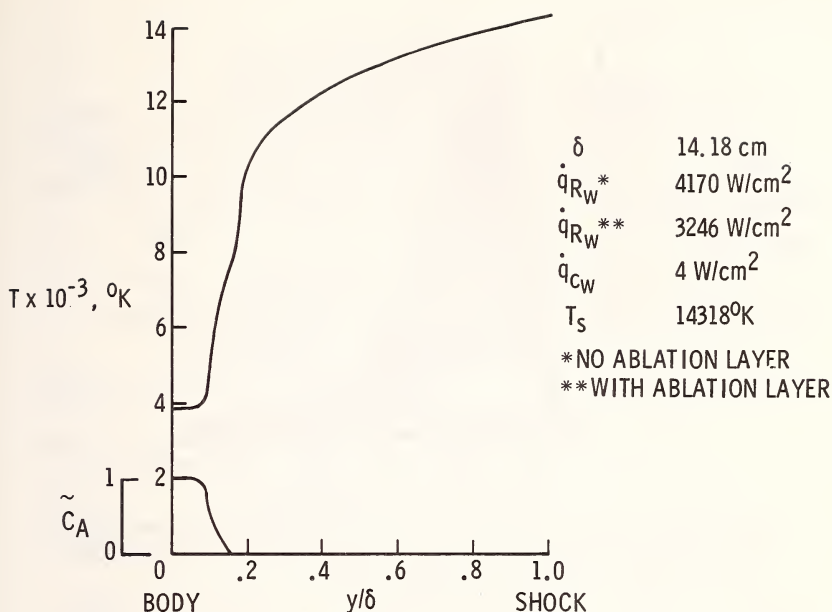


Figure 9.- Temperature and ablation products profile. Stagnation streamline of 304.8 cm radius sphere, $V_\infty = 15.24$ km/sec, 61 km altitude, carbon phenolic injection, $\frac{\rho_w V_w}{\rho_\infty V_\infty} = 0.2$, $T_w = 3600^\circ$ K (from Ref. 50).

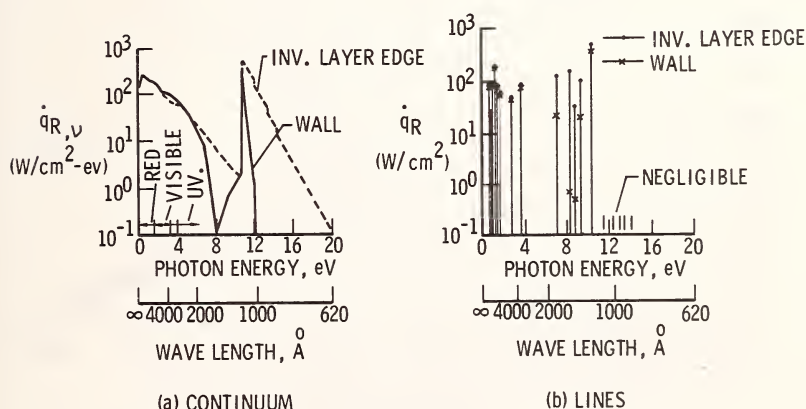


Figure 10.- Spectral distribution of radiation heat flux due to line and continuum processes (from Ref. 50).

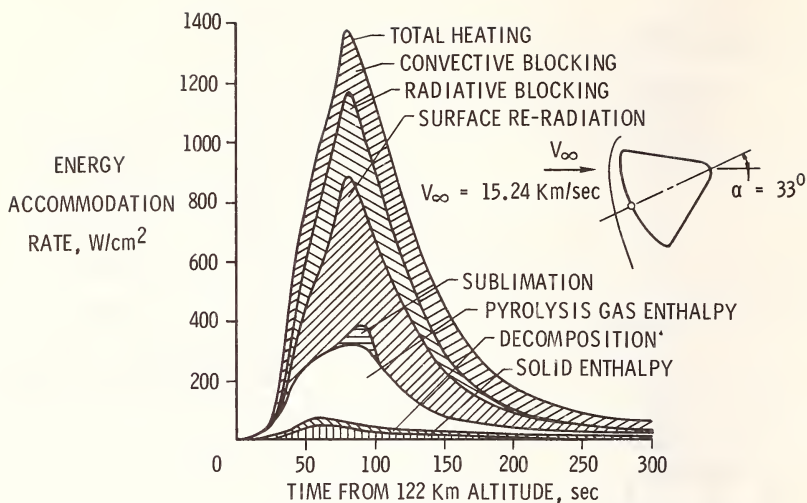


Figure 11.- Ablative energy accommodation mechanism for phenolic-nylon ablator on Apollo-like planetary-return Earth entry vehicle (from Ref. 49).

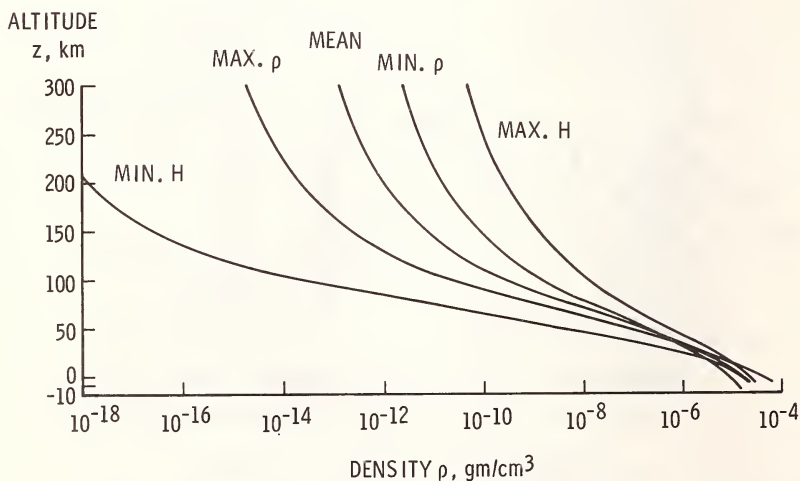


Figure 12.- Density profiles for five Martian atmospheric models.

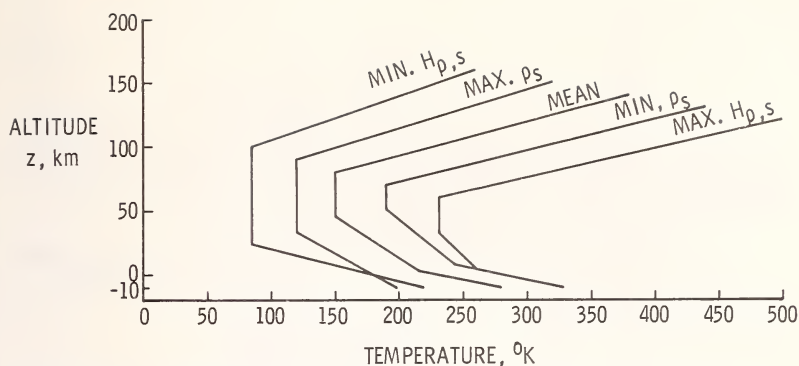
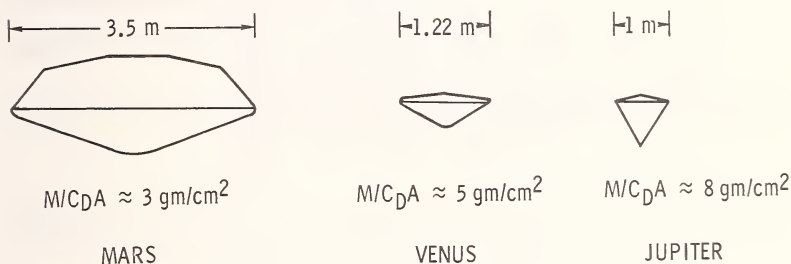


Figure 13.- Temperature profiles for five Martian atmospheric models.



(PROJECT VIKING)

Figure 14.- Configurations for typical planetary entry vehicles.

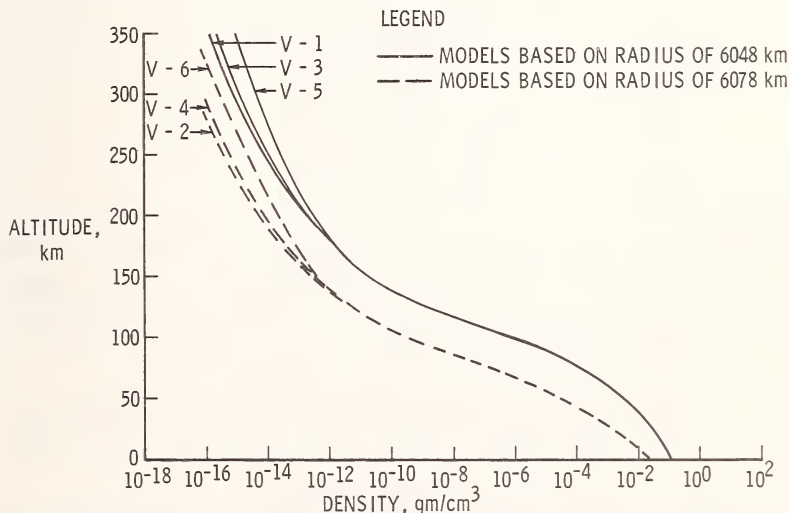


Figure 15.- Density versus altitude for models of Venus atmosphere (from Ref. 55).

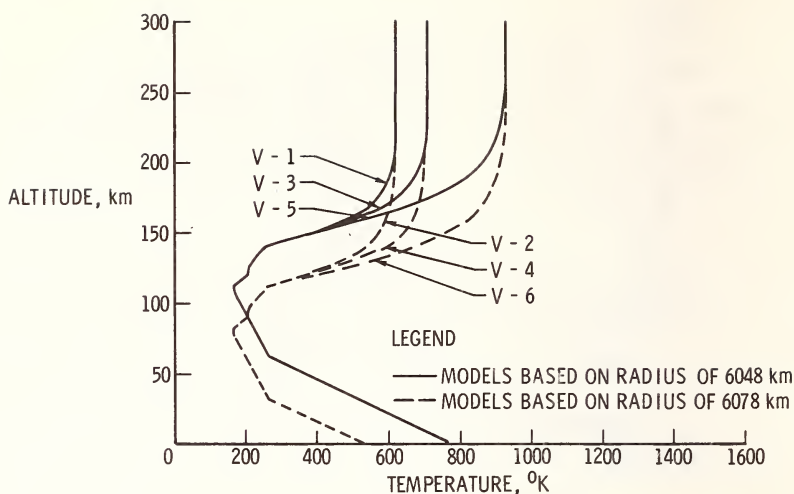


Figure 16.- Temperature versus altitude for models of Venus atmosphere (from Ref. 55).

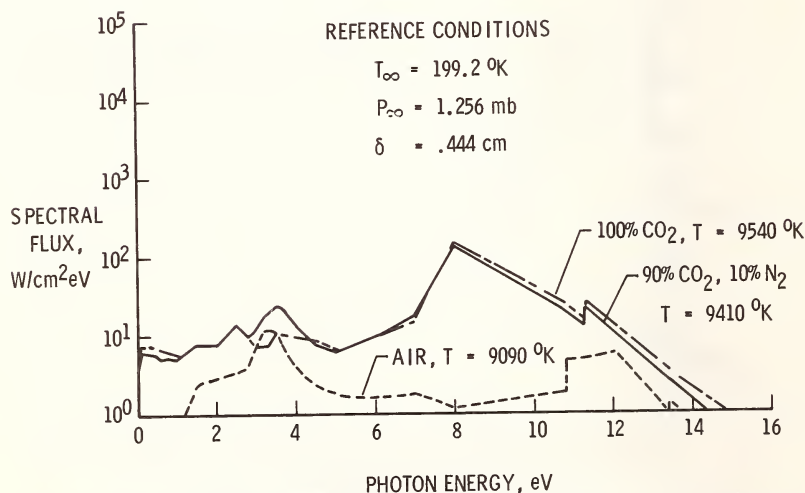


Figure 17.- Comparison of spectral flux from air and proposed Venusian atmospheres.

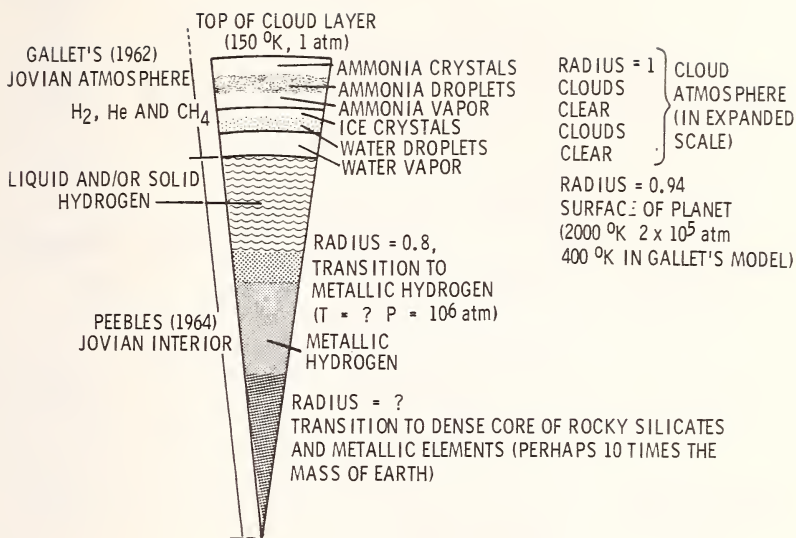


Figure 18.- Jovian cloud layers proposed by Gallet overlying Jovian interior by Peebles (from Ref. 57).

$$V_e = 50 \text{ km/sec}$$

$$R_{e_l} = 5 \times 10^6 \quad r_{N_i} = 1 \text{ cm}$$

$$\epsilon_c = 30^\circ$$

$$r_b = 1 \text{ m}$$

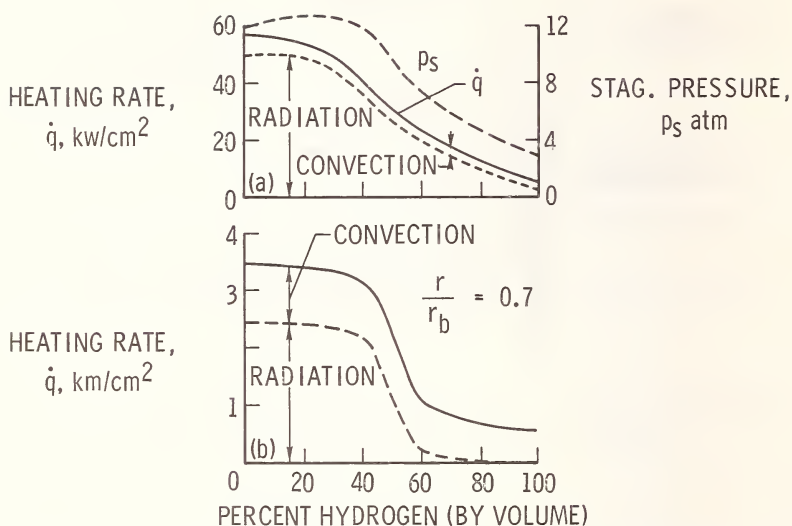


Figure 19.- Maximum heating rates and stagnation pressures for conical body during shallow ballistic entry; (a) stagnation point (ablating nose), (b) flank (at 0.7 of length point). (From Ref. 83.)

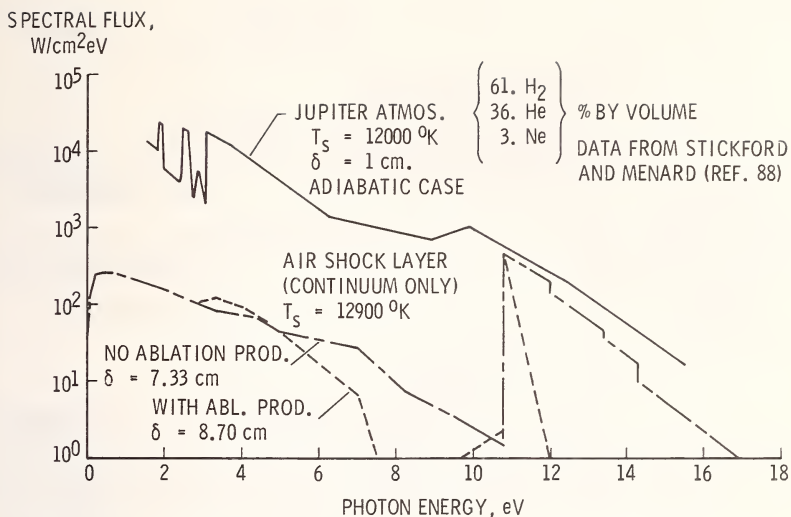


Figure 20.- Comparison of typical shock layer spectra for Jovian and Earth entries.

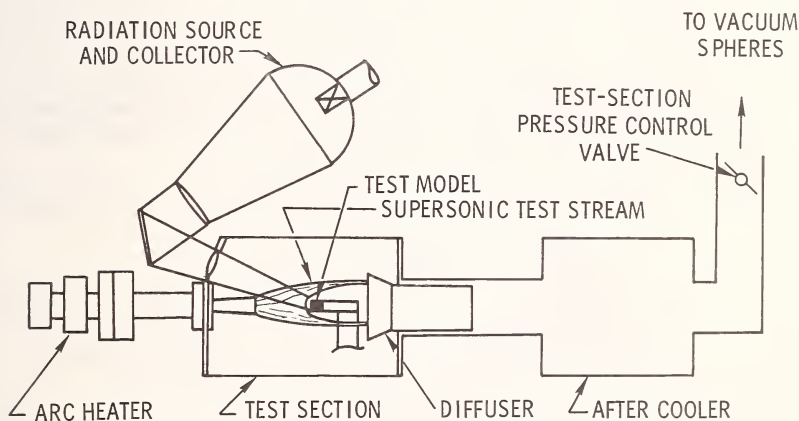


Figure 21.- Schematic of ground test facility.

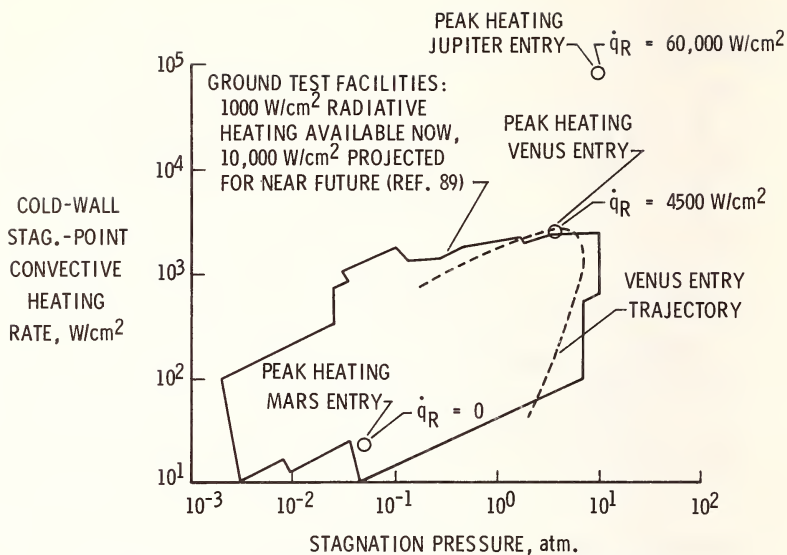


Figure 22.- Ground facility test capabilities.

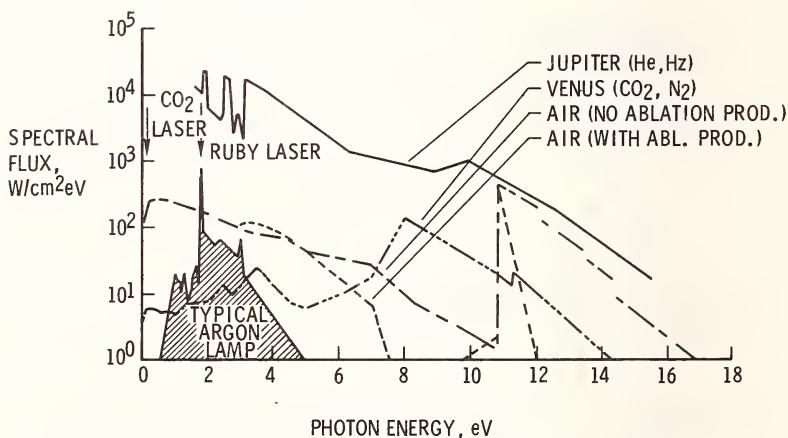


Figure 23.- Comparison of typical shock-layer spectra for various planetary atmospheres with spectra for ground test radiation sources.

ABLATION PHENOMENA IN SUPERSONIC LAMINAR AND
TURBULENT FLOWS

E. M. Winkler,¹ M. T. Madden,² R. L. Humphrey,²
and J. A. Koenig³

REFERENCE: Winkler, E. M., Madden, M. T.,
Humphrey, R. L., and Koenig, J. A., "Ablation
Phenomena in Supersonic Laminar and Turbulent Flows,"
ASTM/IES/AIAA Space Simulation Conference, 14-16
September 1970

ABSTRACT: Arc tunnel experiments using pipe spec-
imens of TFE-7 examine the ablation of Teflon under
a supersonic laminar and turbulent boundary layer.
Test conditions include Mach numbers of 2.3 and 3.0,
supply pressures of 2×10^6 N/m² to 3×10^6 N/m² and
supply temperatures of 2200°K to 5000°K. Experi-
mental results are compared with computer predictions.
In two laminar boundary-layer tests, parallel stri-
ations appear; in all turbulent boundary-layer tests,
criss-cross striations appear.

KEY WORDS: ablation, Teflon, ablation-induced
transition, cross-hatched striations

NOMENCLATURE

A = cross-sectional area of node
A₀ = original cross-sectional area of node
B = factor in density law

¹Chief, High-Temperature Aerodynamics Group,
Aerophysics Division, Naval Ordnance Laboratory (NOL)

²Aerospace Engineers, NOL

³Aerospace Engineering Technician, NOL

E/R	= activation energy divided by gas constant
f	= stream function
h	= local enthalpy per unit mass
H_T	= total enthalpy per unit mass
K_k	= mass fraction of the k^{th} element
k	= thermal conductivity
M	= Mach number
m	= meter
\dot{m}_g	= mass removal rate of gas per unit area which enters the boundary layer without phase change
N	= Newton
P	= pressure
t	= time
T	= temperature
u	= velocity
X	= axial distance into duct
y	= coordinate normal to ablating surface with origin fixed relative to back wall
z	= depth, measured from receding surface
ρ	= density
ρ_o	= original density
ρ_r	= final density
Γ	= volume fraction of resin in plastic
η	= transformed normal coordinate in boundary layer
τ	= wall shear stress

SUPERSCRIPT

m = reaction order

SUBSCRIPTS

A,B,C = constituents

g = gas

k = element

o = supply or original

∞ = free stream

INTRODUCTION

The use of ablative materials and the prediction of their performance for protection of re-entering vehicles has not always been successful. Some of the difficulties encountered are traceable to the inability of ground test facilities to accurately duplicate critical flight regimes, and the lack of analytical techniques to analyze experimental data and to make accurate predictions about future performance. A series of successful experiments have been performed at the U. S. Naval Ordnance Laboratory (NOL) in which the ablative performance of Teflon was examined under supersonic laminar and turbulent boundary layers (1)⁴. It is the purpose of this paper, then, to present the results of these tests and show their successful comparison with analytical techniques. Results of skin-friction measurements are presented for the first time and compared with the predictions of a computational technique known as the BLIMP-CMA computer programs (2,3).

Teflon was chosen as the sample material for two reasons. First, and most pragmatically, Teflon is relatively simple to analyze. It is a homogeneous material not possessing the complexities of multi-component ablaters, thus reducing the number of ways in which errors of analysis may arise. Second, Teflon has practical applications as a desirable heat shield material (4). The desirable qualities include predictable ablative performance, high specific heat, and low thermal conductivity; detrimental to its performance are the relatively high density and low tensile and compressive properties.

⁴The numbers in parentheses refer to the list of references appended to this paper

EXPERIMENTAL PROCEDURE

The experimental set-up is depicted in Figure 1. Air is heated in the 3 Megawatt four-ring, three-phase, ac arc (5) and expanded through an axially symmetric, contoured nozzle. The emerging supersonic air is then passed through the TFE-7 Teflon duct, and exits into a diffuser and exhaust system. The nozzle as well as the Teflon ducts have been contoured to insure uniformity of flow by use of a non-ablating boundary-layer program developed at NOL (6,7). Pressure data indicate this initial contour maintained uniform flow throughout the duct for the duration of the test. The decision to pass air through the model, rather than over a shape such as a cone or a wedge, was based on the ease of instrumentation of the pipe specimen. Flight conditions encountered at certain stations on a re-entering, blunted vehicle can be duplicated by this arrangement. Air is expanded in a supersonic nozzle to a Mach number that equals the local Mach number at the vehicle's station to be studied; the supply conditions correspond to the stagnation point conditions on the body in flight. Even for high free-stream Mach numbers, the local Mach number may be quite low. Typically for a small blunted cone re-entering at $M = 15$, the local Mach number may be $M \approx 3$.

The test conditions called for supply pressures of 20 to 30 atmospheres, (i.e., 20 to $30 \times 10^5 \text{ N/m}^2$), Mach numbers of 2.3 to 3.0, and testing times of 3 to 13 seconds. The specimens numbered 1L through 6L were exposed to a boundary layer predicted to be laminar, while specimens 1T through 5T were exposed to a predicted turbulent boundary layer. The complete running conditions are summarized in Table I.

All of the ducts were fabricated from TFE-7 polytetrafluoroethylene. The inner diameter was one inch (25.4 mm), and the wall thickness was 0.75 inch (19 mm). A length of six inches (152 mm) was used for all the ducts; this length had been shown in prior tests to maintain uniform flow throughout the length of the duct. This removed the limitations of internal shock waves. The uniformity of flow was verified by pressure measurements. With the exception of one duct, all ducts were instrumented with static pressure taps located 0.25 (6.35 mm), 1.25 (31.75 mm), 2.375 (60.32 mm), 3.5 (88.9 mm) and 4.625 (117.47 mm) inches from the exit plane of the water-cooled nozzle. At the $X = 4.625$ inches location there were two taps 90 degrees (1.570 rad) apart to check for asymmetries of flow. In addition to these static pressure taps,

the Pitot pressure was recorded at the exit of each duct. For tests requiring a measurement of the Pitot pressure to verify that the running conditions were proper, a quick injection mechanism was used to insert an uncooled probe into the flow centerline. This mechanism is detailed in Reference 8. The uniformity of flow was confirmed by a centerline traverse conducted with a water-cooled probe; the performance of these probes was not completely satisfactory as their small size hampered effective cooling during exposure for the duration of the traverse.

For the ablation measurements the ducts were variously instrumented as indicated in Table I. The ducts were fitted to record surface and in-depth temperatures. Receding thermocouples were used to measure surface temperature while the in-depth readings used a thermocouple plug. This plug arrangement is shown in Figure 2. Wall shear stress was recorded in four tests. The balance used in these tests was developed at NOL and is described in Reference 9. This instrument, which records continually, uses a floating element head. In Figure 3, a Teflon element head is shown with the disassembled balance. Finally, mass loss due to ablation was determined by comparison of contour measurements of the ducts before and after each test.

ANALYTICAL PROCEDURES

The analysis of the data was performed with the assistance of two computer programs. The first of these, the Boundary Layer Integral Matrix Procedure, referred to by its acronym BLIMP, (2), allows the computation of steady-state ablation and laminar boundary-layer response. The second was the Charring Material Ablator program, known as CMA (3). Together with the CMA, iterative use of the BLIMP allows the transient response of the ablating laminar boundary layer and the in-depth response of the material to be specified.

In particular, the BLIMP, at least the version used at NOL in the present analysis, performs a nonsimilar solution of the laminar, ablating boundary layer. This program has great versatility, and the user is free to select from options in six categories:

1. Body shape: axisymmetric or planar
2. Upstream effects: nonsimilar or similar solution
3. Chemistry: homogeneous, equilibrium, or equilibrium-frozen with rate controlled reactions

4. Transport properties: equal or unequal diffusion or thermal diffusion coefficients

5. Surface boundary conditions: specify component mass fluxes of char, pyrolysis, and edge gas; or perform mass-energy balances

6. Edge conditions: specify total enthalpy, pressure, and pressure distribution, or assigned edge conditions including entropy layer

As used for the NOL tests, the BLIMP was set to solve the nonsimilar, multicomponent, equilibrium, laminar boundary layer through the axisymmetric nozzle and duct. Unequal diffusion and thermal diffusion coefficients were allowed. To account for the difference in surface material between the non-ablating nozzle and Teflon, a discontinuous stream-wise surface was selected with the nozzle wall temperature being held fixed while the duct wall temperature was solved for by an energy balance across the ablating teflon surface.

The BLIMP solves the conservation equations and boundary condition equations by an integral-matrix procedure using a generalized Newton-Raphson technique to reduce the errors to zero. The conservation equations are expressed in terms of the primary dependent variables, f , H_T and K_k and their derivatives with respect to η . These equations are integrated across nodes within the boundary layer and across these nodes the primary variables are represented by a cubic spline fit.

The CMA specifies the transient, in-depth, thermochemical response of the ablator. Basically the CMA solves the one-dimensional, unsteady, heat conduction problem by a method of finite differences. The basic assumptions are:

1. maximum of three components for the ablator - two resins and one reinforcement
2. density history follows an Arrhenius type law
3. pyrolysis gas is in equilibrium with the char
4. pyrolysis out-gassing is immediate
5. no coking
6. cross-sectional area can vary
7. one-dimensional conduction

Within the program, the user is free to select one of three options for boundary conditions:

(a) specified surface chemistry (i.e., species concentration), (b) specified surface temperature and recession rate and (c) specified radiation view factor and flux. For the present experiments option (b) was used with the Teflon composed of only one constituent, i.e., $\rho_B = \rho_C = 0$.

The fundamental equations are:

1. The energy balance

$$\frac{\partial}{\partial t} (\rho h A)_y = \frac{\partial}{\partial y} (k A \frac{\partial T}{\partial y})_t + \frac{\partial}{\partial y} (\dot{m}_g h_g)_t$$

2. density history

$$(\frac{\partial \rho}{\partial t})_y = - B e^{-E/RT} \rho_o (\frac{\rho - \rho_r}{\rho_o})^m$$

3. composition

$$\rho = \Gamma (\rho_A + \rho_B) + (1 - \Gamma) \rho_C$$

Allowing the ablating surface to recede, the material is considered as an array of arbitrary in-depth nodes and solved by a finite difference technique.

RESULTS OF LAMINAR BOUNDARY-LAYER TESTS

A total of six ducts were tested at $M = 3$, $p_o \approx 21$ atmospheres ($21.2 \times 10^5 \text{ N/m}^2$), and $T_o = 9000^\circ \text{R}$ (5000°K). These laminar boundary-layer tests lasted from 11 to 13 seconds. During this time the pressure distribution within the ducts was observed to be relatively steady with time and distance, thus discounting the possible existence of internal shocks. The data in Figure 4 show that there was a slight favorable pressure gradient within the duct due to over-compensation for boundary-layer growth.

The temperature measurements were partially successful. The surface thermocouples did not recede with the ablating surface, and as a consequence, they became exposed to the flow. Upon exposure the readings became erratic; the onset of this irregular behavior, however, allowed us to fix the onset of ablation to be at about four seconds from the start of the test. The in-depth thermocouple plugs performed well. There are some limitations imposed, though. The spacing between the thermocouples, 0.025 inch (0.63 mm) was too wide to accurately evaluate the wall heat transfer. Furthermore, there was perhaps a 10 percent inaccuracy in the data as a result of tolerance errors in the placement of the wires. The data are in Figure 5. The apparent discrepancy of trend between experimental data and theoretical predictions is due to the method of

computation which assumes an instantaneously hot wall rather than a transiently heated wall. During none of the tests was steady-state completely reached, as predicted by the CMA "heat storage" term:

$$\int \frac{1}{\rho C_p} \left(\frac{\partial T}{\partial t} \right)_z \frac{Adz}{A}$$

which never vanished and was still approximately six or seven percent of the surface heat transfer.

After the tests the gas-wetted surface of the ducts developed a glossy or waxy appearance; in some instances portions of the surface were slightly brown.

As shown in Figure 6 a pattern of parallel striations formed in two of the ducts tested under the predicted laminar conditions. The ducts were supposedly tested under the same conditions as those that did not exhibit the longitudinal grooving. It is held possible that these grooves are the result or manifestation of Görtler vortices resulting from a concavity in the duct (10) immediately behind the nozzle junction, or represent the existence of longitudinal vortices behind a rearward facing step at the junction of the nozzle and duct (11). This type of parallel grooving has also been observed on ablating Teflon cones (12).

The final diameter increase of two of the ducts is shown in Figures 7 and 8. In each case the resulting profile is compared with that predicted by the BLIMP-CMA procedures. The agreement between the resulting contour and predicted contour is quite good-up to a point. In all of the supposedly laminar boundary-layer tests, a pronounced increase in ablation was observed to begin at about 3.5 inches (88.9 mm) into the duct and reach a maximum at about 4.3 (109.2 mm) to 4.5 inches (114.3 mm). Supporting data indicate this increase in ablation was due to transition from laminar to turbulent flow. Predictions by the BLIMP program indicate a momentum-thickness Reynolds number, Re_θ , of 450 at this point; this value is high enough to support transition. The calculated boundary-layer profiles also support transition. As shown in Figure 9 the profiles at three locations within the duct exhibit, first, a normal behavior and then an increasing degree of inflection as the point of ablation increase is approached and then passed. This inflection in the velocity profile is indicative of instability that leads to transition. Transition may also be the

cause of the parallel striation pattern previously noted; this effect is described in References 13 and 14.

Finally, for the laminar tests, the wall shear response was recorded. In the first test the balance was placed in the region subject to transition. Figure 10 shows the balance response. The initial transient declines to a minimum at about 5.8 seconds, and then rises toward steady state at about 13 seconds. To further examine this response, two balances were installed in one duct; one balance was located as before, and the other was placed upstream in the laminar region. The balance in the transitional region repeated its behavior; the laminar zone balance responded as shown in Figure 11. The comparison with the BLIMP-CMA curve is not quantitatively as good as hoped, although the qualitative behavior is as predicted. The final value of measured wall shear is about 36 percent of the predicted cold wall shear.

TURBULENT BOUNDARY-LAYER TESTS

The ducts numbered 1T through 5T in Table I were tested under conditions designed to produce a turbulent boundary layer. The general conditions were $M = 2.3$, $P_0 = 21$ to 28 atmospheres (i.e., $21.2 - 28.3 \times 10^5 \text{ N/m}^2$) and $T_0 = 4300$ to 4600°R (2388 to 2555°K). The specific purpose of these tests was to examine the behavior of a cracked ablating surface (15). The results described here are those pertinent only to the surface response of the Teflon.

The ablative performance of the ducts was uniform. Mass loss increased from zero to a maximum loss about one inch down the duct and then decreased to about 70 percent of the maximum for the remainder of the duct. The ablation spike observed in the laminar tests was not observed in any of the turbulent tests. The mass loss was found to vary linearly with time as shown in Figure 12. The ablation was very pronounced and the pressure was observed to drop so that the Mach number increased from 2.3 to 2.6. Because of this change in running conditions, testing times for the turbulent tests were kept between 2.7 and 6.5 seconds. Wall shear was recorded in two tests, at 21 ($21.2 \times 10^5 \text{ N/m}^2$) and 28 atmospheres ($28.3 \times 10^5 \text{ N/m}^2$). The balance reading indicated a rapid approach to steady-state, within two seconds, reaching a value of 60 percent of the cold wall shear.

Finally, the now famous cross hatching was observed in all of the turbulent tests. The pattern started at the duct entrance and formed over the length of the duct. Typical of the patterns formed is that shown in Figure 13. The pressure taps were seen to cause a change in the pattern from a criss-cross to a more pronounced "V" form. The general pattern is that of a depressed groove with a raised, diamond-shaped, internal island. The pattern angle for these $M = 2.3$ tests was 32 degrees (0.55 rad); this is consistent with data reported by Laganelli and Nestler (12). There was no observed liquid layer run-off during these tests. At present no attempt at correlation among the various theories (16,17,18, 19,20,21) is being attempted.

SUMMARY

A successful series of ablation tests have been carried out on Teflon ducts exposed to supersonic laminar or turbulent boundary layers. Static pressure, surface and in-depth temperature, mass loss, and skin friction were recorded and compared with a sophisticated, theoretical approach. There was good agreement between the data and predictions. The wall shear response was measured under laminar, transitional, and turbulent ablating boundary layers.

In a series of turbulent tests, ablation rate was found to vary linearly with time, wall shear was reduced to 60 percent of the predicted cold wall value, and striations were observed. For the same test Mach number, the pattern angle was constant and compares well with previously measured values.

REFERENCES

- (1) Winkler, E. M., Madden, M. T., Humphrey, R. L., and Koenig, J. A., "Supersonic Ablation Studies with Teflon," NOLTR 69-125, U. S. Naval Ordnance Laboratory, White Oak, Md., Oct. 1969
- (2) Bartlett, E. P. and Kendall, R. M., "Nonsimilar Solution of the Multicomponent Laminar Boundary Layer," Aerotherm Report No. 66-7, Pt III, Aerotherm Corp., Palo Alto, Calif., Mar. 1967
- (3) Moyer, C. B. and Rindal, R. A., "Finite Difference Solution for the In-Depth Response of Charring Materials Considering Surface Chemical and Energy Balances," Aerotherm Report No. 66-7, Pt II, Aerotherm Corp., Palo Alto, Calif., Mar. 1967
- (4) Schmidt, D. L., "Ablation of Fluorocarbon Resins and Components," Technical Report AFML-TR-68-393, Air Force Materials Laboratory, Oct. 1969
- (5) Winkler, E. M., Humphrey, R. L. and Koenig, J. A., "The NOL Four-Ring, Three Phase, AC Arc Heater, Mark IV," NOLTR 70-12 (to be published), U. S. Naval Ordnance Laboratory, White Oak, Md.
- (6) Solomon, J. M., "Calculation of Laminar Boundary Layers in Equilibrium Dissociated Air by an Extension of the Cohen and Reshotko Method," NOLTR 61-143, U. S. Naval Ordnance Laboratory, White Oak, Md., Feb. 1962
- (7) Glowacki, W. J., "Fortran IV Program for Calculating the Turbulent Boundary Layer Growth for Contoured Axisymmetric Nozzles Using Air or Nitrogen," NOLTR to be published, U. S. Naval Ordnance Laboratory, White Oak, Md.
- (8) Aerodynamics Department Staff, "The NOL 3 Megawatt Arc Tunnel," NOLTR 66-80, U. S. Naval Ordnance Laboratory, White Oak, Md., Sept. 1966
- (9) Bruno, J., Yanta, W., and Risher, D., "Balance for Measuring Skin Friction in the Presence of Heat Transfer," NOLTR 69-56, U. S. Naval Ordnance Laboratory, White Oak, Md., June 1969
- (10) Görtler, M., "On the Three-Dimensional Instability of Laminar Boundary Layers on Concave Walls," NACA TM 1375, June 1954, translation of original 1940 paper
- (11) Ginoux, J. J., "The Existence of Three Dimensional Perturbations in the Reattachment of a Two Dimensional Boundary Layer after Separation," AGARD Report 272, Apr. 1960

- (12) Laganelli, A. L. and Nestler, D. E., "Surface Ablation Patterns: A Phenomenology Study," AIAA Journal, Vol 7, No. 7, July 1969, pp 1319-1325
- (13) Gregory, N., Stuart, J. T. and Walker, W. S., "On the Stability of Three Dimensional Boundary Layers with Applications to the Flow Due to a Rotating Disk," Boundary Layer Effects in Aerodynamics, Philosophical Library Inc., 1957
- (14) Knapp, C. F. and Roache, P. J., "A Combined Visual and Hot-Wire Anemometer Investigation of Boundary Layer Transition," AIAA Journal, Vol 6, No. 1, Jan. 1968, pp 29-36
- (15) Winkler, E. M., Humphrey, R. L., Koenig, J. A., and Madden, M. T., "Investigation of Substructure Heating on Cracked Ablative Heat Shields," NOLTR 69-122, U. S. Naval Ordnance Laboratory, White Oak, Md., July 1969
- (16) Larson, H. K. and Mateer, G. G., "Cross-Hatching A Coupling of Gas Dynamics with the Ablation Process," AIAA Paper 68-670, Los Angeles, Calif., 1968
- (17) Inger, G. R., "Discontinuous Supersonic Flow Past an Ablating Wavy Wall," Report DAC-62375, McDonnell Douglas Corp., Santa Monica, Calif., 1968
- (18) Nachtsheim, P. R., "Analysis of the Stability of a Thin Liquid Film Adjacent to a High-Speed Gas Stream," NASA TN D-4976, Jan. 1969
- (19) Tobak, M., "Hypothesis for the Origin of Cross-Hatching," AIAA Paper 69-11, New York, N. Y., 1969
- (20) Mirels, H., "Origin of Striations on Ablative Materials," AIAA Journal, Vol 7, No. 9, Sept. 1969, pp 1813-1815
- (21) Probst, R. F. and Gold, H., "Cross-Hatching a Material Response Phenomena," AIAA Journal, Vol 8, No. 2, Feb. 1970, pp 364-366

TABLE 1
OPERATING CONDITIONS AND INSTRUMENTATION

Duct Number	Mach Number	Supply Pressure (MN/m ²)	Supply Temperature (°K)	Test Time (sec)	Instrumentation
1L	3.03	2.056	4277	13	6 static-pressure orifices
2L	3.04	2.168	4888	13	4 surface thermocouples - 6 static-pressure orifices
3L	3.03	2.229	4372	13	4 thermocouple plugs with 3 thermocouples per plug 6 static-pressure orifices
4L	3.06	2.275	3666	13	1 skin-friction balance 6 static-pressure orifices 4 thermocouple plugs
5L	3.03	2.229	4200	13	6 static-pressure orifices 1 longitudinal and 1 transverse crack, each with one heat gauge
6L	3.06	2.259	3455	12	2 skin-friction balances
1T	~2.3	2.087	2405	2.7	3 static-pressure orifices 1 longitudinal and 1 transverse crack, each with one heat gauge

TABLE 1 (Cont.)

Duct Number	Mach Number	Supply Pressure (MN/m ²)	Supply Temperature (°K)	Test Time (sec)	Instrumentation
2T	~2.3	2.087	2600	5.7	1 static-pressure orifice - longitudinal crack with three heat gauges 1 transverse crack with one heat gauge
3T	~2.3	2.127	2400	4.2	1 static-pressure orifice 2 transverse cracks, each with one heat gauge
3AT	~2.3	2.127	2400	6.4	2 static-pressure orifices 2 transverse cracks, each with one heat gauge 1 skin-friction balance
4T	~2.3	2.887	2405	4.4	2 static-pressure orifices 3 transverse cracks, each with one heat gauge
5T	~2.3	2.887	2405	4.6	3 static-pressure orifices 3 in-depth thermocouples 1 skin-friction balance

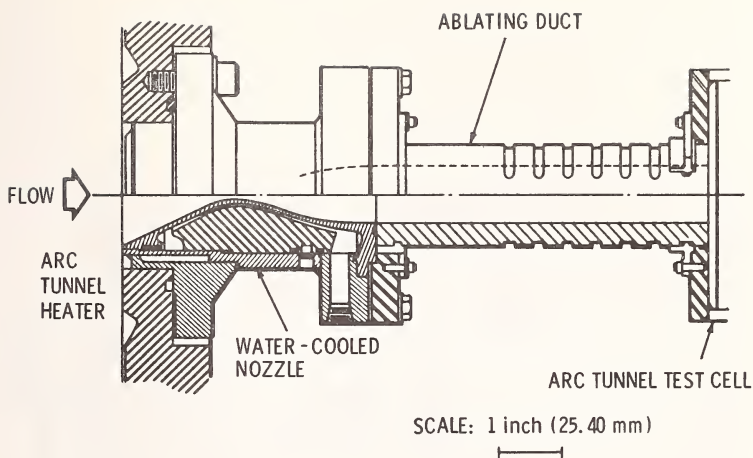


FIG. 1 NOZZLE AND ABLATION DUCT ARRANGEMENT

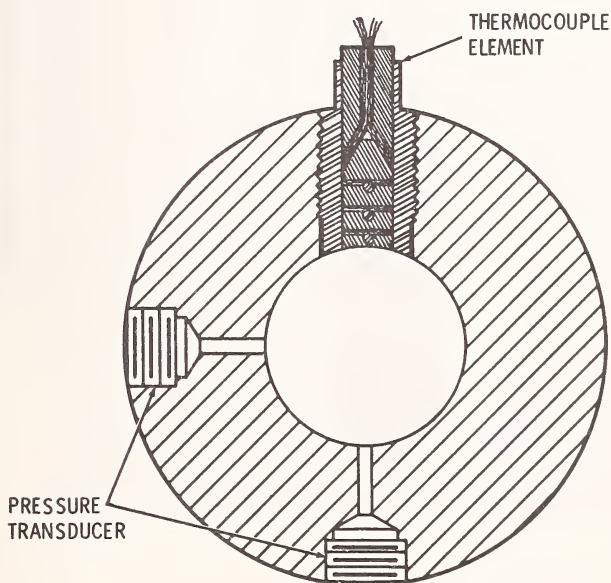


FIG. 2 THERMOCOUPLE PLUG FOR IN-DEPTH TEMPERATURE MEASUREMENT

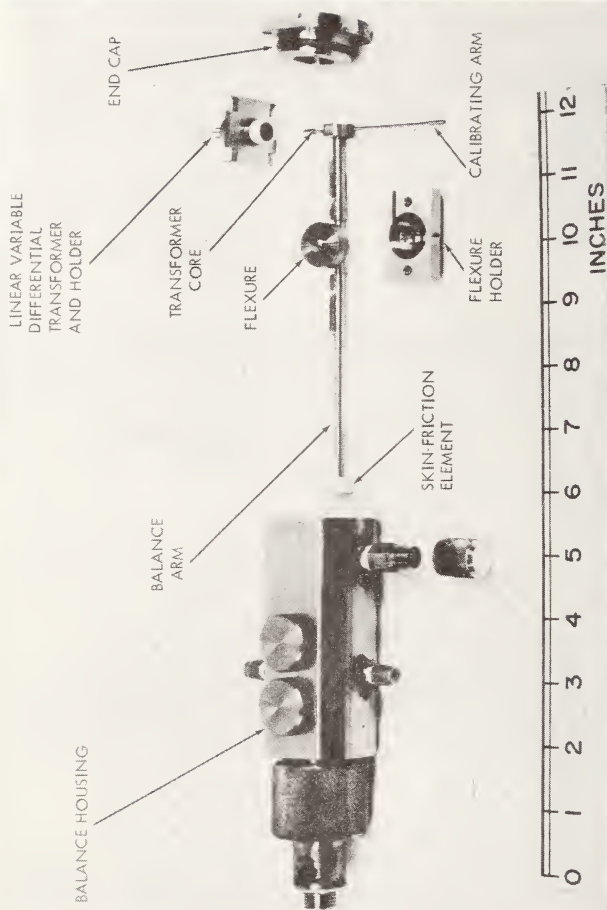


FIG. 3 EXPLODED VIEW OF SKIN FRICTION BALANCE

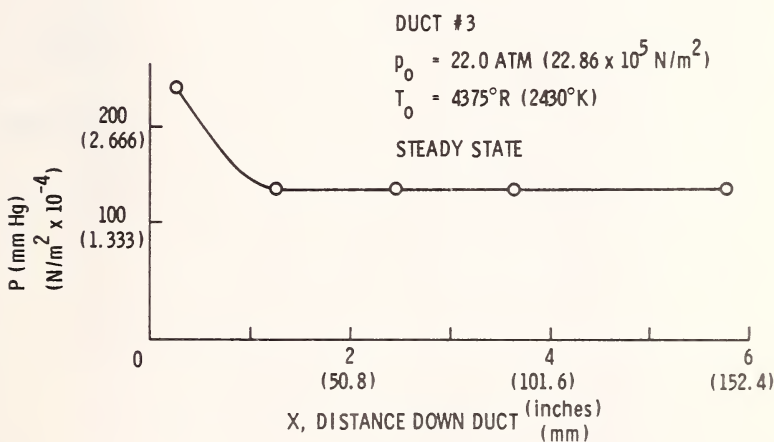
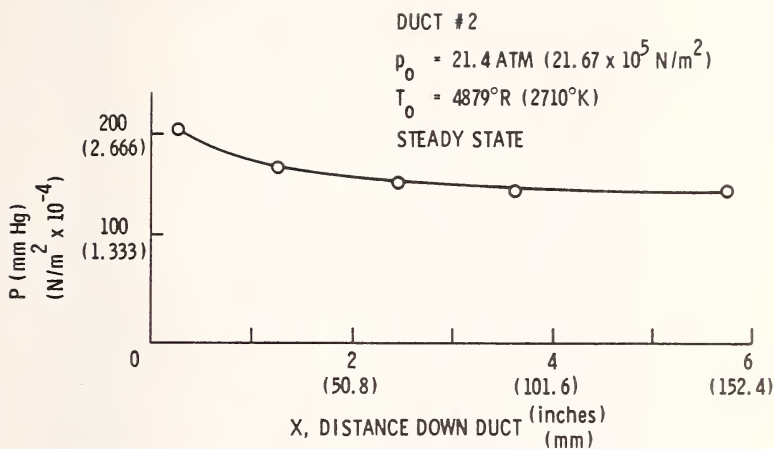


FIG. 4 PRESSURE DISTRIBUTION IN TEFLON DUCT

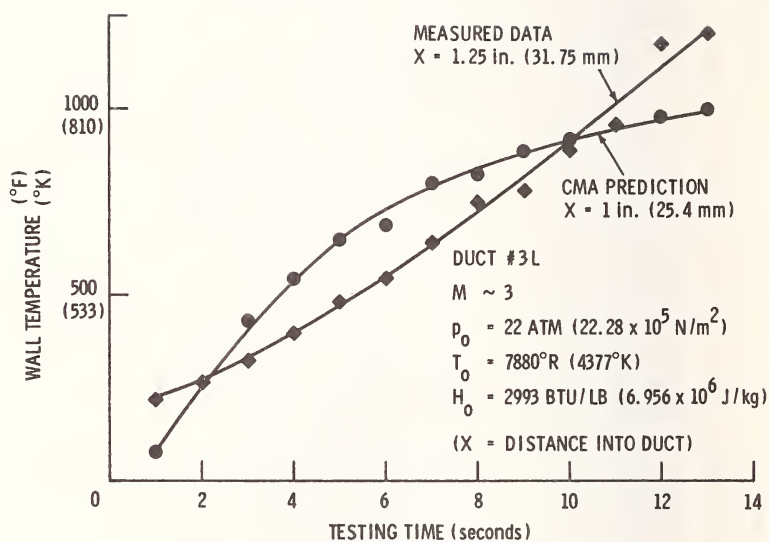


FIG. 5 PREDICTED AND MEASURED IN-DEPTH TEMPERATURES


FLOW 



FIG. 6 INSIDE VIEW OF DUCT NUMBER 5L AFTER TEST

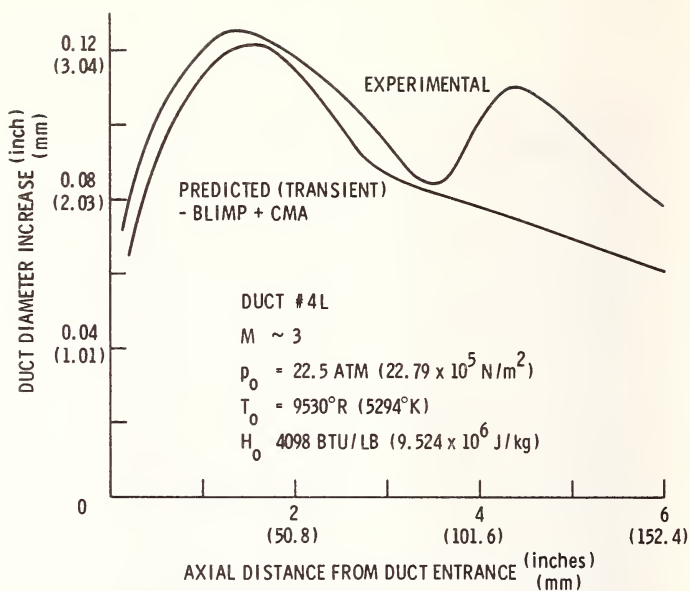


FIG. 7 PREDICTED AND MEASURED TOTAL RECESSION

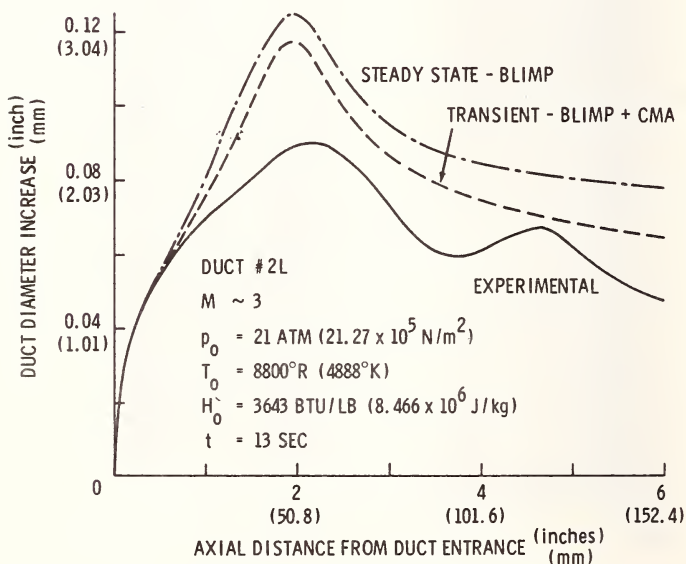


FIG. 8 PREDICTED AND MEASURED TOTAL RECESSION

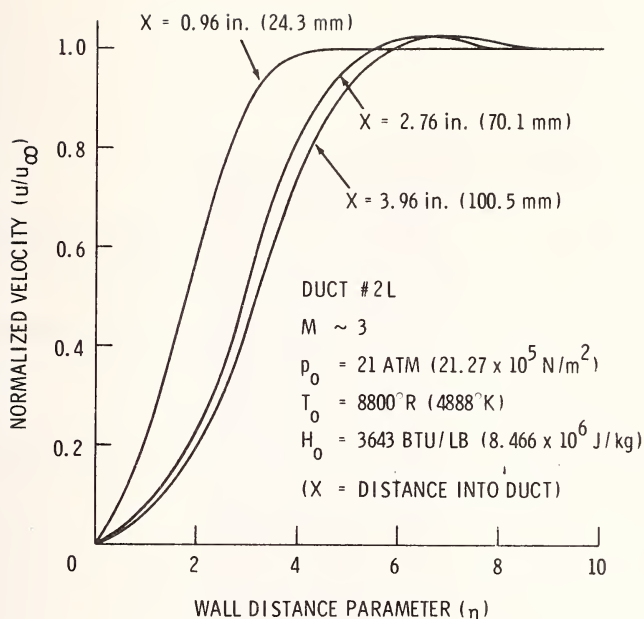


FIG. 9 CALCULATED VELOCITY PROFILES

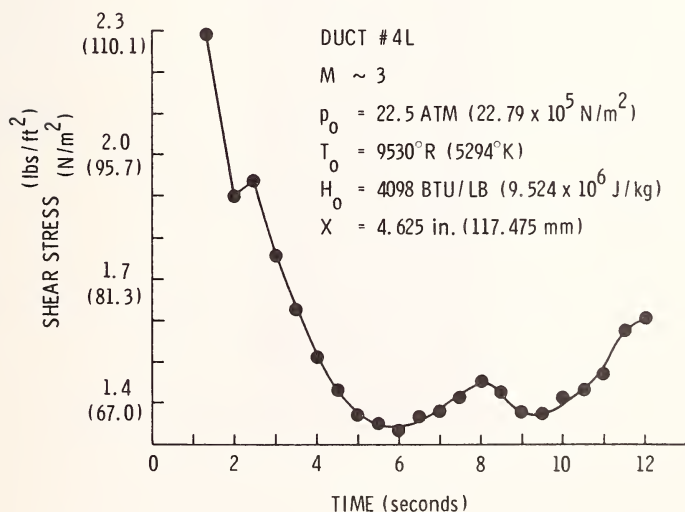


FIG. 10 WALL SHEAR RESPONSE

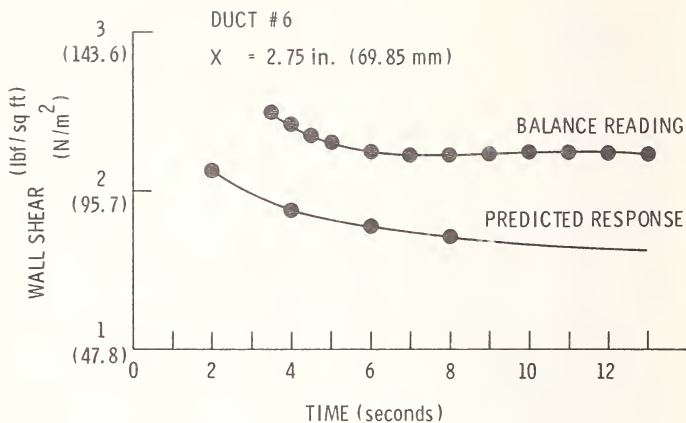


FIG. 11 WALL SHEAR RESPONSE

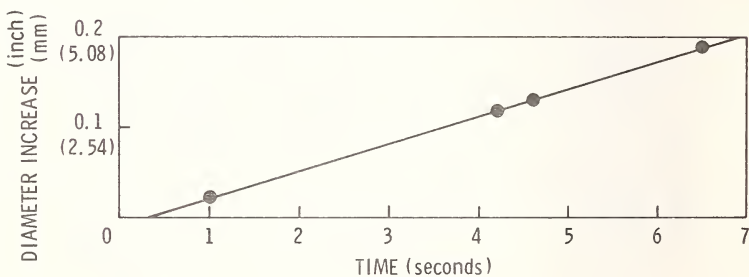


FIG. 12 VARIATION OF TOTAL ABLATION OF FOUR DUCTS AS A FUNCTION OF TESTING TIME

FLOW 



FIG. 13 CROSS-HATCHED STRIATION PATTERN

PREDICTION OF MECHANICAL EROSION OF CHARRING ABLATORS

Lauri H. Hillberg¹

REFERENCE: Hillberg, Lauri H., "Prediction of Mechanical Erosion of Charring Ablators," ASTM/IES/AIAA Space Simulation Conference, 14-16 September 1970.

ABSTRACT: A simple method has been developed for predicting the mechanical erosion of charring ablators exposed to an aerodynamic environment. The method requires the knowledge of two variables: the aerodynamic shear stress at the ablating surface and the surface temperature. Test data are used to obtain two empirical constants necessary for correlating the erosion recession rate in terms of these two variables. The empirical constants have been determined for phenolic cork, phenolic carbon, epoxy-novolac, and high density silicone rubber.

KEY WORDS: ablation, char, erosion, aerodynamic shear, phenolic carbon, cork, epoxy-novolac, silicone rubber.

Nomenclature

A	=	erosion constant, $\text{lbm/ft}^2\text{sec/lbf/in}^2$ ($\text{kg/m}^2\text{sec/N/m}^2$)
B	=	erosion constant, $^{\circ}\text{R} (^{\circ}\text{K})$
M	=	Mach number
m	=	mass erosion rate, $\text{lbm/ft}^2\text{sec}$ ($\text{kg/m}^2\text{sec}$)
P	=	pressure, lbf/in^2 (N/m^2)
\dot{s}	=	surface recession rate, in/sec (m/sec)
ΔS	=	thickness lost, inches (m)
t	=	time, sec
T	=	temperature, $^{\circ}\text{R} (^{\circ}\text{K})$

¹ Senior Engineer; Aerospace Group, The Boeing Company, P.O. Box 3999, Seattle, Washington 98124

- α = angle of attack, deg (rad)
 ρ = density, lbm/ft³ (kg/m³)
 τ = aerodynamic shear stress, lbf/in² (N/m²)
 Ψ = blocking function

Subscripts

- e = erosion
 f = final
 o = at onset
 s = at surface
 t = total
 w = wall

Introduction

One of the strongest factors affecting the performance of a charring ablator is the recession of the char surface. This recession is detrimental to the performance of the ablator since additional material must be provided to compensate for the material loss. In order to determine the amount of this loss and also to provide a means for evaluating the overall ablator response, it is necessary to evaluate all mechanisms which contribute to the surface recession. One such mechanism is mechanical erosion, a term which represents the material loss attributed to factors which include aerodynamic shear, thermal stress, and internal gas pressure.

Analytical prediction of mechanical erosion has been extremely difficult. The most successful method has been to use sophisticated computer programs which incorporate an integrated thermal-structural analysis (1,2,3)². The purpose of the structural analysis is to provide a means for examining the stress state in the material and determining structural failure of the char layer. This failure, occurring repeatedly during ablation, is then considered to constitute the mechanical erosion. The disadvantage of this type of approach lies in the need to define numerous structural properties of both the virgin plastic and char over a wide range of environmental conditions. These properties often require extensive testing to determine (e.g., Reference 4) and may be erroneous or may have been determined at conditions incompatible with the

² The number in parenthesis refers to the list of references appended to this paper.

intended environment. Consequently, the accuracy and usefulness of a complex structural analysis for predicting mechanical erosion may be lost because of the lack of well defined structural properties.

It is apparent that there is a need for a mechanical erosion prediction method which has greater simplicity than the complex structural analysis and which can be presented in terms of easily defined variables. Two such methods have already been proposed (5,6). In both of these methods, the mechanical erosion rate is determined by specifying a maximum char thickness permissible under certain conditions. When these conditions are reached the char fails at the point determined by that maximum thickness. Repetition of this failure process constitutes the mechanical erosion. The maximum char thickness used in these two methods is presented in terms of aerodynamic shear (5) or pressure (6) and a few empirical constants.

A third simplified method for predicting mechanical erosion is presented in this paper. In this method the only external force influencing the mechanical erosion rate is assumed to be the aerodynamic shear. Thus, this method is not applicable to stagnation regions or regions having insignificant aerodynamic shear levels. Use of Reference 6 or the simplified stress analysis in Reference 5 may be utilized in these areas.

Theory

Several assumptions are necessary for developing this method. First, as was mentioned above, only aerodynamic shear loads are assumed to act on the char. Pressure effects are neglected. However, the necessary empirical constants are determined under conditions having both aerodynamic shear stress and normal stresses induced by the pressures exerted by the gaseous ablation products as they flow through the char layer. In this respect, pressure effects are included.

The second assumption is that mechanical erosion is a continuous process and not a series of discrete failures of the char layer. If discrete failures do occur, then it is assumed that the frequency of the failures and the thicknesses of the material lost are such that the recession can be handled as a continuous process.

The third assumption is that the aerodynamic shear acting on the ablating surface is equal to the shear in the absence of ablation times the blocking function, Ψ , which accounts for the effects of mass injection.

The final assumption is that all thermo-chemical processes such as oxidation, sublimation, and decomposition can be readily analyzed. This assumption is in keeping with the capabilities of ablation computer programs now available. The mechanical erosion rate can then be

determined from tests by measuring the total recession rate and subtracting the thermo-chemical contribution.

Utilizing the above assumptions, an analytical prediction method based on the model developed by Gaudette (7) is proposed. Gaudette's model, which analyzed the mechanical erosion of silica-filled epoxy-novolac, assumed that the erosion rate was a function of the surface temperature, this temperature reflecting the resistance of the viscous melt layer formed on the surface of the char layer. His equation for the mechanical erosion rate has the form

$$\dot{m}_e = f(\Psi \tau K^{10^4/T_W})$$

where K is a constant set at 0.5 for epoxy-novolac. The original erosion data obtained in Reference 7 along with the curve representing the selected functional relationship are shown in Figure 1.

The method proposed here assumes that Gaudette's model may be extended to apply to all charring ablators and not just those which form a viscous melt layer. This assumption implies that the surface temperature also reflects the structural failure resistance of the char layer. Reference 8 briefly discusses this assumption.

It is possible upon examining the erosion data of Reference 7 (and the data discussed subsequently) to simplify Gaudette's model. The erosion data shown in Figure 1 has been replotted on linear scales in Figure 2. A straight line drawn through these data intercepts the origin and yields an equation for the erosion rate of the form

$$\dot{m}_e = C \Psi \tau K^{10^4/T_W}$$

or, after converting to the base e ,

$$\dot{m}_e = A \Psi \tau e^{-B/T_W}$$

Dividing through by the shear stress at the ablating wall, $\Psi \tau$, yields the erosion model proposed in this paper,

$$\boxed{\frac{\dot{m}_e}{\Psi \tau} = A e^{-B/T_W}}$$

This model shows the mechanical erosion rate divided by the aerodynamic shear stress at the ablating wall is dependent only on the surface temperature. It is thus possible to easily predict the mechanical erosion rate for a charring ablator through the knowledge of three parameters and two empirical constants which can be readily determined from tests.

Results

The two empirical constants required for the proposed mechanical erosion method can be directly determined from wind tunnel or free flight tests. Determining them involves plotting the variable \dot{m}_e/Ψ_T versus $1/T_w$ on semi-log graph paper. The slope is constant B and the intercept at $1/T_w$ equal to zero is constant A . These empirical constants have been determined for four distinctly different ablators: epoxy-novolac, high density silicone rubber, phenolic cork, and phenolic carbon.

Epoxy-Novolac

The equation for the straight line drawn through the data shown in Figure 2 is used directly to obtain the necessary empirical constants for Avcoat 5026-39H/CG epoxy-novolac. The equation for the mechanical erosion, after converting the exponential base from 0.5 to e , is

$$\frac{\dot{m}_e}{\Psi_T} = 0.52 e^{-6930/T_w}$$

High Density Silicone Rubber

The empirical constants have been determined for Dow Corning DC 93-072 silicone rubber ($\rho = 70 \text{ lbs/ft}^3$). These constants were determined from tests conducted in the Boeing Supersonic Combustion Wind Tunnel (BSCWT). The nominal wind tunnel conditions were:

$$\begin{aligned} M &= 2.2 \\ P_t &= 37 \text{ to } 112 \text{ psi} \\ T_t &= 1130 \text{ to } 2020^\circ \text{ F} \end{aligned}$$

The model was a sharp flat plate with boundary layer trips located 0.2" from the leading edge. A 2" x 4" x 0.2" ablator specimen was bonded to a plate which was then bolted into a recession located 0.7 inches behind the boundary layer trips. The ablator surface initially is flush with the leading edge. The flat plate was set at either 0° , 10° , or 15° angle of attack during the tests.

The mechanical erosion rates required to obtain the erosion constants were reduced using the following equation

$$\dot{m}_e = \rho_s \Delta S / 12(t_f - t_o)$$

The surface density of the ablator required in the above equation was determined using a transient ablation analysis computer program (9) which utilizes an Arrhenius decomposition rate law. The thickness lost was determined directly from before and after measurements of 10X photographs. It had previously been found from TGA tests conducted on the char in air that chemical reactions did not contribute to surface recession. Finally, the onset time, or the time when surface erosion began in the tests, and the time terminating the test were determined from slow motion movies.

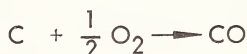
The three unknowns remaining in the correlation equation, the blocking function, the aerodynamic shear stress, and the surface temperature, were determined analytically using known material properties and measured wind tunnel conditions. Several iterations using various erosion constants were required to obtain the correct values for these three parameters.

The erosion data from these series of tests are summarized in Table 1. The resulting data are plotted in Figure 3. The straight line drawn through these data is represented by

$$\frac{\dot{m}_e}{\Psi \tau} = 2070 e^{-16930/T_W}$$

Phenolic Cork

Erosion constants were obtained for Armstrong AC-2755 phenolic cork using a combination of wind tunnel tests and flight test data. Wind tunnel test data obtained from two tests conducted in the Boeing Hypersonic Wind Tunnel (BHWI) were reduced in the same manner as the DC 93-072 silicone rubber with the exception that surface recession attributed to chemical oxidation was included. Constants used for the reaction limited oxidation were obtained from TGA tests conducted on the cork char in air; constants for the diffusion limited oxidation were obtained assuming



The wind tunnel test model was a 15° half-angle cone having a sharp steel nose tip. The wind tunnel conditions were

$$\begin{aligned} M &= 6.05 \\ P_t &= 850 \text{ and } 1000 \text{ psi} \\ T_t &= 1000^\circ\text{F} \end{aligned}$$

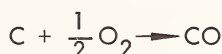
The second of the two tests used a quartz lamp to supplement the aerodynamic heating rates. The wind tunnel test data are summarized in Table 2 and plotted in Figure 4.

Missile flight test data were also used to supplement the wind tunnel data. Flight ablation meters yielded thickness ablated as a function of time. The local slope of this curve yielded the ablation rate, also as a function of time. Using the known flight trajectories and a transient ablation analysis computer program (9), the surface density, surface temperature, blocking function, and aerodynamic shear stress were determined. Utilizing the measured ablation rates and the supplemental analytical data, the necessary erosion data were determined. These data are also plotted in Figure 4. The erosion equation resulting from these data is

$$\frac{\dot{m}_e}{\Psi \tau} = 1.09 \times 10^{11} e^{-37540/T_W}$$

Phenolic Carbon

Erosion constants were obtained for Avco X6300 phenolic carbon having a 90° fabric layup using the data presented in Reference 10. The mechanical erosion rates were determined by taking the recession rates indicated in Reference 10, converting them to mass loss rates by assuming a char density of 70 lbm/ft³, and subtracting the recession attributed to oxidation. The oxidation recession was assumed to be that for diffusion limited combustion for the reaction



The aerodynamic shear stresses and the surface temperatures shown in Reference 10 were used, except that a Reynolds analogy factor of 1.2 was applied to the shear stress. The final variable, the blocking function, was determined analytically using a transient ablation analysis computer program (9). The results are tabulated in Table 3 and are plotted in Figure 5. From this figure it was found that the erosion rate can be represented by

$$\frac{\dot{m}_e}{\Psi \tau} = 7.5 \times 10^5 e^{-77000/T_W}$$

Discussion

The results obtained for the proposed erosion rate equation indicate that mechanical erosion can be correlated, at least for the materials and conditions examined. It is interesting to note that such a simple equation does correlate as well as it does for the different ablator types and the different ranges of test environments.

It is realized that the results may be limited. Except for the missile flight tests for the phenolic cork, the tests were essentially steady state tests. Consequently, the temperature profiles and char depths may not match flight conditions. The data shown for phenolic cork in Figure 4 do, however, indicate a correlation between wind tunnel and flight test data. However, the cork char is very fragile and was quite thin in both the wind tunnel and flight tests. Consequently, it is very difficult to make any significant conclusions from these data.

To test the ability of the erosion model to aid in correlating temperature data, several instrumented DC 93-072 silicone rubber ablation models were run in the same test series that were used to obtain the empirical constants. The results of one such test are shown in Figure 6. The conditions of the test were

$$\begin{aligned}M &= 2.2 \\P_t &= 70 \text{ psi} \\T_t &= 1850^\circ\text{F} \\\alpha &= 15^\circ\end{aligned}$$

The temperatures were predicted for a location 2.0" aft of the leading edge. The correlation between the predicted and measured values can be seen to be excellent. Correlation without the mechanical erosion model was extremely poor, largely due to the fact that no recession was predicted.

Conclusions

A simple, straight forward method has been developed for the prediction of mechanical erosion of charring ablators in a shear environment. By virtue of the ability to reduce test data in terms of the proposed equation, the method appears valid, at least for the materials and test conditions which were examined.

Empirical constants for use in the proposed erosion equation have been determined for epoxy-novolac, high density silicone rubber, phenolic cork, and phenolic carbon.

References

1. Schneider, P.J., Dolton, T.A., and Reed, G.W.; "Mechanical Erosion of Charring Ablators in Ground-Test and Re-Entry Environments," *AIAA J.*, Vol. 6, No. 1, Jan. 1968, pp 64-72.
2. Hillberg, L.H.; "Influence of Material Properties on Re-Entry Vehicle Heat Shield Design," *AIAA/ASME 8th Structures, Structural Dynamics and Materials Conference*, March 1967.
3. Hoglund, R.F., Babcock, S.E., and Grovens, R.N., Jr.; "Ablation Test Specimens Environment at High Temperature," *AIAA/ASME 10th Structures, Structural Dynamics and Materials Conference*, April 1969.
4. Ching, A., and Welsh, W.E., Jr.; "Strength and Stress-Strain Properties of Rapidly Heated Laminated Ablative Materials," *AIAA J.*, Vol. 6, No. 12, Dec. 1968, pp 2312-2315.
5. Mathieu, R.D.; "Mechanical Spallation of Charring Ablators in Hyperthermal Environments," *AIAA J.*, Vol. 2, No. 9, Sept. 1964, pp 1621-1627.
6. Bishop, W.M. and DiCristina, V.; "A Prediction Technique for Ablative Material Performance Under High-Shear Re-Entry Conditions," *AIAA J.*, Vol. 6, No. 1, Jan. 1968, pp 59-63.
7. Gaudette, R.S., del Casal, E.P., and Crowder, P.A.; "Charring Ablation Performance in Turbulent Flow, Volume I," Document D2-114031-1, The Boeing Company, June 1967.
8. Rindal, R.A.; "An Evaluation of Design Analysis Techniques for High Performance Ballistic Vehicle Graphite Nose Tips, Appendix D: Thermo-chemical and Thermomechanical Ablation," Air Force Materials Laboratory, AFML TR-69-73, Volume IV, January 1970.
9. Hillberg, L.H.; "The Improved Convective Heating and Ablation Program (CHAP)," Document D2-26104-2, The Boeing Company, June 1969.
10. Mitchel, B.J.; "Ablative Material Tests Under Transient Heating Simulating Ballistic Re-Entry," *AIAA Paper 69-150*, January 1969.

TABLE 1--Erosion Data for DC 93-072 Silicone Rubber

Run	$\Psi\tau$ (psi)	ΔS (in)	$t_f - t_o$ (sec)	$\dot{m}_e / \Psi\tau$ (*)	T_W (°R)
1	.055	.015	26.8	4.0×10^{-2}	1560
2	.102	.035	23.2	5.9×10^{-2}	1620
3	.117	.037	14.2	9.0×10^{-2}	1680
4	.114	.076	41.7	6.4×10^{-2}	1660
5	.108	.024	24.4	3.6×10^{-2}	1520
6	.105	.036	54.8	2.4×10^{-2}	1480
7	.056	.016	22.8	4.9×10^{-2}	1610
8	.080	.022	27.4	3.9×10^{-2}	1530
9	.121	.043	10.5	14.0×10^{-2}	1760
10	.083	.044	19.8	11.0×10^{-2}	1750
11	.122	.135	21.7	19.0×10^{-2}	1810
12	.061	.025	19.1	8.5×10^{-2}	1690
13	.055	.033	27.7	8.7×10^{-2}	1660
14	.050	.006	37.2	1.2×10^{-2}	1410
15	.098	.013	42.2	1.2×10^{-2}	1390

* $(\text{lbm}/\text{ft}^2 \text{sec})/(\text{lbf}/\text{in}^2)$

TABLE 2--Erosion Data For Armstrong AC-2755
Phenolic Cork

Run	$\Psi\tau$ (psi)	t (sec)	$\dot{m}_e/\Psi\tau$ (*)	T_W (°R)
1	.069	30.0	5.1×10^{-3}	1230
2 ⁺	.077	30.0	1.8×10^{-2}	1310

* $(\text{lbm}/\text{ft}^2 \text{sec})/(\text{lbf}/\text{in}^2)$

+ aerodynamic heating supplemented by quartz heating lamps

TABLE 3--Erosion Data For Avco X6300 Phenolic
Carbon (90° Fabric Layup)

Specimen Code	\dot{s} (in/sec)	\dot{m}_t^* (lbm/ft ² sec)	\dot{m}_e (lbm/ft ² sec)
X6300-4	.026	.152	.134
X6300-5	.051	.297	.265
X6300-3	.024	.140	.104

Specimen Code	Ψ	$\tau +$ (psi)	$\dot{m}_e/\Psi\tau$ (**)	T_W (°R)
X6300-4	.62	.20	1.10	5780
X6300-5	.63	.35	1.20	5680
X6300-3	.73	.29	0.49	5150

* based on a surface density of 70 lbm/ft³

+ values shown in Reference 10 corrected for a Reynolds analogy factor of 1.2

** (lbm/ft²sec)/(lbf/in²)

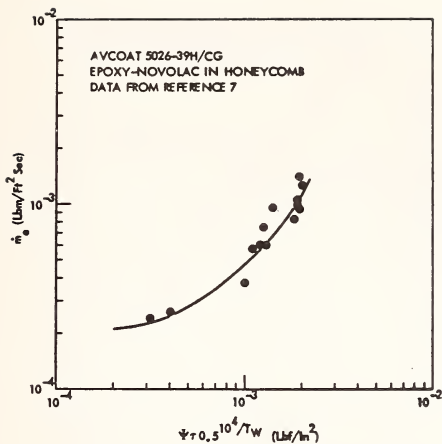


Fig. 1--Mechanical Erosion Data for Avcoat 5026-39H/CG.

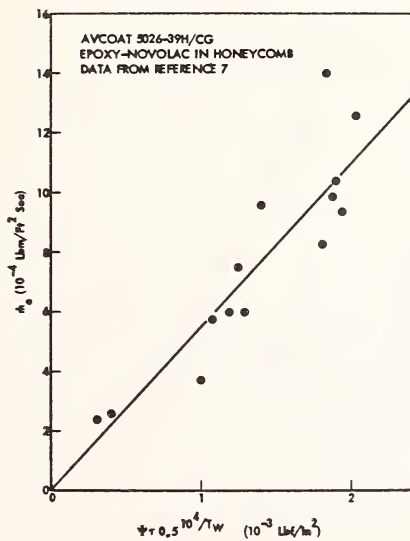


Fig. 2--Mechanical Erosion Data for Avcoat 5026-39H/CG.

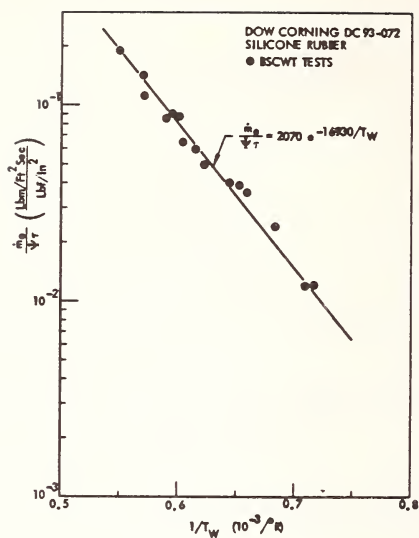


Fig. 3--Mechanical Erosion Data for Dow Corning DC 93-072.

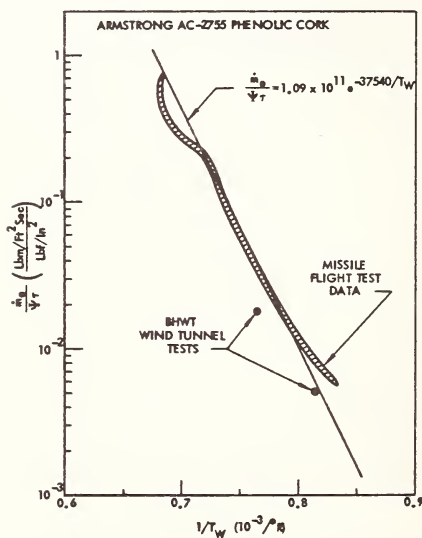


Fig. 4--Mechanical Erosion Data for Armstrong AC-2755 Phenolic Cork

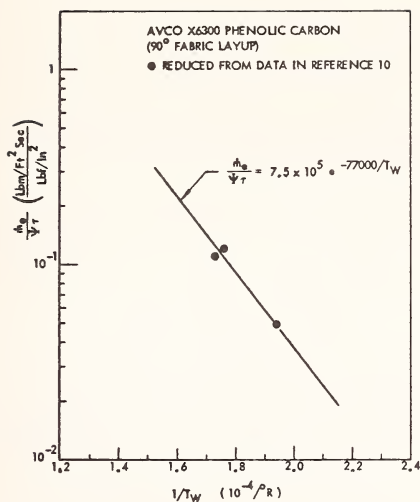


Fig. 5--Mechanical Erosion Data for Avco X6300 Phenolic Carbon

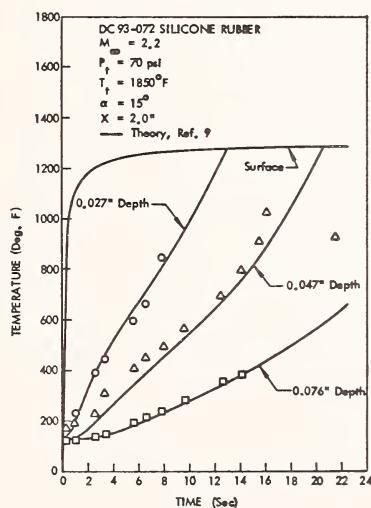


Fig. 6--Temperature Test Data for Dow Corning DC 93-072.

HEATING IN CRACKS ON ABLATIVE HEAT SHIELDS

E. M. Winkler,¹ R. L. Humphrey,² M. T. Madden,²
and J. A. Koenig³

REFERENCE: Winkler, E. M., Humphrey, R. L., Madden, M. T., and Koenig, J. A., "Heating in Cracks on Ablative Heat Shields," ASTM/IES/AIAA Space Simulation Conference, 14-16 September 1970

ABSTRACT: An experimental program has been carried out in the U. S. Naval Ordnance Laboratory (NOL) 3 Megawatt Arc Tunnel to study the effect of cracks in an ablative heat shield on the substructure heating. The tests used a supersonic contoured nozzle with a Teflon duct attached to it. The ducts had transverse and longitudinal cracks machined into the surface. They were instrumented for pressure, temperature, heat transfer and skin-friction measurements. The cracks were found to have pronounced effects on the ablative behavior. The heating is moderate under a laminar boundary layer, but can be catastrophic when the boundary layer is turbulent, depending upon the size and direction of the crack. The results for the transverse cracks were compared with an available analytical prediction. The heat-transfer measurements tend to support the concept of vortex cells existing within the cracks. Cracks that are deep as compared with their width result in very little substructure heating.

KEY WORDS: ablation, substructure heating, catastrophic ablation, surface cracks

¹Chief, High-Temperature Aerodynamics Group,
Aerophysics Division, Naval Ordnance Laboratory (NOL)

²Aerospace Engineers, NOL

³Aerospace Engineering Technician, NOL

NOMENCLATURE

b	= crack width
H	= enthalpy
h	= crack depth
M	= Mach number
\dot{m}	= material loss per unit time
q	= heat-transfer rate
Re	= Reynolds number
St	= Stanton number
u	= velocity
x	= distance from duct entrance
y	= depth of crack
δ^*	= boundary-layer displacement thickness
ρ	= density

SUBSCRIPTS

c	= bottom of crack
s	= surface of duct
w	= wall
θ	= momentum boundary-layer thickness
τ	= shear stress
∞	= free-stream values

INTRODUCTION

Ablative materials are an accepted means for protecting re-entry vehicles from the intense heating encountered during certain phases of the flight. There is concern, however, that when cracks develop in the ablative heat shield, the substructure may be subjected to excessive heating. The ablative

behavior of the heat shield may be altered in the vicinity of cracks which in turn can affect the aerodynamics of the vehicle. The analytical description of the processes is inadequate to allow a safe design of heat shields. A moderate number of studies have been performed on non-ablating, shallow cavities, rectangular notches of various aspect ratios, and on the upstream and downstream sides of protrusions as, for example, reported in References 1 through 4. Most of the studies were done for low-speed flow. Early experimental studies were done by Wieghardt and Tillmann, References 1 and 2. They illustrated the vortex flow pattern in the cavities and obtained empirical relations for the effect of the cavities, or notches on the total drag of the vehicle. Analytical studies (3,4)⁴ established a dependency of the number of vortices within given notches on the flow Reynolds number. Heat-transfer data are reported in References 5 and 6, for example. These studies serve as a guide, but since they do not cover a sufficiently wide range of conditions, they did not lead to a satisfactory theoretical treatment that could be applied to ablating surfaces in high-speed flow. The present research program was formulated to look into this matter.

APPROACH

NOL's approach, primarily experimental, endeavors to produce actual flight conditions in the 3 Megawatt Arc Tunnel and to measure parameters and material responses that can be used to further the understanding of the processes involved. Re-entry bodies except for manned space vehicles are typically conical with a small to moderate amount of nose bluntness. The heat shield may be Teflon, silica or carbon phenolic, or a number of other materials.

Representative flow parameters over the conical part of a re-entry heat shield are: Mach number = 2.0 to 10, wall enthalpy (H_w)/stream enthalpy (H_o) = 0.2 to 0.4, friction Reynolds numbers (Re_τ) = 70 to 2000. Cracks in the heat shield may have width over boundary-layer thickness (b/δ^*) ratios of 0.05 to 10 while crack heights to width ratios (h/b) could range from 0.1 to 10.

Such conditions can be duplicated in an arc heated tunnel by using the similarity of flow down a nozzle from stagnation conditions to that around the forward region of a re-entry body. If one makes the reservoir conditions of the arc tunnel equal to the

⁴The numbers in parentheses refer to the list of references appended to this paper.

stagnation point values on the re-entry body, the correct flight conditions on the initial portion of the conical surface can be duplicated. This allows the options of studying the flow external or internal to a model with equal validity of the results. The latter approach was selected because it is experimentally quite convenient. Even small models can be easily instrumented for obtaining pressure, temperature, heat-transfer and skin-friction data. In this case, the model can be simply an axially symmetric duct as described in the next section. Instrumentation supports and leads can be arranged externally, thus eliminating the difficulty of providing aerodynamic and thermal shields for them.

For the study of substructure heating due to cracks, parameters other than Mach number, pressure and enthalpy ratio need to be considered. From flow studies in cavities, or cracks, with non-ablating walls (1,2,3,4,5,6) one knows that the friction Reynolds number, Re_τ , characteristic sizes such as b/δ^* and h/b , as well as the geometry may influence the flow patterns in the cavity and the heat transfer to its walls. Geometry factors include orientation of the cavity with respect to the flow direction, spacing of the cavities, if there are more than one, and the cavity edge geometry. With ablation present, the blowing rate parameter, $c_q = \dot{m}/\rho_\infty u_\infty St$ also has to be considered. The critical, actual size, b , of a crack is somewhat speculative until studies on this subject matter are concluded. But it appears plausible that cracks of 0.25 mm (0.01 inch) width or larger on the conical part of an ICBM heat shield may lead to problems for the substructure depending on the time of exposure to intense heating. The blowing rate parameter, essentially an indication of the amount of shielding provided by the ablator, will vary with the material. The aspect ratio h/b will depend on the thermal shock resistance of the heat-shield material and the cause of the cracks. It is, however, conceivable that it may range from 0.1 to 10.

EXPERIMENTAL ARRANGEMENT

The experimental set-up is shown in Figure 1. The arc heater, part of NOL's 3 Megawatt Arc Tunnel (7), is a three-phase, four-ring, arc which operates on dry air supplied from a high-pressure storage field. The heater is followed by an axially symmetric contoured nozzle designed by the method of Reference 8. Two nozzles have been used during

the present investigations, one was designed for a Mach number 3, the other for a Mach number of 2.3. From the nozzle, the flow enters an axially symmetric duct made of the ablative material. The Teflon ducts (TFE-7, E.I. DuPont Co.) with nominal inside diameter of 25.4 mm (1 inch) and length of 152 mm (6 inches), are tightly connected to the nozzle exit which has the same diameter. The nozzle as well as the duct contours have been corrected for the boundary-layer growth. The Mach number 3 nozzle and ducts were designed for laminar flow, while the Mach number 2.3 nozzle and ducts had turbulent boundary-layer corrections applied to them. Exiting from the ducts, the flow then discharges into a test cell, diffuser and exhaust system.

The Teflon ducts are instrumented with copper-constantan thermocouples, and static and Pitot pressure gauges. The transverse and longitudinal cracks machined into the ducts are equipped with heat gauges on the end walls and bottom to measure local heat transfer rates (Fig. 2). In some ducts the local skin friction was measured with a specially developed balance (9).

Crack sizes, orientation, and instrumentation of the ducts are summarized in Tables I and II. This covers a representative but limited range of conditions of interest for the substructure heating problem.

ANALYTICAL PROCEDURES

Several analytical programs have been used in the analysis of the experimental data. Test results obtained under conditions where the duct boundary layer was predicted to be laminar were compared with the BLIMP-CMA programs (Boundary Layer Integral Matrix Procedure-Charring Material Ablator)(10). In the present test series only one run was laminar. The BLIMP-CMA procedures are quite versatile and permit the calculation of Teflon ablation rates, boundary-layer parameters, and in-depth material response in non-similar, multi-component, chemically-reacting, equilibrium, laminar boundary layers along axisymmetric or planar surfaces. Quasi-steady or transient solutions can be obtained.

Unfortunately, a turbulent boundary-layer option was not available for the BLIMP-CMA procedures. As a consequence, the data obtained with turbulent boundary layer along the duct wall, could not be compared with predictions. However, a numerical

procedure was devised to analyze the experimental data to the extent considered essential for the sub-structure heating studies. It combines a computation applicable to turbulent boundary layers (8) on non-ablating walls, experimental information, and wall-species and temperature data obtained from the use of BLIMP. These are quasi-steady-state computations. It was felt that this is acceptable since the experimental shear-stress data indicate that for the turbulent boundary-layer test runs, steady-state conditions are reached in less than one second.

RESULTS

Laminar Boundary-Layer Test

There was only one test carried out under conditions where the boundary layer was predicted to be laminar through the duct. This was done at a Mach number of 3, a supply air pressure of 2.13 MN/m^2 (21 atm) and stagnation temperature of about 5000°K (9000°R). The test duration was 13 seconds. The duct had two cracks, one in the flow direction, the other transverse to it. The size, aspect ratio, and location of the cracks are listed in Table I. Both cracks were instrumented with a heat gauge.

There was a small favorable pressure gradient along the duct due to an overcompensation of the boundary-layer growth along the duct. The surface texture of all ducts became glossy and waxy (11); this texture is presumably attributable to one of the Teflon degradation species (12). Ablation increased from zero at the duct entrance - because of the contact with the cooled nozzle - to a maximum at $x = 30$ to 50 mm (1.2 to 2 inches) from the duct entrance, then decreased as expected for a laminar boundary layer. At $x = 90 \text{ mm}$ (3.5 inches), the ablation increases, reaches a maximum and then decreases again. This anomaly is observed in all "laminar runs," and was analyzed as evidence of boundary-layer transition. This duct also showed the longitudinal, almost parallel striations which are further evidence of laminar boundary-layer instability and transition, as discussed in References 13 and 14. At the downstream side of the longitudinal crack a pronounced wake-like additional ablation pattern is observed as seen from Figure 3. The transverse crack shows only a slight rounding on the downstream side.

The heat gauge in the longitudinal crack began to respond as soon as hot air from the arc heater reached it, about 10 ms. The temperature rise was

linear with time but at a moderate rate. There was a 13.6°C (24.5°F) temperature rise in the 13 seconds of the test. For the transverse crack there was no response discernible for the first second of the test. Thereafter the temperature rose very slowly at a varying rate. The temperature variations correspond to a heating rate of $2.7 \times 10^3 \text{ W/m}^2$ ($2.4 \times 10^{-1} \text{ BTU/ft}^2\text{sec}$) for the longitudinal crack and to a maximum of $7.9 \times 10^2 \text{ W/m}^2$ ($0.7 \times 10^{-1} \text{ BTU/ft}^2\text{sec}$) for the transverse crack. In terms of q/q_s the values are .0042 and .0016, respectively.

Turbulent Boundary-Layer Tests

Six tests were performed at a Mach number of 2.3. The boundary layer was turbulent throughout the duct. The test conditions were 2.13 and 2.84 MN/m² (21 and 28 atm) and temperatures of 2390 and 2560 degrees Kelvin (4300 and 4600°R). Ablation was very pronounced under these conditions, requiring that the testing times be kept to six seconds or less. Five of the six ducts had several cracks, longitudinal and transverse to the flow, as listed in Table I. The instrumentation varied, providing for pressure readings, in-depth temperature recordings, and skin-friction measurements along the ducts, and heat-transfer measurements at the bottom and side walls of the cracks. (See Table I.) The listed values of h/b and b/δ^* refer to the cold wall conditions. The sixth duct was used for a reference test for duct number 4T. This became necessary since duct number 4T was run at conditions for which no reference data existed from previous tests. Pressure, wall temperature and skin-friction data were needed for the evaluation of the results. The amount of instrumentation required was in excess of what could be accommodated in one duct.

The overall ablation behavior of the ducts in this test series was very uniform. The mass loss increased from zero at the entrance to a maximum at $x \approx 25 \text{ mm}$ (1 inch) and then leveled off to an almost constant value of about 70 percent of the maximum, Figure 4. The ablation rates varied from 0.776 to 0.561 kg/m²-sec (.159 to .115 lb/ft²sec) along duct number 5T. Expressed in terms of the blowing rate parameter, $\dot{m}/\rho_\infty u_\infty St$, the turbulent ablation was 0.99.

The experiments showed that the total amount of ablation for a given value of wall heat transfer varied linearly with time, allowing the onset of ablation to be deduced. It was determined to be 0.3 second. All of the turbulent ducts exhibit

cross-hatched striation patterns as shown in Figure 5. The patterns start more or less immediately at the duct entrance and form in a more uniform fashion if a pressure orifice is not located there. A pressure orifice seems to enhance the wave pattern and promote its formation. The cracks have a pronounced effect on the striation pattern, they alter the spacing or even cause them to disappear, Figure 6. At the downstream side of longitudinal cracks, the interference between the crack "wake" and the striations produces a complex pattern, as seen in Figure 7. Analytical studies are under way attempting to explain the observed patterns.

The heat gauges at the bottom and sides of the cracks responded within 30 ms after arc ignition. Some of the temperature readings are shown in Figure 9. For the longitudinal cracks the center of the downstream wall experiences practically the cold-wall surface heating rate, at least initially. The temperature rose to 950°K (1250°F) within the first half second, then the rapid ablation caused the destruction of the heat gauge and the recording ceased. At the bottom of the crack, Figure 9, the heating rate varies, first almost linearly with time, from zero to 0.20 of the averaged surface heating during the first 1.23 seconds of the testing time and then reaches 100 percent of the surface heating within the next $3/4$ second. Burn-out of the heat gauge occurred at this time. A faint pattern of transverse vortices is discernible at the bottom of the cracks. The center of the upstream wall showed an erratic behavior probably indicative of a changing vortex formation. Gouging, both laterally and longitudinally occurs at the downstream end of the crack. It is particularly severe when a longitudinal and a transverse crack interact.

The transverse crack heating rates read from continuous oscillograph recordings showed a more moderate behavior, reaching at best eight percent of the surface heating rate.

Unfortunately, the number of runs and the range of variation of parameters was insufficient to draw firm conclusions. The following are the observations:

- a. For aspect ratios of four, the heat transfer to the bottom of the transverse crack at $t = 1$ second is about four percent of the duct surface heat transfer. At the end of a four second test it may be as high as eight percent. At this time, the nominal aspect ratio has changed to $h/b \approx 2.5$. However, the geometry has also changed, i.e., the edges are rounded, and there is evidence of gouging

due to the vortices that had established in the cracks.

b. The value of h/b does not seem to be a unique correlating parameter nor does b/δ^* or Re_τ . However, the absolute width, b , seems to be of some significance, both in the substructure heating rate and the deformation of the initial crack geometry. This is evidence that a transverse crack will cease, with increasing width, to be an "open cavity" and the flow pattern in it will change to that of a "closed cavity".

c. With increasing depth of the crack, the heat transfer decreases very sharply, and is only 1.8 percent of the surface heating under a turbulent boundary layer for an aspect ratio of 7. This is consistent with the studies reported in Reference 15. Detailed analysis and flow studies in transverse cracks have led to relations for the variation of the crack heat transfer q_c/q_s with the depth parameter y/b , where y is the distance from the surface and b the width of the crack. The analysis indicates that the ratio of q_c/q_s is not a function of Mach number and is not affected by ablation if the data is given in terms of the changing crack depth as ablation progresses. The discontinuity in the curve is due to the transition between the solutions chosen for the regions of y/b . The predicted variation, for the transverse cracks, is shown in Figure 10 (solid and dashed lines) together with the present results and other experimental data. It can be seen that the crack heat transfer depends only weakly upon the value of b/δ and moderately on the friction Reynolds numbers.

d. The temperature records show some very interesting trends. The short duration run, duct number 1T, shows a uniform rise in temperature. For all other runs a periodic behavior is exhibited, or at least suggested by the temperature traces. After a uniform rise of the crack-bottom temperature for a certain time there follows a period where the temperature remains constant for some time, then the temperature rises again at about the initial rate, there may even be a decrease of temperature. This may repeat itself several times during one recording, as seen from the temperature traces of Figure 11. The same periods of temperature rise and constant temperature are not necessarily maintained in two cracks in the same duct. This observation strongly suggests that vortex flow exists in the cracks, with the number of the counter-rotating vortices being some multiple of the crack width.

Then, as ablation progresses, the crack height is reduced and its width increased to a degree that the vortex at the bottom of the crack can no longer be maintained. The lowest vortex breaks up, and the gas becomes more or less stagnant. The bottom temperature then remains constant, or even decreases if the vortex core temperature was lower than that of the outer region, as seen from Figure 11. When the next vortex has reached the bottom, or a reformation of vortex patterns has taken place to fit the changed height and width of the crack, the temperature rises again. If one adopts the results of Reference 5, namely that 30 percent of the heat transferred across the dividing streamline atop of a cavity is transferred at the bottom of the first vortex, and so on, the present results suggest that at the end of the tests two or three vortices existed in the transverse cracks.

SUMMARY AND CONCLUSIONS

Supersonic substructure heating studies were carried out in the NOL 3 Megawatt Arc Tunnel. The purpose was to assist the analysis of the effects of cracks in ablative heat shields on the performance of the vehicle. Teflon TFE-7 was selected as the ablator.

The test conditions were chosen so that the boundary layer in the Teflon duct was predicted to be either all laminar or all turbulent. Transverse and longitudinal cracks in the ducts were instrumented to obtain heating rates at the bottom and side walls of the cracks. In addition, wall-static pressures, in-depth temperatures, and skin-friction data were obtained for the duct itself. Total ablation was evaluated from the wall recession.

The repeatability of test conditions and results was very good.

The non-dimensional heating rate for transverse cracks was found in good agreement with other recent experimental data and the prediction of an unpublished analytical procedure. The temperature records obtained from gauges on the bottom and side walls of the cracks indicate a changing vortex flow in the cracks.

The heating rate and ablation rate at the bottom and downstream walls of one-inch long longitudinal cracks of aspect ratios of 4 and 8 will lead to catastrophic failure of the substructure. There are indications of transverse vortices on the bottom of the longitudinal cracks.

Parallel striations, in the flow direction were observed in the laminar duct and cross-hatched striations in all turbulent ducts. Pressure orifices and cracks have a pronounced effect on the striation pattern and the ablative behavior of the material.

A procedure that combines measured pressure and wall shear data with theoretical chemistry information and a NOL-developed boundary-layer prediction procedure is judged successful in evaluating the surface heating rate for a Teflon surface under a turbulent boundary layer. More complete details may be found in Reference 19.

REFERENCES⁴

- (1) Wieghardt, K., "Increase of the Turbulent Frictional Resistance Caused by Surface Irregularities," translated from Jahrbuch der deutschen Luftfahrt forschung, Vorabdruck 1A 022, 1943
- (2) Tillman, W., "Additional Measurements of the Drag of Surface Irregularities in Turbulent Boundary Layers," NACA TM 1299 (translation) Jan. 1951
- (3) Pan, Frank and Acrivos, Andreas, "Steady Flows in Rectangular Cavities," Journal of Fluid Mechanics, 28, Pt A, 643, 1967
- (4) Fox, Jay, "Heat Transfer and Air Flow in a Transverse Rectangular Notch," International Journal of Heat and Mass Transfer 8 269, 1965
- (5) Haugen, R. L. and Dhanak, A. M., "Heat Transfer in Turbulent Boundary-Layer Separation over a Surface Cavity," Journal of Heat Transfer, Trans. ASME, Vol 89, Series 6, No. 4, 1967
- (6) Nicoll, K. M. and Bogdonoff, S. M., "Experimental Studies of a Specific Cavity Configuration in Laminar Hypersonic Flow," Archiwum Mechaniki Stosowanej 1 16, 1964
- (7) Aerodynamics Department Staff, "The NOL 3 Megawatt Arc Tunnel," NOLTR 66-80, U. S. Naval Ordnance Laboratory, White Oak, Md., Sept. 1966

- (8) Glowacki, W. J., "Fortran IV Program for Calculating the Turbulent Boundary Layer Growth for Contoured Axisymmetric Nozzles Using Air or Nitrogen," (to be published as a NOLTR)
- (9) Bruno, J. R. and Risher, D. B., "Balance for Measuring Skin Friction in the Presence of Ablation," NOLTR 68-163, U. S. Naval Ordnance Laboratory, White Oak, Md., Sept. 1968
- (10) Kendall, R. M. and Bartlett, E. P., "A Procedure for Calculating the Non-Similar, Laminar, Chemically Reacting Boundary Layer over an Ablating Teflon Body with Coupled Quasi-Steady or Transient Wall Boundary Conditions," Aerotherm Final Report No. 68-32, Aerotherm Corp., Palo Alto, Calif., Apr. 1968
- (11) Winkler, E. M., Madden, M. T., Humphrey, R. L., and Koenig, J. A., "Supersonic Ablation Studies with Teflon," NOLTR 69-125, U. S. Naval Ordnance Laboratory, White Oak, Md., Oct. 1969
- (12) Wentrick, T., Jr., "High Temperature Behavior of Teflon," AF BMD-TN-59-15, Research Report No. 55, July 1959
- (13) Gregory, N., Stuart, J. T. and Walker, W. S., "On the Stability of Three-Dimensional Boundary Layers with Application to the Flow Due to a Rotating Disk," Boundary Layer Effects in Aerodynamics, Philosophical Library, Inc., 1957
- (14) Knapp, C. F. and Roache, P. J., "A Combined Visual Transition," AIAA Journal, Vol 6, 29, 1968
- (15) Donaldson, Coleman, D. P. and Dunn, J. R., "Final Report on Flow and Heat Transfer Studies in Transverse Cracks," ARAP Report No. 133 (DASA 2301), June 1969
- (16) Settlege, P. H. and Siegle, J. C., "Keeping Cool with 'Teflon'," an evaluation of "Teflon" TFE resins as heat-barriers in high-speed flight, The Journal of Teflon, Polychemicals Dept., Dupont Co., 1960
- (17) Scala, S. M., "A Study of Hypersonic Ablation," Proceedings of the 10th International Astronautical Congress, Springer-Verlag, Vienna, 1959

- (18) Siegle, J. C. and Muus, U. T., "Pyrolysis of Polytetrafluoroethylene," address to American Chemical Society Meeting, Sept. 1956
- (19) Winkler, E. M., Humphrey, R. L., Koenig, J. A., and Madden, M. T., "Investigation of Substructure Heating on Cracked Ablative Heat Shields," NOLTR 69-122, U. S. Naval Ordnance Laboratory, White Oak, Md., July 1969

TABLE 1
OPERATING CONDITIONS AND INSTRUMENTATION

Duct Number	Mach Number	Supply Pressure MN/m ² (atm)	Supply Temperature °K (°R)	Test Time (sec)	Instrumentation
1T	~2.3	2.09 (20.6)	2400 (4300)	2.7	3 static-pressure orifices 1 longitudinal and 1 transverse crack, each with one heat gauge
2T	~2.3	2.09 (20.6)	2600 (4680)	5.7	1 static-pressure orifice 1 longitudinal crack with three heat gauges 1 transverse crack with one heat gauge
3T	~2.3	2.13 (21)	2400 (4320)	4.2	1 static-pressure orifice 2 transverse cracks, each with one heat gauge
3AT	~2.3	2.13 (21)	2400 (4320)	6.4	2 static-pressure orifices 2 transverse cracks, each with one heat gauge 1 skin-friction balance

TABLE 1 (Cont.)

Duct Number	Mach Number	Supply Pressure MN/m ² (atm)	Supply Temperature °K (°R)	Test Time (sec)	Instrumentation
4T	~2.3	2.89 (28.5)	2405 (4330)	4.4	2 static-pressure orifices 3 transverse cracks, each with one heat gauge
5T	~2.3	2.89 (28.5)	2405 (4330)	4.6	3 static-pressure orifices 3 in-depth thermocouples 1 skin-friction balance, no cracks
5L	3.03	2.23 (22.0)	4200 (7560)	13	6 static-pressure orifices 1 longitudinal and 1 trans- verse crack, each with one heat gauge

TABLE 2
CHARACTERISTICS OF CRACKS

Duct Number	Type of Crack	Height h mm (in.)	Width b mm (in.)	h/b	b/ δ^*	Re τ
1T	transverse	2.92 (0.115)	0.79 (0.031)	3.7	2.16	1200
	longitudinal (1-inch long)	3.38 (0.133)	0.79 (0.031)	4.3	3.86 to 3.35	1900
2T	transverse	5.08 (0.200)	0.79 (0.031)	6.5	2.28	1200
	longitudinal (1-inch long)	5.74 (0.226)	(0.050)	4.5	3.95 to 3.43	1900
3T	transverse	5.59 (0.220)	0.79 (0.031)	7.1	3.96	1600
	transverse	5.59 (0.220)	0.79 (0.031)	7.1	3.35	1850
3AT	transverse	3.15 (0.124)	0.79 (0.031)	4	3.96	1600
	transverse	3.18 (0.125)	0.79 (0.031)	4	3.35	1850

TABLE 2 (Cont.)

Duct Number	Type of Crack	Height h mm (in.)	Width b mm (in.)	h/b	b/ δ^*	Re $_{\tau}$
4T	transverse	3.15 (0.124)	0.76 (0.030)	4.1	2.52	1300
	transverse	10.2 (0.400)	2.54 (0.100)	4	7.13	4000
	transverse	3.15 (0.124)	0.76 (0.030)	4.1	1.88	1200
5L	transverse	6.35 (0.25)	0.79 (0.031)	8.0	1.78	124
	longitudinal (25 mm long) (1-inch long)	6.35 (0.25)	0.79 (0.031)	8.0	3.25 to 5.25	124

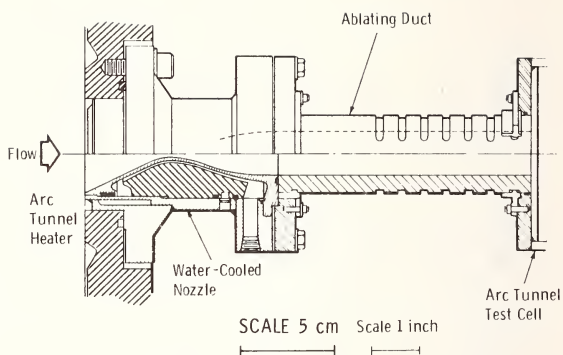


FIG. 1 NOZZLE AND ABLATION DUCT ARRANGEMENT

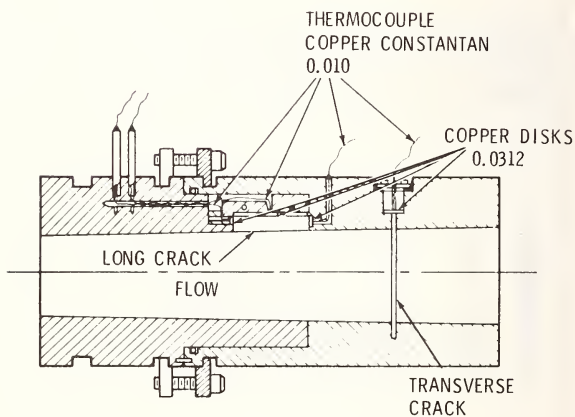


FIG. 2 HEAT GAUGE INSTALLATION IN CRACK



FIG. 3 ABLATION PATTERN IN TEFLON DUCT OBTAINED IN "LAMINAR" RUN

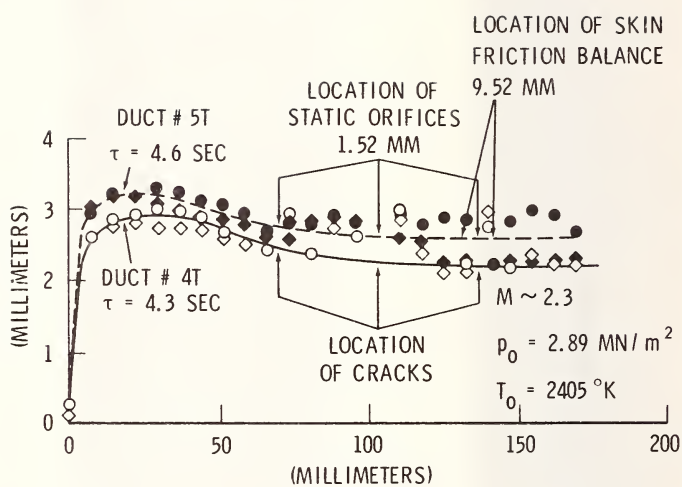


FIG. 4 TOTAL SURFACE RECESSION
 ($\diamond \circ$ MEASURED 180° APART)

FLOW 



FIG. 5 CROSS - HATCHED STRIATION PATTERN

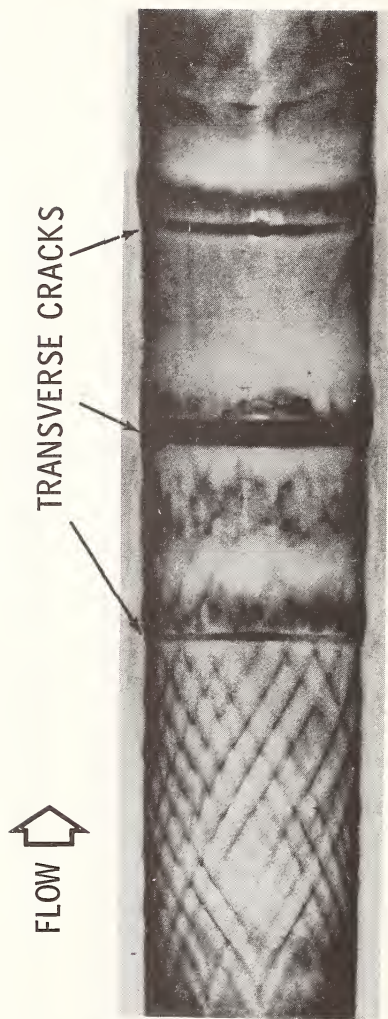


FIG. 6 MODIFICATION OF STRIATION PATTERNS DUE TO TRANSVERSE CRACKS

FLOW 

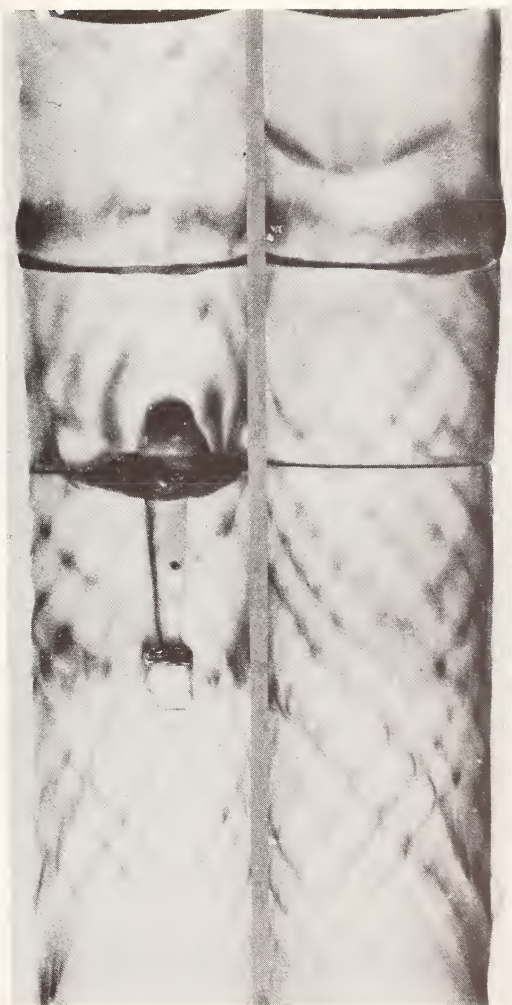


FIG. 7 MODIFICATION OF STRIATION PATTERNS DUE TO A LONGITUDINAL CRACK
(TWO HALVES OF DUCT LAID SIDE BY SIDE)

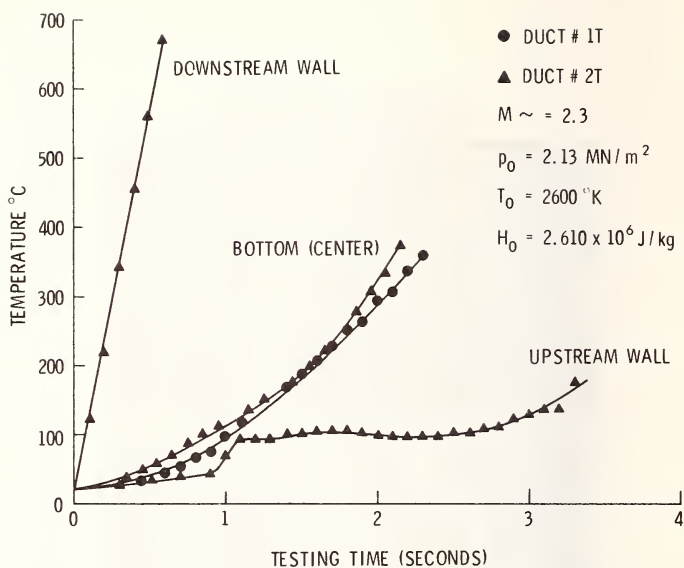


FIG. 8 TEMPERATURE VARIATION FOR LONGITUDINAL CRACK

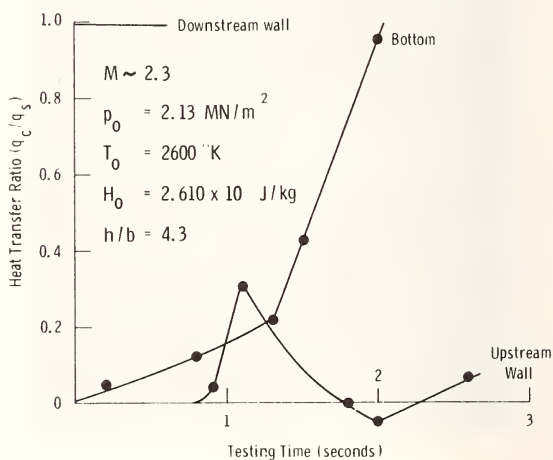


FIG. 9 HEAT TRANSFER TO SIDE WALLS AND BOTTOM OF A LONGITUDINAL CRACK

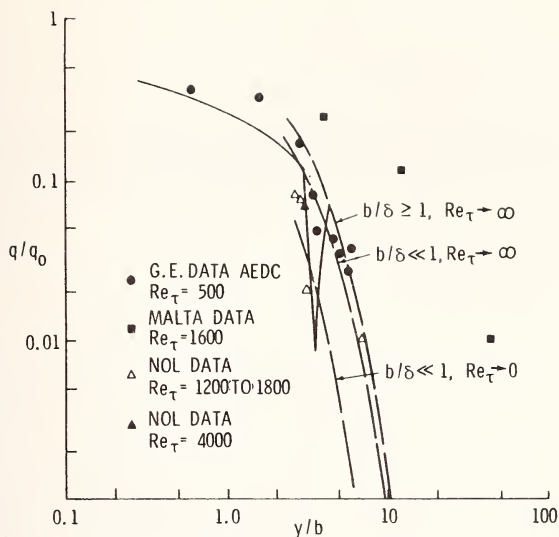


FIG. 10 TRANSVERSE CRACK HEATING SUMMARY

Courtesy of the Aeronautical Research Associates of Princeton.

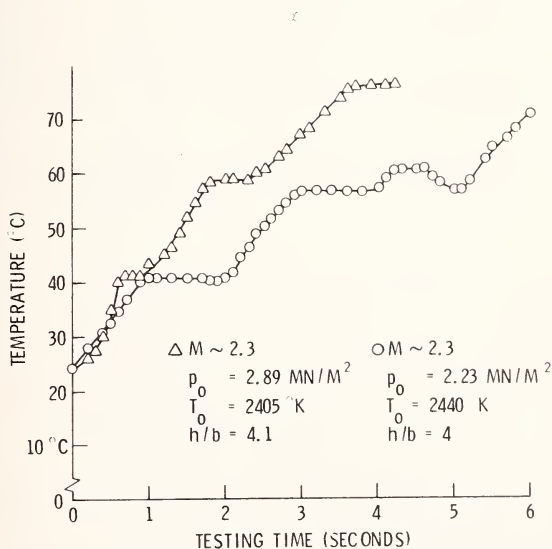


FIG. 11 TEMPERATURE VARIATION IN TRANSVERSE CRACKS

APPARENT OPERATING LIMITS OF ARC HEATERS WITH RESPECT TO TOTAL ENTHALPY AND STAGNATION PRESSURE²

R. Richter¹

REFERENCE: Richter, R., "Apparent Operating Limits of Arc Heaters With Respect to Total Enthalpy and Stagnation Pressure," ASTM/IES/AIAA Space Simulation Conference, 14-16 September 1970.

ABSTRACT: For many years arc heaters have been operated over a wide range of operating conditions. An apparent upper limit with respect to stagnation pressure and total enthalpy was found which could not be exceeded. It is attempted to show that this limit is not imposed by the enthalpy-pressure combination but is caused by the limit in total power input that can be achieved with the non-segmented constricted arc heater. The failure or fast deterioration of arc heater components is found to be primarily due to high arc currents which are employed to heat the gas to maximum temperature. It is concluded that the enthalpy-stagnation limit of nonsegmented constricted arc heaters operating under similar constraints can be exceeded.

KEY WORDS: arc currents, arc heaters, constricted arc, enthalpy, operational limits, stagnation pressure

NOMENCLATURE: C = Constant (Relation (1)); D = Diameter, cm; H = Enthalpy, Btu/lb or joules/kg; I = Current, amps; P = Power, watt; V = Voltage, volt; W = Mass flow rate, g/sec.; T = Temperature, °R; h = Heat transfer coefficient, Btu/sec-°R-ft²; k = Heat conductivity, Btu-ft/sec-°R-ft²; p = Pressure, atm; q = Heat load, Btu/ft²-sec or kW/cm²; t = Wall thickness, inch; σ = Stress, psi

SUBSCRIPTS: A = arc; a = anode; all = allowable; c = constrictor; c = cathode; c = copper; M = melting; T = total; W = water; o = stagnation.

¹Senior Scientist, Electro-Optical Systems, Pasadena, California.

²Work reported in this paper was performed under several NASA and USAF contracts.

Arc heaters have long been employed for chemical processing and reentry simulation because of their capability to raise gases to high temperatures. Presently they are primarily used for testing of heat shield materials for manned and unmanned spacecrafts and missiles under conditions encountered during reentry into the atmosphere of the earth or other planets.

For the simulation of the environment encountered during the reentry phase with respect to heat transfer and fluid dynamics, an arc heater has to heat air at a combination of high enthalpy and stagnation pressure. The approximate operating point of an arc heater for simulating the reentry conditions into the earth atmosphere of a manned spacecraft is 40,000 Btu/lb at a stagnation pressure of 1 atm, while that for simulating the reentry conditions of a missile is about 4,000 Btu/lb at a stagnation pressure of 200 atm. The operating conditions for the manned spacecraft have now been achieved, while attempts are still under way to reach the operating conditions needed for the simulation of the reentry conditions of missiles. The obtainment of the desired conditions is apparently subject to limitations. Figure 1 shows the apparent operating limits of arc heaters with respect to stagnation pressure and total enthalpy as they have been experienced by many investigators. It is therefore of great interest to find the physical limits for reaching, with arc heaters, the desired total enthalpy at a given stagnation pressure as well as to determine the operating parameters that set these limits.

The limit to the achievable enthalpy at a given stagnation pressure appeared primarily to be determined by the structural integrity of the arc heater components. In attempts to raise the total enthalpy at a given operating pressure, failures of the electrodes and/or of the containment walls would occur. Failures of the electrodes would be attributed to exceeding the average local heat load on an electrode surface which is a function of the total arc current, the operating pressure, and the attachment point velocity over the surface. The failure of the containment walls could be attributed to stray arc attachments and/or local over-heating.

During the development of several arc heaters and in the course of a special Air Force supported program, a better understanding of the apparent operating limits for arc heaters has been generated. A substantial amount of experimental data was obtained which permitted some correlations of the most important parameters. But as had been found previously by many other investigators, the number of operating parameters in arc heaters is fairly large and their inter-relation rather complex. The main parameters appear to be:

1. Arc Current
2. Operating Pressure
3. Mass Flow Rate
4. Constrictor Design

- a. Diameter
- b. Length
- c. Wall Thickness
- d. Cooling
- 5. Electrode Design
 - a. Magnetically Forced Arc Movement
 - b. Magnetic Field Strength
 - c. Gas Induced Arc Movement
 - d. Vortex Strength
- 6. Electrode Separation
- 7. Gas Properties as Function of Pressure and Temperature
 - a. Radiation
 - b. Electrical Conductivity
 - c. Thermal Conductivity
 - d. Viscosity
 - e. Absorptivity

The possible number of permutations between these parameters is so large that it would be unrealistic to hope for establishing absolute operating limits of arc heaters by an experimental process of elimination. Some form of analysis has therefore to be developed but whose basic assumptions are well supported by a broad experimental background.

The first attempts in that direction have been made by a new analysis of the arc heating process in arc heaters. This analysis still requires some additional refinements and extensions, though it already permits the evaluation and design of constricted arc heaters over an operating regime in which absorption of radiation has no major influence. The author has primarily worked with constricted arc heaters. However, many of the results that will be discussed are applicable to all arc devices, radiation sources included.

Many attempts have been made to analyse the heating process in arc heaters, primarily of constricted arc heaters (Refs. 1,2,3, and 4). These analyses did not predict too well the experimentally obtained results of the author. The author feels that the main reason for the discrepancies between analytical predictions and test data is the inconsistency between the model underlying the analyses and the actual processes taking place in the constrictor. Many investigators, for instance, have based their analysis on the laminar flow through a smooth tube (Refs. 1 and 4). This condition is rarely encountered in a segmented constrictor which has been the type of arc heater investigated by the author. Furthermore, most analyses assumed the flow as well as the arc to develop in a continuous process along the constrictor (Ref. 1). The results of these analyses predict the heat transfer to the constrictor wall to be primarily determined by the local total enthalpy of the gas

The numbers in parentheses refer to the list of references appended to this paper.

which increases along the constrictor. This, however, was not borne out by our test data and therefore a different analytical approach appeared to be indicated.

The author approached the analysis of the very complicated arc heating process by synthesizing the various physical processes which apparently take place in the constrictor of an arc heater. These processes are individually analyzed and then combined by demanding an overall energy balance as well as stipulating an arc operation with minimum entropy rise. The complete analysis will be presented at a later date in a separate paper.

The main difficulty in applying the synthesized analysis to test data and/or the design of arc heaters lies in the inavailability of fully substantiated material properties for the various gases. The author employed primarily the thermal conductivity, radiation, electrical conductivity, and viscosity data of Ref. 5. With these material properties for nitrogen, fairly good agreement between test data and calculated heat transfer rates and electric fields were obtained over a very wide range of operating conditions, i.e., from less than 1 atm to 97 atm. The analysis was also applied to data reported in the literature. A good agreement with measured arc diameters of an arc operating in a cross flow was found (Ref. 6). The largest variations between test data and calculated values was about 20 percent. This discrepancy is quite acceptable considering not only the uncertainties associated with the measurement of absolute local heat transfer rates and electric fields in arc heaters but also the uncertainty in the materials properties used.

Two types of constricted arc heater designs have to be distinguished. In one type of design the electric arc operates with what the author will call a "natural" arc length, while in the other type of design the arc length is determined by the distance between the two electrodes. These two types of heaters are illustrated in Figure 2. Many variations for each type of heater are possible, though the basic design must be considered unalterable. It is also possible that in both types of arc heaters the polarity of the two electrodes might have an influence but it will become clear from the future discussions that such influence must be minor and can be included into the overall picture of arc heater operation.

In the first type of arc heaters which is shown schematically in Figure 2a, the natural arc length appears to be a function of all major operating parameters, i.e., mass flow rate, operating pressure, arc current, and gas, as well as the arc heater component configuration and the magnetic field strength, if a magnetic field is employed for the control of the arc. When correlating a substantial number of experimental

The numbers in parentheses refer to the list of references appended to this paper.

data of non-segmented constricted arc heaters (Refs. 7 and 8), an interesting relation between the major parameters appears to be applicable. This relation could be best expressed by

$$V_T = \frac{C \times \dot{W}^m}{I_A^n \times p_o^l \times D_c^x} \quad (1)$$

The exponents of the parameters were found to be

$$\begin{array}{ll} m = 0.835 & n = 0.267 \\ l = 0.129 & x = 1.34 \end{array}$$

and the constant for air, $C = 1617$.

Naturally this relation cannot be justified in the strictest sense of an analysis as it is well known that the total voltage is the sum of several individual voltage drops, all of which are dependent on the operating parameters in a different way, i.e.,

$$V_T = V_a + V_c + V_A \quad (2)$$

In most cases the arc voltage is very much larger than the sum of the electrode voltages. This is especially true for high power, high pressure arc heaters.

But, nevertheless, the relation as it stands conveys the interesting effects of the most important parameters on the total voltage. The total voltage-arc current characteristic shows a negative slope with a power of approximately 0.267. This slope prevails at current levels at which investigators of stationary arcs have observed arc operation with a positive slope. The negative slope of nonsegmented arc heaters has therefore to be attributed to a shortening of the arc length with increasing arc current. This deduction is further substantiated by the positive voltage current characteristics of arc heaters which do not permit the arc to shorten itself (Refs. 9 and 10). If the total voltage is divided by the electric field which was found to be also a function of the major operating parameters, the effect of the major operating parameters on the arc length would be expressed.

When multiplying the total voltage by the arc current, relation (1) leads to a relation between the major operating parameters and total input power

$$P_T = V_T I_A \quad (3)$$

The numbers in parentheses refer to the list of references appended to this paper.

$$P_T = \frac{C \dot{W}^m I_A^{1-n}}{P_O^\ell D_C^x} \quad (4)$$

From this relation it is seen that the total input power, P_T , is primarily a function of the arc current, the main flow rate, the operating pressure, and the constrictor diameter. The mass flow rate and the constrictor diameter have a strong influence in contrast to the relatively weak influence of the operating pressure. The medium influence of the arc current on the total power input was always quite obvious by the negative slope of the voltage-current characteristic of such heaters. But the most important aspect of this relation is the influence of the mass flow rate, \dot{W} , on the total power input. The relation points out quite clearly that if a current limit exists, then there exists also an enthalpy limit. Because the mass averaged total enthalpy is a fraction of the total input power divided by the mass flow rate, the fraction being the efficiency, η ,

$$H_T = \eta \frac{V_T I_A}{\dot{W}} \quad (5)$$

or

$$H_T = \frac{\eta C I_A^{1-n}}{D_C^x P_O^\ell \dot{W}^{1-m}} \quad (6)$$

The efficiency was found to be a strong function of the arc current. If we set as a first approximation

$$\eta \sim I^{-z}$$

where the value for z is found to vary between 0.12 and 0.35, the enthalpy, H_T , is given by

$$H_T = \frac{C' I^{1-n-z}}{D_C^x P_O^\ell \dot{W}^{1-m}} \quad (7)$$

The exponent $1-n-z$ is very much less than 1. For that reason we find that for a given arc heater configuration a limit to the achievable total enthalpy at a given pressure exists regardless of arc current.

The important results of this exercise are the following:

1. The arc heater does not have an operating limit that is determined by the total enthalpy of the gas. Quite the opposite, the enthalpy limit is determined by the arc heater.

2. An enthalpy limit is established by the total electric power input for a given gas flow rate and arc heater configuration, as indicated by the strong influence of the constrictor diameter and the mass flow rate on the total voltage.

Relation (7) seems to indicate that the total enthalpy at a given pressure could be increased by decreasing the constrictor diameter, D_c . This is indeed possible. But, when decreasing the constrictor diameter, a new limit is being approached.

When a segmented constricted arc heater was operated over a wide range of operating conditions, heat transfer rates to the constrictor wall could be measured under various operating conditions. In Figure 3 the heat loads on a constrictor when operating with a stagnation pressure of around 1 atm are shown (Ref. 9) while in Figure 4 heat transfer rates for a second constrictor operating at stagnation pressures ranging from 38 atm to 51 atm are shown (Ref. 10). It can be seen in both figures that the heat transfer rates are almost constant over the entire length of the constrictor. This result seems to indicate that the heat loads under the conditions under which the heaters were operated are predominantly a function of the arc current. Some arc devices were tested under conditions and with constrictor configurations for which this was not at all the case (Ref. 9). Under some conditions it could be clearly shown that the measured heat transfer rates were the sum of two heat transfer processes; one as shown in Figures 3 and 4 was almost constant along the constrictor, the other was directly proportional to the local mass averaged total enthalpy. But those were cases which the author does not consider applicable to the present discussion. In Figure 5, calculated heat loads for various arc currents and constrictor diameters are shown. Experimental correlations between local heat transfer rates and constrictor diameters are not available as it was not possible to build a representative number of segmented constrictors of different diameters. Since good agreement was found between measured and calculated heat transfer rates, the use of analytical values can be justified. These correlations show that the heat load increases quite rapidly with decreasing constrictor diameter and that, therefore, a limit exists to how small a constrictor diameter can be made.

This limit to the permissible heat load cannot be a simple one. It is determined by the operating pressure as well as the yield strength at elevated temperature of the material of which the constrictor is built. For any given heat load the wall thickness of a container under pressure has two limits, one limit is set by the maximum allowable temperature of the material; the other limit by the tensile or compressive strength of the material as a function of the effective temperature. If

The numbers in parentheses refer to the list of references appended to this paper.

the allowable temperature is the melting temperature, T_m , then the maximum wall thickness as a function of heat load is given by

$$t = k \left(\frac{T_m + T_w}{\dot{q}} - \frac{1}{h} \right) \quad (8)$$

For simplicity, a thin wall tube is being considered. When the same assumption is applied to the stress consideration, the relation between pressure and wall thickness is given by

$$t = \frac{\Delta p D_c}{2 \sigma_{all}} \quad (9)$$

Elimination of the wall thickness t between relations 8 and 9 produces the following limit

$$\dot{q}_{all} = k (T_m + T_w) / \left(\frac{\Delta p D_c}{2 \sigma_{all}} + \frac{k}{h} \right) \quad (10)$$

This relation has been plotted for copper into Figure 5. The combined results show clearly the constraint on the size of the constrictor diameter.

SUMMARY

The preceding discussion has attempted to explain the observed stagnation pressure - total enthalpy limit of nonsegmented constricted arc heaters by the rather complex relations between the major operating parameters and the physical dimensions of the arc device. When expanding the experimentally determined relation between total voltage, constrictor diameter, arc current, mass flow rate and stagnation pressure it is realized that the apparent enthalpy limit that was found experimentally with such heaters is effectively a design limit. The destruction of heater components is not at all caused by the stagnation pressure-total enthalpy combination. The destruction or excessive deterioration of components has to be attributed to the high arc current which is employed in an unsuccessful attempt to overcome the basic limit on the total power input imposed by the heater design. The stagnation pressure - total enthalpy limit has been exceeded by the use of a segmented constrictor which makes the arc length independent of the stagnation pressure, the mass flow rate, and the constrictor diameter. Arc heaters with segmented constrictors are subject to new limits whose dependence on the major parameters are not included in this discussion.

REFERENCES

1. Stine, H. A. and Watson, V. R., "The Theoretical Enthalpy Distribution of Air in Steady Flow Along the Axis of a Direct-Current Electric Arc," NASA TN D-1331 (1962).
2. Stine, H. A., Watson, V. R., and Shepard, C. E., "Effect of Axial Flow on the Behavior of the Wall-Constricted Arc," NASA TM X-54,065, presented to the AGARD Specialists' Meeting on Arc Heaters and MHD Accelerators for Aerodynamic Purposes, Rhode-Saint-Genese, Belgium, September 21-23, 1964.
3. Weber, H. E., "Growth of an Arc Column in Flow and Pressure Fields," AGARD Specialist Meeting on Arc Heaters and MHD Accelerators for Aerodynamic Purposes, Rhodes-Saint-Genese, Belgium, September 1964, (Published as AGARDograph No. 84, pp 845-881).
4. Skifstad, J. G. and Murthy, S. N. B., "Analysis of Arc-Heating Phenomena in a Tube," International Symposium on Plasma Phenomena and Measurements, IEEE-PTGNS, Tenth Anniversary Meeting, San Diego, California, October 29 - November 1, 1963 (IEEE Transaction on Nuclear Science, January 1964, Pg. 92).
5. Yos, J. M., "Transport Properties of Nitrogen, Hydrogen, Oxygen and Air to 30,000°K," AVCO Tech. Memo RAD-TM-03-7, 22 March 1963.
6. Roman, W. C., and Myers, T. W., "Investigation of Electric Arc Interaction with Aerodynamic and Magnetic Fields," ARL Report 66-0191, October 1966.
7. Eschenbach, Richard C., Skinner, G. M., and Arc Laboratory Staff, "Development of Stable, High Power, High Pressure Arc Air Heaters for a Hypersonic Wind Tunnel," WADD Technical Report 61-100 ASTIA AD No. 266 907 (July 1961).
8. Brown, St. George, and Patton, J. B., "Calibration and Operation of the Linde Model N4000 Arc Heater with 1/2- and 3/8-inch-Diameter Constrictors," AEDC-TR-65-102, June 1965.
9. Richter, R., and Buhler, R. D., "High Enthalpy Gas Heater," Final Report Contract No. NAS9-3564 (December 1965).
10. Richter, R., "Ultrahigh Pressure Arc Heater Studies," AEDC Report No. AEDC-TR-69-180 (September 1969).

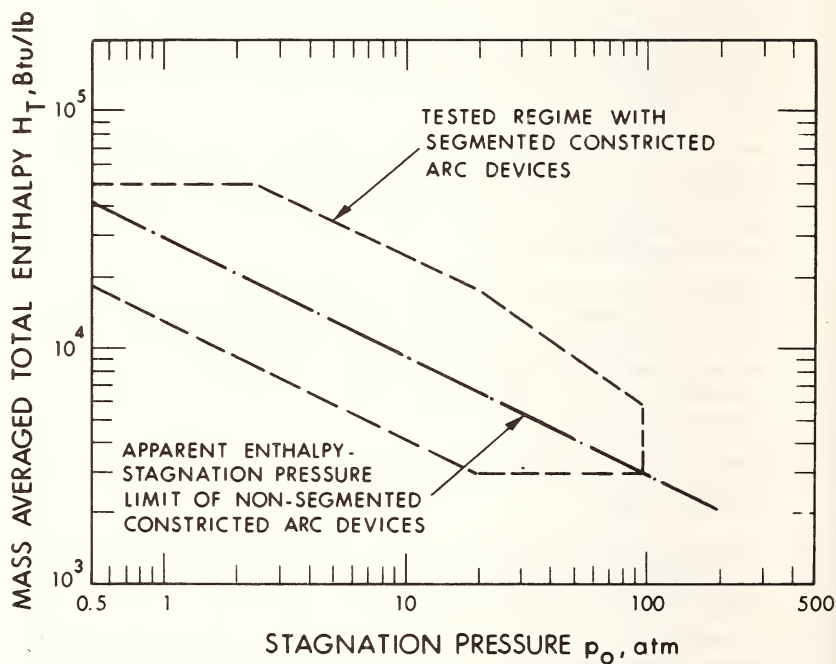
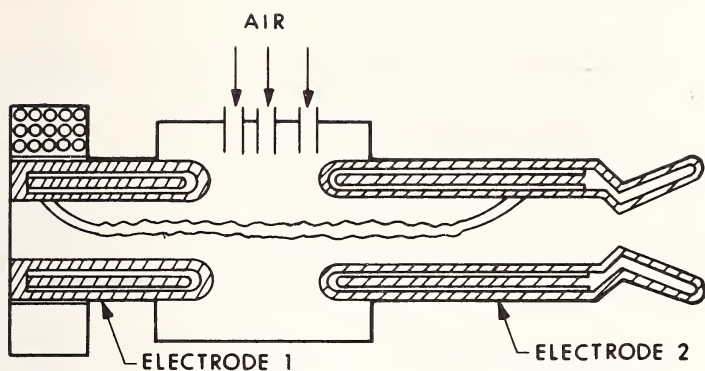
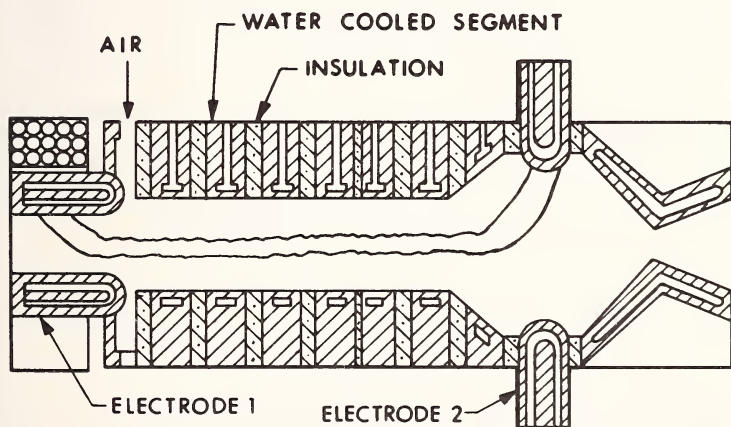


Fig. 1--Experimentally established operating regimes of constricted arc heaters.



a. NONSEGMENTED CONSTRICTED ARC HEATER CONFIGURATION



b. SEGMENTED CONSTRICTED ARC HEATER CONFIGURATION

Fig. 2--Two basic types of constricted arc heater configurations.

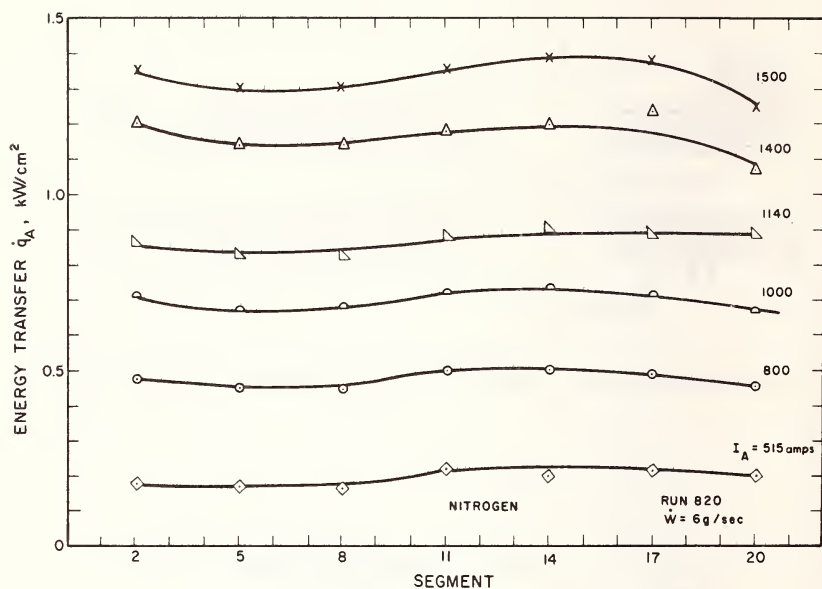


Fig. 3--Measured heat transfer rates along the constrictor of a low pressure arc heater (≈ 1 atm).

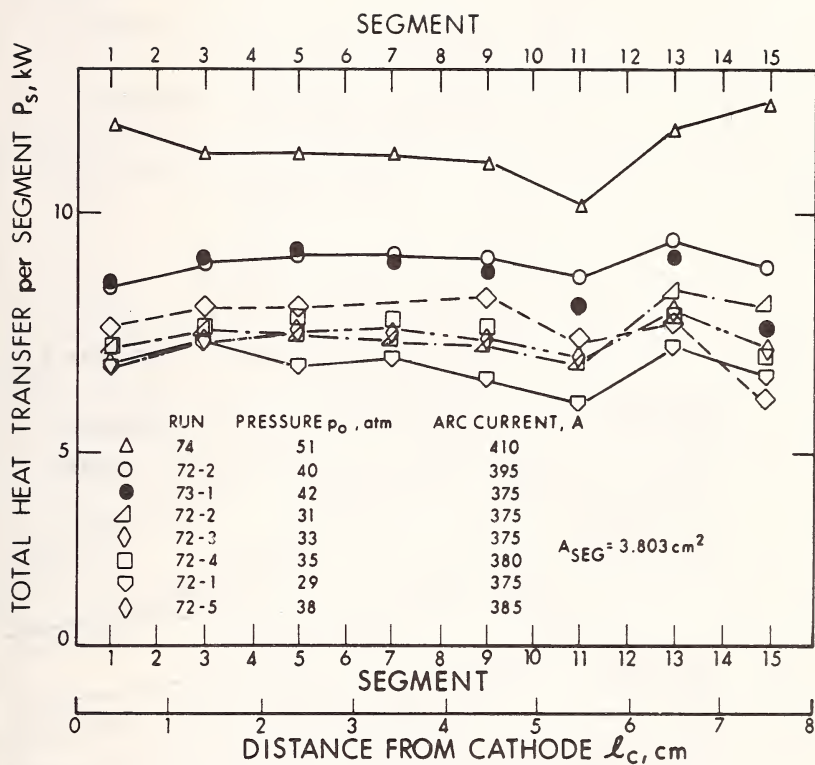


Fig. 4--Heat transfer rates along the constrictor of a high pressure arc heater.

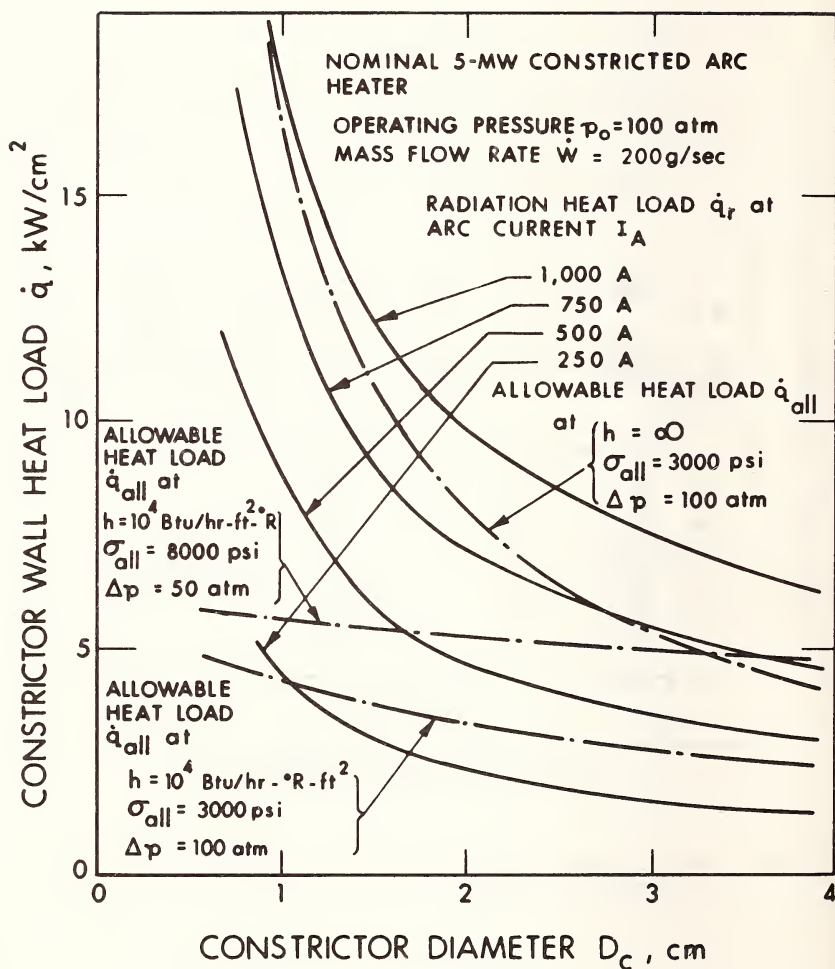


Fig. 5--The effect of constrictor diameter on the maximum heat load and the allowable heat load.

OPERATING CHARACTERISTICS OF THE AIR FORCE FLIGHT
DYNAMICS LABORATORY REENTRY NOSE TIP (RENT)
FACILITY

J. C. Beachler

Research Aerospace Engineer, Air Force Flight
Dynamics Laboratory, Wright-Patterson AFB, Ohio

ABSTRACT: Reentry missile nose tip development requires ground test facilities capable of simultaneously producing extreme pressures and heat transfer rates. The Reentry Nose Tip (RENT) Facility was developed by the Air Force Flight Dynamics Laboratory to produce this high pressure hyper-thermal environment. The present and planned capability of this facility is described and typical pressure and heat transfer profiles of the test jet are shown.

KEY WORDS: reentry, test facility, heat protection, ballistic missiles

The continuing requirement for higher performance ballistic reentry vehicles has placed greatly increased demands on thermal protection techniques. Improved ablation materials and several new heat protection methods have been brought to bear on the problem.

These programs have required extensive ground and flight test efforts to screen and develop better materials and methods for heat protection. The

Reentry Nose Tip (RENT) Facility was recently developed by the Air Force Flight Dynamics Laboratory to extend the nation's ground test capability for thermal protection system evaluation.

Facility Description and Performance

The RENT Facility is a high pressure high power arc heated continuous supersonic wind tunnel which produces a high pressure high shear test environment with stagnation temperatures up to $14,000^{\circ}\text{R}$. Figure 1. is a schematic of the facility.

The primary component of the Facility is its high pressure high voltage arc heater which heats up to 8 lbm/sec of high pressure air to stagnation enthalpies of 6400 Btu/lbm at 125 atmospheres pressure using 37 megawatts of electrical power. This air is expanded from a .900 inch throat to Mach 1.8 at the nozzle exit. A cross section view of the heater is shown in Figure 2.

The test models are injected to the arc jet centerline at a station .100 inches downstream of the nozzle exit plane by a hydraulically actuated linear drive system capable of producing model speeds from 4 to 150 inches per second. The model carriage drives 5 models and/or probe struts through the test jet in either a sweep or sweep-pause mode. This system produces up to 7g decelerations as it stops the model in the test flow.

The RENT exhaust system consists of a collector cone 18 inches downstream of the nozzle exit followed by a water-spray-cooled 18 inch diameter duct leading to a 7 foot diameter centrifugal water separator and a 40 foot long vertical exhaust stack.

The operating range of the facility was determined in a series of tests conducted in mid-1969. A typical operating characteristic for 2400 amps current and a nozzle throat diameter of .900 inches is shown in Figure 3. The DC power to the arc heater is determined by monitoring the operating voltage and current. The air mass flow rate is measured with a subsonic venturi located upstream of the heater. The air pressure in the heater was measured at the outside wall of the swirl chamber and at the center of the rear electrode as indicated in Figure 2. Based on References 1-3 the rear electrode pressure (P_{OR}) is considered to be the most representative heater stagnation pressure. The flow rates and the temperature rise of the heater cooling

water were used to determine the energy loss to the heater for calculation of the heater efficiency and heat balance enthalpy:

$$H_o = [EI - (\dot{w} C_p \Delta T)_{H_2O}] / \dot{w}_{air}$$

Since the heat balance or bulk enthalpy is an average measurement, it is typically not a true test jet centerline value due to the use of highly cooled nozzle and front electrode walls and the centrifuging action of the arc stabilizing vortex which tends to concentrate the hot, less dense plasma near the centerline of the heater. However, since accurate direct measuring total enthalpy and heat flux probes are beyond present technology for the conditions of these tests, the data is presented using the heat balance values of H_o . A summary of facility performance is shown in terms of arc heater stagnation pressure and heat balance total enthalpy in Figure 4.

Typical radial impact pressure profiles taken with graphitic probes for nominal Mach 1.8 conical, flared and contoured nozzles are shown in Figure 5. The maximum heater pressure (P_{OR}) of 125 atmospheres produces a model stagnation pressure of about 100 atmospheres at a station 0.100 inches downstream of the nozzle exit. Radial and axial pressure surveys have been made with both conical and flared expansion contours on $d^* = 1.00$ and 0.900 inch nozzle throats. Reference 4 discusses the performance and relative merits of each of these nozzles for high shear testing.

A characteristic stagnation point heating rate profile taken with null point calorimeters in the contoured nozzle at 100 atmospheres heater pressure is shown in Figure 6. The ratio between centerline and intermediate plateaus of heating rate is approximately 2:1. The centerline H_o estimated for laminar heating is 6000 Btu/lbm which is about 2.5 times the heat balance value.

Pressure and temperature measurements were made to determine the mass handling and cooling system performance of the RENT Exhaust System. Facility operation demonstrated that it had adequate cooling and mass handling capacity at maximum heater operating conditions. With an arc heater mass flow of 6.5 lb/sec an additional 24 lb/sec of air is entrained through the exhaust system by the test jet.

Acoustic levels of up to 163 dbm with a frequency peak at 1000 Hertz were observed with a microphone at the exhaust collector cone. Since the facility is enclosed by concrete and an acoustic barrier, this sound level caused no damage to equipment and all operational personnel were safe without ear protection at their normal work stations. Power spectral density analyses indicated the sound was generated at the free jet boundary.

High speed photography, high speed digital data and pyrometer measurements are normally used for analysis of ablation tests conducted in the RENT Facility.

Arc Heater Performance

The general operating characteristics of the $N=4^1$ heater with 1.00 inch and 2.00 inch nozzle throats are described in Reference 2. However, the high shear tests in the RENT required extending the pressure capability to the limit of a new less restrictive air supply system and improving heater enthalpy at all conditions.

Tests were made with a 96 inch front electrode to determine the maximum P_{OR} attainable without blowing the arc through the heater nozzle throat. An extended pressure range is available when a front field coil is used to hold the downstream arc termination in the heater. The data in Figure 3 represents the maximum achievable P_{OR} with the 0.900 inch nozzle throat as limited by the existing air supply capacity.

A front electrode burnout problem previously thought to be a radiation heating performance limit (Reference 2) was found to be a backside cooling problem and has been remedied by redesign of the cooling passage. Cooling water velocities have been raised from 80 to 120 ft/sec to prevent film boiling on the electrode.

A test series was run with a 96 inch front electrode to determine the maximum attainable enthalpy at heater pressures corresponding to a model stagnation pressure of 60 atmospheres. Since the impact pressure at the model test station was about 77% of P_{OR} , the tests were conducted at a heater stagnation pressure of 1100 psia. The heater enthalpy increased with increasing arc current up to the 5400 amp level where front electrode erosion at

¹ Heater scale factor described in Reference 3.

the arc termination became excessive. Improvements in front electrode cooling permitted extending the operable arc current from 2800 to 5400 amps at this pressure. All figures are shown with H_0 from heat balance.

Summary and Future Plans

The pressure capability of the AFFDL N=4 arc heater has been extended to 123 atmospheres at 37 MW through improved front electrode cooling, the use of a front spin coil and improvements in the air supply system. The current capacity of the heater has also been extended from 2800 to 5400 amps at 75 atmospheres through improved electrode cooling.

Facility operation at maximum heater conditions has demonstrated the adequacy of the RENT exhaust and model injection systems and shown that sound levels produced by the test jet are acceptable.

Pressure and heat flux surveys of the test jet with conical and flared nozzles and ablation tests for AF Materials Laboratory have demonstrated the quality and steadiness of the test flow. Use of a front spin coil has also precluded the possibility of arcing to the test models and assisted in producing uniform pressure profiles with fluctuations of less than $\pm 5\%$ in jet impact pressures. Test flows appear very clean and axisymmetric.

The RENT Facility is operational and has been routinely performing ablation tests for the Air Force Materials Laboratory and the Air Force Space and Missile Systems Organization.

Future plans include extending the operating pressure of the N=4 heater to 140 atmospheres, design and development of a 200 atmosphere heater and increasing the heater power supply capacity.

REFERENCES

1. R. T. Smith and W. A. Kachel, "Design and Performance of a Small (8-Megawatt) Arc Heater for the AFFDL 50 Megawatt Hypersonic Facility," AFFDL-TR-68-17, February 1968.
2. R. T. Smith and J. L. Folck, "Operating Characteristics of a Multi-Megawatt Arc Heater Used with the Air Force Flight Dynamics Laboratory 50 Megawatt Facility," AFFDL-TR-69-6, April 1969.
3. R. C. Eschenbach and G. M. Skinner, "Development of Stable High Power, High Pressure Arc Air Heaters for a Hypersonic Wind Tunnel," WADD-TR-61-100, Linde Company, Indianapolis, Indiana, July 1961.
4. F.J.A. Huber, "A Tailored Plume Nozzle for Testing Fast Reentering Missile Nose Tips," Paper to be Presented at AIAA 6th Aerodynamic Testing Conference, March 1971.

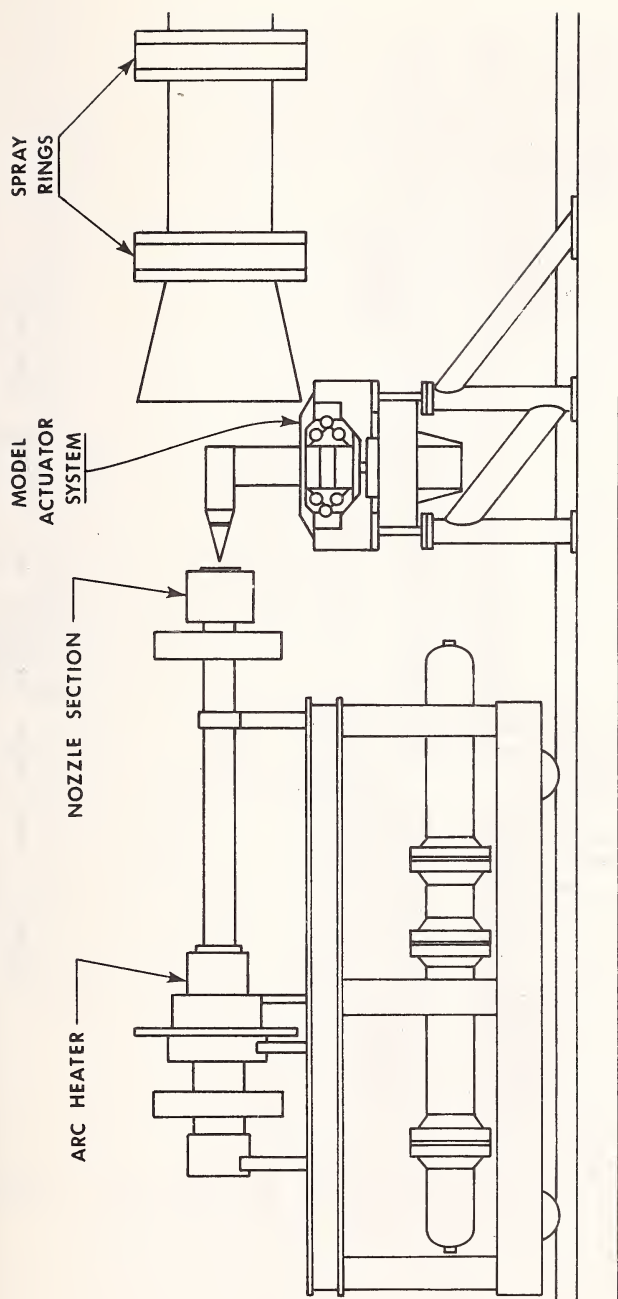


FIGURE 1 RENT FACILITY SCHEMATIC

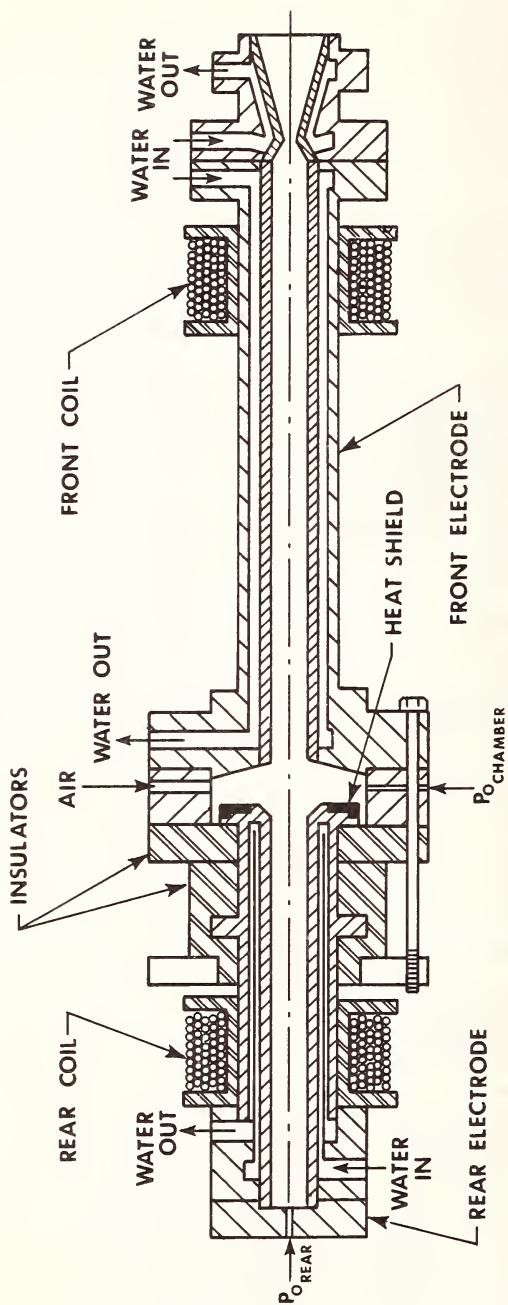


FIGURE 2 N=4 HIGH PRESSURE ARC HEATER SCHEMATIC

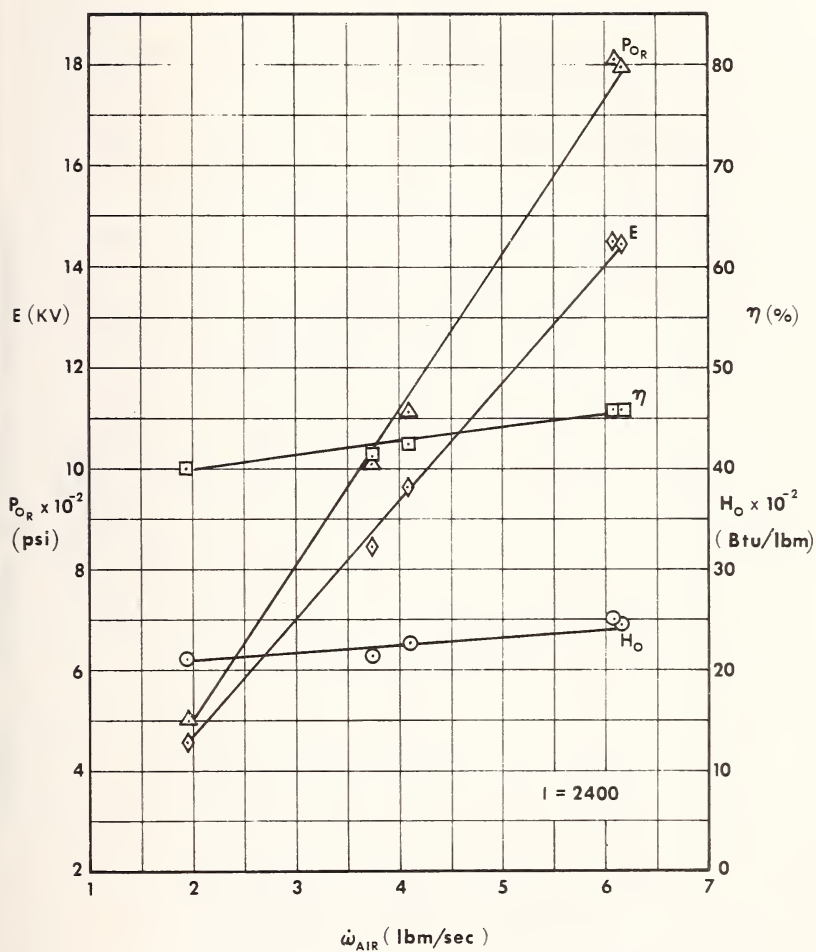
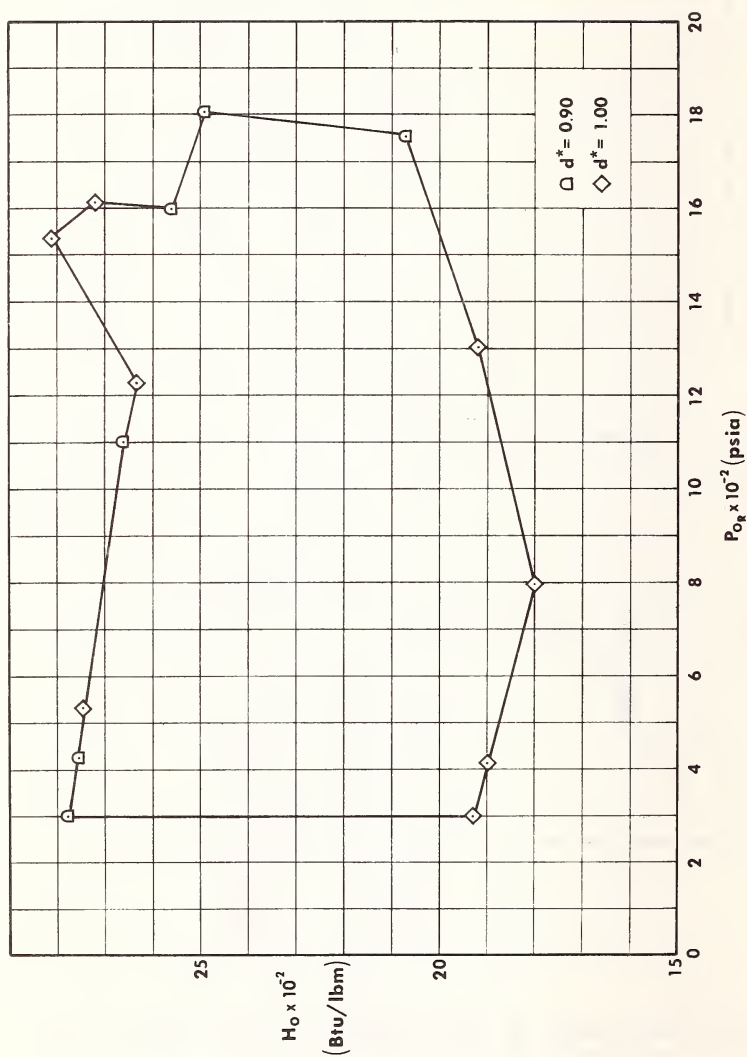
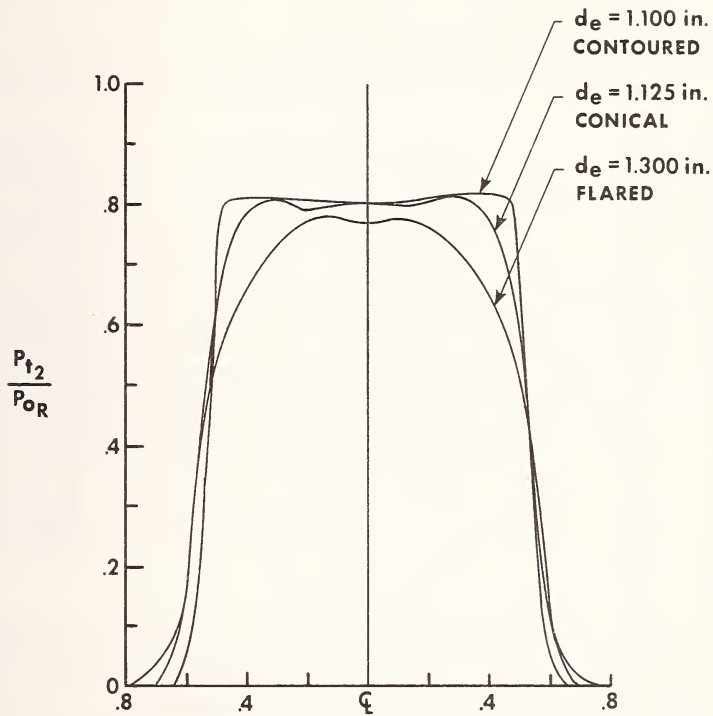


FIGURE 3 N=4 OPERATING CHARACTERISTICS, $d^* = .900$, 96 INCH FRONT ELECTRODE, WITH FRONT COIL

FIGURE 4 SUMMARY OF FACILITY PERFORMANCE



$P_{OR} = 1500 \text{ psi}$
 $I_{ARC} = 2600 \text{ A}$
 $d^* = 0.900 \text{ in.}$



RADIAL DISTANCE FROM NOZZLE ζ , inches

Axial Station 0.100 from Exit Plane

FIGURE 5 IMPACT PRESSURE
 PROFILES OF RENT NOZZLES

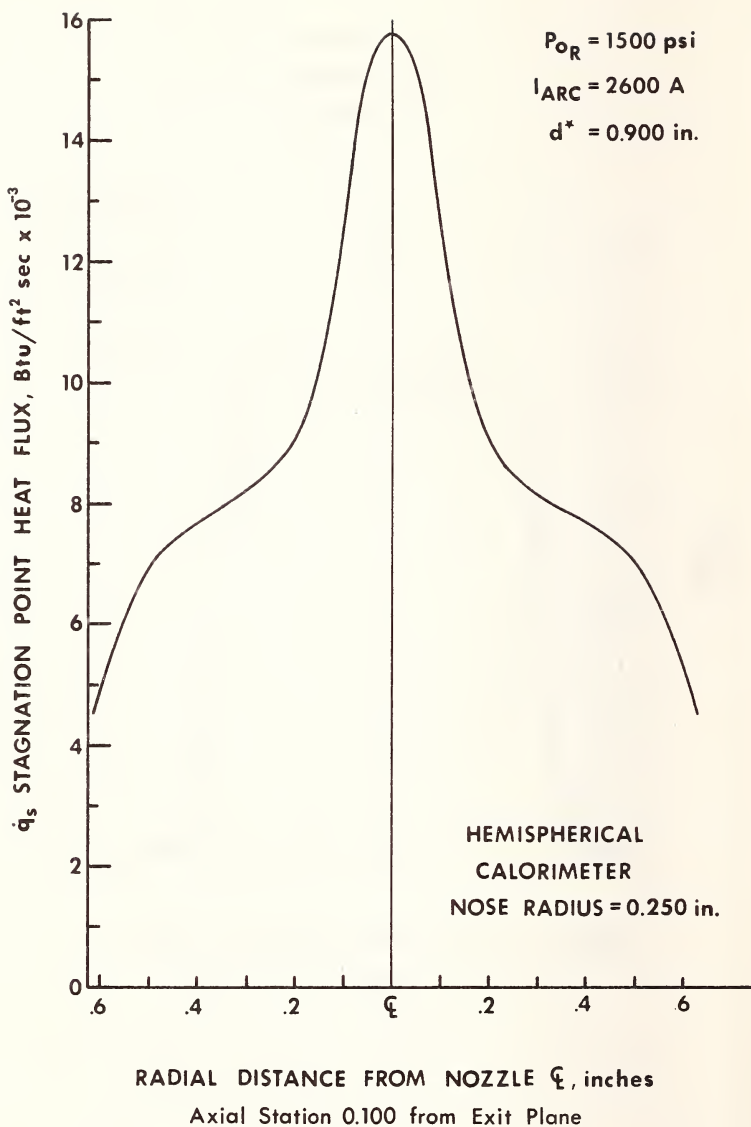


FIGURE 6 HEAT FLUX PROFILE
OF CONTOURED RENT NOZZLE

INVESTIGATION OF THE CHARACTERISTICS
OF FLUIDS VENTED INTO A VACUUM

Riddle Steddum,¹ Dupree Maples,¹ and Frank M. Donovan ¹

ABSTRACT: For manned space stations planned for the future, it becomes necessary to eject fluids into the space environment. These ejected fluids form ice clouds which remain in the vicinity of the spacecraft and could interfere with optical instrumentation. In order to study the dynamics of fluid jets in a space environment, a high vacuum system was modified to allow the injection of fluids into a vacuum region while maintaining a pressure below 0.1 N/m^2 . The cone angles, individual particle velocities, and mass flow rates of water sprays under vacuum conditions were measured. The individual particle velocities of sprays produced by outgassed water were lower than the particle velocities of sprays produced by water with a definite amount of dissolved gas.

KEY WORDS: vacuum tests, particle velocities, flow rate tests, high speed movies, water jet

INTRODUCTION: During long duration space missions liquid wastes must be ejected from spacecrafts. The behavior of liquids in a space environment becomes important because the possibility exists that the ice particles formed from ejected liquids could interfere with optical instrumentation.

Major characteristics of jets produced by ejecting fluids into a space environment which should be investigated are the total included cone angle of the spray; the velocities of individual particles within the spray; the size, shape, and distribution of particles; the state of the particles, i.e., whether they are liquid or solid; and the total volume flow rate. The above characteristics are functions of at least two important general parameters: the nature of the ejected fluid - its chemical and physical composition and its thermodynamic

¹Louisiana State University, Baton Rouge, Louisiana

properties; and the physics of the injection process - orifice size and geometry and injection pressure and temperature.

Some previous investigations of this problem include a study presenting both theoretical and experimental work by Simmons, et al of the Atlantic Research Corporation (1)*. The experimental program included static tests where bulk samples of liquid were suddenly exposed to vacuum, orifice and gasket leak tests, and vent line tests. Some work was done to determine individual particle size and velocity by using still photographs. Other work includes that done at the Boeing Company by Dawley (2). This investigation had three stated objectives: to confirm that there exists a problem of flow stoppage due to freezing; to determine the effects of flow rates, water temperature, and initial nozzle tip temperature on nozzle performance; and to record the ice formations photographically. A report by B. L. Mann and O. T. Stoll (3) also deals primarily with the problem of flow stoppage due to freezing. Jet dynamics were not considered. In the Journal of Spacecraft and Rockets, Mikatarin and Anderson (4) report studying liquid jets expelled into a vacuum, but could not obtain particle velocity measurements. A report by the Brown Engineering Company's Research Laboratories (5) considers work which has been done to determine the drop sizes which form from jets and the expected life times of ice spheres in a space environment as a function of radius.

This investigation has been directed toward the study of cone angles and individual particle velocities of water jets under vacuum conditions. Sprays produced by distilled, out-gassed water were compared to sprays produced by water with a known amount of gas (CO_2) dissolved in it as a function of injection pressure and orifice size. The degree of vacuum was kept below 0.1 N/m^2 .

EXPERIMENTAL APPARATUS AND PROCEDURE: This investigation was conducted in a Murphy and Miller Vacuum Chamber at the National Aeronautics and Space Administration's Mississippi Test Facility - an overall view of the apparatus is shown in Figure 1. The test chamber is approximately 1.25 m in diameter by 1.5 m long and is evacuated by a Stokes mechanical pump, a Roots high volume blower, and an oil diffusion pump. The system is capable of producing a minimum pressure of $3.33 \times 10^{-3} \text{ N/m}^2$. Chamber pressure was measured by a thermocouple and an ionization gage. A hole 0.6 m in diameter covered by a plate provided a mounting for various feedthroughs.

A cylindrical, liquid nitrogen cooled, cryogenic liner was designed and installed within the test chamber to provide cryopumping for the water vapor. A fluid injection system was

*The numbers in parentheses refer to the list of references appended to this paper.

also designed and installed in place of a glass port on the door of the test chamber. A close-up view of this system is shown in Figure 2. This system consisted of a tank approximately 10^{-3}m^3 capacity which held the fluid to be injected into the vacuum system, a slight glass arrangement in the side of the tank, a valved fill-drain line and a pressurization line, a plunger for starting and stopping the injection of the fluid, a threaded hole for mounting various nozzles and orifices, a hot water line for heating the nozzle, and a small port and mirror for close viewing of the nozzle surface. The vacuum side of this system is shown in Figure 3.

Tank pressurization was supplied by a cylinder of high pressure gas which fed a ballast tank (capacity approximately 10^{-2}m^3) through a pressure regulator. The ballast tank was connected directly to the fluid injector tank by a rubber vacuum hose. Ballast tank pressure was measured by a pressure gage which read from 30 inches of mercury vacuum to 15 pounds per square inch above atmospheric pressure. This fluid pressurization system is shown schematically by Figure 4.

The fluid spray was photographed using both still and high speed cameras. The still photographs were taken with a 4 x 5 inch view camera with a 135 mm focal length lens. Exposure times varied between 1/60 and 25 seconds. The high speed motion pictures were made with a model WF-145 Wollensak Fastex "S" high speed camera. The particle velocity measurements were made from movie film taken at approximately 4,000 frames per second with a 35 mm focal length lens. Successful high speed motion picture photography of sprays in a vacuum depends greatly on obtaining proper lighting. Experience gained thus far in this project indicates a modified backlighted spray photographs best. A diagram of the lighting arrangement used in the footage from which velocity measurements were made is shown in Figure 5.

The fluid tested was distilled water which was boiled for one hour to expell dissolved gasses and then cooled in a closed flask. The first series of tests used helium as the pressurizing gas because it is nearly insoluable in water. In the second series, carbon dioxide was used as the pressurizing gas and is quite soluble in water. The mole fraction of gas dissolved in the water was obtainable from Henry's Law. The water was injected into the vacuum at temperatures between 24C and 27C.

RESULTS: During the first few runs, a slot approximately 3.2 mm wide was put directly in front of the spray in order to obtain a thin section through the middle of the spray and hence photograph only a section of the spray parallel to the film plane. Icing problems were anticipated for previous investigators (references 1 and 2) had reported the formation and growth of ice structures whenever a water jet struck a surface. Therefore, the slot was provided with a heater.

Nevertheless, ice would still form on the slot, occasionally bridging the slot and blocking flow although the slot material was heated to a temperature in excess of 38C. Although the slot material was kept in excess of 38C, generally one-half hour was required for the ice formation to melt sufficiently for gravity to break it away from the slot. One other problem arose with the slot: the sprays tended to be unstable and sweep from side to side and miss the slot. This was particularly true of sprays produced by the smaller orifices sizes and at lower pressures. These sprays would issue from the orifice as a thin, pencil-like jet for a length of several jet diameters and then break into a cone spray of small particles. Just before this pencil-like jet broke into a spray it would begin to weave, causing the entire cone to sweep. For these reasons the slot was abandoned and the entire spray photographed.

A series of tests were conducted to obtain particle velocities as a function of injection pressure for outgassed water and for water with dissolved carbon dioxide in it. The results of this series of tests is presented in Figure 6. Each velocity plotted is the average of the velocities of approximately twenty particles tracked at each pressure. These velocities were obtained by photographing the spray with a high speed 16 mm movie camera. By proper choice of camera location and lens focal length, it was possible to photograph the spray such that individual particles could be tracked for about fifty frames. This corresponded to an actual distance of about 150 mm. A time base was provided by timing marks put on the edge of the film at one thousand per second. Due to reasons discussed above it was not possible to obtain only a section of the spray, but rather the entire spray had to be photographed; thus, some dispersion of particle velocities would be expected because many particles would not be moving exactly parallel to the film plane. This dispersion did occur but not to the degree which might have been expected. This is probably due to small cone angles. Table 1 compares results from this work to the results obtained by the Atlantic Research Corporation group (1). The latter did measure the velocity of particles which were moving only parallel to the film plane. However, these velocities were obtained using still photographic equipment and a single flash strobe and the time which a particle track registered on the film was difficult to measure and they reported that their tabulated velocity measurements were probably in error by a factor of two. Note also the large range of velocities reported. This group did not attempt to outgas the water.

Since the range of velocities observed in this work is not unduly large and the velocities fall within the range of the few observations of previous investigators, it is felt that the average velocities presented in Figure 6 are representative of the particle velocities of the entire spray under

the various conditions. There was some error because some particles were not moving parallel to the film plane. Corresponding to earlier reports (1), many particles appeared to be rotating. When viewing the high speed movies, many particles appear dim but their brightness will increase sharply and then decrease as they move across the screen. This is probably due to specular reflections from uneven particle surfaces.

Another series of tests was conducted to measure the volume flow rate of outgassed water through seven nozzle sizes (orifice diameters of 0.34, 0.51, 0.66, 0.79, 0.84, 1.0, and 1.17 mm) at five injection pressures. These results are presented in Figure 7. As would be expected and as seen from Figure 7, the volume flow rate and injection tank pressure are related by the following equation:

$$\dot{V} = c p^{\frac{1}{2}} \quad \text{where: } \dot{V} = \text{volume flow rate}$$

$$p = \text{injection pressure}$$

$$c = \text{constant (different for each nozzle)}$$

Included cone angles as a function of injection pressures as shown in Figure 8 were obtained from still photographs of sprays produced by outgassed water. It appears from this figure that cone angles and injection pressure could be correlated by an equation of the form:

$$\alpha = a p^m \quad \text{where: } \alpha = \text{cone angle}$$

$$p = \text{injection pressure}$$

$$m, a = \text{constants.}$$

A problem arises when attempting to obtain cone angles of sprays photographically. The sprays are dense near the center and become progressively less dense away from the axis of the jet and no clear boundary at the jet's edge exists. The intensity of the photographic image of the spray depends on the size and concentration of the drops comprising the spray, the arrangement and intensity of the lighting of the spray, as well as the film speed, exposure time and aperture used. It is quite likely therefore, that small and widely separated drops at the periphery of the spray did not register on the film and the total included angles of the sprays were somewhat larger than those measured. The data shown in Figure 8 for the large nozzle (0.99 mm) does not have nearly as much scatter about its representative line as does that of the small nozzle (0.51 mm). It is felt that this is due to the spray from the small nozzle being finer and more diffuse than the spray from the larger nozzles, making it more difficult to correctly define the boundaries of the small jet.

CONCLUSIONS: Experience gained in this program indicates that

icing will occur whenever a spray impinges on a surface, even a relatively hot surface. The work accomplished to date demonstrates that sprays in a vacuum can successfully be analyzed photographically if the spray is properly lighted. Additional work is proceeding to determine particle velocities, sizes, and distributions within water sprays for various nozzle sizes, injection pressures, and dissolved gas content. Another series of experiments will attempt to define the freezing time of the individual particles comprising the sprays.

REFERENCES:

1. Simmons, Gift, and Markels, "Investigation of the Effects of Vacuum on Liquid Hydrogen and Other Cryogenes Used on Launch Vehicles," Final Summary Report, Atlantic Research Corporation, Contract No. NASA-11044, December 18, 1964, NASA Assesstion X65-12159.
2. Dawley, Richard A., "Expulsion of Water Based Liquids into a Hard Vacuum," 02-84191-1, Boeing Company, 1966 (N66-30440).
3. Mann, B. L., and U. T. Stoll, "Experimental Investigation of the Freezing Problem Presented in Discharging Water Based Fluids to Space," SAE Paper 912D, SAE/NASA Engineering & Manufacturing Meeting, Los Angeles, California, October 5-9, 1964.
4. Mikatarian, R. R., and R. G. Anderson, Journal of Spacecraft and Rockets, Vol. 3, No. 2, February, 1966, pp. 267-268.
5. Sodek, B. A., "The Resultant State of Water Expelled into the Near-Earth Orbital Environment," RL-SSL-207, Brown Engineering, July, 1968.
6. Brennan, J. A., "A Preliminary Study of the Orifice Flow Characteristics of Liquid Nitrogen and Liquid Hydrogen Discharging into a Vacuum," Advances in Cryogenic Engineering, Vol. 9, Plenum Press, New York, 1964.
7. Schmidt, J. M., "An Experimental Study of the Behavior of Liquid Streams Injected into a Low Pressure Chamber," Jet Propulsion Lab., California Institute of Technology, Pasadena, California, April, 1949.

Table 1

Comparison of the Distribution of
Particle Velocities Between Current
Work and Previous Work

Velocities from this Investigation	Velocities Presented in Reference 1
Injection Pressure: 85.5 KN/m ²	Injection Pressure: 101.3 KN/m ²
Fluid: outgassed water	Fluid: water
Particle Velocity $\frac{m}{s}$	Particle Velocity $\frac{m}{s}$
16.05	11.05
16.55	42.10
17.30	21.00
15.00	22.70
16.05	13.35
14.80	22.10
15.45	10.18
14.55	23.20
16.55	34.60
15.05	12.37
15.30	10.61
14.70	10.40
16.40	12.03
16.75	11.17
14.70	11.70
16.90	
15.90	
16.30	

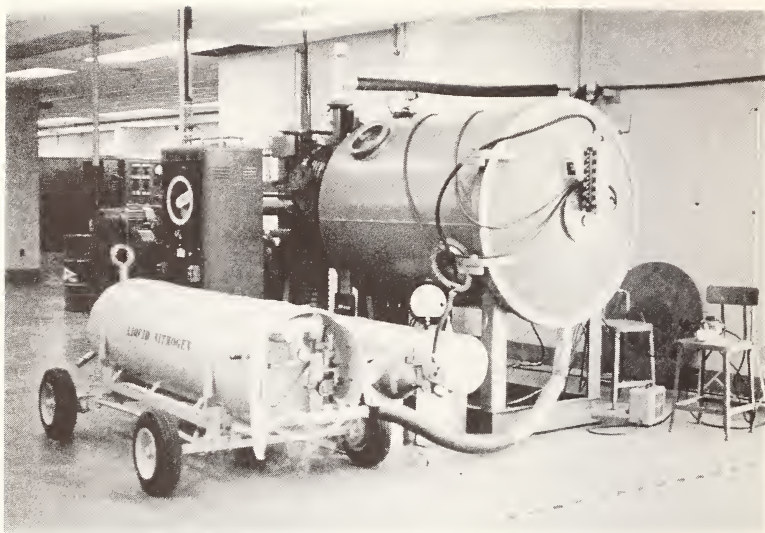


Fig. 1--Overall View of the Test Apparatus

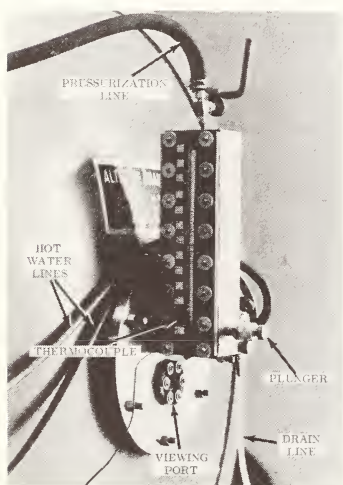


Fig. 2--Injection Tank System



Fig. 3--Vacuum Side of the Injection System

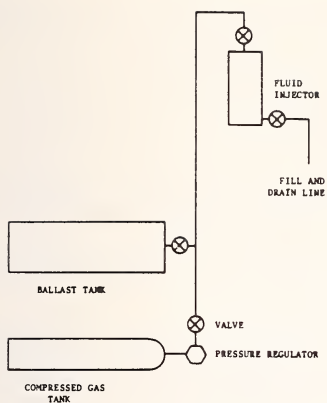


Fig. 4--Fluid Injector Pressurization System

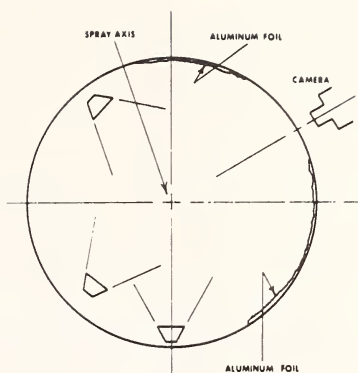


Fig. 5--Lighting Arrangement for High Speed Movies

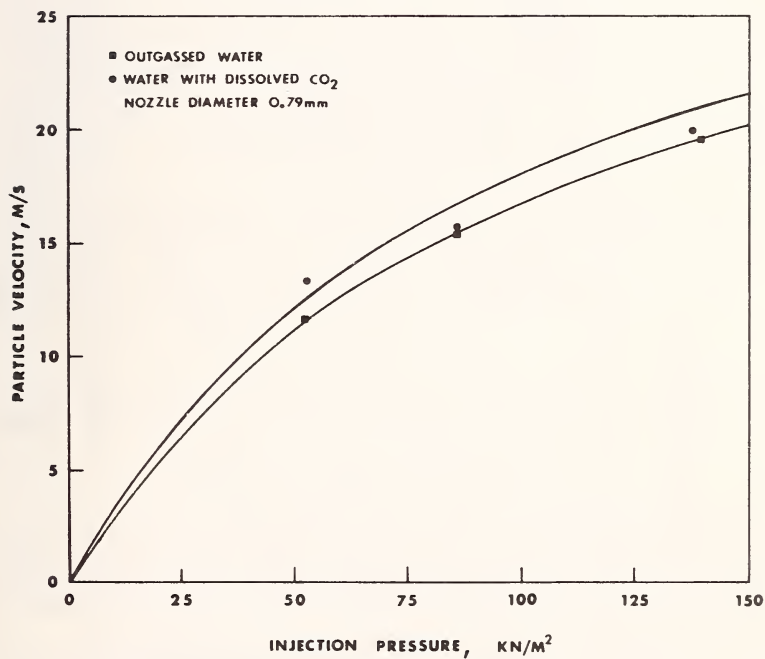


Fig. 6--Average Particle Velocity vs Injection Pressure

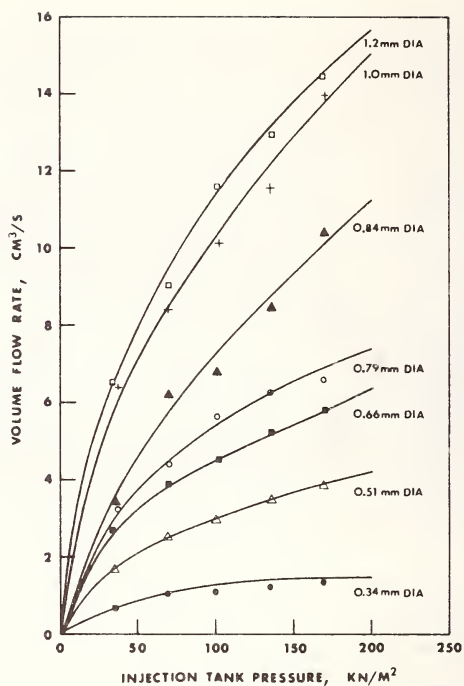


Fig. 7--Injection Tank Pressure vs Volume Flow Rate

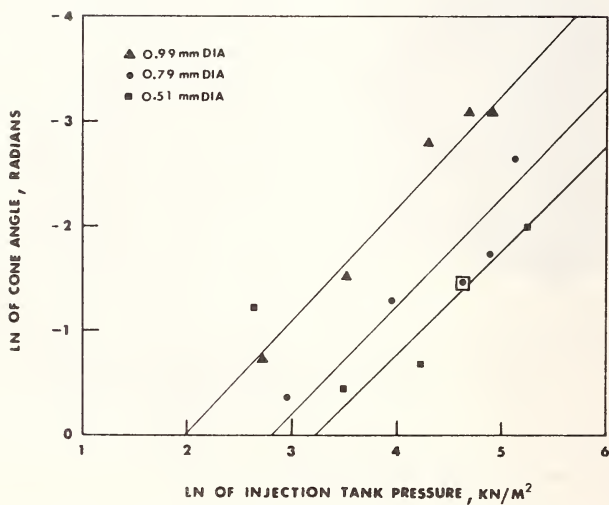


Fig. 8--Cone Angle vs Injection Pressure

MICROMETEOROID IMPACT SIMULATION SYSTEM

Robert A. Golub¹ and John R. Davidson²

REFERENCE: Robert A. Golub and John R. Davidson, "Micrometeoroid Impact Simulation System," ASTM/IES/AIAA Space Simulation Conference, 14-16 September 1970.

ABSTRACT: This paper describes a Micrometeoroid Impact Simulation System (MIMS) at NASA Langley Research Center and outlines current research efforts. The MIMS electrostatically accelerates electrically charged, micrometer-size particles to velocities in excess of 30 km/s. Particles can be accelerated one at a time or at various rates to above 10/s. The major components of the MIMS are a microparticle charger-injector, a horizontal 4-million-volt Van de Graaff accelerator, an assemblage of particle detectors, a particle deflection system, a data system, and a series of target chambers. The data system is a computer-controlled, real-time system which records information to determine the velocity, mass, and diameter of each particle which enters the target area. The system also controls and selects particles, and rejects particles which do not have the desired velocities. The system is used to study damage to sensitive surfaces, develop micrometeoroid detectors, and obtain data about meteoroid entry physics.

KEY WORDS: micrometeoroid, hypervelocity, particle detectors, impact damage

The existence of meteoroids in space presents a hazard to vehicles and satellites outside of the earth's atmosphere. The particle sizes vary greatly, with the smallest being about $1\mu\text{m}$ in diameter. Their velocities vary from about 11 to 72 km/s.

¹Aerospace Technologist, NASA Langley Research Center, Hampton, Va.

²Aerospace Technologist, NASA Langley Research Center, Hampton, Va.

The small particles, called micrometeoroids, can damage the surfaces of space telescopes, external windows on spacecraft, lenses, protective coatings, and exposed instrumentation. The damage is the result of both a high particle flux and long exposure time which causes a gradual deterioration of the surface efficiency. To establish a damage criteria and degradation rates, the cumulative effect of micrometeoroid impacts must be measured.

A Micrometeoroid Impact Simulator (MIMS) was built to measure these phenomena. The major components of the simulator system are a microparticle charger-injector, a horizontal 4-million-volt Van de Graaff accelerator (VDG), an assemblage of particle detectors, a particle deflection system, a unique data acquisition system, and a series of target chambers. The simulator has accelerated micrometer-size, spherical particles to velocities in excess of 34 km/s. It can provide particles at rates in excess of 10/s.

The purpose of this paper is, first, to describe the MIMS and, second, to outline the current experimental studies.

MIMS THEORY OF OPERATION

The basic principle under which the system functions is the conservation of energy. It states that a particle with charge, q , put in a potential field V , will change kinetic energy by an amount equal to the product of V and q . Mathematically,

$$\frac{1}{2} mv^2 = Vq$$

where m is the mass of the particle and v is the velocity of the particle. Solving the equation for the velocity:

$$v = \sqrt{2 Vq/m}$$

The resultant velocity, then, is a function of the potential field V , the charge on the particle q , and the particle mass m . From theory and geometry q varies as $\sqrt{V/d}$ and since the machine voltage is usually fixed and the charger-injector maintains a relatively constant charging efficiency, the velocity will vary with particle size; the smallest particles will have the highest velocities. Figure 1 shows the variation of the velocity with particle size. With the simulator system at 4-MV, 0.1 μ m diameter particles are accelerated to velocities about 35 km/s and 10 μ m diameter particles to velocities of about 4 km/s.

A diagram of the system is shown in Figure 2. The vacuum environment through which the particles travel is maintained by the VDG vacuum system and the vacuum systems of the adjoining

target chambers. A particle is accelerated as follows: The particles are initially at rest in a cavity in the charger-injector. A particle is given a charge and then injected into the VDG along the accelerating axis. Once in the field of the VDG, the particle is focused and accelerated through the full potential of the machine. After it leaves the VDG, the particle is traveling at a constant velocity. It then traverses several particle detectors where its charge-induced voltage, time of flight, and the potential by which it was accelerated are measured by the data system. If the particle is within preset time-of-flight limits, it is counted, has its measured parameters recorded, and is allowed to pass through the deflection system without being deflected. On the other hand, if the particle does not have the proper velocity it is considered unacceptable, is not counted, does not have its parameters recorded, and the deflection system deflects it into a deflection aperture plate where it is stopped before it can enter the target chamber. The data system records the parameters for those particles which it has allowed to pass into the target area.

The particle beam size is controlled with the VDG focusing system. A focused particle beam would contain about 90 percent of the particles within a 1-mm-diameter area. A defocused beam, which is useful in some experiments, can be as large as about 6 mm in diameter.

The particles normally used are carbonyl-iron. Their density is $7.86 \times 10^3 \text{ kg/m}^3$ and their diameters range from about 0.1 to 10 μm . Particles can be injected either by manual operation or by automatic operation at rates of 0.5, 1, 2, 5, or over 10 per second.

PARTICLE CHARGER-INJECTOR

The charger-injector is shown in Figure 3. Details of operation are available in reference 1. The methods for charging and injecting particles will be described briefly. The particles are initially at rest in the particle cavity. The charging electrode-particle cavity assembly and the plate are maintained at a potential of about 12 to 14 kV. A negative pulse is then applied to the plate which causes the topmost layer of particles to achieve erratic motion. This motion is similar to that of particles in a gas. Some of these particles will effuse through the cavity exit into the forward charging chamber. Of the particles which pass into the forward charging chamber which are still in motion, some will strike the electrode and gain a very high charge. When one of these highly charged particles passes through the collimating apertures, it is focused and accelerated by the VDG.

A charging electrode is shown in the figure inset. It is basically a tapered shaft with a small ball at the end. The shaft length is about 2.5 mm and the diameter of the ball is

about 30 μ m. The electrode is usually tungsten. For particle rates of about 10 per second, the average operating lifetime of a good charging electrode is about 40 to 80 hours. The application of a 12 to 14 kV potential on the electrode results in a charge transfer to a particle amounting to about 12 to 14 percent of the theoretical maximum charge that the particle can hold. If the electrodes are operated at higher potentials, the charging efficiency does not increase appreciably but the electrode lifetime is shortened considerably.

ACCELERATOR

The 4-MV Van de Graaff Accelerator (Model KN-4000) is operated in a positive mode. The high potential is attained by transferring charge from a power supply located at the base of the machine (via a specially woven, continuous belt) to the high voltage dome. Figure 4 is a photograph of the VDG with the outer tank and the dome removed to show the high voltage end of the column where the terminal electronics of the machine are mounted. The primary components of the column are porcelain insulating supports, a series of rings coupled by resistors, the accelerating tube, and a drive motor and alternator pulley which hold the belt. The alternator also supplies power for use inside the high-voltage dome. The particle charger-injector and its electronics can be seen in the end of the column. The column is cantilevered from a heavy base plate which is anchored to the floor. In order to operate the accelerator, the tank must enclose the column and be sealed to the base plate. The tank is pressurized to about 550 kN/m² (80 psig) with sulfur hexafluoride gas. The SF₆ is an excellent insulating gas and allows operation at 4 to 4.5 MV with almost no machine sparking. The accelerator operates stably if it has been properly prepared for running. At 4 MV the terminal voltage variation can be held below ± 10 kV with some effort.

DETECTORS

The velocity, charge, and position detectors are identical electrically and differ only in the configuration of the active elements. Figure 5 shows a diagram of a typical detector. The detector is a coaxial capacitive pickup consisting of an inner active element through which the particles pass, a bootstrap shield, and a vacuum-enclosure support outer tube. The detector active element behaves like a capacitor and senses a passing charged particle. The governing equation is:

$$q = CV_0$$

where q is the particle charge, C the detector capacitance, and V_0 the induced voltage. A typical detector waveform showing the voltage V_0 as a function of time for a passing charge particle is shown in Figure 5. The bootstrap shield is operated by negative feedback from the detector amplifier and drives the electrical capacitance of the assembly to a lower effective value. This bootstrap shield action increases the sensitivity of the detectors. These detectors can reliably sense charges as small as about 1 fC.

TARGET AREA

The arrangement of the target chambers is shown in Figure 6. The target chambers are deliberately arranged in a "piggyback" style. The arrangement facilitates quick experimental change-overs by minimizing the alignment problems. Each chamber is independent of the others because each has its own vacuum system and can be closed off from the others. The first chamber, which is called the single-impact chamber, contains a movable, remotely controlled, target positioner. The positioner can move the target across the beam horizontally and vertically to about 5 cm from the center line. The positioner also contains a gimbal system and can allow pitch and yaw motions of the target to $\pm 45^\circ$. The chamber has two 12.5-cm glass ports so that the target can be seen from the front at angles of 45° .

The second chamber is used for mirror surface tests and impact flash experiments. It has two chamber sections on a common axis. The first section contains two sets of parallel plates which are aligned along the particle beam axis; one set is perpendicular to the other. The plates deflect the particle beam when a modulated high voltage is applied to each set of plates. In this way, the surface of a mirror can be scanned with the beam. The impact flash section has four equally spaced, 5-cm front viewing ports and one 5-cm rear viewing port. All of the 5-cm ports have retainers for mounting filters and photo-multiplier tubes.

The third chamber is a specially designed, two-stage, differentially pumped system used for luminosity and drag experiments. The chamber test section, which can be at pressures as high as 300 N/m^2 , can be coupled to the other vacuum systems which are at about 10^{-4} N/m^2 (10^{-6} torr). The test section is about 15 cm in diameter and over 1 m in length. It has fifteen 5-cm diameter ports along its axis to view particle luminosity.

DATA SYSTEM

The data system, in addition to recording data, also controls the particle beam. The computer-controlled interface coupled to the multielement detector system selects particles

with desired velocities and controls the number of particles which strike the target. The data system can accept particles with velocities from less than 1 km/s to velocities greater than 40 km/s. It measures the charge-induced voltage of the particle, time of flight of the particle, and the potential of the VDG for each particle within preset velocity limits. From these three parameters the velocity, mass, and diameter of a particle can be calculated.

Equipment

The MIMS control room is shown in Figure 7. The three instrument racks at the left contain the controls and monitoring equipment for the VDG and the particle charger-injector. The other components are parts of the data system; they are the computer, the interface rack, the magnetic tape unit, the keyboard/printer-punch/reader, and the card reader.

The computer has a 16-bit word length and multiple hardware registers. It contains 16,000 words of core memory to hold the MIMS control program. The control program is a real-time program and uses the interrupt features of the computer for selection of functions. The operator controls program functions with the data switches and the interrupt switch on the computer control console.

The magnetic tape unit, the card reader, and the keyboard/printer-punch/reader are standard computer peripheral devices. They are used to store data, to modify the program, and for operator control of the data system.

The interface rack is a specially designed unit. It contains:

1. A dual counter scaler unit for counting particles.
2. A time interval counter for measuring particle time of flight.
3. An analog-to-digital converter (ADC) for measuring charge-induced voltage and VDG potential.
4. The control unit for the deflection system.
5. Two logic chassis which handle the real-time signals for the system.

Figure 8 shows the multielement detection system and the deflection system. Detectors V1, V2, and V3 are particle velocity sensors. Detector CH-1 is used to sense the particle charge-induced voltage. Detectors P1 and P2 are position detectors and are used only to align the detector system to the particle beam. The deflection plates, the deflection aperture plate, and the deflection system power supply can be seen between detectors V3 and P2.

Method of Operation

Basically, the system works as follows (see Fig. 9): A particle passes through detector V1 and starts the time interval counter and a 1-MHz clock counter. If the particle gets to detector V2 (40 cm downstream from detector V1) it stops the 1 MHz clock counter; the clock counter value is stored in a storage register, and the clock counter is reversed so that it counts down to zero. Meanwhile the stored count (from the 1-MHz clock counter) is compared to two preset time-of-flight limits which form a "window." If the particle is within the limits then it is tentatively accepted; otherwise the system is reset and waits for another particle. When the 1-MHz clock counter reaches zero, the particle should be within the active element of detector CH-1. The analog-to-digital converter is given a convert pulse which tells it to convert the charge-induced voltage of the particle. The stored count (time value) is now loaded back into the 1-MHz clock counter and the clock counter is started to count down a second time. If the particle gets to detector V3, which is 1 m from V1, then the time interval counter is stopped and the particle is counted as an acceptable particle. Now the charge-induced voltage and velocity of the particle are read into the computer. The particle should reach the entrance to the deflection plates (40 cm downstream from detector CH-1) when the 1-MHz clock counter reaches zero for the second time. This clock counter triggers a pulse to remove the 10 kV from the deflection plates for a short period of time to allow the particle to continue in a straight line path. The particle is then free to enter into the first of the target chambers. If, for some reason, the particle had been unacceptable, that is, had either an unacceptable velocity or had struck one of the detectors and failed to get through the detection system in the proper timing sequence, the 10-kV potential would not have been removed from the deflection plates and the unwanted particle would have been deflected into the downstream deflection aperture plate. During the period in which a particle was between detector V3 and the deflection plates, the ADC was given a signal to convert a value from the VDG for the accelerating potential and subsequently store it in the computer. When sufficient particles have been accepted, the data stored in the computer memory are automatically transferred to magnetic tape for later analysis. Each time a particle is counted by the system it is compared to a preset maximum allowed particle count which, when reached, automatically terminates data system activity.

Data Output

Data can be output during real-time operation to a printer and stored on magnetic tape. In Figure 10 is shown a printer

listing from a typical experimental run. At the top is the computer program initialization which tells the operator about his system options. In this case Mode A has been selected. This is a real-time mode where the accumulated data will be automatically transferred to the magnetic tape for storage. The alphabetic information starting with "PROJECT NUMBER" and ending with "USE DS, AND INTERRUPT TO GO" is typed out automatically in sequence. At the end of each line the operator supplies the numeric information. When the last numeric digit is typed, the project number, specimen number, and file reference number are automatically transferred onto the magnetic tape for identification. After the run has begun, the operator may print particle data on the printer at any time. If the operator interrupts the computer, the parameters will be printed for the next particle the system accepts after the interrupt was performed. When the operator terminates a run or (automatically) when the maximum allowed particle count limit is reached, the data system will stop operation, type out "END OF RUN," and await further instructions from the operator.

Mode B is like Mode A except that the tape identification is not generated (PROJECT NUMBER through FILE REFERENCE NUMBER) and the data are not stored on magnetic tape.

Mode C prints out any data which have been stored on the magnetic tape for checking or analysis.

Mode D is a test mode which gives a quick and simple system test of the velocity limits, the ADC conversions, and the time-of-flight measurement.

The data collected on magnetic tape are analyzed on a digital computer at Langley Research Center. Programs exist which read the data from the tapes and calculate parameters such as particle charge, velocity, mass, radius, momentum, and kinetic energy. Typical outputs of data are shown in Figure 11. Figure 11(a) shows a data display for the relative frequency of occurrence (for particle velocity). Figure 11(b) shows the results of a more extensive analysis and shows the log of kinetic energy versus relative frequency of occurrence.

Listed in Table 1 are some data which illustrate the system capabilities. Time-of-flight limits were selected in deliberate groups. The system was required to allow only one particle to be accepted during each run. The data illustrate that the data system can control the particle velocity by using the preset velocity limits. Particles in the 10-km/s range are available at rates of several particles per minute. For particles with velocities in excess of 30 km/s, the rate is about one particle in about 15 minutes when the system is set to shoot particles of 10/s. The calculated radii and masses for each particle are listed. The velocities and radii listed show that the smaller particles are the fastest, as predicted by theory.

EXAMPLES OF MICROMETEOROID EXPERIMENTS

The experimental programs presently underway are concerned with damage to sensitive surfaces, micrometeoroid detectors, and meteoroid entry physics.

Mirror surfaces, such as those to be used in the reflecting telescopes proposed for the manned space station, will be struck by micrometeoroids. A study is underway at the MIMS facility to show how the specular and diffuse reflectance change when such surfaces are bombarded with microparticles. Coated aluminum mirror surfaces have been bombarded with up to 10^9 particles/m². The narrow angle specular reflectance changes are being measured.

The simulator is being used to test and evaluate thin-film, capacitor-type micrometeoroid detectors. These detectors will be flown on the Meteoroid Technology Satellite. The satellite has three objectives: to measure meteoroid penetration rates in bumper protected structures (the rates will be compared with data from previous satellites which had unprotected sensors); to measure the velocities of meteoroids which penetrate stainless-steel sheets 13 μ m thick; and to measure the impact flux of small mass meteoroids in near-earth space. The thin-film capacitor detectors (about 1 or 2 μ m) are part of the velocity measuring sensors, and also detect the small-mass meteoroids. The characteristics of the detector discharge and the meteoroid parameters which trigger the discharge are not fully understood. Particle characteristics are being correlated with discharge signal characteristics to establish specifications for flight hardware. Also, because the velocity measuring device uses a thin-film capacitor bumper, the effect of the bumper on possible particle breakup is being studied. Thin-film capacitor detectors of 0.2 and 0.4 μ m thickness are also being studied.

When micrometeoroids hit a surface a flash of light is given off; this could be detrimental to space experiments which use photosensitive materials. The intensity-history of the flash and the spectral characteristics are being measured. If these are known, it may be possible to discriminate against them. Various kinds of targets, both hard and soft, are being tested. Preliminary measurements indicate that the flash from soft targets is somewhat different from the flash from hard targets. Other experiments suggest that the impact flash characteristics can be correlated with projectile characteristics, consequently the flash may be used both to detect micrometeoroid impacts and to identify the velocity and mass of the impacting particle; correlations of this type are being studied.

The MIMS solid-state detector studies are an effort to develop a reliable, long-life micrometeoroid impact detector for particles with masses as low as approximately 10^{-16} kg. Presently, no detector exists for these particles. Solid-state detectors are used by nuclear physicists to analyze particulate

radiation. Three types of these solid-state detectors being studied for micrometeoroid measurements are:

1. Lithium-drifted silicon detectors
2. Silicon heavy-ion detectors
3. Silicon surface-barrier detectors

To date, two of the lithium-drifted silicon detectors have been tested with encouraging results. Every microparticle which struck the first detector generated a signal. The second detector was bombarded by over 700,000 particles intermittently during a several-day period and was still giving out signals when the run was terminated. Two surface-barrier-type detectors were tested but both of these failed after only a few impacts.

For the luminosity and drag experiments, a program is being developed at the MIMS facility on the laboratory simulation of meteor phenomena and associated atomic collision processes. A differentially pumped vacuum chamber is being used to provide a rarefied atmosphere. The particle is shot into the gas and, depending upon conditions, may cause a streak of light or be decelerated. Both the light trail and the particle deceleration will be measured. It is hoped that the results will supply data about the luminous efficiencies of meteors and help calibrate meteor photographs and radar observations.

CONCLUDING REMARKS

The Micrometeoroid Impact Simulator is one of the few apparatus which can accelerate particles of known mass to meteoric speeds (above 11 km/s). With the data acquisition system now in operation, the velocities of the impacting particles can be controlled and all particle parameters recorded for future automatic data analysis. The automatic features of the system permit the effect of thousands of particles on sensitive surfaces to be measured and analyzed. The simulator is being used to study the effect of micrometeoroids' impacts upon sensitive surfaces, and to develop new micrometeoroid sensors for flight experiments.

TABLE 1--Demonstration of Particle Velocity Control

Particle No.	Time of Flight Limit (μ s) Slow	Fast	Particle Time of Flight (μ s)	Velocity (km/s)	Diameter (μ m)	Mass ($\text{kg} \times 10^{-16}$)
1	100	5	95.14	10.51	0.774	10.92
2	100	5	81.57	12.25	.476	4.44
3	100	5	80.71	12.39	.472	4.34
4	100	5	86.48	11.56	.714	15.01
5	100	5	88.35	11.31	.526	6.04
6	75	5	66.46	15.04	.456	3.91
7	75	5	54.13	18.47	.510	5.51
8	75	5	61.49	16.26	.496	5.03
9	75	5	68.80	14.53	.534	6.83
10	40	5	35.54	28.14	.272	.836
11	30	5	28.92	34.58	.236	.551

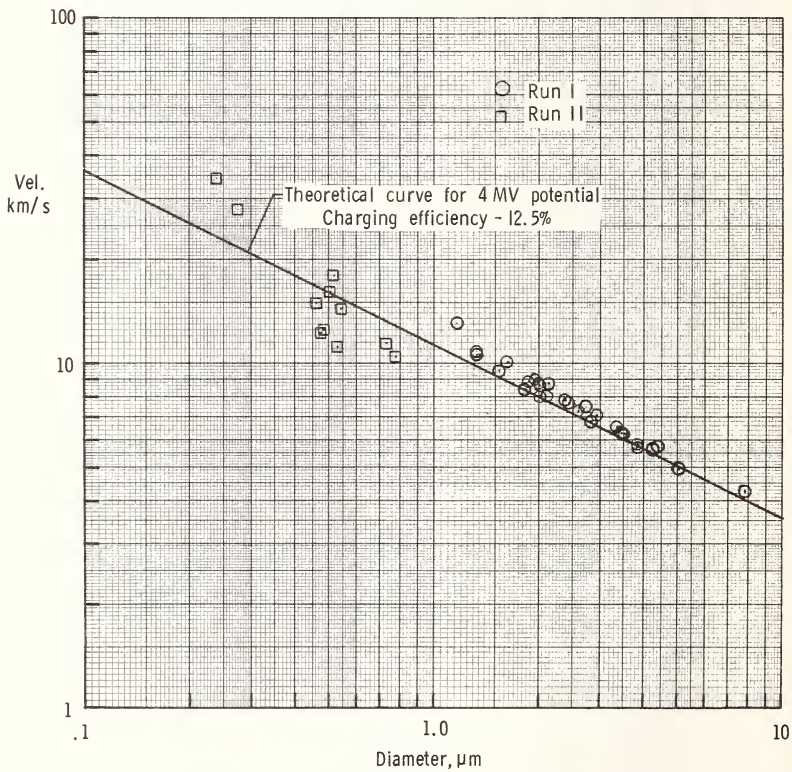
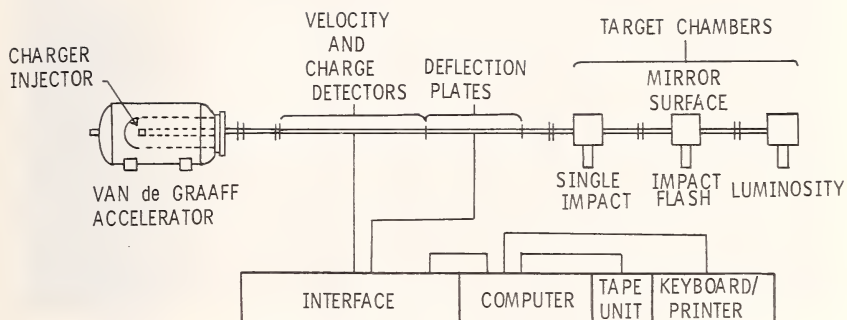


Figure 1. -- Variation of microparticle velocity with diameter for 4-million-volt potential.



DATA ACQUISITION SYSTEM PERFORMANCE CHARACTERISTICS

CARBONYL IRON PARTICLES; DENSITY $7.86 \times 10^3 \text{ kg/m}^3$

PARTICLE DIAMETER RANGE; 1 to 10 μm

PARTICLE RATES TO GREATER THAN 10/s

PARTICLE VELOCITY RANGE; $1 > v > 35 \text{ km/s}$

MEASURES AND RECORDS PARTICLE PARAMETERS

Figure 2. —Micrometeoroid Impact Simulator System.

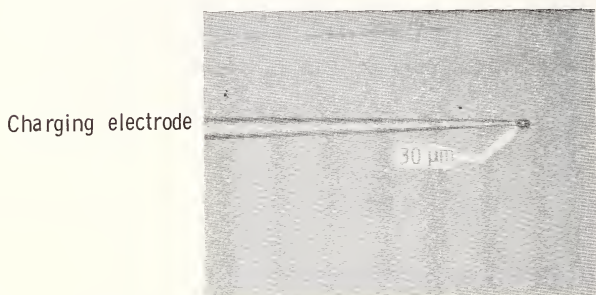
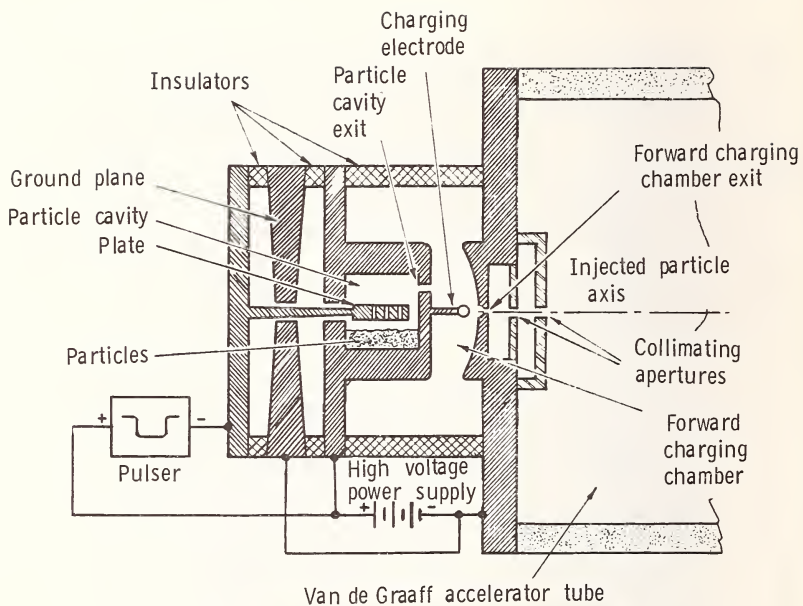


Figure 3. --Microparticle charger-injector.

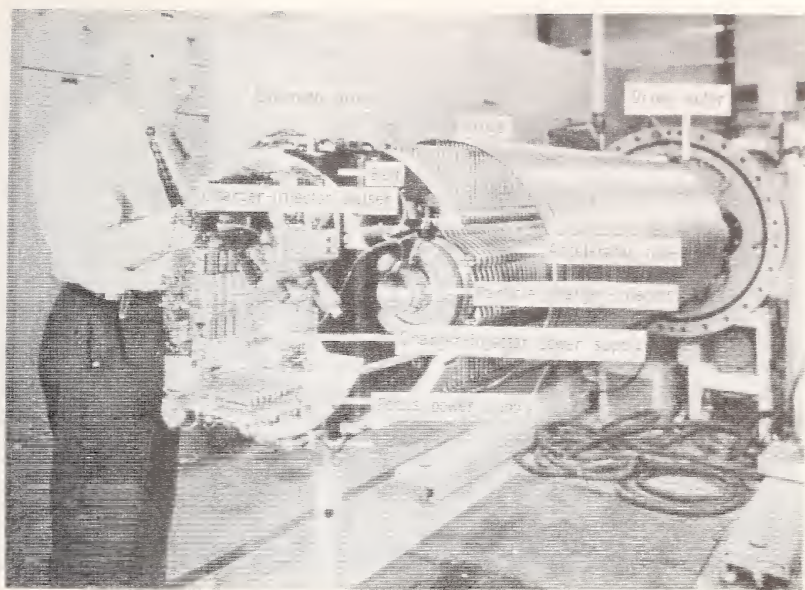
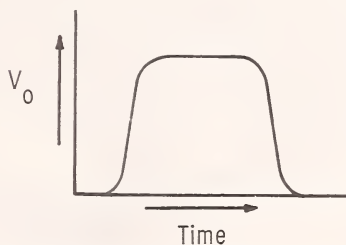
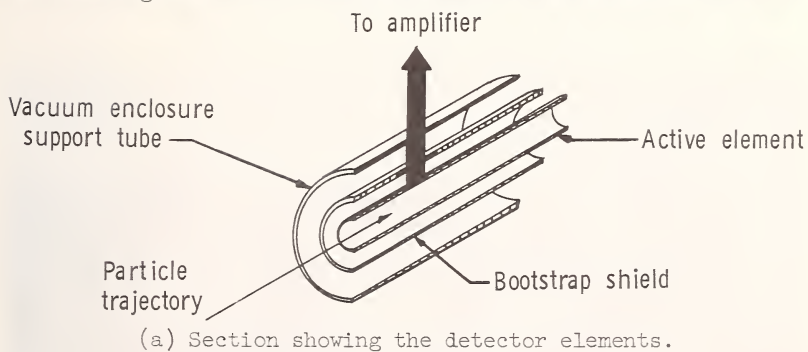


Figure 4. -Van de Graaff accelerator column.



(b) Typical detector waveform.

Figure 5. -Detector schematic and waveform.

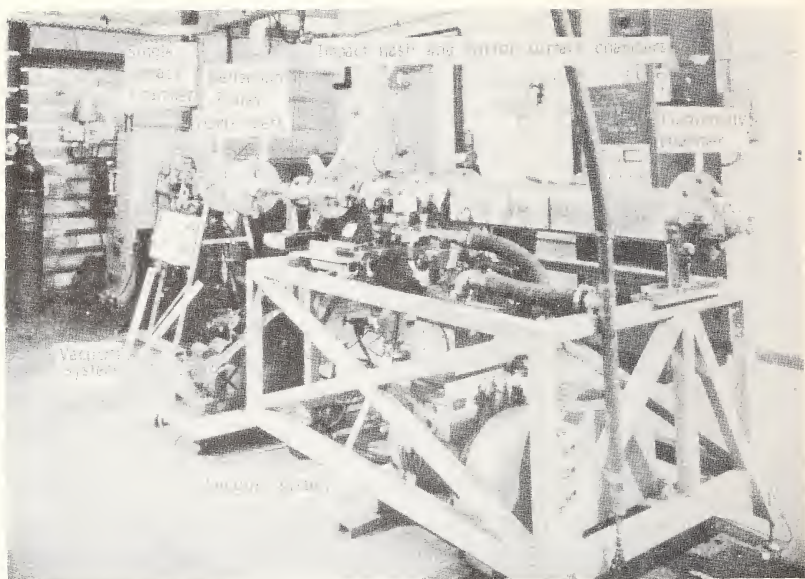


Figure 6. --Target chambers.



Figure 7. --MIMS control room.

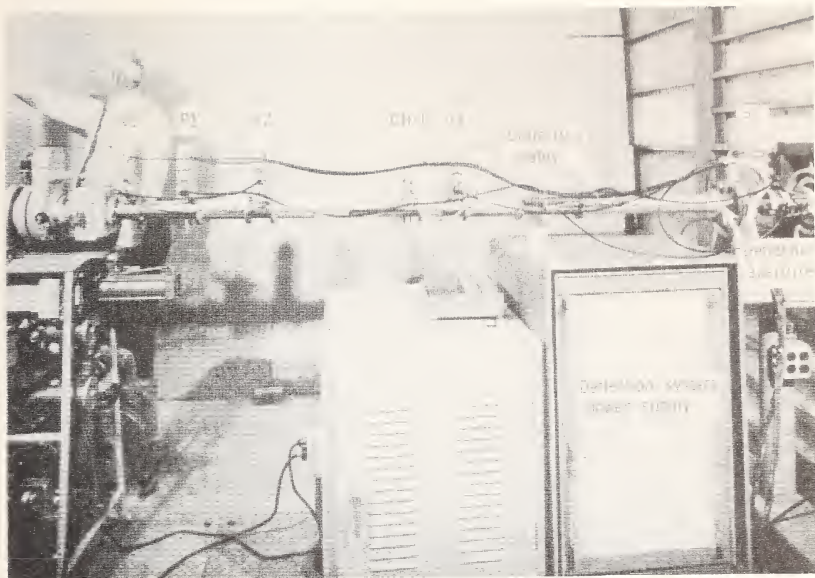


Figure 8. -Detector and deflection systems.

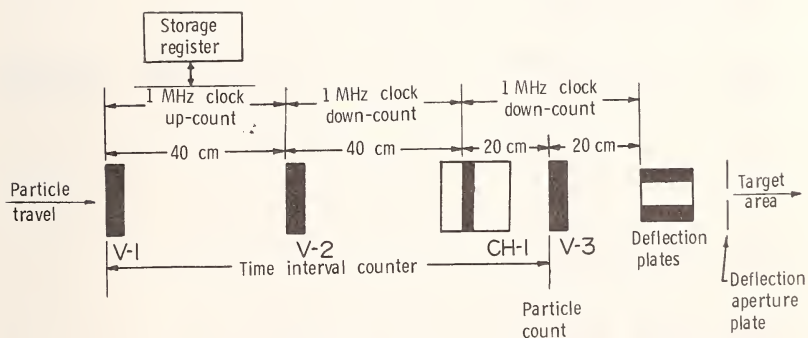


Figure 9. -Data system schematic.

DATA SWITCH	MODE
14 15	
0 0	A REAL-TIME
0 1	B BY-PASS TAPE
1 0	C PRINT OUT OF TAPE
1 1	D SYSTEM TEST

INITIALIZATION

SET MODE DS, INTERRUPT

PROJECT NUMBER	333
TEST NUMBER	003
SPECIMEN NUMBER	023
FILE REFERENCE NUMBER	000001
MAX. PARTICLES ALLOWED	0015000
MAX. ENTRIES ALLOWED	0015000
MINIMUM FLT TIME	0005
MAXIMUM FLT TIME	0250
READY FOR REAL-TIME.	
USE DS, AND INTERRUPT TO GO.	

IDENTIFICATION

CHRG FLT TIME	VOLTMETER
00025 017075	00389
PARTICLE COUNT	0000023

CHRG FLT TIME	VOLTMETER
00019 016082	00387
PARTICLE COUNT	0000072

CHRG FLT TIME	VOLTMETER
00012 015444	00390
PARTICLE COUNT	0000117

CHRG FLT TIME	VOLTMETER
00014 015004	00390
PARTICLE COUNT	0000180

DATA FROM PRINTER

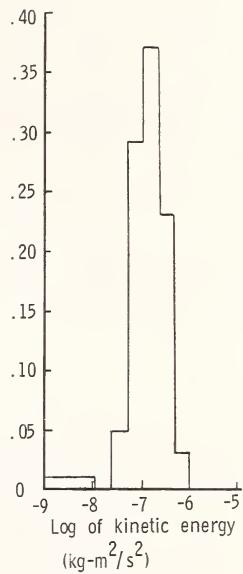
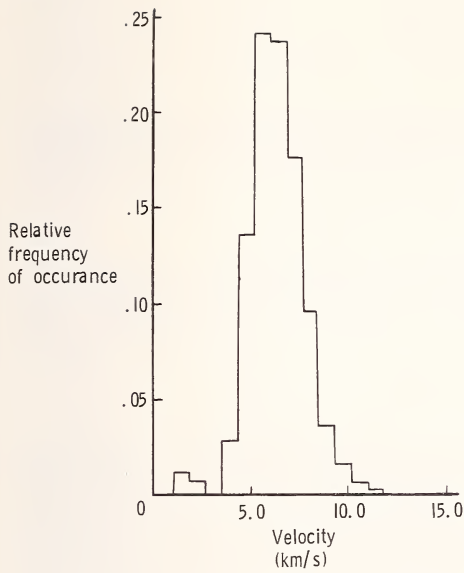
CHRG FLT TIME	VOLTMETER
00014 015215	00388
PARTICLE COUNT	0000241

CHRG FLT TIME	VOLTMETER
00017 015108	00391
PARTICLE COUNT	0000301

CHRG FLT TIME	VOLTMETER
00043 017982	00386
PARTICLE COUNT	0000375

END OF RUN

Figure 10. —Data from printer list of experimental run.



(a) Velocity distribution.

(b) Kinetic energy distribution.

Figure 11. —Typical results from Data Acquisition System.

A SPACE RADIATION ENVIRONMENT SIMULATOR FOR THE EVALUATION OF SOLAR CELLS

P. A. Newman, J. J. Hirshfield, H. E. Wannemacher, NASA, Goddard Space Flight Center, Greenbelt, Md., and M. Eck, Howard Slack Associates, Baltimore, Md.

ABSTRACT: A facility for studying the properties of solar cells and other optically sensitive devices under a wide range of environmental conditions such as could be found on extra-terrestrial space missions has been developed at the NASA Goddard Space Flight Center. The system includes control of temperature, vacuum and solar irradiation while irradiating a 23 cm by 23 cm array of samples with 4 MeV protons or electrons. Typically the samples can be controlled in temperature between -170°C and 150°C , while a shroud, used to control radiative coupling, can be independently controlled between -196°C and 150°C . The vacuum system, which is virtually free of hydrocarbon contamination, will evacuate the chamber to less than 1×10^{-8} torr in less than 4 hours. A 400 l/s Noble Vac-Ion pump backed by a titanium bulk sublimator and a titanium filament evaporator has been designed to accommodate the large gas loads possible during irradiation. A 4.2 KW compact Xenon arc solar simulator provides a close match to the solar spectrum from low irradiances to an irradiance of four solar constants. An automatic data acquisition system modified to generate digital solar cell I-V characteristics is used to collect data in a form suitable for computer processing.

KEY WORDS: space simulation, space radiation, solar cells, tests, thermal control, high vacuum.

INTRODUCTION

A facility for the in-situ testing of solar cells and other optically sensitive devices under a simulated space environment has been built and is in use at the Goddard Space Flight Center of NASA. The system is capable of irradiating a 23 cm \times 23 cm array of solar cells with both particulate radiation (protons or electrons) and simulated solar radiation while being maintained under a vacuum of 10^{-8} torr or less and controlled in temperature over a range of -170°C to 150°C . Data acquisition is accomplished automatically using a conventional system with a number of special modifications.

CHAMBER DESIGN

A plan view of the system is shown in Figure 1. The main chamber is a stainless steel (304) cylinder 45 cm in diameter and 203 cm long with a Wheeler flange holding the sample holder and all of the electrical feedthroughs at one end and an entrance port for the particulate radiation at the other. A port with a u.v. grade quartz window is located at right angles to the particulate beam adjacent to the beam entrance port. The use of a slightly off-axis turning mirror permits the simultaneous irradiation of the samples by photons and protons or electrons. The length of the chamber is needed to accommodate the divergence of the particulate beam. A cryogenic shroud that covers the region from the sample holder to the turning mirror is used to prevent unwanted radiative coupling. The sample holder can be rotated about 5° on an axis normal to the plane of the particulate beam and the simulator beam so that measurements can be made with each of the components normal.

VACUUM SYSTEM

All of the high vacuum pumping equipment is located below the main chamber (Fig. 2). The various pumps used are listed in Table 1 along with their pumping speed and range of operation. The basic pump is a 400 l/s Noble Vac-Ion¹ pump that is assisted in its various ranges by a titanium filament evaporator and a titanium bulk sublimator. The roughing system is mounted on a separate cart and is connected to the system by a flexible line. It consists of a gas aspirator and three cryogenic sorption pumps. Under ideal conditions (system

¹Varian Assoc. Palo Alto, Calif.

not opened to atmosphere for too long) the chamber can be evacuated from atmosphere to 1×10^{-8} torr in less (Fig. 3) than four hours. With the exception of one viton "O" ring used to seal the quartz window all openings are closed with copper gaskets to provide a hydrocarbon free system. The system pressure is monitored by a nude ion gauge located in the main chamber. The introduction of high energy protons into the system during irradiation of the solar cells could provide for a substantial gas load both from induced outgassing of the chamber walls and substrate and from the protons themselves. Fortunately the titanium bulk sublimator has an enormous pumping speed in this region so that the pressure can be kept under control for these peak gas loads.

SAMPLE PLATEN

Solar cells to be irradiated are mounted on a temperature controlled copper platen (Fig. 4) located at the end of the chamber. The platen size is 23 cm \times 23 cm and can accommodate about 50 solar cells at one time. A series of 9 Faraday cups are mounted at various points on the platen so that their apertures are in the plane of the solar cells. The walls of the Faraday cups are fabricated from tungsten so that the wall thickness could be made greater than the range of 4 MeV electrons. The Faraday cups are used to monitor the uniformity of the radiation over the surface area. Thermocouples are mounted on some of the cells to record the actual cell temperature during the experiment.

The wires used to transmit the cell characteristics are run along the platen surface and are shielded by copper guides. The thermal coupling of the solar cells can be monitored under various experimental conditions by measuring the open circuit voltage. It has been found that the cell junction temperature can be kept within 3 or 4°C of the sample platen with 1400 W/m² (approximately one solar constant) incident on the solar cell. This is about what one would expect based on the published values of the thermal conductivity of silicon.

TEMPERATURE CONTROL SYSTEM

The thermal system is used to control the temperature of the cryoshroud and the sample platen. Several critical design constraints had to be met. These were:

1. Rapid shroud temperature response over a range of -170°C to 150°C.

2. A shroud gradient of less than $\pm 5^{\circ}\text{C}$ over this temperature range under a distributed load of 1400 W/m^2 .
3. Accurate shroud temperature control over the desired temperature range.
4. Rapid specimen temperature response.
5. Accurate specimen temperature control ($\pm 2^{\circ}\text{C}$) while being subjected to varying incident solar radiation intensities.

In addition both the shroud and the sample platen had to have an accumulated leak rate that was less than $1 \times 10^{-9}\text{ ml/s}$ referred to standard pressure and temperature over the operational temperature range.

The thermal conditioner for the shroud consists of a pumped gaseous nitrogen loop, a series of heaters, and a gaseous nitrogen to liquid nitrogen shell and tube heat exchanger. The entire system is housed in an equipment cabinet 76 cm wide, 137 cm long and 183 cm high. A block diagram of the system is shown in Figure 5.

A three stage centrifugal blower is used to circulate approximately 104 l/s (220 CFM) of nitrogen gas through the system. Modulating butterfly valves proportion the gas flow through the heat exchanger. This variation in flow combined with a variation in power input to the heater produces a very precise means of effecting temperature control. There is also a large potential heat source or heat sink reserve. The response time and temperature overshoot of the system can be minimized by biasing the system source and sink against each other.

Rapid transients require that system mass be minimized. This is especially critical in the heater design since this element runs at the highest temperatures of any system component. The system heater shells are fabricated from thin wall stainless steel tubing 7.6 cm in diameter. Each heater module contains a 1.6 KW quartz infra red lamp and a set of thin aluminum fins. The fins are radiatively heated by the infra red lamp and are convectively cooled by the gaseous nitrogen stream. The weight of the heater extended surface is approximately 450 g.

The system heat sink is a liquid nitrogen boiler. Gaseous nitrogen is pumped through the tube side of the shell and a tube heat exchanger. The shell side of the unit is flooded with liquid nitrogen. The liquid level is maintained by the use of a temperature probe, controller, and a solenoid valve to permit filling from an external reservoir. Boil-off from the liquid nitrogen is mixed with the exit gas flow stream to further lower the circulating gas stream temperature. A pressure relief valve is located in the main gas stream to prevent excessive pressure buildup either from the introduction of boil off gas or from gas expansion during loop temperature up-transients. The relief valve maintains the gaseous nitrogen loop pressure at 21 KN/m^2 (3 psig).

The shroud thermal system tests showed that the system met the design goals. The transient performance of the system is shown in Figure 6.

To meet the temperature control requirements of the sample platen stated previously requires the use of a secondary cooling medium to eliminate the temperature rise that would otherwise result from the incident radiation.

It was desired to have a work surface temperature change capability of -170°C to 150°C . Conventional mechanical refrigeration temperature control techniques were examined and discarded as being too massive and slow in response.

The sample platen is shown in Figure 4. The surface that the samples are mounted on is made of 1.3 cm thick copper plate to obtain uniform temperature distribution. Heat removal from the platen is accomplished by conduction to a liquid nitrogen boiler and heat sink. Heat addition is provided by the use of four (4) 300 W infrared quartz lamps. The conduction path between the liquid nitrogen boiler and the platen is a square box section fabricated from stainless steel. The dimensions of this section are carefully selected and controlled. The infra red lamps are mounted inside copper "U" sections which are welded to the conduction path box section. The resultant thermal network provides the rapid response and ability to absorb varying amounts of incident flux without changing the surface temperature outside the design limits. Platen temperature control is provided by sensing the surface temperature, comparing it to a setpoint temperature, and varying the power input to the infrared lamps to effect a balance. A schematic representation of the system conduction paths and their electrical analogues is shown in Figure 7. The results of the system transient tests are shown in Figure 8.

RADIATION SOURCE AND BEAM OPTICS

The radiation source initially employed was a horizontally mounted 4 MeV Dynamitron² that was located in a shielded room adjacent to the environmental chamber. The Dynamitron, a d.c. charged particle accelerator, whose equivalent circuit is shown in Figure 9, is basically a set of cascaded vacuum tube rectifiers capacitively coupled to an r.f. power supply operating at 130 KHz. Two large r.f. electrodes, located along with the vacuum tubes and the ion source in a large pressure vessel filled with 1800 Kg of sulphur hexafluoride as an insulating gas (552 KN/m^2) (80 psi), induce an r.f. potential in a set of

²Radiation Dynamics, Westbury, N.Y.

corona rings causing a d.c. flow through the rectifiers and establishing a large potential at the output in the high voltage terminal. The capacitance from the r.f. electrodes to the pressure vessel and the previously mentioned inductive load result in resonant circuit operation.

An electron gun or duoplasmatron type ion source with an einzel lens, located in the high voltage terminal, provides an electron beam. The duoplasmatron and einzel lens is also used for the production of ion beams.

The beam is accelerated thru an evacuated accelerator tube across which the full d.c. terminal voltage appears. The mult-section glass and electrode acceleration tube assembly with an external resistance bleeder network provides a voltage gradient across the tube and establishes beam focussing by the tube electrodes. Typical base vacuum in the accelerator tube and its drift tube extensions is between 5×10^{-8} and 5×10^{-7} torr. Operational pressure is on the order of 10^{-6} torr. After acceleration from the terminal potential to ground the beam leaves the grounded pressure vessel and is transported to the target through evacuated stainless steel drift tubes with the aid of electrostatic and electromagnetic lenses and deflection elements as well as beam defining apertures.

The beam, after entering the beam transport system, is passed through a horizontal 46 cm circular pole face switching magnet. The magnet has a focussing effect in the horizontal plane but its primary function is to deflect the beam through a selected angle for transport to the target area in the adjacent room. In positive ion operation the magnet acts as a momentum analyzer insuring the purity of ion species and mono-ergic properties of beams reaching the target.

After deflection of the beam into a drift tube aligned with the center line of the environmental chamber, beam focussing and/or defocussing is accomplished with electromagnetic lenses. The beam focussing properties in the horizontal plane of the switching and analyzing magnet are also utilized.

Electrostatic fields are used to provide slight beam deflections for alignment of the beam within the drift tube. All of these beam optic elements are designed to introduce a minimum of beam aberration or energy spread.

A large cross-section electron beam can be produced at the target plane by placing a scattering foil in the path of a well focussed beam. This technique has limitations, particularly for the evaluations described here, but has been used. An air core solenoid lens is also used with the electron beam to produce a beam convergence that will allow entry into the environmental chamber with subsequent cross-over and divergence.

The solenoid lens is not a practical method of handling proton or ion beams. These beams are focussed and defocussed with

electro-magnetic quadropole lenses. It should be noted that the accelerator without supplemental focussing elements provides a low emittance beam with 90% of its charged particles located within a 1 cm diameter circle. A quadropole magnet is used to supplement the focussing of the beam by the analyzing magnet. Pairs of quadropoles or quadropole doublets are used to introduce the required beam convergence for entry into the chamber. Quadropole lenses produce convergence in one plane and divergence in a 90° displaced plane. Doublet lenses with poles displaced 90° will thus permit control of circular beams and the introduction of convergence or divergence as desired.

SOLAR SIMULATOR³

The solar simulator (Fig. 10) uses a high pressure, compact arc, Xenon lamp as the energy source. It can be operated as high as 4.2 KW for high intensity simulation. The short term intensity is regulated by a feedback amplifier that uses the output of a solar cell in its feedback loop and controls the firing angle of a silicon controlled rectifier power supply. The long term intensity is maintained by a calibrated solar cell mounted at the same distance from the simulator as the cells being studied but outside the chamber. The solar beam is diverted by an external mirror and the lamp intensity is periodically adjusted to maintain the calibrated short circuit current. The external standard is maintained at a temperature close to ambient by a separate control system. A Lenticular lens system is used to achieve a uniform irradiance at the sample plane that is better than 2% uniform over a 23 cm by 23 cm area.

DATA ACQUISITION

It is desired to measure the current-voltage characteristics of the solar cells in their active region after each dose of radiation. Various experiments have been designed to study the effects of temperature and solar intensity during irradiation to simulate certain extra-terrestrial missions. The data system has been designed to record the data in digital form so that computer processing can be utilized. To achieve this the circuit shown in block form in Figure 11 is used in conjunction with a data acquisition system. The cell characteristic is traversed by driving current from a separate supply and measuring the voltage across the cell and the current by measuring

³Spectrolab Inc., Sylmer, Calif.

the voltage drop across a precision resistor. The current is driven in stepwise fashion by an I.C. operational amplifier used as a staircase generator triggered by the data acquisition system; an I.C. voltage comparator; an I.C. integrator; an I.C. gated feedback amplifier and a power transistor. The feedback amplifier is used to modify the voltage step of the staircase generator as a function of the change in the cell current so that the data points on the I-V curve are uniformly spaced. The gating of the feedback amplifier is required to suppress the transient caused by the cell being switched by the cross-bar scanner in the data acquisition system.

In the data acquisition system each cell is assigned to a data channel. A tape controlled programmer selects the channel, the range, the integration period and the measurement mode. The current and voltage are measured simultaneously on separate digital voltmeters and are recorded on punch paper tape sequentially. The number of data points collected for each cell can be varied to suit the particular experiment. While the data acquisition system provides precision of better than $\pm 0.5\%$ the actual precision is limited at present to $\pm 2\%$ due to short term fluctuations on the intensity of the simulator believed to be due to the wandering of the arc. Because of long lines necessary to connect the data acquisition system and the samples in the chamber a Kelvin connection is used to eliminate the problem of the voltage drop in the 1800 cm of wire.

A typical data run would sample and record the Faraday cup currents, the thermocouple voltages, the system pressure and the time during the particulate irradiation and the cell I-V characteristics and temperature after each irradiation. Thus from the data tape it is possible to computer generate plots of I_{sc} , V_{oc} , and P_{max} vs. fluence for each cell with cell temperature and light intensity as parameters.

CONCLUSION

The Space Radiation Environment Simulator can be used to create in the laboratory a wide range of conditions that could be encountered on space missions and that could degrade solar cells, solar cell cover glasses and solar cell cover glass adhesives. Properties of these devices and materials can be studied as a function of particle fluence, simulated solar intensity and temperature over a wide range. Raw data output in digital form can be used with a computer to provide any significant type of analysis as required.

ACKNOWLEDGEMENT

The authors would like to express their gratitude to a number of people who gave valuable inputs at various points in the design of this chamber. We owe special thanks to W. Gdula and M. Moore formerly of this center, W. Wappaus, GSFC, A. Lauer of Varian and H. Slack of Howard Slack Assoc.

TABLE 1

Pump	Max. Pumping Speed	Pressure Range
Noble-Vac-Ion . Titanium Filament Evaporator..	4×10^2 l/s @ 4×10^{-6} Torr	below 10^{-3} Torr
Titanium Bulk Sublimator..	1×10^4 l/s @ 1×10^{-7} Torr*	below 10^{-3} Torr
	7×10^4 l/s @ 1×10^{-5} Torr*	below 5×10^{-5} Torr

*Area/Conductance limited at lower pressures.

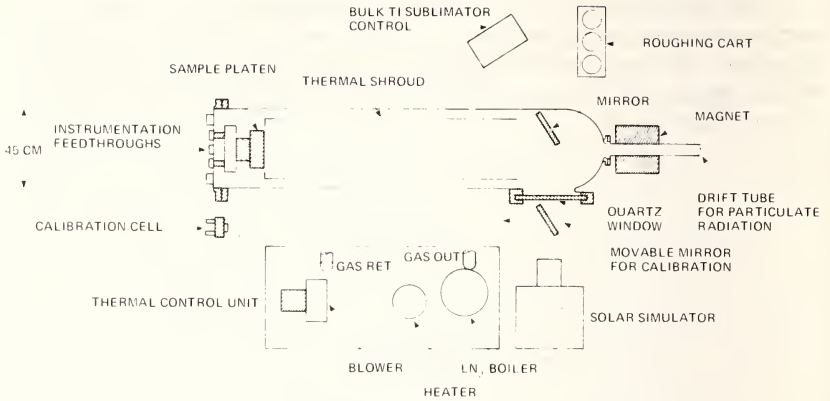


Fig. 1—Space radiation environment simulator — plan view.

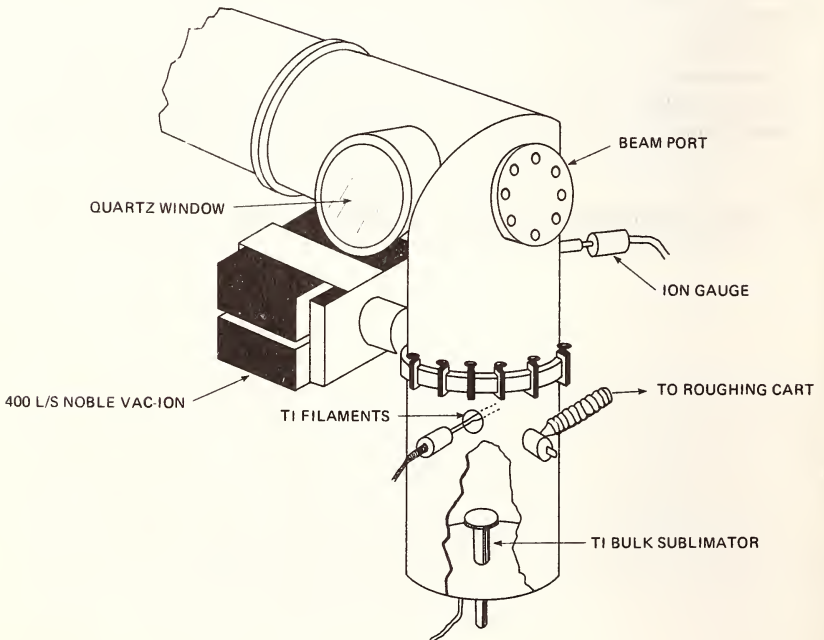


Fig. 2—Space radiation environment simulator — vacuum pumping components.

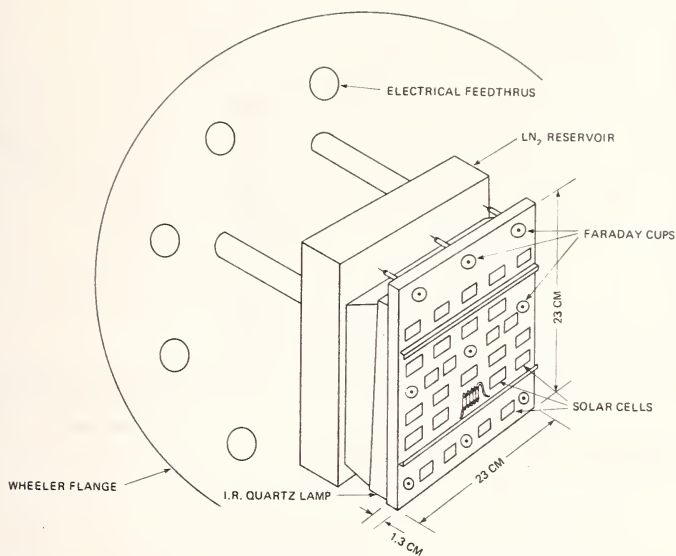


Fig. 3—Space radiation environment simulator — sample platen.

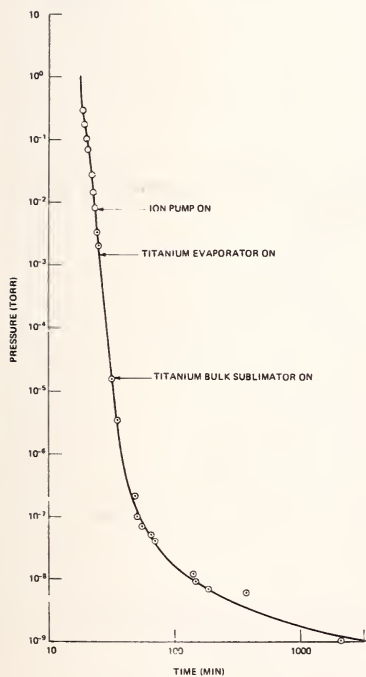


Fig. 4—Typical pump-down cycle.

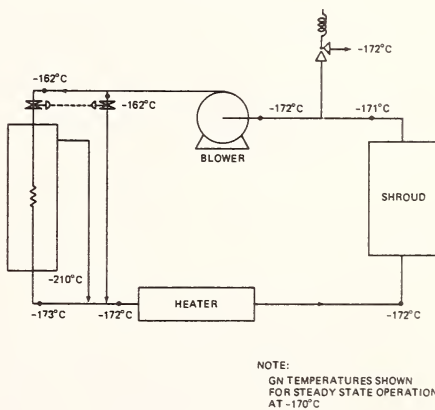


Fig. 5—Thermal control system for shroud — gas mode.

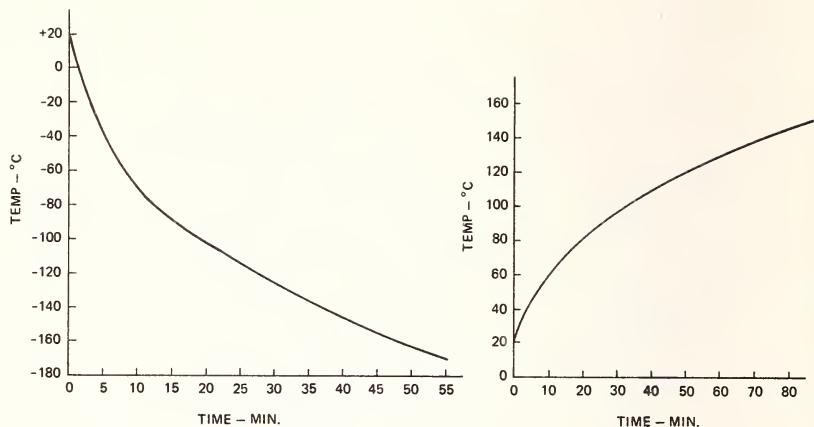


Fig. 6—Shroud transient performance.

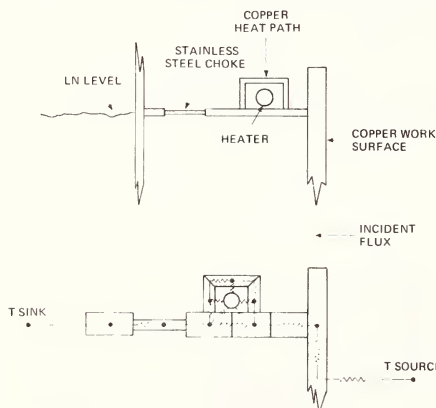


Fig. 7—Thermal mock-up of platen.

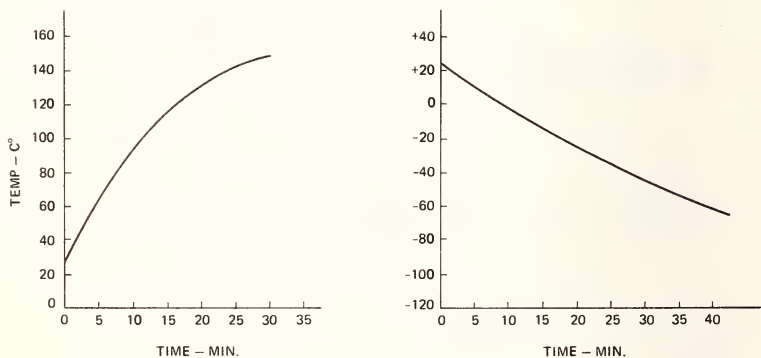


Fig. 8—Platen transient performance.

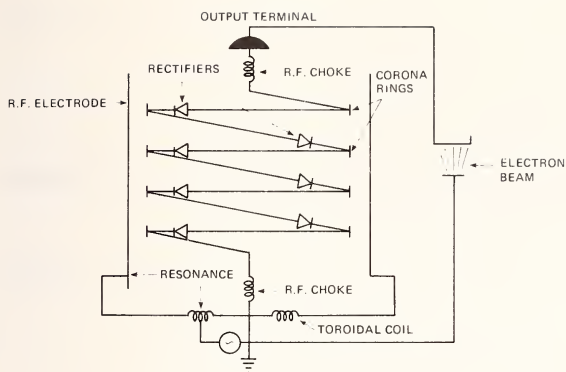


Fig. 9—Dynamitron equivalent circuit.

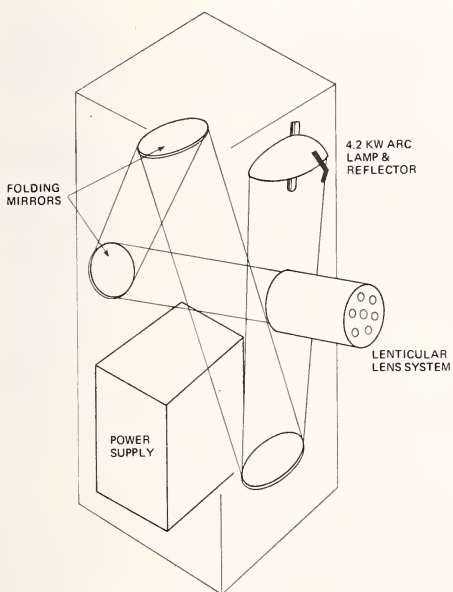


Fig. 10—Solar simulator.

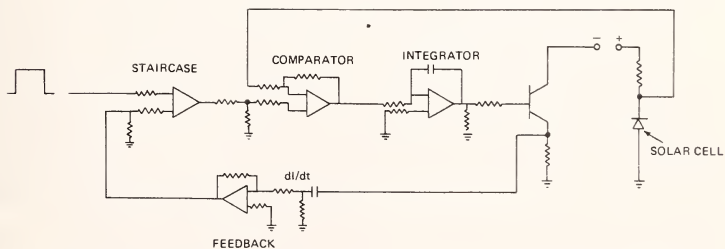


Fig. 11—Circuit for producing solar-cell I-V characteristics.

PROPERTIES OF OPTICAL MATERIALS IN SPACE

Fred W. Paul¹

REFERENCE: Paul, Fred W., "Properties of Optical Materials in Space," ASTM/IES/AIAA Space Simulation Conference, 14-16 September 1970.

ABSTRACT: A program has been established to provide a central clearinghouse for information about the effects of space environment on the optical and other physical properties of optical materials. Information is being collected and organized on the effects of space environment on refractive index, dispersion, transmittance, reflectance, thermal expansion coefficient, Young's modulus, birefringence, and yield and breaking points of all materials of interest for the transmission or reflection of optical radiation in space.

In technical areas where information about the behavior of materials does not exist a program of laboratory investigations will provide the required information. In preparation for some in-house studies of materials at very low temperatures and also during exposure to a charged particle flux an experiment has been devised and instrumented to provide measurement of dimensional changes and refractive index changes at several wavelengths. The essence of the method is the use of Fabry-Perot interferometry to measure independently the dimensions of the sample of material and the optical path length through the material.

¹Test and Evaluation Division, Goddard Space Flight Center, Greenbelt, Md. 20771

KEY WORDS: optical materials, physical property changes, space environment, information center, interferometric measurements

Introduction

The behavior of optical materials and components and systems in space is of primary interest to the designers and users of space borne optical devices. Questions often arise, at all phases of a program, i.e., design, manufacture and use, as to what effect the environment will have on a particular element. During the years of space studies a substantial body of knowledge about this subject has been developed. It has often been difficult to locate the required information to answer a question about what behavior can be expected. The program which is being described in this paper is an effort to collate and codify this knowledge to make it more readily available to those who need it.

The environment of space is not a single definable thing. Depending on where in space one intends to operate there may be a variety of atomic ions, or a concentration of electrons, or trapped radiation belts, or solar wind and a variety of electromagnetic radiation, and low or high temperature. There are also environmental components which are carried with the spacecraft, for example condensible vapors or a nuclear power plant. It may or may not be desirable to include the environments of manufacturing, test, prelaunch and launch in this discussion. The material properties that are to be included are transmittance, absorptance, emissivity, reflectance, scattering, refractive index, dispersion, birefringence, thermal expansion coefficient. Also Young's modulus, hardness, yield point and breaking point for all materials of interest for the transmission and reflection of radiation in space. If it is decided that photovoltaic devices and various detectors should be included, then the electric properties of these devices and materials must also be included. The complexity of this

subject, which is illustrated by the above remarks, is one of the reasons that answers to questions about the behavior of materials in space are difficult to find. Another factor is that the determination of what material will serve for a specific mission is often a routine engineering task which is forgotten as soon as it is accomplished. However, there are some notable exceptions to this, e.g., the vigorous and effective program on spacecraft coatings by the Thermophysics Specialist Group of AIAA and ASTM has established a solid and well publicized basis for choice of materials and methods of evaluating new materials.

Information Center

A program has been established at GSFC to collect and interpret and interrelate information about optical materials suitable for use in space borne systems. The optical properties like transmittance and refractive index and the other physical properties like moduli and expansion coefficients will be recorded and the effect on these properties of exposure to the various factors of the use environment will be determined. In instances where available publications such as periodic literature, meeting reports, and conference proceedings do not provide adequate information studies will be established to fill the gaps. This program is expected to produce extensive and adequately cross referenced bibliographies. In addition it is planned that several summaries or position papers will be issued which will provide comparative information on candidate materials for specific applications. It is intended that the bulk of the literature research, extraction and compiling of pertinent information and the studies to provide new information will be done under contract, probably with research institutes or academic departments. In this period of shrinking budgets this program has not competed successfully for funds with some of the more glamorous items like manned flight and orbiting observatories. Nonetheless a small start has been made as an in-house task and some interesting items about

materials behavior in space or in simulated space environment have been noted.

There is a very extensive and well-known literature about radiation effects on optical materials (for example, Reference 1) which has evolved from nuclear studies and from solid state physics. It is usually time-consuming to extract from this large volume of literature information pertinent to a particular space application problem. Bibliographies of materials directly related to space applications (Reference 2) are very helpful and more of them are needed. There are also some very useful general articles (References 3, 4) which elucidate the problem areas and the practically possible solutions. In addition there are a number of studies of more restricted scope which confine their attention to a certain class of materials or a single environmental factor, (References 5,6,7,8) or similar restriction. Information in this form is the easiest to use, provided that the circumstances involved in the engineering application fall within the scope of the study. There are also two handbooks (References 9, 10) which provide guidance for the use of optical materials in space.

It would not be appropriate at this time when but a small fraction of the available and desirable information has been collected, to draw conclusions or to summarize. However there are one or two items which might be mentioned briefly. One is that reflecting surfaces appear to endure the space environment very well. Canfield, Hass and Waylonis (Reference 11) showed that aluminum mirrors overcoated with magnesium fluoride will stand years of space exposure without loss of reflectance. Pittman, et al (Reference 7) and Gunter, et al (Reference 12) have observed that diffraction gratings, both original rulings and replicas, show only very small adverse effects of exposure to a simulated space environment. The chief hazard to reflecting surfaces seems to be contamination by deposits of condensible materials. Gunter also found that some mirror substrate materials are better than others in resisting change of optical figure at high doses of electrons. Among fused quartz, pyrex, borosilicate crown glass, synthetic fused silica, and Cervit, the

synthetic fused silica retained its shape best and also showed least discoloration due to the irradiation. Another item of interest is the study of changes of refractive index of optical glass due to gamma rays (Reference 13) and electrons (Reference 14). Malitson, et al observed substantial changes in refractive index, as much as a few parts in the fourth decimal place due to irradiations. The refractive index showed continuing instability for long periods after the irradiation. Unfortunately this study was left incomplete due to lack of funds. A third item that might be mentioned is the conclusion reached by Heath and Sacher (Reference 6) that magnesium fluoride, barium fluoride and synthetic sapphire will provide the most stable high transmittance for ultraviolet wavelengths. These are but a few of the interesting bits of information about the behavior of optical materials in space. They serve to illustrate that many useful and sometimes unexpected results have appeared in the literature. Perhaps the above few paragraphs may serve to introduce the literature search and organization of information which is planned. I would like now to describe a modest in-house laboratory program which is being undertaken to provide information in an area which seems not to be well covered elsewhere.

An Experiment

Malitson, Dodge and Gonschery have reported^{13, 14)} on the effects of penetrating radiation on the refractive index of some optical glasses. Gunter, et al¹²⁾, have observed changes in optical figure of diffraction gratings and their substrate material due to doses of 1 MEV electrons. It seems that it would be interesting and useful to know at what rate these changes occur during exposure to the radiation environment and whether the changes in refractive index and figure exhibit any rapid increases or decreases when the radiation field is removed. In order to provide the required information a system has been built which permits continuous measurement of refractive index and physical dimensions and optical figure during exposure of materials to

penetrating radiation. The essence of the method is use of interferometry to measure index of refraction and dimensions during exposure. This is done without mechanical contact of the measuring system with the sample to be measured.

The method being used is illustrated in Figure 1. Plates A and B are arranged as a Fabry-Perot interferometer. The sample is inserted part-way between the F-P plates and is held parallel to them. By patch-work coating of the sample four different interference patterns are obtained. The first pattern, formed by the rays indexed (1), is used to determine the interferometer spacing, d , by conventional Fabry-Perot procedures¹⁵). Rays (2) are used to determine the optical path length between the interferometer plates when the rays pass through the sample. This length is $d + (n - 1)t$ where n is the refractive index and t is the thickness of the sample. Rays (3) and (4) are used to determine respectively the distance between the upper interferometer plate and the top surface of the sample, and between the lower interferometer plate and the bottom of the sample. The difference between the distances found from rays (3) and (4) and (1), when appropriate corrections are made for phase changes on reflection and for thickness of the coatings, gives the thickness of the sample, t .

To consider the required measurements in a little more detail the following equations may be written:

$$P_1\lambda = 2d + 2\delta_1 \quad (1)$$

$$P_2\lambda = 2[d + (n - 1)t] + 2\delta_1 \quad (2)$$

$$P_3\lambda = 2L_1 + \delta_1 + (\delta_3 + \epsilon_3) \quad (3)$$

$$P_4\lambda = 2L_2 + \delta_1 + (\delta_4 + \epsilon_4) \quad (4)$$

Where P_1, P_2, P_3, P_4 are the experimentally found orders of interference for the four sets of rays. λ is wavelength. d is the F-P interferometer spacing. δ_1 is the phase change on reflection at

the F-P plates, assumed to be the same for both plates. n is refractive index and t is the thickness of the sample. L_1 and L_2 are the distances between the Fabry-Perot plates and the nearest surface of the sample. δ_3 and ϵ_3 are the phase change on reflection and the thickness of the patch coating in the upper side of the sample and δ_4 and ϵ_4 are the corresponding quantities on the lower side.

If equation (1) is subtracted from (2) one has

$$P_2\lambda - P_1\lambda = 2(n - 1)t \quad (5)$$

The phase change drops out and the left hand side contains only measurable quantities. If we subtract the sum of (3) and (4) from (1) we have

$$P_1\lambda - (P_3\lambda + P_4\lambda) = 2d - 2(L_1 + L_2) - (\delta_3 + \epsilon_3 + \delta_4 + \epsilon_4) \quad (6)$$

Since

$$d - (L_1 + L_2) = t, \text{ we have}$$

$$P_1\lambda - (P_3\lambda + P_4\lambda) = 2t - (\delta_3 + \epsilon_3 + \delta_4 + \epsilon_4) \quad (7)$$

Once more the left side contains measurable quantities. However, to evaluate the δ 's and ϵ 's on the right side a separate experiment is required. For this fringes of equal chromatic order will be used as described by Bennett¹⁶⁾. In this method the coated area for which δ and ϵ are to be determined will be partially overcoated with an opaque layer of aluminum. The equal chromatic order fringes which are formed by interference between reflected light from the double coated surface and a uniformly coated flat comparison surface can be analyzed to determine values for both δ and ϵ of the coated area for which these quantities are to be measured. Inserting all the measured values in equation (7) yields a value for t . Putting this value of t in equation (5) yields a value of n . This process is repeated for as many wavelengths as necessary.

The principal application envisioned for this

method of measurement is in situ measurement in intense penetrating radiation fields. For several reasons, however, the first application will be measurements at reduced temperatures. For one thing, a new method always required "shaking down" and the available radiation facilities are so heavily loaded with work that to take up facility time for shake-down operations is undesirable. Another factor is that information about the performance of some ultraviolet transmitting materials at low temperatures has not been published and such information has been requested for planning purposes on some space missions. Also the measurement of refractive index and thermal expansion coefficient of some twenty optical glasses by Molby¹⁷⁾ and the thermal expansion of some infrared transmitting materials by Browder, et al¹⁸⁾ provide a convenient means of comparing results obtained with the new method with those obtained by older methods.

For the low temperature work a liquid helium cryostat is used which is provided with both electrical heaters and pumping tubes so that temperature can be stabilized at points both below and above the boiling point of helium at atmospheric pressure. The sample is attached to the liquid helium chamber by a massive OFHC copper block to which the sample is attached with indium solder to provide good thermal contact. The Fabry-Perot etalon, which consists of fused silica plates separated by an invar spacer ring, is held in position by thin stainless steel strips with adjusting screws so that the etalon plates can be maintained parallel to the surfaces of the sample which is positioned between the two plates, as shown in Figure 1. The cryostat has two fused silica windows through which observations of the fringe pattern are made.

The cryostat is evacuated by a turbomolecular pump with a large liquid nitrogen cooled trap between pump and cryostat followed by two room temperature right angle bends and finally a right angle bend at the liquid nitrogen shield wall of the cryostat. Pumpout and backfill operations are carefully managed to reduce the likelihood of contamination of the cryostat. Monitor mirrors are frequently inserted in place of the interferometer and are

measured for contamination effects by the method recommended by Hass and Hunter¹⁹). No contamination has been detected in three months of operation.

The interferometer is illuminated by an argon ion laser, which provides five strong lines in the range 476 nm to 514 nm. On occasion when longer wavelength information is desired a helium-neon laser radiating at λ 633 nm is substituted. The fringe patterns are photographed either with a view camera or with a Hilger constant deviation spectrometer with camera attachment. To avoid confusion among the several interference patterns that exist due to the various rays shown in Figure 1, an aperture is used which limits the area of the interferometer which is recorded by the camera to dimensions of the order of 1 mm x 3 mm for any particular photograph. The chosen area is moved sequentially to obtain pictures of the fringe pattern formed by rays (1), then rays (2), etc., as shown in Figure 1. A set of four pictures, which can be taken in an elapsed time of 5 to 10 minutes, gives the necessary information for determining the refractive index at several wavelengths and the mechanical thickness of the sample for a specific temperature. The temperature of the specimen is measured with a thermocouple embedded in the specimen but outside the portion used for optical measurements. A series of measurements with several thermocouples simultaneously has shown that the temperature measured at the thermocouple is not significantly different from that where the optical measurements are made.

The apparatus which has been described has been completely assembled. Preliminary experiments have been run on temperature sensing, on determination of phase changes on reflection, on contamination and on photography of the Fabry-Perot fringes. The first complete experiments to determine refractive index and linear thermal expansion coefficient at temperatures between room temperature and liquid temperature will be done this month. Further work will include additional materials in a temperature range of interest to space missions followed by a transfer to a radiation facility.

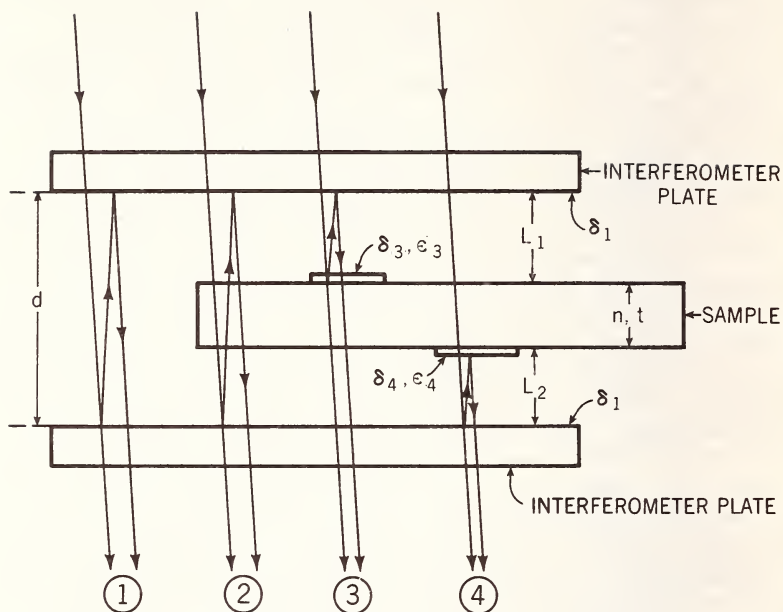


Figure 1. Schematic of Fabry-Perot Interferometer with Sample of Material to be Measured Inserted

References

- (1) "Radiation Effects on Glass - An Annotated Bibliography," Sept. 1965, Radiation Effects Information Center, Battelle Memorial Institute.
- (2) Avery, L., "A Bibliography on the Effects of Short Wave and Particle Radiation on Glasses," Astrogeophysical Memo #164, July 1964, High Altitude Observatory, Boulder, Colo.
- (3) Becker, R. A., Applied Optics, Vol. 6, p. 955, (1967).
- (4) Barnes, W. P. Jr., Applied Optics, Vol. 5, p. 701 (1966).
- (5) Neu, J. T., Philbin, E. J., Mahadwan, P., Compton, J., "Evaluation of the Effects of Space Environment Exposures on Index of

Refraction and Extinction Coefficients of Apollo Window Materials," NASA CR 1019, April 1968.

- (6) Heath, D. F. and Sacher, P. A., Applied Optics, Vol. 5, p. 937 (1966).
- (7) Pittman, M. A., Ofelt, G. S., Becher, J., Kernell, R. L., Applied Optics, Vol. 8, p. 209 (1969).
- (8) Lusk, T. E., Electronic Design, 26 Oct. 1960.
- (9) Cooley, J. L., Janda, R., Handbook of Space Radiation Effects on Solar Cells, NASA SP 3003 (1963).
- (10) Rittenhouse, J. B., Singletary, J. B., "Space Materials Handbook," 3rd ed., (especially chapter 8) NASA SP 3051 (1969).
- (11) Canfield, L. R., Hass, G., Waylonis, J. E., Applied Optics, Vol. 5, p. 45 (1966).
- (12) Gunter, R. C. Jr., Kennedy, E. F., Kaseta, F. W., Jour. Opt. Soc. Am., Vol. 57, p. 1430 (1967).
- (13) Malitson, I. H., Dodge, M. J. and Gonshery, M. E., Jour. Opt. Soc. Am., Vol. 55, p. 1583 (1965).
- (14) Dodge, M. J., Malitson, I. H., Gonshery, M. E., Jour. Opt. Soc. Am., Vol. 56, p. 1432 (1966).
- (15) Meissner, K. W., Jour. Opt. Soc. Am., Vol. 31, p. 405 (1941).
- (16) Bennett, J. M., Jour. Opt. Soc. Am., Vol. 54, p. 612 (1964).
- (17) Molby, F. A., Jour. Opt. Soc. Am., Vol. 39, p. 600 (1949).
- (18) Browder, J. S. and Ballard, S. W., Applied Optics, Vol. 8, p. 793 (1969).
- (19) Hass, G., and Hunter, W. R., "Laboratory Experiments to Study Surface Contamination and Degradation of Optical Coatings and Materials in Simulated Space Environments," presented at the Optical Contamination in Space Symposium, Aspen, Colo., Aug. 13-15, 1969 and submitted for publication in Applied Optics.

AUTHOR INDEX

Baurer, T. [5] External Spacecraft Contamination Modeling and Countermeasures	72
Beachler, J.C. [55] Operating Characteristics of the Air Force Flight Dynamics Laboratory Reentry Nose Tip (RENT) Facility	593
Bean, B.L. [24] Ultraviolet and Charged Particle Degradation of Aluminum and Silver Coated FEP Teflon Second Surface Mirrors	345
Blado, L.D. [9] In Situ Vacuum Gage Calibration by the Reference Transfer Method	141
Bortner, M.H. [5] External Spacecraft Contamination Modeling and Countermeasures	79
Bullis, W.M. [31] Measurement Methods for Micro-circuits	449
Buna, T. [48] Operation of a Large Thermal Vacuum Chamber at Martian Pressure Levels	725
Cappel, K.L. [40] The Dynamic Environment Simulator, A Multienvironmental Man-Rated Centrifuge . . .	587
Carden, W.H. [39] Explosive Oxidations Initiated by Simulated Meteoroid Penetration into Spacecraft Atmosphere	569
Chamberlin, P.G. [15] Method for Rock Property Determination in Ultrahigh Vacuum	209
Chuan, R.L. [6] Particulate Contaminant Measurement by Quartz Crystal Microbalance	105
Cooper, A.M. [5] External Spacecraft Contamination Modeling and Countermeasures	79
Corbin, W.E.Jr. [7] Space Measurements of the Contamination of Surfaces by OGO-6 Outgassing and their Cleaning by Sputtering and Desorption	113

Cridlin, M.S. [44] A Method to Obtain an Ultraclean Environment	661
Cunningham, F.G. [24] Ultraviolet and Charged Particle Degradation of Aluminum and Silver Coated FEP Teflon Second Surface Mirrors	345
Davidson, J.R. [57] Micrometeroroid Impact Simulation System	915
Donohoe, M.J. [26] The Degradation of Alzak by Short Wavelength Ultraviolet Radiation	383
Donovan, F.M. [56] Investigation of the Characteristics of Fluids Vented into a Vacuum	905
Dubinin, E.M. [20] Laboratory Experiment on Solar Wind Interaction with Geomagnetic Field	297
Eck, M.G. [45] A Programmable Dynamic Thermal Vacuum System for Solar Array Component Testing	669
[58] A Space Radiation Environment Simulator for the Evaluation of Solar Cells	935
Enlow, D.L. [4] Contamination Studies in a Space Simulated Environment	51
Evlanov, E.N. [13] Apparatus for Laboratory Simulation of Ionospheric Flow Over On-Board Instruments of an AES . .	189
Fairbanks, J.W. [45] A Programmable Dynamic Thermal Vacuum System for Solar Array Component Testing	669
Fayet, Ph., [23] Some Problems Concerning the Simulation of Plastic Films Degradation by Ionizing Radiations	323
Ferguson, M. J. [41] Use of the Ben Franklin Submersible As A Space Station Simulator	599
Flanagan, T.M. [36] Charged Particle Track Implications for Accelerated Testing	525
Fleming, R.M. [14] Thermal Conductivity Measurements of a Candidate Viking Heat-Shield Material After Sterilization, and During Exposure to Vacuum, and to a Simulated Martian Atmosphere	197
Foley, T.P. [37] A Simulation to Validate Future Space Missions	535

Foreman, K.M. [47] Simulation of Surface- Atmosphere Interaction Processes for Mars	699
Goldsmith, J.C. [2] Molecular Contamination in Environmental Testing at Goddard Space Flight Center	1
Golub, R.A. [57] Micrometeroroid Impact Simulation System	915
Greenwood, L.R. [14] Thermal Conductivity Measurements of a Candidate Viking Heat-Shield Material After Steri- lization, and During Exposure to Vacuum, and to a Simulated Martian Atmosphere	197
Harvey, W.L. [33] Establishment of an Optimum Duration for Spacecraft Component Thermal Vacuum Tests	473
Hearst, P.J. [21] Effect of Photodegradation on Organic Coatings	299
Henninger, J.H. [26] The Degradation of Alzak by Short Wavelength Ultraviolet Radiation	383
Hillberg, L.H. [52] Prediction of Mechanical Erosion of Charring Ablators	837
Hirschfield, J.J. [58] A Space Radiation Environ- ment Simulator for the Evaluation of Solar Cells	935
Humphrey, R.L. [51] Ablation Phenomena in Supersonic Laminar and Turbulent Flows	813
[53] Heating in Cracks on Ablative Heat Shields	853
Karafiath, L. L. [16] Friction Between Solids and Simulated Lunar Soils in Ultrahigh Vacuum and Its Significance for the Design of Lunar Roving Vehicles	225
King, H.J. [19] Solar Wind Simulator	279
Koenig, J.A. [51] Ablation Phenomena in Supersonic Laminar and Turbulent Flows	813
[53] Heating in Cracks on Ablative Heat Shields	853
Kostkowski, H.J. [12] Radiometry Standards - Present and Future	185
Leonas, V.B. [13] Apparatus for Laboratory Simulation of Ionospheric Flow Over On-Board Instruments of an AES	189

Lilienkamp, R.H. [9] In Situ Vacuum Gage Calibration by the Reference Transfer Method	141
[10] Methods of Determining Residual Gas Composition from Residual Gas Analyzer Data	151
MacInnis, J.B. [43] Advanced Diving Techniques Applicable to Extended Mission Neutral Buoyancy Space Simulation	651
Madden, M.T. [51] Ablation Phenomena in Supersonic Laminar and Turbulent Flows	813
[53] Heating in Cracks on Ablative Heat Shields	853
Mains, R.M. [35] Some Effects of Equalization on Acceleration Response and Fatigue Life Expectancy	509
Managadze, G. G. [20] Laboratory Experiment on Solar Wind Interaction with Geomagnetic Field	297
Maples, D. [56] Investigation of the Characteristics of Fluids Vented Into a Vacuum	905
May, C. B. [41] Use of the Ben Franklin Submersible as a Space Station Simulator	599
McCally, M. [40] The Dynamic Environment Simulator, A Multienvironmental Man-Rated Centrifuge	587
McClung, R.W. [29] Monitoring Service Testing by Nondestructive Testing	405
McClure, C.M. III [42] Development of an Open Circuit Cryogenic Life Support System for Use in Neutral Buoyancy Space Simulation	623
[43] Advanced Diving Techniques Applicable to Extended Mission Neutral Buoyancy Space Simulation	651
McIntosh, R. [26] The Degradation of Alzak by Short Wavelength Ultraviolet Radiation	383
McKeown, D. [7] Space Measurements of the Contamination of Surfaces by OGO-6 Outgassing and their Cleaning by Sputtering and Desorption	113
Metz, A.W. [37] A Simulation To Validate Future Space Missions	535
Nakagawa, Hiroshi [46] The Cryopumping System for the Space Simulation Chamber	683
Nelson, E.R. [2] Molecular Contamination in Environmental Testing at Goddard Space Flight Center	1

Newman, P.A., Jr. [8] Simulation of Radiation from R.T.G. Power Sources	129
[58] A Space Radiation Environment Simulator for the Evaluation of Solar Cells	985
O'Connor, J.W. [44] A Method to Obtain an Ultraclean Environment	661
Paillous, A. [17] Real Time Simulation of Atmospheric Balloon Environment	245
[23] Some Problems Concerning the Simulation of Plastic Films Degradation by Ionizing Radiations	323
Paul, F.W. [59] Properties of Optical Materials In Space	949
Parameswaran, V.R. [34] Equipment to Study High Velocity Dislocations in Matter	487
Park, S.G. [24] Ultraviolet and Charged Particle Degradation of Aluminum and Silver Coated FEP Teflon Second Surface Mirrors	345
Pikus, I.M. [5] External Spacecraft Contamination Modeling and Countermeasures	79
Podgorny, I.M. [20] Laboratory Experiment on Solar Wind Interaction With Geomagnetic Field	297
Podnieks, E.R. [15] Method for Rock Property Determination in Ultrahigh Vacuum	209
Rabinowicz, E. [32] Life Testing Using Continuous Acceleration	457
Ratliff, J. [48] Operation of a Large Thermal Vacuum Chamber at Martian Pressure Levels	725
Reetz, A.Jr. [1] Introduction to Contamination Session (Not Available)	
Richter, R.L. [54] Apparent Operating Limits of Arc Heaters with Respect to Total Enthalpy and Stagnation Pressure	879
Riggs, W.E. [49] A Cryopump for Steady-State Testing of Rocket Engines under Altitude Conditions	749
Ritter, A.L. [3] Contaminant Measurement In Space Environment Simulation Chambers	25

Rogers, D.B. [40] The Dynamic Environment Simulator, A Multienvironmental Man-Rated Centrifuge	587
Roizès, A. [22] Relation Between Dose Rate Effects and Laboratory Simulation of Space Radiation Damage	313
Roussel, H. [17] Real Time Simulation of Atmospheric Balloon Environment	245
Roux, J.A. [11] Spectral Absolute Reflectance Measurements of CO ₂ Frosts in the 0.5 to 12.0 Micron Region	165
Schutt, J.B. [25] The Interaction of Low Energy Electrons with Polymeric Perfluorinated Ethylene-Propylene (FEP)	359
Schuttler, R. [22] Relation Between Dose Rate Effects and Laboratory Simulation of Space Radiation Damage	313
Seiber, B.A. [11] Spectral Absolute Reflectance Measurements of CO ₂ Frosts in the 0.5 to 12.0 Micron Region	165
Shane, R.S. [28] Plans and Status of NMAB ad hoc Committee on Testing for Prediction of Material Performance in Structures and Components	403
Shiralkar, B. [32] Life Testing Using Continuous Acceleration	457
Smith, A.M. [11] Spectral Absolute Reflectance Measurements of CO ₂ Frosts in the 0.5 to 12.0 Micron Region	165
Smith, K.A. [30] Signature Analysis - Non-Intrusive Techniques for Incipient Failure Identification Application to Bearings and Gears	407
Steddum, R.E. [56] Investigation of the Characteristics of Fluids Vented Into A Vacuum	905
Sullivan, E.M. [50] Ablative Heatshields for Planetary Entries - A Technology Review	751
Triplett, M.J. [49] A Cryopump for Steady-State Testing of Rocket Engines Under Altitude Conditions	749

Tsunoda, R. [46] The Cryopumping System for the Space Simulation Chamber	683
Umansky, S.V. [13] Apparatus for Laboratory Simulation of Ionospheric Flow Over On-Board Instruments of an AES	189
Van Lint, V.A.J. [36] Charged Particle Track Implications for Accelerated Testing	525
Walberg, G.D. [50] Ablative Heatshields for Planetary Entries - A Technology Review	751
Wannemacher, H.E. [58] A Space Radiation Environment Simulator for the Evaluation of Solar Cells	935
Wappaus, W.A. [27] The Photo-Response at an Alkaline Paint Interface with Aluminum	393
Weertman, J. [34] Equipment to Study High Velocity Dislocations in Matter	487
Weichbrodt, B. [30] Signature Analysis - Non-Intrusive Techniques for Incipient Failure Identification Application to Bearings and Gears	407
Williams, C.W. [42] Development of an Open Circuit Cryogenic Life Support System For Use in Neutral Buoyancy Space Simulation.	623
Winkler, E.M. [51] Ablation Phenomena in Supersonic Laminar and Turbulent Flows	813
[53] Heating in Cracks on Ablative Heat Shields	853
Wolff, C.M. [3] Contaminant Measurement in Space Environment Simulation Chambers	25
Wood, B.E. [11] Spectral Absolute Reflectance Measurements of CO ₂ Frosts in the 0.5 to 12.0 Micron Region	165
Yonda, A.W. [37] A Simulation to Validate Future Space Missions	535
Zuccaro, D. [18] Analysis of the Simulation of the Solar Wind	261
Zupan, Frank [38] General Purpose Centralized Automatic Testing for Improvement of Shipboard System Performance	549

Latest developments in the subject area of this publication, as well as in other areas where the National Bureau of Standards is active, are reported in the NBS Technical News Bulletin. See following page.

HOW TO KEEP ABREAST OF NBS ACTIVITIES

Your purchase of this publication indicates an interest in the research, development, technology, or service activities of the National Bureau of Standards.

The best source of current awareness in your specific area, as well as in other NBS programs of possible interest, is the **TECHNICAL NEWS BULLETIN**, a monthly magazine designed for engineers, chemists, physicists, research and product development managers, librarians, and company executives.

If you do not now receive the **TECHNICAL NEWS BULLETIN** and would like to subscribe, and/or to review some recent issues, please fill out and return the form below.

Mail to: Office of Technical Information and Publications
National Bureau of Standards
Washington, D. C. 20234

Name _____

Affiliation _____

Address _____

City _____ State _____ Zip _____

☐ Please send complimentary past issues of the Technical News Bulletin.

☐ Please enter my 1-yr subscription. Enclosed is my check or money order for \$3.00 (additional \$1.00 for foreign mailing).

Check is made payable to: SUPERINTENDENT OF DOCUMENTS.

SP 336

(cut here)

